

Details of illustrations in  
this document may be better  
studied on microfilm.

REPRODUCED 1971



Approved for public release; distribution unlimited.

ARMY RESEARCH HUMAN LABORATORY  
A RESEARCH AND DEVELOPMENT  
ACTIVITY SYSTEM COMMAND  
WRIGHT-PATTERSON AIR FORCE BASE OHIO 45433

Reproduced by  
NATIONAL TECHNICAL  
INFORMATION SERVICE  
SPR 010 d VA 72151

The ~~and~~ <sup>experiments</sup> reported herein were conducted according to the Guide for Laboratory Animal Facilities and Care, ~~also prepared~~ <sup>prepared</sup> by the Committee on the Guide for Laboratory Animal Resources, National Academy of Sciences - National Research Council.

The voluntary informed consent of the subjects used in this research was obtained as required by A: F: 1964 Regulation 80-33.

CLASSIFICATION	
COSTI	WHITE SECTION
DOO	BOIF SECTION
UNAL	GER
JUSTIFICATION	
BY	
DISTRIBUTION/AVAILABILITY CODE	
SIST.	AVAIL. 230/01/02/03



AD739501

Security Classification		DOCUMENT CONTROL DATA - R & D	
(Security classification of title, body of abstract and indexing annotation must be entered when the overall report is classified)			
1. ORIGINATING ACTIVITY (Corporate author)		2a. REPORT SECURITY CLASSIFICATION	
Aerospace Medical Research Laboratory Aerospace Medical Div, Air Force Systems Command Wright-Patterson Air Force Base, Ohio 45433		Unclassified	
2. REPORT TITLE		2b. GROUP	
SYMPOSIUM ON BIODYNAMIC MODELS AND THEIR APPLICATIONS.		N/A	
3. DESCRIPTIVE NOTES (Type of report and inclusive dates)			
4. AUTHOR(S) (First name, middle initial, last name)			
5. REPORT DATE		7a. TOTAL NO. OF PAGES	7b. NO. OF REFS
December 1971		980	
8a. CONTRACT OR GRANT NO.		9a. ORIGINATOR'S REPORT NUMBER(S)	
b. PROJECT NO 7231		AMRL-TR-71-29	
c.		9b. OTHER REPORT NO(S) (Any other numbers that may be assigned this report)	
d.			
10. DISTRIBUTION STATEMENT			
Approved for public release; distribution unlimited			
11. SUPPLEMENTARY NOTES		12. SPONSORING MILITARY ACTIVITY	
Details of illustration in this document may be better studied on microfilm		Aerospace Medical Research Laboratory Aerospace Medical Div, Air Force Systems Command, Wright-Patterson AFB, OH 45433	
13. ABSTRACT			
<p>The Symposium on Biodynamics Models and Their Applications took place in Dayton, Ohio, on 26-28 October 1970 under the sponsorship of the National Academy of Sciences - National Research Council, Committee on Hearing, Bioacoustics, and Biomechanics; the National Aeronautics and Space Administration; and the Aerospace Medical Research Laboratory, Aerospace Medical Division, United States Air Force. Most technical areas discussed included application of biodynamic models for the establishment of environmental exposure limits, models for interpretation of animal, dummy, and operational experiments, mechanical characterization of living tissue and isolated organs, models to describe man's response to impact, blast, and acoustic energy, and performance in biodynamic environments.</p>			

AD  
REC  
APR 4 1972  
AIR FORCE

DD FORM 1 NOV 65 1473

Security Classification

Reproduced From  
Best Available Copy

14.	KEY WORDS	LINK A		LINK B		LINK C	
		ROLE	WT	ROLE	WT	ROLE	WT
	Biomechanics Biodynamics Biodynamic Model Biomechanic Model Human Body Response to Mechanical Stress Tissue Properties Modeling Mechanical Body Response Modeling Mechanical Tissue Properties Mechanical Properties of Bone Modeling Mechanical Response of Bone Bone Strength Tissue Strength Human Impact Tolerance Spinal Impact Tolerance Human Tolerance to Escape System Forces Model of the Human Spine Effect of Blast on Man Mechanical Response of Thorax-Abdomen Model of Man's Response to Air Blast Vertebral Injury Human Crash Tolerance Kinematic Model of Man Dynamic Model of Man Effects of Shock and Vibration on Man						

## FOREWORD

The Symposium On Biodynamic Models And Their Applications 1970, held in Dayton, Ohio, on 26, 27, and 28 October 1970, was jointly sponsored by the National Academy of Sciences - National Research Council, Committee on Hearing, Acoustics, and Biomechanics; the National Aeronautics and Space Administration; and the Aerospace Medical Research Laboratory (AMRL) of the United States Air Force. Dr. Henning E. von Gierke served as Symposium Chairman. Mr. Leon E. Kazarian served as Chairman of the Technical Committee. Committee members consisted of Dr. Hans L. Oestreicher, Mr. Ints Kaleps, and Mr. John Carmichael, all from Aerospace Medical Research Laboratory. Mr. Carmichael also served as Program Coordinator. The Symposium was organized and administered by the Aerospace Medical Research Laboratory under Project 7231, Biomechanics of Aerospace Operations. Administrative and Logistics support to the Symposium was provided by the University of Dayton Research Institute (UDRI) under Contract F33615-71-C-1207 with Mr. Joseph Miltello acting as Administrative Coordinator for the Symposium. Mr. Douglas Patton, also of UDRI, deserves special thanks for his assistance in the preparation of the proceedings of the conference. Thanks are also extended to Mrs. Louise Bolton of Technical Information, Support Services Division, AMRL, for her technical editing services on the Symposium papers.

Acknowledgement is made, on behalf of the sponsoring organizations, to the speakers for their response and contributions to this report on biodynamic models. We wish to thank all of the above listed organizations and individuals for their efforts on behalf of the Symposium On Biodynamic Models And Their Applications 1970.

## TABLE OF CONTENTS

	Page
Introduction	1
Welcome Col C. L. Holt	9
Opening Remarks W. L. Jones	11
Keynote Address Lt Col N. P. Clarke	15
<b>SESSION I - APPLICATION OF BIODYNAMIC MODELS FOR THE ESTABLISHMENT OF ENVIRONMENTAL EXPOSURE LIMITS</b>	<b>25</b>
Chairman - H. von Beckh Co-chairman - Lt Col G. C. Mohr	
1. A Model to Simulate Thoracic Responses to Air Blast and to Impact R. Fletcher	27
2. Dynamic Simulation Techniques for the Design of Escape Systems: Current Applications and Future Air Force Requirements J. W. Brinkley and J. Shaffer	71
3. Some Current Biomechanical Research in the United Kingdom, as Related to the Effects of Impact and Vibration on Man J. Sandover	105
4. Use of a Mathematical Model for the Evaluation of Head Injury Criteria J. Benedict	123

	Page
5. Mechanical and Physiological Response of the Human Cervical Vertebral Column to Severe Impacts Applied to the Torso W. Lange	141
SESSION II - MODELS FOR THE INTERPRETATION OF ANIMAL, DUMMY, AND OPERATIONAL EXPERIMENTS	169
Chairman - A. Hirsh Co-Chairman - T. Moore	
6. Biodynamic Modeling and Scaling: Anthropomorphic Dummies, Animals, and Man M. Kornhauser	171
7. Multidegree, Nonlinear Mathematical Models of the Human Body and Restraint Systems: Applications in the Engineering Design of Protective Systems R. R. McHenry	193
8. A Five-Degree-of-Freedom Mathematical Model of the Body I. Kaleps and H. E. von Gierke	211
9. Some Aspects of Biodynamic Modeling for Aircraft Escape Systems P. R. Payne	233
10. Two Biodynamic Models Used to Determine Optimum Energy Absorber Characteristics R. W. Carr	337
11. Bone Atrophy by Inactivity J. H. Eichler	359
SESSION III - MECHANICAL CHARACTERIZATION OF LIVING TISSUE AND ISOLATED ORGANS	381
Chairman - H. L. Cestreicher Co-chairman - L. Kazarian	

	Page
12. The Mechanical Characteristics of Skin and Other Soft Tissue and their Modeling R. Kenedi	383
13. On Some Geometric Properties of Human Ribs - I S. B. Roberts and P. H. Chen	403
14. The Interaction of the Components of the Human Back G. A. Olsen	429
15. The Ultimate Strength and Failure Mechanism of the Anthropoid Knee Joint J. O. Outwater, C. H. Jacobs, and R. W. Castle	459
16. The Effects of Hypogravic and Hypodynamic Environments on the Skeletal System and Acceleration Tolerance L. E. Kazarian and H. E. von Gierke	475
17. Testing Dynamic Material Properties of Brain Arteries C. H. Daly, J. D. Chalupnik, and J. D. Danberg	501
18. A Theoretical Analysis of the Mechanical Characteristics of the Patella and Quadriceps Mechanisms E. H. Miller, D. Miller, and R. Kroll	515
19. Biomechanics in Motor Skeletal Structures C. Hirsch	533
20. The Implication of a Cerebellar Model for the Mammalian Response to Movement T. W. Calvert and F. Meno	541
21. The Effect of Initial Curvature on the Dynamic Response of the Spine to Axial Acceleration T. F. Li, S. H. Advani, and Y-C. Lee	553



	Page
SESSION IV - MODELS TO DESCRIBE MAN'S RESPONSE TO IMPACT, BLAST, AND ACOUSTIC ENERGY	571
Chairman - V. L. Roberts Co-chairman - I. Kaleps	
22. Modeling the Circulatory System under Biodynamic Loads J. T. Apter	573
23. An Analysis of the Pressure Wave Generated in Seated Spinal Impact P. J. Torvik	595
24. The Transverse Response of the Lumbar Spine Under Longitudinal Loads H. E. Krause and M. Shirazi	621
25. Nonlinear Lumped Parameter Mathematical Model of the Dynamic Response of the Human Body G. R. Hopkins	649
26. Control of the Human Forearm During Abrupt Acceleration P. A. Stewart, J. Duffy, J. Soechting, H. Litchman, and P. R. Paslay	671
27. An Approach to Head Impact Analysis G. Moskowitz, J. Rose, and S. Gordon	693
28. The Biomechanics of Spinal and Head Impact: Problems of Mathematical Simulation Y. K. Liu	701
29. The Effect of Vibration on Blood Flow and Pressure in the Major Arteries of Dogs R. G. Edwards, C. F. Knapp, E. P. McCutcheon, K. O. Lange, and W. O. Griffin	737

	Page
SESSION V - PERFORMANCE IN BIODYNAMIC ENVIRONMENTS	767
Chairman - L. Young	
Co-chairman - Lt Col C. J. Hodgson	
30. Interfacing Man-Machine Performance in Dynamic Environments H. R. Jex	769
31. Human Operator Performance in Hypoxic Stress C. Replogle, L. Kulak, R. Gold, F. Holden, and G. Porter, Jr.	791
32. The Use of Models in the Study of Wound Ballistics A. A. Woodward	807
33. Analysis of Gait Using a Minimum Energy Approach R. E. Beckett and K. C. Pan	823
34. Response of the Spine in Biodynamic Environments M. Shirazi	843
35. A Dynamic Model of the Spine Using a Porous Elastic Material E. F. Rybicki and A. T. Hopper	851
36. A Mathematical Model to Determine the Brain Damage When the Human Head is Subjected to Impulsive Loads A. Engin and V. Roberts	877
37. A Mechanical Impedance Model for Head Injury Due to Linear Impact R. Stalnaker, J. McElhaney, and V. Roberts	905
38. The Biological Responses of the Spinal Canal and Its Contents to Surgical Trauma of the Axial Skeleton J. H. Moore	933
Closing Remarks: The Future Col J. P. Stapp	975

# SYMPOSIUM SPEAKERS and SESSION CHAIRMEN

Julia T. Apter  
Presbyterian-St. Luke's Hospital  
Mathematical Biology  
1753 N. Congress Parkway  
Chicago, Illinois 60612

James V. Benedict  
Technology Incorporated  
Life Sciences Division  
8531 N. New Braunfels Ave.  
San Antonio, Texas 78217

James W. Brinkley  
AMRL  
Impact Branch  
Wright-Patterson Air Force Base  
Ohio 45433

Thomas W. Calvert  
Carnegie-Mellon University  
Biotechnology Program  
500 Forbes Avenue  
Pittsburgh, Pennsylvania 15213

Richard W. Carr  
Beta Industries, Inc.  
2763 Culver Avenue  
Dayton, Ohio 45429

Neville P. Clarke  
Aerospace Medical Division  
Directorate of Res. and Dev.  
Brooks Air Force Base  
Texas 78235

Colin H. Daly  
Dept. of Mechanical Engineering  
University of Washington  
Seattle, Washington 98105

Richard G. Edwards  
Wenner-Gren Aero Research Lab.  
University of Kentucky  
Lexington, Kentucky 40506

Joachim H. Eichler  
Orthopaedische Universitaetsklinik  
Freiligrathstrasse 2  
63 Giessen/Germany

Ali E. Engin  
University of Michigan  
Biosciences, HSRI  
Baxter Road and Huron Parkway  
Ann Arbor, Michigan 48105

Royce Fletcher  
Lovelace Foundation for Medical  
Education and Research  
5200 Gibson Blvd., S. E.  
Albuquerque, New Mexico 87108

Steve Gordon  
Naval Air Development Center  
A. C. E. D.  
Warminster, Pennsylvania 18974

Arthur E. Hirsch  
National Highway Safety Bureau  
Vehicle Structures Division  
7th and D Street, S. W.  
Washington, D. C. 20591

Carl Hirsch  
Department of Orthopaedics  
Karolinska Institute  
Stockholm, Sweden

Corrin J. Hodgson  
6570th AMRL  
Vibration Branch  
Wright-Patterson Air Force Base  
Ohio 45433

Col. C. L. Holt  
Commander  
AMRL  
Wright-Patterson Air Force Base  
Ohio 45433

Gordon R. Hopkins  
West Virginia University  
Theoretical & Applied Mechanics  
Engineering Science Bldg.  
Morgantown, West Virginia 26506

Henry R. Jex  
Systems Technology, Inc.  
13766 South Hawthorne Blvd.  
Hawthorne, California 90250

Walton L. Jones  
NAS Chairman CHABA  
2150 Constitution Avenue  
Washington, D.C. 20037

Ints Kaleps  
6570th AMRL  
Wright-Patterson Air Force Base  
Ohio 45433

Leon E. Kazarian  
6570th AMRL  
Wright-Patterson Air Force Base  
Ohio 45433

R. M. Kenedi  
Strathclyde University  
James Weir Building  
(BioEng. Dept.)  
Montrose Street  
Glasgow, C.1. Scotland

Horst E. Krause  
University of Dayton  
Research Institute  
Dayton, Ohio 45409

W. Lange  
Max-Planck-Institut  
Department of Biomechanics  
201 Rheinlanddamm  
4600 Dortmund, West Germany

Teng-Fang Li  
West Virginia University  
Dept. of Theor. & Applied Mechanics  
Engineering Sciences Building  
Morgantown, West Virginia 26506

Y. Kirg Liu  
Tulane University School of Medicine  
Biomechanics Laboratory  
1430 Tulane Avenue  
New Orleans, Louisiana 70112

Edward H. Miller  
Orthopaedics University of Cincinnati  
Cincinnati General Hospital C-4  
Cincinnati, Ohio 45229

George C. Mohr  
6570th AMRL  
Environmental Med. Div.  
Wright-Patterson Air Force Base  
Ohio 45433

Thomas J. Moore  
AMRL  
Neurophysiology Branch  
Wright-Patterson Air Force Base  
Ohio 45433

Raymond R. McHenry  
Cornell Aeronautical Lab., Inc.  
Transportation Research Dept.  
4455 Genesee Street  
Buffalo, New York 14221

Hans L. Oestreicher  
6570th AMRL/BBM  
Wright-Patterson Air Force Base  
Ohio 45433

Gerner A. Olsen  
City College of New York  
Civil Engineering  
140th Street and Convent Avenue  
New York, New York 10031

John O. Outwater  
University of Vermont  
Burlington, Vermont 05401

Peter R. Payne  
Wyle Labs., Payne Division  
12221 Parklawn Drive  
Rockville, Maryland 20852

Sanford B. Roberts  
University of California  
School of Engineering  
405 Hilgard Avenue  
Los Angeles, California 90024

Verne L. Roberts  
University of Michigan  
HSRI  
Ann Arbor, Michigan 48105

Edmund F. Rybicki  
Battelle Memorial Institute  
Advanced Solid Mechanics Division  
505 King Avenue  
Columbus, Ohio 43201

Jack Sandover  
University of Technology  
Dept. of Ergonomics and Cybernetics  
Loughborough, Leicestershire  
England

Mehdi Shirazi  
University of Dayton  
Research Institute  
Dayton, Ohio 45409

Richard L. Stalnaker  
University of Michigan  
HSRI, Biosciences  
Huron Street and Baxter Road  
Ann Arbor, Michigan 48105

John P. Stapp  
Scientific Advisor  
National Highway Safety Bureau  
Department of Transportation  
5208 Nassif Building  
Washington, D.C. 20591

Peter J. Torvik  
AFIT  
Department of Mechanics  
Wright-Patterson Air Force Base  
Ohio 45433

Harold J. von Beckh  
Aerospace Medical Research Dept.  
Naval Air Development Center  
Johnsville  
Warminster, Pennsylvania 18974

Henning E. von Gierke  
AMRL  
Wright-Patterson Air Force Base  
Ohio 45433

Arthur A. Woodward  
U. S. Army Aberdeen R & D Center  
Ballistics Research Laboratory  
Aberdeen Proving Ground  
Maryland 21005

Laurence R. Young  
M. I. T. Center of Space Research  
Man-Vehicle Laboratory  
M. I. T. Building 37-207  
Cambridge, Massachusetts 02139

J. J. Zwislocki  
Laboratory of Sensory Communications  
Syracuse University  
821 University Avenue  
Syracuse, New York 13210

## INTRODUCTION

Henning E. von Gierke

The Symposium on Biodynamic Models and Their Applications took place in Dayton, Ohio on 26-28 October 1970 under the sponsorship of the Aerospace Medical Research Laboratory, USAF, the National Academy of Sciences - National Research Council Committee on Hearing, Bioacoustics and Biomechanics (CHABA), and the National Aeronautics and Space Administration. It was the purpose of the meeting to bring together those scientists, engineers, physicians and operations experts who have worked on biodynamic models over the past decade or have used the models to the benefit of their work. Many of the participants have worked on these problems as individuals or groups, representing one discipline or a broad multidisciplinary spectrum, but were seldom aware of the general, broad developments in these areas and how their individual efforts fit into the wide spectrum of biodynamic models. Some of them might still wonder where exactly their place is and what the relationship of their particular model to similar models is - and this shows that the effort was timely and worthwhile, that it helped to take stock of and crystalize a rapidly developing and not yet too well defined field. It was realized that biodynamic models and their applications are only small areas of the overall general biodynamics field. The decision to concentrate on this restricted topic grew out of the observation that it was a relatively new and active area, pursued by several laboratories and supported by various Government Agencies. And since the goals for the modeling efforts and their support varied widely, communication between these groups is limited and closer contact between workers appeared profitable.

The emphasis on biodynamic models should not give the impression that the final goal of the symposium was removed from and neglected the biomedical



and practical problems of the real world, the problems of tolerance limits for biodynamic environments, of injuries, of clinical treatment and hardware protection. On the contrary, the opposite was the case, the group of scientists assembled was probably most united by the common conviction that major future progress in applied biodynamics will come from a refined quantitative mathematical description of the biomechanical and biological processes, or in other words, from an understanding of function and behavior of biomechanical systems through realistic models.

In soliciting, selecting and discussing the papers presented no attempt was made to define the field of biodynamics, to delineate the various types and definitions of models, nor to judge the extent and value of their applications. The operational definition of the symposium title was accepted and most of the topics proposed and covered by the participants were accepted and are included in these conference proceedings. The technical program committee exercised its prerogative only with respect to the time allotted to the various topics and not by deleting some at the expense of others. The material was roughly organized under 5 session topics with some invited and review papers in each session. The session topics, with their dedicated chairmen were as follows:

1. Application of Biodynamic Models for the Establishment of Environmental Exposure Limits (H. von Beck, M.D., Lt Col G. C. Mohr, USAF (MC)).
2. Models for the Interpretation of Animal, Dummy and Operational Experiments (A. Hirsch, Dr. T. Moore).
3. Mechanical Characterization of Living Tissue and Isolated Organs (Dr. H. L. Oestreicher, Dr. J. Apter).
4. Models to Describe Man's Response to Impact, Blast and Acoustic Energy (Dr. V. L. Roberts, I. Kaleps).

5. Models to Describe Performance in Biodynamic Environments (Dr. L. Young, Lt Col C. H. Hodgson, USAF (MC)).

I would like to thank all contributors for their active participation and the submission of their complete manuscripts. I would particularly like to thank the invited speakers for their critical reviews and enlightening outlooks into the future. All are well-known experts in their fields and many came from foreign countries and overseas to participate in the symposium. In addition to all the speakers, session chairmen, participants, and discussants, I would like to thank Colonel C. L. Holt, Commander of our Aerospace Medical Research Laboratory, for his Welcoming Address and general support of the symposium, Dr. W. L. Jones representing NASA as well as CHABA for his Opening Remarks and Lt Col N. P. Clarke, USAF (VC), who with his unique training in Veterinary Medicine as well as human physiology and biophysics and his laboratory as well as Headquarters management experience gave us the keynote address: "Biodynamic Models: A View from the Customer."

A description of the symposium would not be complete without mentioning with great gratitude our banquet speaker, Dr. J. Zwislocki, Directory Laboratory of Sensory Communications, Syracuse University, New York, who reviewed for us probably the most complete and refined biodynamic studies of a biological system ever conducted and described by models.<sup>1</sup> He showed that these complex models which were derived in ideal cooperation with biodynamic, biological and psychological observations can serve as models for biodynamic research and modeling in general. He talked on "The Mechanism of the Ear: How to take it apart and put it together." The brilliance of his presentation exposed many of the attendees to a stimulating research area they had not been aware of before.

A special note of thanks is given to Colonel J. P. Stapp, USAF (Ret.) MD, PhD, now with the National Highway Safety Bureau, for his closing remarks: "The Future," which reviewed the achievements of our symposium with appropriate critical analysis and inspiring encouragement for our future struggle in this field. Having started his pioneering work in biomechanics in our laboratory here at Wright-Patterson AFB, it was particularly nice to have him with us and share with him the contributions of the theoretical disciplines to the too easily discouraging complexity of biomedical observations.

In my evaluation, the symposium papers give a good indication of where we stand scientifically with respect to biodynamic models and where we stand in terms of practical applications; i.e., what we have to offer to the operational users. Scientifically, in my opinion, the problem of the immediate future is not so much a theoretical-mathematical one to build more sophisticated models. I think it is rather the need to obtain better and more refined measurements of the body's passive and active dynamic properties. These measurements must be made in close interaction with a model hypothesis and the application of the model. Some papers, particularly the ones dealing with spinal models, clearly demonstrated the critical need for better and more complete experimental data; the models are ahead of the experimental knowledge and no spinal model, no matter how sophisticated or appealing, will give us the capability to treat other than longitudinal deformations of the spine and predict injury probability for other than longitudinal loads, unless we start to collect the basic dynamic and strength data on which to base or through which to verify our model. Work in this direction has hardly started. The second remark with respect to the scientific status of biodynamic models has to do with the final integration of the various models into one unified mechanical model of the whole body. I don't think I am asking for an impossible dream. A

sophisticated mathematical modeling technology for the analysis of extremely complex structures is available in the aerospace field and similar methodology could be applied to the mechanical body system: the overall body system should be broken down into subsystems to whatever level is necessary to obtain adequate dynamic representation or to arrive at a simplified system satisfying the specific question at hand. However, further breakdown and/or simplification should not only clearly state what is neglected or included mathematically but also what anatomical or physiological dysfunction or pathological processes can or cannot be expected to be described by the subsystem model. It is in this area, where some of our modeling efforts are still weak and the task of integrating all subsystems together again to obtain one overall system appears at present still hopeless. But here too, the problem is probably less a mathematical one than one of having the right data on which to base more sophisticated subsystem models, and on how the subsystems interact. And this leads me to the third remark on the scientific status and future of modeling that the most important scientific contribution of modeling should be in guiding more economical and meaningful collection of biological data. It emphasizes what was felt all through the symposium: biodynamic modeling must be pursued as a strong, inseparable part of clinical and experimental biodynamic research and only true interdisciplinary cooperation can fully exploit its potential.

The second point I want to summarize relates to the important question: What practical applications for biodynamic models do we have to offer today? Although several important engineering and biomedical engineering applications were discussed, I think an integration and assessment of the broad spectrum of potential applications would lead us to the conclusions that we have more to offer than is being used. We heard in several papers of the need for dynamic

hardware dummies for aircraft, escape systems, tractor and automobile vibration and impact testing. There is no reason why such anthropodynamic dummies replacing present anthropomorphic dummies cannot be designed, fabricated and commercially available. In explaining crash injuries, establishing and defining human tolerance specifications and in designing and testing protection systems use of mathematical models is still in its infancies. Some of the models as they exist today and their application to the scaling of animal data have a lot to offer to respiratory physiology, stress physiology and physiology in general. The passive biodynamic models must become an important subsystem in the human operator performance models used to assess manual control capability and other performance parameters under mechanical stress. "Active" responses of the body to the mechanical environments have already been modeled in isolated cases, but should now be combined with the most complete and sophisticated passive models available. And finally the same models have to offer valuable information to clinical medicine, orthopaedic surgery and cardiopulmonary problems. A combination of one of the whole body models to describe major responses to vibration or sustained acceleration with the well developed models for the circulatory system is only one of the intriguing possibilities which comes to mind to extend the application of present model technology in support of environmental physiology (circulation under hypo- and hypergravic conditions as well as under vibration and impact) as well as in support of clinical problems (cardiovascular assist by vibrations or alternating pressure applications).

In conclusion, the intensive discussions covering the broad spectrum of biodynamic models and their applications by 165 dedicated scientists from here and abroad did not necessarily lead to the cliché conclusions that more centers of biomechanics research and more students of this field are needed.

It rather was convincing evidence that the time is gone when biomechanics was an interesting and rewarding part-time occupation of experts in mechanical engineering or an equally rewarding hobby for mathematically inclined physicians. What is needed is an interdisciplinary expertise of stable teams and a few well equipped centers which concentrate on these problems and go about their solution in a logical, step-by-step program. I hope that the conference and this publication of its proceedings contributed towards this goal scientifically as well as organizationally by bringing the large team, devoted to this area closer together. To all participants and particularly to those untiring organizers of this meeting, my sincere thanks.

HENNING E. VON GIERKE  
Chairman, Symposium on Biodynamic  
Models and Their Applications  
February 1971



## REFERENCES

1. Zwislocki, Josef, "Analysis of Some Auditory Characteristics," Chapter 15, Vol III of "Handbook of Mathematical Psychology," R. D. Luce, R. R. Bush and E. Galanter (editors), John Wiley and Sons, Inc., New York, 1965.

## WELCOME

Clinton L. Holt, Colonel, USAF, MC

Commander  
Aerospace Medical Research Laboratory  
Wright-Patterson Air Force Base, Ohio

This Symposium on Biodynamic Models and Their Applications is jointly sponsored by National Aeronautics and Space Administration, National Research Council-National Academy of Sciences, Committee on Hearing, Bioacoustics and Biomechanics (CHABA), and the Aerospace Medical Research Laboratory, United States Air Force.

This international meeting of distinguished scientists and engineers is being held at the cradle of manned aeronautical flight. Wright Field is a place where advancement in aerospace sciences and technical achievement in aeronautics is an accepted principle and way of life for thousands of highly specialized people, as well as a host of multidisciplinary teams. The charisma of aeronautical science has accelerated from a mere spark on the fields of the Huffman Prairie in 1904 with canvas and bent wood to the mightiest concentration of aeronautical development in the world today, exemplified by the C-5A, F-111A, F-15, and the new B-1A.

A vital part of this expanding aeronautical technology is man in the system. Putting man in an advanced aircraft system requires a fundamental description of his anatomical and physiological capabilities and limitations. That description needs to be related to optimizing man's role in the total weapon system design. Achieving that objective in today's and tomorrow's aircraft development requires the evolution and application of highly specialized and definitized mathematical models which adequately describe appropriate biological parameters. This symposium is concentrating on technology which is fundamental, exciting and extremely relevant to the future of

manned aeronautical system design and development. The broad spectrum of the program indicates a truly multidisciplinary approach to the problem. The extremely diverse geographical locations of the scientists and their laboratories shows that a continuing means must be established for implementing and maintaining the vital personal communications which is so necessary on a frequent basis. The technological cycle in aeronautical development is too rapid for the use of conventional communications processes. I hope this symposium will help fill that need.

## OPENING REMARKS

W. L. Jones

Chairman, Executive Council, CHABA  
Director, Biotechnology and Human Research Division  
National Aeronautics and Space Administration  
Washington, D. C.

Good morning ladies and gentlemen. I would like at this time as Chairman of CHABA to welcome you to this conference on "Biodynamic Models and Their Applications." For those of you who might not be familiar with this organization, CHABA refers to the Committee on Hearing, Bioacoustics and Biomechanics of the National Academy of Sciences - National Research Council. This Committee, by its charter, is established to resolve issues of concern in areas its name suggests. It is advisory to the U. S. Government in general and specifically to its sponsors, the Army, Navy, Air Force, NASA, FAA, NIH, and Public Health. Over the past 25 years the attention of this Committee has been primarily focused on problems in hearing and bioacoustics. In particular the Committee has been concerned with measurement and evaluation of hearing; conservation of hearing; study of the ear and associative central nervous system function; protection against intense sound; speech communication in the presence of noise; nonauditory effects of intense sound fields; physiological, psychological and social effects of man exposed to sounds, such as, for example, noise produced by airplanes, rockets, gunfire, weapons and vehicles; and finally, the physical and engineering problems of the generation, measurement and control of acoustical energy.

In the past few years a part of the attention of the Committee has turned toward the area of biomechanics. In fact, the recent entry of the Committee into the domain of biomechanics has been the result of the farsightedness of such of its members as Dr. von Gierke and Dr. Goldman, who saw the problems to be met and, at the same time, recognized the possibility that the Committee on Hearing, Bioacoustics and Biomechanics could become the vehicle for the consideration of

many of these problems. The area of biomechanics has been delineated by the Committee to include the specification of the mechanical properties of the human body and its components; the effects of mechanical force fields, including vibration, upon human performance, health and comfort; the protection of man from mechanical force fields; and, finally, the physiological and engineering problems of the generation, measurement and control of mechanical force fields. For the past two years the Committee has maintained a small, but active working group under the guidance of Dr. Goldman which is addressing the problems of head injury from a multiplicity of viewpoints ranging from the physical engineering problems of measurement and control of head impact, through the physiological and mechanical problems of dealing with temporary and permanent brain damage, through to the problems of psychological response to the injury and, ultimately, techniques of protection therefrom as well as a consideration of the epidemiology of head injury. Nevertheless, the symposium beginning this morning represents the first large-scale meeting we have sponsored dealing exclusively with topics in the field of biomechanics.

It may well be that major advances in the biological and medical sciences in the foreseeable future will come as the result of conceptual and mathematical models now being developed. For this reason, the National Academy of Sciences is bringing the prestige of CHABA in full support of this growing technology and, through the conduct of meetings such as this, is striving to encourage even greater advances that have been made to date.

Inasmuch as we in NASA have been supporting work both in universities and industry for the development of mathematical modeling techniques, I thought I might take just a moment to discuss these procedures and to indicate why we feel they are of value to our program. To begin with, much as we in the biological sciences might like to take credit for the development of these procedures, the fact is that we probably are the

last of three major movements to make extensive use of math models. The first movement, of course, came in the physical sciences and it was here that the basic rules of modeling were developed and refined. With the tremendous increase in technology since World War II, the old rules of build, test and rebuild become hopelessly out of date. This has been particularly true in the space program. Whereas, we always will test a new system as fully as possible before committing it to operational use, this on occasion simply is not possible. In this case, it becomes necessary to rely heavily on the predictive power of the math models we have developed to describe the behavior of the system under operational conditions.

The second major movement to make significant use of math modeling has been in the development of intricately contingency plans for the control of events ranging from natural disasters to civil disorders. The stockpiling of control forces, supplies, and logistics support materials is all dictated by the results obtained through exercising the math model. The best example, of course, is the use of math models in the planning of urban transportation systems. Urban mass transportation involving freeways, subways, airports, trains, buses, and the personal automobile represents a complex system which, as we all have seen, can become hopelessly congested if not developed and controlled in accordance with a realistic, long-term plan. As has been documented time and time again, however, long-term plans can fall far short of expectations in just a few years. The best technique for developing an optimum strategy for dealing with the problems of mass transportation seems to be through use of math models. The Department of Transportation now is making considerable use of such procedures.

The third movement now making use of math modeling is, of course, taking place in the biological sciences. For those who espouse these procedures, this, I feel, will represent a most challenging subject material. The variables with which any model must deal in biology are very complex, quite interrelated, and, as a rule, not easily described by simple, or



even complex, equations. The materials of the human body are far more complex than are the materials, for example, with which one might construct the Lunar Module. Yet, even taking into account these great complexities, progress is being made in describing the functioning of various systems and components of the body through modeling techniques. A number of the papers to be presented here during the next three days attest to this.

I might also note that the use of information generated through biodynamics models here at Wright Field was of use to NASA in dealing with a very specific problem. A question arose concerning emergency landings in which the spacecraft might return to land rather than water. NASA called on Dr. Henning von Gierke whose research in biodynamics verified the landing couch design and provided assurance for a land recovery.

Recognizing the difficulties of dealing with biological materials in mathematical terms, I would like to encourage all of you to continue this type of work with the utmost vigor. As the models of body systems become more precise, we will be able to obtain answers to critical questions concerning human behavior and human problems without the need for extensive laboratory research and without having to rely so heavily on extrapolations from animal research. I feel the development and utilization of the techniques of math modeling in the biological sciences represent one of the most important advances we have made in recent years. I am pleased that CHABA is able to play some part in the support of this movement. Thank you.

## KEYNOTE ADDRESS

### BIODYNAMIC MODELS: A VIEW FROM THE CUSTOMER

Neville P. Clarke, Colonel, USAF, VC

Assistant Director of Research and Development  
Aerospace Medical Division (AFSC)  
Brooks Air Force Base, Texas

#### INTRODUCTION

As the title indicates, I will approach this introduction from the standpoint of the customer, that is the one who uses the output of biodynamics research (in particular, biodynamic models) to form the basis for solutions to practical problems. I hope to show not only that biodynamics modeling is already producing such practical answers, but also to identify classes of unanswered questions for which models may provide solutions.

This paper considers the following topics: (1) definition of operational biodynamics environments, (2) scope of R&D activities addressing these problems, (3) pay-off areas for the modeling approach and (4) an example of a practical problem to illustrate areas in which we still lack quantitative answers.

#### OPERATIONAL BIODYNAMICS ENVIRONMENTS

Biodynamics models have been used to describe normal functions such as hearing, proprioception, locomotion, etc. These models have been used to explain pathophysiologic deficiencies in function as well as to provide design improvements for various forms of prosthetic devices. In addition to this aspect of biodynamics research, there are major efforts devoted to the study of effects of mechanical force environments imposed by the environment or by man-made devices on people.

Of the mechanical force environments of concern to Air Force operations, almost all have corresponding concern to the other military services, NASA, operators of commercial aircraft and to the general civilian population.

Noise is a continuing environment of concern from the standpoint of establishing adequate exposure criteria, particularly for those exposed to high intensity engine noise on a career basis. This involves ground maintenance as well as flight personnel. Adequate means of testing and protecting these personnel is also a matter of continuing concern. Communication in noise environments is a necessary aspect of aircraft, spacecraft and industrial operations. With the new federal legislation on pollution control, there is a re-emphasis on noise as an environmental pollutant.

Blast forces transmitted through either air or water are important components of the environment produced by nuclear and nonnuclear explosions. The sonic boom, in terms of its effect on general civilian populations, may pose a limiting condition for design or utilization of supersonic aircraft. Vibration exposures may limit performance or cause acute or chronic injury or disease. This form of energy varies widely in frequency and intensity; its sources are both from the environment (turbulence) and from the operation of machinery (dynamic air pressures, engine-induced vibration). Although the variables are somewhat different, this form of mechanical force pervades almost all forms of transportation and is an important consideration for both crew and passengers. Impact forces are, of course, responsible for the majority of the staggering number of deaths and injuries on the highways. Aggressive programs sponsored by the Department of Transportation and by the automotive industry attest to the seriousness of concern over this problem. Although it involves smaller populations, there are similar types of unacceptably high injury rates associated with crashlanding impact of passenger aircraft, with escape from military aircraft using ejection systems and in the ground-landing

impact of vehicles such as spacecraft and escape capsules. Under operational conditions, combinations of these environments commonly occur. For instance, high amplitude vibrations produced by unstable flight of escape systems are followed by impact type loadings from parachute deployment and ground landing. Mechanical force environments may be associated with other environmental extremes such as heat, terrain following acceleration and vibration during low altitude high speed flight.

#### SCOPE OF R&D ACTIVITIES

The approach to study and solution of problems associated with each of the environments described above is similar. Each aspect is interrelated with the others. The first task is to adequately define the environment either by measurement or by calculation. For example, measurement of noise intensity and frequency spectra associated with operations around ground maintenance stations for aircraft must be made to assess hazards to the ground crew. By theoretical acoustics techniques, one can predict the noise levels and characteristics for large engines of future systems. Such data can be used to forecast the siting and land use requirements in advance. The second R&D activity is the definition of nominal and emergency exposure limits. The concern here is to define standards such that acute or chronic exposure does not result in damage to personnel. In this area falls the major scope of work directed toward defining limits beyond which tissue damage or destruction of the organism occurs. Our speakers at this symposium will address many of the problems associated with defining these limits of safe exposure. The third class of R&D activity applicable to the environments described above is the definition of several of the environments above on performance. Usually in this case one is concerned with less severe environmental conditions in which there is not threat of injury to the man but in which the mechanical forces are sufficiently severe to pose limits, for instance, to his ability to perform complex control tasks

associated with operation of modern aircraft or spacecraft. Here, modeling of man's ability to perform classes of tasks in such environments offers particular promise in that the output of such a model can be in a format that can be used by the designer to optimize the overall system in terms of the various subsystems, including the human operator. The fourth kind of R&D activity is that directed towards providing for improved protection of man and for extending his limit of performance either in time or intensity of environment. It is at this point where the designer and the biomedical scientist must communicate in quantitative terms and on a common basis in order to achieve the goal.

#### PAY-OFF OF THE MODELING APPROACH

The preceding discussion shows that R&D activities in biodynamics research are closely interdependent. Models provide a structure and format for assuring that it is possible to obtain internally consistent descriptions of man's response to the several aspects of the overall environment. Injury limit models should ultimately be based on biomechanical characteristics of the component tissues. Performance limit models should apply to realistic aspects of the operational environment and should be readily miscible with models describing the engineering designer's problems and options in providing controls, displays, attenuation, restraints and the like. From the engineer's domain, protection of man in mechanical force environments entails a range of disciplines of considerable breadth. On one extreme, basic characteristics of attenuation and restraint materials must be optimized for human use, not only from the protection but also from the comfort standpoint. At the other end of the spectrum, the aerodynamic properties of the system which determine "ride quality" must be traded against other performance requirements for the system. A system optimized for vibration isolation and protection must also provide adequate protection against the impact forces associated with ejection.

The modeling approach has added a great deal of confidence in the extrapolation of data from experimental animals to man in evaluating environments too extreme for experimental use of human subjects. Several of the people who have been major contributors to our knowledge about scaling laws are participants in this symposium. An example of how such information is used will follow. The ability of models to predict effects on the basis of experimental data is particularly important in biodynamics in areas where simulator ability does not exist to recreate predicted environments of new or even existing systems. The dynamic response index is an example of the recent development of a model to serve this purpose. I will not treat this model in detail since it will be described in a later paper. However, it serves to illustrate a useful point. A common cause of injury in escape from aircraft is a compression fracture of one or more vertebrae as a result of catapult loads. Using data obtained from cadaver studies and measurement of whole body responses to vibration, a model was developed which can be used to compute from the input acceleration-time history, the probability of producing vertebral fractures from  $+G_z$  impact loads. This model can be used to predict the effect of arbitrarily complex spinal impact loads where in earlier times, empirical guesses based on "eyeball" comparison of test data with laboratory studies was required.

#### TEST AND EVALUATION OF THE B-58 ESCAPE SYSTEM

I turn now to the final portion of this presentation: a brief review of some of the biodynamics problems which we encountered several years ago in testing and evaluating the B-58 escape system. Since man represents a significant percentage of the total mass of this system, and since this mass is displaced by the forces imposed on the system, the aerodynamic stability of the system is influenced by the alteration in center of mass which occurs as the man is deformed and displaced by mechanical forces. For this reason, it was important in the test program to use a subject similar in dynamic response characteristics to man. As an erect animal, the bear

has some characteristics in vertebral configuration similar to man and at the time of the tests some limited use of the animal had been made as an impact test subject. The deciding factor in selecting this specimen for our test program was the similarity in whole body mechanical impedance between the bear and man shown in Figure 1. If differences in mass are accounted for, one can see that the bear and man have a striking similarity in their mechanical impedance in comparison to a rather marked difference between them and an anthropomorphic dummy available at that time.

This test program, even though it is ten years old, serves well to point out some of the unanswered questions which were present then and which we still face each time we evaluate data from such an escape system. Figure 2 shows the three translational acceleration patterns recorded from a test ejection which occurred prior to design improvements in stabilizing the deceleration of the capsule. Similarly complex angular accelerations were present in these early tests. How does one evaluate the effect of these environments on man? We don't have simulator ability to experimentally study the environment at this time. We don't have an objective endpoint for impact accelerations in other than the spinal direction. We don't know much about how forces acting in different directions as a function of time in the impact regime interact with one another. We don't know much about the effect of one segment of this operational environment on the response of man to a subsequent exposure seconds later. So, it is clear that there remain a number of unanswered questions in this example of the broader field of biodynamics research. And, this is not an isolated example. It is also clear that the modeling approach is an important aspect of treating the complex problems such as those I have illustrated.

## CONCLUSIONS

This meeting is focused on the modeling approach. However, this is obviously only one aspect of the overall area of biodynamics research.

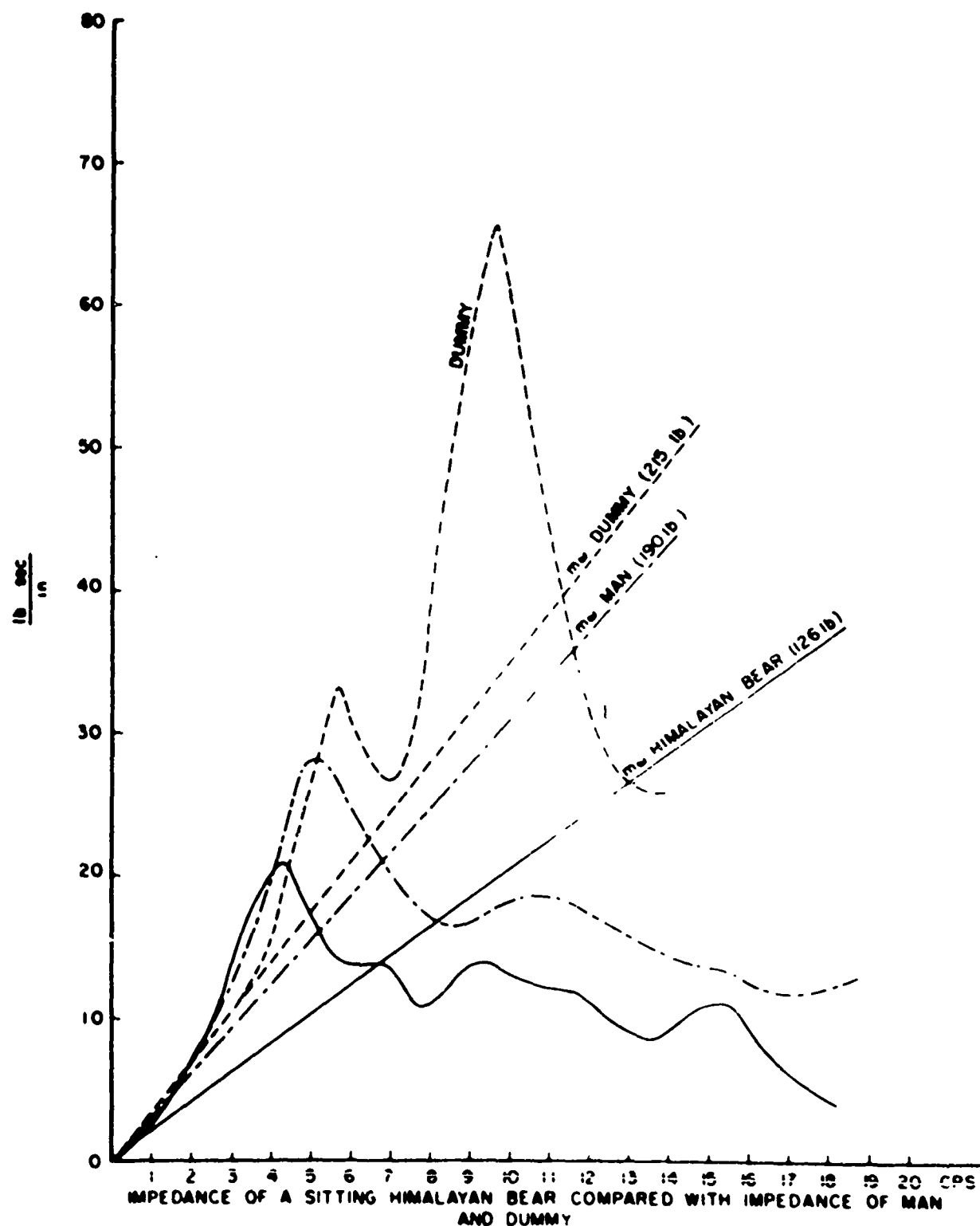
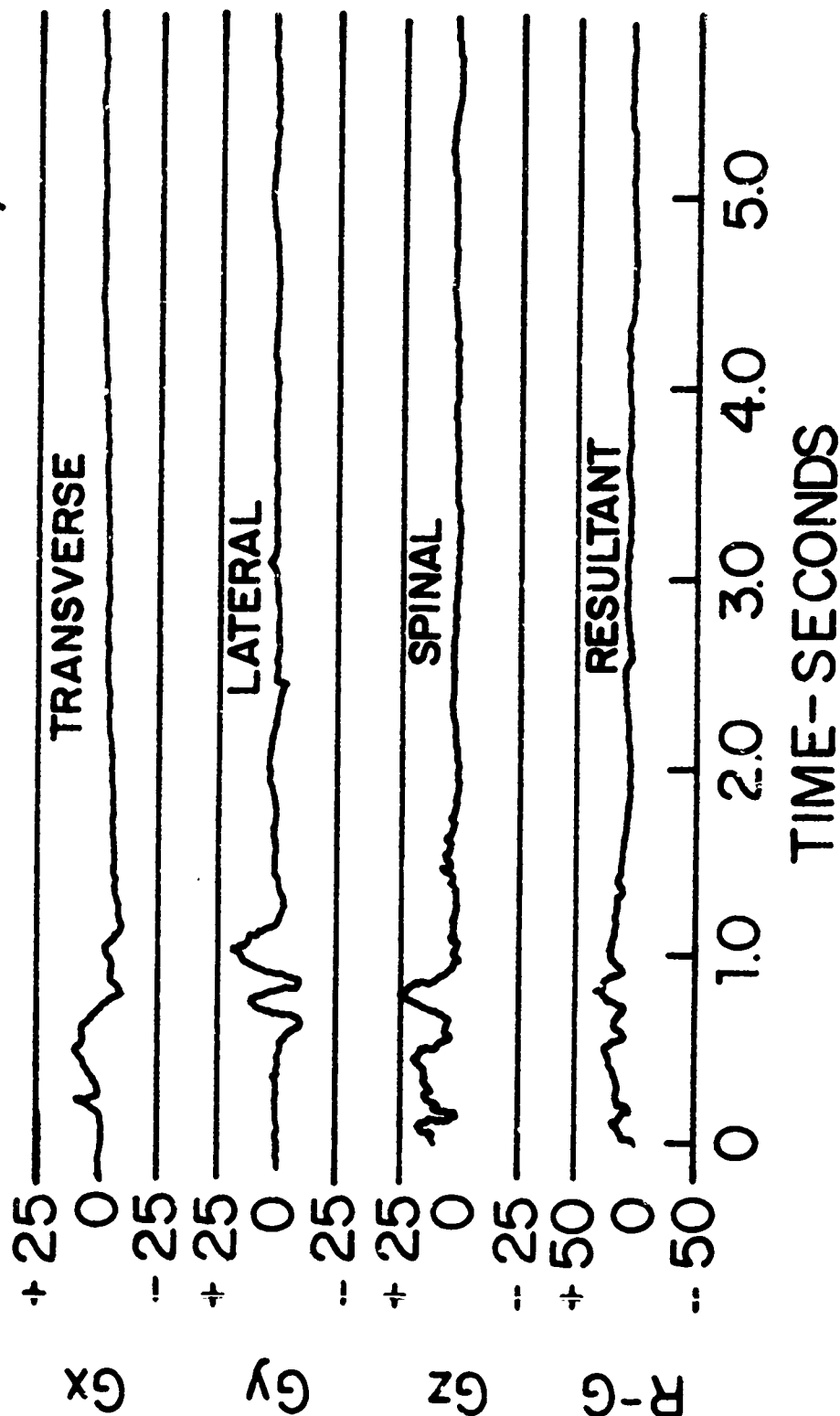


Fig. 1 - Whole Body Mechanical Impedance of Man, Bear and Dummy <sup>(1)</sup>



INFLIGHT EJECTION 2-9 BEAR OCCUPANT  
 KEAS = 436 MACH = 1.62 ALT = 45,800'



NOTE: ACCELERATION MEASURED AT CAPSULE  
 SEAT AREA

Fig. 2 - Translational Acceleration Patterns from Test Ejection of B-58 Escape Capsule<sup>(2)</sup>

A working interface between modelers and others in this field can do much to identify what kinds of data are missing and can guide further efforts in data acquisition.

I have attempted to develop the story to show that there are practical unanswered questions in biodynamics which need to be addressed. Models which permit application of theoretical and experimental data to operational situations offer a conceptual breakthrough in our ability to achieve this end.

Current efforts by diverse groups are rapidly developing information which ought to be readily exchanged. We are only beginning to achieve the kind of communication which needs to exist between the various disciplines and agencies which bear on the area of biodynamics. This meeting provides what we hope will be a useful forum for such an interdisciplinary exchange over the next few days. Perhaps more importantly, it will establish lasting exchanges of information and ideas between the participants.

In this context, I bring you the best wishes of General Roadman, the Commander of the Aerospace Medical Division, for success in this meeting and in achieving our common objectives in biodynamics research and development.

## REFERENCES

1. Coerman, Rolf R. Companion of the Dynamic Characteristics of Dummies, Animals and Man. Impact Acceleration Stress, NAS-NRC Publ. 977, pp 173-184, 1961.
2. Clarke, N. P. Biodynamic Response to Supersonic Ejection. Aerospace Med., 34:1089-94, 1963.

AMRL-TR-71-29

SESSION I

APPLICATION OF BIODYNAMIC MODELS FOR THE ESTABLISHMENT  
OF ENVIRONMENTAL EXPOSURE LIMITS

Chairman

H. von Beckh  
Director of Research  
(AMRD), Naval Air  
Development Center

Co-chairman

Lt Col G. C. Mohr  
AMRL

A MODEL TO SIMULATE THORACIC  
RESPONSES TO AIR BLAST AND TO IMPACT\*

E. R. Fletcher

Lovelace Foundation for Medical Education and Research  
Albuquerque, New Mexico

ABSTRACT

A fluid-mechanical model of the thorax is described which has been useful in explaining biophysical mechanisms and scaling procedures applicable in assessing responses of the thorax energized by air-blast overpressures or by nonpenetrating missiles. Methods of parameter estimation are discussed. Comparisons are made between measured and computed intrathoracic pressures and chest-wall motions. The tested mammalian species are shown to divide into two approximately similar groups and the implications of this are discussed. Suggestions are made concerning possible future areas of research.

---

\* This work, an aspect of investigations dealing with the Biological Effects of Blast from Bombs, was supported by the Defense Atomic Support Agency of the Department of Defense, Contract No. DA 01-70-C-0075.

The experimental work discussed in this manuscript was conducted according to the principles enunciated in the "Guide for Laboratory Animal Facilities and Care," prepared by the National Academy of Sciences-National Research Council.

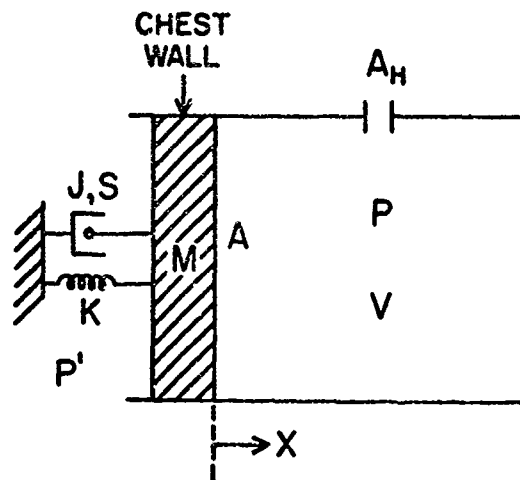
PRECEDING PAGE BLANK

## INTRODUCTION

Air-blast overpressures have been observed to produce injury and mortality in animals. For some time it has been known that when an animal is exposed to a shock wave the principal target organ (i.e., the major site of the initial injuries) is the lung.<sup>14</sup> Starting in 1963, personnel of the Lovelace Foundation for Medical Education and Research have in a series of papers<sup>8,2,3,4</sup> reported the development, refinement, and applications of a fluid-mechanical model of the thorax. This model has been useful in explaining biophysical mechanisms and scaling procedures applicable in assessing responses of the thorax energized by air-blast overpressures or by nonpenetrating missiles. The objective of this paper is to review the accomplishments to date (by summarizing the earlier papers and by reporting more recent studies) and to suggest in which areas future efforts might profitably be directed.

## THE MODEL

Figure 1 shows a somewhat modified version of the model as it was envisioned to assess responses of the thorax to air blast. The complex airways and lungs of an animal are approximated by a simple orifice opening into a single chamber containing only gases. The chest wall is approximated by a rigid mass attached to a spring simulating tissue elasticity and attached to a dash pot simulating frictional effects. Clearly one could reasonably expect to simulate only the gross fluid-mechanical responses of the lung with such a simplified model. However, it was thought from the start that this modified spring-mass system could, by a proper choice of



- |  |                                   |
|--|-----------------------------------|
| A : Effective area                                   | P : Internal air pressure         |
| A <sub>H</sub> : Effective orifice area              | P' : External air pressure        |
| M : Effective mass                                   | K : Spring constant               |
| V : Gaseous volume of lungs                          | J : Damping factor                |
| X : Displacement                                     | S : Power of velocity to which    |
| V <sub>0</sub> : Gaseous volume at zero displacement | the damping force is proportional |
| γ : Polytropic exponent for gas in lungs             | t : Time                          |

#### MODEL EQUATIONS

$$M \frac{d^2 X}{dt^2} + J \left| \frac{dX}{dt} \right|^S \frac{dX/dt}{|dX/dt|} + KX = A(P' - P)$$

$$\frac{dP}{dt} = -\gamma \frac{P}{V} \frac{dV}{dt} + \frac{1.334 \times 10^7 A_H}{V} |P' - P|^{1/2} \frac{P' - P}{|P' - P|} \quad \text{cgsu}$$

$$V = V_0 - AX$$

Fig. 1. Mathematical model of the thorax (incorporating a single gaseous volume) to simulate fluid-mechanical responses to rapid changes in environmental pressure.

parameters, be made to oscillate when it was engulfed by a blast wave in the same manner that intrathoracic pressures had been observed to oscillate in animals subjected to air blast.<sup>5, 12</sup> This was later shown to be the case.

The model in Fig. 1 differs from the original model<sup>8, 2</sup> in two respects:

(1) The damping force (see first equation in Fig. 1) is assumed to be proportional to the piston velocity to the  $S$  power, where any positive number may be chosen for  $S$ , while in the original model only a value of 1.0 could be used.

(2) A single piston is used, while the original model contained two pistons, one to simulate the chest wall and one to simulate that part of the abdomen which moves with the diaphragm. However, the values of the parameters for the original model were always (except in the first paper<sup>8</sup>) chosen in such a way that the two pistons moved exactly together so that in effect there was only one piston. (In the later version of the model<sup>3</sup> the abdominal piston was omitted because reported acoustic data indicate that the motion of the abdomen is much slower than that of the chest wall.)

In all other respects (such as the assumptions that [1] the spring is linear and [2] the pressure-volume changes in the lung are polytropic) the two models are identical. We can thus use Fig. 1 in discussing calculations made with the original model provided we assume  $S$  to be equal to 1.0.

The equations in Fig. 1 can be used to compute the motion of the piston, the gas flow through the orifice, and the internal pressure as functions of time for a specified blast wave. Solving these equations



requires the use of numerical techniques and is most easily accomplished with the aid of an electronic computer. Before this can be done, however, it is necessary to have estimates of the magnitudes of  $A$ ,  $A_H$ ,  $M$ ,  $V_0$ ,  $\gamma$ ,  $K$ ,  $J$ , and  $S$  (see Fig. 1).

#### PARAMETER ESTIMATION

Many sources and kinds of information have been examined in trying to estimate numerical values for the required animal parameters, and these have been discussed in the previous model papers. Among others, we have considered (1) measured gaseous lung volumes and lung masses, (2) experiments in which either an entire cat or dog was exposed to a sinusoidal pressure wave or such a wave was introduced into the airways of the animal, (3) rapid-decompression tests on man, (4) illustrations showing cross-sections of cadavers, and (5) measured intrathoracic pressures in rabbits and a dog exposed to blast waves. As might be expected, some of the parameters (listed in Fig. 1) could be estimated for one species of mammal while others could be estimated for other species. Thus in order to have an estimate of all the parameters for one species, it became necessary to scale some of the parameters from one species to another. This interspecies scaling was accomplished by using dimensional analysis and by assuming that all mammals are "similar" in that they have the same shape and equivalent distributions of various physical parameters.<sup>2</sup> It is interesting to note that all of the conclusions reached in regard to scaling between mammalian species agree with what could be predicted if we assumed the various species had "electrodynamical similitude."<sup>6</sup> The basic criteria for this

similitude are a constant shape and density, and a constant propagation velocity of electromagnetic waves in all of the species. The similarity law, which is derived from these criteria, can be expressed in the following form:

A physical quantity which has the dimensions  
 $(\text{mass})^\alpha (\text{length})^\beta (\text{time})^\mu$  will vary among  
 electrodynamically similar animals as  
 $(\text{body mass})^{\alpha + \beta/3 + \mu/3}$ .

Guerra and Günther<sup>6</sup> have found this scaling to hold approximately, although they determined from the periods of biological functions in various species that  $0.31\mu$  was the "most probable value" in the exponent of body mass rather than the  $\mu/3$  predicted by theory.

Having obtained (with the aid of interspecies scaling) estimates of all the animal parameters as functions of body mass, the model (Fig.1) was used to compute intrathoracic pressures in animals exposed to shock waves. These computed pressure waves were then compared to the measured waves, and it was found that by making moderate adjustments in the estimated animal parameters, reasonable agreement could be obtained between theory and experiment. Figure 2 shows measured and computed intrathoracic pressures for a rabbit exposed near the closed end of a shock tube to the indicated blast wave. Note that both the computed and measured internal pressure waves oscillate around the external pressure, and that the frequencies and the amplitudes of the oscillations in the two waves are in good agreement.

Intrathoracic pressure records undoubtedly represent the best single source of information for estimating the effective or average

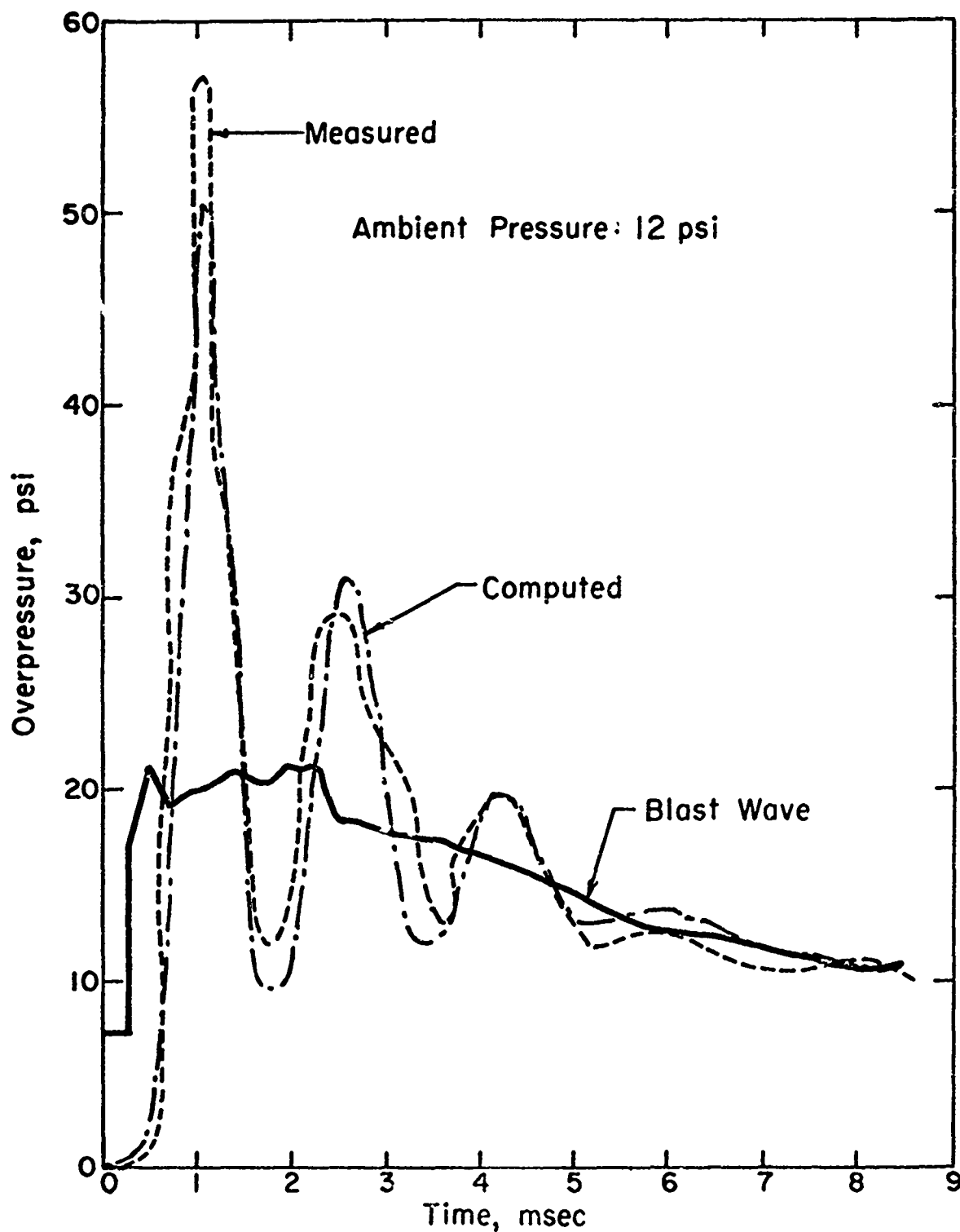


Fig. 2. Measured and computed intrathoracic overpressures for a rabbit exposed near the closed end of a shock tube to the indicated blast wave.<sub>33</sub> Taken from Reference 2.

animal parameters needed in the model. This is because, by looking at the internal pressure records, we are seeing the effective areas, masses, volumes, spring constants, and damping factors "in action," so to speak, in the very circumstances we are trying to approximate with the model, namely an animal's being exposed to an air-blast wave. It should, however, be realized that the fact that only relatively small adjustments were required in the initial estimates of the animal parameters in order to obtain good agreement between the measured and computed intrathoracic pressures does not mean that all of those animal parameters have been "closely" determined. The effects of varying one parameter can to some extent be counterbalanced by an appropriate adjustment in another parameter. Also, the computed internal pressure records have been found to be quite insensitive to the values of some of the parameters. Let us consider in particular three facts that we have been able to determine by solving the model using various animal parameters:

- (1) The response of the thorax when energized by air-blast overpressures is so fast (see Fig. 2) that there is not enough time for a significant amount of air to flow in or out of the orifice,  $A_H$
- (2) Because the air is essentially trapped in the lungs during exposure to air blast (see statement 1), there is a nonlinear "air spring" acting on the piston, and the effective air-spring constant is much larger than the tissue-spring constant,  $K$ .
- (3) The computed internal pressures are highly dependent on the power,  $S$ , of velocity to which the

damping force is assumed to be proportional.

However, the four intrathoracic pressure records that have been published to date (three recorded in rabbits<sup>8,2</sup> and one in a dog<sup>3</sup>) provide insufficient data to determine if S actually has a value of 1.0 as has always been assumed.

An attempt has been made to determine a numerical value for the parameter S by using a group of unpublished intrathoracic pressure records<sup>12</sup> for several species exposed to approximately square-wave overpressures. In order to do this the model was solved many times using various overpressures and animal parameter values. In view of the facts listed above and in order to simplify the calculations,  $A_{\bar{H}}$  and K were set equal to zero, and  $\gamma$  was always assumed to be equal to 1.2, the average of the polytropic exponents for isothermal and adiabatic processes for air.\* For these conditions it can be shown (using the equations in Fig. 1) that if S is equal to 1.0, the peak internal overpressure in atmospheres is a function of only two quantities:

---

\*No accurate intrathoracic temperature measurements have been made in animals during exposure to air blast. Because of the enormous heat capacity of water and the vast surface area between pulmonary gas and tissue, the pressure-volume changes may not be adiabatic. To date, none of the model calculations have required that the compromise  $\gamma$  of 1.2 be changed in order to approximate the data. This is not proof, however, that a  $\gamma$  of 1.2 corresponds to reality in the lungs, and more theoretical and/or experimental effort is needed to resolve this issue.

the external overpressure in atmospheres and a scaled damping factor,  $\alpha_0$ , which is equal to  $(J/2A) (V_0/1.2 \text{ MP}_0)^{1/2}$ . It can be demonstrated<sup>2</sup> that  $\alpha_0$  is equal to the damping ratio (i.e., the damping factor divided by the critical damping factor) for small oscillations (i.e., small enough that the air spring is essentially linear) about the ambient pressure,  $P_0$ . The computed curves of constant  $\alpha_0$  are shown in Fig. 3 as a function of the external overpressure and the difference between the peak internal pressure and the external pressure. The time,  $t_m$ , to peak internal pressure multiplied by the quantity  $A (P_0/V_0 M)^{1/2}$  can also be expressed as a function of the same two parameters which define the peak internal overpressure in atmospheres;  $t_m$  when scaled in this manner is given the symbol  $Z$ , and curves of constant  $Z$  are also shown in Fig. 3.

The data in Fig. 3 were plotted using the measured external, peak internal, and ambient (12.0 psi) pressures. These data were obtained with animals either located (1) against the end-plate of a closed shock tube (in which case the external pressure was taken to be the reflected pressure) or (2) in a shallow chamber in the side of an open shock tube (in which case the external pressure was taken to be the incident pressure). It was earlier assumed<sup>2</sup> and it can be predicted using the electrodynamic similitude law that  $\alpha_0$  should be constant for similar animals (at a constant  $P_0$ ); this follows from the fact that  $\alpha_0$  is dimensionless. From Fig. 3 it can be seen that although all the data seem to line up fairly well, except for the monkey point, these data could not be reasonably approximated by a curve of constant  $\alpha_0$ . At the low pressures the data correspond to an  $\alpha_0$  of about 0.3 while at the higher pressures they correspond to an  $\alpha_0$  of

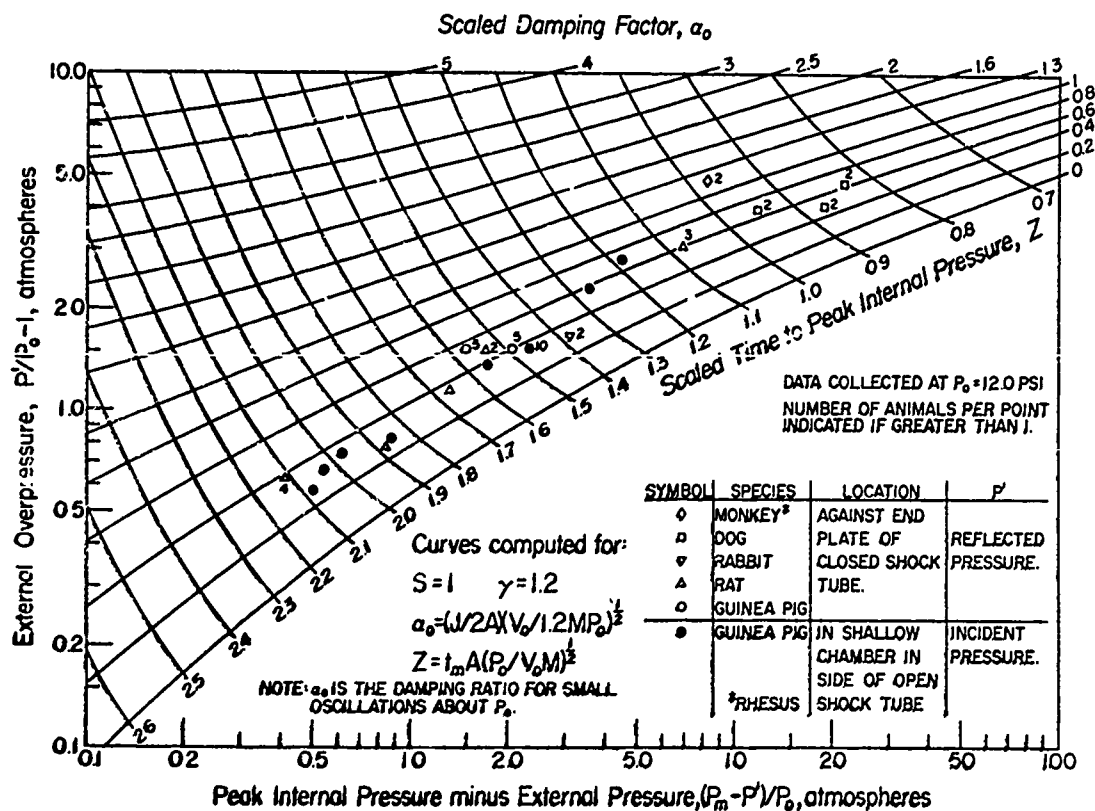


Fig. 3. Peak internal pressure minus external pressure vs external overpressure for animals exposed to a long-duration shock wave. The scaled time to peak internal pressure and scaled damping factor curves were computed with the model by assuming the damping force to be proportional to piston velocity.

about 0.6. As would be expected, the  $\alpha_0$ 's that have been used in previous papers lie in this range.

Since the data do not correspond to a constant  $\alpha_0$  as has been predicted for  $S$  equal to 1.0, it was decided to assume an  $S$  of 2.0 (i.e., a damping force proportional to velocity squared) in order to see if the data would then fit the predictions. The model solutions that were made for  $S=1.0$  were repeated with the only change being that  $S$  was set equal to 2.0. The scaled damping factor,  $E$ , is then equal to  $(JV_0/AM)$  which cannot be interpreted in terms of a damping ratio as was done for  $S=1.0$ \*. The scaled time,  $Z$ , has the same form for  $S=2.0$  as it did for  $S=1.0$ . Figure 4 shows the results of the calculations for  $S=2.0$  and the data shown on Fig. 3 are also shown on Fig. 4. Since  $E$  is dimensionless, the data should fall along a curve of constant  $E$ . We can see, however, that at the low pressures the data correspond to an  $E$  of 2.0 and at the high pressures to an  $E$  of 1.0 (excluding the monkey data). Thus once again the data do not fall along a curve of constant scaled damping factor, but they do cut across the  $E$  curves in the opposite sense from the way in which they cut across the  $\alpha_0$  curves. For this reason it seemed that in order to have the data fall along a curve of constant scaled damping factor, a value of  $S$  between 1.0 and 2.0 would have to be chosen. Therefore, the model calculations were repeated for  $S=1.5$ , and the data and predicted curves are shown in Fig. 5. The dimensionless scaled

---

\*When  $S$  is greater than 1.0, the damping ratio is effectively zero for small oscillations and varies with the peak piston displacement (even with a linear spring) for larger oscillations.



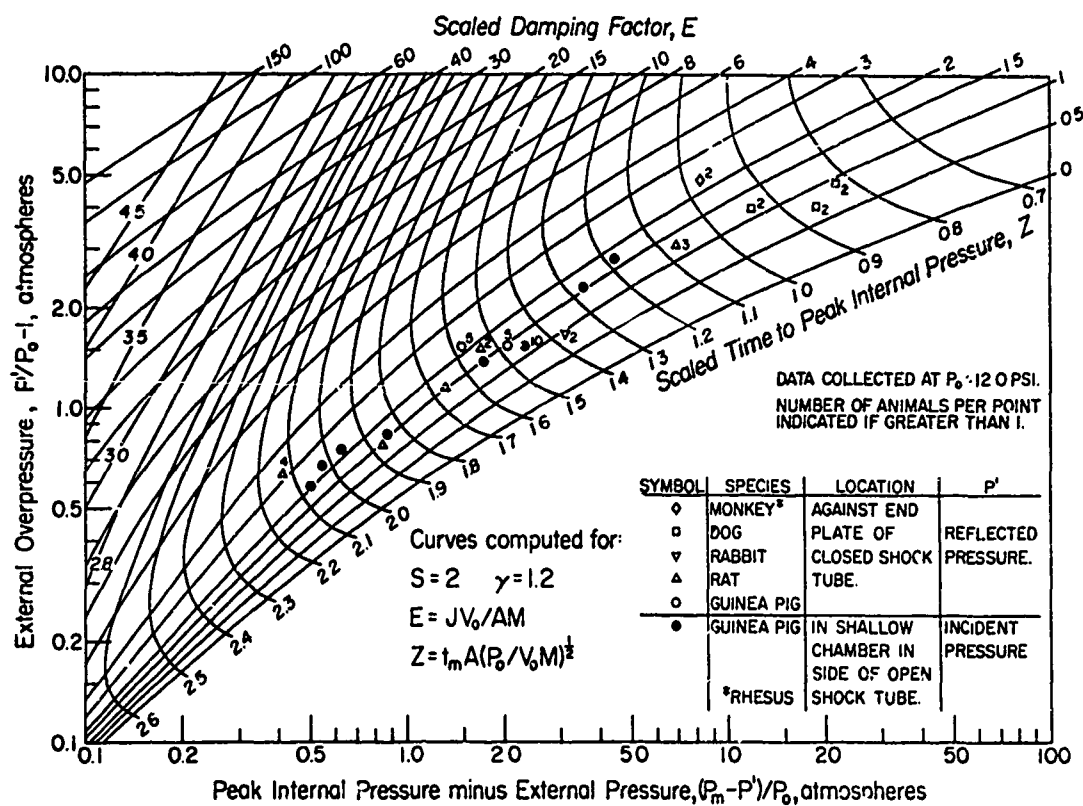


Fig. 4. Peak internal pressure minus external pressure vs external overpressure for animals exposed to a long-duration shock wave. The scaled time to peak internal pressure and scaled damping factor curves were computed with the model by assuming the damping force to be proportional to piston velocity squared.

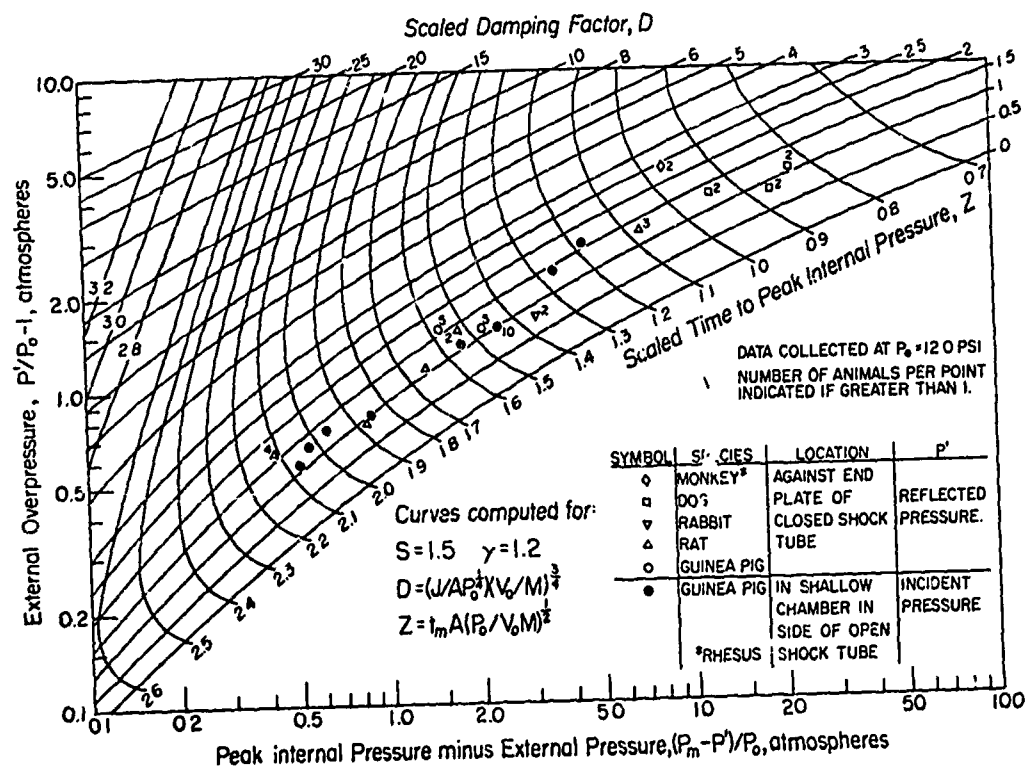


Fig. 5. Peak internal pressure minus external pressure vs external overpressure for animals exposed to a long-duration shock wave. The scaled time to peak internal pressure and scaled damping factor curves were computed with the model by assuming the damping force to be proportional to piston velocity to the 1.5 power.

damping factor,  $D$ , is equal to  $(J/A) (V_0/M)^{3/4} P_0^{-1/4}$  and the scaled time,  $Z$ , has the same form as before. For  $S=1.5$  the data do, as predicted, seem to fall along a curve of constant  $D$  with a value of  $D=1.3$  being the estimated best fit to the data. The rhesus monkey data, however, fall at a  $D$  value of about 2.4. Since this point represents only two tests (both at essentially the same external overpressure), the possibility of some error should not be entirely ruled out, and it would therefore be premature to try to speculate as to the cause of this anomaly. If the point is substantiated, it would mean that for a given external overpressure the peak internal pressure would be considerably smaller in a rhesus monkey than it would be in any of the other four species tested.

Having concluded that the peak internal pressure can be reasonably predicted by choosing  $\gamma=1.2$ ,  $S=1.5$ , and  $D=1.3$ , the next step is to consider the time to peak internal pressure. The actual times were determined from the intrathoracic pressure records by considering both the time when the internal record first moved above zero and the time when the external pressure wave struck a second gauge (which was triggered at the same time as the intrathoracic gauge) mounted in the side of the shock tube at a known location with respect to the animal. The scaled times were estimated from the  $Z$  lines and the data points on Fig. 5. It can be seen, however, that if Fig. 3 or 4 had been used, these scaled times would not have been very different. Point by point the actual time to peak pressure was divided by the scaled time to peak pressure and the resultant values of  $t_m/Z$  for each species showed no systematic variation with incident

or peak internal pressure. Therefore, the values were averaged for each species,\* and these averages are shown in Fig. 6 plotted against mean body mass of the animals. From considerations of dimensional analysis or the electrodynamical similitude law it can be predicted that  $t_m/Z$  should vary as animal body mass,  $m$ , to the  $1/3$  power, and indeed the points on Fig. 6 can be reasonably approximated by the equation  $t_m/Z = 0.6 (m/1\text{kg})^{1/3} \text{msec}$ .

To summarize, we have found that for dogs, rabbits, rats, and guinea pigs exposed to square-wave overpressures it is possible to reasonably estimate the peak internal pressure and time to peak while not violating the laws of dimensional analysis or the electrodynamical similitude law by choosing:\*\*

$$K = 0, A_H = 0, \gamma = 1.2, S = 1.5,$$

$$(J/A) (V_0/M)^{3/4} (12 \text{ psi})^{-1/4} = 1.3,$$

$$\text{and } (1/A) (V_0 M/12 \text{ psi})^{1/2} = 0.6 (m/1\text{kg})^{1/3} \text{msec}.$$

However, more data are needed, and the calculations should be repeated for other values of  $\gamma$ . It is interesting to note that in order to predict the correct peak pressure and correct time to peak it is not

---

\*Since the guinea pigs were tested in two locations in the shock tube, a separate average was computed for each location.

\*\*The 12-psi value appears in the following equations because this was the ambient pressure where the data were collected. The 1-kilogram value and the msec unit are included to keep the equations dimensionally correct. Care should be taken in using these equations to keep the units consistent.

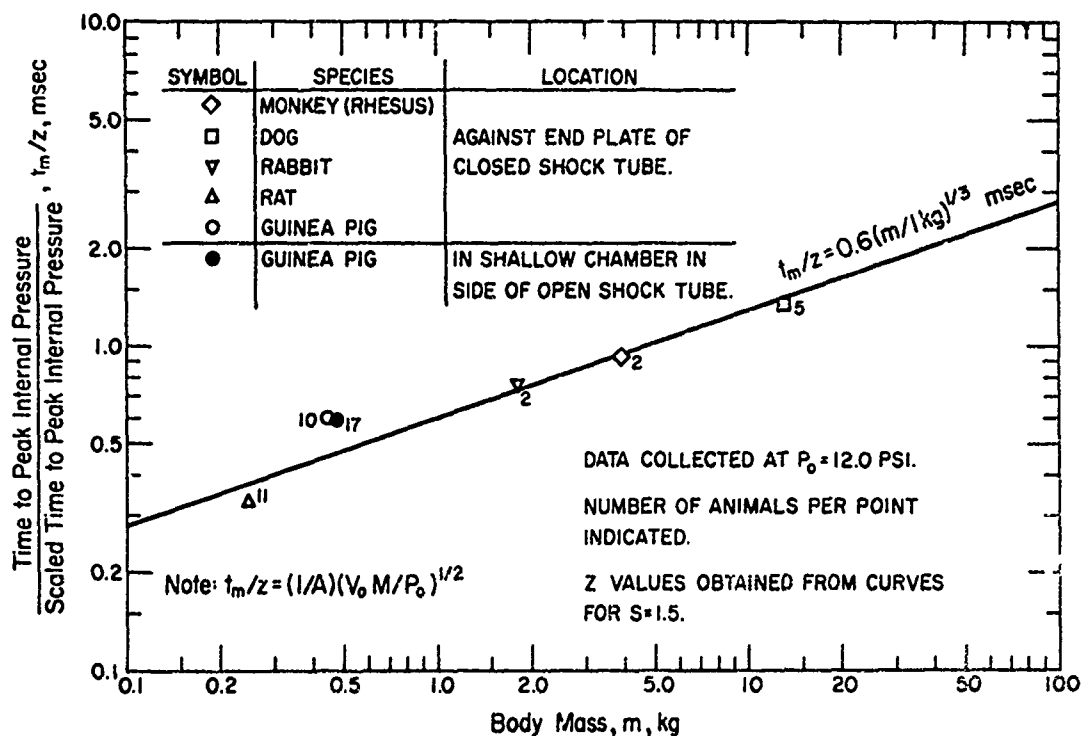


Fig. 6. Time to peak internal pressure divided by scaled time to peak internal pressure vs body mass for animals exposed to a long-duration shock wave. The scaled times were computed with the model by assuming the damping force to be proportional to piston velocity to the 1.5 power. The line is an estimated best fit to the data with the theoretical slope of  $1/3$ .

necessary to have good estimates of  $J$ ,  $A$ ,  $V_0$ , and  $M$  separately, but it is necessary to have good estimates of  $(J/A) (V_0/M)^{3/4}$  and  $(1/A) (V_0 M)^{1/2}$ .

### PRIMARY BLAST APPLICATIONS

As was mentioned earlier, the thorax model was first developed to study the consequences of exposure to blast-induced variations in environmental pressure (i.e., primary blast effects). In that regard, the ability of the model to duplicate intrathoracic pressures (see previous section) during such exposure strongly suggests that we understand the gross mechanisms which produce those pressures. The question is: How can we use this model to predict levels of injury and mortality and, hopefully, to increase our understanding of how the various pressures and motions precipitate the observed<sup>14</sup> wounds? As a first step toward answering this question, we should see if the available mortality data are consistent with the predictions for inter-species scaling as derived from dimensional analysis or electro-dynamical similitude concepts. If this turns out to be true, we can reasonably assume that similar mechanisms are producing similar injuries in the various species; if this can be assumed, the data for all of the species can be considered in estimating injury in any one of the species, and this should considerably reduce the amount of experimental and theoretical (obtained with the model) data needed to predict and explain injury mechanisms, types, and levels. If, however, the data and the predicted scaling relationships do not agree, there can be little hope for using the model to estimate injury levels in some species (like man) that has not been systematically subjected to a

variety of blast waves in the laboratory.

A considerable amount of data, most of which has been published previously,<sup>4</sup> is available on mortality in animals exposed near a normally reflecting surface to shocked blast waves whose durations ranged from 0.24 to 400 msec. It was found<sup>4</sup> that for each duration and species a linear relationship existed between the probit of mortality and the logarithm of the peak reflected overpressure, and that (except for the guinea pig) all the lines had a common slope. By using this approach, the overpressures required to produce 50 percent mortality were estimated from the data for the various durations and species tested. These LD<sub>50</sub> values are plotted in Fig. 7, and curves, which were estimated by eye, have been drawn to connect the data points for each species (if there was more than one point for that species). As would be expected, the curves indicate that the required pressure increases with decreasing duration and approaches a constant value with increasing duration. It is difficult to conclude much about interspecies scaling from this plot, or to estimate where the curve for an untested species should fall. However, it can be noted that the curves do seem to be roughly divided into two groups, although the curve for the squirrel monkey extends into both groups, and the datum for the chicken (the only non-mammal tested) falls below all of the other data.

Using dimensional analysis it has been predicted<sup>2</sup> that the data for all species should fall approximately on a single curve if the LD<sub>50</sub> overpressure were plotted as a function of duration divided by animal body mass to the 1/3 power rather than as a function of duration alone. The data (from Fig. 7) have been plotted in this way

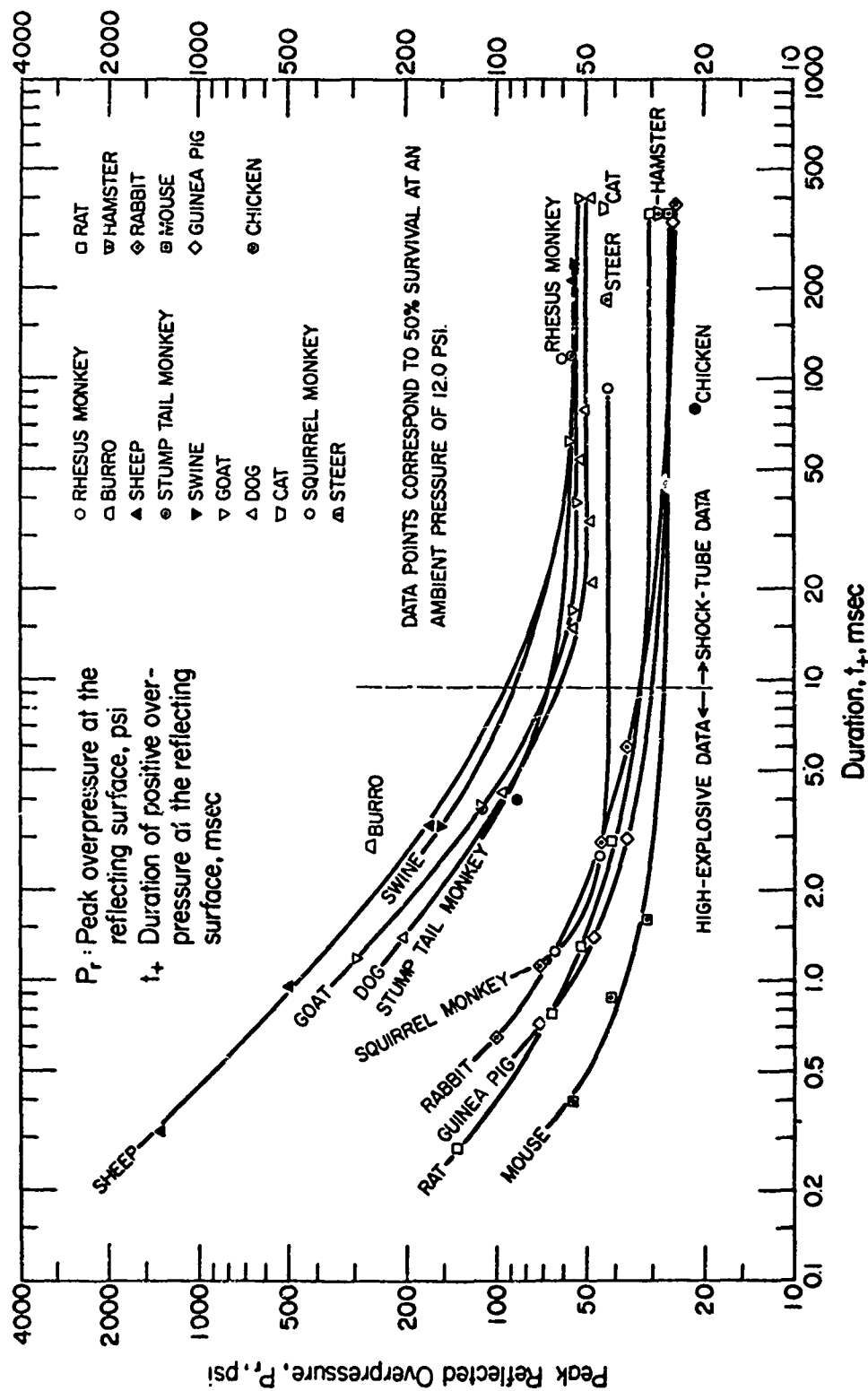


Fig. 7. Peak reflected overpressures and durations for sharp-rising blast waves which will result in 50 percent mortality in various species. The curves were estimated by eye.



in Fig. 8, and the overpressures and durations have been multiplied by the appropriate factors to make them directly applicable to a 70-kg animal (i.e., an animal the size of man) and an ambient pressure of 14.7 psi. In other words, if we assume that any one of the species tested is similar to man (the meaning and consequences of animal similitude having been discussed earlier from the points of view of dimensional analysis and electrodynamics), then the data in Fig. 8 for that species may be assumed to apply directly to a 70-kg man at sea level. Since it is apparent from Fig. 8 that all of the mammals tested are not approximately similar to each other, some discretion must be exercised in applying these data to man. The mammals do, however, seem to divide into two approximately similar groups which have been broadly designated in the figure as "small mammals" and "large mammals," even though some of the species classified as small mammals have a greater mass than some of the species classified as large mammals. Note that although the shock-tube data point for squirrel monkeys is lower than the data points for any other large mammal, it is certainly high enough to indicate that the squirrel monkey should be considered as a large mammal. The reason why the two high-explosive data points (marked by arrows) for squirrel monkeys fall so far below the rest of the data for the large mammals is not known at this time. Since these two points represent a total of only 16 monkeys, it would be premature to conclude that for some reason the overpressure tolerance of squirrel monkeys rises more slowly with decreasing duration than it does for other mammals.

In an earlier report<sup>4</sup> it was concluded that a family of curves which adequately fit the data for the various species could be obtained

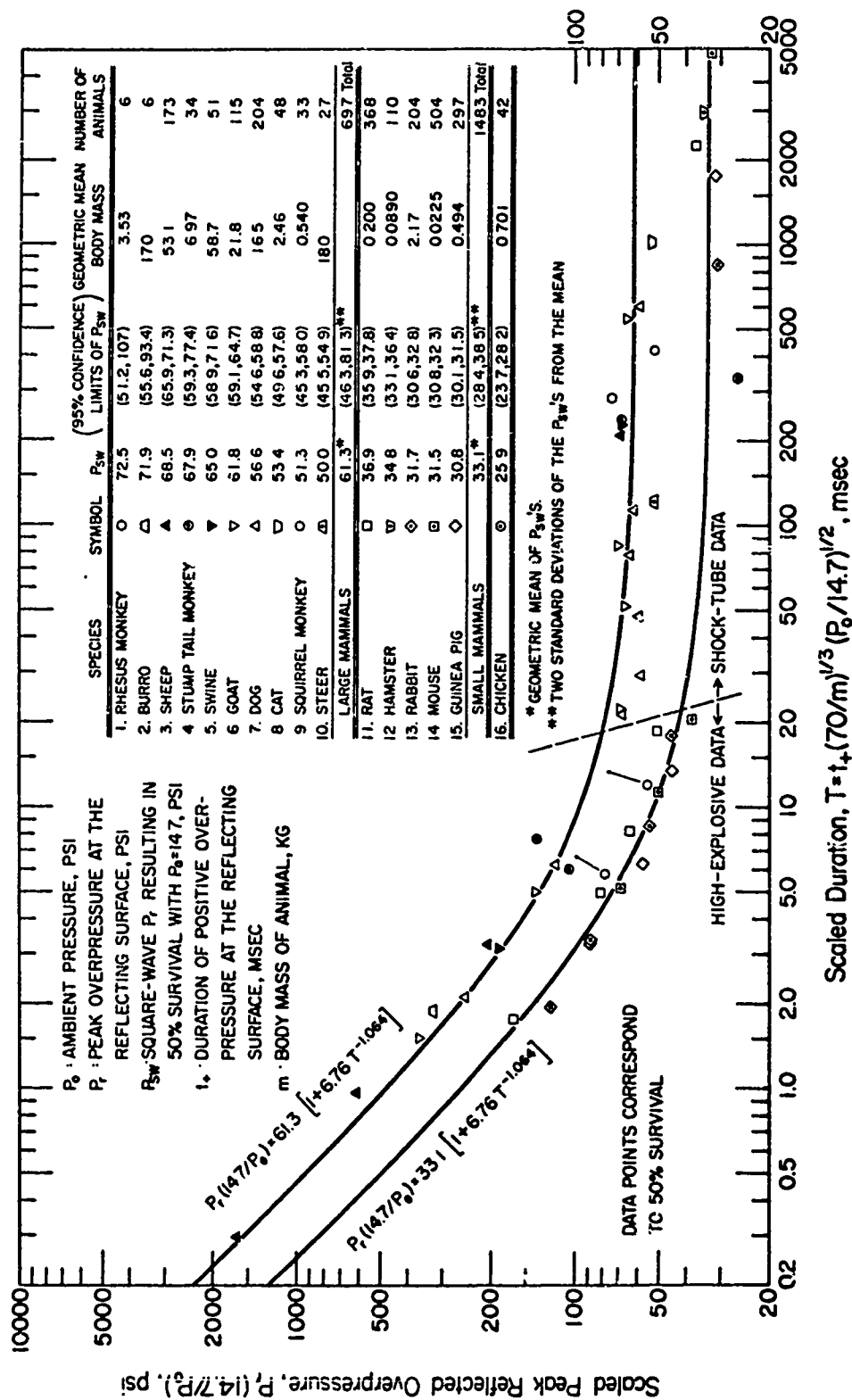


Fig. 8. Scaled peak reflected overpressures and scaled durations

for sharp-rising blast waves which will result in 50 per cent mortality in various species. The curves, computed for a hypothetical average large mammal and a hypothetical average small mammal, were derived from Reference 4.

by translating (in Fig. 8) a single curve in the vertical direction only. Thus, a family of curves could be drawn in Fig. 8 for the various species which would differ by only one parameter; namely, the scaled overpressure that each curve approaches for long-duration blast waves. This scaled overpressure,  $P_{sw}$ , is listed in the figure (along with 95 percent confidence limits) for each species. It should be noted that  $P_{sw}$  is the square-wave (or long-duration) overpressure which will result in 50 percent mortality for an ambient pressure of 14.7 psi. Listed in Fig. 8 are approximate 95 percent confidence limits for the  $P_{sw}$  of an untested species which is known to belong to one of the two groups. From these limits it can be seen that the  $P_{sw}$ 's of the small and large mammals differ significantly even though there is scatter in both groups, and that the  $P_{sw}$  of the chicken is significantly below those of the mammals. The geometric averages of the  $P_{sw}$ 's for the large and small mammals are 61.3 and 33.1 psi, respectively. The two curves in the figure can be thought of as applying to a hypothetical average small mammal with a  $P_{sw}$  of 33.1 psi, and a hypothetical average large mammal with a  $P_{sw}$  of 61.3 psi. The equations for the curves were taken from Ref. 4. It is instructive at this point to quote from this reference as to how a curve was estimated for man: "To which of the blast-tolerance groups formed by the experimental animals is man likely to belong? Previous estimates place him in the high-tolerance group. Assuming that man is a member of this group but lacking further evidence, his tolerance was arbitrarily but tentatively taken to be the geometric mean of those for the members of his group. . . ." (Thus, man has been assumed to correspond to the hypothetical average large mammal for which a curve was drawn in

Fig. 8.) This would still seem to be the best procedure for estimating the blast tolerance of a mammalian species for which a  $P_{sw}$  has not been established provided there is reasonable evidence to suggest that the species is similar to the members of one of the two groups. Several possible sources for evidence of this type will be discussed later.

Having determined that in regard to lethality there are two groups of approximately similar mammals instead of one, there is some question as to what influence this will (or should) have on our attempts to use the model to predict and explain injury mechanisms, types, and levels. We might, for instance, assume that similar mechanisms are producing similar injuries in the species of each group taken separately, but that the mechanisms and injuries for one group have nothing to do with those for the other. This would not be reasonable, however, because:

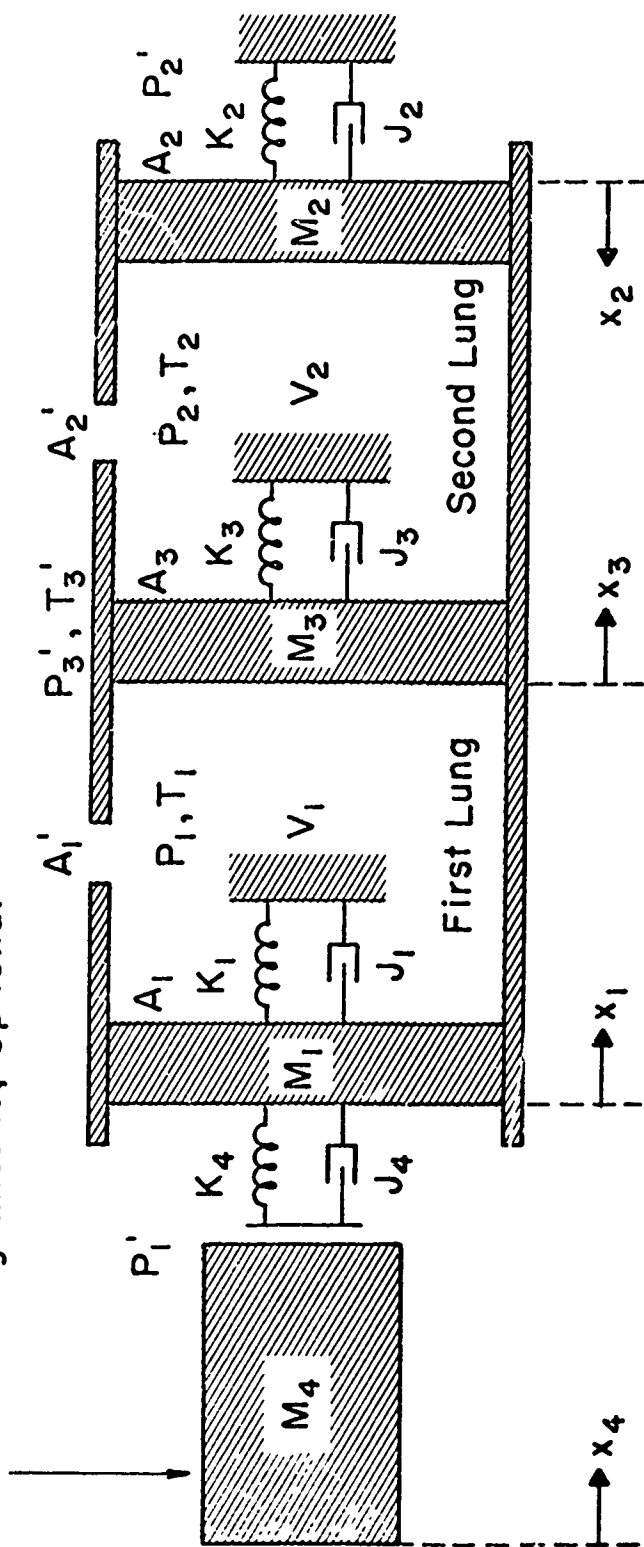
- (1) The same types of injuries have been observed in species of both groups.<sup>14</sup>
- (2) The data for both groups fall along the same curves in Figures 5 and 6.
- (3) The curves for both groups have the same shape in Fig. 8. and the same scaled time,  $T$ , applies to all species.

It, therefore, seems more reasonable to assume that the same mechanisms and types of injuries occur in both groups of mammals, even though the blast load required to produce a given level of injury varies between the groups. In terms of the model, it is to be hoped that observed injury (or mortality) levels in mammals can be correlated

with some physical quantity that can be computed with the model, such as peak piston velocity, peak internal pressure, impulse under the internal pressure wave, etc. If such a physical quantity can be found for one species, the value of the quantity required to produce a given level of injury can probably be scaled (by the methods discussed) to other species in the group of which the first species was a member. Further, the same physical quantity could probably be used to predict injury levels for the other group, and be scalable in the same way among the species of that group, but it is to be expected that the quantity might not be scalable between groups.

To date, only a limited number of calculations have been performed in an attempt to determine a physical quantity which can be computed with the model and which correlates well with mortality. A more complicated version of the thorax model was used in this study<sup>3</sup> (see Fig. 9) which has a separate chamber for each lung and three pistons, the outside ones representing the chest walls and the middle one the mediastinal tissue between the lungs. (The nonpenetrating missile shown in the figure was disregarded for the air-blast calculations, but it will be discussed later.) By having the two lungs separated, it was hoped that the relative damage to each lung could be estimated. When the model was used to compute the pressures in a dog exposed to an LD<sub>50</sub>, square-wave overpressure at the end-plate of a closed shock tube, the average of the predicted pressures in the two lungs agreed well with the measured intrathoracic pressures. It was determined that a peak internal pressure of approximately 250 psi (for a  $P_0$  of 12.0 psi) was required to produce 50 percent mortality, and that the peak pressure in the lung against the end-plate should be

# Non-Penetrating Missile, Optional



- |                                 |                                |
|---------------------------------|--------------------------------|
| $A_i$ : Effective Area          | $J_i$ : Damping Factor         |
| $A_i'$ : Effective Orifice Area | $K_i$ : Spring Constant        |
| $M_i$ : Effective Mass          | $P_i$ : Internal Air Pressure  |
| $V_i$ : Gaseous Volume          | $P_i'$ : External Air Pressure |
| $x_i$ : Displacement            | $T_i$ : Internal Temperature   |
|                                 | $T_i'$ : External Temperature  |

Fig. 9. Mathematical model of the thorax (incorporating two gaseous volumes) to simulate fluid-mechanical responses to rapid changes in environmental pressure and to nonpenetrating missile impact with the chest wall. Taken from Reference 3.

higher than the peak in the other lung. Experimentally it has been observed that in similarly exposed mammals more damage occurs in the lungs nearest the end-plate.<sup>12</sup> Similar calculations were made to estimate the response of a dog in a free-stream exposure in a broad-side standing posture to an LD<sub>50</sub> shock wave (as estimated from guinea pig data; see Ref. 3). For both "long"- and "short"-duration waves it was determined that the average of the peak pressures in the two lungs was about 250 psi, with the two pressures being approximately equal for the long-duration wave, and the pressure in the upstream lung being greater than that in the downstream lung for the short-duration wave. Unfortunately no published experimental data are available at this time to allow for direct comparison with the predictions. If the calculations are later substantiated by experiments, it would tend to indicate that the computed peak internal pressure (or the average of the two peaks if the lungs are considered separately) might be a reasonable physical quantity with which to estimate lethality, at least for the animals and exposure conditions considered. More effort is needed in this area if any firm conclusions are to be reached.

Another application of the model to primary blast problems concerns a group of experiments<sup>11, 12</sup> in which animals were exposed side-on at the end-plate of a shock tube and at various distances away from it to long-duration waves. It was observed that for a constant overpressure the mortality declined as the distance from the end-plate increased, with larger distances being required to provide a given degree of protection for animals with larger masses than were needed for animals with smaller masses. The overpressure at the animal

rises in two steps, the first corresponding to the arrival of the incident shock and the second corresponding to the arrival of the reflected shock which results when the incident wave strikes the end-plate. The mortality in a given species can be expressed as a function of the reflected overpressure and time,  $t_g$ , between the arrivals of the two shocks at the center of the thorax of the animal. It was found that for each  $t_g$  and species a linear relationship existed between the probit of mortality and the logarithm of the reflected overpressure, and that the lines had a common slope. This is analogous to what was found earlier in regard to the duration and peak overpressure for animals exposed against the end-plate to a blast wave. Likewise in an analogous manner, an attempt was made to scale the step-load data between species by dividing the  $t_g$ 's by animal body mass to the  $1/3$  power, and by dividing the reflected overpressure which will result in 50 percent mortality when animals are away from the end-plate by the corresponding overpressure when they are against the end-plate.\* The available step-load data are displayed in this form in Fig. 10. Note that  $t_g$  is not zero for an animal against the end-plate; rather it corresponds to the time required for the incident wave to traverse one-half the animal's body width (at the thorax) plus the correspondence time for the reflected wave. The data for all species are quite scattered and may reasonably be approximated by a single curve.

---

\*The technique of normalizing various overpressures for a species by dividing them all by one particular overpressure for that species was used in Ref. 4; when the pressure-duration data for 13 species of mammals (some in the large group and some in the small) were normalized in this manner, they all fell approximately on one curve.



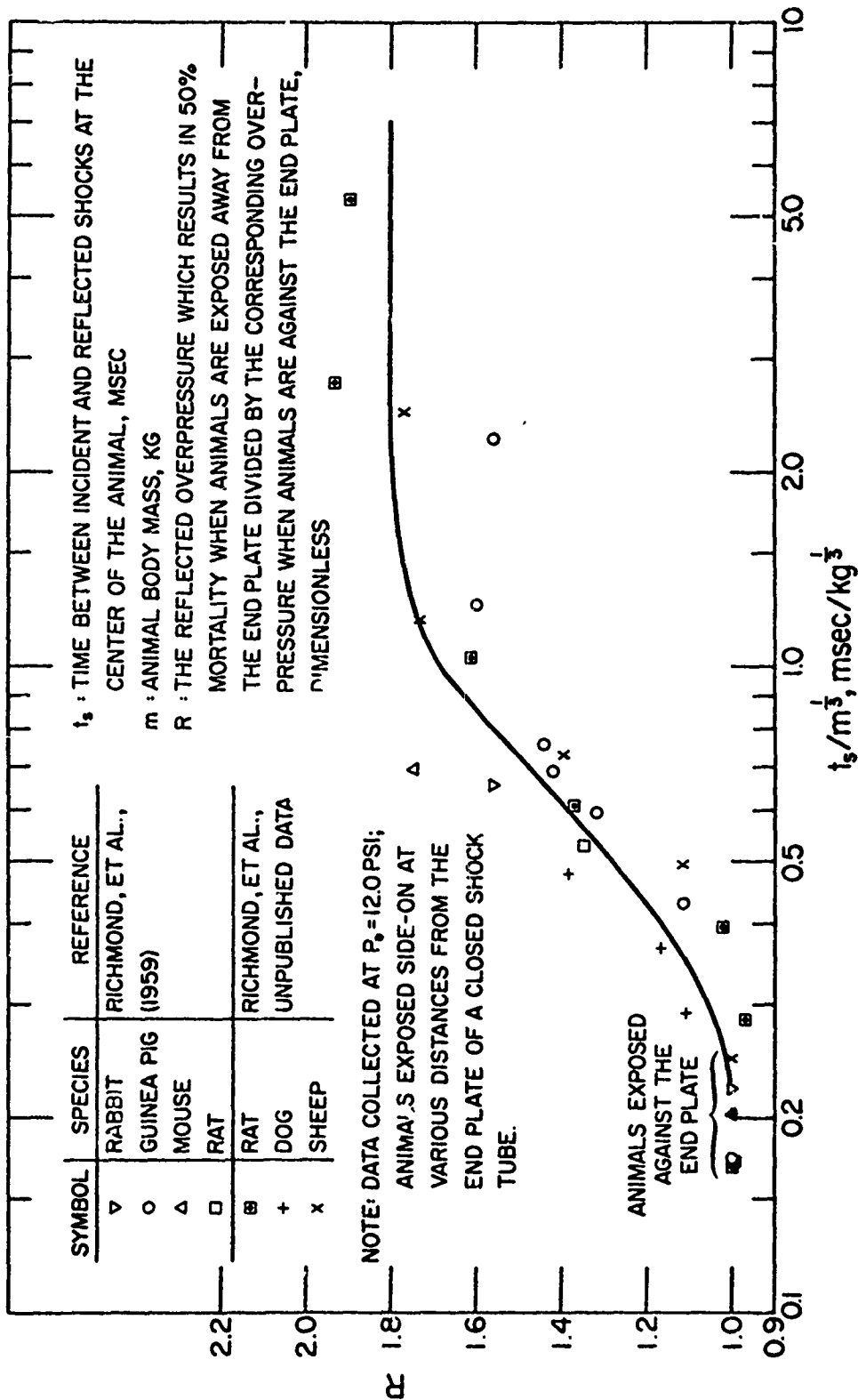


Fig. 10. Scaled reflected overpressure which will result in 50 percent mortality when various animals are exposed away from the end-plate of a closed shock tube vs scaled time between the arrivals of the incident and reflected waves. The curve was estimated by eye.

This curve would suggest that the LD<sub>50</sub> reflected overpressure increases by about 80 percent as an animal is moved from against the end-plate to a "long" distance from the end-plate. It should be noted that in theory the data in Fig. 10 could be displayed in such a way as to show the two groups of mammals (as in Fig. 8). This was not attempted, however, since the data from Ref. 11 were obtained with the animals in metal cages which partially protected them. (Cages were not used in the more recent experiments.<sup>12</sup>) Even though this is true, the relative protection provided by moving a constant scaled distance away from the end-plate was evidently approximately the same whether the animals were in cages or not.

Although the step-load data have not been analyzed extensively by using the model, the few calculations that have been made indicate that the peak intrathoracic pressure should, at least for short distances, decrease as the animal is moved away from the end-plate. This is illustrated in Fig. 11 which shows the external and computed internal pressures as functions of time for a rabbit at four different distances from an end-plate and exposed to a reflected overpressure of 52.1 psi. Two reasons have been proposed<sup>2</sup> for the reduced peak internal pressure when the animal is moved away from the reflecting surface: (1) the driving pressure (i.e., the difference between the external and internal pressures) of the reflected shock is reduced because of the increased pressure in the lungs due to the incident shock and (2) the increased internal pressure also results in a stronger air-spring's being active at the time of arrival of the second pulse, and this tends to inhibit further motion of the chest wall. The peak internal pressure is smallest if the reflected shock arrives at the

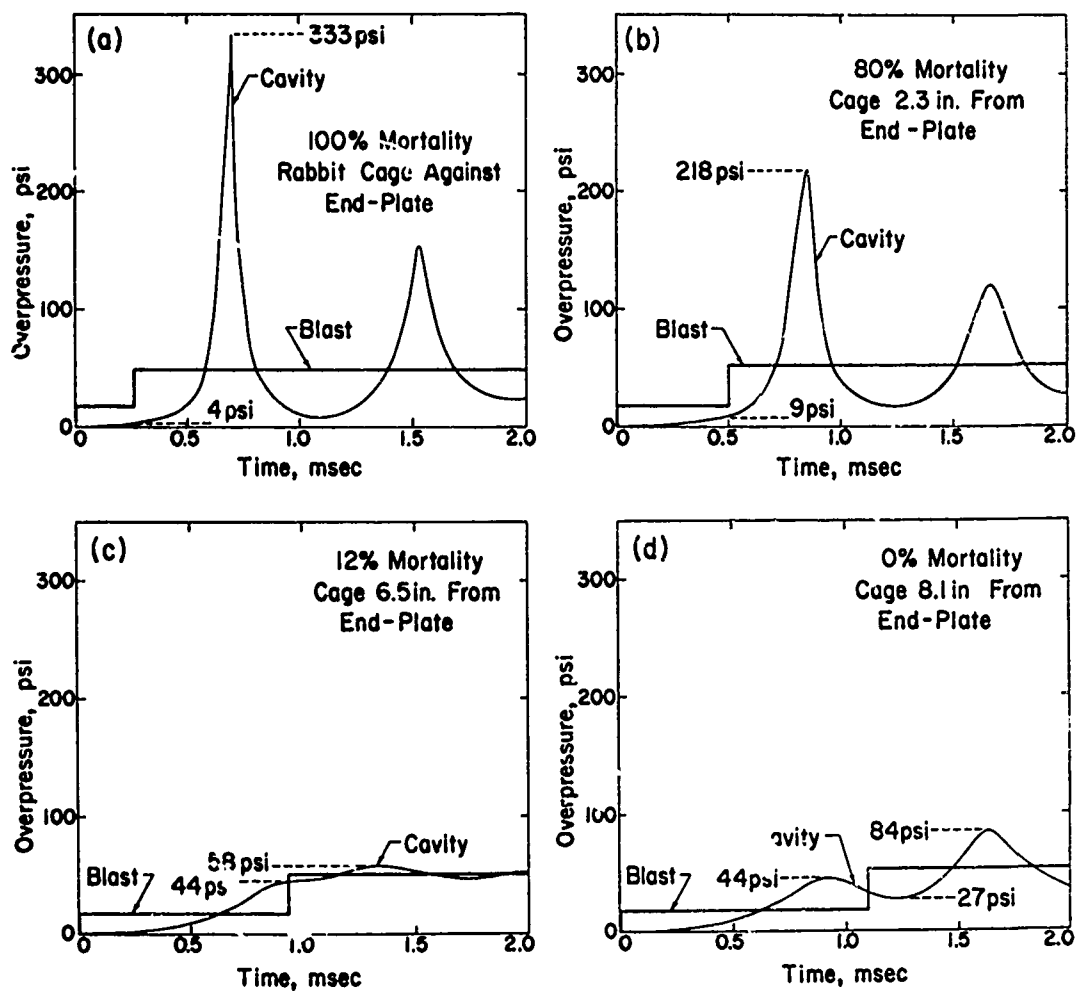


Fig. 11. Computed intrathoracic overpressure vs time for rabbits exposed at various distances from the end-plate of a shock tube to an incident and a reflected shock of 17.2 and 52.1 psi, respectively. Taken from Reference 2.

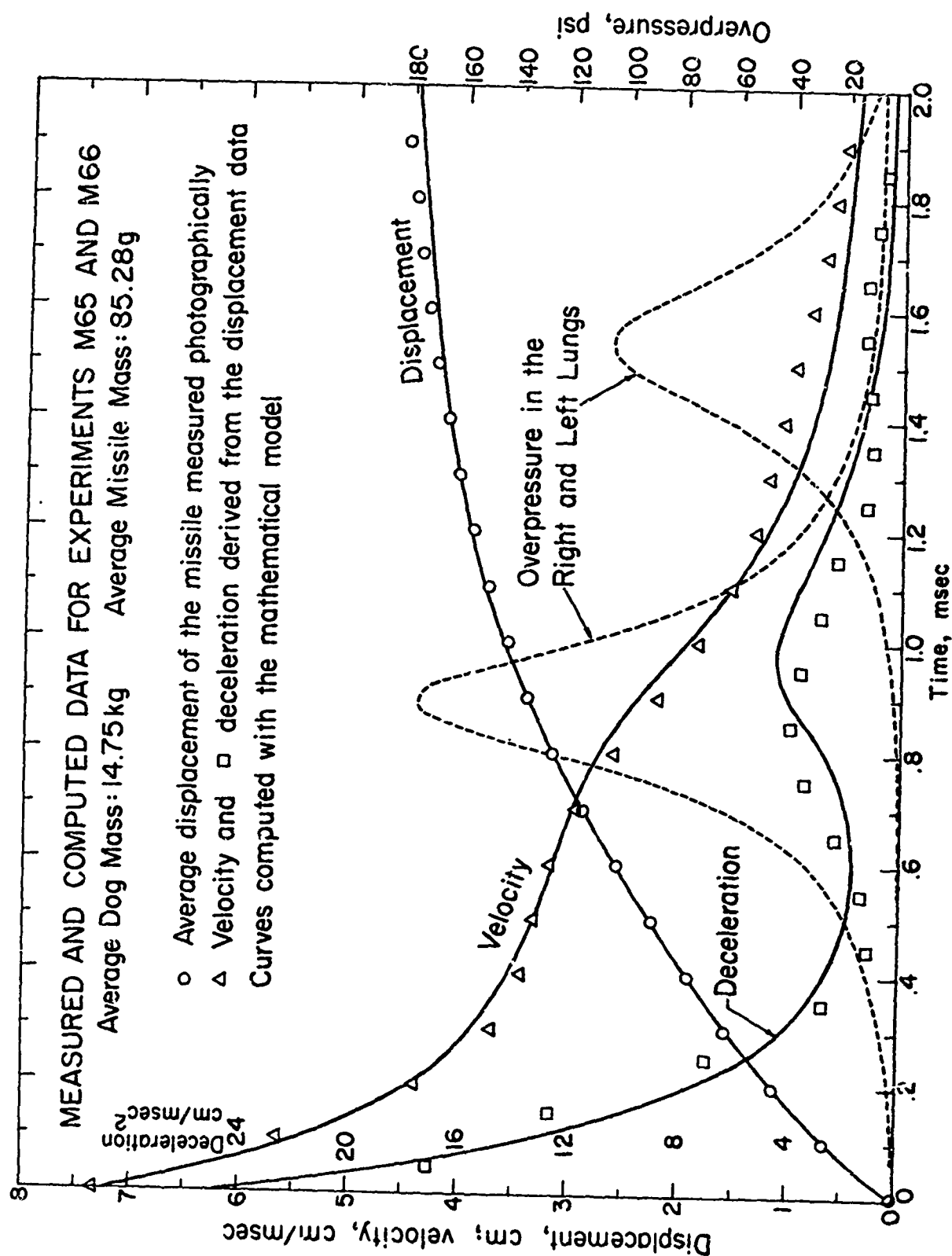


Fig. 12. A comparison of computed and measured displacement parameters for a nonpenetrating missile experiment. Taken from Reference 3.

time when the lung pressure has reached a peak value due to the incident wave; compare Fig. 11 (b), 11 (c), and 11 (d). The available experimental data do not indicate that the mortality, like the computed peak internal pressure, decreases to a minimum as the animals are moved away from the reflecting surface and then increases to a smaller secondary maximum (the primary maximum occurring when the animals are against the end-plate) as the distance is further increased, beyond which it again decreases with increasing distance. This is not surprising, however, since these data are limited and the predicted secondary maximum is rather small. Although the predictions agree qualitatively with the tentatively proposed criterion of peak internal pressure as a predictor of mortality (in that by moving away from the end-plate both measured mortality and predicted peak internal pressure decrease), the calculations to date are insufficient to determine if this criterion is quantitatively consistent with the step-load mortality data.

#### NONPENETRATING MISSILE APPLICATIONS

Experiments<sup>3</sup> have been performed in which flat circular (7-cm diameter) missiles of various masses were impacted against the rib cage near the mid-lateral point of the right side of the thorax of a dog which was positioned on a pendulum-like mount that was free to swing. The time-displacement histories of the missiles were obtained from motion pictures. Numerical differentiation techniques were used to obtain the velocity and deceleration of the missiles from the displacement data. The model in Fig. 9 was used to predict the motions of the missiles and the internal pressures. The methods for estimating

the additional animal parameters that were needed for these calculations have been discussed previously.<sup>3</sup> Fig. 12 shows the measured and calculated displacement, velocity, and acceleration for a missile striking a dog as well as the calculated pressures in both lungs. It can be seen that the computed and measured motions of the piston agree remarkably closely. Unfortunately, no internal pressure record was obtained on this experiment. Figure 13 shows the measured and calculated internal pressures on a similar missile impact experiment.<sup>7</sup> Note that the measured peak pressure and time to peak agree closely with the averages of the values computed for the two lungs.

The post-impact lung mass as a percentage of body mass was used as an index of damage in these experiments, particularly since there were insufficient mortalities for a rigorous lethality analysis. It was shown that experimental conditions which produced a constant value for this percentage resulted (when they were analyzed on the model) in an approximately constant value of average (for the two lungs) maximum overpressure.<sup>3</sup> Thus, as in the study of air blast, it was found that injury correlates reasonably well with predicted average peak overpressure in the lungs. Although the data are scanty, it appears that the predicted peak internal pressure associated with 50 percent mortality from exposure to a blast wave is higher than the corresponding pressure from impact with a nonpenetrating missile.

#### MAMMALIAN SIMILARITIES

It has been established (see Fig. 8) that in regard to primary blast effects the mammals can be divided into two approximately similar groups which we have designated as large and small mammals.

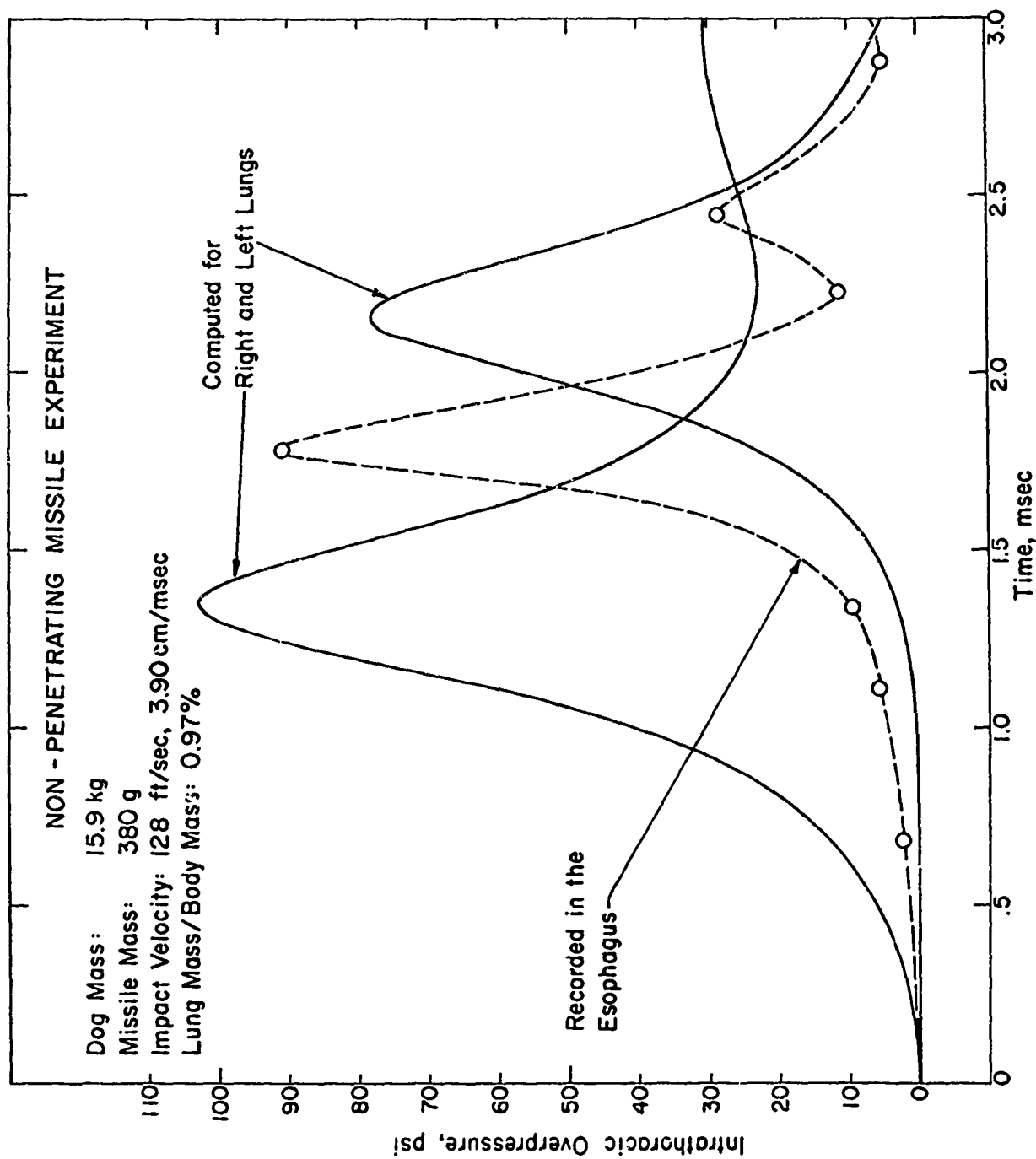


Fig. 13. A comparison of computed and measured internal pressures for a nonpenetrating missile experiment.

However, the rationale for this dichotomy remains unknown. One might ask: Is this division observable in regard to other biological responses or some physical features of the mammals? The reason for asking this is not so much in the hope of confirming the observed division as it is in the hope that these other responses or features could suggest that an untested species (i.e., a species which has not been used in air-blast experiments) is more likely to be similar to the species in one group than it is to those in the other, and might further suggest the existence of additional groups, or subgroups of the known groups, as yet unobserved. The physical features of the mammals that have been considered in this regard were those concerned with the thorax, since it was supposed that these would be the features most likely to correlate with blast tolerance. It has been determined that average lung density and gaseous lung volume divided by body mass (both quantities which should be constant for similar species) seem to show the same division of the mammals.<sup>2</sup> These quantities are plotted in Fig. 14 as a function of animal body mass, and lines have been drawn to show the average values of the quantities for each group. It can be seen that the large mammals have relatively larger gaseous lung volumes and less dense lungs than the small mammals. Note that both the monkey (assumed to be rhesus) and man points are reasonably close to the values for the other species of the large-mammal group. The LD<sub>50</sub> square-wave overpressure values ( $P_{sw}$  values from Fig. 8) are also plotted as a function of body mass in Fig. 14, and the chicken point has been included for reference.

Another biological response (i.e., in addition to the response to air blast) in which the mammals have been observed to divide into



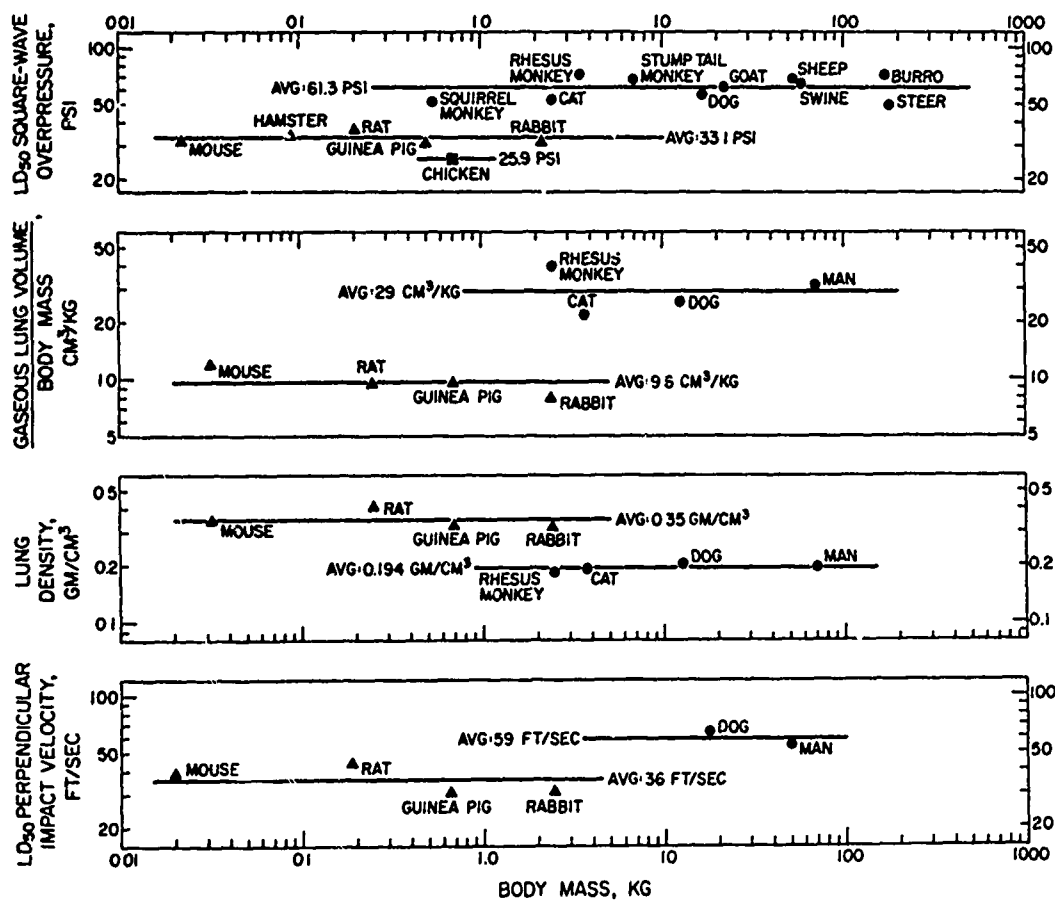


Fig. 14. Animal body mass vs

(1) LD<sub>50</sub> square-wave overpressure for  $P_0 = 14.7$  psi,  
 (2) average gaseous lung volume divided by animal body mass, (3) average lung density, and (4) LD<sub>50</sub> velocity for perpendicular impact with a non-yielding surface. Note that in each case the mammals are divided into two groups. Average values of the various parameters are indicated for both groups.

two approximately similar groups concerns mortality following perpendicular impact with a non-yielding surface. It can be predicted, by using a dimensional analysis or electrodynamical similitude approach, that an approximately constant impact velocity should be required to produce 50 percent mortality in similar species. Experimentally determined LD<sub>50</sub> impact velocities (taken from Ref. 9) are plotted in Fig. 14 as a function of body mass. The average velocity for the mouse, rat, guinea pig, and rabbit is 36 ft/sec while the average for the dog and man is 59 ft/sec. From Fig. 14 it can be seen that lines with a small negative slope would fit the data for both groups somewhat better than the horizontal average-velocity lines drawn. However, the data are insufficient to establish that this apparent decrease in impact tolerance with increasing body mass is significant for either group. It should be realized that the connection between whole-body impact and air-blast exposure is only partial at best. Although the thorax is likely to be injured during impact, it is not necessarily the site of the bulk, or even the most serious, of the injuries.

The lung-volume, lung-density, and impact-velocity data in Fig. 14 are scanty. However, they do provide evidence of three ways in which man is more similar to the large mammals than to the small. Since each of these involves the thorax, it is reasonable to assume that man is more likely to be similar to the large mammals in regard to air-blast tolerance also. Although the data tend to confirm the existence of two groups of mammals, they do not seem to suggest any additional groups or subgroups of the two established groups.

It is interesting to consider Simpson's classification of mammals<sup>13</sup>

(which he indicates is only tentative in many respects) wherein these animals have been divided into a hierarchy of groups of categories in such a way as to try to make the divisions consistent with phylogeny and with animal affinities. In large measure this classification is based upon the assumptions that structural similarity is (1) indicative of common phyletic origin and (2) proportional to natural affinity. The nonextinct mammals, excluding those that lay eggs or have pouches, have been divided into four groups called cohorts: Unguiculata (containing the primates and the other direct descendants of the insectivores which can generally be characterized as mammals with nails or claws), Ferungulata (containing the carnivores and hoofed mammals), Glires (containing the rodents and rabbits), and Mutica (containing the whales and porpoises). It can be seen that all of the small mammals tested are members of the Cohort Glires and all of the large mammals are members of either the Cohort Unguiculata or the Cohort Ferungulata. After reviewing the rationale behind Simpson's classification, it seems not unreasonable to tentatively replace our term small mammals with Glires and our term large mammals with Unguiculata and Ferungulata. It should be noted, however, that we have found no conclusive evidence to suggest that blast tolerance correlates with any of the given subdivisions (such as orders) of the cohorts.

#### PROSPECTUS

The model discussed in this paper has been helpful in assessing responses of the thorax to air blast and impact, and, perhaps in a modified form, it may prove to be useful in regard to other problems

concerning the thorax as well. Several studies involving this model, all of which are either under way or being contemplated, would seem to be particularly worthwhile. In the following brief description of these studies, they have been divided into four categories, each based upon the physical phenomenon energizing the thorax:

Air Blast. An attempt will be made to determine if peak intrathoracic pressure correlates reasonably well with mortality when animals are exposed to an air-blast wave where the overpressure does not rise to its peak value in a single step. If this is not the case, an attempt will be made to find another physical quantity which can be used to predict levels of injury and mortality. Internal pressure records have been obtained<sup>12</sup> in guinea pigs at various distances from a reflecting surface (i.e., in step-load situations) to provide data for this study. When our understanding is sufficient to allow us to predict injury levels in animals exposed in the vicinity of a single reflecting surface, we hope to extend the use of the model to more complicated exposure geometries, such as in a room or some other structure. Also, it is hoped that more internal pressure records can be obtained in monkeys in order to better determine the parameters needed for the model, and to try to resolve the apparent anomalies in the monkey data obtained to date. After the new data are available, it would be desirable to recalculate the curves in Figs. 3 through 5 for  $\gamma$  values other than 1.2.

Impact. A few intrathoracic pressure records have been obtained in dogs during impact with a nonpenetrating missile.<sup>7</sup> These should be more thoroughly compared with model predictions in order to determine better effective animal parameters for impact applications.

Predictions should then be made for impacts involving a more extensive area than that struck by the missiles. Although there are additional sites of injury, it is hoped that the model of the thorax will be useful in assessing mammalian tolerance to whole-body impact.

Rapid Decompression. Although the model could be used to predict the responses of the thorax to any type of rapid environmental pressure changes, only responses to overpressures (i. e., blast waves) have been studied to date. However, data (including intrathoracic pressures) are available on human response to rapid decompression.<sup>10</sup> An attempt should be made to use the model to explain these data.

Underwater Blast. It is known that the lungs are injured when animals are exposed to underwater blast waves.<sup>1</sup> Unfortunately, the author is aware of no intrathoracic pressure data for animals so exposed. Such data could prove to be very helpful if, as would seem desirable, the model is to be used to predict responses of the thorax to underwater blast.

## REFERENCES

1. Andersen, P. and S. Løken, "Lung Damage and Lethality by Underwater Detonations," Acta Physiol. Scand. 72: 6-14, 1968.
2. Bowen, I. G., A. Holladay, E. R. Fletcher, D. R. Richmond and C. S. White, "A Fluid-Mechanical Model of the Thoraco-Abdominal System with Applications to Blast Biology," Technical Progress Report, DASA-1675, Defense Atomic Support Agency, Department of Defense, Washington, D.C., June 1965.
3. Bowen, I. G., E. R. Fletcher, D. R. Richmond, F. G. Hirsch and C. S. White, "Biophysical Mechanisms and Scaling Procedures Applicable in Assessing Responses of the Thorax Energized by Air-Blast Overpressures or by Nonpenetrating Missiles," Technical Progress Report, DASA-1857, Defense Atomic Support Agency, Department of Defense, Washington, D. C., November 1966. Also: Ann. New York Acad. Sciences 152 (Art. 1): 122-146, Oct. 28, 1968.
4. Bowen, I. G., E. R. Fletcher and D. R. Richmond, "Estimate of Man's Tolerance to the Direct Effects of Air Blast," Technical Progress Report, DASA-2113, Defense Atomic Support Agency, Department of Defense, Washington, D.C., October 1968.
5. Clemedson, C.-J. and A. Jönsson, "Distribution of Extra- and Intrathoracic Pressure Variations in Rabbits Exposed to Air Shock Waves," Acta Physiol. Scand. 54: 18-29, 1962.

6. Guerra, E. and B. Günther, "Mechanical and Electro-Dynamic Similitude in Biology," Bol. Soc. Biol., Concepcion, (Chile) 29: 87-91, 1956. Translated by J. W. Palmer, Original title: "Similitud Mecánica y Electrodinámica en Biología," Royal Aircraft Establishment Library Translation No. 1155, March 1966.
7. Hirsch, F. G. and Staff, Lovelace Foundation for Medical Education and Research, Albuquerque, New Mexico, Unpublished data.
8. Holladay, A. E. and I. G. Bowen, "A Mathematical Model of the Lung for Studies of Mechanical Stress," Proceedings of the San Diego Symposium for Biomedical Engineering, 1963, pp 39-50.
9. Jones, R. K., D. R. Richmond and E. R. Fletcher, "A Re-appraisal of Man's Tolerance to Indirect (Tertiary) Blast Injury," To be published in the Proceedings of Panel N-5, Subgroup N of the Technical Cooperation Program Working Group on Therapy Regimes meeting in London, April 16-18, 1969.
10. Luft, U. C. and R. W. Bancroft, "Transthoracic Pressure in Man During Rapid Decompression," J. Aviation Med. 27: 208-220, June 1956.
11. Richmond, D. R., R. V. Taborrelli, F. Sherring, W. B. Wetherbe, R. T. Sanchez, V. C. Goldizen and C. S. White, "Shock Tube Studies of the Effects of Sharp-Rising, Long-Duration Over-Pressures on Biological Systems," Technical Progress Report, AEC, TID-6056, USAEC Office of Technical Information Extension, Oak Ridge, Tennessee, March 10, 1959.
12. Richmond, D. R. and Staff, Lovelace Foundation for Medical Education and Research, Albuquerque, New Mexico, Unpublished Data.

13. Simpson, G. G., "The Principles of Classification and a Classification of Mammals," Bulletin of the American Museum of Natural History 85: i-xvi, 1-350, 1945.
14. White, C. S. and D. R. Richmond, "Blast Biology," Technical Progress Report, AEC TID-5764, Oak Ridge, Tennessee, September 18, 1959.



DYNAMIC SIMULATION TECHNIQUES FOR THE DESIGN OF ESCAPE SYSTEMS:  
CURRENT APPLICATIONS AND FUTURE AIR FORCE REQUIREMENTS

James W. Brinkley and John T. Shaffer

Aerospace Medical Research Laboratory  
Wright-Patterson Air Force Base, Ohio

INTRODUCTION

The applications of biodynamic data within the United States Air Force are numerous and many are vitally important but the most critical of these applications is in the development of emergency escape systems for aircraft. In this application these data determine, to a large extent, the actual capabilities or performance limitations of the systems that are designed. These capabilities or the lack of capabilities ultimately determine whether the aircraft crewman will survive an aircraft emergency. The designer of escape systems must be able to provide a design that is capable of meeting this life or death situation and still produce a design that is lightweight, requires minimum cockpit space, requires little maintenance, withstands high crash loads, and yet provides a reasonably comfortable platform for the performance of flight control, instrumentation monitoring, and other crew duties. In such a design problem, constrained by so many factors, the design criteria must be defined with appropriate precision for there is no latitude for overdesign since it will be reflected in weight, size, and ultimately in the compromise of the performance of the aircraft.

The biodynamic properties of the crewman that directly effect the design of escape systems include those influencing acceleration exposure limits, the inertial response of the human body to acceleration and the response of the body to a high velocity airstream. The relationships between these properties and the performance capability of an escape system can be understood more completely by studying the performance envelope of an escape system. Figure 1

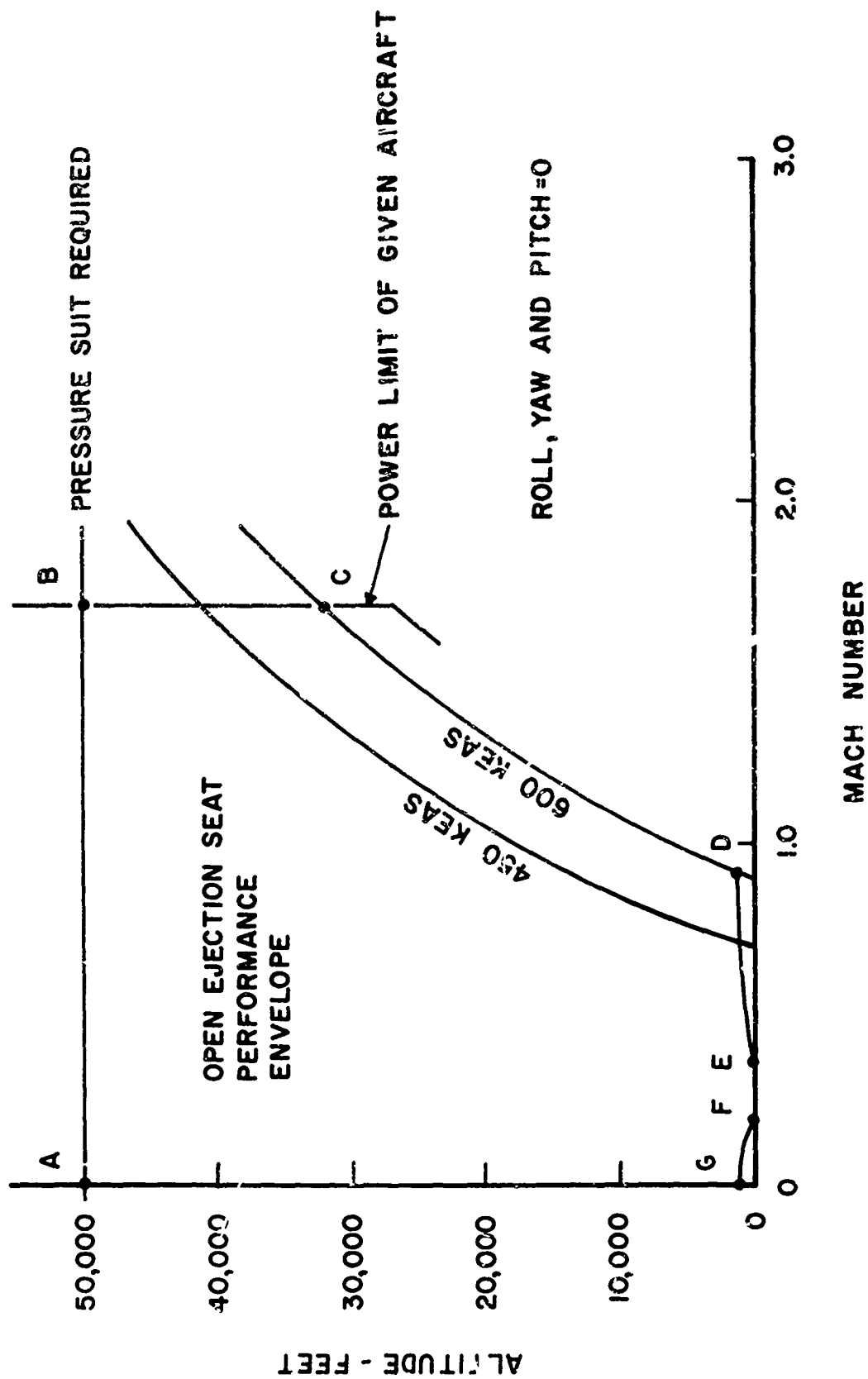


Figure 1. Typical Escape System Performance Envelope (Ref 1).

depicts the performance limits of an open ejection seat for aircraft altitudes and Mach number combinations if the aircraft flight is straight and level at the time of ejection initiation. The region within the area defined by the line connecting the points ABCDEFG is usually accepted as a region where survivable escape is probable. Note that this type of a representation of system performance is a gross simplification as other graphs are actually necessary to more completely describe the capabilities of a system for other combinations of altitude, speed, and aircraft flight conditions, i. e., attitude and sink rate.

The line CD is a limit created by two factors, flailing of the crewman's head and limbs and rapid deceleration of the crewman and seat after entry into the airstream. These factors are interrelated and have caused most of the major injuries and one-half of the fatalities experienced in Air Force ejections initiated at airspeeds above 500 KEAS. Furthermore, all ejections initiated above 500 KIAS during the period of January 1968 to December 1970 have resulted in fatality or major injury to the ejectee (ref 2). Shannon's study of Air Force operational ejection experience in this time period has shown that limb flailing has occurred with violence sufficient to cause injury in ejections at airspeeds as low as the 250-300 KIAS range and is the second largest cause of major injuries associated with escape system use (the primary cause is ejection acceleration), accounting for 12 percent of the total number of major injuries.

Human tolerance to parachute opening shock and the structural adequacy of the parachute canopy form the criteria for establishment of the limit between points E and D. The ejectee must have adequate altitude at the time of ejection to permit deceleration to a velocity which will not produce injurious opening shock or destroy the parachute canopy. Fortunately, the number of parachute opening shock injuries that have been experienced during Air Force operations is low. Shannon reported only five major injuries resulting from parachute opening shock in his study of 384 ejections (ref 2). This area is receiving some renewed interest, however. Parachute canopies currently under development

employ new stronger materials which are capable of withstanding loads as much as 30 percent higher than those that can be tolerated now without destruction of the canopy.

The trajectory height that the escape system achieves is the critical factor in establishing the limit from point E through F and G. This limit represents the airspeeds and altitudes beyond which the trajectory height will not be adequate to provide complete deployment of the personnel parachute prior to contact with the ground. Point G is the maximum aircraft altitude where safe escape can be accomplished without forward airspeed. The improved performance in the area between points G and F results from the fact that the stabilization of the seat by a drogue parachute and deployment of the recovery parachute are aided by the horizontal velocity at the time of ejection. Some escape systems can provide escape in the area between the points F and E in cases where the ejection is initiated at ground level. Such capability is possible for several reasons. First, the ejection catapult produces an impulse that is adequate to achieve a trajectory to meet the parachute deployment altitude requirement. Second, the seat is relatively stable during the burning of the sustainer rocket. Early ejection seat designs employed a ballistic catapult that would propel the ejection seat up guide rails. The seat velocity that could be achieved was limited by the relatively short acceleration stroke thereby available and the human tolerance to acceleration in the  $+G_z$  direction. The capability of this concept was so limited that it was difficult to provide clearance of the vertical stabilizer of the aircraft at higher airspeeds without exceeding human tolerance. Addition of a rocket catapult solved the fin clearance problem and provided the total impulse necessary to reach adequate parachute deployment altitudes during ground level ejections. Nevertheless, safe escape at ground level was not immediately attainable if the airspeed was low since, without an effective drogue parachute, the seat would usually pitch forward and much of the rocket thrust would be used to drive the seat toward the ground. This reaction was caused by the initial pitching moment that was usually required to overcome the tendency for the seat to pitch backward at high speed and the inertial response

of the ejectee to the catapult acceleration which causes a misalignment between the rocket thrust vector and the seat-man center-of-gravity as shown in Figure 2. Studies of the inertial response characteristics of the human body and the incorporation of stabilization systems such as gyro-controlled vernier rockets have led to solutions to this problem.

Additional critical operational problems that are not shown by our review of the escape system performance envelope but which represent serious challenges to biodynamic research are the problems of ground impact acceleration environments associated with encapsulated ejection seats and crew module escape systems and, a similar problem, the accelerations associated with fixed wing aircraft or helicopter crash. These problems are both characterized by acceleration environments of irregular waveform, varying acceleration vector directions, and multiple impacts. The human response to these environments can not be satisfactorily assessed using simple geometric approximations of the waveforms to extrapolate to laboratory data; furthermore, the existing data are generally inadequate to completely define human acceleration exposure limits in any but the  $+G_z$  direction. The importance of correcting this situation cannot be overemphasized since this problem has crucial effects on civilian safety programs as well as the design of protective equipment for military applications.

The use of modeling techniques to guide in the development of pertinent experimental hypotheses and the analysis of experimental data provides a proven method to approach these problems in the most expeditious and meaningful fashion. Furthermore, the use of these techniques provides a method to handle the complexities of the environmental inputs as well as the complexities of the human response and yet do so in a format that can be relatively easily used by designers of safety equipment.

The intent of this paper is to describe applications of this approach that have been made by the Air Force and its contractors and to highlight problem areas where more work is required to meet Air Force requirements for crew safety.

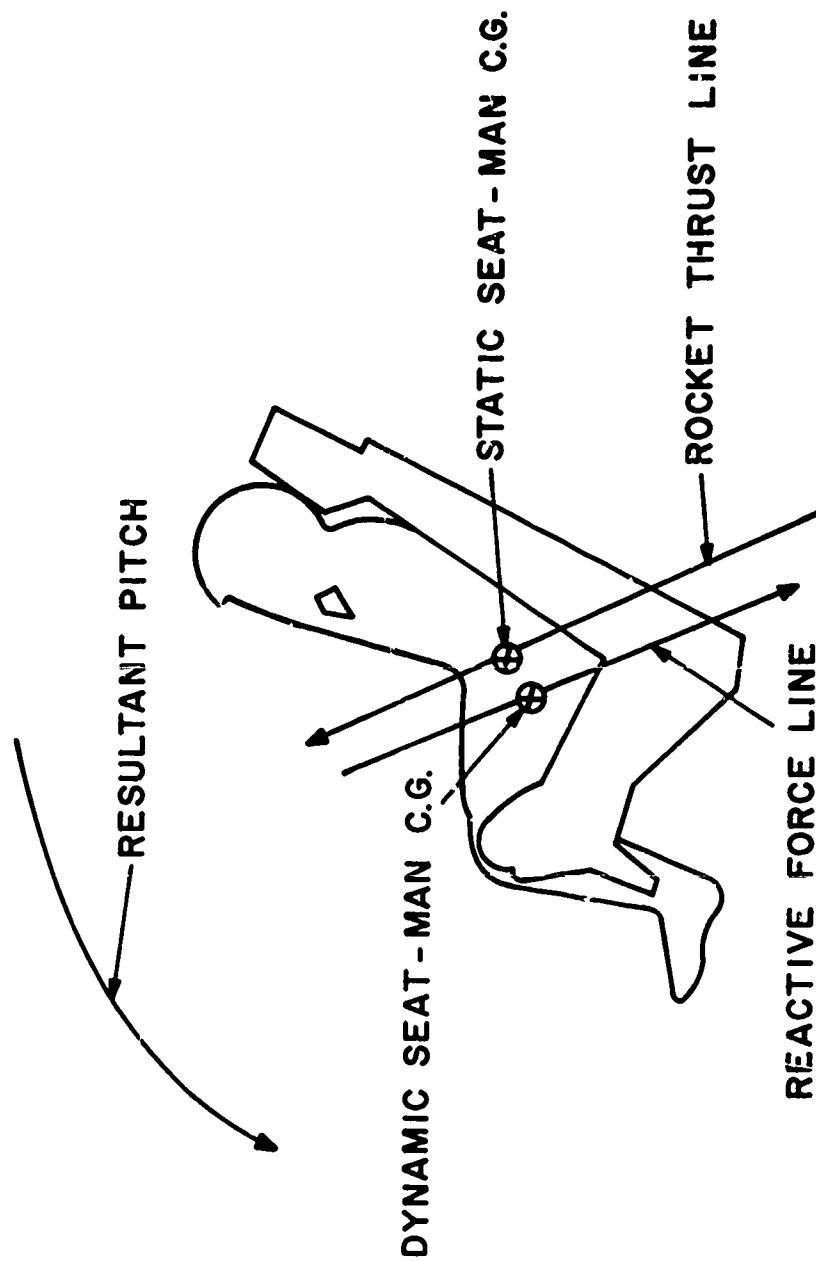


Figure 2. Pitching Caused by Misalignment of Rocket Thrust Vector and Seat-man C.G.

## SPINAL INJURY MODEL

The method currently in use by the Air Force and its contractors to determine exposure limits for short duration  $+G_z$  acceleration produced by ejection catapult is perhaps the most important recent aeromedical contribution to the field of ejector system design. This method is used in the Air Force specifications for upward ejection seats and encapsulated escape systems (refs 3, 4). It involves the use of a simple mechanical model to predict the probability of spinal injury, i.e., compression fracture of the vertebral body segments. The model is a simple mechanical system composed of the common lumped-parameter elements, a mass, a spring and a viscous damper. The response of the model, shown in Figure 3, is computed by solving the equation:

$$\frac{d^2 \delta}{dt^2} + 2 \zeta \omega_n \frac{d\delta}{dt} + \omega_n^2 \delta = \frac{d^2 z}{dt^2}$$

where:

- $\delta$  = deflection (in.)
- $\zeta$  = damping ratio
- $\omega_n$  = natural frequency of the model (rad/sec)
- $z$  = acceleration input (in/sec<sup>2</sup>)

Assuming failure of the vertebral column can be related to the deflection of the structure, the deflection of the model is determined and used to calculate the Dynamic Response Index:

$$DRI = \frac{\delta_{\max} \omega_n^2}{g}$$

where:

- $\delta_{\max}$  = the maximum deflection of the model (in.)
- $g$  = 386 in/sec<sup>2</sup>

Although biodynamic application of this type of procedure was first described by Payne in reference 5 the properties of the model used in the Air Force escape systems specification were determined by Stech and Payne

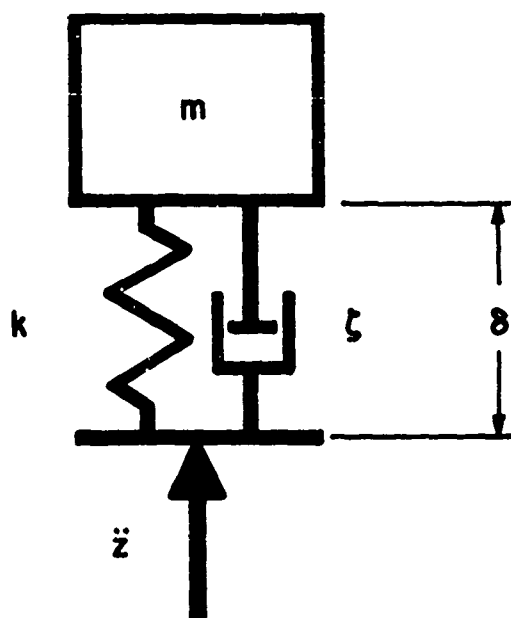


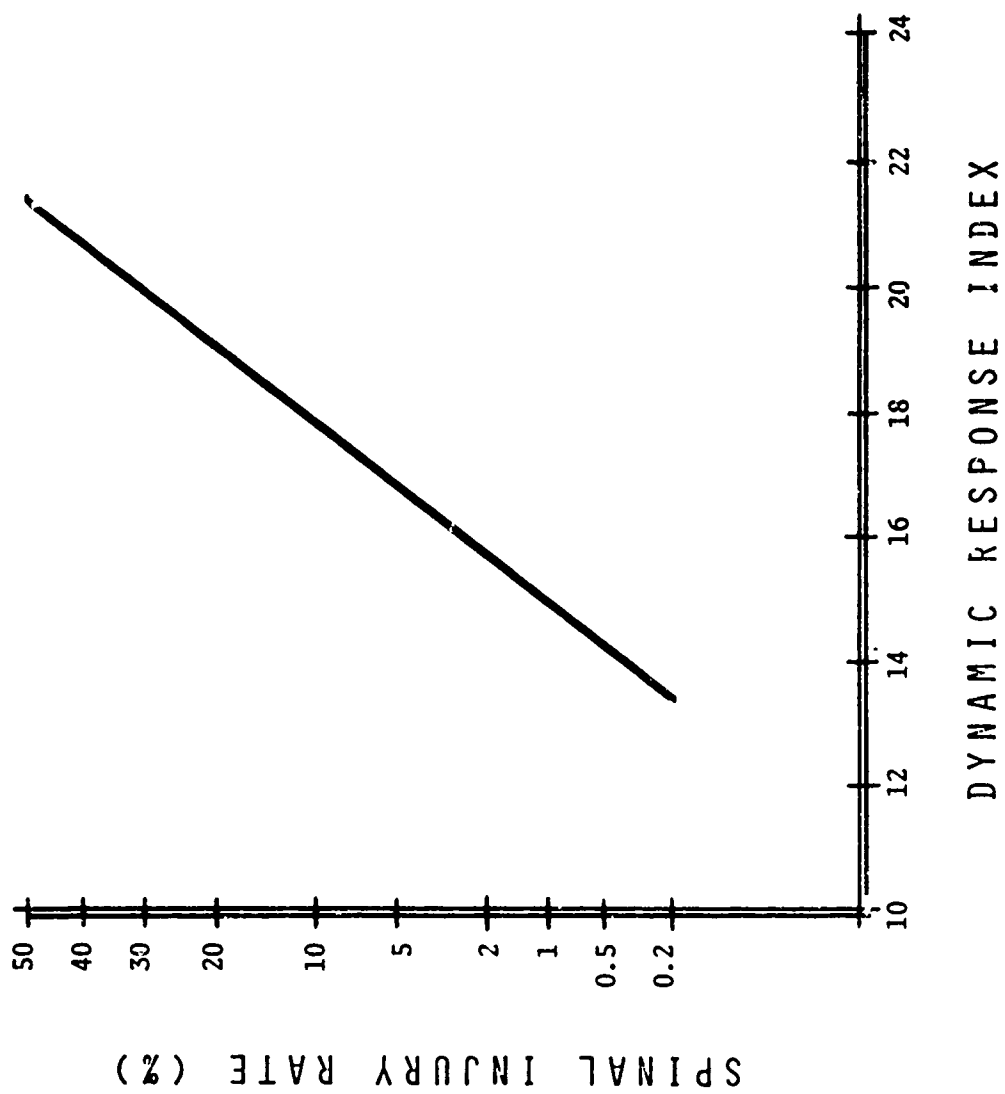
Figure 3. Spinal Injury Model.



using existing experimental data. The reader is directed to reference 6 for the sources of data and the procedures that were used. The values of  $\zeta$  and  $\omega_n$  that were chosen for use in the specifications, 0.224 and 52.9 radians per second, were selected as values that had been computed by Stech and Payne as representative of the mean age of the Air Force flying population (ref 8) at acceleration levels of approximately 20G. The breaking strength of the vertebral bodies was also calculated by Stech and Payne using data obtained from tests of cadaver specimens. To develop an initial estimate of the probability of injury, i. e., probability of a compression fracture of the spine, for given DRI values, Stech and Payne determined the 50 percent probability of injury levels for several age groups. For age 27.9 years, the mean of the Air Force flying population, the 50 percent probability of injury level was estimated to be at a DRI of 21.3.

The probability of injury over a range of DRI values can be calculated assuming a normal distribution and that the relationship between vertebral breaking strength and body weight is random. The validity of a normal distribution is discussed more thoroughly by Payne elsewhere in this Symposium. The assumption of no relationship between breaking strength and body weight is at least partially supported by Shannon (refs 2, 9) in his reviews of spinal injuries due to ejection force. Using these assumptions the estimate shown in Figure 4 was computed by determining the variance of the quotient of breaking strength and body weight distributions (ref 10). Band, in the appendix to Payne's presentation within this Symposium has computed the distribution for several levels of dependence of breaking strength on body weight which serves to provide some insight into the influence of the assumption that has been used.

Before the model could be introduced in the specifications a study was conducted to determine the accuracy of the model when its predictions were compared to operationally experienced spinal injury rates (ref 1). DRI values were calculated using data obtained from ejection catapult test programs. The calculations were accomplished for the case of a 50th percentile weight crewman



PROBABILITY OF INJURY ESTIMATED FROM LABORATORY DATA

Figure 4. Initial Estimate of Probability of Spinal Injury

and his personnel equipment. The catapult acceleration that was used was representative of the performance of the catapult if the pre-ignition temperature is 70°F, the nominal aircraft cockpit temperature. The results of these calculations are plotted in Figure 5. Only compression fractures that were attributed to ejection acceleration by the accident investigation have been considered. The initial estimate of the injury probability distribution based on cadaver data is also shown in Figure 5 and compared to the distribution estimated from the operational data. Since the data obtained from the analysis of operational injuries was not considered adequate to determine a unique distribution, the slope of the line drawn through the data points was established on the basis of the slope of the initial estimate but the breaking strength was increased to coincide with the operational findings.

The spinal injury model was first used as a design and evaluation tool during the development of the F-111 crew escape module. Although this application was originally intended only to be an experimental application, the unusual acceleration environment measured during rocket sled ejections could not be evaluated using more conventional methods. The  $+G_z$  acceleration-time history shown in Figure 6 was measured at the c. g. of the crew module during ejection. The initial portion of the acceleration profile, caused by rocket gas pressure buildup between the crew module and the aircraft fuselage prior to module separation, represented the most difficult problem. The rate of onset was at minimum at least 1000 G/sec while the maximum allowable rate of onset by the existing design limitations was 300 G/sec. Analysis of the pulse using the spinal injury model revealed that the DRI values were relatively lower than had been anticipated and the probability of spinal injury, at least for lower airspeed (450 KEAS), was not considered to be excessive, and thus, a redesign of the crew module and the aircraft fuselage was avoided.

Since adoption of the spinal injury model in Air Force specifications it has been used in the evaluation of several operational problems and is currently being used in the development of the Advanced Concept Ejection Seat for the Air Force Life Support Systems Program Office and in the development

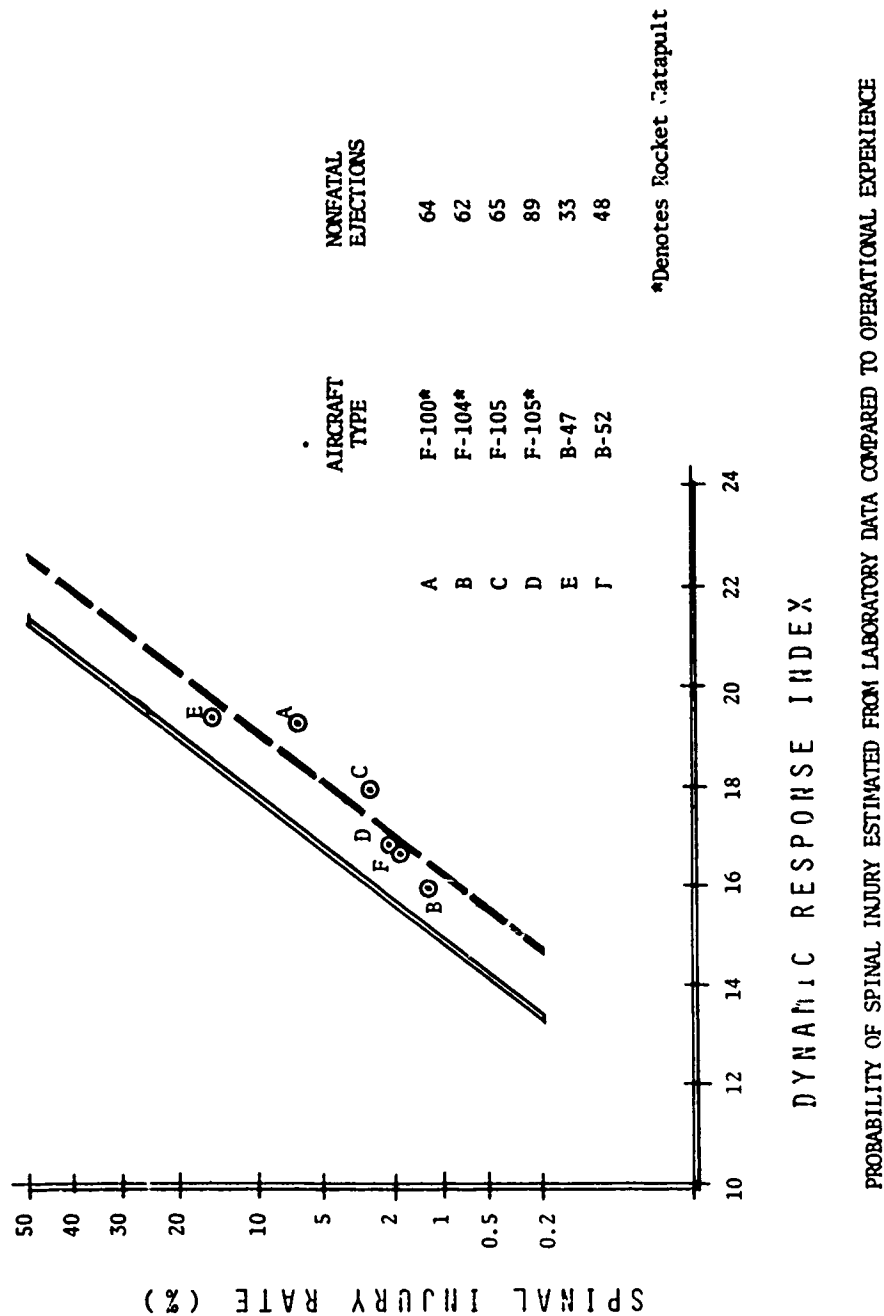


Figure 5. Probability of Spinal Injury Estimated from Operational Experience.

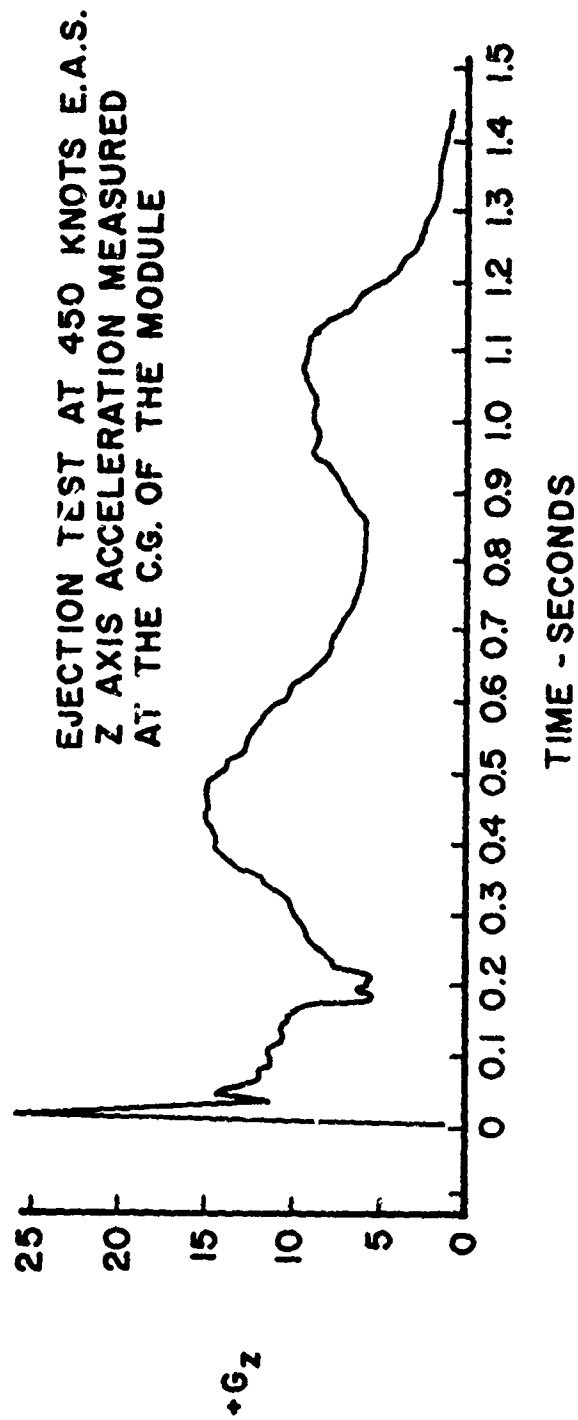


Figure 6. F-111 Acceleration-time History.

of the B-1 Crew Escape Module. The technique is also being applied on a consultative basis in the development of the SIIS-3 ejection seat development program for the Naval Air Systems Command. Carr and Phillips (ref 11) have used the technique to study the design of energy absorption systems for helicopter crash environments. Payne (refs 12, 13) has described the application of the spinal injury model in the development of personnel restraint systems and ejection seat cushions. The application that has had the most pronounced operational effect is the assessment of the spinal injury problem that existed with use of the ejection seat in the F-4 aircraft. During the period of 1966 to 1968 use of the F-4 escape system by Air Force crewman resulted in an unusually high incidence of vertebral compression fracture. The spinal injury rate during this period averaged approximately 41 percent of the total number of nonfatal ejections. An estimated 84 percent of these injuries (34 percent of the total nonfatal ejections) were attributed to the ejection force. These statistics contrasted sharply with the relatively low spinal injury rate averaging approximately 4 percent experienced with other Air Force ejection seats during the same period. The DRI that was calculated for the F-4 catapult was 19 which would be related to an injury rate of approximately 9 percent if the model prediction could be directly applied to this case. However, the ejection seat (Fig. 7) used in the F4 does not permit the crewman's vertebral column to be aligned with the catapult acceleration vector as in other Air Force ejection seats (ref 14). Furthermore, the Air Force procedure of using the D-ring ejection initiation handle to decrease the time required to eject eliminated the upper torso restraint advantage obtained with use of the face curtain initiation technique. The advantages of the face curtain technique have been described by such investigators as Martin, Latham, Boses, and Kazarian (refs 15, 16, 17, 18). Although the spinal injury model predictions of injury are intended to be used in only those cases where there are less than 5 degrees of misalignment, Brinkley and Mohr (ref 19) hypothesized that the injury threshold would be lower in the misalignment case but the variance might be the same. On the basis of this proposition a spinal injury rate of 5 to 10 percent was estimated for a reduced charge catapult producing a DRI of 16, the minimum charge allowable without



Figure 7. F-4 Ejection Seat Compared to other Air Force Ejection Seat.

serious compromise to the performance envelope of the F-4 escape system. Incorporation of the reduced charge catapult in addition to a more easily tightened lap belt and an optimally contoured seat resulted in a major reduction in the spinal injury rate. As of 31 December 1969 the overall spinal injury rate had been reduced to 8 percent of the total nonfatal ejections (ref 20). \* Ejection force was attributed to be the cause of injury in 9 ejections and 1 injury was related to parachute landing impact. The medical investigators designated 3 injuries as caused by either ejection force or landing impact. The marked reduction of landing impact injuries is generally attributed to be the result of incorporation of a lower sink rate parachute, i.e., a 28 ft. diameter canopy rather than the 24 ft. canopy that had been used.

#### INERTIAL RESPONSE MODEL

The primary reason for the development of a model to represent the inertial response characteristics of the entire human body was the practice to represent the crewman as a rigid mass in attempts to study escape system stability analytically. This procedure was known to be erroneous by observation of the trajectory of ejection seats during ground level test firings of these seats at zero airspeed. The pronounced forward pitching of the seat was related to the "body slump" of the dummy or, in the operational case, the crewman and the corresponding displacement of the seat-man center-of-gravity with respect to the rocket thrust vector as discussed earlier. To correct the performance, changes have been made to the rocket nozzle angle on a cut and try basis during development test until a successful recovery could be made. This approach has been quite uneconomical and furthermore it is fallacious as it assumes that the dummy will respond to the acceleration in the same manner as the human body. Coermann's study of the mechanical impedance of both human subjects and anthropomorphic dummies (ref 21) demonstrated that such an approach would be incorrect. The final result of this cut and try approach has been the development of a center-of-gravity envelope which is believed to cover the full range of variations of c.g. due to anthropometrics, personnel equipment configurations

\*See Figure 8.



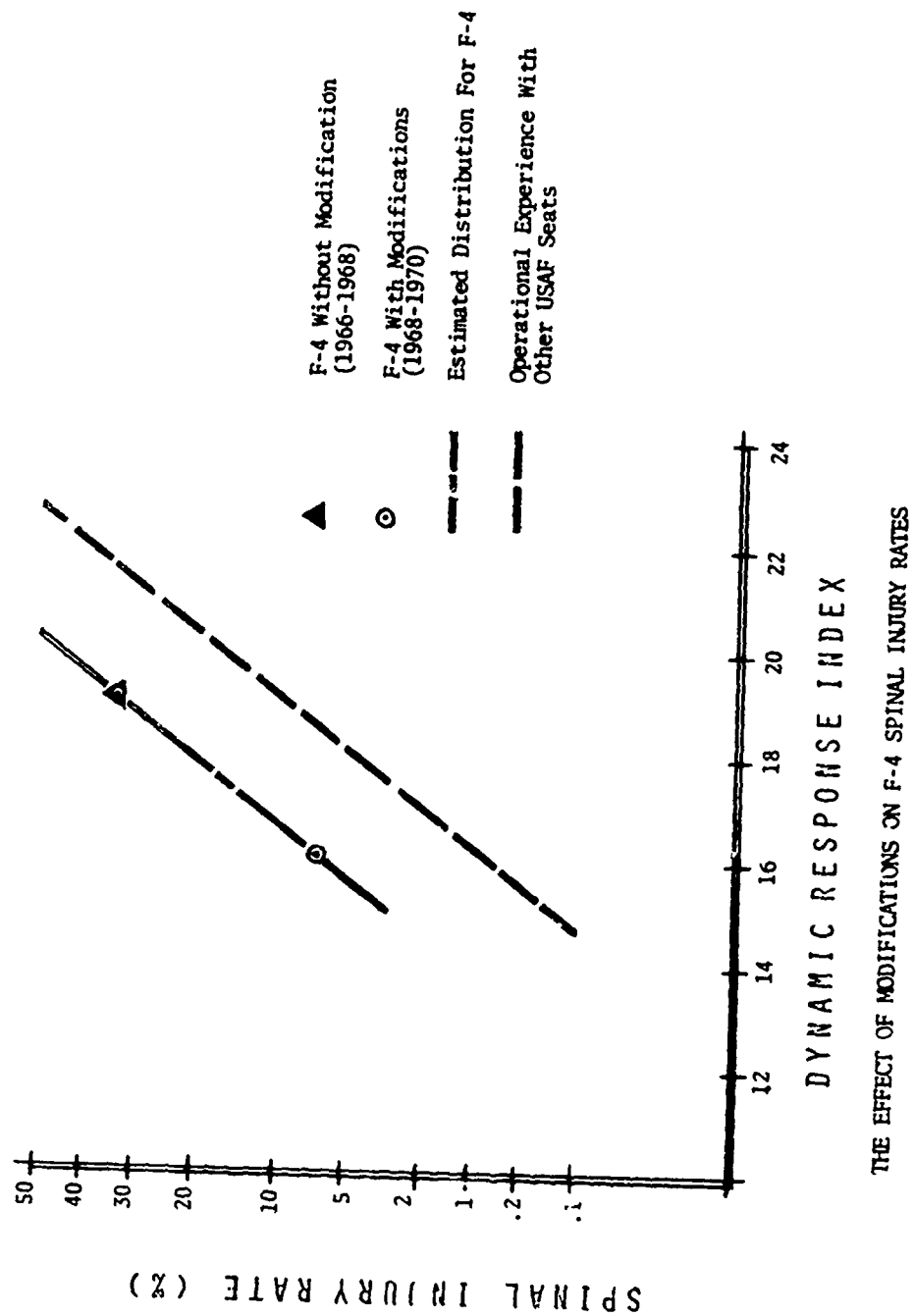


Figure 8. Comparison of Spinal Injury Rates before and after Modification of F-4 Ejection Seat.

and movement of the c. g. due to the acceleration. This empirical procedure ignores the dynamic response characteristics of the human body and therefore, will work only if it works at all, for similar ejection acceleration wave forms.

The initial attempts to provide data to improve the procedure were all directed toward the measurement of the c. g. shift of the human body during acceleration. Douglas Aircraft attempted to determine the maximum excursion of the c. g. by measuring the position of the c. g. during centrifuge tests with human subjects (ref 22). Further work was accomplished by McDonnell Aircraft and the Naval Aircrew Equipment Laboratory to measure the motion of the c. g. by photometrically measuring the motion of targets placed on body segments of human test subjects (ref 24). The centrifuge technique was, of course, limited to the evaluation of steady-state response but beneficial nonetheless as the measurements of the static excursions of the whole body c. g. provide important limit condition data for the eventual development of a dynamical description. The photometric data that was collected must be approached with considerable caution, however. Although it is possible to determine the position of the c. g. of a multisegment system by knowing the weights of the segments and measuring the position of the segments, in actual practice an accurate measurement of the position of the major segments of the human body is impossible to achieve since the motion of the internal viscera cannot be determined photometrically. Nevertheless, the data contained in reference 23 represented a step forward into a more complete understanding of the dynamic phenomenon.

The Aerospace Medical Research Laboratory began experimental work in 1963 to measure the movement of the c. g. of the human body as a function of time. The initial work that was done was fraught with considerable difficulty. Attempts to measure the c. g. shift in the plane perpendicular to the acceleration vector produced erroneous data as described by Brinkley in reference 24. A theoretically accurate scheme was then developed and a test seat supported by six force cells was designed and fabricated as shown diagrammatically in Figure 9. Briefly, the procedure used consisted of measurement of the inertial response of the seat-man combination and the acceleration of the seat, calculation

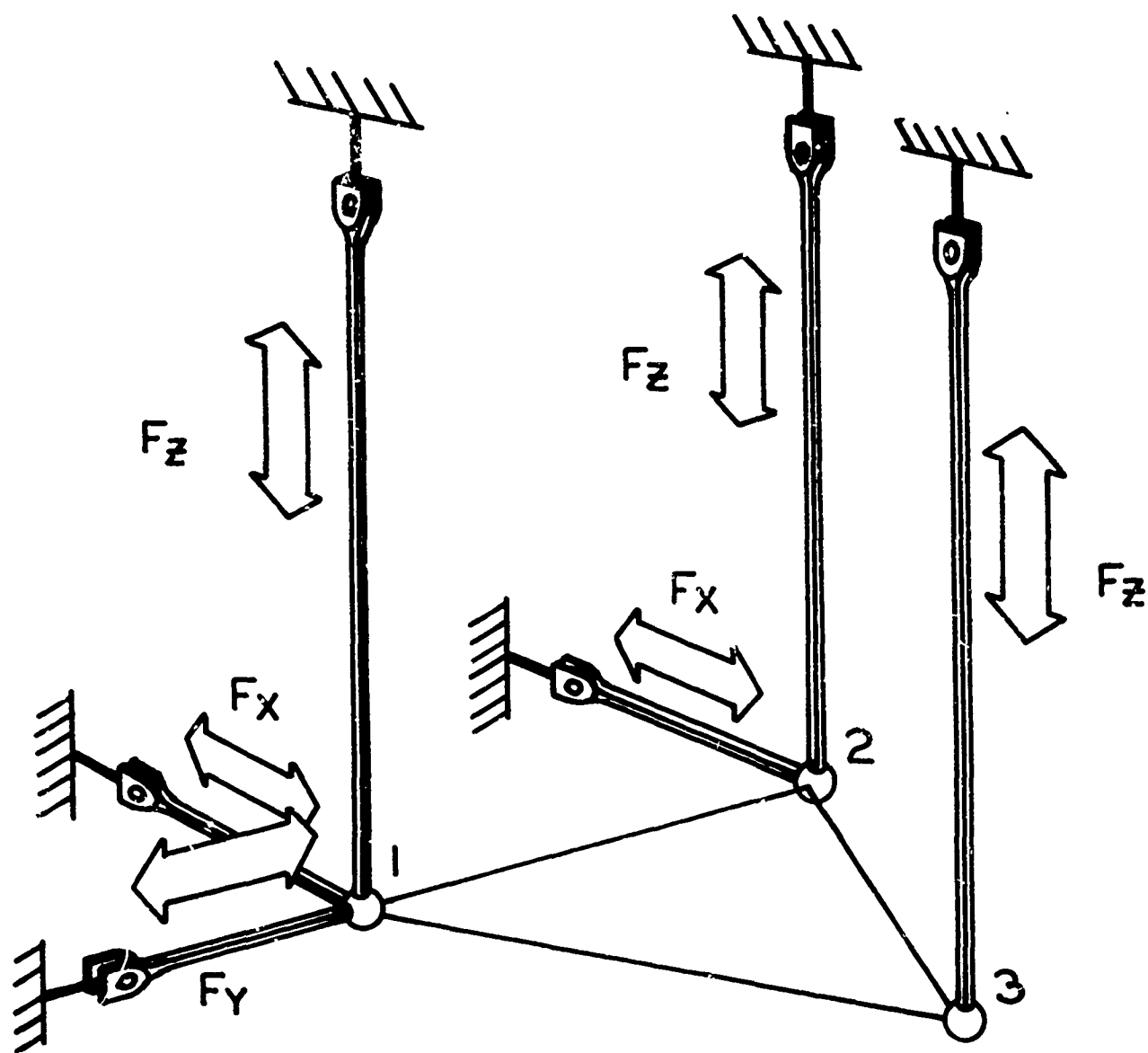


Figure 9. Test Apparatus to Measure Center of Mass Shift.

of the inertial response of the seat by multiplication of the measured acceleration by the mass of the seat, subtraction of the calculated seat force from the measured forces to determine the forces attributable to the human response dividing the human response by the mass of the subject and then integrating the resulting subject acceleration to determine the displacement. Since this procedure involved a double integration over the period of the entire test, including both free-fall and impact, any error in the measurement was accumulated and biased the results to an unacceptable degree. This same procedure has recently been used by Yeager (ref 26) with considerably better results using the Naval Aerospace Crew Equipment Department Linear Accelerator at Philadelphia, Pennsylvania.

After concluding that the displacement of the human c. g. could not be determined within an acceptable degree of accuracy, using the AMRL Vertical Deceleration Tower, other approaches were studied. The simplest method seemed to be to measure the inertial forces exerted by the human subject during the acceleration and to develop a force or inertial response model that could be used by the escape system dynamicist within a multidegree of freedom model of the man-seat combination. The data that were collected were then analyzed by Whitmann and a mechanical analog of the test seat and human subject was developed (ref 27). The analog of the human consisted of a simple spring-mass-damper system with a natural frequency of 10 Hertz, a damping ratio of 0.3 and a mass equal to the entire mass of the test subject. This model has proven to be a good approximation of the whole body inertial forces exerted on the seat structure in the  $+G_z$  direction for impact accelerations ranging from 10 to 14G.

Once a system has been designed using the inertial response model in the design process a demonstration of system performance is usually required to verify the design analysis and qualify the resulting hardware. Emergency escape systems or crash attenuation systems are generally designed to exposure limit conditions with narrow margins of safety and therefore, too hazardous to evaluate using human subjects. The approach that has been pursued by the Aerospace Medical Research Laboratory has been the development of

a mechanical surrogate or a physical analog of the human body. Such a system has been developed for the AMRL under a research contract with the Wyle Laboratories (ref 29). This "anthropodynamic dummy" was designed to meet a number of objectives listed in order of their relative priority:

- a. to duplicate the whole body inertial response characteristics in the  $+G_z$  direction.
- b. to duplicate the whole body inertial response characteristics in the x-z on sagittal plane.
- c. to duplicate the center of gravity and moment of inertia of a human body.
- d. to approximate the kinematic properties of the human at the major joints providing adjustment of muscle tension.
- e. to provide a dummy with a shape similar to the human body so that a gross approximation of the aerodynamic properties could be simulated.

Figure 10 shows the basic skeletal structure of the resulting dummy. Ball joints have been used at four points within the shoulder mechanism as well as in the lower portion of the neck, in the lumbar region of the spine and the ends of the femurs. Articulation at the knees and elbows has been provided by simple pin joints. Friction dampers are used at each of the joints to provide adjustment of joint torques. Adjustment of the inertial response in the  $+G_z$  direction is provided by changing the spring that represents the spinal column. Figure 11 shows the dummy in its final configuration with a solid viscoelastic material covering. Soft rubber bags that can be filled with water or soft rubber are used in the abdominal and thoracic cavities.

Impact tests of the dummy have been conducted by the authors using the Vertical Deceleration Tower to evaluate the  $+G_z$  inertial response simulation. Measurements were made by placing the dummy on a rigid, cast aluminum seat pan which was connected to the seat support structure and impact carriage by three force transducers. Acceleration was also measured at the seat pan. The dummy was restrained to the seat pan by a lap belt. A shoulder harness was

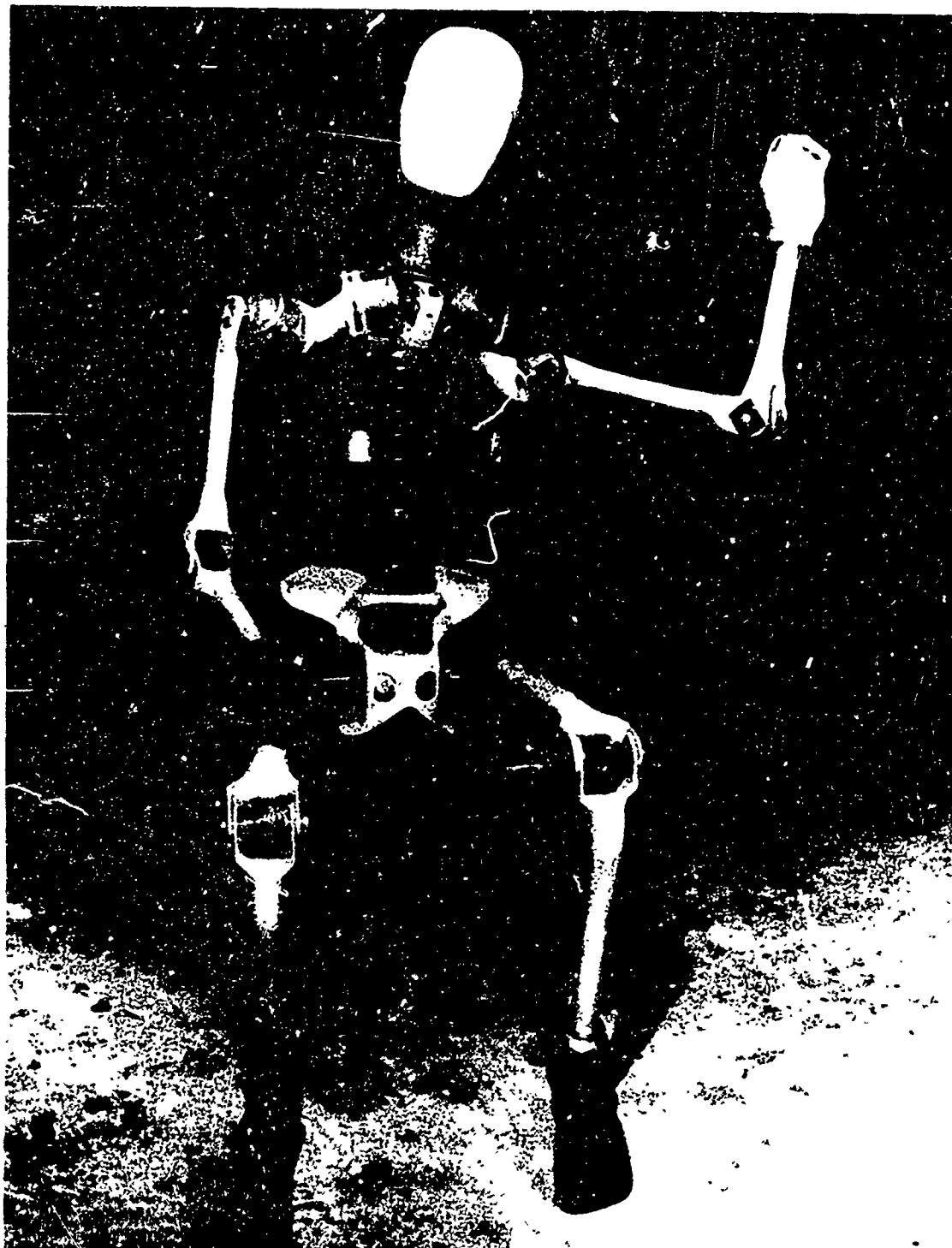


Figure 10. Skeletal Structure of Physical Analog Prototype.

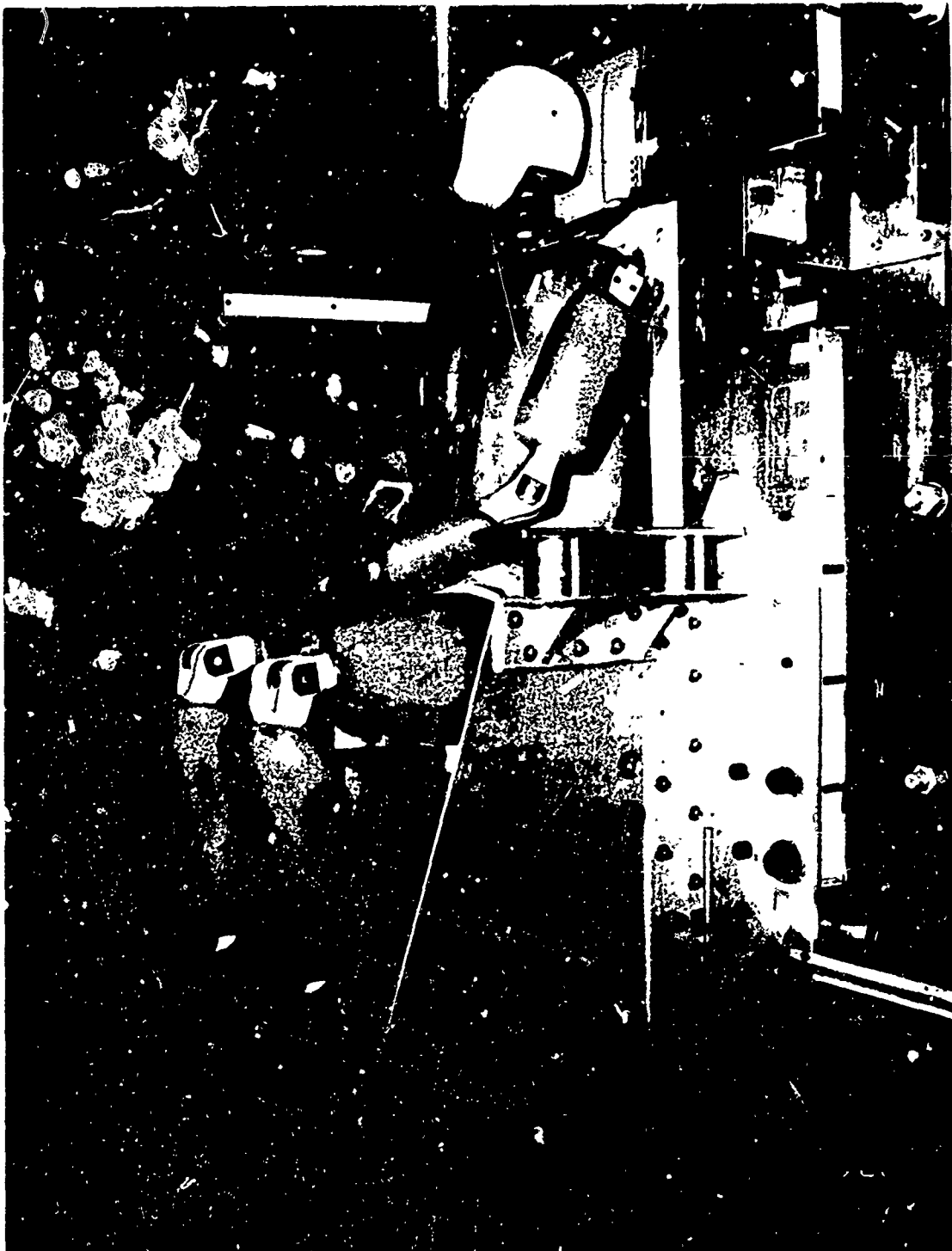


Figure 11. Final Configuration of Physical Analog Prototype.

used but was not tightened; its only function was to prevent the dummy from pitching forward out of the seat. Tests were conducted at 10G and the measured forces were compared to the same measurements taken with human subjects and another anthropomorphic dummy. The comparison of human and the prototype dummy in Figure 12 shows a very good simulation of the peak response but considerable more oscillation than the human at the end of the acceleration. The comparison of the forces measured with the conventral dummy and a human subject shown in Figure 13 dramatically illustrates the large dissimilarity that could grossly effect the performance of an escape system. Moment of inertia and center of gravity measurements were taken on the model by the Air Force Flight Dynamics Laboratory using the procedure described in reference 30. The results of these measurements shown in Figure 14 and Table I compare reasonably well with other measurements made with human subjects in similar body positions (ref 31). Additional tests to determine the  $+G_x$  inertial response characteristics of the dummy prototype are forthcoming.

#### SUMMARY OF REQUIREMENTS

To define the design criteria required to extend the capabilities of contemporary aircraft escape systems and other protective equipment to eliminate, or at least decrease, the injury and fatality rates that have been experienced, a biodynamics research program must encompass the study of a wide range of environmental hazards that are associated with aircraft emergencies. Only a cursory review of the available design guidance and research literature is necessary to understand that the existing biodynamic information does not provide the technology base that is required to completely support a significant advancement in escape system design or crash protection equipment development. For any given stress the criteria that are provided to the designer must define the level of the stress (as a function of time) required to cause a specific injury, the probability of injury associated with the stress level, the effects of combinations of stress such as windblast and aerodynamic deceleration, the effects of sequential applications of stress as well as the effects of other



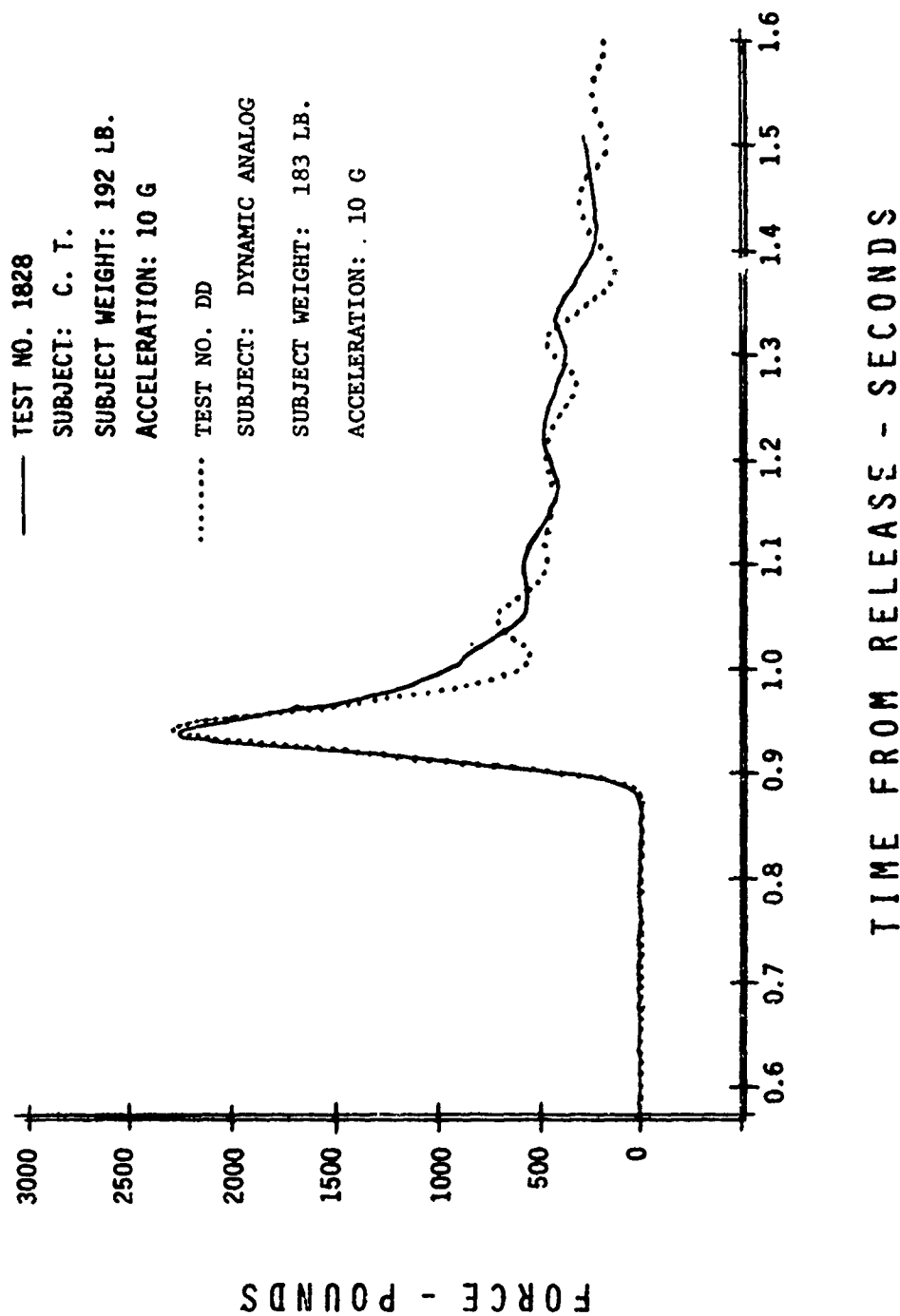
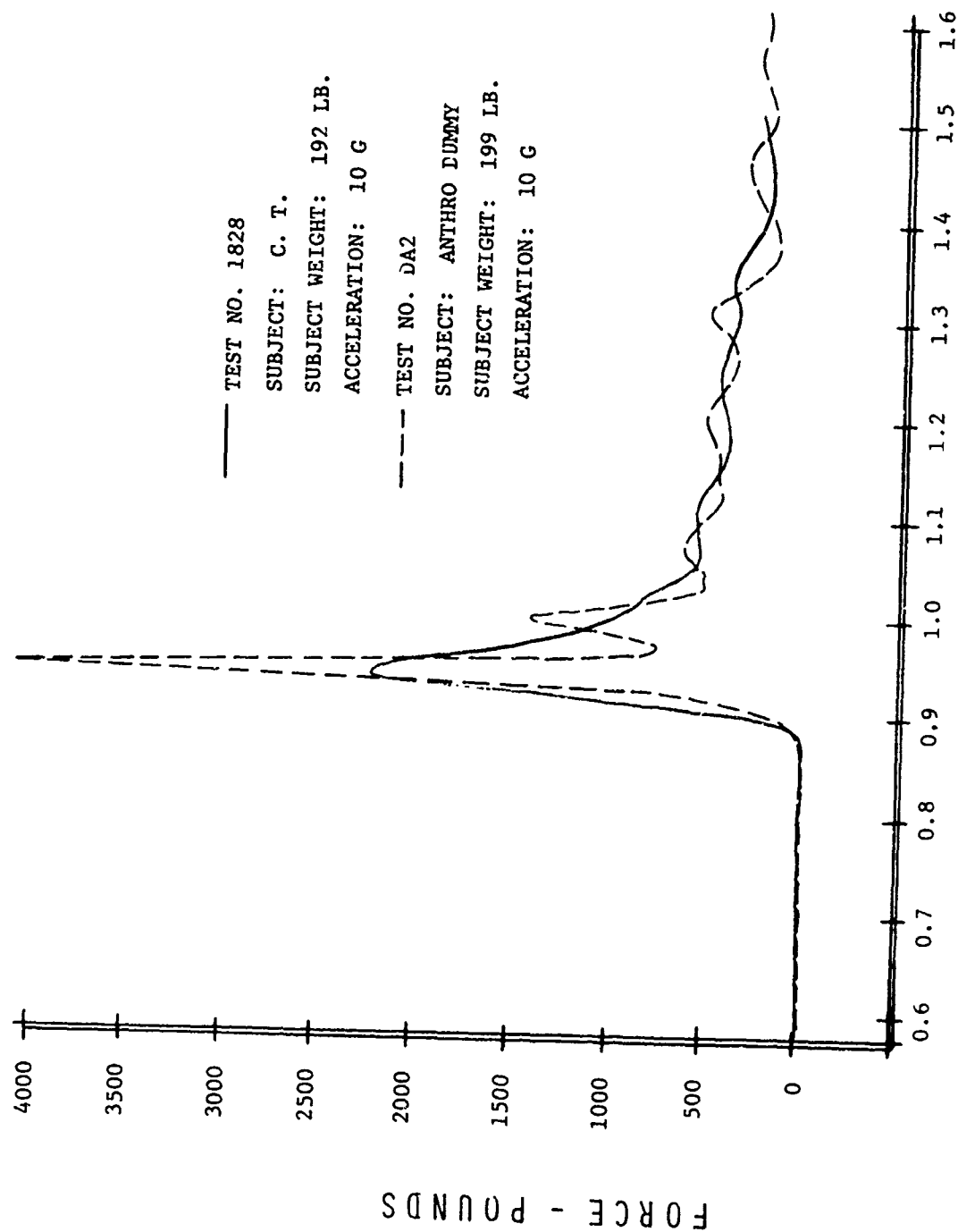
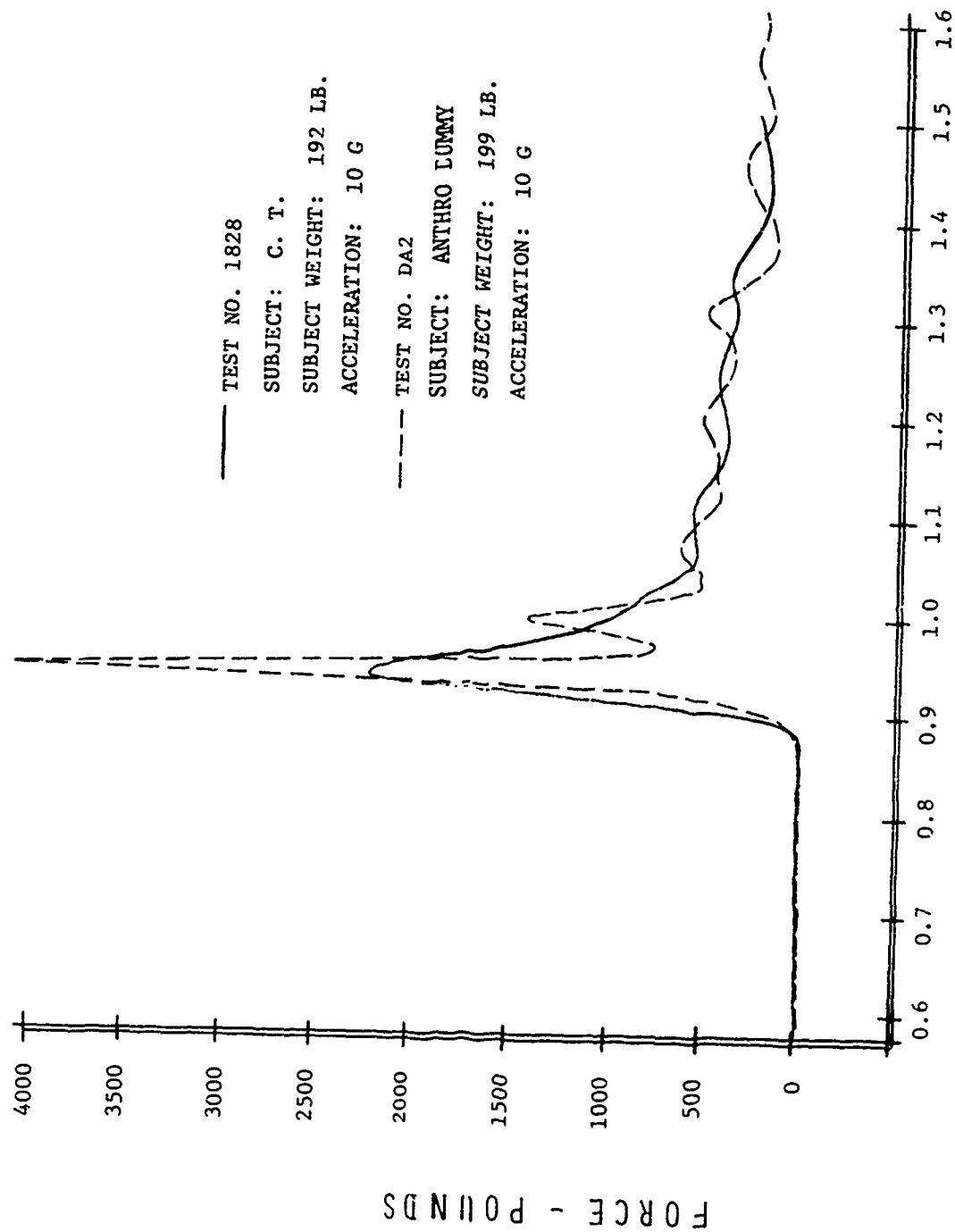


Figure 12. Comparison of Human and Analog Prototype Inertial Response Measurements.



### TIME FROM RELEASE - SECONDS

Figure 13. Comparison of Conventional Dummy and Analog Prototype Response Measurements.



### TIME FROM RELEASE - SECONDS

Figure 13. Comparison of Conventional Dummy and Analog Prototype Response Measurements.

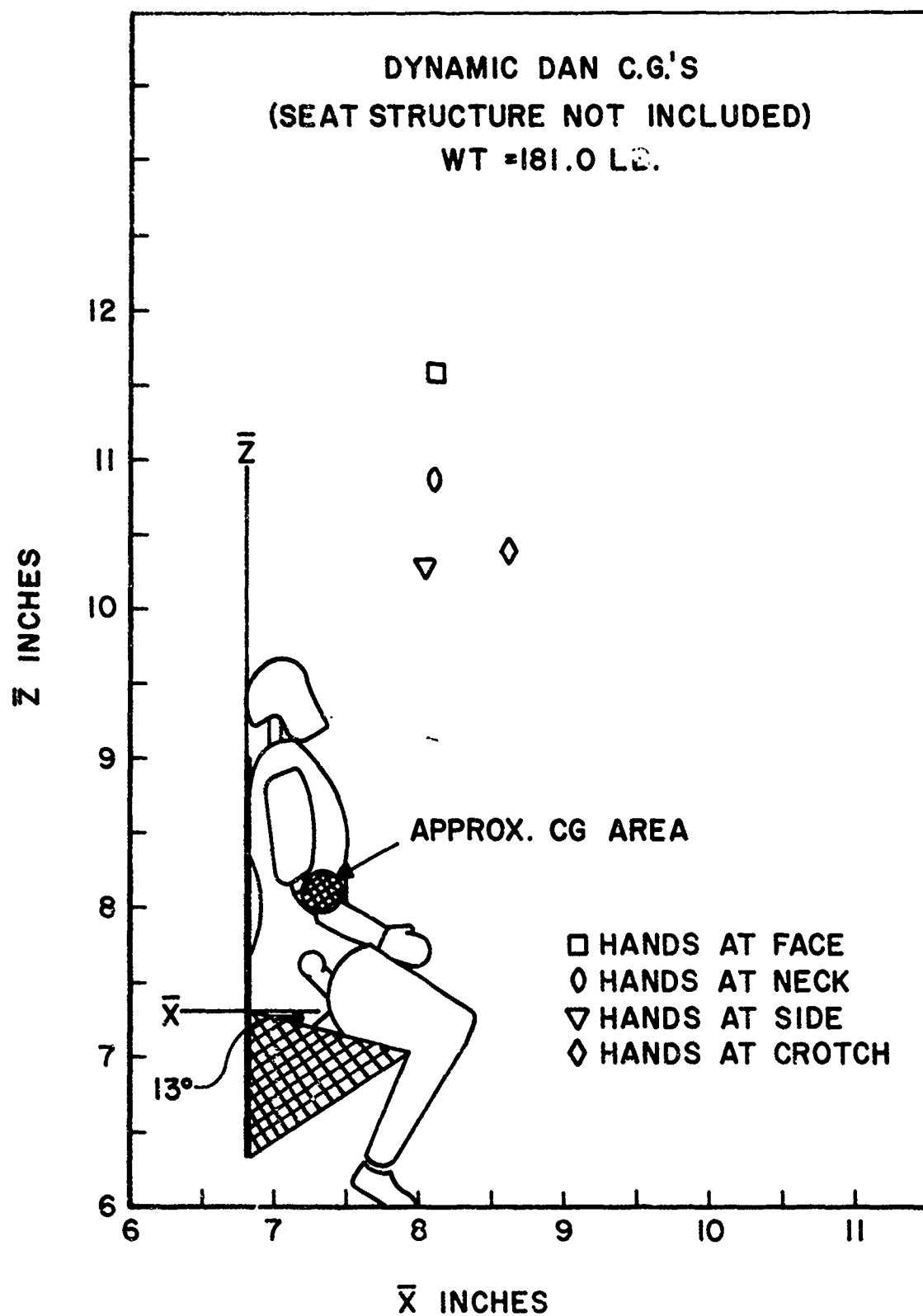


Figure 14. Positions of Center of Gravity of Analog Prototype for Four Positions.

	Weight Lbs.	$I_{yy}$ (Pitch) $2$ lb-ft-sec	$I_{xx}$ (Roll) $2$ lb-ft-sec	$I_{zz}$ (Yaw) $2$ lb-ft-sec	$\bar{x}$ inches	$\bar{y}$ inches	$\bar{z}$ inches
F-106 Seat - Dynamic Dan	332.6	17.06	16.03	7.56	11.18	0.16	19.95
F-106 Seat - 95th Pct.	354.4	19.88	19.73	8.41	10.62	0.24	19.85
F-106 Seat - 5th Pct.	285.4	15.46	14.08	7.29	10.00	0.14	18.51
Dynamic Dan - Hands at Face	181.0	9.08	7.07	1.29	8.14	0.66	11.57
Dynamic Dan - Hands at Neck	181.0	7.26	5.50	1.04	8.16	0.36	10.86
Dynamic Dan - Hands at Side	181.0	7.92	5.47	0.96	8.06	0.69	10.30
Dynamic Dan - Hands at Crotch	181.0	7.94	5.66	1.00	8.64	0.49	10.39

TABLE I

variables such as crew age and conditioning, personal equipment configuration, restraint system dynamics and escape system stability. The design criteria that are available for the  $+G_z$  direction represent the closest approximation to this type of comprehensive description. Although considerable research has been conducted to define the human response to the short duration acceleration environments generated during the escape sequence, only vaguely defined exposure limit criteria are available for body axes other than the  $+G_z$  direction. The operationally critical modes of injury\* remain to be defined for each of the other acceleration directions before any serious attempt can be made to provide more comprehensive descriptions.

More work is necessary to fully determine the effects of body support and restraint systems not only with respect to their ability to maintain body position but to the manner in which they modify the acceleration environments transmitted through them. The results of this work must be reduced to practical design and evaluation guidance. Efforts in this area have suffered from two major deficiencies. First, we have not been able to satisfactorily determine the appropriate dynamic properties of the restraint and support materials and then define their effects in a given design configuration; for example, in a specific restraint system configuration the interplay between the properties of the webbing material, the harness geometry and elasticity of the restrained body obscures the effects of a single factor. Second, without exposure limit criteria it is impossible to evaluate the efficiency of given protection system in any way other than a comparison with other operationally acceptable systems or, in a limited fashion, by evaluation using animal subjects.

---

\* Critical modes of injury are defined herein as those types of injuries that will limit the airman's ability to survive after ejection, prevent him from assisting in his own rescue and/or prevent him from regaining flight status soon after the ejection. From an operational as well as an economical viewpoint a practical limitation of the investigation is necessary since the study of minor injuries resulting from an emergency procedure where the alternative is usually death is certainly pointless.

As in the area of acceleration exposure limit criteria the inertial response characteristics of the human body and body segments are undefined for directions other than  $+G_z$ . The lack of such data not only deters the development of escape systems and impact attenuators as discussed earlier but greatly limits the designers ability to develop lightweight seat structures that will successfully withstand crash loads. Current seat design practice is to assume that the human body is a rigid mass whose load is uniformly distributed over the seating surfaces. Although this procedure is obviously inaccurate and leads to a significant structural deficiency, a correction of this practice will not be made until inertial response data are available and exist in a form that is useful to the seat designer.

The gap that exists between the designers needs and the available data has become so extensive that the most radical departure from conventional design within the last decade, the yankee extraction system design by Stanley Aviation, Inc., has been conceived and developed without such data. As a result, the limitations of this system at higher airspeeds remain undefined and may eventually be determined only by operational experience. This situation isn't too surprising since research on the windblast problem has been practically nonexistent in this country for nearly two decades. Although some action is now being taken by our Laboratory to correct this situation more emphasis will be required within the aeromedical research community to provide the necessary guidance to the designer. Initial efforts must be directed toward the definition of the aerodynamic properties of the human body and body segments. These data must be used to predict the forces acting on the crewman to initiate flailing and then verified in windtunnel tests. Only after the acquisition of such data and the development of predictive aerodynamic models can simple, objective methods of personnel protection be developed.

### CONCLUSIONS

Research in biodynamics has made very significant contributions to the fulfillment of Air Force operational requirements in the area of emergency

escape system design in certain select aspects. The development of dynamic models to describe the response of the human to given environments has provided the aircraft designer with a powerful design and evaluation tool expressed in his own engineering language. Multiple degree-of-freedom models currently used to study the performance of escape systems and the effects of the design of their subsystems can be modified to incorporate the biodynamic model to assess the influence of escape system model outputs on the human. The parameters of escape system components may thereby be varied analytically to study their effect on human response and, conversely, the analysis can also show the influence of human body dynamics upon the performance of the escape system. Since the approach that has been used avoids the specification of exposure limits in absolute "safe" or "intolerable" terms it facilitates a more realistic assessment of the operational impact of a specific design and thus, allows the risk to the using population to be more commensurate with mission requirements.

The models that have been developed for use by the designer have been relatively simple systems for two important reasons. First, although much more complex models have been developed, the biological data that exist have not been adequate to verify these models. Although more complex models may eventually be capable of predicting the precise nature and extent of an injury, in most Air Force design applications such precision is usually of only academic interest. Second, to be useful tools the biodynamic models must be relatively simple to avoid introducing an unreasonable complexity to the overall escape system-man simulation or implying by their complexity a degree of accuracy that is not actually provided or, for that matter, even required in such design analysis calculations.

The scope of development and application of biodynamic models is extensive in the area of escape system design and practically limitless when other applications such as the field of transportation safety are considered. The primary limitation to the extension of their usefulness and the incorporation of the large inventory of modeling techniques that are available from other fields of science and engineering is the availability of meaningful experimental data.



## REFERENCES

1. Brinkley, J. W., "Development of Aerospace Escape Systems," Air University Review, Vol. XIX, No. 5, pp. 34-49, July - August 1968.
2. Shannon, R. H., "Operational Aspects of Forces on Man During Ejection/Extraction Escape in the U. S. Air Force 1 Jan 1968 - 31 Dec 1970," Linear Acceleration (Impact Type), AGARD Conference Preprint No. 88, Harford House, London, June 1971.
3. Military Specification. Seat System: Upward Ejection, Aircraft, General Specification for. MIL-S-9479A (USAF), 16 June 1967.
4. Military Specification. Capsule Emergency Escape Systems, General Requirements for. MIL-C-25969B (USAF).
5. Payne, P. R., "The Dynamics of Human Restraint Systems," Impact Acceleration Stress, National Academy of Sciences-National Research Council, Publication 977, Washington, D. C., 1962.
6. Stech, E. C. and P. R. Payne, Dynamic Models of the Human Body, AMRL-TR-66-157, Aerospace Medical Research Laboratory, Wright-Patterson Air Force Base, Ohio, AD 701 383, November 1969.
7. Coermann, R. R., The Mechanical Impedance of the Human Body in Sitting and Standing Positions at Low Frequencies, ASD Technical Report 61-492, Aerospace Medical Research Laboratory, Wright-Patterson Air Force Base, Ohio, AD 413 478, September 1961.
8. Hertzberg, H. T. E., G. S. Daniels and E. Churchill, Anthropometry of Flying Personnel -1950, WADC Technical Report 52-321, Wright Air Development Center, Wright-Patterson Air Force Base, Ohio, AD 47 953, April 1959.
9. Chubb, R. M., W. R. Detrick and R. N. Shannon, Compression Fracture of the Spine During USAF Ejections, Report No. 3-66, Deputy Inspector General for Inspection and Safety, Norton Air Force Base, California, 21 April 1965.
10. Volk, W., Applied Statistics for Engineers, McGraw-Hill Book Company, Inc., New York, 1958.
11. Carr, R. W. and N. S. Phillips, Definition of Design Criteria for Energy Absorption Systems, NADC-AC-7010, Naval Air Engineering Center, Philadelphia, Pennsylvania, AD 871 040, June 1970.

12. Payne, P. R., Personnel Restraint and Support System Dynamics, AMRL-TR-65-127, Aerospace Medical Research Laboratory, Wright-Patterson Air Force Base, Ohio, AD 624 487, October 1965.
13. Payne, P. R., "Injury Potential of Ejection Seat Cushions," Journal of Aircraft, Vol. 6, No. 3, pp. 273-278, May-June 1969; also published as AMRL-TR-69-134.
14. Mohr, G. C., J. W. Brinkley, L. E. Kazarian and W. W. Millard, "Variations of Spinal Alignment in Egress Systems," Aerospace Medicine, Vol. 40, No. 9, pp. 983-988, September 1969; also published as AMRL-TR-67-232.
15. Martin, J., Report on Research and Development Carried Out by Martin-Baker Aircraft Co., Ltd., in Connection with Ejection Seats for High Speed Aircraft, Martin-Baker Aircraft Company, Ltd., England.
16. Latham, F., "A Study in Body Ballistics: Seat Ejection," Proceedings of the Royal Society of London, Series B-Biological Sciences, Vol. 147, pp. 121-139, December 1957.
17. Bosee, R. A. and C. F. Payne, "Theory on the Mechanism of Vertebral Injuries Sustained on Ejections From Aircraft," Presented at the meeting of the Aerospace Medical Panel of the Advisory Group for Aeronautical Research and Development, North American Treaty Organization (NATO), April 1961.
18. Kazarian, L. E., D. D. Boyd and H. E. von Gierke, "The Dynamic Biomechanical Nature of Spinal Fractures and Articular Facet Derangement," Linear Acceleration (Impact Type), AGARD Conference Preprint No. 88, Harford House, London, June 1971; also published as AMRL-TR-71-17.
19. Brinkley, J. W. and G. C. Mohr, Presentation to Headquarters USAF Air Staff personnel, Pentagon, Washington, D. C., 26 October 1966.
20. Shannon, R. N., Written communication.
21. Coermann, R. R., "Comparison of the Dynamic Characteristics of Dummies, Animals and Man," Impact Acceleration Stress, Publication 977, National Academy of Sciences-National Research Council, Washington, D. C., 1962.
22. Douglas Aircraft Company, Report No. LB 32116, February 1965.
23. Horne, G. B. and J. J. McDonnell, Studies to Determine Dynamic Displacement of Seat/Man Center of Gravity Due to Rocket Thrust, NAEC-ACEL-531, U.S. Naval Air Engineering Center, Philadelphia, Pennsylvania, 30 July 1965.

24. Brinkley, J. W., E. B. Weis, P. J. Martin and N. P. Clarke, Shift of the Center of Mass of a Man-Seat System During Transient Acceleration, Presented at the 35th Annual Scientific Meeting of the Aerospace Medical Association, 11-14 May 1964.
25. Weis, E. B., and F. P. Priamano, The Motion of the Human Center of Mass and Its Relationship to the Mechanical Impedance, AMRL-TR-65-50, Aerospace Medical Research Laboratory, Wright-Patterson Air Force Base, Ohio, AD 637 182, June 1966.
26. Yeager, R. R., Transient Deviations of the Human Body's Center of Mass, Report No. NADC-AC-7012, Naval Air Development Center, Johnsville, Warminster, Pennsylvania, October 1970.
27. Whittmann, T. J., An Analytical Model to Duplicate Human Dynamic Force Response to Impact, ASME Publication 66-WA/BHF-12 and AMRL Technical Report 66-126, Aerospace Medical Research Laboratory, Wright-Patterson Air Force Base, Ohio, AD 724 544, November 1966.
28. Payne, P. R. and E. G. U. Band, Development of a Dynamic Analog Anthropomorphic Dummy for Aircraft Escape System Testing, AMRL-TR-70-10, Aerospace Medical Research Laboratory, Wright-Patterson Air Force Base, Ohio, August 1971.
29. Winsteadley, W. C., T. J. Whittmann and M. C. Eifert, Special Equipment for Measurement of Mechanical Dynamic Properties of Emergency Escape Systems, AFFDL-TR-68-8, Air Force Flight Dynamics Laboratory, Wright-Patterson Air Force Base, Ohio, January 1968.
30. Santschi, W. R., J. DuBois and C. Omoto, Moments of Inertia and Centers of Gravity of the Living Human Body, AMRL-TDR-63-36, Aerospace Medical Research Laboratory, Wright-Patterson Air Force Base, Ohio, AD 410 451, May 1963.

PAPER NO. 3

SOME CURRENT BIOMECHANICAL RESEARCH IN THE UNITED KINGDOM,  
AS RELATED TO THE EFFECTS OF IMPACT AND VIBRATION ON MAN

J. Sandover

Department of Ergonomics and Cybernetics,  
Loughborough University of Technology, England.

Although current research into models is not widely dispersed in the United Kingdom, models are used extensively as an aid to discussion.

Current research includes the dynamics of wrist movements, the use of a model for tractor seat testing, and the properties of body tissue. Work at the author's establishment is directed towards providing a range of information on the human dynamic response to impact and vibration. Studies range from transient and steady-state impedance experiments, to internal and external transmissibility measurements. It is suggested that a wider understanding of variations and non-linearities is required before useful analytic, and synthetic models can be evolved.

## INTRODUCTION

The United Kingdom can lay claim to probably some of the earliest uses of models to explain man's response to shock and vibration. In 1957 Wing Commander Latham (1) used a single degree of freedom model to obtain a better understanding of the problems of pilot ejection. His work was, in fact, very advanced for the time, and he used one of the first analogue computers available in England. Unfortunately, since Latham's studies, there has been little published work on modelling in the United Kingdom. However, the importance of the shock and vibration environments is becoming increasingly apparent. Models are used extensively as an aid to discussion, but current research into models is not widely dispersed.

This paper will describe work relevant to this meeting which is being carried out at some institutions in the United Kingdom. However, other groups are also carrying out research into other aspects of the effect of shock and vibration on man. At Loughborough University of Technology, there is a considerable interest in modelling, and a large proportion of this paper deals with the Loughborough work. It is hoped that this does not indicate any undue bias on the part of the author.

#### THE UNIVERSITY OF STRATHCLYDE

The Bio-mechanics Unit at Strathclyde is the major research centre in the United Kingdom studying the mechanical properties of body tissue. Professor Kenedi will no doubt describe some of the activities of his unit in his paper tomorrow. However, one particular piece of work by Dr. J. B. Finlay (2) on the dynamic properties of skin is of interest. Dr. Finlay carried out skin torsion tests using a 15 m/m diameter disc rotating inside a 23 m/m inside diameter guard ring. The disc rotational movements were sinusoidal, and a servo system was used to ensure constant displacement amplitude. He found that from 0.004 Hz. to 1 Hz. a constant phase relationship existed, with torque leading displacement by  $10^{\circ}$ . From 1 Hz. to 10 Hz. there was a noticeable rise in the phase curve, with a maximum lead of  $15^{\circ}$  at 10 Hz. He found that this constant phase relationship occurred in both the low amplitude case (linear region) and the high amplitude case (non-linear region).

The skin is thus behaving thixotropically (as the synovial fluid, it contains a considerable proportion of long chain molecules). Finlay has pointed out that one should consider the possibility of rate dependent damping in models of the body.

Finlay's results are similar to those of Vlasblom. However, Vlasblom used a constant current driving system which has a constant torque characteristic at low frequencies, but not at high frequencies. Probably for this reason Vlasblom's phase changes at higher frequencies were greater than those obtained by Finlay.

#### THE UNIVERSITY OF EDINBURGH

Dr. Walsh of the Department of Physiology has for some time been interested in body movements during vibration. In a paper given at a recent informal meeting on human response to vibration (Reference 4), Dr. Walsh has described experimental studies of hand movement. General studies of the effects of vibration on tracking performance are made difficult by lack of knowledge of the movement of body parts. Dr. Walsh has attempted to study wrist movements, isolated from the effects of whole body vibration. He used a printed circuit motor to give flexion and extension at the wrist. The printed circuit motor affords a drive system which can be servo-controlled to provide constant torque. Dr. Walsh found that wrist displacement showed a resonance at about 5 Hz. The resonant frequency increased, or decreased as the wrist was stiffened or relaxed respectively. By using velocity feed-back, he was able to induce tremor at the resonant frequencies.

#### THE NATIONAL INSTITUTE OF AGRICULTURAL ENGINEERING

This Institute has long been concerned with the effects of vibration on tractor drivers. In order to assess the value of different anti-vibration seats for tractors, Tomlinson (5) has developed a dummy similar to that of Suggs (6) at Raleigh. The usual approach in this situation is to use impedance techniques to compare the dummy with man. However, Tomlinson is only interested in the value of the seat in attenuating the

tractor vibration, and methods of standardization of measurement of the attenuation. Consequently, Tomlinson rates the acceptability of his model in terms of the transmissibility of the seat using the dummy, compared with that occurring when a man sits on the seat. Tomlinson based his dummy on a Coermann type parallel two degree of freedom model, and then varied the parameters until seat transmissibility was similar to that when carrying a human. Tomlinson's final design had the following parameters:

First System: Mass - 13.1 Kg., Stiffness - 19.7 Kg/cm.  
Damping factor - 0.35, Damped natural frequency - 7.2 Hz.

Second System: Mass - 24.9 Kg., Stiffness - 13.4 Kg/cm.  
Damping factor - 0.30, Damped natural frequency - 3.8 Hz.

A rigid framework and fibre-glass seat moulding brought the total weight of the dummy to 57.3 Kg. The model is therefore equivalent to a 76 Kg. human, if one assumes 75% of body weight carried by the seat. Using different tractor seats, Tomlinson compared seat displacement transmissibility measures obtained for four subjects (of weights 65-75 Kg.) with those for the dummy. The results for a typical seat are shown in Fig. 1. Bearing in mind the range of variation between the subjects, the dummy is obviously useful as a means of simulating man in comparisons of seat transmissibility.

#### THE ROYAL AIRCRAFT ESTABLISHMENT

The Human Engineering Division of the Engineering Physics Department have underway a variety of research programmes dealing with human responses to shock and vibration. A single degree of freedom model concept has been used by J. Rayne (7) in considerations of flying helmet design. Rayne is considering the rotational movement obtainable from linear blows to explain concussion phenomena.

A warning to many research workers in the vibration field is evident in the work of Rowlands (8). He was faced with the need to carry out transmissibility measurements using a dynamic simulator which had extensive harmonic distortion in the acceleration waveform. Rowlands has taken into account the harmonic content at each frequency in order to obtain a better approximation to true sinusoidal transmissibility. Very few vibrators useful for human response studies have a true sinusoidal acceleration waveform and Rowlands' work indicates that one should at least consider the harmonic distortion present. He found that harmonics certainly affect the apparent transmissibility obtained. Non-linear systems can generate harmonics in the output regardless of the input, and Rowlands is considering the use of this phenomenon as a method of indicating non-linearities in the human system.

#### THE UNIVERSITY OF SURREY

Another disturbing fact for researchers in the modelling field arises from work by Mr. Hayden and Wing Commander McKenzie-Pratt (9) in the Mechanical Engineering Department at Surrey. They were attempting to model the human chest response to the type of blow received in a motor-car accident. Initially, they found that the static response of a cadaver chest was similar to that of the live human. However, under dynamic conditions the similarity no longer existed. They applied blows of about 160 m.sec. duration (sine pulses) to the chest of standing subjects. The tolerable force level was about 200 lbs. (4 to 5 times the static tolerance). However, when they applied the same impacts to fresh cadavers (supine in this case) over 50% of the ribs cracked.

The use of cadavers for injury simulations would obviously be wrong in these studies. Bearing in mind the expected similarity between actual bone strength of the cadavers and live subjects, the results suggest that the mechanical responses of the chest are completely different. One would, of course, expect differences due to muscle tone and thorax pressure, but the degree of difference demonstrated should give a severe warning against neglect of these factors. The experimenters are now designing more sophisticated equipment so that the mechanical responses of the human chest can be studied more fully.

#### LOUGHBOROUGH UNIVERSITY OF TECHNOLOGY

In the Department of Ergonomics and Cybernetics there is a strong interest in the effects of shock and vibration on man, with the present research programme centred on investigations into the mechanical responses. However, before considering this work in detail, another piece of work carried out in the Department is of interest.

Mitchelson (10) is concerned generally with the possibility of using upper arm movements to control a lower arm prosthesis, and this preliminary study was to investigate the relationships between upper and lower arm movements. The subject was asked to move a stylus between two points on a board placed horizontal, at 45°, and vertical. Thus, the upper arm had the same total angular movement, but followed different time/displacement patterns. The movements were filmed and the arm co-ordinates obtained from each frame of film.

Mitchelson found that the initial angular velocity of the upper arm movement was least for the vertical hand motion and greatest for the horizontal hand motion. He considers that his results generally support the possibility of the existence of unique relationships between upper and lower arm movements, and therefore the possibility of prosthetic control. Equipment is now being designed that will give direct electrical signals indicative of the arm positions. This will eliminate the time consuming scanning of the cine film required at the moment.

This work is mentioned not so much for its immediate interest, as for the possibilities it introduces for research into the effects of vibration on manual control.



The work of the bio-dynamics group is centred on the need for a better understanding of the responses to the mechanical environment. Studies range from the long and short duration impact situation to the vibration situation.

The Department is under contract to the Ministry of Technology to study the mechanical responses of man during impact with the aim of providing parameters for the design of a dummy to be used in ejection seat testing.

During the development of the investigation, it soon became clear that initially, it would be necessary to restrict the study to the first part of the ejection sequence, when the direction of impact is approximately parallel to the spine.

The need to provide parameters for a piece of hardware leads to important considerations. The high initial cost of a dummy, and the large number likely to be damaged in testing, result in the need for only a simplified representation - two or three degrees of freedom at the most. If the dummy is to be representative of the aircrew population, then it must be capable of taking into account the variation in mechanical response likely to occur. In general, one would expect these two requirements to be mutually opposed, and in consequence a great deal of emphasis has been placed on gaining an understanding of the variations in response over the population concerned.

In order to provide some form of reference where variations are likely to be least, the experiments are initially quite consciously restricted. The subject sits directly on a hard-faced measuring cell with no restraint, so that seat and restraint dynamics are eliminated. Normally the subject is asked to sit erect (at present he is assisted by a free-moving vertical support, and in the future attempts will be made to use electromyographic techniques to standardize posture), although he is also asked to slump slightly so that indications are obtained of the effects of postural change.

The experiments are restricted to low impact levels, so that large numbers of subjects can be used in safety.

Simple anthropometric measurements are taken, and the numbers of subjects will be sufficient to satisfy statistical testing of the hypothesis that variations in response are due to differences in body build.

Measurements are taken of the transient force and acceleration at the buttock-seat interface. The measurements are used to calculate the input mechanical impedance of the human system, and these measures are in turn used to propose analogue equivalents of the human system.

The subject is seated on a table which can fall freely for 2 metres onto a braking system using nylon tear webbing. An ejection seat may be fitted to the table if required. The table runs on two vertical guides, and is fitted with brakes sufficient to hold the table after its first

The work of the bio-dynamics group is centred on the need for a better understanding of the responses to the mechanical environment. Studies range from the long and short duration impact situation to the vibration situation.

The Department is under contract to the Ministry of Technology to study the mechanical responses of man during impact with the aim of providing parameters for the design of a dummy to be used in ejection seat testing.

During the development of the investigation, it soon became clear that initially, it would be necessary to restrict the study to the first part of the ejection sequence, when the direction of impact is approximately parallel to the spine.

The need to provide parameters for a piece of hardware leads to important considerations. The high initial cost of a dummy, and the large number likely to be damaged in testing, result in the need for only a simplified representation - two or three degrees of freedom at the most. If the dummy is to be representative of the aircrew population, then it must be capable of taking into account the variation in mechanical response likely to occur. In general, one would expect these two requirements to be mutually opposed, and in consequence a great deal of emphasis has been placed on gaining an understanding of the variations in response over the population concerned.

In order to provide some form of reference where variations are likely to be least, the experiments are initially quite consciously restricted. The subject sits directly on a hard-faced measuring cell with no restraint, so that seat and restraint dynamics are eliminated. Normally the subject is asked to sit erect (at present he is assisted by a free-moving vertical support, and in the future attempts will be made to use electromyographic techniques to standardize posture), although he is also asked to slump slightly so that indications are obtained of the effects of postural change.

The experiments are restricted to low impact levels, so that large numbers of subjects can be used in safety.

Simple anthropometric measurements are taken, and the numbers of subjects will be sufficient to satisfy statistical testing of the hypothesis that variations in response are due to differences in body build.

Measurements are taken of the transient force and acceleration at the buttock-seat interface. The measurements are used to calculate the input mechanical impedance of the human system, and these measures are in turn used to propose analogue equivalents of the human system.

The subject is seated on a table which can fall freely for 2 metres onto a braking system using nylon tear webbing. An ejection seat may be fitted to the table if required. The table runs on two vertical guides, and is fitted with brakes sufficient to hold the table after its first

rebound from the braking system. To make better simulation feasible if required, the complete apparatus is operable at an angle to the vertical (maximum  $30^{\circ}$ ).

The braking system consists of several strips of "ply-tear webbing" hung across the path of the table (thus cradling it as it falls). This braking system enables a trapezoidal waveform to be synthesized, although the waveform is rather noisy. The acceleration pulse of Fig. 2 shows a typical waveform. The pulse is, in fact, very similar to measured ejection seat accelerations. The equipment is illustrated in Fig. 3.

At the time of writing, insufficient results are available to enable any firm statements to be made about human responses. However, there are sufficient results to indicate the viability of the system. Figures 4a and 4b shows typical modulus, and phase-angle values obtained from four impacts using cast-iron weights totalling 80 Kg. The results indicate satisfactory performance up to about 30 Hz.

Figures 5a and 5b were obtained from five runs with a well built male subject sitting erect. The acceleration level was about 6 g. The impedance spectra are reasonably repeatable, and indicate series resonances at 5 to 6 Hz., and 9 to 10 Hz. However, only the 9 to 10 Hz. resonance is verified by the phase-angle plot. This resonance is in agreement with other authors (Yeager (11) and Wittman (12)). At lower acceleration levels (3 g.) the slight variation at 4 Hz. becomes more apparent. However, contrary to expectations, there is little change in the spectrum when the posture is changed.

Although the scatter is great, the modulus of impedance tends to increase with frequency above 30 Hz. (i.e. 'mass-like' response). This is not expected in simple systems, and has previously been observed by Weis (13). He considered that the effect may be due to restraint artifacts or non-linearities in the human system. The Loughborough equipment eliminates restraint effects, and one is faced with the possibility of non-linearities in the system.

A large number of subjects are being tested in a variety of situations, (long duration, low acceleration and short duration, high acceleration) and this should lead to a clear picture of human response before postulating the responses under the more severe conditions of pilot ejection. In another series of tests, Coermann's vibratory impedance experiments are being repeated. There are surprisingly few reports of large scale vibratory impedance studies. Using improved techniques, it is intended that large numbers of subjects, in a variety of postures will be measured.

This range of experiments varying from short duration impact to vibration, should enable conclusions to be drawn on the degree of non-linearity to be expected, variations in response due to posture, subject anthropometry, etc. With this basic information, more complex experiments necessitating small numbers of subjects can be considered with greater confidence in the results.

It is recognised that impedance techniques are valid only if the system is linear, and even then do not give all the information necessary for complex models (see Payne, 14). However, until methods of measurement of body movement are more accurate, the techniques give a basic datum for considerations of possible non-linearities, and model configurations.

At Loughborough we are anxious to know as much as possible about the transmission of mechanical energy through the body. Included in the experimental programme are such measurements as external transmissibility, internal transmissibility (e.g. intra-abdominal pressure), and muscle tone, so that more can be learnt of the human responses to impact and vibration.

### CONCLUSIONS

The ultimate aim of modelling is surely the development of analytic models (from response studies) which are related to the descriptive models one would expect from a knowledge of the human anatomy and physiological responses.

If this aim is to be attained, then more knowledge is required of the propagation of forces through the body and body parts, the non-linearities to be expected in the human system, and the range of variations to be expected due to posture, subject anthropometry, etc. Although the work in the United Kingdom is widely varied, it is probably a good indication of the range of studies necessary for the evolution of useful models.

## REFERENCES

1. LATHAM, F. 1957. A study in body ballistics; seat ejection. Proc.Roy.Soc. Vol. 147.
2. FINLAY, J.B. 1970. Biodynamic studies of human skin. Doctorial Thesis. University of Strathclyde. Oct. 1970.
3. VLASBLOM, D.C. 1967. Doctorial Thesis. University of Utrecht. (Also at 7th Int.Conf. on Medicine and Bio Eng. Stockholm. 1967).
4. WALSH, E.G. 1970. The use of torque generators to study bodily resonances. Informal meeting on human response to vibration. Loughborough University of Technology. Sept. 1970.
5. TOMLINSON, R.W. and KYLE, D.J. 1970. The development of a dynamic model of the seated human operator. Nat. Inst. Agricultural Engineering. (Private communication of work to be published.)
6. SUGGS, C.W., ABRAMS, C.F. and STIKELATHER, L.F. 1969. Application of a damped spring-mass human vibration simulator in vibration testing of vehicle seats. Ergonomics. Vol. 12. pp 79-90.
7. RAYNE, J. 1970. Royal Aircraft Establishment, Farnborough. Human Engineering Divn. Private communication.
8. ROWLANDS, G.F. 1970. Royal Aircraft Establishment, Farnborough. Human Engineering Divn. Private communication.
9. HAYDEN, F. and MCKENZIE-PRATT, R. 1970. University of Surrey, Dept. Mech. Eng. Private communication of work not yet published.
10. MITCHELSON, D.L. 1970. An investigation into some aspects of the dynamic anthropometry of the arm. Postgraduate thesis. Loughborough University, Department of Ergonomics and Cybernetics. Sept. 1970.
11. YEAGER, R.R., MACHOWSKY, G.V., and SHANAHAN, R.J. 1969. Development of a dynamic model of unrestrained, seated man subjected to impact. Technology Incorporated. NADC-AC-6902.
12. WITTMAN, T.J. 1966. Analytical model to duplicate human dynamic force response to impact. A.S.M.E. 66-WA/BHF-12. (A.M.R.I. -TR-66-126.)
13. WEIS, E.B., CLARKE, N.P., and VON GIERKE, H.E. 1963. Mechanical impedance as a tool in biomechanics. A.S.M.E. 63-WA-280.
14. PAYNE, P.R., and BAND, E.G.U. 1969. A four-degree-of-freedom humped parameter model of the seated human body. Wyle Laboratories, Payne Division. Working Paper No. 59101-6. Nov. 1969.

### ILLUSTRATIONS

- Figure 1: Comparison of displacement transmissibility of dynamic model and male subjects.
- Figure 2: Acceleration and force transients for 62.3 Kg. human, sitting slightly slumped, 60 m/sec.<sup>2</sup>.
- Figure 3: Subject seated on table.
- Figure 4a: Modulus of impedance of 80 Kg. weight (data from four consecutive runs).
- Figure 4b: Phase angle of impedance of 80 Kg. weight (data from four consecutive runs).
- Figure 5a: Modulus of impedance of 62.3 Kg. human, sitting erect, 60 m/sec.<sup>2</sup> (data from five consecutive runs).
- Figure 5b: Phase angle of impedance of 62.3 Kg. human, sitting erect, 60 m/sec.<sup>2</sup> (data from five consecutive runs).

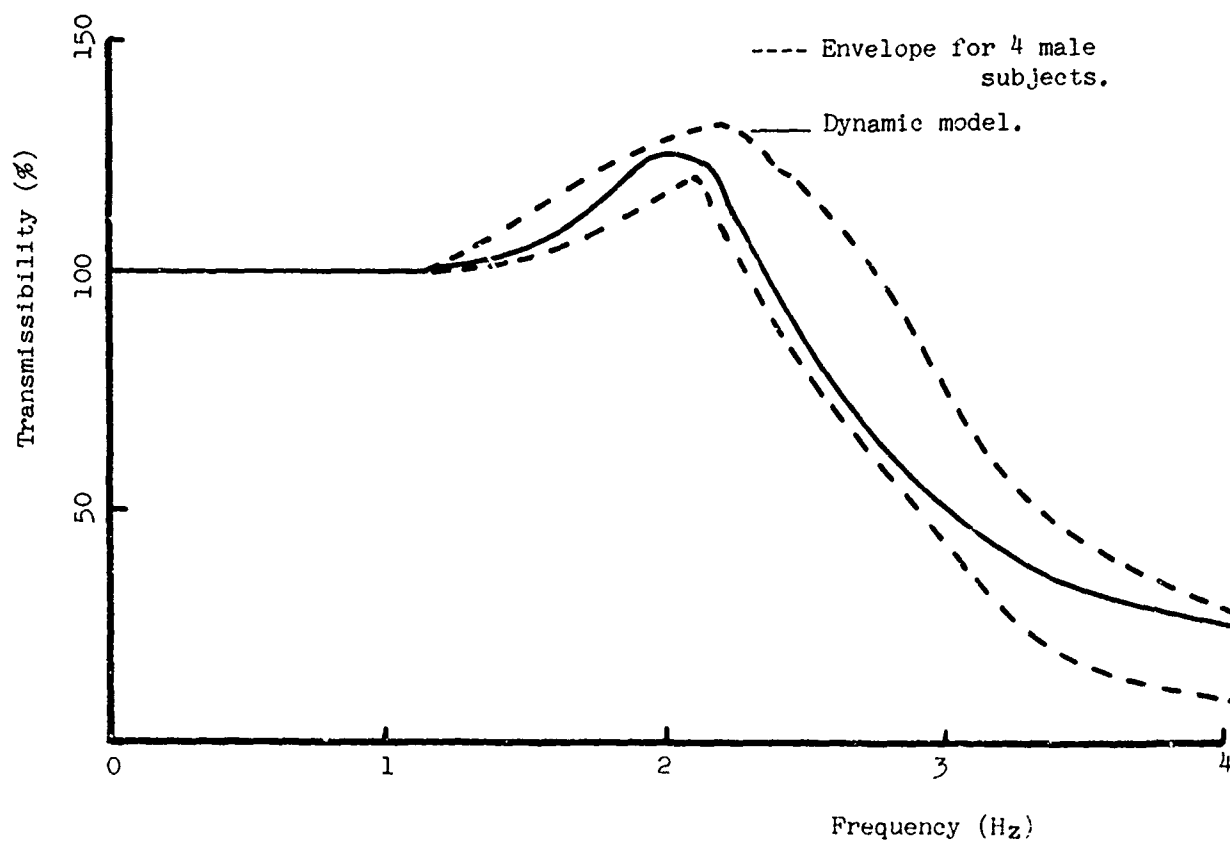


Fig. 1. Comparison of displacement transmissibility of dynamic model and male subjects.



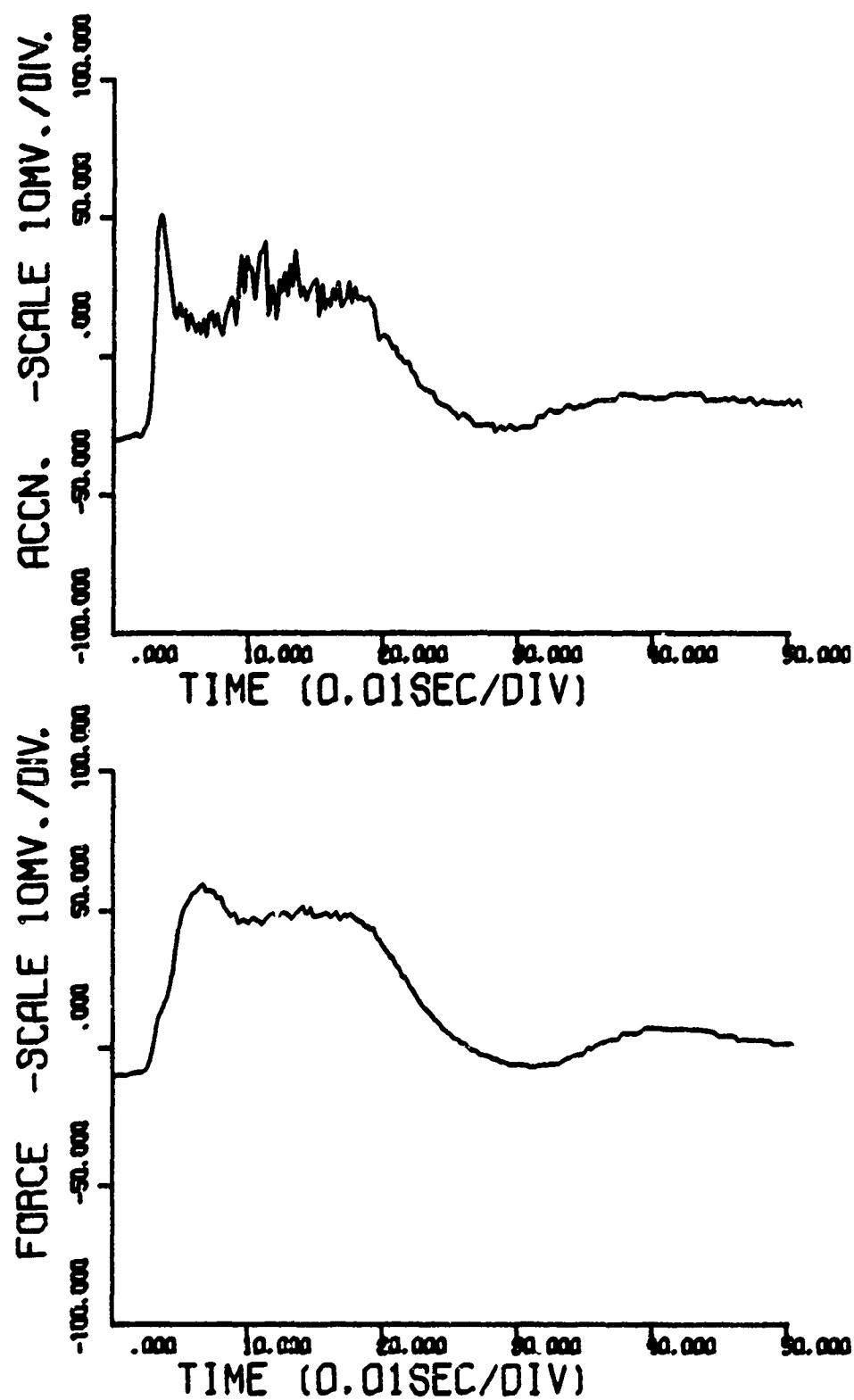


Fig. 2. Acceleration and force transients for 62.3 Kg. human, sitting slightly slumped, 60 m/sec.<sup>2</sup>.



Figure 3: Subject seated on table

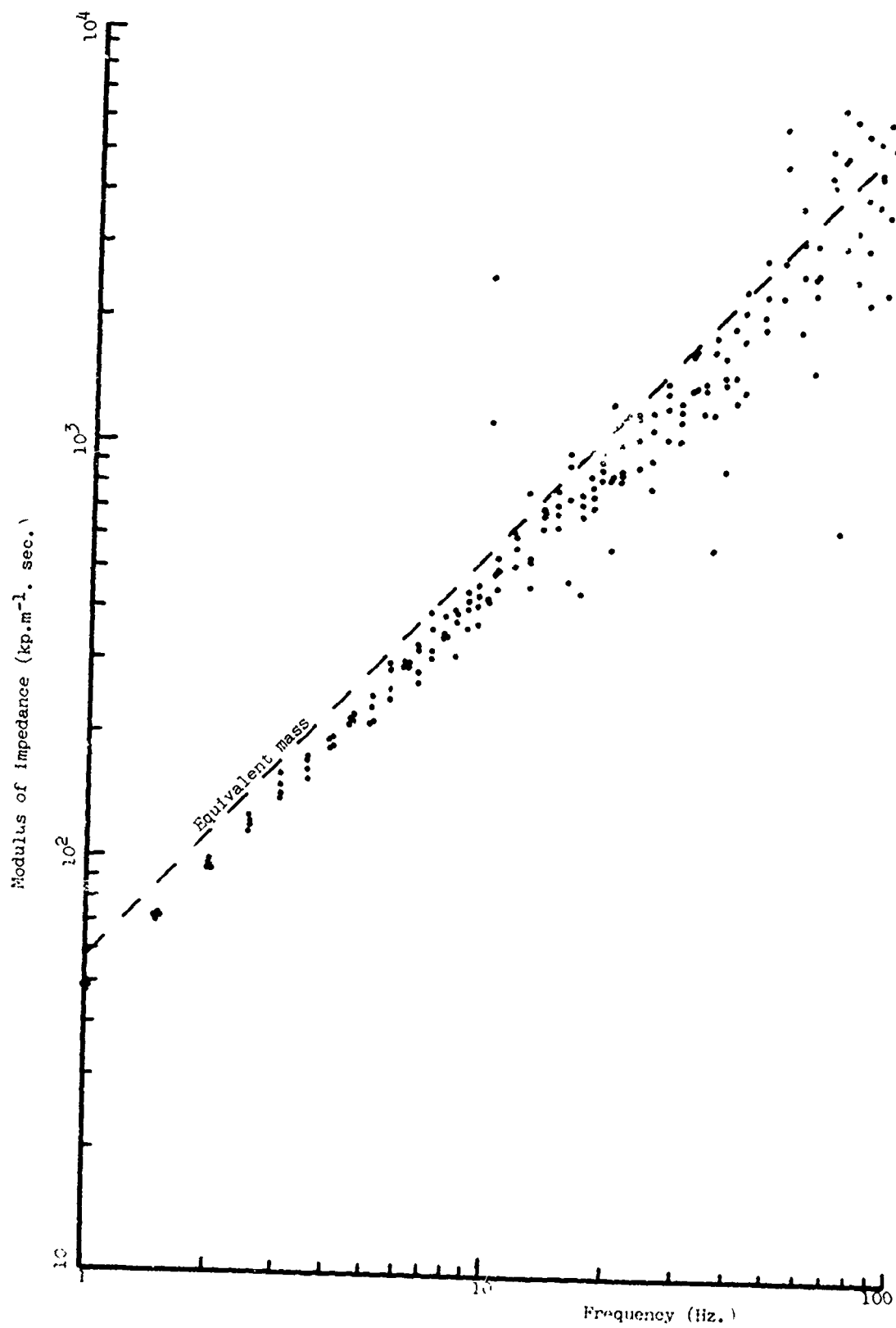


Fig. 2a. Modulus of impedance of 50 g. weight (data from four consecutive runs).

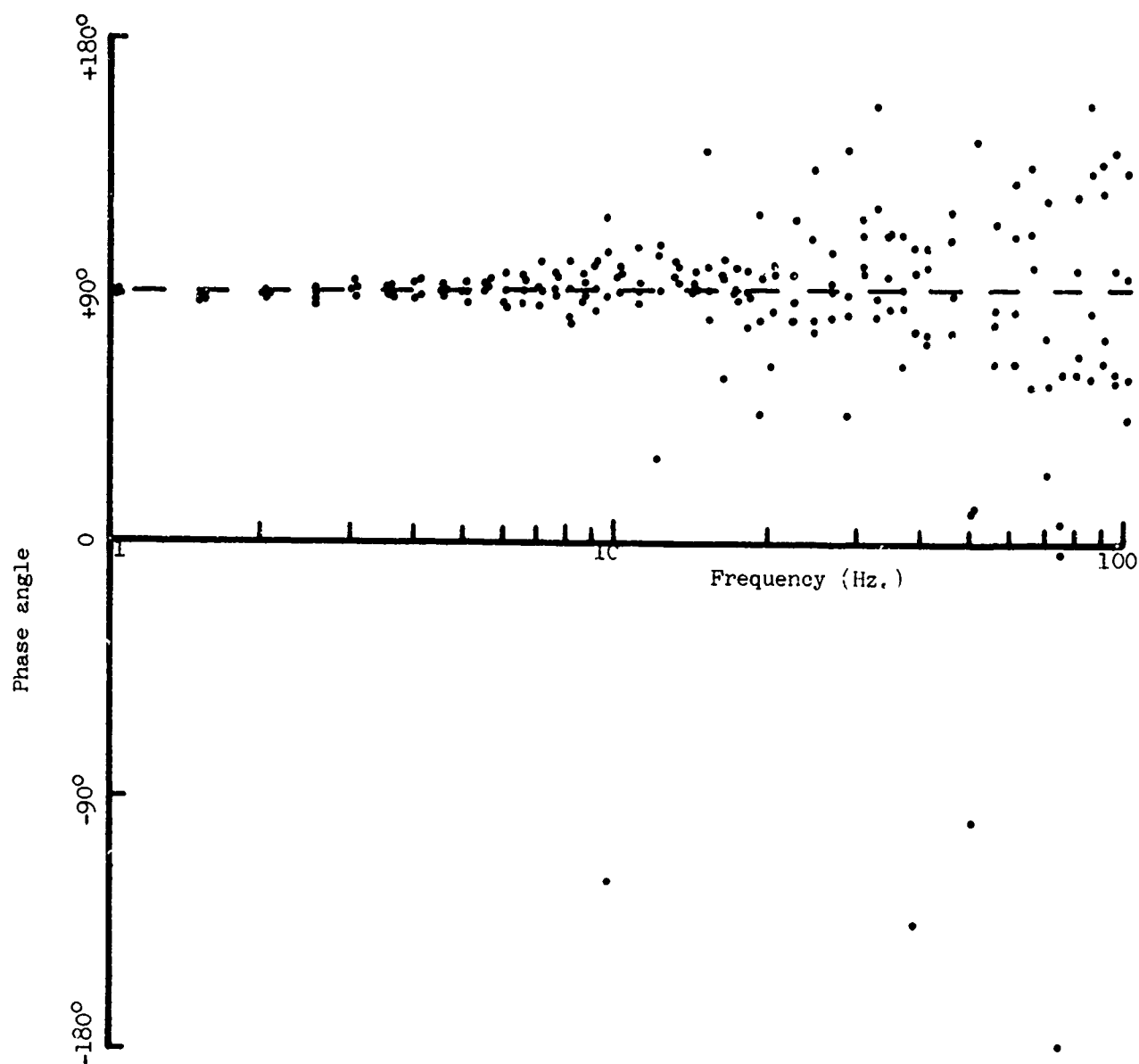


Fig. 4b. Phase angle of impedance of 80 Kg. weight (data from four consecutive runs).

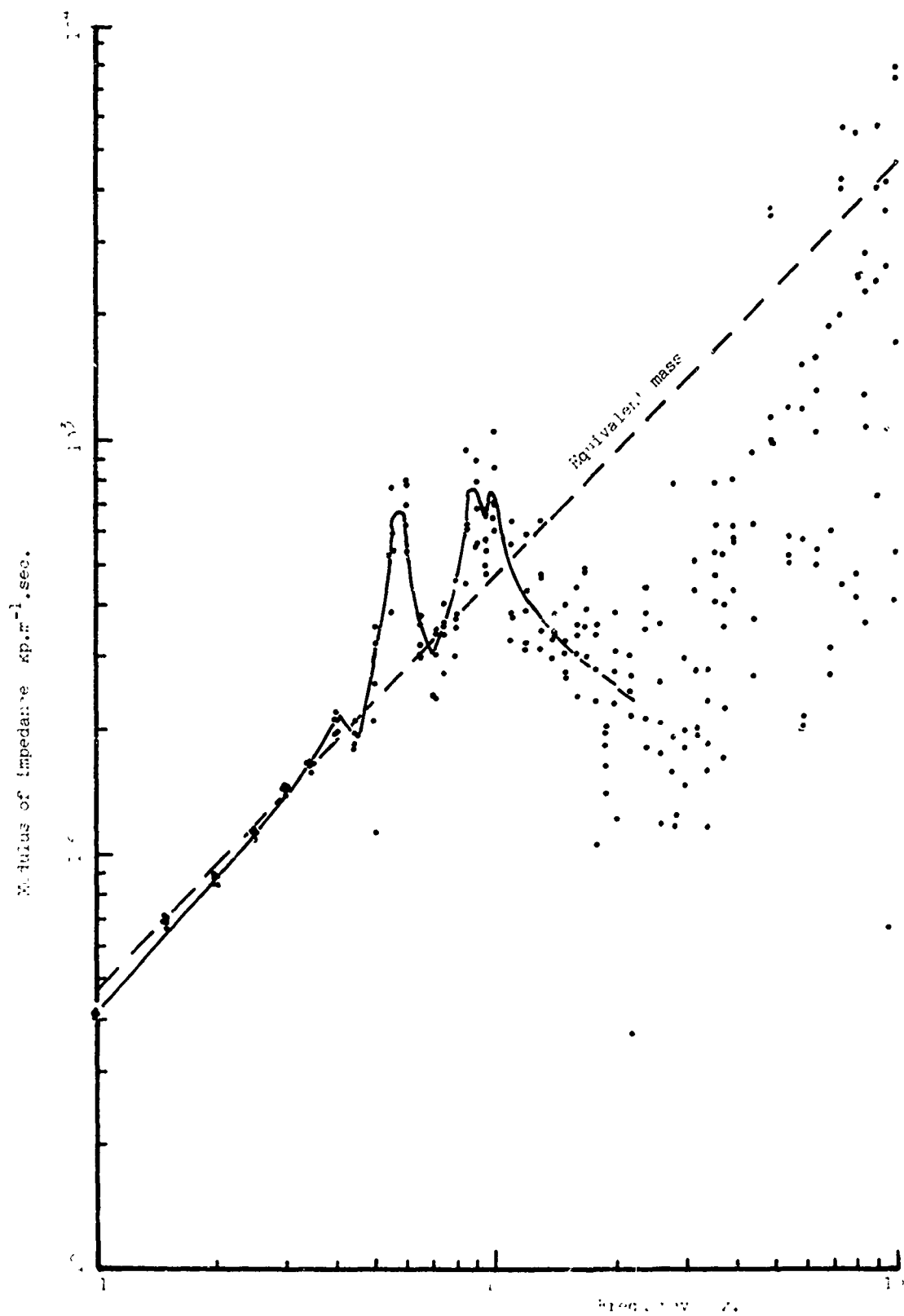


Fig. 2. Modulus of impedance of the system, calculated from the data of the experiment.

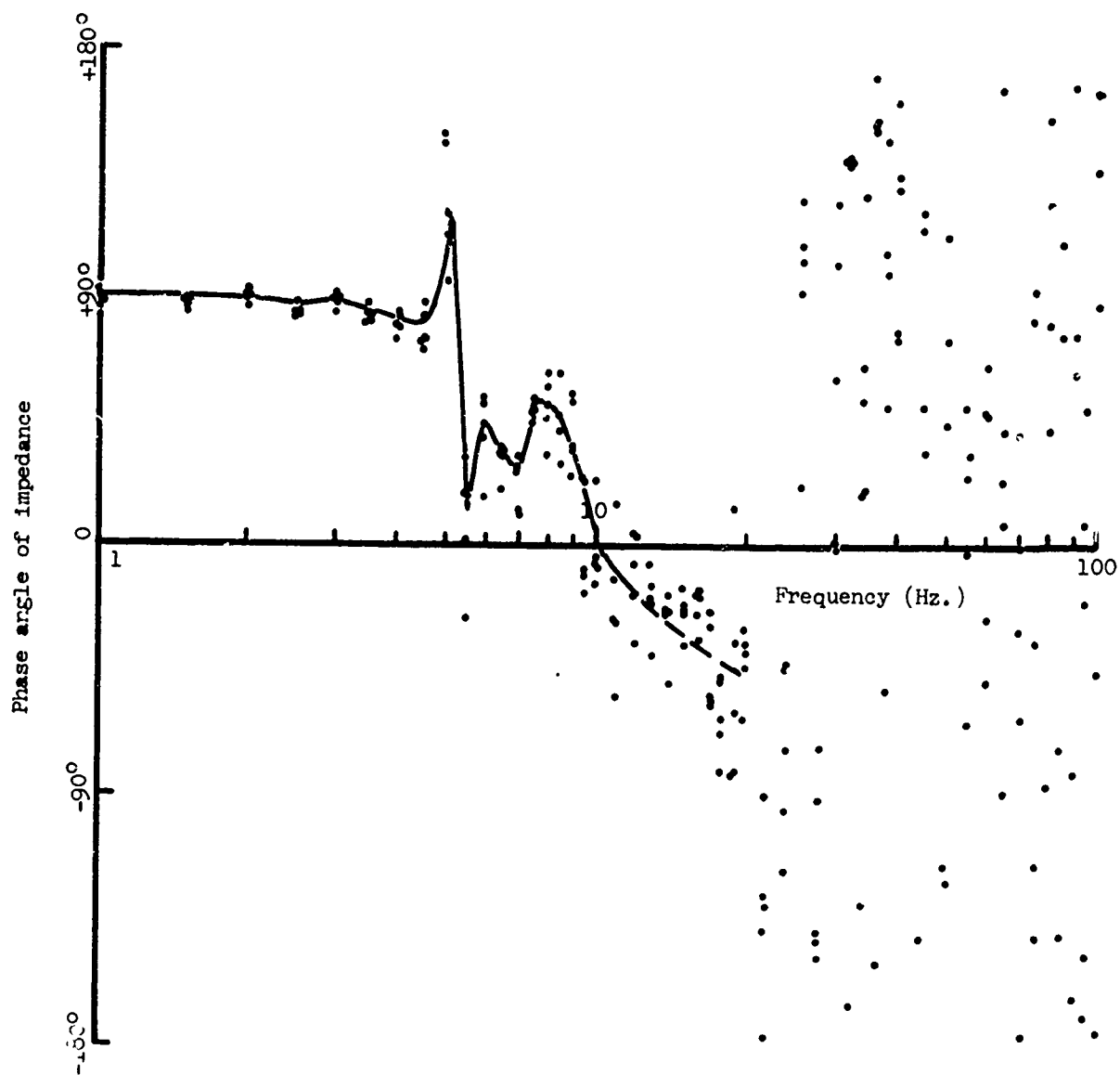


Fig. 5b. Phase angle of impedance of 62.3 Kg. human, sitting erect, 60 m/sec.<sup>2</sup> (data from five consecutive runs).

USE OF A MATHEMATICAL MODEL FOR  
THE EVALUATION OF HEAD INJURY CRITERIA

James V. Benedict

Technology Incorporated  
Life Sciences Division  
8531 North New Braunfels Avenue  
San Antonio, Texas 78217, U. S. A.

ABSTRACT

The present study concerns the use of an analytic model for closed brain injury to evaluate General Motors' Severity Index for head injury. This index, which considers the relative importance of the duration and intensity of the pulse by means of an impulse-integration procedure, has been demonstrated empirically to be an excellent means of comparing the severity of pulses of varying shapes. Four pulses (square, half-sine, skewed and triangular), each having the same Severity Index but different magnitudes, were employed as inputs to the model.

The model response to each of the four impacts was determined. Graphs of the time variation of stresses in the shell and pressures in the fluid at both the impact pole and at the counter pole demonstrate excellent correlation between model response and Severity Index, independent of the shape and magnitude of the impact force.

Criteria to assess the severity of impacts classically have been based upon specific parameters of the pulse wave-form. Maximum force or acceleration sustained, rate of onset, pulse shape, duration, and the rate of change of acceleration are representative of characteristics of the pulse which have been selected as injury criteria. However, as von Gierke<sup>1</sup> has noted, the situations in which any single aspect of the impact wave-form characterizes the system response are limited. This observation is substantiated by the work of Kornhauser and Gold<sup>2</sup> who have found that the incidence of injury depends on both the magnitude and the duration of the impact. Their tolerance curves of velocity change ( $\Delta v$ ) versus average acceleration ( $\bar{a}$ ) indicate that threshold values for both  $\Delta v$  and  $\bar{a}$  must be exceeded before injury will occur. Thus, a relation between both magnitude and duration must be considered in assessing impact severity.

Based on the assumption that the severity of an impulse wave-form is a function of both duration and intensity, Gadd<sup>3</sup> developed an exponentially weighted-impulse criterion for estimating head injury resulting from frontal impacts. From the work of Lissner<sup>4,5</sup> in which tolerance curves of intracranial pressure versus time indicated that the time required to produce severe concussion in dogs decreased as the pressure increased, and from that of Eiband<sup>6</sup> which demonstrated a similar trend for sled-test tolerance curves of acceleration versus time, Gadd noted that both results demonstrated a downward sloping tolerance curve in the range of vehicle occupant cranial impacts. He further noted that when the data was represented on a log-log plot the curve could be approximated by a straight line at an angle of less than 45° with the horizontal. He concluded that an impulse-area criterion would not satisfactorily predict injury. The resulting severity index which Gadd devised is depicted in Figure 1.

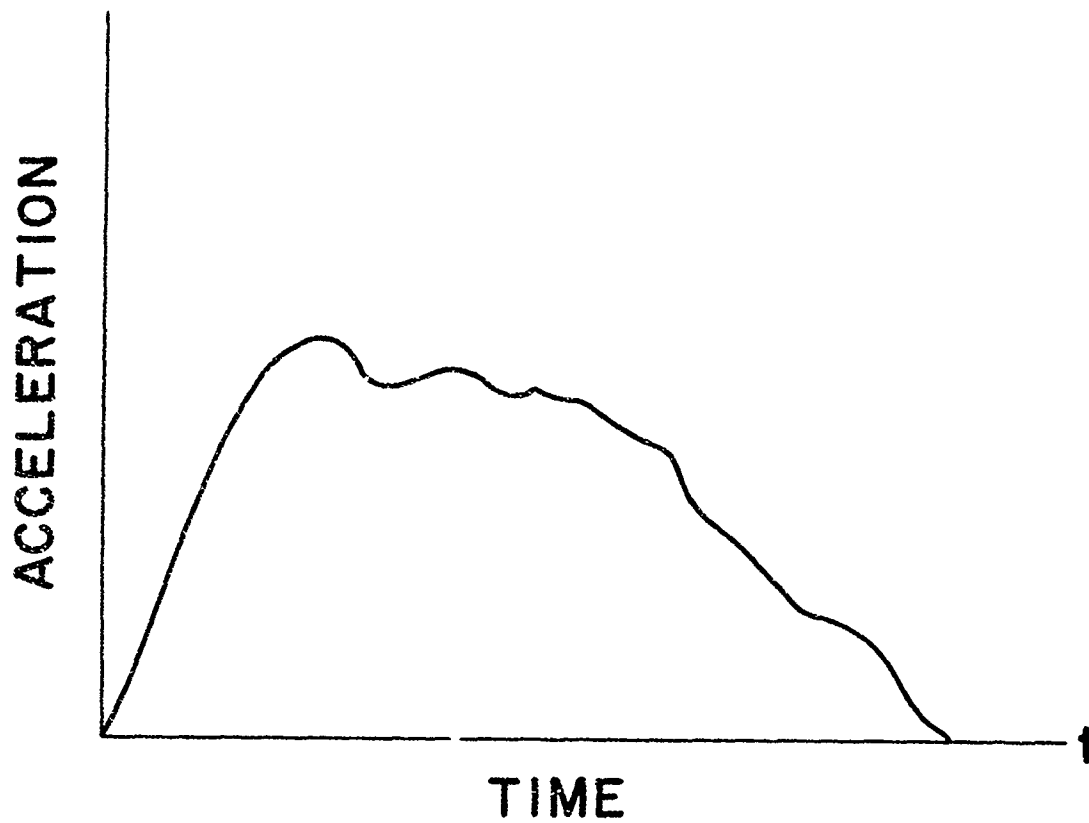
In general, the severity index (S. I.) may be expressed mathematically as:

$$S. I. = \int (\bar{a})^n dt$$

where S. I. is the severity index (a number);  $\bar{a}$  is the acceleration, pressure, or force producing an injury threshold of a specified degree;  $n$  is the exponential weighting factor; and  $t$  is time in seconds.

For head injury resulting from frontal impacts,  $\bar{a}$  is the acceleration of the head expressed in "g" units, and  $n$ , based upon empirical results, is 2.5. The exponential weighting factor signifies the importance of the high intensity segments and the insignificance of the low intensity portions of the impacts, while the integral accounts for the





$$S.I. = \int_0^t a^{2.5} dt$$

Figure 1. General Motors Severity Index

effect of the duration of both the high intensity and the low intensity portions of the curve.

The purpose of this study is to investigate the usefulness of the severity index in comparing the severity of pulses of different peak magnitude and varying wave-form. The severity index has been used primarily to investigate the injury potential of various pulses of one to fifty milliseconds duration applied to the frontal bone of the head. A previously developed mathematical model for head injury<sup>7</sup> has been used therefore to study various pulses having the same severity index but differing in wave-form and peak magnitude.

The head injury model assumes that the skull is a linear, homogeneous, isotropic, thin spherical shell and that the brain is an ideal (acoustic) fluid. Using extensional shell theory and assuming axisymmetry of the load, the following set of three coupled, second order, linear partial differential equations with variable coefficients obtain in spherical polar coordinates:

$$\frac{\partial^2 u}{\partial \phi^2} + \cotan \phi \frac{\partial u}{\partial \phi} - (\mu + \cotan^2 \phi) u + (1 + \mu) \frac{\partial w}{\partial \phi} - \lambda^2 \frac{\partial^2 u}{\partial t^2} = 0, \quad (1)$$

$$\frac{\partial u}{\partial \phi} + \cotan \phi u + 2w + \frac{\lambda^2}{(1 + \mu)} \frac{\partial^2 w}{\partial t^2} + \frac{\eta \lambda^2}{(1 + \mu)} \left( \frac{\partial \Phi}{\partial t} \right)_R - \frac{\epsilon (1 - \mu)}{E} F_{\text{ext}} = 0, \quad (2)$$

and

$$\frac{\partial^2 \Phi}{\partial r^2} + \frac{2}{r} \frac{\partial \Phi}{\partial r} + \frac{1}{r^2} \frac{\partial^2 \Phi}{\partial \phi^2} + \frac{\cotan \phi}{r^2} \frac{\partial \Phi}{\partial \phi} - \frac{\partial^2 \Phi}{\partial t^2} = 0 \quad (3)$$

Figure 2 depicts the relationship between the displacements  $u$ ,  $v$ , and  $w$  and the coordinate axes.

Equations (1) - (3) are solved by finite difference methods using backwards difference analogs and employing techniques described in references 7 and 8. Figure 3 shows the segmentation of the shell for

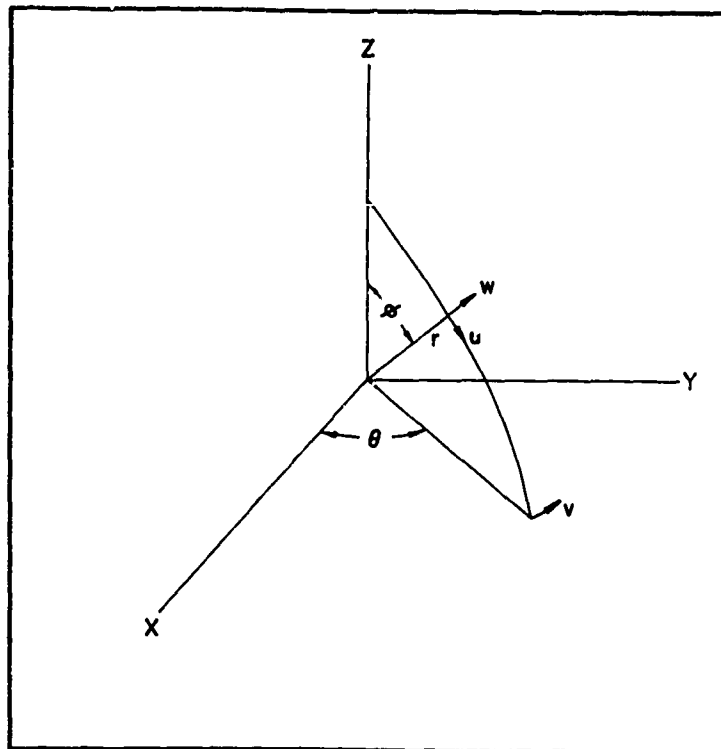


Figure 2. Coordinate System used to Describe the Model.

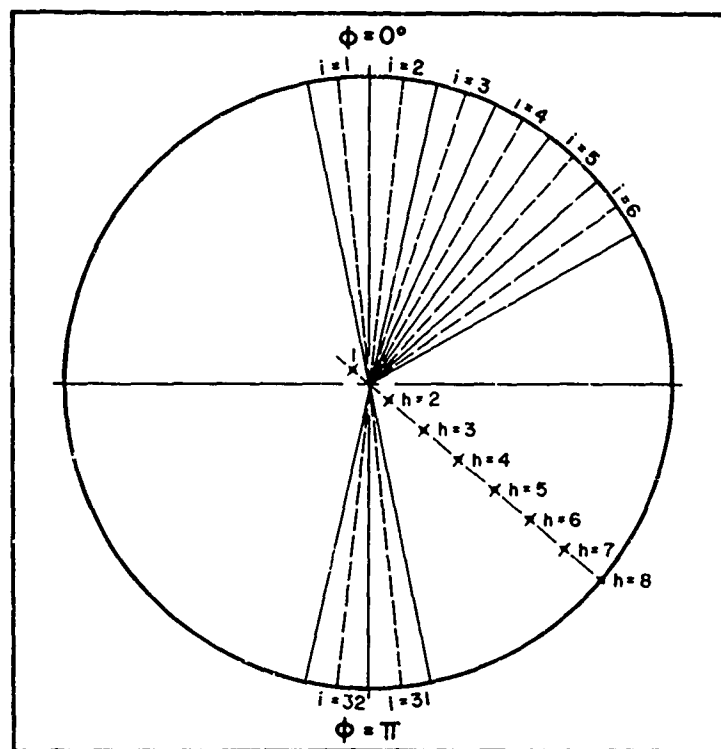


Figure 3. Shell segmentation for Finite Difference Analogs.

application of the finite difference analogs.

The model may be applied to an input with arbitrary temporal and spatial distributions, provided axisymmetry is maintained. Four different inputs were selected to evaluate the severity index, and the model responses for each have been compared. The four acceleration pulse shapes chosen to represent those which might be encountered in actual vehicle-interior impact situations are square pulse, half-sine pulse, triangular pulse and an arbitrary impact pulse as suggested by Goldsmith<sup>9</sup>. These four acceleration pulses are depicted schematically in Figure 4. The mathematical representations of the four pulses are shown in Figure 5, in which  $t$  is the independent variable, time, and  $T$  is the duration of the impact.

A pulse duration of 0.0001 sec was selected for each of the four input functions. The intensity of the pulses was selected by requiring that each of the four pulses yields the same severity index. That is,

$$(S. I.)_i = \int (\bar{a})_i^{2.5} dt_i = 500.$$

The input to the model, represented by the term  $F_{ext}$  in equation (2), has units of  $\text{lbf/in}^2$ . Each of the four input pulses was expressed in these units by assuming a head weight of 10 pounds and an even distribution of the load over a polar cap of  $15^\circ$  polar angle. Figure 6 depicts the four inputs as functions of both time and polar angle.

### Numerical Results

The following properties of the shell and the encased fluid are used in the calculations:

Shell:	$E = 2 \times 10^6 \text{ lbf/in}^2$
	$\mu = 0.25$
	$a = 3 \text{ in.}$
	$h = 0.15 \text{ in.}$
	$\rho_s = 2.00 \times 10^{-4} \text{ lb sec}^2/\text{in}^4$

## ACCELERATION PROFILES

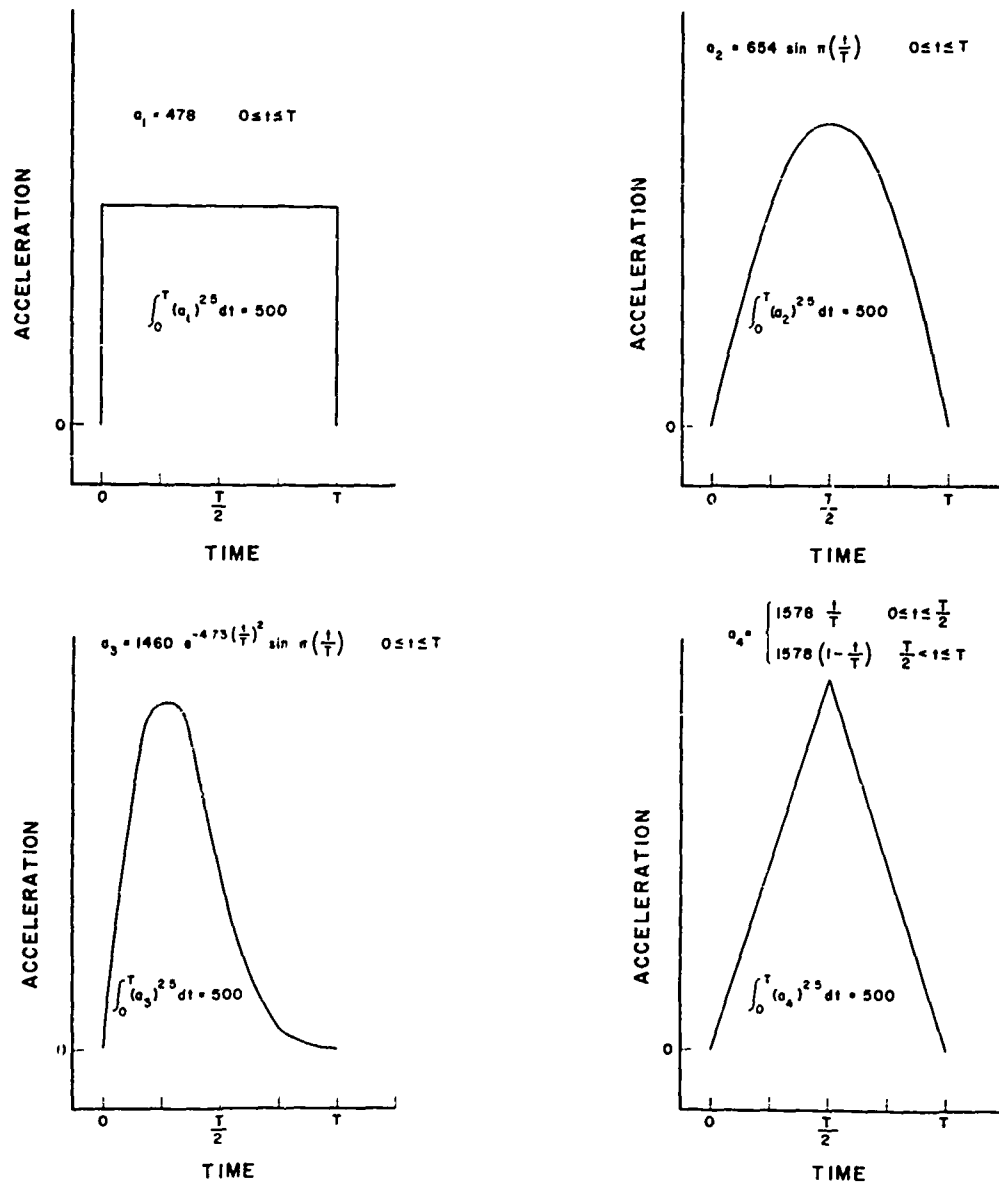


Figure 4. Schematic Representation of the Four Input Pulses.

TYPE OF PULSE	MATHEMATICAL DESCRIPTION	TIME DOMAIN
SQUARE	$a_1 = A_1$	$0 \leq t \leq T$
HALF - SINE	$a_2 = A_2 \sin \frac{\pi t}{T}$	$0 \leq t \leq T$
ARBITRARY	$a_3 = A_3 e^{-b\left(\frac{t}{T}\right)^2} \sin \frac{\pi t}{T}$	$0 \leq t \leq T$
TRIANGULAR	$a_4 = A_4 \frac{t}{T}$ $a_4 = A_4 \left(1 - \frac{t}{T}\right)$	$0 \leq t \leq \frac{T}{2}$ $\frac{T}{2} < t \leq T$

Figure 5. Mathematical Description of the Four Input Pulses.

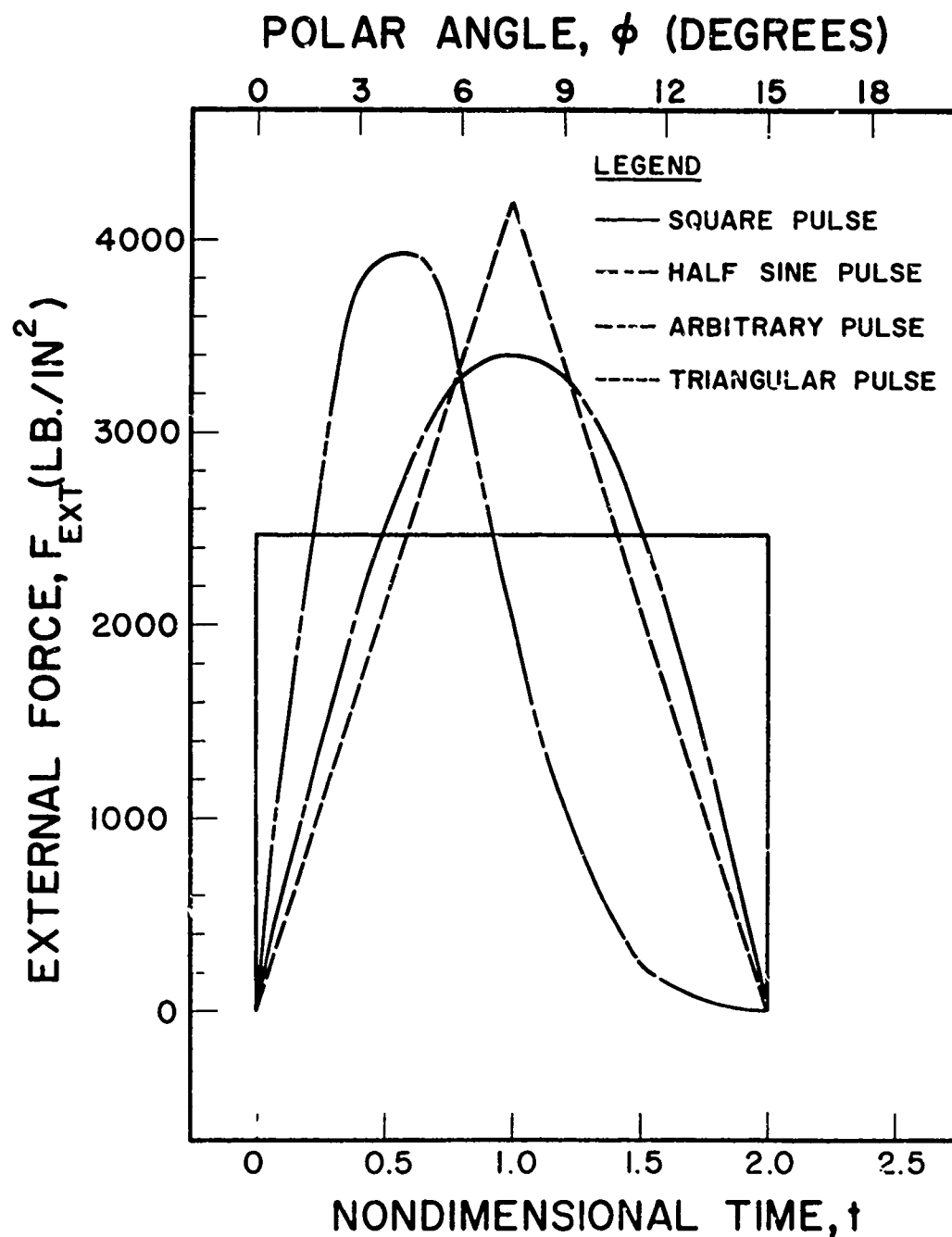


Figure 6. Forcing function versus time,  $t$ , and polar angle,  $\phi$ .

Fluid:

$$\begin{aligned}K &= 300,000 \text{ lbf/in}^2 \\ \rho_f &= 0.938 \times 10^{-4} \text{ lb sec}^2/\text{in}^4 \\ C_o &= 56,553 \text{ in/sec.}\end{aligned}$$

Using this data and determining the model response to each of the four input pulses yields the results shown in Figures 7 - 11. The resting position is considered to be a zero datum, and all pressures are gage rather than absolute pressures.

Pressure variation with time at polar angles of  $3^\circ$  and  $177^\circ$ , the positions approximating the impact pole and the counter pole, respectively, are shown in Figures 7 and 8. Fluid pressures are studied at  $r = 1.0$  (immediately adjacent to the shell) since this location is where the greatest pressure fluctuations occur. The fluid at the impact pole is compressed initially and as the impact load decreases in intensity the compression diminishes and the fluid is subjected to a tensile stress. The duration of this tensile stress is approximately 125  $\mu\text{sec}$ . The pressure at the counterpole does not reflect a change from the zero datum until the stress wave in the shell, which generates instantaneous centers for wave propagation as it traverses the shell, approaches the counterpole. As the shell attempts to separate from the fluid, tensile stresses occur in the fluid. These stresses are more diffuse, less severe and longer lasting than the tensile stresses at the impact pole. Although the solution has not been obtained for a period that is sufficiently long to determine the duration accurately, it is estimated that the tensile stress at the counterpole is maintained for approximately 300  $\mu\text{sec}$ .

The variation of the shell radial displacement as a function of time for both the impact pole and the counterpole are shown in Figures 9 and 10. The load produces an initial indentation at the impact pole followed by an elastic recovery as the load is removed. There is a continual outward displacement at the counterpole which assists in producing the tensile stresses in the fluid at that point. Membrane stresses in the shell are shown in Figure 11 for the impact pole. Initially high compressive stresses are generated during the impact period, followed by elastic recovery when the load is relieved.

Each of Figures 7 - 11 shows the model response for the four impact pulses selected. Inspection of these five graphs reveals a similar model response for the four pulses although the pulse shapes, rates of onset, and peak intensities differ.



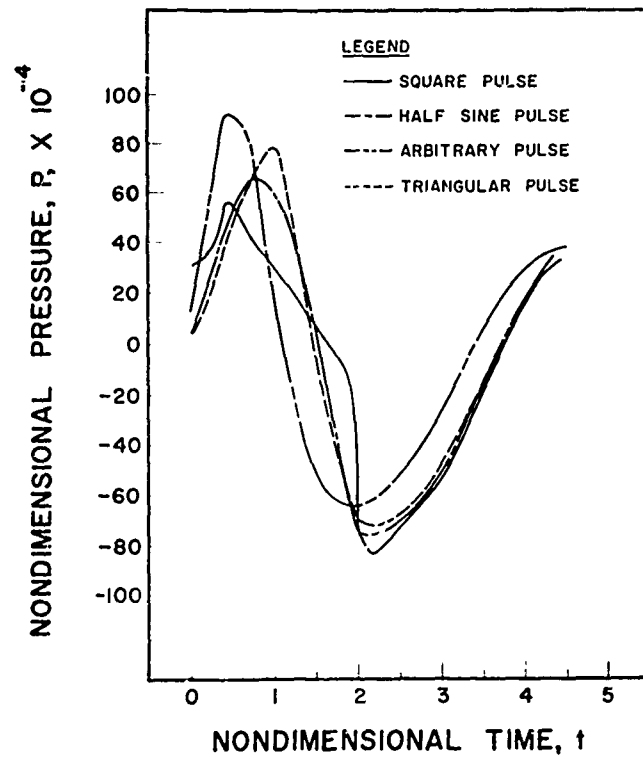


Figure 7. Pressure versus time,  $\phi = 3^\circ$ ,  $r = 1.0$

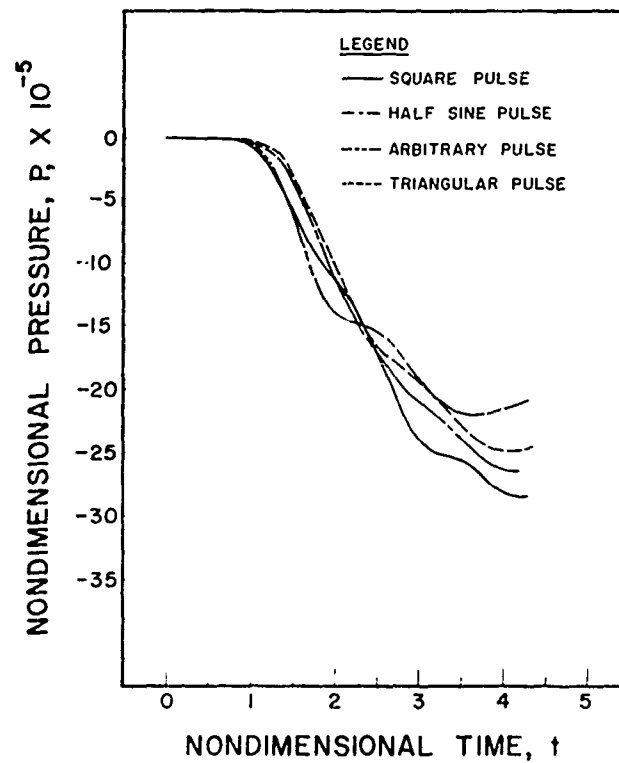


Figure 8. Pressure versus time,  $\phi = 177^\circ$ ,  $r = 1.0$

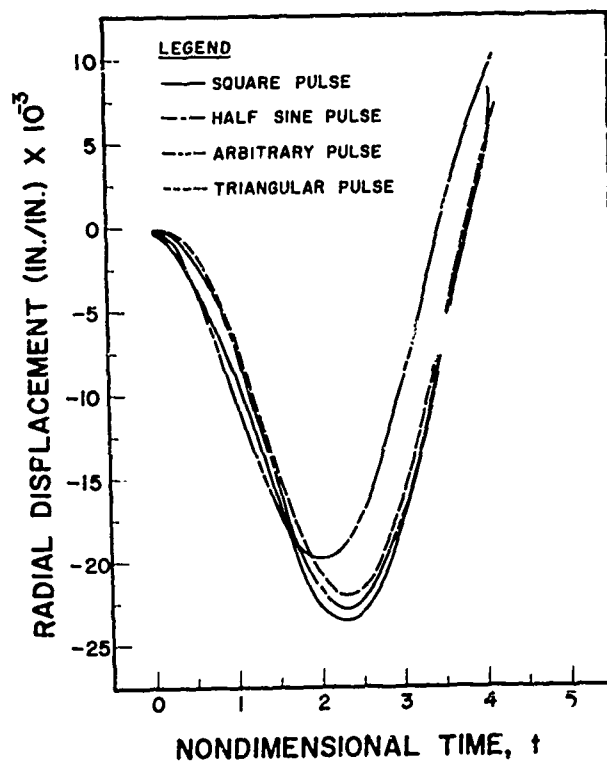


Figure 9. Radial displacement versus time,  $\phi = 3^\circ$

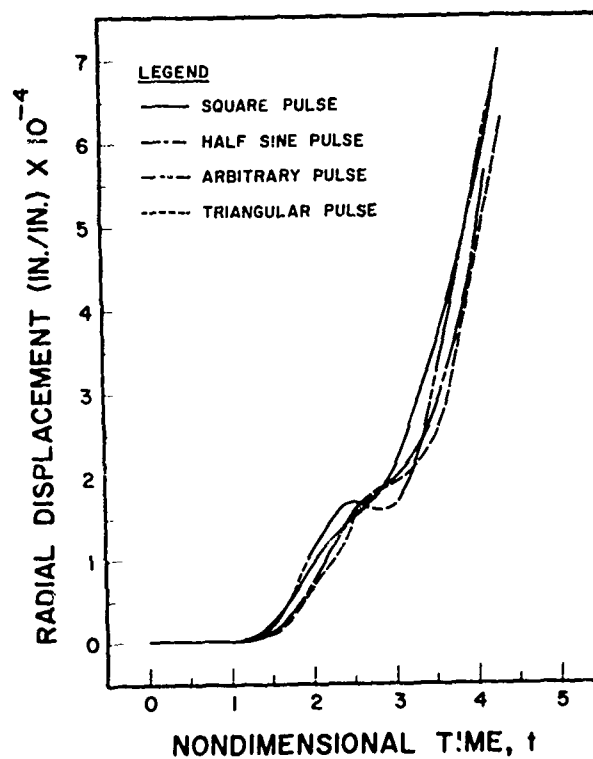


Figure 10. Radial displacement versus time,  $\phi = 177^\circ$

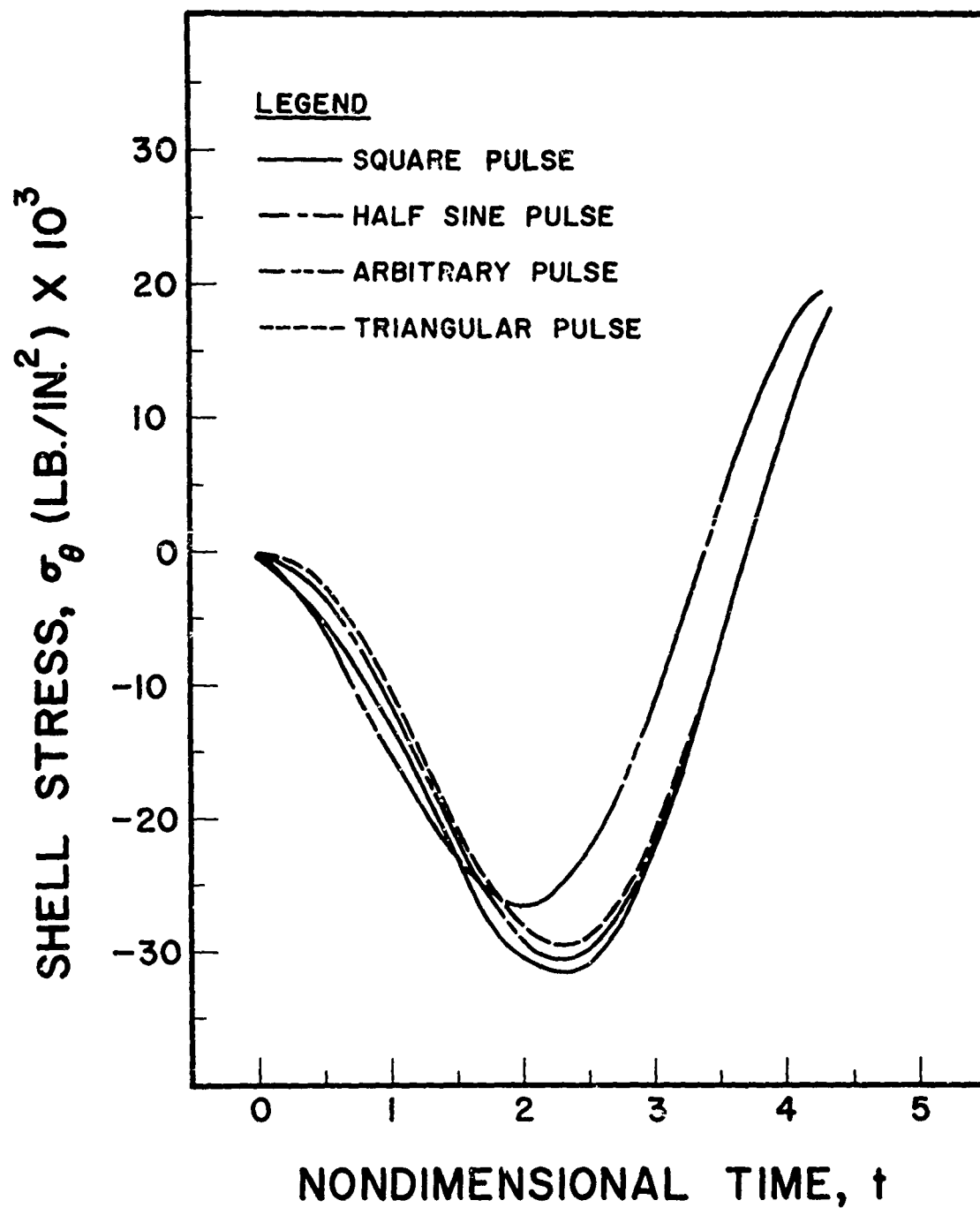


Figure 11. Normal stress in the  $\theta$ -direction versus time,  $\phi = 3^\circ$

### Conclusions

The intent of this study has not been to determine the effectiveness of the General Motors' Severity Index in predicting injury thresholds, since this result could be accomplished only in a program which combined analytic and experimental or clinical investigation. The objective of this study has been to assess the value of the Severity Index in predicting a single parameter equivalent for pulse wave-forms of varying shapes and magnitudes. As evidenced by the results shown in Figures 7 - 11, the Severity Index does appear to be an excellent means of comparing impact functions.

The current work may be extended to an investigation of model response to pulses of durations within the range of known vehicle interior impacts, or to a study of pulses of identical peak intensities but different durations. The predictive capability of the severity index under these conditions could therefore be determined.

### Acknowledgments

The author expresses his appreciation to the Life Sciences Division of Technology Incorporated for support of this study.

# NOMENCLATURE

$a$	Radius of the shell middle surface (L)
$\bar{a}$	Average acceleration
$A_1, A_2, A_3, A_4$	Constants, determine magnitude of the acceleration functions
$b$	Constant, determines decrement rate of the loading function
$C_o$	Compressional wave speed in the encased fluid, $[K/\rho_o]^{1/2}$ (L/T)
$C_s$	Wave speed in the shell, $[E/\rho_s(1 - \mu^2)]^{1/2}$ (L/T)
$E$	Young's modulus for the shell material ( $F/L^2$ )
$F_{ext}$	External loading function ( $F/L^2$ )
$h$	Shell thickness (L)
$K$	Bulk modulus of the fluid ( $F/L^2$ )
$n$	Exponential weighting factor
$P(\phi, t)$	General loading function ( $F/L^2$ )
$P'$	Pressure in the fluid measured with the undisturbed state as zero datum ( $F/L^2$ )
$P$	Nondimensional pressure, $P'/K$
$R$	Value of the discrete radial variable at the shell boundary
$SI$	Severity index
$r'$	Dimensional radial coordinate (L)
$r$	Nondimensional radial coordinate, $r'/a$
$T$	Nondimensional duration of loading
$t'$	Dimensional time (T)
$t$	Nondimensional time, $C_o t'/a$

# NOMENCLATURE

$a$	Radius of the shell middle surface (L)
$\bar{a}$	Average acceleration
$A_1, A_2, A_3, A_4$	Constants, determine magnitude of the acceleration functions
$b$	Constant, determines decrement rate of the loading function
$C_o$	Compressional wave speed in the encased fluid, $[K/\rho_o]^{1/2}$ (L/T)
$C_s$	Wave speed in the shell, $[E/\rho_s(1 - \mu^2)]^{1/2}$ (L/T)
$E$	Young's modulus for the shell material ( $F/L^2$ )
$F_{ext}$	External loading function ( $F/L^2$ )
$h$	Shell thickness (L)
$K$	Bulk modulus of the fluid ( $F/L^2$ )
$n$	Exponential weighting factor
$P(\phi, t)$	General loading function ( $F/L^2$ )
$P'$	Pressure in the fluid measured with the undisturbed state as zero datum ( $F/L^2$ )
$P$	Nondimensional pressure, $P'/K$
$R$	Value of the discrete radial variable at the shell boundary
$SI$	Severity index
$r'$	Dimensional radial coordinate (L)
$r$	Nondimensional radial coordinate, $r'/a$
$T$	Nondimensional duration of loading
$t'$	Dimensional time (T)
$t$	Nondimensional time, $C_o t'/a$

$u'$	Dimensional meridional displacement (L)
$u$	Nondimensional meridional displacement, $u'/a$
$v'$	Dimensional parallel displacement (L)
$v$	Nondimensional parallel displacement, $v'/a$
$w'$	Dimensional radial displacement (L)
$w$	Nondimensional radial displacement, $w'/a$
$x, y, z$	Cartesian coordinates
$\Delta v$	Incremental change in velocity
$\epsilon$	Dimensionless parameter, $a/h$
$\eta$	Dimensionless parameter, $a\rho_o/h\rho_s$
$\phi, \theta$	Spherical coordinates
$\lambda$	Dimensionless parameter, $Co/Cs$ , the speed ratio
$\mu$	Poisson's ratio
$\rho_f$	Density of the fluid ( $FT^2/L^4$ )
$\rho_s$	Density of the shell ( $FT^2/L^4$ )
$\psi$	Dimensional velocity potential ( $L^2/T$ )
$\Phi$	Nondimensional velocity potential, $\psi/aCo$
Subscripts	
$h$	Refers to discrete variables in the radial direction
$i$	Refers to discrete variables in the $\phi$ direction

## REFERENCES

1. von Gierke, H. E. , "Biomechanics of Impact Injury." Impact Acceleration Stress - Proceedings of a Symposium with a Chronological Bibliography. National Academy of Science, National Research Council Publication 977, 1962, pp. 121-122.
2. Kornhauser, M. and A. Gold, "Application of the Impact Sensitivity Method to Animate Structures." Impact Acceleration Stress - Proceedings of a Symposium with a Comprehensive Chronological Bibliography. National Academy of Sciences, National Research Council Publication 977, 1962, pp. 333-344.
3. Gadd, C. W. , "Use of a Weighted Impulse Criterion for Estimating Injury Hazard." Proceedings of Tenth Stapp Car Crash Conference, 1966. Published by SAE, New York. pp. 95-100.
4. Lissner, H. R. , et. al. , "Experimental Studies on the Relation between Acceleration and Intracranial Pressure Changes in Man." Surgery, Gynecology and Obstetrics, 1960, pp. 329-338.
5. Lissner, H. R. and E. S. Gurdjian, "Experimental Cerebral Concussion." ASME Paper No. 60-WA-273, 1960.
6. Eiband, A. , "Human Tolerance to Rapidly Applied Accelerations." NASA Memorandum 5-19-59E, June 1959.
7. Benedict, J. V. , E. H. Harris and D. U. von Rosenberg, "An Analytical Investigation of the Cavitation Hypothesis of Brain Damage." J. Basic Engineering - Transactions of the ASME, Vol. 92, Series D, No. 3, September 1970, pp. 597-603.
8. von Rosenberg, D. U. , Methods for the Numerical Solution of Partial Differential Equations, New York. American Elsevier, 1969, p. 128.
9. Goldsmith, W. , Private Communication, 1968.



MECHANICAL AND PHYSIOLOGICAL RESPONSE OF  
THE HUMAN CERVICAL VERTEBRAL COLUMN TO  
SEVERE IMPACTS APPLIED TO THE TORSO

Wolfgang Lange

Max-Planck-Institut für Arbeitsphysiologie  
Rheinlanddamm 201, 46 Dortmund, Germany

ABSTRACT

In experiments with human cadavers, severe frontal and rear-end automobile collisions were simulated on an acceleration sled. A wide range of angles of rotation between head and torso resulted from the impacts. The magnitude of the torque exerted at the cervical spine was estimated using the mass moments and lever arms.

Autopsies after the experiments indicated certain types of injuries to the intervertebral disks and the ligaments caused by torque, axial forces and shear forces. Obviously, preexperimental damages to the column by spondylitis and/or athrosis deformans are important parameters for the impact trauma.

PURPOSE

A series of experiments with human cadavers was performed to gain information on the response of the cervical column to severe impacts applied to the torso. Specifically, the purpose of this research was

- 1) to study the motion of the head relative to the torso, depending on the direction of impact
- 2) to assess the effects of a headrest in rear-end collisions
- 3) to assess the effects of the steering wheel in frontal collisions, using different types of safety harnesses
- 4) to categorize and localize damage to the cervical column after the impact
- 5) to ascertain whether or not there is a relation between preexperimental damage of the cervical column and trauma caused in a simulated collision.

**PRECEDING PAGE BLANK.**

## EQUIPMENT

The equipment used consisted essentially of a hydraulic catapult applying an impulse to a guided sled. The maximal impact force was 12 Megapond (4600 lb), the maximal sled speed attained was about 15 m/s (45 ft/sec). The acceleration of the sled could be controlled between 0 and 30 g. After the impact the sled travelled 3.5 metres before being decelerated with 1.3 g.

Acceleration of the head was measured by a pick-up mounted on a 200 gram helmet. In some experiments chest acceleration was also measured. In the head-on collisions, seat belt force was recorded too. A wide angle high-speed camera mounted on the sled could take 500 frames per second of the cadaver. Catapult, sled and camera are shown in figure 1.

## CADAVERS

The cadavers were of men and women who had died some days before the experiments. They were kept at about 15°C for at least three days before the experiment, by which time they had lost their rigidity. The cervical column of each cadaver was examined by x-ray for damage existing before the experiment. After the impact each cadaver was dissected to detect injuries caused by the collision.\*

Damage to the cervical column existing before the experiment ("pre-damage") was classified into four groups [5]:

- 1) (0) sound, without damage
- 2) (+) moderate modification by deforming spondylitis
- 3) (++) strong modification by spondylitis and/or athrosis deformans
- 4) (+++) severe damage by osteochondrosis.

---

\* The medical examinations were performed by P. Hinz, M. D., Dept. of Orthopaedics, University of Heidelberg, Germany.

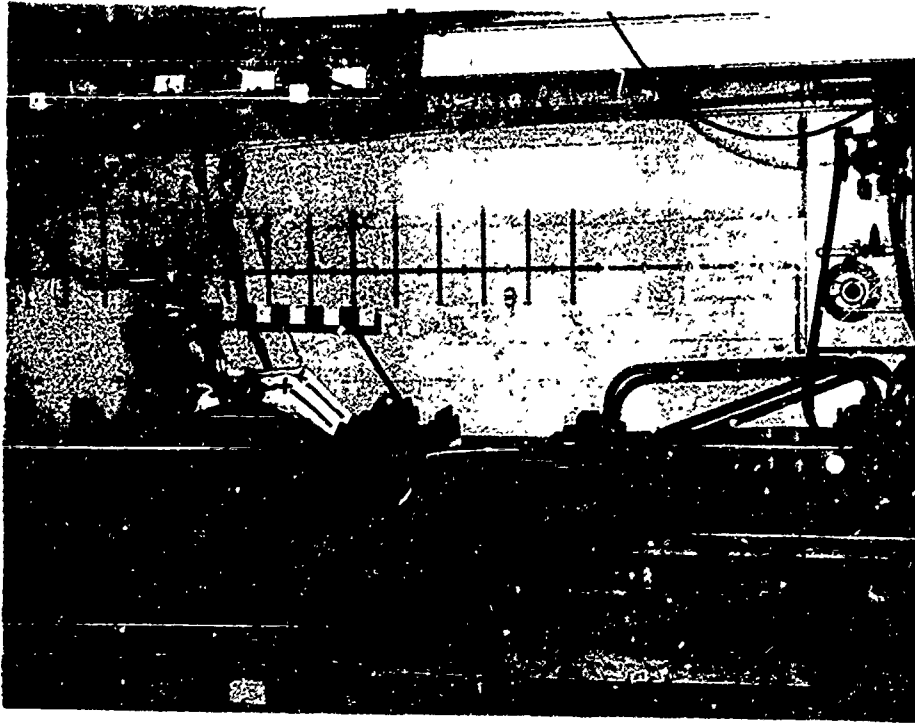


Figure 1: Electro-hydraulic catapult and sled. Overall view.

Figure 2 shows a cervical column belonging to group 1, figure 3 a column classified into group 3.

Impact injuries caused in the collision experiments were classified into three groups.

- 1) ( ☐ ) without macroscopical damage caused by the impact
- 2) ( ☒ ) moderate damage, namely haematoma or partial tearing of the intervertebral disks
- 3) ( ☒ ) severe ruptures of ligaments and intervertebral disks with resulting compression of the spinal cord as shown in figure 4.

#### REAR-END IMPACTS

The cadavers were placed into standard automobile bucket seats, reinforced to withstand the impact force. The pick-up on the helmet measured a combination of linear and angular acceleration during the impact. Four typical phases are shown in figure 5.



Figure 2: Human cervical vertebral column.  
Sound vertebrae, without damage.

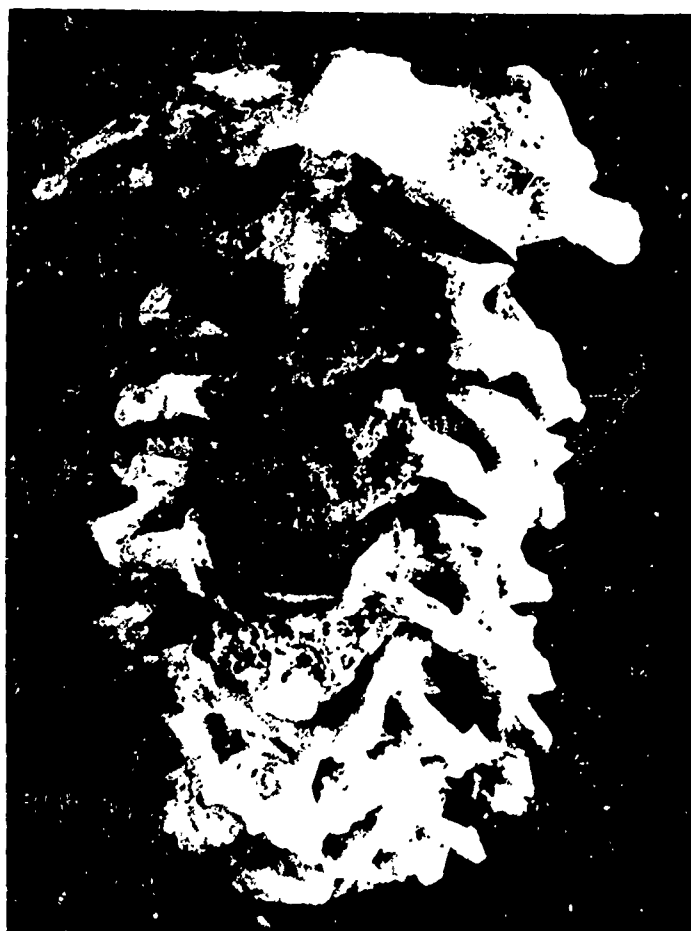


Figure 3: Human cervical vertebral column.  
Strong modification by spondylitis deformans.



Figure 4: Severe rupture of ventral ligaments and the intervertebral disk with resulting compression of the spinal cord.

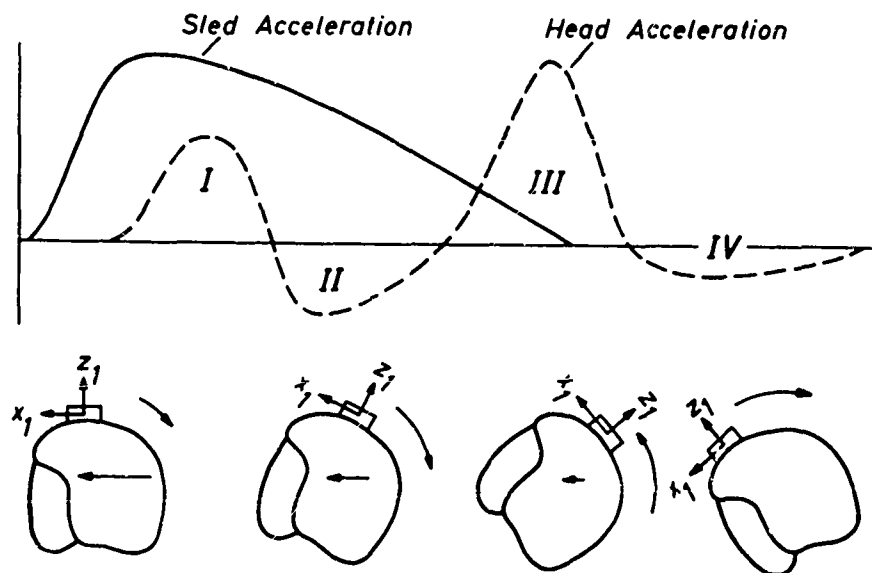


Figure 5: Phases of head acceleration in rear-end collisions.

In phase I, the neck is mainly stressed by shear force. During phase II, the shear force is smaller but the bending torque increases because the sled is still accelerating. In phase III, with very little additional forces applied to the sliding sled, the neck is stressed by the inertial moment of the head, especially if there is no headrest. During phase IV, an opposite bending moment strains the neck. The acceleration in  $x_1$ -direction has its maximal value in phase III.

In nine rear-end impacts the seats were without headrests. In six of these nine runs the sled was accelerated to velocities of 18 to 39 km/h in about 60 ms. The maximal sled acceleration was between 19 and 29 g. Under these conditions the heads rotated backwards 75 to 108 degrees with respect to the longitudinal axis of the torso. The maximal acceleration of the head, measured on the helmet varied between 4 g and 31 g in phase II and between 15 and 34 g in phase III.

In three other runs without headrests, the maximal acceleration of the sled was 25 or 26 g during an acceleration period of about 110 ms. Hence the sled reached a velocity of, respectively, 52 and 53 km/h. In these runs,

the angle of rotation between head and trunk was between 112 and 140 degrees. The maximal acceleration at the helmet was between 22 and 24 g in phase II and between 24 and 47 g in phase III. The results of the nine runs are compiled in table 1.

Severe damage to the intervertebral disks and a rupture of ligaments resulting in spinal cord pressure occurred in runs no. II and no. VIII. In three runs moderate damage was detected, while no macroscopic damage was apparent in four other cases. It is noteworthy that the ruptures occurred only in the lower part of the cervical column. No relation between bending angle and injuries to the column was found. However, the upper edge of the seats used was so low that bending occurred not only in the cervical but also in the thoracic column. This was clearly demonstrated in run VII, where the head bent 140 degrees from the torso; however, only a torn thyroid cartilage of the larynx was found in the autopsy.

The maximal torque between the 6th and the 7th cervical vertebra in phase III was approximated by computing the mass moment of the head with respect to the center of mass (CM) of the head and by estimating the distance between CM and the disk between C6 and C7. A torque of only 680 kpc<sub>m</sub> (590 in lb) was calculated for run no. III. The highest torque of 2100 cmkp (18,300 in lb) occurred in run no. VIII. A positive correlation between amount of torque and severeness of damage is apparent. However, in some instances we also observed low torque with trauma (run no. III) and high torque and no injury (run no. V). It seems that in these cases the predamage affected the response of the cervical column.

In another series of simulated rear-end collisions, we used several different kinds of headrests attached to the seat. In these runs, the duration of impact was about 114 ms, the maximal acceleration about 25 g and the velocity about 50 km/h. Before the impact, the head was spaced about 6 CM in front of the headrest. All cadavers used had a predamaged cervical vertebral column.



run no.	impact parameters			cadaver data				experimental results				
	max. sled acceleration	duration of impact	velocity	age	sex	stature	predamage	height of the seat back above CM of the head	max. head rotation relative to torso	torque between C6/C7	impact damage to disks	rupture of ligaments
	(g)	(ms)	$\left(\frac{\text{km}}{\text{h}}\right)$	(yrs)		(cm)		(mm)	(deg)	(cmkp)		
I	25	58	28	49	m	174	0	-235	75	1160	<input type="checkbox"/>	ventral
II	24	55	26	58	m	171	+	-165	90	1450	<input checked="" type="checkbox"/> C6/C7	
III	19	60	24	56	m	170	+	-215	100	680	<input checked="" type="checkbox"/> C6/C7	ventral
IV	19	55	18	72	m	169	++	-185	93	900	<input type="checkbox"/>	
V	28	67	39	54	m	172	0	-170	108	1550	<input type="checkbox"/>	ventral
VI	29	66	32	53	f	160	0	-250	88	1250	<input checked="" type="checkbox"/> C7/TH 1	
VII	25	113	52	34	m	170	0	-235	140	1500	<input checked="" type="checkbox"/> larynx	ventral and dorsal
VIII	26	109	52	68	f	164	+++	-185	112	2100	<input checked="" type="checkbox"/>	
IX	26	167	53	42	f	166	0	-160	138	1100	<input type="checkbox"/>	

Table 1: Simulated rear-end collisions without headrests

Table 2 summarizes the experiments. Bending of the head with respect to the torso occurred in the range of 30 to 119 degrees. The amount of bending depended on the distance between the center of mass of the head and the point of support at the headrest. The rotation was also related to the type and quality of the headrests, some of which were bent backwards by the impacting head.

Neck torque could not be computed because an unknown portion of the bending force was absorbed by the headrest.

Post-experimental investigation of the cervical column showed that only 3 cadavers were without macroscopical damage caused by impact: In run no. X, the cadaver of a 46 year old man with only minor predamage had been bent 112 degrees. In run no. XIV, with a 72 year old man, the bending angle was only 30 degrees because a well designed headrest kept the head up. In run no. XVI, the neck of a severely predamaged man of 76 was bent 70 degrees.

Figure 6 shows the data of run no. XVI. Fifteen milliseconds after sled impact, the head is accelerated in the direction of the impact. Another 15 ms later, the head suddenly begins to rotate in the opposite direction. When the head is nearly erect, it hits the headrest, as indicated by oscillations in the head acceleration curve, with the peak reaching 60 g. The head then rotates farther backwards until it reaches its maximal bending angle of 70 degrees 160 ms after the beginning of the impact. Then the head returns slowly. Head rotation is stopped when the chin touches the chest 450 ms after the initial impact. In this case, an effective headrest protected the cervical column by absorbing much of the impact energy.

Generally, however, the vertebral disks of the lower part of the cervical vertebral column were injured and the ventral ligaments were torn. In two runs (no. XV and XXI), ventral and dorsal ligaments were lacerated. A typical example for an ineffective headrest is given in figure 7 (run no. XII). The support rotates backwards and the neck is bent at the axis of rotation of the headrest. This resulted in torn intervertebral disks and ruptured ligaments

run no.	impact parameters			cadaver data				upper edge of the headsupport above CM of the head	experimental results			
	max. sled acceleration	duration of impact	velocity	age	sex	stature	predamage		max. head rotation relative to torso	max. inertial force of the head (phase 3)	impact damage to disks	rupture of ligaments
	(g)	(ms)	$\left(\frac{\text{km}}{\text{h}}\right)$	(yrs)		(cm)		(mm)	(deg)	(kp)		
X	26	116	55	46	m	176	+	-85	112	54	□	
XI	26	111	54	69	m	169	+++	-30	119	37	■ C4/C5 ■ C7/TH 1	ventral
XII	26	115	54	82	m	175	+++	+10	80	87	■ C5/C6 ■ C7/TH 1	ventral
XIII	not recorded			62	f	163	+	-30	80	152	■ C6/C7	ventral
XIV	23	115	51	72	m	168	+	+35	30	186	□	
XV	24	113	49	40	m	172	++	-70	107	130	■ C6/C7	ventral and dorsal

Table 2: Simulated rear-end collisions with headrests

run no.	impact parameters			cadaver data				upper edge of the headsupport above CM of the head	experimental results			
	max. sled acceleration	duration of impact	velocity	age	sex	stature	predamage		max. head ro- tation relative to torso	max. inertial force of the head (phase 3)	impact damage to disks	rupture of ligaments
	(g)	(ms)	( $\frac{\text{km}}{\text{h}}$ )	(yrs)		(cm)		(mm)	(deg)	(kp)		
XVI	25	115	47	76	m	174	+++	+ 90	70	74	<input type="checkbox"/>	ventral
XVII	25	118	51	66	m	169	+++	+ 60	68	130	<input checked="" type="checkbox"/> C5/C6	ventral
XXVIII	25	114	51	60	m	168	+	+130	100	100	<input checked="" type="checkbox"/> C6/C7	ventral
XIX	25	110	51	73	m	158	+	- 45	105	72	<input checked="" type="checkbox"/> C3/C4 <input checked="" type="checkbox"/> C6/C7	ventral
XX	24	112	46	70	m	170	++	+ 90	70	170	<input checked="" type="checkbox"/> C6/C7	
XXI	not recorded			79	f	162	+++	----	----	----	<input checked="" type="checkbox"/> C7/TH 1	ventral and dorsal

Continuation of Table 2

run no.	impact parameters			cadaver data				upper edge of the headsupport above CM of the head (mm)	experimental results			
	max. sled acceleration (g)	duration of impact (ms)	velocity (km/h)	age (yrs)	sex	stature (cm)	predamage		max. head rotation relative to torso (deg)	max. inertial force of the head (phase 3) (kp)	impact damage to disks	rupture of ligaments
XVI	25	115	47	76	m	174	+++	+ 90	70	74	<input type="checkbox"/>	ventral
XVII	25	118	51	66	m	169	+++	+ 60	68	130	<input checked="" type="checkbox"/> C5/C6	ventral
XVIII	25	114	51	60	m	168	+	+130	100	100	<input checked="" type="checkbox"/> C6/C7	ventral
XIX	25	110	51	73	m	158	+	- 45	105	72	<input checked="" type="checkbox"/> C3/C4 <input checked="" type="checkbox"/> C6/C7	ventral
XX	24	112	46	70	m	170	++	+ 90	70	170	<input checked="" type="checkbox"/> C6/C7	ventral
XXI	not recorded			79	f	162	+++	----	----	----	<input checked="" type="checkbox"/> C7/TH 1	ventral and dorsal

Continuation of Table 2

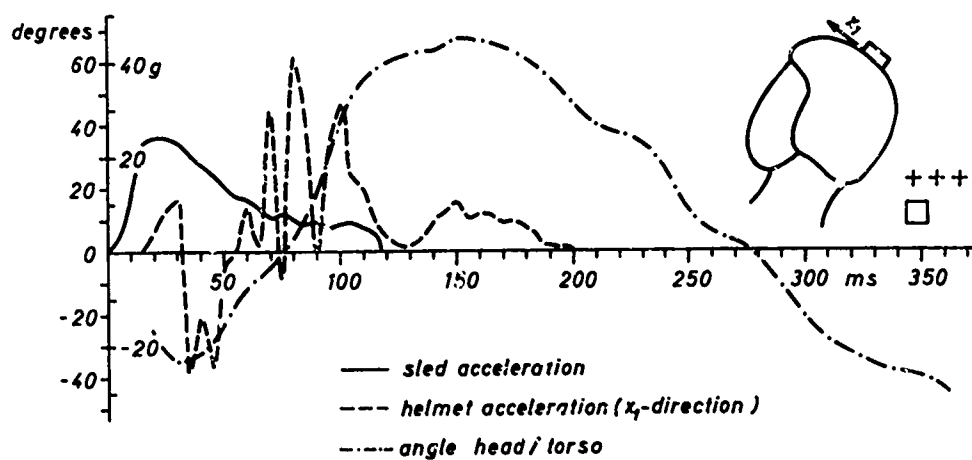


Figure 6: Whiplash in test no. XVI

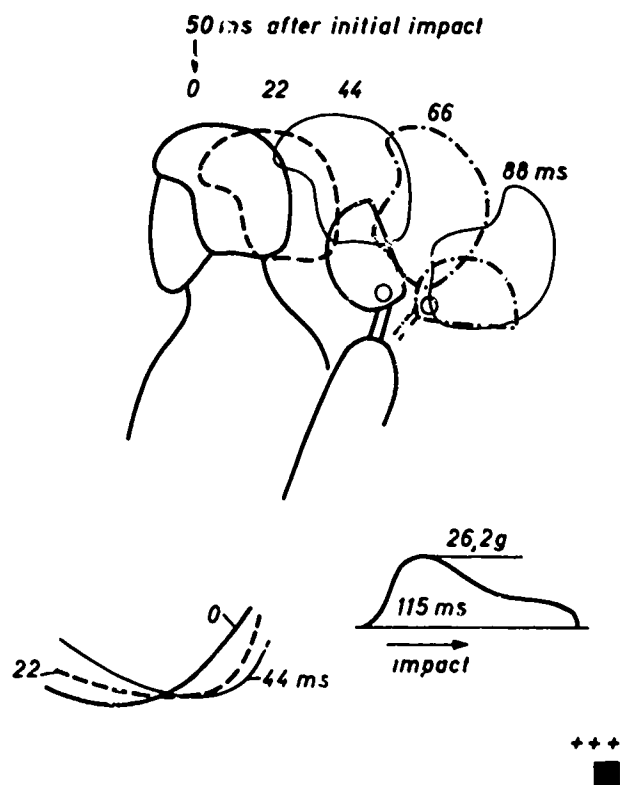


Figure 7: Whiplash in test no. XII

between vertebral C4/C5 and C7/T1. The time history of acceleration and of the angle head to torso is shown in figure 8. Here, the maximal bending occurs during sled acceleration and at about the same time when the head is subjected to its highest angular acceleration. The backrest is not strong enough to resist the inertial force of the head and gives way. In this case, the torque of the neck is superimposed by significant shear forces and by axial forces resulting from the sled acceleration. The severely predamaged cervical column was not able to resist the strain and suffered extensive trauma.

#### HEAD-ON COLLISIONS

In 15 simulations of frontal collisions, cadavers were placed into standard bucket seats. They were held in position with a 3-point-harness and in one case with a double diagonal shoulder belt.

In the first 10 runs, a steering wheel was in front of the cadaver to which the hands were tied. In addition to the accelerations of the sled and the head the acceleration of the chest and the forces within the safety belts were recorded. In these simulations of severe frontal collisions with steering wheel and seatbelt (21% stretch when loaded with 1000 kp) installed, the head hit the wheel. This limited the amount of bending of the neck, but brought about additional shear forces that strain the column.

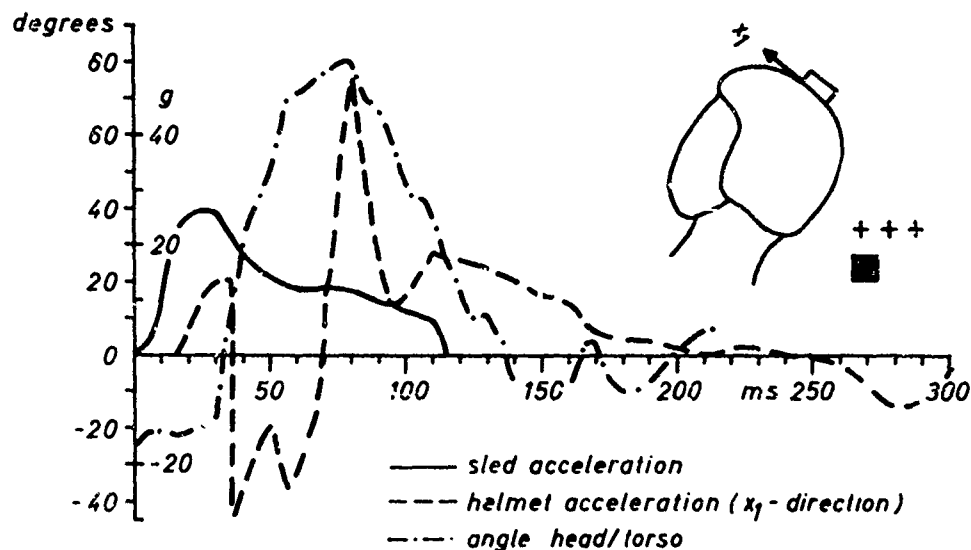


Figure 8: Investigation of whiplash, test no. XII

Figure 9 shows the motion of the cadaver as well as the seat belt forces and the accelerations recorded in test no. VII. The head bends only 30 to 40 degrees before striking the steering wheel during the sled acceleration. In this case only haemorrhages of the neck muscles round the upper part of the cervical column were confirmed although the column was evidently predamaged.

Another impact situation is shown in figure 10. Here, the head rotates nearly 90 degrees and then hits the steering wheel after sled acceleration has ceased. The different motions of the cadavers in runs no. VII and IX may be explained by their different anthropometric characteristics (stature, weight, mass distribution etc.). In test no. VII, force F2 amounted to 430 kp and force F3 to 350 kp, versus 350 and 450 kp, respectively, in test no. IX. In test no. IX, the lower part of the torso was more effectively restrained than in test no. VII. Thus, in test IX, the upper part of the torso could bend forward farther than in test VII. After run IX, three injured intervertebral disks (C3/C4, C4/C5, C5/C6) were found but no ligament was torn.

Table 3 summarizes the frontal collisions with steering wheels and belts installed. The acceleration of the chest is, with one exception, generally higher than that of the sled. This is due to and depends on the stiffness of the belt, and on how the belt is located on the cadaver. Chest acceleration also depends on how and when the chest hits the steering wheel. This is indicated by the belt forces recorded with and in absence of a steering wheel, as discussed later.

Injuries to the cervical column sustained in the frontal collision with steering wheel are quite different from those observed after the rear-end collision. After the frontal impact, a fracture of the dens was discovered (run no. IV); a partial rupture of the intervertebral disks between C2 and C3 occurred in run no. V; four adjacent vertebrae were damaged in run no. IX. On the other hand, only severe bleeding of the neck muscles was discovered in runs VII and VIII. Ruptures of ligaments occurred only three times: In one case, only on the ventral side, in two cases both on the dorsal and the



run no.	impact parameters				belt forces			cadaver data					experimental results	
	max. sled acceleration	duration of impact	velocity	max. chest acceleration	F <sub>1</sub> max.	F <sub>2</sub> max.	F <sub>3</sub> max.	age	sex	stature	weight	predamage	impact damage to disks	rupture of ligaments
	(g)	(ms)	( $\frac{km}{h}$ )	(g)	(kp)	(kp)	(kp)	(yrs)		(cm)	(kp)			
I	21	60	18		480	360	210	69	m	181	92	+	☐ C6/C7	ventral and dorsal
II	22	122		22	590	400	-	49	f	168	45	+	☐ C5/C6, C6/C7	
III	21	123	49	25	470	400	70	68	f	168	65	++	■ C6/C7	ventral and dorsal
IV	23	120	44	38	660	400	350	78	f	168	58	+++	■ dens	
V	22	140	51	45	630	470	280	69	m	169	67	+++	☐ C2/C3	
VI	27	123	47	51	550	420	280	80	m	178	85	+++	☐ C5/C6, C6/C7	ventral
VII	20	126	48	40	860	430	350	53	m	185	90	++	☐	
VIII	20	86	37	37	480	340	240	82	f	155	77	+	☐	
IX	21	86	34	38	840	350	440	60	m	176	80	++	■ C3/C4, C4/C5, C5/C6	
X	23	120	48	39	500	300	260	62	f	155	50	+	☐	

Table 3: Simulated frontal collisions with steering wheel, lap belt and single diagonal safety belt

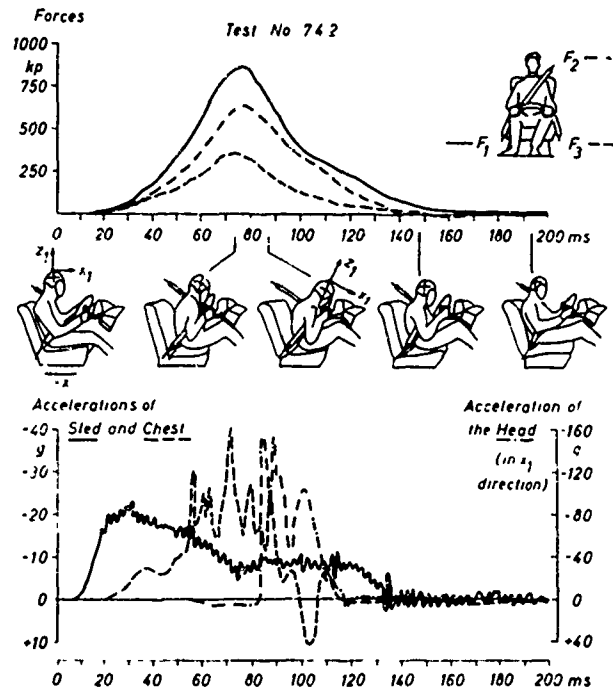


Figure 9: Accelerations and belt forces in a simulation of a frontal collision (test no. VII)

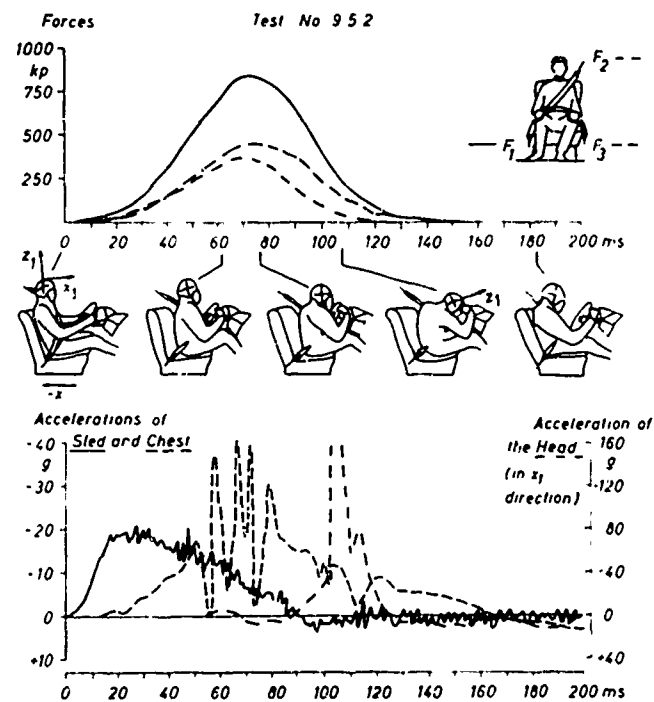


Figure 10: Accelerations and belt forces in a simulation of a frontal collision (test no. IX)

ventral side. Thus, quite a variety of injuries is present, no "typical" reaction of the cervical column to a severe frontal collision with steering wheel apparent. However, shear forces and axial forces seem to be mainly responsible for the injuries sustained.

Another five head-on collisions were simulated without a steering wheel. These are the runs nos. XVII to XXI listed in table 4. Run no. XXI with a severe bending of the neck is illustrated in figure 11.

Chest acceleration begins 10 ms after sled acceleration and then increases to 35 g in 30 ms. This steep onset is due to the stiffness (12% stretch at a load of 1000 kp) of the belt and the fact that it was attached to the cadaver very tightly. The head rotated by as much as 123 degrees. A torque of about 4200 cmkp (3650 in lb) at the C6/C7 interface was estimated to result from the inertial energy of the head. This explains why the predamaged column of the cadaver was severely injured at C5/C6 and C6/C7 with the dorsal ligaments torn.

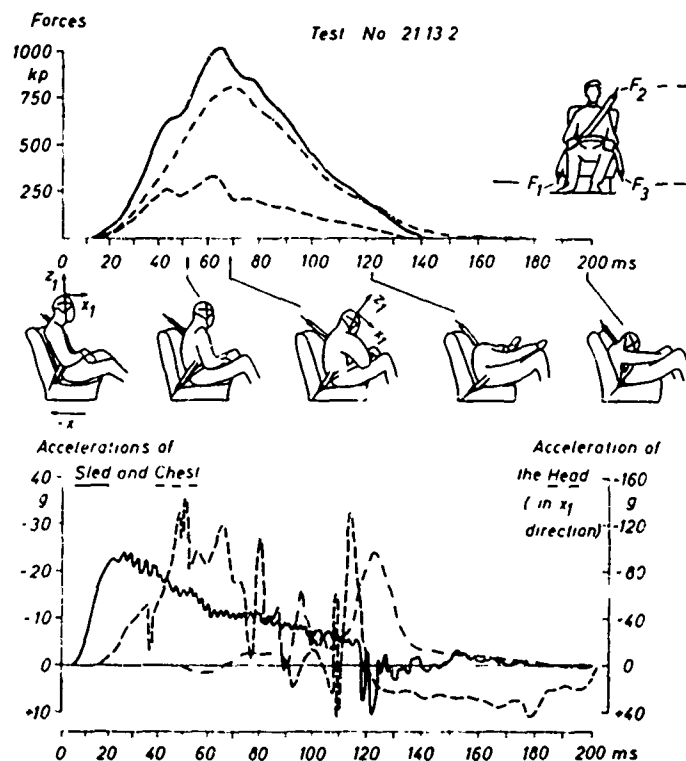


Figure 11: Accelerations and belt forces in a simulation of a frontal collision (test no. XXI)

run no.	impact parameters				belt forces			cadaver data					experimental results			
	max. sled acceleration	duration of impact	velocity	max. chest acceleration	F <sub>1</sub> max.	F <sub>2</sub> max.	F <sub>3</sub> max.	age	sex	stature	weight	predamage	max. head rotation relative to torso	torque between C6/C7	impact damage to disks	rupture of ligaments
	(g)	(ms)	( $\frac{km}{h}$ )	(g)	(kp)	(kp)	(kp)	(yrs)		(cm)	(kp)		(deg)	(cmkp)		
XVII	23	122	44	28	730	610	440	75	m	172	91	+++	52	2750	☑ C6/C7	
XVIII	26	122	48	38	1020	760	380	32	m	170	86	0	52	2900	☐	
XIX	27	112	50	47	950	780	460	32	f	170	58	0	127	3200	☑ C7	dorsal
XX	26	115	46	36	780	300	560	52	m	175	80	0	86	3400	☑ C5/C6	
XXI	25	125	50	38	1000	800	340	56	m	178	71	+++	123	4200	■ C5/C6, C6/C7	dorsal

protected by a (V-type) double shoulder harness

Table 4: Simulated frontal collisions without steering wheel but with lap belt and single (double) diagonal shoulder belt

Figure 12 illustrates run no. XX. Here, a (V-type) double shoulder harness protected the cadaver from moving forward more than about 20 cm, and drew the cadaver back into the seat after the impact. The head rotated 86 degrees, the maximal torque was computed to be 3400 cmkp (2960 in lb). Only some bleeding nerve roots near cervical vertebra 7 were found in the autopsy.

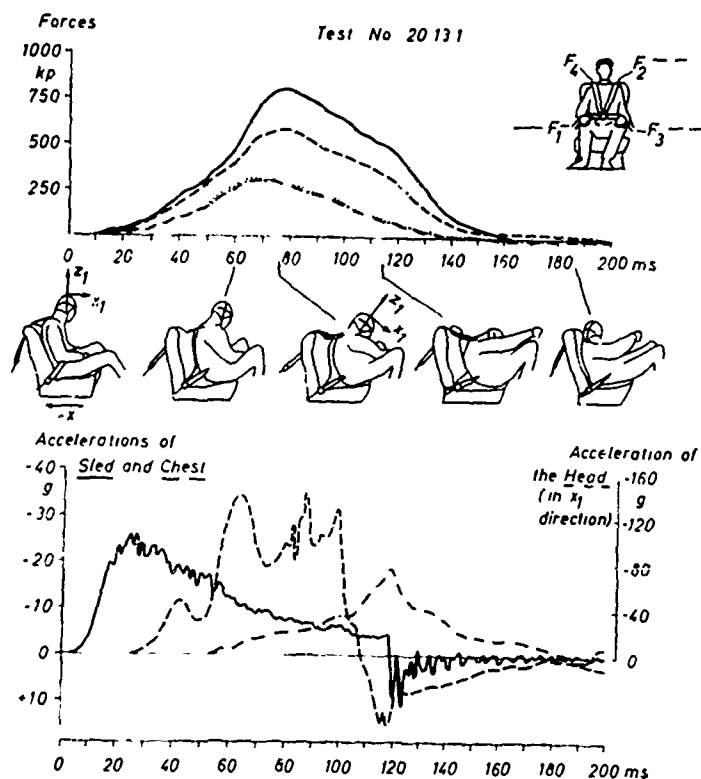


Figure 12: Accelerations and belt forces in a simulation of a frontal collision (test no. XX)

The curves in figure 13 indicate the rotation of the head relative to the torso observed in runs nos. XVII to XXI. The maximal rotations are between 90 and 120 degrees. The peaks occur about 120 ms after the initial impact. They happen simultaneously with the maximal angular acceleration of the head. Figure 13 also shows that the stiff belts used in runs XIX (6% stretch) and XXI (12% stretch) seemed to bring about extensive head rotations while the softer belts in runs XVII and XVIII (21% stretch under a static load of 1000 kp) stretched more easily and caused less head rotation.

As table 4 shows, maximal torques at the disks between C6 and C7 were in the range of 2750 to 4200 cmkp. Only the lower part of the cervical column was damaged, no ventral ligaments were torn. Both predamaged columns suffered additional disk ruptures. In run no. XVIII, with a column sound before the experiment, no macroscopical injuries at all were caused by the impact. Run no. XIX caused a fracture of the 7th spinal process and a partially torn dorsal ligament of an initially undamaged cadaver.

#### 45 DEGREE-COLLISIONS

Six additional experiments were performed with simulated 45 degree-collisions. Three of them (nos. XI - XIV in table 5) were rear-end collisions, the other three were frontal ones. Table 5 contains some of the experimental data. Figure 14 illustrates a frontal collision under 45 degrees left. Because of his inertia, the cadaver restrained by lap belt and a diagonal belt passing over his left shoulder, rotated on the seat into the direction of the impact. Thus, his neck was stressed in about the same manner as in a straight head-on collision. Forward rotation of the head was estimated to be about 90 degrees. The autopsy showed a ruptured disk between C6 and C7, but no torn ligaments.

The possible effects of rear-end collision under 45 degrees left are shown in figure 15. Here the upper torso slips away from under the belt passing over his right shoulder. Then the body moves backwards and upwards along the backrest being supported mainly by its upper edge. During this motion even the helmet strikes the backrest, as indicated by oscillating accelerations about

run no.		impact parameters			cadaver data					experimental results	
		max. sled acceleration	duration of impact	velocity	age (yrs)	sex	stature (cm)	weight (kp)	predamage	impact damage to disks	rupture of ligaments
		(g)	(ms)	$\left(\frac{\text{km}}{\text{h}}\right)$							
XI	rear-end collisions at 45° left	24	124	46	62	m	180	75	+	<input type="checkbox"/>	
XII		23	121	44		m	179	78	0	<input type="checkbox"/>	
XIII		21	114	46	62	f	168	62	+++	<input checked="" type="checkbox"/> C4/C5, C5/C6 (TH 11)	
XIV	frontal collisions at 45° left	not recorded			36	m	174	72	0	<input checked="" type="checkbox"/> C6/C7	
XV		21	119	48	25	m	190	88	0	<input checked="" type="checkbox"/>	
XVI		23	124	48	65	m	164	67	+++	<input checked="" type="checkbox"/> C6/C7	

Table 5: Simulated collisions at 45 degrees

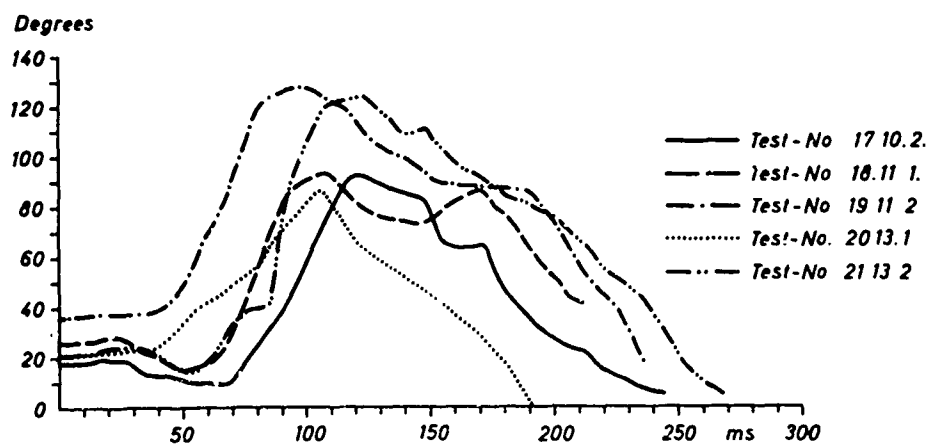


Figure 13: Rotation of the head relative to the torso observed in runs nos. XVII to XXI

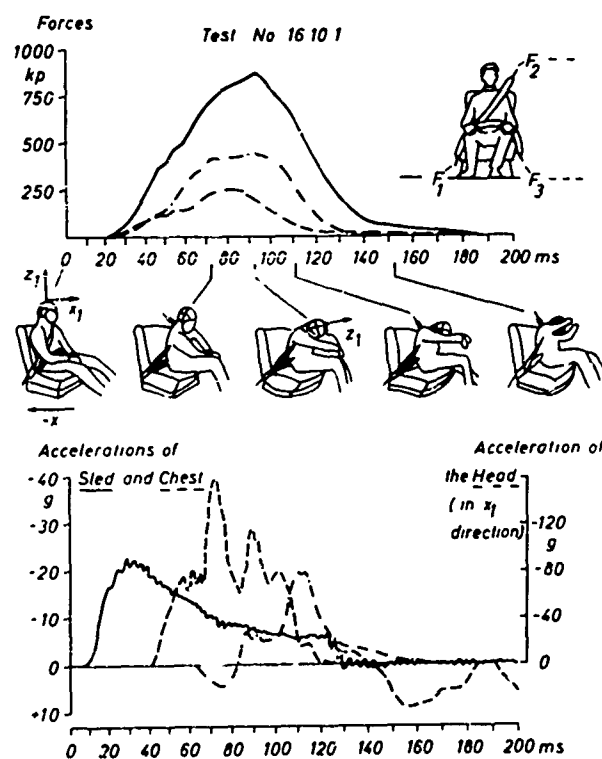


Figure 14: Accelerations and belt forces in a simulation of a frontal collision at 45 degrees left



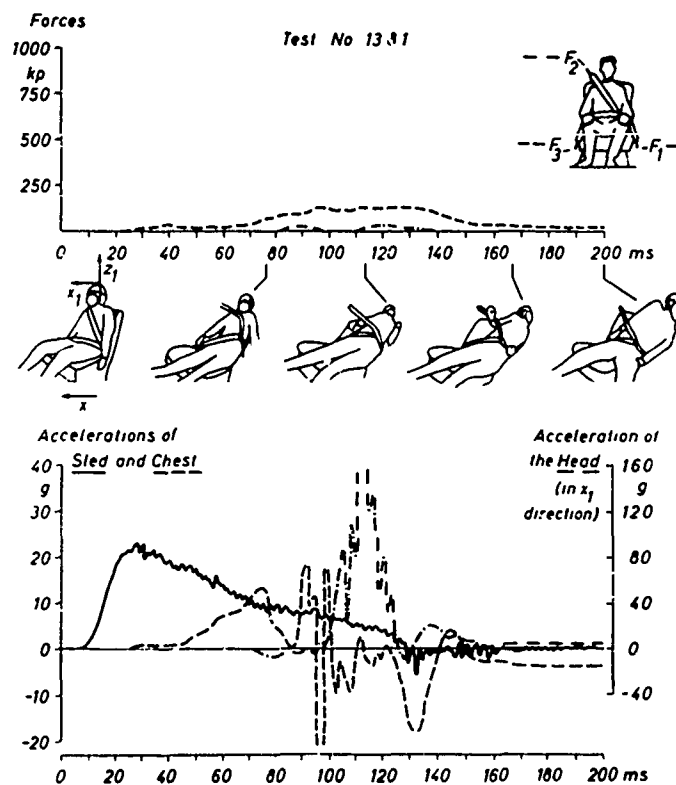


Figure 15: Accelerations and belt forces in a simulation of a rear-end collision at 45 degrees

120 ms after the initial impact. The autopsy unveiled ruptured disks between C4/C5 and C5/C6 and a fraction of the 11th thoracic vertebra. In two further rear-end collisions of this kind no macroscopic damage occurred.

### SUMMARY AND CONCLUSIONS

The reported investigations of the response of the cervical vertebral column of cadavers to severe impacts indicate that at least three variables significantly affect type and severity of macroscopic damage:

- 1) the angle of rotation between head and torso
- 2) the torque exerted at the spine
- 3) the predamage of the column.

The magnitudes of rotation and torque in turn depend on the amount and the direction of impact, on the support offered to the body by a backrest, a headrest and the steering wheel. Rotation and torque also depend on the type of safety belts used, on their plasticity, and on the snugness or slack with which they are worn.

In our experiments, especially the lower part of the cervical vertebral column was injured when the head was not caught by a suitable headrest. Severe damage to intervertebral disks was generally found to coincide with tearing of ligaments. Frontal impacts affected mainly the dorsal ligaments while impacts from the rear often resulted in ruptures of the ventral ligaments. The experiments showed that pre-experimental damage to the cervical column can aggravate succeeding impact injuries. This is of some practical importance since at only 50 years of age about every second woman's and man's spinal column is affected by spondylosis deformans. As figure 16 shows, 9 of 10 columns are affected at age 60.

Despite the many difficulties encountered when trying to extrapolate results of cadaver experiments to the living body, it is hoped that the reported experimental findings help to understand the response of the mechanisms of the human body to severe impacts.

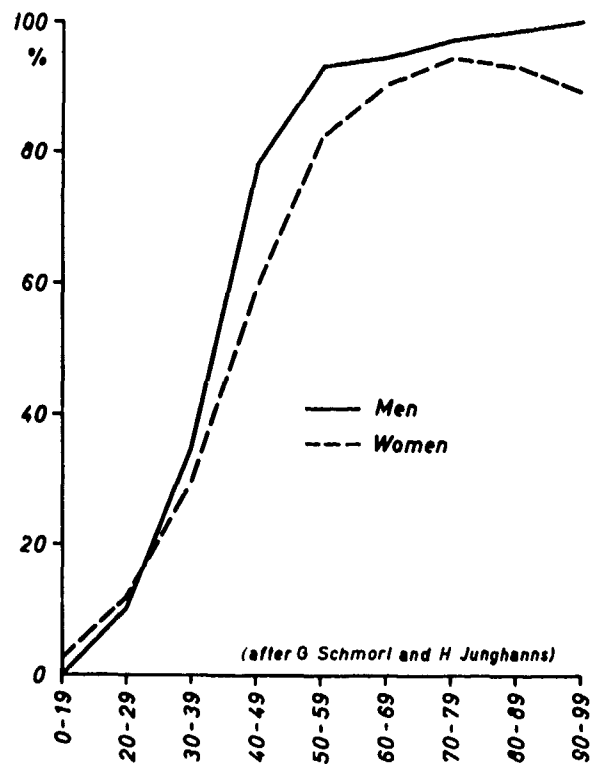


Figure 16: Occurrence of spondylosis deformans at men and women in different ages (n=4.253)

\*Redrawn from Schmorl and Junghanns, 1968 [8]

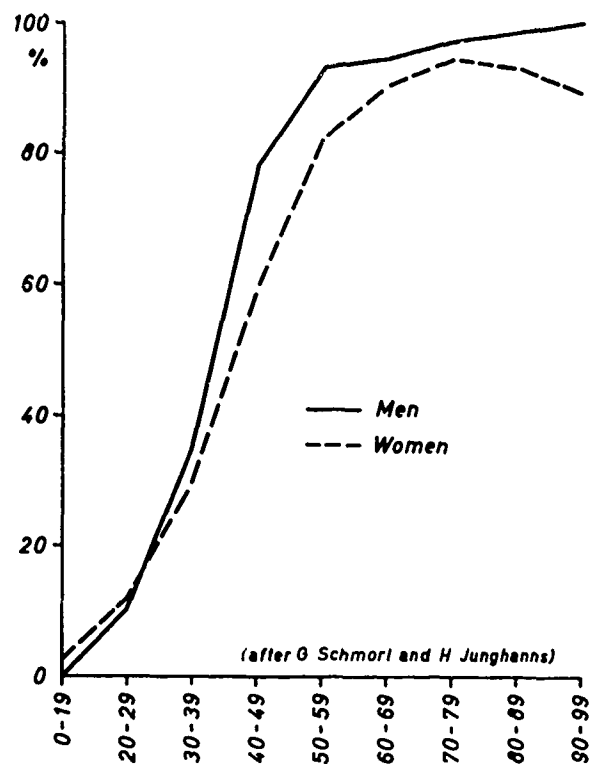


Figure 16: Occurrence of spondylosis deformans at men and women in different ages (n=4.253)

\*Redrawn from Schmorl and Junghanns, 1968 [8]

## LITERATURE

1. Emori, R.I. : Analytical Approach to Automotive Engineering Congress, Detroit, Mich., 1968
2. Fiala, E., and B. Fabricius : Stobartige Beschleunigung von Fahrzeuginsassen bei Auffahrunfällen. Forschungsbericht Nr. 52, Institut für Kraftfahrzeuge, Technische Universität Berlin 1968
3. Hinz, P., and L. Tamaska : Arteria Vertebralis und Schleuderverletzung die Halswerbelsäule. Archiv für orthopädische und Unfall-Chirurgie 64, 268-277(1968)
4. Hinz, P. : Vielschichtige Untersuchungsmethoden zur Erfassung pathomorphologischer Sektionsbefunde nach Schleudertraumen der Halswirbelsäule. Dtsch. Z. ges. gerichtl. Med. 64, 204-216 (1968)
5. Hinz, P., R. Coermann, and W. Lange : Das Verhalten der Halswirbelsäule bei der Simulation von Auffahrunfällen. Monatsschrift für Unfallheilkunde, Heft 8, 321-328 (1969)
6. Lange, W., and P. Hinz : Auffahrunfälle mit und ohne Kopfstütze. VDI-Zeitschrift 20/1970
7. Mertz, H. J., and L. M. Patrick : Investigation of the Kinematics and Kinetics of Whiplash. 11th Stapp Car Crash Conference, Anaheim, California, October 10-11, 1967
8. Schmorl, G., and H. Junghanns : Die gesunde und die kranke Wirbelsäule in Röntgenbild und Klinik. Georg Thieme Verlag, Stuttgart 1968

AMRL-TR-71-29

SESSION II

MODELS FOR THE INTERPRETATION OF ANIMAL,  
DUMMY, AND OPERATIONAL EXPERIMENTS

Chairman

A. Hirsh  
National Highway Safety  
Bureau

Co-chairman

T. Moore  
AMRL

re: 10/10/71 Page 1000

BIODYNAMIC MODELING AND SCALING:  
ANTHROPOMORPHIC DUMMIES, ANIMALS AND MAN

M. Kornhauser

Consulting Services  
Wynnewood, Pennsylvania

ABSTRACT

After a brief outline of the applications and methods of biomechanics and the major sources of biodynamics data, this paper reviews the status of mathematical modeling, physical modeling (dummies) and scaling of models and damage levels.

Biomechanics data required for preparing mathematical models, as well as for adjusting and validating the computer programs, are found to be insufficient for computational applications. Because of this paucity of supporting data, computer models are in general oversimplified and rudimentary, despite the availability of adequate computational techniques used in the aerospace industry.

Physical models and the requirements for dynamic similarity are discussed. Although quantitative simulation is warranted under some circumstances, anthropomorphic dummies are expected to be of most value as visual aids and for purposes of demonstrating kinematic relationships between man and vehicle.

Scaling from dummies to man and from animals to man is difficult to justify theoretically because of differences in structure, size and modes of failure. However, damage scaling in terms of the inputs (G and  $\Delta V$ ) required for failure, is shown to be accurate enough for purposes of rough approximation.

The mathematical model approach, with proper validation, is concluded to offer ultimately the greatest promise of accurate quantitative prediction.

PRECEDING PAGE BLANK

## INTRODUCTION

Biomechanics is an interdisciplinary blending of the biomedical and the physical sciences applied to the effects of dynamic mechanical environments on living organisms. In its broadest terms, biomechanics covers a wide range of mechanical environments such as shock and vibration, acoustic inputs, air blast, underwater explosion effects, etc.; as well as applications to a variety of organisms. The discussions of this paper are restricted to the narrower subject of the effects of whole body impact or deceleration (not direct impact of projectiles, etc.) on man and other animals.

The primary purpose of biomechanics is to predict response and injury, via the following route:

(1) Input - Definition of the force application or input to the biological system, spatially and in terms of its time history. In many cases the loading system is coupled to the biomechanical system, for example in the cases of vehicular crashes, and it may become necessary to define inputs to the entire vehicle-man coupled system.

(2) Response - Observation, analysis or prediction of the response of the organism to the inputs. In the cases of analysis and prediction, it is necessary to obtain some kind of biomechanical definition, or model, of the organism and to subject this model to the mechanical inputs.

(3) Failure - Observation, analysis or prediction of failure, damage, or injury to the organism. For purposes of prediction, it becomes necessary to determine the various mechanisms of injury and to ascertain whether one or more mechanisms have been excited to the point of failure.

(4) Prediction - Prediction of response and failure of the animal, or another animal, to other inputs.

The latter three steps are discussed further in this paper in terms of the methods employed, an evaluation of accomplishments to date, and recommendations for the future.



## METHODS OF BIOMECHANICS

Four broad sources of data are employed to assist in the process of prediction human response and injury:

- (1) Results of experimentation on man and natural incidents involving humans.
- (2) Animal experimentation.
- (3) Mathematical "experiments" with computer models.
- (4) Physical experimentation with dummies.

Table 1 presents in capsule form the relative advantages and disadvantages of each approach to obtaining useful data.

The above listing of methods of obtaining data is generally in the direction of less direct applicability to man (requiring more adjustment, interpretation, or scaling) for numbers (2), (3), and (4), although their sequence is not intended to be exact. Mathematical and physical models are discussed below in terms of the sources of inaccuracy and methods of application.

## MATHEMATICAL MODELING

The process of mathematical modeling of the human body may be compared directly with the similar process employed in the aerospace industry to model a large aircraft or space structure. Table 2 lists the main steps required to develop and validate a mathematical model.

Although the aerospace industry has matured and developed a sophisticated technology of mathematical modeling, the biomechanics community has not been able to justify complex models (because of the paucity of the biomechanical data required for modeling and validation of models) and only very recently has begun to adopt aerospace methods. The best work has been done in the biomedical areas (1) and (3) of Table 2, but the potentialities of the engineering areas (2) and (4) have not been exploited well.

METHOD	ADVANTAGES	LIMITATIONS
MAN: Experimentation, results of accidents	Realistic: • Material properties • Neuromuscular reactions • Injury modes	<ul style="list-style-type: none"> <li>• Experimentation only to point of discomfort</li> <li>• Accident details hard to reconstruct</li> <li>• Accident data statistical</li> </ul>
ANIMALS: Experimentation	<ul style="list-style-type: none"> <li>• Tissue properties similar to man</li> <li>• Neuromuscular reactions</li> <li>• Injury modes similar to man</li> </ul>	<ul style="list-style-type: none"> <li>• Structures different from man</li> <li>• Organic differences</li> <li>• Size scaling necessary</li> </ul>
COMPUTER MODELS	<ul style="list-style-type: none"> <li>• Ease of "experimentation"</li> <li>• Programs reproducible and permanent</li> <li>• Model may be improved to any degree of fidelity</li> </ul>	<ul style="list-style-type: none"> <li>• Parameters must be adjusted per experiment results.</li> <li>• Need a good set of subsystem (organs, etc.) models for good overall system model</li> </ul>
PHYSICAL MODELS: Anthropomorphic dummies	<ul style="list-style-type: none"> <li>• A superb visual aid</li> <li>• Inexpensive way of observing kinematic effects</li> </ul>	<ul style="list-style-type: none"> <li>• Expensive to model internal organs adequately.</li> <li>• Serious problems of friction damping, mat'l properties</li> <li>• Injury hard to predict</li> </ul>

Table I

STEP	AEROSPACE MODELING	BIODYNAMIC MODELING
(1) Idealization of actual structure into lumped parameters or continuous element in order to prepare the subsystem models.	Reduction of beams, plates, shells, etc. to mass-spring elements. Nonlinearities, large deflection effects, and damping estimated.	Tissue properties, joint properties, organic geometry must be reduced to lumped or distributed elements. Non-linearities, damping estimated.
(2) Subsystems are coupled to form a system model	The math modeler's skill enters here in developing an efficient (short running time) system model. Coupling techniques are discussed in the text.	
(3) Model exercised to obtain modes, frequencies response, and failure	Failure defined in terms of excessive deflection (performance affected) or permanent strain.	Failure criteria include strain (fracture, rupture) deflection (cervical stretch, for example), pressure (a concussion mechanism).
(4) Model adjusted and validated by comparison with subsystem and system tests.	Comparison of free-free modes and frequencies, static deflection tests, influence coefficients <sup>3</sup>	Modes, frequencies <sup>1</sup> , impedance measurements <sup>2</sup> from vibration and low-level impact tests.

Table 2

Much work has been done to define tissue and joint properties. Without tabulating the actual properties, Table 3 lists some sources and examples of the data available. Data of this kind must be available in order to accomplish Step (1) of Table 2.

Step (2) of Table 2 involves formation of the system model, which may be one or more organs, the entire body, the body plus restraints, etc., depending on the application to be simulated. The human body is a structurally complex system, composed of subsystems (organs, limbs, etc.) made of dissimilar materials and coupled to each other in complex ways. In certain loading regimes such as high frequency vibrations, grossly different transmission properties of the bony skeleton and the "hydraulic" vascular system will result in parallel structural systems responding out of phase, but coupled throughout by interconnecting tissues. With lower frequency inputs, however, the parallel systems may react essentially as one system. Modeling such a system poses formidable challenges to the structural dynamics analyst who is accustomed to modeling aerospace structures. He must learn to select the significant breakdowns of mass, elasticity and damping in order to construct the biodynamic model; and the selection techniques will be somewhat different from those he has used for steel or titanium in plates, shells, I beams, etc. However, the general methods of analysis are identical, and the aerospace industry can provide a powerful tool for computer modeling the complex human structure.

Hurty<sup>16</sup>, Bamford<sup>17</sup> and others develop a most fruitful method for computer modeling of exceedingly complex structures. In the component mode approach to modeling, the subsystems are first broken down to whatever level of detail is required for adequate dynamic representation. Experience and judgment are, of course, required to determine adequacy. Besides, however, the subsystem may be tested experimentally to ascertain whether enough modes have been represented, and how accurately. There may, of course, turn out to be a limitation in computer capacity or running time, which could force the modeler to split the subsystem into smaller

TISSUE, JOINT, ORGAN	SOURCE OF DATA
Soft tissues, muscle, bone	Goldman & von Gierke <sup>4</sup> , Nickerson & Drazic <sup>5</sup> , von Gierke <sup>6</sup> , Fung <sup>7</sup> , Starr et al <sup>8</sup> , Sittel <sup>9</sup> , Roberts et al (ref) <sup>14</sup>
Blood, arteries	Fung <sup>7</sup> , Roberts et al (ref) <sup>14</sup> , Starr et al <sup>8</sup>
Intervertebral disc	Hanzel <sup>10</sup> , Sonnerup <sup>11</sup> , Orne & Liu (ref) <sup>13</sup>
Spine	Henzel <sup>10</sup> , Orne & Liu (ref) <sup>13</sup>
Knee joint	Edwards <sup>12</sup>
Leg, foot	Hirsch & White <sup>15</sup> , Roberts et al <sup>14</sup>
Skull	Goldman & von Gierke <sup>4</sup> , Starr et al <sup>8</sup>

Table 3

subsystems. However, with a large machine which can handle of the order of 100 elements comfortably, it should be possible to develop good dynamic lumped models of each human organ as a subsystem. The subsystem program is then run to obtain output modes. Subsystems are now tied together at their physical points of connection to obtain overall system response to a set of inputs. The final step is to go back to each subsystem to read out its response (perhaps to failure) in its own modes.

The basic advantage of working in modal coordinates is economy. The overall coupled system modes are approximately equal to the number of subsystems times the modes represented in each subsystem. Therefore if an average of 10 modes were found adequate to represent each of 10 different subsystems, the coupled system program would have 100 elements. A single program for all subsystems taken together could have required 1,000 elements, which would have been prohibitive in size. Therefore the component mode approach appears suitable for modeling the human body, with its hundreds of bones and muscles.

A comment is in order on the question of continuum mechanics programs vs. lumped parameter programs. There is really no difference between these approaches if a fine enough breakdown of lumped parameters is made. Stress wave behavior will be exhibited without an inordinate degree of definition. A beam or column, for example, will require of the order of 10 subdivisions to exhibit minimum "continuous" properties.

Nonlinearities do pose a special problem in the component mode approach, since the modes will shift with change in amplitude of input and response. For example, it is known that a steady linear acceleration will cause increased stiffness, less damping, and higher energy transmission to internal organs when the human body is then subjected to vibration. It is therefore necessary to adjust the subsystem modes to be consistent with the response obtained, and this will be somewhat of an iterative process.

After the computer model has been assembled and exercised (step 3 of Table 2), it is desirable to make adjustments at all levels possible within the system. Test data<sup>1,2,3</sup> on modes, frequencies, etc. should be used to validate and adjust the subsystem programs. Table 4 presents some data on first mode frequencies.

Besides response data, static and dynamic failure data should be employed to validate computer models. (Some of these data will be presented below in a discussion of damage scaling). The end product is an adjusted and validated computer program which should provide some predictive value when applied to a situation for which experimental data do not exist.

How well has the biomechanics rationale described above been applied to the human body subjected to impact? The answer is, generally, in a rudimentary and perfunctory fashion. A fair (but not complete) picture of the history of computer models applied to human impact is presented in Table 5, in chronological order.

The earlier models were oversimplified one-or-two degree of freedom models, and they had limited predictive value. Some recent models (Turnbow, McHenry and Naab) treated the man as a kinematic linkage without internal flexibility, so that only external (to the body) loads could be determined. Other more detailed models (Coermann, Starr) were still not fine enough in breakdown to yield significant load and failure results within the human body. Only the most recent work of Orne and Liu<sup>13</sup> appears to have sufficient detail to be a truly significant tool for predicting spinal response and failure. Unfortunately, their model does not appear to have been adjusted by comparison with experiment, and validation of its predictive utility remains to be demonstrated.

To summarize the state of the art, it appears that only this year has an (apparently) adequate model of the human spine been developed. Obviously, much work remains in developing adequate models of the other human subsystems (limbs, organs, etc.), and coupling them to finally obtain a good system model of the human body.

MODE	FREQUENCY, CPS	SOURCE
Human viscera	3, 4	Coermann et al <sup>2</sup> , Roberts et al <sup>14</sup>
Standing man	5.7, 10	Stech & Payne <sup>20</sup> , Hirsch <sup>18</sup>
Seated man	6	Stech & Payne <sup>20</sup> , Hirsch <sup>18</sup>
Supine man	7.4-9.7	Stech & Payne <sup>20</sup>
Skull	700	Goldman & von Gierke <sup>4</sup>
Spine and head	6	Terry & Roberts <sup>19</sup> , Stech & Payne <sup>20</sup>
Thorax-abdomen (pressure excit.)	45-60	von Gierke <sup>6</sup>

Table 4



YEAR	MODEL	ELEMENTS IN COMPUTER PROGRAM	INVESTIGATOR	CORRELATION WITH EXPERIMENT
1941, 1943	Fluid-filled rigid skull		Anzelius, Goggio <sup>14</sup>	
1957	Man-seat	Two	Latham <sup>19</sup>	Seat load only
1958	Head on spine	Continuous elastic rod	Hess & Lombard <sup>19</sup>	Good, head accel.
1958	Supine man	One	Korhauser <sup>26</sup>	Good, survival only
1960	Standing man	6 masses, 7 springs	Coermann et al <sup>4</sup>	Good, vibrations
1962, 3	Head	Lumped, continuous	Payne <sup>14</sup>	
1966	Head on spine	One mass, continuous	Liu & Murray <sup>23</sup>	None
1966	Seated man	8 masses (kinematics only), spring restraint	McHenry & Naab <sup>14</sup>	Good, seat loads only
1967	Man-seat	"	Turnbow et al <sup>21</sup>	"
1968	Skull-brain	10 elements	Starr et al <sup>8</sup>	Qualitative only
1968	Head on spine	Cont viscoelastic rod	Terry & Roberts <sup>19</sup>	Good, head accel.
1969	Head on spine	One mass, continuous	Liu <sup>25</sup>	None
1969	Seated man	One, two	Yeager et al <sup>24</sup>	Good, seat loads
1970	Fluid-filled elastic skull	Continuous	Benedict <sup>22</sup>	None
1970	Head on spine	25, 3 degrees of freedom	Orne & Liu <sup>13</sup>	None

Table 5

## PHYSICAL MODELING AND SCALING

Table 1 summarizes the major advantages and limitations of using dummies as biodynamic tools, and these will not be expanded in more detail. Further, although it would be useful to discuss the practical problems of material selection (physical simulation of properties) and model construction (friction in joints, etc.), the present discussion will be restricted to the questions of scaling "laws" and what they predict about the adequacy of dummies and animals to represent the human body.

Hudson<sup>27</sup> presents a rather thorough discussion of scale model principles, although he does not address the special problems of anthropomorphic dummies. It is not appropriate to present here the theory of dimensional analysis and dynamic similarity. Instead, the conclusions reached by Hudson and others on the conditions required for dynamic similarity are presented in Table 6.

For dynamic similarity in general, it appears that geometric similarity and identical material properties are required. Hudson, however, indicates some structures for which complete geometric similarity is not required and for which all material properties need not be identical. Likewise, Baker and Westine<sup>30</sup> and Horowitz and Nevill<sup>31</sup> discuss modeling with dissimilar materials, although the former require materials with similar stress-strain curves while the latter use the area under the stress-strain as the correction criterion. Thus it appears possible to justify relaxation of the requirements for dynamic similarity under special circumstances.

Since humans and other animals are exceedingly complex structures, it is not possible to justify simulation by dummies on any theoretical basis. Only under very restrictive conditions, as for example when using kinematic dummies (no flexibilities, but simply masses and linkages with correct moments of inertia) to find motions and loads on restraint systems, can physical models serve useful quantitative purposes. As tools for purposes of visualization, or for demonstrating kinematic relationships of human and vehicle dynamics, anthropomorphic dummies are very helpful.

SOURCE	STRUCTURE	REQUIREMENTS FOR DYNAMIC SIMILARITY
<sup>28</sup> Hermes	Beams Plates Frames	(1) Geometric similarity, boundary conditions same (2) Velocity/speed of sound in mat'l = constant (3) Young's modulus of proto. & model must be same (4) Poisson's ratio " " " " " "
<sup>29</sup> Heller	Armor, non-penetrating impacts	(1) Geometric similitude (2) Identical material (3) Equal impact velocities
<sup>27</sup> Hudson	Beam ----- Plate	Area/length <sup>2</sup> = constant, radius of gyration/length = constant (rather than complete geometric similarity). ----- Geometric similarity, Poisson's ratio the same

Table 6

The scaling difficulties mentioned above apply, of course, to animal-to-human comparisons. Structure and size differences present serious obstacles to quantitative scaling. However, as with dummies, animal experimentation is invaluable in uncovering responses and failure mechanisms which often suggest similar qualitative behavior of human.

An invaluable animal-to-man correlation approach is to work with non-human primates of similar construction and to scale directly to man. This approach, of course, allows experimentation with primates which would not be permitted with humans. Besides this direct scaling for clinical purposes, the primate-series experimentation offers exciting possibilities for measuring tissue and organ properties and responses required for developing and validating computer models, which models may later be scaled for applications to humans.

#### DAMAGE SCALING

Despite the differences in structure which precludes any rationale for scaling between animals and man, it has been possible to do some fairly successful scaling based on the inputs required to produce damage. This is even more surprising when one considers the different modes of failure possible with any animal and man. Table 7 presents some modes of damage and the inputs required to produce them.

The two main input parameters found most useful for scaling purposes are acceleration level, or number of g's, and velocity change, delta-v. There exists a background of structural dynamics technology (see, for example, Kornhauser<sup>42</sup>) which presents the rationale for employing these two parameters to characterize the input shock, even though some not-quite-second-order effects are omitted (rise time, pulse shape, etc. ), and the two parameters do indeed prove useful in presenting animal survival data. Kornhauser and Gold<sup>43</sup> show the following very approximate scaling laws for a wide range of animal sizes:

$$G \cong 40/L \qquad \text{Eq. (1)}$$

MODE OF FAILURE	LOAD, LBS.	ACCEL., g	DELTA-V, fps	P, psi	SOURCE OF DATA
Standing man (leg) " , voluntary	1,600	20 10	10 10		Hirsch <sup>18</sup> Swearingen et al <sup>32</sup>
Seated man (vertebrae) " , voluntary	1,400	10-30 10	13-26 15		Hirsch <sup>18</sup> Swearingen et al <sup>32</sup>
Supine man (?)		20	53 (50%)		Stech & Payne <sup>20</sup>
Squatting man, voluntary		5	25		Swearingen et al <sup>32</sup>
Head, lateral (brain?)		50	15.4 (21 with helmet)		Hirsch <sup>34</sup>
" " , voluntary		38	6.5		Lombard et al <sup>33</sup>
Concussion (?)		-	15-25		Rayne & Maslen <sup>35</sup>
" , intracranial pressure				18-40	Gurdjian et al <sup>36</sup>
" , " " , dogs				25-95	Gurdjian et al <sup>37</sup>
" , cervical stretch					von Gierke <sup>38</sup>
Skull fracture			14-20		Lissner <sup>39</sup>
" " , flat	600 in-lbs.		~17		Goldman & Von Gierke <sup>4</sup>
" " , 90° corner	60 in-lbs.		~ 6		Goldman & Von Gierke <sup>4</sup>
Ribs, lungs, diaphragm, heart					Evans & Patrick <sup>40</sup>
Aorta, rupture					Starr et al <sup>8</sup>
Hydraulic effects					Payne <sup>41</sup>

\* There would appear to be a discrepancy between this and the 53 fps for the supine man, unless the lateral head damage really reflects the mode of cervical stretch which does not occur in the case of supine, whole body impact.

Table 7

where  $L$  is a characteristic length (in feet) in the direction of acceleration, and

$$27 < \Delta v < 53 \text{ fps} \quad \text{Eq. (2)}$$

for all animals tested to date.

The first scaling law makes sense if animal tissues have approximately equal densities and strengths. If the tissues behave as fluids with the density of water, then the pressure produced by 1 g of acceleration is equal to about 1/2 psi per foot of "depth". Equation (1) above would then be equivalent to the statement that animal structures can withstand about 20 psi of pressure, induced by inertia loading of the tissues.

The second law shows the relative invariance of the  $\Delta v$  required to produce injury, over a wide variety of animals from mice to men. At first glance this is most surprising, because of differences in size and structure. However, size in itself may be explained away, since Kornhauser<sup>42</sup> shows that  $\Delta v$  is almost constant for uniform beams of any size, with small variations to account for different boundary conditions or methods of support. Structural differences, unfortunately, are not that easy to rationalize since beams and shells with concentrated masses may have much lower  $\Delta v$  for failure than uniform beams.

Despite structural differences, there is a mechanism for explaining why animal  $\Delta v$ 's are not too different; namely, Darwinian natural selection. Land animals live in an environment which produces falls from various heights, and impact tolerance should be a definite factor in survivability and natural selection. By this token, of course, the tree-dwelling creatures would be expected to survive higher  $\Delta v$ 's than surface dwellers. To test this hypothesis, Table 8 separates various animals into these two groups. Some correlation does show, but not enough to be conclusive. Perhaps some impact testing of fish would reveal whether or not Darwinian selection has had much to do with the existing  $\Delta v$  tolerances of animals.

SURFACE ANIMALS	Delta-v, LD <sub>50</sub>	CLIMBING ANIMALS	Delta-v, LD <sub>50</sub>
Mice <sup>43</sup>	39	Man <sup>20</sup>	53
Rats <sup>43</sup>	44	Rhesus monkey <sup>44</sup>	40
Guinea Pigs <sup>43</sup>	31	Squirrel monkey <sup>44</sup>	48
Rabbits <sup>43</sup>	32		
	Avg. 36		Avg. 47

Table 8

## CONCLUSIONS

(1) Because of the paucity of biomechanical data required for modeling and validation of analytical models and for definition of failure points, biomechanical models have been rudimentary. Sophisticated computer modeling techniques are available, however, for modeling the most complex biological systems.

(2) Scaling of anthropomorphic dummy data is seldom justifiable on a theoretical basis, but some quantitative results of a kinematic (rather than deformational) nature may be obtained. Dummy experimentation is therefore of greatest value in producing kinematic data as well as qualitative data.

(3) Animal-to-man scaling is most fruitful with primates, and this suggests the value of developing and validating primate computer models in order to help in validating the human analytical models.



## REFERENCES

1. Nickerson, J. L. and Coermann, R. R. "Internal Body Movements Resulting from Externally Applied Sinusoidal Forces", AMRL-TDR-62-81, July 1962
2. Coermann, R. R. et al "The Passive Dynamic Mechanical Properties of the Human Thorax-Abdomen Systems and the Whole Body System" Aerospace Medicine, 31, June 1960
3. Rodden, W. P. "A Method for Deriving Structural Influence Coefficients from Ground Vibration Tests" AIAA Journal, 5, 5, May 1967, 991-1000
4. Goldman, D. E. and von Gierke, H. E. "Effects of Shock and Vibration on Man", Shock and Vibration Handbook, vol. 3, chap. 44, McGraw-Hill, 1961
5. Nickerson, J. L. and Drazic, H. "Young's Modulus and Breaking Strength of Body Tissues" AMRL-TDR-64-23
6. von Gierke, H. E. "Biodynamic Response of the Human Body" Applied Mech. Rev., 17, 12, Dec. 1964, 951-958
7. Fung, Y. B. "Biomechanics, its Scope, History, and some Problems of Continuum Mechanics in Physiology" Applied Mech. Rev., 21, 1, 1968
8. Starr, C. et al "UCLA Motor Vehicle Safety Project" Report No. 68-52, Oct. 1968
9. Sittel, K. et al "Fiber Elasticity from Cineradiography using Anisotropic Model", 8th ICMBE, Chicago, July 20-25, 1969
10. Henzel, J. H. et al "Reappraisal of Biodynamic Implications of Human Ejections", Aerospace Medicine, 39, 3, March 1968
11. Sonnerup, L. "Mechanical Analysis of the Human Intervertebral Disc", 8th ICMBE, Chicago, July 20-25, 1969
12. Edwards, R. G. et al "Ligament Strain in the Human Knee Joint" ASME 69-WA/BHF-4, J. Basic Engin., March 1970, 131-136
13. Orne, D. and Liu, Y. K. "A Mathematical Model of Spinal Response to Impact", ASME Paper No. 70-BHF-1

## REFERENCES (Continued)

14. Roberts, V. L. et al "Review of Mathematical Models which Describe Human Response to Acceleration", ASME 66-WA/BHF-13
15. Hirsch, A. E. and White, L. A. "Mechanical Stiffness of Man's Lower Limbs", ASME Paper No. 65-WA/HUF-4, 1965
16. Hurty, W. C. "Dynamic Analysis of Structural Systems using Component Modes", AIAA Journal, 3, 4, April 1965, 678-685
17. Bamford, R. M. "A Modal Combination Program for Dynamic Analysis of Structures", JPL, Pasadena, Calif., Aug. 1966
18. Hirsch, A. E. "Man's Response to Shock Motions", Navy Dept., DTMB Report 1797, Jan. 1964, AD 436809
19. Terry, C. T. and Roberts, V. L. "A Viscoelastic Model of the Human Spine Subjected to +G<sub>z</sub> Accelerations", J. Biomechanics, 1, 161, 1968
20. Stech, E. L. and Payne, P. R. "Dynamic Models of the Human Body", AMRL-TR-66-157, Nov. 1969, AD 701383
21. Turnbow, J. W. et al "Aircraft Passenger-Seat-System Response to Impulsive Loads", ASA/VLABS Tech. Rept. 67-17, Aug. 1967
22. Benedict, J. V. et al "An Analytical Investigation of the Cavitation Hypothesis of Brain Damage" ASME Paper 70-BHF-3
23. Liu, Y. K. and Murray, J. D. "A Theoretical Study of the Effect of Impulse on the Human Torso", Biomechanics, Y. C. Fung (Ed.), ASME, 1966, 167-186
24. Yeager, R. R. et al "Development of a Dynamic Model of Unrestrained, Seated Man Subjected to Impact" Technology Inc. Rept. No. NADC-AC-6902, March 1969
25. Liu, Y. K. "Towards a Stress Criterion of Injury - an Example in Caudocephalad Acceleration", J. Biomechanics, 2, 145, 1969
26. Kornhauser, M. "Impact Protection for the Human Structure" Proc. AAS, Western Regional Mtg., Palo Alto, Calif. 1958

# REFERENCES (Continued)

27. Hudson, D. E. "Scale Model Principles", Chap. 27, Vol. 2 of Shock and Vibration Handbook, McGraw-Hill Book Co., 1961
28. Hermes, R. M. "Dynamic Modeling for Stress Similitude" ONR Contract N8 onr-523, Closing Report June 1953
29. Heller, S. R. Jr. "Structural Similitude for Impact Phenomena" DTMB Report 1071, April 1952
30. Baker, W. E. and Westine, P. S. "Modeling the Blast Response of Structures using Dissimilar Materials", AIAA Journal, 7, 5, May 1969, 951-957
31. Horowitz, J. M. and Nevill, G. E. Jr. "A Correction Technique for Structural Impact Modeling using Dissimilar Materials" AIAA Journal, 7, 8, Aug. 1969, 1637-1639
32. Swearingen, J. J. et al "Human Voluntary Tolerance to Vertical Impact" Aerospace Medicine, 31, 1960
33. Lombard, C. F. et al "Voluntary Tolerance of the Human to Impact Accelerations of the Head" J. Av. Medicine, 22, 2, 1951
34. Hirsch, A. E. "Current Problems in Head Protection", Head Injury Conf. Proc., Lippincott, Philadelphia, 1966
35. Rayne, J. M. and Maslen, K. R. "Factors in the Design of Protective Helmets", J. Aviation Medicine, June 1969, 631-637
36. Gurdjian, E. S. et al "Observations on the Mechanism of Brain Concussion, Contusion, and Laceration" Surgery, Gynecology, and Obstetrics, 101, 1955
37. Gurdjian, E. S. et al "Quantitative Determination of Acceleration and Intracranial Pressure in Experimental Head Injury" Neurology Journal, 3(6), June 1953
38. von Gierke, H. E. "On the Dynamics of some Head Injury Mechanisms" Head Injury Conf. Proc., Lippincott Co., 1966
39. Lissner, H. R. et al "Mechanics of Skull Fracture", Proc. SESA, 7, 1, 1949

#### REFERENCES (Continued)

40. Evans, F. G. and Patrick, L. M. "Impact Damage to Internal Organs" Symp. on Impact Accel. Stress, Nov. 27-29, 1961, Brooks AFB, San Antonio, Texas
41. Payne, P. R. "The Dynamics of Human Restraint Systems" Symp. on Impact Accel. Stress, Nov. 27-29, 1961, Brooks AFB, San Antonio, Texas
42. Kornhauser, M. "Prediction and Evaluation of Sensitivity to Transient Accelerations" J. Appl. Mech., 21, 371, 1954
43. Kornhauser, M. and Cold, A. "Application of the Impact Sensitivity Method to Aircraft Structures", Symp. on Impact Accel. Stress, Nov. 27-29, 1961, Brooks AFB, San Antonio, Texas
44. Kozarian, L. - Private communication, to be published.

PAPER NO. 7

MULTIDEGREE, NONLINEAR MATHEMATICAL  
MODELS OF THE HUMAN BODY AND RESTRAINT  
SYSTEMS: APPLICATIONS IN THE ENGINEERING  
DESIGN OF PROTECTIVE SYSTEMS

By  
Raymond R. McHenry

Cornell Aeronautical Laboratory, Inc.  
Buffalo, New York 14221

ABSTRACT

The role of mathematical models of whole-body kinetics in the engineering design of protective systems for acceleration exposures of humans is discussed. A number of specific models of this type and corresponding engineering applications are described. Present limitations of the research technique and probable future developments are discussed.

## INTRODUCTION

The development of several forms of mathematical models of the human body to aid the engineering design of protective systems has received increasing attention in recent years. This is a natural approach to be taken by engineers confronted with a physical problem, since mathematical modeling of physical systems constitutes the basis for most forms of engineering analysis.

For the case of a crash victim exposed to vehicular accelerations with either partial or no restraint (e.g., automobile occupants), the kinetics of the whole-body responses assume a major role in determining both the occurrence and the extent of injury. For this reason, a number of multidegree, nonlinear mathematical models of whole-body kinetics either have been or are being developed for application as aids to the design of protective systems for automobiles and aircraft. Since the pertinent, direct experience of the author is limited to this form of modeling of the human body, the present paper will be limited accordingly.

Whole-body models for prediction of the kinetics of automobile and aircraft occupants, while primitive from the viewpoint of biomechanics, have recently become quite elaborate analytically, including as many as forty degrees of freedom (1) in three-dimensional simulations. As a result of the analytical complexity that has developed in this form of modeling, there has been a tendency on the part of some experimentalists to misunderstand the limited objectives of the research approach.

For example, Patrick and Sato (2) suggest that proponents of mathematical models intend "to replace all other subjects in crash research ... when enough data and large enough computers become available". Further, they indicate that the long-range objective is "to design a vehicle and evaluate its safety characteristics without going farther than the computer". They also point out that existing models do not "approach the number of variables required for a complete human simulation". By no stretch of the imagination can the existing forms of whole-body kinetic models be considered to be potential replacements for experiments, particularly in the establishment of human tolerance levels (the topic of Reference 2). Rather, they are intended only to serve as aids in the engineering application of existing tolerance data and in the planning of meaningful experiments.

Snyder (3) refers to the "delusionary validation" of mathematical models based on dummies. It is highly doubtful that knowledgeable researchers, who are familiar with the primitive stages of development of existing whole-body models of the human body, can be deluded about limitations on validity. A number of further points made by Snyder (3) regarding the limitations on all forms of mathematical modeling in biomechanics research, that are imposed by "complexities, variations, and unknowns of the human body", might well be interpreted as a strong case for the need to develop additional

analytical aids to experimentation. How else can one ever hope to logically organize, interpret and apply the singular test results that are obtained with individual animals or cadavers under specific conditions of exposure?

The application of available human tolerance information to the design of protective systems requires an intermediate means of relating the system design features to occupant responses and loading under given exposure conditions. While instrumented volunteer subjects can be used in mild-exposure tests of protective systems, experimentation at dangerous exposure levels requires the use of instrumented anthropometric dummies, cadavers or animals. Each of the test subjects involves its own particular kind of difficulties with interpretation in terms of the corresponding responses and/or injuries of a living human subject. In fact, reconstructions of injury-producing accidents constitute the only available means to approximate the actual responses of living humans at injurious levels of acceleration exposures.

The adequacy of any mathematical model of a physical system is dependent, of course, on the nature and objectives of the particular application. If anthropometric dummies are being used in the experimental development of a protective system, an analytical aid that correlates adequately with dummies can obviously be useful. It can serve as a means of interpolating between test conditions, exploring the sensitivities of system parameters, and selecting the more meaningful test conditions. When one considers the large number of variables involved in the testing of a protective system, the need for analytical aids to the planning of a test series becomes obvious.

Mathematical models of the human body and restraint systems are relatively recent additions to the available selection of applicable research tools. Within the recognized limitations of their validity, they can serve as preliminary design tools as well as means of supplementing experiments. This paper will briefly review the form, features and limitations of some representative, whole-body models. A number of specific applications will then be discussed.

## TYPICAL FORMS, FEATURES AND LIMITATIONS

Most of the past efforts related to modeling whole-body kinetics in acceleration exposures have been restricted to plane motions. The extent of analytical complexity has varied widely, ranging from one to ten degrees of freedom in the representation of the human body and including a wide range of detail in the treatment of contacts with the vehicle interior. Recent trends toward the incorporation of refinements and extensions in existing planar models (e.g., References 4, 5 and 6) and toward the development of three-dimensional representations (References 1, 7 and 8) may be attributed both to the demonstrated utility of such analytical aids and to favorable trends in the costs of computer applications (Figure 1).

analytical aids to experimentation. How else can one ever hope to logically organize, interpret and apply the singular test results that are obtained with individual animals or cadavers under specific conditions of exposure?

The application of available human tolerance information to the design of protective systems requires an intermediate means of relating the system design features to occupant responses and loading under given exposure conditions. While instrumented volunteer subjects can be used in mild-exposure tests of protective systems, experimentation at dangerous exposure levels requires the use of instrumented anthropometric dummies, cadavers or animals. Each of the test subjects involves its own particular kind of difficulties with interpretation in terms of the corresponding responses and/or injuries of a living human subject. In fact, reconstructions of injury-producing accidents constitute the only available means to approximate the actual responses of living humans at injurious levels of acceleration exposures.

The adequacy of any mathematical model of a physical system is dependent, of course, on the nature and objectives of the particular application. If anthropometric dummies are being used in the experimental development of a protective system, an analytical aid that correlates adequately with dummies can obviously be useful. It can serve as a means of interpolating between test conditions, exploring the sensitivities of system parameters, and selecting the more meaningful test conditions. When one considers the large number of variables involved in the testing of a protective system, the need for analytical aids to the planning of a test series becomes obvious.

Mathematical models of the human body and restraint systems are relatively recent additions to the available selection of applicable research tools. Within the recognized limitations of their validity, they can serve as preliminary design tools as well as means of supplementing experiments. This paper will briefly review the form, features and limitations of some representative, whole-body models. A number of specific applications will then be discussed.

## TYPICAL FORMS, FEATURES AND LIMITATIONS

Most of the past efforts related to modeling whole-body kinetics in acceleration exposures have been restricted to plane motions. The extent of analytical complexity has varied widely, ranging from one to ten degrees of freedom in the representation of the human body and including a wide range of detail in the treatment of contacts with the vehicle interior. Recent trends toward the incorporation of refinements and extensions in existing planar models (e.g., References 4, 5 and 6) and toward the development of three-dimensional representations (References 1, 7 and 8) may be attributed both to the demonstrated utility of such analytical aids and to favorable trends in the costs of computer applications (Figure 1).



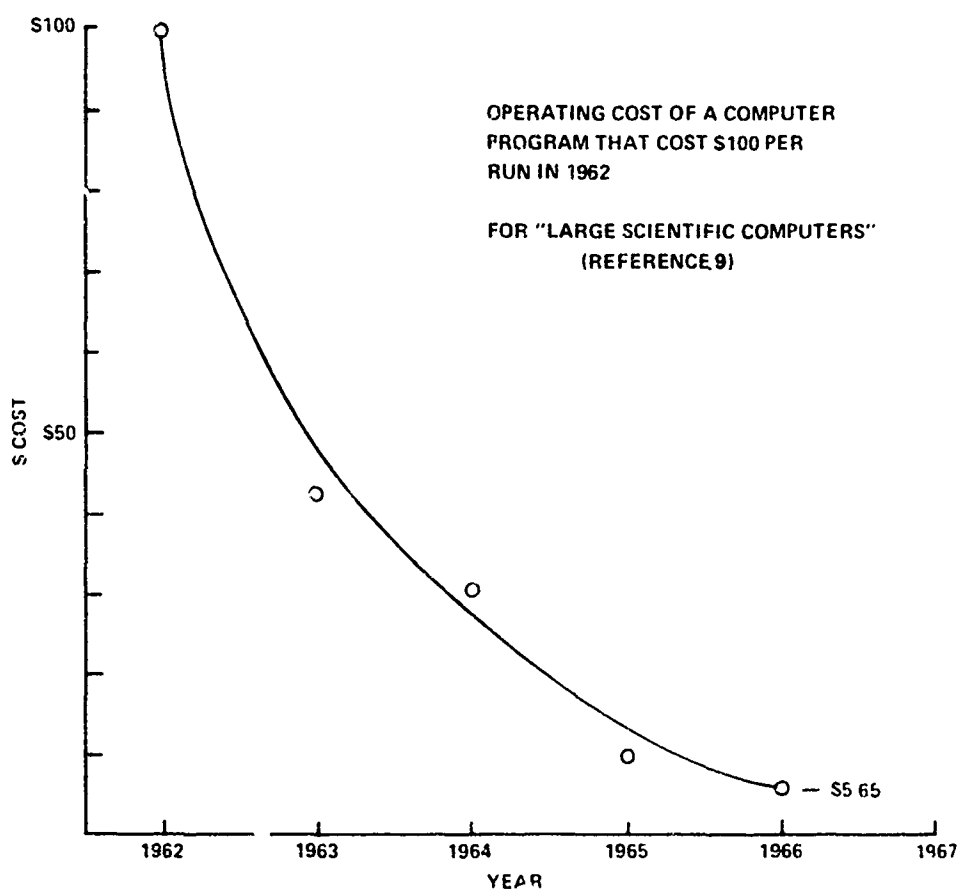


Figure 1 COMPUTER COSTS vs YEARS

One of the earlier planar models (Figure 2) was that of Ryan and BeVier (10), which was developed for study of the effects of the waveform of the deceleration time history, in frontal collisions, on the responses of a lap belted occupant. The model was limited to two degrees of freedom, and interpretations of injury potential were based on the magnitude of the predicted pelvic acceleration.

In 1963, McHenry (11) developed a somewhat more elaborate, six-degree-of-freedom model of a belted occupant (Figure 3), which included the option of inertial interactions with the simulated single-degree-of-freedom vehicle. The model of Reference 11 included nonlinear representations of the seat cushion, the lap and shoulder restraint belts, and a knee stop to prevent reverse bending. Muscular restraints were simulated by constant restoring couples in the manner of the early Model 120 Sierra dummy (12).

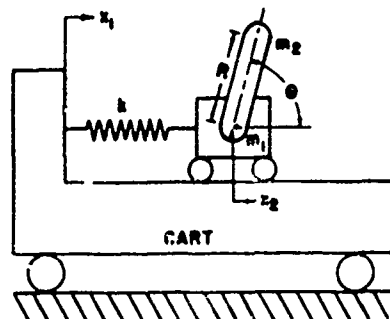
The cited early models established both the feasibility and the utility of analytical models of this type. As a result, a number of models based on a similar general approach, but differing in analytical details, have been developed (e.g., References 4, 13, 14, 15).

Whole-body models generally make use of three separate forms of analytical definitions of the body which share a common, body-fixed coordinate system.

Inertial and internal constraint properties are defined corresponding to an articulated assembly of rigid mass segments (e.g., see Figure 4) in which empirically fitted constraints are imposed on the degree and extent of joint articulations (e.g., see Figure 5).

Forces produced by contacts with the vehicle interior are approximated through the use of analytically defined surfaces for the contacted regions of the body, in the form of simple geometric shapes (e.g., see Figure 6), and by determination of the occurrence and extent of interferences of these body surfaces with the vehicle interior (Figure 7). The corresponding magnitudes of contact forces are determined by application of empirically fitted load-deflection characteristics of the type depicted in Figure 8. Restraint belt forces are calculated on the basis of elongation, as determined from analytic geometry, and using fitted characteristics similar to the type displayed in Figure 8.

A third form of analytical definition of the body consists of line drawings of the profiles of body segments that are sometimes used to produce graphic displays of simulated responses (e.g., Figure 9). Such displays constitute a convenient means of checking the gross behavior for aspects of predicted responses that may have exceeded the applicable ranges of simplifying assumptions. They also permit direct comparisons of predicted kinematic responses with high speed films of experiments (Figure 9), and they provide a format for presentation of results.



#### NOTATIONS

- $m_1$  - mass of body excluding upper part of body
- $m_2$  - mass of upper part of body.
- $k$  - stiffness of belt
- $z_2$  - displacement of hip.
- $\theta$  - angular displacement of upper part of body
- $x_1$  - displacement of cart

Figure 2 TWO-MASS MODEL  
(RYAN & BEVIER, REF. 10)

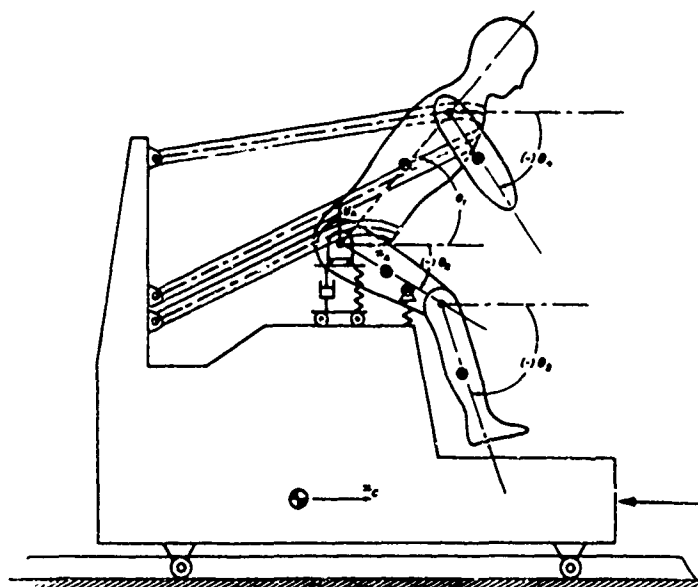
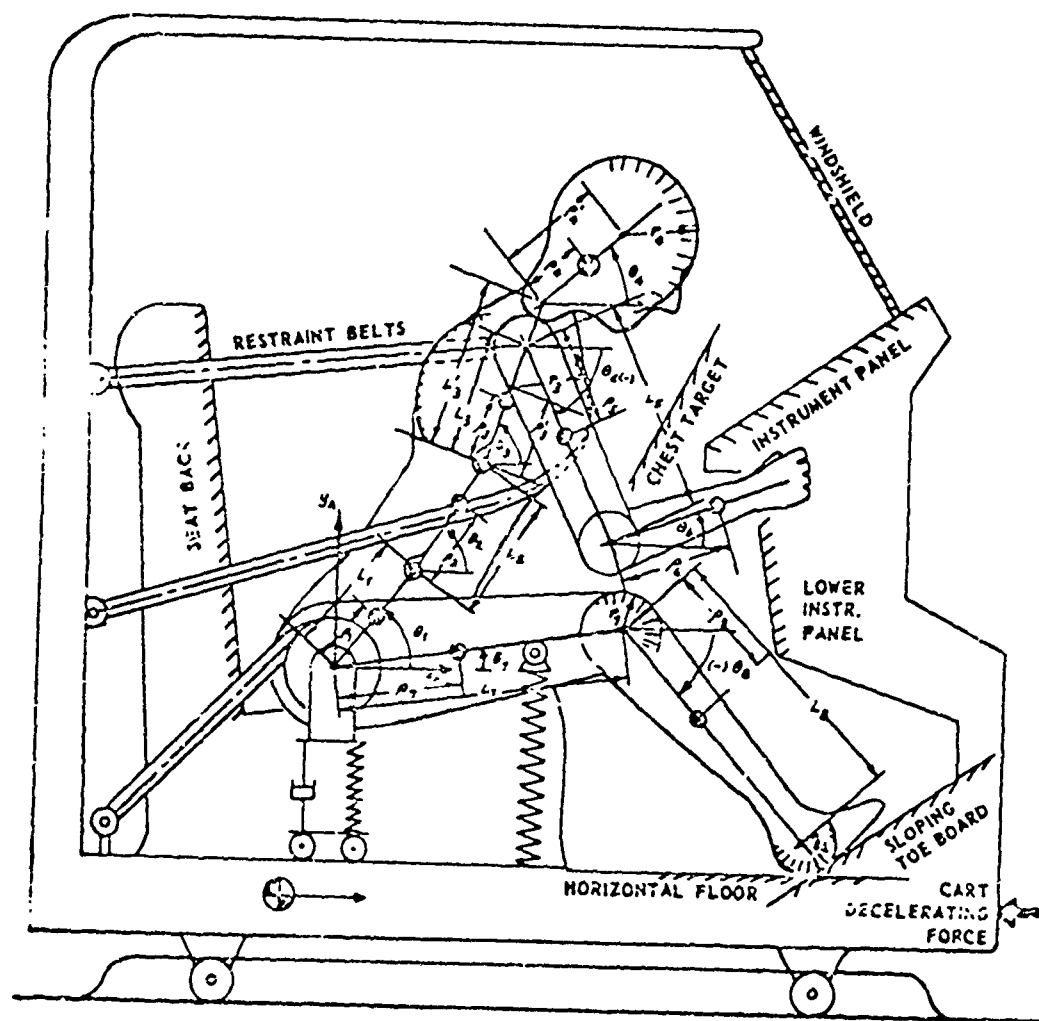


Figure 3 MATHEMATICAL MODEL OF HUMAN BODY AND RESTRAINT  
SYSTEM ON TEST CART (7 DEGREES OF FREEDOM)



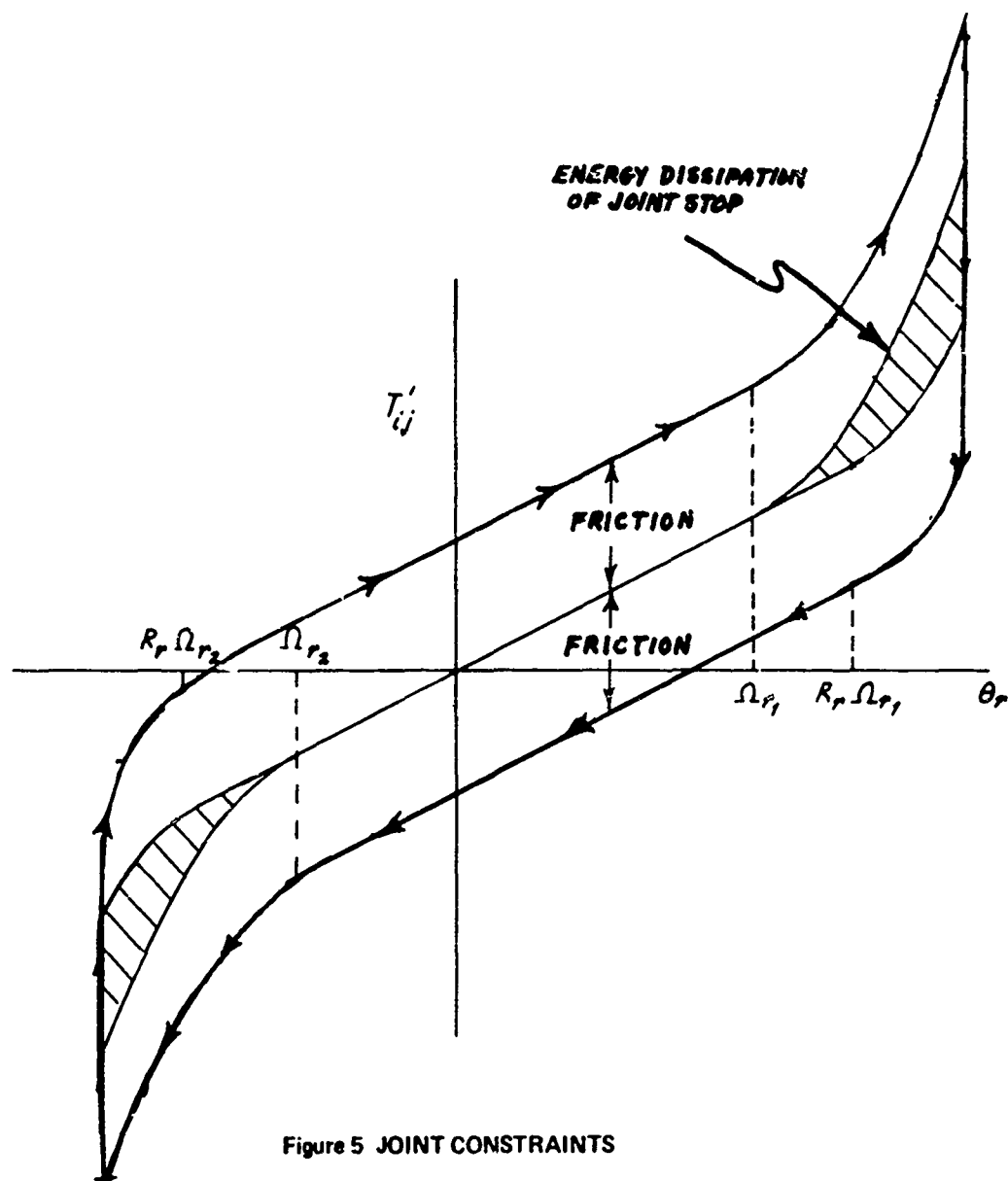


Figure 5 JOINT CONSTRAINTS

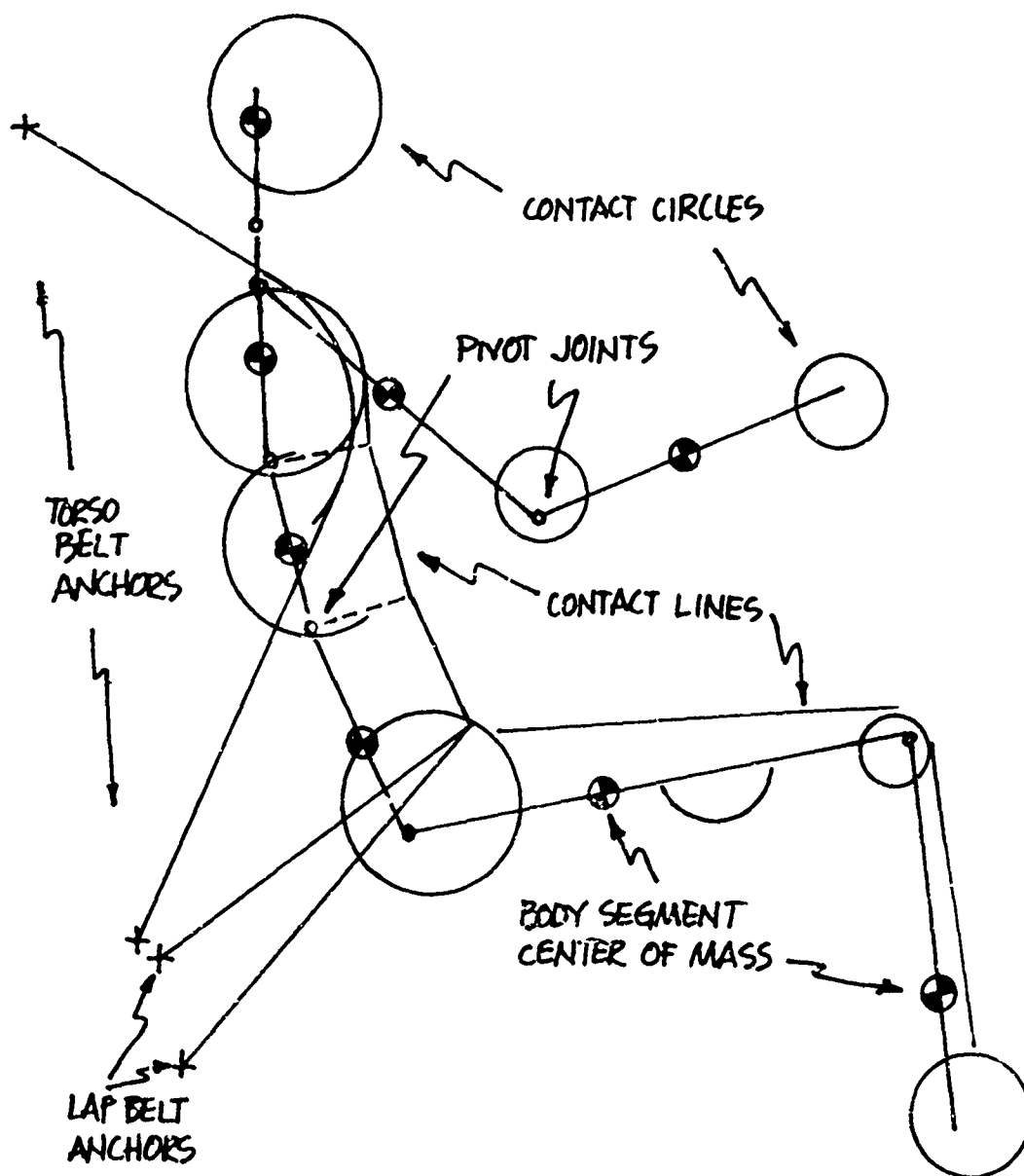


Figure 6 OCCUPANT CONTACT AND BELT CONFIGURATION

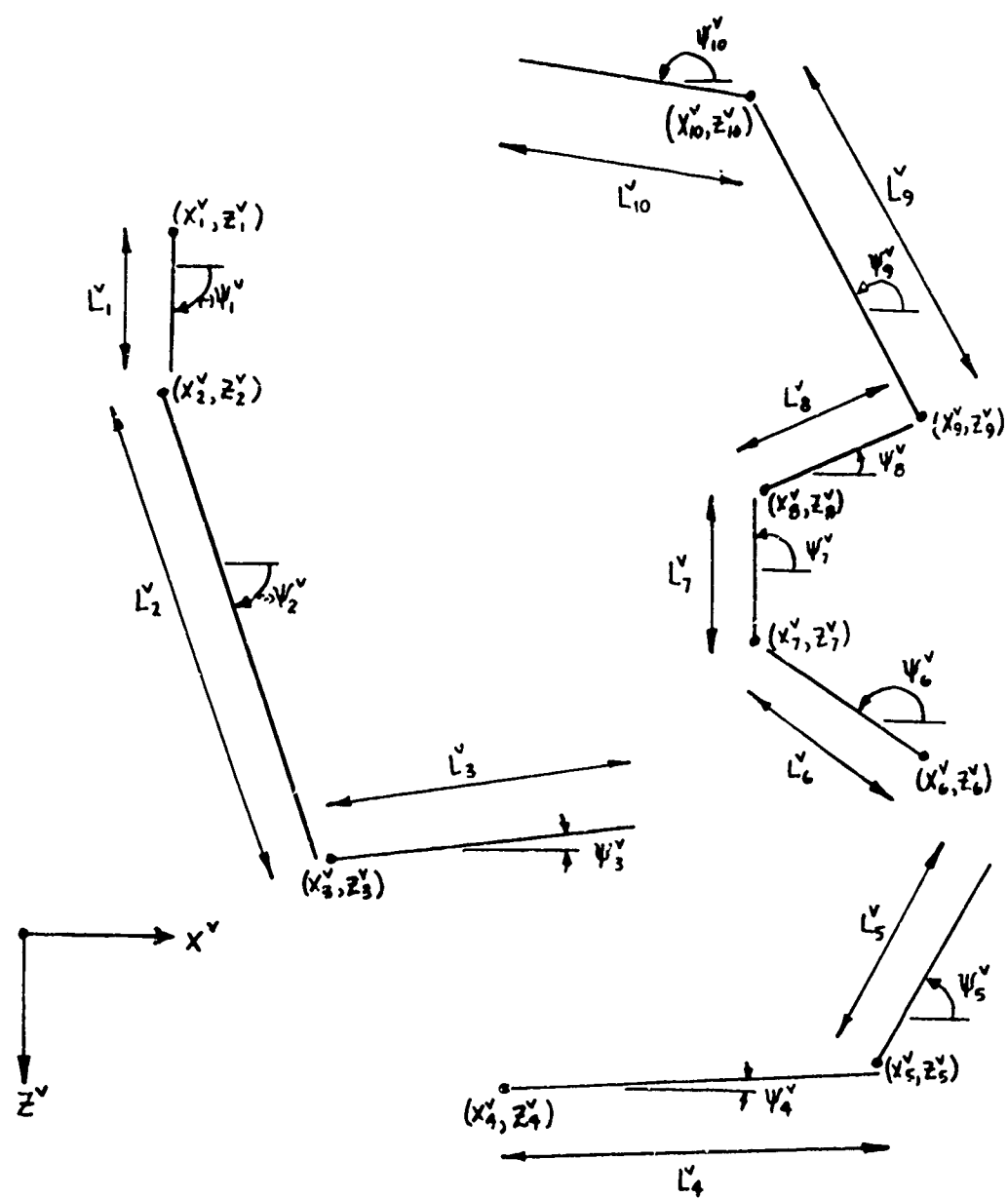


Figure 7 VEHICLE CONTACT SYSTEM

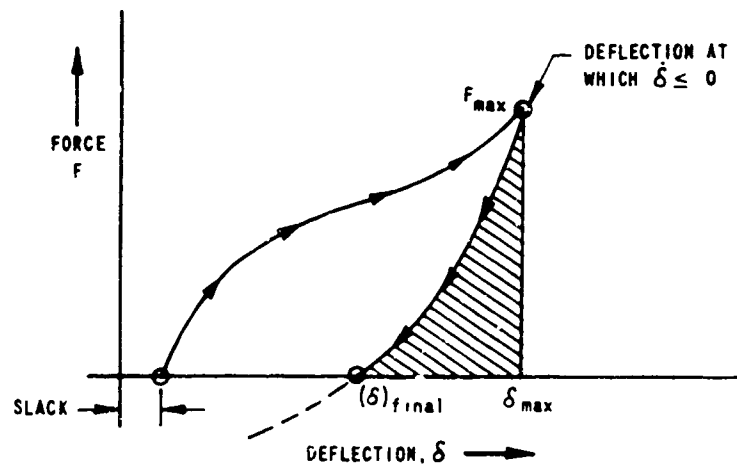


Figure 8 GENERAL FORM OF CONTACT, BELT, AND CART-STOPPING FORCES



EXPERIMENTAL DATA



The dummy elbows were locked in this test. Since the simulation does not permit complete locking of joints, there are significant differences in arm kinematics

SIMULATION DATA

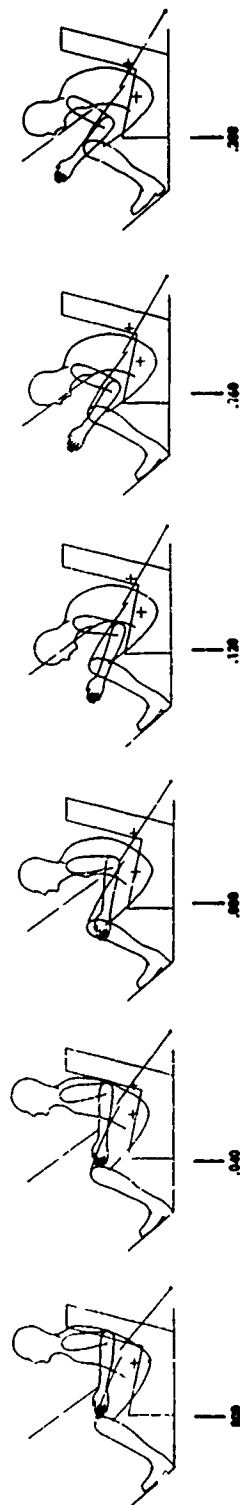


Figure 9 DUMMY KINEMATIC COMPARISON  
LAP BELT RESTRAINT - CART VELOCITY 10 MPH

Because of the nonlinear nature of the simulated physical system, solutions of the equations of motion are obtained in the form of time histories of the displacements, velocities and accelerations of the degrees of freedom and of the magnitudes and positions of applied forces. The equations are solved by means of stepwise numerical integration. Filtering of predicted acceleration responses is sometimes used to achieve a frequency content compatible with that present in experimental data (5).

By far the most elaborate operational model of this general type is that developed by Young (8). His model is three-dimensional, including a twelve-segment representation of the crash victim and a twenty-five plane representation of the vehicle interior. With the selected joint constraints, a total of thirty-one degrees of freedom are included in the simulated occupant. A three-dimensional formulation that is being developed by CAL (1) is very similar to that of Young (8). The primary difference is the inclusion by CAL of three additional segments, which raises the total number of degrees of freedom to forty. The earliest known three-dimensional simulation of the crash victim is that of Robbins (7), which included only twelve degrees of freedom.

Obviously, models of the type described are limited to indirect predictions of injury. They do not model the mechanisms of injury. Rather, they predict the inertial loading of restraint systems and of body areas that impact the vehicle interior. The injury potential of these items must be evaluated in terms of separately determined tolerance information. In this respect, applications of the models require the same interpretation procedure as that followed with most anthropometric dummies. The dummies are, in general, designed to withstand extreme exposures without damage, while producing acceleration and force measurements that are interpreted in terms of separately determined tolerance information. Therefore, the present forms of whole-body mathematical models may be viewed as being equivalent to highly adjustable dummies with identical repeatability of responses. The addition of features such as time-varying representations of muscular effects, particularly with some form of closed-loop control, can serve to make the mathematical models respond in a manner more realistic than that of the passive dummies.

#### SOME SPECIFIC APPLICATIONS

A number of specific applications of this type of model have been made by CAL and others, under a variety of sponsorship. The limited time available for preparation of this paper has precluded the preparation of detailed definitions of qualifying conditions associated with each application and the request of sponsor clearances for presentation of findings. Therefore, the discussion will be limited to descriptions of representative applications.

- (1) Locations and inertial loadings of contacts on the vehicle interior, for the case of minimum or no restraint.

Note that the case of no restraint has assumed greater importance with the growing interest in passive, inflatable restraints. For minor collisions, below the threshold of restraint deployment, the interior configuration and padding must provide the maximum possible protection of the unrestrained occupants. The results of a representative study of this type are presented by Martin and Kroell (16).

- (2) Exploratory parameter studies of inflatable occupant restraints.

Parameters of interest include the threshold and timing of deployment, the restraint configuration, the maximum pressure in the restraint, and the venting rate. A computer simulation of an inflatable restraint, for use with a whole-body kinetic model of the human body, is presented by Hammond (17).

- (3) Investigation of the causes of "submarining" responses of anthropometric dummies in tests of automobile restraint harnesses.

The results of this study are presented in Reference 18.

- (4) Energy absorption requirements for compartment interiors as a function of impact speed, occupant size and weight, compartment configuration, and occupant restraints.
- (5) Interpolation of test results for different occupant sizes and weights.
- (6) Exploratory studies of the effects of vehicle exterior crush properties on the responses of restrained and unrestrained occupants.

The results of an early study of this topic are presented in Reference 11.

- (7) Preliminary evaluations of new concepts for protective devices (e.g., yielding seat structures, load-limiters in restraint anchorages, etc.).

## FUTURE DEVELOPMENTS

The incorporation of time-varying muscular restraints, with some form of closed-loop control (i.e., to simulate attempted position control by the test subject), is seen as an early development. However, the feasibility of integrating detailed submodels of body components, in an attempt to directly model the mechanisms of injury, is considered to be doubtful in view of the present complexity of the three-dimensional models. Such an endeavor might well go beyond the point of diminishing returns.

A distinct need is seen for the development of detailed submodels of body components for conditions of three-dimensional loading, in order to gain a better understanding of the mechanisms of injury and to provide readily available measures of tolerance (when adequately validated). However, in exposure conditions where gross, whole-body motions occur, the extent of interactions may be of secondary importance (e.g., interactions between visceral and whole-body responses). If this is found to be the case, the whole-body models can be applied to provide definitions of loading conditions for auxiliary, injury predicting submodels. It should be noted that this same general approach of neglecting effects of inertial interactions is currently taken in isolated studies of the crash vehicle and its occupants.

## REFERENCES

- (1) Research in progress at Cornell Aeronautical Laboratory, Inc., under Contract No. FH-11-7592 with the National Highway Safety Bureau and Contract No. CAL 7001-C7 with the Automobile Manufacturers Association.
- (2) Patrick, L. M. and Sato, T. B., "Methods of Establishing Human Tolerance Levels", Impact Injury and Crash Protection, Chapter XIII, Published by Charles C. Thomas, Springfield, Illinois, 1970.
- (3) Snyder, R. G., "Human Impact Tolerances", 1970 International Automobile Safety Conference Compendium, Society of Automotive Engineers.
- (4) Becker, J. M. and Robbins, D. H., "Mathematical Simulation of Collision, I", Volume IV of IV, Highway Safety Research Institute, Ann Arbor, Michigan, October 1967.
- (5) Segal, D. J. and McHenry, R. R., "Computer Simulation of the Automobile Crash Victim - Revision No. 1", CAL Report No. VJ-2492-V-1, March 1968.
- (6) Patten, J. S. and Theiss, C. M., "Auxiliary Program for Generating Occupant Parameter and Profile Data", CAL Report No. VJ-2759-V-1R, January 1970.
- (7) Robbins, D. H., "Three-Dimensional Simulation of Advanced Automotive Restraint Systems", 1970 International Automobile Safety Conference Compendium, Society of Automotive Engineers.
- (8) Young, R. D., "A Three-Dimensional Mathematical Model of an Automobile Passenger", Research Report 140-2, Texas Transportation Institute, Texas A&M University, August 1970.
- (9) Knight, K. E., "Evolving Computer Performance 1963-1967", DATAMATION, January 1968, pages 31-35.
- (10) Ryan, J. J., BeVier, W., "Safety Devices for Ground Vehicles", Mechanical Engineering Department, University of Minnesota, Minneapolis, 1 September 1960.
- (11) McHenry, R. R., "Analysis of the Dynamics of Automobile Passenger-Restraint Systems", Proceedings of the Seventh Stapp Car Crash Conference (1963), Published by Charles C. Thomas, Springfield, Illinois, 1965.
- (12) Kindred, R. A., "The Design and Construction of Sierra Engineering Company Model 120 Anthropometric Dummy", Sierra Engineering Company, Technical Report No. 120-901, Sierra Madre, California, November 1953.

- (13) McHenry, R. R. and Naab, K. N., "Computer Simulation of the Crash Victim - A Validation Study", Proceedings of the Tenth Stapp Car Crash Conference, SAE, November 8-9, 1966.
- (14) Haley, J. L., et al, Crashworthiness Study for Passenger Seat Design, Arizona State University Engineering Report No. 65-01, 1966.
- (15) Furusho, H., Yokoya, K. and Fujiki, S., "Analysis of Occupant Behavior During Collision", Society of Automotive Engineers of Japan 1969 Spring Meeting.
- (16) Martin, D. E. and Kroell, C. K., Vehicle Crush and Occupant Behavior, SAE Paper No. 670034, Detroit, January 9-13, 1967.
- (17) Hammond, R. A., "Digital Simulation of an Inflatable Safety Restraint", to be presented at 1971 SAE Meeting, Detroit, January 1971.
- (18) McHenry, R. R. and Naab, K. N., An Analytical Investigation of the Causes of "Submarining" Responses of Anthropometric Dummies in Tests of Automobile Restraint Harnesses, CAL Report No. YM-2250-V-1, December 1966.

- (13) McHenry, R. R. and Naab, K. N., "Computer Simulation of the Crash Victim - A Validation Study", Proceedings of the Tenth Stapp Car Crash Conference, SAE, November 8-9, 1966.
- (14) Haley, J. L., et al, Crashworthiness Study for Passenger Seat Design, Arizona State University Engineering Report No. 65-01, 1966.
- (15) Furusho, H., Yokoya, K. and Fujiki, S., "Analysis of Occupant Behavior During Collision", Society of Automotive Engineers of Japan 1969 Spring Meeting.
- (16) Martin, D. E. and Kroell, C. K., Vehicle Crush and Occupant Behavior, SAE Paper No. 670034, Detroit, January 9-13, 1967.
- (17) Hammond, R. A., "Digital Simulation of an Inflatable Safety Restraint", to be presented at 1971 SAE Meeting, Detroit, January 1971.
- (18) McHenry, R. R. and Naab, K. N., An Analytical Investigation of the Causes of "Submarining" Responses of Anthropometric Dummies in Tests of Automobile Restraint Harnesses, CAL Report No. YM-2250-V-1, December 1966.

PAPER NO. 8

A FIVE-DEGREE-OF-FREEDOM  
MATHEMATICAL MODEL OF THE BODY

Ints Kaleps  
Henning E. von Gierke

Aerospace Medical Research Laboratory  
Wright-Patterson Air Force Base, Ohio

E. B. Weis

Riverside Methodist Hospital  
Columbus, Ohio

ABSTRACT

A linear, five-degree-of-freedom, lumped parameter model is proposed to simulate thoracic, abdominal and spinal response to various dynamic environments. Five characteristic body segment masses are chosen, corresponding to the pelvis, abdomen, torso, chest wall and respiratory gas. The effects of blast, acoustic fields, steady-state pressure variations and mechanical forces can be simulated with the model to provide insight into actual body response. Relations are given for scaling from or to geometrically similar animals as a function of mass. The model formulation also provides a basis for a systematic set of biodynamic experiments for man or similar primate.

PRECEDING PAGE BLANK



## INTRODUCTION

For the past 30 years numerous investigators have generated considerable information concerning the dynamic response characteristics of the human body to mechanical excitations and proposed lumped parameter mathematical models to characterize particular body reactions [Refs 1-6]. Total body as well as segmental body excitations of the thoracic cage and abdominal viscera have been observed for sitting, standing and supine subjects [Refs 7-10]. Several mathematical body models based on these experiments have been developed, but each model has been specific to one particular dynamic environment. However, the body is one coupled system and it should be possible to combine the various body models into a single model capable of simulating any body reaction within the limits of the particular modeling technique employed.

Most of man's total body responses to mechanical excitations occur at low frequencies ( $< 50$  Hz), and can be viewed as relative displacements of certain anatomical segments of the body. The motion of this system may be analyzed if each segment is assigned a mass, the masses coupled in the proper manner, and the elasticity and damping of each of the couples specified. One further necessary simplification is that all the mass resides in the specific segments and the elasticity and damping of the internal organs are only within the connecting elements. Thus a lumped parameter mathematical model is formulated. Displacements are limited to small amplitudes to allow the assumption of linear model behavior.

A linear lumped parameter mathematical model of the type proposed is restricted in many specific aspects but it does provide considerable insight into the dynamic behavior of the internal organs; body mass coupling; energy transfer, distribution, and dissipation; relative subsystem excursions, and provides indirect injury predictions - all in the proper time sequence. Driving point impedances are also easily computed and form an initial basis to guide the analytical model's validity.

A unified model using lumped parameter techniques is proposed, as shown in Fig. 1, which combines the dynamic characteristics of the various individual models used to simulate response to impact, vibration, blast, and acoustic fields, as well as possessing proper passive physiological characteristics.

The availability of animal data from experiments too dangerous or impractical to be performed with human subjects, requires methods of animal-to-human data extrapolation. For animals geometrically similar to humans, the proposed model, with proper scaling relations, can be used to draw conclusions from the dynamic response of animals to the corresponding response for humans.

The proposed model also serves as a basis for establishing a set of systematic subhuman primate or human experiments which are clearly defined in terms of a mechanical model and a set of equations. The experimental results, in turn, can be used to refine or, if necessary, alter the proposed model.

#### MODEL DESCRIPTION

The model as shown in Fig. 2 simulates the anatomical configuration of the torso. The arms, legs, and head have not been included in this model, as their influence on the dynamic response of the torso is considered secondary. The basic element of the model is the mass,  $M_t$ , which represents the loaded spine. It is tightly coupled to the pelvic mass,  $M_p$ , which in turn is coupled to the buttocks and the abdominal mass,  $M_a$ .

The thorax is simulated by an air-filled cavity with the abdomen, chest wall, and airway to the mouth acting as pistons. The coupling of these masses is achieved by the gas pressure acting on the effective piston areas:  $A_a$ ,  $A_w$ , and  $A_r$  respectively.

The mathematical formulation of the model is given by Eq 1-5. These five, coupled, linear second-order differential equations describe the model for  $+G_z$  longitudinal excitations only. The coupling for the lower body is

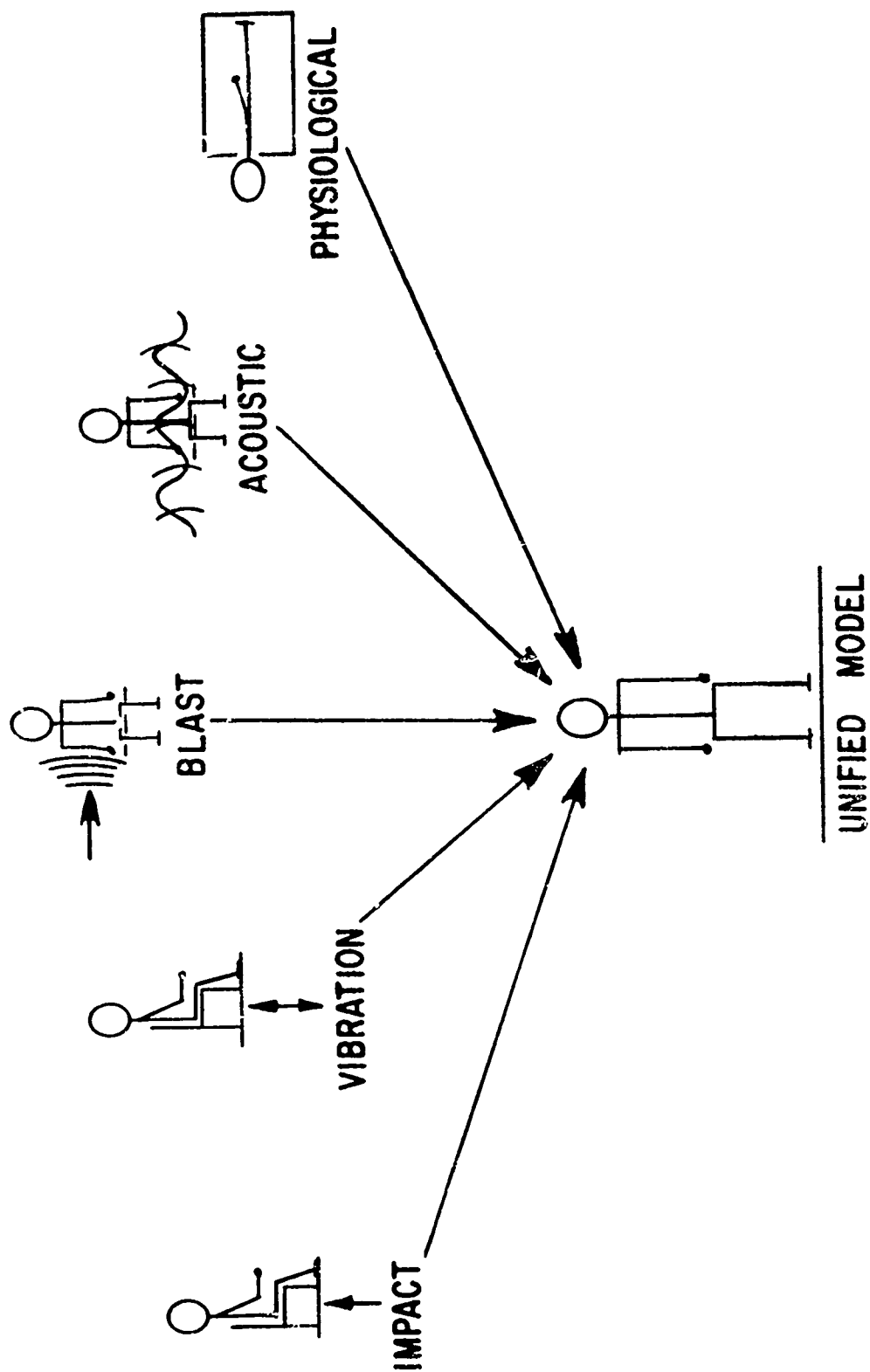


Figure 1. Unified Model

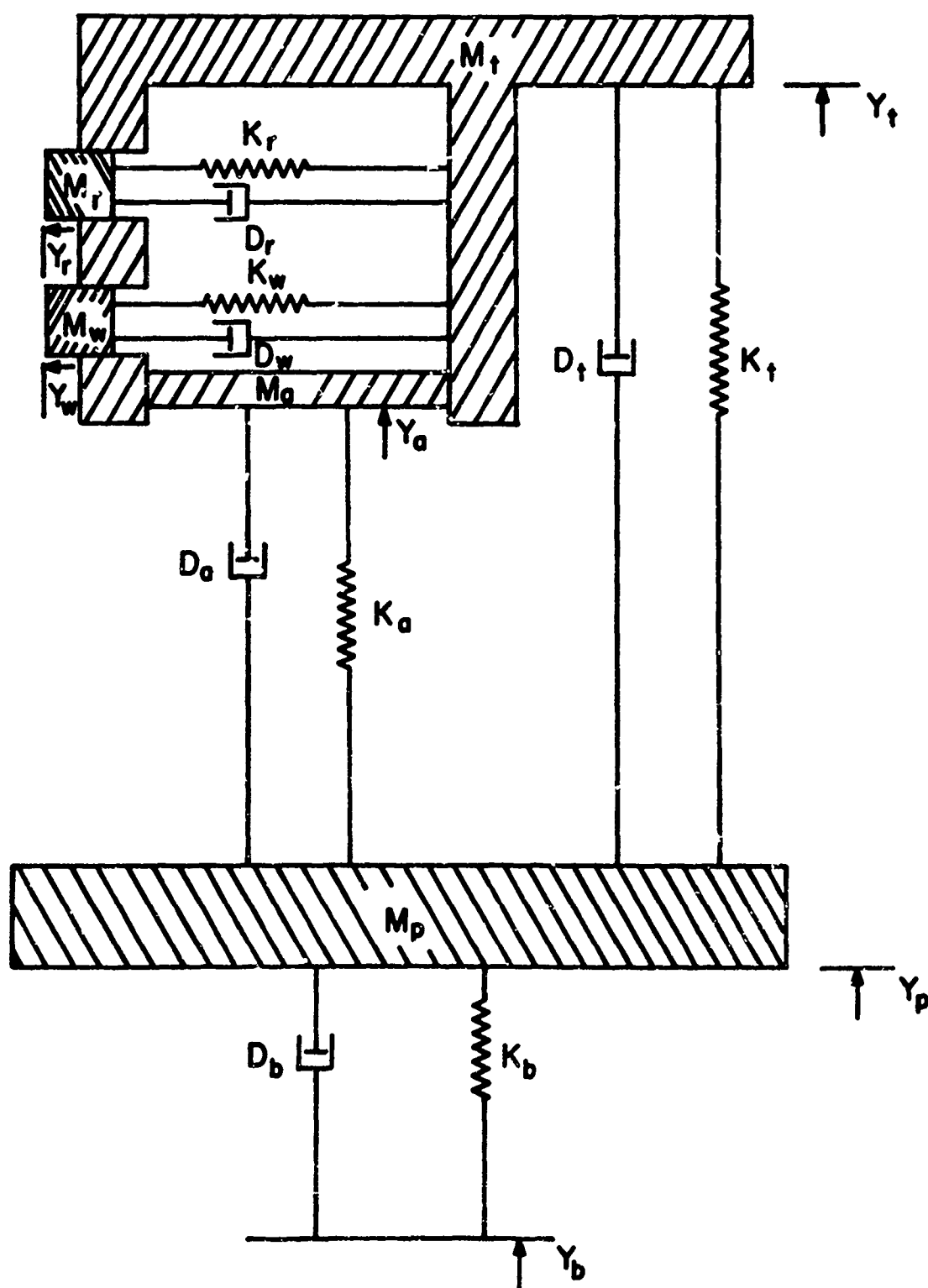


Figure 2. Five-Degree-of-Freedom Body Model

assumed to be mechanical, while for the thorax the ideal gas equation is used. Eq 6 gives the pressure volume relationship, where  $P_0$  and  $V_0$  are equilibrium values of the pressure and volume respectively, and  $P$  and  $V$  are variations from the equilibrium values. For small changes in the volume, Eq 6 may be approximated by Eq 7, which is linear. Eq 8 gives the volume change within the thoracic cavity due to mass surface area displacements of the abdominal, chest wall, and effective respiratory mass.

Note that for  $V$  much smaller than  $V_0$ , the gas equation introduces only elastic terms where the effective spring constant is  $P_0/V_0$  times the area of the respective mass being displaced.

Due to the air coupling in the thorax, the chest wall and respiratory mass are excited orthogonally to the  $G_z$  axis but move as an integral part of the torso longitudinally or parallel to the  $G_z$  axis and have their masses included in  $M_t$ .

With slight modifications to the equations describing the response of the model, excitations in the  $G_x$  direction can also be studied. For example, vibration of a subject in the supine position is simulated by adding a coupling term for the relative displacement of the chest to the torso in Eq 4 and by assuming the coupling constants of the abdominal mass to be isotropic for motion in the  $G_z$  and  $G_x$  directions.

The variables used in this model can be derived from various experimental measurements and the physical constraints imposed during experiments; for example, an envelope surrounding the abdomen or a blocked trachea can, in turn, be easily simulated on the model.

Each of the masses can be excited individually or in combination with one or more of the others to simulate various body stresses. The buttocks, though not an independent variable in this model, does serve as a driving point with  $f_b$  in Eq 9 as the input force for vibrations or impact exposures or for the measurement of total body impedance for the seated subject.

## MODEL EQUATIONS

1.  $M_p \ddot{Y}_p = K_b (Y_b - Y_p) + D_b (\dot{Y}_b - \dot{Y}_p) + K_a (Y_a - Y_p) + D_a (\dot{Y}_a - \dot{Y}_p) + K_t (Y_t - Y_p) + D_t (\dot{Y}_t - \dot{Y}_p)$
2.  $M_a \ddot{Y}_a = K_a (Y_p - Y_a) + D_a (\dot{Y}_p - \dot{Y}_a) - A_a P$
3.  $M_t \ddot{Y}_t = K_t (Y_p - Y_t) + D_t (\dot{Y}_p - \dot{Y}_t) + A_a P$
4.  $M_w \ddot{Y}_w = A_w P - K_w Y_w - D_w \dot{Y}_w$
5.  $M_r \ddot{Y}_r = A_r P - K_r Y_r - D_r \dot{Y}_r$
6.  $P = -\frac{P_0 V}{V + V_0}$
7. If  $V \ll V_0$ ,  $P = -\left(\frac{P_0}{V_0}\right)V$
8.  $V = (Y_t - Y_a) A_a + Y_w A_w + Y_r A_r$
9.  $f_b = K_b (Y_b - Y_p) + D_b (\dot{Y}_b - \dot{Y}_p)$

For large volume changes, Eq 7 is no longer valid and Eq 6 must be used. Although the differential equations are no longer linear, they can be solved, and must be used in this form when the model is used to study lung compression due to large amplitude blast waves. Experiments have shown that the injury mechanisms of primary interest occur when relatively large lung volume changes take place.

### MODEL ANALYSIS

Two basically different computer approaches were used to solve the differential equations and to readjust the equation parameters to give solutions best approximating the experimental data available.

A digital computer program called MIMIC [ Ref 11] was used to solve the differential equations in the time domain. SYSTRAN [Refs 12,13,14], a program developed for biodynamic signal analysis, was used to analyze the equations in the frequency domain.

The equations were also simulated on analog and hybrid computers which allowed direct observation of system response and were used to study the effects of variations of the system parameters on the dynamic behavior of the model.

Both the digital and analog computer programs allowed great versatility in the modes of system excitation and provided readouts of any desired model variable. The five masses as well as the buttocks could be excited individually or in combination to simulate various dynamic environments.

Nonperiodic and periodic forcing functions were used to study the characteristic response of the model. By use of the MIMIC and SYSTRAN programs, it was possible to obtain transient solutions as well as frequency domain response amplitudes from the nonperiodic driving function.

Sinusoidal functions were used in the analog and hybrid computer analysis to study the resultant changes in the dynamic response characteristics upon variation of the model parameters.

## MODEL RESPONSE

A number of dynamic experiments have been simulated on the model, these include (1)  $+G_z$  square wave and sinusoidal excitations of a sitting subject; (2) human blast-wave exposures resulting in pressure on the abdomen, chest wall and trachea; and (3) individual tracheal, chest wall, and abdominal pressure excitations corresponding to cases of physiological interest.

The linear analysis of a nonlinear system can at best provide predictions only within certain displacement or acceleration ranges. Thus, for each case when the response of the present model is compared to experimental results, the system parameters are adjusted for the particular levels of amplitude under consideration.

From Coermann's [Ref 8] low level vibration experiments and  $+G_z$  impact studies done at this laboratory, it seems evident that as levels of acceleration are increased, there occurs a stiffening of the body's response as indicated by the shifting of the impedance profile to higher frequencies. Fig. 3 compares the model impedance response for a preloaded case to impact impedance measurements. A reduction in the buttocks stiffness,  $K_b$ , shifted the impedance profile to lower frequencies, and model behavior was similar to that measured by Coermann [Ref 3] in his low level vibration studies.

Excitations at different points of the model showed resonances of the chest wall and abdomen to lie between 5 and 10 Hz, depending on the point of input. Chest wall resonance was consistently about 1 to 2 Hz higher than the abdominal resonance as expected from experimental results [Ref 9].

The  $+G_x$  excitation of a supine subject was also simulated by adding chest-torso coupling terms in the differential equations and by driving the model at the torso and pelvis simultaneously. An increase in the resonance frequency of the chest wall and abdomen was observed as expected from experiments [Ref 9].

The behavior of the thoracic-abdominal system for ramp, sawtooth, N-wave and sinusoidal pressure variation excitations was also studied.



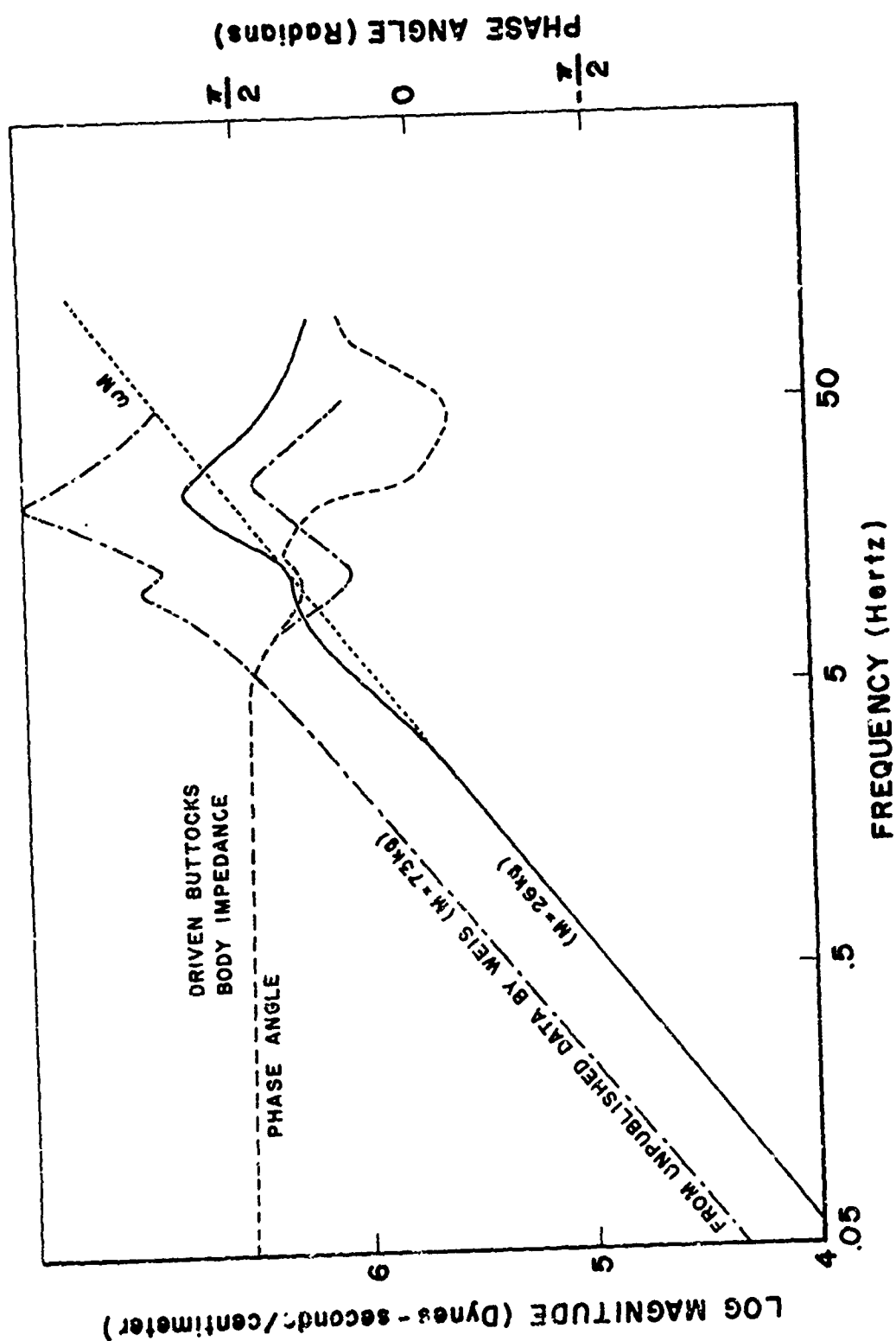


Figure 3. Measured and Calculated Impact Impedance

Input was applied to the abdomen, chest wall and mouth for the open trachea case, and only to the abdomen and chest wall (with trachea blocked) for the closed trachea case. Intensity versus duration of three dynamic pressure fields resulted in lung compression to one-eighth static volume for open and closed trachea as shown in Fig. 4. The model predicts that greater pressure intensities can be tolerated if the trachea is open to the incident pressure wave.

Since strain can be directly related to the difference of various mass displacements for the model, it is possible to excite the model at a given strain level by defining input displacements and observing the accelerations necessary to produce the given strain. Since for many injury mechanisms strain is directly related to the likelihood of injury, it is possible to derive curves of equal injury potential. Fig. 5 shows curves of equal strain analytically derived for the abdomen and spine. Note that for shorter durations the softer system, in this case the abdomen, can withstand higher loads, whereas for longer duration accelerations it becomes more susceptible to injury than the spine.

Typical parameter values used for the model are given in Table 1. These values, representative for a 70 kg body mass, were selected as a compromise from segmental and whole body dynamic and static measurements, other lumped parameter models, and the requirements for stability and proper behavior of the present model.

The scaling relations applied to this model are given in Table 2. These relations were used to scale the model to any desirable size as a function of the total mass. Fig. 6 shows abdominal and chest wall deflections due to constant velocity amplitude buttocks excitations for an equivalent 70 kg body mass. These were scaled down to a 6 kg body, with the resulting shifts shown in Fig. 7. Two basic changes are observed: the resonances shift from about 5 to 6 Hz up to between 11 and 12 Hz; the relative magnitude of the chest displacement to the abdominal displacement is also reduced by one half for the smaller mass. The upward shift in the resonance frequency is as would be expected for a smaller subhuman primate and agrees well quantitatively

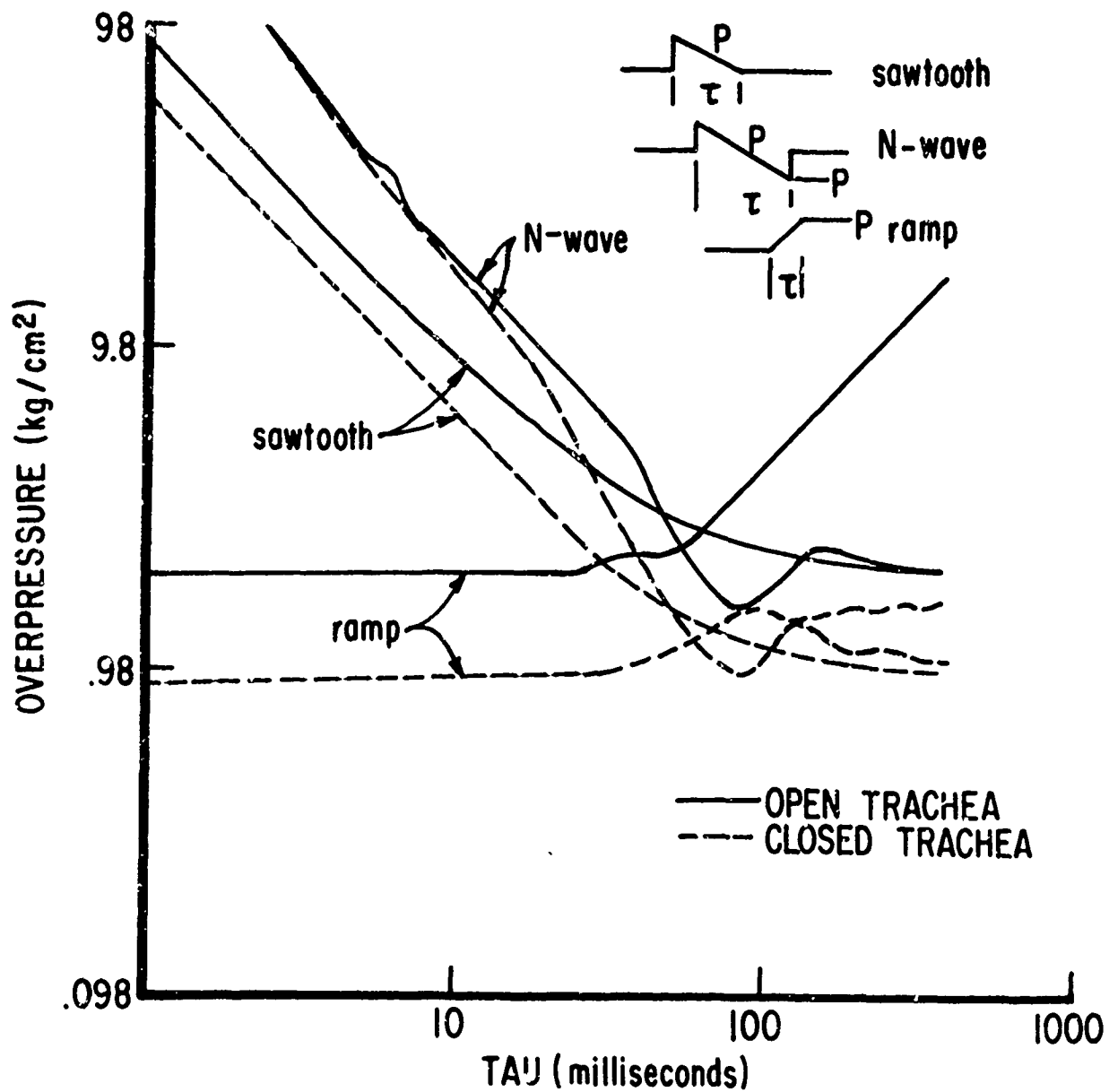


Figure 4. Intensity vs. Duration of Three Dynamic Pressure Fields Resulting in Lung Compression to One-Eighth Static Volume for Open and Closed Trachea

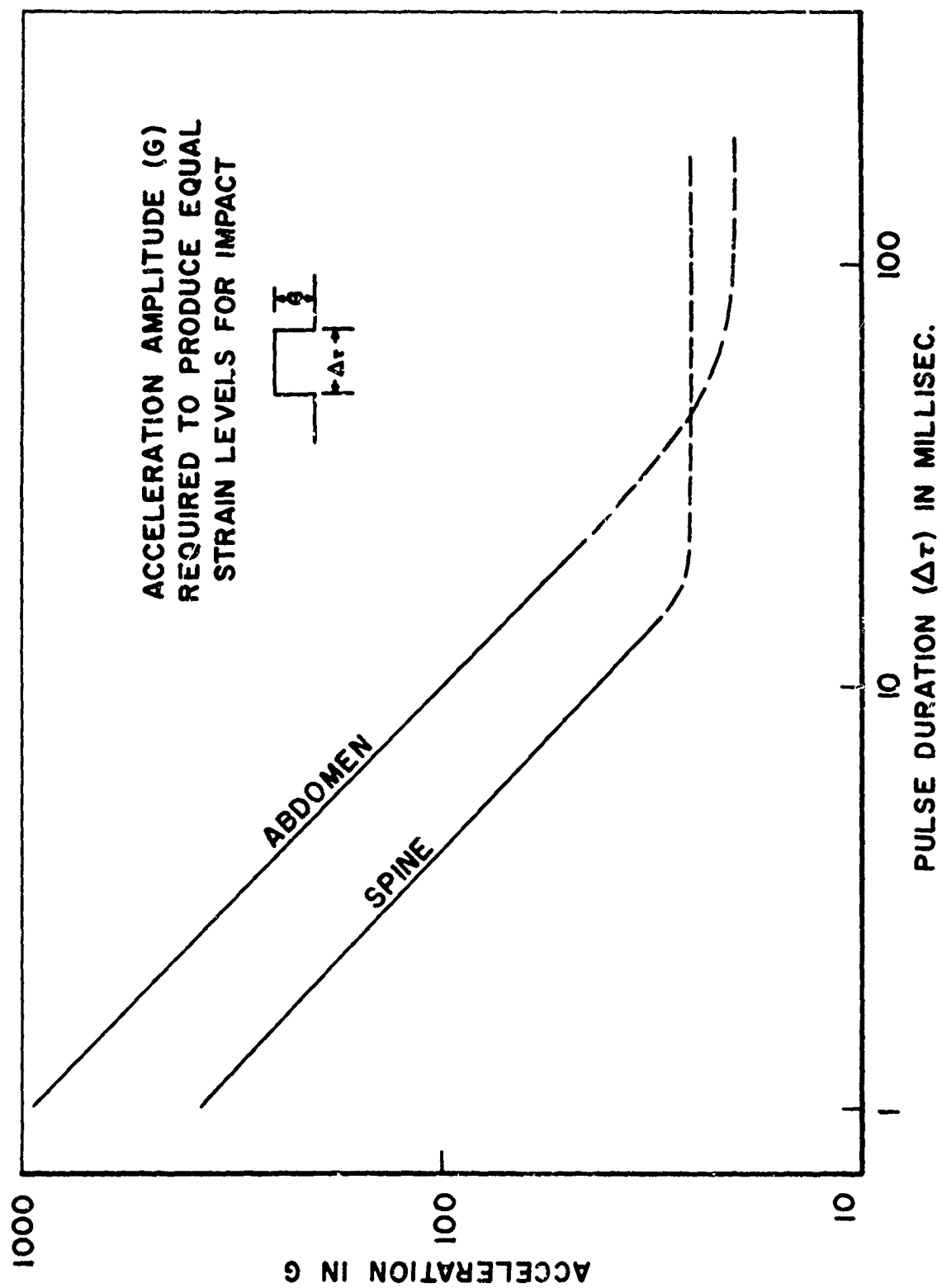


Figure 5. Calculated Curves of Equal Strain for the Abdomen and Spine

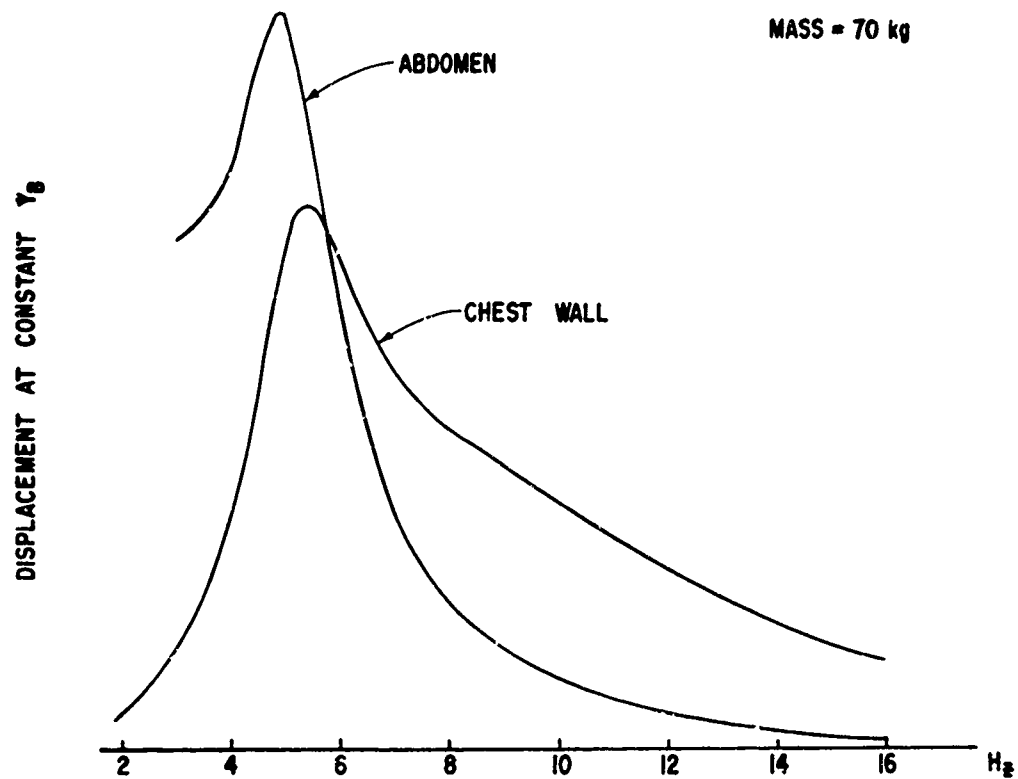


Figure 6. Abdominal and Chest Wall Deflections Due to Constant Velocity Amplitude Buttocks Excitations for 70 kg Body Mass

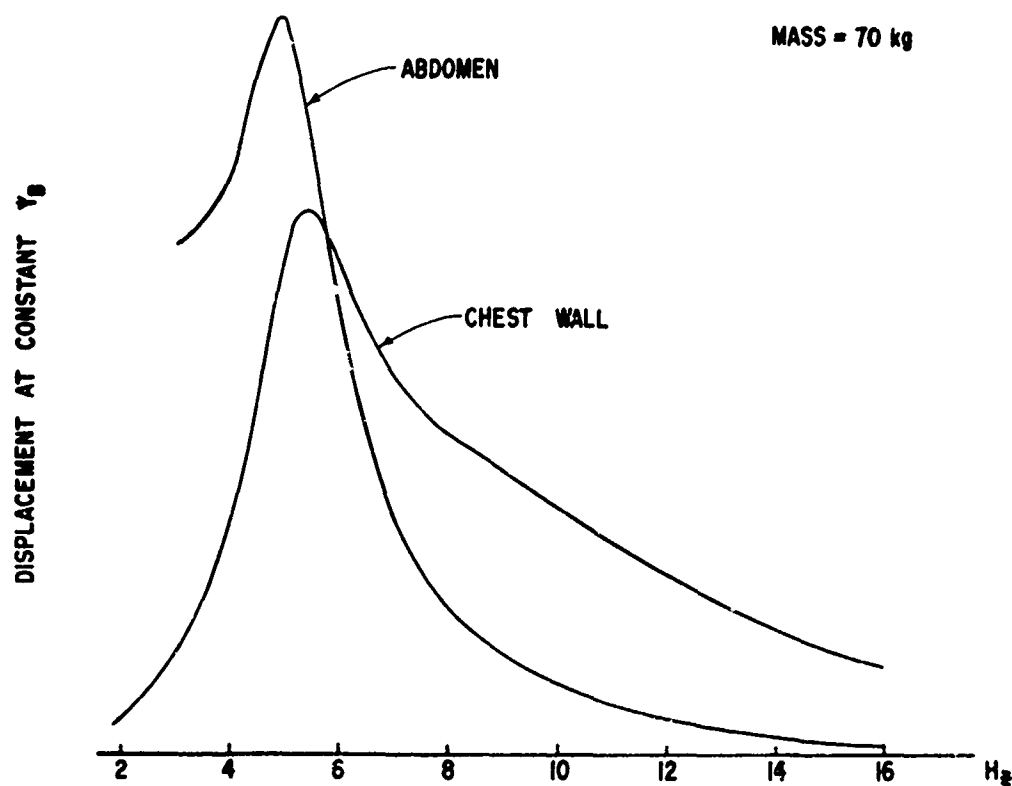


Figure 6. Abdominal and Chest Wall Deflections Due to Constant Velocity Amplitude Buttocks Excitations for 70 kg Body Mass

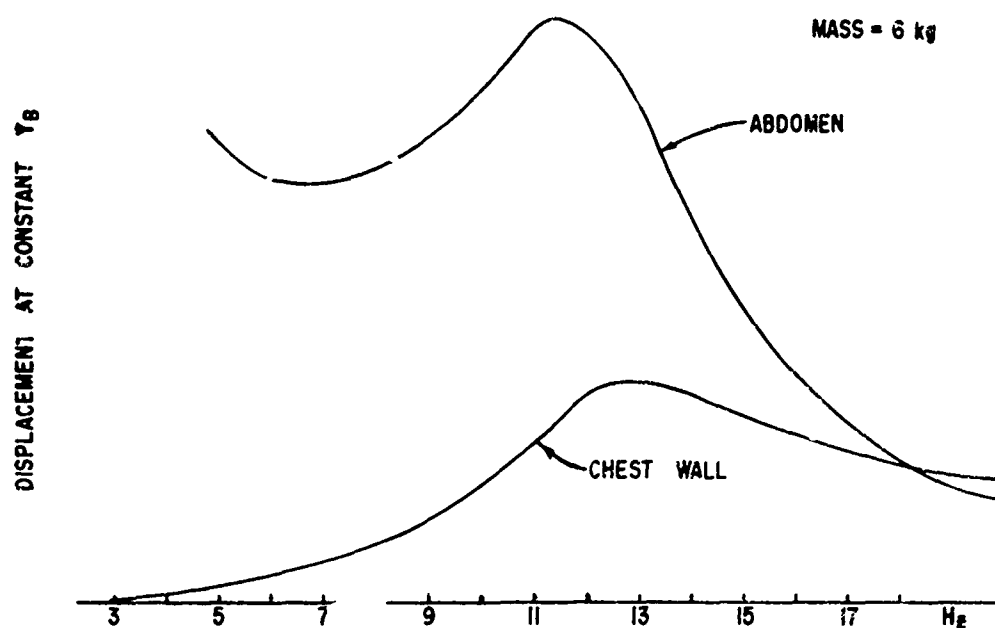


Figure 7. Abdominal and Chest Wall Deflections Due to Constant Velocity Amplitude Buttocks Excitations for 6 kg Body Mass

# PARAMETERS

$V_0$ (CM <sup>3</sup> )	$4 \times 10^3$
$A_R$ (CM <sup>2</sup> )	2
$M_R$ (GMS)	$1 \times 10^{-1}$
$D_R$ (DYNES - SEC/CM)	$1.6 \times 10$
$K_R$ (DYNES/CM)	0
$A_W$ (CM <sup>2</sup> )	$2 \times 10^2$
$M_W$ (GMS)	$1 \times 10^3$
$D_W$ (DYNES - SEC/CM)	$6 \times 10^5$
$K_W$ (DYNES/CM)	$1 \times 10^8$
$A_A$ (CM <sup>2</sup> )	$2 \times 10^2$
$M_A$ (GMS)	$4 \times 10^3$
$D_A$ (DYNES - SEC/CM)	$1 \times 10^4$
$K_A$ (DYNES/CM)	$8 \times 10^6$
$M_T$ (GMS)	$4 \times 10^4$
$D_T$ (DYNES - SEC/CM)	$4 \times 10^6$
$K_T$ (DYNES/CM)	$1 \times 10^9$
$M_P$ (GMS)	$8 \times 10^3$
$D_B$ (DYNES - SEC/CM)	$6.5 \times 10^5$
$K_B$ (DYNES/CM)	$6 \times 10^7$

Table 1. Typical Model Parameters



## SCALING RELATIONS

LENGTH:  $L_1 = L_2 (M_1/M_2)^{1/3}$

AREA:  $A_1 = A_2 (M_1/M_2)^{2/3}$

VOLUME:  $V_1 = V_2 (M_1/M_2)$

MASS  
ELEMENTS:  $m_1 = m_2 (M_1/M_2)$

DAMPING  
COEFFICIENT:  $D_1 = D_2 (M_1/M_2)^{2/3}$

SPRING  
CONSTANT:  $K_1 = K_2 (M_1/M_2)^{1/3}$

RESONANT  
FREQUENCY:  $f_1 = f_2 (M_2/M_1)^{1/3}$

Table 2. Parameter Scaling Relations

with measurements by Kazarian [Ref 15], who has observed maximum abdominal displacements at 12 to 13 Hz for a 6-8 kg Rhesus monkey (*macaca mulatta*).

### SUMMARY

The present model is only an approximation, as any biodynamic model must be, but it does provide considerable insight into the dynamic response of the human body to various mechanical stress environments and it permits predictions to be made concerning the relative displacements of the major torso organs due to various acceleration-time histories applied to different parts of the body. The resonances of body segments under steady-state vibrational input can be observed, and the effects of body constraints on the resonance frequencies and displacement, velocity, and acceleration amplitudes can be predicted. The dynamic behavior of the thorax can also be better understood in terms of the interaction of the chest wall and abdomen as mechanical elements, with the air modeled as an ideal gas.

Not only can the model predict excursions of the system's variables for any input function and changes in these excursions for differing constraints, it can also, given strain injury correlations, predict curves of equal injury potential as functions of acceleration-time profiles.

The present model also serves as a vehicle for the application of scaling relations to geometrically similar primates differing only in total mass. Use of the scaling relations in combination with the model provides an easy check on its validity, as animal data can be scaled to the human, but also human data can be scaled down to the animal. Certainly a two-way correspondence for low input data would give more credence to high input animal-to-man extrapolations using the same model.

The model can also be extremely helpful in establishing a systematic set of both animal and human experiments. Although with only five degrees of freedom it can not deal in detail with individual organs or their internal reactions, its five degrees do correspond to some of the most frequently measured variables.

The set of experiments delineated by this model - including thoracic and buttocks impedance measurements, studies of resonances of the spine, abdomen and chest wall, and relative body segment motion, and the changes produced on them by imposing various body constraints - will not only provide needed biodynamic data, but will in turn allow further refinements; including, if necessary, alterations of the present model.

## REFERENCES

1. DuBois, A. B., A. W. Brody, D. H. Lewis, B. F. Burgess, Jr., "Oscillation Mechanics of Lungs and Chest in Man," J. Appl. Physiol., 8:587, 1956.
2. von Gierke, H. E., "Biodynamic Response of the Human Body," Applied Mech. Review, Vol 17, No 12, p 951, Dec 1964.
3. Holladay, A. E. and I. G. Bowen, "A Mathematical Model of the Lung for Studies of Mechanical Stress," Proc. of the San Diego Symp. for Biomedical Engineering, p 39, 1963.
4. Otis, A. B., Fenn and H. Rahn, "Mechanics of Breathing in Man," J. Appl. Physiol., 2:592, 1950.
5. Brody, A. W., "Mechanical Compliance and Resistance of the Lung-Thorax Calculated from the Flow Recorded During Passive Expiration," Am. J. Physiol., Vol 178, No 2, p 189, 1954.
6. Long, E. C., W. E. Hull and E. L. Gebel, "Respiratory Dynamic Resistance," J. Appl. Physiol., 17(4), p 609, 1962.
7. Coermann, R. R., G. H. Ziegenruecker, A. L. Wittwer, and H. E. von Gierke, "The Passive Dynamic Mechanical Properties of the Human Thorax-Abdomen System and of the Whole Body System," Aerospace Medicine, Vol 31, p 443, June 1960.
8. Coermann, R. R., "The Mechanical Impedance of the Human Body in Sitting and Standing Position at Low Frequencies," Human Vibration Research, S. Lippert editor, Pergamon Press, 1963.
9. Clark, W. S., K. O. Lange and R. R. Coermann, "Deformation of the Human Body due to Uni-directional Forced Sinusoidal Vibration," Human Factors, pp 255-274, Oct 1962.
10. Edwards, R. G. and K. O. Lange, A Mechanical Impedance Investigation of Human Response to Vibration, AMRL-TR-64-91, Aerospace Medical Research Laboratories, Wright-Patterson Air Force Base, Ohio, 1964.
11. Sansom, F. J. and H. E. Peterson, Mimic Programming Manual, SEG-TR-67-31, Systems Engineering Group, Wright-Patterson Air Force Base, Ohio, July 1967.
12. Lajeunesse, D. J., E. B. Weis, Jr. and T. J. Hogan, SYSTRAN (Systems Analysis Translator): A Digital Computer Program, AMRL-TR-65-133 (AD 624468), Aerospace Medical Research Laboratories, Wright-Patterson Air Force Base, Ohio, July 1965.

13. Weis, E.B., Jr. and D. J. Lajeunesse, SYSTRAN (Systems Analysis Translator): A Digital Computer Program, Supplement One. AMRL-TR-65-133 (Sup I), Aerospace Medical Research Laboratories, Wright-Patterson Air Force Base, Ohio, March 1966.
14. Weis, E.B., Jr. and D. J. Lajeunesse, SYSTRAN (Systems Analysis Translator): A Digital Computer Program, Supplement Two, AMRL-TR-65-133 (Sup II), Aerospace Medical Research Laboratories, Wright-Patterson Air Force Base, Ohio, Dec 1967.
15. Kazarian, L.E., Aerospace Medical Research Laboratory, Wright-Patterson Air Force Base, Ohio, Personal Communication, 1970.

# SOME ASPECTS OF BIODYNAMIC MODELLING FOR AIRCRAFT ESCAPE SYSTEMS

Peter R. Payne

Wyle Laboratories  
Rockville, Maryland 20852

## INTRODUCTION

### The Basic Problem

Not long after the parachute was invented, people wearing them started jumping out of airplanes. At first this was a fairly simple exercise because the flight speeds were so low, and if one did accidentally hit part of the airplane, such as the fin or stabilizer, during the course of falling away, this was usually no great problem. Because of the low air speed, the crew member would not have achieved much relative velocity, and in any case the airplane was very flimsily constructed.

By the end of World War II, however, egress was getting to be much more of a challenge, and pilots were being taught specific escape techniques for each aircraft. Escape was starting to get both difficult and hazardous, and it is not surprising that around this time development of the ballistically-fired ejection seat started in various countries. In today's high-speed aircraft there is little possibility of escape unless an ejection seat or capsule is employed, and future flight envelopes are extending to the point where even an escape seat may be inadequate, partly because of the injuries caused by wind blast, and partly because the amount of vertical acceleration required to clear the aircraft structure (usually the fin) may be so great that the seat occupant will be seriously injured by the escape system itself.

Assuming incompressible flow, constant crew member drag area, and constant airplane velocity, elementary mathematics shows that the velocity decrement of the crew member with respect to the aircraft is given by

$$\frac{(C_{DS})_{px}}{2m} = \frac{\frac{\Delta u}{u_o}}{1 - \frac{\Delta u}{\Delta_o}} - \ln \left| \frac{1}{1 - \frac{\Delta u}{u_o}} \right|$$

PRECEDING PAGE BLANK

where  $u_o$  = the (constant) aircraft velocity  
 $\Delta u$  = the velocity change of the crew member with respect to aircraft axes  
 $x$  = the distance traveled, relative to aircraft axes, from the point of departure  
 $(C_D S)$  = the drag area of the crew member  
 $m$  = the mass of the crew member  
 $\rho$  = mass density of air .

Taking typical figures of  $(C_D S) = 6.0 \text{ ft}^2$

$m = 165/32.2$ , and sea level air density, we find that  $\frac{\Delta u}{u_o} = .146$  at a distance 10 ft behind the point of departure, and .203, 20 ft behind. The following table gives solutions for three different practical cases corresponding to different dates in aircraft history:

<u>Year</u>	<u>1920</u>	<u>1945</u>	<u>1970 A. D.</u>
Airspeed	80 knots E. A. S.	300 knots E. A. S.	600 knots E. A. S.
$\Delta u$ at twenty feet	27.4 ft/sec	102.8 ft/sec	205.5 ft/sec
Time to twenty feet	1.353 secs	0.362 secs	0.181 secs
Free-fall distance	29.5 ft	2.11 ft	0.53 ft
Initial horizontal acceleration	0.79 g	11.1 g	44.5 g
Wind blast pressure	21.7 lb/ft <sup>2</sup>	305 lb/ft <sup>2</sup>	1220 lb/ft <sup>2</sup>

(Of course, these figures are very idealized, being based on incompressible flow assumptions, and assuming that only a drag force acts on the escaping crew member. They do serve to illustrate the magnitude of the problem, however.)

The ejection seat mitigates the problem of escape by accelerating rapidly out of the aircraft, so that it has acquired a substantial velocity normal to the direction of flight when it leaves its guide rails. This escape velocity must be sufficient for the seat and its occupant to clear the aircraft structure, and in practice, this requires very high levels of acceleration in the initial, or catapult acceleration phase; and often a subsequent rocket powered "boost" as well. In order to design such a system, therefore, we need to know how much acceleration the escape seat occupant can be subjected to.

The human body can always be damaged by sufficiently high acceleration levels. Even the gravitational acceleration of  $32.2 \text{ ft/sec}^2$  can cause injuries (damage to the circulatory system, for example) in some individuals, after a sufficient period of time has elapsed. The higher acceleration levels associated

with re-entry of a space vehicle, which are maintained for a few minutes, give rise to "hydraulic problems," caused by the displacement of blood and other fluids from their normal location in the body. In contrast, the "brief acceleration" or "short period" acceleration associated with an ejection seat, and which endures for a period of less than a second, can cause structural damage, if the level is high enough, but cannot significantly distort fluid flow patterns. It is this short period category of acceleration then, and the body's response to it, which is the subject of this paper.

The precise nature of the structural injury caused by short period acceleration depends upon the orientation of the acceleration vector with respect to the human body, the restraint of the human body, the magnitude of the acceleration and the way in which the magnitude varies with time.\* The basic problem to be studied can be summarized as follows. Given an acceleration time history, such as that associated with the initial trajectory of an escape system will it cause injury when applied to a human subject, and what will be the nature of the injury? Of course, there is a simple and direct way of determining the answer to this question by experiment, but we are prevented from using it because of obvious moral, legal, humanitarian and other prohibitions. Yet we cannot avoid answering the question because we could then be condemning some of our fighting men to death or injury in the future, either because they will have to use escape systems with excessively dangerous acceleration characteristics, or because their escape envelope is unnecessarily restricted in relation to the total envelope of their vehicle.\*\*

It is now generally agreed that the best way to answer the question is to develop an accurate description of the human body, including both its dynamic characteristics and the static load bearing capability of its many complex components, so that we can accurately calculate the effect of a given input acceleration time history, and also that we may be able to design a restraint or support system which optimally couples it to the driving force associated with the acceleration. The construction of such a "dynamic model" is a task routinely undertaken in the aerospace industry (among others) for structures which are built from well understood materials. A simple example is an

---

\* This is sometimes referred to as the "frequency content" of the input acceleration, but such terminology can be misleading. A reference to "frequency content" implies that such descriptors as the power spectral density of an input acceleration pulse can be correlated with injury mode, and at the present time this is not proven; indeed, quite cogent arguments can be made for the contention that power spectral density is not correlatable with injury, at least in a simple way.

\*\* We should also like to find an answer to this question because of the thousands of people who unnecessarily lose their lives in automobile accidents and other crash environments; deaths which might often be avoided, given adequate restraint and protection.



aircraft, for which the strength of each element is accurately calculated,\* in order to ensure that it can perform its function without failure. We also determine the deformation of the aircraft's structure, and construct dynamic models which tell us how it will behave in response to gusts, how aeroelastic deformation influences its stability and handling characteristics, and to assure that flutter and divergence cannot occur with the flight envelope. But such a task is very much harder in the case of the human body, firstly because it is so much more complex than an aircraft, and secondly because many of its constituent materials are not "simple" linear materials obeying Hooke's law and having small damping. Additionally, the dynamic characteristics can be varied by tensing or relaxing the muscles which make up so much of the body. Other variations occur because the various body materials tend to change their characteristics with age, environment, and the degree of physical fitness of the subject, and because people are not manufactured to the same close tolerances as aircraft.

At first sight one might suppose that an adequate description of the human body could be built up by measuring the various quantities of interest from cadaver material. Information of this type is certainly very helpful, and indeed a pioneer of biodynamics, Arno Geertz [12], obtained a remarkably accurate estimate of the ability of the human spine to withstand ejection seat acceleration in this way. It does have limitations, however, because cadaver material is hard to obtain for the age groups of primary interest, and its dynamic and even static properties are often different from the in vivo case. Additionally, the important contributions of the muscle structure and fluids are almost entirely absent in the cadaver.

It is, therefore, necessary to devise experiments with live human subjects from which meaningful data can be obtained. Since it is essential to avoid injury to the subjects, the acceleration levels used in such tests must be substantially lower than those which would cause injury, and the results have to be extrapolated in some way in order to predict the level at which injury would occur. It is also necessary to devise tests which will enable us to determine the damping in the various elements of a dynamic model, and the primary dynamic characteristics, such as resonant frequencies.

Needless to say, there is no "right way" to discover the "right model" for the human body. We must laboriously build a model piece by piece, sometimes relying upon intuition, sometimes on the biologist, and sometimes relying on the results of a fortuitous experimental observation, but constantly comparing the apparent external behavior of our model with experimental observations (such as those obtained on the AMRL drop test facility) in order to make sure that it is not straying from the reality of physical measurements. It will be a long time before we can feel that we have a completely adequate model, and many hundreds of workers will by then have contributed to its construction, just as in any other scientific discipline.

---

\*Spectacular exceptions to this prove the rule!

## The Development of Ejection Seat Biodynamics in Germany

The practical development of the ejection seat apparently started in Germany during 1939, and escape systems were operational by the end of the war. Lovelace [24], et al, have provided an in-depth review of this development, including translations of many original german papers as appendices to their report. Geertz [12] has also given a review which is more restricted, emphasizing the work carried out at Heinkel Flugzeugwerke, where he was employed. Much of Geertz' work was later summarized in a well-known paper by Ruff [36], and it is interesting to note that Ruff is listed as a co-advisor in Geertz's thesis.

It is clearly impractical to review this early work with the detail and attention which it deserves, but as a fluid dynamicist, the writer feels bound to observe that he is often delighted by the simple and straightforward manner in which many German workers approach the solution of a technical problem. Just after World War II, for example, we were fumbling around with the problem of designing jet engine intakes, and the whole subject seemed to be very abstruse and ill-defined. The writer will always remember the delight with which we received the German reports of wartime work on the subject (work which was later summarized in Kuchemann and Weber's "Aerodynamics of Propulsion") and which said almost everything there was to say, and in a most elegant manner.

In the case of the ejection seat problem one imagines them starting off by computing the acceleration necessary to give sufficient vertical velocity to clear the tail. They must then have realized that the seat must push the man out by the seat of his pants.

"What is going to push the top of the man out? "

"The spine is the only compression member between the top half of the man and the bottom half, so clearly the spine is going to push the top half of the man out of the aircraft. We must not ask the spine to push with a force greater than it can withstand. "

"How much force can the spine withstand? "

"We do not know. We get some spines and measure their breaking strength. "

This was done, principally by Geertz, and the critical ejection seat acceleration calculated. As a check other workers accelerated subjects in ejection seats, at increasing acceleration levels, until injuries were sustained. A few calculations were made to generalize the results, and the team moved on to other endeavors. According to Lovelace, et al, seats designed to the criteria so developed were "entirely satisfactory" in approximately sixty operational ejections.

Until recently, the earliest (and in some ways still the best) data on the strength of individual vertebrae was generally attributed to Ruff [36]. In fact, Ruff does acknowledge Geertz as the originator of this data. Geertz also measured the load-deflection curves of two large spinal segments, his results being reproduced as Figures 1 and 2 of this paper. His experimental techniques for these investigations were quite excellent, and one could perhaps wish they had been emulated by some later investigators.

It is interesting to note that, in common with Wiesehofer [47], Geertz based his earliest acceleration tolerance calculations on vertebral strength data given by Junk [20] (1925) in *Tabulae Biologicae*; which was something of a surprise to the present (data-starved) writer. Wiesehofer complains that "it is not possible to tell from the available table whether the measured values (of Junk) were averages for 30 year old men, or were based on a single individual, and ... it (is) not clear whether exceptionally strong men were selected and whether the vertebrae were fresh ...". Geertz is also rather wary of Junk's data and says of his own experiments "the present results have to be considered more correct." In order to evaluate these comments, the writer obtained a copy of the original Junk reference and found to his surprise that Junk was referencing Messerer [26] (1880). Reference to the Rare Book Department of the Library of Congress revealed that Messerer had measured the breaking strengths of vertebrae between C-4 and L-5 from seven subjects, ages 25 to 81, and that his results are in excellent agreement with modern data. Indeed, above T-8, Messerer (1880) still provides the only data available today.

The Messerer data is reproduced in Table 1. Comparing it with modern data, one must conclude that Messerer's (1880) testing technique was much more sophisticated than that of Perey [33] (1957), say. Most probably he filled the irregular end-plate surfaces with some plaster-like material, or placed intervertebral discs between the end-plates and the jaws of the testing machine.

Returning to Geertz' vertebral strength data, it is very surprising, in view of the high quality of his work, that he did not notice the relatively large hysteresis and strain rate effects of the intervertebral discs. (Virgin [43] (1951) first reports this in the literature.) One suspects that the spinal segment shown in Figure 2 has a greater stiffness than that of Figure 1 because of this effect, in that the second test went faster than the first; as is so often the case!

One of Geertz' most remarkable experiments involved measuring the upper torso acceleration of subjects during simulated ejection up a tower, using an early piezoelectric accelerometer (developed by a Dr. Nier of Dresden)

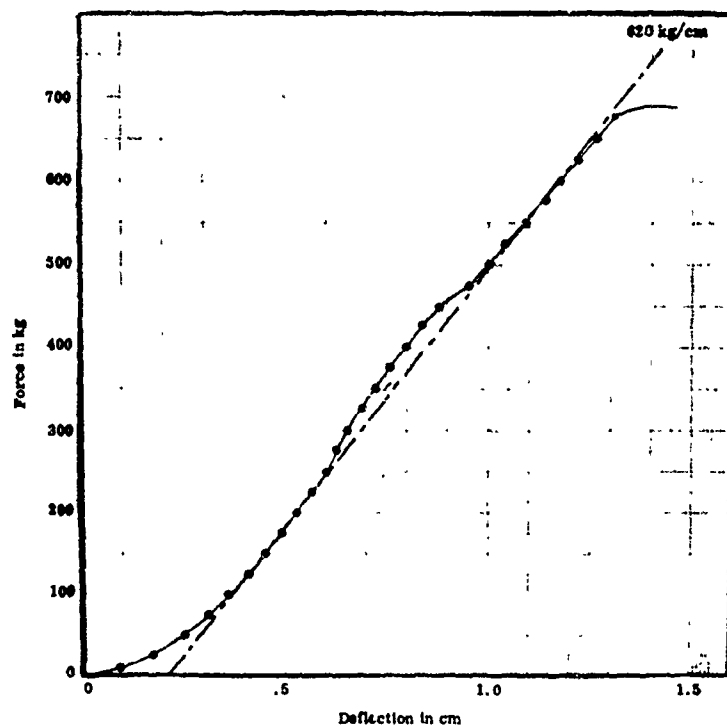


Figure 1. Load Against Deflection for a Spinal Segment, T-11 to L-2, Including the Processes of T-10 and L-3, According to Geertz. (Subject age 21.) [12]

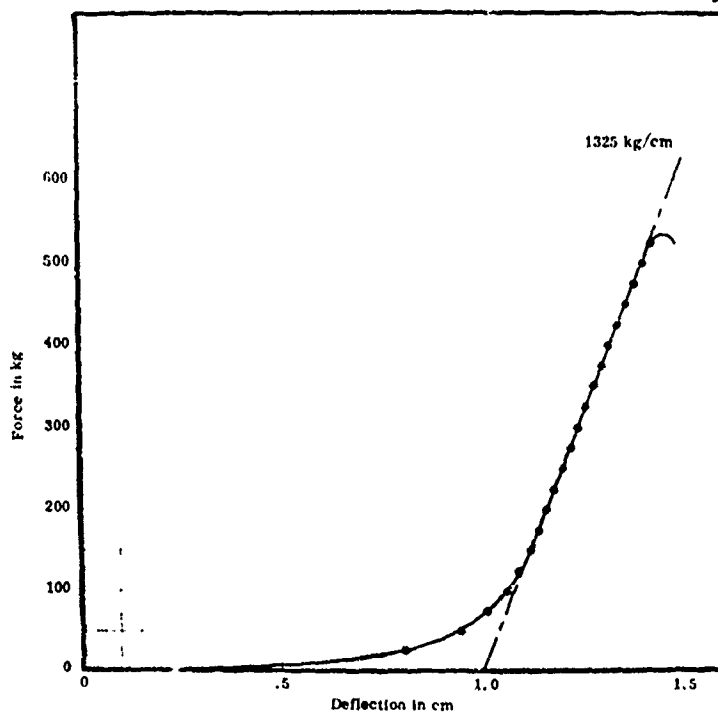


Figure 2. Load Against Deflection for a Spinal Segment, T-8 to T-12, Including the Processes of T-7 and L-1, According to Geertz. (Subject age 23.) [12]

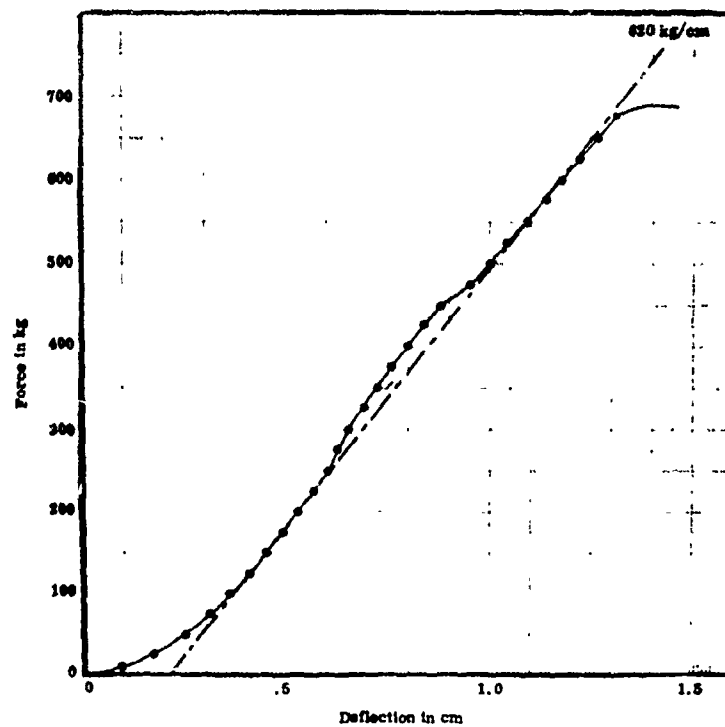


Figure 1. Load Against Deflection for a Spinal Segment, T-11 to L-2, Including the Processes of T-10 and L-3, According to Geertz. (Subject age 21.) [12]

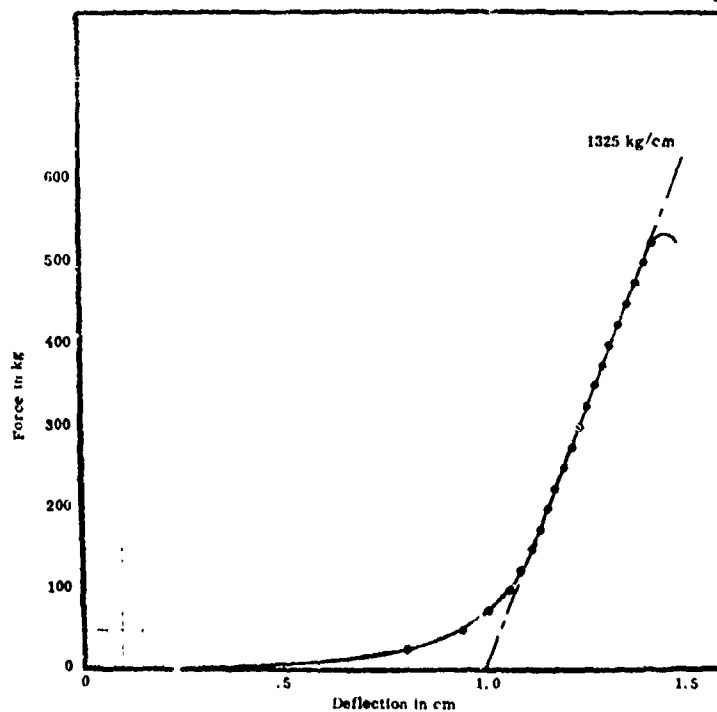


Figure 2. Load Against Deflection for a Spinal Segment, T-8 to T-12, Including the Processes of T-7 and L-1, According to Geertz. (Subject age 23.) [12]

TABLE 1  
VERTEBRAL STRENGTH DATA OF MESSERER (1880) [26]

56 year old man

C-3	150 Kg	T-1	200 Kg	L-1	400 Kg
C-4	150	T-2	200	L-2	425
C-5	170	T-3	190	L-3	350
C-6	170	T-4	210	L-4	400
C-7	170	T-5	210	L-5	425
		T-6	220		
		T-7	250		
		T-8	250		
		T-9	320		
		T-10	360		
		T-11	400		
		T-12	375		

	<u>C-4</u>	<u>T-1</u>	<u>T-6</u>	<u>T-10</u>	<u>L-1</u>	<u>L-4</u>	<u>L-5</u>
25 year old woman	-	300	360	480	620	-	740 Kg
30 year old man	275	450	600	850	1000	-	875 Kg
34 year old woman	-	-	-	-	-	800	-
51 year old woman	240	250	280	420	540	-	560 Kg
56 year old man	-	-	220	360	400	400	425 Kg
80 year old woman	-	-	-	-	-	250	-
81 year old woman	-	-	-	-	240	-	-

in conjunction with a cathode-ray oscilloscope\*. His experimental results are reproduced in Figure 3, and the upper torso acceleration is compared with the MIL-S-9479A Dynamic Response Index model in Figure 4. Considering that the DRI model is only single degree of freedom, and that it was developed as a spinal injury model, the agreement seems to be remarkably good.

Another interesting experiment involved an attempt to measure, in vivo, the amount of body weight carried by each vertebra. To do this, vertebral deflection was measured (using x-ray photography) when a horizontal subject was loaded in compression, and compared with the corresponding deflections when the subject stood vertically under 1 g. Since a considerable amount of soft tissue, including part of the viscera, loads up the spine under these conditions, but not during short period transients, Geertz' results are of limited value. As shown in Figure 5, however, the raw data does give a low load stiffness for two intervertebral discs, and this value is in excellent agreement with more recent measurements at the same force levels, using cadaver material.

The writer cannot leave the subject of Geertz' work without one direct quotation:

"Under a certain load every body bends, before it breaks; if its breaking tension is less than the distance which a freely suspended mass can possibly cover during the short time which the acceleration is effective, the body will not break. Thus, whether or not a break occurs depends in every case upon the time.

We may say: An acceleration of any magnitude may be safe regardless of the tensile strength of the skeleton, as long as it is of short duration."

At the time of the last symposium a few people, including Kornhauser and the writer, were spending considerable effort arguing that this was so, and that the very short duration HIAD allowables were nonsense. But since Geertz had succinctly stated the entire case twenty years earlier, our efforts do not now appear to be as pioneering as they perhaps seemed at the time. Geertz' mathematical analysis of this regime is perhaps a little unsophisticated, and he suggests a critical velocity change of only 4.2 ft/sec (26 g for .005 seconds) because he did not have a dynamic model which would permit him to differentiate between the critical velocity change and critical acceleration regimes. With our better understanding of biodynamics, we would today be inclined to say that the Geertz data indicates a critical velocity change (75% P.I.) of 15.3 ft/sec for the case of no arm rests and no shoulder harness; a result which is not inconsistent with the present DRI model.

---

\* Geertz says, "One disadvantage of this device is that its calibration is difficult and uncertain and is affected by various external influences." This must strike a responsive chord in all our hearts!

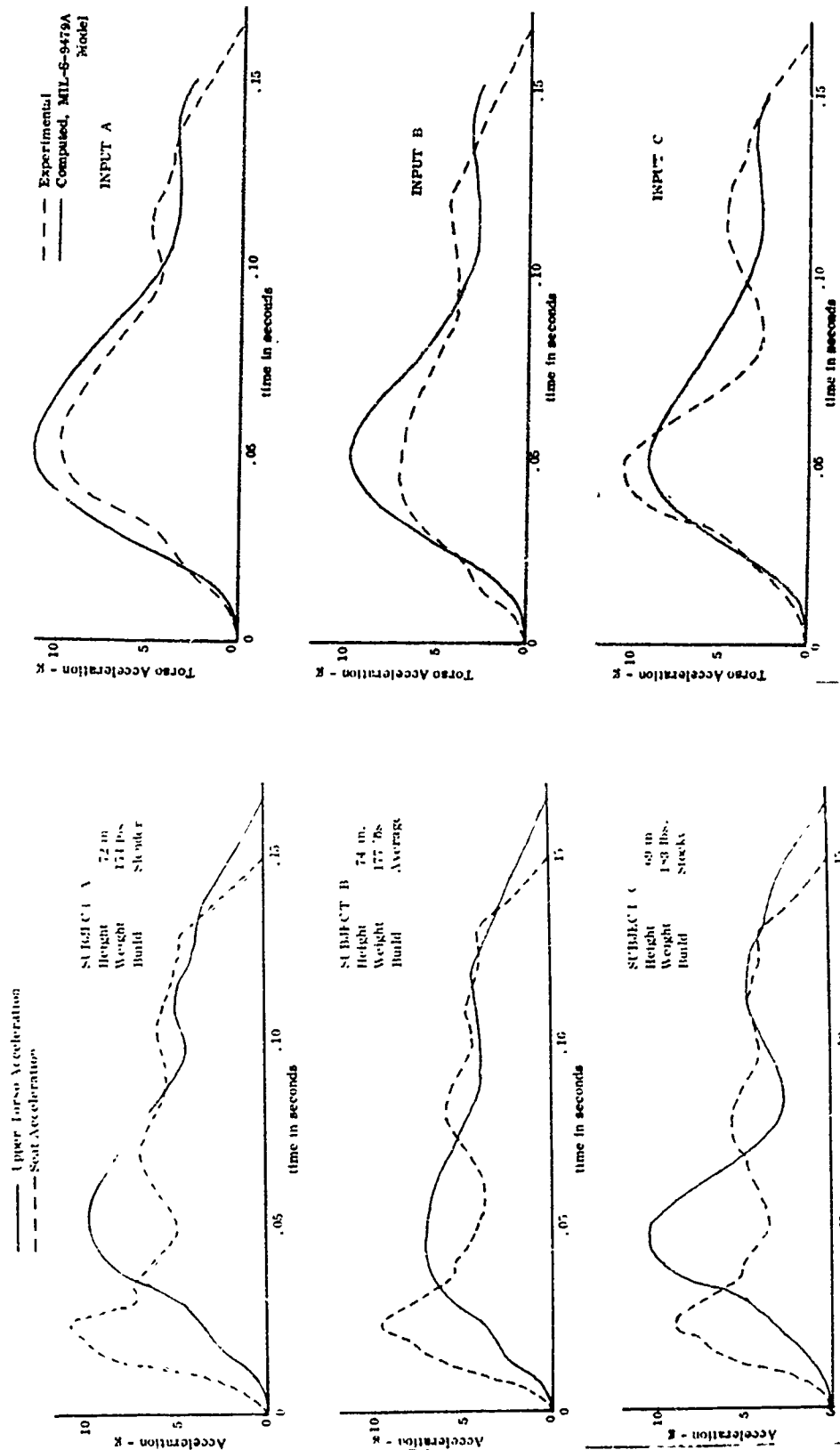


Figure 3. Geertz (1943) Measurements of Seat and Upper Torso Acceleration on an Ejection Tower [12]

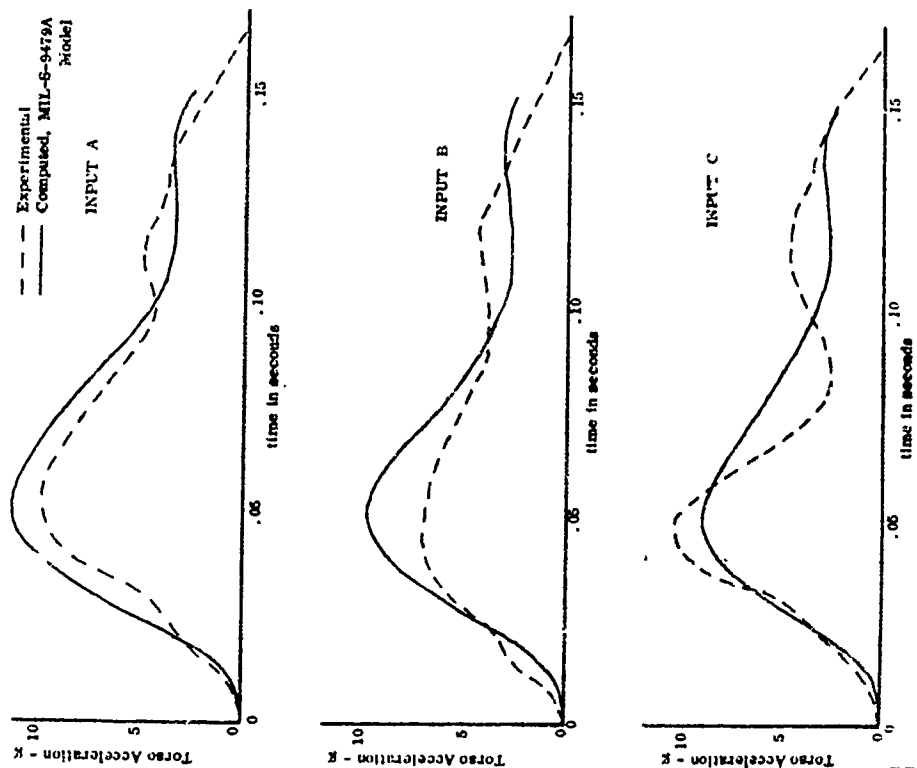


Figure 4. Comparison Between Geertz' Experiments and the Single-Degree-of-Freedom DRI Model [12]



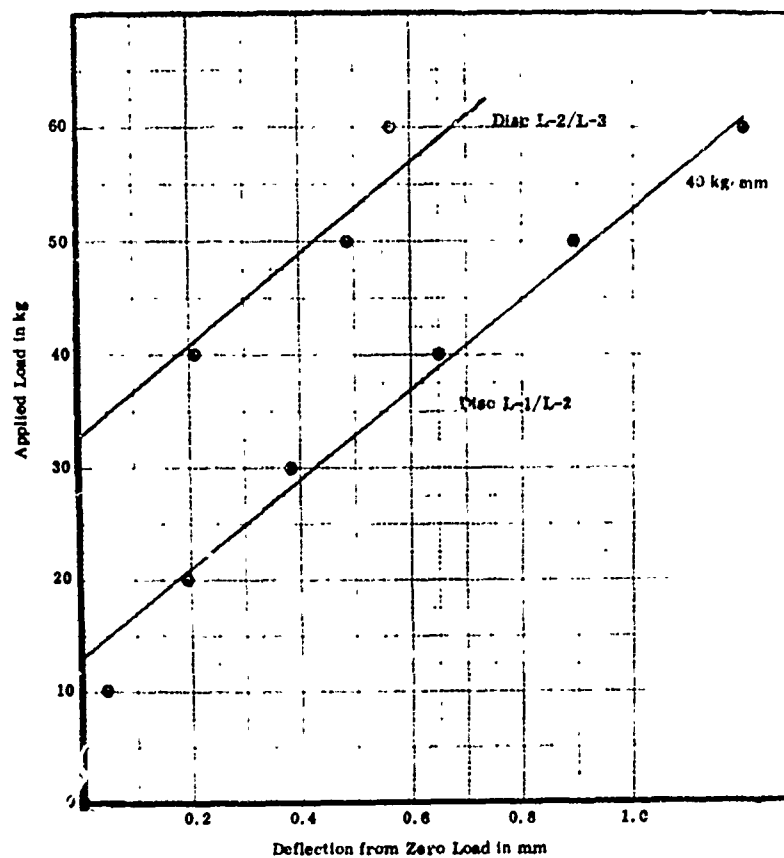


Figure 5. Analysis of Geertz Results for Disc Deflection in vivo (67.5 kg male) [12]

Another quotation, this time from Ruff\* (1941) seems quite topical today. Of parachute opening shock he says:

"In order to determine the opening impact which actually occurs in the case of man, the values obtained with a (rigid) dummy cannot be used without qualification . . . . Significantly higher impacts occurred in experiments with the dummy than in the case of a human subject of the same weight and under otherwise identical conditions. In one case an impact-like stretching force of 2020 Kg was measured with the dummy and 1290 Kg with a human being of the same weight."

In summary, the wartime German workers produced a wealth of data and ideas, and laid much of the basic groundwork in escape biodynamics. It is a thousand pities that much of this work was "lost" in the archives during the ensuing quarter of a century, that some of those people who knew of its existence were unable to appreciate its importance, and that the reproductions available today are so poor. One hopes that some agency will find it possible to retrieve the original documents and republish the material in a form which makes it readily available to all workers in the field.

#### A NEW LOOK AT DATA FOR SPINAL MODELS

The history and purpose of dynamic modelling for the prediction of spinal injury has already been reviewed by Brinkley before this symposium, and is also well covered in the previous literature. The present "standard" model is the single degree of freedom, lumped parameter model defined in MIL-S-9479A [1], and some of its past and future applications have also been described by Brinkley. In the present paper, therefore, it seems appropriate to review and update some of the basic assumptions inherent in the use of this model, and to indicate possibly fruitful ways of improving it.

#### Statistical Variability in Vertebral Fracture

We cannot expect that all ejectees will suffer the same consequences of seat acceleration. In the case of injury defined as vertebral fracture, we must expect that some ejectees will be injured and some will not, and define the probability of injury as

$$P.I. = \frac{\text{Number of ejectees sustaining a vertebral fracture}}{\text{Total number of ejectees}}$$

The causes of this variability are as follows:

- (a) Variability in the acceleration-time history of the catapult/rocket-catapult.

---

\* in Lovelace, et al. [24]

- (b) Variability in the stiffness and bottoming depth of the resiliency transmitting the acceleration to the pelvic girdle; primarily variability in the cushion and in the size and tone of the crew members' buttocks.
- (c) Variability in the pre-loading of the transmitting resiliency, such as the difference between ejection initiation at 1g or -1g, or the degree of lap belt tension.
- (d) Variation in the seat occupants posture and restraint system support.
- (e) Variation in the amount of arm weight which is supported by the shoulders, and hence transmitted through the spine.
- (f) Variability in the dynamic response of the crew member to the input acceleration, because of variations in stiffness and damping.
- (g) Variability in the weight of the crew member's head and torso.
- (h) Variability in the strength of the vertebrae in the ejectee's spine.

In this section we are concerned only with items (g) and (h); the strength of the spine and the load which it has to support.

Let us first look at the population of likely ejectees, based on Hertzberg and Daniels [16] (1954) for the Air Force, and Gifford, Provost and Lazo [13] (1965) for the Navy.

#### Height and Weight

As indicated in Figure 6, the height distribution is normal (Gaussian) and the total range of variation rather small, as might be expected. The normal distributions given by the authors of these two reports do not give a particularly good fit to the weight data, however, as indicated in Figures 7 and 8. Instead the Gamma distribution seems to give the best fit, i. e.,

$$p(x) = \frac{x^{\alpha} e^{-x/\beta}}{\beta^{\alpha+1} \Gamma(\alpha+1)}$$

where  $\alpha$  and  $\beta$  are parameters with  $\alpha > -1$ , and  $\beta > 0$  the properties of this distribution are given by

$$\begin{aligned} \text{Mean} & \quad \mu = \beta (\alpha + 1) \\ \text{Variance} & \quad \sigma^2 = \beta^2 (\alpha + 1) \\ \text{Standard Deviation} & \quad \sigma = \beta \sqrt{\alpha + 1} \end{aligned}$$

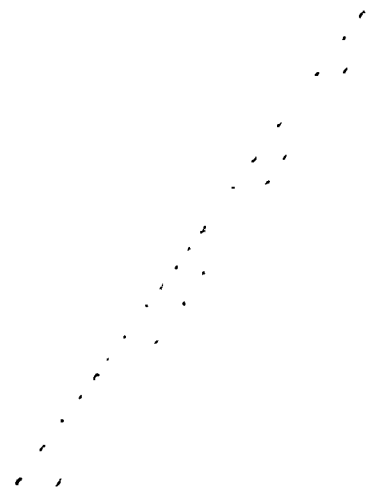
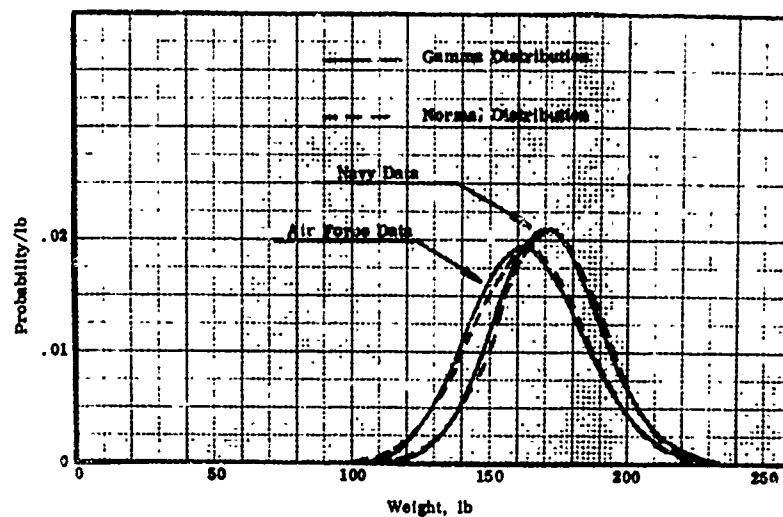
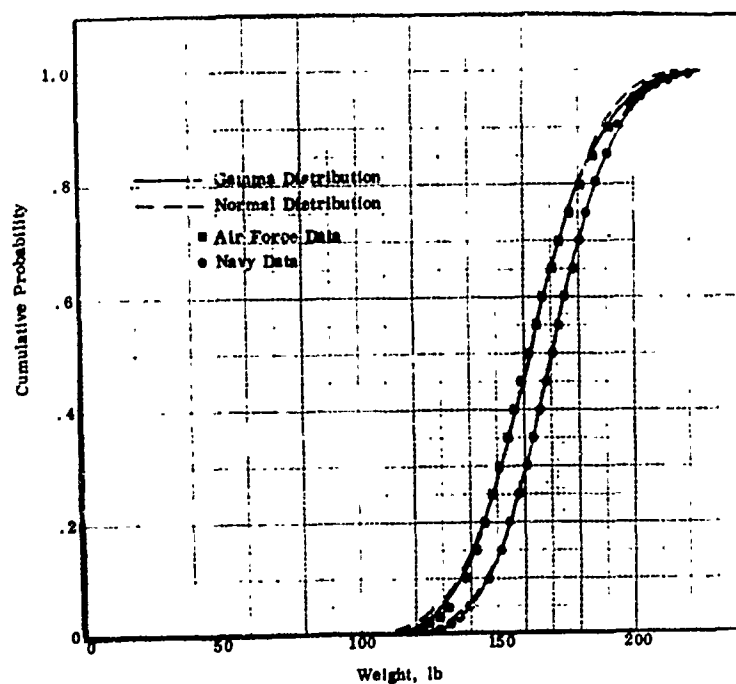


Figure 6. Height Distribution for Air Force [16] and Navy [13]  
Flight Crew Personnel



Data:	Air Force [16]	Navy [13]
Number of Data Points:	4052	1549
Mean ( $\mu$ ):	163.66 lb	171.4 lb
Std. Dev. ( $\sigma$ ):	20.86 lb	19.09 lb
$\alpha$ :	60.554	79.614
$\beta$ :	2.659	2.126

Figure 7. Weight Density Distribution of Air Force and Navy Air Crew



Data:	Air Force [16]	Navy [13]
Number of Data Points:	4052	1549
Mean ( $\mu$ ):	163.66 lb	171.4 lb
Std. Dev. ( $\sigma$ ):	20.86 lb	19.09 lb
$\alpha$ :	60.554	79.614
$\beta$ :	2.659	2.126

Figure 8. Weight Distribution of Air Force and Navy Air Crew

(We shall find that the Gamma distribution applies to much of the biological size and strength data analyzed in the paper; perhaps the statisticians can supply a reason as to why this should be so.)

There is, of course, a connection between the height and weight distributions, and it would be very useful to know the weight deviation from the mean at a given height.

#### Vertebral Size, Strength and Stiffness

The variation in vertebral size is clearly of interest in connection with the variation of strength. Perey [33] reports end-plate areas for 185 lumbar vertebrae.

The first step is to determine if there is any systematic change in area along the spine. The mean areas for each vertebra were found to be as follows:

Vertebra	L-1	L-2	L-3	L-4	L-5
Mean area	14.88	16.30	17.01	17.85	18.19 cm <sup>2</sup>

Since there is clearly a systematic variation, all areas were normalized to L-5 on the basis of these mean values. As shown in Figures 9 to 11, the resulting data is better described by a Gamma distribution than a normal one.

For vertebral breaking strength we have two main sources of data, Geertz and Perey. Bell, Dunbar, and Beck [3] also measured failing strength of 63 vertebral bodies, and their measurements were perhaps the most careful ever carried out, but unfortunately they only report their results in terms of stress and strain, so that the basic information is not recoverable. (This unfortunate procedure was also used in reference 46, and seems to be the beginning of a trend.)

The basic Perey failing strength data is presented in Figures 12 to 15. At first sight the cloud of data points in Figure 12 might appear discouraging, particularly to the engineer! However, as will be shown later, the "over age 60" data points must be eliminated because they are definitely lower than the rest of the data. Secondly, we note that the mean strength varies along the lumbar spine, and we use this fact to normalize the data to L-5. The normalized strength and stiffness data then give the distributions shown in Figures 13 to 15.

Because Perey did not attempt to "true-up" his vertebrae, except for partially removing the posterior spines, the stresses induced by the jaws of the testing machine must have been much larger than those for pure compression at the same load. This would have the effect of reducing the load at which failure occurred and also reducing the apparent stiffness. (Perey also notes that his

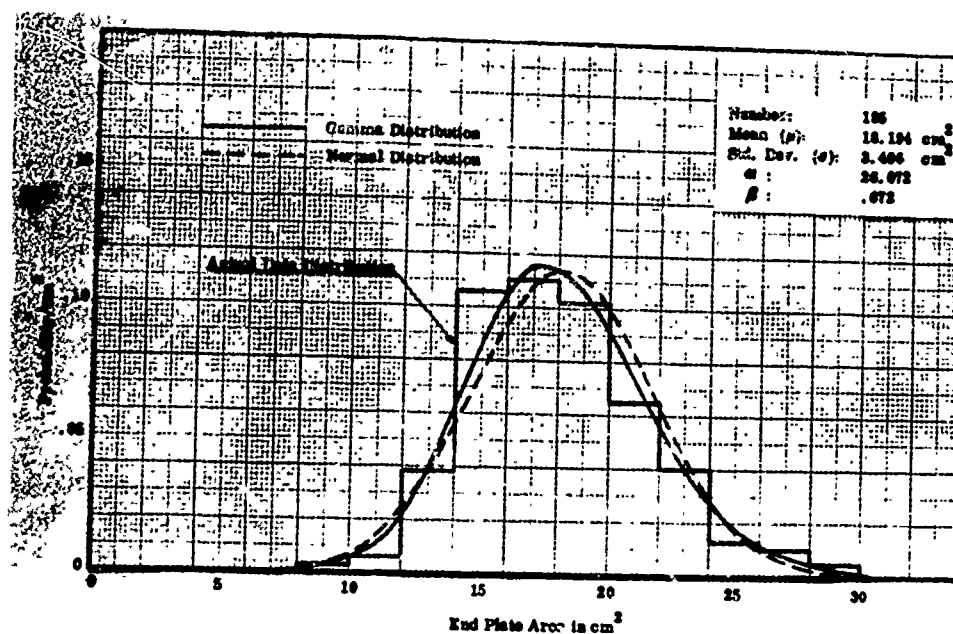


Figure 9. Vertebral Cross Sectional Area Normalized to L-5, from Perey [33]

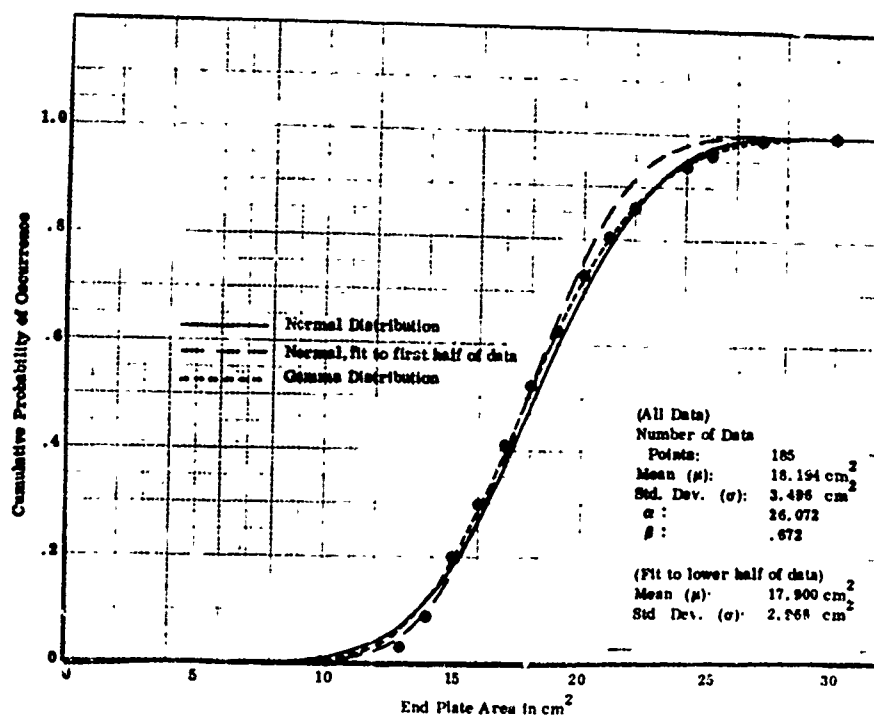


Figure 10. Vertebral Cross Sectional Area Normalized to L-5, from Perey [33]



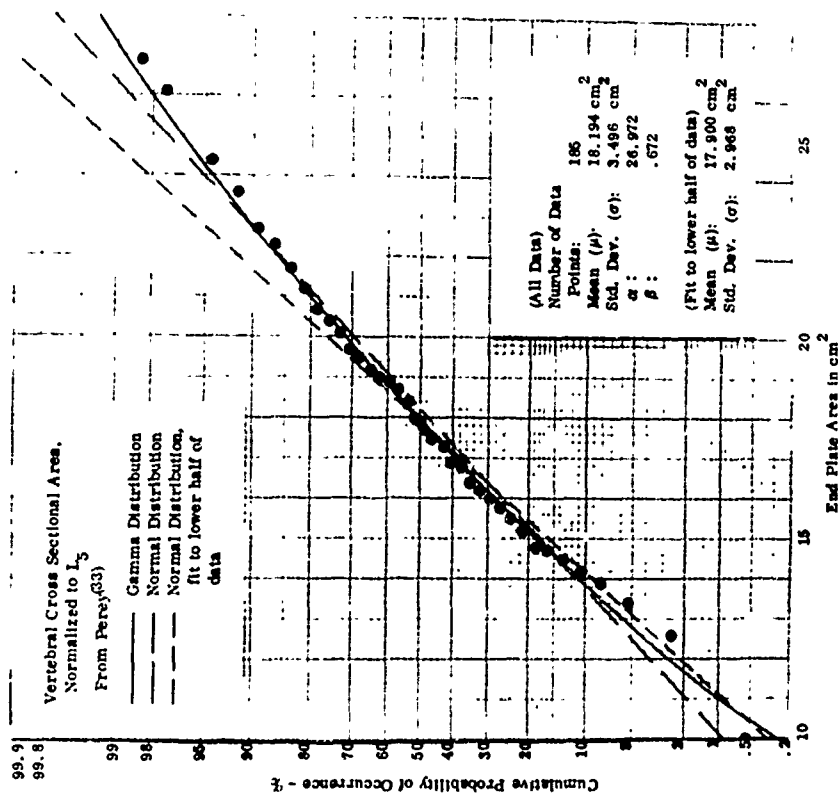


Figure 11. Vertebral Cross Sectional Area Normalized to L-5, from Perey [33]

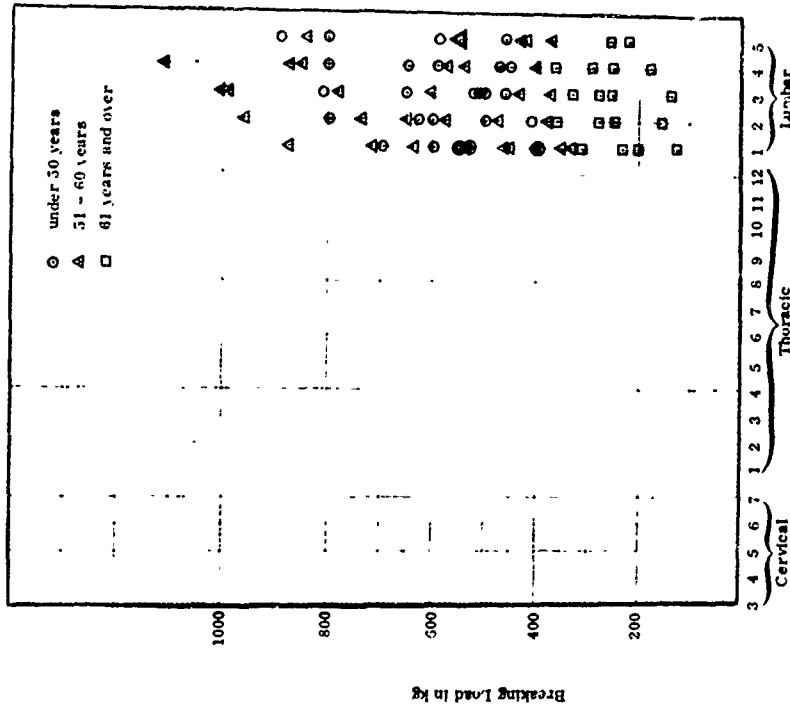


Figure 12. Perey's Measurements of the Strength of Single Vertebral Bodies [33]

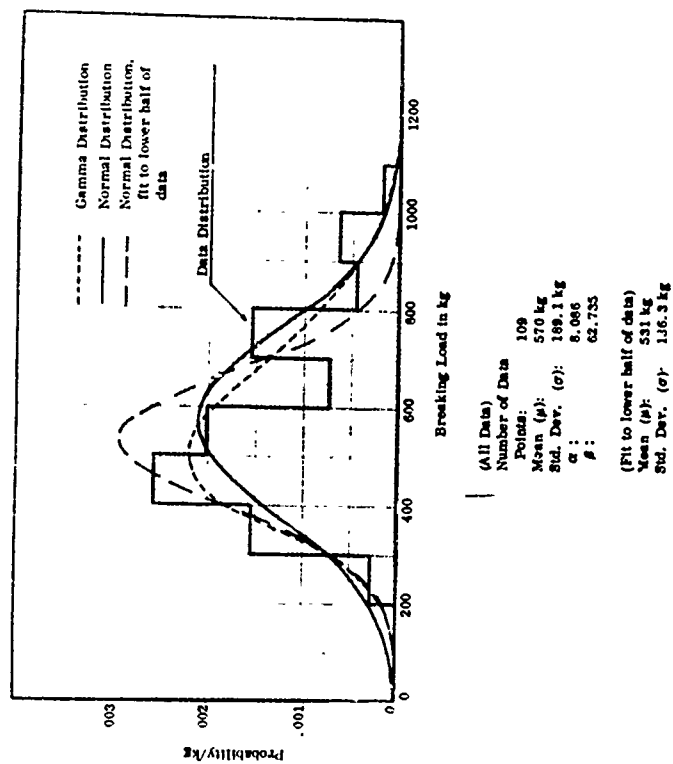


Figure 13. Vertebral Failing Load Normalized to L-5. Age less than 60 Years from Perey [33]

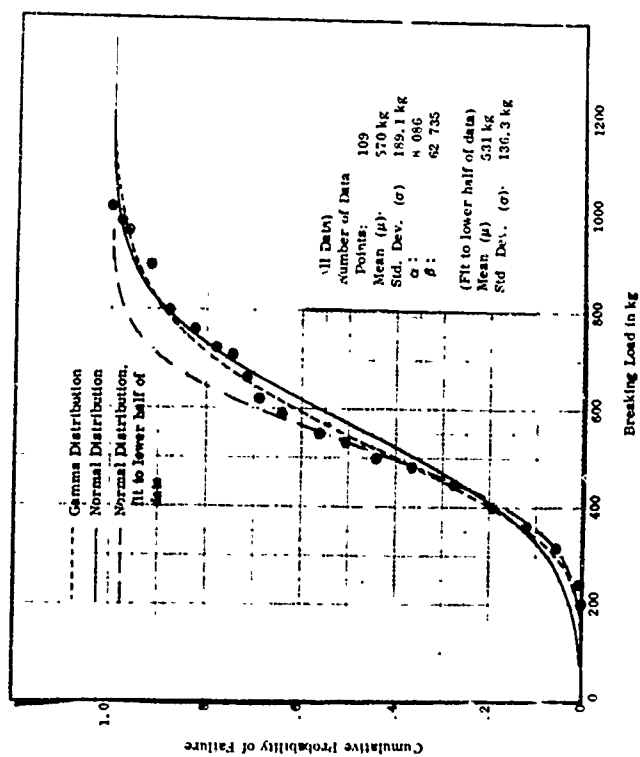


Figure 14. Vertebral Failing Load Normalized to L-5. Age less than 60 Years from Perey [33]

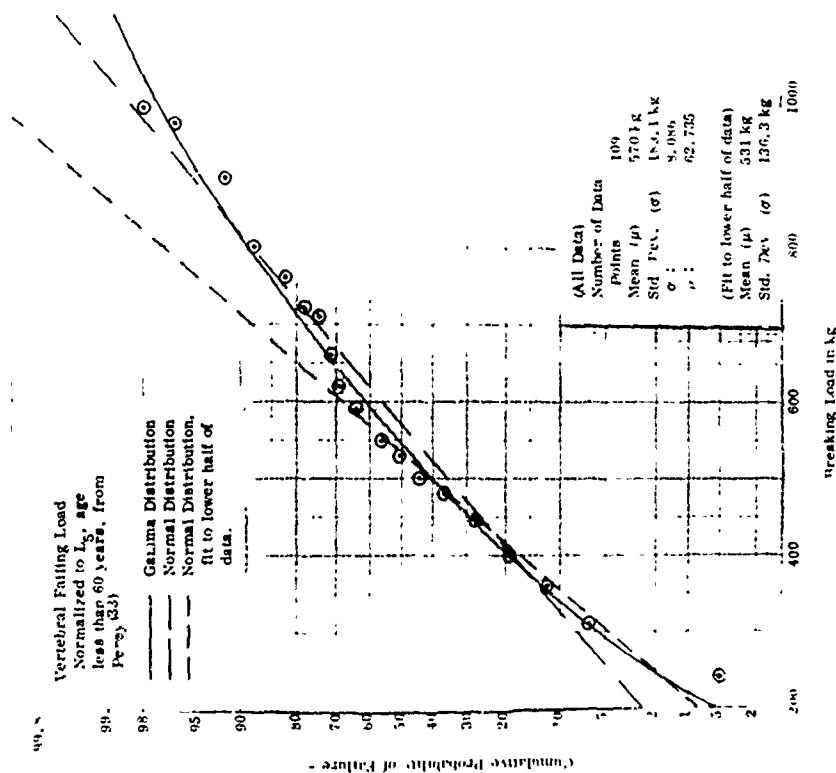


Figure 15. Vertebral Failing Load Normalized to L-5. Age less than 60 Years from Perey [33]

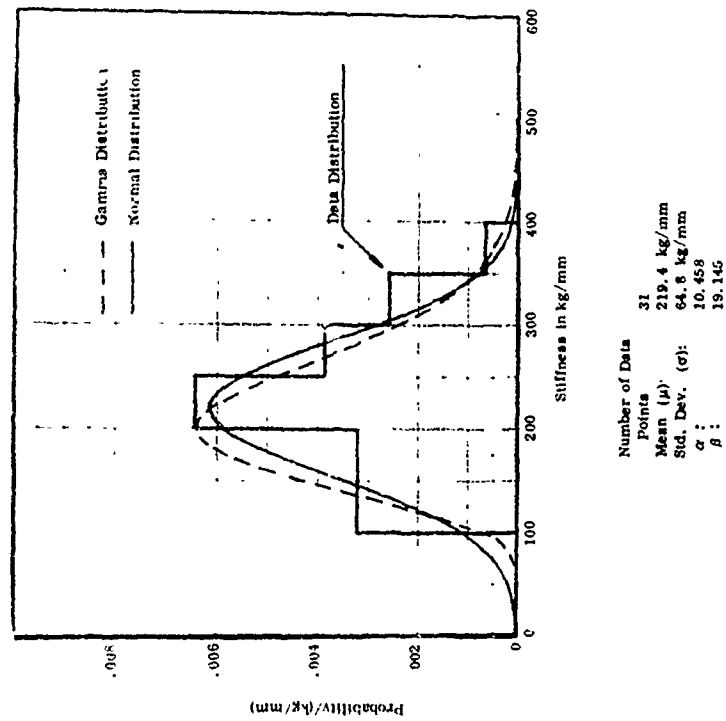


Figure 16. Vertebral Stiffness from Perey [33] Age less than 51 Years

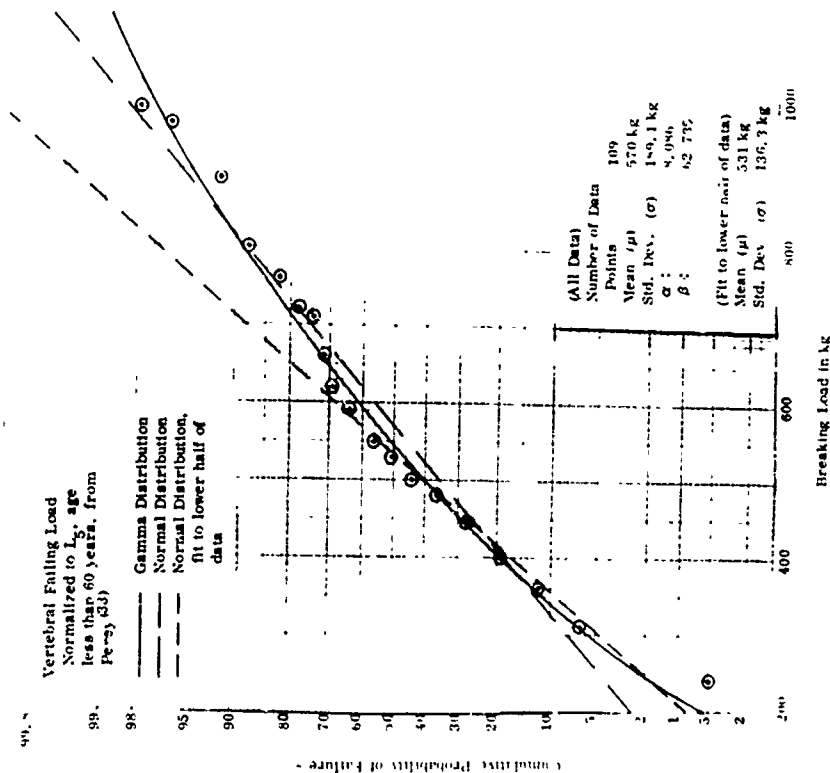


Figure 15. Vertebral Failing Load Normalized to L-5.  
Age less than 60 Years from Perey [33]

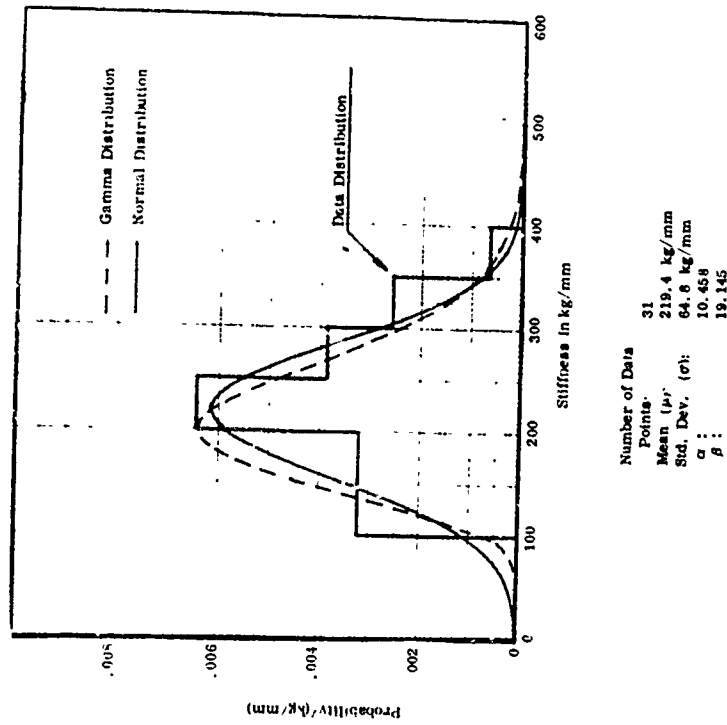


Figure 16. Vertebral Stiffness from Perey [33]  
Age less than 51 Years

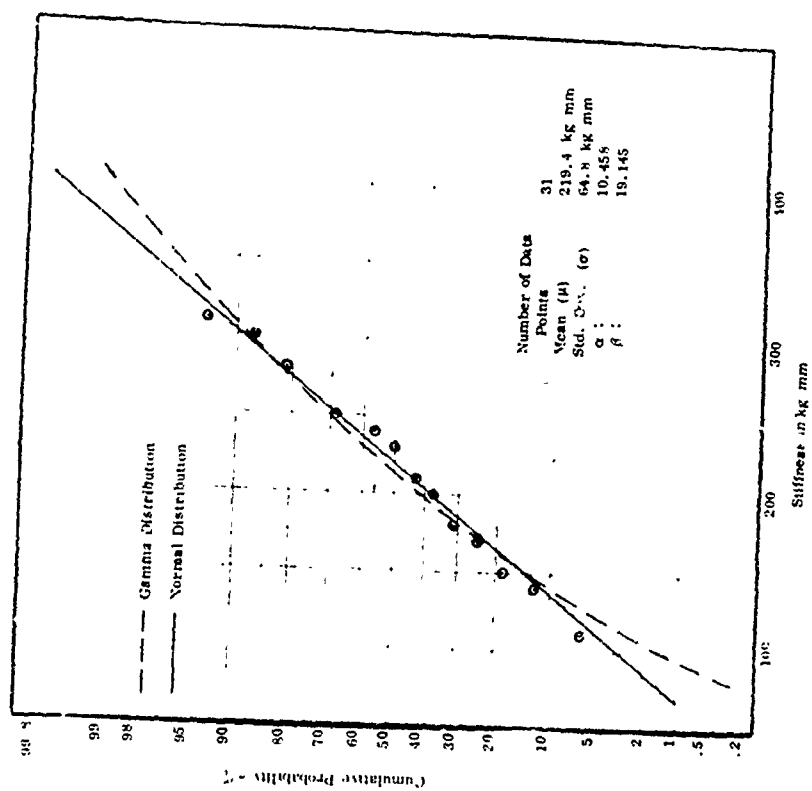


Figure 17. Vertebral Stiffness from Perey [33]  
Age less than 51 Years

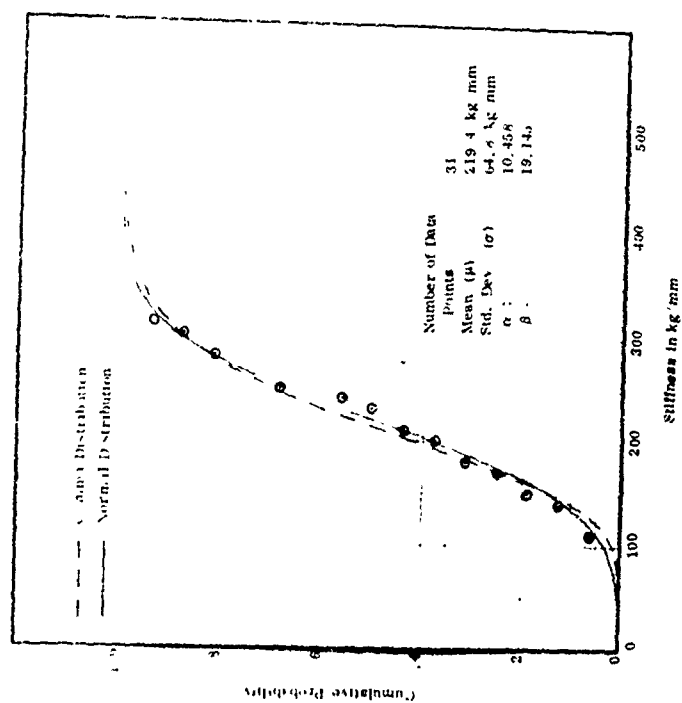


Figure 18. Vertebral Stiffness from Perey [33]  
Age less than 51 Years

force deflection curves were always nonlinear to start with, and often through the range to failure, which directly contradicts the findings of other investigators using bone alone. \*) Thus, the Perey strength and stiffness data is of general interest, but not of much quantitative value.

The Geertz strength data is given in Figures 19 to 22 and is listed in Table 2. These results are obtained by first plotting breaking strength for each test as a function of position along the spine, as in Figure 19. A least mean square regression analysis is then used to determine the best fit line, which in this case turns out to be linear. (Since some vertebrae have more test points than others, such a procedure is more accurate than a best fit to the means for each vertebra.) This mean line is then used to normalize all the data to L-5 in Table 3.

Geertz protected the vertebra under test by an intervertebral disc and part of the adjacent vertebra on either side, the latter being chambered to ensure pure compression. Three data points obtained by Crocker and Higgins [8] (T-8, T-12, and L-1) are included in this analysis, an additional test where L-5 failed at 270 kg being rejected. Also included are two points (T-12, L-1) ascribed to Nachemson [27] by Crocker and Higgins, although we have not so far been successful in tracing down the original reference. Other data is undoubtedly available, but has unfortunately not been reported in suitable form. Typical references are the paper by Bell, Dunbar, and Beck and Reference 41, both of which report values in terms of "stress" (on a nominal end-plate area) and strain, without giving the dimensions used.

#### The Effect of Age on Strength and Stiffness

Stech and Payne [39] (1964) reported Stech's analysis of Perey's data, which showed a linear decrease of both stiffness and strength with increasing age. Considering that Perey identified only the age groups "up to 50," "50 - 60," and "over 60," the identification of such a variation could not be expected to have much precision. Additionally, as noted earlier, Perey's static testing techniques were so poor that it now seems dangerous to place much reliance upon any conclusions derived from his data. Hence it was decided to see if a more precise analysis was possible.

As a first step, the breaking load data of Geertz, and Crocker and Higgins, (Tables 2 and 3) embracing ages 19 to 46 years, was plotted against age, after normalizing to L-5, as described earlier. It was found that the mean breaking strength was not influenced by age at all, or if there was a discernible trend, it indicated a slight increase of strength with age! The raw Perey data, shown in Figure 23 indicated the same result. On the other hand, the much earlier work of Messerer (1880) (Table 1, shown in Figure 24)

---

\* For example, see Bell, Dunbar; and Beck [3]

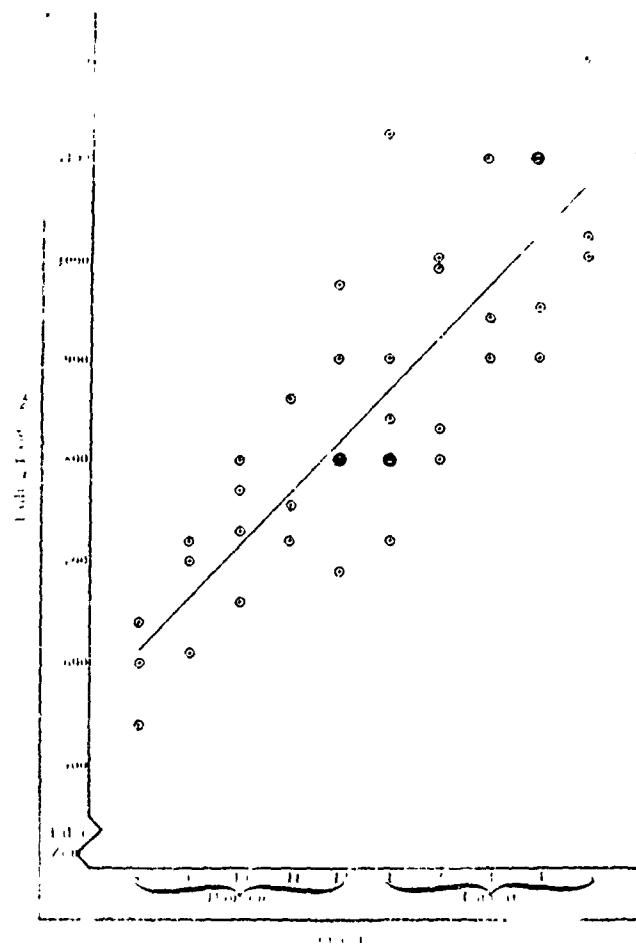


Figure 19. Vertebral Failing Load from Geertz [12], Crocker & Higgins [8], and Nachemson

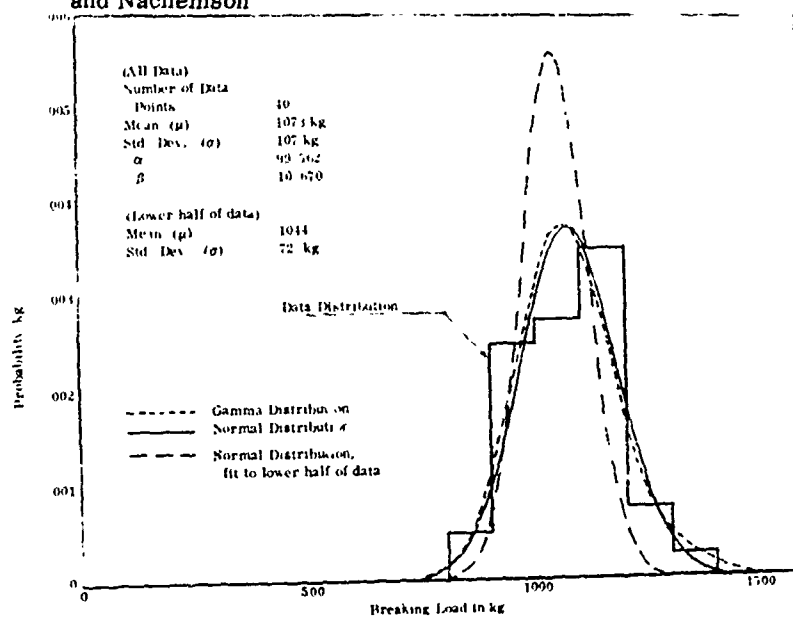


Figure 20. Vertebral Failing Load, Normalized to L-5 from Geertz [12], Crocker & Higgins[8], and Nachemson

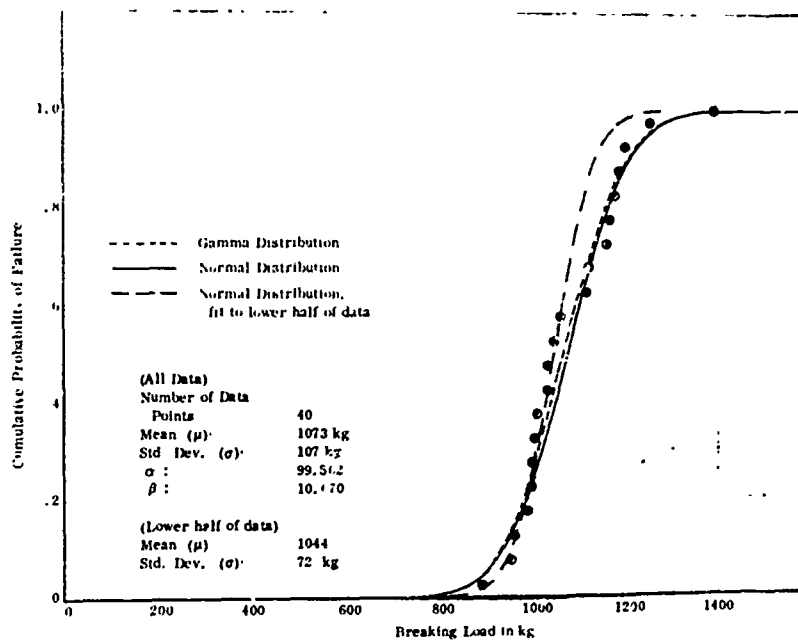


Figure 21. Vertebral Failing Load, Normalized to L-5 from Geertz [12], Crocker & Higgins [8], and Nachemson

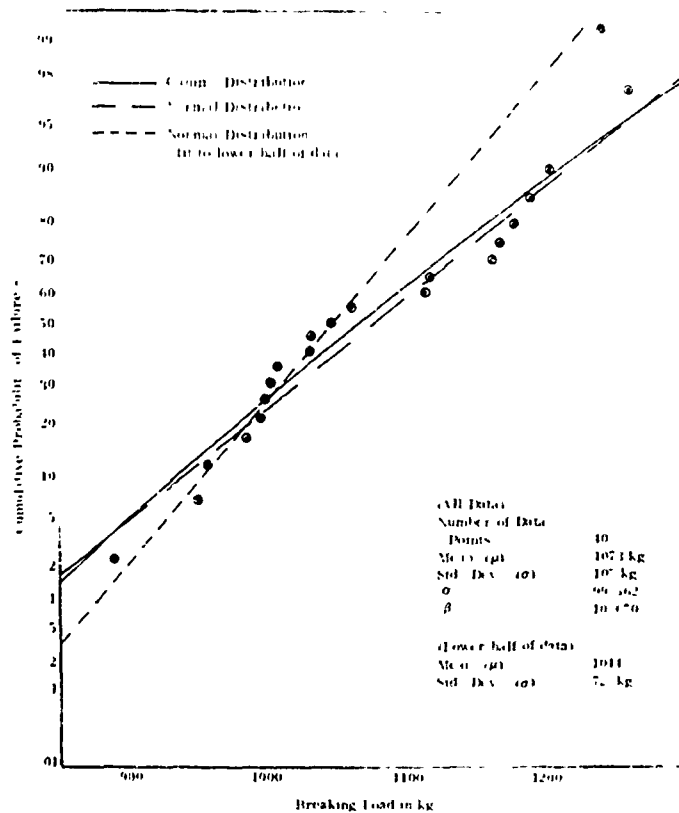


Figure 22. Vertebral Failing Load, Normalized to L-5. From Geertz [12], Crocker & Higgins [8], and Nachemson



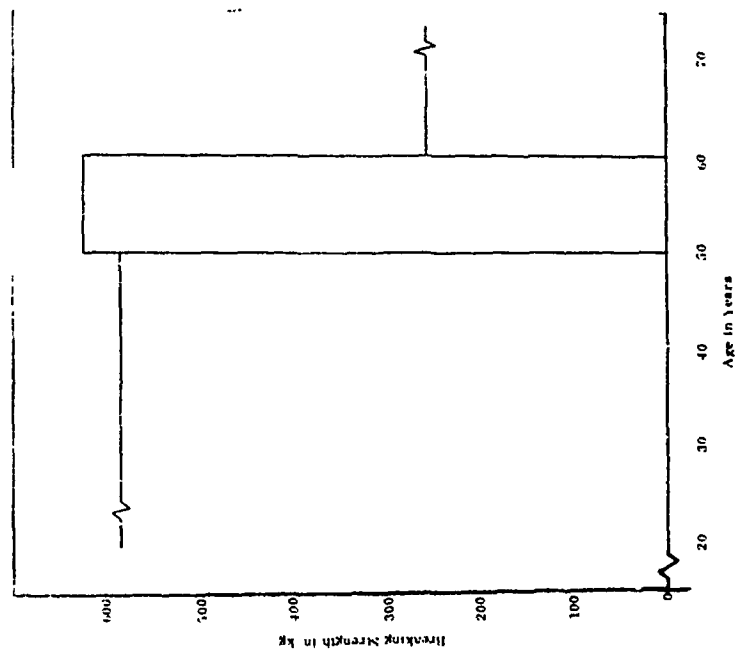


Figure 23. The Effect of Age on Static Vertebral Body Strength, According to Perey [33]

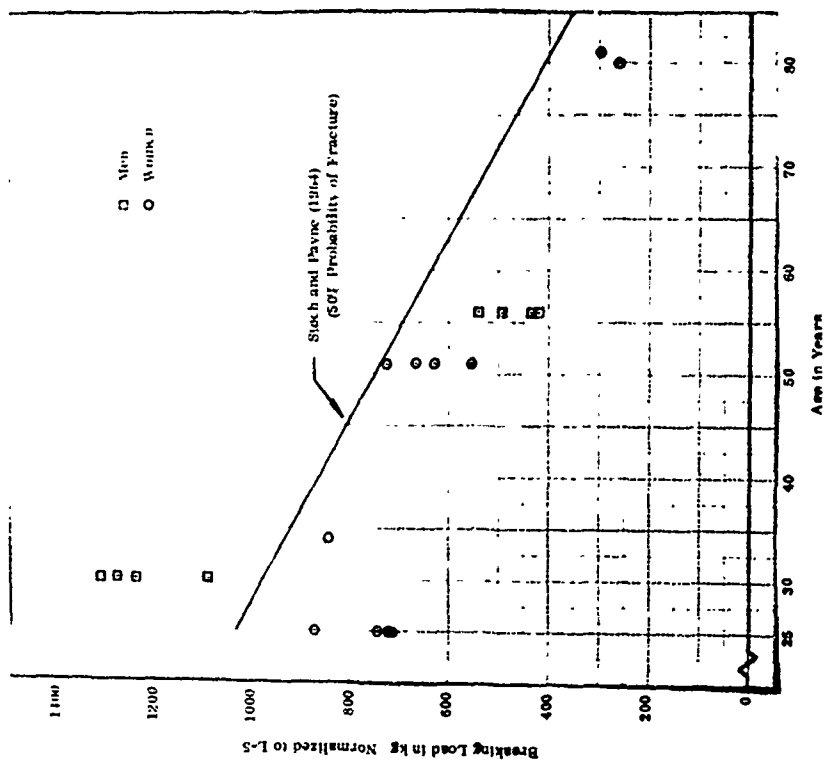


Figure 24. Effect of Age on Vertebral Breaking Strength, From the Data of Messerer [26] (1880)

TABLE 2  
BREAKING LOAD DATA

Age (years)	Breaking load in Kg									
	T-8	T-9	T-10	T-11	T-12	L-1	L-2	L-3	L-4	L-5
<u>Geertz Data [12]</u>										
19				750		720		900		
21	640		800		900		990			1020
21				720	690	840				
23	540	610								
33			660		800		800		1100	
36	600	720	770							
38					800		830		900	
43		700		860		900		940		1000
44			730			800			950	
46				755		800		1100		1200
<u>Crocker and Higgins Data [8]</u>										
40					974	1125				
47	536									

TABLE 3

## BREAKING STRENGTH DATA NORMALIZED TO L-5

Age (years)	Factor	Normalized Breaking Load in Kg									
		T-8	T-9	T-10	T-11	T-12	L-1	L-2	L-3	L-4	L-5
		.570	.619	.666	.713	.760	.809	.856	.904	.952	1.0
<u>Geertz Data [12]</u>											
19					1052		890		995		
21		1123		1200		1183		1157			1020
21					1010	909	1038				
23		948	985								
33				990		1053		935		1157	
36		1052	1163	1157							
38						1053		970		945	
43			1132		1205		1110		1040		1000
44				1097			988			997	
46					1058		988		1218		1200
<u>Crocker and Higgins Data [8]</u>											
40						1280	1390				
46		940									

makes one suspect a decrease in strength after about age 40, although his data points are so few that there is clearly a question as to whether such a trend is statistically significant. Additionally, there is some evidence of a reduction in vertebral bone density above about age 45. To illustrate this, the raw data of Trotter, Broman, and Peterson [42] is plotted in Figures 25 and 26 for thoracic and lumbar vertebrae. The trend is clearly toward decreased density with increasing age, at least after early middle age. It seems clear that a reduction in bone density would imply a reduction in mechanical properties.

To resolve these questions, we appeal to the data of Bell, Dunbar, and Beck, although one has to perform a few conjuring tricks because the results are presented in the form of stress and strain. The authors state that the end-plate area of their L-4 and L-5 specimens varies in the range 1.8 in<sup>2</sup> to 3.76 in<sup>2</sup>, from which one might guess the mean to be near 2.77 in<sup>2</sup>. The Perey area data (Figures 9 through 11) gives a normalized L-5 mean of 18.2 cm<sup>2</sup> = 2.82 in<sup>2</sup>, so that the figure of 2.77 in<sup>2</sup> is probably about right for tests equally divided between L-5 and L-4. This average area can then be used to convert stress to load.

Applying the same (very loose) procedure to the quoted volume range of between 32.0 and 73.5 ml, we arrive, in conjunction with the mean area of 2.77 in<sup>2</sup>, at an estimated mean height of 1.16 in, so that the quoted strains can be converted to compressive deflections.

The failing stresses reported by Bell et al are plotted against age in Figure 27. If A is age in years, and  $f_{\max}$  the breaking stress\*, then the mean line

$$f_{\max} = 2269.5 e^{-.02239A} \quad (\text{lb/in}^2)$$

gives a least squares best fit with a correlation coefficient of 0.41. (The straight line shown in Figure 27 has a coefficient of 0.36.)

When these results are multiplied by the mean area of 2.77 in<sup>2</sup>, we obtain the breaking load variation shown in Figure 28. This line seems to be quite compatible with the average of the Geertz et al data, since the latter is probably not statistically significant, in terms of a trend with age, above about age 35, while the Bell et al data, by itself, is not significant below about age 50. In conjunction, the two sets of data make a convincing argument for breaking load being independent of age up to 42.5 years, and then decreasing exponentially above that.

---

\* Bell et al state that all samples followed Hooke's law up to about three quarters of the breaking load, and that no nonlinearity was observed at low loads.

Reproduced from  
best available copy.

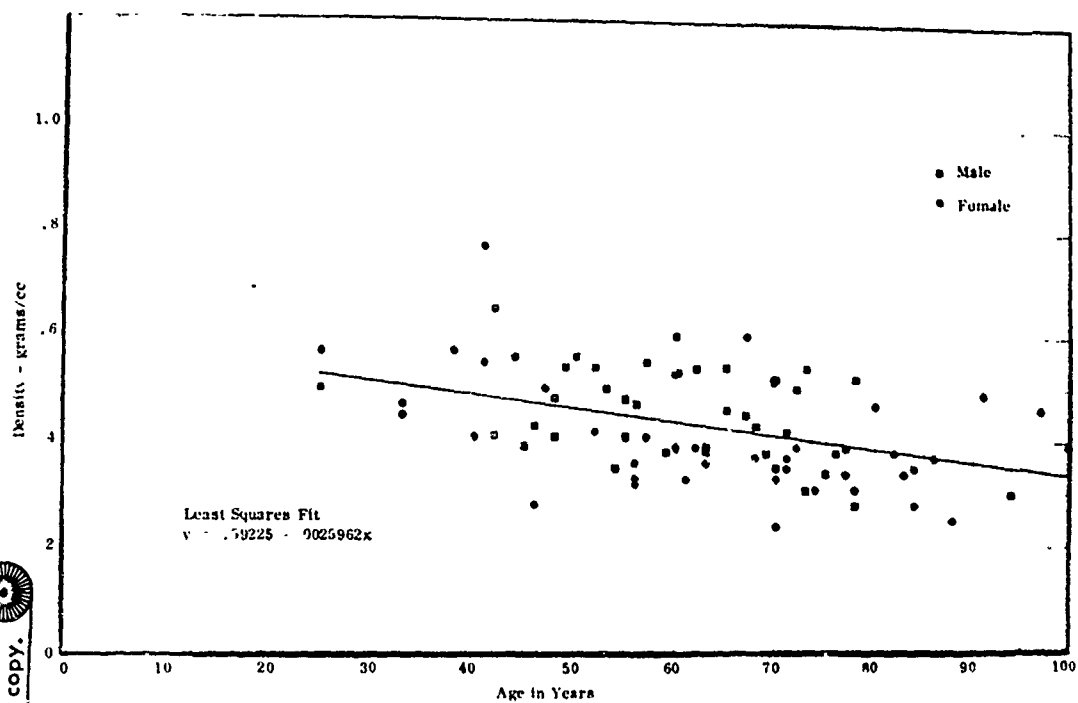


Figure 25. Thoracic Vertebra Density [42]

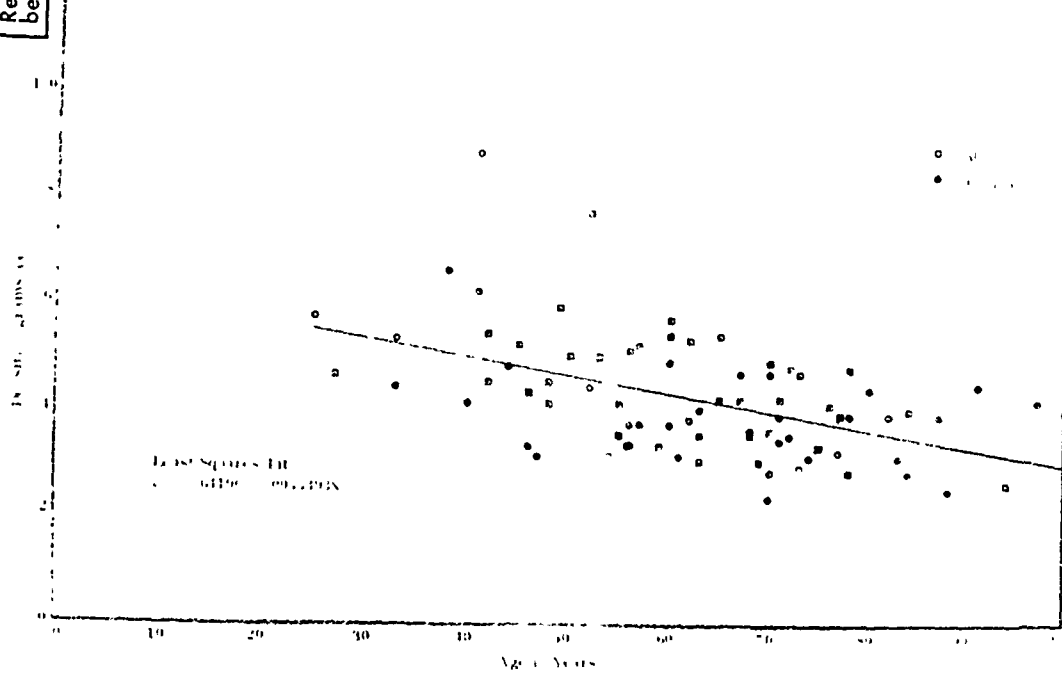


Figure 26. Lumbar Vertebra Density [42]

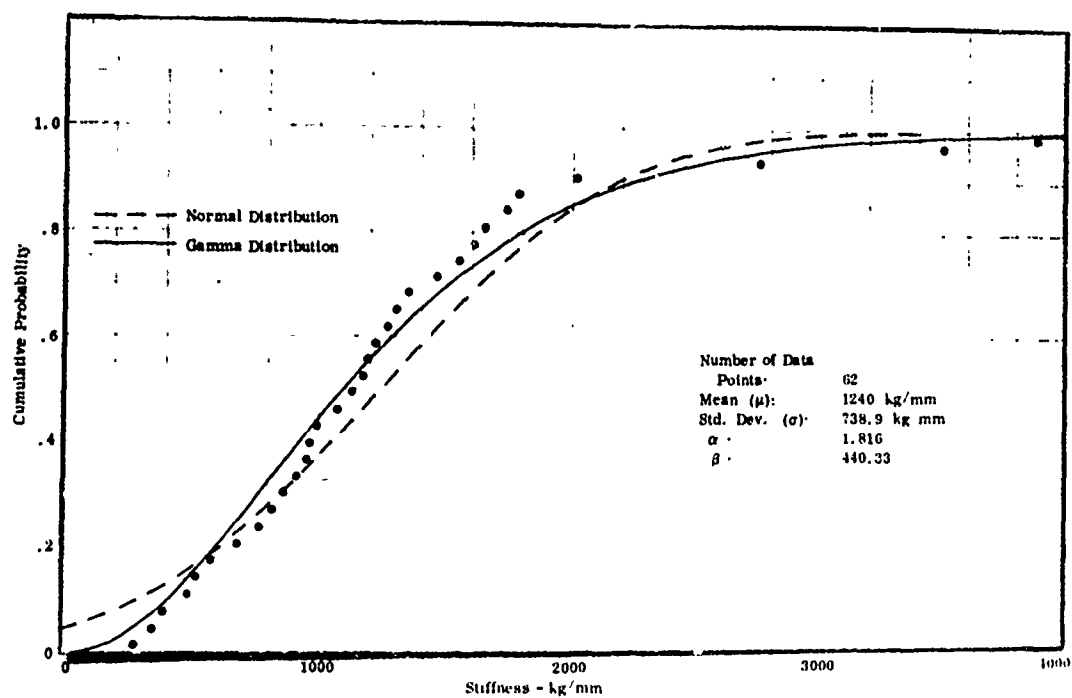


Figure 31. Vertebral Stiffness, Normalized to Age 42.5, From Bell, Dunbar, and Beck [3]

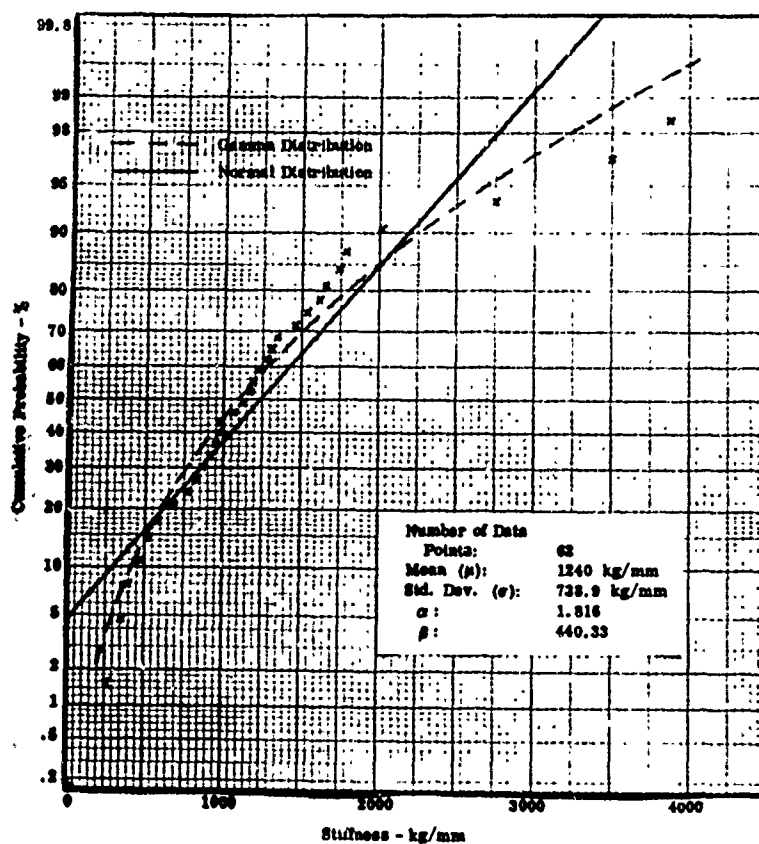


Figure 32. Vertebral Stiffness, Normalized to Age 42.5, from Bell, Dunbar, and Beck [3]

It is intellectually satisfying to get away from the concept of a linear decrease in mechanical properties with age, partly because nearly all life processes are inherently exponential, and partly because Stech's figure of zero strength at 117 years (refined to 107 years in the present analysis) reminds some of us too strongly of our inevitable end. The maintenance of our youthful bone strength to middle age is also in better accord with subjective clinical and postmortem examinations, with what we see at ski resorts, and with what we would like to believe.

One can hypothesize that the decrease in the physical properties of bone starts when one is no longer "physically fit," and that the critical age of 42.5 years may be substantially higher for aircrew members. None of the Bell et al subjects were fit at the time of their death, so that there may be an inherent bias to low properties in the data.

Whether this is so or not, it seems clear that, as a practical matter, we may neglect the effect of age when considering the problem of aircrew injury in ejection seats.

Bell et al also present stiffness data from their experiments\*, given in the form of a plot of elastic limit stress against the corresponding strain. The raw data, converted to stiffness as described above, is plotted against age in Figure 29 and the best least mean squares fit is found to be

$$\text{Stiffness} = 2415.0 e^{-.02005A} \text{ (Kg/mm)}$$

Using this relationship to normalize the data to age 42.5 years, we obtain the stiffness distribution shown in Figures 30 to 32, and the failing load distribution of Figures 33 to 35. It is of great interest to note that the mean strength value is 1242 kg, against 1073 kg for the Geertz data, even though the standard deviation is much larger. The indirect method of analysis may be part of the reason for the greater scatter, but once again we should remember that the Bell et al subjects were not fit, and that we might expect to find a considerably smaller mean deviation in the case of aircrew members and other "fit" subjects.

The mean stiffness shown by this analysis is 1100 Kg/mm. This is much less than the value of 6000 Kg/mm given by Crocker and Higgins for a "dynamic" test (at an unknown deflection rate), but otherwise seems to agree quite well with the implications of other experimental data.

It is interesting to note that the Bell et al data also confirms quite well Stech's original hypothesis of a linear relationship between failing load and

---

\* That is, stiffness with the end-plate capped, giving higher values than in vivo, because the end-plate cannot deflect.

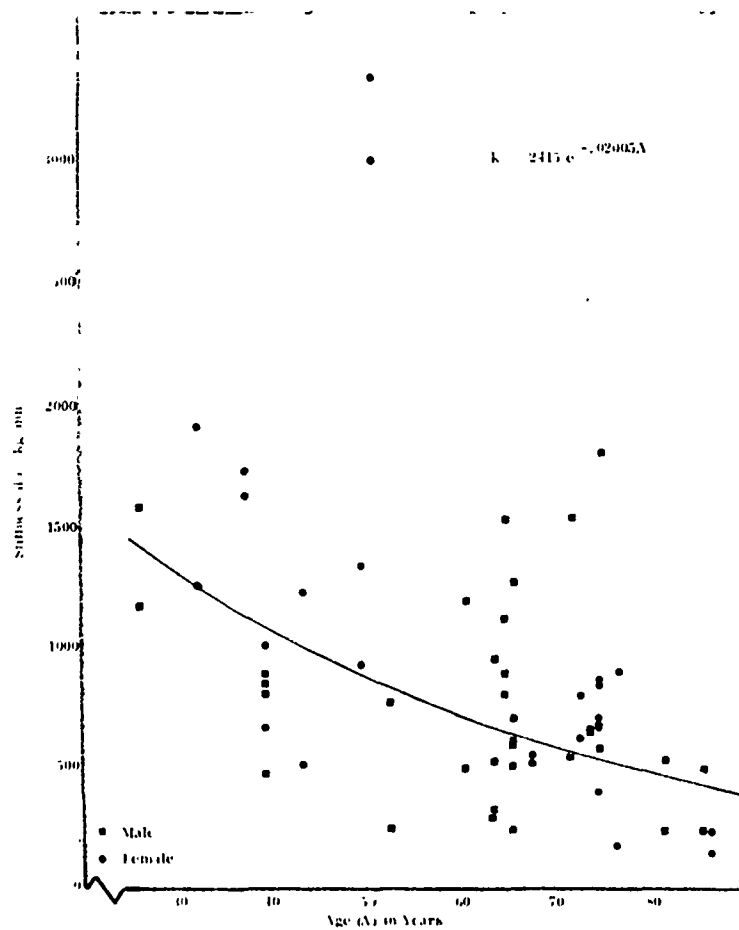


Figure 29. Variation of Vertebral Stiffness with Age, From Bell, Dunbar, and Beck [3]

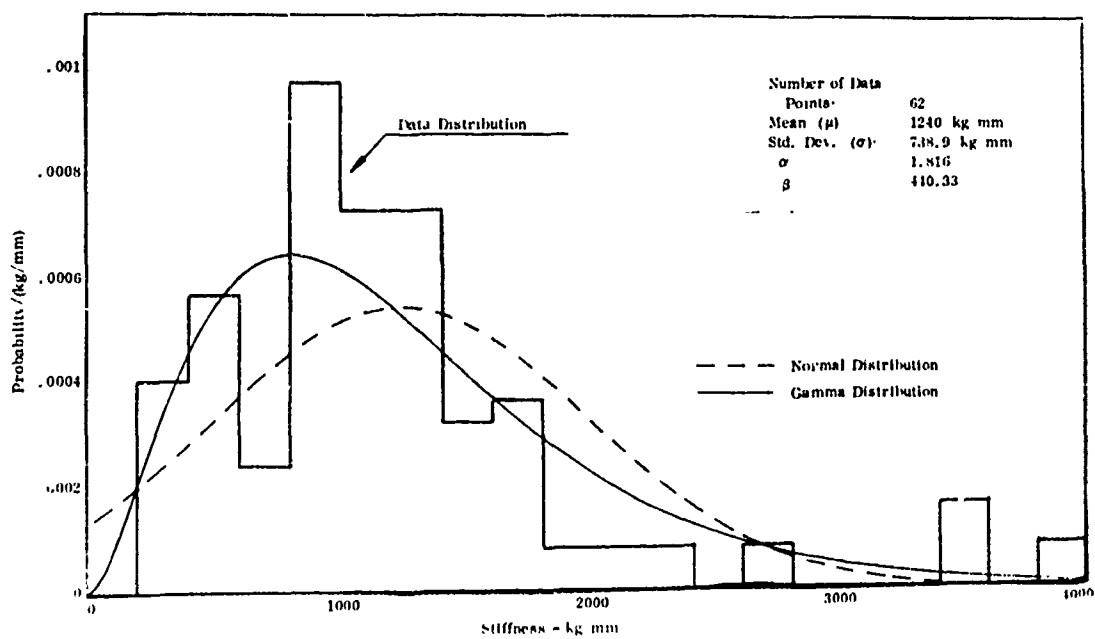


Figure 30. Vertebral Stiffness Normalized to Age 42.5, From Bell, Dunbar, and Beck [3]



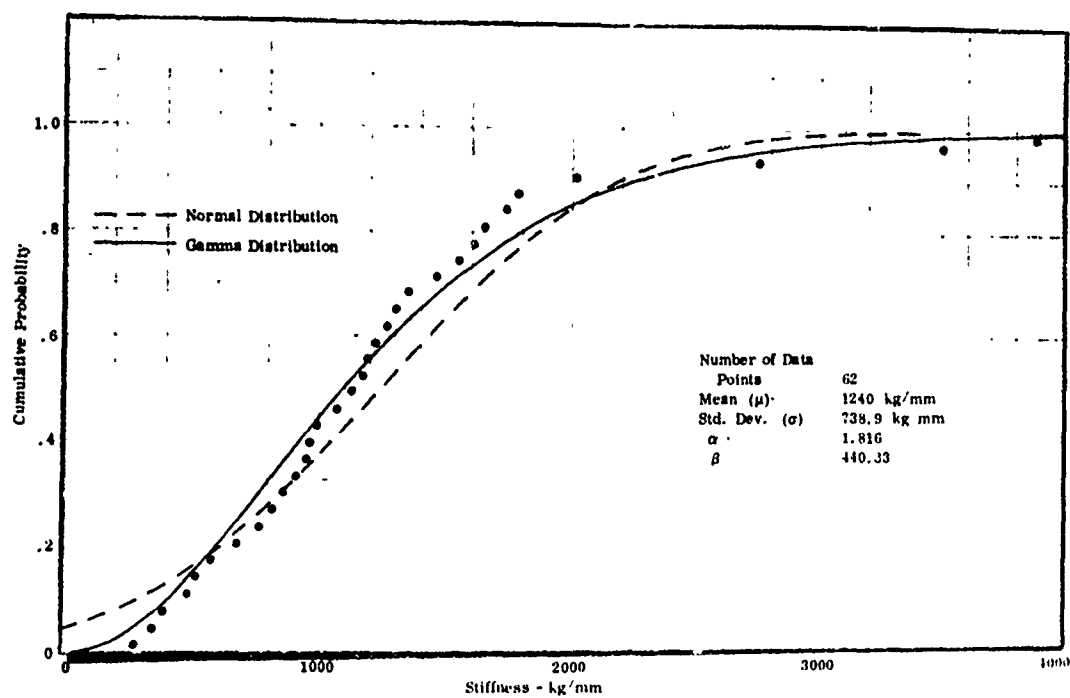


Figure 31. Vertebral Stiffness, Normalized to Age 42.5, From Bell, Dunbar, and Beck [3]

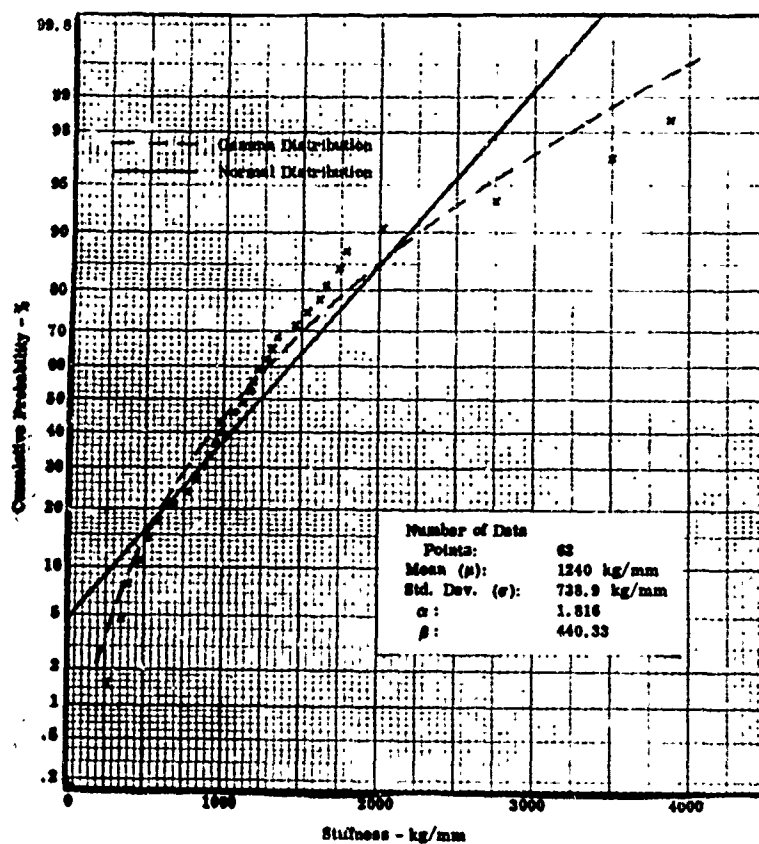


Figure 32. Vertebral Stiffness, Normalized to Age 42.5, from Bell, Dunbar, and Beck [3]

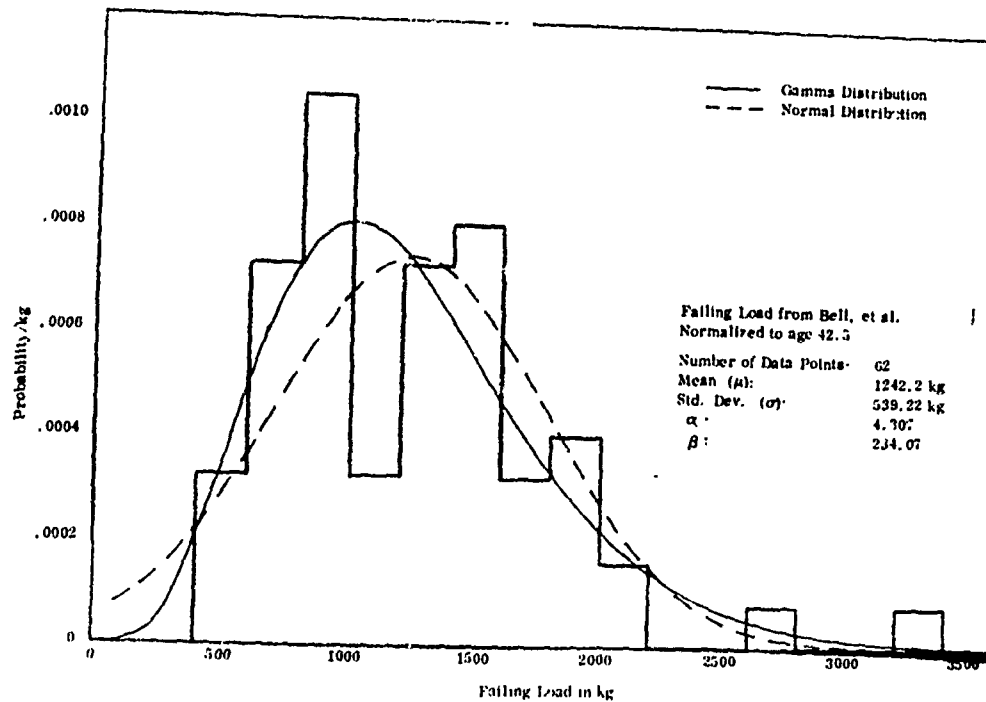


Figure 33. Vertebral Strength, Normalized to Age 42.5, Based on 2.77 in<sup>2</sup> Area, From Bell, et al [3]

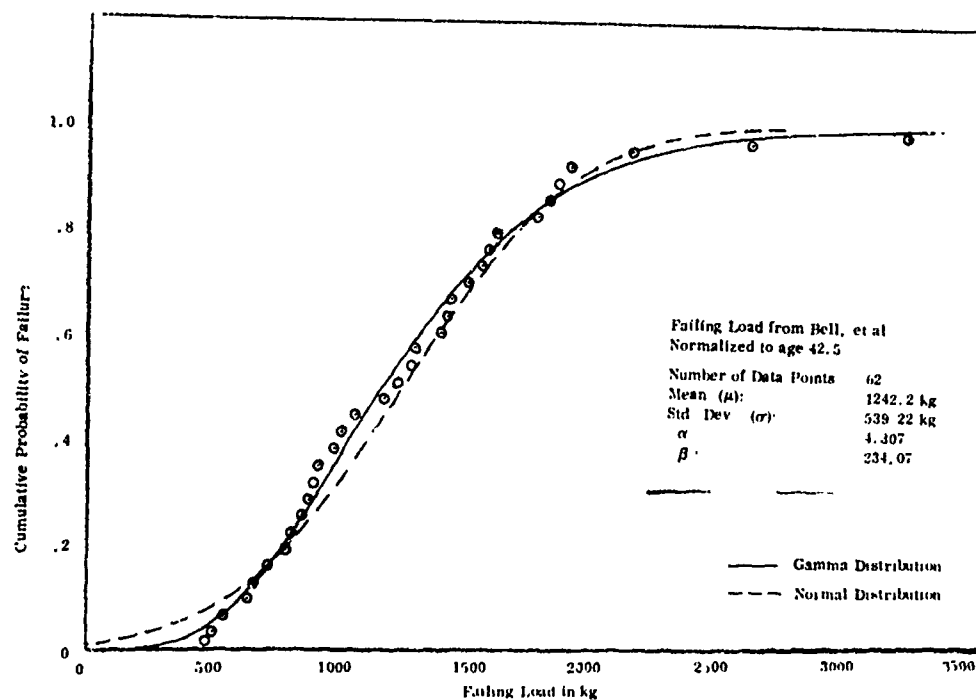


Figure 34. Vertebral Strength, Normalized to Age 42.5, Based on 2.77 in<sup>2</sup> Area, From Bell, et al [3]

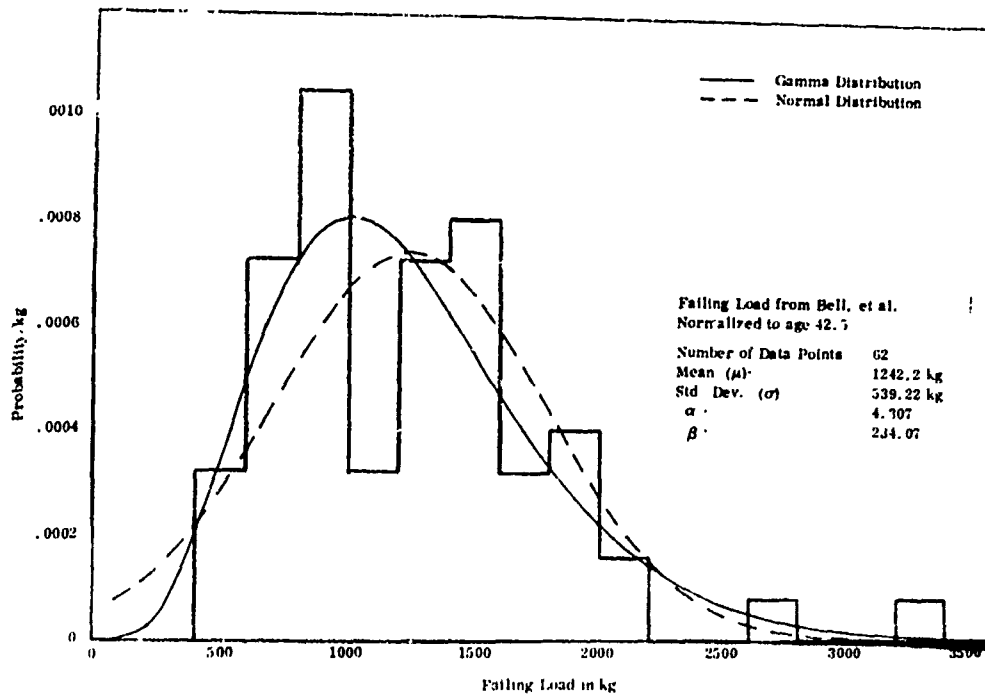


Figure 33. Vertebral Strength, Normalized to Age 42.5, Based on 2.77 in<sup>2</sup> Area, From Bell, et al [3]

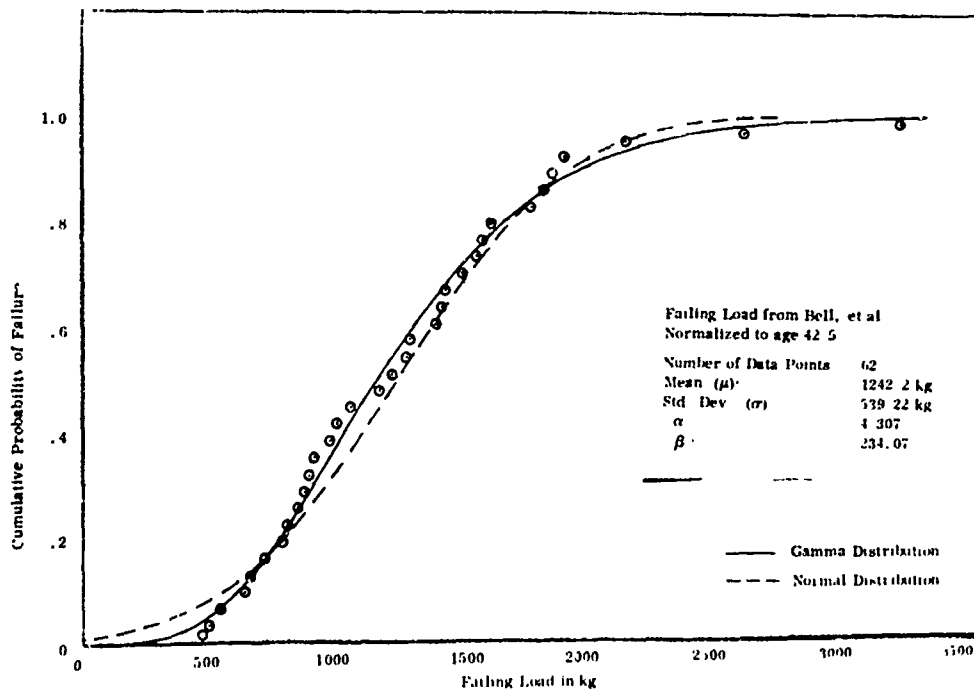


Figure 34. Vertebral Strength, Normalized to Age 42.5, Based on 2.77 in<sup>2</sup> Area, From Bell, et al [3]

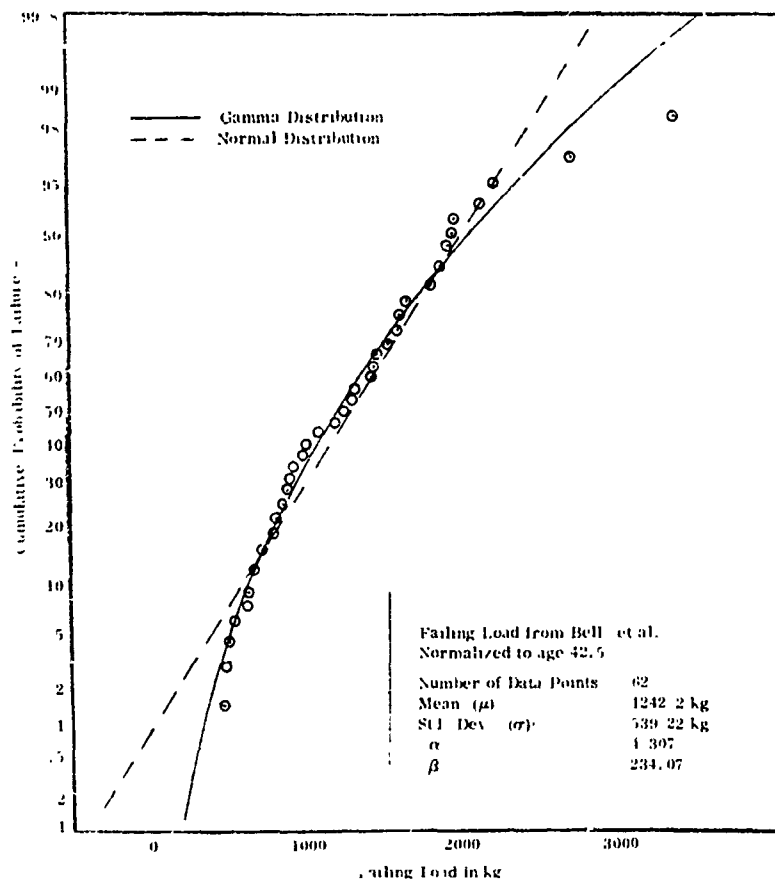


Figure 35. Vertebral Strength, Normalized to Age 42.5  
 Based on 2.77 in<sup>2</sup> Area, from Bell, et al [3]

stiffness\*, (shown in Figure 36), which was based upon the Perey static data. As shown in Figure 37, the slope of load against stiffness derived from the Bell et al data is only half that indicated by the Perey data. The coefficient of correlation is .873 for the line

$$F_{\max} = 167.5 + .7793k \text{ (Kg)}$$

Needless to say, this relationship is expected to be much closer to the truth, in absolute terms.

### The Mechanics of the Spine

In earlier modelling we have been content to treat the spinal column as a spring, without inquiring too deeply into the details of its structure. Stech and Payne [39] (1964) did show that a measurement by Yorra [50] of the stiffness of two vertebrae and a disc, when ratioed up to the rest of the spine, gave a stiffness (T-1 to L-5) which was compatible with the MIL-S-9479A DRI model. However, subsequent work has shown this analysis to be fallacious, in that the entire upper torso mass was assumed to react on T-1 (which is poor physiology) while the static compression measurements of Yorra ought to give a much lower stiffness than is experienced in a dynamic environment, indicating bad dynamics! It is clearly time to examine the available data on the spine more closely.

If one ignores the processes, which are generally assumed to transmit no load, the structure of the spine appears deceptively simple, from a load transmission and deflection point of view. The important part of the spine consists of 17 bony vertebral bodies, roughly cylindrical in shape, with a pancake-shaped disc between each pair. Primarily as a result of the work of Bell et al, we are now free of the misconceptions perpetrated by Perey, and can say that the vertebral body is composed of perfectly normal engineering material (at low strain rates, at least) and obeys Hooke's law up to about 75% of its ultimate load. This is confirmed by the many experiments made with other types of bone samples, by other workers. The only real peculiarity we observe with bone is that both its modulus and breaking strength have been observed to increase substantially with strain rate. (See McElhaney [25], for example.) We also have an upper limit for vertebral stiffness and the associated variability, again based on the work of Bell et al.

One might think that the task of constructing a spinal spring model would be easy, therefore. Alas, this is not so, partly because of the inter-vertebral discs, which together constitute almost one third of the spine's length. The problem is to discover the dynamic properties (stiffness and damping) of these discs.

---

\* This linear relationship seems true for a particular vertebrae, at any age. It cannot be used to determine the stiffness of other vertebrae when their failing load is known, unless the length of the vertebra is also known.

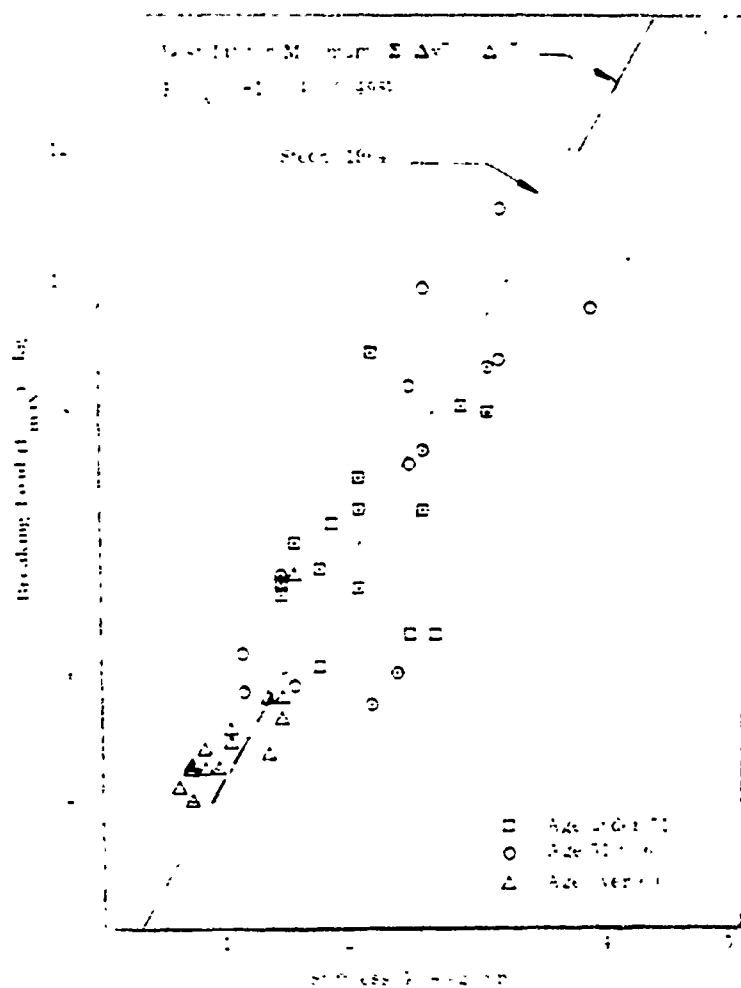


Figure 36. Stech's Relationship Between Vertebral Strength and Stiffness, Based on the Data of Perey [33]

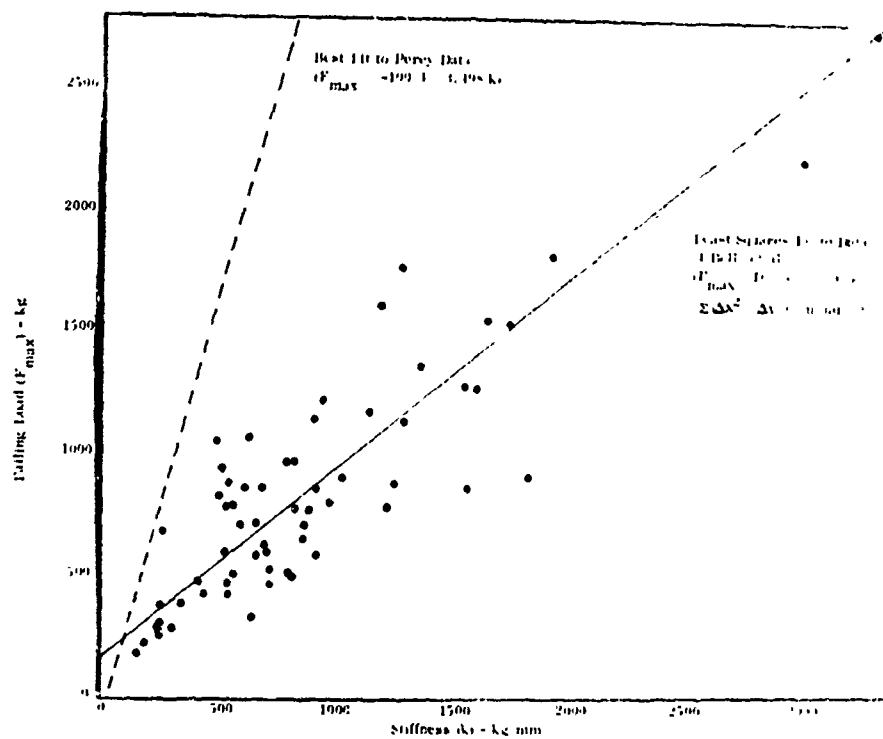


Figure 37. Variation of Vertebral Failing Load with Stiffness from Bell et al [3]

The first hint of the problem comes from Virgin [43] (1951) who showed that, in static compression and relaxation, a disc shows substantial hysteresis. A more recent illustration of this is provided by some raw data of Yorra, plotted in Figure 38. (Yorra apparently did not attach much significance to this phenomenon, since he suppressed it in his published curves.)

Hirsch and Nachemson [19] (1954) showed that a disc tended to "creep" under load, and published Figure 39 as an illustration of the phenomenon. Of course, this can be regarded as another manifestation of hysteresis, or internal damping.

Once one realizes how powerful a damper the disc is, one can see an important cause of variability in the published measurements of disc stiffness; namely, the loading rate. A modern fully automated testing machine will indicate a higher "static" stiffness than one for which the deflection has to be read manually at each load setting! One can also see that none of these measurements is likely to have any application to loads which are dynamically applied! However, for the record, Table 4 summarizes some of the data which has been accumulated.

In the next section we discuss two attempts to wrest some dynamic information about the disc from data which was manifestly not intended to be used in such a way.

#### An Analysis of the Dynamic Disc Test Data of Hirsch and Nachemson

Hirsch and Nachemson conducted some experiments with single inter-vertebral discs in an apparatus represented by Figure 40. The use of the principal vibrating mass  $m_2$  at the end of the arm provides a simple relationship for static force/deflection measurements, but requires careful interpretation in the dynamic cases. Figure 40 shows a representation of the test set-up and two equivalent simple linear models.

Assuming that the lever in Figure 40(a) is massless so that the moving parts rotating about the point A have mass  $m_2$  and radius of gyration  $\ell_2$ .

$$\begin{aligned}\text{Then} \quad F &= k\delta + 2K\dot{\delta} \\ &= m_2 \ell_2^2 \ddot{\theta} / \ell_1\end{aligned}$$

$$\begin{aligned}\text{but} \quad \ddot{y}_1 &= \ell_1 \ddot{\theta} \\ \therefore F &= m_2 \ddot{y}_1 (\ell_2 / \ell_1)^2\end{aligned}$$



The first hint of the problem comes from Virgin [43] (1951) who showed that, in static compression and relaxation, a disc shows substantial hysteresis. A more recent illustration of this is provided by some raw data of Yorra, plotted in Figure 38. (Yorra apparently did not attach much significance to this phenomenon, since he suppressed it in his published curves.)

Hirsch and Nachemson [19] (1954) showed that a disc tended to "creep" under load, and published Figure 39 as an illustration of the phenomenon. Of course, this can be regarded as another manifestation of hysteresis, or internal damping.

Once one realizes how powerful a damper the disc is, one can see an important cause of variability in the published measurements of disc stiffness; namely, the loading rate. A modern fully automated testing machine will indicate a higher "static" stiffness than one for which the deflection has to be read manually at each load setting! One can also see that none of these measurements is likely to have any application to loads which are dynamically applied! However, for the record, Table 4 summarizes some of the data which has been accumulated.

In the next section we discuss two attempts to wrest some dynamic information about the disc from data which was manifestly not intended to be used in such a way.

#### An Analysis of the Dynamic Disc Test Data of Hirsch and Nachemson

Hirsch and Nachemson conducted some experiments with single inter-vertebral discs in an apparatus represented by Figure 40. The use of the principal vibrating mass  $m_2$  at the end of the arm provides a simple relationship for static force/deflection measurements, but requires careful interpretation in the dynamic cases. Figure 40 shows a representation of the test set-up and two equivalent simple linear models.

Assuming that the lever in Figure 40(a) is massless so that the moving parts rotating about the point A have mass  $m_2$  and radius of gyration  $\ell_2$ .

$$\begin{aligned} \text{Then} \quad F &= k\delta + 2K\dot{\delta} \\ &= m_2 \ell_2^2 \ddot{\theta} / \ell_1 \end{aligned}$$

$$\begin{aligned} \text{but} \quad \ddot{y}_1 &= \ell_1 \ddot{\theta} \\ \therefore F &= m_2 \ddot{y}_1 (\ell_2 / \ell_1)^2 \end{aligned}$$

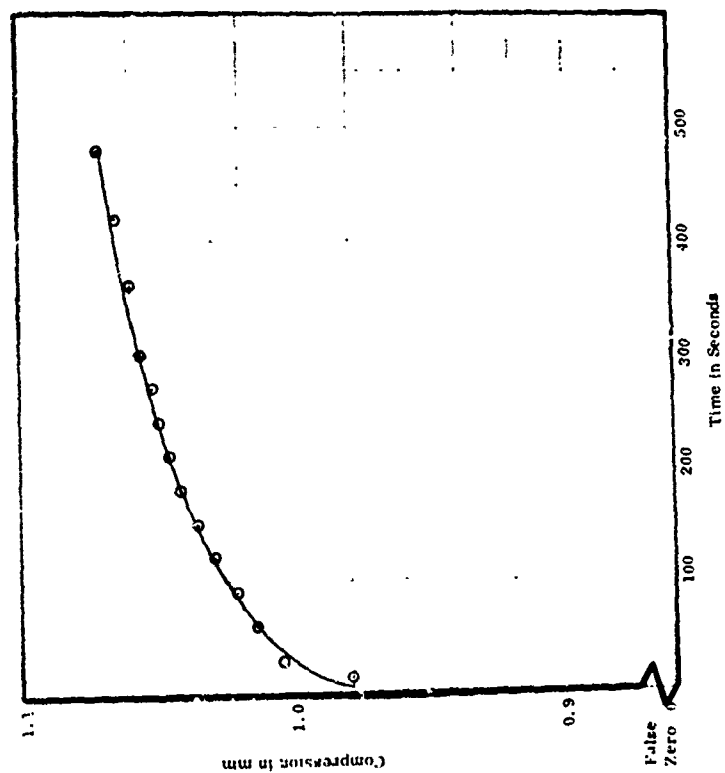


Figure 39. Variation of Disc Deflection with Time, Under a 100 Kg Load, According to Hirsch and Nachemson (L-4 disc, male, aged 46) [19]

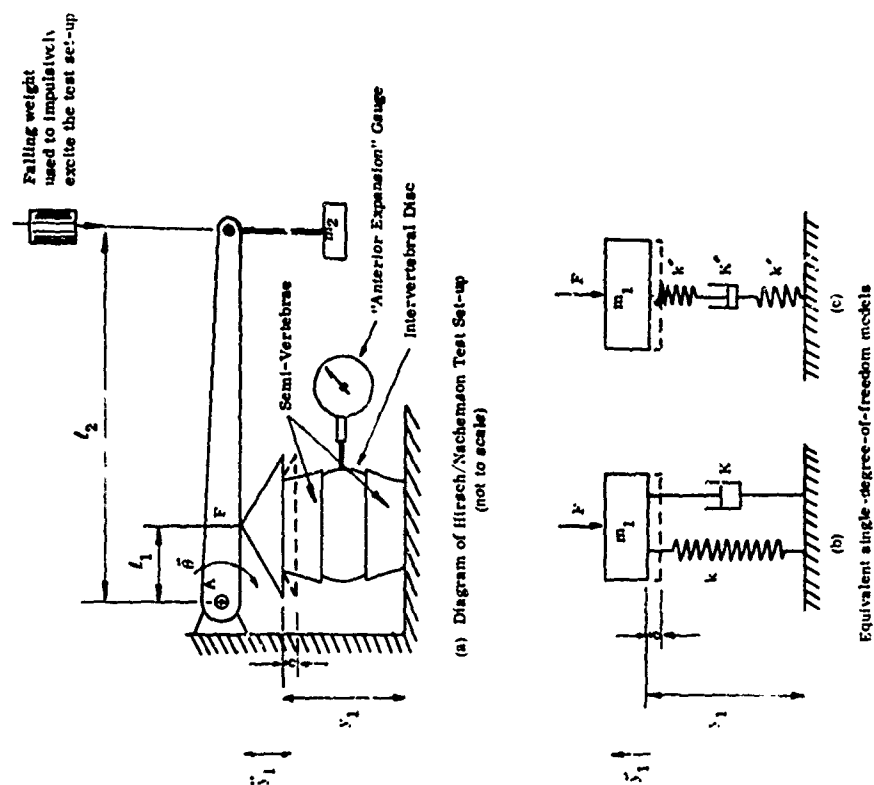


Figure 40. Diagram of Intervertebral Disc Dynamic Model

TABLE 4  
"DISC" STIFFNESS RESULTS OF VARIOUS  
WORKERS WITH LOW SPEED LOAD APPLICATION

	<u>Low Load</u> 0-50 kg	<u>Medium Load</u> 50-150 kg	<u>Large Load</u> 150-1000 kg	<u>Remarks</u>
Geertz (1943) ( <u>in vivo</u> ) (one sample)	40 kg/mm	-	-	Very approximate measurement.
Geertz (1943) (11 samples, two tests)	-	-	High 795 kg/mm (T-10 to L-3) Low 313 kg/mm (T-7 to L-1)	Averaged from two vertebral assemblies including 6 and 5 discs respectively.
Virgin (1951) (six samples)	-	97 kg/mm	276 kg/mm (High 435 kg/mm Low 143 kg/mm)	Average "static" load rate. Virgin identified hysteresis in disc force-deflection curve. Only a "thin slice" of vertebral bone on each side of disc.
Hirsch and Nachemson (1954) (94 samples, but no individual data)	-	92 kg/mm (see Fig. )	-	Lcw speed load application. Half of each adjacent body used.
Hirsch (1955) (one sample)	51 kg/mm	101 kg/mm	-	Lcw speed load application. Half of each adjacent vertebral body used.
Yorra (1956) (five samples)	-	119 kg/mm (High 226 kg/ mm Low 68 kg/mm)	300 kg/mm (High 372 kg/ mm Low 222 kg/mm)	Nearly complete (trued-off) vertebra on each side of disc.
Crocker & Higgins (1966) (one sample)	-	-	686 kg/mm	0.1 mm/sec deflection rate of disc plus L-1 and L-2 of 40 year old male.
" "	-	-	1150 kg/mm	Stiffness of disc alone.

for the model in Figure 40(b)

$$F = k\delta + 2K\dot{\delta}$$

$$= m_1 \ddot{y}_1$$

for equivalence,  $m_1 = m_2 (\ell_2 / \ell_1)^2$

It should be noted that this is not identical to the equivalence required for static deflection ( $m_{1s} = m_{2s} (\ell_2 / \ell_1)$ ) which is the only figure used by Hirsch and Nachemson. Thus, as the ratio  $\ell_2 / \ell_1$  is about six (measured from Figures 10 and 11 of Reference 18) the equivalent mass of the single degree of freedom system represented in Figure 40(b) should be about six times the mass corresponding to the "preload" applied to the specimen in the Reference 17 and 18 tests.

The deflection-time history traces of the anterior expansion gauge recorded in Figures 18 and 19 of Reference 18, are interpreted in Table 5 to allow an equivalent dynamic model to be calculated from the theory of Appendix A. The scales on the two figures, especially Figure 19, are extremely small so that very little accuracy can be expected. Cases E and A represent the best traces so that the best estimate of the damping coefficient is about

$$2K = 35.0 \times 10^3 \text{ lb sec/ft}$$

The average of the four experiments gives

$$2K = 23.9 \times 10^3 \text{ lb sec/ft}$$

Due to other sources of damping and loss in the test rig, these estimates are expected to be on the high side of the correct value.

#### An Analysis of Perey's Dynamic Test Data

Perey describes a series of tests in which a weight (mass  $m_1$ ) was placed on a pair of lumbar vertebrae, complete with the intervening disc. (The arches with the intervertebral joints and spinal processes with their ligaments were undisturbed.) A second weight (mass  $m_2$ ) was then dropped on the first weight, from a known height, and the specimen examined for injury.

For each value of  $m_1$  and  $m_2$ , Perey quotes forces, as (for example) "1250 kp during 0.006 sec." This is presumably the force needed to stop the lower weight, after it has acquired velocity from the impact, assuming constant force for 0.006 seconds. Such a number is clearly very approximate and bears no simple relationship to the peak force developed in the specimen. Additionally, for what it is worth, most vertebra tested did not fail at "loads" much in excess of static failure loads reported by Perey elsewhere in his report; although to be sure, as McElhaney shows, dynamic failure loads can considerably exceed their static equivalents.

TABLE 5

## ANALYSIS OF HIRSCH AND NACHEMSON'S DYNAMIC DATA

CASE	E	A	B	C
Figure	18	19	19	19
Case	99	87	87	87
Sex	F	M	M	M
Age	Ref. 19 Data	18	48	48
Vertebra	L2	L3	L3	L3
$m_2(l_2/l_1)$ (Kg)	100	130	100	70
$m_1 = m_2(l_2/l_1)^2$ (Kg)	600	780	600	420
$m_1$ (slugs)	41.2	53.6	41.2	28.8
$\lambda/2\pi$ (cps) *	10.42	9.82	9.73	12.5
$\lambda$ (rad/sec)	65.6	61.8	61.1	78.6
n	3	1	2	2
$y_{\max}/y_{\max_o}$ *	0.5	.742	.33	.227
$\bar{c}$ (from Fig. A7)	.038	.049	.088	.118
$(1 - \bar{c}^2)$	.999	.998	.992	.986
$\omega = \lambda(1 - \bar{c}^2)^{1/2}$ (rad/sec)	65.5	61.7	60.9	78.0
$k = m_1\omega^2$ (1000 lb/ft)	176	204	153	175
$k =$ (Kg/mm)	262	304	228	260
$c = \bar{c}\omega$ (1/sec)	2.49	3.02	5.36	7.17
$2K = 2cm_1$ (lb sec/ft)	202.5	324	441	413
$k' = m_1\omega^2$ (1000 lb/ft)	176	204	153	175
$k' =$ (kg/mm)	262	304	228	260
$2K' = \frac{k}{2c}$ (1000 lb sec/ft)	35.4	33.8	14.3	12.2

\* Values measured from Ref. 19, Fig. 18 and 19.

# An Analysis of Perey's Dynamic Test Data

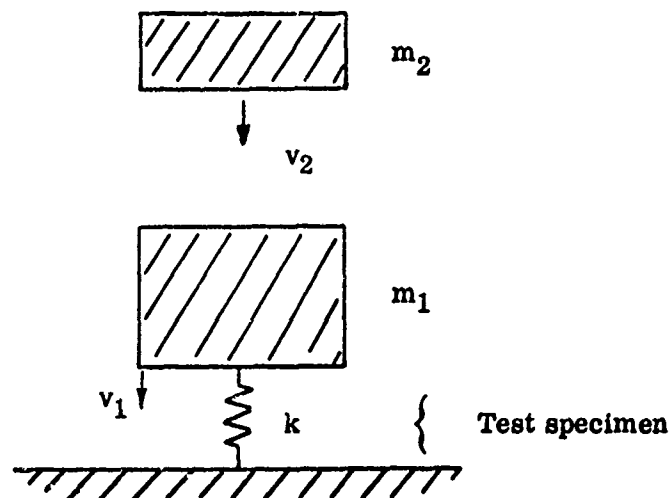


Figure 41. Dynamic Model of Perey's Dynamic Test Rig

The velocities of the weights after impact can be computed from the standard results for elastic collision; namely,

$$v_{12} = \frac{(1+e) m_2 v_{21}}{m_1 + m_2}$$

$$v_{22} = \left[ 1 - \frac{(1+e) m_1}{m_1 + m_2} \right] v_{21}$$

The following table gives the weight values used in Perey's experiments:

Drop height	50	50	50	50	60	60	cm
$gm_2$	15	18	15	15	5	3.5	kg
$gm_1$	25	25	15	10	30	35	kg
$\frac{m_2}{m_1 + m_2}$	.375	.418	.5	.6	.143	.091	
$\frac{m_1}{m_1 + m_2}$	.675	.582	.5	.4	.857	.909	

The weights are assumed to be of steel, for which the coefficient of restitution is  $e = 0.555$ . Also the initial impact velocities are assumed to be  $v_{21} = 10.28$  ft/sec and  $11.25$  ft/sec from  $50$  cm and  $60$  cm respectively, which implies negligible friction\*. Thus, the velocities and initial kinetic energy are as follows:

$m_2$	15	18	15	15	5	3.5	kg
$m_1$	25	25	15	10	30	35	kg
$v_{12}$	5.99	6.68	7.98	9.58	2.505	1.592	ft/sec
$v_{22}$	.278	.977	2.28	3.88	-3.75	-4.64	ft/sec
$\frac{1}{2} m_1 v_{12}^2$	30.7	38.1	32.6	31.35	6.45	3.4	ft/sec

If the two vertebrae and the intervening disc could be adequately represented by a linear spring, of stiffness  $k$ , then it is easy to show that the initial kinetic energy of the mass is related to the maximum potential energy in the spring by

$$\frac{1}{2} m_1 v_{12}^2 = \frac{F_{\max}^2}{2K}$$

If we assume that Perey's dynamic test specimens fail at the same load which he measured statically, then this equation can be used to find the equivalent linear stiffness, which turns out to average  $1.86 \times 10^4$  lb/ft =  $27.7$  Kg/mm. This is clearly much too low, so it seems clear that an adequate model requires a series damping element. This hypothesis is strengthened by noting that although failure rate shows no discernible trend with impact energy (Fig. 42) it does show a trend against impact velocity (Fig. 43).

We, therefore, employ, in Table 7, the series damper model theory of Appendix A to calculate the damping coefficient, and arrive at an average value of  $2K = 76.0$  lb ft/sec. The assumptions needed to obtain this result are as follows:

- (a) The dynamic failure load is the same as that measured statically. In the dynamic case only one end of each vertebra is in contact with a flat plate, the other end being supported naturally by the disc, so that the total amount of vertebral body material distorted by the test fixture is less; perhaps about half. But the peak stresses which initiate failure are assumed to be unaffected.
- (b) The elastic stiffness of the vertebral bodies will clearly be greater, during the dynamic tests, because one end is properly

---

\* which is almost certainly not true.

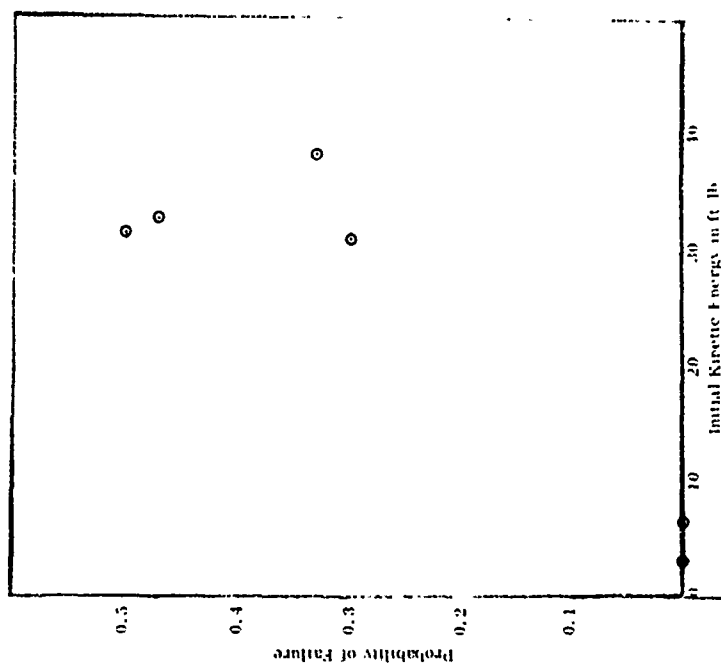


Figure 42. Relationship Between Impact Energy and Failure Rate in Perey's Tests of Pairs of Lumbar Vertebrae [33]

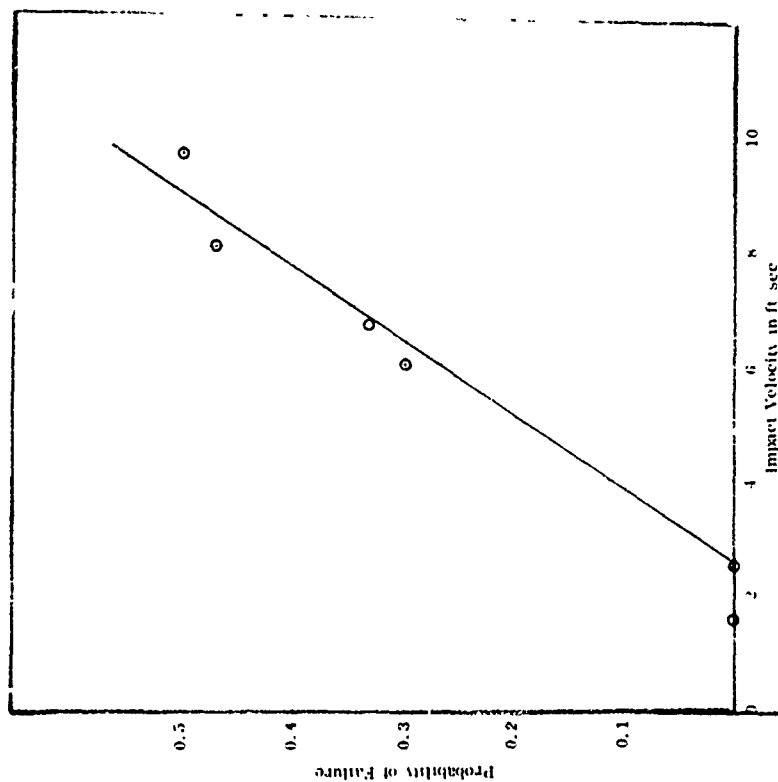


Figure 43. Relationship Between Impact Velocity and Failure Rate in Perey's Tests of Pairs of Lumbar Vertebrae [33]



TABLE 6

## SUMMARY OF PEREY'S DYNAMIC LOADING TESTS

(Pairs of Lumbar Vertebra, plus T-12/L-1)

Impact Energy (ft./lb)	Initial Velocity	Number of Tests	End Plate Failures	Compressive Fractures	<u>Total Failures</u> <u>Total Tests</u>
3.04	1.592	2	0	0	0
6.45	2.505	1	0	0	0
30.70	5.990	20	6	0	0.3
38.10	6.640	21	6	1	0.333
32.60	7.980	17	8	0	0.471
31.35	9.580	16	3	5	0.5

Subject's aged over 60 eliminated from Perey's data. Reduction in vertebral height without fracture classed as failure.

TABLE 7  
ANALYSIS OF PEREY'S DYNAMIC DATA

Pre-load Weight	25	25	15	10	Kg
Impact Energy	30.7	38.1	32.6	31.35	lb ft
Initial Velocity after Impact ( $\dot{y}_0$ )	5.99	6.68	7.98	9.58	ft/sec
Number of Tests	20	21	17	16	
Failures/Total tests ( = P. I. )	0.300	0.333	0.471	0.500	
Static Failure Load for P. I. (Fig. )	453	470	532	545	Kg
Pre-load Mass ( $m_1$ )	1.715	1.715	1.03	0.687	slugs
$\ddot{y}_{\max} = F_{\max}/m_1$	583	605	1140	1748	ft/sec <sup>2</sup>
Undamped Frequency <sup>1</sup> ( $\omega$ )	360.5	360.5	465.0	570.0	rads/sec
$\ddot{y}_{\max}/\omega \dot{y}_0$	0.27	0.2515	0.3075	0.32	
$\tau$ (from Fig. )	1.54	1.68	1.29	1.22	
$m_1 k'$	$38.3 \times 10^4$	$38.3 \times 10^4$	$23.0 \times 10^4$	$15.3 \times 10^4$	(lb sec/ft) <sup>2</sup>
$2K (= mk'/2c^2)$	$80.7 \times 10^3$	$67.9 \times 10^3$	$69.1 \times 10^3$	$51.4 \times 10^3$	lb sec/ft

Average  $2K = 67.0$  lb sec/ft

---

<sup>1</sup> Based on mass (m) and a stiffness for two vertebra of  $k' = 22.3 \times 10^4$  lb/ft. This is the average of Percy's and Bell, et al's 50% stiffnesses.

supported by the disc. In Table 7 we have assumed a stiffness mid-way between Perey's and the results of Beil et al. It turns out that the calculation is not particularly sensitive to stiffness, so that the crudity of this assumption is relatively unimportant.

The result of  $2K = 67.0 \text{ lb sec/ft}$  is about twice the most reliable values deduced from the Hirsch and Nachemson data in the previous section, which is quite good agreement, under the circumstances. Neglected factors such as friction in Perey's test set-up could easily explain the difference, or indeed, a very much larger one. But possibly these analyses have served to indicate, albeit crudely, an upper bound to the damping effect of the disc. They do not reveal its dynamic stiffness, but with such large damping terms a precise stiffness value is probably unimportant.

#### Construction of a Simple Spinal Model

Conceptually, a dynamic model of the torso for  $+C_z$  acceleration is very simple, as was realized by Geertz in 1943, and possibly even earlier by other workers. It consists of the relatively rigid mass of the head and upper torso, superimposed on the spine, which acts as a compression spring. A small amount of series damping is provided by the intervertebral discs, and considerably more by the muscles and other tissues in parallel with the spine.

The present DRI model (29) [1] was originally derived rather indirectly from acceleration tolerance data, without appeal to detailed biodynamic information. We now consider the construction of a spinal model from a physiological point of view, using the statistical data already analyzed in this paper.

Using the data given by Dempster [9], it is fairly simple to estimate a value for the "mass" of the dynamic model, as indicated in Table 8. This value is given with and without arms, because the spine may carry all the arm mass (as in the case of the D-ring system) or almost none, at the other configuration extreme, when arm rests are used. Our simple model assumes that these loads are distributed as shown in Figure 44. The model is evidently a distributed parameter one above T-10, with a massless spring between T-10 and L-5.

Both Junk and Geertz show a continual increase in spinal load down to L-5, but this is based on static conditions. In a dynamic environment it is to be expected that most of the visceral mass will be reacted on the pelvic girdle, and by tension in the appropriate skin, musculature and restraint system. Of course, the lower portion of the spine must react its own mass, and that of the musculature intimately attached to it, so that the true picture will be somewhere between the dynamic and static load distributions shown in Figure 44. The error involved in neglecting these effects is likely to be small, however.

The mean variation of strength along the spine is given in Figure 45. The values between T-8 and L-5, inclusive, are obtained from the statistical

TABLE 8

## HEAD AND "UPPER TORSO" WEIGHT OF 50% MAN

Total Weight = 161.9 lb

Component	<u>Component Weight</u> Total Weight	Component Weight (lb)
(a) Both arms	.099	16.0
(b) Trunk, minus limbs	.565	91.5
(c) Abdomen, plus pelvis	.264	42.7
(d) Head and neck	.079	12.8
(e) Thoracic organs and blood	.056	9.1
Head and "upper torso" weight (with arms)	=	(a) + (b) - (c) + (d) - (e)
	=	<u>68.5 lb</u>
Head and "upper torso" weight (without arms)	=	(b) - (c) + (d) - (e)
	=	<u>52.5 lb</u>

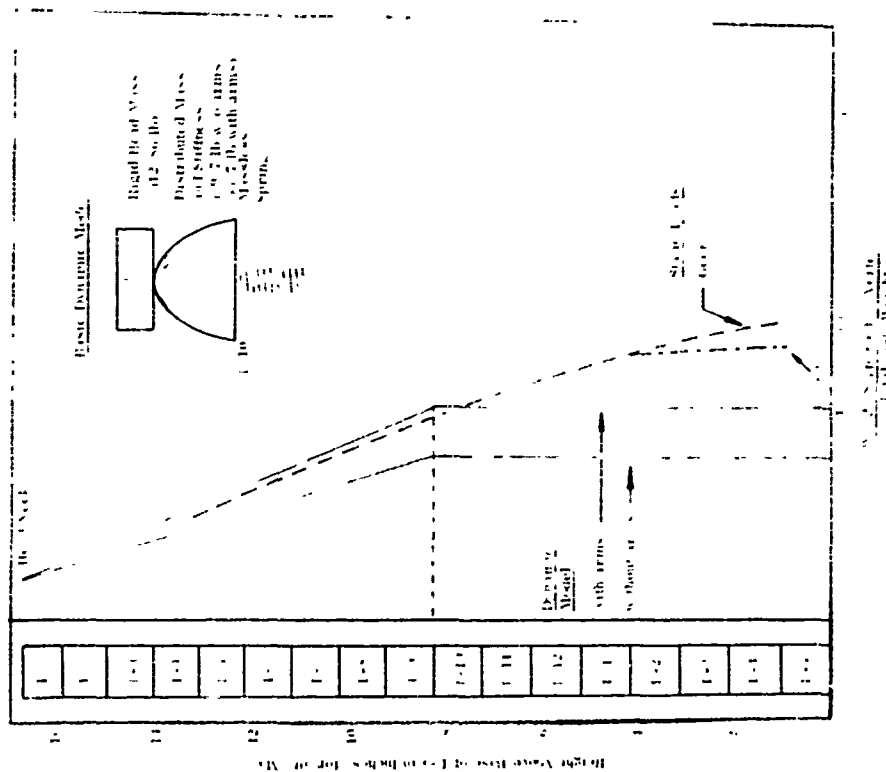


Figure 44. Dynamic and Static Loads on the Spine and an Equivalent Dynamic Model

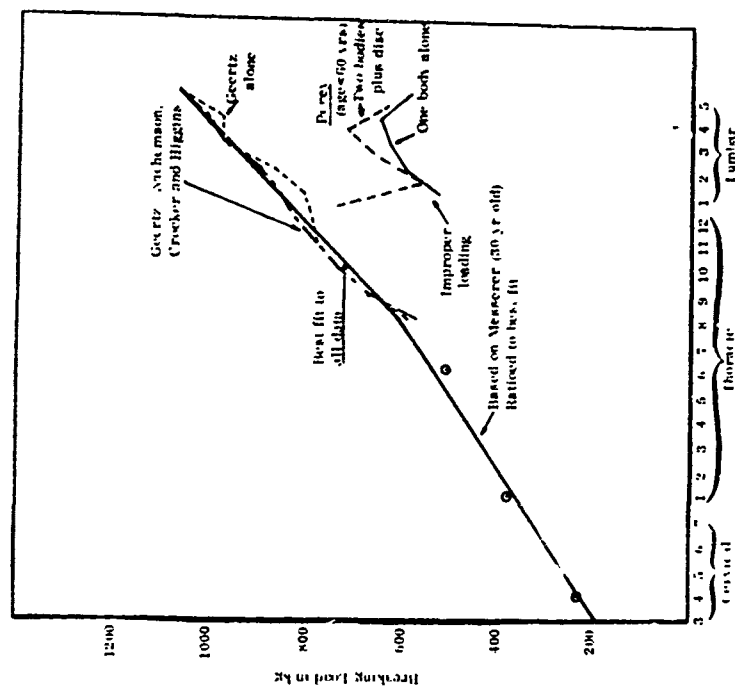


Figure 45. Average Falling Loads for Individual Vertebrae, Ages Less than 42.5 Years

analysis given earlier. The only known data for vertebrae above T-8 is by Messerer, and this is adapted (with a slight adjustment to the mean values below T-8) to give the strength values shown in Figure 45.

Knowing the strength of each vertebra, and the load which it carries, it is easy to determine which vertebra is most likely to fracture, under steady state (nontransient) conditions. For the simple dynamic model of Figure 44, T-10 is clearly the critical one. The Geertz weight distribution would place the critical vertebra somewhat lower in the spine, -- in some unpublished work Stech has calculated that L-1 is critical in this case -- and in either case, we can compute curves of relative probability of fracture, as shown in Figure 46, based on the Geertz et al failure distribution of Figure 20. (It is interesting to note from Figure 46 that the relative probability of injury distribution changes with the overall probability of injury.)

The Geertz et al distribution of Figure 20 can also be used to calculate the relationship between the Dynamic Response Index (DRI) and the probability of injury, since

$$DRI = \frac{\text{Peak Force}}{\text{mass} \times g} = \frac{\text{Peak Force}}{\text{Weight}}$$

For the model of Figure 44, the failing force is that of T-10 (Geertz distribution of Figure 20 ratioed by 713/1075 from Figure 45) and the weight, from Table 8, is either 32.4% or 42.2% of the body weight, depending on whether or not the arms are included in the model.

Of course, the Geertz distribution is one of failing load alone, and does not include the effect of variation in body weight. To accomplish the latter, the distribution of Figure 20 is divided by the weight distribution of Figure 7 (the latter being ratioed by 42.2%) to give the solid line distribution in Figure 47. As can be seen, it agrees quite well with Brinkley's [5] correlation between DRI and injury rate for various escape systems in the Air Force inventory.

Details of the procedure employed to combine the failure and weight distributions are discussed in Appendix B. We should note here, however, that the solid line corresponding to  $g/(\sigma_1/\sigma_2) = 0$  assumes that there is no mutual dependency, and that this is almost certainly incorrect, since tall, heavy men are likely to have stronger spines. The foregoing analysis needs to be repeated when more detailed weight data (in the form of weight deviation from the norm at a given height) becomes available. However, it is interesting to note that the curve for  $g/(\sigma_1/\sigma_2) = 0.5$  is still in good agreement with operational data, so far as slope is concerned, albeit displaced somewhat to the right in terms of absolute values.

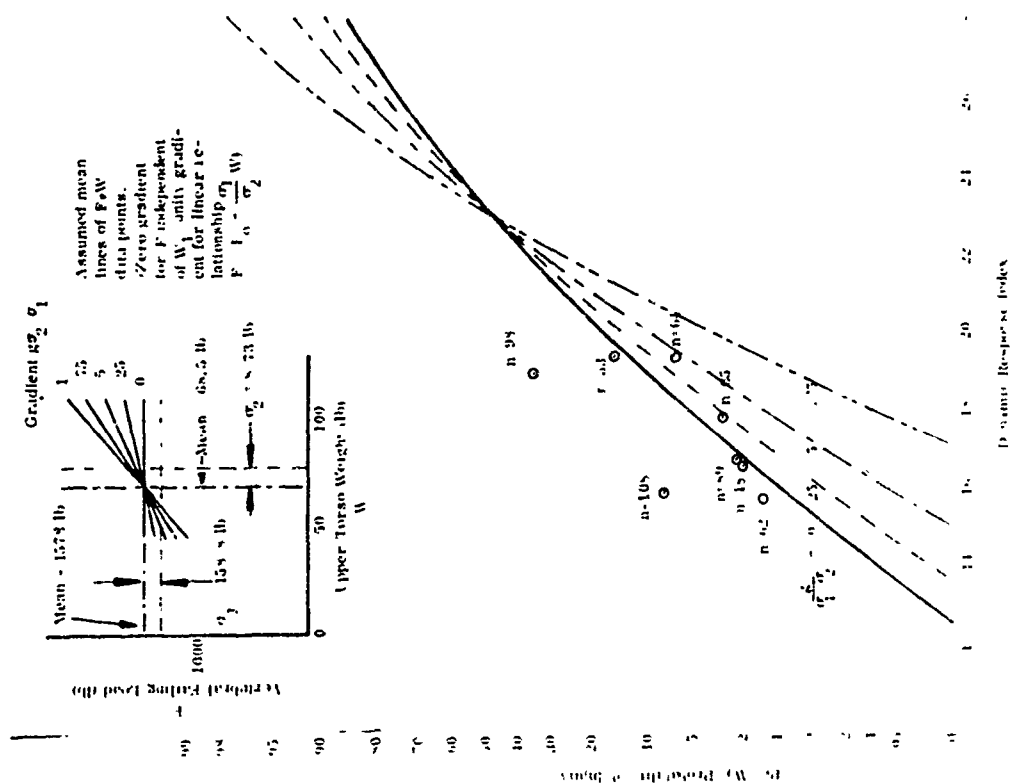


Figure 46. Relative Probability of Fracture Location for the Simple Model of Figure 44, Assuming Steady State Acceleration Loading

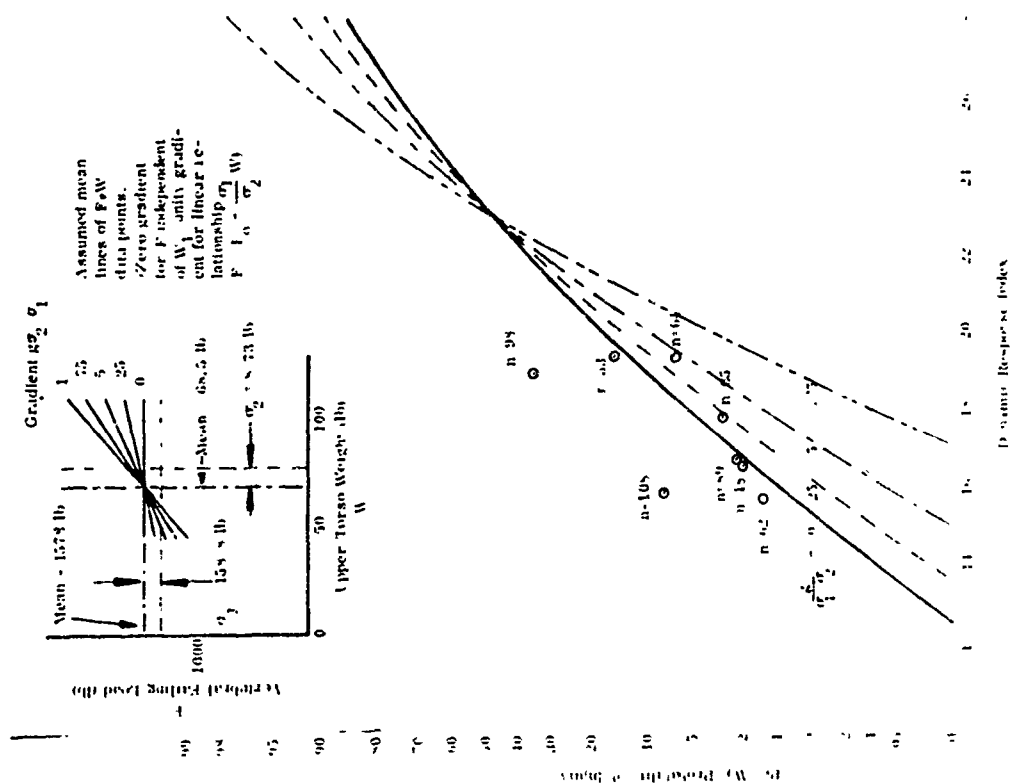


Figure 47. Relationship Between Probability of Injury and Dynamic Response Index (DRI) using the Geertz, et al Falling Distribution

Needless to say, Brinkley's calculations must gloss over many other sources of variability than the two identified. One can hope that they are all of second order importance, however, based on the evidence of Figure 47.

Such calculations, based upon quasi-static conditions, cannot tell us about the most probable location of injury in the dynamic environment of an ejection, of course. Although there is nothing inherently difficult about rigorously analyzing a model which combines lumped and distributed parameter elements\*, it is more convenient for our present purposes to represent the distributed upper torso mass by two point masses at each end of its resiliency, as indicated in Figure 48.

For illustrative purposes the values of these masses ( $m_1, m_2$ ) at either end of the distributed parameter section, connected by a weightless spring of stiffness  $k$  can be calculated as follows. The natural frequency of such a system would be

$$\omega_{n1} = \sqrt{\frac{k}{m_1 m_2} (m_1 + m_2)} = \sqrt{\frac{k}{m_2} \frac{(1 + \phi)}{\phi}}$$

where

$$\phi = \frac{m_1}{m_2}$$

For a distributed parameter longitudinal bar with free ends, the first natural frequency is

$$\omega_n = \pi \sqrt{\frac{k}{(m_1 + m_2)}} = \pi \sqrt{\frac{k}{m_2 (1 + \phi)}}$$

Equating these two

$$\frac{\pi^2}{1 + \phi} = \frac{1 + \phi}{\phi}$$

or

$$\phi^2 - (\pi^2 - 2) \phi + 1 = 0$$

$$\therefore \phi = 0.129$$

Thus the masses required are

$$m_1 = \left(\frac{\phi}{1 + \phi}\right) m_T = 0.1144 m_T$$

$$m_2 = \left(\frac{1}{1 + \phi}\right) m_T = 0.8856 m_T$$

\* See, for example, H. Kolsky [21]



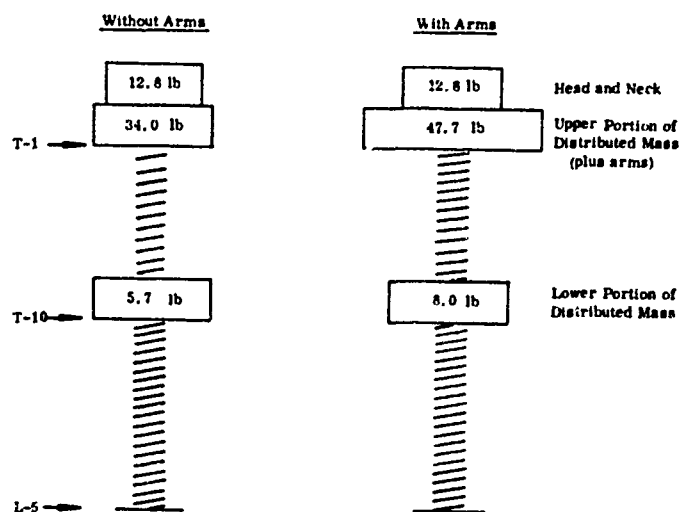


Figure 48. A Lumped Parameter Representation of the Spine and Upper Torso Mass Model of Figure 44

To complete a simple dynamic model, we need to know values for the resiliencies and dampers which will represent the spine. The measurements of Bell et al give a median bone stiffness of about 1100 Kg/mm, a figure which is known to be too high because it does not include end-plate flexure. The analysis of the "dynamic experiments" of Perey and of Hirsch and Nachemson leads us to suspect that the lumbar intervertebral discs each act as dampers, with a damping coefficient of about  $2K = 35.0 \times 10^3$  lb sec/ft. For the lack of any better information, we assume this value to hold for all discs. The "large load" stiffness measurements of Virgin lead us to suspect that the disc is also resilient, with a stiffness, in parallel with its damping effect, of about 300 Kg/mm; again we must assume this to be true for all discs, but forces associated with this stiffness will be so low, in relation to the damper forces, that they can be neglected in any case.

The computation of the bone stiffness which follows is illustrated in Table 9. Assuming that the load bearing portions of all vertebrae are geometrically similar, the stiffness will vary directly with cross-sectional area (and hence with breaking strength) and inversely with height. The average breaking strengths are given by Figure 45. The heights of individual vertebrae along the spine was measured on a representative model, and the resulting measurements smoothed as shown in Figure 49. These values were then used in Table 9 to calculate the stiffness of individual vertebrae and the cumulative stiffness:

$$k_c = \frac{1}{\sum_1^n \frac{1}{k_n}}$$

Finally, it is necessary to provide an estimate for the damping provided by the musculature in parallel with the spine. Payne and Band [32] (1969) have given a tentative value of 19.4 lb sec/ft, for a single damper, and (with reservations) this same value is used for the two dampers required in the present mode.

The final basic spinal model is illustrated in Figure 50.

#### Additional Degrees of Freedom in the Escape System Dynamic Model

So far we have confined our modelling to those elements of the body directly associated with the spine. As indicated in Figure 51, the first resonant frequency of this sub-model of the body is over twice that of the DRI model, indicating that the spine is significantly stiffer than we previously thought, or that end-plate flexure accounts for most of the vertebral body resiliency.

It is a simple matter to indicate all but one of the obvious remaining degrees of freedom; namely, the thoracic, visceral, and head on neck modes indicated in Figure 52. Payne and Band have shown that the measurements of Dieckmann [10] for the head on neck mode indicate an undamped natural frequency

To complete a simple dynamic model, we need to know values for the resiliencies and dampers which will represent the spine. The measurements of Bell et al give a median bone stiffness of about 1100 Kg/mm, a figure which is known to be too high because it does not include end-plate flexure. The analysis of the "dynamic experiments" of Perey and of Hirsch and Nachemson leads us to suspect that the lumbar intervertebral discs each act as dampers, with a damping coefficient of about  $2K = 35.0 \times 10^3$  lb sec/ft. For the lack of any better information, we assume this value to hold for all discs. The "large load" stiffness measurements of Virgin lead us to suspect that the disc is also resilient, with a stiffness, in parallel with its damping effect, of about 300 Kg/mm; again we must assume this to be true for all discs, but forces associated with this stiffness will be so low, in relation to the damper forces, that they can be neglected in any case.

The computation of the bone stiffness which follows is illustrated in Table 9. Assuming that the load bearing portions of all vertebrae are geometrically similar, the stiffness will vary directly with cross-sectional area (and hence with breaking strength) and inversely with height. The average breaking strengths are given by Figure 45. The heights of individual vertebrae along the spine was measured on a representative model, and the resulting measurements smoothed as shown in Figure 49. These values were then used in Table 9 to calculate the stiffness of individual vertebrae and the cumulative stiffness:

$$k_c = \frac{1}{\sum_1^n \frac{1}{k_n}}$$

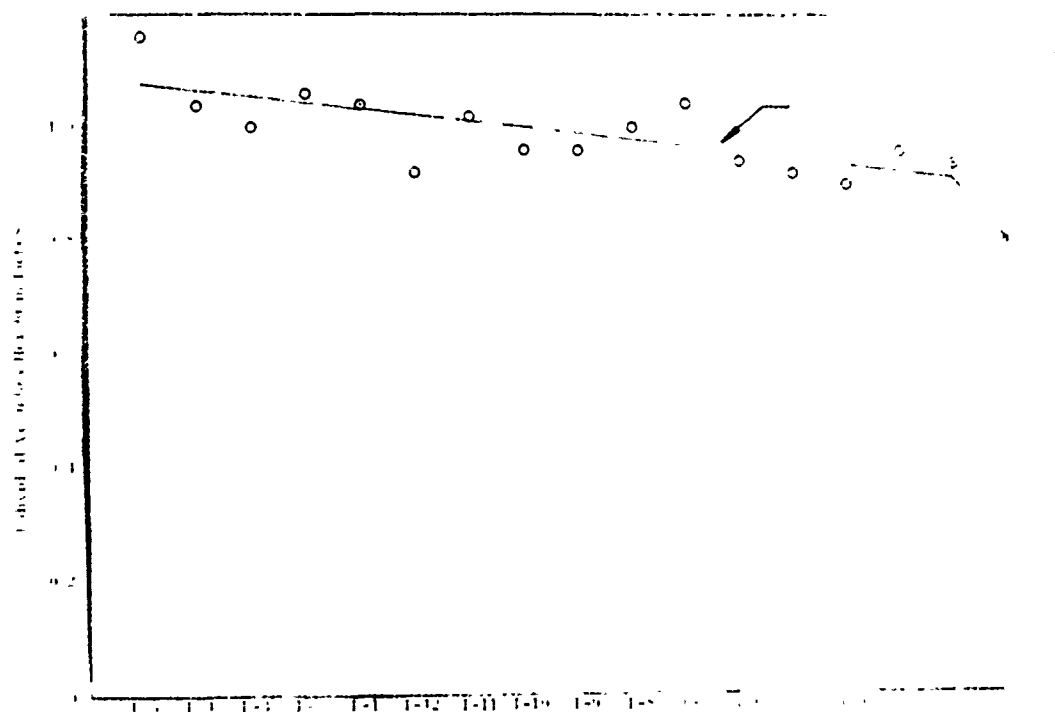
Finally, it is necessary to provide an estimate for the damping provided by the musculature in parallel with the spine. Payne and Band [32] (1969) have given a tentative value of 19.4 lb sec/ft, for a single damper, and (with reservations) this same value is used for the two dampers required in the present mode.

The final basic spinal model is illustrated in Figure 50.

#### Additional Degrees of Freedom in the Escape System Dynamic Model

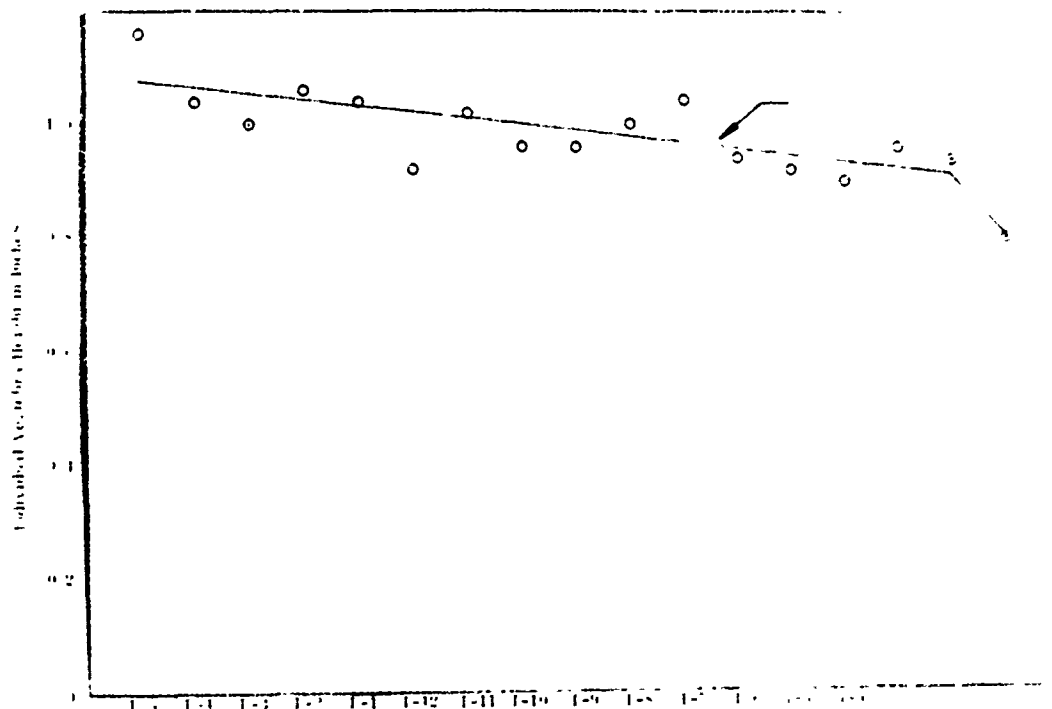
So far we have confined our modelling to those elements of the body directly associated with the spine. As indicated in Figure 51, the first resonant frequency of this sub-model of the body is over twice that of the DRI model, indicating that the spine is significantly stiffer than we previously thought, or that end-plate flexure accounts for most of the vertebral body resiliency.

It is a simple matter to indicate all but one of the obvious remaining degrees of freedom; namely, the thoracic, visceral, and head on neck modes indicated in Figure 52. Payne and Band have shown that the measurements of Dieckmann [10] for the head on neck mode indicate an undamped natural frequency



Reproduced from  
best available copy.

Figure 49. Individual Vertebral Height for a Fifty Percentile Man



Reproduced from  
best available copy.

**Figure 49. Individual Vertebral Height for a Fifty Percentile Man**

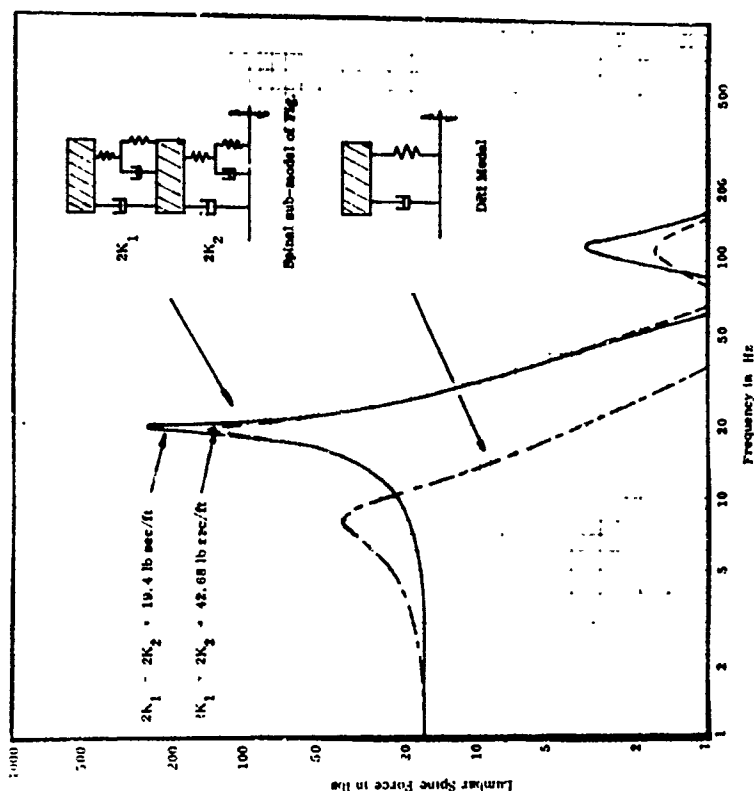


Figure 51. Variation with Frequency of the Peak Force in the Lumbar Region of the Spinal Model when Subjected to Sinusoidal Excitation at  $\pm 0.25 \text{ g}$

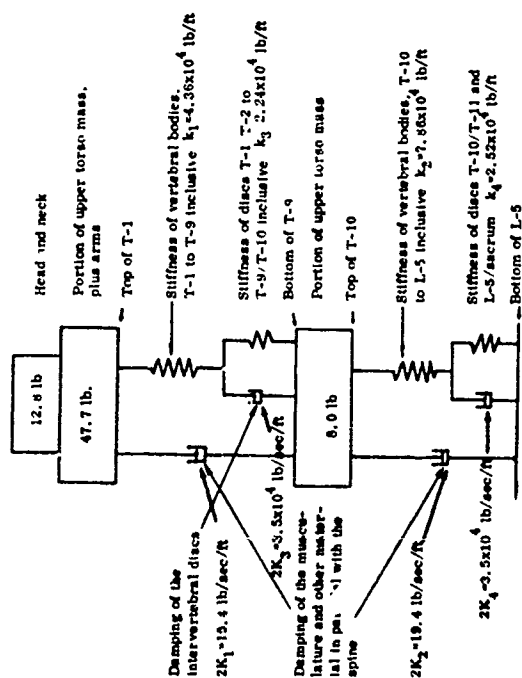


Figure 50. The Basic Spinal Model for  $+G_z$  Acceleration (arms included)

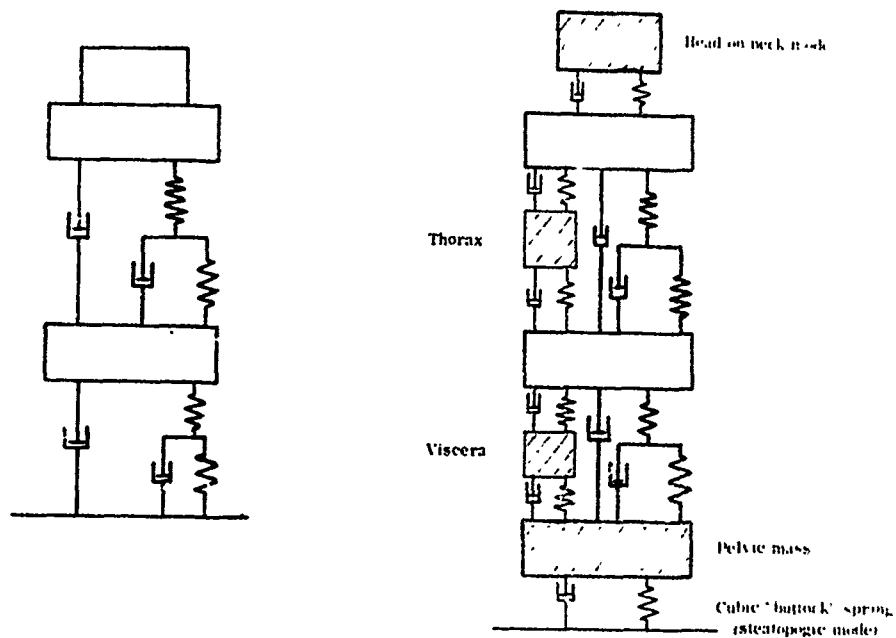


Figure 52. Incorporation of the Basic Spinal Model into a More Complete Model of the Seated Man

of 192.3 rads/sec, with which is associated a critical damping ratio of 0.15. By analogy with the lower portions of the spine, there is no reason to believe that this mode is significantly nonlinear. The thoracic and visceral modes present more difficulty, although Payne and Band have shown that if the visceral mode frequency (at low amplitudes) is assumed to be between 3.0 and 3.5 Hz, as determined by Coermann [7] et al, then for low damping of the mode, a peak will show up in a mechanical impedance plot, as shown in Figure 53. They suggest that since such peaks are not observed in practice, the low amplitude damping ratio must be at least  $\bar{c} = 0.5$ , based on a visceral mass of 15.0/32.2 slugs. On the other hand the visceral "spring" must stiffen up with increasing deflection, or else the viscera would deflect a foot or so beneath the pelvis during a high-force impact. (Weiss and Mohr [46] present some evidence of such stiffening, measuring apparent frequencies of 6.0 - 10.0 Hz during positive spinal impact.) Thus, the visceral spring is assumed to be linear for small amplitudes and stiffen in a cubic manner for larger amplitudes.\*

We can hardly even hazard a guess for the thoracic mode's dynamic characteristics, at the present time. Fortunately, the mass involved is relatively small, so that the neglect of this mode will not influence a model's overall response, to any great extent.

This leaves only the dynamics of the extremities, which do not seem to be of much importance in the escape acceleration environment, and that of the system between L-5 and the seat cushion or pan.

#### The Steatopogic Mode

It is clear to anyone that a resilience exists beneath the skeletal structure in the seated position. Phillips [34] has made some measurements in vivo from which it can be inferred that this spring force is approximately given by

$$F = 17.2 \times 10^4 \delta^3 \quad (\delta \text{ in feet})$$

(It is interesting to note from Figure 54 that this cubic relationship is not limited to the buttocks.) Payne and Band suggest that the buttock resiliency "bottoms out" above a deflection of 0.1 ft, at which point the seat pan is effectively driving the skeletal framework directly.

After the buttocks have bottomed out, the remaining resilience is due to deformation of the skeletal structure between the femurs and L-5, and at the present time there is no way of estimating a value for this.

As shown by Payne and Band, the steatopogic mode dominates impedance measurements, and it seems likely that much of the variability in such measurements is due to variations in buttock size, muscle tension, and tonus.

---

\* The only justification for cubic stiffening is that some other nonlinear elements of the body seem to follow this rule.



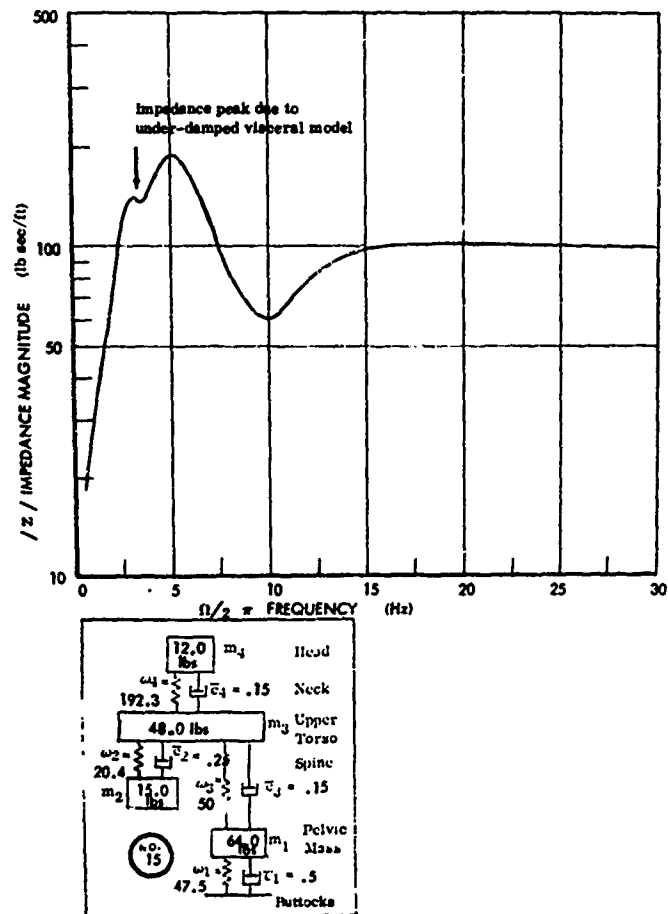


Figure 53. Illustration of a Visceral Mode Peak in Model Impedance

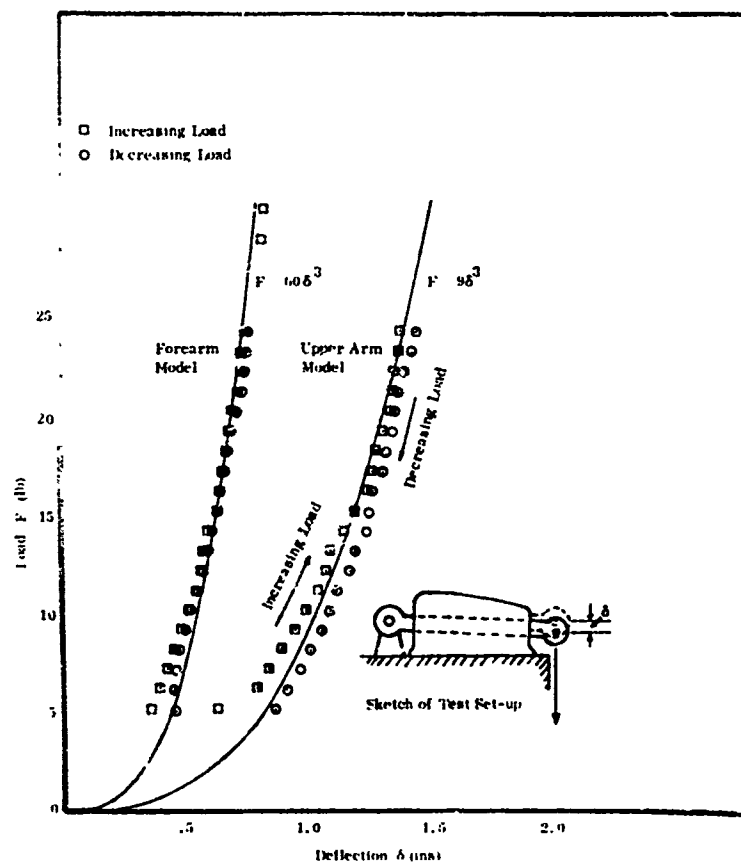


Figure 54. Force/Deflection Test Results from the Arm Components of an Anthropodynamic Analog of the Human Body

## SOME TYPICAL RESULTS WITH MULTI-DEGREE OF FREEDOM MODELS

Since the development of the multi-degree of freedom model described in the previous section is not yet completed, it may be of interest to examine some typical results obtained with our earlier model (Payne and Band [32]) as an illustration of what can be expected. This earlier model, illustrated in Figure 55, is not too dissimilar to the new one under development, except that one degree of freedom is missing from the spinal mode, and the spine plus pelvic girdle resilience is significantly less stiff (about  $0.75 \times 10^4$  lb/ft) than the figure of  $2.8 \times 10^4$  lb/ft obtained for the spine alone in the present analysis.

Sinusoidal excitation of the model gives the response shown in Figure 56. The general similarity between this and the experimental observations of Latham [22], Dieckmann [10] and Woods [49] is obvious.

The mechanical impedance of the model is shown in Figures 57 and 58, the buttock resiliency being shorted out in Figure 58 to simulate "bottoming out" under centrifuge acceleration bias effects. Figures 59 and 60 show the corresponding experimental data available.

Finally, Figure 61 shows an acceleration pulse imposed on a live human subject with the AMRL vertical acceleration tower, together with an analytical approximation to it, and Figure 62 compares the model's response with that observed experimentally.

## AN OBSERVATION ON THE COLLECTION OF BIOLOGICAL DATA

In most other scientific disciplines today we at least pay lip service to the merits of an interdisciplinary approach, even though we may have private reservations about a procedure which sounds suspiciously like "research by committee."

I hope I may be forgiven for repeating, in this regard, something which I said ten years ago [29], when we last had a meeting of this nature.

"From a long term point of view there can be little doubt that the 'integrated research' effort achieved when a team of medical, engineering and mathematical workers are employed on a continuing program is by far the most effective means of increasing our knowledge... Too many of our research programs today are being undertaken by workers with a capability in only one of the several disciplines involved, with the result that their work loses much of its value .."

This situation has changed all too little in ten years, so perhaps I may be permitted to be more blunt than I was last time in illustrating the sort of thing which happens when an isolated worker goes off alone to his ivory tower.

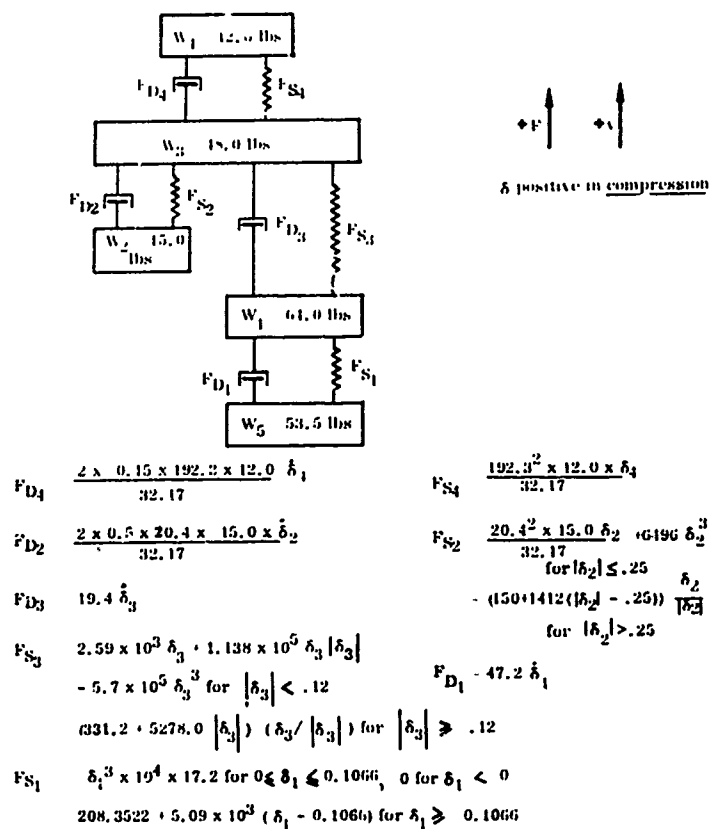


Figure 55. Four Degree of Freedom Model of a Seated Man from Payne and Band [32]

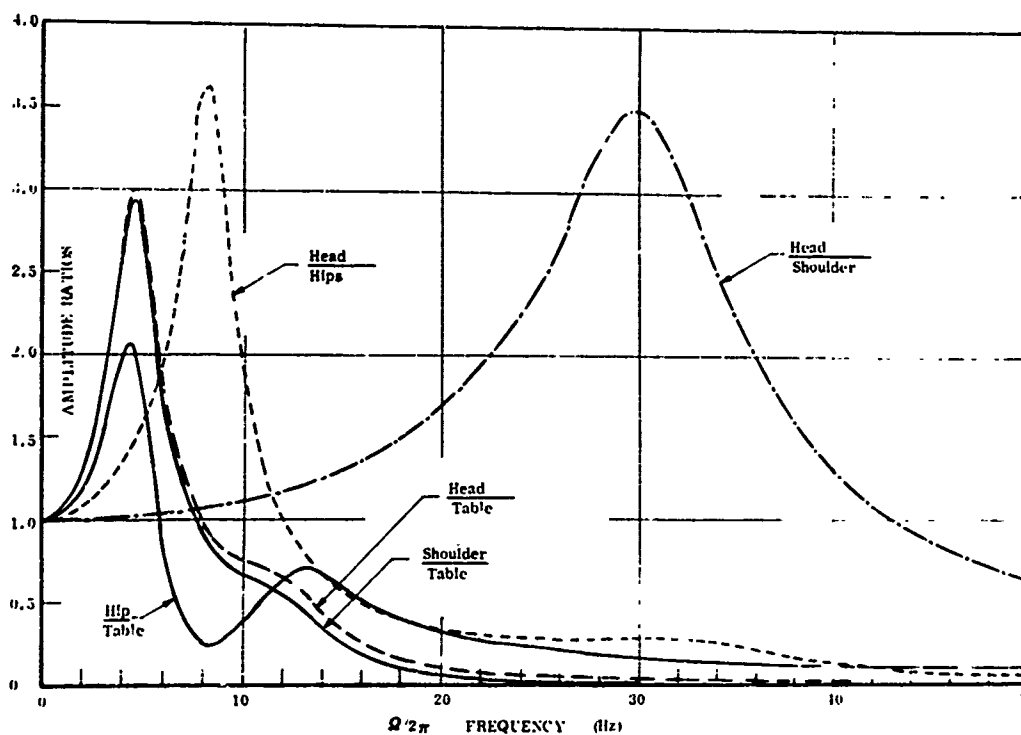


Figure 56. Response of the Model of Figure 55 to +1g Sinusoidal Excitation

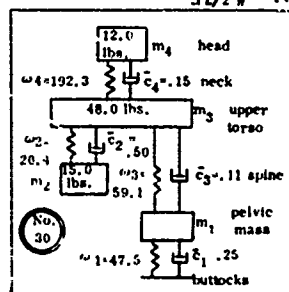
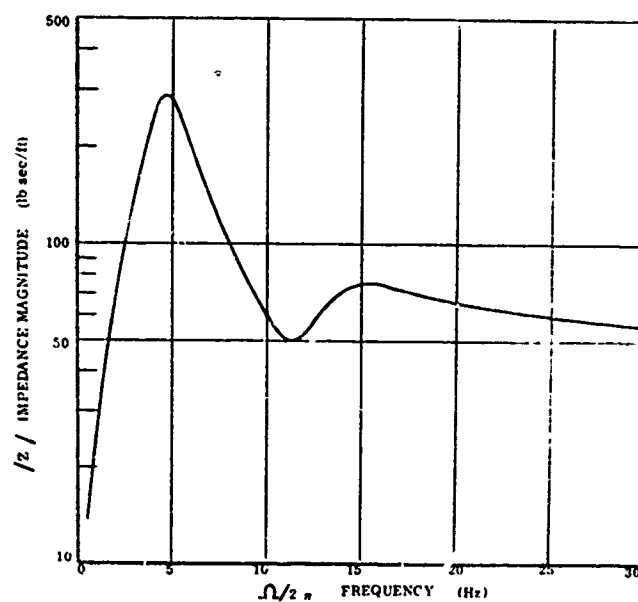


Figure 57. Mechanical Impedance of the Four Degree of Freedom Model

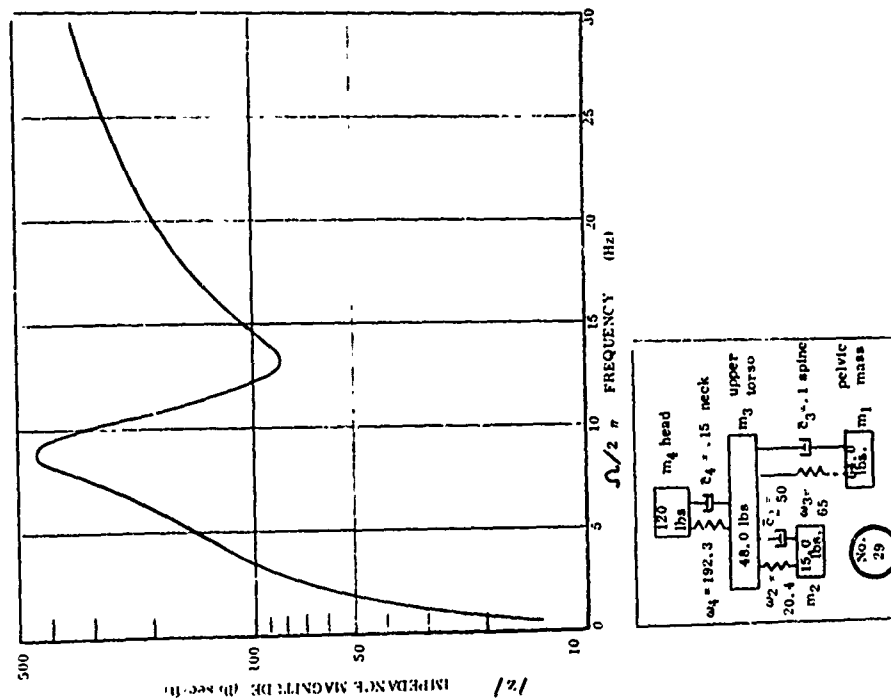


Figure 58. Mechanical Impedance of the Four Degree of Freedom Model with the Buttock Spring and Damper Shorted Out

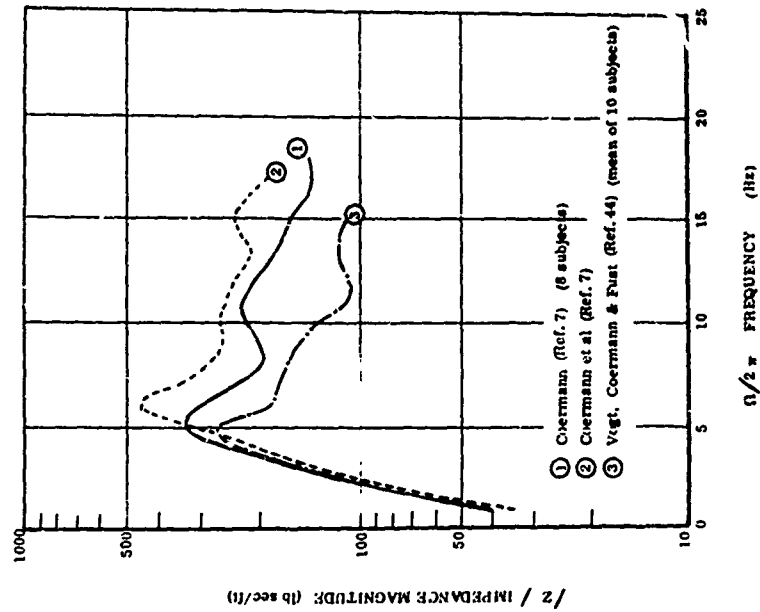


Figure 59. Average Experimentally Measured Impedance of Seated Human Subject Under 1 g Conditions

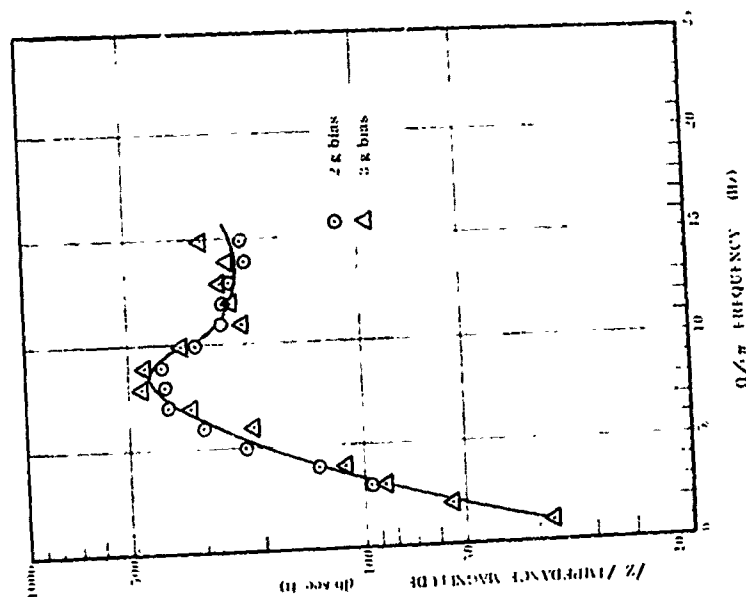


Figure 60. Inferred Experimental Data Points for the Impedance Measurements of Vogt, Coermann and Fust[44] under 2 g and 3 g bias.

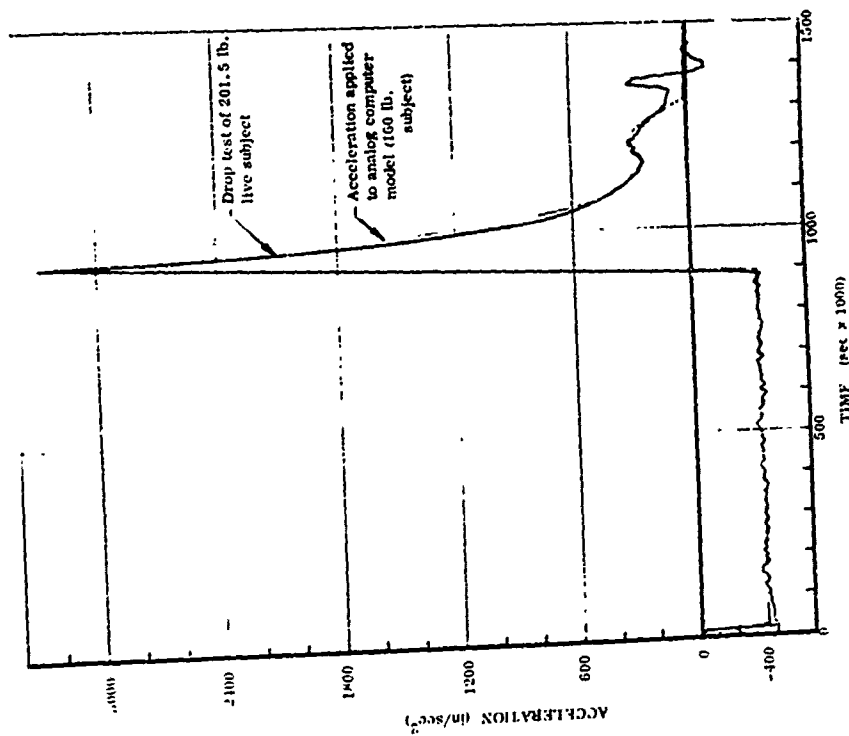


Figure 61. Acceleration Measured During Drop Test of Live Subject on the AMRL Vertical Deceleration Facility

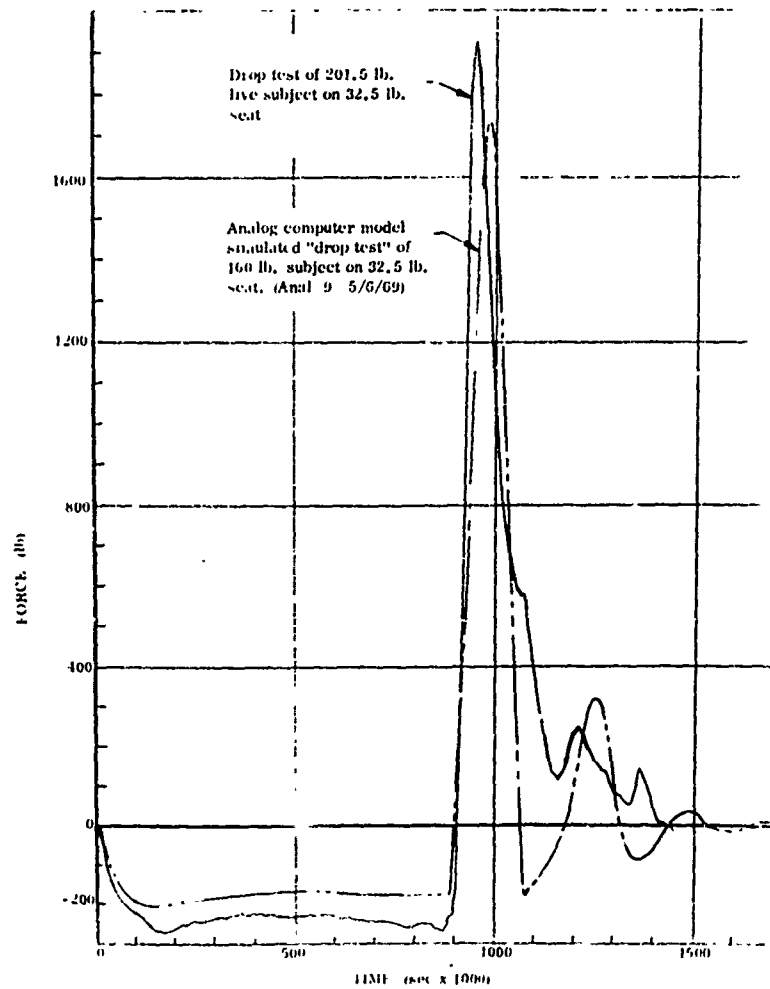


Figure 62. Comparison of Measured and Theoretically Calculated Force on Live Subject During a Drop Test



Let us consider for a moment the reports reviewed in the effort to construct a better dynamic model of the spine. In each case the investigator was interested in the dynamic properties of a biological structure, usually one or more vertebrae and/or intervertebral discs - meaning that he primarily wanted to measure force against deflection at different strain rates, and observe at what load failure occurred. We might expect such a task to be assigned to a materials test engineer, experienced in viscoelastic material testing, with a biologist, a dynamicist, and a statistician acting as consultants. In fact, more of the vertebral experiments seem to have been carried out by biologists, after being briefed on the operation of a compressive testing machine, by a not-very-interested materials man. The dynamicist was rarely consulted! The experimental results obtained in this way are often worthless. (Personally, I do not find this too surprising. As an engineer, I doubt I should be able to perform even a routine appendectomy after receiving only a casual description of what to look for and how to cut it off!)

The earliest spinal work reviewed here was that of Messerer (1880). He restricted himself to reporting the failing load of individual vertebrae, and his results agree well with the best modern data, where the latter is available for comparison. One concludes that his specimens were properly prepared (trued-off, filled with plaster or discs left in place) so that they fitted into a compression testing machine without developing spurious, test-induced stresses. Reporting procedure a hundred years ago was not as formalized as it is today, unfortunately, so that Messerer did not record his test techniques. If he had, perhaps Perey, seventy-five years later, would not have made the mistake of putting irregularly shaped vertebrae straight into the jaws of his compression tester.

Next came Geertz (1943), an engineer. Because he was in the middle of World War II Geertz was probably in a hurry, needing data to solve the problem of how much acceleration would be tolerated by an ejection seat occupant. He made very few mistakes, nevertheless, and his data on breaking strength is certainly the most comprehensive available, and probably also the most reliable. With a good grasp of the physical picture he was also able to apply his results to the steady state acceleration problem, and predict tolerance levels which we would not quarrel with today. His only failing was in dynamics. Here he calculated a much too low critical velocity change (4.2 ft/sec) from a velocity change spike which had caused injury when superimposed on a large acceleration pulse, and using an erroneous method of analysis to boot. His dynamical naivete also caused him to originate, so far as we can tell, the famous "rate of onset" ( $d^3y/dt^3$ ) fallacy which so bedeviled biodynamics in the postwar era.\* But one one is perfect, particularly when the pressure is on, and Geertz was clearly an outstanding pioneer in biodynamics.

---

\* Despite Routh's [35] much earlier observation, "We notice that the velocity and acceleration are dynamical names for the first and second differential coefficients of (distance)  $s$  with regard to the independent variable  $t$  (time). If the third differential coefficient were required, we should use some such name as the hyper-acceleration, but this extension is not necessary to dynamics."

In 1951, Virgin noted that "the highly resilient elastic nature of the vertebral column is provided by the intervertebral discs, which constitute one-third of the whole length of the column." Virgin showed that compression and relaxation of a disc gave a hysteresis loop on a plot of load against deflection, something which is characteristic of viscoelastic materials, of course. He did not record compression rate, however, so that his data cannot be used to estimate the strain rate dependency.

Hirsch and Nachemson in 1954, and Hirsch in 1955, studied discs supported by half vertebrae on either side. They did not repeat Virgin's discovery of hysteresis, but did note that a loaded disc took a long time to reach equilibrium (Fig. 39).

They also noted that when a compressive load was applied to a disc it was squashed down by the load ("compressed") and at the same time bulged out sideways; behavior which they explained by describing the disc as a fluid-filled bag.

Hirsch and Nachemson pre-loaded a specimen with a large mass on top of it and impulsively excited it by dropping a weight on the mass. Not surprisingly, with the vertebrae and disc column supporting it as a spring, the mass vibrated up and down after such excitation, and naturally, the disc bulged in and out at the same frequency. The frequency, of course, should be given by

$$\text{frequency in rad/sec}^* = \sqrt{\frac{\text{specimen stiffness}}{\text{mass}}} - (\text{a damping term})$$

Increasing the pre-loading mass reduced both the frequency and the apparent damping of these oscillations, as we would expect from elementary single degree of freedom lumped parameter theory. Hirsch and Nachemson seem to be quite unaware of this simple explanation of why the disc "bulged in and out" after an impulsive loading, however. Here are some of their conclusions:

"3. The mechanical behavior of the disc differs according to how fast the stresses set in. If a disc is kept loaded a certain amount of compression occurs until an equilibrium is reached. If a disc is subjected to a short momentary load it starts to oscillate. (Our emphasis.)

"7. If the disc is under load and has assumed an equilibrium and is then subjected to an increasing strain for a short period of time, it resumes the form it had before the additional load was brought on. The disc has the power of adaptation to mechanical stresses. However, the greater the load applied, the less will be the capacity for shock absorbing.

---

\* This equation is an oversimplification, since they used a beam to apply the load with a mechanical advantage, as shown in Figure 40. The natural frequency of the mass on the end of the beam was 5 - 15 cps.

"8. When an intervertebral disc is subject to rapidly acting forces it starts to oscillate. (Our emphasis.)

"9. Oscillations have been registered while the disc has been under a static load from 10 to 130 kg. This means that, even if a disc has reached a static equilibrium, additional rapid forces can increase deformations to a very great extent, even if these forces are relatively small. Because the deformations occur frequently during a short period of time (tenths of seconds), this means a hitherto unknown stress of considerable magnitude.

"10. The smallest trauma can produce great stress in the low back if the force acts rapidly. The changes in shape in a disc are of such intensity and frequency that it is hardly believable that muscular reaction can stabilize and protect a back from these variations in form. They are entirely due to the biophysical construction of the disc material itself.

#### "DISCUSSION"

"It has previously been considered that, in consequence of its solid construction, an intervertebral disc reacted slowly, that it could be compressed or could change shape, relatively speaking, fairly gradually. Further, it was assumed that, having reached a certain equilibrium, it retained that position until the strain upon it was relaxed. The intervertebral disc was said to have what was called an elastic quality, a fact which our investigations described here have confirmed. The disc has a capacity for statically adjusting itself to different mechanical demands.

"In addition, however, to these slow ways of reacting there are also extremely rapid changes in form, oscillations which arise quite irrespective of the point of static equilibrium at which the disc may find itself. Thus an intervertebral disc represents a dynamic system in which the disc's mass is constantly in motion. Even very small rapidly exerted strains induce shiftings of the mass that are measurable in tenths of a millimetre. Measurements of the movements of the disc with a greater degree of accuracy show that those forces which are required in order to induce such rapid movements at all may be extremely small. Seeing that the body is never in a, mechanically speaking, absolute state of rest, we cannot expect that any such state of rest will arise in an intervertebral disc either. The more frequently the strains are brought to bear, the higher the frequency of the oscillations.

"We are here concerned with biomechanical phenomena, or changes in tension, in the material which occur within fractions of a second - phenomena that are merely a consequence of the physical

properties of the material. It has been possible to register movements that are far more rapid than we have previously had any cause to take into account.

"It is possible, indeed probable, that other tissues also show similar conditions ..."

It seems obvious that these conclusions would have been modified if the research team had included a dynamicist, and that a test engineer would have modified the experimental techniques to give much more valuable data.

Two years later, in 1957, Perey reported his well-known series of experiments. As mentioned earlier in this paper, his static strength and stiffness data appears to be of little value, presumably because the sections were placed in the jaws of the testing machine without any attempt at "trueing-off" the irregular end-plates to avoid stress concentrations. His "dynamic tests" measured nothing at all, since he had no way of measuring the forces developed in the specimen. (Perey refers to a "calculated force" of so many Kg for "approximately .006 seconds" but his method of calculation has so far eluded us and we do not believe his numbers. Also, they are rather more than twice the failing loads which he reports from static testing.) Of course, it is possible that biologists may be able to glean information from his illustrations of vertebrae fractured at these high strain rates, in comparison with "static" failures.

Lest it be thought that, as an engineer, I am unfairly singling out biologists, I will conclude this critical review of experimental vertebral studies with an unauthored Technology Incorporated report (1967). The investigators decided to check out their equipment by measuring the modulus of elasticity of known materials, before commencing tests with vertebral sections. Using blocks of aluminum and pine they measured moduli of  $3.4 \times 10^6$  and  $0.26 \times 10^6$  lb/in<sup>2</sup> respectively, or about one-third and one-sixth of the correct values. One is, therefore, completely up in the air as to whether the figures quoted for vertebral stiffness can be believed. Additionally, the data is mostly reported as strain, without the load or deflection being specified, and modulus, without any dimensions. Finally, the rate of compression is given as strain rate, without any dimensions which would permit one to convert back to absolute compression rate.

#### An Appeal for Data

In 1970 we still do not know what the stiffness of a vertebral body is. We have a fair idea of the stiffness when the end-plates are capped with plaster, but suspect that this figure is much higher than is appropriate to nature, because much of the deflection occurs in the end-plates.

Much of this paper is taken up with a description of rather torturous analyses which have been made in an attempt to recover some information from

properties of the material. It has been possible to register movements that are far more rapid than we have previously had any cause to take into account.

"It is possible, indeed probable, that other tissues also show similar conditions . . ."

It seems obvious that these conclusions would have been modified if the research team had included a dynamicist, and that a test engineer would have modified the experimental techniques to give much more valuable data.

Two years later, in 1957, Perey reported his well-known series of experiments. As mentioned earlier in this paper, his static strength and stiffness data appears to be of little value, presumably because the sections were placed in the jaws of the testing machine without any attempt at "trueing-off" the irregular end-plates to avoid stress concentrations. His "dynamic tests" measured nothing at all, since he had no way of measuring the forces developed in the specimen. (Perey refers to a "calculated force" of so many Kg for "approximately .006 seconds" but his method of calculation has so far eluded us and we do not believe his numbers. Also, they are rather more than twice the failing loads which he reports from static testing.) Of course, it is possible that biologists may be able to glean information from his illustrations of vertebrae fractured at these high strain rates, in comparison with "static" failures.

Lest it be thought that, as an engineer, I am unfairly singling out biologists, I will conclude this critical review of experimental vertebral studies with an unauthored Technology Incorporated report (1967). The investigators decided to check out their equipment by measuring the modulus of elasticity of known materials, before commencing tests with vertebral sections. Using blocks of aluminum and pine they measured moduli of  $3.4 \times 10^6$  and  $0.26 \times 10^6$  lb/in<sup>2</sup> respectively, or about one-third and one-sixth of the correct values. One is, therefore, completely up in the air as to whether the figures quoted for vertebral stiffness can be believed. Additionally, the data is mostly reported as strain, without the load or deflection being specified, and modulus, without any dimensions. Finally, the rate of compression is given as strain rate, without any dimensions which would permit one to convert back to absolute compression rate.

#### An Appeal for Data

In 1970 we still do not know what the stiffness of a vertebral body is. We have a fair idea of the stiffness when the end-plates are capped with plaster, but suspect that this figure is much higher than is appropriate to nature, because much of the deflection occurs in the end-plates.

Much of this paper is taken up with a description of rather torturous analyses which have been made in an attempt to recover some information from

incompletely reported experiments which were never intended to yield data of this type in the first place. We have attempted to deduce the damping coefficient of the spine from Perey's "dynamic" experiments in which he measured nothing at all, other than the number of vertebrae which suffered fractures. We have also attempted to deduce damping and stiffness from the microscopic traces reproduced by Hirsch and Nachemson, putting aside the discouraging thought that the test apparatus had resonances in the same range as the frequencies being measured, so that the analysis cannot be very inaccurate. In these and other cases the process of trying to extract useful data from the experimental reports often reads like something from the pen of Conan Doyle, and it is clear that none of this would be needed if a suitable number of the right experiments were performed correctly. The experimental methods required are obvious from the preceding discussion and the need for them is equally obvious. Surely all we need to do now is divert some money from more esoteric investigations and get on with performing the experiments.

©

## APPENDIX A

### IMPACT RESPONSE OF A SYSTEM WITH $q$ SPRINGS AND $p$ DAMPERS IN SERIES

# IMPACT RESPONSE OF A SYSTEM WITH $q$ SPRINGS AND $p$ DAMPERS IN SERIES\*

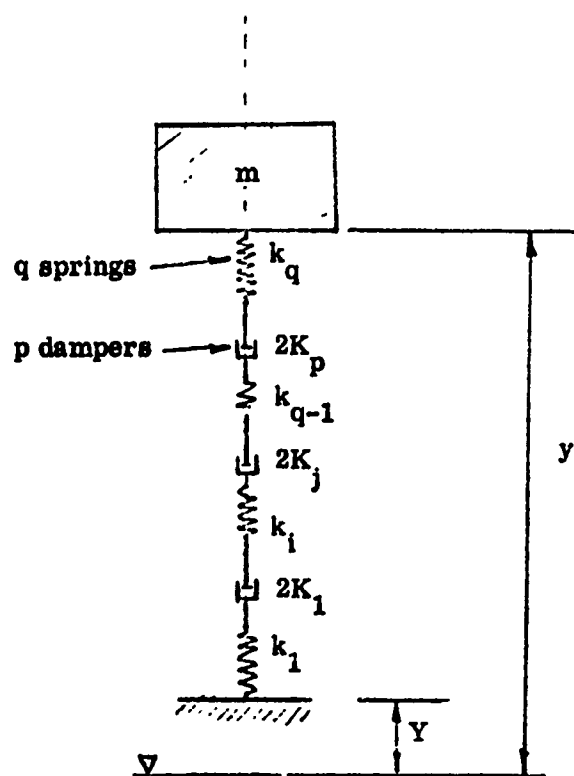


Figure A1. System Geometry

Figure A1 shows a system of a single mass  $m$ ,  $p$  dampers, each with an individual damping coefficient  $2K_j$ , initial length  $l_{D_j}$  and deflection  $\delta_{D_j}$  and  $q$  springs, each with an individual spring constant  $k_i$ , initial lengths  $l_{S_i}$  and deflections  $\delta_{S_i}$ . The spring and dampers are considered to be massless, so that the force  $F(t)$  in each element is equal:

$$F = F_S = F_D$$

The relationships between the length, deflections and overall  $y$  ordinates are given in equation (1):

$$y = y_o + \sum_{j=1}^p l_{D_j} + \sum_{i=1}^q l_{S_i} - \sum_{j=1}^p \delta_{D_j} - \sum_{i=1}^q \delta_{S_i} \quad (1)$$

\*This appendix is taken from Wyle Laboratories Working Paper 59111-10, 1 Oct. 1970.



$$\therefore \delta D_i = \frac{F}{2K_j}$$

$$\begin{aligned} \delta D_j &= \int \frac{F}{2K_j} dt \\ &= \frac{1}{2K_j} \int F dt \end{aligned} \quad (2)$$

Similarly  $F = K_i \delta s_i$  and is equal for each spring

$$\therefore \delta S_i = \frac{F}{k_i} \quad (3)$$

Substituting in (1) from (2) and (3)

$$y = Y + \sum_{j=1}^p \ell_{D_j} + \sum_{i=1}^q \ell_{S_i} - \left( \int F dt \right) \sum_{j=1}^p \frac{1}{2K_j} - F \sum_{i=1}^q \frac{1}{k_i} \quad (4)$$

Differentiating (4) with respect to t:

$$\dot{y} = \dot{Y} - \left[ \sum_{j=1}^p \frac{1}{2K_j} \right] F - \left[ \sum_{i=1}^q \frac{1}{k_i} \right] \frac{dF}{dt} \quad (5)$$

putting  $F = m \ddot{y}$  and assuming  $\dot{Y} = 0$  and rearranging we have (6)

$$\ddot{y} + \left[ \frac{\sum_{j=1}^p \frac{1}{2K_j}}{\sum_{i=1}^q \frac{1}{k_i}} \right] \ddot{y} + \left[ \frac{1}{m \sum_{i=1}^q \frac{1}{k_i}} \right] \dot{y} = 0$$

This is a differential equation of the familiar form:

$$\frac{d^2(\dot{y})}{dt^2} + 2c \frac{d(\dot{y})}{dt} + \omega^2(\dot{y}) = 0 \quad (7)$$

where

$$\begin{aligned} 2c &= \frac{\sum_{j=1}^p \frac{1}{2K_j}}{\sum_{i=1}^q \frac{1}{k_i}} \\ \text{and } \omega^2 &= \left[ \frac{1}{m \sum_{i=1}^q \frac{1}{k_i}} \right] \end{aligned} \quad (8)$$

Note that if all the spring constants are equal ( $=k$ ) and all the damping coefficients are equal ( $=K$ ) then:

$$\text{and } \left. \begin{aligned} 2c &= \frac{pk}{2qK} \\ \omega^2 &= \frac{k}{mq} \end{aligned} \right\} \quad (9)$$

Further, if only one spring  $k'$  and damper  $K'$  were used then  $p = q = 1$  and:

$$\text{and } \left. \begin{aligned} 2c &= \frac{k'}{2K'} \\ \omega^2 &= \frac{k'}{m} \end{aligned} \right\} \quad (10)$$

so that we may treat the multiple spring/damper case as a single spring/damper system with the following characteristics [compare (9) and (10)]:

$$\text{and } \left. \begin{aligned} k' &= 1 / \sum_{i=1}^q (1/k_i) \\ 2K' &= 1 / \sum_{j=1}^p (1/2K_j) \end{aligned} \right\} \quad (11)$$

Thus the solution for equation (7) is generally true for all such systems regardless of the individual values of  $p$ ,  $q$ ,  $k_i$ , and  $K_j$  by making the substitutions shown in (10) and (11). The solution to equation (7) is:

$$\frac{\dot{y}}{\dot{y}_0} = e^{-ct} \left( \cos \lambda t + \frac{c}{\lambda} \sin \lambda t \right) \quad (12)$$

$$\text{where } \lambda^2 = \omega^2 - c^2$$

It should be noted that  $\lambda$  may be real, zero, or imaginary, corresponding to a damped oscillation, critical damping, or a supercritical damped motion respectively. Equation (12) may be rewritten:

$$\frac{\dot{y}}{\dot{y}_0} = e^{-ct} \cos \left( \lambda t - \cos^{-1} \frac{\lambda}{\omega} \right) \quad (13)$$

From equation (13)  $\dot{y} = 0$  if  $t = t'_n$ , where  $t'_n$  is given by:

$$\left. \begin{aligned} \lambda t'_n &= \left( \frac{2n+1}{2} \right) \pi + \cos^{-1} \frac{\lambda}{\omega} \\ \text{or} \quad &= \left( \frac{2n+1}{2} \right) \pi + \sin^{-1} \frac{c}{\omega} \end{aligned} \right\} \quad (14)$$

$$\text{where } \bar{c} = \frac{c}{\omega}$$

The values for  $t'_n$  from (14) give the value of  $t$  for maximum deflections  $y_{\max_n}$ .

From equation (13) we have:

$$\left. \begin{aligned} y &= \frac{-\dot{y}_0 e^{-ct}}{\omega^2} \left( 2c \cos \lambda t - \left( \frac{\lambda^2 - c^2}{\lambda} \right) \sin \lambda t \right) \\ \dot{y} &= \dot{y}_0 e^{-ct} \left( \cos \lambda t + \frac{c}{\lambda} \sin \lambda t \right) \\ \ddot{y} &= \frac{-\dot{y}_0 e^{-ct}}{\lambda} (\omega^2 \sin \lambda t) \end{aligned} \right\} \quad (15)$$

Initial values when  $t = 0$  are:

$$y_0 = - \frac{2c\dot{y}_0}{\omega^2}$$

$$\dot{y}_0 = \dot{y}_0$$

$$\ddot{y}_0 = 0$$

and the final values when  $t \rightarrow \infty$  are:

$$y_\infty \rightarrow 0$$

$$\dot{y}_\infty \rightarrow 0$$

$$\ddot{y}_\infty \rightarrow 0$$

By substituting the value for  $t'$  from (14) in the equation for  $y$  in (15), the maximum values of the deflection  $y$  are obtained

$$y_{\max_n} = - (-1)^n \frac{\dot{y}_0}{\omega} e^{-\frac{c}{\lambda} \left( \frac{2n+1}{2} \pi + \sin^{-1} \bar{c} \right)}$$

Similarly the acceleration  $\ddot{y}$  (and consequently the force  $F$ ) have maximum values when  $\ddot{y} = 0$ . This may be shown to occur at time  $t''_n$  given by:

$$\lambda t''_n = \frac{2n+1}{2} \pi - \sin^{-1} \bar{c}$$

and the corresponding maximum values for the acceleration are.

$$\ddot{y}_{\max_n} = - (-1)^n y_0 \omega e^{-\frac{c}{\lambda} \left( \frac{2n+1}{2} \pi - \sin^{-1} \bar{c} \right)}$$

Expressed in nondimensional terms equations (15) for the sub-critically damped case where  $\lambda > 0$  and  $\bar{c} < 1$  become:

$$\left. \begin{aligned} \left( \frac{\ddot{y}}{\dot{y}_0 \omega} \right) &= -e^{-\tau} \left( 2\bar{c} \cos \sqrt{\frac{1-\bar{c}^2}{\bar{c}^2}} \tau + \frac{2\bar{c}^2-1}{\sqrt{1-\bar{c}^2}} \sin \sqrt{\frac{1-\bar{c}^2}{\bar{c}^2}} \tau \right) \\ \left( \frac{\dot{y}}{\dot{y}_0} \right) &= e^{-\tau} \left( \cos \sqrt{\frac{1-\bar{c}^2}{\bar{c}^2}} \tau + \frac{\sqrt{\bar{c}^2}}{1-\bar{c}^2} \sin \sqrt{\frac{1-\bar{c}^2}{\bar{c}^2}} \tau \right) \\ \left( \frac{\ddot{y}}{\dot{y}_0 \omega} \right) &= -e^{-\tau} \left( \frac{\sin \sqrt{\frac{1-\bar{c}^2}{\bar{c}^2}} \tau}{\sqrt{1-\bar{c}^2}} \right) \end{aligned} \right\} \quad (16)$$

where  $\tau = ct$

The maximum values for  $y$  and  $\dot{y}$  in equation (16) are given by:

$$\begin{aligned} \left( \frac{y_{\max}}{\dot{y}_0 \omega} \right) &= -(-1)^n e^{-\frac{\bar{c}}{\sqrt{1-\bar{c}^2}} \left( \frac{\pi}{2} + \sin^{-1} \bar{c} \right)} \\ \text{when } \tau' &= \frac{\left( \frac{2n+1}{2} \right) \pi + \sin^{-1} \bar{c}}{\sqrt{\frac{1-\bar{c}^2}{\bar{c}^2}}} \\ \text{and } \left( \frac{\dot{y}_{\max}}{\dot{y}_0 \omega} \right) &= -(-1)^n e^{-\frac{\bar{c}}{\sqrt{1-\bar{c}^2}} \left( \frac{\pi}{2} - \sin^{-1} \bar{c} \right)} \\ \text{when } \tau'' &= \frac{\left( \frac{2n+1}{2} \right) \pi - \sin^{-1} \bar{c}}{\sqrt{\frac{1-\bar{c}^2}{\bar{c}^2}}} \end{aligned}$$

In the special critically damped case where  $\bar{c} = 1$  then equations (16) become:

$$\left. \begin{aligned} \left( \frac{y}{\dot{y}_0 \omega} \right) &= -e^{-\tau} (2 + \tau) \\ \left( \frac{\dot{y}}{\dot{y}_0} \right) &= e^{-\tau} (1 + \tau) \\ \left( \frac{\ddot{y}}{\dot{y}_0 \omega} \right) &= -\tau e^{-\tau} \end{aligned} \right\} \quad (17)$$

and  $\left( \frac{\ddot{y}_{\max}}{\dot{y}_0 \omega} \right) = -\frac{1}{e}$  when  $\tau'' = 1$

there is no maximum deflection in this case and the deflection and velocity slowly subside to zero when  $\tau \rightarrow \infty$ .

For the supercritically damped case of  $\bar{c} > 1$  equations (16) become:

$$\left. \begin{aligned} \left( \frac{\dot{y}}{y_0 w} \right) &= -e^{-\tau} \left( 2\bar{c} \cosh \frac{\sqrt{\bar{c}^2 - 1}}{\bar{c}^2} \tau + \frac{(2\bar{c} - 1)}{\sqrt{\bar{c}^2 - 1}} \sinh \frac{\sqrt{\bar{c}^2 - 1}}{\bar{c}^2} \tau \right) \\ \left( \frac{\dot{y}}{y_0} \right) &= e^{-\tau} \left( \cosh \frac{\sqrt{\bar{c}^2 - 1}}{\bar{c}^2} \tau + \frac{\sqrt{\bar{c}^2 - 1}}{\bar{c}^2 - 1} \sinh \frac{\sqrt{\bar{c}^2 - 1}}{\bar{c}^2} \tau \right) \\ \left( \frac{\ddot{y}}{y_0 w} \right) &= -e^{-\tau} \frac{\sinh \frac{\sqrt{\bar{c}^2 - 1}}{\bar{c}^2} \tau}{\sqrt{\bar{c}^2 - 1}} \\ \left( \frac{\ddot{y}_{\max}}{y_0 w} \right) &= -e^{-\tau''} \frac{\sinh \frac{\sqrt{\bar{c}^2 - 1}}{\bar{c}^2} \tau''}{\sqrt{\bar{c}^2 - 1}} \text{ where } \tau'' = \frac{1}{2} \left[ \ln \left( \frac{1 + \sqrt{(\bar{c}^2 - 1)/\bar{c}^2}}{1 - \sqrt{(\bar{c}^2 - 1)/\bar{c}^2}} \right) \right] \end{aligned} \right\} (18)$$

which also reverts to the values shown in equations (17) when  $\bar{c} \rightarrow 1$  and, as expected, there is no maximum value of  $y$ .

Expressed in terms of exponentials, equations (18) become:

$$\left. \begin{aligned} \left( \frac{\dot{y}}{y_0 w} \right) &= - \left( \bar{c} + \frac{2\bar{c}^2 - 1}{2\sqrt{\bar{c}^2 - 1}} \right) e^{-\left(1 - \frac{\sqrt{\bar{c}^2 - 1}}{\bar{c}^2}\right)\tau} - \left( \bar{c} - \frac{2\bar{c}^2 - 1}{2\sqrt{\bar{c}^2 - 1}} \right) e^{-\left(1 + \frac{\sqrt{\bar{c}^2 - 1}}{\bar{c}^2}\right)\tau} \\ \left( \frac{\dot{y}}{y_0} \right) &= \left( \frac{1}{2} + \frac{1}{2} \frac{\sqrt{\bar{c}^2 - 1}}{\bar{c}^2 - 1} \right) e^{-\left(1 - \frac{\sqrt{\bar{c}^2 - 1}}{\bar{c}^2}\right)\tau} - \left( \frac{1}{2} - \frac{1}{2} \frac{\sqrt{\bar{c}^2 - 1}}{\bar{c}^2 - 1} \right) e^{-\left(1 + \frac{\sqrt{\bar{c}^2 - 1}}{\bar{c}^2}\right)\tau} \\ \left( \frac{\ddot{y}}{y_0 w} \right) &= \frac{1}{2\sqrt{\bar{c}^2 - 1}} \left( e^{-\left(1 + \frac{\sqrt{\bar{c}^2 - 1}}{\bar{c}^2}\right)\tau} - e^{-\left(1 - \frac{\sqrt{\bar{c}^2 - 1}}{\bar{c}^2}\right)\tau} \right) \end{aligned} \right\} (19)$$

For all the cases described by equations (16), (17), (18), and (19), the initial and final values are as follows.

when  $\tau = 0$

$$\left(\frac{\dot{y}}{\dot{y}_0 \omega}\right)_0 = -2\bar{c}$$

$$\left(\frac{\ddot{y}}{\ddot{y}_0}\right)_0 = 1$$

$$\left(\frac{\ddot{\dot{y}}}{\ddot{\dot{y}}_0 \omega}\right)_0 = 0$$

(20)

and when  $\tau \rightarrow \infty$

$$\left(\frac{y}{\dot{y}_0 \omega}\right)_\infty = \left(\frac{\dot{y}}{\dot{y}_0}\right)_\infty = \left(\frac{\ddot{y}}{\ddot{\dot{y}}_0 \omega}\right)_\infty \rightarrow 0$$

Figures A2 to A5 show non-dimensional time histories of displacement ( $y \omega / \dot{y}_0$ ), velocity ( $\dot{y} / \dot{y}_0$ ) and acceleration ( $\ddot{y} / \ddot{\dot{y}}_0 \omega$ ) for a range of damping coefficients from 0.25 to 2.0. The maximum acceleration ( $\ddot{y}_{max} / \dot{y}_0 \omega$ ) and the time at which this maximum occurs are plotted against damping ratio in Figure A6. The relationship between the amplitude of successive cycles and the damping ratio  $\bar{c}$  is shown in Figure A7, and Figure A8 shows the required values of  $K / \sqrt{mk}$  to obtain a range of damping ratios  $\bar{c}$  for each of the series and parallel spring/damper systems. It is interesting to note to obtain a  $\bar{c} = .5$ , the components of the parallel and series systems are interchangeable.

The principal characteristics of the two systems are given in Table A1. These formulae are used in the main body of the report to analyze the experimental data of Hirsch and Nachemson.

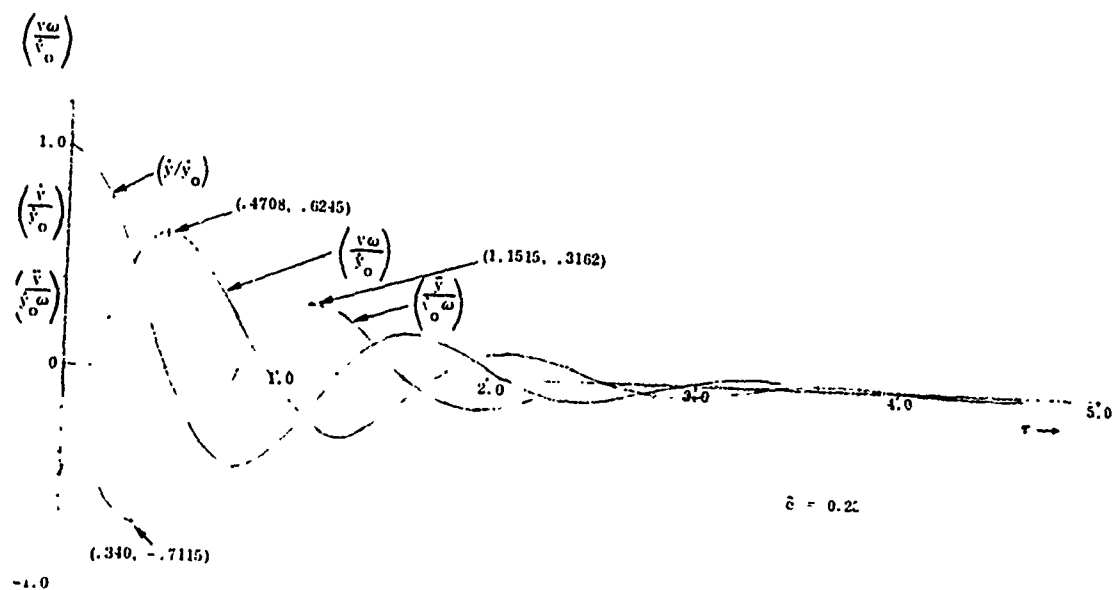


Figure A2. Non-Dimensional Time History of Subcritically Damped Motion ( $\bar{c} = 0.25$ )

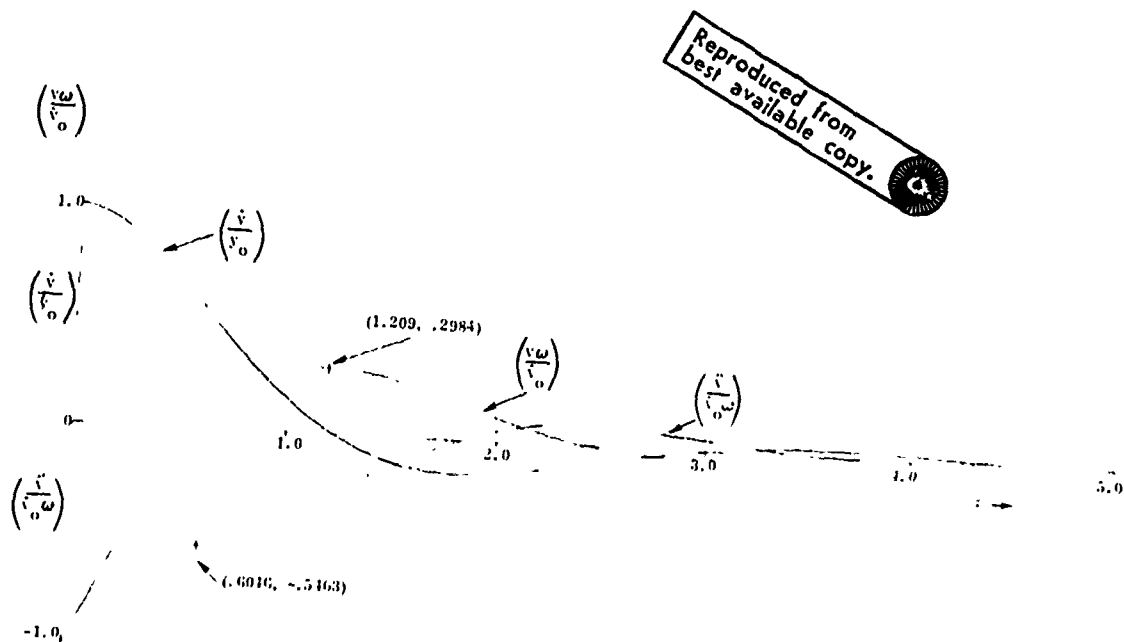
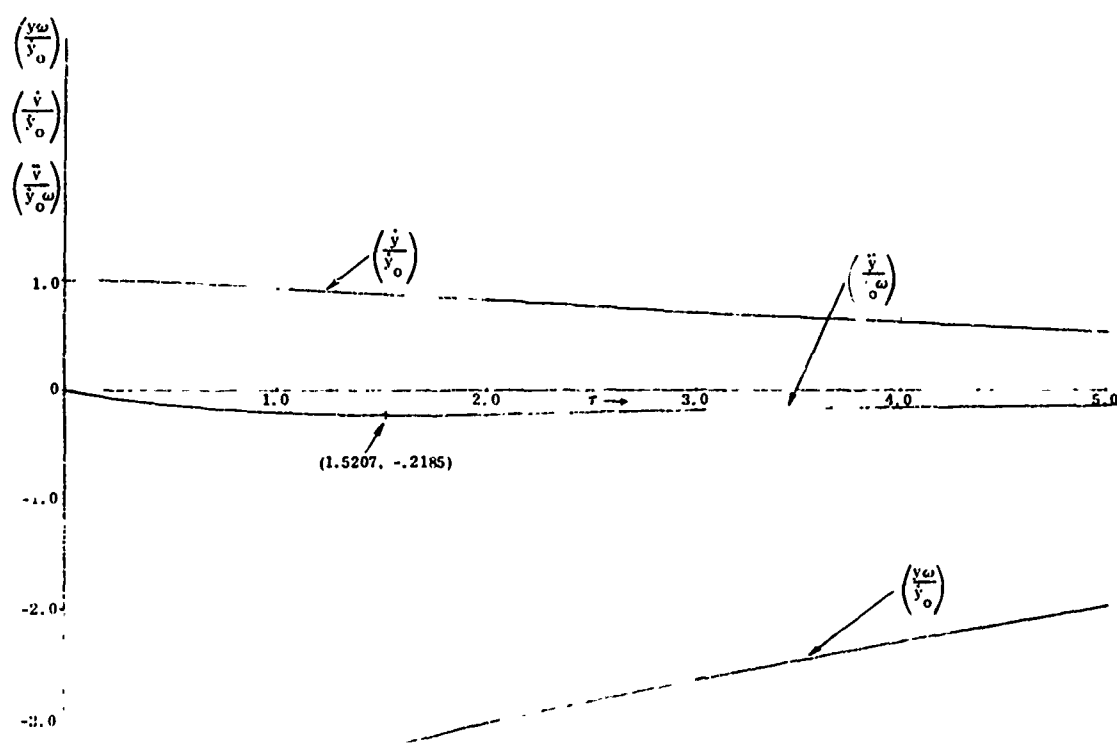
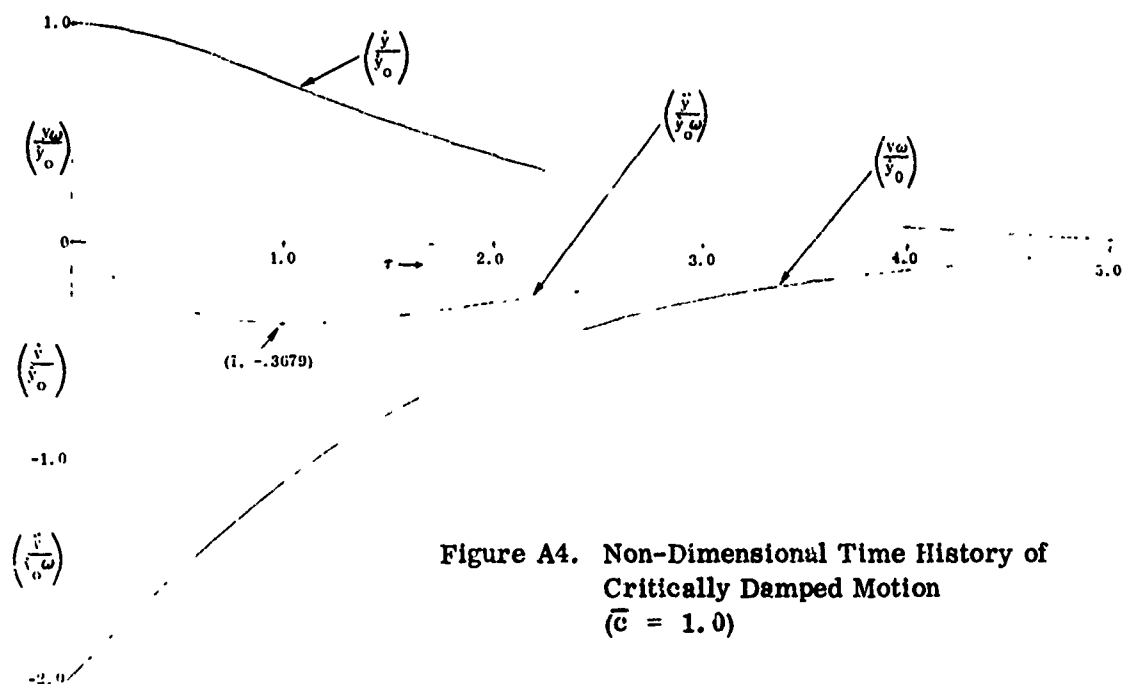


Figure A3. Non-Dimensional Time History of Subcritically Damped Motion ( $\bar{c} = 0.5$ )





Reproduced from  
best available copy.

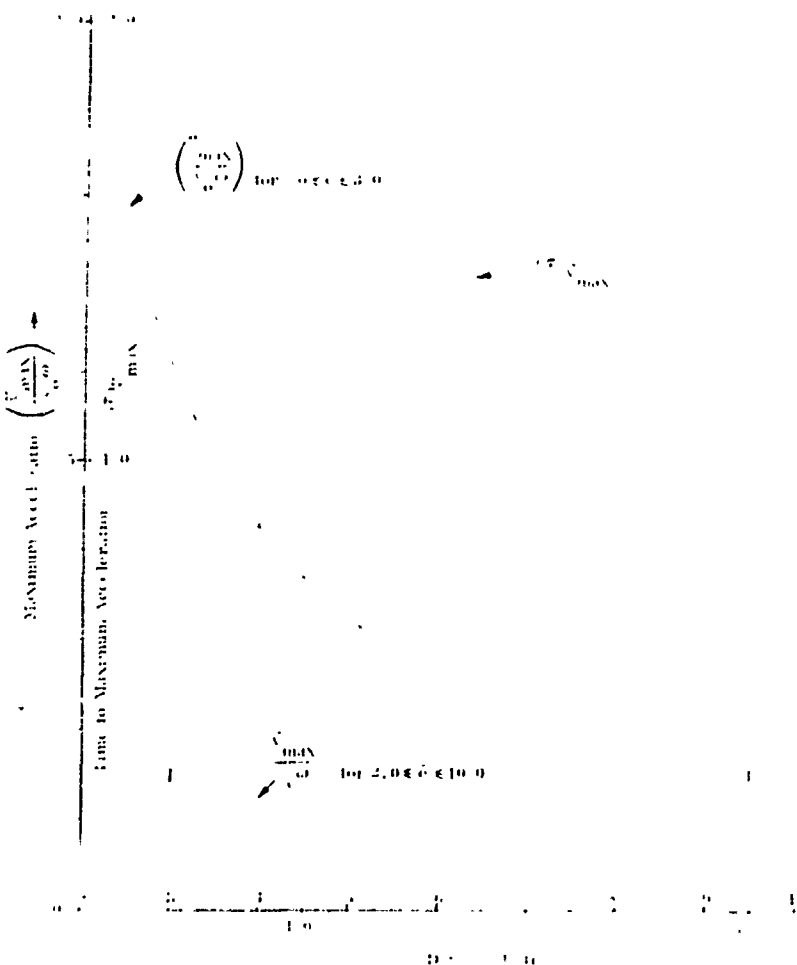


Figure A6. Variation of Maximum Acceleration and Time to Maximum Acceleration with Damping Ratio  $\bar{c}$

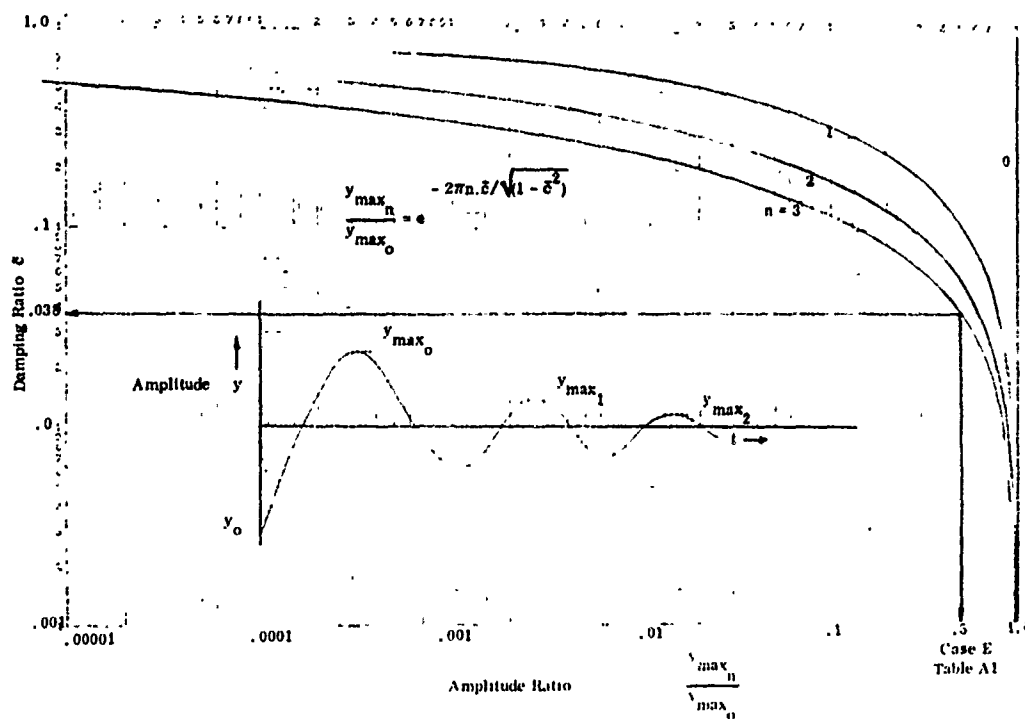


Figure A7. Relationship Between Amplitude and Damping Ratio

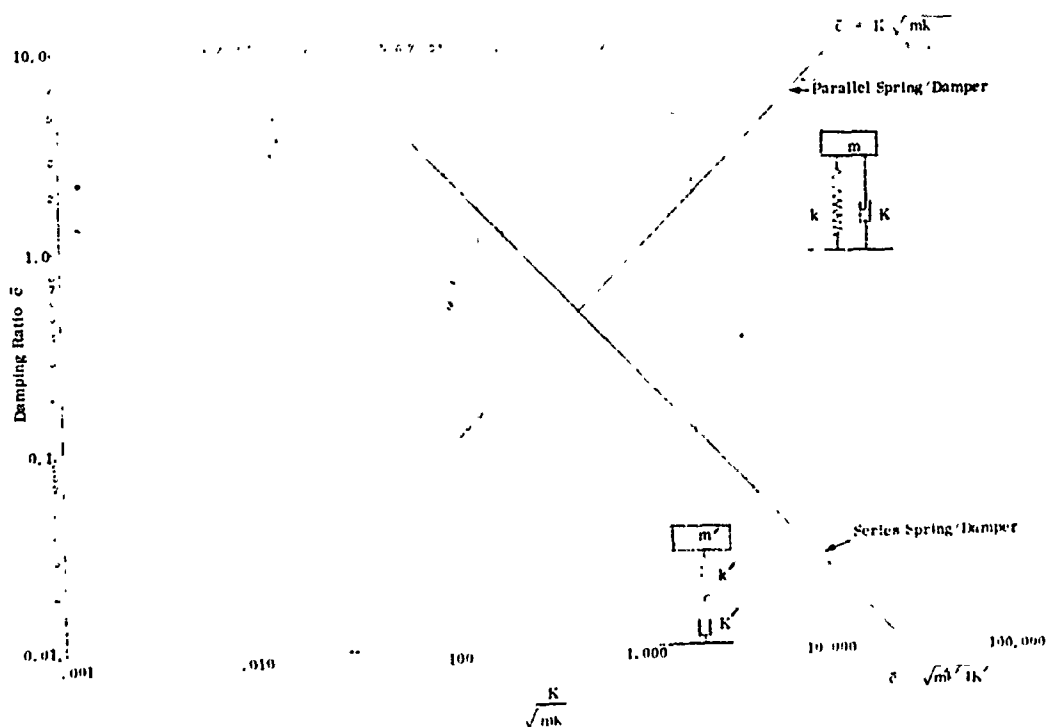


Figure A8. Equivalence of Parallel and Series Spring Damper Systems

Table A1. Comparison of Parallel and Series Spring Damper Models

		Parallel Spring/Damper	Series Spring/Damper
Equation of Motion		$\ddot{y} + 2c\dot{y} + \omega^2 y = 0$ or $\ddot{y} + \frac{2K}{m}\dot{y} + \frac{k}{m}y = 0$	$\ddot{y} + 2c\dot{y} + \omega^2 y = 0$ or $\ddot{y} + \frac{k'}{2K}\dot{y} + \frac{k'}{m}y = 0$
Initial Conditions when $t = 0$	$y_0 =$  $\dot{y}_0 =$  $\ddot{y}_0 =$	$0$  $\dot{y}_0$  $-2c\dot{y}_0$	$-\frac{2c}{\omega^2} \dot{y}_0$  $\dot{y}_0$  $0$
Deflection	$y =$	$\frac{\dot{y}_0}{\lambda} e^{-ct} \sin \lambda t$ (from ref. A3)	$\frac{\dot{y}_0}{\lambda} e^{-ct} \sin (\lambda t - \theta')$ where $\theta' = \sin^{-1}(2c\lambda/\omega^2)$ (from eq. 15)
Velocity	$\dot{y} =$	$\dot{y}_0 e^{-ct} \frac{\omega}{\lambda} \sin (\theta' - \lambda t)$	$\dot{y}_0 e^{-ct} \frac{\omega}{\lambda} \sin (\theta' + \lambda t)$ where $\theta' = \sin^{-1}(\lambda/\omega)$
Acceleration	$\ddot{y} =$	$\dot{y}_0 e^{-ct} \frac{\omega^2}{\lambda} \sin (\lambda t - \theta')$	$\dot{y}_0 e^{-ct} \frac{\omega^2}{\lambda} \sin \lambda t$
Mass	$m$	$m$	$m'$
Natural Frequency	$\omega$	$\sqrt{k/m}$	$\sqrt{k'/m'}$
Spring Stiffness	$k$	$k = \omega^2 m$	$k' = \omega'^2 m' = k$
Damping Constant	$2c$	$2c$	$k'/2K' = k/2K'$ (see eq. 10)
Damping Coefficient	$2K$	$2K = 2cm$	$2K' = k m/2K = k/2c$
Damping Ratio	$\bar{c}$	$\bar{c} = c/\omega = K/\sqrt{km}$	$\bar{c} = \frac{c}{\omega} = \frac{k/4K'}{\sqrt{k'/m}} = \frac{\sqrt{k'm}}{4K'}$

Ref.A3. Shock & Vibration Handbook, Vol. 1, pp 2-2

Table A1. Comparison of Parallel and Series Spring Damper Models

		Parallel Spring/Damper	Series Spring/Damper
Equation of Motion		$\ddot{y} + 2c\dot{y} + \omega^2 y = 0$ or $\ddot{y} + \frac{2K}{m}\dot{y} + \frac{k}{m}y = 0$	$\ddot{y} + 2c\dot{y} + \omega^2 y = 0$ or $\ddot{y} + \frac{k'}{2K'}\dot{y} + \frac{k'}{m}y = 0$
Initial Conditions when $t = 0$	$y_0 =$  $\dot{y}_0 =$  $\ddot{y}_0 =$	$0$  $\dot{y}_0$  $-2c\dot{y}_0$	$-\frac{2c}{\omega^2} \dot{y}_0$  $\dot{y}_0$  $0$
Deflection	$y =$	$\frac{\dot{y}_0}{\lambda} e^{-ct} \sin \lambda t$ (from ref. A3)	$\frac{\dot{y}_0}{\lambda} e^{-ct} \sin (\lambda t - \theta')$ where $\theta' = \sin^{-1}(2c\lambda/\omega^2)$ (from eq. 15)
Velocity	$\dot{y} =$	$\dot{y}_0 e^{-ct} \frac{\omega}{\lambda} \sin (\theta' - \lambda t)$	$\dot{y}_0 e^{-ct} \frac{\omega}{\lambda} \sin (\theta' + \lambda t)$ where $\theta' = \sin^{-1}(\lambda/\omega)$
Acceleration	$\ddot{y} =$	$\dot{y}_0 e^{-ct} \frac{\omega^2}{\lambda} \sin (\lambda t - \theta')$	$\dot{y}_0 e^{-ct} \frac{\omega^2}{\lambda} \sin \lambda t$
Mass	$m$	$m$	$m'$
Natural Frequency	$\omega$	$\sqrt{k/m}$	$\sqrt{k'/m'}$
Spring Stiffness	$k$	$k = \omega^2 m$	$k' = \omega'^2 m' = k$
Damping Constant	$2c$	$2c$	$k'/2K' = k/2K'$ (see eq. 10)
Damping Coefficient	$2K$	$2K = 2cm$	$2K' = k m'/2K = k/2c$
Damping Ratio	$\bar{c}$	$\bar{c} = c/\omega = K \sqrt{km}$	$\bar{c} = \frac{c}{\omega} = \frac{k'/4K'}{\sqrt{k'/m}} = \frac{\sqrt{k'm}}{4K'}$

Ref. A3. Shock & Vibration Handbook, Vol. 1, pp 2-4

APPENDIX B

DETERMINATION OF THE PROBABLE DISTRIBUTION OF  
THE RATIO OF VERTEBRAL FAILING LOAD TO  
SUBJECT WEIGHT (F/W)

# DETERMINATION OF THE PROBABLE DISTRIBUTION OF THE RATIO OF VERTEBRAL FAILING LOAD TO SUBJECT WEIGHT (F/W)

Different sources of data for vertebral failing load, F, (Figures 20, 21, and 22) and for the weight, W, of Air Force personnel (Figures 7 and 8) have been analyzed to show that both of these sets of data may be represented fairly by normal distributions, or, rather more closely, by gamma distributions.

The object of this appendix will be to show how these two distributions can be compounded to provide a probable distribution of the ratio F/W. This can only be done by assuming that the F and W data refer to a statistically similar set of subjects.

It is not known whether there is any significant dependence of F on W so that a general case will be assumed, as shown in Figure B1, in which the distribution of F is represented on the vertical axis by the mean  $F_o$  and the standard deviation  $S_1$  and the distribution of W is represented on the horizontal axis by the mean  $W_o$  and the standard deviation  $S_2$ . A typical line of  $F/W = K_j$  (=constant) is represented by the line o u v. To allow the generality mentioned above, the mean line  $m_o = o$  with gradient  $g_1$  represents a line drawn through the mean of the F values in each elemental area width dw. If the two distributions of F and W may be assumed to be normal, then the data is distributed about the mean line with a standard deviation  $\sigma_1$  given by:

$$\sigma_1 = \sqrt{S_1^2 - \epsilon_1^2 S_2^2} \quad (\text{ref. B-1}) \quad (1)$$

Thus the gradient  $g_1$  defines the dependence of F on W. For example, if  $g_1 = 0$ , F is independent of W and the mean value of F is the same ( $F_o$ ) for all elemental areas dx, and  $\sigma_1 = S_1$ . If  $g_1 = S_1/S_2$  then F is directly dependent on W and all the data should be on a single line. The value of  $g_1$  cannot exceed  $S_1/S_2$ .

The Reference B-1 also shows that  $\sigma_1$  is constant for all values of W. Thus the mean line in Figure 1 is represented by:

$$m = m_o + g_1 x \quad (2)$$

and

$$F_o = m_o + g_1 W_o \quad (3)$$

---

Ref. B-1. E. G. U. Band, "Statistical Relationships for Analysis of Ship Stress Data," Webb Institute of Naval Architecture, July 25, 1965.

The probability  $\Omega(\frac{F}{W} > K_j)$  of  $\frac{F}{W}$  exceeding a particular value  $K_j$  is, therefore, given by the double integral representing the probability of lying in the area above the line  $o u v$  on Figure 31:

$$\Omega(\frac{F}{W} > K_j) = \int_{-\infty}^{\infty} (2\pi S_2^2)^{-\frac{1}{2}} \cdot e^{-\frac{(x-W_o)^2}{2S_2^2}} \int_{K_j x}^{\infty} (2\pi \sigma_1^2)^{-\frac{1}{2}} \cdot e^{-\frac{(y-F_o)^2}{2\sigma_1^2}} dy \cdot dx^* .$$

This integral can be calculated numerically without difficulty, but it also lends itself to a simplified treatment as a single two-dimensional elliptically-normal distribution. This two dimensional, elliptically-normal distribution is characterized by the parallelogram ABCD. Reference 1 shows how this elliptical distribution may be transformed to a simple, circular-normal distribution about the origin of a new set of axes  $X, Y$  by the transforming equations:

$$X = (x - W_o) / S_2 \quad (4)$$

$$Y = (y - m) / \sigma_1 \\ = (y - F_o - g(x - W_o)) / \sigma_1 \quad (5)$$

The standard deviation of the data about the  $X$  or  $Y$  axes, or any other diameter is now unity.

The problem of determining the probability of  $\frac{F}{W}$  exceeding  $K_j$ , is to determine the percentage of the data points lying above the line  $o u v$  in the  $x y$  plane, which will be identical to the percentage of data lying above the line  $o u v$  in the  $X Y$  plane. The coordinates of  $u$  and  $v$  in  $x y$  plane are given by:

\* In this development both distributions have been assumed to be normal. A similar treatment can be applied to the gamma distribution in which case:

$$\Omega(\frac{F}{W} > K_j) = \int_0^{\infty} x^{\alpha_1} e^{-x/\beta_1} / \left[ \Gamma(\alpha_1 + 1) \beta_1^{\alpha_1 + 1} \right] \int_{K_j x}^{\infty} y^{\alpha_2} e^{-y/\beta_2} / \left[ \Gamma(\alpha_2 + 1) \beta_2^{\alpha_2 + 1} \right] dy \cdot dx$$

$$\text{where } \beta_1 = S_1^2 / W_o \quad \text{and} \quad \beta_2 = S_2^2 / F_o$$

$$\alpha_1 = (W_o / S_1)^2 - 1 \quad \alpha_2 = (F_o / S_2)^2 - 1$$

This can be evaluated numerically.

$$x_v = W_o$$

$$y_v = K_j W_o$$

$$\frac{x_u}{W_o} = \frac{m_o}{m_o + y_v - F_o}$$

$$x_u = m_o W_o / (m_o + K_j W_o - F_o) \quad (6)$$

$$= (F_o - g_1 W_o) / (K_j - g_1)$$

$$y_u = K_j m_o W_o / (m_o + K_j W_o - F_o)$$

$$= K_j (F_o - g_1 W_o) / (K_j - g_1)$$

The coordinates of u and v in the X Y plane may be obtained by applying the transforming equations (4) and (5):

$$X_v = (x_v - W_o) / S_2 = 0$$

$$X_u = (F_o - K_j W_o) / S_2 (K_j - g_1) \quad (7)$$

$$Y_v = (y_v - F_o - g_1 (x_v - W_o)) / \sigma_1 = (W_o K_j - F_o) / \sigma_1$$

$$Y_u = 0$$

The perpendicular distance  $n_j$  is given by:

$$\frac{n_j}{y_v} = \frac{X_u}{\sqrt{X_u^2 + Y_v^2}}$$

$$\therefore n_j = \frac{-(F_o - K_j W_o)^2 / \sigma_1 S_2 (K_j - g_1)}{\left[ \frac{(F_o - K_j W_o)^2}{S_2^2 (K_j - g_1)^2} + \frac{(W_o K_j - F_o)^2}{\sigma_1^2} \right]^{1/2}}$$

$$= \frac{(F_o - K_j W_o)}{(\sigma_1^2 + S_2^2 (K_j - g_1)^2)^{1/2}} \quad (8)$$



and by substituting for  $\sigma_1$  from equation (1):

$$n_j = \frac{-(F_o - K_j W_o)}{(S_1^2 + K_j^2 S_2^2 - 2g_1 K_j S_2^2)^{1/2}} \quad (9)$$

Note that when  $g_1 = \frac{S_1}{S_2}$  then  $Y_v \rightarrow \infty$  and  $n_j \rightarrow X_u$ .

In the special case when  $g_1 = 0$

$$n_j = \frac{-(F_o - K_j W_o)}{\sqrt{S_1^2 + K_j^2 S_2^2}}$$

Note that when

$$K_j = 0$$

$$n_j = \frac{-F_o}{S_1}$$

when

$$K_j = \frac{F_o}{W_o}$$

$$n_j = 0$$

and when

$$K_1 \rightarrow \infty$$

$$n_j \rightarrow \frac{W_o}{S_2}$$

All of these results are as expected.

The probability of  $\frac{F}{W}$  exceeding  $K_j$  is therefore governed by the normal probability distribution of  $n_j$  with unit standard deviation:

$$f(n) = (2\pi)^{-1/2} e^{-(n^2/2)}$$

and the problem of determining the percentage  $\rho$  of experimental points expected to be in the region  $F/W > K_j$  reduces to the determination of the percentage of the normal distribution  $\int f(n) dn$  lying in the region  $n > n_j$ .

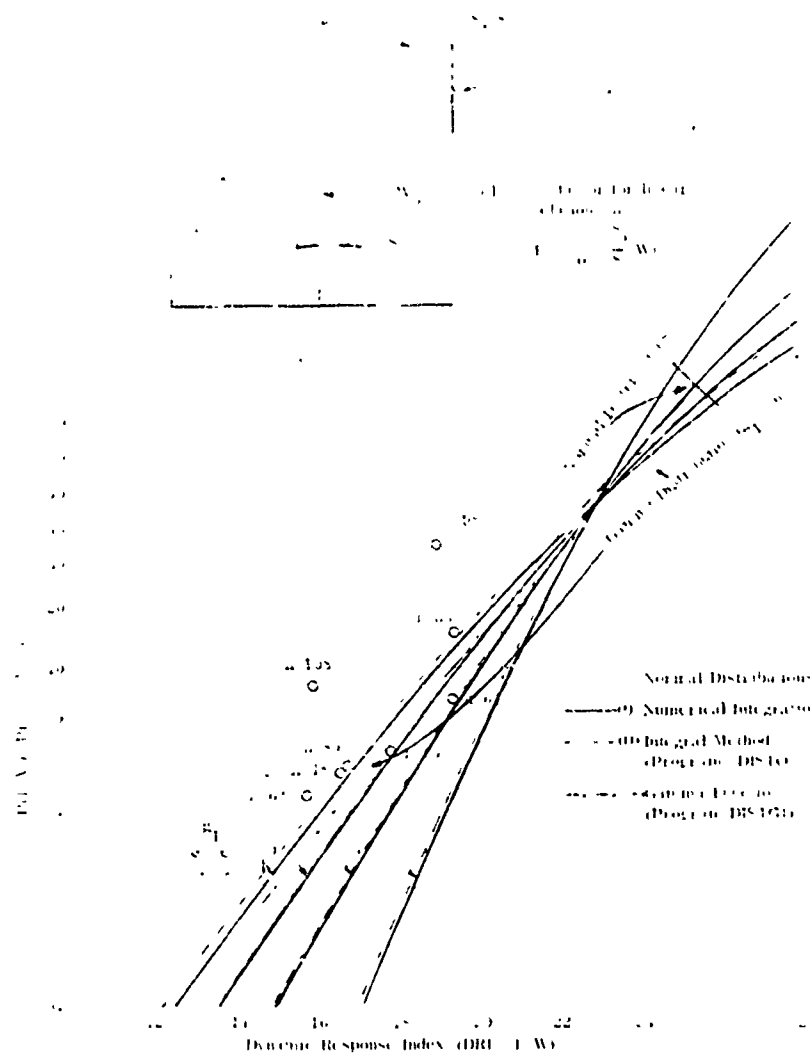


Figure B3. Relationship Between Probability of Injury and Dynamic Response Index (DRI) Using the Geertz, et al Failing Distribution

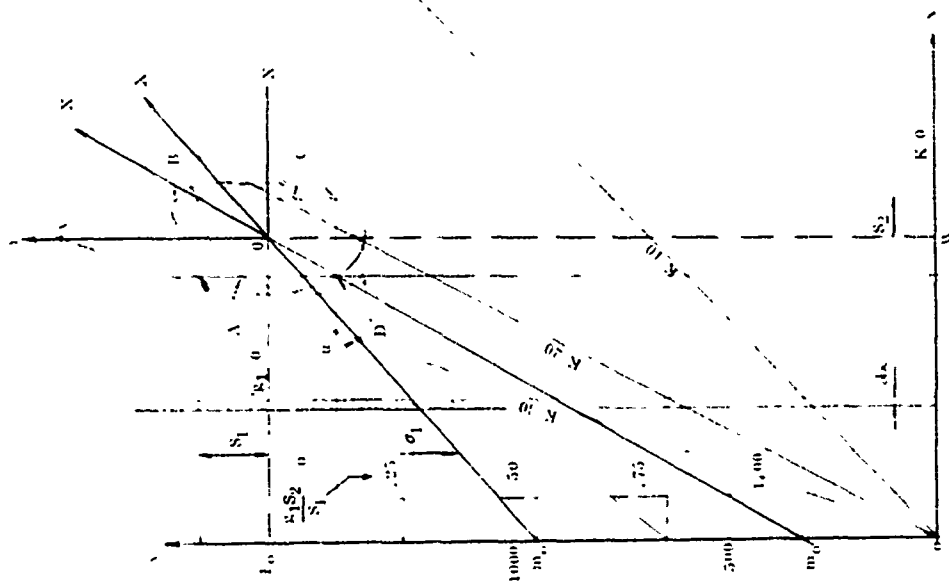
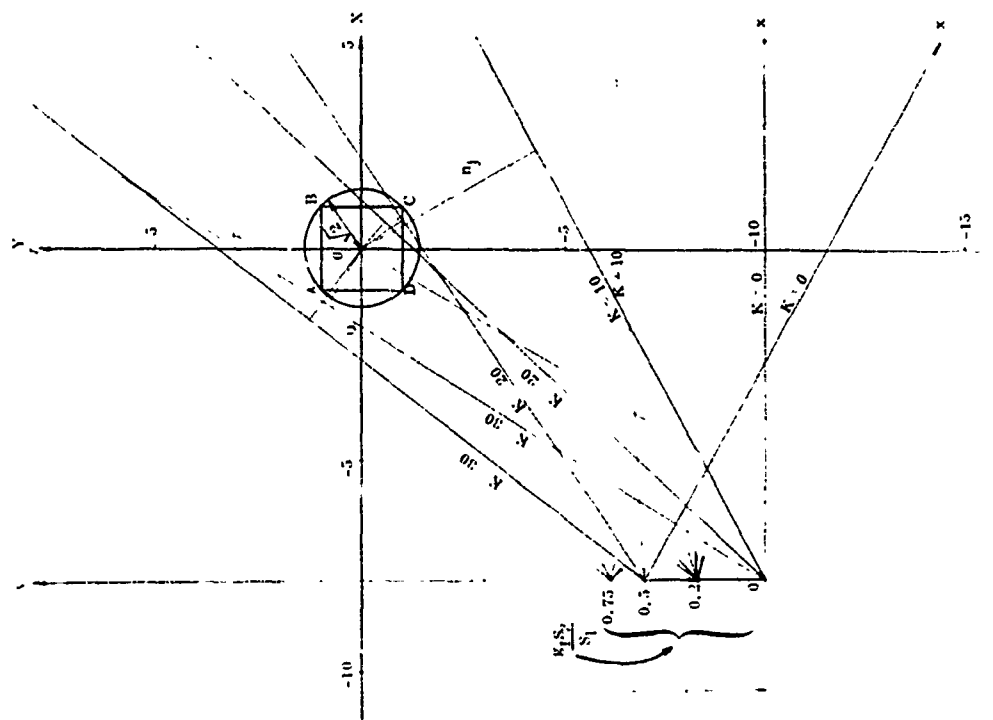


Figure B1. Distributions of F and W



Thus  $\Omega \left( \frac{F}{W} > K_j \right) = \Omega (n > n_j)$

$$= \int_{n_j}^{\infty} f(n) dn$$

$$= \int_{n_j}^{\infty} (2\pi)^{-1/2} e^{-(n^2/2)} dn$$

numerical values of which are tabulated in most sets of mathematical tables, for various values of  $n_j$ .

This distribution can be expressed directly in terms of K by making the substitution from equation (9)

$$n = -(F_o - KW_o) / (S_1^2 - 2g_1KS_2^2 + S_2^2K^2)^{1/2}$$

The distributions represented in Figures B1 and B2 are the distributions of F and W with the following characteristics:

$$F_o = 1578 \text{ lb}$$

$$S_1 = 158.8 \text{ lb}$$

$$W_o = 68.5 \text{ lb}$$

$$S_2 = 8.73 \text{ lb}$$

Five values of  $g_1$  are represented, namely

$$g_1 S_2 / S_1 = 0, .25, .5, .75, 1.0$$

four values of K

$$K = 0, 10, 20, \text{ and } 30.$$

These values of  $F_o$  and  $W_o$  refer to the failing load of the L-5 vertebra and the upper torso mass supported by the L-5 vertebra. An example of the resulting distributions, calculated both numerically and by the integral, compound distribution method as described above, are shown in Figure B3 and are compared with the values derived by Payne from experimental data in the main body of the paper. In this case a corrected vertebral load is used and the distribution of upper torso weight is assumed to be proportional to the total body weight. The very small differences between the two methods of calculation may be ascribed to the inaccuracies inherent in the simple numerical integration used. The best agreement is achieved by assuming  $g_1 = 0$ , in other words, by assuming that there is no significant dependence of F on W for the sample used, although this does not seem to be physically probably. Also shown

on Figure B3 is the result obtained by assuming gamma distributions for  $F$  and  $W$  rather than the normal distributions. This was only carried out by numerical integration for the case corresponding to  $g_1 = 0$ . The difference between the  $g_1 = 0$  lines for the gamma and normal distributions is quite small, as would be expected, and there are insufficient data points to enable a choice to be made between the two.

## REFERENCES

1. U. S. Air Force, "Seat System: Upward Ejection, Aircraft, General Specification for, "MIL-S-9479A (USAF) (16 June 1967).
2. Band, E. G. U., "Statistical Relationships for Analysis of Ship Stress Data," Webb Institute of Naval Architecture, (25 July 1965).
3. Bell, G. H., Olive Dunbar, and J. S. Beck, "Variations in Strength of Vertebrae with Age and their Relation to Osteoporosis," Calcified Tissue Research 1, 75-86 (1967).
4. Brillouin, Leon, Wave Propagation in Periodic Structures, 2nd edition. New York: Dover Publications Inc. (1953).
5. Brinkley, James W., "Development of Aerospace Escape Systems," Air University Review (July-August 1968).
6. Brown, Thornton, Robert J. Hanse, and Alvin J. Yorra, "Some Mechanical Tests on the Lumbosacral Spine with Particular Reference to the Intervertebral Discs," J. of Bone and Joint Surgery, Vol. 39-A, No. 5 (October 1957).
7. Coermann, R. R., Gerd H. Ziegenruecker, Albert L. Wittwer, and Henning von Gierke, "The Passive Dynamic Mechanical Properties of the Human Thorax-Abdomen System and of the Whole Body System," Aerospace Medicine, Vol. 31, No. 6 (June 1960).
8. Crocker, Jeremy F., and Lawrence S. Higgins, "Phase IV - Investigation of Strength of Isolated Vertebrae," Final Technical Report TI 1313-66-4, Technology Incorporated, Life Sciences Division (October 1966).
9. Dempster, W. T., "Space Requirements of the Seated Operator," WADC-TR-55-159 (July 1955).
10. Dieckmann, D., Intern. Z. angew. Physiol. einschl. Arbeitsphysiol., 16:519 (1957).
11. Eiband, A. Martin, "Human Tolerance to Rapidly Applied Accelerations: A Summary of the Literature," NASA Memorandum 5-19-59E (June 1959).
12. Geertz, Arno, "Limits and Special Problems in the Use of Seat Catapults," AAF Aero Medical Center ATI No. 56946, (Translated August 1946).

13. Gifford, Edmund C., Joseph R. Provost, and John Lazo, "Anthropometry of Naval Aviators - 1964," U. S. Naval Air Engineering Center ACCEL-533, AD No. 626322 (October 1965).
14. Goldman, David W., and Henning von Gierke, "Effects of Shock and Vibration of Man," Shock and Vibration Handbook, Harris and Crede, Vol. 3, pp. 44-1 through 44-51, McGraw-Hill Book Co., New York (1961).
15. Henzel, John H., James W. Brinkley, and George C. Mohr, "Acceleration Profile Associated with Thoracic Vertebral Compression," J. of Trauma, Vol. 6, No. 6, pp. 756-766 (1966).
16. Hertzberg, H. T. E., and G. S. Daniels, "Anthropometry of Flying Personnel - 1950," WADC-TR-52-321, AD No. 47953 (September 1954).
17. Hess, John L., "The Approximation of the Response of the Human Torso to Large Rapidly Applied Upward Accelerations by that of an Elastic Rod and Comparison with Ejection Seat Data," Douglas Aircraft Company Inc., Report No. ES 26472 (26 November 1956).
18. Hirsch, Carl, "Reaction of Intervertebral Discs to Compression Forces," J. of Bone and Joint Surgery, Vol. 37-A, No. 6 (December 1955).
19. Hirsch, Carl, and Alf Nachemson, "New Observations on the Mechanical Behavior of Lumbar Discs," 19 Acta Orth. XXIII, 4.
20. Junk, W., Tabulae Biologicae, Berlin (1925).
21. Kolsky, H., Stress Waves in Solids, New York. Dover Publications Inc. (1963).
22. Latham, F., "A Study in Body Ballistics: Seat Ejection," Proceedings of the Royal Society, B, Vol. 147, pp. 121-139 (1957).
23. Liu, Y. King, "Towards a Stress Criterion of Injury - An Example in Caudocephalad Acceleration," J. of Biomechanics, Vol. 2, No. 2, pp. 145-149 (May 1969).
24. Lovelace II, W. Randolph, Edward J. Baldes, and Verner J. Wulff, "The Ejection Seat for Emergency Escape from High-Speed Aircraft," AAF Aero Medical Laboratory TSEAL-3-696-74C, ATI No. 7245 (August 1945).
25. McElhaney, James H., "Dynamic Response of Bone and Muscle Tissue," J. Appl. Physiol. 21 (4):1231-1236 (1966).

26. Messerer, Otto, "Uber Elasticitat und Festigkeit der Menschlichen Knochen," Stuttgart: J. G. Cotta'schen Buchhandlung (1880).
27. Nachemson, Alf, "The Influence of Spinal Movements on the Lumbar Intradiscal Pressure and on the Tensile Stresses in the Annulus Fibrosus," Acta Orthopaedica Scand., 33(3):183-207 (1963).
28. Payne, Peter R., "An Analog Computer which Determines Human Tolerance to Acceleration," Presented at the National Academy of Sciences Symposium on Impact Acceleration Stress, Brooks Air Force Base, San Antonio, Texas (November 1961).
29. Payne, Peter R., "The Dynamics of Human Restraint Systems," Presented at the National Academy of Sciences Symposium on Impact Acceleration Stress, Brooks Air Force Base, San Antonio, Texas (November 1961).
30. Payne, Peter R., "Optimizations of Human Restraint Systems for Short-Period Acceleration," TR-65-108, Aerospace Medical Research Laboratories (June 1965).
31. Payne, Peter R., "Personnel Restraint and Support Systems Dynamics," AMRL-TR-65-127 (October 1965).
32. Payne, Peter R., and Edward G. U. Band, "A Four Degree-of-Freedom Lumped Parameter Model of the Seated Human Body," Wyle Laboratories, Payne Division Working Paper No. 59101-6 (25 November 1969).
33. Perey, O., "Fracture of the Vertebral End-Plate in the Lumbar Spine: An Experimental Biomechanical Investigation," Acta Orthopaedica Scand., Supp. 25 (1957).
34. Phillips, Norman S., "Research on Human Responses to Complex Vibrations and Design Principles for Body Support, Restraint and Vibration Isolation Systems," Final Report Contract No. AF 33(557)-1894, AMRL, Wright-Patterson Air Force Base, Ohio (November 1967).
35. Routh, Edward John, "A Treatise on Dynamics of a Particle," Dover Publication, New York (1960).
36. Ruff, Sigmund, "Brief Acceleration: Less Than One Second," German Aviation Medicine in World War II, Chapter IV-C, Vol. 1, pp. 584-597 Department of the Air Force, U. S. Government Printing Office, Washington, D. C. (1950).



37. Smith, Jr., Richmond W., and David A. Keiper, "Dynamic Measurement of Viscoelastic Properties of Bone," Amer. J. of Medical Electronics, pp. 156-160 (October-December 1965).
38. Stech, Ernest L., and Peter R. Payne, "The Effect of Age on Vertebral Breaking Strength, Spinal Frequency, and Tolerance to Acceleration in Human Beings," Aerospace Medical Laboratory BD Technical Report (January 1963).
39. Stech, Ernest L., and Peter R. Payne, "Dynamic Models of the Human Body," Frost Engineering Development Corporation (February 1964).
40. Stech, Ernest L., and Peter R. Payne, "Dynamic Models of the Human Body," TR-66-157 Aerospace Medical Research Laboratories (February 1966).
41. Technology, Inc., "The Investigation of Vertebral Injury Sustained During Aircrew Ejection. Phase 2a: Basic Science Experimental Design and Investigation of Dynamic Characteristics of Vertebral Columns Considered as an Engineering Structure," Annual Technical Report. Technology Inc. Life Sciences Division (October 1967).
42. Trotter, Mildred, George E. Broman, and Roy R. Peterson, "Densities of Bones of White and Negro Skeletons," J. of Bone and Joint Surgery, Vol. 42-A, No. 1 (January 1960).
43. Virgin, W. J., "Experimental Investigations into the Physical Properties of the Intervertebral Disc," J. of Bone and Joint Surgery, Vol. 33-B, No. 4 (November 1961).
44. Vogt, H. L., R. R. Coermann, and H. D. Fust, "Mechanical Impedance of the Sitting Human Under Sustained Acceleration," Aerospace Medicine, Vol. 39, No. 7 (July 1968).
45. Vykukal, Hubert C., "Dynamic Response of the Human Body to Vibration when Combined with Various Magnitudes of Linear Acceleration," Aerospace Medicine, Vol. 39, No. 11 (November 1968).
46. Weis, Jr., Edmund B., and George C. Mohr, "Cineradiographic Analysis of Human Visceral Responses to Short Duration Impact," Aerospace Medicine, Vol. 38, No. 10 (October 1967).
47. Wiesehofer, H., "Aviation Medical Principles for the Construction of Emergency Ejection Seats," (October 1943) in "The Ejection Seat for Emergency Escape from High-Speed Aircraft," by Lovelace, et al.

48. Wittmann, Thomas J., and Norman S. Phillips, "Human Body Nonlinearity and Mechanical Impedance Analysis," J. of Biomechanics, Vol. 2, No. 3 (July 1969).
49. Woods, A. G., "Human Response to Low Frequency Sinusoidal and Random Vibration," Aircraft Engineering, Vol. 39 (July 1967).
50. Yorra, Alvin J., "The Investigation of the Structural Behavior of the Intervertebral Disc," Thesis Submitted in Partial Fulfillment of the Requirements for the Degree of Master of Science in Civil Engineering, Massachusetts Institute of Technology (1956).

48. Wittmann, Thomas J., and Norman S. Phillips, "Human Body Nonlinearity and Mechanical Impedance Analysis," J. of Biomechanics, Vol. 2, No. 3 (July 1969).
49. Woods, A. G., "Human Response to Low Frequency Sinusoidal and Random Vibration," Aircraft Engineering, Vol. 39 (July 1967).
50. Yorra, Alvin J., "The Investigation of the Structural Behavior of the Intervertebral Disc," Thesis Submitted in Partial Fulfillment of the Requirements for the Degree of Master of Science in Civil Engineering, Massachusetts Institute of Technology (1956).

Two Biodynamic Models Used to Determine  
Optimum Energy Absorber Characteristics

Richard W. Carr  
Beta Industries, Inc.

ABSTRACT

Energy absorbers are generally designed to generate a constant force over their stroke length. The reason for this is that constant force or "square wave" devices are the most efficient. For any peak force level, a square wave absorber will dissipate a given amount of energy in the shortest stroke. If this energy absorber is used to protect a rigid mass, then a constant force device is the most suitable. But is this type of energy absorber suitable for protecting a seated man from high level accelerations such as those present in potentially survivable airplane crashes?

This question was answered by using two biodynamic models of the seated human. The first model employed was developed to determine human dynamic response to impact accelerations. Using this model placed on a seat and energy absorber, the equations of motion of the system were determined. The crash input accelerations were applied as an input and a computer program was used to solve for the seat acceleration. The seat acceleration was then used as an input to a second biodynamic model. This was a physiological model whose output is a Dynamic Response Index (D. R. I.) that provides a measure of spinal injury probability. By adjusting the force deflection characteristics on the computer program, a seat acceleration was found which generated an ideal D. R. I. response. This force-displacement curve was defined to be an optimum energy absorber characteristic. The form of this force-deflection profile differed from the square wave by having a high amplitude force "spike" at the beginning of the stroke followed by a low level "notch" and ending with a medium level constant force.

PRECEDING PAGE BLANK

## INTRODUCTION

Energy attenuators or absorbers are currently being used in a multitude of applications, from providing an impact surface for a typewriter carriage to protecting heavy equipment air-dropped from aircraft into isolated areas. The operation of all energy absorbers is governed by the same basic principle. All energy attenuators dissipate energy by providing a reaction force that is displaced over some distance. The amount of energy dissipated can be expressed as:

$$E = \int_0^x F_r(x) dx \quad (1)$$

where  $E$  = energy dissipated  
 $F_r$  = reaction force  
 $x$  = displacement

The above equation simply states that the amount of energy a particular device can dissipate is equal to the area under force-displacement curve.

The majority of applications for energy absorbers today generally specify the reaction force required and an allowable stroking distance. Normally the force is determined by the strength of the object to be protected and stroking distance is as small as practicable since space is usually at a premium. For these applications, an energy absorber which reaches the specified force very quickly and stays at that force through the remainder of the stroke is the most desirable. That is, an energy attenuator whose force-deflection curve closely approximates a rectangular pulse or square wave is normally considered the best and most efficient.

If the object or system to be protected by an energy absorber can be considered a rigid body, then the square wave attenuator is ideally suited for protection of the object. However, if the system to be protected is not rigid but dynamic in nature (i. e., the system possesses dynamic characteristics such as stiffness and damping in addition to mass) an energy absorber with a rectangular force-deflection curve is not necessarily the optimum. This is because a lightly damped dynamic system can generate higher forces and accelerations than those applied and this must be taken into account if the system is to be adequately protected.

A special case of system protection is isolation of a seated human from abrupt vertical accelerations. This can

be accomplished by installing an energy attenuating device between the man and the point of application of the acceleration. But the question quickly arises as to what the force-deflection characteristics of the energy absorber should be. Is it reasonable to assume that a constant force or square wave attenuator would provide the optimum protection? If the seated man reacted as a rigid mass a square wave absorber would be the optimum, but previous studies have indicated this is not the case.

A simple dynamic analytical model that duplicates human body dynamic response to impact accelerations was recently developed by T. J. Wittmann (Ref. 1). The model is a single-degree-of-freedom, spring mass damper system with a natural frequency 10 Hz, a damping ratio of 0.3, and a mass equal to that of the man (Ref. 1). Using this model in place of a seated man, the force that a man would exert on the seat can be determined. This force must be balanced by the energy absorber force, and since a lightly damped system will overshoot, a square wave attenuator will cause higher accelerations than anticipated to be present at the seat. It should be expected, therefore, that an optimum energy absorber would have a force-deflection curve other than a square wave.

To actually calculate an optimum energy absorber waveform, a method of determining acceleration profiles that are tolerable to seated humans must be used in addition to the dynamic force model. A biodynamic model currently employed by the U. S. Air Force (Ref. 2) that relates randomly applied accelerations to probability of injury can be used to find tolerable accelerations. This model is also a single-degree-of-freedom spring mass damper system and is illustrated in Figure 1. The output of this injury model is a Dynamic Response Index or D. R. I. which is defined as:

$$\text{D. R. I.} = \frac{W_n^2 \int_{\max}}{g} \quad (2)$$

where  $W_n$  = natural frequency of system  
 $\int$  =  $X - x$   
 $g$  = gravitational acceleration

The D. R. I. is a measure of the forces carried in the spine and can be related to the probability of spinal injury. The current limit used by the U. S. Air Force is 18 (Ref. 2), which corresponds to a probability of spinal injury of 0.05.

Before attempting to define an optimum energy absorber, the ideal or optimum response of the seated man should be de-

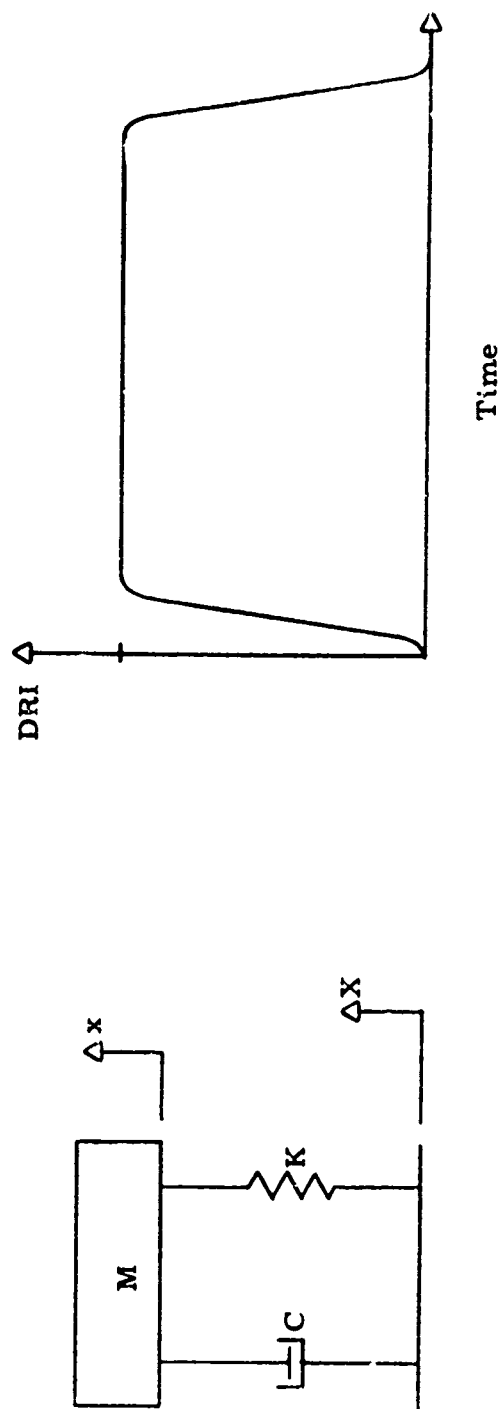


FIGURE 1 DRI Model and Optimum Response

finer. Since the purpose of the energy attenuator is to reduce the probability of injury for the man, an optimum output of the injury or D. R. I. model must be determined. The Dynamic Response Index provides a measure of injury probability that is determined by the maximum compression of the model's spring (i. e.,  $\delta_{\max}$ ). This implies the probability of injury only depends on the maximum or peak D. R. I. and is independent of the time the D. R. I. is at a given level.

Another point to consider is what happens when the D. R. I. varies. When the D. R. I. varies with respect to time, the physiological model is dissipating energy through the motion of the damper. This can be shown as follows:

$$\text{D. R. I. (t)} = \frac{W_n^2 \delta(t)}{g} = k \delta(t) \quad (3)$$

$$\begin{aligned} \delta &= X(t) - x(t) \\ E &= \text{energy dissipated} \\ E &= \int_{t_1}^{t_2} (c \dot{\delta}) \cdot \dot{\delta} dt \end{aligned} \quad (4)$$

From Equation 3 it is seen that the D. R. I. varies directly with the displacement  $\delta$ . When the D. R. I. varies,  $\delta$  has a first derivative and energy is dissipated by the system, but when the D. R. I. is constant,  $\delta$  is zero and no energy is dissipated by the model. If no energy is being absorbed by the man, the energy present in the seated man energy absorber system can only be dissipated by the energy absorber. When this condition exists the D. R. I. time history should be as shown in Figure 1 and maximum use of the energy absorber is attained. The curve does not have an infinite rise or decay time because a rectangular wave is not physically realizable. The D. R. I. is the result of the response of an elastic system and must change values in a smooth fashion. Some energy will be dissipated by the model in reaching and declining from the maximum level, but this cannot be eliminated from a dynamic system and is negligible when compared with the total energy dissipated.

#### THEORETICAL APPROACH

The two biodynamic models, one for the dynamic response and one for physiological measure or injury prediction, along with an optimum D. R. I. response, provide the necessary tools to solve the problem of defining optimum energy absorber characteristics. Using the dynamic model, the equations of motion that describe the seated man system shown in Figure 2 were written.



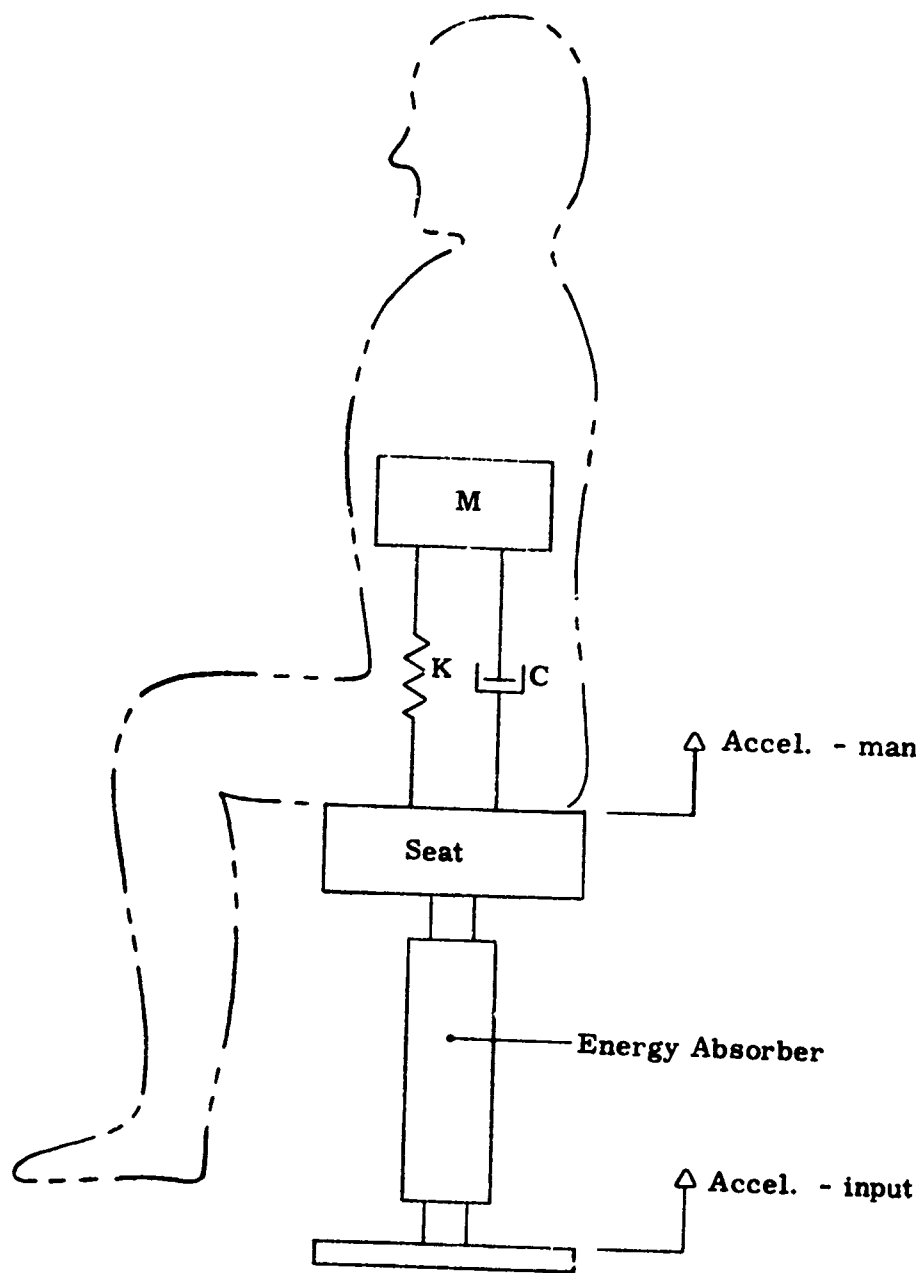


FIGURE 2 Seated Man Model

As shown in Figure 2, the input acceleration acts upon the energy absorber which develops forces within it that accelerate the seat and the seat then accelerates the man. The motion of the seat and the man are described by the equations:

$$M_2 \ddot{X}_2 = C_1 \dot{X}_1 + K_1 X_1 - C_1 \dot{X}_2 - K_1 X_2 + F_{ea} + F_{st} - W_2$$

$$M_1 \ddot{X}_1 = K_1 X_1 - C_1 \dot{X}_1 + C_1 \dot{X}_2 + K_1 X_2 - W_1$$

where  $X_2$  = seat displacement

$M_2$  = seat mass

$W_2$  = seat weight

$C_1$  = damping coefficient, dynamic man model

$K_1$  = stiffness, dynamic man model

$X_1$  = displacement dynamic man model

$M_1$  = mass of the man

$F_{ea}$  = energy absorber force

$F_{st}$  = structural force developed when energy absorber bottoms

This system of equations can be solved for  $X_2$  when the input acceleration and energy absorber characteristics are known. The solution can then be used to solve the equation of motion of the injury model shown below, where seat motion  $X_2$  drives the system but is not coupled to it.

$$M_3 \ddot{X}_3 = C_3 \dot{X}_2 + K_3 X_2 - C_3 \dot{X}_3 - K_3 X_3 - W_1$$

where  $M_3$  = mass of the man

$C_3$  = damping coefficient, injury model

$K_3$  = stiffness, injury model

$X_3$  = displacement injury model

The solution of this equation can be used to determine the D. R. I. which is a measure of the force developed in the spring and is equal to  $K_3 (X_3 - X_2) / M_3 g$ .

A computer program for solving the above equations using MIMIC (Ref. 3), a digital computer subroutine, was written. The input acceleration and the force deflection characteristics of the energy absorber were both entered into the program as tabulated data points. The input acceleration was selected from available data on full scale crash tests and a typical crash acceleration profile for a helicopter is shown in Figure 3. When this acceleration is applied to the system shown in Figure 2, with a man weight of 170 pounds and a seat weight of 150 pounds, the energy absorber force-deflection characteristics can be adjusted until the optimum D. R. I. response is obtained.

For optimization purposes, the primary effort was to determine whether or not an energy absorber force deflection curve could be defined that would take advantage of the dynamic response of the man. Does the man's response significantly influence the design of the energy attenuator? The computer program was developed and used to test the hypothesis that a force displacement curve exists that offers the seated man better protection than an energy absorber that generates a constant force.

The initial approach to the problem is an intuitive one. The energy absorber characteristics to be developed must create a tolerable environment for the man but still maintain a minimum stroke. This is because tolerable accelerations could be obtained by energy absorbers with low force levels but extremely long stroke lengths. Unfortunately, long stroke lengths are generally undesirable and high force levels that could cause dynamic overshoot of the man must be used.

An energy absorber with a constant force level will cause a long duration acceleration pulse to be applied to the seated man. Since a long acceleration pulse will cause the man to overshoot, what will be the effect of a very short duration pulse? The limit of a short duration acceleration pulse is the impulse input and for this input a linear system responds not to the magnitude of the waveform but to the area underneath it, or the velocity change. A single impulse input and the system response is shown in Figure 4. This figure implies that if a linear system is struck impulsively the system response will reach a peak value that depends on velocity change and then decrease to zero. If this peak value is a tolerable limit, then it would be desirable to reach this value and hold it. Since a linear system obeys the superposition principle, additional impulses added at the proper time can be used to keep the response at a constant value. This is illustrated for two impulsive inputs in Figure 5. It is apparent that the first pulse is used to achieve the desired level and that subsequent pulses can be added to maintain

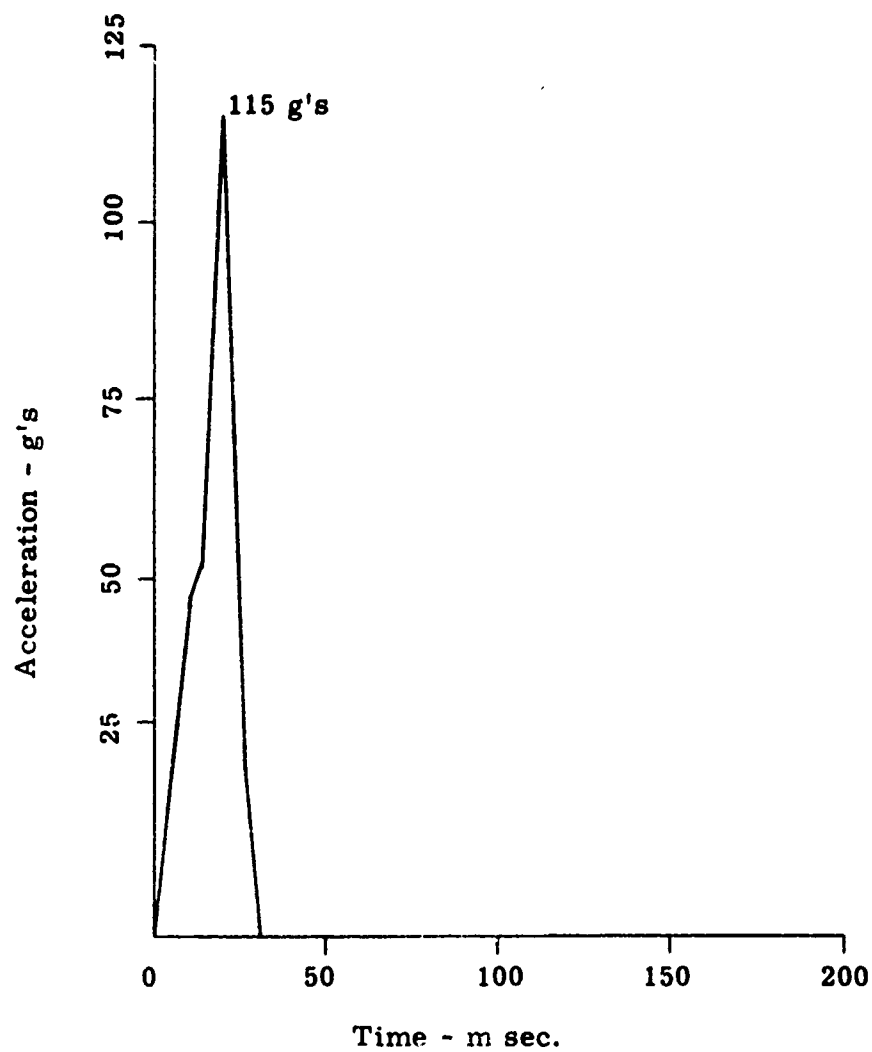
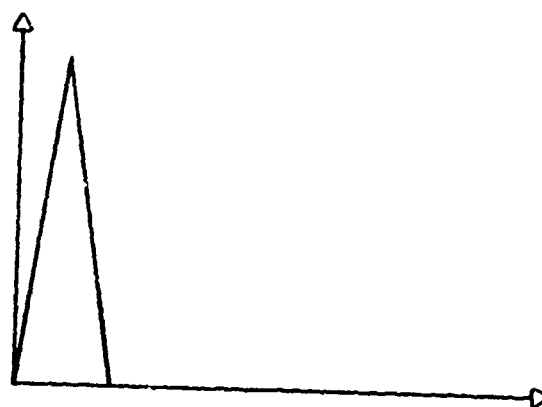


FIGURE 3 Helicopter Crash Pulse

Input



Time

Response



Time

FIGURE 4 Single Impulse and Response

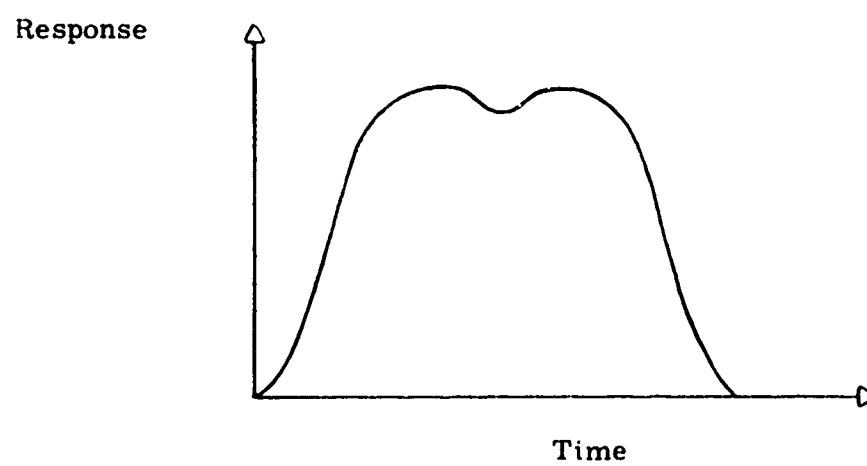
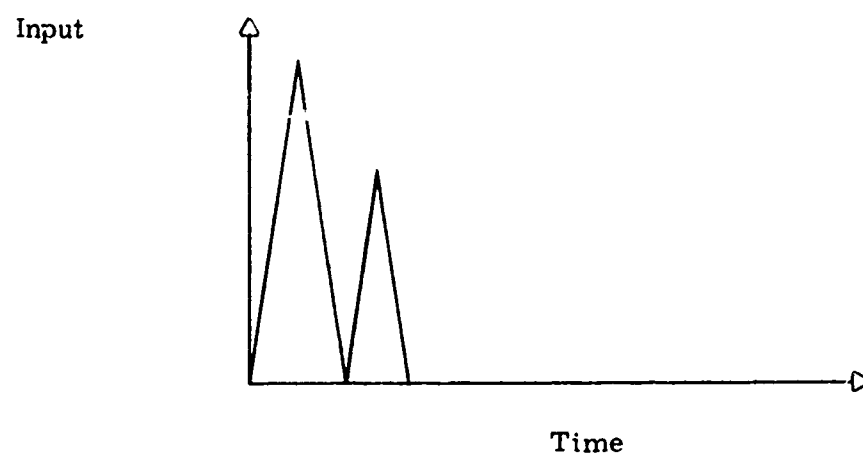


FIGURE 5 Two Impulses and Response

that value. The initial pulse determines the peak value of the response and additional pulses can only be added when the total response does not exceed the desired level. This means that there will be a large initial spike, a "valley" or "notch" and then a series of lower level pulses as required to keep the response at a constant level.

The description just given is directly applicable to the man and seat. It is desirable for an acceleration to be applied to the man that will cause him to compress up to a given level and remain there. If this is to be achieved the acceleration of the seat must have the "notched" appearance. Since the seat acceleration is dictated by the forces of the energy absorber and the dynamic response of the man, the energy absorber force-deflection curve must create the force-time profile desired. During the initial acceleration, the man will lag the input and not generate large forces. The seat, however, will have accelerations nearly equal to the input and the force generated by the energy absorber will be approximately equal to the seat mass times its acceleration. Therefore, the force-time profile of the energy absorber must have the same notch as the desired seat acceleration. Since energy absorbers generally strick in one direction, the force-deflection curve should be of the same form as the force-time profile, so that an energy absorber with a "notched" force-displacement curve should cause the seat acceleration to generate the proper response of the man.

## RESULTS

Knowing what general wave shape an optimum energy absorber would have, the next step was to quantitatively define a force-displacement curve for an energy attenuator that would provide the best protection for a seated man from the helicopter crash pulse shown in Figure 3. From existing crash criteria a level of 40 g's was first used as an estimate of the acceleration that could be carried by the energy absorber structure. By estimating the seat weight at 150 pounds and using a 50th percentile man of 170 pounds, the peak force due to the inertial dead weight would be 12,800 pounds. Existing energy absorber data (Ref. 4) indicated that a triangular pulse of this peak could be obtained by an initial stroke of 0.42 inches.

The plateau or final portion of the force-displacement curve is dictated partially by the impulsive response but is also the limit for the inertial forces of the man and seat. After the impulse response has decayed, the D. R. I. level must be indicative of the seat acceleration, and the D. R. I. of 18 was used as a tolerable

limit (Ref. 2). Since this is the inertial acceleration of the seat and man after transient response, the force level of the absorber for this region must be approximately 5,750 pounds ( $18 \times 320$ ). The only level left to be determined for the initial waveform is the value to be used for the "notch". Since this value should be indicative of a practical energy absorber, a value of 1,000 pounds was chosen and the preliminary optimum waveform shown in Figure 6 was inserted into the computer program and adjusted until an optimum response was achieved.

At first it was not known where or how long the notch should be, so several variations of impulse peak and "notch" locations were attempted. The best response was achieved when the waveform had an impulse of 14,200 pounds followed by a 1,000 pound "notch" of 3.5 inches and a plateau of 5,300 pounds. This force-deflection curve and the D. R. I. response it generates are shown in Figure 7.

The energy absorber waveform shown in Figure 7 can be called the optimum waveform for the conditions which were used to determine it. These conditions were a 170 pound man, a 150 pound seat, and the helicopter crash pulse as an applied input. If any of these conditions or parameters change then the response will change and a different optimum waveform might be required. A preliminary investigation of the effects of these parameters indicate that a variation of the input acceleration has the most effect on the D. R. I. response. A change in the seat or man weight appears to only change the D. R. I. level and stroke length. An increase in system weight will lower the peak D. R. I. and increase the stroke length, but a decrease in system weight will have just the opposite results.

Since the input acceleration governs the dynamic response of the system the variation of this parameter was investigated. The input acceleration to the seated man is determined by the nature of the crash and the response of the aircraft. Since the response of a system subjected to a transient input is indicative of its natural frequency, the acceleration input to the seated man should vary in amplitude but not in time duration. Therefore, responses to input accelerations having the same time base but with reduced amplitudes were examined.

The optimum energy absorber waveform for the full input acceleration has an initial force spike of 14,200 pounds. This requires a certain amount of input acceleration to actuate the absorber. As the input acceleration is reduced, a point is reached where the input does not generate the 14,200 pounds



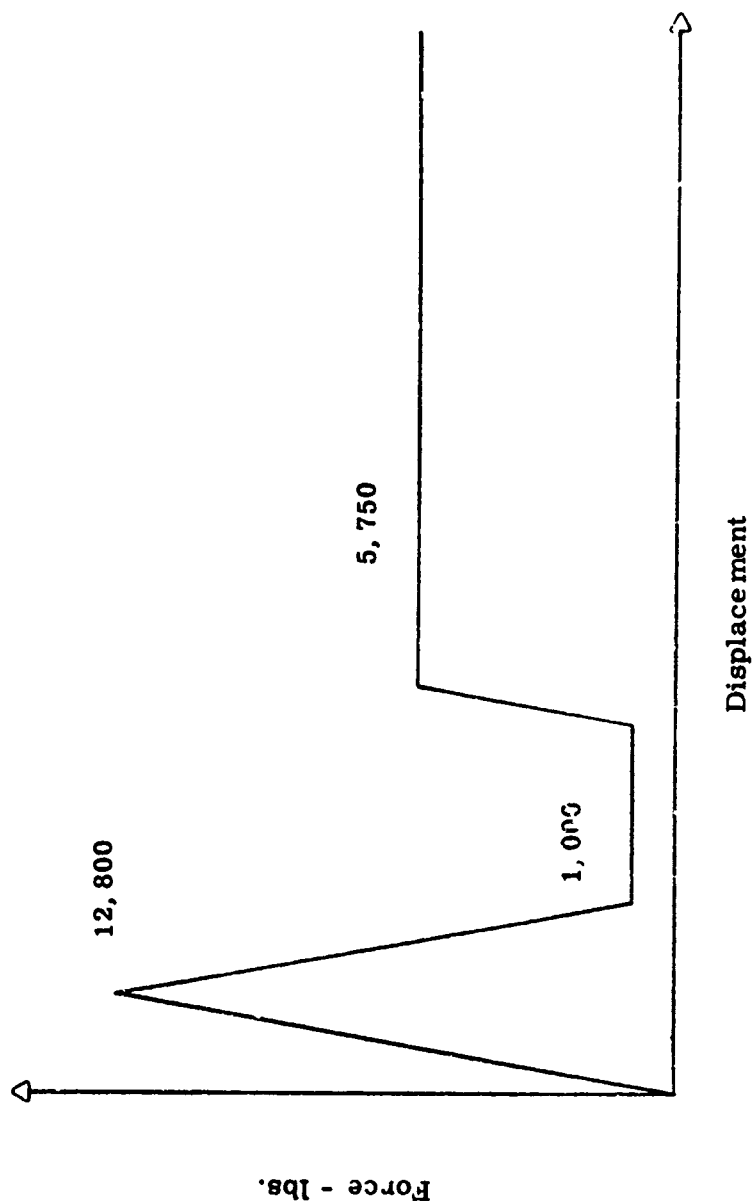


FIGURE 6 Preliminary Optimum Energy Absorber Waveform

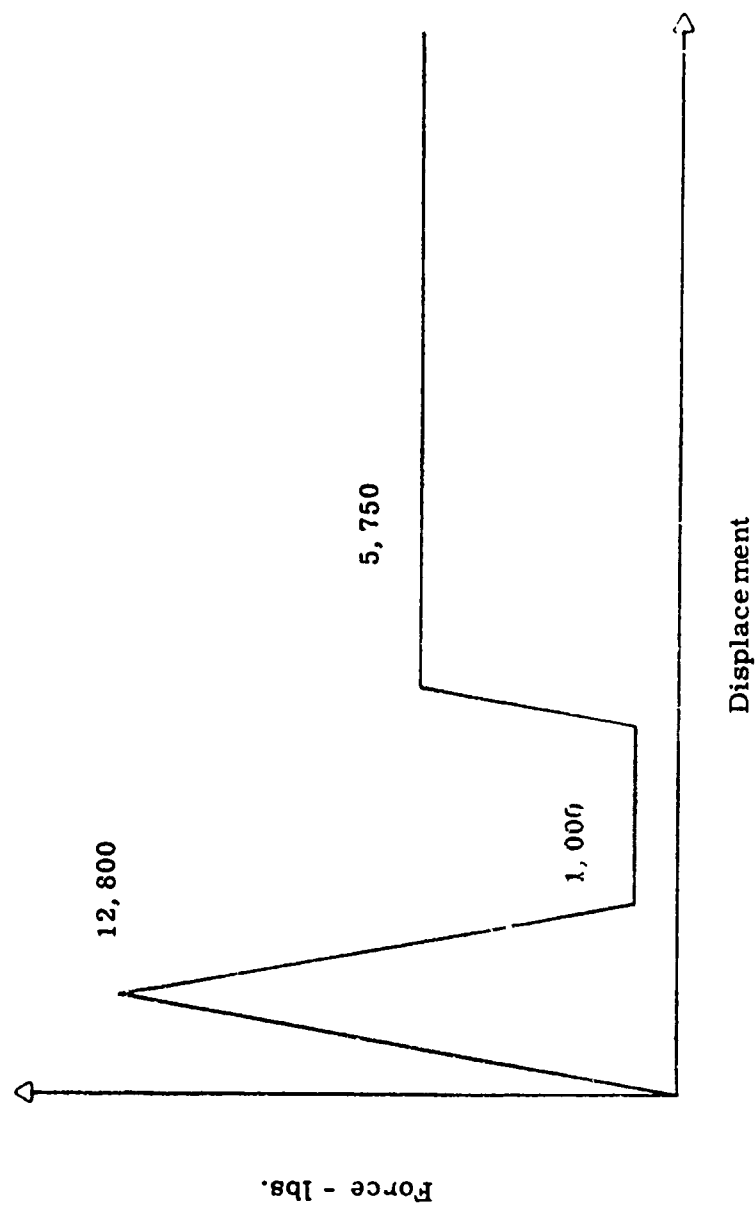


FIGURE 6 Preliminary Optimum Energy Absorber Waveform

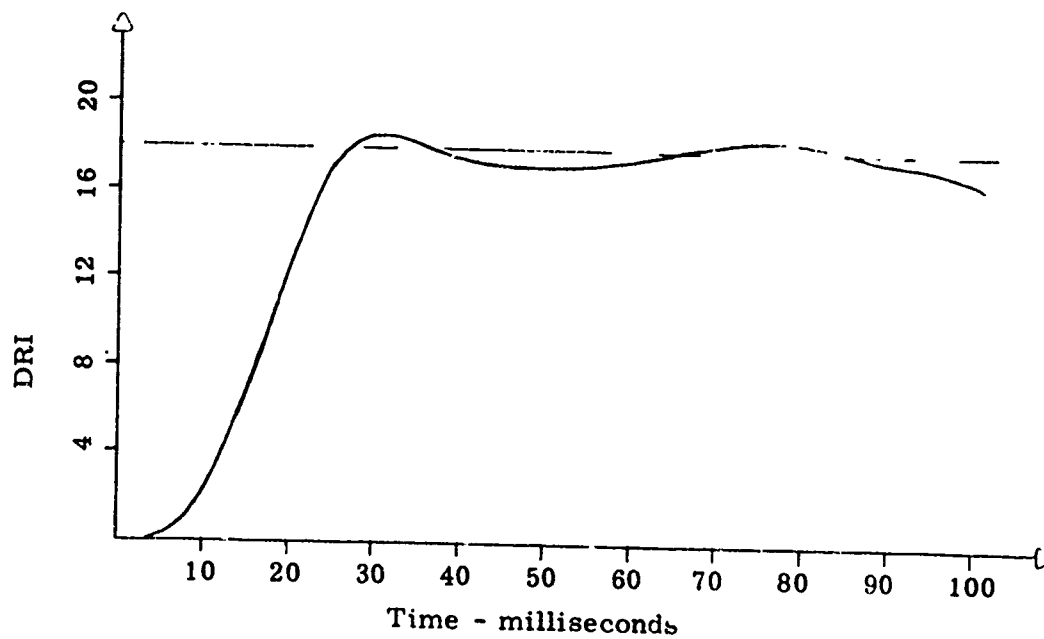
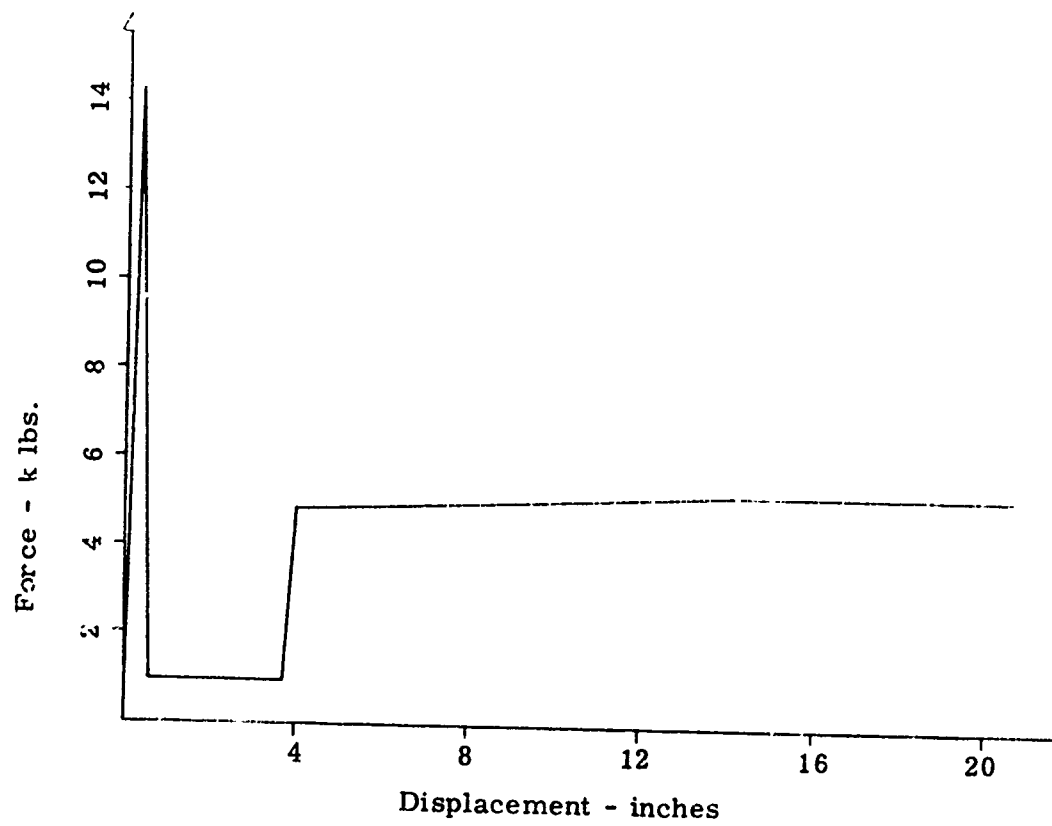


FIGURE 7 Optimum Energy Absorber Waveform and Response

and the absorber acts as a high stiffness element causing the man's response to overshoot. As the input is reduced further the amplitude of the overshoot will decrease and eventually will not exceed allowable limits. Therefore, a force-displacement waveform with a large initial force spike may be optimum for high peak input accelerations but it may create a band of reduced acceleration inputs, as shown in Figure 8, that would produce dangerous acceleration levels for the man.

To investigate this problem several variations of the energy absorber waveform were studied. The first variation shown in Figure 9, reduced the peak value to 7,100 pounds and increased the displacement of this initial peak to one inch. This waveform was adjusted until an acceptable D. R. I. response for all levels of input was obtained. The final force-deflection waveform has an initial peak force of 6,500 pounds, a "notch" force of 1,000 pounds, and a plateau force that increases from 4,500 to 5,300 pounds. Figure 10 illustrates this final waveform and the D. R. I. responses that result from reducing the input acceleration magnitude. Examination of the D. R. I. curves show that the modified waveform generates D. R. I. responses which have a peak level of 19.2 or lower except the curve for 0.4A which has a peak D. R. I. of 19.9. These peak values could be reduced to a tolerable level of 18 by lowering the forces of the energy absorber. Therefore, it appears that the modified "notched" energy absorber force-deflection curve can be optimized to protect a seated man from any peak acceleration level up to the maximum peak anticipated, provided the stroke length is long enough.

### CONCLUSIONS

The results of this investigation indicate an optimum force-displacement curve for protection of a seated man can be found for a given set of conditions: man weight, seat weight and input acceleration. As long as the input is impulsive the dynamic response of the man creates a force-overshoot and this can be compensated for by having a "notched" absorber. This type device differs drastically from the traditional square wave force-displacement absorber. The square wave device will dissipate the most energy for a given stroke length, but will generate an acceleration input to the seated man which will result in a higher probability of injury than the notched absorber. Because the man responds as a lightly damped dynamic system, a square wave absorber causes higher seat accelerations than anticipated. This also subjects the man to greater accelerations which generate higher forces in the spine resulting in a greater probability of injury. A safer design takes the man's response into account and for an energy absorber that

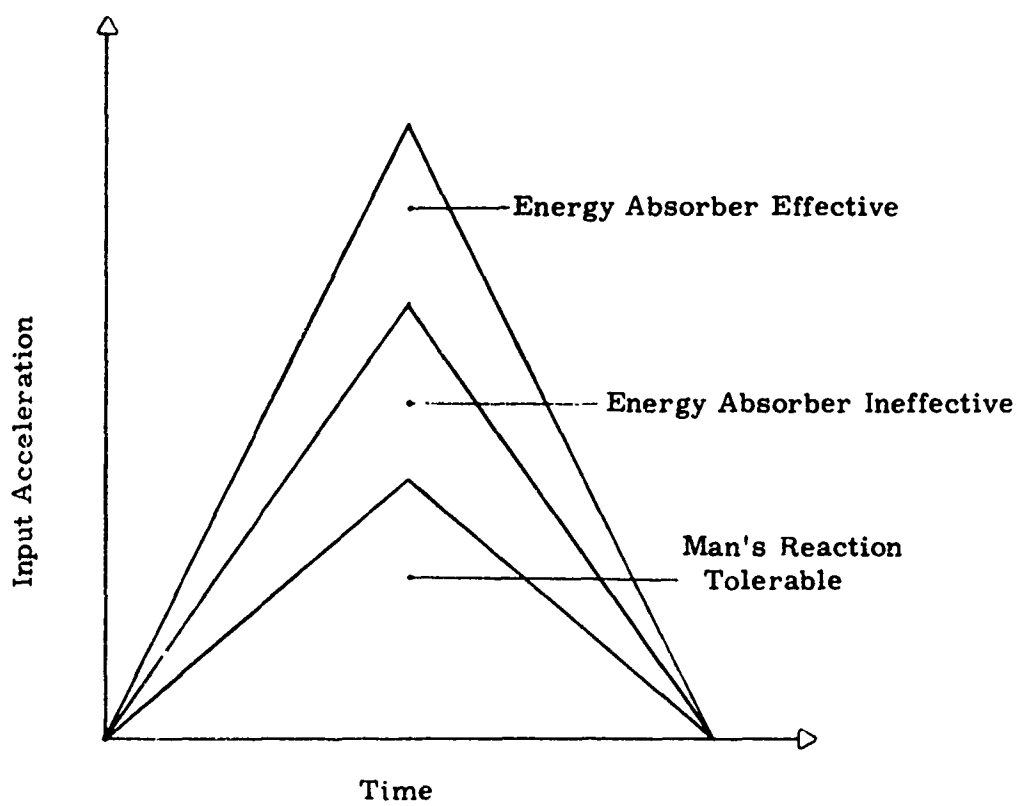


FIGURE 8 Input Acceleration Ranges

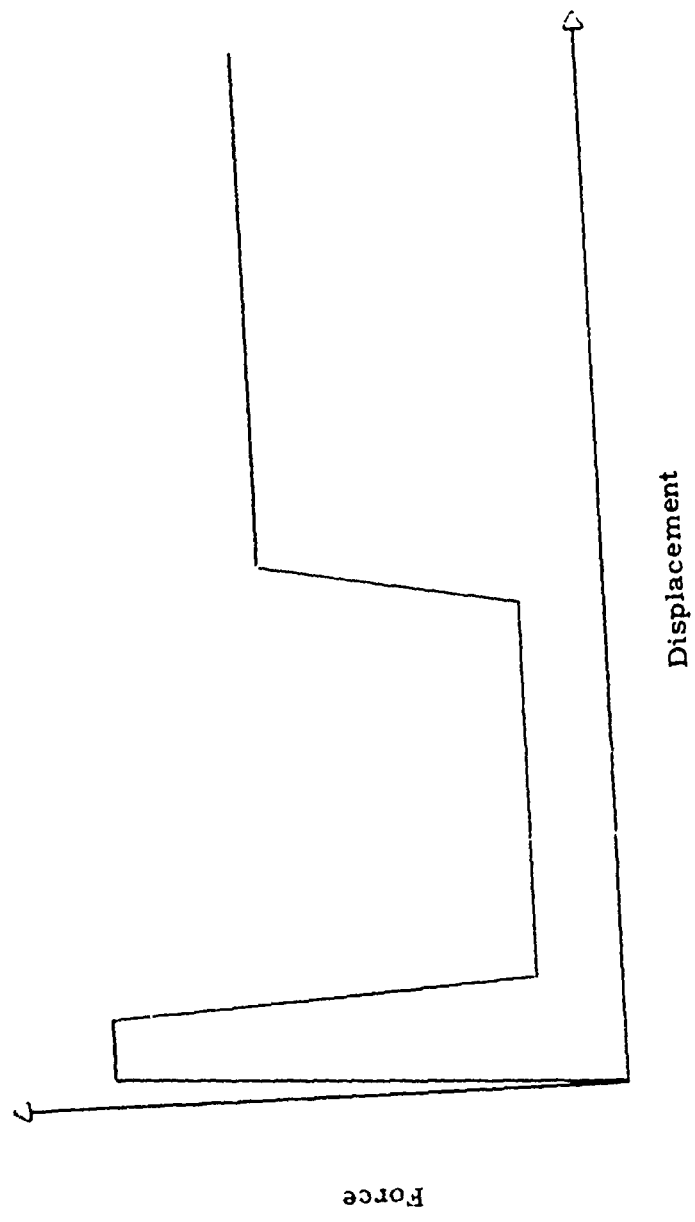
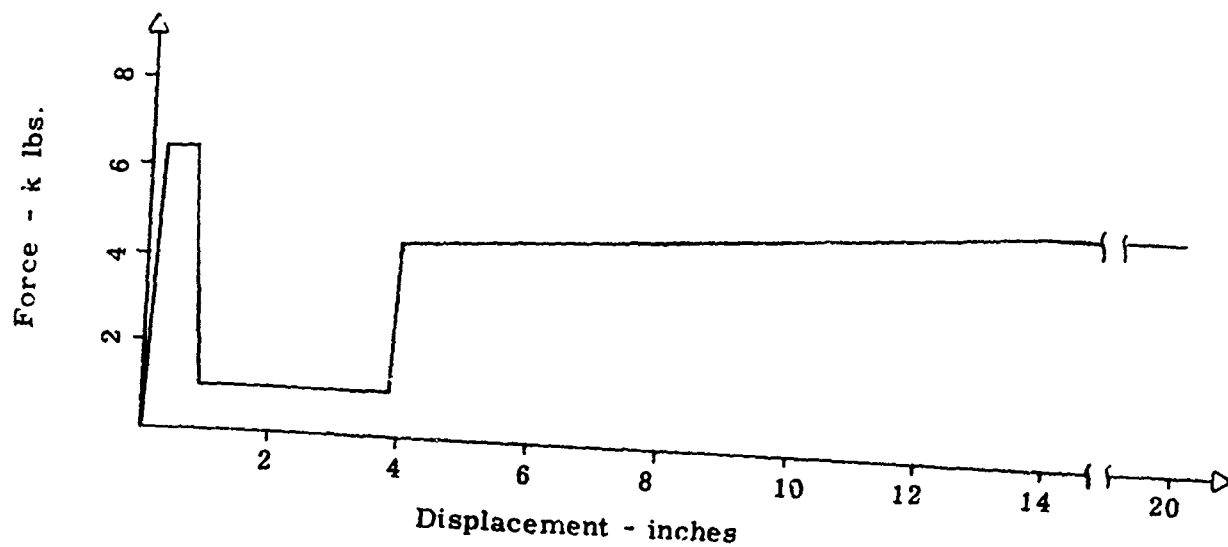


FIGURE 9 Modified Energy Absorber Waveform



Input	Stroke - in.
□ A*	19.1
○ 0.8A	12.1
△ 0.6A	6.9
◇ 0.4A	0.34
○ 0.3A	0.02

A\* - helicopter crash pulse

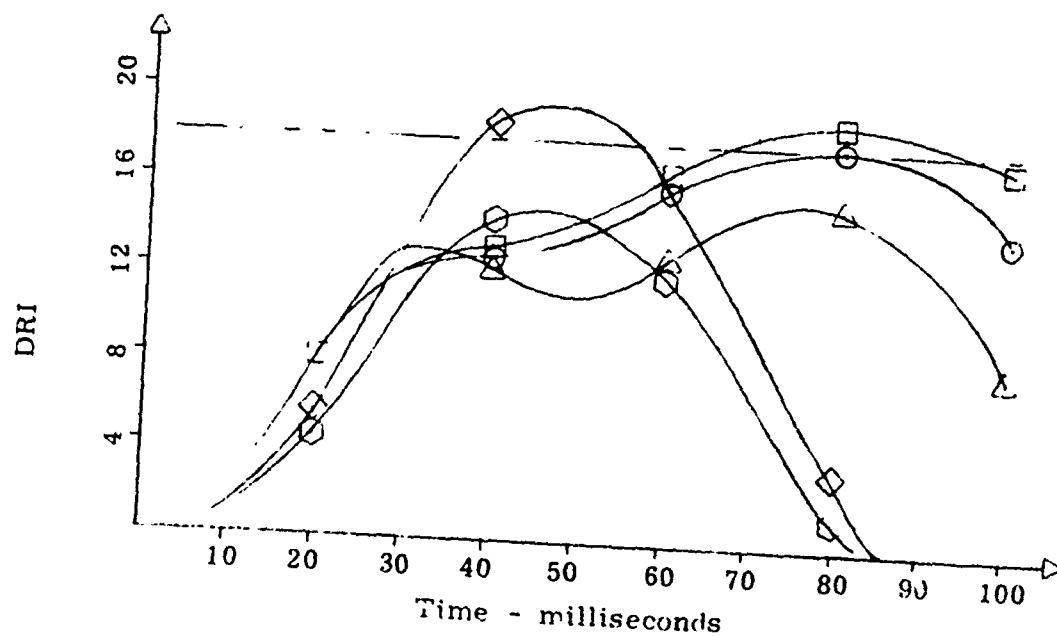


FIGURE 10 Modified Energy Absorber Waveform and Response

is a passive elastic element, the optimum for a given set of conditions is a "notched" force-displacement absorber.

It is usually not possible to design for a given set of fixed parameters and a range of values must be considered. The absorber must act in conditions of less severe inputs. If the absorber has a high peak value initially it is possible that an input less than the maximum anticipated could generate dangerous acceleration levels. This can be overcome by truncating the initial peak value and compromising on the efficiency of the absorbers. The truncated and notched absorber will work for reduced acceleration input levels provided that the force levels of the absorber are low enough and the stroke lengths are long enough. The force levels are not necessarily dictated by the maximum input but by some lesser input that creates a maximum response.

Therefore, it appears that truly optimum energy absorber characteristics exist for every possible combination of man weight seat weight and input acceleration, but a single element energy absorber can only provide an optimum waveform for one set of conditions. A single element energy absorber can be modified to provide protection for a greater range of conditions but the force deflection curve is no longer a true optimum for any of the conditions.

#### ACKNOWLEDGEMENTS

The research reported in this paper was sponsored by the Aerospace Crew Equipment Department, Naval Air Development Center, Johnsville, Pennsylvania, under contract N00156-70-C-1374 with Beta Industries, Incorporated, Dayton, Ohio. During the contractual period, Mr. Marc Schwartz of the Acceleration Branch, Aerospace Crew Equipment Department served as the contract monitor.

The author is grateful for the assistance lent by his associates at Beta Industries, Inc. and by Mr. Marc Schwartz of the Naval Air Development Center. Special appreciation is extended to Mr. Norman S. Phillips and Mr. Joseph Kramer of Beta Industries, Inc. for their technical assistance and editorial comments.



## REFERENCES

1. Wittman, T. J., An Analytical Model to Duplicate Human Dynamic Force Response to Impact: AMRL-TR-66-126, Aerospace Medical Research Laboratories, Wright-Patterson Air Force Base, Ohio 1966.
2. MIL-A-9479 (USAF), Seat System; Upward Ejection, Aircraft, General Specification for, U. S. Air Force, June 1967.
3. Sansom, Frederick J. and Peterson, Harry E., MIMIC Programming Manual, SEG-TR-67-31, Aeronautical Systems Division, Wright-Patterson Air Force Base, Ohio, July 1967.
4. Schwartz, Marcus, Dynamic Testing of Energy Attenuating Devices, NADC-AC-6905, U. S. Naval Air Development Center, Johnsville, Pennsylvania, October 1969.

**BONE ATROPHY BY INACTIVITY**

by Joachim H. Eichler

Dozent an der Orthopädischen  
Universitätsklinik Giessen, Germany  
Direktor: Prof. Dr. H. Rettig

**Abstract**

The development of bone atrophy caused by inactivity was investigated in experiments with Guinea pigs. 300 animals of an inbred strain were fixed by a pelvic plaster for different times. The breaking strength of femora was measured and the reduction of spongy bone determined by uncalcified bone sections. Moreover, bone remodelling, dry mass of bone, and mineral balance were tested in our experiments. Bone atrophy is developing rapidly depending upon time of immobilization, age, and sex. The calcium balance is negative from the first day of immobilization.

Osteoporotic changes produced by inactivity are compared with results obtained after space flights. According to our animal experiments it is suggested, that in addition to the loss of static load by weightlessness the limited possibility of movements by the astronauts within the spacecraft, therefore plainly the inactivity, is responsible for the bone atrophy.

**PRECEDING PAGE BLANK**

Until today, relatively little was known about the effect of inactivity upon the skeletal system. REIFENSTEIN and ALBRIGHT (1944) reported an increased elimination of calcium by the urine during treatment by plaster. Balance experiments undertaken by WHEDON and co-workers of 9 completely paralyzed patients suffering from poliomyelitis, revealed a progressive increase of calcium elimination between 3 and 5 weeks after onset of the disease. After this time, the calcium concentration revealed increased at the same level. The maximum calcium elimination was 572 mg per day. One of these patients lost 58g of calcium, nearly 5% of the whole calcium content of the body, within 7 months of poliomyelitis.

BIRKHEAD (1965) showed for the first time by radiostrontium that calcium losses in paralyzed patients originated from the skeletal system. The changes were explained partly by the disturbance of the autonomous nervous system by polio-viruses and partly by the increase of callus formation which is often observed in spontaneous bone fractures. These conclusions were confirmed by TRUETA (1965) and GEISER (1963) who found osteoporosis of the leg bones in rats, after resection of the nervous ischiadicus.

Our own investigations reported here are dealing with the effect of inactivity upon the skeleton. In these experiments Guinea pigs of the inbred strain PIRBRIGHT WHITE were used, since they were the only ones of the small laboratory animals that tolerated a pelvic plaster (Figure 1). Their nutrition was sufficient despite the handicaps of the plaster. By a little technical trick, a small piece of metal attached to the plaster, the animals were able to crawl around in the cage using the plaster like a sled. The movements were connected with an isometric muscle contraction of the fixed hindlegs. Hip and knee joints were fixed at an angle of 90°. In this position the head of the femur is brought under pressure by tension of the adductor muscles. There is, however, no increased load on the knee. This was the reason for our using for microscopic sections only material originating from the shaft of the femur, or from the condylus close to the knee.

The results reported here were obtained from over 300 male Guinea pigs of 5 different weight groups. The average time of fixation was 3 weeks. Within one group of medium weight which corresponds to adolescent animals; immobilization was carried out for 1, 2, 3, 4, 5 and 6 weeks.

#### Results:

The breaking strength of the femur was tested by a device that I constructed myself. There was no possibility of testing the dynamic maximum load capacity of the femora which is well known by material tests! The static stability, however, was measured by a slow increase of the load. The constant test

MADE IN GERMANY

interval used for the technical comparison of different materials was avoided since the whole length of the bone, and not a part there of is subjected to a dynamic load. We called this type of dynamic load of the bone the physiological breaking strength.

There was a linear decrease of the physiological breaking strength noted up to six weeks. At the same time, the physiological breaking strength of the humerus increased in comparison to controls. This result is explained most literally by the compensatory and intensified use of the forelegs by the immobilized animals.

We suggest that muscle exercises lead to a higher physiological breaking strength of the long bones.

3 out of 20 Guinea pigs which were immobilized by the pelvic plaster had spontaneous fractures. All these fractures were observed in the transitional zone between the cortical bone of the knee and the compact bone of the femur. The shape of these fractures was different from controls. The healthy animals had a triangular limitation of the fractured sides and a dislocation of the wedge shaped fragments at the side of the maximum strain. The femora of the immobilized animals, however, showed a nearly smooth-faced limitation of the fractured sides (Figure 2). This type of fracture is regarded as typical for a damaged bone structure by immobilization. Besides the loss of mineral salts, there is a damage of collagenous fibres which might be responsible for this behavior. Immobilization by pelvic plaster causes a reduction of the physiological breaking strength of the femora depending upon time age and sex (Table 1). The youngest Guinea pigs have the highest loss of physiological breaking strength within the weight class around 150g. They lost 55% of the physiological breaking strength after immobilization for 2 weeks. The femora of adult animals lose 43.7% after 3 weeks and after an additional 6 weeks 23.0% which amounted to a total loss of 61% of the original breaking strength.

The influence of immobilization upon the spongy-bone of the femur was determined in uncalcified microscopic bone sections embedded into methylmetacrylate. Surface measuring by an integration eyepiece revealed a loss of 36% trabecula after an immobilization time of 2 weeks (Table 2). After 4 weeks, only one third of the original spongy-bone is still present at this side (Figure 3).

The atrophy of the compact bone was measured by the NORDIN index in the transitional zone between the condylus and shaft of the femur (Figure 4). In contrast to the spongy-bone the atrophy of the compact bone is proceeding remarkably slower.

The NORDIN index of the femur is unchanged by a 5 day fixation, measurable symptoms of 20% atrophy appear after 3 weeks of fixation.

The quantitative calculations of bone remodelling were carried out by tetracycline labelling. The antibiotic tetracycline forms so called chelates with bivalent metal ions, especially with complex calcium compounds. Moreover, tetracycline shows fluorescence in ultraviolet light. Therefore tetracycline can be used for studies of bone remodelling instead of radioactive calcium.

The amount of active and inactive osteons can be analysed after a single labelling with tetracycline. At the same time the present bone resorption is determined as well. Therefore, tetracycline labelling in well defined intervals permits the calculation of bone remodelling and resorption.

According to FROST's Index the amount of osteons which active osteoid limbus per  $\text{mm}^2$  of compact bone was calculated. Femora of tetracycline labelled animals were used for these experiments. The Guinea pigs received two doses of 10 mg/kg body weight of methyltetracycline intermuscular on day one and ten of the experiment (Figure 5).

The function of the osteons is highly dependable upon the immobilization. 3 weeks after plaster treatment the amount of active osteons decreases to 50% (Table 3). Moreover, the amount of resorption channels is increasing about tenfold. The inactive osteons are doubled. This response to inactivation is also reflected by the amount of osteons, with active osteons limbus per  $\text{mm}^2$ . Since the small areas of bone sections can be included by this method. The above mentioned FROST Index is reduced to 50% by immobilization of 3 weeks.

Determination of osteoblasts and osteoclasts shows a two to fourfold increase of osteoclasts in comparison to controls. According to UEHLINGER an osteoclast destroys the amount of bone which is produced by 20 osteoblasts at the same time. Therefore the observed increase of osteoclasts explains the rapid resorption of spongy bone very well. This is only an indirect method for determination of bone resorption and formation since osteoblasts are also phagocytize any bone.

The calculation of the yearly rate of bone formation reflects the same results found by the FROST Index (Table 4). During an immobilization of 3 weeks the bone remodelling is reduced to 50%. Moreover, the microscopic bone sections revealed the following changes:

Immobilized bones show a remarkable reduction of osteocytes, the animals have smaller osteons with fewer canaliculi and smaller osteoid limbus. The results obtained with a polarising microscope revealed a resorption of fibrils by immobilization. The collagenous fibrils are thinner and atrophic in

the area of the outer and inner general lamellae (Figure 6).

The dry mass of bone substance was determined by interferential microscopic methods. Unstained and uncalcified sections longitudinal of the femur condyle were used for this purpose. The microscopic sections were tested for their thickness by interferometric in comparison with water. Sections with a deviation of more than  $0.1 \mu\text{m}$  of the ideal thickness of  $6.0 \text{ mm}$  were excluded. The average dry mass of the bone after 3 weeks of immobilization was  $6.48 \times 10^{-12} \text{ gm}/\mu\text{m}^2$  in comparison to controls which had  $8.05 \times 10^{-12} \text{ gm}/\mu\text{m}^2$  (Table 5). Therefore the loss of mineral substance was between 10.8% and 19.5% of the remaining bone. Our results are not in accordance with NORDIN's theory, that a deficiency of bone tissue, but a normal mineral content of the remaining bone, is marking osteoporosis. NORDIN, however, obtained his results by chemical analysis. As a result of the rapid resorption of spongy bone a recovery of bone minerals was expected from the excrements.

In preliminary experiments, the normal elimination of calcium, phosphorus and potassium by faeces and urine was measured under conditions of a dry standard fodder. The 3 weeks experimental period was preceded by a 2 weeks period of daily measurement of mineral balance (Table 6).

The calcium balance becomes significantly negative during 3 weeks of immobilization ( $p < 0.01$ ). The daily excretion was  $17.5 \text{ mval/l}$  and therefore exceeded the average uptake of  $15 \text{ mval/l}$ . The excretion of calcium increases continuously during the period of immobilization (Table 7).

The elimination of phosphorus is also significantly increased ( $p < 0.01$ ). In contrast to the elimination of calcium the mean differences of the daily balance of phosphorus are high especially during the first days of immobilization.

Fixation by pelvic plaster has no significant influence upon the elimination of potassium. The normal balance of this mineral is proving the normal functioning of the digestive system and the kidneys under experimental conditions.

The balance of sodium is slightly negative, but without significance. The negative balance of sodium is increased with high losses of calcium.

These experimental results obtained with Guinea pigs can be applied to the human organism only to a limited extent, considering the relative time of bone development one might suggest that comparable damage to the skeleton by immobilization in man is expected after a fivefold time.

The analysis of the urine and faeces of astronauts showed increased losses of calcium. Weightlessness as well as a certain immobility caused by, the narrowness of the

spacecraft could be made responsible for this observation. The Russian cosmonaut and physician JEGOROW reported high losses of calcium in the skeleton during his space flight. The 2 American astronauts who undertook the 8 days trip in gemini 5 had losses of 15% of the skeletal calcium. According to MACK and co-workers (1967) who measured the calcium content at peripheral sides of the skeleton of the gemini-astronauts the loss of calcium is significantly lower under calcium enriched nutrition. Moreover, the loss of minerals can be reduced by isometric and isotonic muscle contractions.

This observation seems to be in contrary to the former suggestion of MACK that the decrease of bone mass is provoked by the loss of gravity which might cause a disturbance within the crystal structure of the hydroxylapatite.

We, however, suggest, that only the limited possibility of movement by the astronauts within the spacecraft is responsible for the bone atrophy. This would be avoided to a certain extent by a programm of muscle exercises which could be carried out even under space flight conditions.

Unpublished experiments of BENEXE revealed, that calcitonin prevents osteoporosis in animals immobilized by plaster. Employing this method, it could be possible to reduce the development under space flight conditions. This in my opinion, seems to be an attractive method for the prevention of osteoporosis during extended space flights.



Figure 1

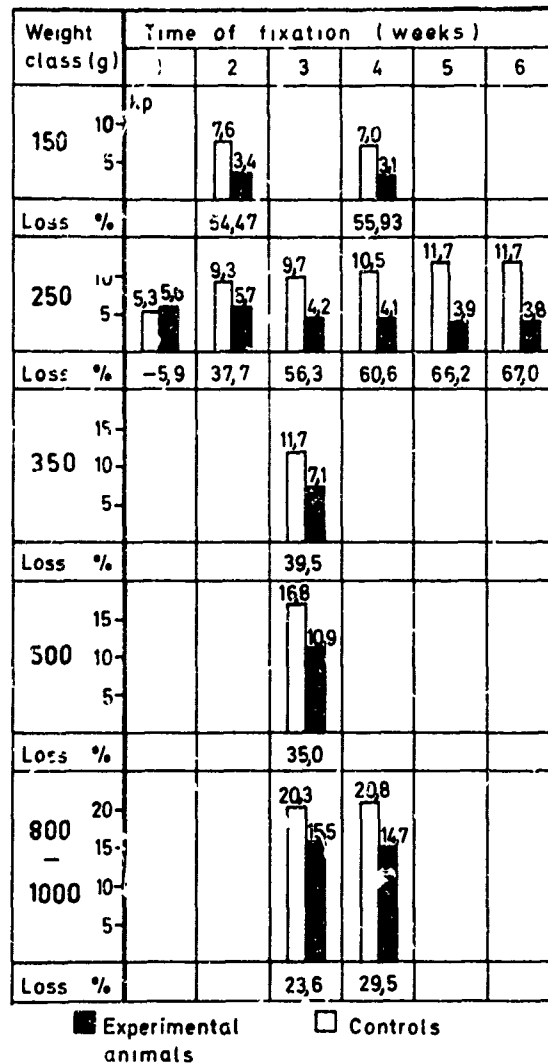
Male Guinea pig (body weight 336 g) with the pelvic plaster.  
The x-ray picture on the left side shows the position of  
the knee joint used for all experiments





Figure 1

Male Guinea pig (body weight 336 g) with the pelvic plaster.  
The x-ray picture on the left side shows the position of  
the knee joint used for all experiments



Reduction of the physiological breaking strength of femora by pelvic-plaster immobilization (guinea pigs)

Table 1

Fixation in a pelvic plaster in comparison with a clear reduction of the breaking strength of the immobilized femora

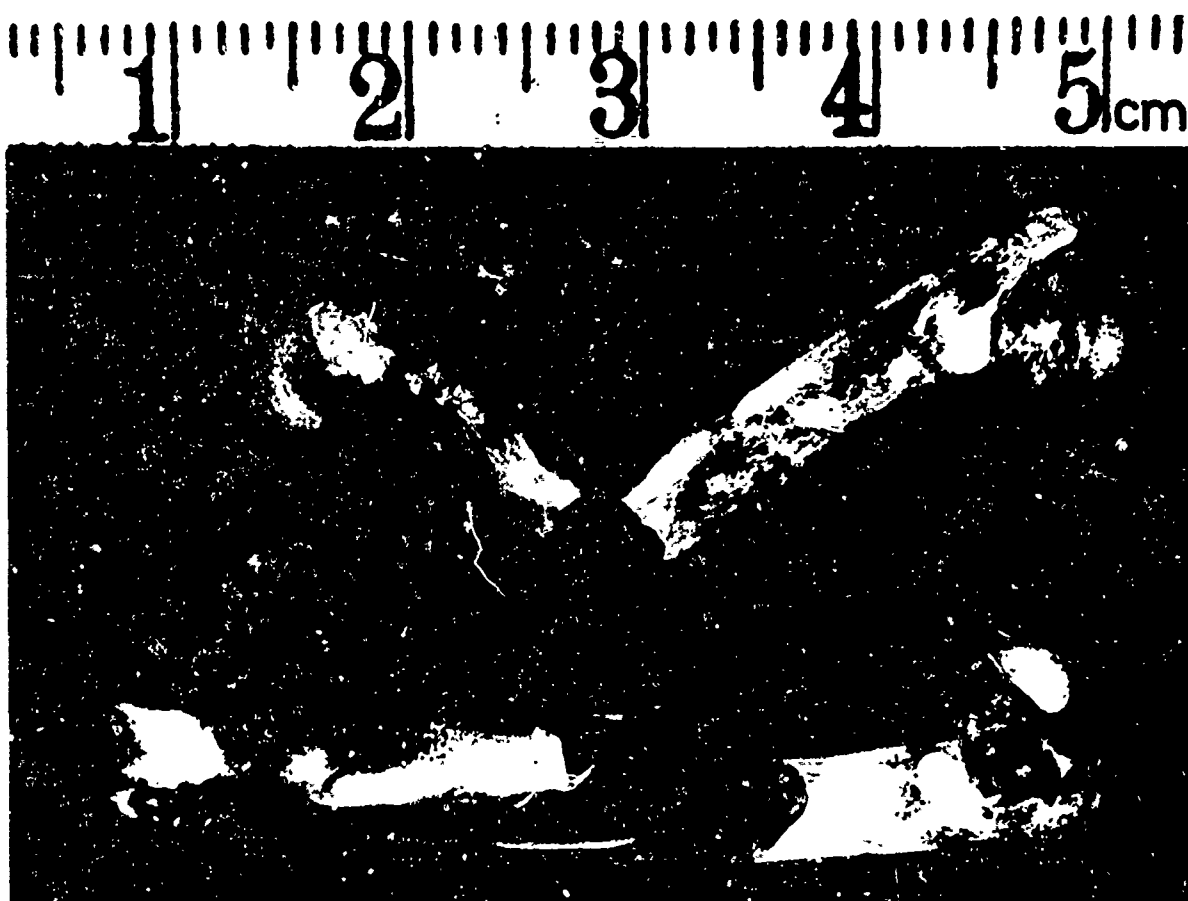
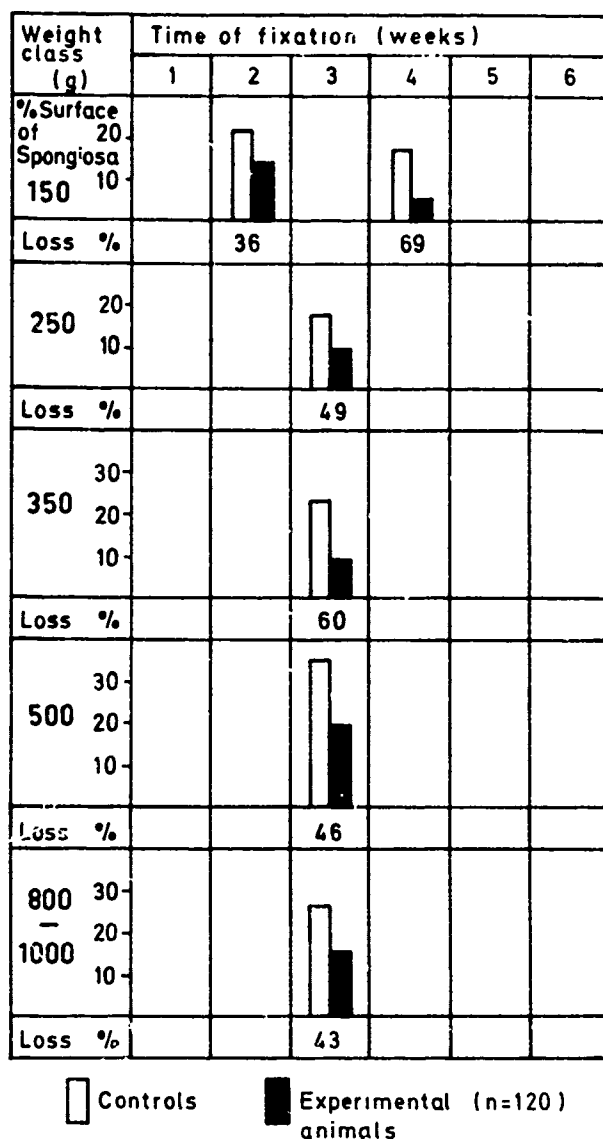


**Figure 2**

**Above: smooth fracture sides of osteoporotic bone**  
**Below: normal bone fracture with typical splintered pieces**



Atrophy of spongy bone by immobilization  
(120 guinea pigs with pelvic plaster)

Table 2

Rapid atrophy of spongy bone as result of immobilization



Figure 3

Uncalcified sections of the condylus of the femur. Thickness  
6  $\mu$ m, staining azur eosine. Magnification about 80 x.  
Above: plaster treatment for 3 weeks  
Below: control

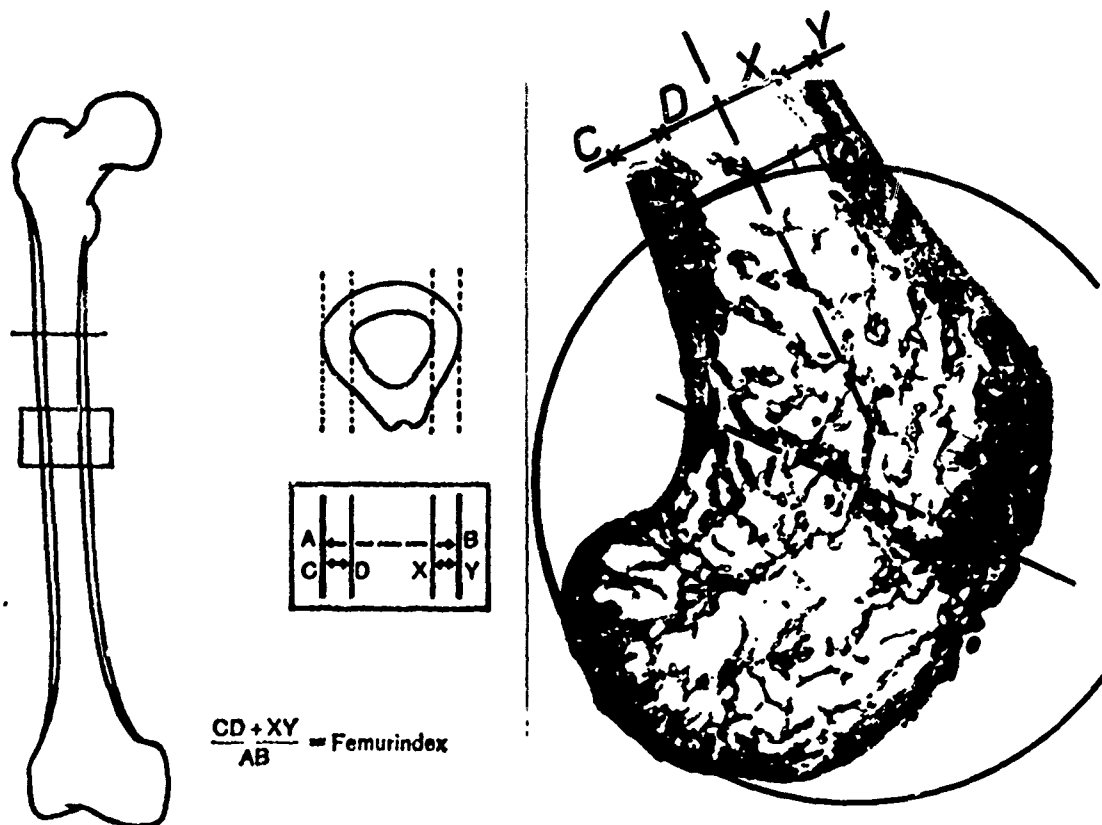


Figure 4

Left: femur index (NORDIN) for determination of atrophy of compact bone  
 Right: longitudinal section of the femur condyle and determination of NORDIN index

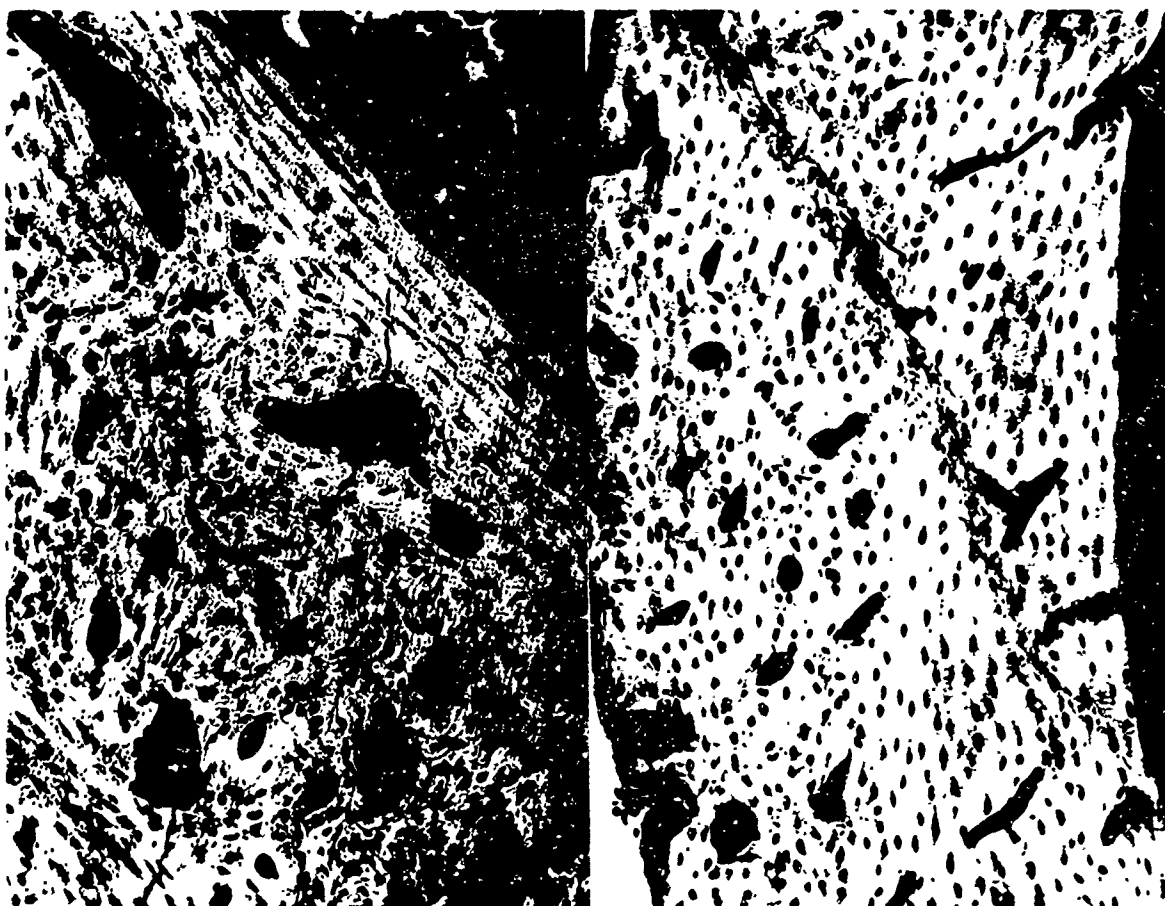


Figure 5 a

Uncalcified sections (6  $\mu$ m) of the compact bone of  
the femur under normal light  
Right: control  
Left: atrophy of bone surface and reduction of the  
amount of osteocytes 3 weeks after immobilization



Figure 5 b

The same sections as shown in figure 5 under ultraviolet light

Right: active osteons with doubled rings

Left: reduction of active osteons



no. of animals	starting weight g	weight at autopsy g	labelled % osteons	inactive % osteons	resorption channels	osteoid seam index (FROST)			
20 controls	480	610	80	62	48	37	2	1	15.0
20 exp. animals	490	590	33	32	60	58	11	10	6.7
20 controls	195	290	60	25	122	51	57	24	13.9
20 exp. animals	210	240	17	7	140	64	60	29	4.7

Measuring of bone remodelling during immobilization

Table 3

Reduction of active osteons and increase of resorption channels by immobilization

Influence of immobilization  
upon the average yearly bone  
formation rate

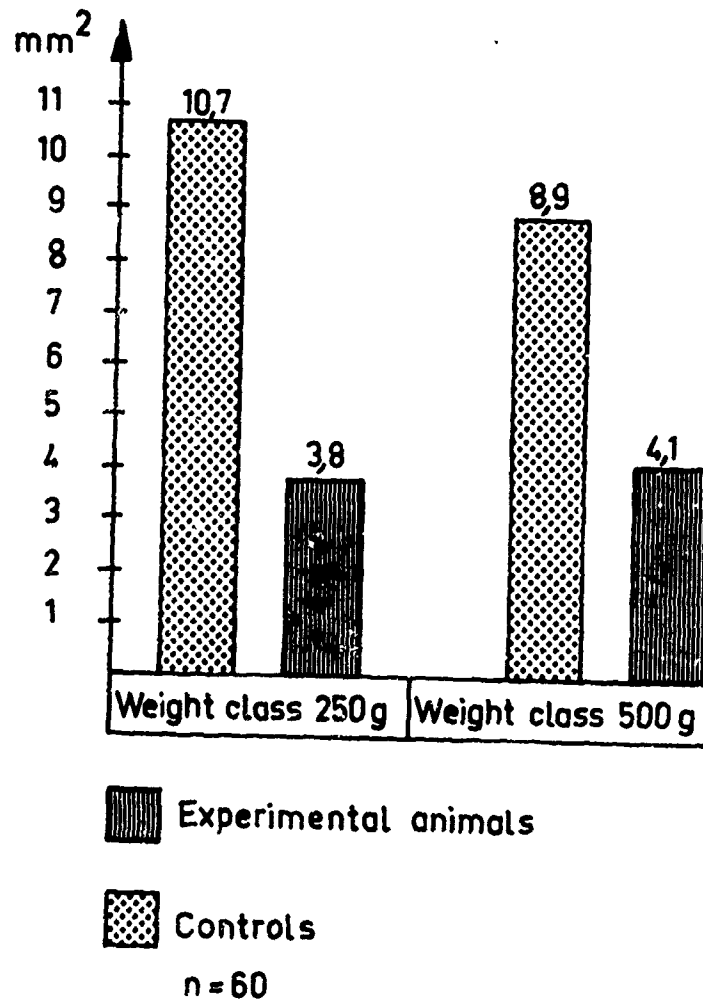


Table 4

Reduction of bone remodelling after immobilization

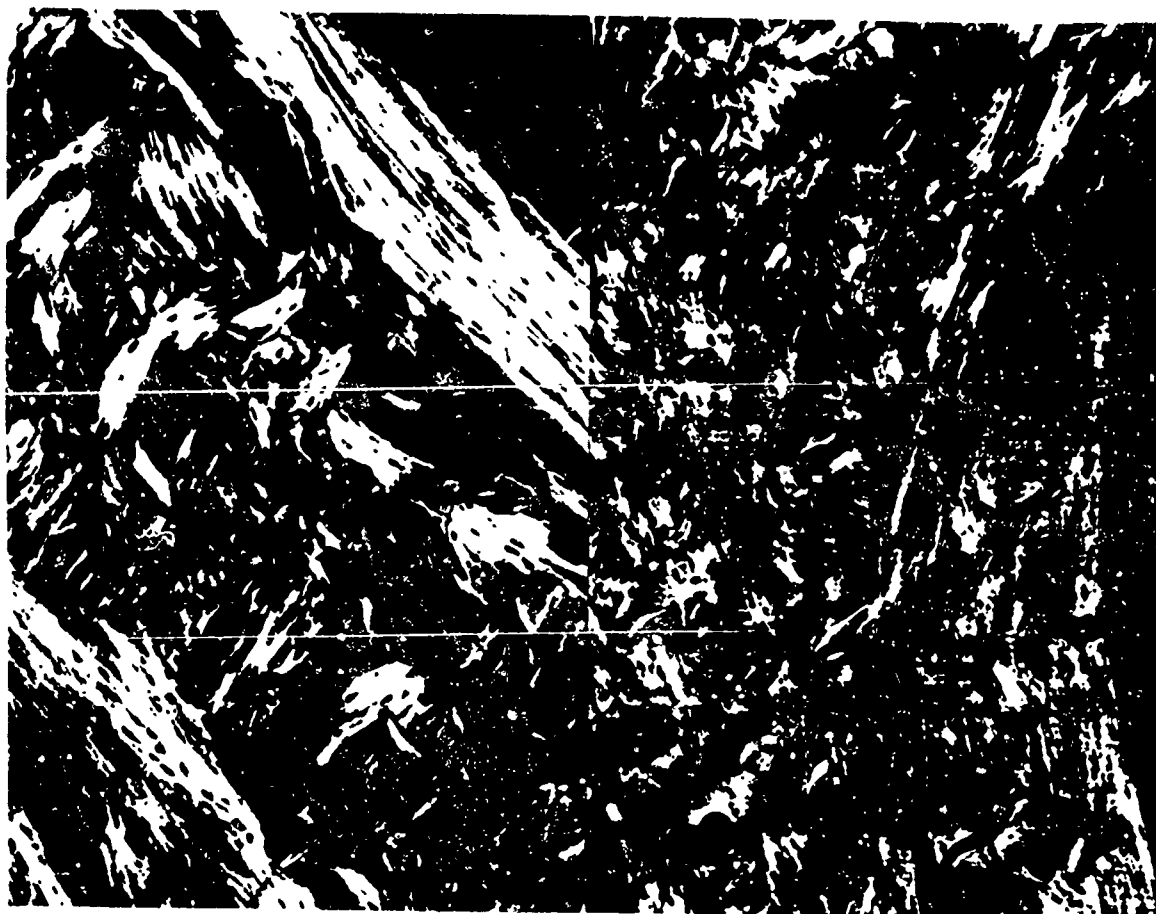


Figure 6

Sections of figure 5 under polarising light  
Right: control, normal structures  
Left: experimental animal with atrophy of the fibres

	starting weight g	sex	no. of animals	time of fixation (weeks)	dry bone mass $10^{-12} \text{g}/\mu\text{m}^2$	weight of anorganic bone mass $10^{-12} \text{g}/\mu\text{m}^2$
K	350	m	10	0	7,46	4,90
	350	f	10	0	7,68	5,05
V	350	m	10	3	6,66	4,67
	350	f	10	3	6,56	4,60
percentage of loss of weight by immobilization					10,8% 14,6%	4,7% 8,9%
K	800-1000	m	10	0	8,02	5,27
	800-1000	f	10	0	8,05	5,28
V	800-1000	m	10	3	6,40	4,48
	800-1000	f	10	3	6,48	5,54
percentage of loss of weight by immobilization					10,4% 19,5%	15,0% 14,1%

#### Dry weight of the femur—compacta revealed by interferometry

( V = Test animals, K = controls )

( m = male              f = female )

Table 5

Weight reduction of the matrix 3 weeks after immobilization

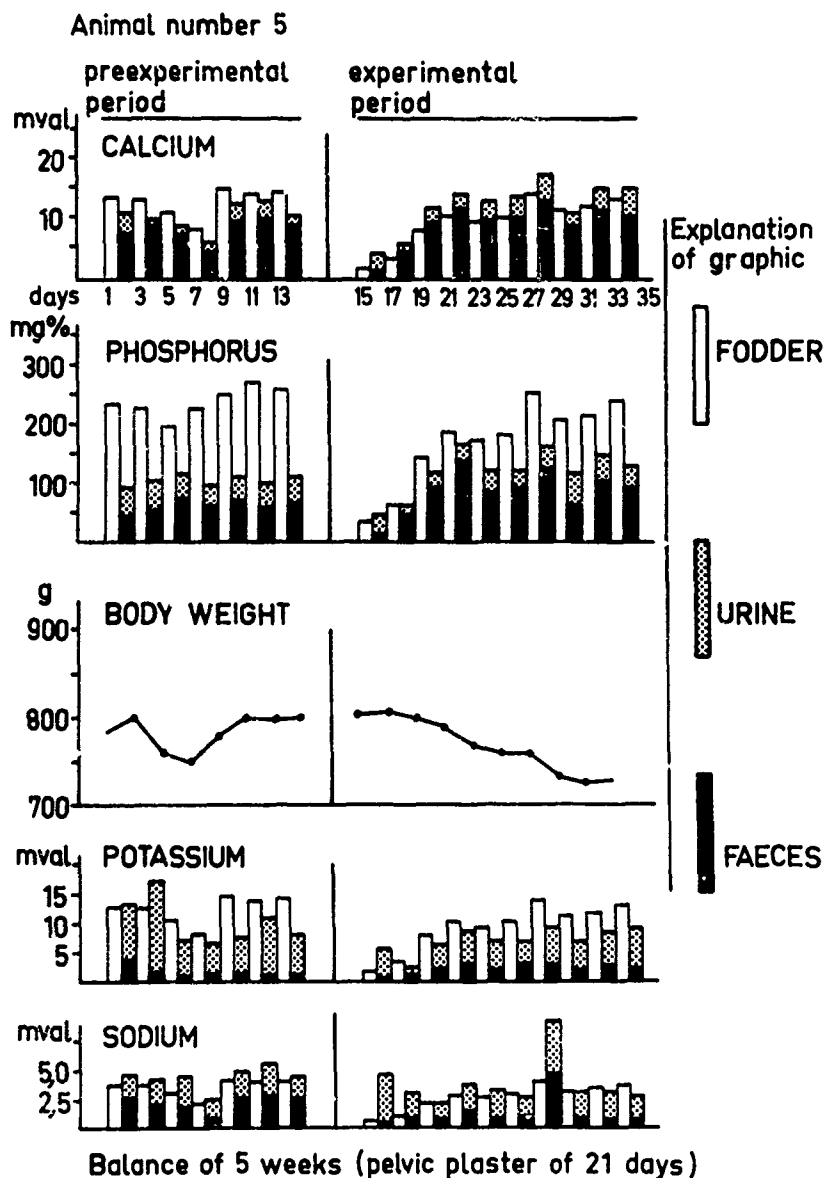
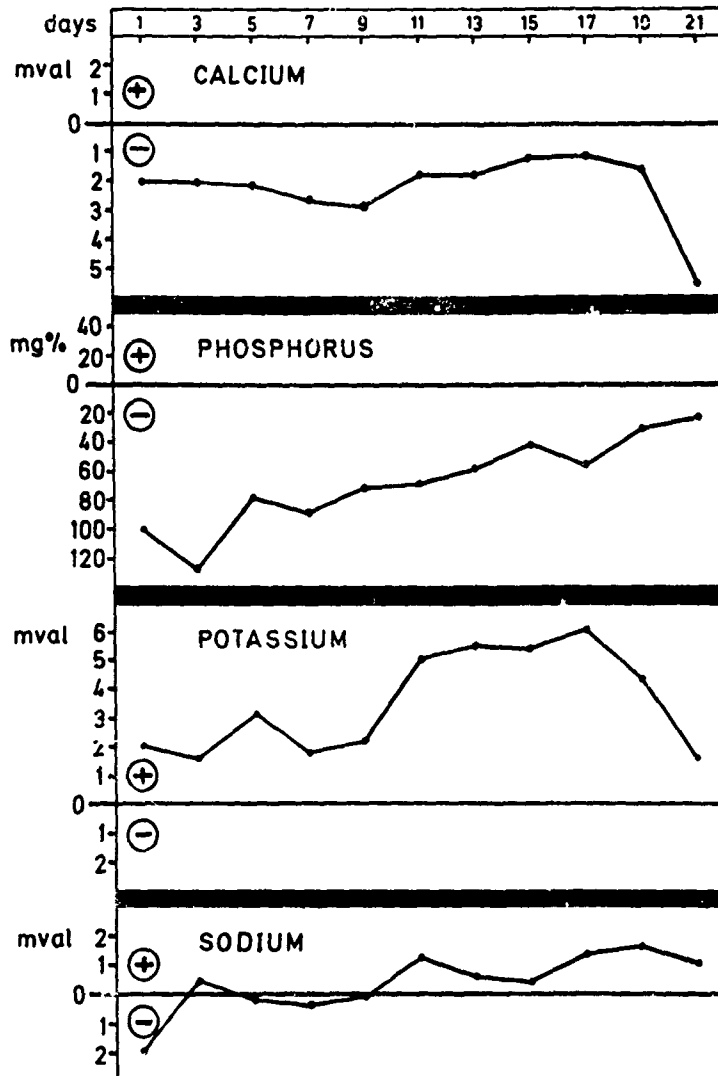


Table 6

Mineral elimination in comparison with the average elimination of the preexperimental period



Mineral elimination compared to the average  
elimination of the preexperimental period  
(6 guinea pigs)

Table 7

Mineral balances of 6 Guinea pigs during plaster  
treatment for 3 weeks

## References

BIRKHEAD, B.: zit. by ALBANESE, A.A.: Effect of exercises on nutritional requirements. In: Gordon research conf. food and nutrition colby junior coll. New London 1966

DEITRICK, J.E., G.D. WHEDON, E. SHORR: Effect of immobilization upon various metabolic and physiologic functions of normal men. Amer. J. Med. 4 (1948) 3

EICHLER, J.: Inaktivitätsosteoporose, Aktuelle Orthopädie Heft 3, G.Thieme, Stuttgart (1970).

GEISER, M., J. TRUETA: Muscledaction, bone rarefication and bone formation, J. Bone Jt. Surg. (Edinb.) 40 (1958) 282

JEGOROW, E.: zit. by: KROKOWSKI, E., E. HAASNER: Aktuelle Bedeutung der quantitativen Bestimmung des Skelett-Calciumgehaltes, Wehrmed. Mschr. 12 (1968) 229

MACK, P.B., P.A. LACHANCE, G.P. VOSE, F.B. VOGT: Bone demineralization of foot and hand of gemini-titan VI, V and VII astronauts during orbital flight, Am. J. Roentgen. 100 (1967) 3

NORDIN, B.E.C.: The pathogenesis of osteoporosis, Lancet, (1961) 1011

REIFENSTEIN, E.C., F. ALBRIGHT: Paget disease: its pathologic physiology and the importance of this in the complications using from fracture and immobilization. New Engl. J. Med. (1944) 231

## R e f e r e n c e s

BIRKHEAD, B.: zit. by ALBANESE, A.A.: Effect of exercises on nutritional requirements. In: Gordon research conf. food and nutrition colby junior coll. New London 1966

DEITRICK, J.E., G.D. WHEDON, E. SHORR: Effect of immobilization upon various metabolic and physiologic functions of normal men. Amer. J. Med. 4 (1948) 3

EICHLER, J.: Inaktivitätsosteoporose, Aktuelle Orthopädie Heft 3, G.Thieme, Stuttgart (1970).

GEISER, M., J. TRUETA: Musculation, bone rarefaction and bone formation, J. Bone Jt. Surg. (Edinb.) 40 (1958) 282

JEGOROW, E.: zit. by: KROKOWSKI, E., E. HAASNER: Aktuelle Bedeutung der quantitativen Bestimmung des Skelett-Calciumgehaltes, Wehrmed. Mschr. 12 (1968) 229

MACK, P.B., P.A. LaCHANCE, G.P. VOSE, F.B. VOGT: Bone demineralization of foot and hand of gemini-titan VI, V and VII astronauts during orbital flight, Am. J. Roentgen. 100 (1967) 3

NORDIN, B.E.C.: The pathogenesis of osteoporosis, Lancet, 1 (1961) 1011

REIFENSTEIN, E.C., F. ALBRIGHT: Paget disease: its pathologic physiology and the importance of this in the complications arising from fracture and immobilization. New Engl. J. Med. (1944) 231



AMRL-TR-71-29

SESSION III

MECHANICAL CHARACTERIZATION OF LIVING  
TISSUE AND ISOLATED ORGANS

Chairman

H. L. Oestreicher  
AMRL

Co-chairman

L. Kazarian  
AMRL

PRECEDING PAGE BLANK

PAPER NO. 12

THE MECHANICAL CHARACTERISTICS OF SKIN AND  
OTHER SOFT TISSUE AND THEIR MODELLING.

BY

R. M. Kenedi

BIOENGINEERING UNIT, UNIVERSITY OF STRATHCLYDE,  
GLASGOW, SCOTLAND.

INTRODUCTION

The Tissue Mechanics Division of the BioEngineering Unit has been concerned for some six years with the mechanical characterisation of soft connective tissues such as skin, tendon, ligament, cartilage, etc. The load deformation characteristics have been studied on the macro and micro scales in vitro and in vivo.

At the commencement of its activities some 7 years ago the Unit started with a fairly clearly defined problem - that of the load deformation behaviour of human skin in vivo with special reference to reconstructive plastic surgery. Following some seven years of intensive research activity it can be stated that i) no solutions have been obtained and ii) the problems have multiplied.

In consequence one can only say on behalf of the Division that we are confused, that to some extent we know what confuses us and that all that can be offered in this brief presentation is to pass to you in as clear a manner as I am capable of the confusion that characterises the present state of ignorance in this field.

I propose to deal with the subject broadly in three areas: the mechanical characteristics of tissue as a "material"; the functional role of tissue and the potential influence of this role on mechanical characterisation and modelling concepts.

Prior to commencing the presentation I should make it clear that the work that I am going to outline is that of others in the Strathclyde Tissue Mechanics Division, my role being purely that of the transmitter. In that sense this contribution could possibly be best summed up by a slightly paraphrased version of an oft repeated saying namely "something old, something new, mostly borrowed but possibly not blue".

PRECEDING PAGE BLANK

## MECHANICAL CHARACTERISATION OF TISSUE AS A MATERIAL

It is pertinent at this point to indicate how at Strathclyde interest in the mechanical characteristics of tissue arose. This as mentioned commenced in relation to clinical problems associated with reconstructive surgery.

Figure 1 shows a skin flap design used to excise a skin cancer on the forehead. The first step is to excise the triangle containing the defect. The next step is to raise the rectangular flap A leaving it attached at its base and rotating it in the direction of the arrow so as to cover the excision wound. This uncovers a discontinuity in the original position of this flap which is then covered by the secondary flap B pulled into position as indicated.

Figure 2 shows the operation result. It can be seen that such a topographical rearrangement can only be effected if in addition to body movements of the flaps, they are also extended in a variety of directions. Thus the skin undergoes loading and the deformations corresponding to the loading during such manipulations.

Figure 3 indicates the situation that resulted in a similar case when closure was unsuccessfully attempted. The flap design in this case was ineffective and demonstrated that skin while capable of extending has a limit deformation just like all other materials which cannot be exceeded without onset of rupture. The operation in this instance was completed by a free graft. A variety of similar examples can be quoted from virtually all fields of surgery, which in a broad sense might be regarded as a form of engineering construction in human tissue as its material. In consequence surgeons for example require knowledge of mechanical characteristics of human tissue in the same way as engineers do.

To assess these mechanical characteristics at its simplest figure 4 shows the results of a tensile test on human skin. The load extension graph shown on the right hand of the figure is typical of virtually all tissues -- initially fairly large extensions for relatively low load followed by extensions at a decreasing rate with increasing loads. The "Poisson" effect shown on the left hand side of the diagram follows the same pattern. It is particularly significant that these contractions at right angles to the load are comparable in magnitude to the direct extensions. This implies that the tissue must be subject to volume loss and that the "material" is not a homogenous continuum.

12 2000 00 000000

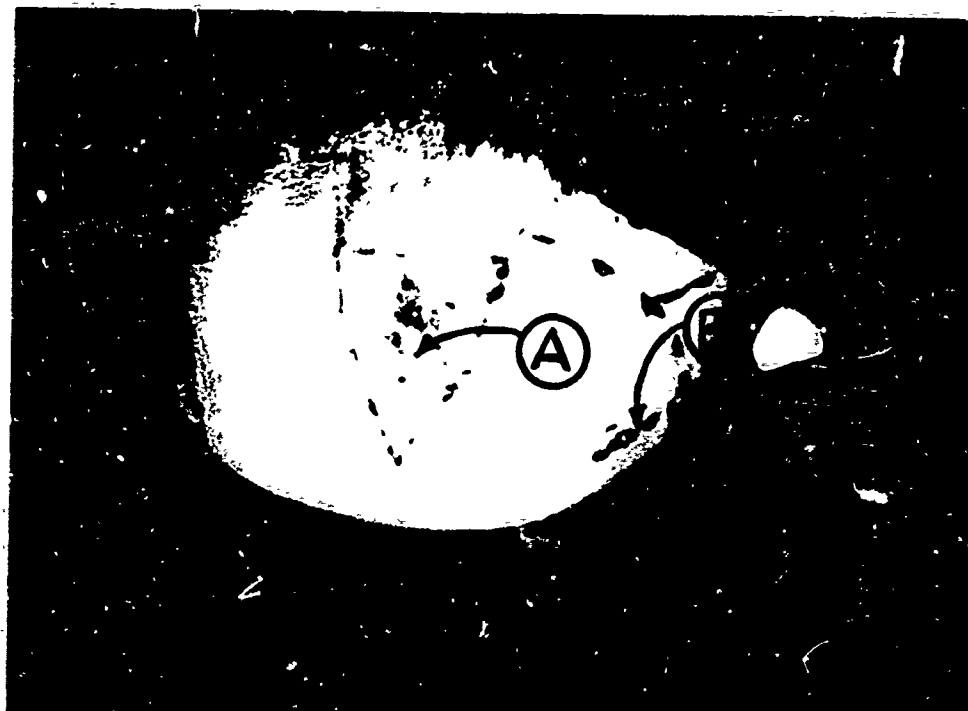


Figure 1



Figure 2

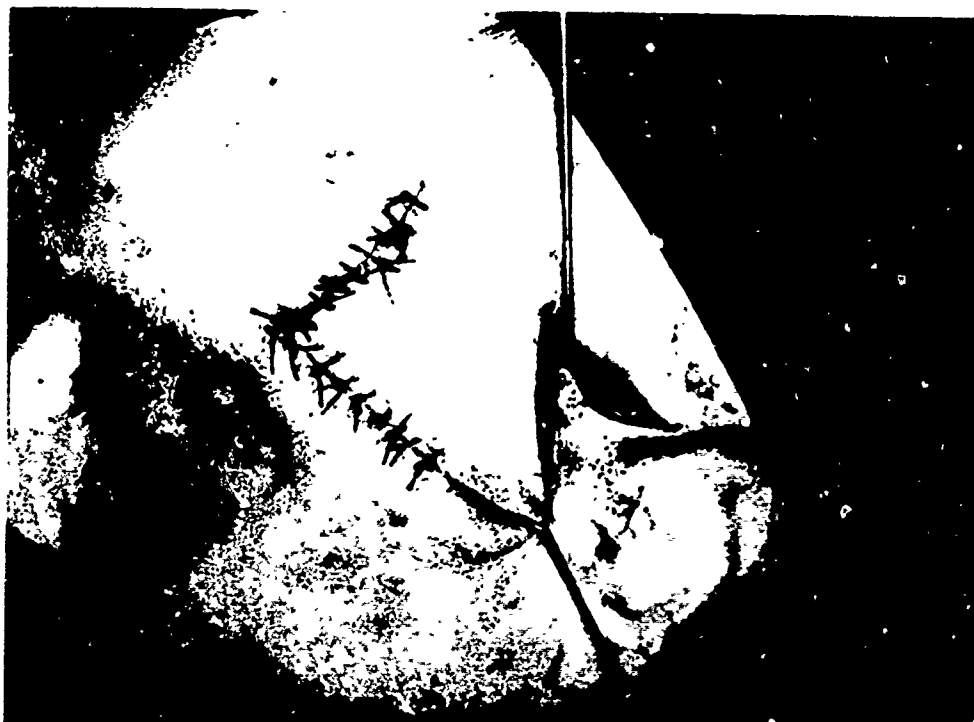


Figure 3

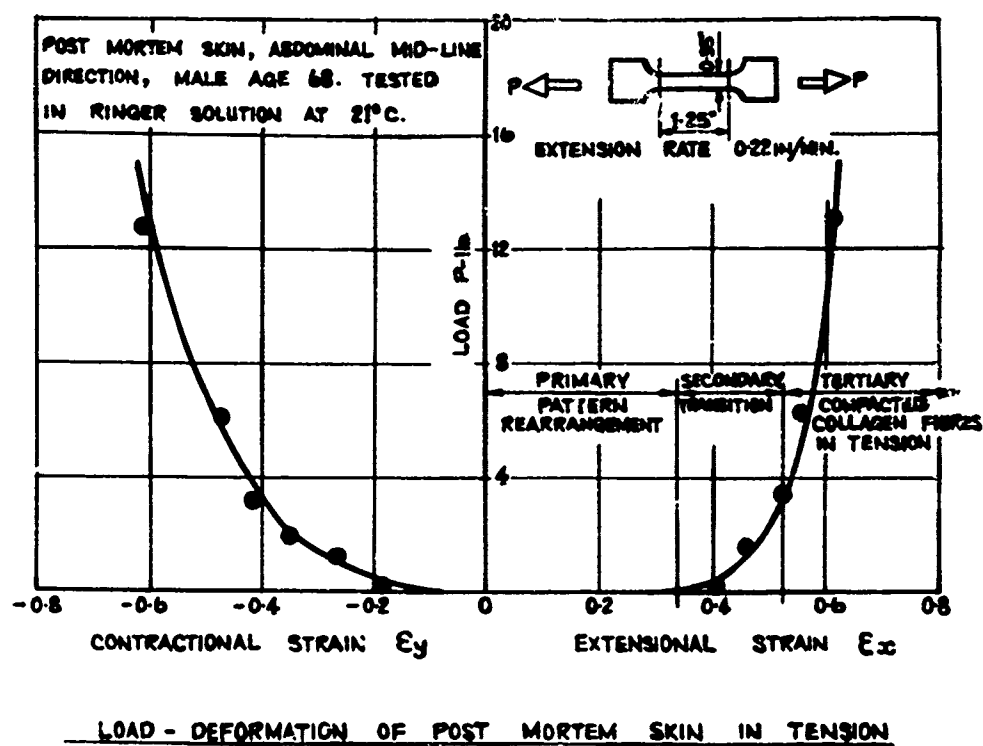


Figure 4

Figures 5 and 6 show similar tensile graphs of a variety of tissues ranging from a single fibre of collagen to a single strand of elastin. It is seen that effectively the same shape of curve is obtained although of widely varying magnitudes in the extension load response.

Figure 7 shows strain rate sensitivity and stress relaxation curves for human skin. It has also been established that other tissues exhibit these effects.

In summary one can describe human tissue from a mechanical point of view as a nonhomogeneous, nonlinear visco-elastic substance. The degree of nonlinearity and visco-elasticity varies to an appreciable extent as between different tissues. It is further suspected that quantitatively the spectrum of random variation that may be encountered in comparable normal individuals is such as to make reliable quantitative forecasts problematical.

#### FUNCTIONAL ROLE OF THE TISSUES

Figure 8 shows Langer's (1861) lines of the human torso. These were obtained by puncturing the skin of a cadaver with a round bladed instrument which on withdrawal left an oval wound. He found that these wounds lined up to form the kind of patterns that are shown in the figure. Various interpretations have been given to these patterns -- Langer himself seemed to think that these were related to the stress actions that obtained in the skin as a result of its containment function for the human body. Recent work by Stark (1970) in vivo has shown that these lines are representative of a phenomenon functional in origin and related to skin extensibility. Figure 9 shows the in-vivo set up. In this two pads are attached to the skin by adhesive. These are then pulled apart at a predetermined time rate until a pre-set tensile load is reached. The corresponding extension on a length marked between the pads is then recorded. At selected points on the body surface such constant loads were applied in eight different directions at each point with the corresponding extension measured in each instance.

In Figure 10 are plotted the variation with orientation of these extension readings for each point. It is seen that these define ellipses and that the minor axes of these ellipses tend to line up with the corresponding Langer's line. These lines therefore may be interpreted in vivo as lines of minimum extensibility. Obviously the extensibilities influence greatly scar formation consequent on incisions which therefore should preferably be made along Langer's lines for minimal wound opening.

The variability of these load/extension variations over the skin surface also implies probable variability of the limit 'stretch' of skin. This in turn

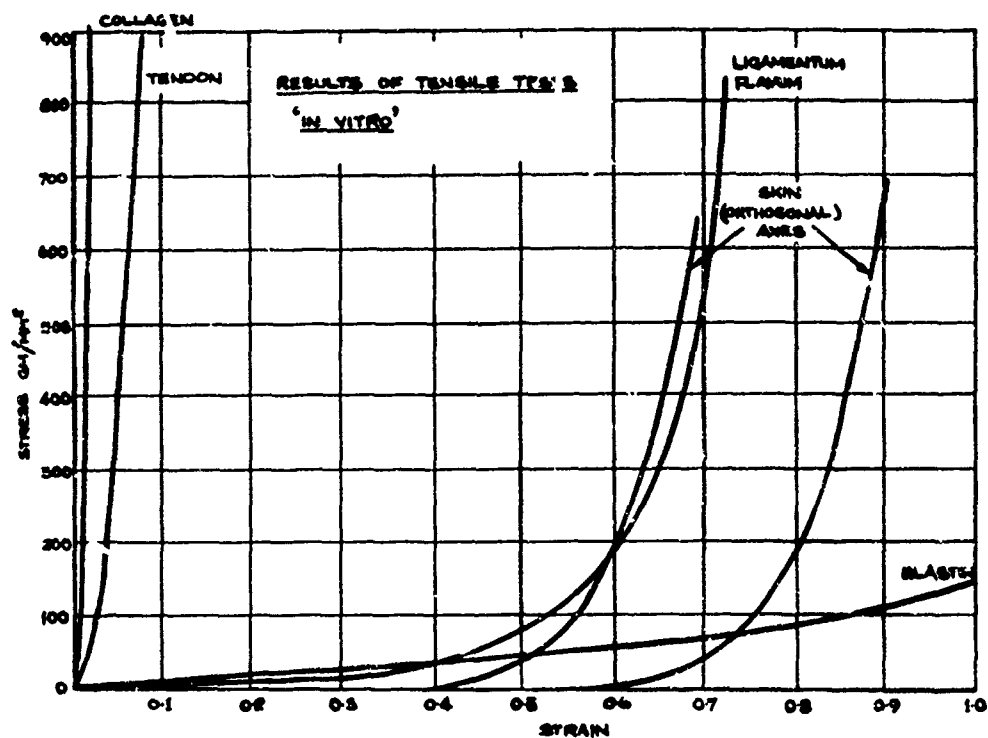


Figure 5

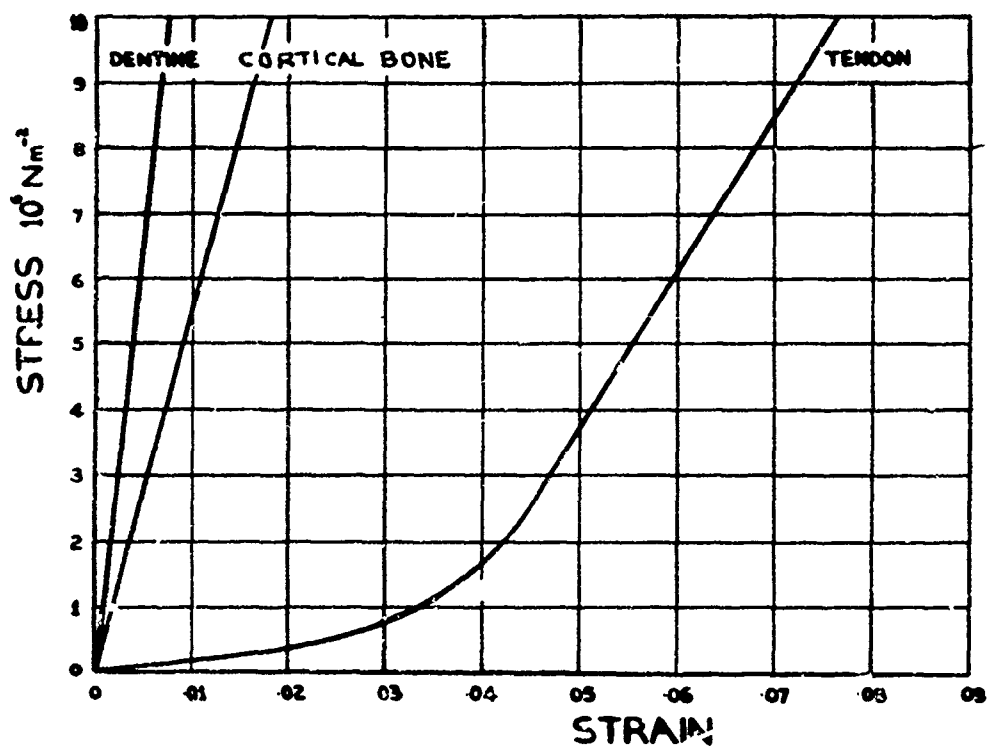


Figure 6

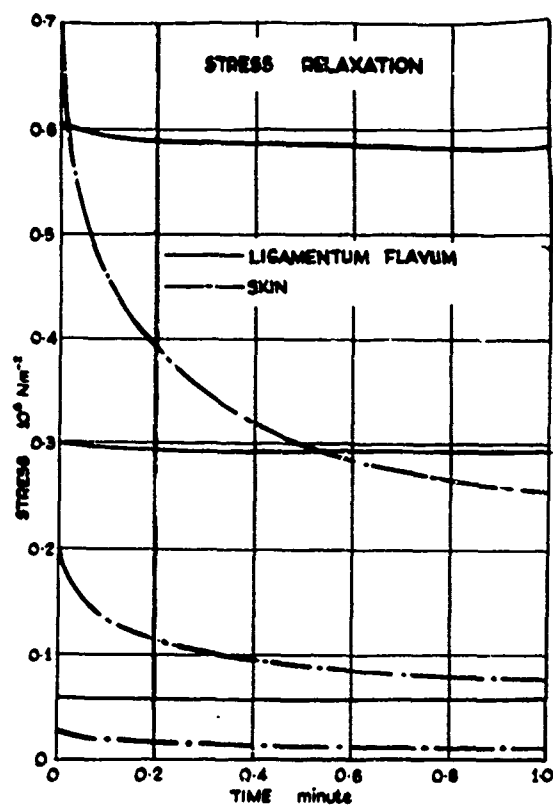


Figure 7

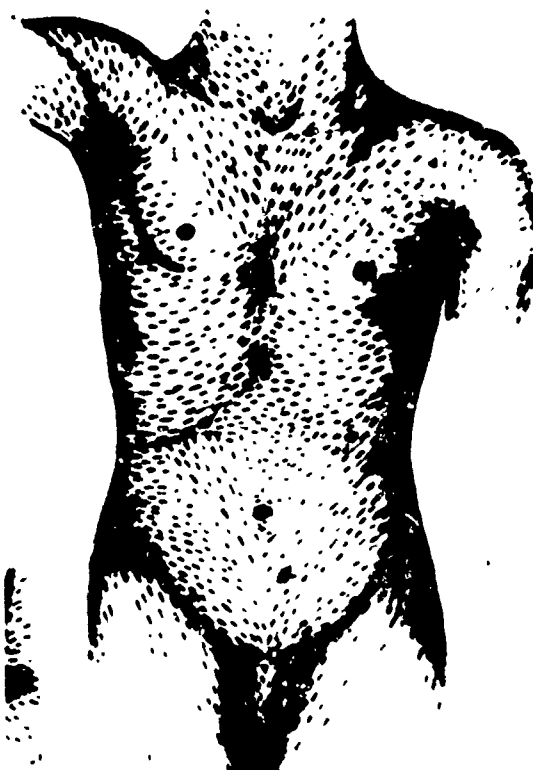


Figure 8



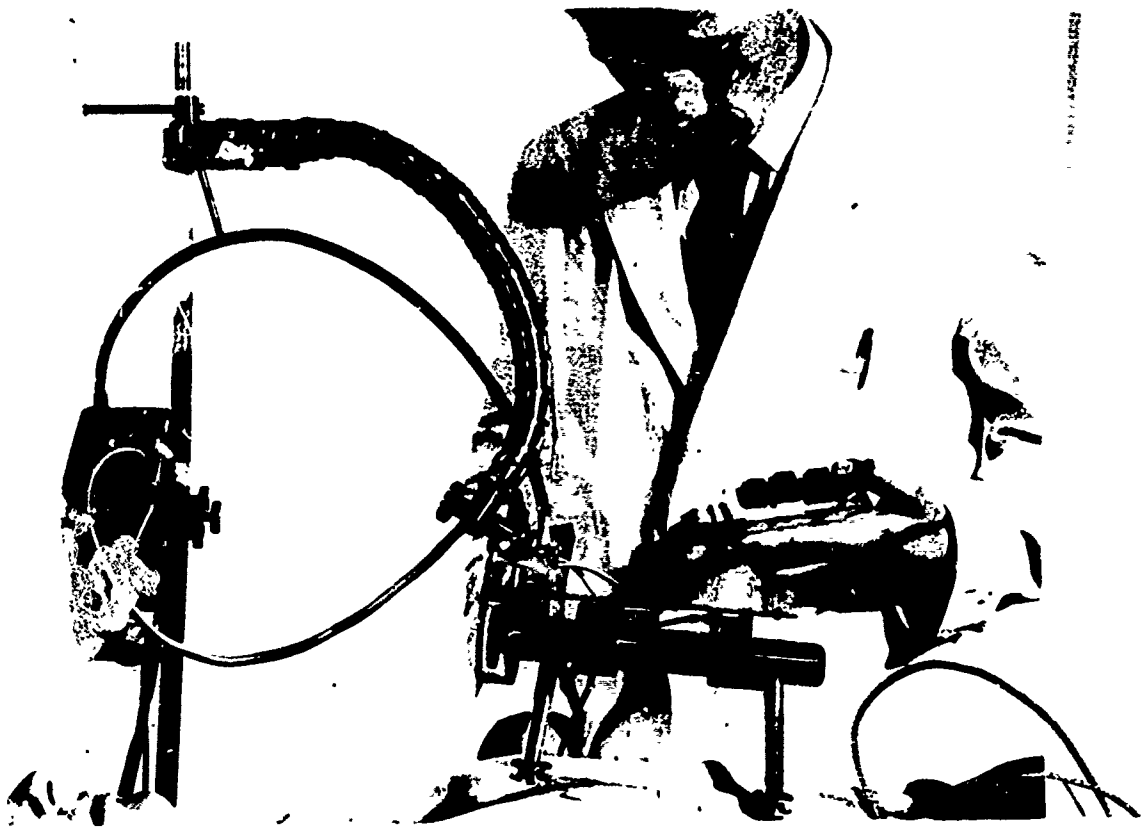


Figure 9

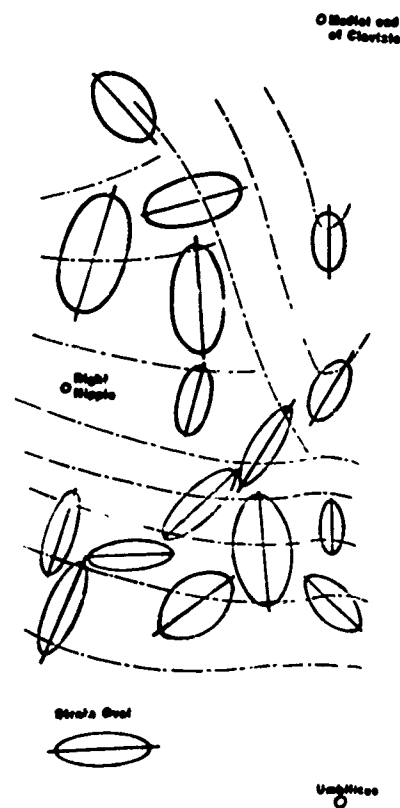


Figure 10

emphasises the very considerable difficulty in arriving at basic criteria to define the permissible limits of body loading. In some of the papers at this Symposium it was suggested for example that the relevant load limits may be definable in terms of certain limiting tissue stretch. Considering Langer's lines it will be appreciated how complex the attempt at arriving at such limits might become: for example it would be necessary in a given biodynamic situation not only to identify the maximal load pattern but also its interaction with the functional variation of the human skin cover. This in turn may imply that it is not necessarily the uniquely maximal load that causes damage but rather certain particular combination of load and deformation response which result in critical levels.

In this connection it is necessary to make a further point. Throughout the preceding discussions in the symposium the 'body limit' in relation to biodynamic loading seems to have been conceived as failure of some kind. (For example rupture of tissue, fracture of bone). It should be emphasised most strongly that in the author's view impending physiological impairment rather than tissue failure should be the criterion. One views with increasing concern certain areas of human experimentation where minor, possibly undetectable, physiological impairment may obtain which on repeated applications of the same circumstance might result in serious body damage as a result of cumulative effects.

"Functional" patterns similar to Langer's lines in skin can be obtained in other tissues such as articular cartilage. (Mital 1970\*) Figure 11 shows the kind of puncture pattern that one obtains in the articular cartilage of the head of the femur when puncturing the head with a round bladed instrument. It is seen that the puncture lines run roughly radially following the lines of compressive stress resulting from the type of loading that obtains on the head of the femur in normal circumstances. When one pictures in the same fashion the acetabulum, the articular cartilage there exhibits the patterns shown in figure 12. These again tend to follow the lines of compressive stress which in the case of the acetabulum (roughly a hemispherical bowl subject to radial load) are circumferential. Figure 13 represents a somewhat speculative correlation of the femoral and acetabular patterns with the subject in a standing position with feet together. The patterns appear to be matched, the puncture trajectories crossing roughly at right angles. It is interesting to speculate whether this kind of complimentary pattern is functionally conducive to more effective lubrication by enhancing fluid interchange between the matching surfaces. If such speculation is correct it is somewhat sobering to reflect that quite a number of surgical procedures (such as osteotomies with femoral head rotations) disturb this relationship. One would surmise that such disturbance is likely to be detrimental although the clinical significance of this is not known.



Figure 12



Figure 11

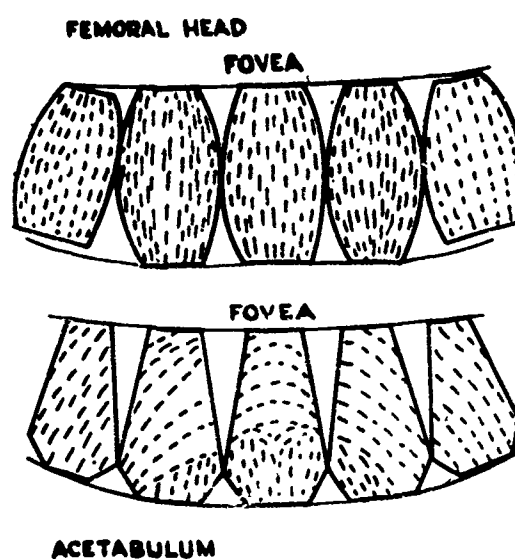


Figure 13

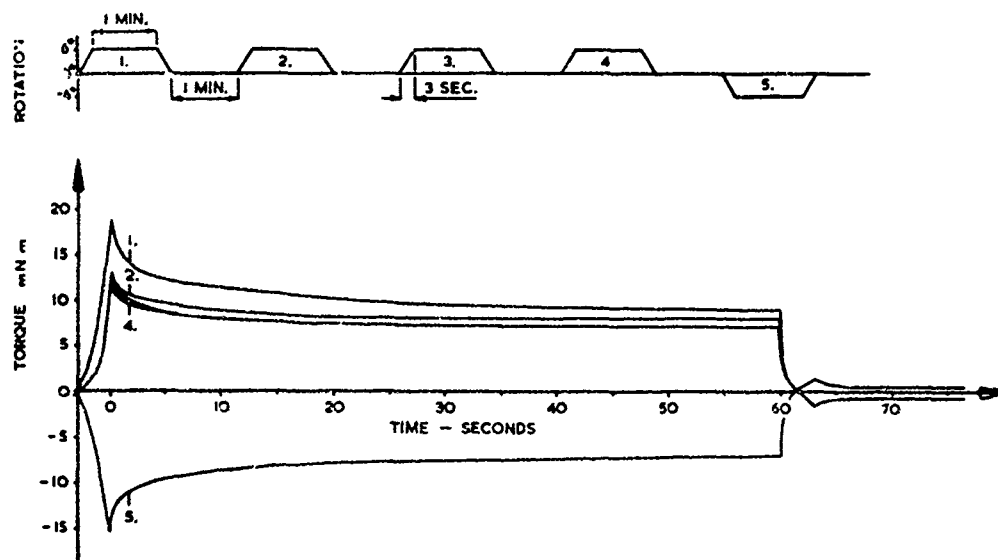
Again these speculations react on the question of biodynamic modelling in two ways: firstly by highlighting the complexity of the likely deformation response of a human body component as opposed to the idealised whole body and secondly, by emphasising the dangers of disturbance of the tissues' functional role, through external interference. This point must be emphasised and re-emphasised as the author's background experience in this area tends increasingly to show that our sum total of knowledge of the mechanical behaviour of tissue particularly in relation to these functional aspects is pityfully restricted. We might be permitting body interference particularly in the field of biodynamics on the basis of inadequate data and this may lead because of cumulative effects to catastrophic results.

The work presented up to now has been primarily static and quasistatic. Certain dynamic work has been performed by Duggan (1967), Daly (1966) and Finlay (1979). The last named whose work represents the establishment of a definitive technique carries out "torsion tests" on human skin in vivo. The technique consists of attaching a disc (commonly 15 mm diameter) by means of a suitable adhesive to the skin surface. The area of skin under test is delineated by attaching an annular disc of 25 mm diameter encompassing the 15 mm disc. This is then oscillated in a torsional manner by feeding to it angular displacement inputs, normally in the form of trapezoidal ramps as shown in figure 14. This figure shows the results of repeated ramp inputs. It is seen that the resulting torque versus time graphs exhibits the typical deformation response encountered in static tests followed by stress relaxation and on removal of load, restitution. It is interesting to note that on removal of the displacement the torque values do not return to zero immediately but switch across to the negative domain, and further that the maximum torque values tend to drop on repetition of action in the same direction while on reversal reach magnitudes of the order of the first input.

Figure 15 shows a most interesting phenomenon -- that of effective independence of phase lag (displacement leading torque) from frequency up to about 10 Hertz. This is well established and probably indicates that the tissue fluid within the skin substance is thixotropic i.e. its viscosity varies indirectly with shear rate which in turn is proportional to frequency.

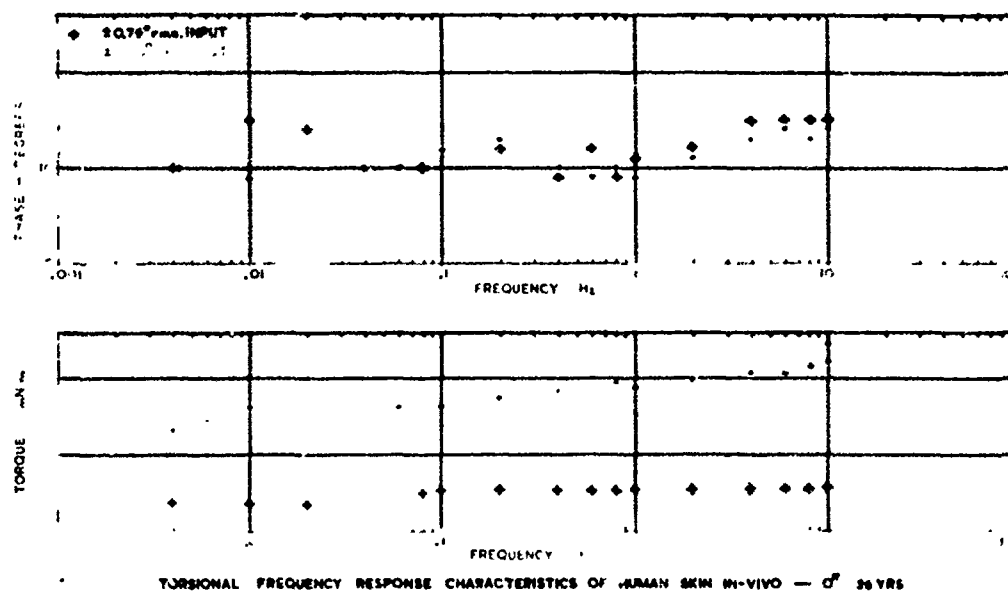
#### MICRO ARCHITECTURE

Anyone who works with tissue particularly from the engineering point of view becomes aware of its somewhat unique nature as a "material." It has already been indicated that its behaviour is highly complex. Such complexity necessitated extensive micro scale investigations primarily, because the information that was available from micro anatomy for body tissues was exceedingly sketchy and grossly inadequate for mechanical analysis. In the following, random examples of tissue structure and its interrelation with mechanical characteristics is presented.



REPEATED TRAPEZOIDAL TORSIONAL TEST - LEFT CALF  $\sigma$  72 YRS.

Figure 14



TORSIONAL FREQUENCY RESPONSE CHARACTERISTICS OF HUMAN SKIN IN-VIVO -  $\sigma$  30 YRS

Figure 15

Figure 16 shows Scanning Electron Microscopy (SEM) photographs of normal and arthritic articular cartilage surface. The typical irregularity of the normal surface has been ascribed to a lubrication enhancing feature. The concept is that the irregularities retain portions of synovial fluid and thus permit a kind of "squeeze" lubrication. (Walker et al, 1968). It is worthy to note that the nature of these irregularities is now a matter of some controversy as Clarke (1970) has shown that the undulating appearance is probably artefact although there are irregularities mostly of a figure 'eight' outline. The arthritic surface is characteristically littered with debris.

Figure 17 is that of a chondrocyte in articular cartilage. The photograph shows the basically fibrous structure of articular cartilage. It can also be seen that there is a degree of shrinkage due to dehydration in preparing the specimen. The author may be forgiven if he comments that he finds these SEM photographs fascinatingly impressive. It is always a pleasure to realise how elegant one's internal aspects are even if one's external appearance does not come up to expectation.

Figure 18 to 20 inclusive show SEM photographs of skin at increasing magnifications. It is seen that what appear to be collagen fibres in figures 18 and 19 are in fact composed of fibrils.

Figure 21 shows the effect of load - the specimen was subjected to tensile load and then fixed in that position. It is seen that there appears to be a layering effect, the first layer of closely interlinked fibres actually split at right angles to the direction of the applied load, while the layer below it of more mobile fibres is shown to have aligned itself in the direction of load.

Figure 22 shows the micro architectural appearance along and at right angles to Langer's lines. Layering is again clearly visible and in addition there appears to be a greater density of fibres running parallel to Langer's lines than at right angles to them.

Figure 23 shows the typical macro scale age effect in tension and the corresponding SEM diagrams. The primary effect of age on the tensile load extension graph is a reduction in the initial extension at low load and it is seen that this correlates with a less mobile and more closely interlinked fibre structure.

#### MODELLING TRENDS AND CONCEPTS

Broadly there have been three basic approaches to tissue modelling. The first one consists basically of attempts to find an artificial material that will behave not unlike the tissue to be modelled. In connection with human tissue virtually every new man made material that comes on the market is tried out, in the author's opinion with an outstanding lack of success. Figure

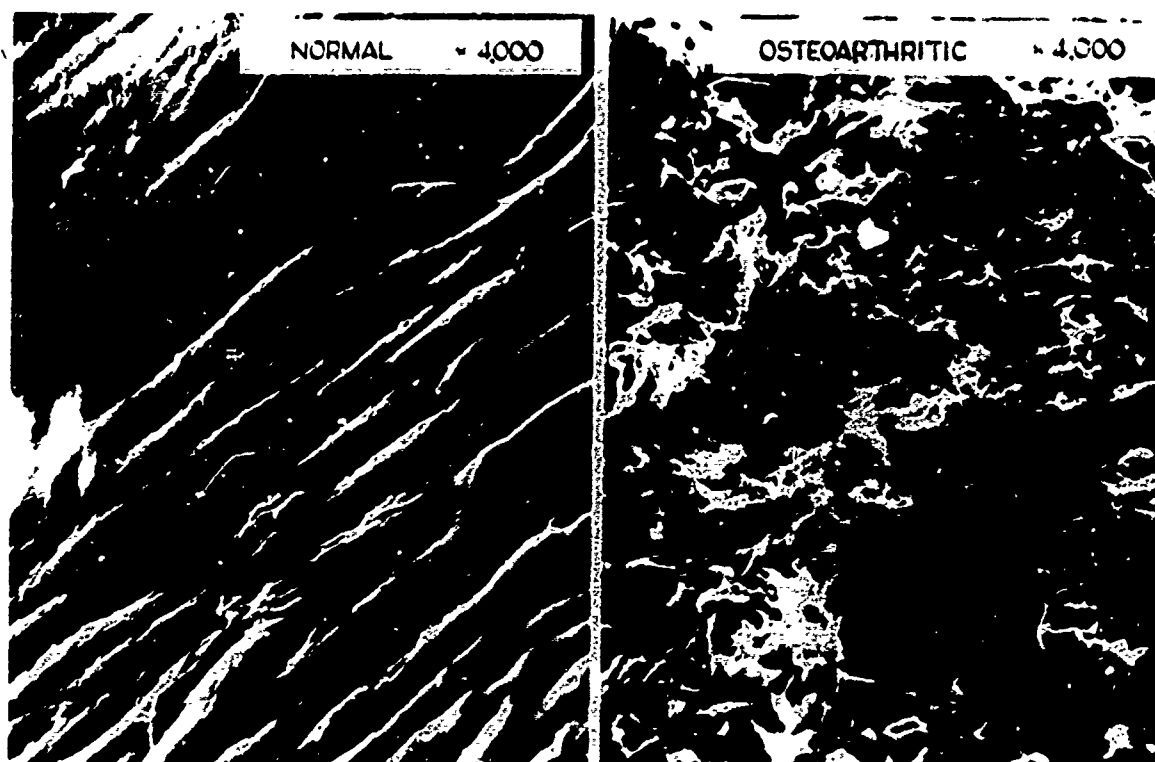


Figure 16

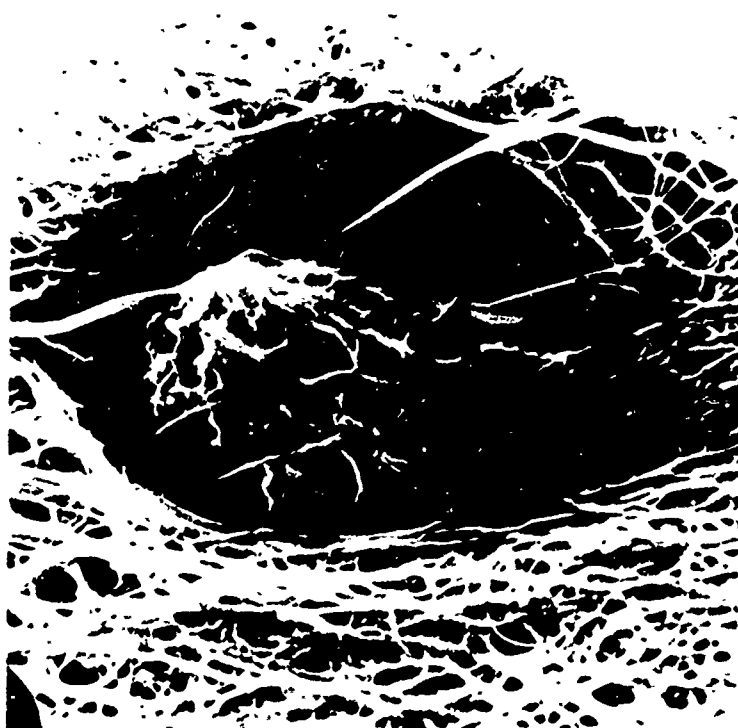


Figure 17

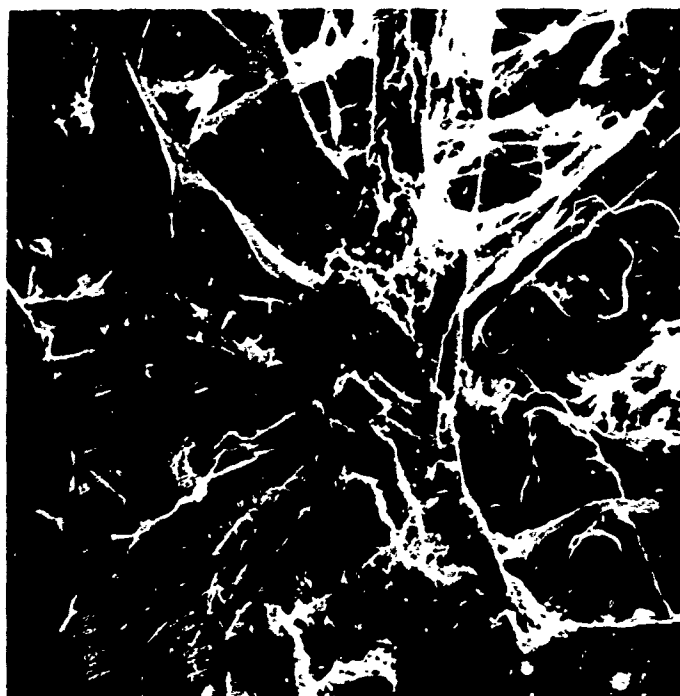


Figure 18



Figure 19





Figure 20



Figure 21

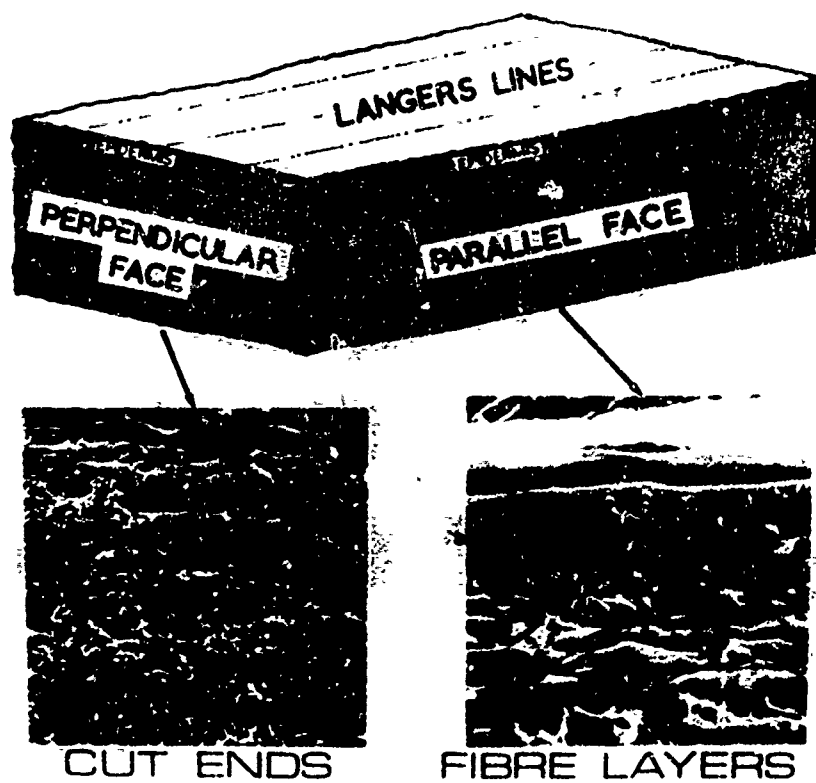


Figure 22

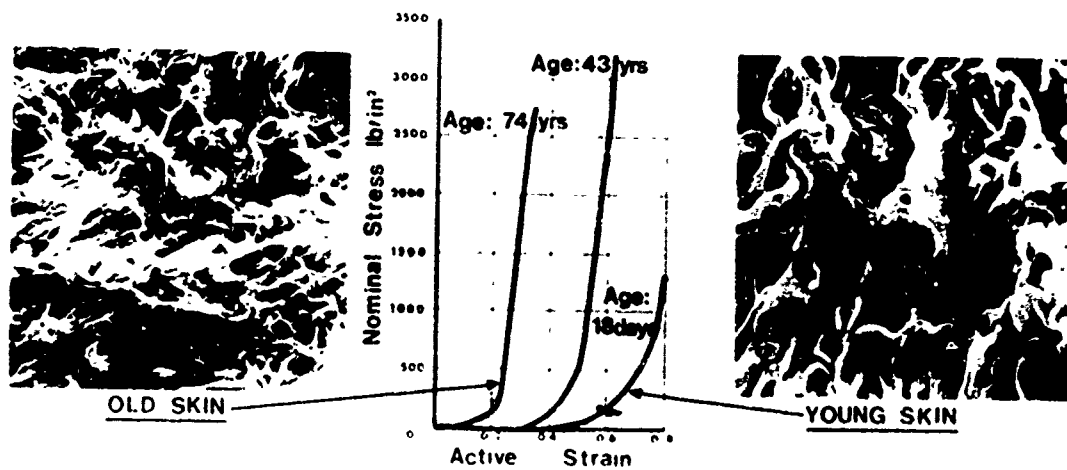


Figure 23

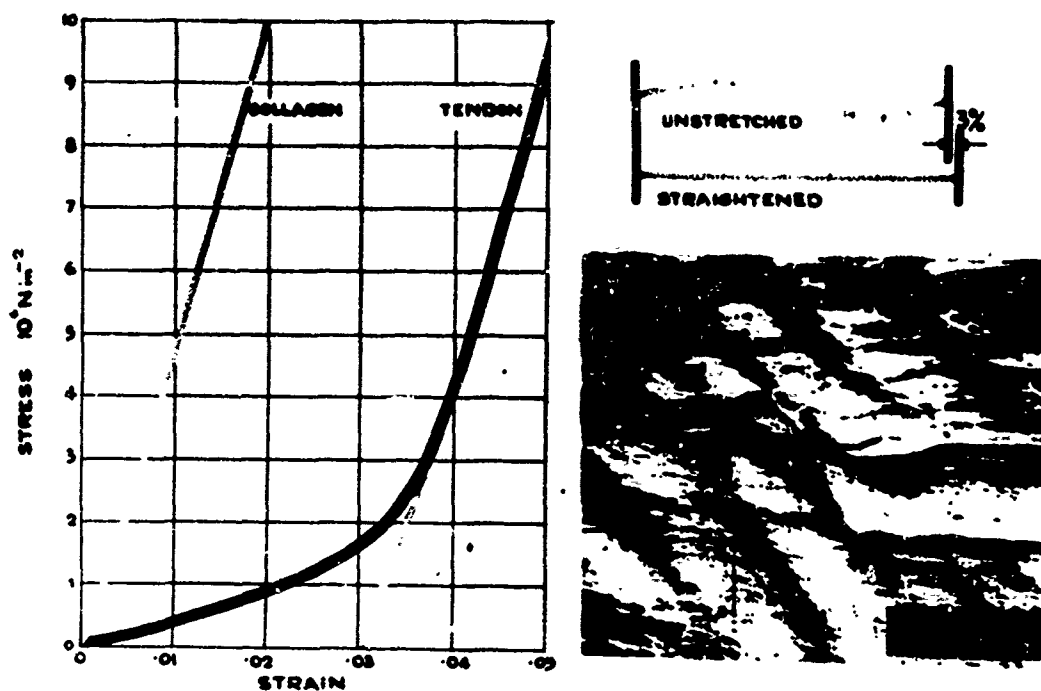


Figure 25

INFLUENCE OF MICROSTRUCTURE AND COLLAGEN/ELASTIN RATIO ON TENSILE PROPERTIES OF TISSUES

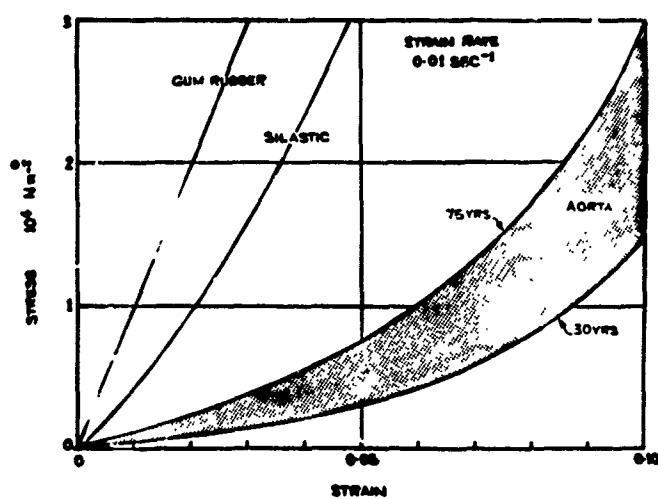


Figure 24

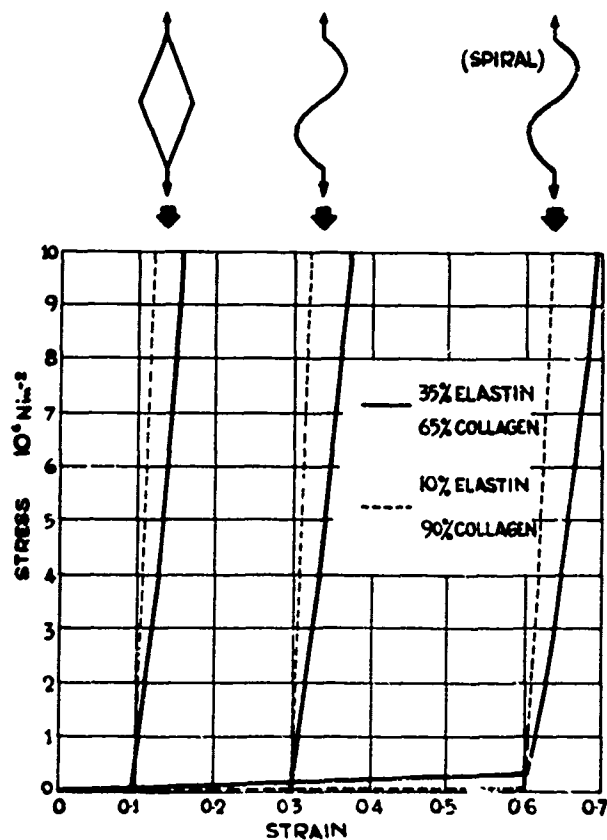


Figure 26

24 shows for example the behaviour of natural and silicone rubbers in comparison with human aorta. The differences are obviously very significant. It is a sobering thought that silicone based materials are used in arterial implants, yet in view of the difference in load/deformation characteristics, obvious mechanical incompatibilities must be introduced at the junction of implant and natural tissue.

The second approach for ligamentous tissue is that of the rheological model. Such models have their place and have proved exceedingly useful if employed the way they are supposed to be employed: namely, to provide a model representative of the integrated overall effect. In biorheology very unfortunately certain somewhat over optimistic practitioners have started to identify specific tissue components (such as mucopolysaccharides, collagen fibres, elastin, etc) with elements of the model. This is obviously not tenable and one hopes that such practices, which only lead to erroneous concepts incorrectly expressed, will be discontinued. In the author's belief effective modelling certainly for human tissue can only result from the third approach of physically rational models. Obviously a degree of simplification from the physical complexity that exists is needful but can be effected. Figure 25 shows for example a suggested model for tendon. Tendon micro architecture as shown in the scanning micrograph consists primarily of parallel bundles of collagen laid down in a wavy pattern. On initial loading the first stage is straightening of the wavy pattern achieved by a strain of the order of 3% followed by stretching of the collagen itself. The straight lines, one horizontal and the other parallel to the stress strain graph of collagen, can be looked upon as adequately representing the load deformation relation in tension. The figure also shows the actual curve obtained for tendon.

Figure 26 shows similar relationships for human skin. In these the effects of various microarchitectural configurations (rhomboidal, sinusoidal, helical) are examined together with the effect of different relative proportions of two of the major components, collagen and elastin. It is seen that the micro architecture governs the initial elongation while the relative proportion of the major components governs the slope of the second straight line composing the mathematical model.

## SUMMARY

A brief survey of attempts at mechanical characterisation of human tissue as components of the body have been presented. It is concluded that human tissue from a mechanical point of view is a multi-component material, nonhomogeneous, anisotropic and clearly non linearly visco-elastic. As regards effective modelling it is suggested that both material simulation

and rheologic modelling are likely to prove abortive and that the most promising attempts to date are based on simplified models of actual physical structure. It is patently obvious that much more factual data is needed over the whole spectrum not the least in respect of limit load carrying capacity of the body and its components. It is further suggested that such limit capacity should preferably be related to the onset of physiological impairment than to palpable tissue damage.

#### THE STRATHCLYDE TISSUE MECHANICS DIVISION

This Division of the BioEngineering Unit is headed by Dr. P. F. Millington, under the general supervision of the BioEngineering Unit's Clinical Director, Professor T. Gibson. Its staff consists of Mr. J. H. Evans and Mr. J. C. Barbenel (Senior Lecturers), Dr. J. B. Finlay and Miss R. Wilkinson (Lecturers).

Doctoral students attached to the Division are Messrs. J. A. Brown, I. Clarke, G. R. Fernie, J. F. North, A. W. Parker and H. Stark.

As indicated, the lecture presented an outline of the work of this Division in which all the above-named participated.

#### BIBLIOGRAPHY

Langer, A. K. (1861) "Zur Anatomie und Physiologie der Haut." I Uber die Spaltbarkeit der Cutis, S. B. der Akad, in Wein, Vol. 44, pp. 19-46

Daly, C. H. (1966) The biomechanical characteristics of human skin. PhD. Thesis, University of Strathclyde, Glasgow.

Duggan, T. C. (1967) Dynamic mechanical testing of living tissue. 7th Int. Conf. on Medical and Biological Engng, Stockholm, 27-1.

Walker, P. S., Dowson, D., Longfield, M. D., Wright, V. (1968). "Boosted lubrication in synovial joints by fluid entrenchment and enrichment." Journal of the Annals of Rheumatic Diseases.

Mital, M. A., (1970). Unpublished report on the biomechanical characteristic of articular cartilage. University of Strathclyde, Glasgow.

Finlay, B., (1970). "Dynamic mechanical testing of human skin "in vivo". Journal of Biomechanics, Vol. 3, No. 6. November, 1970.

Stark, H. L., (1971). The surgical limits of extension and compression of human skin. PhD. Thesis, University of Strathclyde, Glasgow.

ON SOME GEOMETRIC PROPERTIES OF HUMAN RIBS-I

Sanford B. Roberts and Ping Heng Chen

School of Engineering and Applied Science  
University of California, Los Angeles

ABSTRACT

The cross-sectional geometric properties of ribs 1 through 8 of a medium-framed female cadaver specimen were studied. Specifically, each rib was cut into 10 sections, the exposed cross-sections photographed, a finite element grid superimposed, and with the aid of a digital computer, the geometric properties (total area, compact bone area, centroid, principal axes, principal moments of inertia and torsional constant) of the compact bone region were determined. Although most of these quantities exhibit wide variations some trends do emerge. Of particular significance is a simple geometric construction for the location of the centroid and principal axes and the general result that a thin-walled ellipse is a reasonably accurate model from which the approximate cross-sectional properties may be calculated.

INTRODUCTION

Human ribs can be categorized as "long bones," (Frost 1967)<sup>\*</sup> in that they possess the characteristic structure of a thin cortex of compact bone surrounding a medullary canal of marrow and trabecula. The architecture of long bones (especially the femur) and its relationship to the load carrying function has been studied since the later part of the 19th century (Evans 1957). There have also been attempts at detailed stress analysis with the usual objective of relating the shape of the compacta and trabecula to a simplified notion of the stress and/or strain state under load (Evans 1957). In spite of an extensive history (Evans 1967) of investigations, there do not appear in the literature any significant studies which provide detailed quantitative data on the geometry, especially cross-sectional geometry, of any human bones. It goes without saying that a meaningful stress analysis (e.g. Roberts 1970) of the components of the skeletal system under normal or traumatic conditions is impossible without knowledge of (among other things) the geometry. As part of a study of the response of the

---

<sup>\*</sup> See list of References at end of paper.

thoracic skeleton to dynamic forces, a program aimed at defining the cross-sectional and global properties of human ribs was undertaken. This is a first report, focusing upon our findings within the cross-sections of human ribs.

The judgment was made at the outset that the trabecula would be neglected and only the compact bone geometry would be considered. Since the geometric quantities determined are those necessary for stress analysis, this decision implies that the compact bone is the primary load carrying component whereas the contribution of the cancellous bone is insignificant. Although it appears intuitively correct, this hypothesis requires further experimental evidence for its full justification.

The information presented herein was obtained by direct observation and measurements on the rib cage of an embalmed female cadaver specimen with an apparent small frame. The cause of death was coronary vascular arteriosclerosis in June 1968 at age 77.

Observations made on one cadaver specimen are hardly sufficient to permit drawing general conclusions. We are however, strongly motivated to find conceptually simple unifying principles from which approximate geometric properties of typical ribs can be constructed. For example, it would be advantageous to be able to make two measurements (say "width" and "depth") at a particular station along the longitudinal axis of a rib and calculate the cross-sectional properties, such as location of centroid and principal moments of inertia, without actually exposing the internal cross-section and making direct measurements. Motivated by this objective we have intentionally flavored this report with what appear to be generalizations applicable to most human ribs. We trust that a desire on the part of other researchers to further substantiate or contradict our hypotheses will help stimulate the production of a statistically valid collection of data.

#### EXPERIMENTAL AND ANALYTIC PROCEDURES

The rib cage from the specimen 6901 was excised, the individual ribs (designated 6901-Rib Number) separated and the superficial soft tissue was removed. Each rib (except No. 1) was cut into 10 sections (see Fig. 1), the cuts being made in a plane approximately normal to the longitudinal axis of the rib. The longitudinal axis being approximated by the imaginary line parallel to the superior and inferior borders and halfway between them. The interior surface thus exposed is designated herein as the rib cross-section. The cross-section contains two regions, namely a thin border of compact bone and an interior region of cancellous bone and marrow. From the perspective that the bony thorax is a force transmitting structure, only the compact bone is considered effective. Consequently, it is to it which our attention is directed. The compact bone region is not easily distinguishable from the cancellous bone interior. The interior "border" requires careful scrutiny and judgement for its definition. We found that close examination under magnification, and the removal of all soft tissue and

as much cancellous bone as possible is necessary since it would otherwise render the border definition extremely difficult.

The exposed cross-sections of each rib were photographed under 10 power magnification with a scale having 0.01 in. divisions placed in the field of view and in the plane of the cross-section (Figs. 2-6) Tracings of the outline of the compact bone regions were made from the developed photographs. A network of 36 quadrilateral elements (72 nodal points) and a cartesian coordinate system describing the geometry of the cross-section\* was then superimposed. The coordinates of each nodal point were scaled and entered as input data into an augmented finite element computer program (Mason 1967) which calculated

- a) The cross-sectional area of compact bone ( $A_c$ ) and total cross-sectional area ( $A_t$ )
- b) The orientation of the principal axes ( $y, z$ ) of inertia
- c) The location of the centroid
- d) The principal moments of inertia

$$I_y = \int_R y^2 dA, \quad I_z = \int_R z^2 dA \quad R = \text{Compact bone region}$$

- e) The torsional constant ( $J$ ), where

$$J = \int_R \left[ y^2 + z^2 + y \frac{\partial \phi}{\partial z} - z \frac{\partial \phi}{\partial y} \right] dA \quad (1)$$

$$\frac{\partial^2 \phi}{\partial y^2} + \frac{\partial^2 \phi}{\partial z^2} = 0 \quad (2)$$

where  $\phi = \phi(y, z) = \text{St. Venant warping function}$

The calculation of the torsional constant ( $J$ ) based upon Equations (1) and (2) and appropriate boundary conditions assumes, among other things, that the material is isotropic in that  $G_{xz} = G_{yx}$  ( $G = \text{elastic shear modulus}$ ). Although there is strong evidence (Dempster 1952) indicating that bone is not isotropic, there is presently insufficient information on the dependence of the shear modulus upon orientation normal to the long axis of the bone. This is, at this time it is reasonable to assume that  $G_{xz} = G_{yx}$ .

In addition to the "exact" analysis described above, an approximate analysis based upon

- a) The assumption that the cross-section is a thin-walled ellipse with constant effective thickness ( $t_e$ )

\* Hereinafter the term cross-section will refer to the compact bone portion thereof unless otherwise defined.



- b) The use of the actual "major" and "minor" axes (A,B) measured along actual principal axes, and the ratio of compact bone to total cross-sectional area  $A_c/A_t$

was carried out.

In a thin-walled elliptic cross-section, using a) above it can be readily shown that (see Hudson 1917 and Shanley 1957)

$$4 t_e = (A+B) - \sqrt{(A+B)^2 - 4EAB} \quad , \quad s = \frac{A_c}{A_t} \quad (3)$$

$$64I_y = \pi [BA^3 - (B-2t_e)(A-2t_e)^3] \quad (4)$$

$$64I_z = \pi [B^3A - (B-2t_e)^3(A-2t_e)]$$

$$J = \frac{4 a^2 t_e}{s}$$

$$a = \frac{\pi(A-t_e)(B-t_e)}{4}$$

$$s = \frac{\pi(A+B)}{8} \left[ 3(1+\lambda) + \frac{1}{1-\lambda} \right] \quad (5)$$

$$\lambda = \left[ \frac{A-B}{2(A+B)} \right]^2$$

#### GENERAL RESULTS

The shape of the thin wall of compact bone in the typical rib cross-section is more or less "elliptic." It can be qualitatively characterized by the ratio of the lengths along the "minor" and "major" principal axes (B/A). Figure 7 shows a plot of B/A as a function the nondimensional position parameter (S/L) for ribs 6901-3 thru 6901-8. Observe that at the costochondral junction (S/L=0) the compact bone shape is somewhat cylindrical ( $0.5 \leq B/A \leq 0.8$ ). Proceeding posteriorly into the shaft region it immediately begins to flatten ( $0.2 \leq B/A \leq 0.4$ ) and then gradually expands becoming more "cylindrical" again approaching the angle with maximum values of B/A in the neighborhood of the tubercle.

### THICKNESS OF COMPACT BONE

The thickness ( $t$ ) of the compact bone cortex varies both as a function of  $S/L$  and within each cross-section without any apparent pattern in either respect. The maximum and minimum values of  $t$  were measured in each cross-section and plotted as a function of  $S/L$ . These curves for ribs 3, 5 and 7 are shown in Figs. 8 to 10. The value of  $t_{min}$  is reasonably constant over the rib length, being on the order of 0.01 in. for the three ribs. However,  $t_{max}$  exhibits extensive excursions along the length of any one particular rib. The peak values are usually associated with a highly localized thickened region in a cross-section.

The equivalent thickness ( $t_e$ ) given by Equation (3) was also plotted in Figs. 8 to 10. It is interesting to note that  $t_e$  is reasonably close to the median wall thickness.

### PRINCIPAL AXES OF INERTIA AND CENTROID

The calculated location of the centroid (c.g.)<sup>\*</sup> and the orientation of the principal axes of inertia for specimen 6901-3 Sections 1, 3, 5, 7 and 9 are shown in Figs. 2 to 6. Note that the compact bone boundary has been exaggerated and the principal axes superimposed upon the actual photographs of the cross-sections. One observes that the centroid is approximately at the center of the overall cross-section and that the minor principal axis is nearly parallel to a line connecting the extremum points. The observation suggests the following construction procedure for the approximate centroid location and the local orientation of the principal axes (refer to Fig. 11).

- a) Connect the two points ( $a_1$  and  $a_2$ ) on the extreme superior and inferior edges by a straight line.
- b) Enscribe the outer boundary with a rectangle having sides parallel and perpendicular to  $a_1 - a_2$ .
- c) The intersection of the diagonals of this rectangle locates the c.g. and lines through the c.g. parallel and perpendicular to  $a_1 - a_2$ , are the minor and major principal axes respectively.

The accuracy of this procedure was tested using ribs, 6901-3, 5 and 7. The actual c.g. was located and its position compared with that of the approximate c.g. (designated c.g'.) by the dimensions  $\delta_A$  and  $\delta_B$  (Fig. 11). Also, the angular orientation,  $\alpha$  of the approximate principal axes ( $y'$  and  $z'$ ), with respect to the actual principal axes ( $y, z$ ) was determined. The relative magnitudes of these quantities are given in Table 1. We observe that

---

<sup>\*</sup>Under the assumption that rib compact bone is homogeneous we will use the designations centroid and center of gravity (c.g.) interchangeably.

TABLE 1

RIB NO.- SEC.	S/L	$\delta_A$ (in)	A (in)	$\frac{\delta_A}{A}$ %	$\delta_B$ (in)	B (in)	$\frac{\delta_B}{B}$ %	$\alpha$ Deg.
3-1	0.0	0.010	0.485	2.06	0.005	0.305	1.64	7.0
3-2	0.104	0.005	0.550	0.90	0.002	0.135	1.48	0.5
3-3	0.200	0.002	0.550	0.36	0.002	0.130	1.54	2.0
3-4	0.306	0.011	0.510	2.16	0.001	0.125	0.80	2.0
3-5	0.392	0.010	0.485	2.06	0.010	0.175	5.70	1.0
3-6	0.485	0.010	0.440	2.27	0.023	0.210	10.90	2.0
3-7	0.598	0.020	0.360	5.55	0.004	0.210	1.90	7.2
3-8	0.695	0.012	0.375	3.20	0.030	0.200	15.00	5.5
5-1	0.0	0.030	0.545	5.50	0.038	0.342	11.10	10.0
5-2	0.125	0.010	0.580	1.73	0.00	0.165	0.00	0.0
5-3	0.241	0.010	0.498	2.01	0.00	0.175	0.00	1.2
5-4	0.345	0.035	0.410	8.54	0.005	0.192	2.60	1.75
5-5	0.427	0.030	0.378	7.94	0.00	0.240	0.00	1.0
5-6	0.618	0.012	0.430	2.79	0.012	0.235	5.10	3.3
5-7	0.740	0.032	0.370	8.65	0.026	0.280	9.30	3.3
7-1	0.0	0.046	0.570	8.10	0.020	0.280	7.14	2.5
7-2	0.107	0.008	0.610	1.30	0.010	0.210	4.76	5.5
7-3	0.238	0.028	0.530	5.30	0.020	0.200	10.00	4.0
7-4	0.352	0.001	0.527	1.90	0.017	0.200	8.50	2.0
7-5	0.527	0.030	0.505	5.95	0.007	0.240	2.92	4.5
7-6	0.665	0.060	0.520	11.50	0.025	0.264	9.47	1.5
7-7	0.775	0.005	0.475	1.05	0.028	0.300	9.35	6.0

$$\frac{\delta_A}{A} < 12\%, \quad \frac{\delta_B}{B} < 15\%, \quad |\alpha| < 10^\circ$$

with the average values for the three ribs being

$$\left. \frac{\delta_A}{A} \right|_{\text{avg.}} \approx 4\%, \quad \left. \frac{\delta_B}{B} \right|_{\text{avg.}} \approx 5\%, \quad |\alpha|_{\text{avg}} \approx 3.5^\circ$$

Considering the inherent inaccuracies in defining the compact bone boundaries, these errors are within acceptable limits.

#### CROSS-SECTIONAL AREA

The cross-sectional area of compact bone  $A_c$  (see Figs. 12 to 15) is reasonably constant over the entire length of each rib (especially in the shaft) showing significant perturbations only in the tubercle-neck region and in some cases at the costochondral junction. The value of  $A_c$  at the costochondral junction (C.C.J.) is particularly difficult to determine due to the indistinct transitioning of cartilage to bone. In particular, ribs 5 and 6 showed extensive ossification at this location, thereby giving rise to relatively large values of  $A_c$ . In the shaft region of a typical rib  $A_c$  is of the order 0.035 in.<sup>2</sup>

The calculated values of  $A_c$ , based upon an elliptic cross-section shape produces an excellent approximation. This appears to be uniformly true except at a few isolated sections wherein there is a sharply indented costal groove.

The ratio of  $A_c$  to the area of the entire cross-section ( $A_t$ ) for ribs 1-8 is shown in Fig. 16. The average values of  $A_c/A_t$  are greatest for ribs 1 and 2, (approximately 60% and 50% respectively) decreasing with increasing rib number to essentially a constant 40% in the shaft region of ribs 5-8. The values at the costochondral junction of ribs 5-8 are quite erratic primarily due to the poor definition of this junction as an apparent consequence of cartilage ossification.

#### MOMENTS OF INERTIA AND TORSIONAL CONSTANT

The calculated principal moments of inertia ( $I_y, I_z$ ) and the torsional constant  $J$  are given in Figs. 12 to 15. These quantities are "second moments" of area and are therefore more sensitive to shape and thickness variations than is  $A_c$ . This is exemplified by the lack of uniformity over the length and the more violent changes. For ribs 3-6 the largest values occur at the costochondral junction where the cross section is "flared-out" ( $B/A > 0.5$ ), whereas for ribs 7 and 8, maximum values occur in the tubercle region. Typical values in the shaft region (e.g. for rib 7) are

$$I_y = 0.0007 \text{ in.}^4, \quad I_z = 0.0002 \text{ in.}^4, \quad J = 0.0005 \text{ in.}^4$$

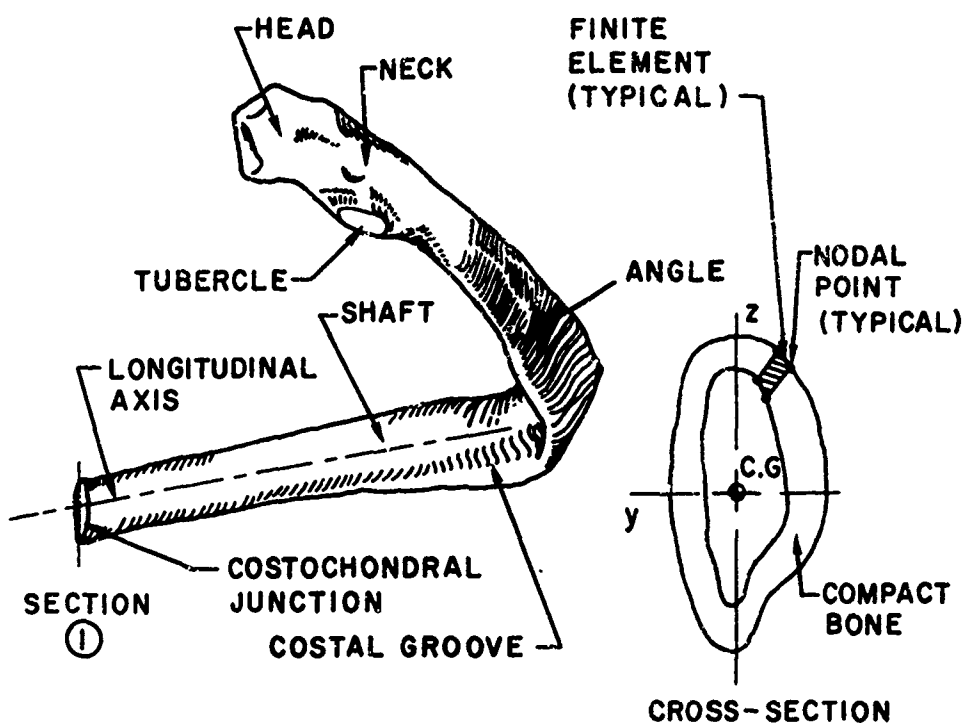
Surprisingly, the results from the elliptic approximation compare favorably with the actual values. There are, of course, isolated regions wherein marked irregularities such as deep costal grooves (e.g. rib 7 Section 6) produce poor agreement.

#### CONCLUSIONS

An analysis of the cross-sectional properties of the first 8 ribs from a female cadaver has been conducted. We have found that the quantities studied ( $t$ ,  $A_c$ ,  $A_c/A_t$ ,  $I_x$ ,  $I_y$ ,  $J$ ) show considerable variation as a function of position along each rib as well as variation between ribs. However, it is also clear that at least for this specimen, certain definite patterns do emerge.

- a) The median wall thickness is greatest in the vicinity of the tubercle.
- b) The compact bone region, c.g. and principal axes of inertia can be approximately located by a simple geometric construction.
- c) The compact bone ratio ( $A_c/A_t$ ) is greatest in rib 1 decreasing to a relatively constant value of about 40% in the shaft regions of ribs 5-8.
- d) All of the geometric quantities studied possess a characteristic variation with rib number. That is, a decrease from rib 1 to a local minimum at rib 3 followed by an increase to a local maximum at ribs 6 or 7 and decreasing thereafter.
- e) The geometric properties can be calculated with reasonably good accuracy by assuming the rib cross-section to be a thin-walled ellipse, provided the major and minor axes and the compact bone ratios are known.

In order to obtain upper-bound estimates of the cross-sectional properties of human ribs, an analysis similar to that described herein has been initiated on a large-framed male specimen. Preliminary results indicate that values of the various geometric quantities in the shaft regions are approximately 20% higher than those of specimen 6901.



**APPROXIMATE LOCATION OF SECTIONS**

RIB NO.	HEAD	TUBERCLE		ANGLE						COSTOCHONDRAL JUNCTION			
	NECK												
6901-1	6			5	4	3	2	1					
2		10	9	8	7	6	5	4	3	2	1		
3		10	9	8	7	6	5	4	3	2	1		
4		10	9	8	7	6	5	4	3	2	1		
5	10	9		8	7	6	5	4	3	2	1		
6	10	9		8	7	6	5	4	3	2	1		
7	10		9	8	7	6	5	4	3	2	1		
8		10	9	8	7	6	5	4	3	2	1		

Figure 1. Rib nomenclature and approximate location of cross-sections



Section 1  
S/L=0.0

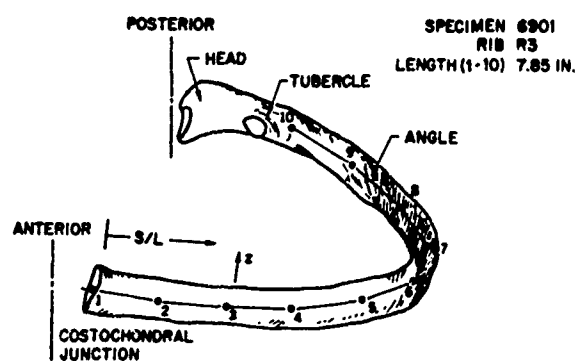
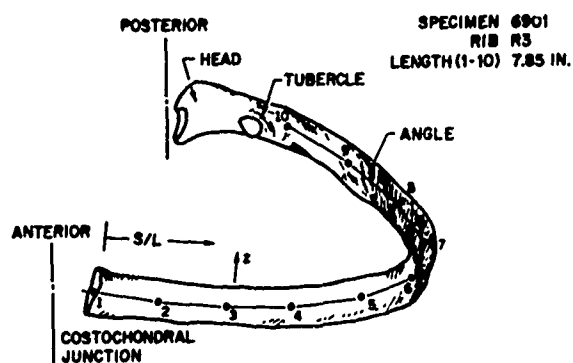


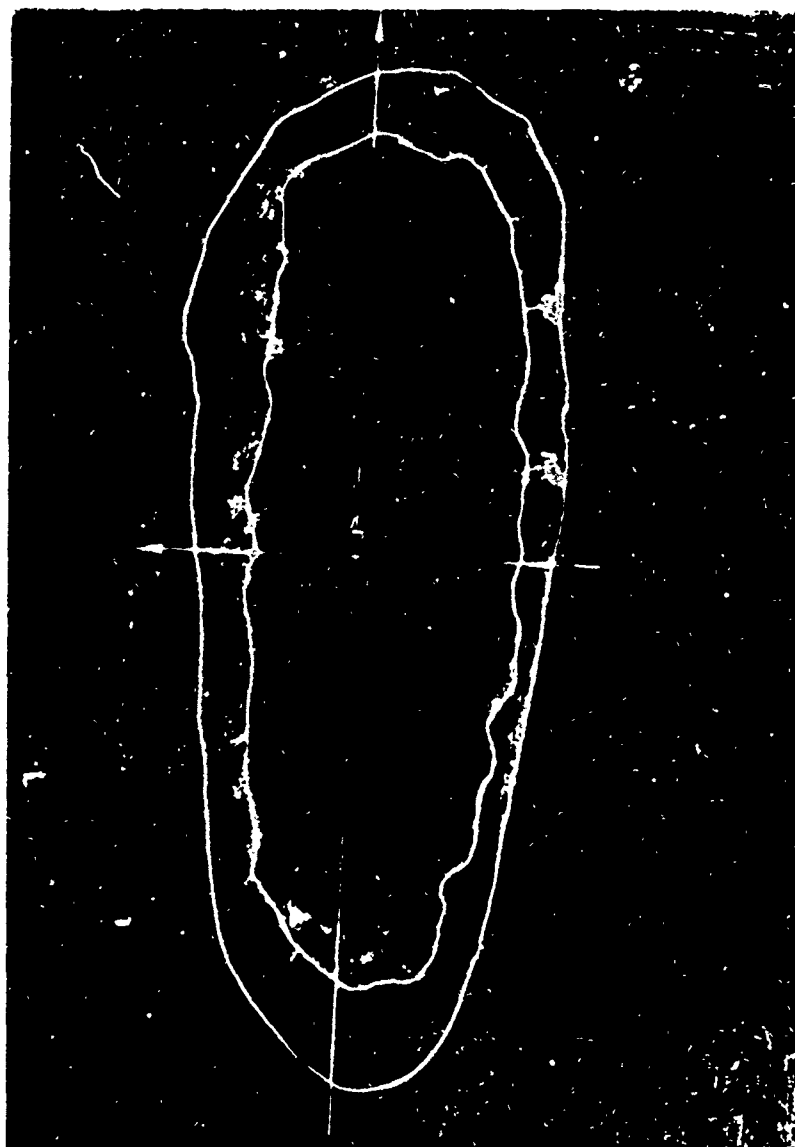
Figure 2. Rib 6901-3 Section 1



Section 3  
S/L=0.200

Figure 3. Rib 6901-3 Section 3





Section 5  
 $S/L=0.392$

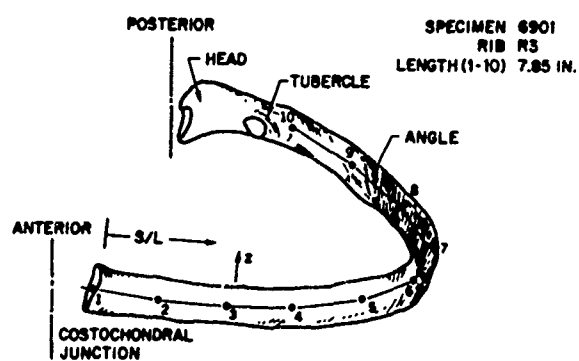


Figure 4. Rib 6901-3 Section 5



Section 7  
S/L=0.598

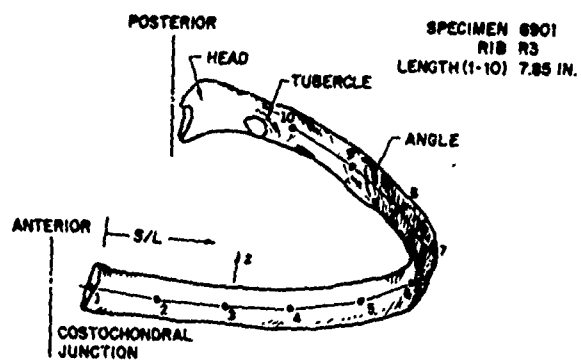
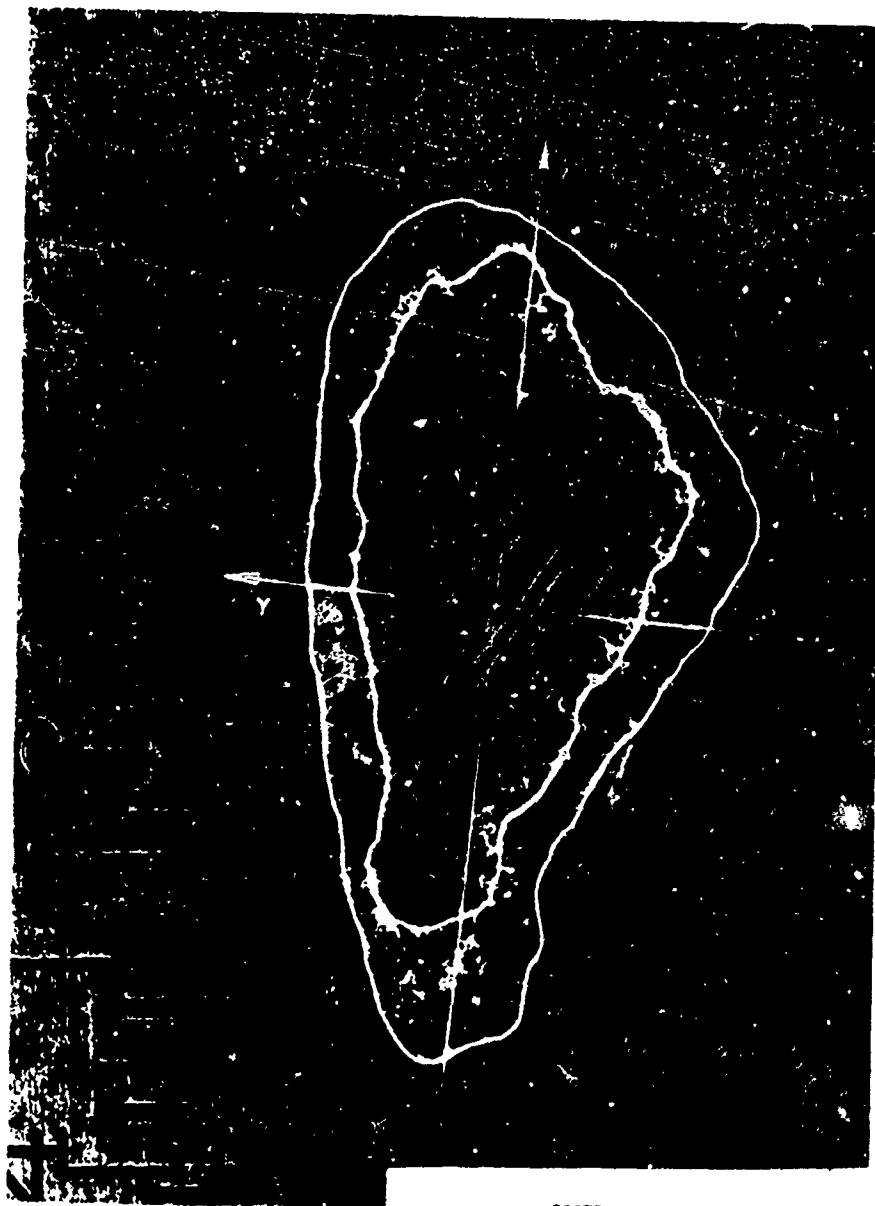


Figure 5. Rib 6901-3 Section 7



Section 9  
S/L=0.801

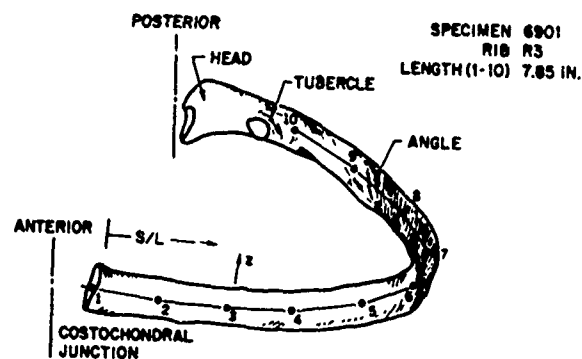


Figure 6. Rib 6901-3 Section 9

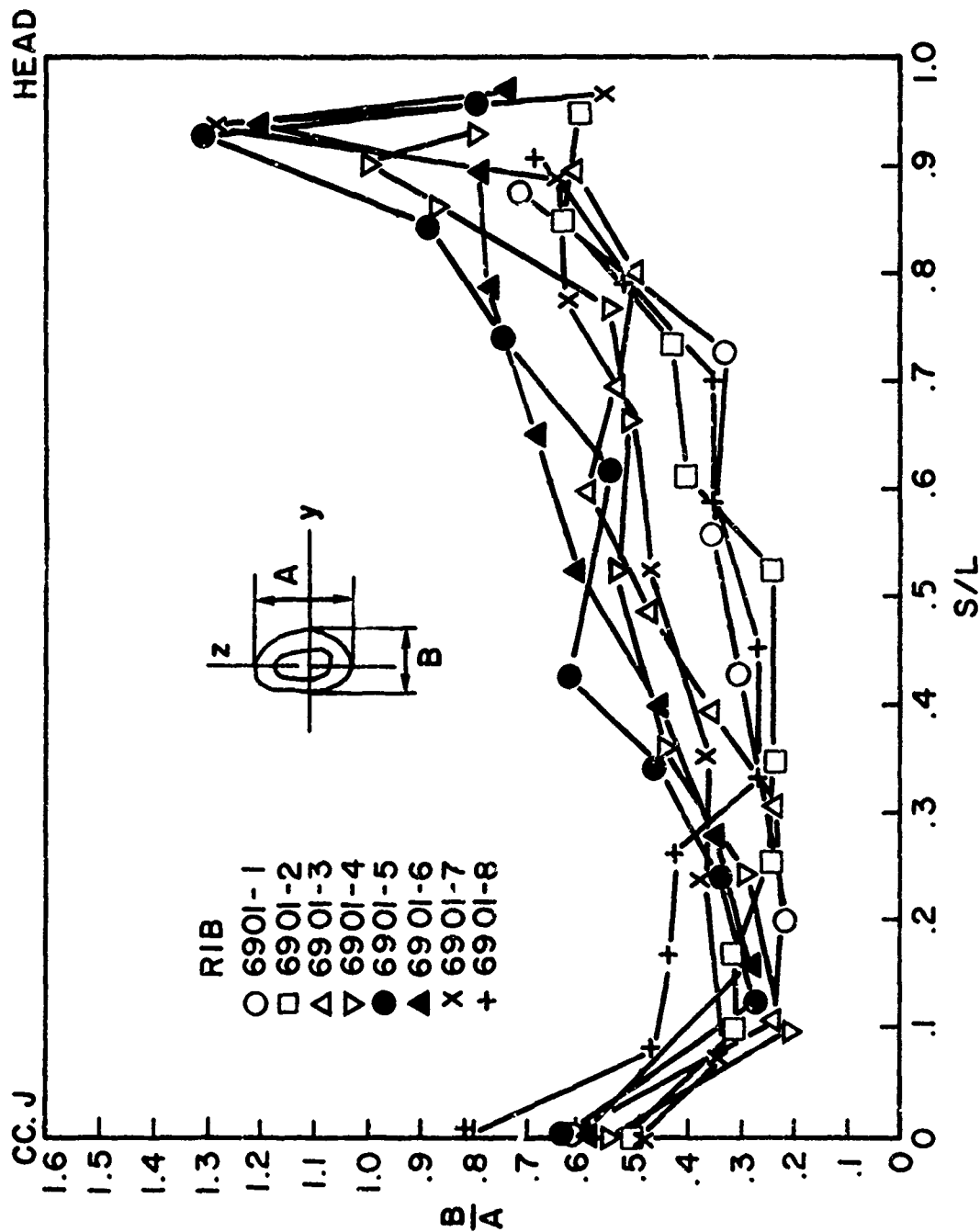


Figure 7. Ratio of principal dimensions (B/A) vs. S/L

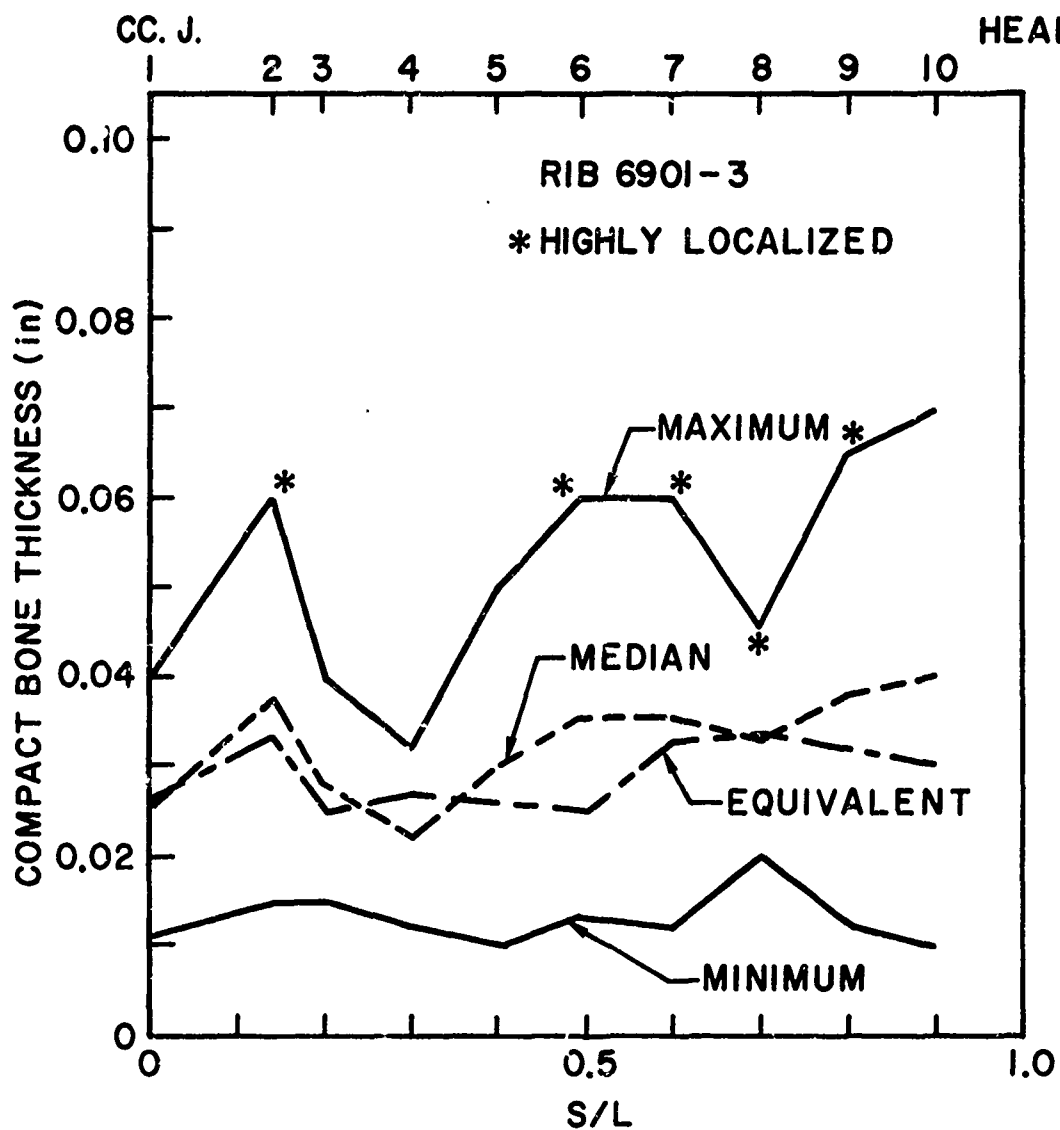


Figure 8. Rib 6901-3 Compact bone thickness vs. S/L

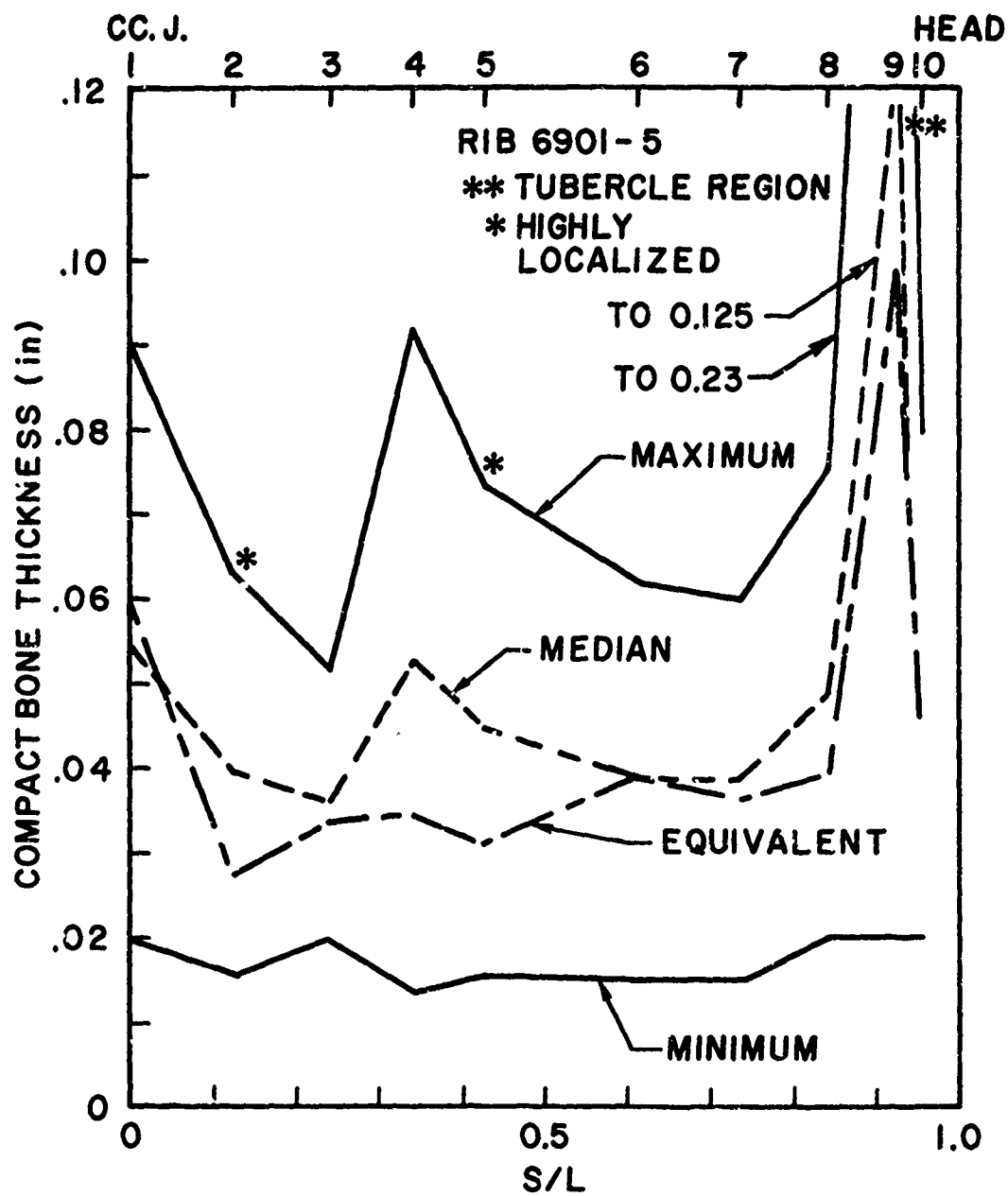


Figure 9. Rib 6901-5 Compact bone thickness vs. S/L

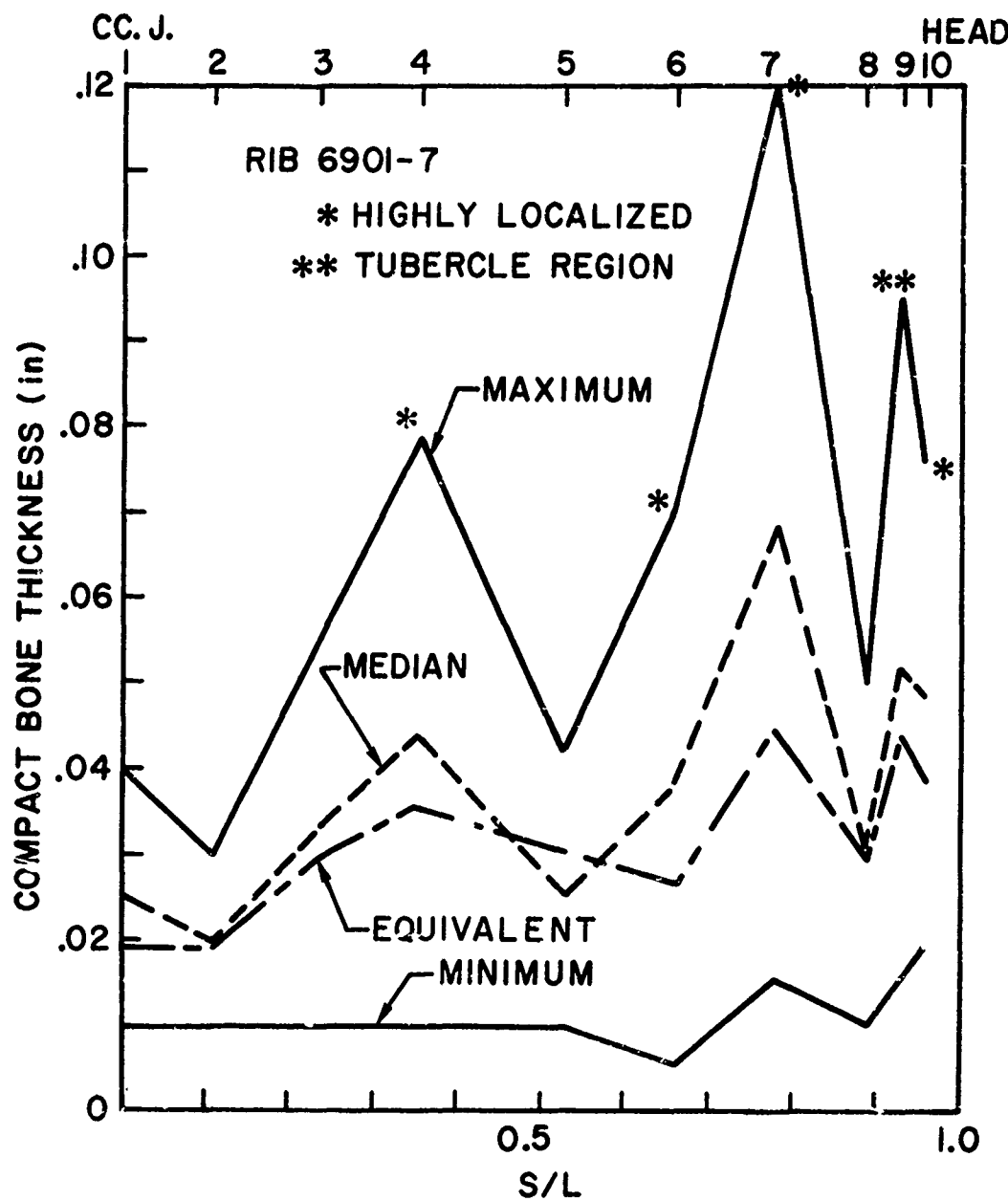


Figure 10. Rib 6901-7 Compact bone thickness vs. S/L

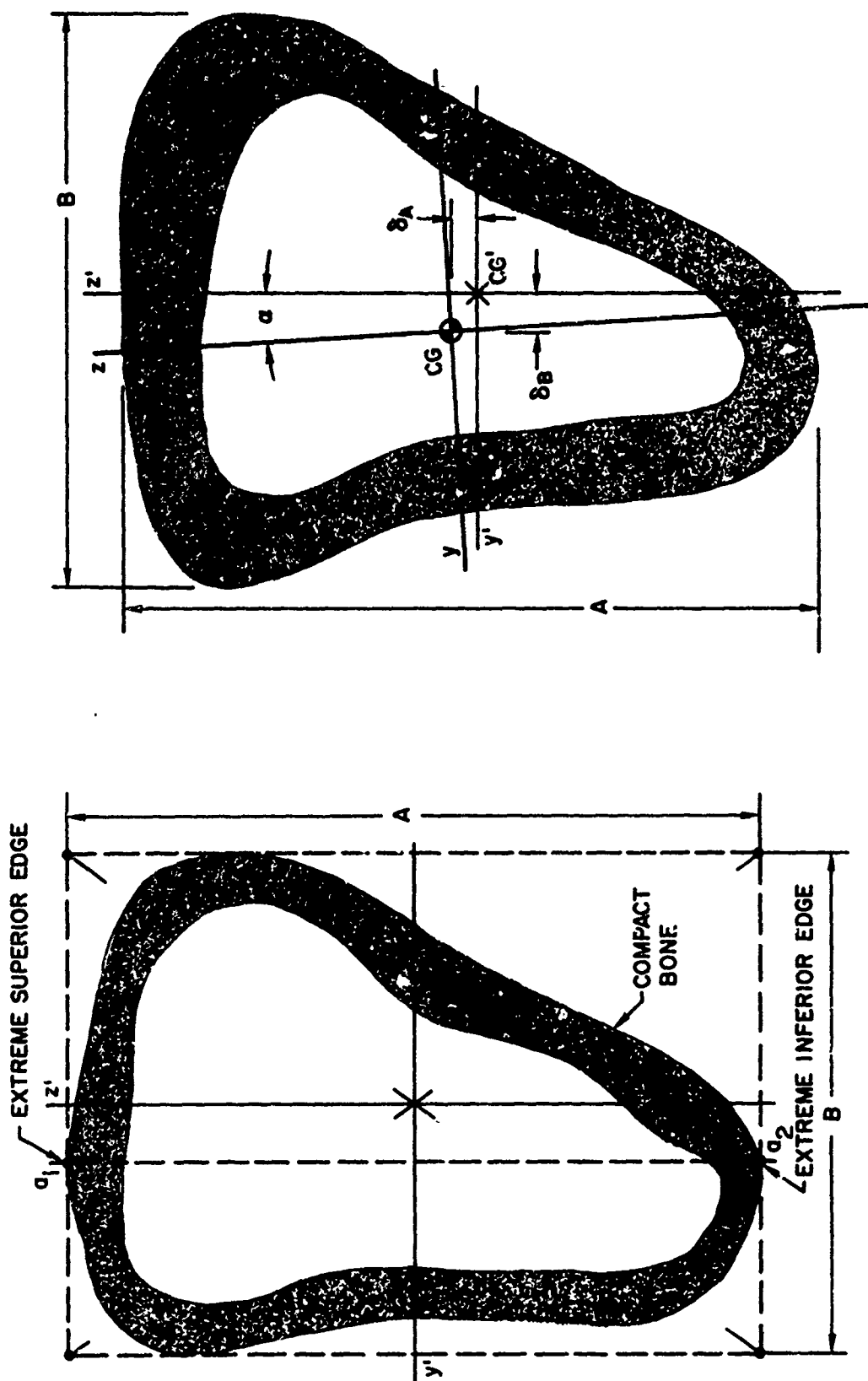


Figure 11. Construction of centroid and principal axes



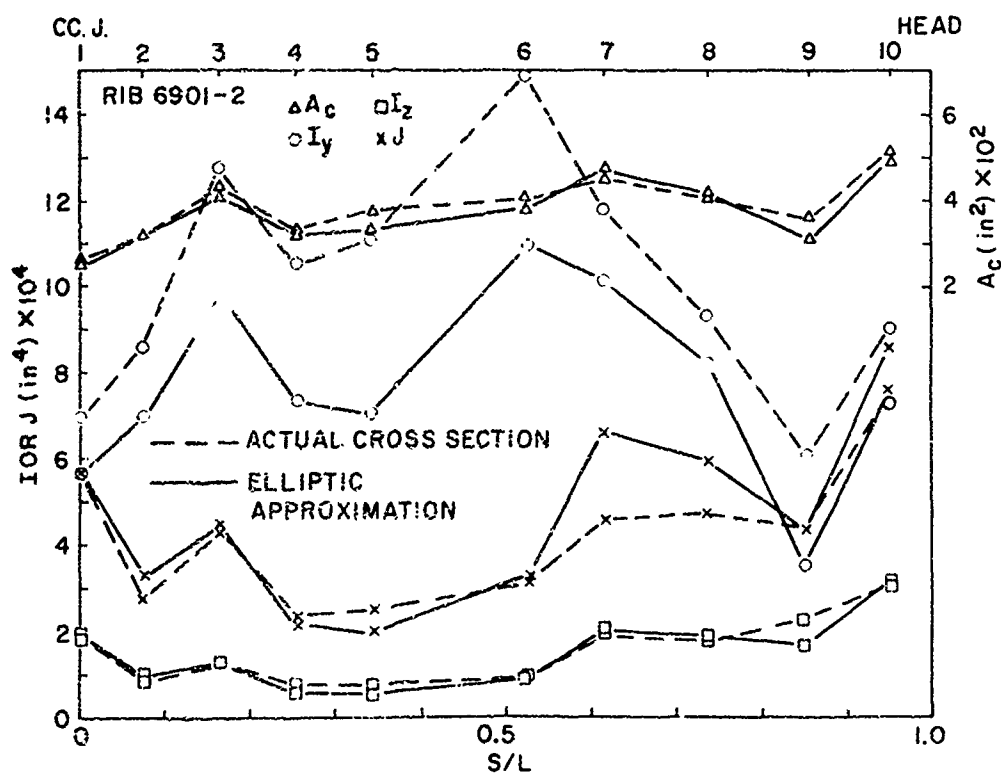
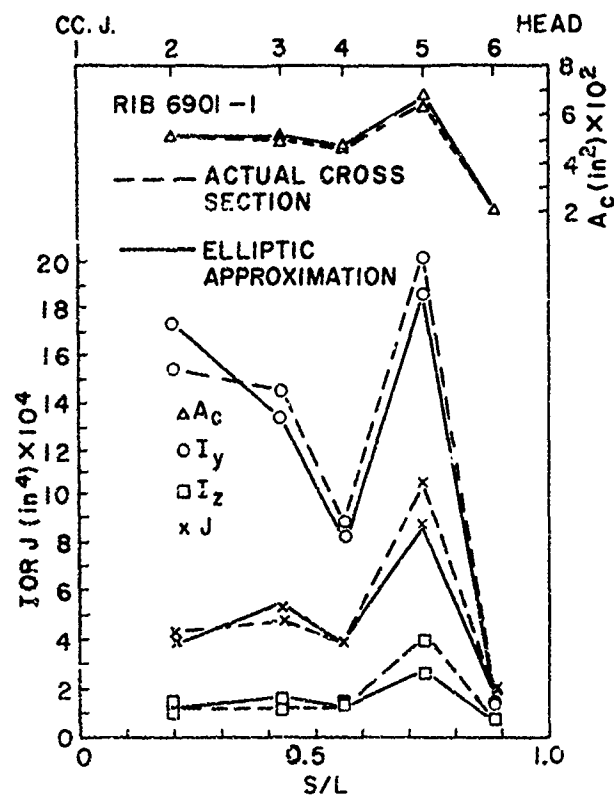


Figure 12. Cross-sectional properties of ribs 6901-1, 6901-2 vs. S/L

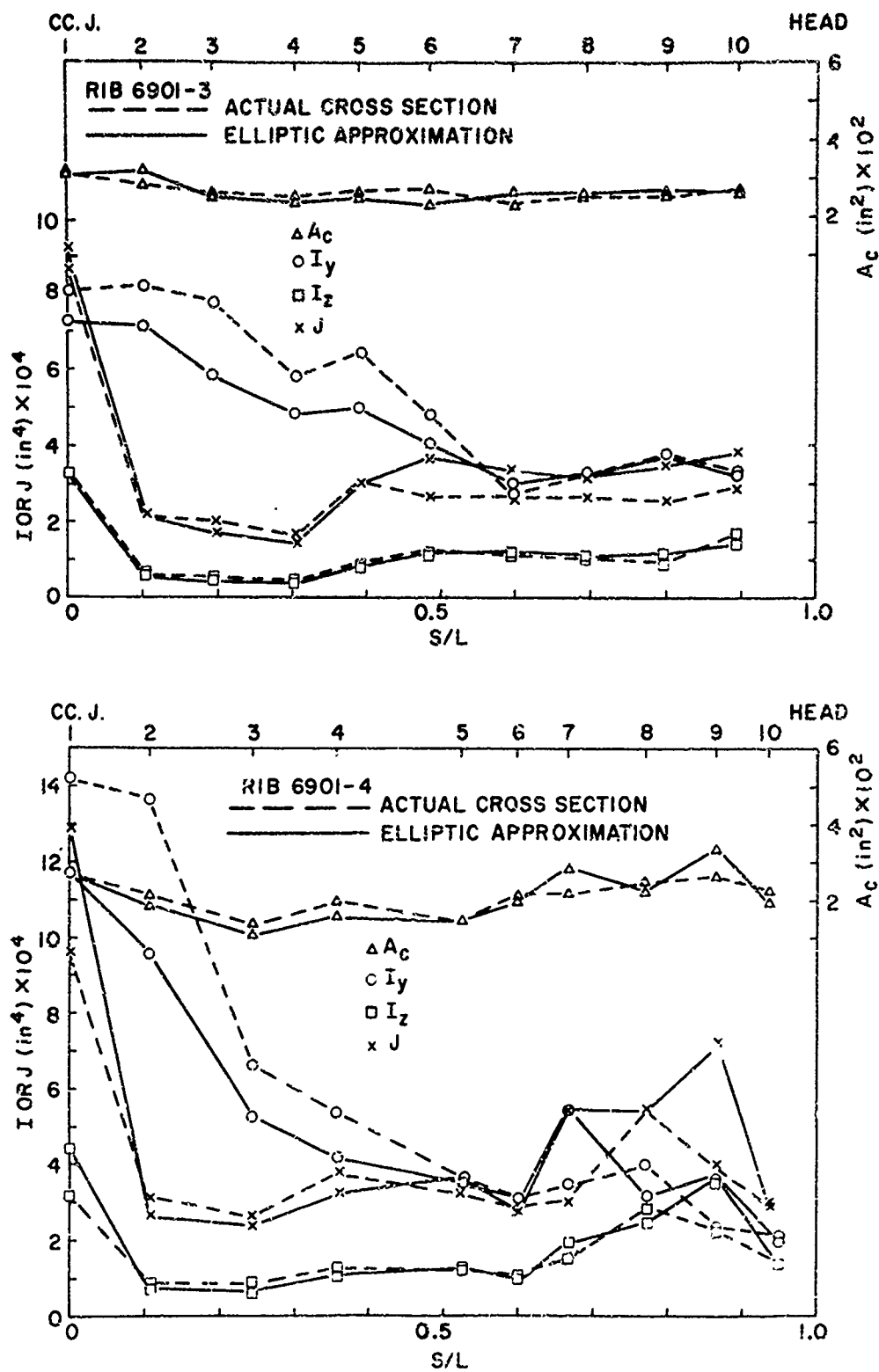


Figure 13. Cross-sectional properties of ribs 6901-3, 6901-4 vs. S/L

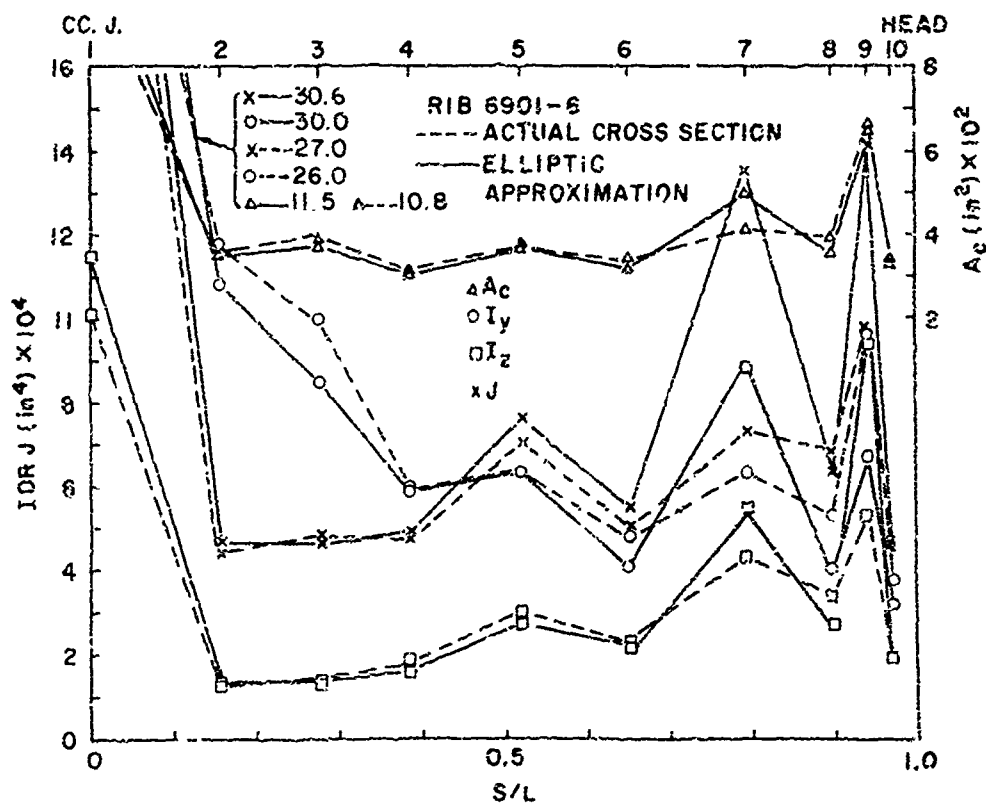
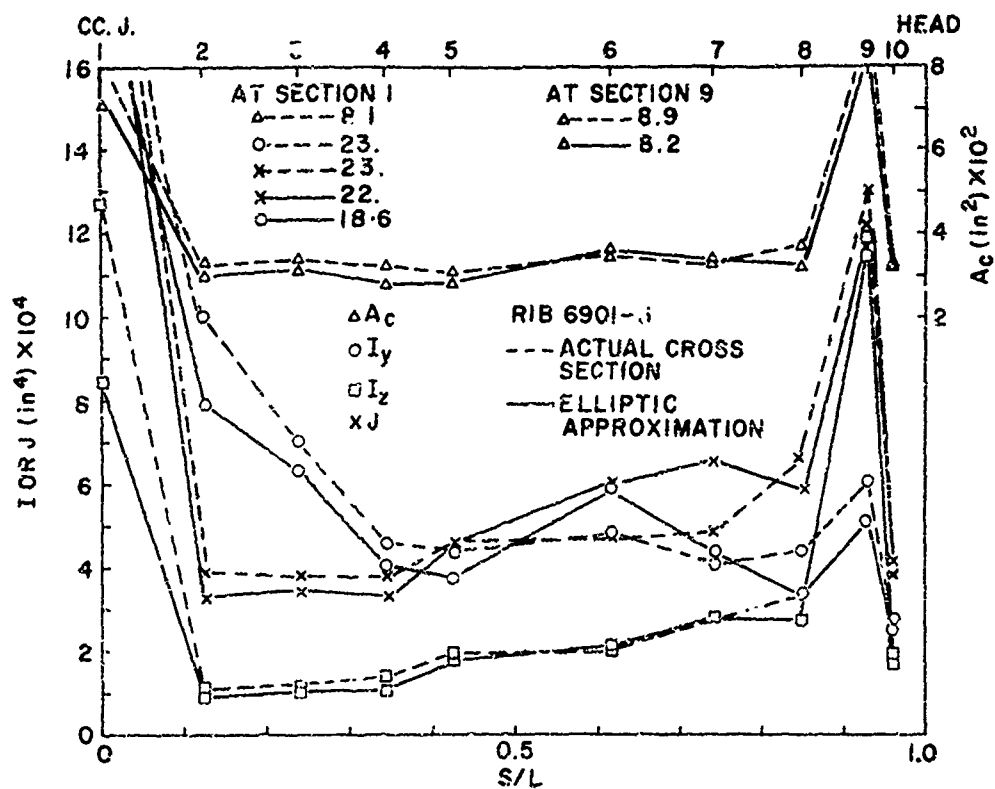


Figure 14. Cross-sectional properties of ribs 6901-5, 6901-6 vs. S/L

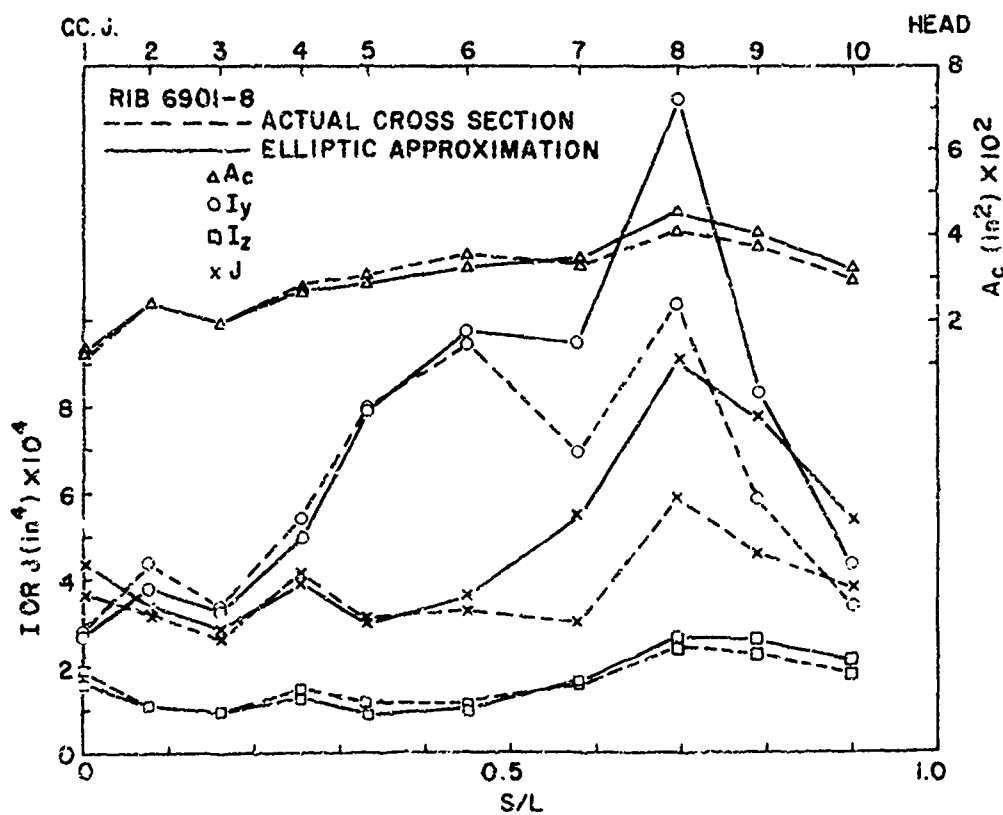
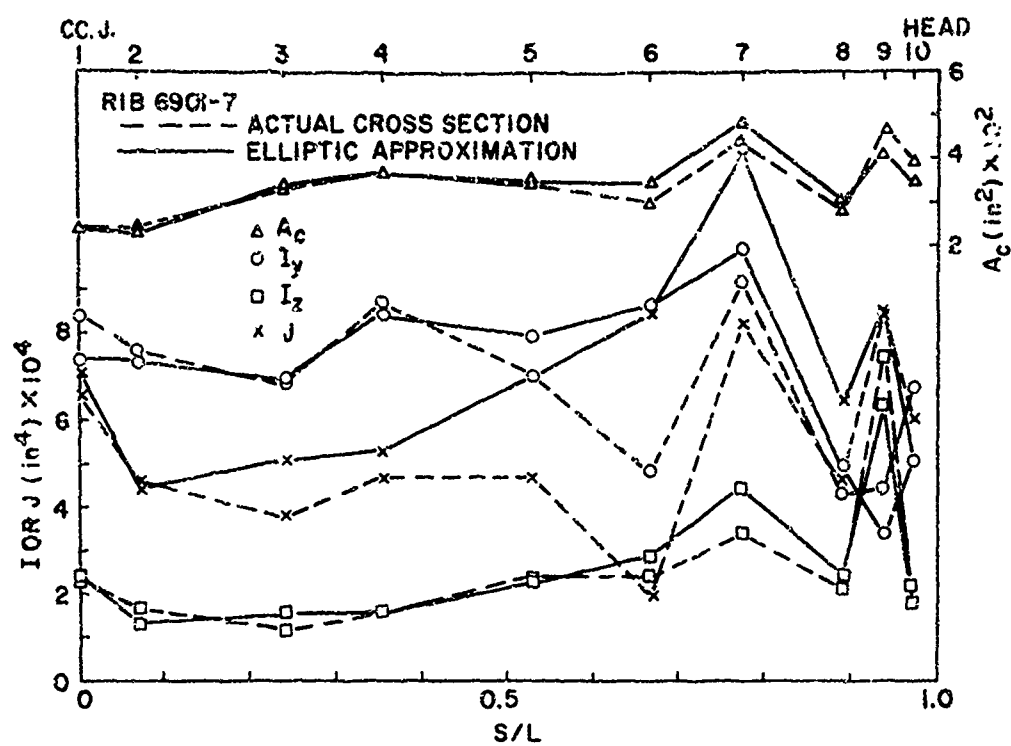


Figure 15. Cross-sectional properties of ribs 6901-7, 6901-8 vs.  $S/L$

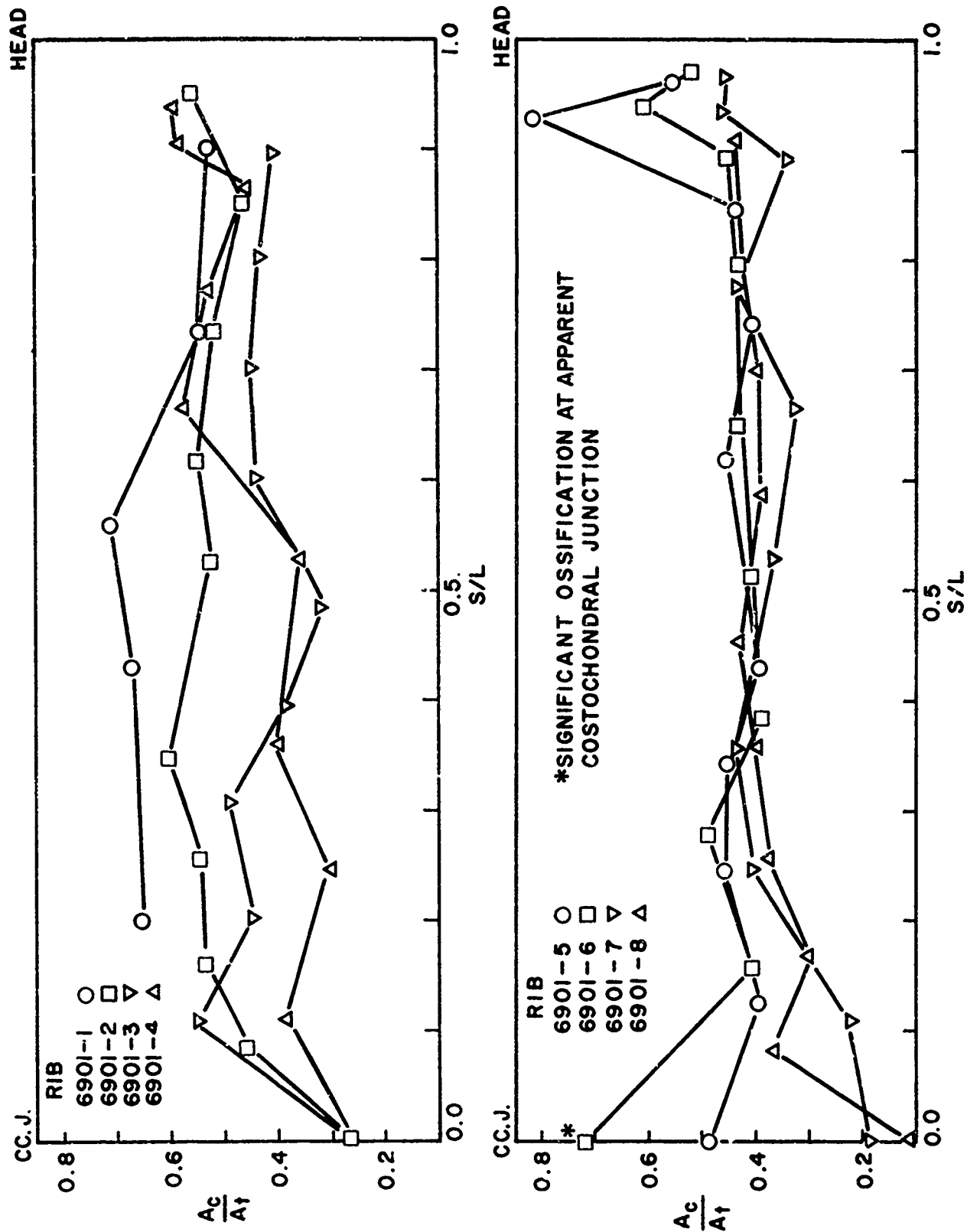


Figure 16.  $A_c/A_f$  vs.  $S/L$  for ribs 6901-1 through 6901-8

## REFERENCES

1. Dempster, W.T., Liddicoat, R.T., (1952) Compact Bone as a Non-Isotropic Material, The American Journal of Anatomy, Vol. 91, No. 3.
2. Evans, F.G., (1957) Stress and Strain in Bones. Ed. O. Glasser, Charles C. Thomas, Illinois.
3. Evans, F.G., (1967) Bibliography on the Physical Properties of the Skeletal System. Artificial Limbs, Vol. 11, No. 2, pp. 48-66.
4. Frost, H.M., (1967) An Introduction to Biomechanics. Ed. C.R. Lam, Charles C. Thomas, Illinois.
5. Hudson, R.G., (1917) The Engineers' Manual, John Wiley & Sons, New York.
6. Mason, W.E., Herrmann, L.R., (1967) Elastic Analysis of Irregular Shaped Prismatic Beams by the Method of Finite Elements. Dept. of Civil Engineering, University of California, Davis, Technical Report No. 67-1.
7. Roberts, S.B., Chen, P.H. (1970) Elastostatic Analysis of the Human Thoracic Skeleton. ASME Paper 70-BKF-2.
8. Shanley, F.R., (1957) Strength of Materials. McGraw-Hill, New York.

PAPER NO. 14

THE INTERACTION OF THE COMPONENTS OF THE  
HUMAN BACK

Gerner A. Olsen

City College Of New York

ABSTRACT

Much of the difficulty retarding progress in treating malfunctions of the human back, stems from a lack of understanding of the interaction of its various components. This paper would attempt to clarify such interaction and present clinical and experimental evidence supporting its concepts.

The actions of the thoracic and lumbar portions of the back are discussed separately. In the thoracic portion lateral stability is shown to be largely dependent on the truss mechanisms resulting from the ribs and attached musculature. The lumbar portion is shown to derive its stability from its inherent spinal components as well as its strong muscular bracing. The result of malfunctions in each of these regions is also emphasized.

INTRODUCTION

Of the many movements that our bodies enact each day—none are more envolved and more beautifully executed than those performed by the mechanisms of the back. Some involve the precise timing and coordination of many muscles, both big and small. Some are delegated to specific muscle groups to perform specific duties. However performed, and not with-

PRECEDING PAGE BLANK

standing their complexity, these movements, once learned, can become quite automatic.

Unfortunately, the beautifully conceived mechanisms controlling these movements can develop-on occasion, functional difficulties (Fig.I) and need repair. It is in these instances that a complete understanding of the normal functioning of the back-and those factors contributing to its stability-is an absolute necessity.

Fundamental to any consideration of the performance of the back is the function of the spinal column. To some the spinal column acts as a rod and remains vertical due to its own inherent stiffness and the supporting intervertebral ligaments. To others the spine is similar to the mast of a ship guyed by muscles to prevent it from buckling. To a degree, these mechanisms do contribute to the lateral stability of the spine. But what about the function of the rib cage? Very little, if anything, has been mentioned in literature concerning the interaction of the rib and muscle structure acting on either side of the spine--and yet it plays a most important part in providing support. Certainly a rib which impinges on the spinal column and applies a force to it should be considered in evaluating its stability.

Another factor to be considered in studying the interaction of the components of the human back is the type of force each component produces. Muscles always develop tensile or pulling forces. Never any other kind. On the other hand, bones are placed in the body to take compression or bending forces.



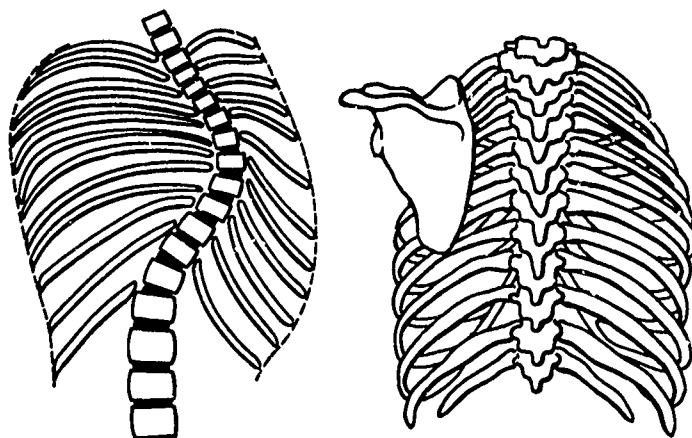


FIG. 1 (left). Typical dorsal scoliosis.

FIG. 2 (right). Normal spine and rib cage, showing supporting action of ribs (Grant's Atlas. Baltimore, The Williams & Wilkins Co., 1962; p. 392).

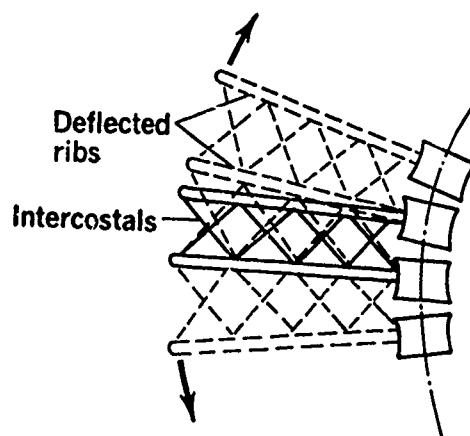


FIG. 3. The effect of the intercostal ligaments on the convex side of the bent spine. These ligaments, placed in tension, hold the ribs rigidly in position while resisting lateral bending.

Any evaluation of a mechanism providing body movements must therefore, assign to each component its proper type of force. Still another factor pertinent to the problem is the relationship of force to deformation. No spine will ever bend or twist of itself. It will bend and twist only as certain forces act upon it-in certain ways. Pathological conditions may contribute heavily to the development of these forces. Whatever their source, the forces applied produce a deformation which reflects their magnitude, direction, point of application and source. These foregoing concepts will be introduced into the following presentation which will have its objectives.

1. To clarify the mechanisms providing motion and lateral stability to the spine.
2. To provide medical evidence substantiating the presence of these mechanisms.
3. To present models showing their action.

#### THE SUPPORTING MEMBERS OF THE HUMAN SPINE

An examination of the human spine reveals a sufficient difference in the manner of support of the thoracic and lumbar regions to consider each region separately.

## THE THORACIC REGION

The rib cage which consists of twelve pairs of ribs, develops the thoracic cavity by support gained in part from the spinal column. The individual ribs butt against the column and are held in place by a complex system of inter-related muscles and ligaments. The motion of the bony framework is promoted by the superimposed ligamentous muscular system.

Included in this system of superimposed ligaments and muscles are the following three groupings:

(a)

The internal and external intercostal ligaments. These ligaments are located diagonally with respect to their attached ribs and 90 degrees to each other around the entire cage. They help form an indeterminate truss system of a cross diagonal pattern. Whenever the ribs diverge, as on the convex side of a spinal curve, these ligaments are in tension, holding the ribs rigidly in position.(Fig. 3)

(b)

The Muscles acting upward and inward. These muscles consist of fibers that arise from or just lateral to the transverse processes and run upward and inward to the spinous processes. They consist of the Serratus Posterior Superior, The Rotators, The Multifidus and Serratus are more obliquely placed in relation to the vertebral column. The Rotators resemble the shorter fibers of the Multifidus. The Levatores costae suspend the individual ribs from the spinal column,

butt them against the spinal segment immediately below their attachment.

(c) The muscles acting upward and outward. The muscles of significant importance in this group are the Iliocostalis, Longissimus, and Serratus posterior inferior. The Iliocostalis system rises with the large erector spinal muscle mass of the lower lumbar area and is extended upward and laterally as an overlapping but continuous muscle inserting into the rib cage. The Longissimus arrangement goes from the mid-line of the spinal column obliquely upward to the lower nine or ten ribs and the Serratus posterior inferior from the spinous processes of the lower two thoracic and upper two lumbar vertebrae to the lower four ribs.

#### THE COLLECTIVE ACTION OF THE MUSCULO-SKELETAL SYSTEM

Individually the muscles described in the foregoing paragraphs do not have very much influence in preventing lateral bending. Collectively however, they can be visualized as acting with the ribs to form superimposed truss systems supporting the spine against the action of lateral forces. (Fig. 8). Some of the truss systems that act to provide stability for the spine are indicated in Figs. 4, 5, 6, & 7.

The trusses on both sides of a normal spine, (Fig. 9a) held in the upright position are perfectly balanced against any lateral or rotational movement. All muscles included in the truss systems are in a normal state of tension.

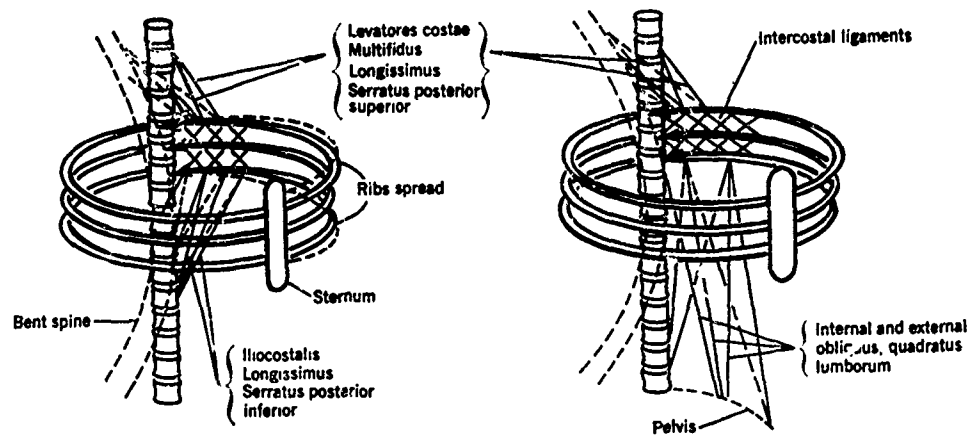


FIG. 4 (left). Truss-like arrangements of musculature and ribs which develop during lateral bend of spine.

FIG. 5 (right). Some of the muscle groups in the lower back inserted in the pelvis. Truss formations are developed with 2 or more ribs acting as a unit.

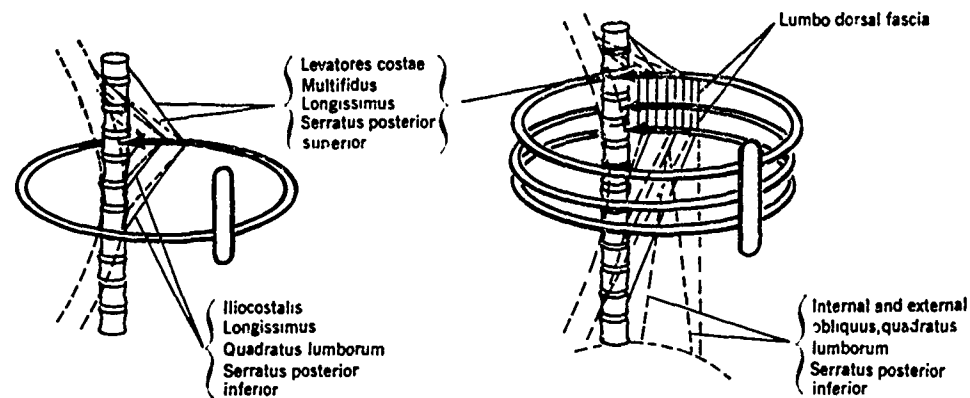


FIG. 6 (left). The effect of musculature on only 1 rib in contributing to the overall lateral stability of the spine.

FIG. 7 (right). The effect of lumbodorsal fascia on the development of lateral stability.

To cause the spine to bend to the left, (Fig. 8) the muscles on that side must first contract with this contraction these muscles pull the spine into a curved position supported in part by the reactive forces developed at the heads and articulating facets of the attached ribs. Simultaneous with this development, the truss systems on the right (convex side) restrain the bending and snap the spine back to a vertical position when normal posture is desired.

The converse of this action results when bending is to the right. In either case, the ribs on the convex side always butt against the spinal column with forces greater than those on the concave side in order to sustain the weight and other forces endeavouring to increase bending.

#### CRITICAL MEMBERS OF THE STRUCTURAL COMPLEXES

The Ribs: One independent and vulnerable member in any of the aforementioned trusses is the rib. Because its attached back muscles act in tension and form obtuse angles directed medially, the rib in the vicinity of the spine is placed in compression. It is in effect a "jig pole" (Fig. 8a) of a derrick and any movements of its base attachments or a transsection along its length would be disastrous to its stability. To transect the costotransverse and radiate ligaments holding the rib to the spine and thus removing its foundation would certainly precipitate a collapse. The resection of the heads and necks of the ribs could have an even more disastrous effect. Resecting the ribs lateral to their tubercle would have

To cause the spine to bend to the left, (Fig. 8) the muscles on that side must first contract with this contraction these muscles pull the spine into a curved position supported in part by the reactive forces developed at the heads and articulating facets of the attached ribs. Simultaneous with this development, the truss systems on the right (convex side) restrain the bending and snap the spine back to a vertical position when normal posture is desired.

The converse of this action results when bending is to the right. In either case, the ribs on the convex side always butt against the spinal column with forces greater than those on the concave side in order to sustain the weight and other forces endeavouring to increase bending.

#### CRITICAL MEMBERS OF THE STRUCTURAL COMPLEXES

The Ribs: One independent and vulnerable member in any of the aforementioned trusses is the rib. Because its attached back muscles act in tension and form obtuse angles directed medially, the rib in the vicinity of the spine is placed in compression. It is in effect a "jig pole" (Fig. 8a) of a derrick and any movements of its base attachments or a transsection along its length would be disastrous to its stability. To transsect the costotransverse and radiate ligaments holding the rib to the spine and thus removing its foundation would certainly precipitate a collapse. The resection of the heads and necks of the ribs could have an even more disastrous effect. Resecting the ribs lateral to their tubercle would have



FIG. 8 B. Stability of crane extension developed through the use of the "jig pole."



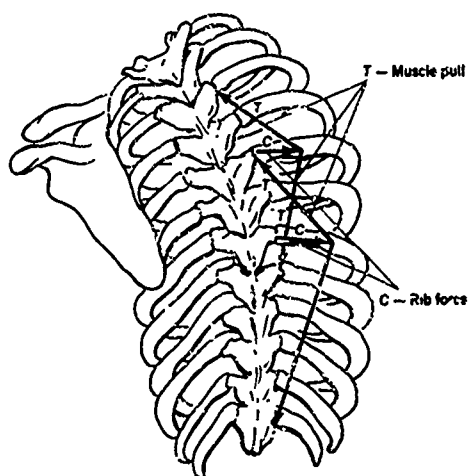


FIG. 8 A. Ribs on convex side butting against spinal column under normal bending condition.

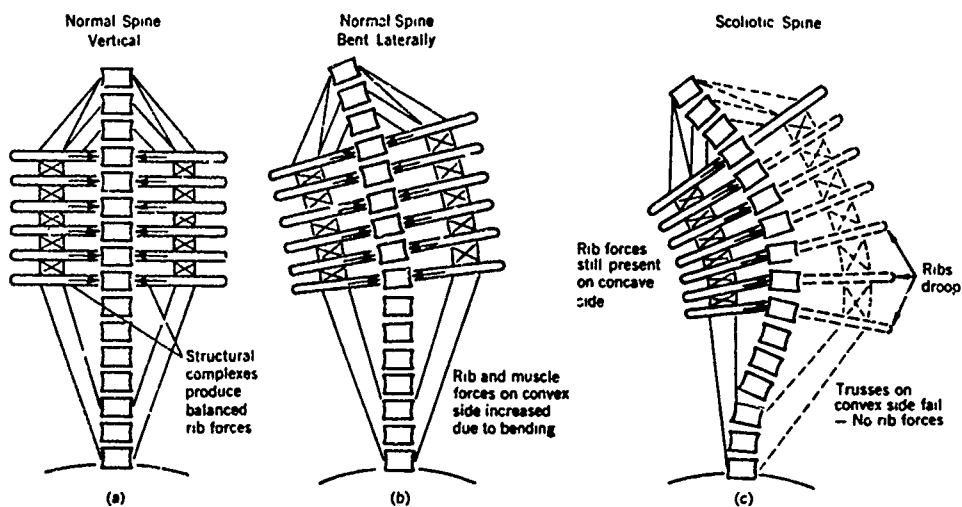


FIG. 9. Forces on normal and scoliotic spines.

a decreased effect, since the costotransverse ligaments would remain intact and with the erector spinal muscle mass would provide partial support. The greater number of transections and resections mentioned above, the greater would be the collapse of the spinal column which requires the support of the abutting ribs for its stability (Fig. 9)

The Muscles: Equally important in providing spinal support are the muscles forming the lateral chords of the symmetrically placed trusses. Any contracture of a muscle on one side of the spine will provide the connecting rib with an increased compressive force which will cause a lateral curve to form towards the opposite side. Conversely a relaxation of a muscle will decrease the rib force and permit a lateral curvature to the same side. Obviously the more muscles affected, the greater the curvature produced.

The Intercostal Ligaments: Another weak spot in the multiple truss system appears to be the network of intercostal ligaments. These ligaments form tensile cross braces between the ribs and prove extremely effective in stabilizing their position. If ruptured, or in some way rendered ineffective, the secondary defense against collapse shown in Figure 6 would be required to prevent loss of stability. This secondary defense comprising longer and more extensible muscles will provide the required resistance but only after a more disadvantageous deflection of the spinal column and more highly stressed components.

#### Rotation Produced By Unbalanced Rib Forces-

Any change in the balance of rib forces on either side of the spinal column will tend toward the development of not only a lateral curve-but a simultaneous rotation as well. (Fig.10). More specifically, rotation is developed where an unbalanced rib force, acting on the vertebral column does not pass through the center of rotational resistance of that cross-section.

In an in vivo study of axial rotation (9) of a normal human thorocolumbar spine, the centers of rotation of the thoracic vertebrae have been indicated as being located anterior to the contact joints of the ribs against the vertebral segments (Fig. 11). A resultant of the rib forces directed to the right posteriorly with respect to the center of rotation produces a tendency of the thoracic spine to rotate counterclockwise with the spinous processes deflected toward the convexity. Clinical evidence derived from scoliotic patients supports this conclusion.

In the same spine rotation study, (9) the centers of rotational resistance of the lumbar spine are shown to be posterior to the intervetebral disc. This is no doubt due to the position of the articulating facets of the lumbar spine which are also located behind the disc and resist rotational movement. Any unbalance of the rib forces in the thoracic region will therefore cause the lumbar vertebrae to rotate clockwise (viewed from above) with the spinous processes deflected to the concavity. Once again, clinical evidence obtained from scoliotic patients has supported this conclusion.<sup>15</sup>

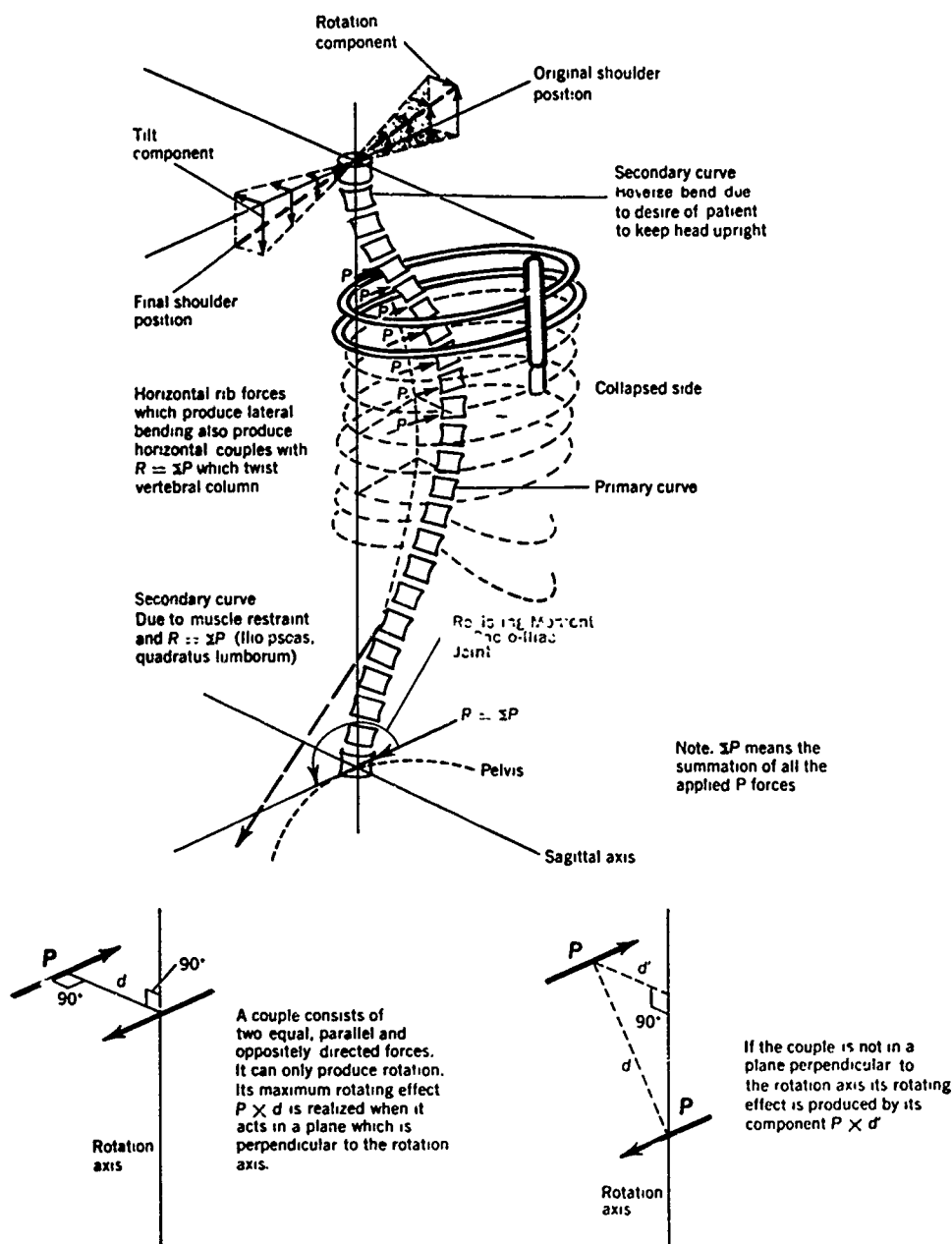


FIG. 10. Lateral bending and spinal rotation produced by rib forces.

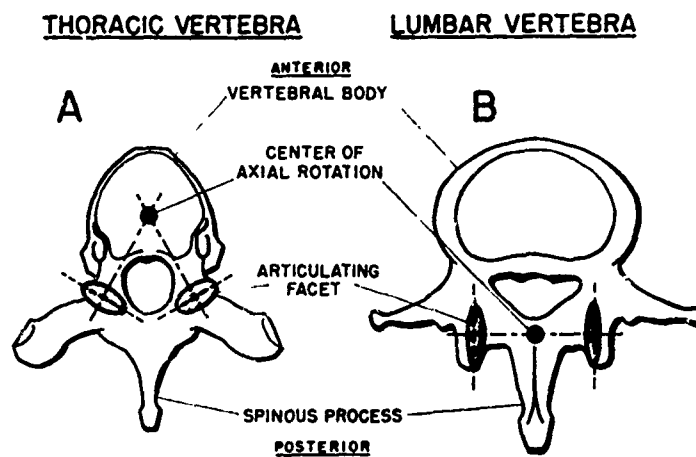


Fig. 11. Centers of Axial Rotation in a Thoracic and a Lumbar Vertebra. (9)

Resisting the rotation of vertebral segments of the spine, are the muscles attached to the spinal processes. These muscles will cause these relatively thin members to have a tendency to bend in a direction opposite to the rotation.

#### TRUSS SUPPORT SYSTEMS

##### CLINICAL AND EXPERIMENTAL EVIDENCE:

Evidence for the support of the multiple truss systems located on either side of the spine has been provided by the following clinical and experimental observations.

In 1934 a thoracic surgeon (2) contended that the ribs were the principal agents for the support of the thoracic vertebrae. It was pointed out that each pair of ribs grips with pressure the vertebrae with which it articulates. If this pressure is unequal on the two sides or if it has been removed from one side by the extensive resection of ribs such as occurs in thoracoplasty operations, the interposed ribs push the vertebrae towards the unsupported side and a curvature occurs.

In 1941 (19) a further study was done of 256 post-thoracoplasty cases in order to determine why lateral bending occurred and in some cases was worse than in others. Scoliosis was present in 219. The convexity was towards the operated side. This study showed that the most important causative factor in the production of a post-thoracoplasty scoliosis appeared to be the removal of the transverse process. This structure was deemed essential in as far as it affords

anchorage for ligaments and muscles which act as stays or guy ropes in maintaining a straight spine.

These observations on the importance of these ligaments were confirmed by a research study (12) which showed that progressive scoliosis would be produced in rabbits by resecting the posterior ends of six ribs. Further experimentation showed that the loss of the posterior costotransverse ligament was a most important factor provoking scoliosis in these experiments. This ligament transfers the effect of the Iliocostalis and the longissimus muscles from the ribs to the vertebrae.

The importance of the rib cage and its truss-like supporting mechanism of muscles and ligaments seems well established by engineering principles backed by clinical and research experience.

#### THE LUMBAR SPINE

The stability of the lumbar spine is developed in three major ways:

1. By the supporting action of its attached symmetrically placed musculature.
2. By the continuing compressive resistance of each vertebral segment and intervertebral disc., and
3. By the tensile resistance of the

intervertebral ligaments developed  
as the spine starts to bend.

We shall consider each of these stabilizing influences in turn - and the development of lateral bending as each is permitted to deteriorate.

1. Muscle weakness of any of the larger independently acting muscles which are stabilizers of the spine will with growth bring about a lateral bending and rotation. In order for a single unbalanced muscle pull to create this type of deformity, it must have a component acting in a plane perpendicular to its longitudinal axis and be eccentrically applied with respect to the center of gravity of the vertebral cross sections. (Fig.12A) Should the unbalanced force have as its other component one directed parallel to the longitudinal axis of the spinal column, an accentuation of the bending will develop due to additional bending moment(16) and compressive force.

Figures 12 and 16a show a vertical column of identical wooden blocks two inches thick, separated by 1/2 inch thick sponge rubber pads, the whole assembly tied together with two vertical lines of 3/8 inch diameter door springs. The bottom joint is fixed, while the top joint is held by a spring which permits it to move laterally about 1/2 inch in any direction. This assembly is presumed to simulate a section of a spinal column.



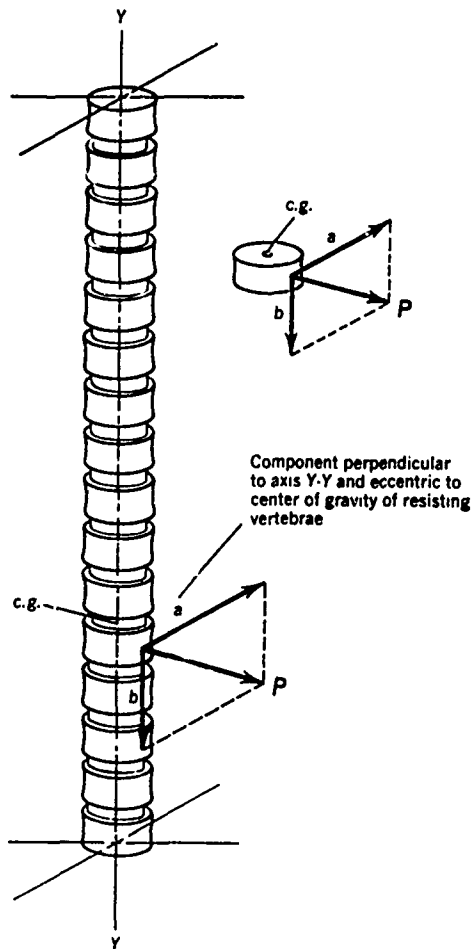


FIG. 12A Unbalanced muscle pull in lumbar region which causes lateral bending and rotation. Component "b" accentuates bending and compressive forces.

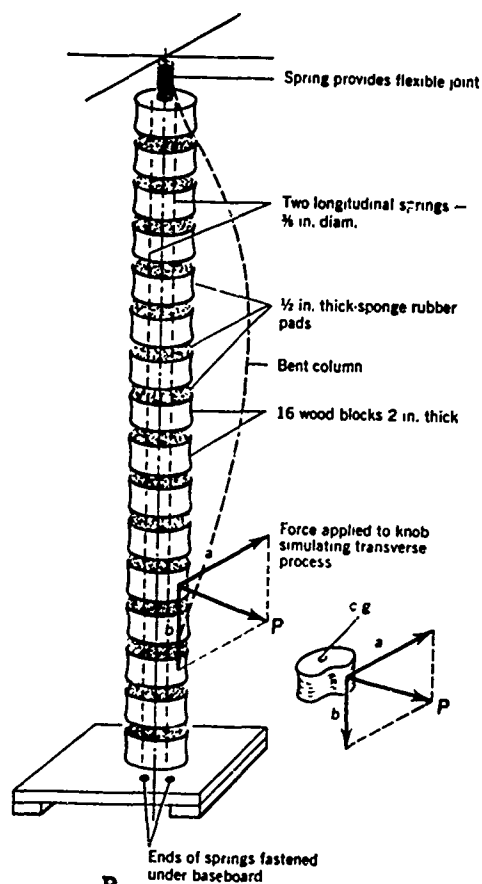


FIG. 12B Lateral bending and rotation resulting from oblique force eccentrically applied.

knobs, representing a transverse process of a spinal segment, and pulled downward and to the right, the elastic curve which results is exactly similar to the curve of a scoliotic spine. This experimental model verifies the type of curve developed by the previous theoretical analysis. Note the rotation and the tilt of the upper segment which in the prototype would bring the right shoulder higher than the left.

Clinical experience(5) has shown that curves with convexity toward the strong muscle group are produced by such extrinsic muscles as the Deltoid, Trapezius, Latissimus dorsi, and Rhomboid in the thoracic spine and by the psoas major in the lumbar spine. Curves may also develop in the lumbar spine when there is unilateral weakness of the rectus abdominis, abdominal obliques(Fig.13b), the abdominal transverse and the quadratus lumborum.

A significant factor in maintaining lateral stability of the spine therefore is the preservation of balance between the two groups of muscles on each side of the body, because an unbalance causes a spinal curvature. If the opposing muscles are equally weak or absent, the curve does not develop. (5).

2. Should any of the intervertebral discs in the lumbar area be pathologically affected causing the disc to become tapered, lateral bending and subsequent rotation will result. This action is shown experimentally in Figs. 14 and 15. Here, on the same experimental column previously described the left half of five successive rubber pads was

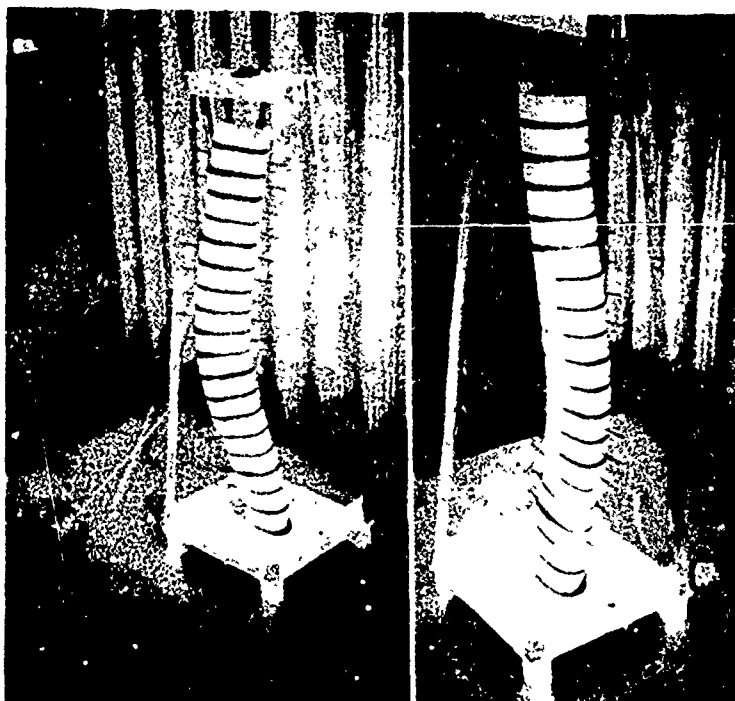


FIG. 13 A, B. A, Experimental model showing bending and rotation resulting from eccentric force directed diagonally downward. B, Model with 5 consecutive bisected rubber pads showing effect of longitudinal springs in producing lateral bending and rotation.

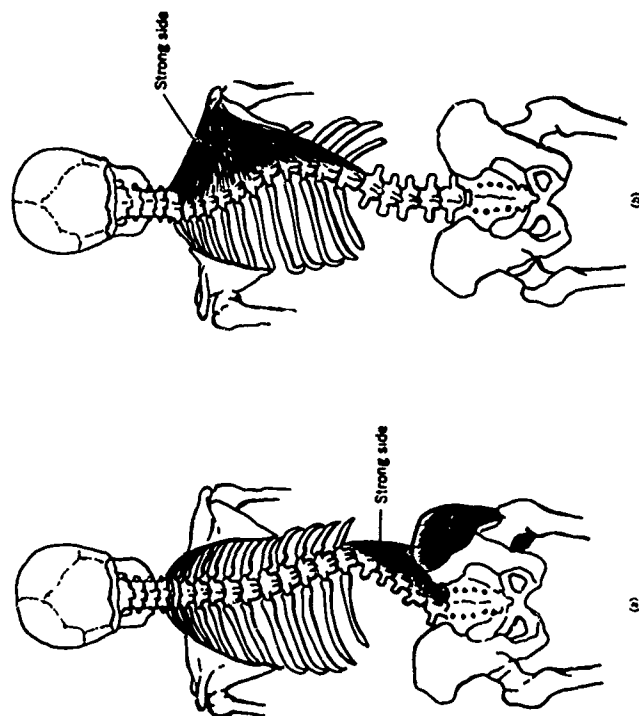


FIG. 14 A, B. A, Unilateral paralysis of the iliopsoas. B, Unilateral paralysis of the trapezius.

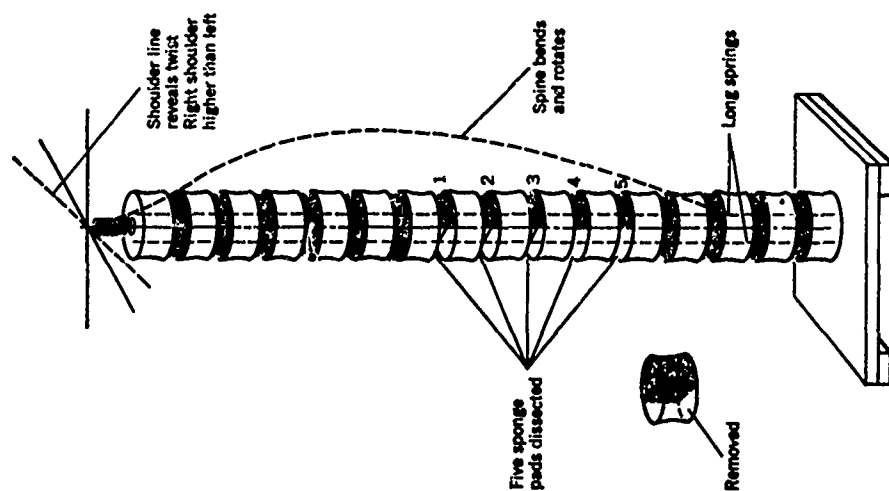


FIG. 15. Bending and rotation of column resulting from bisection and removal of 5 successive sponge pads. Only the longitudinal spring forces are acting.

removed to simulate the taper of the five corresponding spinal discs. Under the action of the longitudinal spring forces alone, the same scoliotic curve developed shown.

The couples responsible for the bending and rotation are shown in Fig. 15. Here the two longitudinal spring forces  $S_1$  and  $S_2$  simulating the intersegmental ligament forces are resolved into a resultant  $R$ . Using the upper part of the column above one of the cut discs as a free body, it is to be noted that the vertical resisting force  $R'$  is not colinear with force  $R$ . The couple thus produced causes the lateral bending (15). Similar couples acting on a scoliotic spine with a normal sagittal plane curvature develop rotation as well.

3. A possibility of longitudinal bending and rotation is developed whenever the resultant of the intervertebral ligamentous forces on any spinal cross-section does not pass through the centroid of resistance of all intervertebral discs. The "normal" spine with its sagittal plane curvature increases this possibly. The weight of the head and shoulder girdle also helps to intensify the effect. The column under these actions, becomes a long coiled spring bending and rotating into a typical scoliosis curve.

This action is revealed in the previously described segmental column by removing one longitudinal spring. Lateral bending and an accompanying rotation is developed when the column is given the

removed to simulate the taper of the five corresponding spinal discs. Under the action of the longitudinal spring forces alone, the same scoliotic curve developed shown.

The couples responsible for the bending and rotation are shown in Fig. 15. Here the two longitudinal spring forces  $S_1$  and  $S_2$  simulating the intersegmental ligament forces are resolved into a resultant  $R$ . Using the upper part of the column above one of the cut discs as a free body, it is to be noted that the vertical resisting force  $R'$  is not colinear with force  $R$ . The couple thus produced causes the lateral bending (15). Similar couples acting on a scoliotic spine with a normal sagittal plane curvature develop rotation as well.

3. A possibility of longitudinal bending and rotation is developed whenever the resultant of the intervertebral ligamentous forces on any spinal cross-section does not pass through the centroid of resistance of all intervertebral discs. The "normal" spine with its sagittal plane curvature increases this possibly. The weight of the head and shoulder girdle also helps to intensify the effect. The column under these actions, becomes a long coiled spring bending and rotating into a typical scoliosis curve.

This action is revealed in the previously described segmental column by removing one longitudinal spring. Lateral bending and an accompanying rotation is developed when the column is given the

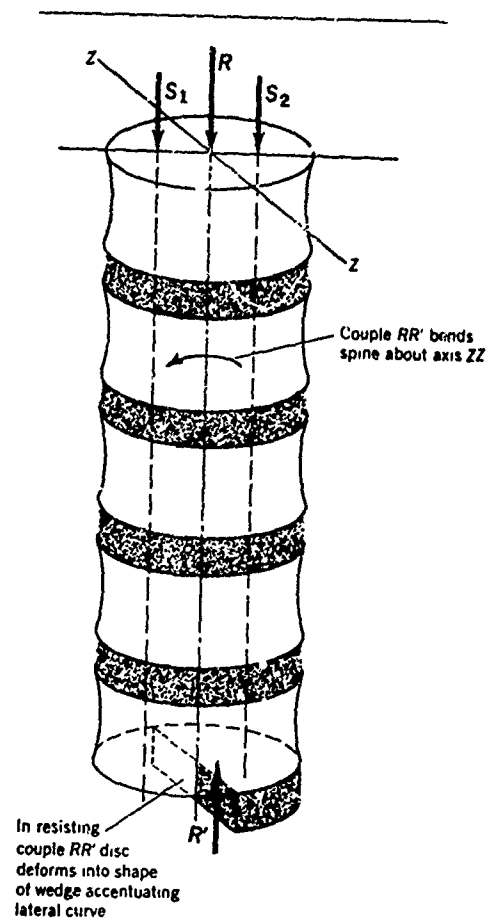


FIG. 16. The free body of the upper portion of Fig. 14 including the uppermost bisected rubber pad.

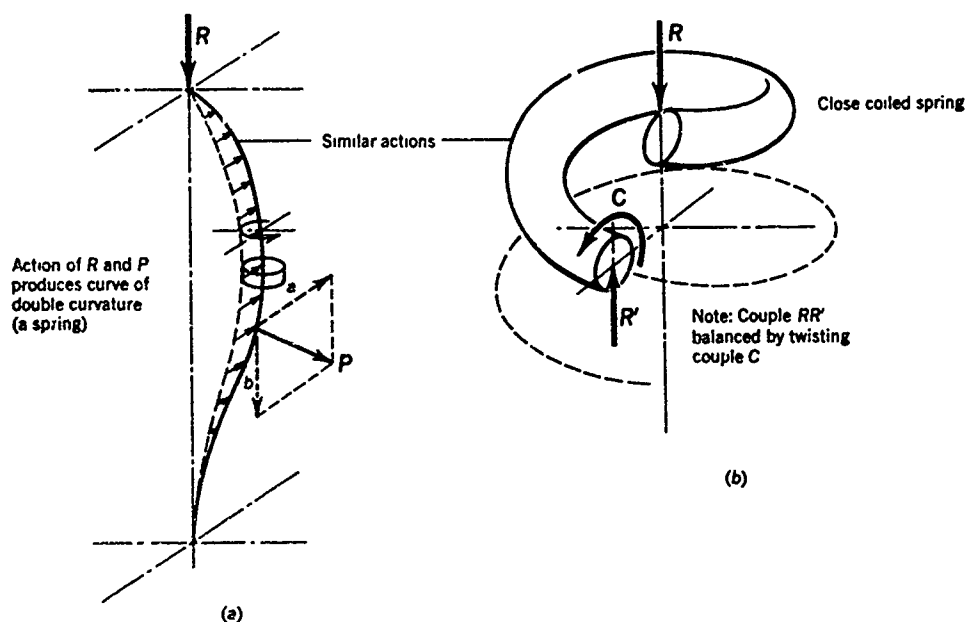


FIG. 17 A and B. Combined effect of the vertical force  $R$  (Due to tension of intersegmental ligaments and weight of head and shoulder girdle) and unbalanced muscle pull  $P$  in producing bending and twisting of column.

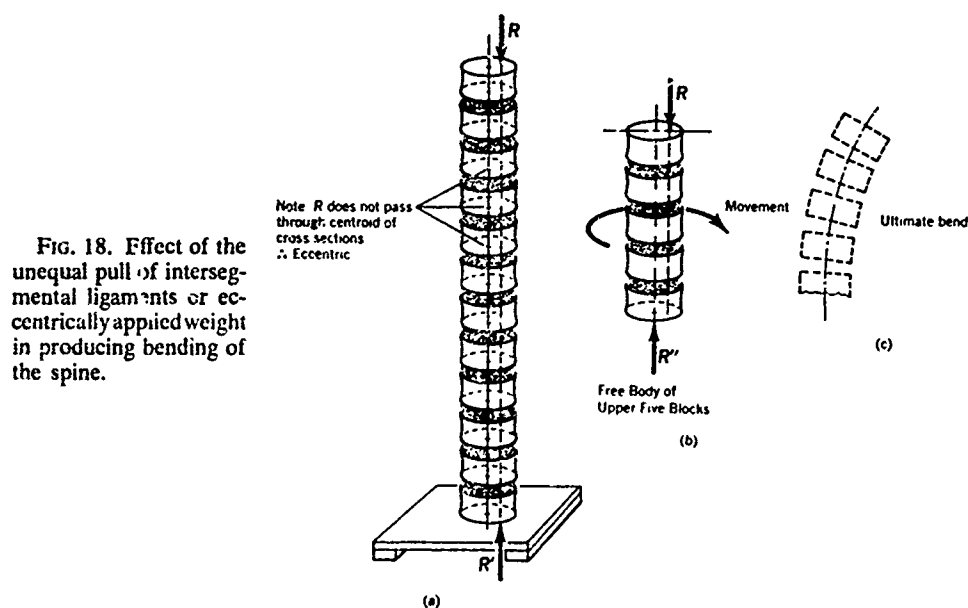


FIG. 18. Effect of the unequal pull of intersegmental ligaments or eccentrically applied weight in producing bending of the spine.



normal saggital curvature of the spine.

#### THE DEVELOPMENT OF A LATERAL BENDING

#### ROTATIONAL DEFORMITY OF THE HUMAN SPINE

#### A SUMMARY

In the Thoracic Region -To produce a lateral bending-rotational deformity in the Human Spine.

As the structural complex on the convex side fails, that on the concave side pushes against the spinal column bending and rotating the spine. The collapse on the convex side is non-elastic. Because of the sustained tension of the muscles on the concave side and the weight of the head and shoulder girdle, the spinal deformation will continue to increase and restoration of the self-supporting vertical spine becomes increasingly difficult. Because irreversible structural changes will occur with increased spinal deformity, time is a critical factor in initiating correction.

In the Lumbar Region- an unbalance of any supporting muscle group will produce a curvature to the side of the heavier muscle pull. A weakness in the intervetebral ligamentous structure will produce a bending toward the weaker side. An unequally compressed intervertebral disc will produce a spinal curve in the direction of the normal side.

### CONCLUSION

With a clear understanding of the fundamentals of mechanics of the back, it is anticipated that substantial improvements will and can be made to the present methods used to correct for spinal curvature. It is with this hope that this paper has been presented.

## REFERENCES

1. Beadle, O.A.: The intervertebral Discs. Observations on their Normal and Morbid Anatomy in Relation to Certain Spinal Deformities, Privy Council, Medical Research Council, Special Report Series #161, London, His Majesty's Stationary Office 193.
2. Bisgard, J. D.: "Deformities of the Chest and Spine Resulting from Thoracic Disease and Operation." Amer. Jour, Surg. 54: 317, 1941.
3. Blount, W. P., and Moe, J. H.: Non-Operative Treatment of Scoliosis with the Milwaukee Brace.
4. Cobb, J. R.: The Problems of the Primary Curve in Idiopathic Scoliosis. American Academy of Orthopedic Surgeons. Annual Meeting 1948 (unpublished data).
5. Colonna, P.C., and Vorn Saal, Frederick: "A study of Paralytic Scoliosis Based on Five Hundred Cases of Poliomyelitis." Journal of Bone and Joint Surgery 23, #1, 335-353, April 1941.
6. Farkas, A: "Pathogenesis of Idiopathic Scoliosis." Journal of Bone and Joint Surgery 36A, 617, 1954.
7. Feiss, H. O.: "Mechanics of Lateral Curvature." Am. J. of Orthopedic Surg. 5: 152, Oct., 1907.
8. Flinchum, D.: "Scoliosis Trouble." J. Med. Assoc., Georgia 52: 67, Feb. 1963.

9. Gregerson, G.G. and Lucas, D. B- "An In Vivo study of the Axial Rotation of the Human Thoracolumbar Spine"Journal of Bone and Joint Surgery. Vol 49A 247-262 March 1967.
10. Harrington, P. R.: "Treatment of Scoliosis." Journal of Bone and Joint Surgery 44-A, #4, 591-610, 1962.
11. Centers of Axial Rotation in a Thoracic and a Lumbar Vertebra. From "An In Vivo study of the Axial Rotation of the Human Thoracolumbar Spine" Gregerson, G. G. and Lucas, D. B.
12. Langenskiold, A. and Michelsson, J. E.: The Pathogenesis of Experimental Progressive Scoliosis. Acta Orthopaedia Scandinavica Supplementum # 59.
13. Lowman, C. L.: Abdominal Fascial Transplants. Edwards Brothers Inc., Ann Arbor, Michigan, 1954.
14. Lucas, D. B., and Bresler, Boris: Stability of the Ligamentous Spine. Biomechanics Laboratory, Univ. of California #40, Jan. 1961.
15. Ober, F. R. and Brewster, A. H.: Lateral Curvature of the Spine 5th Ed. P. Blaikston's Son & Co. 1931.
16. Olsen, G. A.: Elements of Mechanics of Materials. 2nd Ed. Prentice-Hall Inc., Englewood Cliffs, N.J. 1966.

17. Schmidt, A. C.: Fundamental Principles and Treatment of Scoliosis. American Academy of Orthopedic Surgeons, Instructional Course Lectures Vol. 16, 184-212, 1959.
18. Steindler, A.: "The Compensation-Dero-tation Treatment of Scoliosis." Journal of Bone and Joint Surgery Vol. 21, #1, 51-58, Jan. 1939.
19. Weinmann, J.P., and Sicher, H.,: Bone and Bones: Fundamentals of Bone Biology, St. Louis, The C. V. Mosley Co., 1947.
20. Wenger, H.L., and Herman, W.: Role of Transverse Process in Thoragenic Scoliosis, Quart. Bull. Sea View Hospital 7: 45, 1941.

THE ULTIMATE STRENGTH AND FAILURE MECHANISM OF  
ANTHROPOID KNEE JOINTS

John O. Outwater, Carl H. Jacobs and Robert W. Castle

Professor of Mechanical Engineering and Graduate Students  
The University of Vermont  
Burlington, Vermont

ABSTRACT

Testing of the anthropoid knee in three point loading indicates a progressive failure mechanism in an anterior loading situation. This phenomenon is investigated and is shown to be due to the failure of the connective tissue of the knee region as loading progresses. The first response is the patella settling into the intercondyle space of the tibia and contacting the tuberosity. This contact causes the posterior surface of the patella to be bruised. The second response is that of the posterior cruciate ligament failing at its point of insertion into the medial condyle. The ultimate and final failure of the joint occurs when the posterior cruciate ligament completely ruptures and causes the ligament of Wrisberg to tear its lateral condyle insertion allowing the complete collapse of the joint.

The relationships between the angular displacement of the knee joint and the applied bending moment are shown for different size joints. The failure conditions are related also to the joint sizes. The effects of freezing on the angular modulus of the joint and on its ultimate strength is shown to reduce the strength and modulus about 50%.

PRECEDING PAGE BLANK

## INTRODUCTION

The problem of protecting man from serious injury depends in large measure on a knowledge of the ultimate strengths and failure mechanisms of the parts of his body being protected. It is only by such knowledge that we can design accurate and useful protective devices.

If a skier had prior knowledge of the torsional strength of his tibia, then it would be possible to design and adjust devices to prevent its overload<sup>(1,2)</sup>. The skiing problem is well understood and analyzed. This is not the case with many other forms of injury and the purpose of this paper is to determine the strength of the knee joint and its mode of failure so that it may be possible to obtain data for its protection against overload as well as to give insight in regard to the healing needs of the injury.

The mechanics of the knee joint have been extensively studied.<sup>(3,4)</sup> The functions and loads in the various ligaments under different conditions have been measured by the application of strain gages<sup>(5)</sup> and also by inference from the dynamic loading during motion<sup>(6)</sup>. Work is lacking on the ultimate strengths of the joint and it is this strength and concomitant failure mechanism that we seek.

As in all cases where knowledge of ultimate loads and failures is needed, it is not practicable to seek it directly from human specimens and exploratory work is best done with non-human specimens. The loading characteristics can be obtained and the possibility of scaling to human sizes can be reasonably explored using non-destructive methods.

The specimens that we used were the legs of rhesus monkeys (*Macaca Mulata*). Anatomically, these legs are similar to the human leg except for two small bones located anteriorly on the tibia and for a large muscle bundle that extends across the knee on one side.

The knee is a mechanism that is articulated and supported by a variety of different members. Work has been done in severing successive members that contribute to its stability so as to examine the degree of instability that results<sup>(3)</sup>. This demonstrates clearly that it is not only the ligaments that are the support of the knee, but that the menisci, the condyles and the flexing muscles themselves can all

NOT FOR PUBLICATION

contribute to the nearly normal operation of the knee when any one factor is missing. The point to consider, however, when we come to the problem of injury by reverse bending as is so frequently the case with football injuries, is that the muscles do not necessarily have time to react and then, when the leg is straight, the full bending will come on the ligamentous support of the knee acting only in conjunction with the knee geometry. It is this ultimate support that we sought and the mechanism of failure of this support.

The data that we obtained concerned the load-deflection characteristics of the knee joint in anterior loading. The failure mechanisms were related to this curve and the failure loads were further related to body characteristics of the monkey. As frozen specimens were so much simpler to use, the effect of freezing and rethawing on strength characteristics was measured and was shown to be so great as to preclude the use of frozen and rethawed specimens for useful work on strength determinations. Finally, some of the parameters were then compared to similar experiments conducted on humans and speculation is made on scaling our results to human sizes so that our data can be used for the design of knee prostheses for the prevention of knee injuries.

#### EXPERIMENTAL PROCEDURE

After a monkey had been sacrificed, the legs were removed and the muscle bundles of both the upper and lower leg were severed so that no additional strength or support is provided to the knee by these muscles. The leg is then placed in the test support as in Fig. 1 and the loading applied to measure the load-deflection relationship of the knee joint in three point bending.

A typical curve obtained is shown in Fig. 2. It is evident from this curve and the similar curve obtained from the second leg of a pair after it had been frozen, preserved for two weeks, thawed and tested, that there is a pronounced lessening of strength and modulus as a result of freezing and thawing. This change of properties can be inferred by noting that there is far more extensive bleeding in thawed specimens than in those that have been tested when fresh. The freezing apparently causes the blood and body fluids to damage the microstructure of the



cell walls. It not only escapes on thawing, but also lowers the strength of the connective tissues. This lowering of strength is also apparent after rigor mortis has set in as, again, the microstructure is altered with its consequent influence on strength. It may be noted that the loss of strength in the connective tissue is quite distinct from the constancy of values of bone strength before and after freezing<sup>(7)</sup>.

At the same time as the load deflection curves were obtained, it was noted that there were two characteristic deviations in the curves. Each of these deviations signified some internal alteration so dissections were performed to show exactly what had happened to cause the sudden variations.

A total of 21 legs were examined. The load to failure, to the first deviation point on the load deflection curve, to the second deviation point and the associated angular deflections were measured. It was important to relate the strength of the knee joints to some physical dimension of the body so that a prediction might be possible. The monkey weight was used and also a correlation was made with the proximal width of the tibia as this measurement had been so useful as a predictor of strength of the tibia<sup>(1)</sup>.

#### ANALYSIS

The knee joint is essentially a hinge joint permitting angular motion. It permits the lower leg to rotate freely about its end until the hinge is restrained by its internal mechanism when further rotation simply destroys the mechanism by pulling its essential elements free of their anchorage. When this is done the knee joint is seriously damaged. The events leading to this culmination can be traced by noting the load deflection as it occurs.

Three point bending was induced by using an Instron test machine when the force on the knee could be automatically plotted against the movement of the loading point. Such data was interpreted by relating the angular movement of the joint to the angular force or moment needed to effect this angular deflection. The data are all plotted to relate moment in g-cm to the angular deflection in radians.

## DISCUSSION

The failure sequence of the anthropoid knee joint is graphically shown in Fig. 2. It is a three stage process with the first stage occurring at approximately one-third of the collapse load, the second stage at approximately two-thirds of the collapse load and the collapse being complete when it occurs.

Each of these stages was isolated by dissection of the knee after its occurrence to show exactly what had happened: the first stage was found to be due to the fact that the loading was applied to the patella. The patella contacts the capsule above the articulating surfaces and not anteriorly to them. Therefore, when a load is applied to the anterior patella surface, the bone slides down the patellar surface on to the tibial tuberosity (a bone projection above the insertion of the patellar ligament) and then into the joint area protected by the capsular ligaments. Physical evidence of this is apparent upon dissection as the lower posterior surface of the patella is bruised. This bruise is indicated by a hemorrhage located along the bone edge contained in the tissues covering it. It is probably caused by bone to bone contact.

With the patella now resting on the capsule, the joint begins to bend from the front to back until the second stage of failure occurs. As the load is applied to the patella in its slipped position, the anterior cruciate ligament appears to be relaxed while the posterior cruciate is subjected to increasing tension until it fails at its weakest point. This weakest point appears to be at its insertion into the medial condyle. At the second point of failure, the fibrous tissues of the ligament separate from the medial condyle. This is quite evident upon dissection as there is much hemorrhaging about the insertion point and separate fibers are apparent in the torn ligament.

The third and final failure is due to the complete collapse of ligament integrity leading to tissue rupture and bleeding.

The curve in Fig. 2 was characteristic of all the knee joints tested so the values of the three characteristic nodes of failure were noted as well as the slope of the curve and these points were related

to the proximal width of the tibia. These relationships are shown in Figs. 3, 4, and 5. The relationships between the first and second points with the collapse load is shown in Fig. 6 & 7. The relationship between the stiffness of the knee joint and the weight of the specimen is shown in Fig. 8.

The failure values seem reasonably predictable on the basis of body weight and certainly bear a substantially constant ratio with each other. The stiffness of the joint, on the other hand, seems to be independent of the size of the specimen yet it falls within a definite range. A surprising fact that appears to emerge from these results is that the knee joint acts linearly during hyperextension. Many earlier works have shown the partial linearity of tendon substance but recent work<sup>(5)</sup> has shown that the tensions in the knee ligaments during flexure are anything but linear. No work, to the authors knowledge, has, however, been concerned with the extension of the knee mechanism to destruction so it appears that the smaller nonlinearities that are apparent at lower values of extension are overshadowed during the final failure.

Part of the purpose of this paper was to extend the values of strength from that of the monkey to the human leg. Typical values of human proximal width would range from 6 - 12 cms.<sup>(1)</sup> This, on the basis of the curve of ultimate failure load vs proximal width. Fig. 5 would correspond to bending moments ranging from 2700 to 5700 kg-cm. In the absence of any firm evidence of the strengths of knees in reverse bending, these figures would seem reasonable. The values of stiffness of the human knee joints compared to those of the monkey are about 6 times greater. It is questionable whether or not it is reasonable to extrapolate stiffness or strength values but it is certainly reasonable to anticipate the modes of failure and to use such data as a beginning point to seek firm information in regard to the failure of the human knee. We anticipate extending this work to the human knee so that firm data will become available for the design of protective devices against knee overstrain.

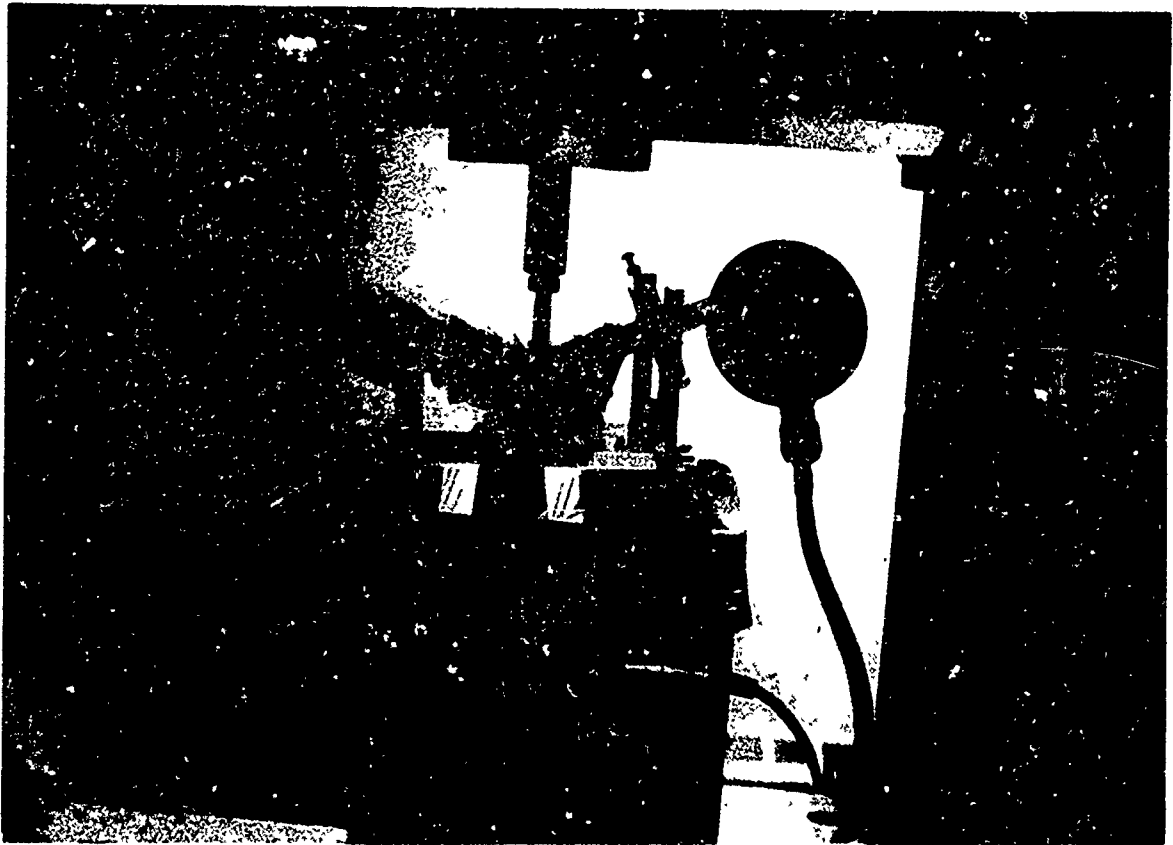


Fig. 1. Leg being tested to failure in reversed anterior bending.

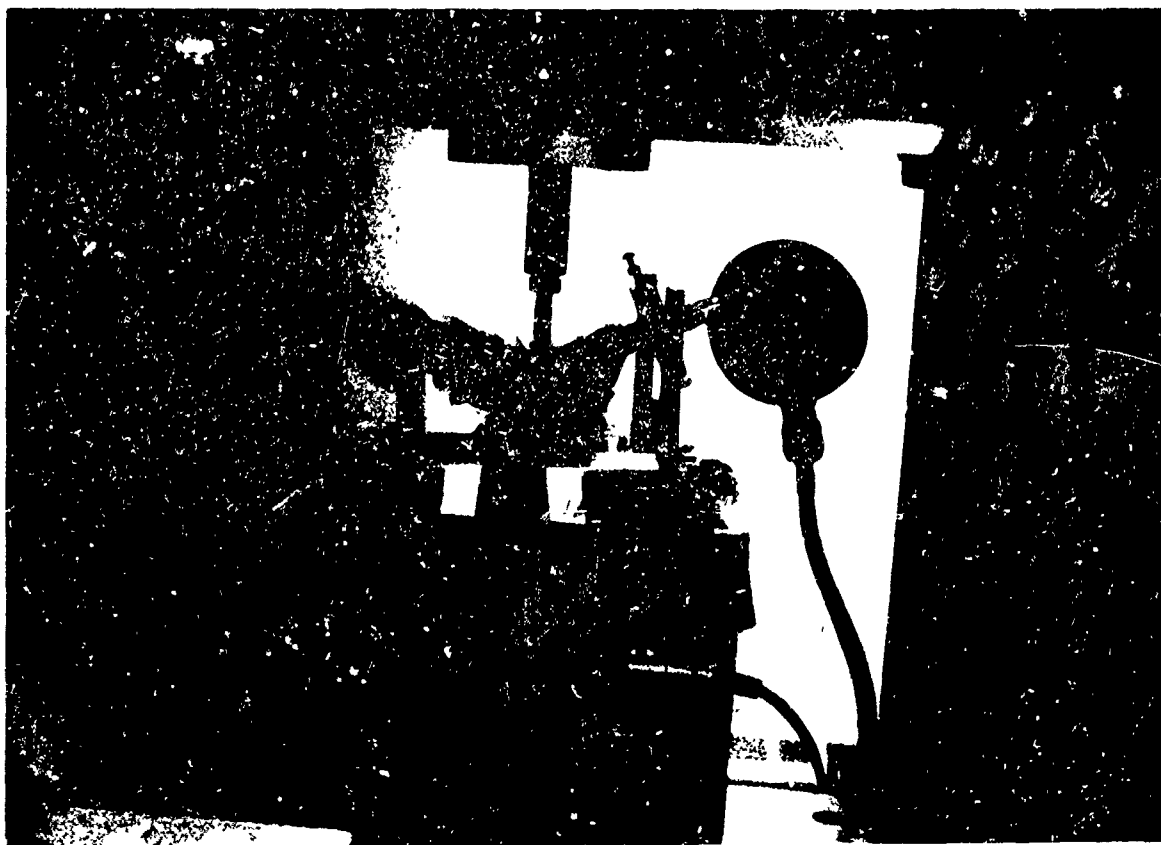


Fig. 1. Leg being tested to failure in reversed anterior bending.

# EFFECTS of FREEZING

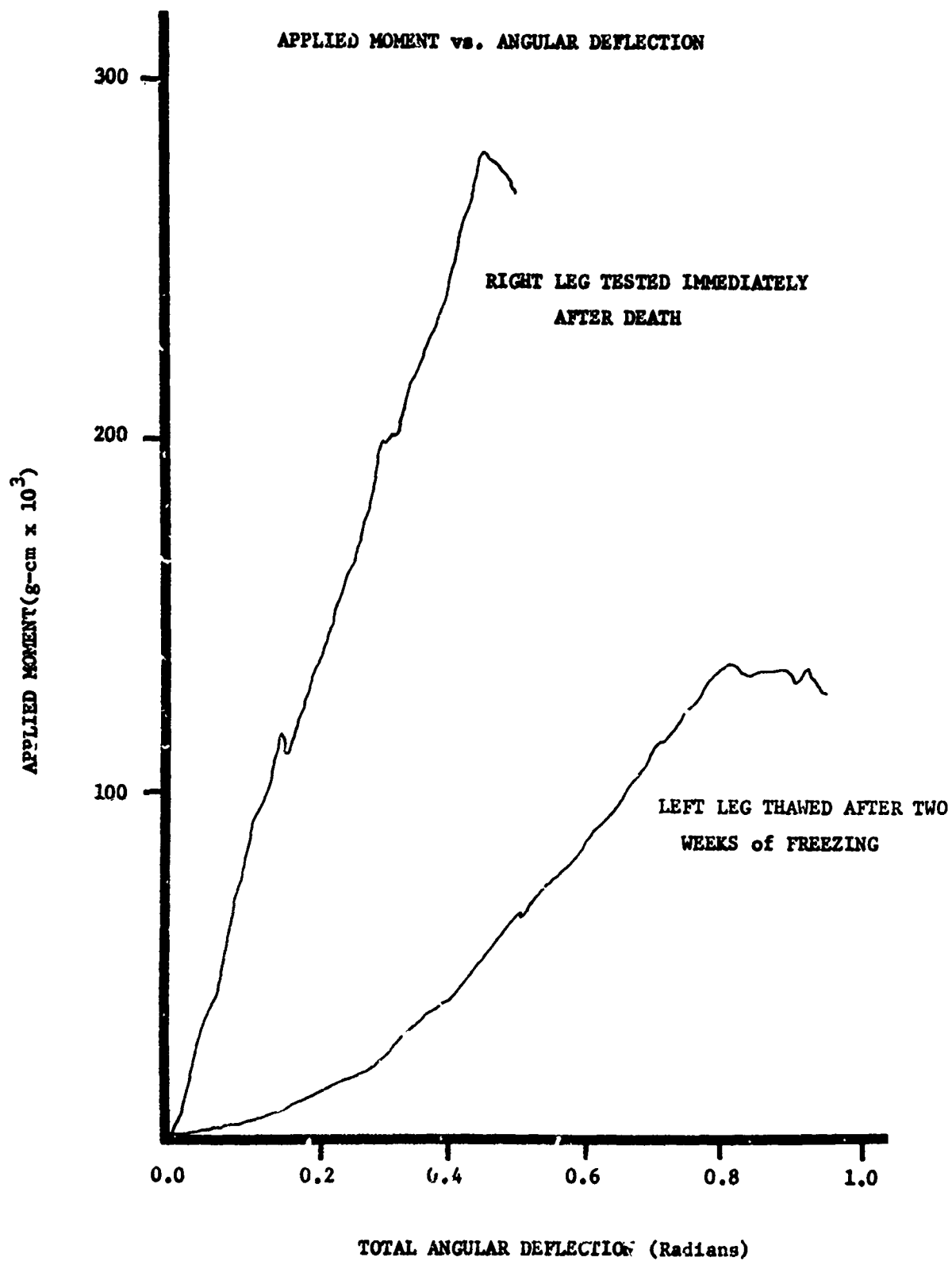


Fig. 2. Typical load deflection curve using fresh and also rethawed frozen specimens.

# FIRST IMPULSE FAILURE MOMENT

## APPLIED MOMENT vs. PROXIMAL WIDTH

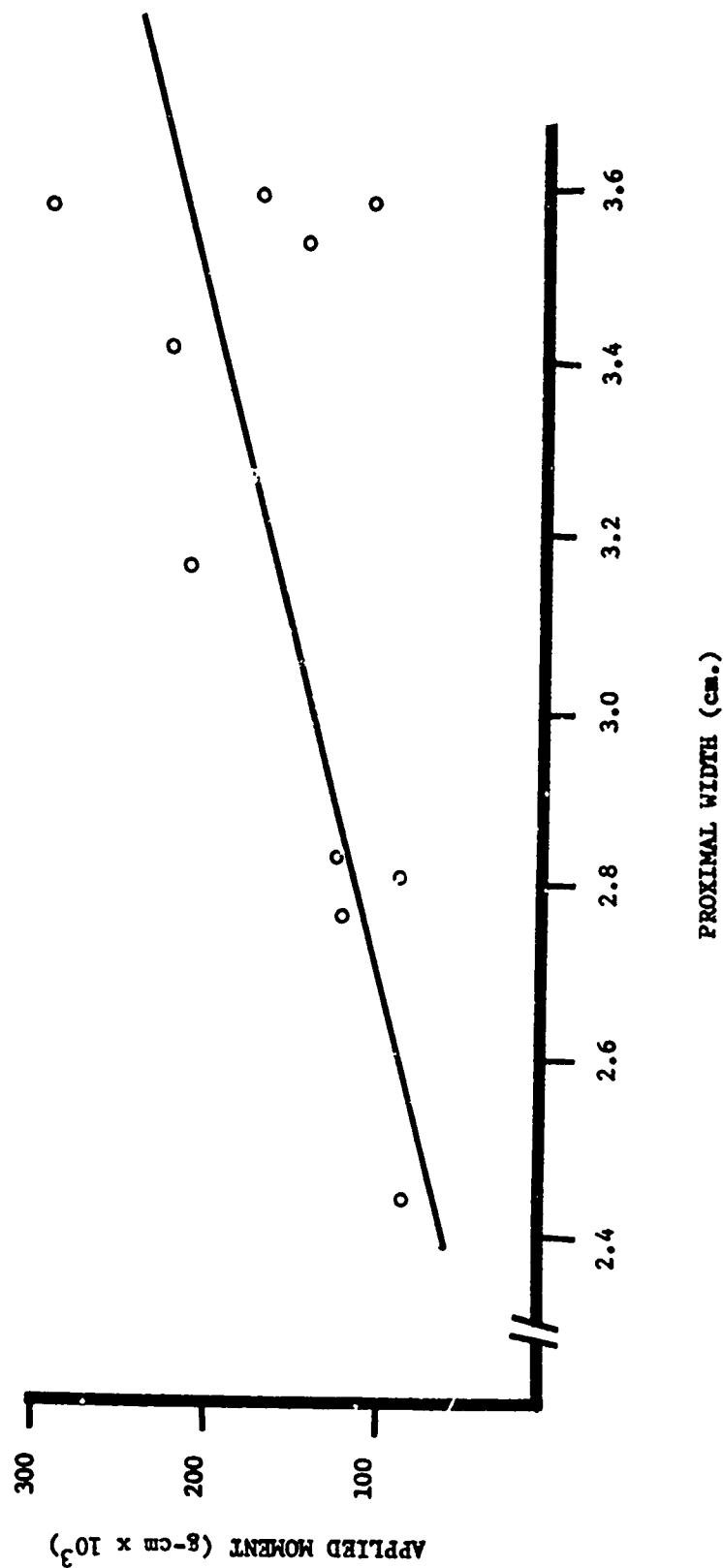


Fig. 3. First failure impulse moment  $M_1$  v. Proximal width.

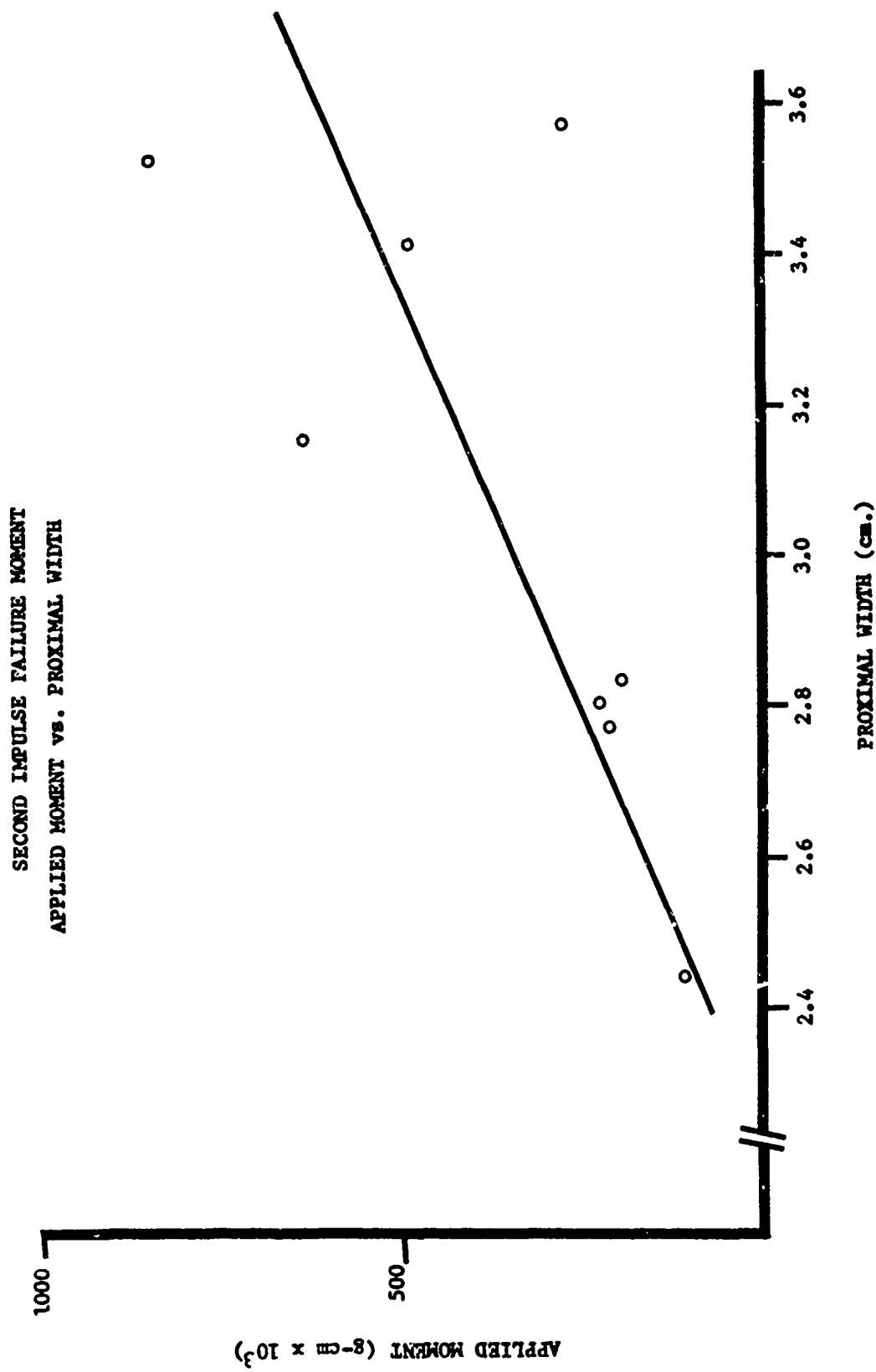


Fig. 4. Second failure impulse moment  $M_2$  v. Proximal width.



FINAL FAILURE MOMENT vs. PROXIMAL WIDTH

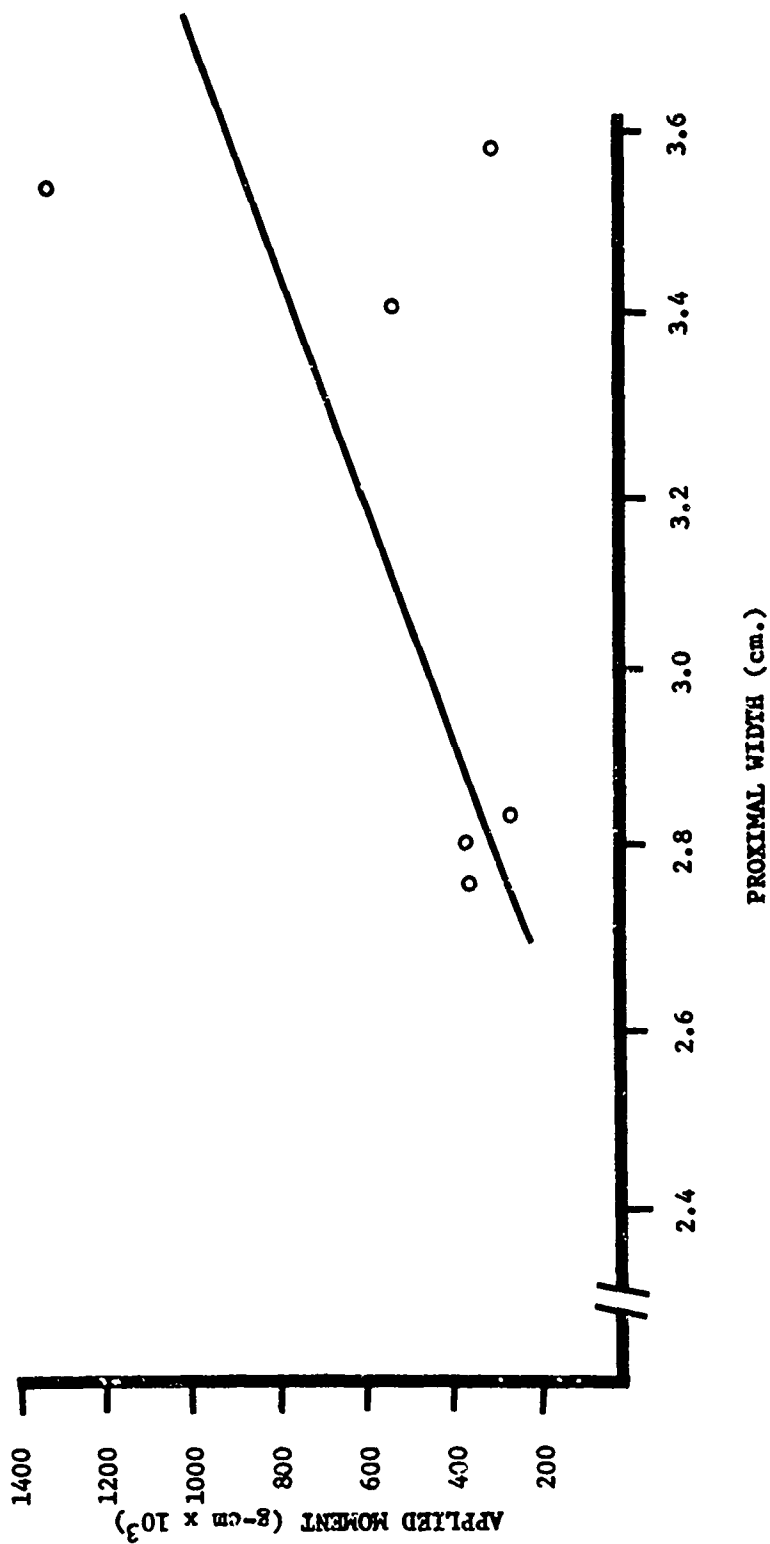


Fig. 5. Final failure moment  $M_f$  v. Proximal width.

INITIAL FAILURE MOMENT  
 FINAL FAILURE MOMENT

vs. FINAL FAILURE MOMENT

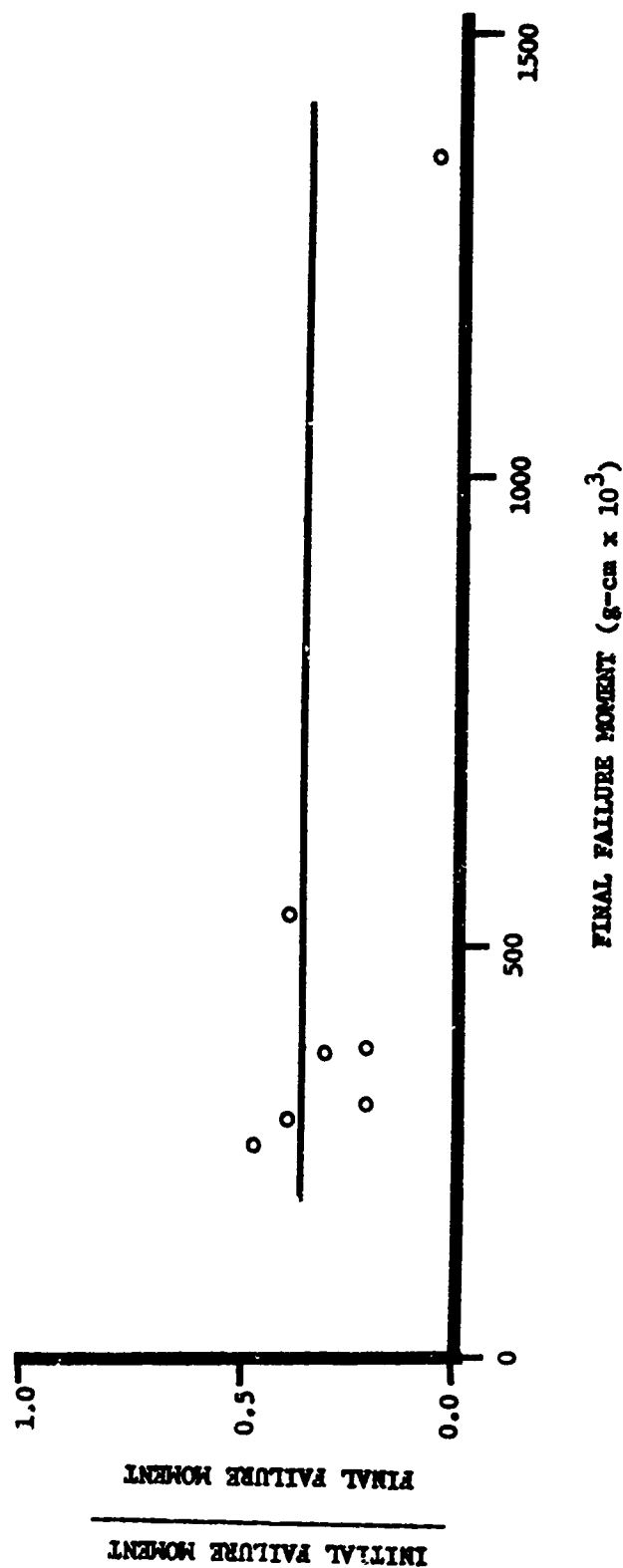


Fig. 6. Ratio of  $M_I/M_F$  v.  $M_F$

SECOND FAILURE MOMENT  
vs. FINAL FAILURE MOMENT

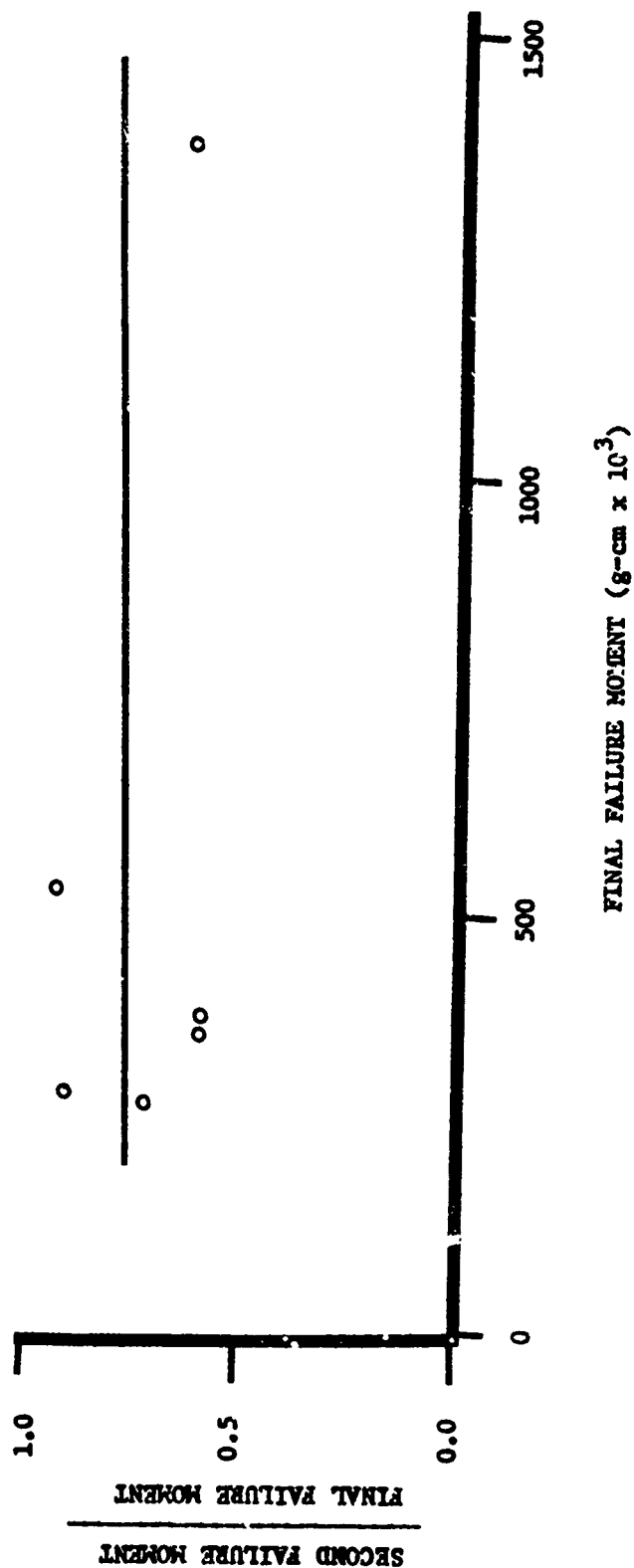


Fig. 7. Ratio of  $M_2/M_f$  v.  $M_f$

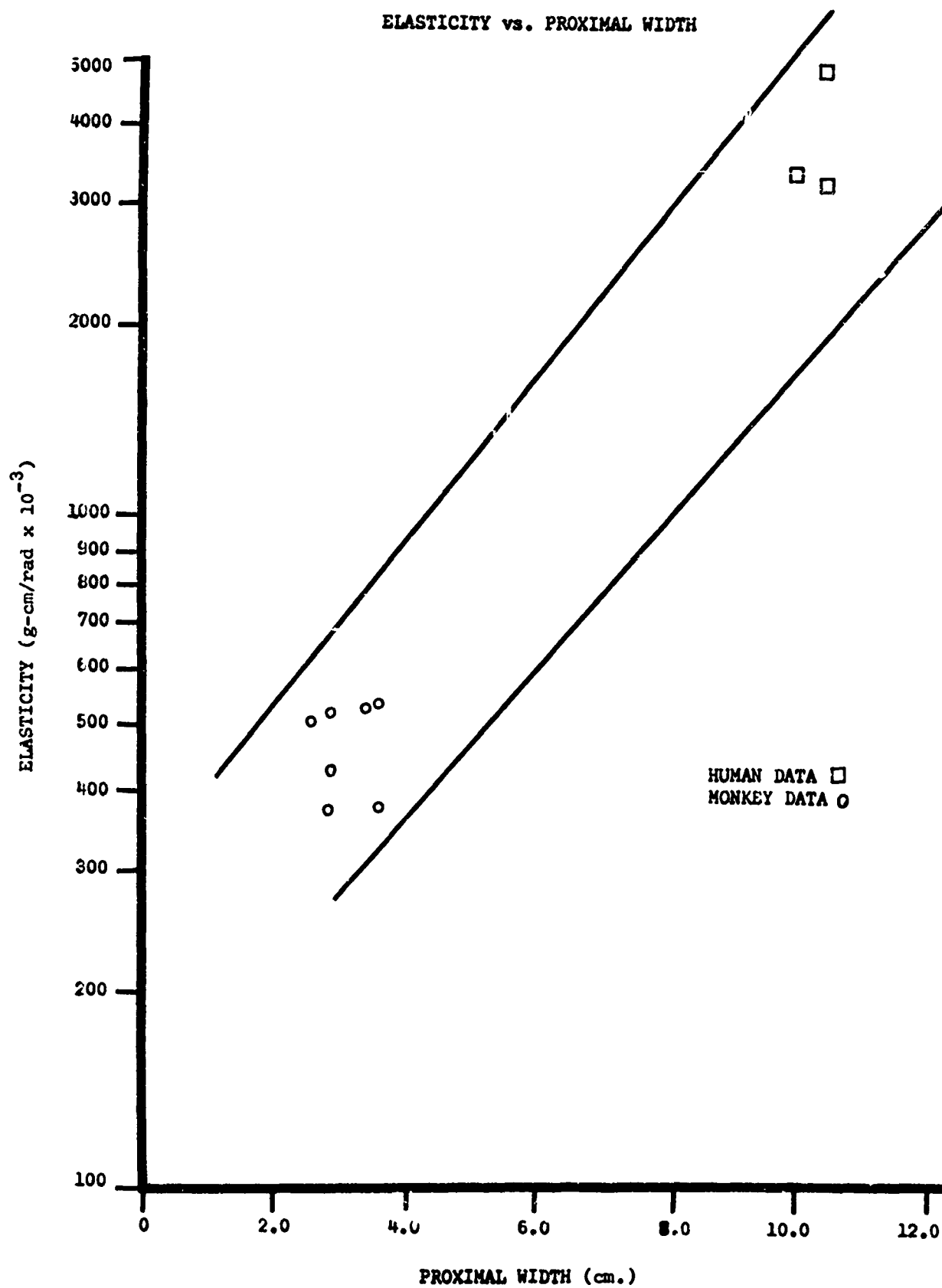


Fig. 8. Elasticity of joint v. Proximal width for men and monkeys.

## CONCLUSIONS

The study of the failure patterns during hyperextension of the knees of rhesus monkeys show the following characteristics:

1. The load deflection relationship is essentially linear from the inception of resistance to the complete collapse of the joint.
2. The elastic stiffness of the joint ranges from 355 to 580 g-cm/rad and is essentially independent of the size of the knee joint.
3. The load deflection curve exhibits two arrest points: the first due to the settling of the patella into the intercondyle space, the second due to the initial pulling out of the posterior cruciate ligament.
4. The ratio of the load at the arrest points to the final failure load is a ratio that is essentially constant regardless of the size of the monkey.
5. The final failure load is linearly dependent on the size of the joint.
6. The effect of freezing on the strength of connecting tissue is severe and leads to both a reduction of strength and joint elasticity of up to 50%.
7. Further work is necessary to reasonably extrapolate strength or stiffness values to those of the human knee.

## ACKNOWLEDGEMENTS

The authors wish to acknowledge the assistance of Drs. H. M. Doremus and D. R. Erickson of the College of Medicine, University of Vermont.

#### REFERENCES

1. Outwater, J.O.; and Woodard, M.S.: Ski Safety and Tibial Forces, ASME Paper 66-WA/BHF-14, 1966.
2. Outwater, J.O.; and Ettlinger, C.F.: The Engineering of Ski Bindings. Med. and Sci. in Sports 1: 4 pp. 200-206, 1969.
3. Brantigan, O.C.; and Voshell, A.F.: "The Mechanics of the Ligaments and Menisci of the Knee Joint." J. Bone and Joint Surg., SS 111, pp. 44-66, 1941.
4. Lindahl, O. et al: The Mechanics of the Extrusion of the Knee Joint. Actn. Orthop. Scand. 38: pp. 226-234, 1967.
5. Edwards, R.G.; Lafferty, J.F.; and Lanze, K.O.: "Ligament Strain in the Human Knee Joint." J. of Basic Eng. Trans. ASME. pp. 131-136, March 1970.
6. Morrison, J.B.: The Mechanics of the Knee Joint in Relation to Normal Walking. Biomech. 3, pp. 51-61, 1970.
7. Sedlin, E.D.; and Hirsch, C.: Factors Affecting the Determination of the Physical Properties of Femoral Cortical Bone. Actn. Orthop. Scand. 37; pp. 29-48, 1966.

THE EFFECTS OF HYPOGRAVIC AND HYPODYNAMIC ENVIRONMENTS  
ON THE SKELETAL SYSTEM AND ACCELERATION TOLERANCE

L. E. Kazarian and H. E. von Gierke

Aerospace Medical Research Laboratory  
Aerospace Medical Division  
Air Force Systems Command  
Wright-Patterson Air Force Base, Ohio 45433

ABSTRACT

One of the rudimentary biomedical aspects of manned space flight, which remains to be investigated, is the long term influence of reduced gravitational forces, extended periods of physical confinement, and inactivity on man's musculoskeletal systems. Particularly, the relationship of altered bone strength to acceleration stress, such as may be encountered during space maneuvers, re-entry into the earth's gravitational environments, parachute opening shock, and ground or water landing impact.

It is common knowledge that the architecture of skeletal tissue is related to its function, of placing static and dynamic stresses on selective hard tissue components which in turn provide guidance in three dimensional space to cellular activity and direct skeletal architecture. The reduction of "normal" static and dynamic mechanical forces on the skeletal system removes or alters to an undetermined degree some of the stimuli controlling normal bone remodeling activity. The skeletal system responds to disuse (or better expressed altered use) by the dissolution of mineral and organic constituents, characterized by a decrease in bone mass while maintaining normal mineral composition. The mechanisms operative in producing these geometric and physiological alterations in calcified tissues, the control mechanisms, and time constants involved in these alterations, are not well understood. To produce a partial answer to the questions raised, adult rhesus monkeys were subjected to plaster of Paris cast immobilization for periods up to 240 days. Skeletal tissue was labelled at predetermined intervals. Following the immobilization period, these animals were exposed to longitudinal spinal impact in order to determine the threshold for mechanical damage to the vertebral column and changes in injury susceptibility as a function of immobilization time. These results seem to indicate that the observed differences in bone remodeling activity, skeletal architecture, as well as spinal impact tolerance, is described best not as an impairment of metabolic activity but rather as

a normal physiological adaptation of the skeletal system to the demands of the "new" environmental habitat. The time constant required by the system to lose over-abundant hard tissue and to stabilize in the new force environment is evident from these experiments. The implications of these animal experiments to future manned space flight and to man's acceleration tolerance is discussed.

## INTRODUCTION

Demineralization of skeletal tissue has been shown to occur in men and animals while under the influence of reduced gravitational environments and hypodynamia. The triggering mechanisms for these radiographically and biochemically observed alterations in homeostatic behavior patterns is yet uncertain. However, there exists an ever increasing amount of experimental and clinical data indicating that bone remodeling activity will vary according to the degree of mechanical forces encountered for a particular environmental habitat and that the establishment, regulation, and control systems associated with mineral metabolism are at least in part, a function of a biological organisms mechanoreceptors responding to stimuli related to the gravitational forces of the earth<sup>(1-12)</sup>.

Future manned space flights, whether they be directed to manned space stations, journeys to the lunar proving ground, or exploration of the nearby planets, will require flight crews to remain in the confined environments of space vehicles and space stations, and to be exposed to the hypodynamic environment for extended periods of time.

One of the rudimentary biomedical aspects of manned space flight, which remains to be investigated, is the influence of reduced gravitational forces, and extended periods of physical confinement and inactivity on man's skeletal system and its relationship to mechanical stress, encountered during space maneuvers, as well as the final phases of space flight such as re-entry into the earth's gravitational environment, parachute opening shock, and ground or water landing impact.



To produce a partial answer to the questions raised and their potential operational significance, osteoporotic rhesus monkeys were exposed to longitudinal spinal impact in order to determine the threshold for mechanical damage to the vertebral column, as well as to provide further insight into the time periods which constitute "skeletal adaptation" in terms of a "new" dynamic equilibria between reduced mechanical forces and the skeletal system.

## EXPERIMENTAL METHODS

### Selection of Primates

Forty-four, male, clinically screened, laboratory rhesus monkeys (*Macaca Mulatta*), ranging in weight from 13 to 15 pounds, were surveyed radiographically to demonstrate maturity by epiphyseal closure of the axial skeleton. The 22 control and 22 experimental animals were housed in an air-conditioned windowless room which was illuminated with fluorescent light. The animals were fed a standard diet of monkey chow. The control and experimental primates were placed in metabolic cages (which enabled urine and feces collection) for seven days. Baseline anteroposterior (AP) and lateral whole-body radiographs were taken of the entire skeletal system on day one of the conditioning period. The radiographic data taken during this period were used as baseline data. After seven days of conditioning, the control, as well as the experimental, monkeys were anesthetized with pentobarbital, 1 cc per 5 pounds, and again radiographed. The control animals were returned to the metabolic cages, and the animals selected for immobilization were prepared for being encased in plaster of Paris casts. Under anesthesia, the animals were wrapped in several layers of cotton gauze; the bony areas and prominences were padded with felt. Quick-setting plaster of Paris was added to construct a full-body cast (Figure 1). The experimental animals were handled (required by the arm immobilization) twice daily; food intake was weighed and recorded. Monkey chow was dropped into the food trays of the controls. Water (distilled) was made available at regular intervals 16 times daily. At two-week intervals control and experimental primates were anesthetized, removed from their restraints, weighed, radiographed, and examined for complications.

Following the prescribed immobilization period, the immobilized and control animals were anesthetized and radiographed. Both primates were similarly restrained on the impact vehicle. The vehicle was raised to the predetermined drop height, released, and allowed to free-fall and decelerate. Immediately following impact exposure, the animals were killed with an overdose of pentobarbital. The entire vertebral column was grossly dissected. Macrophotographs were taken and analyzed in detail for evidence of atrophy. Samples from specific regions of the controls were compared with corresponding regions of the immobilized bone. Radiographs taken in vivo and following necropsy were studied to compare trabecular architecture patterns.

#### Processing of Material

Bones selected for the study were dissected and stripped of all soft tissue. Sagittal and transverse plane segmental sections were prepared using a machinist's circular saw. The trabecular structure and marrow cavity were stripped of haematopoietic and fatty tissue with a high velocity stream of water. Cortical bone was defleshed by hand picking and masceration. The specimens were identified, blotted, and dried in air.

In order to determine the threshold for mechanical damage to the vertebral column, a study was initiated which established the vertebral body compression fracture levels for the normal adult rhesus monkey. The Vertical Deceleration Tower at the Aerospace Medical Research Laboratory was modified to produce the desired acceleration time-histories. The impact vehicle shown in Figure 2 was constructed of glued and doweled laminated maple wood, reinforced with steel buttress plates. The support and restraint system within the shell of the carriage vehicle, although variable, (in terms of postural orientation), remained unchanged for these experiments. Nylon-reinforced cotton restraint straps provided standardized fixation of the primate torso. Tibial flailing was minimized by snugly restraining the lower third of both limbs to the supporting seat structure. Aluminum honeycomb was used as an energy absorbing brake. This hexagonal structure possesses the unique property



Figure 1. Immobilized Monkeys



Figure 1. Immobilized Monkeys

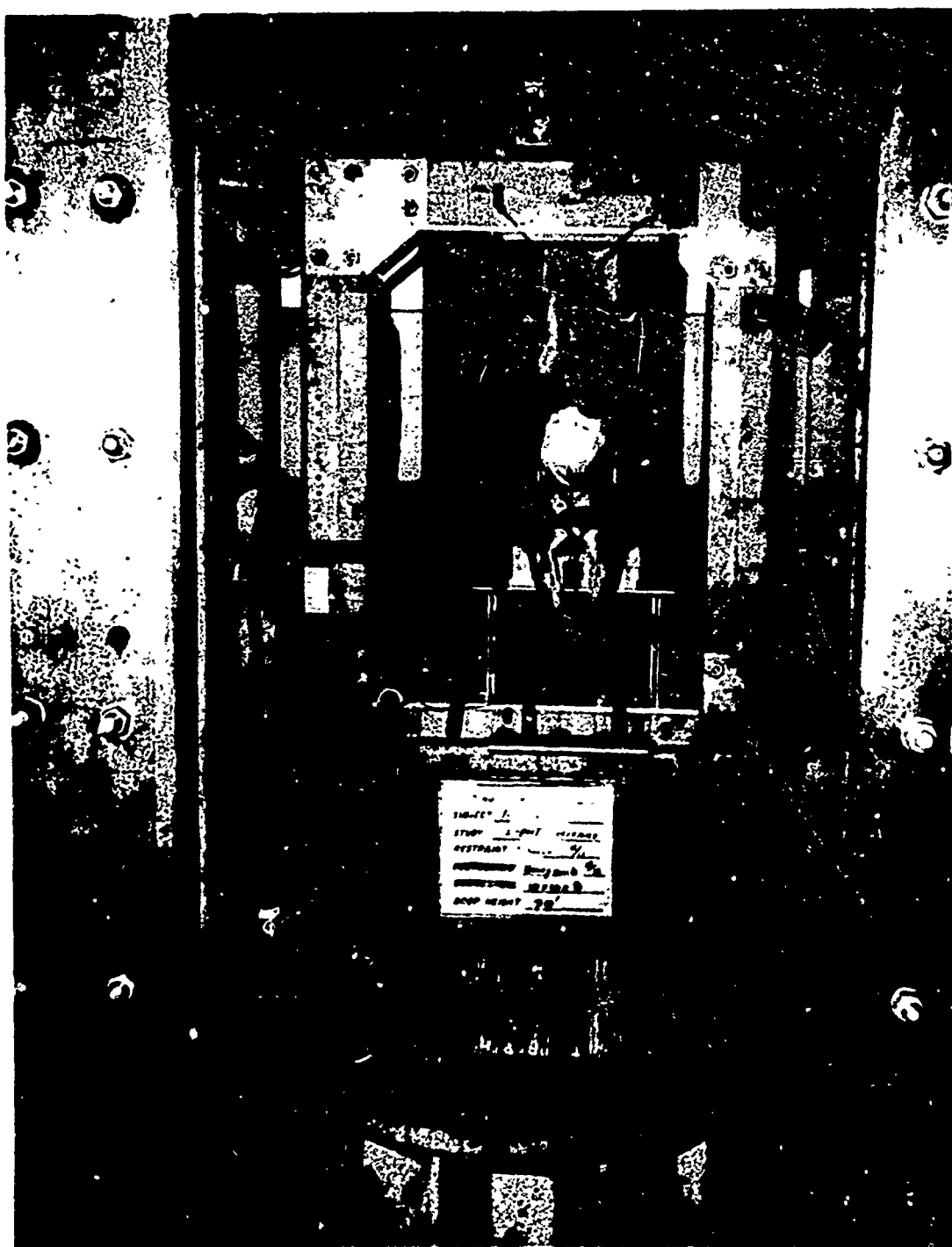


Figure 2. The Impact Vehicle with Experimental (Facing to the Front) and Control (Facing to the Rear) Animals

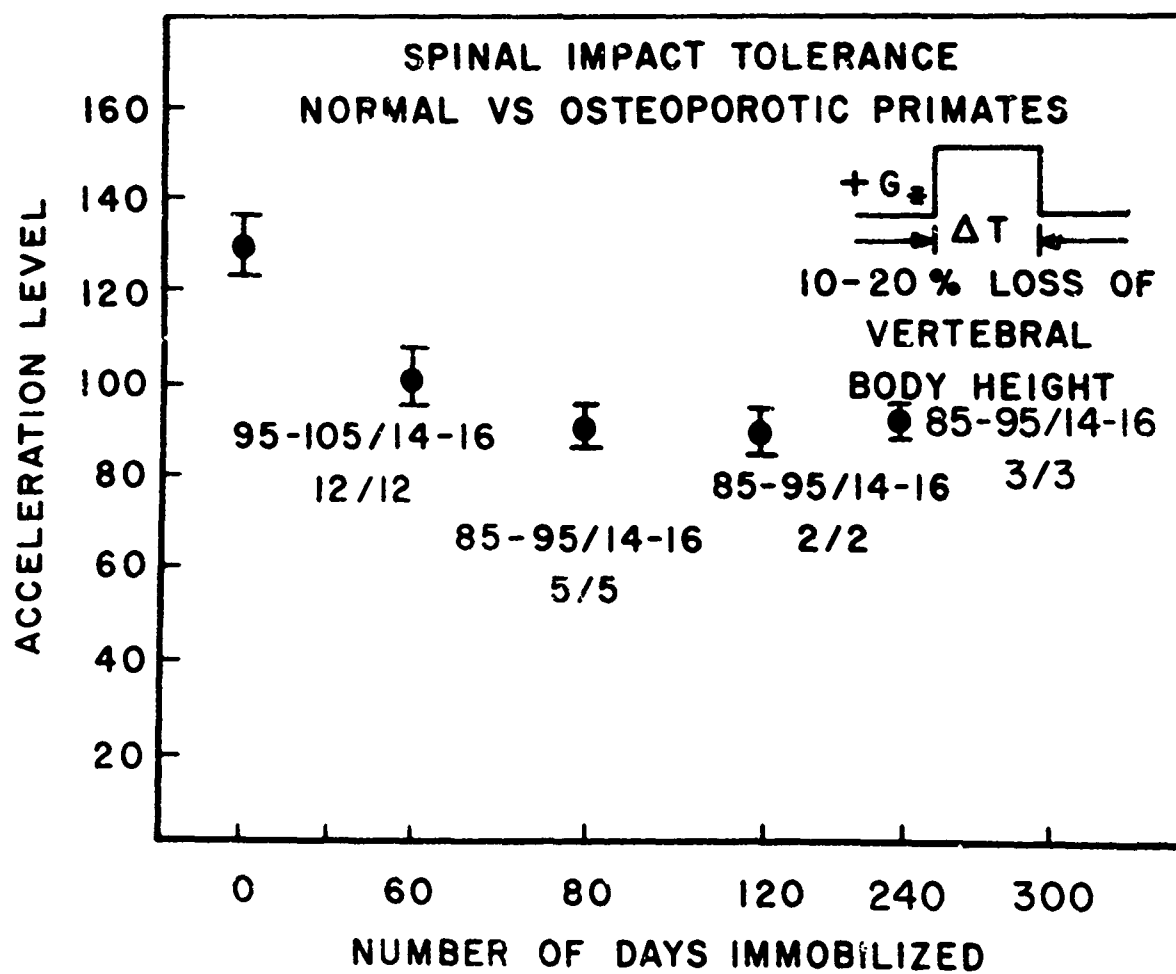


Figure 3. Spinal Impact Tolerance of the Normal and Osteoporotic Primates

of complete energy dissipation during constant load failure. Rectangular acceleration time-histories were selected because of their well-defined, practical, as well as theoretical, significance and interpretability. The magnitude and duration of the acceleration pulses were chosen so that they covered the most probable range of injury predicted from pilot experiments and presently available interspecies scaling data <sup>(13)</sup>. The acceleration pattern was controlled by:

1. Drop Height
2. Aluminum Honeycomb Engineering Specifications
3. Total Surface Contact Area of the Impact Head.

Total time duration was essentially kept constant at 14 to 16 milliseconds. The acceleration level varied from 80 to 140 G's.

The acceleration inputs were in the  $+G_z$  spinal direction. This body axis was selected because the injury mechanisms for this direction of loading are best understood and the results obtained seemed more likely to be more easily explained and incorporated into existing theoretical injury models of the vertebral column.

All primates were restrained in the impact vehicle in an upright position. The primates upper limbs were suspended in such a manner so that the weight of the arms was principally carried by the vehicle structure, thus, minimizing the total weight carried by the total spine, and minimizing anterior lip thoracic fractures of the vertebral body centrum.

### Results

Upon completion of the prescribed immobilization period, the experimental animal was anesthetized, removed from its cast, and radiographed. The control animal was also anesthetized and radiographed. Both were restrained on the impact vehicle (one facing forward, the other facing to the rear) and exposed simultaneously to longitudinal spinal impact at the preselected acceleration time history.

The criteria for injury was a uniform decrease of thoracic vertebral body centrum height. Following impact exposure geometric radiograph measurements of traumatized thoracic vertebrae indicated that, following approximately 80 days of immobilization, spinal impact tolerance is reduced approximately 25 to 30 percent as shown in Figure 3. The range of the acceleration level is indicated by the first value, i. e., for the case of 60 day immobilization, the animals were impacted at an acceleration level of 95 to 105g for a total time duration of 14 to 16 milliseconds. The total number of animals impacted was twelve and the number of animals which received 10 to 20 percent loss of vertebral height is twelve. As the number of days of immobilization increased, spinal impact tolerance decreased and began to plateau somewhere between 60 and 120 days where it essentially remained at this level for up to 240 days of immobilization and resulted in a total decrease in the relationship to normal spinal tolerance of 30 to 35 percent.

The experimental and control animals were immediately killed with an overdose of pentobarbital. A complete necropsy was performed and representative soft tissue samples of all organ systems prepared for histopathological examination. The entire vertebral column was grossly dissected as described earlier. For the immobilized animals, necropsy showed that the mechanism of energy dissipation within the vertebral bodies was to drive the viscous haematopoietic tissue out of the numerous paravertebral sinuses and beneath the surrounding ligamentous structures. The normal animals also showed a similar energy dissipation mechanism, however, less of the haematopoietic was qualitatively observed surrounding the vertebral column.

The entire axial skeleton was removed, grossly examined, defleshed, and macroscopically examined.

Macrographs were taken and analyzed in detail for evidence of hard tissue atrophy. Samples from specific regions of the controls were compared with corresponding regions of the immobilized bone. Serial radiographs taken in vivo, following necropsy and of dry specimens, were studied to compare trabecular architecture and cortical thickness.



Radiographically, following approximately 60 days of immobilization, there is seen coarsening of the trabecular pattern at the distal and proximal ends of the long bones along with thinning of the cancellous bone within the vertebral body. Following approximately eight weeks of immobilization, macerated sagittal sections of vertebral bone compared to normal vertebral bone showed diminution in size and number of trabeculae, accompanied by a decrease in plate size, orientation, and porosity as well as reorientation of the trajectorial lines in cancellous bone. Macerated, vertebral cortical bone showed marked dilatation of bone marrow sinusoids and intraosseous channels (Figures 4 and 5). No gross disturbances were detected in the anatomic outline of the bones of interest. Sixty percent of the sagittal sections showed distinct paucity of spongiosa in the bony terminal end-plates.

Macroscopically, the most striking feature of macerated bone section is the quantitative and qualitative decrease of cancellous bone. The spongiosa of the osteoporotic vertebrae consists of a much more open network of delicate trabeculae. There is considerable atrophy of interconnecting trabeculae and a reduction or disappearance of bony plates (Figures 6 and 7).

The lamina terminalis, normally a well-defined redundant structure, is enforced by a compact layer of calcified material adjacent to the cartilaginous end-plate. The geometry of this structure is related to the function and metabolic state of the annulus fibrosus and nucleus pulposus. Following prolonged immobilization, these vertical trabeculae members enclosed within this structure are coarser, the marrow space larger and trabeculae more irregular.

One distinct type of structural bony failure was shown to be intervertebral disk prolapse (confirmed during necropsy examination) through the adjacent cartilaginous end-plate invoking the cancellous bone of the vertebral body centrum, followed by uniform crushing of the vertebral body centrum as shown in Figure 8 and reported earlier. Central cartilaginous end-plate tearing was not found during the necropsy of the control group.

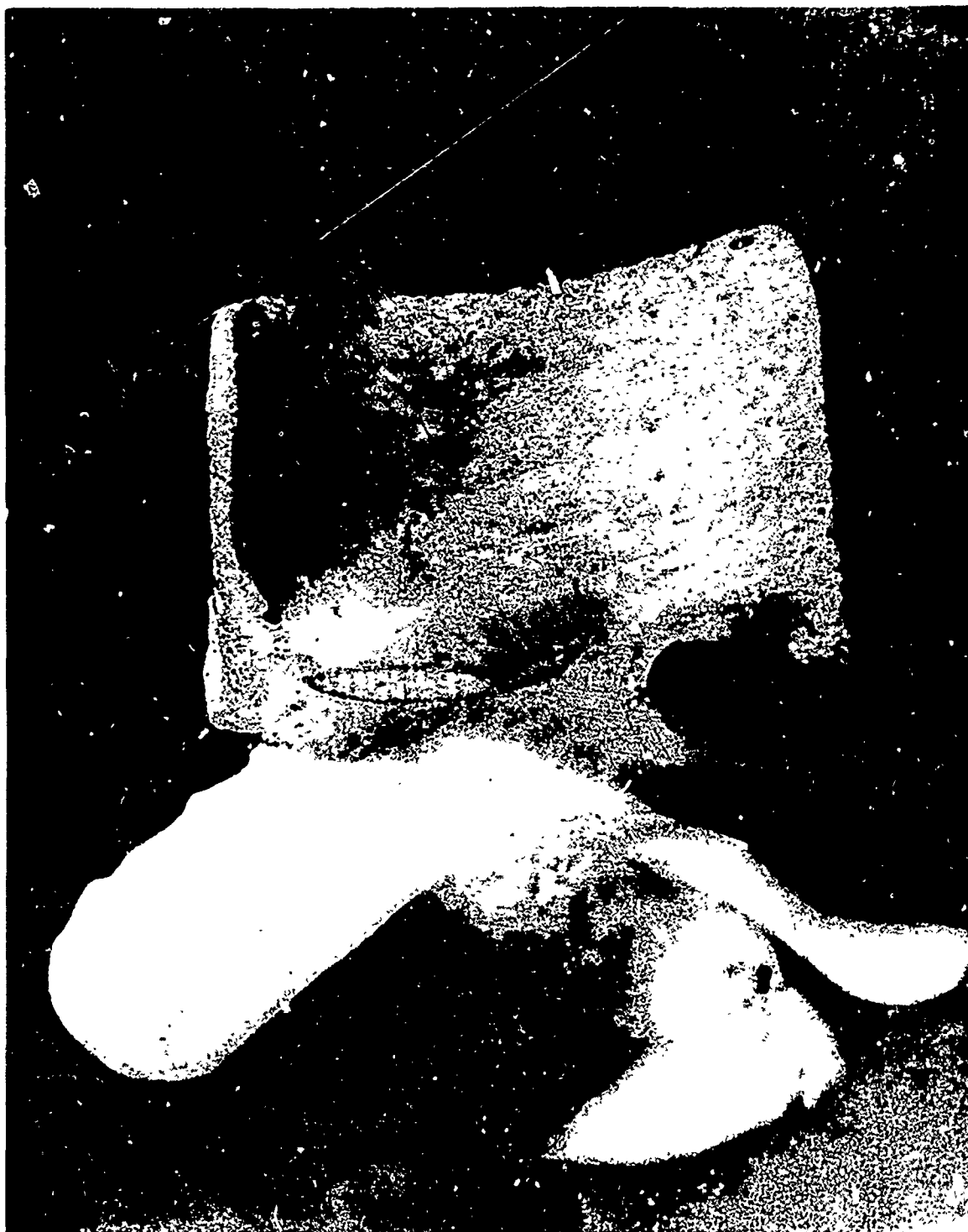


Figure 4. Normal Lumbar-Vertebra (Cortical Bone)



Figure 5. Osteoporotic Lumbar-Vertebra (Cortical Bone)

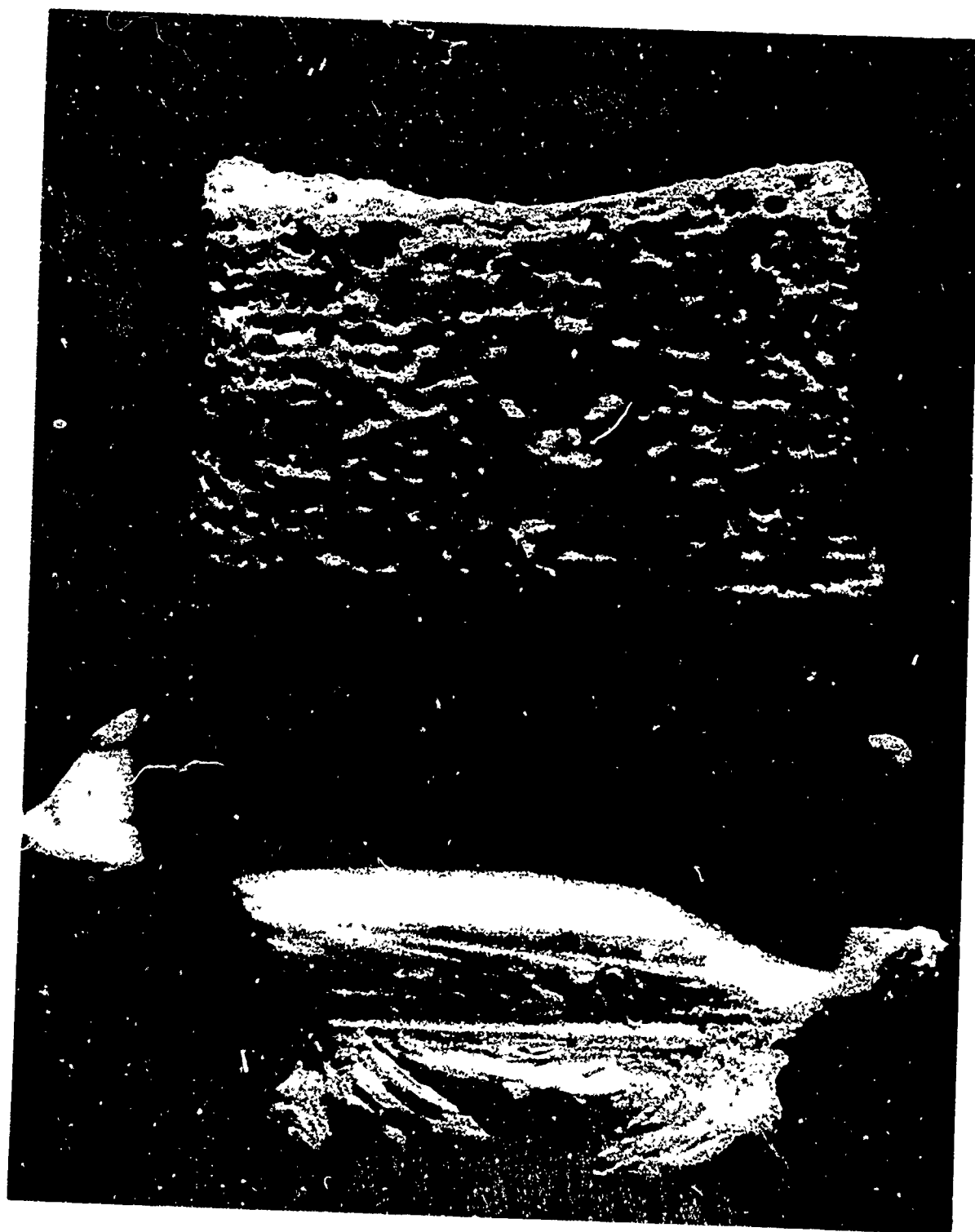


Figure 6. Normal Cancellous Bone (60 Days)

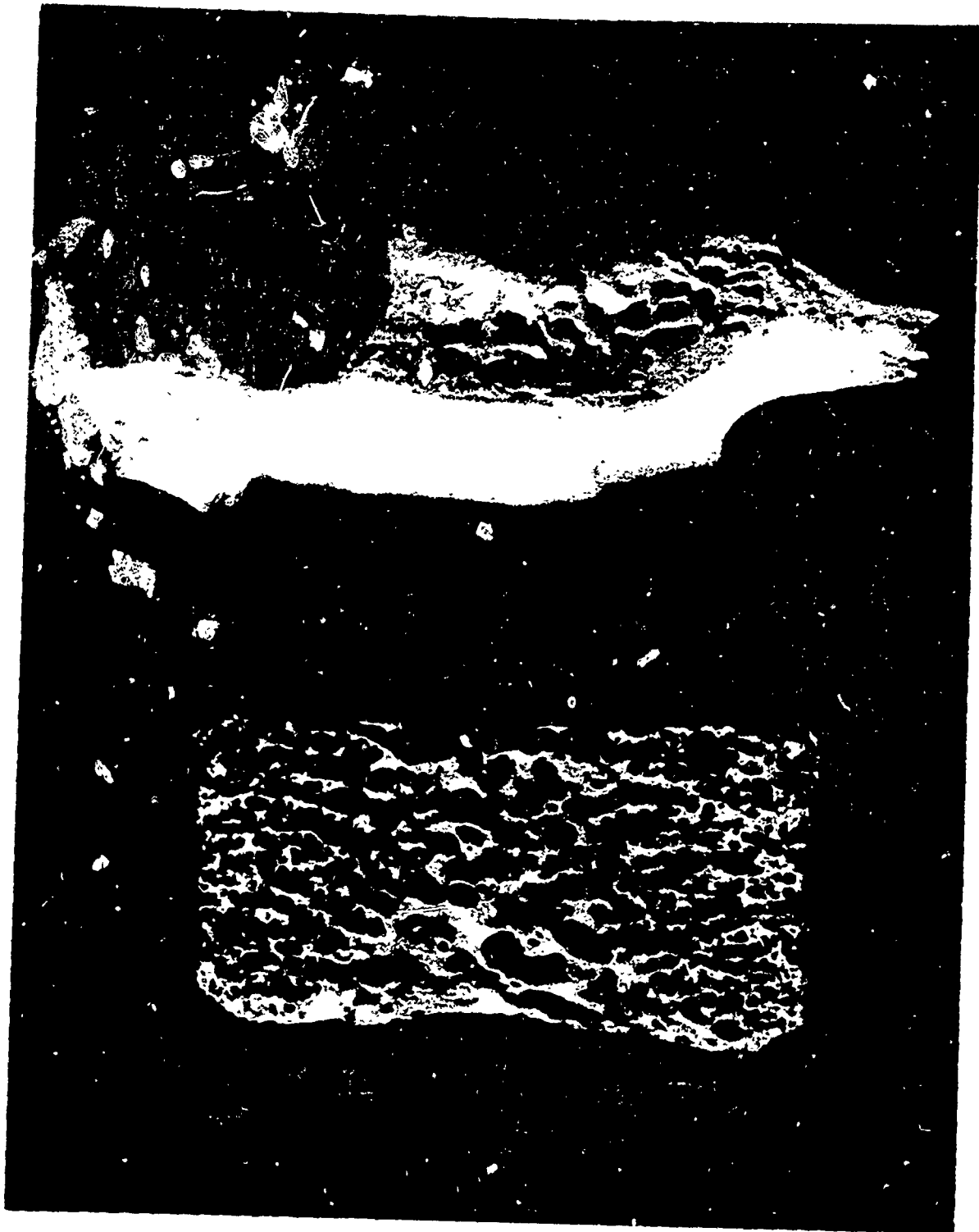


Figure 7. Osteoporotic Cancellous Bone (60 Days)



Figure 8. Disk Prolapse Following Impact

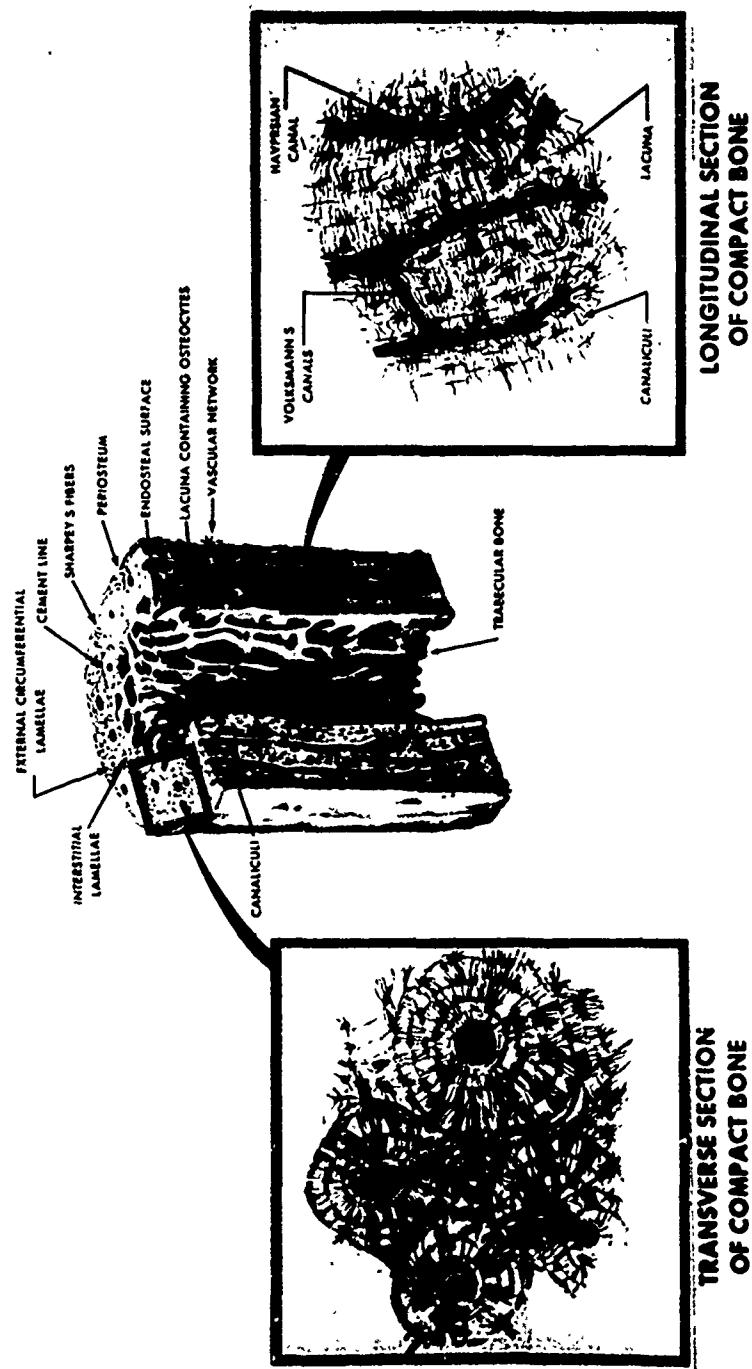


Figure 9. The Surfaces of Bone

## Discussion of Results

The influence of mechanical stress on the skeletal system has been well recognized. As early as Galileo, who derived mathematical relations between fracture resistance and bone geometry, investigators have studied the problem of the load carrying capacity of structural elements in the living system and the mathematical analysis of internal forces and deformations induced by applied loads.

The role of mechanical stress in forecasting bony architecture through influence on the cellular level has been a subject of long debate. The trajectorial theory of bone structure, as developed by von Meyer<sup>(14)</sup>, Bardeleben<sup>(15)</sup>, Roux<sup>(16)</sup>, and Wolff<sup>(17)</sup>, postulated that trabeculae were modeled along paths of compressive or tensile force. Wolff's classical statement was that, "Every change in the form and function of bones, or of their function alone, is followed by certain definite changes in their internal architecture and equally definite secondary alteration in their external configuration, in accordance with mathematical laws."

Koch<sup>(18)</sup>, in his paper, "Laws of Bone Architecture," concluded that cancellous and compact bone are so composed as to produce maximum strength with a minimum of material, and that in form and structure, bones are designed to resist compressive loads.

These concepts have been challenged by numerous investigators on the basis of such arguments that these analyses were based on two-dimensional stress analysis techniques for static conditions, assuming bone to be a homogenous material. However, two factors concerning the architecture of bone cannot be disputed: (1) that the structure of bones is related to the mechanical stress they are subjected to, and (2) there exists a relationship between bone architecture, the physical dynamics of remodeling, and between the geometry and cellular dynamics<sup>(19)</sup>.

When bone is subjected to normal, increased or decreased external forces, whether they be muscle pull, accelerations, or vibrations, its dynamic response characteristics depends not only on the magnitude of the external force and the



inherent strength of the bone, but also the manner in which the forces are applied externally and superimposed internally. The particular combination of forces, along with their rate and direction of application, will cause the bone to deform elastically (deformation without permanent set upon release of the stress), plastically (deformation in the inelastic or plastic range without fracture), or fracture.

Any variations in the magnitude, direction, as well as the rate of application of mechanical stress, will probably result in an alteration of the cellular dynamics of hard tissue, in terms of apposition, resorption (responsible for radiographic differences in bone volume), augmentation, and diminution (responsible for radiographic density changes) of both the mineral constituents and organic protein matrix.

Bone is a highly dynamic organ, anisotropic in organization, construction, and development; each elemental unit of this composite material is made by the deposition of successive layers of highly oriented collagen fibers which are subsequently mineralized. The normal mineralization process of bone requires two sets of factors:

1. an organic protein calcifiable matrix
2. concentration of calcium and phosphate ions in the extracellular fluid

and consists of two processes:

1. the formation of an organic protein matrix (principally protein, collagen, and mucopolysaccharides)
2. the deposition in this matrix of bone material is a complex microcrystalline compound of calcium and phosphate (hydroxyapatite), with a small amount of calcium carbonate.

The organization of the collagen fiber matrix and of the hydroxyapatite crystals is such that these two materials and probably a crystal "binder" all with different elastic moduli and strength, combine to form an optimal composite structure which accounts for the physical and mechanical properties of bone (20).

Bone has been shown to be one of the most plastic organs in the body, able to adapt its architecture, its microscopic composition to chemical and mechanical stress, having a large metabolic turnover of mineral and organic materials and ceaseless chemical and physiological activity throughout life. As it takes part in unnumbered metabolic processes, its high remodeling rate reflects architectural changes, as well as reconstructive adaptations to abnormal functions to a degree surpassed by no other system in the body. The control mechanisms by which these processes are triggered is yet uncertain. It might achieve a state of cyclic relaxation oscillation; it might continually change its behavior or it might have a feedback system whereby deviations lead to a new dynamic equilibrium. Following the cessation of longitudinal growth, and throughout life, the cancellous and cortical bone of the skeletal system is replaced by the progressive resorption and formation of the organic protein matrix and inorganic bone salt at a characteristic rate with a characteristic variation which is a function of an undetermined number of physiological and ecological variables, which are in balance. Any changes in the net balance between the formation and resorption of bone play a critical role in such different phenomena as nucleation and crystal growth, chemistry of calcification, ion transfer between blood and bone, and absolute skeletal volume, and are probably a prerequisite to pathologic conditions.

The cells responsible for the specialization of hard tissue are the osteoblast, found in areas of active bone formation; the osteoclast, found in areas of bone resorption; and osteocyte, found in mature bone responsible for maintenance of normal blood-bone exchange. The precursors of these cells, characteristic of bone, are of mesenchymal origin and are acutely inter-related. During growth, mesenchymal cells frequently transform from one type of bone cell to another, yet are able to return the potencies common to the osteoclast and osteoblast. Little information is available concerning the feedback control systems responsible for the stimulation of the resting mesenchymal cell to activity, which results in the production of specialized cells; the osteoblasts and osteoclasts.

However, what is known is that the net balance between bone formation and bone resorption for a particular time period determines the bone remodeling rate, the architecture, as well as the mass of the skeletal system. The strength of hard tissue is dependent on the quantity of hard tissue per unit volume, the direction of loading, and the geometric configuration of the bone. If net bone resorption is greater than bone formation, a bony porosity develops, the physical and mechanical properties of bone decrease, and the structure becomes susceptible to deformation and fracture during normal weight bearing. If net bone formation is greater than bone resorption, osteosclerosis develops. (For instance, as observed in the changes of vertebral body structure in scoliosis.)

It is a common knowledge that the structure of bone mineral is intimately related to its metabolic activity and that the reduction of normal mechanical forces on the skeletal system removes some of the stimuli for normal bone remodeling activity. The skeletal system responds to disuse or immobilization by the dissolution and removal of organic matrix and inorganic material, characterized by a qualitative and quantitative decrease in bone mass yet with normal mineral composition [Geiser and Trueta <sup>(22)</sup>].

The etiology, clinical, and pathological features of disuse atrophy are by no means uniform, however, its manifestations are quite unvarying. These consist of a diminution in the size and number of trabeculae, accompanied by a decrease in plate size, orientation, and porosity. The thin bony plates of cancellous bone becomes progressively more fenestrated; are reduced to slender rods to be followed by the selective resorption of redundant transverse trabecular structures and the accentuation of primary trabecular trajectories. As the highly active cancellous bone is resorbed, the burden of calcium homeostasis is systematically transferred to the endosteal surface of the skeletal system. Cortical bone is gradually cancellized, accompanied by the marked dilatation of bone marrow sinusoids and intraosseous channels.

In normal bones, osteons have been shown to develop first at the points of muscle attachment [Johnson <sup>(21)</sup>]. Excessive muscle activity has been shown

to accelerate the rate of osteonization. When bone is subject to mechanical stress with no muscular activity (as in the case of poliomyelitis), it is usually devoid of osteons, suggesting the osteonal architecture is not determined by genetics, but by the dynamic mechanical force imposed on bone by muscle pull. In disuse atrophy, the number of osteons in cortical bone decreases and the bone becomes a poorly differentiated structure.

In this study, the increased mineral metabolism and the loss of skeletal volume, along with the observed differences in skeletal architecture, seem to be due to a net loss of the over-abundant hard tissue and specialization or adaptation of the skeletal system to the demands of the "new" particular environmental habitat. However, this is not meant to imply that physiological disturbances and complications will not result from disuse of the biological system. On the contrary, the maintenance of "normal" homeostatic mechanisms of the body are effected by the interaction of numerous physiological systems. For instance, bedrest is an often prescribed non-specific therapy about which very little clinical information is known. Prolonged bedrest has been shown to result in a progressive loss of mineral secondary to bone resorption, increased urinary calcium concentration, and increased susceptibility to renal stone formation. Any alterations in the external environment or physical activity of an organism which produces biochemical or physiological stress, changes in temperature, electrolyte composition, hormone activity, electrical potentials, and Ph, will be counteracted by an unknown number of physiological feedback mechanisms within the organism in an attempt to reestablish the dynamic cellular equilibrium. This adaptative process involves quantitative changes in the control system, yet to be adequately described. It is speculated two types of adaptive changes may occur. One may be an extension of a zone of bone remodeling activity to another level (structural, physiological specialization). The second type results in an altered capacity to maintain an altered bone remodeling rate (general metabolic adaptation). Both types of changes extend the homeostatic mechanisms which eventually shift with time. As the limits of adaptation gradually become

narrower and impose severe limitations on the regulatory and control mechanisms, the end result may very be disturbed relationships in normal cellular dynamics and the possible factors in bone diseases. One other important factor which should be considered in skeletal cytodynamics is the chemical exchange of bone mineral. All bones are richly vascular, and permit the continuous exchange and flow of ions to and from the surfaces of the various holes in bone, namely the osteocyte lacunae, haversian canals, medullary spaces, canaliculae, primary longitudinal canals and volksmans canals (Figure 9).

Throughout life, there exists a continual transport process of ions from the various surfaces of bone which play an important role in the regulation and control of mineral levels in the circulating fluids. Without blood-bone exchange, it can be assumed that the circulation, diffusion impedance, and the exchange of ions within the skeletal system would become restricted; skeletal mineralization would take place, and eventually the skeletal system may become metabolically inert.

Since the skeletal system is "normally" an optimal architectural structure in terms of weight bearing, it would follow that the chemical pathways must parallel and remodel accordingly. The active homeostatic mechanisms in both circulating fluid and hard tissue must work continuously to maintain "normal" levels of circulating chemicals. If a particular mechanical environment constitutes a stressor and results in a prolonged physiological disturbance, the skeletal structure will equilibrate to the new chemical, as well as the functional environment; the end result will be a change of the mechanical and physical properties of the skeletal structure.

#### SUMMARY

The purpose of this study was to determine the effects of disuse atrophy of bone on spinal impact tolerance for the rhesus monkey. This study clearly demonstrates that disuse and inactivity has profound structural and functional effects on the weight bearing spine, in terms of decreased spinal impact tolerance.

The presently used biodynamic injury criteria for impact is based on laboratory experiments and field data, with adult human and animal subjects whose skeletal systems are assumed to be normal and healthy. Disuse atrophy decreases the overall mechanical strength of the skeletal system to such a degree that injury levels for acceleration exposure are significantly altered, for the immobilized rhesus monkey. There are indications that a similar analogy may hold true for man in space for extended periods of time. If this is true, new acceleration stress indices predictive of physiological conditions for the astronaut may become necessary. A considerably more detailed effort is required in order to thoroughly evaluate the consequences of the data reported in this study. Extreme caution must also be exercised to extrapolate quantitatively the time factors studied in this experimental series on the Macaca Mulatta to the human case. Bone remodeling dynamics among primates is probably similar, however, remodeling rates and their magnitude must be compared with reservation.

## BIBLIOGRAPHY

1. Freeman, L. W.: The metabolism of calcium in patients with spinal cord injuries. *Ann. Surg.* 129:177, 1949.
2. Leadbetter, W. F. and Engster, H. C. : The problem of renal lithiasis in convalescent patients. *J. Urol.* 53:269, 1945.
3. Whedon, G. D.: Calcium loss in paralytic poliomyelitis and its quantitative relationship to the development of demonstrable osteoporosis. *J. Clin. Invest.* 31:672, 1952.
4. Lutwak, L., et al: Mineral electrolyte and nitrogen balance studies of the Gemini 7 fourteen day orbital space flight. *Journal of Clinical Endocrinology and Metabolism.* Vol. 29, No. 9, Sept 1969.
5. Abramson, A. S.: Bone disturbances in injuries to the spinal cord and cauda equina (paraplegia); their prevention by ambulation. *J. Bone Joint Surg.* 30A:982, 1948.
6. Brady, L. and Wilson, W. J.: Major urological surgery on poliomyelitis patients confined to respirators; discussion on etiology, prophylaxis against and treatment of calculi in recumbent patients. *J. Urol.* 60:381, 1948.
7. Joelson, J. J.: Urinary calculi in recumbent patients. *JAMA.* 129:157, 1945.
8. Whedon, G. D. and Shorr, E.: Metabolic studies in paralytic acute anterior poliomyelitis. II. Alterations in calcium and phosphorus metabolism. *J. Clin. Invest.* 36:966, 1957.
9. Yegorov, B. B.: Physiological reactions to a possible means of protection against prolonged weightlessness. Third International Symposium on Basic Environmental Problems of Man in Space, Geneva, 19-22 November 1968.
10. McCally, M. and Lawton, R. W.: The pathophysiology of disuse and the problem of prolonged weightlessness. Aerospace Medical Research Laboratory, United States Air Force, AMRL-TDR-63-3, June 1963.
11. Kazarian, L. E. and von Gierke, H. E.: Bone loss as a result of immobilization and chelation. *Clinical Orthopaedics and Related Research*, 65, 1969.

12. Bykov, G. P. and Smirmov, V. P.: Morphological changes in bone and muscle tissue during hypokinesia. *Kosmicheskaya Biologiya i Meditsina*, Vol. 4, No. 2, March-April 1970.
13. Kazarian, L. E., Hahn, J. W. and von Gierke, H. E.: Biomechanics of the vertebral column and internal organ response to seated spinal impact in the rhesus monkey (*macaca mulatta*). *Aerospace Medical Research Laboratory TR-70-85*, 1970.
14. von Meyer, H.: Die Architectur der Spongiosa Reichert und Dubois-Reymonds. *Archiv. S.* 615, 1867.
15. Bardeleben: Beiträge zur Anatomie der Wirbelsaule, Jena, 1874.
16. Roux, W.: Beiträge zur Morphologie der Functionellen Anpassung 2. Über die Selbstregulation der Morphologischen Länge der Skelettmuskeln. 8 Jena: Gustav Fischer 1883 from Jena *Z. Med. Naturk.*, N. F. 16, S. 70, 1882/83.
17. Wolff, J.: Über die Bedeutung der Architectur der Spongiosen Substanz, *Zentralbi. für die med Wissensch.* 54:849-851. 1870.
18. Koch, J. C.: The laws of bone architecture, *Amer. J. Anat.* 21:177-298, 1917.
19. Frost, H. M.: The laws of bone structure. C. C. Thomas, Springfield, Illinois, 1964.
20. Currey, J. D.: Three analogies to explain the mechanical properties of bone. *Biochel.* 2, 1, 1964.
21. Johnson, L.: Armed Forces Institute of Pathology, Washington, D. C., Personal Communication, 1968.
22. Geiser, M. and Trueta, J.: Muscle action, bone rarefaction and bone formation. *J. Bone Joint Surgery.* 40B, 282-311, 1958.



TESTING DYNAMIC MATERIAL PROPERTIES OF BRAIN ARTERIES<sup>\*</sup>

(A Preliminary Report)

C.H. Daly, J.D. Chalupnik and J.D. Danberg

Department of Mechanical Engineering  
University of Washington  
Seattle, Washington

ABSTRACT

Freshly excised arterics of the brain obtained from human autopsy have been tested under dynamic loading conditions for the purpose of determining a suitable dynamic constitutive relation for the material. The results of these tests are to be used in the construction of improved mathematical and physical biodynamic models of the head for use in the Head Injury Program.

Sections of arteries to be tested were marked for length before being excised from the brain. They were then mounted in the testing machine (a modified Instron machine fitted with an electromechanical shaker to provide high rate dynamic loading), where they were stretched to in vivo length and pressurized to physiological pressure with Ringer solution maintained at 37°C. In the tests reported here, the dynamic loading was sinusoidally applied tension of constant displacement amplitude equivalent to about 7 1/2% engineering strain. Frequency of excitation was varied from .01 to 100 Hz. All tests were performed within 4 hours of autopsy. Preliminary results show that the arteries display a nonlinear elastic behavior with no frequency dependent viscoelastic effects over the range of frequencies tested or under static loading.

In addition, ramp function displacement tests (constant strain rate) were performed over a range of .01 to 50 sec<sup>-1</sup> and the results were substantially the same as those given above.

---

\* This work is sponsored by NIH as part of its Head Injury Program (Contract No. NIH-69-2232).

## INTRODUCTION

The National Institutes of Health have instituted a "Head Injury Program" that is aimed at constructing a dynamically equivalent model of the human head. The purpose of this program is to provide a model on which tests can be performed to study the effect of head impact without recourse to animal testing.

In order to construct a dynamically equivalent model, it is necessary first to determine the dynamic material properties of the constituent tissues of the head. The research reported here is part of this effort. It is aimed at determining the dynamic material properties of blood vessels in the brain.

Experience gained from examination of head injuries indicates that damage to the vasculature of the brain is one of the leading sequelae of head trauma. In addition, the vasculature of the brain comprises the major connective tissue component in the brain. For this reason, it is possible that the vessels make a significant contribution to the overall dynamic behavior of the brain, for example, in response to head impact.

## TEST PROGRAM

A test program was initiated to determine the dynamic properties of brain vasculature under conditions representative of those encountered during head impact. In order to collect data that would be comparable to previous results on other blood vessels, it was decided to test the vessel under sinusoidally applied loads. The frequencies over which the material was to be tested were to be varied over a wide range. Low frequency would be on the order of .01 Hz and the high frequency would be as high as was considered practical--this turned out to be 100 Hz.

A ramp test was also proposed in order to more realistically simulate the loading applied to the vessels during impact. The use of a ramp test reduces the difficulty in performing viscoelastic analysis of the test material. Ramp velocities as high as 50 cm/sec are practical and these will lead to strain rates in the test arteries on the order of  $50 \text{ sec}^{-1}$ , depending on the length of the specimen.

## TEST METHODS

### Specimen Preparation and Handling

All specimens to date have been obtained from fresh autopsy human brain tissue. Vessel specimens are selected to be free from obvious pathology and are in the form of cylindrical segments approximately one cm. in length and free from side branches. The great variability in the pattern of the brain vasculature from individual to individual makes it impossible to test precisely the same specimen segments from each brain but it is usually possible to obtain a representative sample covering a range of vessel sizes.

The length of each specimen is measured in situ before it is excised. The specimens are stored in lactated Ringer's solution at 4°C until they are tested (usually within 4 hours of autopsy).

A small segment of each specimen is fixed in formalin and histological sections are prepared. An estimate of the cross-sectional area of the vessel is made from the slide. It is appreciated that this method is subject to error on the order of 15% but it is the only practical method for these very small specimens.

#### Loading Mechanism

Tests are performed over a range of speeds from static loading through high speed dynamic loading on the same testing machine. In order to accomplish this with the required precision, a special testing machine was assembled. The principal components of this testing machine comprise a table top Instron testing machine, and a Ling 50 lb. electromechanical exciter (shaker pot). A schematic diagram of the testing apparatus is shown in Fig. 1.

The shaker pot is mounted to the traveling head of the testing machine in an inverted orientation. A load cell is mounted on the base of the testing machine directly under the armature of the shaker pot. Specimen holding fixtures are mounted on the load cell and on the armature of the shaker pot. The specimen holding fixtures are aligned in the horizontal plane (co-axial along a vertical line). Vertical motion is accomplished either by moving the testing machine cross head for static loading or by moving the armature of the shaker pot for dynamic loading. Also, cross head motion is used to accommodate specimens of different length. (The amplifier that drives the shaker pot is DC coupled and, in consequence, it is possible to apply static loads with the shaker pot, although this is not done in practice.)

This combination of electromechanical and mechanical loading provides sensitive control of the load applied to the specimen over a wide range of frequencies, or velocities. With this apparatus it is possible to test vessels from static loading to a frequency in excess of 100 Hz. The upper frequency limitation is imposed by the frequency response of the load cell, which is discussed in a later section.

Maximum strains permissible under these test conditions are limited by the motion of the moving specimen holder. This is limited by the armature travel of the shaker pot in sinusoidal and ramp testing. In the case of the sinusoidal tests, the armature travel is given as  $\pm 1$  cm. max. up to 45 Hz. reducing to  $\pm 0.2$  cm. max. at 100 Hz. The sinusoidal tests are run one at a time with the operator setting the amplitude manually; therefore, no electrical pre-emphasis is used for these tests.

The shaker pot armature is not capable of precisely following an electrical ramp input, because of mechanical resonances in the range of frequencies at which the tests are performed; consequently, a feedback and pre-emphasis network is inserted between the electrical ramp generator and the driver amplifier.

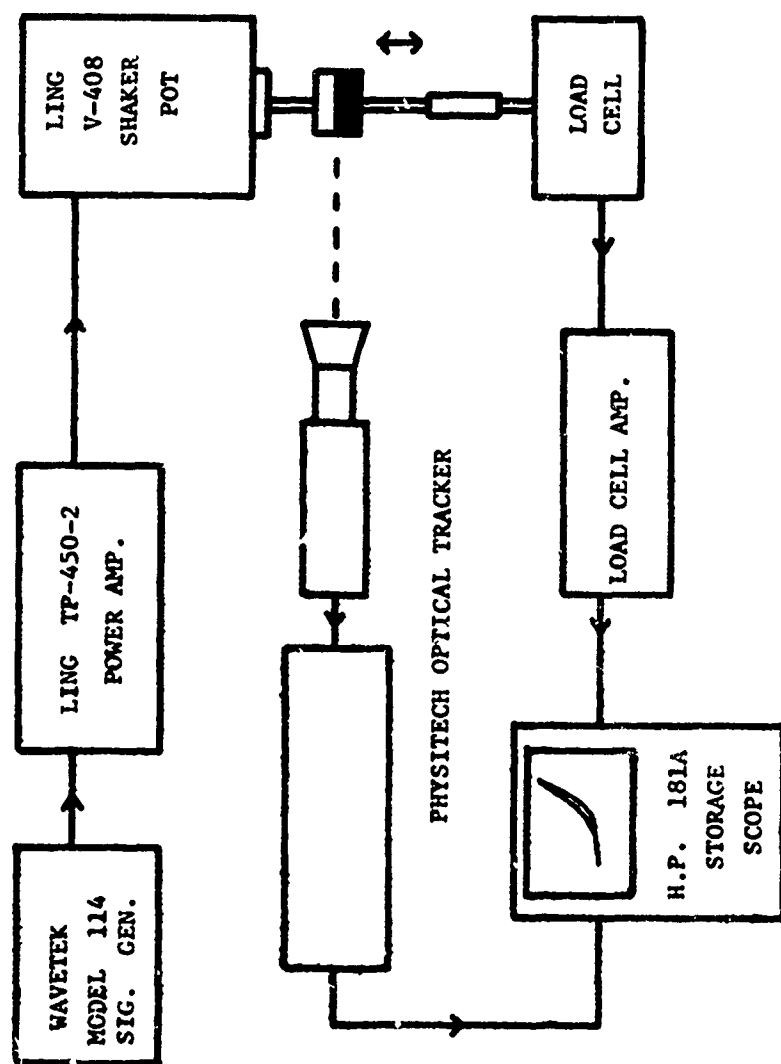


FIG. 1. TEST SETUP FOR SINE-WAVE TESTING

In this system, the displacement signal obtained from the optical tracking unit used for strain determination is compared with the ramp function voltage and an error voltage generated which is fed to the power amplifier through the pre-emphasis network which compensates for the armature dynamics. A circuit diagram of this network is shown in Fig. 2 and representative displacement vs. time oscillograph traces for the armature are given in Fig. 3. The maximum amplitude of the ramp input is essentially 1 cm., unidirectional. However, this is limited to 1.5-2 mm. in actual tests to avoid breaking the specimen. Maximum velocity used in these tests is approximately 50 cm/sec, which corresponds to a strain rate of approximately  $50 \text{ sec}^{-1}$ , depending on the length of the specimen.

#### Load Measurement

The loads encountered in testing these small biological tissue specimens are quite low, on the order of 100 grams. This dictates the use of a highly sensitive loading device. At the same time, the specimens under test are relatively short and the strain is determined from the differential motion of the two specimen holders; thus, it is mandatory that the load cell compliance be held to an absolute minimum. In addition, the resonant frequency of the load cell must be sufficiently above the highest tested frequency to prevent appreciable phase shift in the load signal (compared to the strain signal) over the frequency range under investigation. These latter two conditions are normally incompatible with the first.

In order to solve these problems, a special purpose load cell was designed and constructed. The sensing element is a cantilever beam designed to optimize sensitivity while maintaining a high fundamental frequency and high stiffness. The beam was designed to have a fundamental frequency of 1000 Hz in air, exclusive of fixtures attached to the end of the beam. The maximum deflection at the end under the rated load of 2000 grams was designed to be less than .025 mm. Strain gages (Micro-Measurements type EA-06-062 AQ-350-W) were located in the root area in a four leg temperature compensating bridge configuration.

In order to obtain the desired sensitivity from this load cell, it was necessary to use a high gain low noise pre-amplifier. Dr. Lee Huntsman and Mr. Gary Nichols of the University of Washington Bioengineering Center have developed a suitable amplifier using Fairchild integrated circuit operational amplifiers. Utilizing this design and a low pass filter circuit, it was possible to reduce the equivalent noise level to less than 1 gm. referred to the load input.

The load cell operates submerged in Ringer's solution at  $37^{\circ}\text{C}$ ; therefore, great care was taken to waterproof the strain gages.

#### Strain Determination

It is not practical to measure strain directly by conventional means, because of the small size of the specimen and the low loads obtained. Conventional strain measuring devices are not sufficiently compliant and,

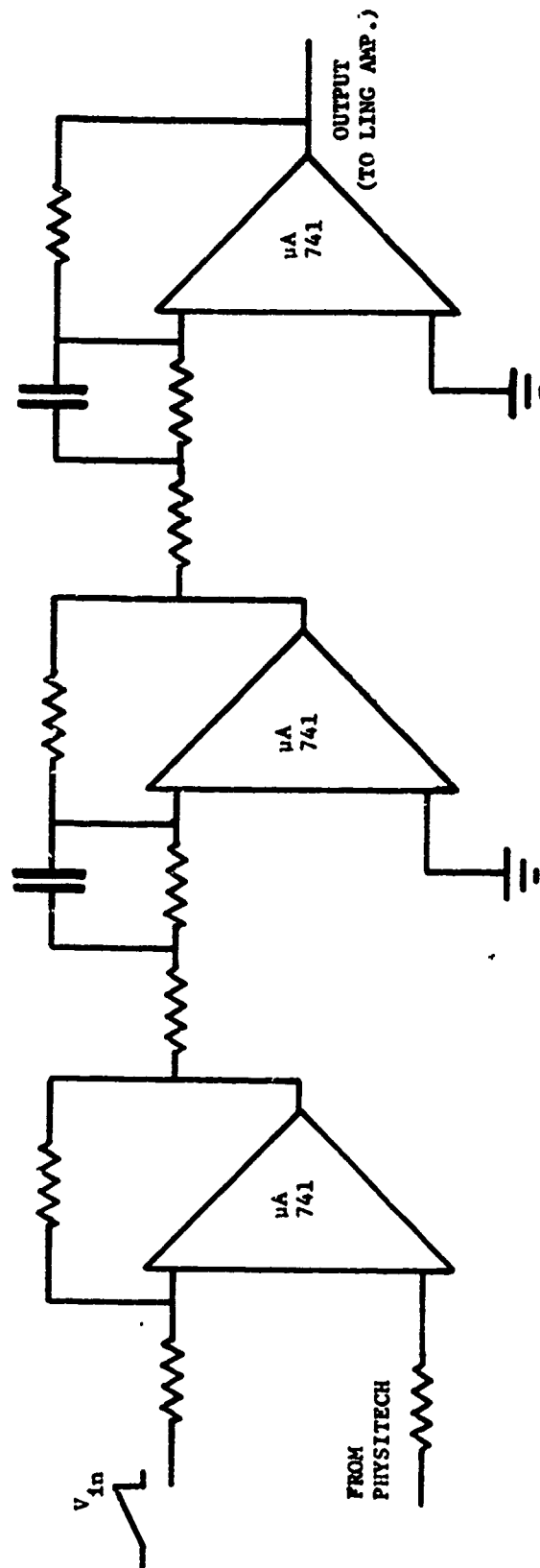
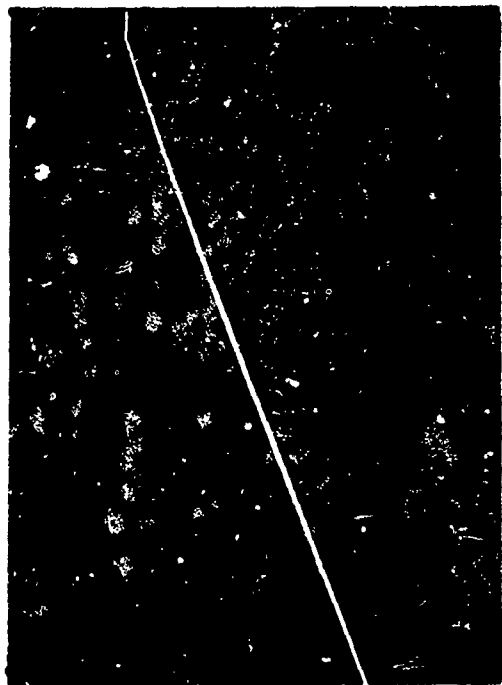
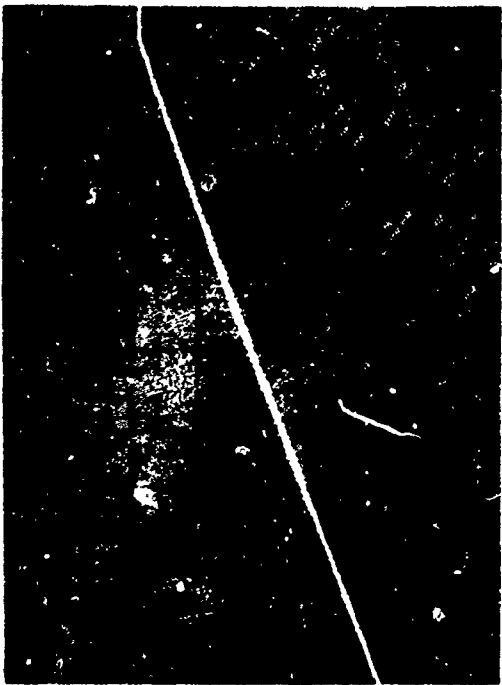


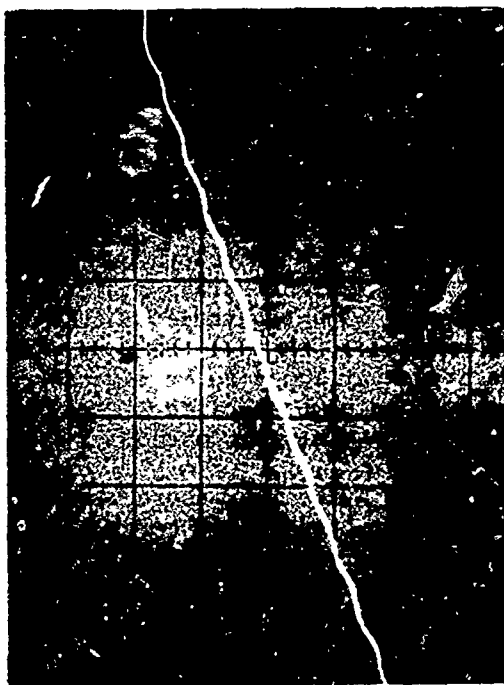
FIG. 2. RAMP FUNCTION TEST FEEDBACK AND COMPENSATION CIRCUIT



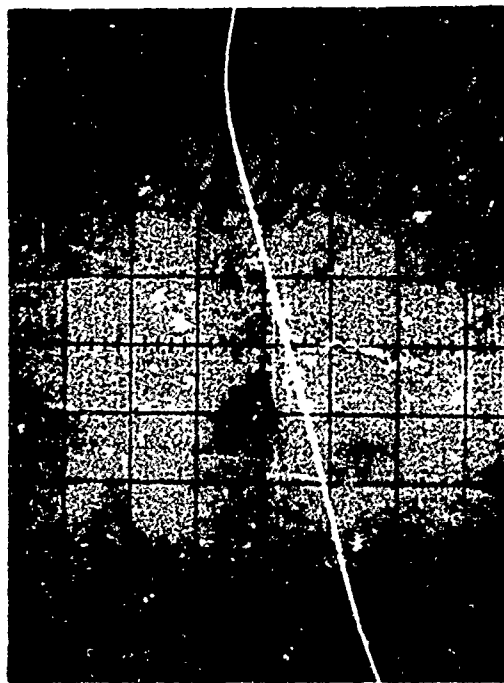
X-AXIS: 1 SEC./DIV.



X-AXIS: 0.1 SEC./DIV.



X-AXIS: 0.01 SEC./DIV.



X-AXIS: 0.001 SEC./DIV.

Y-AXIS: 0.5 MM./DIV. IN ALL CASES

FIG. 3: DISPLACEMENT/TIME TRACES

therefore, they would affect the load readings if they were used. In order to resolve this problem, a Physitec Model 39 electro-optical tracking unit has been employed. This unit is capable of tracking the motion of an illuminated target at frequencies as high as 2000 Hz. The amplitude sensitivity depends on the objective lens used. Typical lenses used range from an 85 mm f/1.4 conventional lens to a 1300 mm catadioptric lens. The output signal from this unit is fed through an identical low pass filter to the one used in the load circuit to ensure the minimum amount of phase shift (of load vs. deformation) through the electronics.

## RESULTS

### Sinusoidal Test

Specimens are taken from a freshly excised autopsy brain and tested as soon as possible. The vessels are marked and measured for length prior to excision from the brain, then placed onto the loading fixtures as indicated in Fig. 4. The lower, stationary loading fixture is hollow and the vessel is infused to a typical mean *in vivo* pressure of 85 mm and the specimen stretched to the previously measured physiological length prior to commencement of the test.

The amplitude of the sinusoidal displacement is then increased until the maximum negative going excursion corresponds to zero stress on the specimen. The frequency is then varied over the range 0.01 to 10 Hz. No significant change in the stress-strain behaviour is seen over this frequency range. A typical result of this test procedure is shown in Fig. 5(a), the specimen in this case being obtained from a 42-year old female. In general it is found that these arteries exhibit non-linear elastic behaviour with a small hysteresis loop. The energy loss per cycle is found to be 15-25% of the strain energy input and does not vary with the frequency of the load cycles.

For frequencies greater than 10 Hz it is found that, because of the very low tangent modulus at low stress which can be seen in Fig. 5(a), wave propagation effects begin to interfere with the measurement. It is, therefore, necessary to restrict this test to the high modulus, high stress part of the stress-strain curve. This is done by varying the pre-load and the sine wave amplitude so that the maximum stress during the cycle is identical to that in the test described above. This procedure allows the frequency range to be extended to 100 Hz. Fig. 5(b) shows the result for the same specimen as that shown in Fig. 5(a). Again no variation with frequency was noted.

It should be noted that these tests are for relatively large strains and, therefore, caution should be used in comparing these results with previously reported results which were taken over relatively small strain amplitudes.



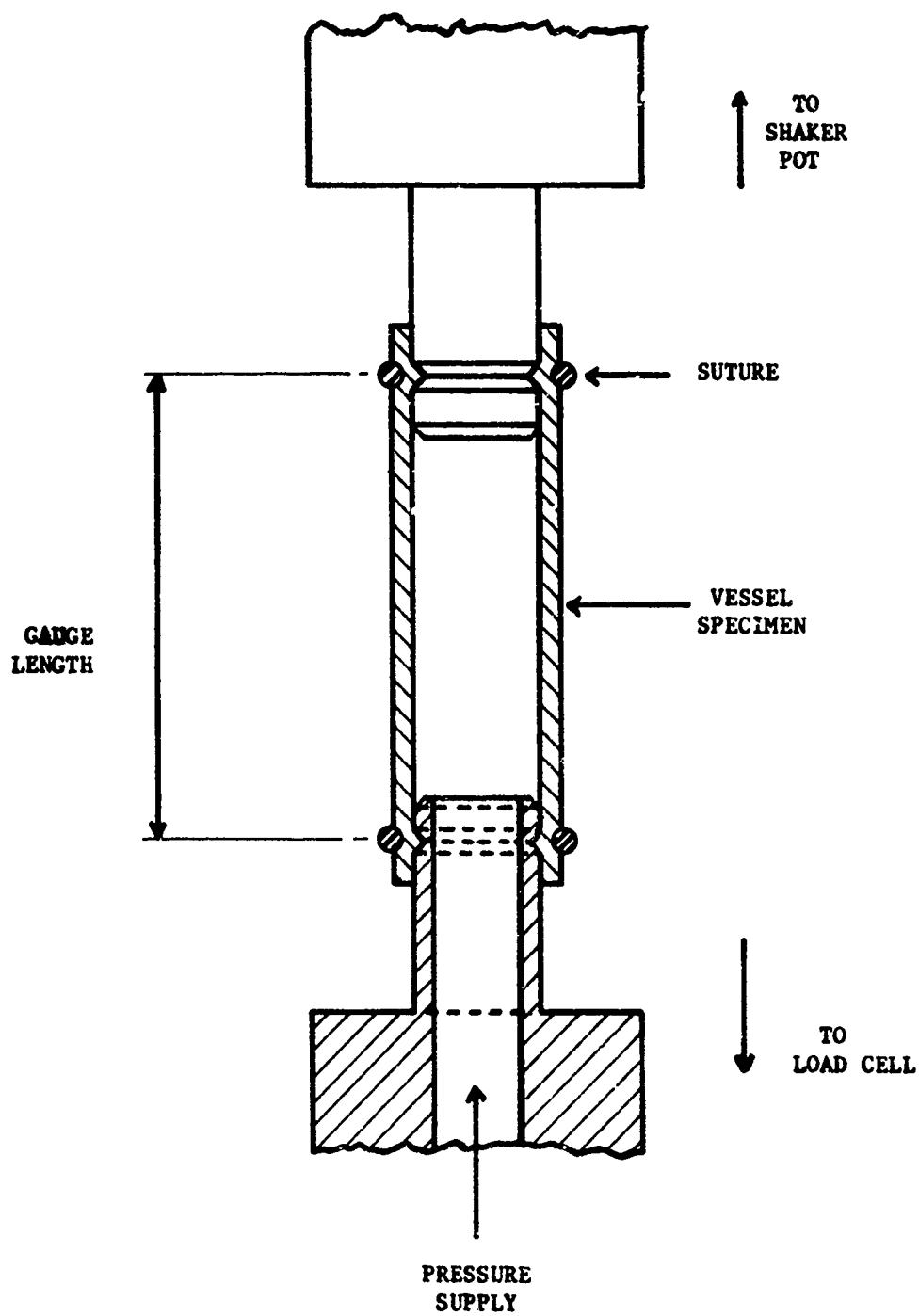


FIG4: SPECIMEN LOADING FIXTURES

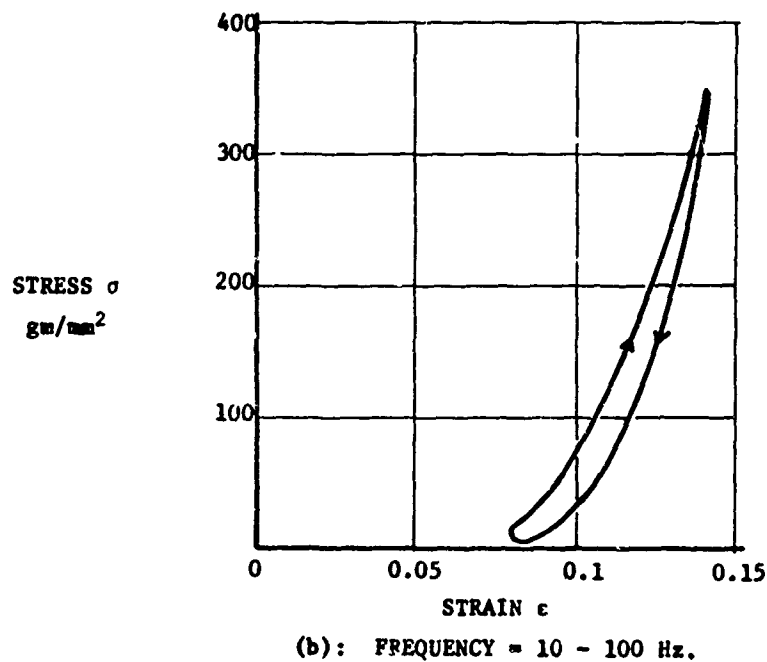
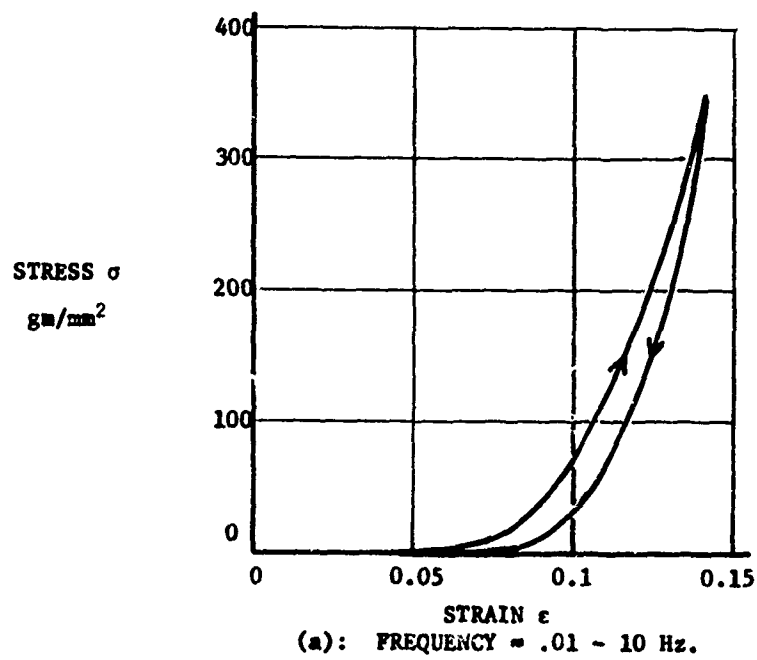


FIG. 5. RESULT OF SINE WAVE TESTS

### Ramp Tests

Preparation for the ramp tests is identical to that for the sinusoidal tests, except that the specimen is not prestretched to physiological length.

Typical results for a series of ramp tests are demonstrated in Fig. 6, which gives results of tests on specimens obtained from a 45 year old male. The results of this test are then plotted in Fig. 7 to show the effect of strain rate on stiffness. The curves are plotted with strain being shown parametrically. It is seen that the behaviour is essentially independent of strain rate.

### CONCLUSIONS

The behaviour of the vasculature of the head has been studied over a range of dynamic loading conditions and found to be essentially non-rate-sensitive over the range tested. The hysteresis loss per cycle was found to be essentially 15-25% of the total strain energy input to the test specimens, and was constant over the range of 0.01 to 100 Hz for sinusoidal tests. The stiffness of the vessels was found to be essentially independent of rate, but strongly dependent upon strain, as is the case in static loading.

This non-linear behaviour is characteristic of all soft tissues and for some tissues it has been shown to be a function of the micro-architecture of the tissue. The relationships between the stress-strain behaviour and the structure of the tissue can be elucidated by histological studies (Kenedi, Gibson and Daly, 1965), use of enzymes which destroy specific components of the structure (Daly, 1969), and by thermoelastic modelling techniques (Apter, 1970). Such studies are presently being carried out on cerebral arteries as part of the study reported here.

### ACKNOWLEDGEMENT

The research upon which this publication is based was performed pursuant to Contract No. NIH-69-2232 with the National Institutes of Health, Public Health Service, Department of Health, Education, and Welfare.

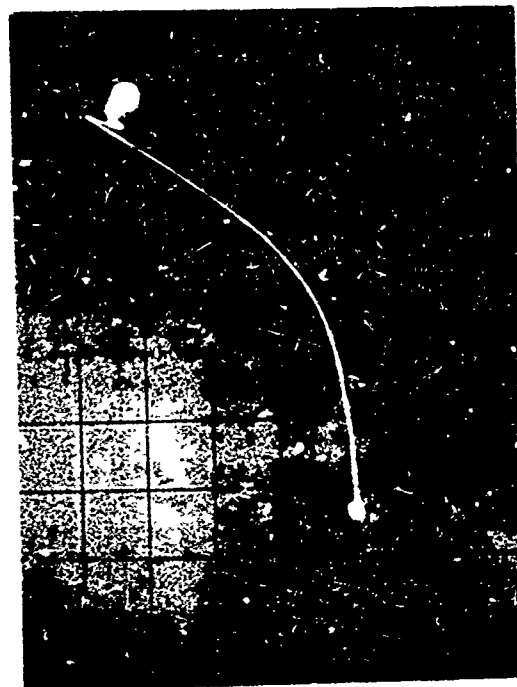
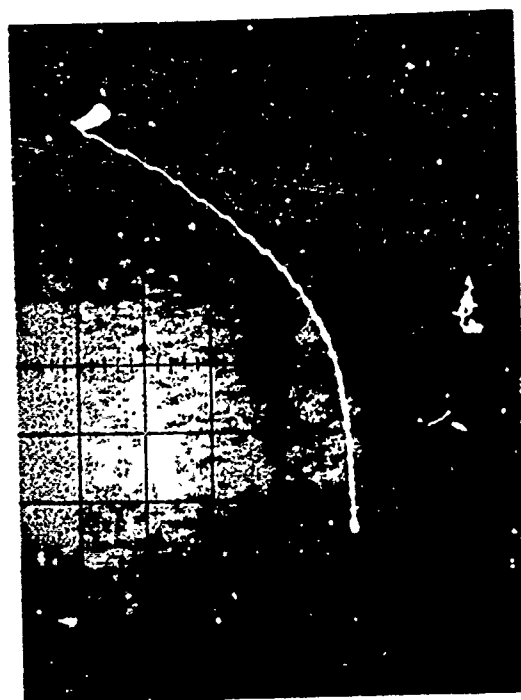
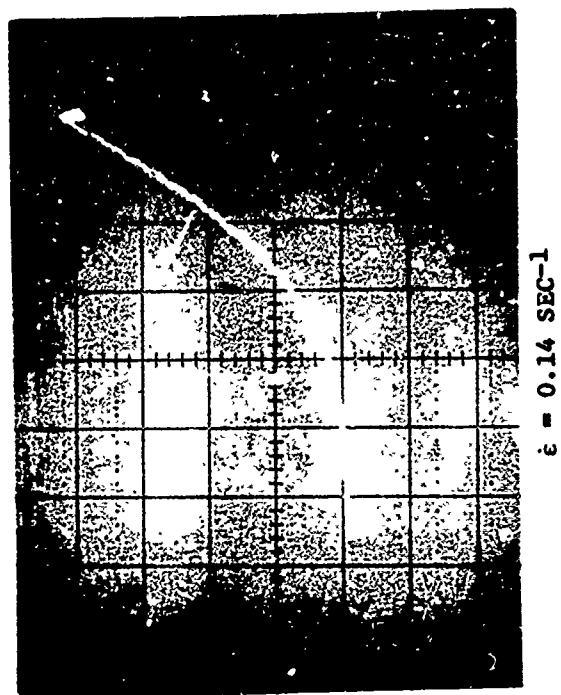
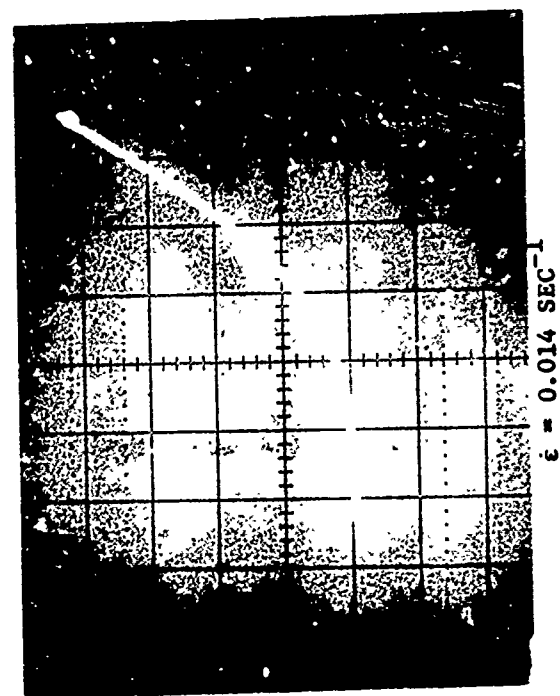


FIG. 6. RAMP FUNCTION TEST RESULTS - STRESS vs. STRAIN FOR VARIOUS STRAIN RATES

SCALES:	X-AXIS:	0.25 MM./DIV.	GAGE LENGTH = 1.05 CM.
	Y-AXIS:	50. CM./DIV.	X-SECTION AREA = 0.95 MM <sup>2</sup>

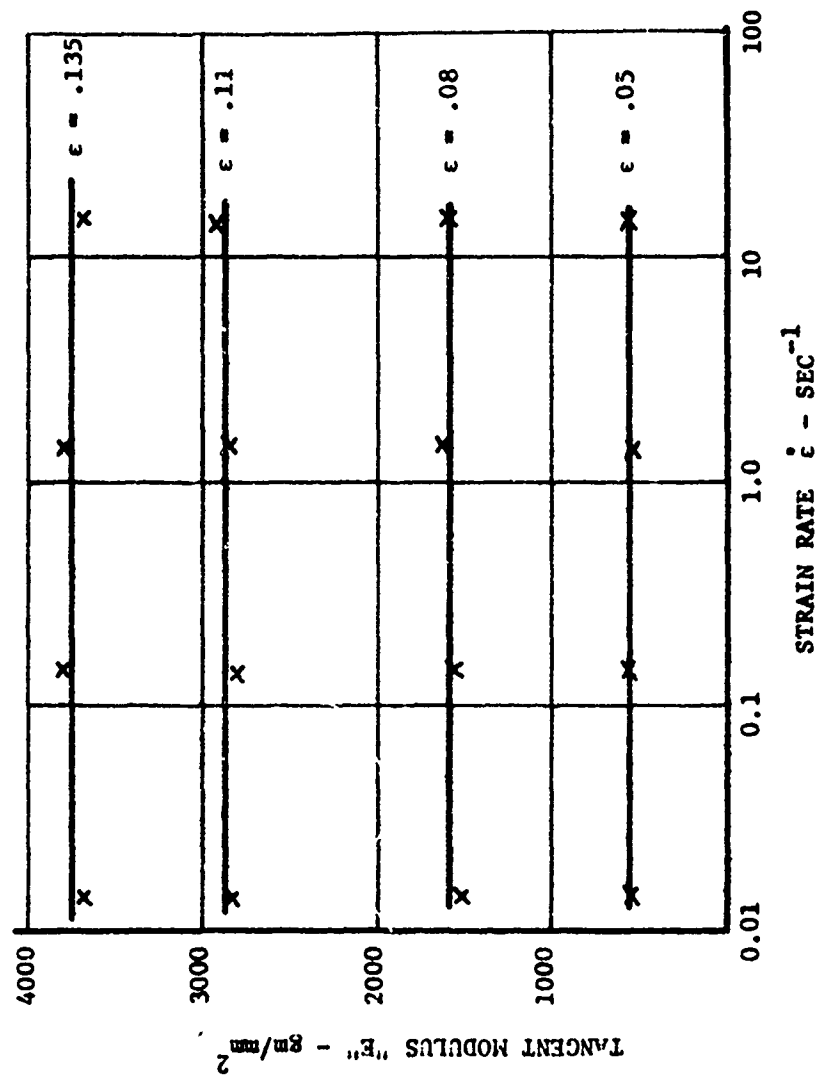


FIG. 7 RAMP FUNCTION TEST RESULTS -- TANGENT MODULUS VS. STRAIN RATE WITH STRAIN PLOTTED PARAMETRICALLY

1. Apter, J.T., P. Mason and J. Hopkinson. "Influence of Composition on Thermal Properties of Tissue." Presented at The Symposium on the Foundations and Objectives of Biomechanics. La Jolla. July 1970.
2. Daly, C.H. "The Role of Elastin in the Mechanical Behavior of Skin." Proceedings of the 8th Int. Conference on Medical and Biological Engineering. Chicago. July 1969.
3. Kenedi, R.M., T.Gibson, and C.H. Daly. "The Determination, Significance and Application of the Biomechanical Characteristics of Human Skin." Digest of the 6th International Conference on Medical Electronics and Biological Engineering, pp. 531-534. Tokyo. 1965.

A THEORETICAL ANALYSIS  
THE MECHANICAL CHARACTERISTICS OF THE PATELLA

Edward H. Miller, M.D., Dane Miller, B.S.M.E.  
and

Robert Kroll, Ph. D., A. E.

Division of Orthopaedic Surgery  
University of Cincinnati College of Medicine  
Cincinnati, Ohio

ABSTRACT

The authors have performed a theoretical static moment analysis of the knee joint, the quadriceps mechanism, and the patella. They have demonstrated that, theoretically, it should be impossible to extend the knee towards  $180^{\circ}$  (maximum extension) against gravity and a theoretical ten pounds active resistive weight at the ankle joint because of the mechanics of the knee joint. They demonstrated that as the quadriceps mechanism lies on the anterior femoral condyle it would seem that, as the knee approached full extension, the line of pull of the quadriceps mechanism would approach  $90^{\circ}$  to the moment at the tibial tubercle. This would produce forces approaching infinity necessary to attain the last few degrees of full extension.

The authors analyzed this system on several voluntary subjects and demonstrated the pulley-shift mechanism of the femoral condyles which prevents this impossible situation from occurring. In this analysis, they demonstrated why the patellectomized patient can indeed obtain full extension against gravity in an active resistive weight.

## CHARACTERISTICS OF THE PATELLA

An important consideration in management of afflictions of the knee involving the patella and consequently the quadriceps mechanism is the mechanical function of the patella. Such afflictions include fracture or degeneration resulting from fracture. This problem arises in fundamental studies of knee joint motion when consideration must be given to removal of the patella. Some have advocated its salvage or replacement by metallic implant, while others have felt this measure unnecessary. It is the purpose of this study to compare the function of the quadriceps mechanism with and without a patella. For the purpose of this determination, static moment analysis has been performed. This seems to be the simplest method, though it should not necessarily be applied to the knee in locomotion. The purpose of using static moment analysis rather than swing phase analysis will be clear upon study of the equations used.

### Knee Moment Equation

It is assumed that all shank movements are confined to the sagittal plane and all physical quantities defined herein are therefore determined for this plan of motion. It is also assumed that the longitudinal axis of the shank is horizontal and, likewise, physical quantities are so determined. Two equations are used for the determination of the final equation and their derivation is herein presented. The first is:

$$(1) \quad F_T = \frac{\bar{r}_A \cdot 0.42 (0.0527W_B + 0.0179W_B)}{\bar{r}_T} + \frac{\bar{r}_A \cdot W_A}{\bar{r}_T}$$

where:

- $F_T$  is the Tibial Tubercle Moment in lb. ft.
- $\bar{r}_A$  is the distance from the center of rotation of the knee joint to the ankle in the feet.
- $\bar{r}_T$  is the distance from the center of rotation of the knee joint to the point of insertion of the patellar tendon into the tibial tubercle.
- $W_B$  is the body weight.



- $W_A$  is a theoretical weight at the ankle joint for "progressive resistive straight leg raising exercises."
- 0.42 is Fisher's coefficient for location of the center of gravity of the shank-foot combination.
- 0.0527 is Fisher's coefficient for the weight of the shank.
- 0.0179 is Fisher's coefficient for the weight of the foot.

and the second equation is:

$$(2) \quad F_Q = \frac{F_T}{\cos \theta}$$

where:

- $F_Q$  is the force necessary in the quadriceps to counteract the moment at the tibial tubercle insertion of its tendon ( $F_T$ )
- $\cos \theta$  is the cosine of the angle subtended by the patellar tendon in relation to the actual direction of the moment at the tibial tubercle.

The final equation used for comparing the force necessary with and without a patella is:

$$(3) \quad \frac{F_{QF}}{F_{QP}} = \frac{\cos \theta_P}{\cos \theta_F}$$

where:

- $F_{QP}$  is the force of pull necessary in the quadriceps tendon with a patella while
- $F_{QF}$  is the same without a patella, and
- $\theta_P$  is the angle subtended by the direction of the patellar tendon with the patella in place as compared to the direction of the moment at the tibial tubercle, while
- $\theta_F$  is the same without a patella when the tendon lies on the femoral condyles.

Equation (3) states that the ratio of the force necessary to extend the knee against gravity, plus an assumed active resistive force with the quadriceps tendon lying over a patella to the same force with the tendon overlying the

femoral condyle, as after patellectomy, is inversely proportional to the cosine of the angles subtended by the direction of these forces. By using this ratio equation, one mathematically eliminates the complicated formula (1) with its inherent inaccuracies: viz., Fischer's coefficients have shown to have as much as 50% variation. This simple ratio reflects the relative forces required.

The derivation of these equations is as follows:

(See Figure 1)

where:

$C_K$	is the location of the center of rotation of the knee joint.
$W_A$	is the active resistive weight assumed to be 10 lbs.
$W_{cg}$	is the weight of the shank-foot combination.
cgSF	is the location of the center of gravity of the shank-foot combination.
T	is the location of the insertion of the patellar tendon into the tibial tubercle.
$\bar{r}_T$	is the distance from $C_K$ to T in feet.
$\bar{r}_{cg}$	is the distance from $C_K$ to cgSF in feet.
$\bar{r}_A$	is the distance from $C_K$ to $W_A$ in feet.
$F_T$	is the force at T necessary to counteract the sum of the forces acting perpendicular to the longitudinal axis of the shank.
$F_{cg}$	is that portion of $F_T$ necessary to counteract $W_{cg}$ .
$F_A$	is that portion of $F_T$ necessary to counteract $W_A$ at A.

Therefore:

$$(4) \quad \bar{r}_T F_T = \bar{r}_{cg} W_{cg} + \bar{r}_A W_A$$

It is obvious that  $F_T$  is the sum of two forces, namely, (1) that which is contributed to by  $W_{cg}$  acting through  $\bar{r}_{cg}$  and (2) that which is contributed by  $W_A$  acting through  $\bar{r}_A$ .



Hence:

$$(5) \quad F_T = F_{cg} + F_A$$

where:

$F_{cg}$  represents the force acting upon and perpendicular to the tibial tubercle necessary to counteract the combined shank-foot weight acting at its center of gravity. Likewise,  $F_{cg}$  has two components; namely, that portion representing the weight of the shank and that representing the foot.

$F_A$  is that component of  $F_T$  representing the counter force necessary to counteract the moment created by the "active resistive weight" at the ankle.

Also:

$$(6) \quad W_{cg} = W_S + W_F$$

Hence, the weight of the shank-foot combination is the sum of the weight of the shank and the weight of the foot. These together act at the cgSF.

Derivation of  $F_{cg}$ :

$$F_{cg} = \frac{\bar{r}_{cg} \times W_{cg}}{\bar{r}_T} \quad \text{sub. eq. (6)}$$

$$(7) \quad \therefore F_{cg} = \frac{\bar{r}_{cg} (W_S + W_F)}{\bar{r}_T}$$

Fisher's coefficients state that:

$$\begin{aligned} W_S &= 0.0527 W_B \\ W_F &= 0.0179 W_B \\ W_B &= \text{Body weight} \\ \bar{r}_{cg} &= 0.42 \bar{r}_A \end{aligned}$$

$\bar{r}_A$  and  $\bar{r}_T$  are obtained from x-rays by direct measurement allowing for parallax.

Hence:

$$(8) \quad F_{cg} = \frac{\bar{r}_A \cdot 0.42 (0.0527 W_B + 0.0179 W_B)}{\bar{r}_T}$$

Derivation of  $F_A$ :

$$(9) \quad F_A = \frac{\bar{r}_A \cdot W_A}{\bar{r}_T}$$

Substituting equations (8) and (9) into equation (5), the quantitation of  $F_T$  is expressed as:

$$(10) \quad F_T = \frac{\bar{r}_A \cdot 0.42 (0.0527 W_B + 0.0179 W_B)}{\bar{r}_T} + \frac{\bar{r}_A \cdot W_A}{\bar{r}_T}$$

Determination of forces necessary in the quadriceps:

(See Figure 2)

$$(11) \quad F_{QP} = \frac{F_T}{\cos \theta_P}$$

where:

$F_{QP}$  is the force necessary in quadriceps contraction to act for  $F_T$  when the quadriceps tendon acts through the center line of the patella.

$\theta_P$  is the angle from the tibial insertion vertical ( $F_T$ ) to a line from the insertion through the center line of the patella and

$$(12) \quad F_{QF} = \frac{F_T}{\cos \theta_F}$$

where

$F_{QF}$  is the same force when the quadriceps mechanism glides over the femoral condyle, as in the absence of the patella.

$\theta_F$  is the angle between  $F_T$  and a line from the tibial tubercle insertion of the quadriceps tendon tangential to the outer surface of the femoral condyles wherein the tendon glides in the absence of the patella.

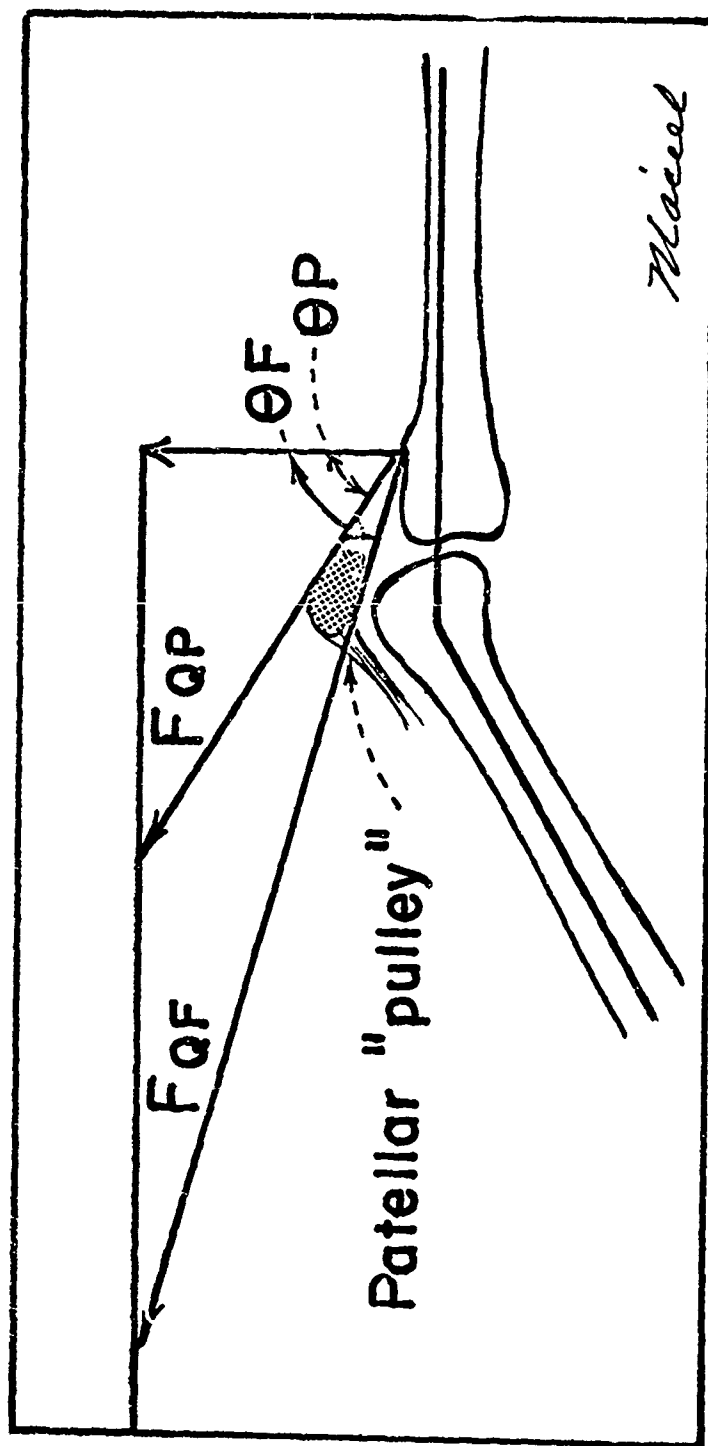


Fig. 2

## The Hypothesis

As the knee extends towards  $180^\circ$ , the tibial tubercle approaches the direct axis of the anterior femur. Thus a ngle  $\theta_F$  approaches  $90^\circ$ , the cosine of  $\theta$  approaches zero. As the cosine of  $\theta$  approaches zero,  $F_{QF}$  approaches infinity. Hence, without other compensatory mechanisms coming into play, it should be impossible to fully extend the knee without a patella against gravity with the long axis of the shank horizontal. It should be noted that during locomotion,  $F_T$  is not at a right angle to the long axis of the shank, rather it is variable and is somewhat less than  $90^\circ$  toward the direction of the quadriceps pull making it possible to have obtainable effective quadriceps contraction. Nonetheless, to expect a patellectomized patient to obtain full extension through the use of active resistive exercises with a weight at the ankle where, when sitting or reclining, the axis of his shank approaches the horizontal when at the same time the knee is approaching full extension would seem to create forces approaching requirement of infinite strength in the quadriceps and be, therefore, unobtainable.

It is well known by the clinician that many patellectomized patients are quite able to fully extend the knee in the manner described. The reason the hypothesis is in err is due to the position of the quadriceps tendon with respect to the proximal tibia and femoral condyle. This factor was not evaluated in this paper.

## Experimental Data

Ten subjects were used. They were all males varying in age from 27 to 32 years and were all resident orthopaedic surgeons. All have normal knees. These subjects had careful lateral x-rays taken of th ir lower legs including their shanks. Measurements of  $\bar{r}_T$  and  $\bar{r}_A$ , as well as  $\theta_P$  and  $\theta_F$  were determined from these roentgenograms. Films were taken in maximum extension and maximum flexion. Additional x-rays were taken with the subjects at  $45^\circ$  flexion and  $90^\circ$  flexion. Tables I through IV demonstrate the results with a numerical average of the ten subjects in Table V.

TABLE I  
Full Extension

Subject	$\theta_P$	$\theta_F$	$\cos \theta_P$	$\cos \theta_F$	$\frac{\cos \theta_P}{\cos \theta_F}$
1	67°	74°	0.39073	0.27564	1.4175373
2	64°	77°	0.43837	0.22495	1.9487441
3	67°	76°	0.39073	0.24192	1.6151207
4	62°	72°	0.46947	0.30902	1.5192220
5	68°	75°	0.37461	0.25882	1.4473765
6	62°	73°	0.46947	0.29237	1.6057393
7	66°	73°	0.40674	0.29237	1.3911824
8	68°	76°	0.37461	0.24192	1.5484871
9	65°	75°	0.42262	0.25882	1.6328723
10	64°	75°	0.43837	0.25882	1.6937253

TABLE II  
45° Flexion

Subject	$\theta_P$	$\theta_F$	$\cos \theta_P$	$\cos \theta_F$	$\frac{\cos \theta_P}{\cos \theta_F}$
1	58°	75°	0.52992	0.25862	2.0490294
2	55°	78°	0.57358	0.20791	2.7587898
3	56°	76°	0.55919	0.24192	2.3114666
4	57°	74°	0.61566	0.27564	2.2335655
5	56°	76°	0.55919	0.24192	2.3114666
6	53°	75°	0.60182	0.25882	2.3252453
7	58°	74°	0.52992	0.27564	1.9225076
8	57°	77°	0.54464	0.22495	2.4211602
9	55°	77°	0.57358	0.22495	2.5498110
10	56°	77°	0.55919	0.22495	2.4858413



TABLE III  
90° Flexion

Subject	$\theta_P$	$\theta_F$	$\cos \theta_P$	$\cos \theta_F$	$\frac{\cos \theta_P}{\cos \theta_F}$
1	54°	68°	0.58779	0.37461	1.5690718
2	51°	69°	0.62932	0.35837	1.7560621
3	51°	68°	0.62932	0.37461	1.6799337
4	48°	63°	0.66913	0.45399	1.4738870
5	54°	68°	0.58779	0.37461	1.5690718
6	53°	69°	0.60182	0.37461	1.6065241
7	51°	67°	0.62932	0.39073	1.6106263
8	57°	69°	0.54464	0.35837	1.5197701
9	54°	68°	0.58779	0.37461	1.5689462
10	54°	67°	0.58779	0.39073	1.5043380

TABLE IV  
Maximum Flexion

Subject	Actual Flexion	$\theta_P$	$\theta_F$	$\cos \theta_P$	$\cos \theta_F$	$\frac{\cos \theta_P}{\cos \theta_F}$
1	115°	53°	67°	0.60182	0.39073	1.5402451
2	122°	48°	67°	0.66913	0.39073	1.7125124
3	117°	49°	66°	0.65606	0.40674	1.6129714
4	124°	45°	60°	0.70711	0.50000	1.4142200
5	120°	51°	67°	0.62932	0.39073	1.6106262
6	123°	45°	62°	0.70711	0.46947	1.5061878
7	122°	48°	66°	0.66913	0.40674	1.6451050
8	113°	50°	67°	0.64279	0.39073	1.6451002
9	125°	48°	66°	0.66913	0.40674	1.6451050
10	127°	51°	66°	0.62932	0.40674	1.5472292

TABLE V  
Average Values for Sampling of 10 Subjects

Leg Position	$\bar{\theta}_P$	$\bar{\theta}_F$	$\cos \bar{\theta}_P$	$\cos \bar{\theta}_F$	$\frac{\cos \bar{\theta}_P}{\cos \bar{\theta}_F}$
Maximum Extension	65°-18'	74°-36'	0.41787	0.26556	1.5958
45° Flexion	56°-06'	75°-54'	0.55775	0.24362	2.2895
90° Flexion	52°-42'	67°-36'	0.60599	0.38107	1.5902
Maximum Flexion (120°-48' Avg.)	48°-48'	65°-24'	0.65869	0.41628	1.5871

TABLE VI

Subject	$W_B$	$\bar{r}_A$ (in)	$\bar{r}_T$ (in)	$\bar{r}_A$ (ft)	$\bar{r}_T$ (ft)
1	185 lb.	17.25	3.75	1.44	0.31
2	153 lb.	16.25	3.25	1.35	0.28
3	172 lb.	17.00	3.50	1.42	0.29
4	168 lb.	17.75	3.75	1.48	0.31
5	188 lb.	17.50	3.50	1.45	0.29
6	160 lb.	17.50	3.50	1.45	0.29
7	174 lb.	17.00	3.25	1.42	0.28
8	184 lb.	17.75	3.50	1.48	0.29
9	158 lb.	16.25	3.00	1.35	0.25
10	190 lb.	17.75	3.75	1.48	0.31

## Results

(See Figure 3)

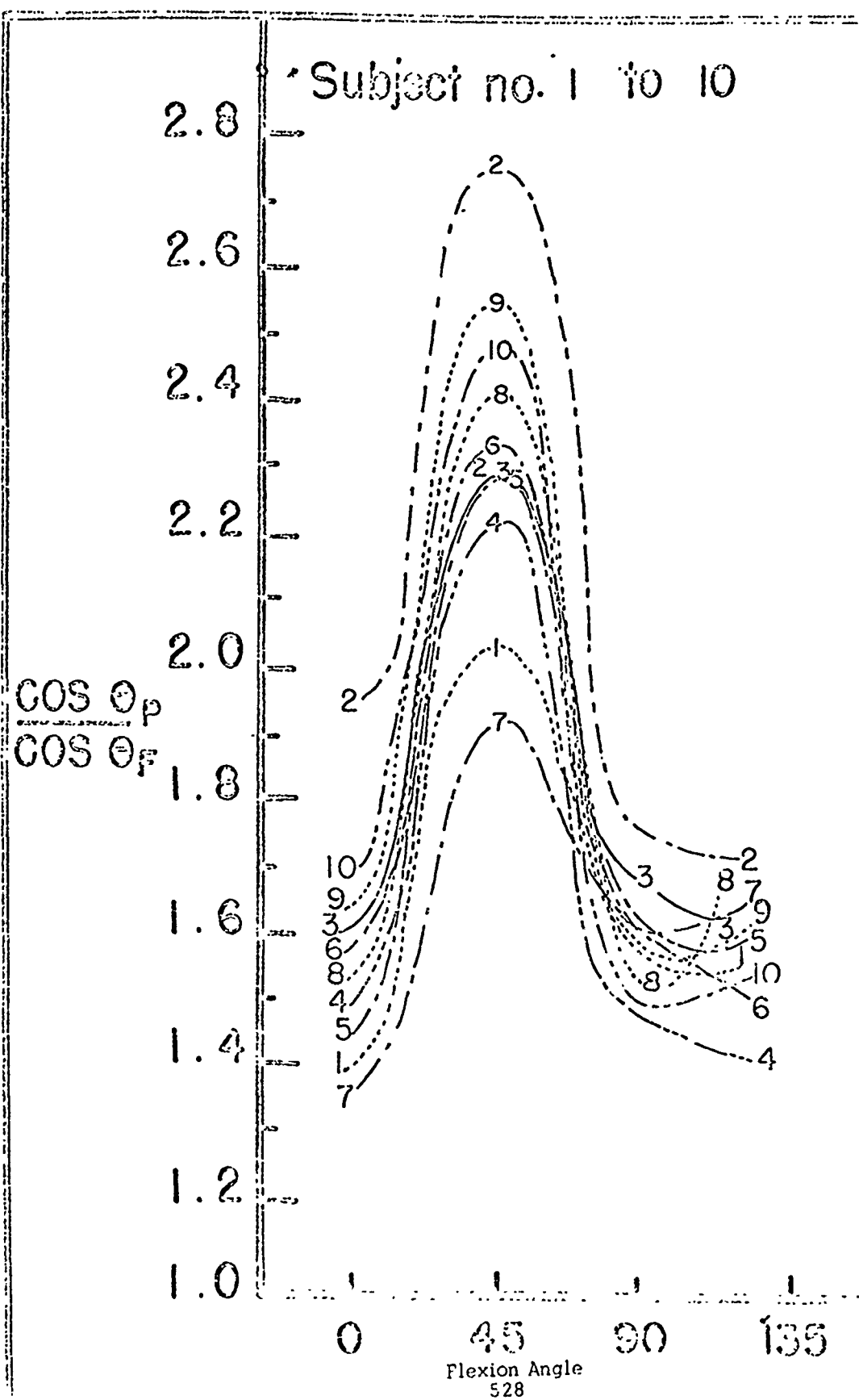
## Conclusions

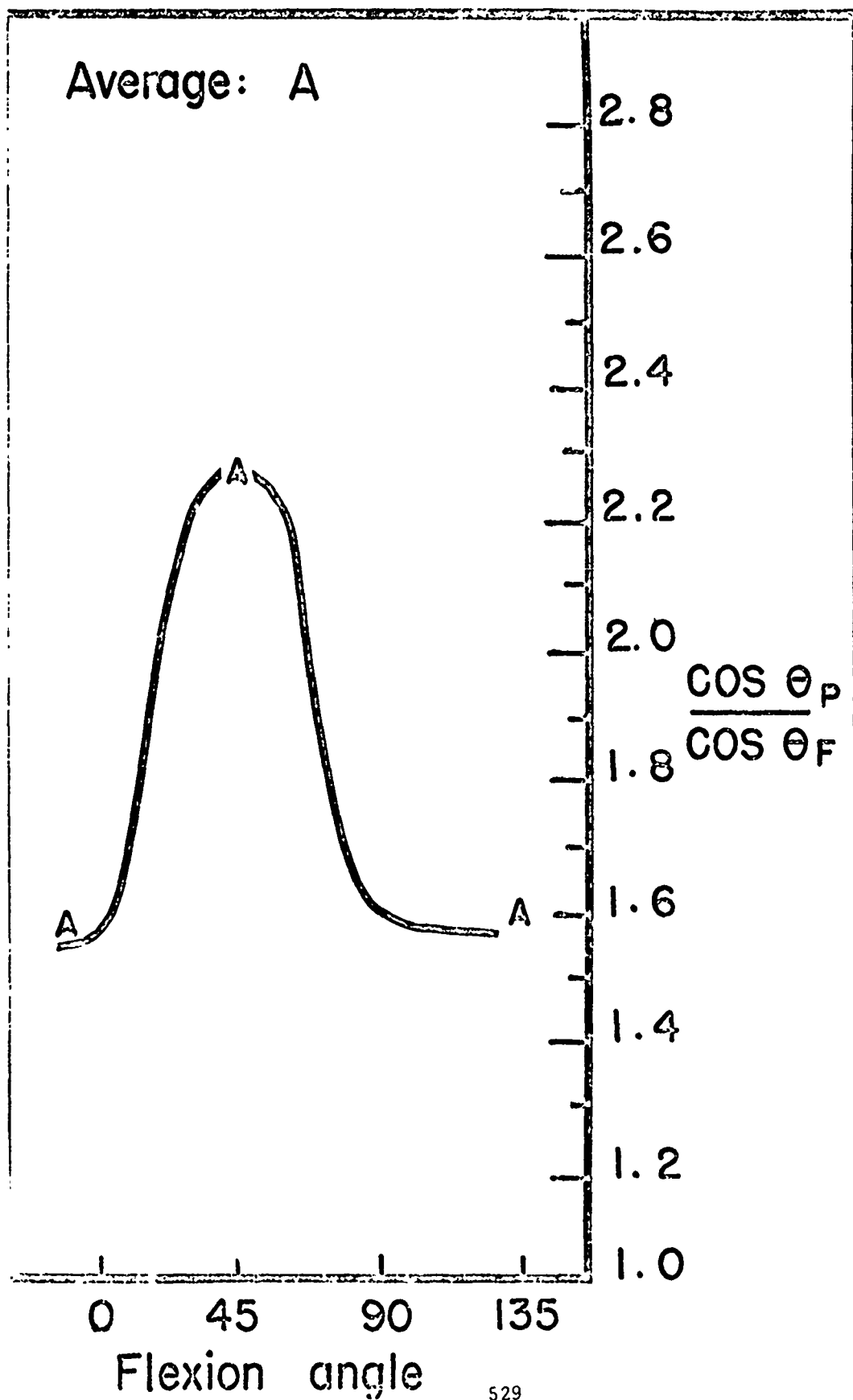
It is obvious from the plotted results that as one extends the knee against active resistive weights and gravity towards the horizontal that the relative forces become greater in the region of  $45^{\circ}$  from full extension. However, somewhere between  $45^{\circ}$  flexion and full extension something happens which causes a reversal, and it becomes easier to obtain the last few degrees of extension. The only mechanism that could explain this peculiarity is that the locus of the pulley would have to increase in radius from the center of rotation of the knee. This is exactly what does happen, because the patella reaches the equator of the anterior femoral condyle and then glides superiorly along the articular cartilage of the anterior femur in a direction tangential to the curvature of the weightbearing portion of the femoral condyle. This in effect increases the efficiency of the mechanical advantage of the system. Consequently, the tibial tubercle is prevented from approaching the longitudinal axis of the quadriceps pull; in fact it, by virtue of anterior tangential displacement of the force mechanism, falls away, as it were, facilitating active extension. The hypothesis then that the patellectomized patient is incapable of full extension in the experimental position is likewise erroneous. This pulley shifting mechanism prevents a potentially irreconcilable situation from occurring.

## Summary

It seems obvious that in the patellectomized patient that, as the knee extends towards  $180^{\circ}$ , the tibial tubercle approaches the direct axis of the anterior femur. As this occurs, the direction of pull of the quadriceps tendon approaches  $90^{\circ}$  to the perpendicular of its insertion into the tibial tubercle. Therefore, necessary forces to complete extension should approach infinity.

An analysis of this mechanism and proof of the actual pulley shift mechanism preventing this impossible situation from arriving is presented.





## REFERENCES

1. Engin, A. D. The axisymmetric response of a fluid-filled spherical shell to a local radial impulse - A model for head injury. J. of Biomech. 2:325-341, 1969.
2. Benedict, J. V. An analysis of an impact loaded, fluid-filled spherical shell as a mathematical model for an investigation of the cavitation theory of brain damage. Ph.D. thesis at Tulane University, 1969.
3. Advanti, S. H., and Lee, Y. Structural investigations of craniocerebral trauma. West Virginia University final report, 1970.
4. Engin, A. E., and Liu, Y. K. Axisymmetric response of a fluid-filled spherical shell in free vibration. J. of Biomech. 3:11-22, 1970.
5. Ommaya, A. K. Mechanical properties of tissues of the nervous system. J. of Biomech. 1:127-138, 1968.
6. West Virginia University. Determination of the physical properties of tissues of the human head. Contract. No. PH-43-67-1137. Final Report, 1970.
7. Galford, J. W., and McElhaney, J. H. A viscoelastic study of scalp, brain and dura. J. of Biomech. 3:211-221, 1970.
8. McElhaney, J. H. and Byars, E. F. Dynamic response of biological materials. ASME 65-WA/HUF-9, 1965.
9. Melvin, J. W., Fuller, P. M., and Barodawala, I. T. The mechanical properties of the diploe layer in the human skull. 1970 SESA Spring Meeting, Huntsville, Alabama.
10. Shuck, L. Z., Haynes, R. R., and Fogle, J. L. Determination of viscoelastic properties of human brain tissue. ASMC 70-BHF-12, 1970.
11. Fallenstein, G. T., Hulce, V. P., and Melvin, J. W. Dynamic mechanical properties of human brain tissue. J. of Biomech. 2:217-226, 1969.
12. Estes, M. S., and McElhaney, J. H. Response of brain tissue of compressive loading. ASME 70-BHF-13, 1970.
13. Janssen, M. L., and Bowman, C. E. The dynamic response of two-dimensional photoelastic models of the human head. ASME 70-BHF-15, 1970.
14. Rose, J. L., and Chou, P. C. Photoelastic study of stress waves generated by exploding wires. 1970. SESA Fall Meeting, Boston, Massachusetts.

## BIBLIOGRAPHY

1. Bartholomew, S. H.: Determination of Knee Moments during the Swing Phase of Walking and Physical Constants of the Human Shank. Prosthetic Devices Research Project, 1957. Institute of Engineering Research, University of California, Berkeley.
2. Beer, Ferdinand P. and Johnston E. Russell: Mechanics for Engineers. Statics and Dynamics. McGraw-Hill Book Company, New York, 1957.
3. Outdermaur, M.: Gross Anatomy and Radiology of the Normal Knee Joint. Documenta Geigy Acta Clinica, Osteoarthritis of the Knee Joint, No. 1, 1963.

BIOMECHANICS IN MOTOR SKELETAL STRUCTURES

CARL HIRSCH

Professor and Chairman, Department of Orthopaedic Surgery  
Karolinska institutet, Stockholm.

ABSTRACT

Abstract: Most lethal biomechanical conditions can be explained by the physical laws which govern inertia, acceleration - deceleration and dissipation or absorption of kinetic energy. These physical laws provide a framework for the quantitative description of the mechanical response of skeletal structures.

The time during which decelerations and forces are generated are of such magnitude to cause sudden fatalities. Traffic injuries and death obviously derive from biomechanical events when power and speed affect the body.

Studies of autopsy materials indicate that just below the level which causes sudden death, there is a narrow margin which may produce serious injuries and yet permit survival. There is thus a maximum tolerance of the body to force. Above this level, death occurs from stresses which exceed the limits of the structures with vital functional capacity.

A complex system, such as the human body, can produce longitudinal, transverse and torsional mechanical responses at any of a series of frequencies. Energy transfer is possible between the various modes. Shape factors may also produce dispersion of energy which can cause large stresses at points remote from the application of the original force.

INTRODUCTION

Injuries and death due to mechanical trauma derive from events where power and speed affect the body. The time during which decelerations and forces occur are contributing factors to most fatalities. In modern society, accidents now rank first as a cause of severe injuries and death in individuals under 35 years of age and are outranked in older age groups, chiefly by cancer, heart conditions and degenerative diseases. The highest lethal rates occur in the very young. This implies an enormous number of life years lost in personal and productive resources.

Most lethal biomechanical conditions can be explained by the physical laws which govern inertia, acceleration - deceleration and dissipation or absorption of kinetic energy. These physical laws provide a framework for the quantitative description of the mechanical response of skeletal structures.



The time during which decelerations and forces are generated are of such magnitude to cause sudden fatalities. Traffic injuries and death obviously derive from biomechanical events when power and speed affect the body.

To avoid these traumatic effects, measures should be taken to protect the body from stresses that it cannot tolerate without failure. Analysis of the physical capacity and of the tolerance of various human tissues to external stresses are therefore important.

Studies of autopsy materials indicate that just below the level which causes sudden death, there is a narrow margin which may produce serious injuries and yet permit survival. There is thus a maximum tolerance of the body to force. Above this level, death occurs from stresses which exceed the limits of the structures with vital functional capacity.

The motor-skeletal system forms a complex articulating system which also serves to protect and to resist mechanical strain. Physical properties of these tissues have long been a matter of interest, and in recent years attempts have been made to define their character in physical terms.

It is difficult to make an interpretation of the stress-strain behaviour of the human body. First of all, the body is a heterogeneous viscoelastic mass within which run large liquid filled channels surrounded by a skeletal frame and various kinds of soft tissues. In fact, the body is polyphasic with liquid, solid and gaseous components.

Secondly, the body is not isotropic, since its properties at given point may be different in different directions. It contains many kinds of materials linked together. Furthermore, the elastic moduli and stress limits for these various parts may change with changes of position or physical state.

Thirdly, the system is highly damped. Free vibrations die away within a few cycles.

A complex system, such as the human body, can produce longitudinal, transverse and torsional mechanical responses at any of a series of frequencies. Energy transfer is possible between the various modes. Shape factors may also produce dispersion of energy which can cause large stresses at points remote from the application of the original force.

The magnitude of stresses can be expressed indirectly as patho-physiological effects. Weaker forces lead to discomfort or fatigue. Increased forces cause vasomotor, neuromuscular, and respiratory compensatory responses. Greater forces lead to injury, and still greater forces, which the body is not able to tolerate, lead to damage or rupture of tissues. Human structures then have reached the point, where the inertial reactions of the organ or its attachments can not tolerate the stresses caused by rapid deceleration.

## METHOD

In this presentation, different anatomical lesions such as fractures, vertebral injuries, or soft tissue ruptures are not discussed in a clinical context. The purpose is rather to try to relate material properties to forces acting in collagen material in general.

Until recently, biomechanics has dealt mainly with interaction between anatomical parts, contact forces in joints, and the relative displacements of structural components. Since the need is increasing for information about how individual components deform under given loads, it, obviously, would be desirable to extend the concept of biomechanics to include continuum mechanical analysis.

Classical continuum mechanics consists of three independent analyses: the analysis of strain, the analysis of stress, and the analysis of material properties. These three analyses give rise to three sets of equations: compatibility equations, equilibrium equations and constitutive equations. The first two sets of equations are independent of the material involved and can be adopted unaltered; only the material analysis is specific in biomechanics. The study of constitutive relations for time-dependent materials is commonly called rheology. The first step towards continuum mechanical analysis of anatomic members is then the macrorheological investigations of its tissues.

In order to obtain information, rheological experiments have until recently only been performed on post-mortem material. This necessitated methods of sampling and testing under conditions that prevented or controlled changes of the material relative to the in vivo state.

Elasticity has previously been determined in biomaterials by measuring slopes in load-deformation diagrams of tension and bending tests. The modulus of elasticity has been calculated by elementary strength of materials theory. These investigations revealed viscous effects in collagen tissues. The material could not be characterized during tension by the modulus of elasticity as is generally done in simple strength of materials.

Because of the time-dependent, viscous effect in the material, the values of load and deformation were registered and the rate of deformation at which the test was performed was also controlled. Three types of tests, as shown in Figs. 1, 2 and 3 were considered of main interest.

The curves in the diagrams are schematic, but show, in principle, the behaviour of collagen tissues under moderate loads at about 50 per cent of the breaking force. The information on the viscoelastic properties obtained from these curves formed the basis for the description of the material under uniaxial states of stress. Creep tests, according to Fig. 1, showed the presence of instantaneous elasticity and delayed elasticity or strain retardation. Stress relaxation is illustrated in Fig. 2, and the cyclic test of Fig. 3 showed the energy dissipation in

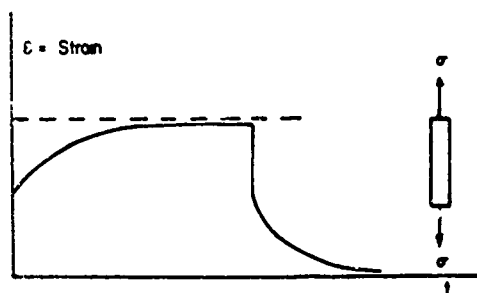


Fig. 1. Suddenly applied constant stress. Sudden unloading at certain time. Registered quantity: strain as a function of time.

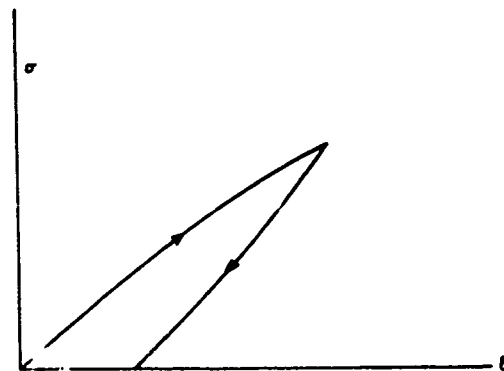


Fig. 3. Cyclic test with either constant rate of strain or stress. Registered quantity: stress as a function of strain.

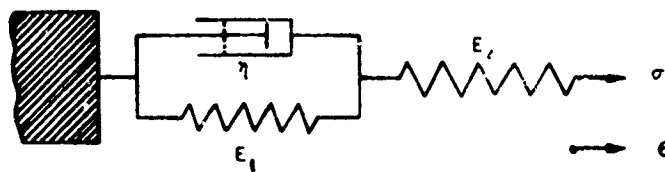


Fig. 4 a Model.

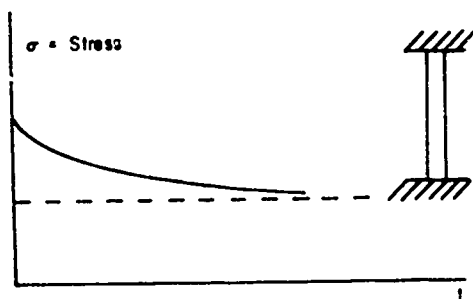


Fig. 2. Suddenly applied constant strain. Registered quantity: stress as a function of time.

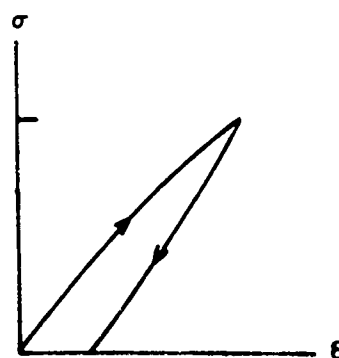


Fig. 4 b Cyclic test curve for the material defined by the model.

the material.

Generalizing the constitutive equations into multiaxial form requires additional information about the anisotropy of the material. Further, in order to analyse a complete anatomic component, variations of mechanical properties from point to point, i.e. inhomogeneity, must be considered. In order to explain the multiaxial behaviour of collagen, these two phenomena represent urgent future research projects in macrobiorheology.

In bone the specific shape of the test curves led to a description of the material in terms of a rheological model. Figs. 4 (a) and (b).

Using standard rheological symbols, the springs represent elastic components in the material, and the dashpot stands for viscous components. The springs are characterized by their moduli of elasticity and the dashpot by their viscosity. The model symbolizes a linear material.

The average slope of the load deformation curve for a material of this type depends on the rate of deformation at which the test is performed. This is easily understood if one considers the two extreme cases of very rapid and very slow rates of deformation. In the first case the dashpot is too slow, and most of the deformation is in the spring. In the second case the dashpot has time to deform. Then the total deformation of the material is composed of the deformations in both springs. Stiffness is decreased corresponding to that of the two springs in series.

This description of bone has been shown to be valid in the lower range of loading (up to about 50 per cent of the breaking strength). For higher loads additional effects are observed, such as permanent deformation after unloading and recovery, or "plastic" deformation. It is necessary to include this phenomenon in the analysis in order to cover a wider range of loading.

Studies of the effect of orientation on the mechanical characteristics of cortical bone revealed that the arrangement of the collagen fibers play a basic role in the strength of the osseous tissue. The stiffness of the bone decreased with increasing angle of the applied force in relation to the longitudinal axis of the diaphyses. Residual deformation and energy dissipation also varied with the angle.

It is possible to grade the energy absorption in bone. By doing so it was found that a simple fall has a relative energy equivalent to 10, a bicycle accident 100 and a car crash, the vehicle moving at 30 Km/hr, 1.000. This explains why an osteoporotic bony area may not have tolerated even an almost innocent twist or slip while the young severe case may have been involved in situations where great energy was generated.

There are, however, many mechanisms present in the body that

prevent injury to bone. The most striking factor is the energy absorbing ability of the muscles. According to recent investigations the quadriceps can absorb 100 times as much energy as the femur. These factors are of course important in the way muscles are taken care of in the clinical management of fractures. Another often overlooked fact is that neuro-muscular mechanisms are participating in energy absorption and limitation of overload.

On the other hand, the muscle contractions might contribute to the injury of the bone. The reactions from muscle forces are moments causing bending, shear and compression. These moments and forces add loads that should be superimposed on the external forces. In panic situations many muscle fibers can be fired subconsciously. Thus mechanisms that under certain conditions prevent injury to the bone, might, under other circumstances make the injury still more severe.

The soft tissues are not only damaged by direct forces during the event of an accident. A fracture in itself releases energy from the bone to the soft tissues. This situation leads to great tissue damage and may not be clinically evident until later during the recovery or when full activity is expected.

Bone may also change its mechanical tolerance due to inactivity or as a result of lack of material. Defects caused by holes due to nails or screws made by the surgeon in his attempt to introduce various kinds of internal fixations or when he is taking grafts to replace loss of bony material may also reduce the tolerance of bone.

Furthermore the need for rigid internal fixation may interfere with the normal mechanical stimulation that is involved in what might be considered biological bone healing and give rise to an osseous material that may not withstand greater demands at a later stage.

Ligaments and tendons are collagenous structures that possesses great strength in combination with little extensibility. They therefore play an important role in transmitting and resisting forces in most organs.

It is known that tendons and joint ligaments have only a limited stretch and have a breaking strength of about 5 - 10 kp/mm<sup>2</sup>. They show a sigmoid stress-strain relationship with a toe-shaped part in the beginning, i.e. initially relatively large deformation with small loads. There is also a viscous component which shows itself as load-relaxation or creep. There is an elastic aftereffect that is completed within five minutes, but some permanent deformation does occur after application of even moderate loads.

Trauma implies destructive external forces acting on living biological material. It is hoped that by identifying accidents

in a biomechanical context, a basis will be created for better clinical understanding of the injurious events and that prophylactic views may emerge.

PAPER NO. 20

THE IMPLICATIONS OF A  
CEREBELLAR MODEL FOR THE MAMMALIAN  
RESPONSE TO MOVEMENT

by

Thomas W. Calvert and Frank Meno  
Biotechnology Program and Electrical Engineering Departments  
Carnegie-Mellon University  
Pittsburgh, Pa. 15213

Abstract

A model for the cerebellum has been developed which shows that the cortex can be regarded as a spatial filter with interesting temporal characteristics. When this model is applied to the vestibulo-cerebellar system it predicts that the signal to the brain which results from acceleration applied to the skull has a trade-off between precision and time response. It appears that slowly changing accelerations will result in high precision information for the brain while a rapidly changing acceleration will result in lower precision information being sent to the brain.

This work was supported in part by Research Grant No. NB 08167 from the National Institute of Neurological Diseases and Stroke. Mr. Meno was supported by a pre-doctoral traineeship on Biomedical Engineering Training Grant No. GM 01455 from the National Institute of General Medical Sciences.

**PRECEDING PAGE BLANK**

### Introduction

When a mammal is subjected to linear or angular acceleration, it generally responds by moving its eyes and adjusting its position. The principal receptor involved is the vestibular apparatus which is known to be sensitive to linear and angular acceleration. It has been observed that the firing rate of the vestibular nerve is a linear function of angular acceleration [1]. However, the output of the cerebellum has an inhibitory effect on the vestibular nucleus.

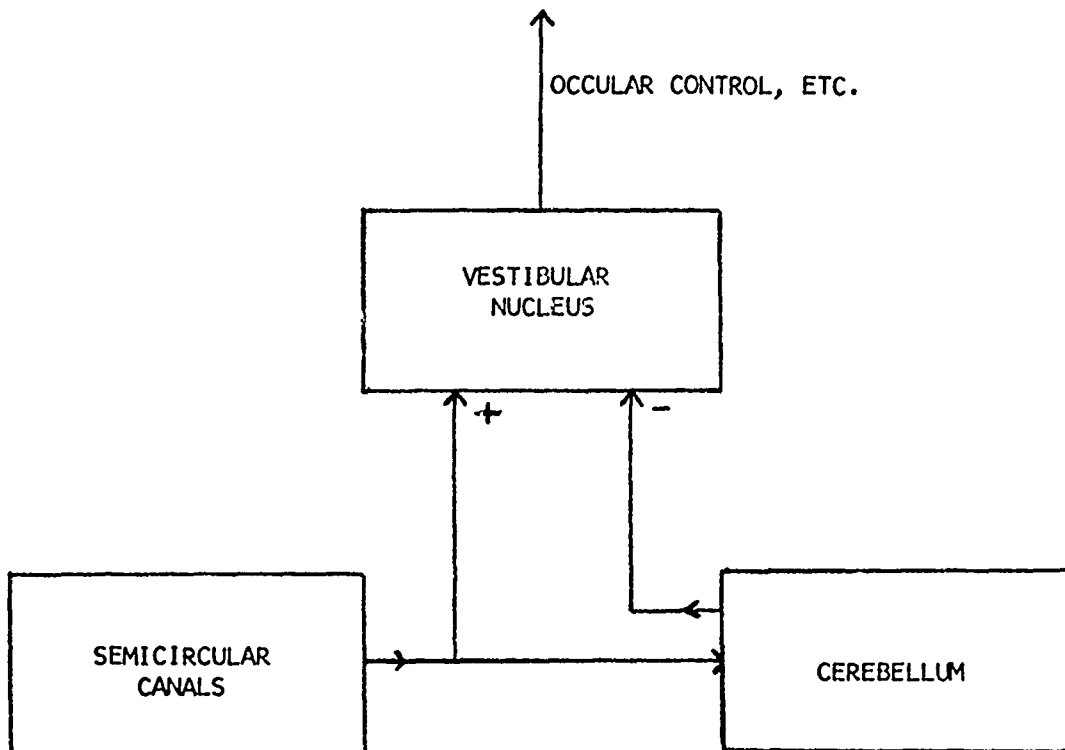


FIGURE 1. THE RELATIONSHIP OF THE CEREBELLUM TO THE VESTIBULAR SYSTEM

Thus, it appears that the output of the vestibular nucleus (which goes to higher centers controlling eye movements, etc.) depends on the difference between a direct signal from the vestibular apparatus and an indirect signal from the vestibular apparatus via the cerebellum. An obvious question concerns what useful role the cerebellum could play in this system. A model which we have recently developed for the cerebellum [2] suggests that the function may be to enhance the precision acceleration information from the vestibular apparatus when it is changing slowly in time. In contrast, acceleration information which is changing quickly may not be transmitted with the same precision.



### A Model of the Cerebellum

The cerebellum is a cortical structure behind and below the cerebrum. The statistics given in Table shown that this must be considered a major part of the central nervous system.

#### HUMAN CEREBELLUM

MEAN VOLUME	162 CM <sup>3</sup>
PERCENTAGE OF WHOLE BRAIN	10.6% (BY WEIGHT)
SURFACE AREA	1000 CM <sup>2</sup>
NUMBER OF PURKINJE CELLS	20 X 10 <sup>6</sup>
GRANULE CELLS	10 <sup>11</sup>
PARALLEL FIBER INPUTS TO ONE PURKINJE CELL	250,000

Table 1.

If the layer of convoluted tissue forming the cortex were unfolded, it would form a sheet approximately 10 cm wide by 100 cm long. There are two inputs, the mossy and climbing fibers and one output, the Purkinje fibers. It is not our purpose here to discuss the anatomy and physiology of the cerebellum since this is well covered elsewhere [3]. However, it is worth noting that the structure of the cerebellar cortex is extremely uniform and consists of the repetition of a few types of cells arranged in a remarkably precise geometrical pattern. Because of its geometry the cerebellum has been thoroughly studied both histologically and by physiological experiments. As a result, there is probably more information available on the cerebellum than for any comparable structure in the brain. In contrast to the detailed knowledge available on the connectivity and function of networks in the cerebellar cortex, relatively little is known about the sources of the inputs or the destinations of the outputs. Our aim has been to model the information processing tasks which this well-defined structure could perform and to use these models to suggest how the cerebellum is involved in the movement control system, etc.

It is known [3] that a mossy fiber input sets up patterns of excitation and inhibition in neighboring Purkinje cells in the cortex. The patterns are unusual in that they are anisotropic. Along a fold in the cortex (defined here to be the x-direction) a mossy fiber input sets up

a strip of excitation extending about 1.5 mm on either side of the input as shown in Figure 2a. In a transverse direction to the folds (defined as the y-direction) a small region of excitation about the input is surrounded by regions of inhibition as shown in Figure 2b.

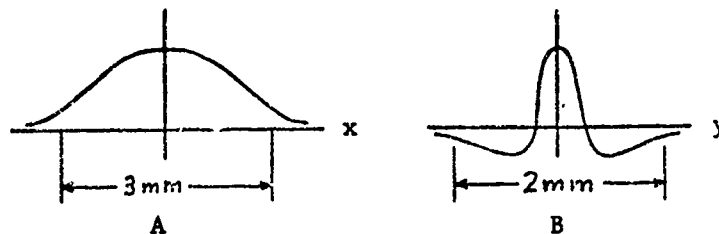


Figure 2. Patterns of excitation and inhibition on the cerebellar cortex.

The result is that an input sets up a "slot" of excitation surrounded by a region of inhibition. The pattern of excitation and inhibition for an input at the origin of our co-ordinate system can be described by

$$f(x,y) = k_1 e^{-x^2/2a^2} \cdot (k_2 e^{-y^2/2b^2} - k_3 e^{-y^2/2c^2}) \quad (1)$$

where  $k_1$ ,  $k_2$  and  $k_3$  are constants to be determined and  $a = 1.5$  mm,  $b = 0.2$  mm and  $c = 0.5$  mm for the cat. The spatial pattern of output on the Purkinje cell fibers can then be described by a continuous function  $p_m(x,y)$  which can be found for any input mossy fiber pattern in  $(x,y)$  from

$$p_m(x,y) = \int_{\text{all } x^1} \int_{\text{all } y^1} m(x^1, y^1) \cdot k_1 e^{-(x-x^1)^2/2a^2} (k_2 e^{-(y-y^1)^2/2b^2} - k_3 e^{-(y-y^1)^2/2c^2}) dx^1 dy^1 \quad (2)$$

The output due to climbing fiber inputs  $c(x,y)$  is quite simple, since for all practical purposes each climbing fiber synapses with only one Purkinje cell and thus

$$p_c(x,y) = k_4 c(x,y) \quad (3)$$

The two inputs can be combined to give a total Purkinje cell activity  $p(x,y)$ :-

$$p(x,y) = p_m(x,y) + p_c(x,y) \quad (4)$$

So far our development has ignored temporal effects. Experiments have shown that an increase in mossy or climbing fiber input causes an increase in Purkinje cell output within 5-10 msec. and that the excitatory influence of the climbing fibers is dissipated within 10 msec. These effects will all be regarded as instantaneous since they are small compared with the time required to dissipate the excitatory or inhibitory effects of mossy fibers on the Purkinje cells. Experimental data indicates that a short pulse of mossy fiber input causes an excitatory effect on the Purkinje cell which decays with a time constant of 20 msec and an inhibitory effect which decays with a time constant of 100 msec. These can be accounted for in our model by the following equations derived from (2), (3) and (4) above:-

$$p(x,y,t) = K \int_{x^1}^{\text{all}} \int_{y^1}^{\text{all}} c(x^1, y^1, t) \delta(x-x^1, y-y^1) dx^1 dy^1 \\ + K \int_{x^1}^{\text{all}} \int_{y^1}^{\text{all}} \int_{-\infty}^t m(x^1, y^1, \tau) e^{-(x-x^1)^2/2a^2} \\ \cdot \left[ 2.5 e^{-(t-\tau)/T_1} e^{-(y-y^1)^2/2b^2} - e^{-(t-\tau)/T_2} e^{-(y-y^1)^2/2c^2} \right] dx^1 dy^1 d\tau \quad (5)$$

where K is a scale constant,

$$a = 1.5 \text{ mm}, b = 0.2 \text{ mm}, c = 0.5 \text{ mm}$$

$$T_1 = 20 \text{ msec and } T_2 = 100 \text{ msec}.$$

The convolution integrals of equation (5) can be written more simply by applying Fourier transformations. A typical transform pair is given by:-

$$P(X,Y,\omega) = \int_{-\infty}^{\infty} \int_{-\infty}^{\infty} \int_{-\infty}^{\infty} p(x,y,t) e^{-j(xX+yY+\omega t)} dx dy dt \quad (6)$$

where linear extension  $x \rightarrow$  spatial frequency  $X$  in cycles/mm  
linear extension  $y \rightarrow$  spatial frequency  $Y$  in cycles/mm  
time  $t \rightarrow$  temporal frequency  $\omega$  in radians/sec or  $f$  in cycles/sec  
(or Hertz) with  $\omega = 2\pi f$ .

Then (5) gives:

$$P(X,Y,\omega) = K.C(X,Y,\omega) + K.M(X,Y,\omega) \pi a e^{-a^2 X^2/2} \left[ \frac{2.5 b e^{-b^2 Y^2/2}}{j\omega + \frac{1}{T_1}} - \frac{c e^{-c^2 Y^2/2}}{j\omega + \frac{1}{T_2}} \right] \quad (7)$$

This is a convenient tool to calculate the response of the cerebellar cortex for any spatio-temporal pattern of inputs on the climbing and mossy fibers. It will be recognized that we are treating the cortex as a spatial filter (but also with temporal characteristics) and that these methods of analysis are well known in optics. Indeed, similar models have been used by Mach for the eye [4] and by Huggins and Licklider for the ear [5].

Some insight into the significance of this model can be obtained by obtaining the transfer function  $\frac{P}{M}(X,Y,\omega)$  between mossy fibers inputs and Purkinje outputs.

$$\frac{P}{M}(X,Y,\omega) = K \pi a e^{-a^2 X^2/2} \left[ \frac{2.5 b e^{-b^2 Y^2/2}}{j\omega + \frac{1}{T_1}} - \frac{c e^{-c^2 Y^2/2}}{j\omega + \frac{1}{T_2}} \right] \quad (8)$$

A plot of  $\left| \frac{P}{M} \right|$  in decibels versus  $Y$  with  $f = \frac{\omega}{2\pi}$  as a parameter is shown in Figure 3. This shows that on the  $y$ -axis, the cortex acts as a spatial filter which enhances high spatial frequencies increasingly as temporal frequency rises.

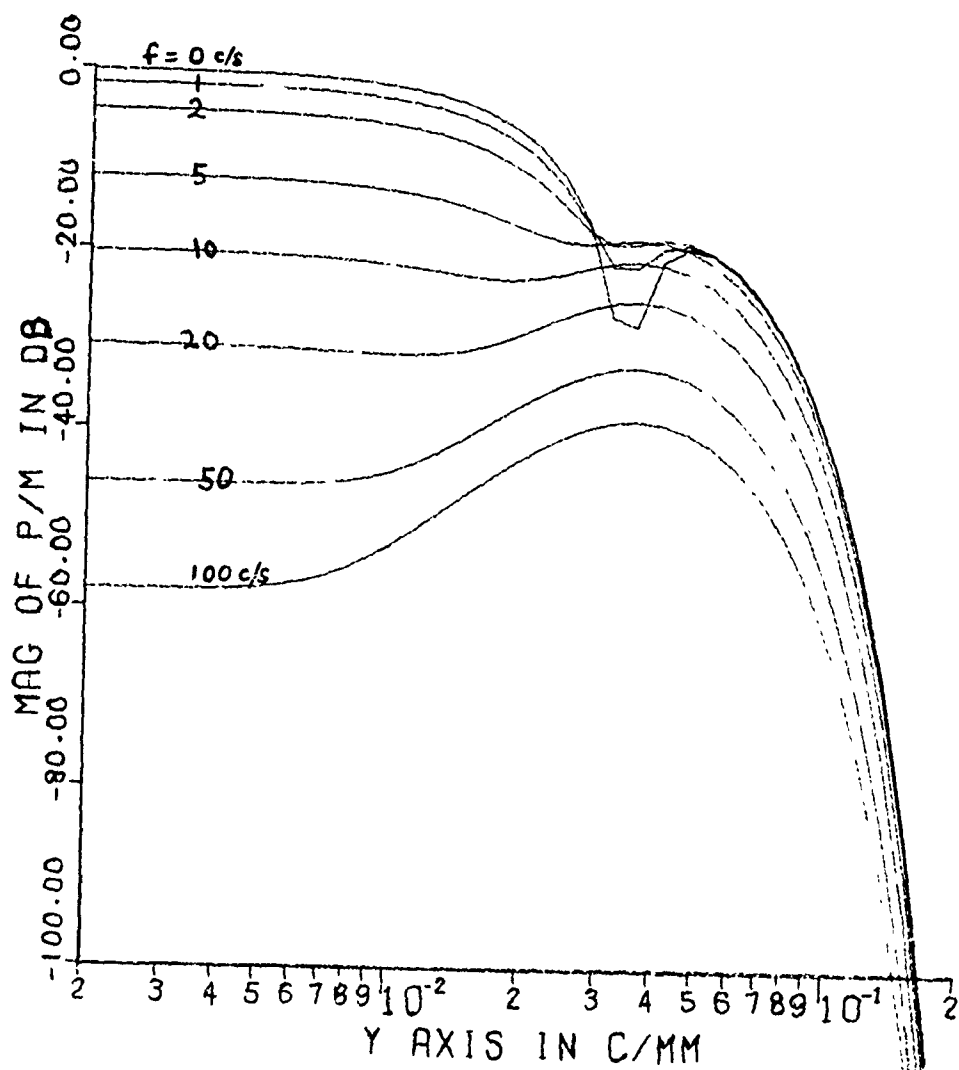


Figure 3. The spatial frequency response of the cerebellar cortex with temporal frequency as a parameter.

### Vestibular-Cerebellar Circuitry

The connections between the vestibular apparatus, the vestibular nucleus and the cerebellum are shown in Figure 1. In contrast to the detailed knowledge of the cerebellar circuitry, relatively little is known about the vestibular nucleus. It is known that the inhibitory Purkinje output  $p(x,y,t)$  from the cerebellum tends to decrease the vestibular output  $v(t)$ . If it is possible to assume some kind of congruent mapping from the vestibular sensors and from the cerebellum to the vestibular nucleus, then it might be possible to represent this in one spatial dimension and time as:-

$$v(y,t) = K_m \cdot M(y,t) - K_p \cdot p(y,t) \quad (9)$$

It must be emphasized that compared to our equations (1)-(8) for the cerebellum, equation (9) represents rather wild speculation and must be treated with caution. If the cerebellar model from (8) is substituted into (9) we obtain:-

$$\frac{V}{M}(Y,\omega) = K_m \left[ 1 - \frac{K_p}{K_m} \cdot \frac{P}{M}(Y,\omega) \right] M(Y,\omega) \quad (10)$$

A plot of  $\frac{V}{M}(Y,\omega)$  is shown in Figure 4 where the magnitude of the transfer function is plotted against  $Y$  with  $f = \frac{\omega}{2\pi}$  as a parameter. ( $K_p$  and  $K_m$  have been set equal to unity). This shows a spatial filter which enhances high spatial frequencies most strongly at low temporal frequencies.

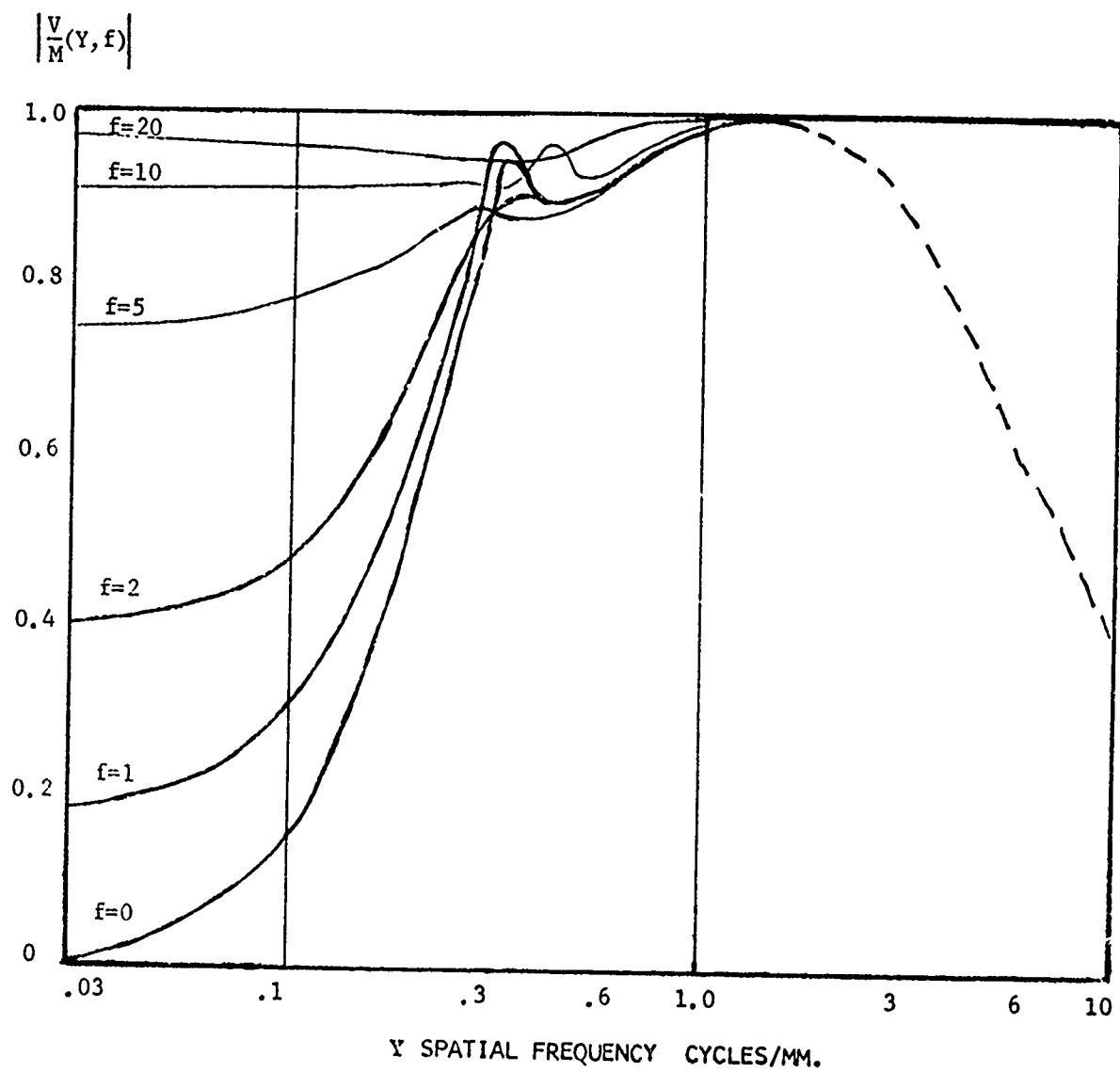


Figure 4. The form of the spatial frequency response of the vestibular-cerebellar system.

### The Implications of the Model

It appears from the development above that the cerebellum serves to enhance the high spatial frequencies in the information from the vestibular organ when the temporal rate of change of the information is low. This implication is based on the assumptions that

- (a) the cerebellar model is valid, and
- (b) congruency exists in mapping to the vestibular nucleus.

We believe that (a) is a good assumption, but that (b) is probably not completely correct. However, whatever type of mapping exists, the cerebellar effect will be most marked at low temporal frequencies.

It remains to examine the meaning of enhancement of high spatial frequencies as applied to nerve fibers originating in a vestibular organ. A semicircular canal is shown in Figure 5. When the skull is subjected to angular acceleration, the fluid in the canal causes the cupula to deflect and nerve cells to discharge.

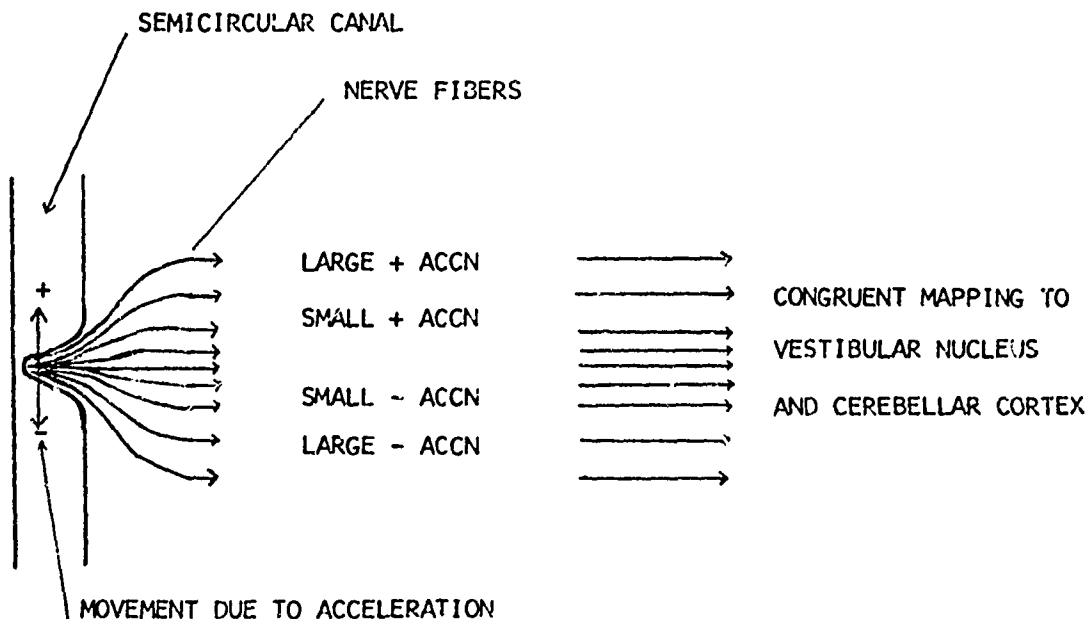


Figure 5. The mapping of nerve fibers from the semicircular canals.



It is known [1] that some cells respond to acceleration in one direction, some to acceleration in the other direction and some to acceleration in both directions. It seems reasonable to assume that some cells are more sensitive to small accelerations and some to large accelerations. Thus, an ensemble of fibers from a semicircular canal has a spatial pattern which changes with the direction and magnitude of the acceleration. It is clear that a loss of definition, or spatial frequencies corresponds to a loss of precision and that an enhancement of high spatial frequencies will tend to maintain precision.

### Conclusion

As a result of our identification of high spatial frequency response with precision, and of our model giving a general form for the spatial frequency response in the vestibulo-cerebellar system, we can draw some conclusions. It appears that if the acceleration applied to the skull is changing slowly (say at a rate below 1 cycles/sec) the information fed to the brain will be of high precision and will allow accurate compensation for this movement. If, however, the acceleration has high temporal frequency components (as in any sudden change) then precision will be lost, but the brain will still receive a signal indicating that there has been a change in acceleration.

This prediction of a trade-off between precision and time response is intuitively satisfying. It implies that given time, the brain can compute and implement accurate compensatory movement. When a sudden change of acceleration occurs, the brain is given low precision information, which is probably all that it can usefully utilize in the short time available.

### References

1. W. Precht and R. Llinas, "Comparative aspects of vestibular input to the cerebellum," in Neurobiology of Cerebellar Evolution and Development, ed., R. Llinas, American Medical Association, 1969.
2. T. W. Calvert and F. Meno, "Models of information processing in the cerebellum," Proceedings of 1970 IEEE Systems Science and Cybernetics Conference, pp. 39-47, October, 1970.
3. J. C. Eccles, M. Ito and J. Szentagothai, The Cerebellum as a Neuronal Machine, New York: Springer-Verlag, 1962.
4. F. Ratliff, Mach Bands: Quantitative Studies on Neural Networks in the Retina, San Francisco: Holden-Day, 1965.
5. W. H. Huggins and J. L. R. Licklider, "Place mechanism of auditory frequency analytics," J. Acoust. Soc. Am., Vol. 23, pp. 290-299, 1951.

THE EFFECT OF INITIAL CURVATURE ON THE DYNAMIC RESPONSE  
OF THE SPINE TO AXIAL ACCELERATION

T.F. Li, S.H. Advani, and Y-C. Lee

Department of Theoretical and Applied Mechanics  
West Virginia University, Morgantown, West Virginia

ABSTRACT

A majority of the studies on the dynamic response of the human torso have considered uni-axial models wherein the initial curvature of the spine is ignored. A detailed discrete parameter vertebral response model incorporating the variable geometry of the spine and subjected to pilot ejection simulated impact conditions has been recently investigated by Orne and Liu. In this work, a simple continuum representation of the spine is formulated and the resulting boundary value problem is solved for the axial and lateral (bending) dynamic response. The assumed model is a constant cross-section, sinusoidally curved, elastic beam with an end mass subjected to an axial acceleration at the other end. The effects of transverse shear and rotational inertia are ignored in the model. The equation governing axial displacement is a non-homogeneous wave equation subjected to non-homogeneous boundary conditions. The governing approximate equation for the lateral deflection is a non-linear second order differential equation with variable coefficients. Short time solutions for these equations are obtained to demonstrate the effect of initial curvature on the spinal dynamic response. Numerical results indicate that the dynamic bending stress is significant in comparison to the axial dynamic stress.

# LIST OF SYMBOLS

Dimensional Quantity	Physical interpretation
A	effective spinal cross-sectional area
$c = \sqrt{E/\mu}$	compressional wave speed
E	instantaneous Young's modulus
$I = Ar^2$	principal moment of inertia
M	concentrated head and upper torso mass
r	effective radius of gyration about spinal bending axis
$\mu$	lumped effective torso and spine mass density

Non-dimensional Quantity	To convert to dimensional form ( $\bar{\quad}$ ) multiply by	Physical Interpretation
a	$c^2/r$	forcing acceleration
L	r	effective spinal length
P	AE	axial force
t	$r/c$	time
u	r	axial column displacement
x	r	axial co-ordinate
$y(x,t)$	r	total column bending displacement
$Y(t)$	r	time function
$y_0(x)$	r	initial column bending displacement
$Y_0$	r	maximum column eccentricity
$\lambda = M/\mu Ar = \bar{\lambda} \bar{L}$		mass parameter

## INTRODUCTION

Crew member protection from hostile aerospace environments is a biomedical engineering problem of grave concern. Rheological and structural response models of human body system components have received particular attention towards defining limiting injury thresholds associated with the governing mechanism(s) of injury. Of special interest is the modelling of the vertebral column response to transient headward accelerations along the spinal axis (+ G<sub>z</sub> ejection mode). Reported data on vertebral fractures resulting from pilot ejection reveals that a majority of these fractures occur between T8 and L1. Several discrete parameter and continuum models of the human torso ranging in complexity and scope have established the desirability of analytical representation of the response variable defining injury. A review of pertinent investigations can be found in studies by von Gierke [1], Roberts, et al [2], and Orne and Liu [3]. Selected contributions are indicated below.

Uniaxial spring mass characterizations of the human torso under impact have been examined by Latham [4], Payne [5], Stech [6], and others [7]. A more refined model described by an eight degree of freedom damped spring mass system has been studied by Toth [8]. Recently, Orne and Liu [3] have investigated a detailed multi-mass representation of the torso incorporating the effects of spinal disk axial, bending, and shear deformations in addition to the variable vertebral geometry. The discrete parameter models involve the (simultaneous) solution of ordinary differential equation(s) formulated from the conditions of dynamic equilibrium. Research on continuum descriptions of the torso includes one dimensional wave propagation models considered by Hess and Lombard [9], Liu and Murray [10], Liu [11], Terry and Roberts [12], and Murray and Tayler [13]. These uniaxial continuum models vary in their degree of sophistication depending on the boundary conditions (head mass), and constitutive relations (linear/non-linear, elastic/visco-elastic). It is noteworthy that experimental results and analytical solutions comparing the rectangular pulse response of an elastic rod-mass system with that of an equivalent spring mass approximation have been obtained by Seigel and Waser [14]. Their work indicates that the rod-mass system experiences "significantly larger" forces for short pulse duration and/or end mass magnitude.

In this paper, we consider a simplified continuum dynamic model representation of the curved spine with the torso mass uniformly distributed along its length. The idealized model is a constant cross-section, sinusoidally curved, elastic column with end mass subjected to a uniform acceleration at the other end. The influence of transverse shear and rotational inertia is ignored in the model. In addition, the effects of moments arising from the head-torso mass eccentricity and the external support-restraint system interaction are not included

in the analysis. The bending stress resulting from these external force and moment intensities can be superposed on the selected basic model under study. Experimental work by Vulcan, King and Nakamura [15] indicates the relative importance of support-restraint systems and head-torso rotation on bending stresses in the vertebral beam-column. The motivation for the assumed model stems from the results of small animal + G<sub>z</sub> impact experiments conducted with flat back and contoured support-restraint systems [16,17]. The large incidence of vertebral fractures and paralysis for the flat back system evidently supports the consideration of initial spinal curvature.

As a problem in theoretical mechanics, the non-linear dynamic response of a simply supported column with sinusoidal initial curvature and a constant velocity forcing function at one end has been studied by Hoff [18], Sevin [19], and Dym and Rasmussen [20]. A comprehensive study of the curved dynamic beam response under constant velocity end loading with combinations of simply supported and clamped boundary conditions has been conducted by Archer and Das [21]. They demonstrate an improved numerical stability of their finite difference solution when the effects of beam transverse shear and rotational inertia are included. Here, the equations and associated boundary conditions governing the axial and bending spinal column motion are formulated and uncoupled. The non-homogeneous wave equation for the axial motion is solved and an approximate equation for the bending response time variable is obtained by using the Ritz-Galerkin procedure. Short time solutions for the spinal response are obtained by the Runge-Kutta method to demonstrate the importance of initial curvature in considering the spinal column response.

#### FORMULATION OF THE BOUNDARY VALUE PROBLEM

The equations governing motion of the basic spinal model (Fig. 1) can be derived by use of Hamilton's principle. The Lagrangian, using this variational energy formulation, considers the strain and kinetic energies of the column and the work done by the axial force. The non-dimensional equations, in terms of the coupled generalized co-ordinates  $y(x,t)$  and  $u(x,t)$  with respect to an inertially defined co-ordinate system are:

- (i) An equation governing the bending motion of the column

$$y'''' + (P'y' + Py'') + \ddot{y} = y_0'''' \quad (1)$$

- (ii) An equation governing compressive motion of the column

$$-P' = \ddot{u} \quad (2)$$

The non-dimensional axial force  $P(x,t)$  in equations (1) and (2) is defined by

$$P = - \left\{ u' + \frac{1}{2} \left[ (y')^2 - (y_0')^2 \right] \right\} \quad (3)$$

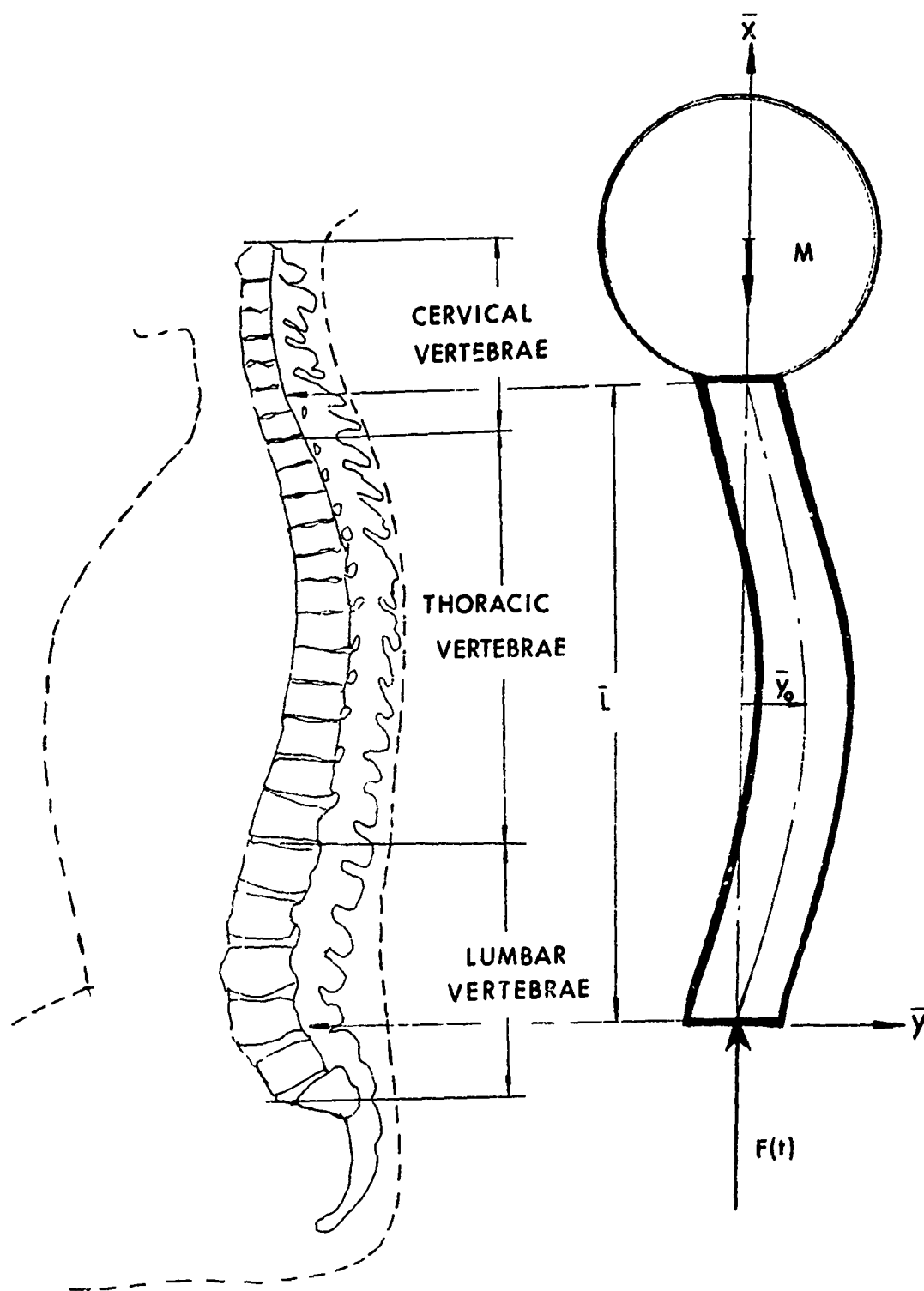


FIG. 1 Vertebral Response Model

In the preceding equations primes and dots denote differentiation with respect to the non-dimensionalized space and time variables respectively. The influence of column transverse shear and column, torso-head rotational inertia is not considered in these equations. A more general representation of equations (1), (2), and (3) is currently under study at Technology Incorporated using the finite difference method [22].

The boundary and initial conditions for the assumed model are

$$u(0,t) = \frac{1}{2} at^2, \quad P(L,t) = \lambda \ddot{u}(L,t) \quad (4a)$$

$$y(0,t) = y(L,t) = y'(0,t) = y'(L,t) = 0 \quad (4b)$$

$$u(x,0) = \dot{u}(x,0) = \dot{y}(x,0) = 0, \quad \text{and } y(x,0) = y_0(x) \quad (4c)$$

#### AXIAL DISPLACEMENT RESPONSE SOLUTION

Equations (2) and (3) can be re-written in the form

$$\ddot{u} - u'' = f'(x,t) \quad (5)$$

$$\text{with } f(x,t) = \frac{1}{2} \left[ (y')^2 - (y_0')^2 \right].$$

The solution to equation (5) can be obtained by considering (i) a homogeneous wave equation subjected to non-homogeneous boundary conditions and (ii) a non-homogeneous wave equation with homogeneous boundary conditions. We therefore write

$$u = u_H + u_P \quad (6)$$

where  $u_H$  satisfies the equation

$$\ddot{u}_H - u_H'' = 0 \quad (7)$$

with the boundary and initial conditions

$$\begin{aligned} u_H(0,t) &= \frac{1}{2} at^2, & u_H'(L,t) &= -\lambda \ddot{u}_H(L,t) - f(L,t), & u_H(x,0) \\ & & & & = \dot{u}_H(x,0) = 0 \end{aligned}$$

and  $u_P$  satisfies the equation

$$\ddot{u}_P - u_P'' = f'(x,t) \quad (8)$$

with homogeneous boundary and initial conditions

$$u_P(0,t) = u_P'(L,t) = u_P(x,0) = \dot{u}_P(x,0) = 0.$$

We obtain the solution to equation (7) in a manner similar to that of Liu and Murray [10] with the modification expressed by the term  $f(L,t)$  in the boundary conditions. The resulting solution after use of the Laplace transform method is



$$\begin{aligned}
u_H(x,t) = & \frac{a}{2} \left\{ (t-x)^2 H(t-x) + \sum_{n=1}^{\infty} \left[ (t-2nL-x)^2 H(t-2nL-x) \right. \right. \\
& \left. \left. - (t-2nL+x)^2 H(t-2nL+x) \right] + \sum_{n=1}^{\infty} \sum_{m=1}^n (-1)^m \frac{2^m \lambda^{-n}}{(m-1)!} n C_m \cdot \right. \\
& \cdot \int_0^t \left[ (\tau-2nL-x)^2 H(\tau-2nL-x) - (\tau-2nL+x)^2 H(\tau-2nL+x) \right] \cdot \\
& \left. \cdot (t-\tau)^{m-1} e^{-(t-\tau)/\lambda} d\tau \right\} \\
& - \sum_{n=1}^{\infty} \int_0^t (-1)^n \left[ f(L, \tau+x-(2n+1)L) - f(L, \tau-x-(2n+1)L) \right] \cdot \\
& \cdot \left\{ L^{-1} \left[ \frac{\varepsilon^n(s)}{s} \right] - \lambda L^{-1} \left[ \frac{\varepsilon^n(s)}{1+\lambda s} \right] \right\} d\tau \quad (9)
\end{aligned}$$

where  $L^{-1}$  denotes the inverse Laplace transform and

$$\varepsilon(s) = (1 - \lambda s)/(1 + \lambda s) \quad .$$

The solution to the non-homogeneous equation (8) can be obtained in the form

$$\begin{aligned}
u_P = & \sum_{n=1,3,5}^{\infty} \frac{4}{n\pi} \sin \frac{n\pi x}{2L} \int_0^t \left\{ f(L, \tau) \sin \frac{n\pi}{2} \right. \\
& \left. - \frac{n\pi}{2L} \int_0^L f(x, \tau) \cos \frac{n\pi x}{2L} dx \right\} \sin \frac{n\pi}{2L} (t - \tau) d\tau \quad (10)
\end{aligned}$$

#### SOLUTION FOR THE BENDING RESPONSE

Equation (1) governing the column lateral response  $y(x,t)$  is simplified by selecting the initial column deviation  $y_0(x)$  from the vertical axis to be sinusoidal. Additionally, in view of boundary conditions (4b) we assume that the column responds in the first spatial mode. We therefore take

$$y(x,0) = y_0(x) = Y_0 \sin (\pi x/L) \quad (11)$$

$$y(x,t) = Y(t) \sin (\pi x/L); \quad (12)$$

Substituting equations (3), (6), (9), (10), (11) and (12) in equation (1) and using the Ritz-Galerkin averaging method, we obtain after considerable simplification a non-linear, variable coefficient, second order differential equation governing  $Y(t)$ . It is

$$\ddot{Y}(t) + \left(\frac{\pi}{L}\right)^4 \left[ (Y - Y_0) + \frac{3}{8} (Y^2 - Y_0^2) Y + \left(\frac{L}{\pi}\right)^4 \cdot \frac{2}{L} A(t) Y - \frac{64}{\pi L} Y \sum_{n=1,3}^{\infty} \frac{n^2 - 4}{n(n^2 - 16)^2} G_n(t) \right] = 0 \quad (13)$$

where

$$A(t) = -\left(\frac{\pi}{L}\right)^2 \int_0^L P_H \sin^2 \frac{\pi x}{L} dx + \frac{\pi}{L} \int_0^L P_H' \sin \frac{\pi x}{L} \cos \frac{\pi x}{L} dx$$

$$G_n(t) = \int_0^t (Y^2 - Y_0^2) \sin \frac{n\pi}{2L} (t - \tau) d\tau$$

and  $P_H$  is the axial force derived from the homogeneous wave equation.

Asymptotic solutions to second order non-linear differential equations with variable coefficients of the type designated by equation (13) have been investigated by Kuzmak (23). However, these solutions are valid for slowly varying time coefficients. A power series solution to (13), with physical constants represented by spinal constitutive and geometric properties and a forcing acceleration ( $\ddot{x}$ ) of 20 G, exhibited numerical instability following a time duration of 15 milliseconds. An improved technique of solution using the Runge-Kutta method in conjunction with an iterative procedure was finally used to yield the transient model response.

#### ASSUMED SPINAL CONSTITUTIVE AND GEOMETRIC PROPERTIES

An extensive literature review revealed that available data is inadequate for characterizing the spinal response in the short time domain. Data surveyed included results on spinal compressive wave propagation experiments and analysis [6,7,22], natural axial frequency data on spinal response [1,7,24], and compression and bending tests on human vertebrae and disks [22,25]. The wide range of reported results is evidenced by comparing (i) a calculated compressive wave velocity of 100 ft/sec obtained by Hess and Lombard [9] versus an experimentally determined spinal cadaveric velocity of 191 ft/sec [22] and (ii) a first resonance axial frequency of around 10 Hz for the spine-upper torso mass [1] as compared to 44 Hz indicated in another study [7]. The static compressive properties of vertebrae and disks are well documented in the literature. Experiments conducted at Technology Incorporated [22] on the compressive response of human vertebrae and disks, using linear visco-elastic theory, indicate that "the average initial elastic modulus" for sets of one bone

plus one disk is 7428 psi. The corresponding reported values for vertebrae and disks are 10,029 psi and 2552 psi respectively [22]. Preliminary results from static moment-curvature tests on human cadaveric spines reveal that its flexural rigidity  $EI$  ranges from  $6 \times 10^3$  to  $10^4$  lb-in<sup>2</sup> [25].

Based on the data and literature reported in the preceding paragraph, a compromised set of constitutive and geometric constants was selected. The values chosen for the assumed model are:

Effective spinal length (L-4 to Cervical Vertebrae)  $\bar{L} = 18$  in

Effective cross-section of area  $A = 1.8$  in<sup>2</sup>

Effective radius of gyration about bending axis  $r = 0.527$  in

Spinal column eccentricity  $\bar{Y}_0 = 2$  in

Head and upper torso concentrated mass  $M = 0.055$  lb sec<sup>2</sup>/in

Non-dimensional mass parameter  $\bar{\lambda} = M/\mu A \bar{L} = 0.33$

Instantaneous elastic modulus  $E = 10,000$  psi

The undamped compressive wave velocity and axial spinal frequency with the above data are 120 ft/sec and 13.5 Hz respectively. The spinal cross-sectional area and radius of inertia take into account the added contribution of the supporting vertebral structure. In addition, based on the "hardening" strain rate characteristics of most biological materials, the assumed instantaneous model elastic modulus is chosen to be larger than reported static values.

#### DISCUSSION AND NUMERICAL RESULTS

Before proceeding to illustrate the results of the numerical computations, a discussion of the assumed model and its inherent limitations will be presented. The selection of a simple half sine wave for describing the initial spinal configuration deserves special mention. Based on geometric data, the sine wave adequately defines the spinal curvature from the cervical vertebrae to the upper lumbar region. The results of Orne and Liu [3] demonstrate a vanishing bending moment for durations up to 90 milliseconds in the vicinity of the L-3 region, thereby justifying the assumed deflection form. In addition, their results indicate that the axial force remains relatively constant in the lumbar region for a specified instant. The continuum model, being an initial attempt towards demonstrating the effect of spinal curvature, neither includes the bending moment contribution of the head-torso mass eccentricities nor the influence of the support-restraint system interaction. These effects can be introduced by refining the model to a beam-column subjected to external distributed dynamic moments and lateral forces (incorporated as a rotational inertia term  $\mu J_0 y_{xxxx}$  and external forcing term  $q(x,t)$  in the beam equation). The effective mass terms participating in the bending and axial modes would also require modification in this model.

Numerical work was performed on an IBM 360, Model 75 computer. The Runge-Kutta routine was combined with an iterative procedure to compute

the lateral deflection. Figure 2 illustrates the mid-span lateral deflection time history computed from equation (13) for acceleration loadings of  $a = 10 \text{ G}$  and  $20 \text{ G}$ . The corresponding total compressive axial displacement is also indicated in this figure. This axial displacement is a superposition of solutions obtained from (i) a homogeneous wave equation (7) with non-homogeneous boundary and initial conditions and (ii) a wave equation (8) with a forcing acceleration term and homogeneous boundary and initial conditions. Since the support-restraint reactions are ignored in the analysis, the results are assumed to be relevant up to a time duration of 40 milliseconds. Figure 3 compares the axial force computed for the uniaxial and axial-bending response models at the load and head ends. The significantly reduced dynamic response factor at the forcing end results from the curvature terms. The head end axial force is also reduced and tends to be tensile for larger elapsed times. The maximum compressive fiber stress time history at the anterior mid-span obtained from the relation  $\sigma = -(P/A + Md/I)$  is shown in Fig. 4. The assumed initial deflection form presupposes a maximum bending contribution at the mid-span (T-8 or T-9) which increases with time in the interval considered. This is in contrast with results which indicate a reversal of sign in the bending moment around this neighborhood [3]. The bending moment stress contribution due to the initial curvature is about 30 percent at  $t = 40$  milliseconds. This effect would be further enhanced if the moments arising from the rotation of the head and movement of the torso were considered. The instantaneous elastic response solutions in the figures represent upper bounds for the visco-elastic vertebral model. However, the early time response for the elastic and damped models is almost identical.

A comprehensive discussion of the mechanisms associated with vertebral injury has been presented by Kazarian, et al [26]. Among these the anterior lip fracture, the compression fracture, and the hyperextension fracture are of particular interest. Coupled with these findings is the reported constitutive experimental data [27,28,29]. In the tests conducted by Crocker and Higgins [29], the intervertebral disks exhibited "hardening" stiffness properties with increasing strain rate. However, their maximum compressive velocity rate of  $4 \text{ mm/sec}$  is well below the corresponding rate encountered in vertebral ejection. Based on the general trend of available experimental results and the model analysis represented by Figs. 2,3, and 4 the mechanisms of injury indicated above lend themselves to analytical definition. For example, data on anterior lip, compression and hyperextension fractures can be correlated with computed dynamic values of compressive stress, tensile stress (due to excessive bending moment) and/or bending and axial displacements. The spinous process fracture with displacement of the pedicle may be interpreted by incorporating the effects of transverse shear in the governing equation.

#### CONCLUSIONS AND RECOMMENDATIONS

The geometrically non-linear, continuum model analyzed here answers some basic questions pertinent to the interpretation and prediction of vertebral column injury resulting from dynamic axial loads. Specifically, the initial spinal curvature introduces a coupled axial-lateral response.

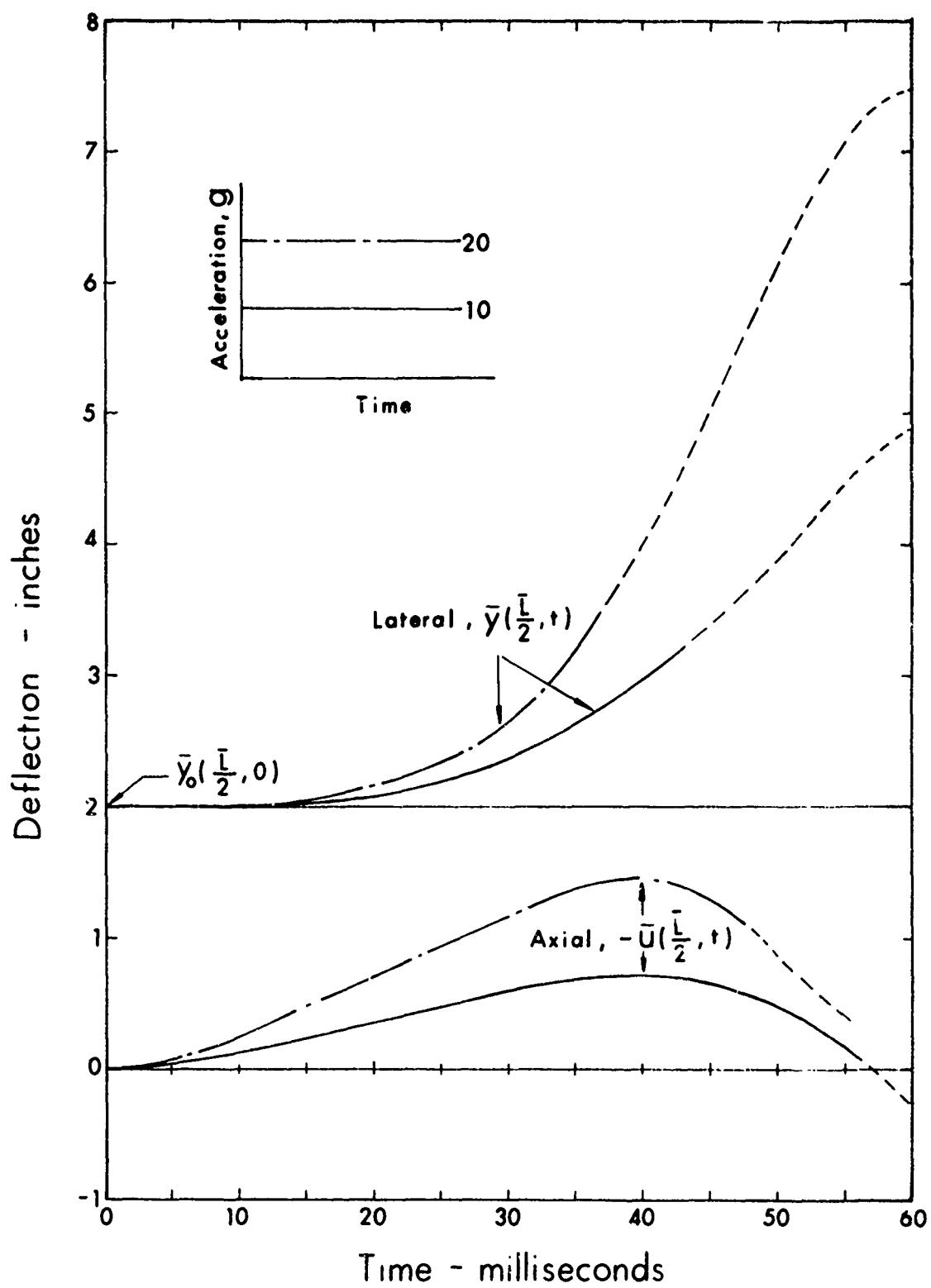


FIG. 2 Mid-span Deflections

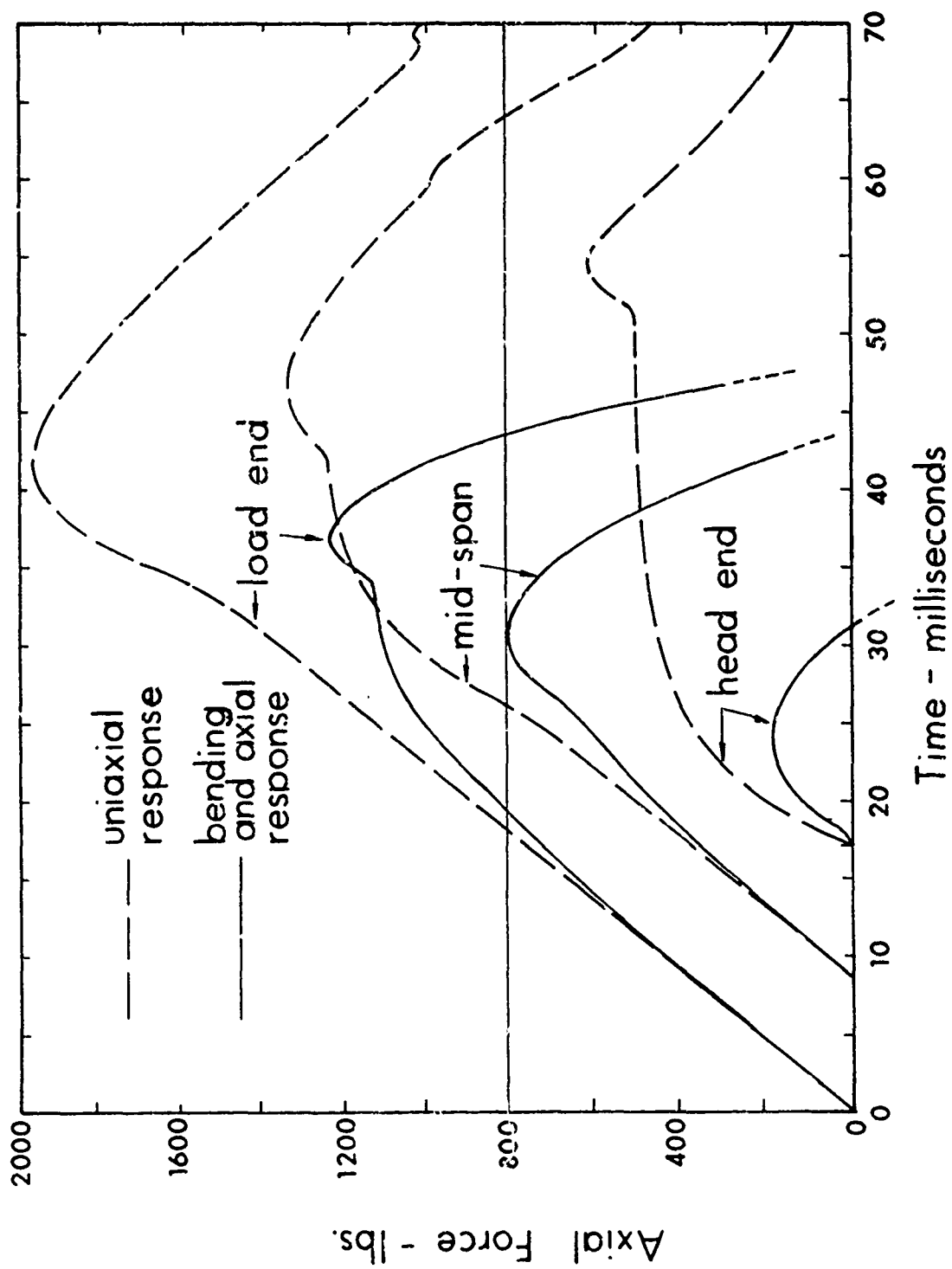


FIG. 3 Axial Force vs. Time, 109

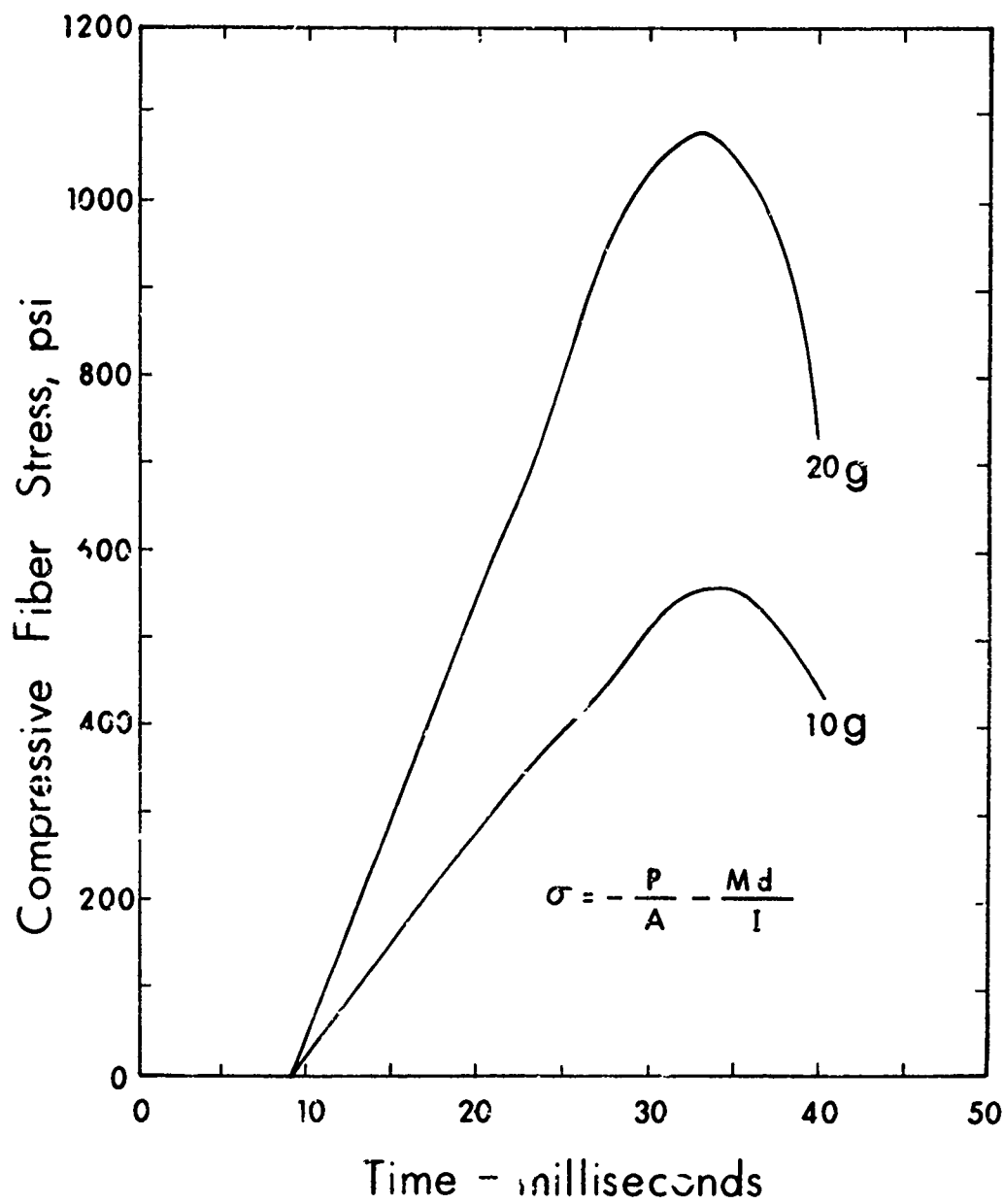


FIG. 4 Mid-span Maximum Fiber Stress

The axial force and stress distribution are significantly influenced by the bending motion response as a result of the mechanical energy distribution between the axial and bending modes.

It is recommended that spinal disk constitutive equations valid in the impact range be determined from high strain rate compressive tests. Finally, it is suggested that more complex continuum models be formulated and the resulting boundary value problem numerically studied to examine the detailed spinal stress response, the torso surface wave response and the associated mechanical energies producing injury.

---

#### Acknowledgements

A portion of this research was conducted by the first author for a Master's degree in Theoretical and Applied Mechanics at West Virginia University. The support by NASA under sustaining grant NGL 49-001-001 is gratefully acknowledged. Computer services were made available by the Computer Center of West Virginia University.



# REFERENCES

- [1] Von Gierke, H.E., "Biodynamic Response of the Human Body," Applied Mechanics Reviews, Vol. 17, No. 4, 1964.
- [2] Roberts, V.L., Stech, E.L., and Terry, C.T., "Review of Mathematical Models Which Describe Human Response to Acceleration," ASME Paper No. 66-WA/BHF-13.
- [3] Orne, D., and Liu, Y.K., "A Mathematical Model of Spinal Response to Impact," ASME Paper No. 70-BHF-1.
- [4] Latham, F., "A Study of Body Ballistics: Seat Ejection," Proceedings of Royal Society, Vol. 147, 1957.
- [5] Payne, P., "The Dynamics of Human Restraint Systems," Impact Acceleration Stress Symposium, National Academy of Sciences - National Research Council Publication 977, 1962.
- [6] Stech, E.L., "Calculation of Human Spinal Frequency from Cadaver Data - a Comparison with Tests on Live Human Subjects," Report 122-100, Frost Engineering Development Corporation, 1963.
- [7] Anon, "A Study of the Dynamic Model Technique in the Analysis of Human Tolerance to Acceleration," NASA TND-2645, 1965.
- [8] Toth, R., "Multiple Degree of Freedom Non-linear Spinal Model," 19th ACEMB, San Francisco, California, 1967.
- [9] Hess, J.L., and Lombard, C.F., "Theoretical Investigations of Dynamic Response of Man to High Vertical Accelerations," J. Aviation Medicine, Vol. 29, 1958.
- [10] Liu, Y.K., and Murray, J.D., "A Theoretical Study of the Effect of Impulse on the Human Torso," Proceedings ASME Symposium in Biomechanics, 1966.
- [11] Liu, Y.K., "Towards a Stress Criterion of Injury - An Example in Caudocephal Acceleration," J. Biomechanics, Vol. 1, 1968.
- [12] Terry, C.T., and Roberts, V.L., "A Viscoelastic Model of the Human Spine Subjected to  $+G_z$  Accelerations," J. Biomechanics, Vol. 1, 1968.
- [13] Murray, J.D., and Tayler, B.A., "An Asymptotic Solution of a Class of Non-linear Wave Equations: A Model for the Human Torso Under Impulsive Stress," SIAM Journal Applied Mathematics, Vol. 18, 1970.

# REFERENCES (Cont.)

- [14] Seigal, A.E., and Waser, R.H., "On the Use of a Spring Mass to Approximate a Bar Mass System Subjected to a Rectangular Force Pulse," International Journal of Solids and Structures, Vol. 5, 1969.
- [15] Vulcan, A.P., King A.I., and Nakamura, G.S., "Effects of Bending on the Vertebral Column During +G Acceleration," Journal of Aerospace Medicine, Vol. 4, 1970.<sup>z</sup>
- [16] Lombard, C.F., and Advani, S.H., "Impact Protection by Isovolu-metric Containment of the Torso," Proceedings 10th Stapp Car Crash Conference, 1967.
- [17] Robbins, W.A., Potter, G.L., Lombard, C.F., "Development of Support and Restraint Technology," AMRL-TR 68-136.
- [18] Hoff, N.J., "The Dynamics of the Buckling of Columns," Journal of Applied Mechanics, Vol. 18, Trans. ASME, Vol. 73, 1951.
- [19] Sevin, E., "On the Elastic Bending of Columns Due to Dynamic Axial Force Including Effects of Axial Inertia," Journal of Applied Mechanics, Vol. 27, 1960.
- [20] Dym, C.L., and Rasmussen, M.L., "On a Perturbation Problem in Structural Dynamics," International Journal of Non-linear Mechanics, Vol. 3, 1968.
- [21] Archer, R.R., and Das, M.L., "A Comparison of Non-linear Dynamic Beam Theories," Developments in Mechanics, Vol. 5, Proceedings 11th Midwestern Mechanics Conference, 1969.
- [22] "The Investigation of Vertebral Injury Sustained During Aircrew Ejection," Technology Incorporated Progress Report, San Antonio, Texas, Contract NAS 2-5062, June, 1970.
- [23] Kuzmak, G.E., "Asymptotic Solutions of Non-linear Second Order Differential Equations with Variable Coefficients," PMM Vol. 23, 1959.
- [24] Rose, L.S., "Rheological Properties of Femoral and Vertebral Elements," M.S. Thesis in Theoretical and Applied Mechanics, West Virginia University, Morgantown, West Virginia, May, 1968.
- [25] Moffatt, C.A., Personal Communications, 1970.
- [26] Kazarian, L.E., von Gierke, H.E., and Mohr, G.C., "Mechanics of Vertebral Injury as a Result of G<sub>z</sub> Spinal Impact," presented at the 39th Annual Meeting of Aerospace Medical Association, 1966.

REFERENCES (Cont.)

- [27] Ruff, S., "Brief Acceleration: Less than One Second," *German Aviation Medicine, World War II*, Vol. 1, Chap. VI-C, Department Air Force Printing, 1950.
- [28] Hirsch, C., "The Reaction of Intervertebral Discs to Compression Force," Journal of Bone and Joint Surgery, Vol. 37-A, No. 6, 1965.
- [29] Crocker, J.F., and Higgins, L.S., "Impact Deformation of Vertebrae," Proceedings of Annual Scientific Meeting, Aerospace Medical Association, 1967.

AMRL-TR-71-29

SESSION IV

MODELS TO DESCRIBE MAN'S RESPONSE TO  
IMPACT, BLAST, AND ACOUSTIC ENERGY

Chairman

V. L. Roberts  
University of Michigan

Co-chairman

I. Kaleps  
AMRL

PRECEDING PAGE BLANK

PAPER NO. 22

MODELING THE CIRCULATORY SYSTEM  
UNDER BIODYNAMIC LOADS

Julia T. Apter, M.D., Ph.D.

Director, Mathematical Biology  
Division of Surgery  
Presbyterian-St. Luke's Hospital

Professor of Surgery  
University of Illinois  
Chicago, Illinois

ABSTRACT

The model developed here was based on the dynamic viscoelastic properties of the components of the cardiovascular system. The model parameters are functions of time and are valid for a wide range of strains. From some limited kinds of behavior numerical values for model parameters can be obtained from data on intact portions of a human cardiovascular system. Almost all behavior can be clarified with this model which, therefore, serves as a valuable teaching aid and as a basis for evaluating the qualitative results to be expected from management of changes induced by large dynamic loads, like impact.

PRECEDING PAGE BLANK

A variety of approaches are currently being used to model the cardiovascular system: computer simulations [1,2], physical models [3], mathematical models [4,5], black boxes [6], automatic control theory [7]. All of these have been heuristic in one way or another. Some, by virtue of their very inability to match real data quantitatively have suggested new models. Some have performed as instructional aids; many have helped design new experiments which, in medical science, can lead to new methods for managing disease states. Only a few have directed new interpretations of experimental data; still fewer have made it possible to quantify verifiable system parameters and then only when the behavior of the model closely resembled real behavior. This last function is one prime purpose of a model. Indeed, it is impossible to quantify biological system parameters without a model. Even the dimensions of an X-ray photograph of a human heart cannot be interpreted without some kind of a model to help sort out signal from noise.

The purpose of the present analysis is to develop some techniques for predicting, for quantifying and for regulating the behavior of the circulatory system of the host organism in the presence of some external forcings. In order to consider the dynamics of the circulatory system when an animal is in an unusual environment, it would be wise to select models that have reliably provided accurate numerical values for system parameters under normal conditions. Several such models exist. One set of models was suggested by the windkessel model of Frank [10,11]. Another relies on compartmental analysis [9] and still another is an analysis via some form of the Navier-Stokes equations [12,13,14]. These models have made it possible to compute cardiac output from a dye dilution curve [8], renal blood flow from the rate of disappearance of a radioactive tracer [9], stroke volume and blood loss from the aorta by analysis of aortic pressure curves [10], and the flow, even if pulsating, through a rubber tube by measuring pressure at two points along the tube [12].

All these models have been used under the assumption of a constant influence from the external environment. The Navier-Stokes method as applied by Womersley has not proved sufficiently accurate to be applied to the human circulation with its special viscoelastic and responsive characteristics [15]. Indeed, when applied to humans, the method has reverted to a black-box type of analysis, certainly unsatisfactory in theory and also in practice [16]. Even more important, the Womersley analysis is appropriate only for small strains, certainly not for even ordinary external forcings.

In general, it is logical to suppose that the models based on the Navier-Stokes equation show promise. However, since even for a rubber tube and for small strains they are exceedingly complex, it is challenging to imagine how complicated they will be for even very simplified versions of a vascular circulation with realistic large strains. But attempts are being made to develop the equations for such conditions [17], and electronic computers could theoretically provide solutions for them. In the meantime, an examination of these and, more usefully, also of the windkessel model can give some information about the behavior of a simplified concept of the circulatory system while being exposed to large external forcings. All of the results obtained

with the windkessel model can, in principle, also be obtained with the Navier-Stokes equations.

An analysis of the effects of external forcings would require some preliminary information obtainable from in vitro or isolated organ studies. These would include (1) tensile strength [18] of each portion of the system, so that the conditions leading to rupture with consequent blood loss from the forcing can be estimated; (2) any differences in viscoelastic properties of various portions of the system [19-23] that might result in pooling of the blood so that vital organs are shunted; (3) effects of the forcing especially on vital organs; i.e., on blood flow to lung, for oxygenation; on flow to heart to maintain the necessary pumping action and on the brain to maintain respiratory and circulatory innervations. It should be emphasized that the information to be gained from an analysis like this would be generally useful in medical practice: in hemorrhagic shock, impact injuries, vascular damage in the aged, organ perfusion, the replacement of arteries with synthetic polymers and many other externally induced events.

There are currently no models that have been used to quantify the influence of any of these factors on normal or abnormal circulation dynamics. What is needed is a model that remains valid in the presence of large strains and that contains factors (1), (2), and (3) as specific parameters. The modified windkessel model appropriate to sequential arrangements of tubes of differing viscoelastic properties might prove to be useful at least for a qualitative analysis. Certainly there are no restrictions on the magnitude of the strains, provided complete understanding of the dynamic stress-strain relationships of the tube walls are available. Many of them are available, and others can be inferred from current knowledge of histology [19-22]. While precise quantification of all system parameters is not yet feasible, the model makes it possible to gain insight into some effects of macroscopic forcings on such a combination of tubes. The model is similar to the circulation with its veins and arteries which are actually two sets of tubes of differing viscoelastic properties. The model suggests ways to quantify "blood pooling" within the circulation under certain kinds of stress. It also suggests ways to understand this pooling process and to modify it. The model includes tensile strength parameters  $E_t$  so that strains which produced restoring forces in excess of  $E_t$ , would cause rupture, and loss of blood from the circulation. In addition, the bending modulus of the tubes would give information about external pressures  $P_0$  that would occlude the tubes if the internal  $P$  became sufficiently low or  $P_0$  became sufficiently high such that some critical  $(P - P_0)^*$  was exceeded.

While the model considers feedbacks, controls, and regulations of parameters, it does not rely on control system theory which generally incorporates black-box transfer functions [7]. Rather, the actual controlling variables and controlled parameters are specified and included in the differential equations of motion and constitutive equations of the model. To be sure, some of these specifications presently are speculative and may not be supported by subsequent research; but they have already been heuristic [7], and will probably continue to be so.

## I. SELF-CONSISTENT MODEL COMMENSURATE WITH LARGE-STRAIN ANALYSIS

The model will, at first, be considered as a self-consistent system entirely independent of the circulation. On the other hand, the model will be developed so that each component is analogous to certain relevant characteristics of the human circulatory system. Other characteristics will be ignored or many will be lumped into a single parameter. In either case, the assumptions will be stated or summarized.

Consider two tubes A and B; superscripts  $\alpha$  and  $\beta$  refer to variables and parameters of these two tubes respectively. The tubes are connected in tandem with a constriction of diameter  $R_\alpha$  between A and B, and  $R_\beta$  between B and A (Figure 1). The tubes are composed of materials which perform as a standard linear solid represented as a Zener element [19] (Figure 2). For generality, the model parameters  $E$  ( $E_1$  or  $E_2$  or  $\eta$  or  $\ell_0$ ) are not taken to be constant [24], but are functions of time and strain. To represent the tubes, curve the model of Figure 2 so that G joins G' and D joins D' to form a circle. Combine many such circles to form a waterproof tube. Then that tube represents our tubes A and B of circumference  $\ell_0^\alpha$  and  $\ell_0^\beta$ .

The set of tubes contains a volume  $V_0$  of fluid which is pumped periodically through the system by a pump  $S$  located at the beginning of tube A (Figure 1) (or just at the end of  $R_\beta$ ). Let us consider that each tube acts as a unit (Windkessel) so that the rate of change of volume  $\dot{V}$  will equal inflow minus outflow, or

$$\dot{V}^\alpha = W^\alpha - F^\alpha \quad (1)$$

and 
$$\dot{V}^\beta = W^\beta - F^\beta \quad (2)$$

where  $W$  is inflow and  $F$  is outflow.

Because of material balance

$$V^\alpha + V^\beta = V_0 \quad (3)$$

and 
$$\dot{V} = \dot{V}^\alpha + \dot{V}^\beta = 0. \quad (4)$$

The form of  $W$  will depend on the pump and, assuming linear flow, the outflow

$$F = \frac{P}{P} \quad (5)$$

where  $P$  is existing pressure and  $T$  is resistance to outflow (dependent on diameter of outlets  $R_\alpha$  and  $R_\beta$ ).

The pressure in a viscoelastic tube of this kind has been shown [23] to be dependent on wall properties as



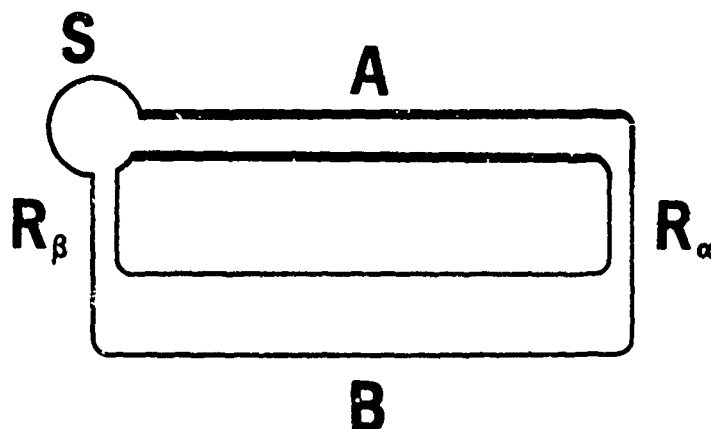


Figure 1. A diagram to show large artery A connected to large vein B by way of a lumped resistance  $R_\alpha$ . Vein B is in series with a pump at S via  $R_\beta$ , a resistance to flow in the pulmonary circuit. The relative thickness of arterial and venous walls and lumen size are indicated. This is the "cardiovascular system" under consideration here.

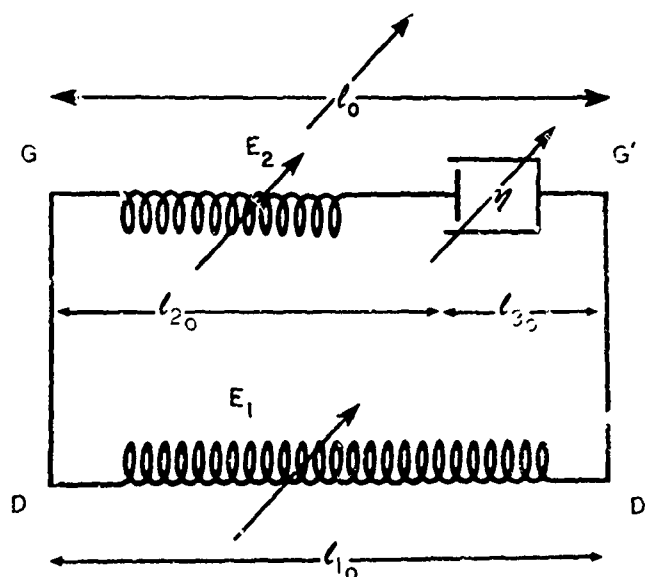


Figure 2. A Zener element with elastic parameters  $E_1$  and  $E_2$ , viscosity parameter  $\eta$  and unstrained length  $l_{1_0}$  all shown as variable with time. Join G to G' and D to D' to form a circle. Combine many such circles to form waterproof tubes. Then those tubes will behave like A, B,  $R_\alpha$  and  $R_\beta$  of Figure 1 to the extent that appropriate values for  $l_{1_0}$ ,  $E_1$ ,  $E_2$  and  $\eta$  are used for aorta, veins, peripheral arteries, and pulmonary capillaries.

$$P = \frac{E_1(\ell_1 - \ell_{1_0}) + E_2(\ell_2 - \ell_{2_0})}{h \ell_1} \quad (6)$$

where  $h$  is  $\frac{1}{2\pi}$  and  $\ell_1 > \ell_{1_0}$ ,  $\ell_2 > \ell_{2_0}$  with  $\ell_{1_0}$  and  $\ell_{2_0}$  defined from Figure 2.

The numerical values for model parameters  $E^\alpha(E_1^\alpha, E_2^\alpha, \eta^\alpha, \ell_0)$  and  $E^\beta$  will be chosen to resemble those already known for arteries [19-22] (A) and veins [23] (B). Even if parameters are not available, they can be deduced from the microscopic structure of arteries and veins. Large arteries are thicker, more muscular, more elastin-containing than veins. Both arteries and veins contain collagen which appears to be stretched only in large deformations (Figures 3 and 4, regions  $\Psi$ ). When muscle is stretched slightly, it responds with a recontraction or an increase in  $E_1$ ,  $E_2$ , and  $\eta$  and a decrease in  $\ell_0$  [24]; and therefore with an increased wall restoring force and a decreased volume. When muscle is stretched a great deal, it cannot respond with a contraction, even if stimulated directly or via nerves or chemicals [19-22]. Instead the adjacent elastin and/or collagen take over the burden of supplying the wall restoring forces, but then there is no stimulus to cause a decrease in  $\ell_0$  as the strain increases. In other words, muscular restoring forces raise pressure and displace volume; elastic and collagenous restoring forces only raise pressure.

In general, under physiological strains

$$E^\alpha > E^\beta \quad (7)$$

$$\ell^\alpha < \ell^\beta \quad (8)$$

and such that

$$p^\beta \ll p^\alpha. \quad (9)$$

We do not have reliable information about  $V^\alpha$  and  $V^\beta$ , but in all likelihood

$$V^\beta > V^\alpha. \quad (10)$$

Whatever these parameter values, however, it appears that the strain in the venous walls is sufficient under normal conditions only to stretch the muscular, not the collagenous elements, of the wall. Thus within the range N on the stress-strain curve of veins in Figure 4, the muscle is stretched and  $\ell^\beta < \ell^{\beta*}$ , where  $\ell^{\beta*}$  is the circumference at which the muscle becomes excessively stretched and collagen comes into play; then the range  $\Psi$  on the stress-strain curve applies. For arteries the muscle is stretched in region  $N_1$  (Figure 3), elastin in region  $N_2$  and collagen in  $\Psi$ . For the present, the aorta, or tube A, has all exits which actually exist along the aorta lumped as the single  $R_\alpha$ . The four-chamber heart is lumped as S and the pulmonary circuit as  $R_\beta$ .

Constitutive equations for each portion of the model are developed as follows for a tube of length L:

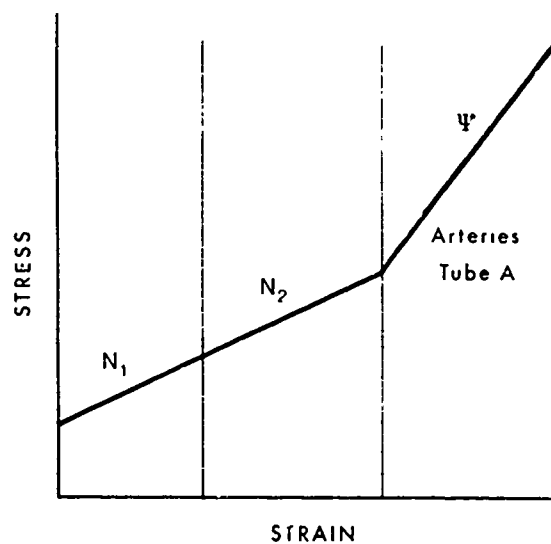


Figure 3. Diagram of stress-strain relationships of arteries, or tube A. In region  $N_1$ , the arterial wall component being stretched is muscle; in region 2 the component is elastin; in region  $\Psi$ , it is collagen. Figure 5 shows the condition of muscular macromolecules in each of these regions.

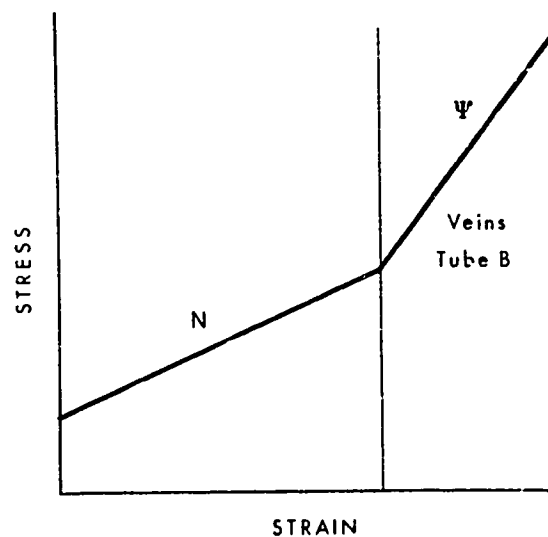


Figure 4. Diagram of stress-strain relationship of veins B. Because veins have very little elastin, in region  $N$  muscle is being stretched throughout; in region  $\Psi$ , collagen is being stretched.

$$V = \frac{\ell^2 L}{4\pi} \quad (11)$$

Thus the rate of change of V with time is

$$\dot{V} = h\dot{\ell} + \frac{h\ell^2}{2} \dot{L} \quad (12)$$

Putting (5), (6), and (12) into (1) and (2) gives

$$\begin{aligned} & \frac{h\ell^{\alpha^2}}{2} \dot{L}^{\alpha} + h\ell^{\alpha} \dot{\ell}^{\alpha} L^{\alpha} \\ & = W - \frac{E_1^{\alpha}(\ell_1^{\alpha} - \ell_{1_0}^{\alpha}) + E_2^{\alpha}(\ell_2^{\alpha} - \ell_{2_0}^{\alpha}) - P_0}{\ell_1^{\alpha} R_{\alpha}} \end{aligned} \quad (13)$$

where  $W^{\alpha}$  is the output from the pump. The  $W^{\beta}$  is simply the outflow from A so that  $W^{\beta} = F^{\alpha}$ , or

$$\begin{aligned} & \frac{h\ell^{\beta^2}}{2} \dot{L}^{\beta} + h\ell^{\beta} \dot{\ell}^{\beta} L^{\beta} \\ & = \frac{E_1^{\alpha}(\ell_1^{\alpha} - \ell_{1_0}^{\alpha}) + E_2^{\alpha}(\ell_2^{\alpha} - \ell_{2_0}^{\alpha}) - P_0}{\ell_1^{\alpha} R_{\alpha}} \\ & - \frac{E_1^{\beta}(\ell_1^{\beta} - \ell_{1_0}^{\beta}) + E_2^{\beta}(\ell_2^{\beta} - \ell_{2_0}^{\beta}) - P_0}{\ell_1^{\beta} R_{\beta}} \quad (14) \end{aligned}$$

If  $P < P_0$  so that the bending modulus were exceeded,  $R^{\alpha}$  or  $R^{\beta}$  would become infinite to indicate collapse of one of the corresponding tubes. Of course the pump must continually be primed with  $F^{\beta}$ , so  $W^{\alpha}$  is a function of  $F^{\beta}$ .

We take  $R_{\alpha}$  to be a function of pressure, that is,  $R_{\alpha}$  is high when  $P^{\alpha}$  is low. We also put a threshold  $P_{\alpha}^*$  on this pressure response and take a maximal resistance to be  $R_{\alpha}^0$ . Then

$$R_{\alpha} = R_{\alpha}^0 - \gamma (P^{\alpha} - P_{\alpha}^*) \quad (15)$$

as already derived elsewhere [25].  $\gamma$  is a constant dependent on the ability of  $R_{\alpha}$  to respond to nervous stimuli from the carotid sinus [25]. The laws governing  $R_{\beta}$  have not yet been investigated, and must be complex since  $R_{\beta}$  lumps the pulmonary circulation. For present purposes it will suffice to consider  $R_{\beta}$  as  $R_{\alpha} < R_{\beta} = \text{constant}$ .

The nonlinearities in the parameters  $E^{\alpha}$  and  $E^{\beta}$  are incorporated as though they depended exclusively on strain  $\epsilon$ , with

$$\epsilon = \frac{l - l_0}{l_0}, \quad (16)$$

and on nervous stimuli. These assumptions are formalized as

$$\dot{E} = k_1 \frac{l - l_0}{l_0} - k_2 E \quad (17)$$

where  $E$  and  $l_0$  are functions of time. This expresses the fact that smooth muscle recontracts ( $l_0$  gets shorter) when stretched at certain frequencies and relaxes if it is stretched at other frequencies [24]. This fact is presently taken empirically but has been developed elsewhere [24] on the basis of the macromolecular structure of muscle. The values for  $k_1$  and  $k_2$  will be functions of the level of nervous stimulation; both  $k_1$  and  $k_2$  and  $k_1/k_2$  are high during stimulation. We must also assume that some values  $L^*$  and  $l^*$  because of  $E_t$  will be associated with rupture or avulsion of a tube. Since rupture does not occur in a normal circulation under normal forcings, the external forcing determines whether  $L^*$  and  $l^*$  would be exceeded. They would be formalized in the computer solution of equations (13) and (14) as upper limits on  $L^\alpha$ ,  $L^\beta$ ,  $l^\alpha$ , and  $l^\beta$ .

The external events of interest include (a) a cut or rupture of a tube, permitting fluid to escape; (b) redistribution of blood so that  $P < P_0$  in one portion of the system; (c) externally applied  $P_0$  so that  $P_0 > P$  in some positions and not in others. All of these can readily be incorporated into the model equations. Their physiological significance will be pointed out below. Note that the model is unrealistic because of the omission of inertial effects of the fluid. These effects are inserted on an ad hoc basis as part of the forcings when the equations are solved.

The equations are amenable to solution with an analog or hybrid computer of suitable size. Indeed, they have already [10] been solved for the case where A and B are neighboring portions of the aorta. Then portion 1 receives blood from the heart and sends it to portion 2, etc. Thus we have a so-called lumped-distributed system with  $E^i \neq E^j$  ( $i = 1, 2, 3, \dots, 20$ ,  $j = 2, 3, \dots, 20$ ), all experimentally determined. Only  $W^1$  was known, but  $F^1 = W^2$ , etc. The solutions were useful and meaningful even though  $W^1$  is not a small strain when the pump is the heart. The form of  $W$  is shown in Figure 6, indicating a most particular kind of pump, indeed. For present purposes, the details of this pump need not be outlined; it has simply been defined by this output. Thus, in the computer solutions,  $W$  is programmed into a function generator which delivers  $W$  once every "heart beat," or is approximated by an equation for a rapidly damped sine curve [10] which repeats itself once every second.

## II. THE EFFECTS OF EXTERNAL FORCINGS ON THE BEHAVIOR OF THE MODEL

All of these analyses will be conducted by expressing the model to simplified, idealized versions of real forcings. The forcings are

idealized in the sense that they can be completely and correctly formalized as equations or as changes in the equations of the model. Naturally, none of these forcings are identical to real forcings. They are, nevertheless, heuristic in helping a clinician to distinguish signal from noise, to recognize probable significance of the signal and to devise means for altering the situation in diseased states.

All the analyses will also rely on the universally observed fact that blood vessel walls containing muscle tend to contract slowly but surely if they are not continually pulsated at frequencies within a "normal range." Pulsation of some kind is necessary to keep the muscles and other components of the walls "in condition." If pulsation stops temporarily, but long enough for the referred to contracture to take place, then renewed pulsation should probably start at low and slowly increasing frequencies to assure effective and durable "warming up."

The conclusions derive from careful observations on the behavior of muscular blood vessels removed from the body. Zatzman et al report [29] and Apter quantifies [20] that blood vessels narrow, shorten and stiffen upon removal. These changes increase and persist for as much as an hour in undisturbed specimens. They take place because section of the artery releases chemical muscular contractants, because the accompanying drop in temperature contracts muscle and because the absence of pulsation also contributes for some reasons still not understood. Zatzman et al [29] found that "stroking" blood vessels immersed in a bath at 37° relaxed their specimens. The frequency of stroking was not mentioned and may be important [24]. Suffice it to say that blood vessels need the warmth of the circulating blood and the pulsation at some particular range of frequencies in order to function in ordinarily expected ways.

This pulsation required by the tubes of our model will not be included in the present formal analysis. All the system parameters have been chosen on the assumption that pulsation is continuous. The pulsation may be induced by nervous impulses from the carotid sinus or by local interruptions in blood flow. Either mechanism seems to be sufficient to keep the peripheral blood vessels ( $R_a$ ) uncontractured [28]. This suggests that cessation of either mechanism can be utilized to increase  $R_a$  if needed. In turn, either mechanism can be maintained, as in non-pulsatile cardiac bypass, to keep  $R$  down. The danger of a high  $R_a$  is that muscle is deprived of blood, letting lactic acid accumulate in the tissues. When the bypass is replaced by pulsatile heart pumping, the lactic acid returns to the circulation with dangerous effects on all tissues. It appears that it is sufficient to keep only the carotid sinus pulsating in order to retain a pulsating effect on  $R_a$ . This pulsation of the carotid sinus could be effected even external stretching of this organ or by electric impulses of suitable frequency in the carotid sinus nerves [28].

Let me emphasize that these considerations and many of those to be outlined below, have not yet been tried or utilized in medical science. They have been brought to light by this model.

### A. EXTERNALLY INDUCED CUT IN TUBE A

Formally, this is a decrease in  $R_\alpha$  and  $W^\beta < F^\alpha$  by an amount  $F_\delta$  determinable by Poisseuille's law

$$F_\delta = \frac{K(P - P_0)}{\chi^4} \quad (18)$$

where  $\chi$  is the radius of the cut and is the amount by which  $R_\alpha$  is decreased.  $K$  incorporates the viscosity of the fluid and other constants. Presumably the flow  $F_\delta$  will continue until  $P = P_0$ . Indeed, if the cut is in the aorta, hemorrhage stops due to tamponade with  $P_0$  rising and  $P^\alpha$  falling. Assume that  $W^\alpha = 0$  if inflow

$$F^\beta < Y \quad (19)$$

the amount of fluid necessary to prime the pump. What we want to know is the number of pump strokes necessary to reach condition (19) or to make  $P^\beta < P_0$  or  $P^\alpha < P_0$ . We might also want to know whether B or A collapses first, as  $V_0$  decreases. This might depend on which of  $\dot{V}^\alpha$  or  $\dot{V}^\beta$  is the greater.

One feedback set into action by these events could be as follows:  $P^\alpha < P^*$  so  $R_\alpha = R_\alpha^0$ . This will reduce flow into B. But the amount of fluid in B is already low because of a decrease in  $V_0$ . Meanwhile, by keeping  $P^\alpha$  up, the  $F_\delta$  is also kept up. Thus, the feedback does not act to control the hemorrhage, but to enhance it. On the other hand, the feedback is regulated to keep  $P^\alpha$  high enough ( $P^\alpha > P^\alpha$ ) to maintain blood flow through vital organs like brain, lungs, heart and kidneys. The body does not regulate life in this situation. An external influence, the first aid man or the doctor must occlude the abnormal opening in the tube to keep the subject alive.

Now suppose that the cut is closed up, with  $V_0^* \ll V_0$ . What kinds of feedbacks or controls would operate to keep the pump primed so that  $W^\alpha \neq 0$ ? The formal conditions to be met are

$$V_0^* = V_\alpha^* + V_\beta^* \quad (20)$$

$$\text{or} \quad V_0^* = k V_0 = k V_\alpha + k V_\beta \quad \text{for } k \ll 1. \quad (21)$$

$$\text{We also have} \quad \dot{V}_0^* = 0 \quad (22)$$

because blood loss has been stopped. One of the events that might take place because  $E^\beta < E^\alpha$  is pooling of the fluid in tube B. Pooling is formalized as

$$V_a^* = k_2 V_a \quad (23)$$

$$V_\beta^* = k_3 V_\beta \quad (24)$$

with  $k_2 < k_3$ , but

$$V_o^* = k V_\alpha = k_2 V_\alpha + k_3 V_\beta \quad . \quad (25)$$

These conditions would be met because  $R_\beta > R_\alpha$  or  $P^\alpha > P^\beta$  and because of the great reduction in inertia of the circulating fluid.

#### B. LOCALIZED COMPLETE OCCLUSION OF TUBE-SYSTEM

Suppose the tube system has been exposed to a whip-like action so that one tube is sufficiently bent to increase  $R$  locally and temporarily to infinity. Now we need some assumptions about the ability of the pump to eject fluid if  $P^\alpha > P_o$ , the pressure inside the pump when it starts to eject fluid into tube B. Ordinarily  $P_o > P^\alpha$  during systole, or the ejection phase of  $W^\alpha$  (Figure 6). If  $R_\alpha$  is infinite (somewhere within tube A and not at  $R_\alpha$  itself), then  $P_o < P^\alpha$  so that fluid flows back into the pump and the action of the pump ceases temporarily. If the pump is the heart, the cessation takes place because the heart muscle is excessively stretched. This cessation may become permanent in the absence of suitable internal controls and external intervention, and is probably one cause of cardiac arrest. The reason for this will be referred to below.

Meanwhile, if the cessation is temporary, the portion of tube A between the bend and  $R_\alpha$  will collapse because  $F^\alpha$  will continue and empty the tube A. When occlusion at the bend is released, the fluid redistributes throughout A, but  $P^\alpha < P_o$  and the pump does not eject enough, even though excessively filled by the temporary backflow.

The overfilling of S physiologically means that the actin and myosin molecules in the muscle fibrils of the heart no longer overlap sufficiently to result in an effectual contraction of the muscle in response to the usual stimuli--nervous and stretch (Figure 5). This excessive stretch may be reversible, if the actin filaments realign themselves normally after the overfilling has been removed. Or, the stretch may be irreversible if the actin and myosin filaments are pulled so far apart that they cannot realign on release or if the muscle membrane has been ruptured. The vascular muscle, too, may be subject to such irreversible changes if excessively stretched for any reason.

#### C. IMPACT

This forcing is likely to influence all elements of the tubal system in question: the pump may simply stop; the feedbacks may cease; the vascular muscle may be overstretched to damage or rupture, the inertia of the fluid may redistribute it so that it stops or even reverses the flow.

The results of vascular rupture have already been handled and can easily be dispensed with. Cardiac arrest, or stopping of the pump S, starts a cycle that is vicious in so far as life support is concerned. One important consequence of the arrest is the effect on the smaller blood vessels, responsible for the "peripheral resistance." These are now exposed to some of the conditions met in in vitro studies. The





Figure 5. Diagram of macromolecules in muscle fibers. Thick lines are myosin; thin lines are actin. In contracted muscle the thin filaments overlap thick filaments as in  $N_1$  (and in region  $N_1$  of Figure 3). In stretched muscle, they are pulled apart as in  $N_2$ , but probably could be made to return towards condition  $N_1$  with suitable muscle stimulants (phenylephrine hydrochloride for aortic muscle). The excessive stretch existing in condition  $\Psi$  is probably irreversible.

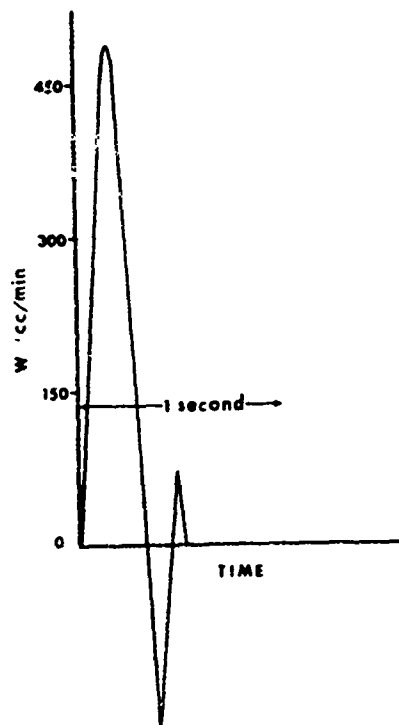


Figure 6. Volume blood flow rate as a function of time as it is forced from pump S of Figure 1. This is, therefore, the forcing function  $W(t)$  for the "cardiovascular system" considered here. This  $W$  closely resembles the output of the human heart.

temperature is reduced because blood is the carrier of warmth to peripheral areas and pulsation stops. Both these events bring on vascular constriction with resulting reduction in blood flow to vital organs and call into play anaerobic metabolism even in muscles, with accumulation of lactic acid. This toxic material may be released into the general circulation when that is restored, either spontaneously or extraneously.

The experience of Zatzman et al that local warmth and "stroking" causes relaxation of muscular blood vessels in vitro suggests similar treatments in the living subject in shock for any reason. When the feedbacks cease, then the pump is no longer effectual because nervous control has been removed, and so the result resembles cardiac insufficiency or arrest. When the fluid becomes redistributed because of inertia, we have a situation not yet dealt with. Here the heart would continue to beat, but blood would be distributed by laws governed by the static properties of the tubes A and B. The usual inertia that keeps blood moving would have momentarily been stopped.

The ability of the vein to store blood is considerably greater than that of the arteries;  $F^v \ll F^a$  and  $\ell^v \gg \ell^a$ . These facts are readily seen in any histological section containing both arteries and veins; arteries have thicker walls and smaller lumens. Thus, while

$$v^v > v^a \quad (26)$$

in general, in the case under consideration

$$v^v \gg v^a \quad (27)$$

While  $P^v$  still remains greater than  $P^a$ , the so-called central venous pressure is higher--signifying possible entrance of veins into the  $\Psi$  region of Figure 4. If the heart should continue to beat normally, the problem would be solved after a few heart beats because the stroke volume would go up, as a result of the increased pressure differential from  $P^v$  to the pump S.

Unfortunately, the heart does not always beat normally after an impact and the redistributed blood exaggerates the problems already discussed in section B above.

This model has been presented with the expectation that it may enhance insights of an engineer into the dynamics of the circulation under certain kinds of stressful situations. The model is not able, however, to clarify observed behavior under some very ordinary situations: sleep versus wakefulness; exercise versus rest; abdominal surgery; inhalation of low oxygen concentrations and many others. It should be emphasized that physicians gain insight into these events the model can handle, but only if the physician can use and accept the language of an equation. On the other hand, the equations help an engineer learn quickly the relationships it would take him many months to learn from reading physiology and pathology texts.

Despite being a decided aid in instruction, the present model has proved adequate for only a limited quantitative evaluation and prediction of circulatory system events. However, it has been useful in suggesting ways to treat shock and has made it possible to analyze aortic pressure curves [25] and obtain verifiable values for cardiac stroke volume [10]. Indeed, the response of the real system to these large external dynamic loads has not been fully investigated; a great deal needs to be learned. Therefore, the prime purpose of this model is to direct attention to a deeper understanding of currently available data, to facilitate communication among those working in this field, and to suggest experiments that might clarify the mechanisms operating in the real system. A summary of the responses of the model to the various forcings referred to here, or to iatrogenic attempts to reverse the problems, are depicted in Figures 7 through 11.

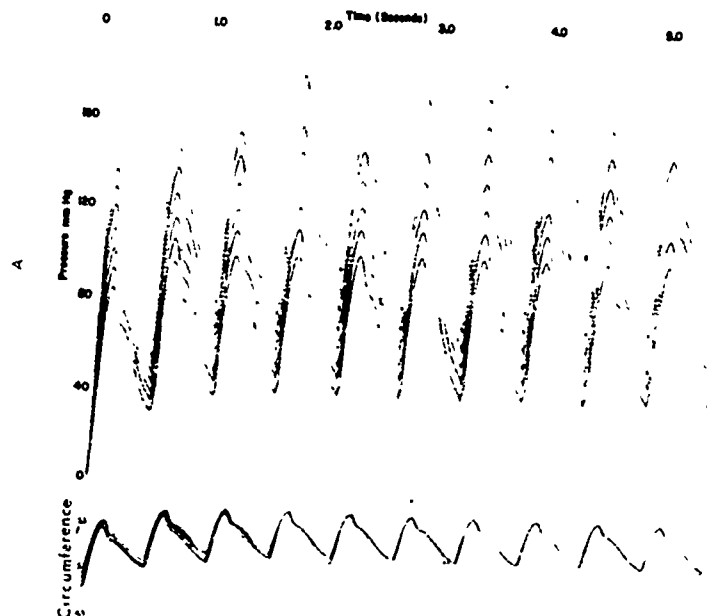


Figure 7. Computer-generated pressure and circumference curves of tube A. Tube A is started full, but not stretched, at  $t = 0$ . Then the pump S initiates "blood" flow as  $W(t)$  of Figure 6. With each beat of the pump, the pressure rises in systole and falls in diastole until a steady state is achieved such that all subsequent pressure and circumference curves are superimposable. This figure shows the effect of giving drugs which would ameliorate the response to impact. The drugs (1) increase the effectiveness of the pump so that stroke volume which is the integral of  $W(t) dt$  for a single cardiac cycle, (2) increase  $R_0$ , (3) make  $R(t)$  less responsive and (4) increase  $E_1$ ,  $E_2$ , and  $\eta$ .

Curve No.	$\eta$	$E_2$	$E_1$	$R_0$	$R(t)$	$W(t)$	$l_{10}$	$\frac{Q}{\text{(stroke volume)}}$
1	0.08	0.35	7	1.0	0.6	0.7	5	42
2	0.1	0.375	7.25	1.05	0.55	0.725	4.9	43
3	0.12	0.40	7.5	1.1	0.5	0.75	4.8	44
4	0.14	0.425	7.75	1.15	0.45	0.775	4.7	44.5
5	0.2	0.5	8.0	1.2	0.4	0.8	4.6	45
6	0.3	0.55	8.25	1.25	0.35	0.825	4.6	46
7	0.4	0.6	8.5	1.3	0.3	0.85	4.6	47
8	0.5	0.65	8.75	1.35	0.25	0.875	4.6	50

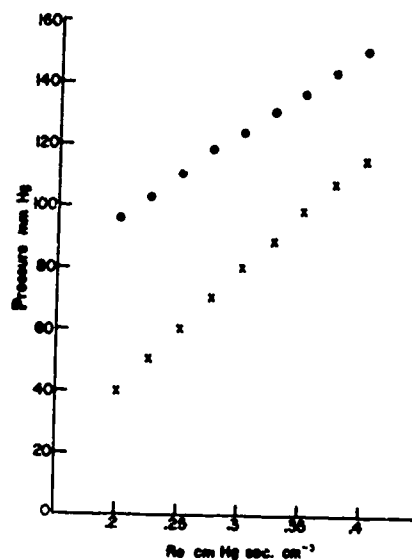


Figure 8. A plot of systolic peak pressure  $P_s$  and diastolic trough pressure  $P_d$  versus peripheral resistance  $R_a$ , all expressed as cm of Hg and generated by the model. Note that both  $P_s$  and  $P_d$  drop as  $R_a$  drops, but also that the pulse pressure  $P_s - P_d$  increases as  $R_a$  drops.

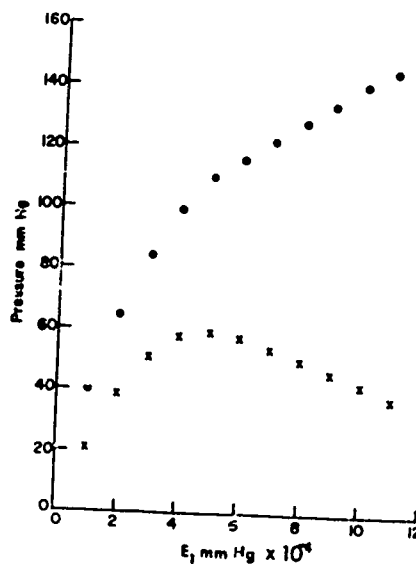


Figure 9. A plot showing  $P_s$  and  $P_d$  versus the equilibrium elastic modulus of tube A. The modulus of A drops when muscle tone is reduced and the modulus of A increases in hypertension or if collagen is under stretch. Collagen is stretched when muscle and elastin are damaged, as from an impact or aging.

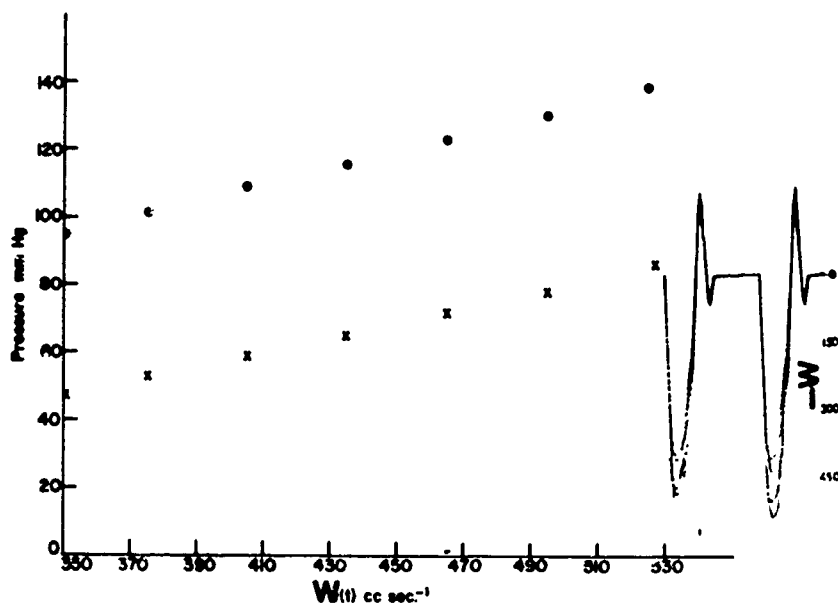


Figure 10. A plot of  $P_S$  • and  $P_D$  x as a function of  $W(t)$ , the stroke volume. In blood loss,  $W(t)$  decreases, with a drop in both  $P_S$  and  $P_D$  and a decrease in  $P_S - P_D$  as well.

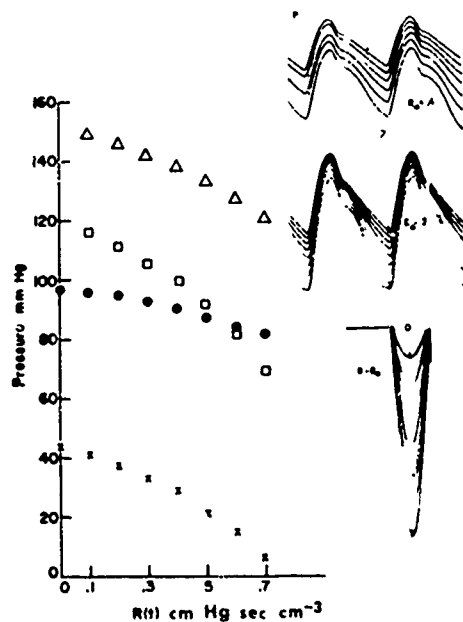


Figure 11. Systolic peak pressures  $P_S$  (• and  $\Delta$ ) and diastolic pressures  $P_D$  (x and  $\square$ ) for two levels of  $R_\alpha$  and 7 levels of responsiveness of  $R(t)$ . If hemorrhage has resulted from a cut in  $R_\alpha$ , so that  $R_\alpha$  and  $R(t)$  both decrease, the effect on pressure is complex, but analyzable with this diagram.

## REFERENCES

1. Jager, G. N., Westerhof, N., and Noordengraaf, A. Oscillatory flow impedance in electrical analog of arterial system. *Circ. Res.* 16:121-133, 1966.
2. Attinger, E. O., Anne, A., and McDonald, D. A. Use of Fourier Series for the analysis of biological systems. *Biophys. J.* 6: 291-304, 1966.
3. Rodbard, S. Biophysical Principles Governing the Flow of Blood in the Vascular System, in Shock and Hypertension, Ed. L. C. Mills and J. H. Moyer, New York, Grune and Stratton, pp. 69-79, 1965.
4. Apter, J. T. An analysis of aortic pressure curves taking into account visco-elastic properties of the aorta and variations in peripheral resistance. *Bull. Math. Biophys.* 27:27-52, 1965.
5. Rosten, S. Mathematical representation of some cardiovascular dynamics using the Laplace Transform. *Bull. Math. Biophys.* 21: 1-11, 1959.
6. Grodins, F. S. Regulation of pulmonary ventilation. *Physiologist* 7:319-333, 1964.
7. Grodins, F. S. Control Theory and Biological Systems, New York, Columbia University Press, 1963.
8. Hamilton, W. F., Riley, R. L., Attyah, A. M., Cournand, A., Forvell, D. M., Himmelstein, A., Noble, R. P., Remington, J. W., Richards, D. W., Jr., Wheeler, N. C., and Witham, A. C. Comparison of the Fick and dye dilution methods of measuring the cardiac output. *Man. Amer. J. Physiol.* 153:309, 1948.
9. Wilson, D., Apter, J. T., and Schwartz, F. A model for measuring renal blood flow from the plasma disappearance of iodopyracet. *J. Appl. Physiol.* 28:79-88, 1970.
10. Morehouse, F., Apter, J. T., and Aniot, L. Use of hybrid computer to analyze behavior of detailed model for aortic blood flow. *Computers in Biology and Medicine* 1:1-10, 1970.
11. Frank, O. Die Grundform des Arteriellen Pulses. *Zeit. Biol.* 37: 483-526, 1899.
12. Womersley, J. R. Oscillatory flow in arteries: The constrained elastic tube as a model of arterial flow and pulse transmission. *Phys. in Med. and Biol.* 2:178-187, 1958.
13. Cox, R. H. Wave propagation through a Newtonian fluid contained within a thick-walled, visco-elastic tube. *Biophys. J.* 8:691-709, 1968.

14. Chow, J., and Apter, J. T. Wave propagation in a viscous incompressible fluid contained in a flexible visco-elastic tube. *J. Acoust. Soc. Amer.* 44(2):427-433, 1968.
15. Fry, D. L., and Greenfield, J. C., Jr. The Mathematical Approach to Hemodynamics with Particular Reference to Womersley's Theory, in *Pulsatile Blood Flow*, Ed. E. O. Attinger, New York, McGraw-Hill, pp. 85-99, 1964.
16. Warner, H. R., Gardner, R., and Toronto, A. F. Computer-based monitoring of cardiovascular functions in post-operative patients. *Circulation* 38:suppl. 2, 68-74, 1968.
17. Rudinger, G. Shock waves in mathematical models of the aorta. *J. Appl. Mech.* 21:34-37, 1970.
18. Taylor, M. G. The elastic properties of arteries in relation to physiological functions of the arterial system. *Gastroenterology* 52:358-363, 1967.
19. Apter, J. T., Rabinowitz, M., and Cummings, D. H. Correlation of visco-elastic properties of large arteries with microscopic structure. II. Collagen, elastin, and muscle determined chemically, histologically, and physiologically. *Circ. Res.* 19:111-115, 1966.
20. Apter, J. T. Correlation of visco-elastic properties of large arteries with microscopic structure. IV. Thermal effects on muscle, elastin, collagen, and intact arteries. *Circ. Res.* 21: 901-918, 1967.
21. Apter, J. T., and Marquez, E. Correlation of visco-elastic properties of large arteries with microscopic structure. V. Sinusoidal forcings at low and at resonance frequencies. *Circ. Res.* 22:393-404, 1968.
22. Apter, J. T., Marquez, E., and Janas, M. Dynamic visco-elastic anisotropy of canine aorta correlated with aortic wall composition. *J. Assoc. Adv. Med. Instrumentation* 4:15-23, 1970.
23. Wood, J. E. The venous system. *Sci. Amer.* 218:86-94, 1968.
24. Apter, J. T., and Graessley, W. W. A physical model for muscular behavior. *Biophys. J.* 10:539-555, 1970.
25. Apter, J. T. An analysis of the aortic pressure curve during diastole. *Bull. Math. Biophys.* 27:27-58, 1956.
26. Apter, J. T. Mathematical development of a mechanical model describing visco-elastic properties of aorta. *Bull. Math. Biophys.* 26:367-388, 1964.



27. Apter, J. T. Biosystems Modeling, in Biomedical Engineering Systems, Eds. M. Clynes and J. H. Milsum, New York, McGraw-Hill, pp. 165-211, 1970.
28. Ead, H. W., Green, J. H., and Neil, E. A comparison of the effects of pulsatile and non-pulsatile blood flow through the carotid sinus on the reflexogenic activity of the sinus baroreceptors in the cat. J. Physiol. 118:509-519, 1952.
29. Zatzman, M., Stacy, R. W., Pandall, J., and Ebanstein, A. Time course of stress relaxation in isolated arterial segments. Amer. J. Physiol. 179:299-302, 1954.

An Analysis of the Pressure Wave  
Generated in Seated Spinal Impact\*

by Peter J. Forvik  
Associate Professor of Mechanics  
Air Force Institute of Technology  
Wright-Patterson AFB, OH 45433

ABSTRACT

Experiments performed on seated pentobarbital anesthetized Macaca Mulatta in order to study the response of the vertebral column and internal organs to spinal impact have revealed a spatio-temporal wave phenomenon along the torso during impact. Associated with this wave is a visible temporary abdominal distension.

A mathematical model for such a mode of propagation is developed in this paper which enables the prediction of the parameters of a pressure wave in terms of certain physical properties of the subject. From the (closed form) results of the analysis, pressure, propagation speed, and skin stretch can be computed in terms of the speed at which the impact occurs.

Although the model is necessarily simplified from the actual complex structure, the predicted relationships between the parameters show encouraging agreement with available experimental results. The predicted values of pressure would produce the internal injuries which have been observed. The model would seem, therefore, to describe the essential features of the phenomenon within the lower torso and can be applied to man.

\*To be presented at the Symposium on Biodynamic Models and Their Applications, Dayton, Ohio, 26-28 October 1970.

PRECEDING PAGE BLANK

## I. Introduction

An analysis of the propagation of a pressure discontinuity through a thin-walled cylindrical vessel filled with an incompressible fluid will be developed. Of interest is the response of a flat-ended cylindrical container to a uniform step increase in pressure over the flat end. The pressure, if maintained, is assumed to produce a planar discontinuity which propagates in the direction of the axis of the cylinder, the plane of the discontinuity being assumed to be normal to the axis of the cylinder. In a deformable cylinder filled with a compressible fluid, such a loading would produce a disturbance in the compressible medium which propagates with the bulk velocity of the fluid and also disturbances propagating through the container walls. These disturbances would, in general, be coupled. In this paper, such modes of propagation will be completely neglected, and it will be demonstrated that another simple mode of propagation exists for this fluid-solid system. The motion considered here is in some respects similar to a mechanism for shock propagation in a fibrous composite which has been previously proposed.<sup>(1)</sup>

While the solution to the problem as stated above has evident application to a vessel filled with fluid and subject to a blast wave impinging normally on one end, the results of this analysis will furnish insight into and have possible application to several other problems of interest. The results are directly applicable to determining the maximum drop velocity which a cylindrical container filled with fluid can be expected to sustain without bursting. The results may also be applicable to analysis of the disturbances propagating through a cylindrical fuel tank due to a crash in which one end of a filled tank is instantaneously stopped. Finally, if the human torso is subjected to a large enough acceleration and the rise time of the disturbance is negligible, as may occur in an aircraft

ejection seat, the conditions assumed in this analysis may be approximately met, and the analysis used to predict the pressures which result within the body from such an acceleration.

## II. Analysis

Consider a right-circular cylinder filled with an incompressible fluid to have a pressure  $P$  applied instantaneously over a plane normal to the axis. This pressure causes a disturbance assumed to be planar to propagate at speed  $D$  into the material at rest. In time  $\Delta t$ , a length  $D\Delta t$  is therefore set into motion at some speed  $U$ , assumed to be in the same direction as  $D$ . All radial motion will be neglected and a uniform state assumed to exist behind the front of the disturbance. Even though radial motion is to be neglected per se, we will assume that the area of the cross section increases from  $A_0$  to  $A_f$  at the front. Figure 1a depicts an exaggerated view of the assumed motion.

We consider the mass and momentum of the volume of fluid contained in a length  $D\Delta t$  and cross section  $A_0$ , as shown in Figure 1b as  $ABCD$ , as it is deformed to the configuration shown in Figure 1c. The length of this cylindrical element changes, as the material line  $CD$  is carried with the fluid, at speed  $U$ , to the new location  $C'D'$ . Region  $A'B'C'D'$  is assumed uniform, with all particles moving at speed  $U$ . Thus the length of segment  $DB$  (initially  $D\Delta t$ ) becomes  $D'B'$ , of length  $(D-U)\Delta t$ . In the same time, the segment  $CD$  has stretched to length  $C'D'$  and the area has changed from  $A_0$  to  $A_f$ . The material line  $AB$  is stretched to  $A'E'$ , but does not translate in the time  $\Delta t$ .

If the fluid initially has density  $\rho_0$ , and in the compressed state has density  $\rho_f$ , then equating the total mass in the cylindrical element before and after the disturbances has passed yields

$$\Delta m_0 = \rho_0 (\pi r_0^2) (D\Delta t) = \Delta m_f = \rho_f (\pi r_f^2) (D-U)\Delta t \quad (1)$$

If the fluid is incompressible, this reduces to

$$\frac{r_0^2}{r_f^2} = 1 - \frac{U}{D} \quad (2)$$

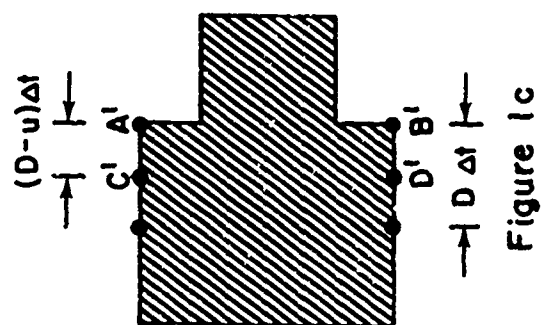


Figure 1c

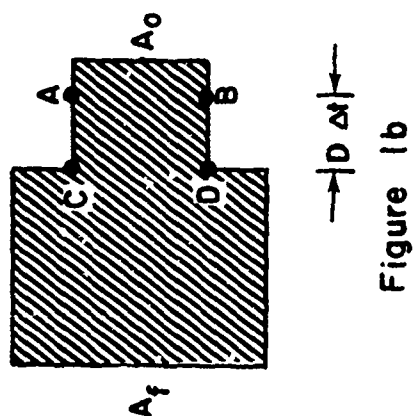


Figure 1b

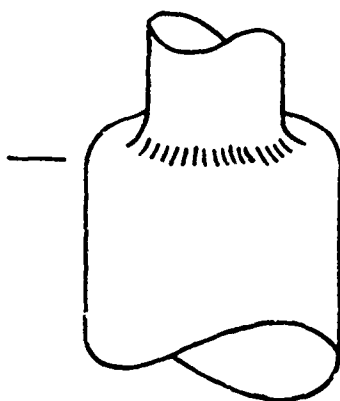


Figure 1a

Fig. 1 Idealization of Pressure Wave Geometry

Considering now the requirement that momentum be conserved, we equate the impulse of the pressure acting on the plane C'D' during  $\Delta t$  to the change in momentum resulting from the acceleration of the mass  $\Delta m_0$  contained in ABCD from rest to the final speed U. Thus

$$PA_f \Delta t = (\rho_0 A_0 D \Delta t) U$$

or

$$P = \rho_0 \frac{r_0^2}{r_f^2} DU \quad (3)$$

The transverse expansion of the fluid filled cylinder is constrained by the circumferential or hoop stresses in the cylinder and therefore depends upon the constitutive relationship for the container. If the walls are thin, the circumferential stress in the container is related to the pressure within the fluid through

$$\sigma = P \frac{r_f}{t_f} \quad (4a)$$

where P is the pressure,

$r_f$  is the final radius of the cylinder

$t_f$  is the final wall thickness and

$\sigma$  is the stress per unit area in the deformed state, i.e. the Eulerian stress.

If we choose instead to define a Lagrangian stress, that is, a stress obtained by dividing the final force by the original area, we obtain

$$\Sigma = P \frac{r_f}{t_0} \quad (4b)$$

where  $t_0$  is the initial wall thickness.

This stress is brought about by the strain in the container wall, assumed to be uniform, which occurs with the change in the cross sectional area. For small deformations, the strain is related to the final and

initial radii through

$$\epsilon = \frac{2\pi r_f - 2\pi r_0}{2\pi r_0} = \frac{r_f}{r_0} - 1 \quad (5a)$$

In terms of the finite Eulerian and Lagrangian strains, the relationship between the radii and strains are, respectively,

$$\epsilon_e = \frac{1}{2} \left[ 1 - r_0^2/r_f^2 \right] \quad (5b)$$

$$\epsilon_L = \frac{1}{2} \left[ \frac{r_f^2}{r_0^2} - 1 \right] \quad (5c)$$

The stress and strain, as defined above, are related through a constitutive relationship which, in general, might be of the form

$$F(\epsilon, \dot{\epsilon}, \sigma, \dot{\sigma}) = 0 \quad (6)$$

where  $\dot{\epsilon}$  and  $\dot{\sigma}$  are strain rates and stress rates. However, we are here concerned only with the instantaneous response, and will assume that even in a material having such a general constitutive relationship that the instantaneous or "jump" stress is related to the instantaneous or "jump" strain through a relationship of the form

$$\sigma = E f(\epsilon_e) \text{ or } \Sigma = E F(\epsilon_L) \quad (7)$$

where  $E$  is a constant having the dimensions of stress and  $\sigma$  and  $\epsilon$  are values of stress and strain immediately behind the discontinuity.

Equations 2, 3, either of Equations 4, one of Equations 5 together with a constitutive relationship of the form of Equation 7 furnish five equations in the six unknowns  $r_f/r_0$ ,  $U$ ,  $D$ ,  $\sigma$ ,  $P$ , and  $\epsilon$ . If Eulerian stress (Eq 4a) is used, some assumption about the final wall thickness,  $t_f$ , must be made. Thus, five parameters of the propagating disturbance can be determined in terms of the sixth.

It is convenient to rewrite the system of equations in a dimensionless form through the introduction of an extension ratio  $\lambda$



$$\lambda = r_f/r_0 \quad (8)$$

and the definition of a dimensionless particle velocity and a dimensionless propagation speed through

$$\hat{U} = U/v \quad (9)$$

$$\hat{D} = D/v \quad (10)$$

where  $v$  has the dimension of a velocity.

Equation 2 (conservation of mass) then becomes

$$\frac{1}{\lambda^2} = 1 - \frac{\hat{U}}{\hat{D}} \quad (11)$$

Equation 3 can be rewritten through the introduction of a dimensionless pressure, defined by

$$\hat{P} = P/\rho_0 v^2 \quad (12)$$

to read

$$\hat{P} = \hat{D}\hat{U}/\lambda^2 \quad (13)$$

Equation 4a and 4b can be made dimensionless through choosing

$$v = \sqrt{\frac{Et_0}{r_0\rho_0}} \quad (14)$$

Equation 4a and 4b then read

$$\sigma/E = \hat{P}\lambda(t_0/t_f) \quad (15a)$$

$$\Sigma/E = \hat{P}\lambda \quad (15b)$$

Equations 5a, 5b and 5c now become

$$\epsilon = \lambda - 1 \quad (16a)$$

$$\epsilon_e = \frac{1}{2} \left[ 1 - 1/\lambda^2 \right] \quad (16b)$$

$$\epsilon_l = \frac{1}{2} \left[ \lambda^2 - 1 \right] \quad (16c)$$

In the next two sections, a linear constitutive relationship will be considered, as well as one possible non-linear relationship. Several other non-linear forms particularly appropriate to metallic materials have also been considered, but are not included in this paper.

### III. A Linear Elastic Container

If the container is assumed to be elastic and the strains infinitesimal, the appropriate constitutive relationship is

$$\Sigma/E = \epsilon \quad (17)$$

Using Equations 11, 13, 15b and 16a, we can solve for all unknown parameters in terms of the extension ratio  $\lambda$ .

$$\epsilon = \lambda - 1 \quad (16a)$$

$$\hat{p} = \frac{\lambda - 1}{\lambda} \quad (18)$$

$$\hat{D}^2 = \lambda^3 / (\lambda + 1) \quad (19)$$

$$\hat{U} = \sqrt{\frac{\lambda + 1}{\lambda}} (\lambda - 1) \quad (20)$$

Eliminating  $\lambda$  between Equations 19 and 20 yields a cubic equation in  $\hat{U}$  and  $\hat{D}$ .

$$\hat{U}\hat{D}^3 - 2(1 + \hat{U}^2)\hat{D}^2 + \hat{U}(2 + \hat{U}^2)\hat{D} + 1 = 0 \quad (21)$$

For any  $\hat{U}$ , only the first positive root yields a propagation speed  $\hat{D}$  which is a solution to the system of equations.  $\hat{D}$  as a function of  $\hat{U}$  is plotted as Figure 2. Values of dimensionless pressure, particle velocity and propagation speed are given for various values of extension ratio  $\lambda$  in Table 1. The physical pressure and velocities may be recovered from the dimensionless forms through the use of Equations 9, 10, 12 and 14.

For large extension ratios, the assumption of infinitesimal strains is not appropriate. Using the Lagrangian strain and assuming the Lagrangian stress to be proportional to the Lagrangian strain with constant of proportionality  $E$ , the necessary equations are

$$\epsilon_L = \frac{1}{2} (\lambda^2 - 1) \quad (16c)$$

$$\hat{p} = \frac{1}{2\lambda} (\lambda^2 - 1) \quad (22)$$

$$\hat{D}^2 = \lambda^3 / 2 \quad (23)$$

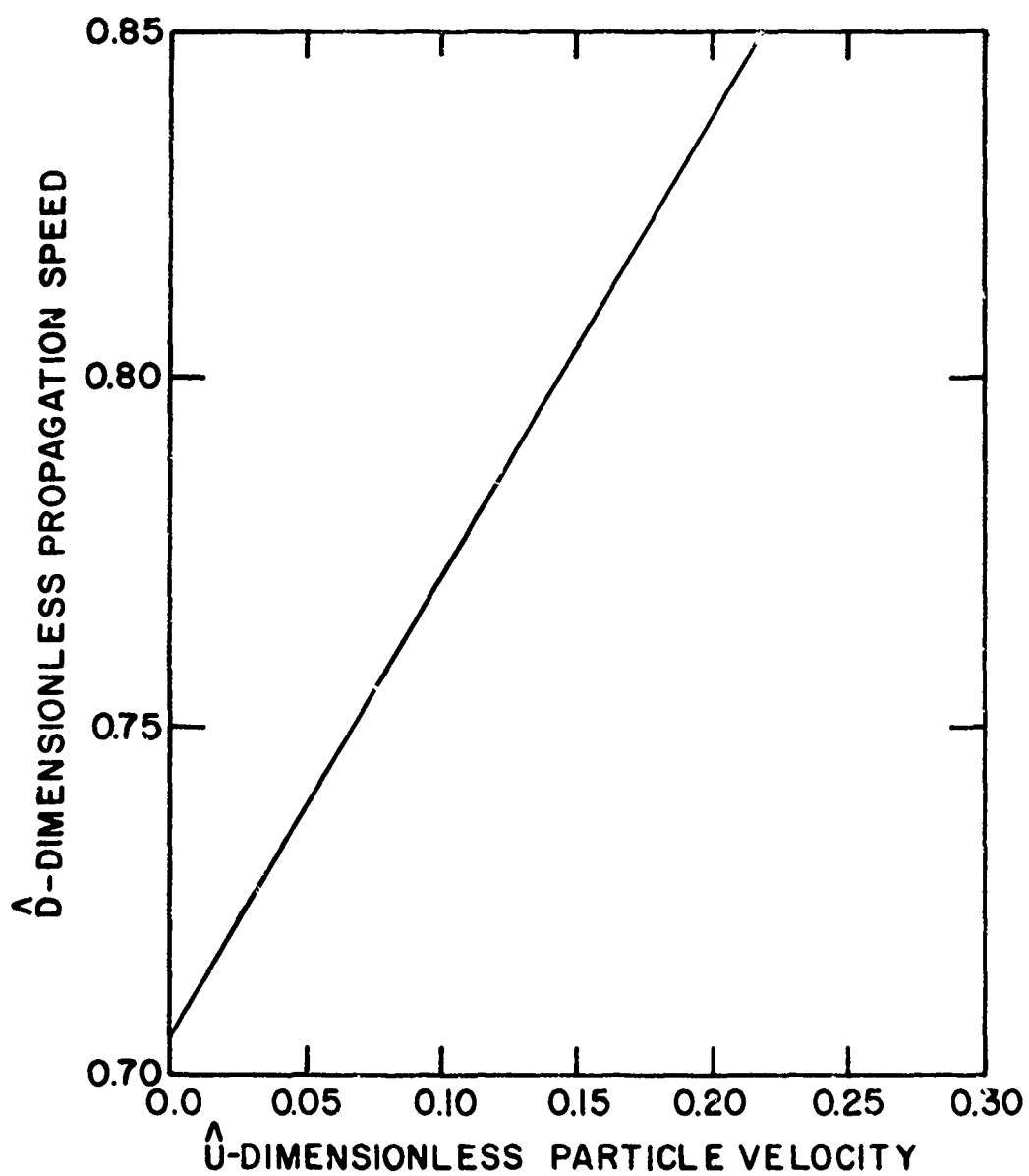


Fig. 2 Propagation Speed as a Function of Particle Velocity for a Linear Material

TABLE 1.

SOLUTION FOR LINEAR CONSTITUTIVE RELATIONSHIP  
INFINITESIMAL STRAIN

$\lambda$	$\rho$	$\theta$	$\delta$
1.02	.0196	.0281	.7248
1.04	.0385	.0560	.7426
1.06	.0566	.0836	.7604
1.08	.0741	.1110	.7782
1.10	.0909	.1382	.7961
1.12	1.071	.1651	.8140
1.14	1.228	.1918	.8321
1.16	1.379	.2183	.8500
1.18	1.525	.2447	.8682
1.20	1.667	.2708	.8863

$$\hat{U} = \frac{(\lambda^2 - 1)}{\sqrt{2\lambda}} \quad (24)$$

Values of dimensionless pressure, particle velocity and propagation speed as functions of extension ratio  $\lambda$  are given in Table IIa.

For an infinitesimal disturbance, ( $\lambda \rightarrow 1$ ), the dimensionless propagation speed  $\hat{D}$  approaches  $1/\sqrt{2}$  (Equation 19 or 23). Hence, from Equation 14, the physical propagation speed approaches

$$D_0 = \sqrt{\frac{Et_0}{2r_0 \rho_0}} \quad (25)$$

From 18 and 20, the relationship between pressure and particle velocity for small strain is

$$\hat{P} = \hat{U}/\sqrt{2} \quad (26)$$

Hence, the physical quantities are related through

$$P = \frac{\rho_0 UV}{\sqrt{2}} = U \sqrt{\frac{E\rho_0 t_0}{2r_0}} \quad (27)$$

Equations 25 and 27 are, in fact, the well known results for water hammer<sup>(2)</sup> in pipes if the pipe wall is so thin, or the fluid so rigid, that compressibility of the fluid can be neglected. The above development for the propagation of a strong disturbance in a cylindrical container could well be modified to include effects of fluid compressibility, as is customarily done in the analysis of the water hammer phenomenon.

An analysis using a linear relationship between Eulerian strain and Eulerian stress may also be performed. In this case, a final value for the thickness is required. If it is assumed that the container wall is incompressible, then  $t_f (2\pi r_f) [(D-U)\Delta t] = t_0 (2\pi r_0) [D\Delta t]$  (28)

Substituting Equation 2

$$\frac{t_f}{t_0} = \lambda \quad (29)$$

Letting  $\sigma = E\epsilon_e$ , Equations 11, 13, 15a and 16b become

TABLE II  
SOLUTION FOR LINEAR CONSTITUTIVE RELATIONSHIP

a. Lagrangian Strain

$\lambda$	$\hat{p}$	$\hat{u}$	$\hat{d}$
1.1	.0955	.1416	.8158
1.2	.1833	.2840	.9295
1.3	.2654	.4279	1.048
1.4	.3429	.5737	1.171
1.5	.4167	.7217	1.299
1.6	.4875	.8721	1.431
1.7	.5559	1.025	1.567
1.8	.6222	1.181	1.708
1.9	.6868	1.339	1.852
2.0	.7500	1.500	2.000

b. Eulerian Strain

$\lambda$	$\hat{p}$	$\hat{u}$	$\hat{d}$
1.1	.0868	.1350	.7778
1.2	.1528	.2593	.8485
1.3	.2041	.3753	.9192
1.4	.2445	.4849	.9900
1.5	.2778	.5893	1.061
1.6	.3047	.6894	1.131
1.7	.3270	.7861	1.202
1.8	.3457	.8800	1.273
1.9	.3615	.9713	1.344
2.0	.3750	1.061	1.414

$$\epsilon_e = \frac{1}{2} \left( \frac{\lambda^2 - 1}{\lambda^2} \right) \quad (16b)$$

$$\hat{p} = \frac{1}{2} \left( \frac{\lambda^2 - 1}{\lambda^2} \right) \quad (30)$$

$$\hat{D} = \lambda / \sqrt{2} \quad (31)$$

$$\hat{U} = \frac{(\lambda^2 - 1)}{\lambda \sqrt{2}} \quad (32)$$

Values of dimensionless pressure, particle velocity and propagation speed are given as functions of extension ratio in Table IIb.

c. Exponential Stress Strain Law

Fung has noted (3) that a relationship

$$\Sigma = \beta [e^{a(\lambda-1)} - 1] \quad 33a$$

is frequently observed in tissue. Here  $\Sigma$  is the Lagrangian stress,  $\lambda$  the extension and  $\beta$  and  $a$  are parameters of the material. From Equation 33a, the modulus at zero strain is  $E = \beta a$ , thus the relationship between stress and elongation becomes

$$\frac{\Sigma}{E} = \left[ \frac{e^{a(\lambda-1)} - 1}{a} \right] \quad 33b$$

This equation, together with Equations 11, 13 and 15b yields a system which may be solved in terms of  $\lambda$ .

$$\hat{P} = \frac{1}{a\lambda} [e^{a(\lambda-1)} - 1] \quad 34$$

$$\hat{D}^2 = \frac{\lambda^3}{\lambda^2 - 1} \left[ \frac{e^{a(\lambda-1)} - 1}{a} \right] \quad 35$$

$$\hat{U} = \hat{D}(\lambda^2 - 1)/\lambda^2 \quad 36$$

Again, the dimensionless velocities and pressures are defined through Equations 9, 10 and 12, using Equation 14. The results of these calculations, for several values of  $a$ , are given in Figures 3, 4, 5 and 6. In Figure 3, the dimensionless pressure is plotted against the extension ratio, and in Figure 4, the propagation velocity is plotted against the particle velocity, with the extension ratio indicated by the dashed lines. Figures 5 and 6 are similar to Figures 3 and 4, with larger values of  $\lambda$  being employed.



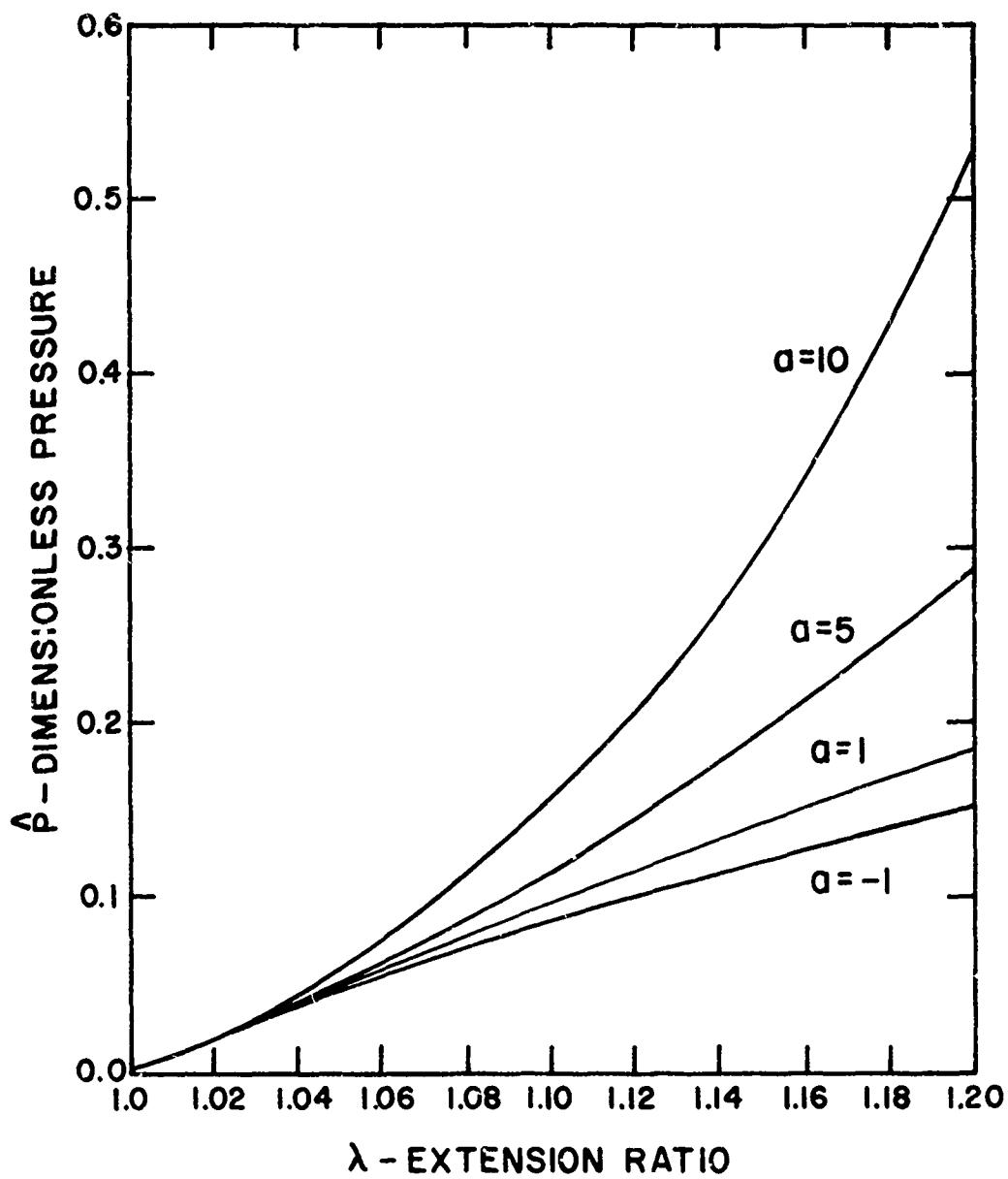


Fig. 3 Pressure as a Function of Extension Ratio for a Non-Linear Material with Small Strain

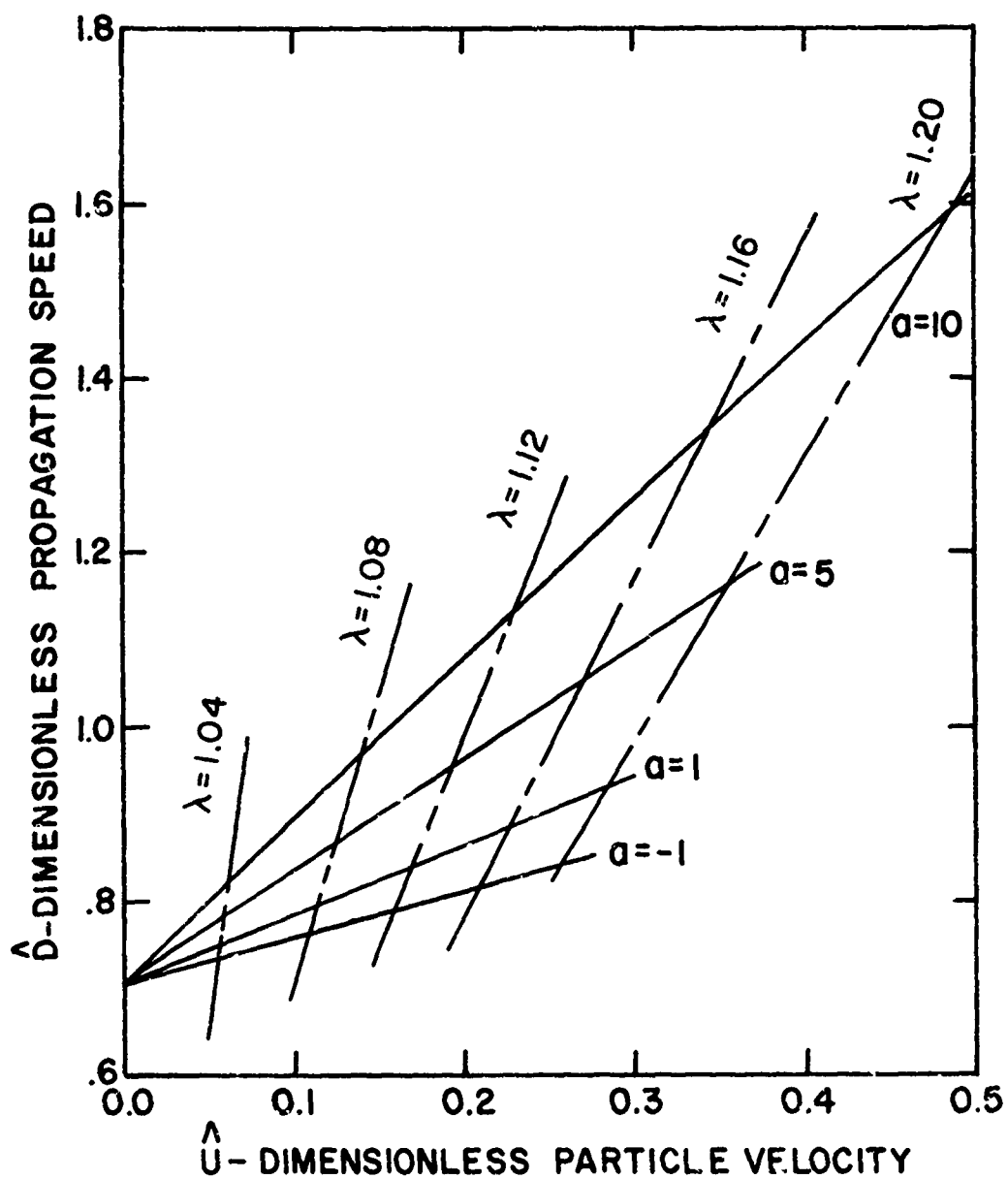


Fig. 4 Propagation Speed as a Function of Particle Velocity for a Non-Linear Material with Small Strain

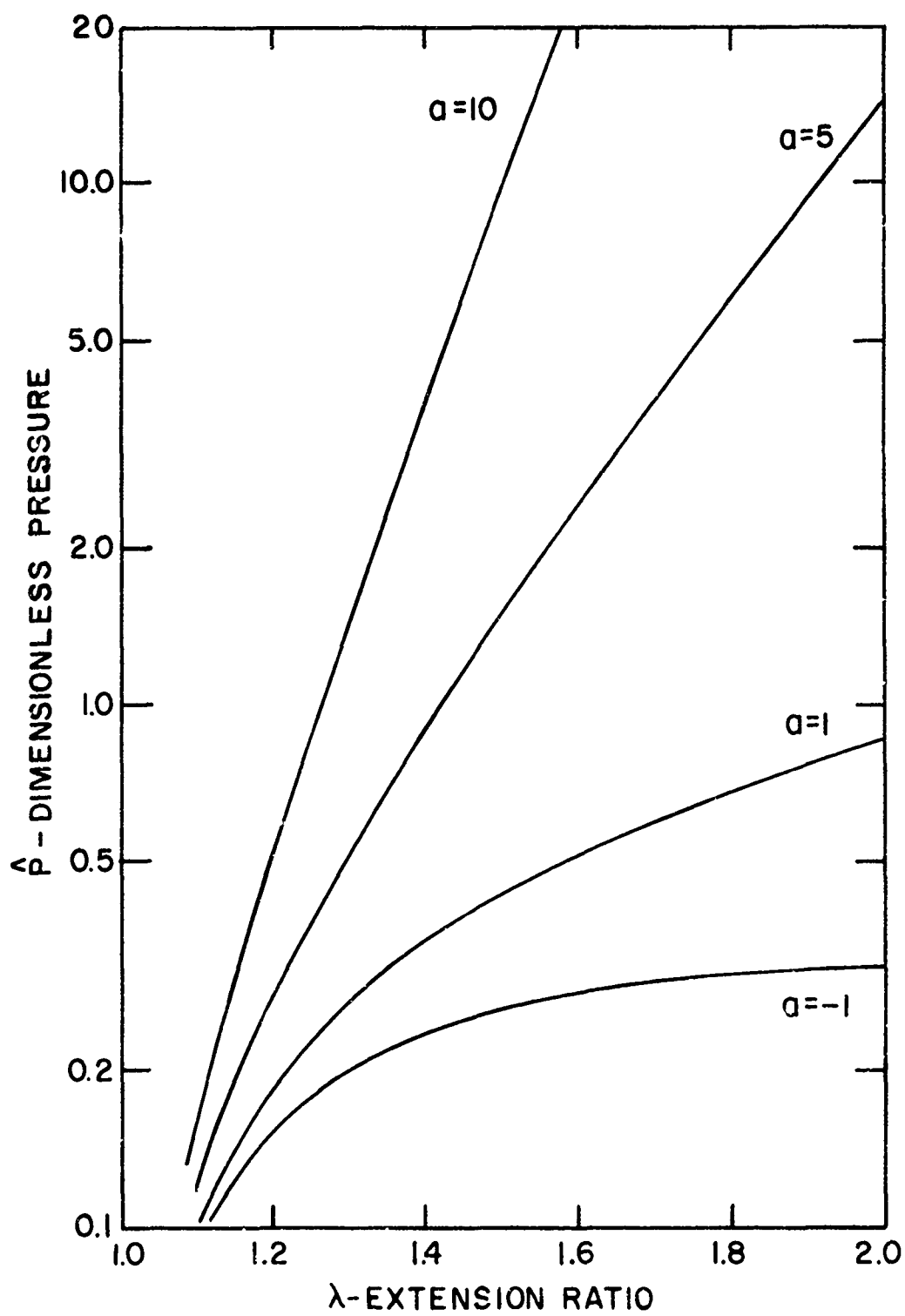


Fig. 5 Pressure as a Function of Extension Ratio for a Non-Linear Material with Large Strain

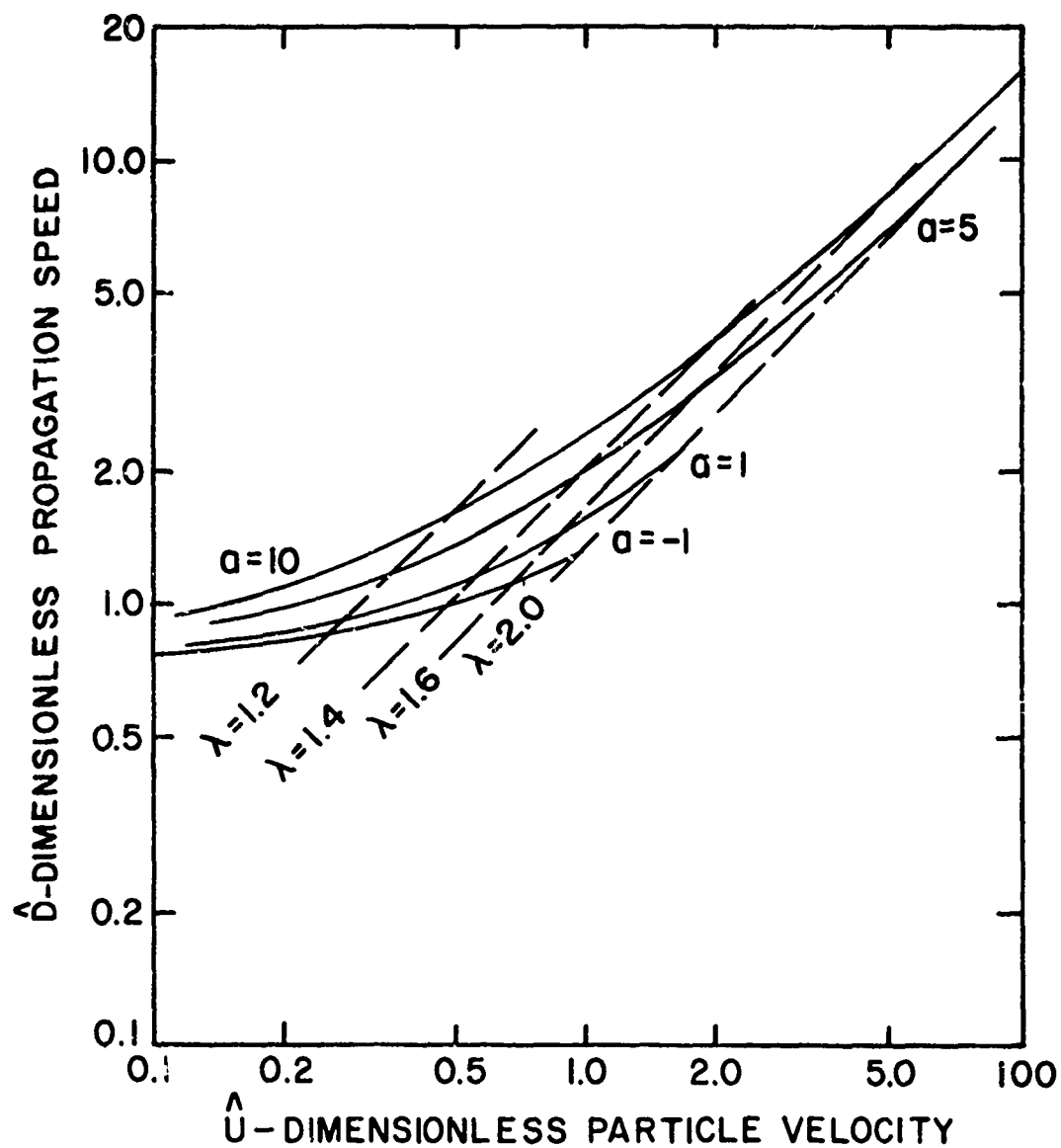


Fig. 6 Propagation Speed as a Function of Particle Velocity for a Non-Linear Material with Large Strain

#### IV. Application

The theory developed in the preceding sections may be readily used to determine the pressure within a flat-ended cylinder filled with an incompressible fluid which impacts normally a rigid barrier at some speed  $V_R$ . Viewed in a coordinate system traveling with the object, a planar pressure wave generated by the impact will sweep along the cylinder imparting a velocity change to the material which it envelops. Since all fluid particles were moving at speed  $V_R$  prior to impact, a velocity change of equal magnitude is required to bring the fluid to rest. Thus, for the case of impact with a rigid wall, the previously given development is applicable if the change in particle velocity due to the disturbance is taken to be the impact speed. The propagation speed in the preceding analysis was assumed to be measured with respect to the undisturbed fluid. In a coordinate system translating with the cylinder at speed  $V_R$ , this material appears at rest. The propagation speed measured with respect to an inertial frame, viz. the rigid object impacted, is  $D - V_R$ .

If we approximate the contents of the lower torso by an incompressible fluid and assume that the skin behaves elastically, the theory may be applied to the determination of the pressure generated within the lower torso of the human body when dropped in a seated position, or equivalently, accelerated as in the ejection seat of a modern aircraft. The torso is, of course, not perfectly cylindrical, but it seems reasonable to so approximate the cross section, as the initial effect in a non-circular cylinder should be the assumption of the maximum section for the given (initial) periphery. It seems plausible to assume that the spinal column will respond quite independently of the internal organs, much as a pencil within a water filled balloon dropped upon a sidewalk. This model, however, can be expected to apply only to the lower torso, for the complicated

structure of the diaphragm, lungs and rib cage within the upper torso will clearly not be adequately described by this elementary model.

Experiments have been carried out (4) on pentobarbital anesthetized Rhesus monkeys (*Macaca Mulatta*) for the purpose of gaining information on the response of primates to a loading of this type. During the course of this investigation, a spatio-temporal wave was observed in the torso, as shown in Figures 7a, 7b, 7c and 7d. These photographs are frames from a motion picture camera monitoring the results of dropping a Rhesus monkey onto a relatively rigid stop at an impact speed of 56 ft/sec. Measurements from the photographs reveal that the width of the torso increases by a factor of 1.5 to 1.8 and that the wave moves along the torso at 100 ft/sec, measured in an inertial coordinate system. With respect to the undisturbed medium, the disturbance therefore moved at a speed of 156 ft/sec. For  $\lambda = 1.5$ , the Lagrangian strain is more appropriate, but the available data for modulus was reduced through the use of Equation 16a so Equations 18, 19 and 20 should be employed. For  $\lambda = 1.5$ , the predicted values are

$$\hat{P} = .333$$

$$\hat{D} = 1.16$$

$$\hat{U} = .645$$

For  $\lambda = 1.8$ , the corresponding values are .443, 1.44 and .995

Available information (5) on Young's modulus for abdominal skin gives  $110 \times 10^8$  dynes/cm<sup>2</sup> for dogs and  $56 \times 10^8$  for humans. Using  $60 \times 10^8$  and taking 1/4 in. as a value for the skin thickness and 2 inches as a torso radius<sup>(6)</sup> together with assuming the density of the contents of the abdominal cavity to be nominally that of water yields 90 ft/sec as a value of  $v$  (Equation 14). Thus, the theory predicts



FIG. 7 PRESSURE WAVE PROPAGATING ALONG TORSO

$U = 58 \text{ ft/sec to } 89.5 \text{ ft/sec}$

$D = 104 \text{ ft/sec to } 130 \text{ ft/sec}$

$P = 37.5 \text{ psi to } 48.7 \text{ psi}$

The agreement between the predicted and observed values is encouraging for the extension ratio can not be read from the photograph with great precision, and the value of Young's modulus is clearly uncertain to a factor of two and possibly very much more, for the layer of muscle underlying the abdominal skin may well behave more like container wall than abdominal content. The assumption of a linear elastic skin is certainly questionable. It should also be noted that the predicted pressure is more than sufficient to induce the soft tissue injuries which were observed (4).

The assumed mode of deformation is that of a uniform region behind the wave front, rather than a disturbance confined to the skin and a shallow underlying region. The agreement between the resulting predictions and the experiment is such that this model can be regarded as being a reasonable description of the phenomenon, which has the appearance of, and has been called, a surface wave. It should be a relatively easy matter to place a few pressure transducers within a subject and repeat the experiment so as to validate or refute the hypothesized pressure distribution and magnitude predicted by the theory.

It should be noted that this theory requires no empirical data to be obtained for one species of subject and then scaled in some manner before predictions on another can be made. Rather, the basic parameters  $\rho$ ,  $E$ ,  $r_0$  and  $t_0$  need only be known. If a complete stress-strain curve can be determined, an appropriate non-linear constitutive relationship such as the one included herein may give more accurate results than the linear case used in the above example.



#### ACKNOWLEDGMENT

The author is indebted to Dr. Von Gierke and Mr. Kazarian for calling the phenomenon to his attention and for making their work available prior to publication.

## LIST OF FIGURES

- Figure 1 Idealization of Pressure Wave Geometry
- Figure 2 Propagation Speed as a Function of Particle Velocity  
for a Linear Material
- Figure 3 Pressure as a Function of Extension Ratio for a Non-Linear  
Material with Small Strain
- Figure 4 Propagation Speed as a Function of Particle Velocity  
for a Non-Linear Material with Small Strain
- Figure 5 Pressure as a Function of Extension Ratio for a Non-Linear  
Material with Large Strain
- Figure 6 Propagation Speed as a Function of Particle Velocity for  
a Non-Linear Material with Large Strain
- Figure 7 Pressure Wave Propagating Along Torso

#### REFERENCES

1. Torvik, P. J., "Shock Propagation in a Composite Material", Journal of Composite Materials, Vol. 4 (July 1970) pp 296-309.
2. Streeter, V. L., Ed. Handbook of Fluid Dynamics, McGraw-Hill, New York, 1961, sec 20, pp 2-10.
3. Fung, Y. C., Continuum Mechanics, Prentice-Hall, Englewood Cliffs, New Jersey, 1969, pp 171-174.
4. Kazarian, L. E., Hahn, J. W., and Von Gierke, H. E., Biomechanics of the Vertebral Column and Internal Organ Response to Seated Spinal Impact in the Rhesus Monkey (Macaca Mulatta), Aerospace Medical Research Laboratories AMRL-TDR-70-85, 1970.
5. Nickerson, J. L. and Drazic, M., Youngs Modulus and Breaking Strength of Body Tissues, Aerospace Medical Research Laboratories AMRL-TDR-64-23, 1964.
6. Kazarian, Personal Communication.

THE TRANSVERSE RESPONSE OF THE LUMBAR  
SPINE UNDER LONGITUDINAL LOADS

H. E. Krause and M. Shirazi

University of Dayton Research Institute  
Dayton, Ohio

ABSTRACT

A novel continuous model of the spine is presented. The transverse motion in the sagittal plane of the spine of sitting human subjects exposed to vertical vibrations revealed considerable bending along the lumbar spine and negligible bending along the thoracic spine. Therefore, the model consists of a curved rod, representing the lumbar spine, longitudinally loaded by a mass, representing the thorax. The differential equation of the transverse motion was derived and solved by making a product assumption. No transverse displacements and no bending moment was assumed at the pelvic end. At the thoracic end, a shear force and a bending moment are applied, representing translatory and rotatory inertia of the attached rib cage.

Eigenfunctions and eigenvalues depend on longitudinal loading. The eigenfunctions correlate well with data obtained over a large range of experimental conditions. The solution for the time distribution contains various distinct harmonic components if an external force, alternating sinusoidally at only one discrete frequency, is applied. This effect is due to a periodic parameter in the differential equation.

INTRODUCTION

Most observed spinal injuries result from external forces applied in the longitudinal direction. Long-time exposure to moderate external loads can develop slowly increasing damages. Compression of the spinal column is the prevailing stress mode.

In recent tests, Vulcan et al.<sup>1</sup> observed considerable bending of the spine of human cadavers that were exposed to spinal-direction impact. Considerable bending of the lumbar spine of sitting human subjects under vertical vibrations was observed by Krause.<sup>2</sup> In view of these findings it seems that transverse displacements as well as longitudinal displacements should be considered.

Bending relieves stress in certain areas and increases it in others, if it is superimposed on existing compression. Therefore, bending may be the factor that determines the location of injury if it is present to a significant magnitude.

This is an exploratory study in which only transverse responses under longitudinal loads will be considered. In particular, we attempt to account quantitatively for the effect of a longitudinal load and initial curvature on the bending stress, its distribution along the lumbar spine, and the conditions of dynamic instability. Longitudinal responses will be neglected. It has been shown by Bolotin<sup>3</sup> that transverse vibrations are significantly disturbed by longitudinal vibrations only at resonance of the latter. Longitudinal vibrations can therefore be neglected if we assume their resonant frequencies and those of the transverse vibrations do not coincide.

#### SPINAL MODEL CONFIGURATION

As a hypothesis, a spine model is assumed that consists of two parts (Figure 1). They are a curved rod to represent the lumbar spine, and a rigid mass connected with it that represents the thorax.

Experimental observations have led to this configuration (Figure 2). The amplitude of the first derivative of the transverse displacement of the thoracic spine above the 10th thoracic vertebra of a sitting human subject under vertical vibrations from 10 to 40 Hz is almost constant. The second derivative is, therefore, almost zero and hardly any bending exists. It is assumed that the rib cage increases the bending stiffness of that part of the spinal column.

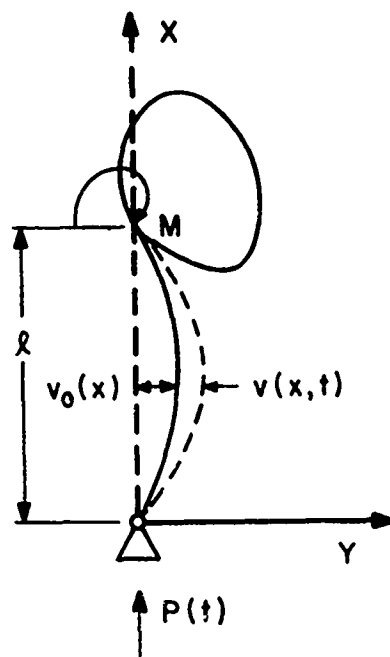


Figure 1. Model Configuration for Lumbar Spine and Thorax.

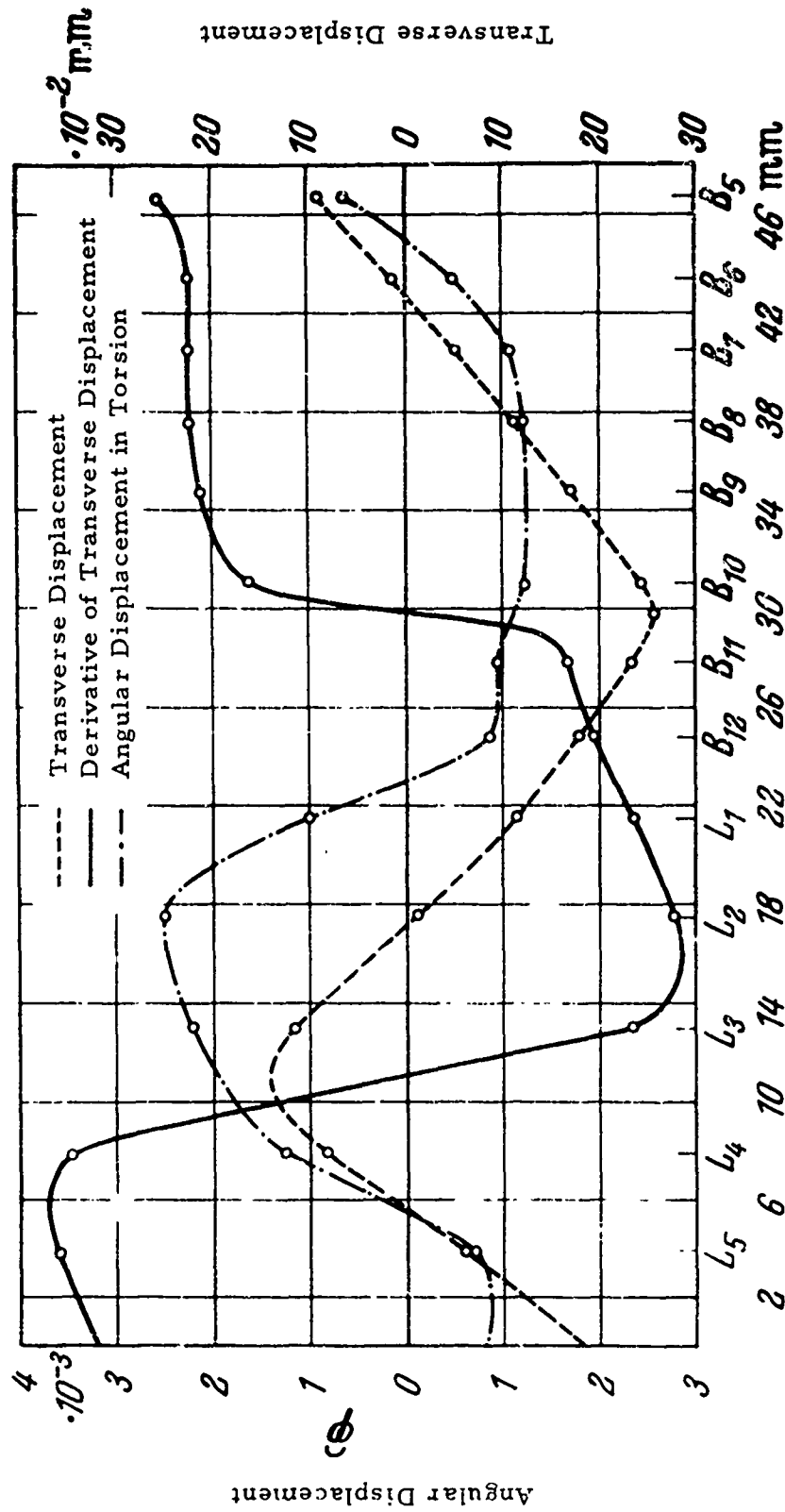


Figure 2. Transverse and Torsional Vibration Amplitude Along the Spine.  $R_{\theta L} z$

It should be noted that Figure 2 includes the torsional deflection under the same experimental conditions. A nodal point can be observed around the 6th and 5th thoracic vertebra. This point was observed for 13 frequencies within the test range from 10 and 40 Hz and for 30 experiments at each frequency. This nodal point coincides with a peak at that point of almost all published curves of injury incidence along the spinal column.

#### EQUATION OF MOTION

The equation of transverse motion of a curved beam has been presented by Bolotin.<sup>3</sup> It is

$$EI \frac{\partial^4 v}{\partial x^4} + P(t) \frac{\partial^2 v}{\partial x^2} + \mu \frac{\partial^2 v}{\partial t^2} = -P(t) \frac{d^2 v_0}{dx^2} \quad (1)$$

where

$E$  = modulus of elasticity

$I$  = areal moment of inertia

$v(x, t)$  = transverse displacement from initial curvature

$v_0(x)$  = initial curvature

$P(t)$  = longitudinal load (compression positive)

$\mu$  = mass per unit length of rod.

The function  $v_0(x) = 0$  if the beam is straight. The nonhomogeneous equation (1) reduces to a homogeneous equation

$$EI \frac{\partial^4 v}{\partial x^4} + P(t) \frac{\partial^2 v}{\partial x^2} + \mu \frac{\partial^2 v}{\partial t^2} = 0. \quad (2)$$

A product assumption

$$v(x, t) = \sum_{n=1}^{\infty} V_n(x) T_n(t) \quad (3)$$

where

$V_n(x)$  = spatial distribution

$T_n(t)$  = time distribution,



decomposes the partial differential equation into a system of ordinary ones. They are

$$\frac{EI}{\mu} V_n^{(4)}(x) + \frac{P(t)}{\mu} V_n'' - \Omega_n^2 V_n = 0 \quad (4)$$

$$\ddot{T}_n + \Omega_n^2 T_n = 0 \quad (5)$$

$P(t)$  is here considered to be constant.

The solutions for these equations are

A. Spatial Distribution

$$V_n(x) = D_{1n} \sin r_2 x + D_{2n} \cos r_2 x \quad (6)$$

$$+ D_{3n} \sinh r_1 x + D_{4n} \cosh r_1 x$$

The  $r_1$  and  $r_2$  are

$$r_{1,2} = \sqrt{-\frac{P}{2EI} + \sqrt{\left(\frac{P}{2EI}\right)^2 + \frac{\mu\Omega^2}{EI}}} \quad (7)$$

B. Time Distribution

$$T_n(t) = A_{1n} \cos \Omega_n t + A_{2n} \sin \Omega_n t \quad (8)$$

where

$$\begin{aligned}\Omega_n &= \text{natural frequencies} \\ D_{mn} &= \text{constants} \\ r_1, r_2 &= \text{eigenvalues}\end{aligned}$$

The constants  $D_{mn}$  will have to be determined by the boundary conditions. Two different sets of boundary conditions will be considered in the following sections. A solution for the homogeneous (that is, straight beam) equation of motion and for the nonhomogeneous (that is, curved beam) equation of motion will be derived for each set of boundary conditions.

### RESTRAINED THORAX

The thorax is supposed to be restrained so that no transverse displacement or rotation can occur. The idealized model for the lumbar spine under these conditions is depicted in Figure 3. This configuration has been treated extensively by Bolotin<sup>3</sup> and other researchers in the field of dynamic instability with the inclusion of nonlinear damping and nonlinear inertia.

#### A. Straight Rod

The solutions for the constants in the spatial distribution equation for the straight beam (equation 6) are determined by the boundary conditions which are

$$\begin{aligned}V(l) &= V(0) = 0 \\ \left( \frac{d^2 V}{dx^2} \right)_{x=l} &= \left( \frac{d^2 V}{dx^2} \right)_{x=0} = 0.\end{aligned}\tag{9}$$

Transverse displacements and bending moments are not admitted at either end of the lumbar spine. This furnishes the equations:

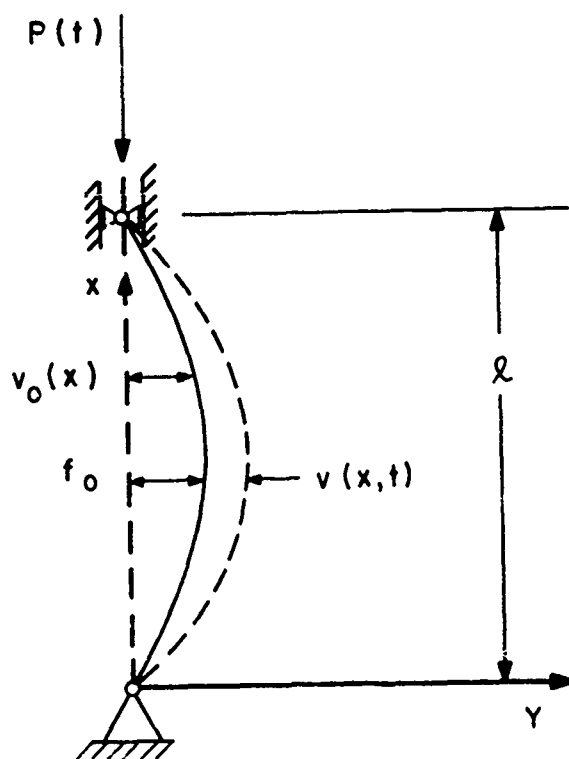


Figure 3. Model Configuration of Lumbar Spine, with Thorax Restrained from Moving.

$$V(l) = 0 = D_1 \sin r_2 l + D_2 \cos r_2 l + D_3 \sinh r_1 l + D_4 \cosh r_1 l \quad (10)$$

$$V(0) = 0 = D_2 + D_4 \quad (11)$$

$$V''(l) = 0 = -D_1 r_2^2 \sin r_2 l - D_2 r_2^2 \cos r_2 l + D_3 r_1^2 \sinh r_1 l + D_4 r_1^2 \cosh r_1 l \quad (12)$$

$$V''(0) = 0 = -D_2 r_2^2 + D_4 r_1^2. \quad (13)$$

These are four homogeneous equations for the four unknowns. In order to obtain solutions, the characteristic determinant has to be zero.

$$\Delta = 0 = \begin{vmatrix} 0 & 1 & 0 & 1 \\ 0 & -r_2^2 & 0 & r_1^2 \\ \sin r_2 l & \cos r_2 l & \sinh r_1 l & \cosh r_1 l \\ -r_2^2 \sin r_2 l & -r_2^2 \cos r_2 l & r_1^2 \sinh r_1 l & r_1^2 \cosh r_1 l \end{vmatrix}$$

$$\Delta = + (r_1^2 + r_2^2)^2 \sin r_2 l \sinh r_1 l = 0 \quad (14)$$

This condition is met if

$$r_2 l = n\pi \quad (15)$$

or

$$r_1 l = 0 \quad (16)$$

The latter condition requires  $P = 0$  and is, therefore, trivial. The eigenvalues are:

$$r_2 = \frac{n\pi}{l} = \sqrt{\frac{P}{2EI}} + \sqrt{\left(\frac{P}{2EI}\right)^2 + \frac{\mu \Omega^2}{EI}} \quad (17)$$

This equation can be solved for the natural frequencies

$$\Omega_n^2 = \frac{(2EI \left(\frac{n\pi}{l}\right)^2 - P)^2 - P^2}{4EI\mu} \quad (18)$$

It is apparent that these frequencies depend on  $P$ . If  $P$  is zero, we obtain

$$\Omega_{n0}^2 = \left(n \frac{\pi}{l}\right)^4 \frac{EI}{\mu} \quad (19)$$

The frequency equation can be rearranged to assume the following form:

$$\Omega_n^2 = \left(\frac{n\pi}{l}\right)^4 \frac{EI}{\mu} - \left(\frac{n\pi}{l}\right)^2 \frac{P}{\mu} \quad (20)$$

The natural frequencies equal those of the straight beam except for

$$\left(\frac{n\pi}{l}\right)^2 \frac{P}{\mu}.$$

The relationship between  $\Omega_n$  and  $P$  is parabolic. The solution  $v(x, t)$  is of a periodic nature if  $\Omega$  is real and it is of a non-periodic nature if  $\Omega$  is imaginary. The transition between both regimes occurs when  $\Omega = 0$ . This is the case if

$$P = P_{\text{crit}} = n^2 \left(\frac{\pi}{l}\right)^2 EI. \quad (21)$$

For  $P > P_{\text{crit}}$  we have buckling and for  $P < P_{\text{crit}}$  the beam is stable.  $P_{\text{crit}}$  is equal to the Euler buckling load for this type of beam support.

The dependence of the natural frequencies on the longitudinal load may be of practical consequence. For example, the response of the spine to external forces seems to be different under different sustained vertical loads as they occur in a dive, pullout, or tight curve. The amplitude of free vibrations is expected to change with the natural frequency if energy is conserved during transition from one longitudinal load to another.

The eigenfunctions for this model are

$$V_n(x) = \sin r_{2n} x. \quad (22)$$

They are identical with the eigenfunctions of the unloaded straight beam. It is easy to see that these functions are orthogonal.

#### B. Curved Rod

The initial curvature will be considered in the following paragraph by solving the nonhomogeneous equation of motion, equation (1). The boundary conditions remain the same.

Again, a product assumption is made:

$$v(x, t) = \sum_{n=1}^{\infty} V_n(x) T_n(t). \quad (23)$$

$V_n(x)$  represents the eigenfunctions that are now known from the preceding paragraph.  $T_n(t)$  are solutions that we seek. Considering the orthogonality of the eigenfunctions, this assumption leads to

$$\begin{aligned} \ddot{T}_n + T_n \left[ \left( \frac{n\pi}{l} \right)^4 \frac{EI}{\mu} - \left( \frac{n\pi}{l} \right)^2 \frac{P}{\mu} \right] = \\ - \frac{\int_0^l P \frac{d^2 v_0}{dx^2} V_n(x) dx}{\mu \int_0^l V_n^2(x) dx}. \end{aligned} \quad (24)$$

The initial curvature may be represented by a Fourier sine series. This series contains only sine functions because the initial curvature can be an odd function with

$$V_0(0) = V_0(l) = 0.$$

The second derivative of the initial curvature is

$$\frac{d^2 v_0(x)}{dx^2} = - \sum_{n=1}^{\infty} g_{0n} \sin \frac{n\pi}{l} x, \quad (25)$$

which results in a set of differential equations

$$\ddot{T}_n + T_n \left[ \left( \frac{n\pi}{l} \right)^4 \frac{EI}{\mu} - \left( \frac{n\pi}{l} \right)^2 \frac{P(t)}{\mu} \right] = \frac{P(t) g_{0n}}{\mu}. \quad (26)$$

These equations are uncoupled due to the orthogonality of the eigenfunctions and due to the orthogonality between the eigenfunctions and the Fourier components of the initial curvature. With the initial conditions

$$v(x, 0) = f_1(x); \quad \left( \frac{\partial v}{\partial t} \right)_{t=0} = f_2(x), \quad (27)$$

we obtain the solution

$$\begin{aligned} T_n(t) = & \frac{2}{\Omega_n l} \left( \int_0^l f_2(x) \sin \frac{n\pi}{l} x dx \right) \sin \Omega_n t \\ & + \left[ \frac{2}{l} \int_0^l f_1(x) \sin \frac{n\pi}{l} x dx - \frac{P g_{0n}}{\mu \Omega_n^2} \right] \cos \Omega_n t + \\ & \frac{P g_{0n}}{\mu \Omega_n^2}. \end{aligned} \quad (28)$$

The longitudinal load  $P$ , as well as the modulus of the Fourier components, is contained in the coefficient of  $\cos \Omega_n t$ . Thus both of them have an effect on the amplitude of the free motion.

The coefficient of the cosine function of the  $n^{\text{th}}$  eigenmode contains only the Fourier coefficient of the  $n^{\text{th}}$  component of the initial curvature. If some of these components are zero, then the equivalent eigenmode amplitude will be unaffected by either the initial curvature or the longitudinal load.

The spine can assume various equilibrium positions. Each one will produce a different shape of its initial curvature. This results in different sets of  $g_{on}$  values. The amplitudes of the various eigenmodes and locations of maximum bending stress will therefore be dependent on the attitude of the subject.

In particular, the interpretation of test results with animal subjects should take differences in curvature between man and animal into consideration.

### C. Dynamic Instability

When a time variable force is added to the longitudinal load, then

$$P(t) = P + P_0 \sin \omega t \quad . \quad (29)$$

The solution that was just discussed does not apply. The differential equation for the time distribution is now

$$\ddot{T} + T \left[ \left( \frac{n\pi}{l} \right)^4 \frac{EI}{\mu} - \left( \frac{n\pi}{l} \right)^2 (P + P_0 \sin \omega t) \frac{1}{\mu} \right] =$$

$$(P + P_0 \sin \omega t) \frac{f_0 \pi^2}{\mu l^2} \quad . \quad (30)$$



This equation represents a Mathieu equation except for the addition of a forcing function. Due to the multiplicative connection of  $T$  and its coefficient, the solution contains also harmonics that are of different frequency than the parameter variation. Which one of these harmonics dominates the solution depends on the relation of the parameter frequency to the natural frequency. Unbounded solutions can be expected at and around frequencies that, according to Bolotin<sup>3</sup>, are

$$\omega = \frac{2\Omega}{k}, \quad k = 1, 2, 3 \dots \quad (31)$$

The solution is of frequency  $\omega$  if  $k$  is even and of frequency  $\omega/2$  if  $k$  is odd. Therefore there are frequencies of parametric resonance in addition to the regular resonant frequencies. These frequencies are load-dependent. The relationship between the first resonant frequency and the longitudinal load, equation (20), is represented by the solid parabola (Figure 4) that intersects the abscissa at  $\omega/\Omega = 1$ . The other parabolas represent locations of possible parametric resonance.

Instability is also possible in areas around these parabolas. Their width depends on the amplitude  $P_0$  of the load variation. These regions of instability are indicated by the shaded areas in Figure 4. Most dangerous, is the first region of instability that is represented by the first region on the right.

Approximate equations for the boundaries between the stable and unstable regions are given by Bolotin<sup>3</sup>. They are:

1st Region of Instability:

$$\omega = 2\Omega \sqrt{\left(1 - \frac{P}{P_E}\right) \left(1 \pm \frac{\epsilon}{2}\right)} \quad (32)$$

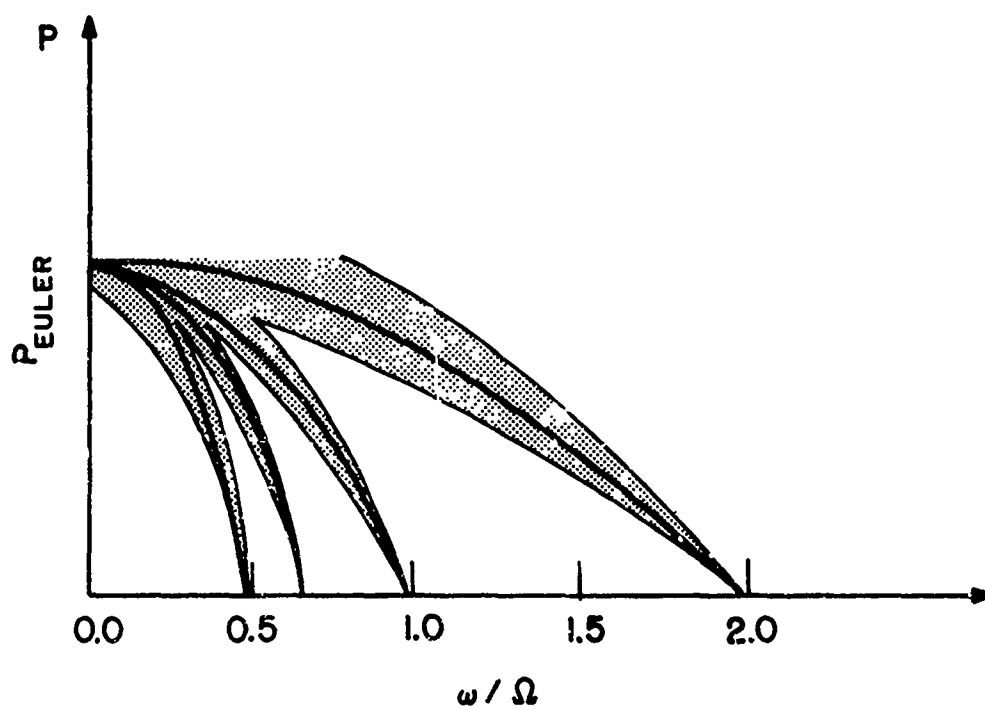


Figure 4. Regions of Instability for Model of Lumbar Spine (Thorax Restrained).

2nd Region of Instability:

$$\omega = \Omega \sqrt{\left(1 - \frac{P}{P_E}\right) \left(1 + \frac{1}{3} \epsilon^2\right)}$$
$$\omega = \Omega \sqrt{\left(1 - \frac{P}{P_E}\right) (1 - 2 \epsilon^2)}$$
(33)

3rd Region of Instability:

$$\omega = \frac{2}{3} \Omega \sqrt{\left(1 - \frac{P}{P_E}\right) \left(1 - \frac{9 \epsilon^2}{8 + 9 \epsilon^2}\right)}$$
(34)

$$\epsilon = \frac{P_0}{2(P - P_E)} ; P_E \text{ Euler buckling Load .}$$

Parametric resonances were occasionally observed when the transverse motion of the spine of a human subject under vertical vibrations was observed. The difference of impedance curves as obtained through vibration and impact tests could perhaps be explained through parametric excitation.

Also the capability of the spine to transfer energy at various frequencies may be of some consequence, in particular with respect to subsystems that are coupled to the spine. Conversely, coupled subsystems may distort parametric resonances.

#### UNRESTRAINED SPINE

The model will now be extended to include the thorax without external restraints. The boundary conditions at the upper end of the rod are determined by the inertia of the thoracic mass to transverse accelerations and the rotational inertia of the thorax (Figure 1). A longitudinal force is acting at the lower end of the lumbar spine. The configuration is somewhat idealized because whole-body accelerations and rotations are assumed to be negligible. The equation of motion is the same as in the previous case and the treatment will follow the

same sequence of steps as before. The homogeneous equation of motion, equation (2), (straight rod) will be solved first and the effects of the longitudinal loading will be discussed. The second step is the solution of the nonhomogeneous equation of motion, equation (1), and a discussion of the results.

#### A. Straight Rod

Equation (2) applies in this case as well as the ordinary differential equations (4) and (5) that were derived from it, and the general solution for the spatial distribution, equation (6), and time distribution, equation (7). The constants  $D_{mn}$  will have to be determined by the boundary conditions which were discussed in the previous paragraph, and are quantitatively defined by the following equations:

$$V(0) = V''(0) = 0 \quad (35)$$

$$EI \left( \frac{\partial^3 v}{\partial x^3} \right)_{x=l} = -m \left( \frac{\partial^2 v}{\partial t^2} \right)_{x=l} \quad (36)$$

$m$  - mass of thorax

$$\theta \left( \frac{\partial^3 v}{\partial x \partial t^2} \right)_{x=l} = -EI \left( \frac{\partial^2 v}{\partial x^2} \right)_{x=l} \quad (37)$$

$\theta$  - dynamic moment of inertia  
of thorax

The characteristic equation as obtained through the usual manipulation is

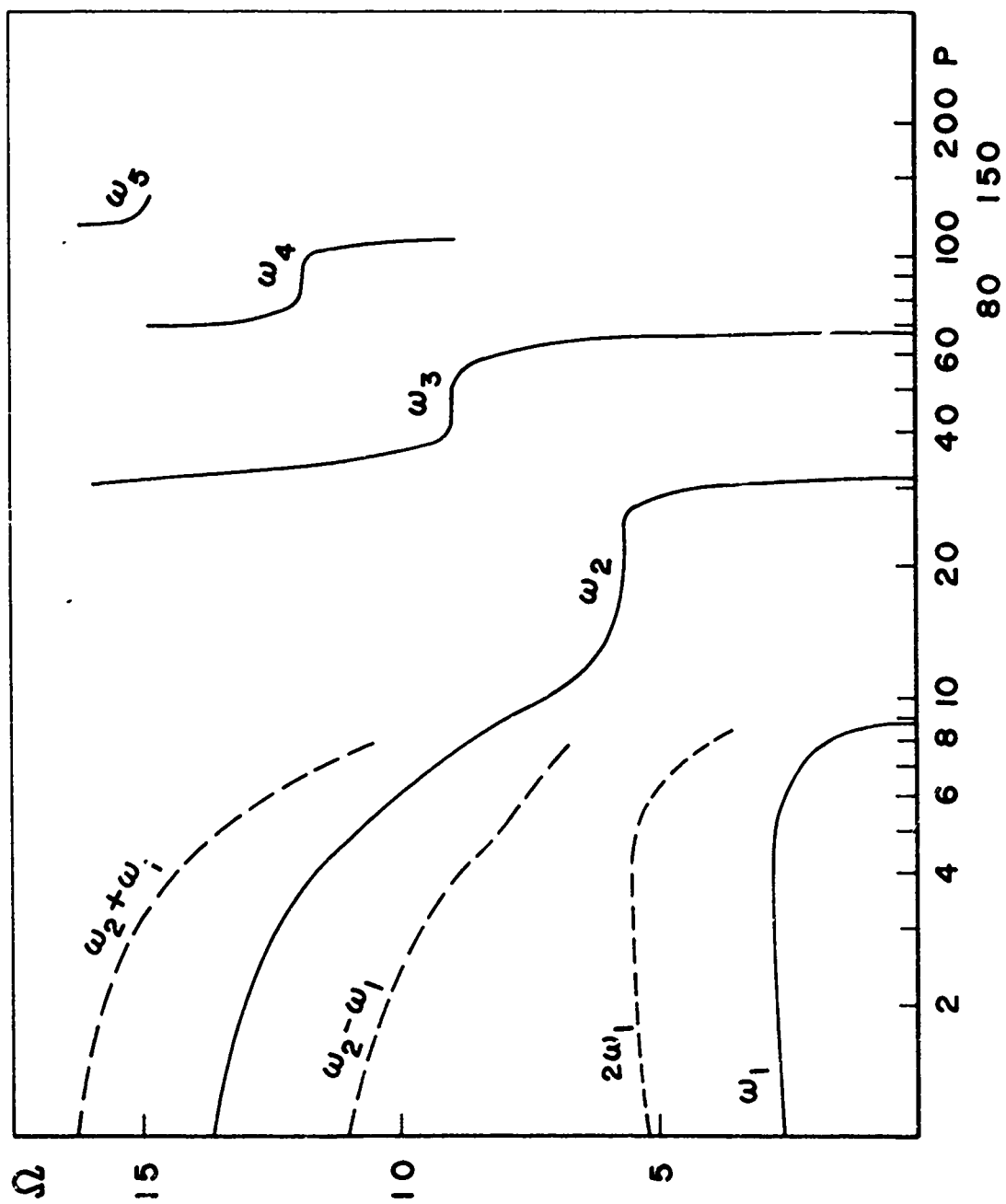


Figure 5. Curves of Possible Instability for the Unrestrained Spine Model.

$$\begin{aligned}
& (r_1^2 + r_2^2) [(-r_2^3 \cos r_2 l - 8 \sin r_2 l)(r_1^2 \sinh r_1 l \\
& - \lambda r_1 \cosh r_1 l) + (r_1^3 \cosh r_1 l \\
& - 8 \sinh r_1 l) \cdot (r_2^2 \sin r_2 l + \lambda r_2 \cos r_2 l)] = 0
\end{aligned} \tag{38}$$

In this equation are

$$\delta = \frac{m \Omega n^2}{EI} \tag{39}$$

$$\lambda = \frac{\theta \Omega n^2}{EI} \tag{40}$$

The characteristic equation contains the natural frequencies as well as the longitudinal load  $P$  which is contained in  $r_1$  and  $r_2$ , (see equation 7). The natural frequencies can therefore be determined as a function of the longitudinal load. This was done by iteration. The results are presented in Figure 5 by the solid curves. Arbitrary values were chosen for the parameters. The only purpose of these preliminary numerical computations was to obtain a graphic picture of the relationship between load and natural frequency. The numerical values for these computations, such as the modulus of elasticity, static moment of inertia, etc. were rough estimates of the various spine materials.

The eigenfunctions for this set of boundary conditions are

$$V_n(x) = \sin r_{2n} x + \frac{r_{2n}^3 \cos r_{2n} l + 8 \sin r_{2n} l}{r_{1n}^3 \cosh r_{1n} l - 8 \sinh r_{1n} l} \sinh r_{1n} x \tag{41}$$

These eigenfunctions depend also on the longitudinal load. The first eigenfunction at three different longitudinal loads is presented in Figure 6. The numerical values for the various parameters were chosen to represent a human subject. The length  $l$  is 30.48 cm which

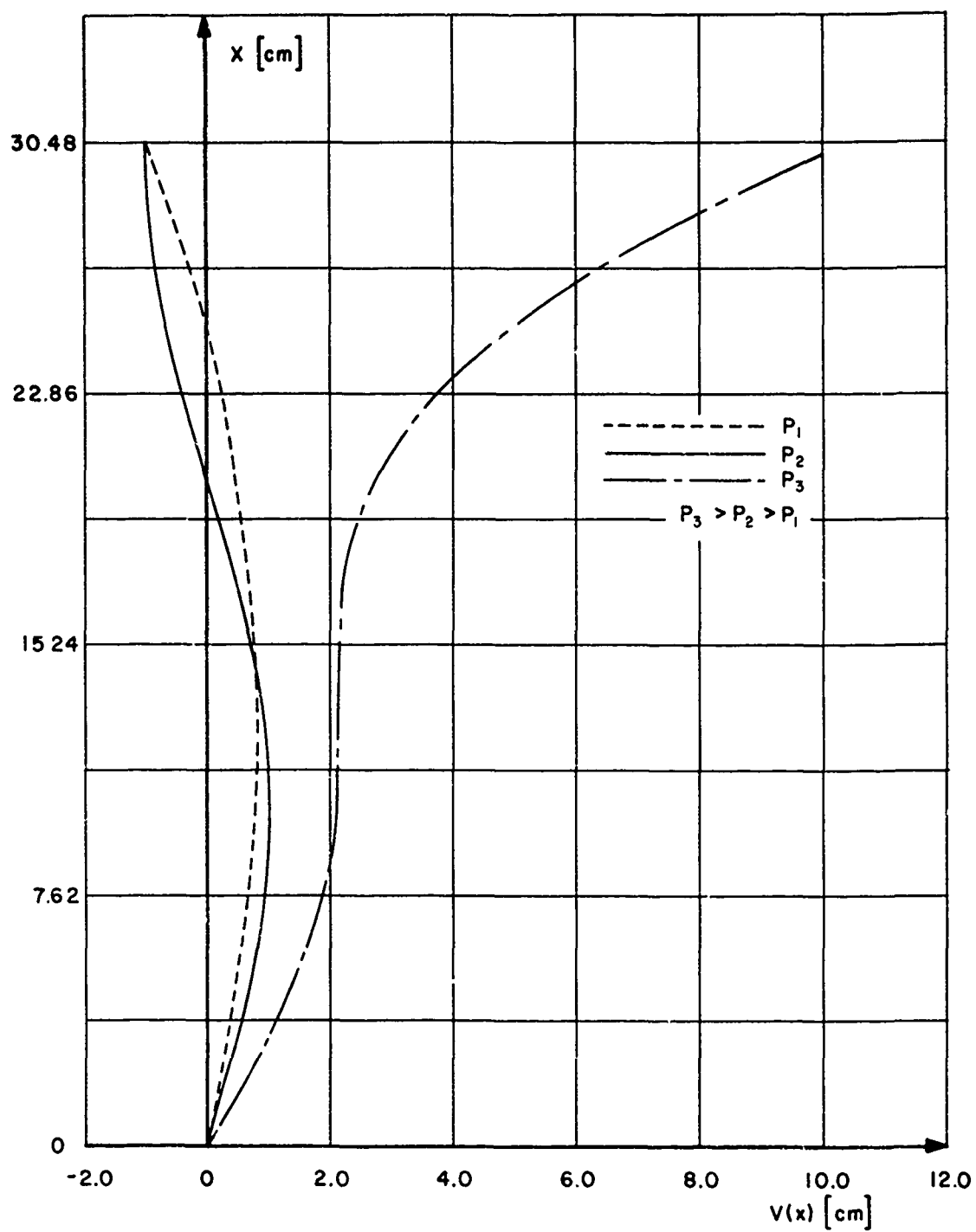


Figure 6. Eigenfunctions of Unrestrained Spine Model Under Various Longitudinal Loads.

represents the length of the average lumbar spine. The lowest of the longitudinal loads,  $P_1$ , is 27 lbs. or 12.27 kp, which is about the weight of the average human thorax. The load  $P_2$  is three times that of  $P_1$  and the load  $P_3$  is ten times that of  $P_1$ . It is very obvious that these eigenfunctions depend very much on the longitudinal load. The curve for the load  $P_2$  is in shape similar to the transverse displacement distribution along the lumbar spine of sitting human subjects under vertical vibration (Figure 2).

The bending moment along the spine in one of its eigenmodes is directly proportional to the second derivative of the eigenfunction. These derivatives are plotted in Figure 7 for the same three longitudinal loads. It is very obvious that these derivatives depend on the longitudinal load. The bending load is rather evenly distributed over the length of the lumbar spine at small longitudinal loads. Peaks of bending loads appear as the longitudinal load increases. The greatest peak occurs at the upper end and a smaller one at the lower section of the lumbar spine. The peaks increase with the longitudinal load and the lower peak moves farther down the spine.

Statistical curves have been published that show the incidence of vertebral injury along the lumbar and thoracic spine. These curves differ somewhat from one author to the other. Hirsch and Nachemson<sup>4</sup> arrive at a distribution along the lumbar spine that is fairly even. Moffatt and Howard<sup>5</sup> present one with an incidence of injury that is low at the lower end of the lumbar spine, increases slowly from there on up, and increases rapidly around the 11th and 12th thoracic vertebra. Another curve published by Higgins et al.<sup>6</sup> is similar to that of Moffatt except for no injuries around the 4th lumbar vertebra and some injury of the coccyx.

It seems that the differences of these curves may be due to differences in the magnitude of the longitudinal loads.



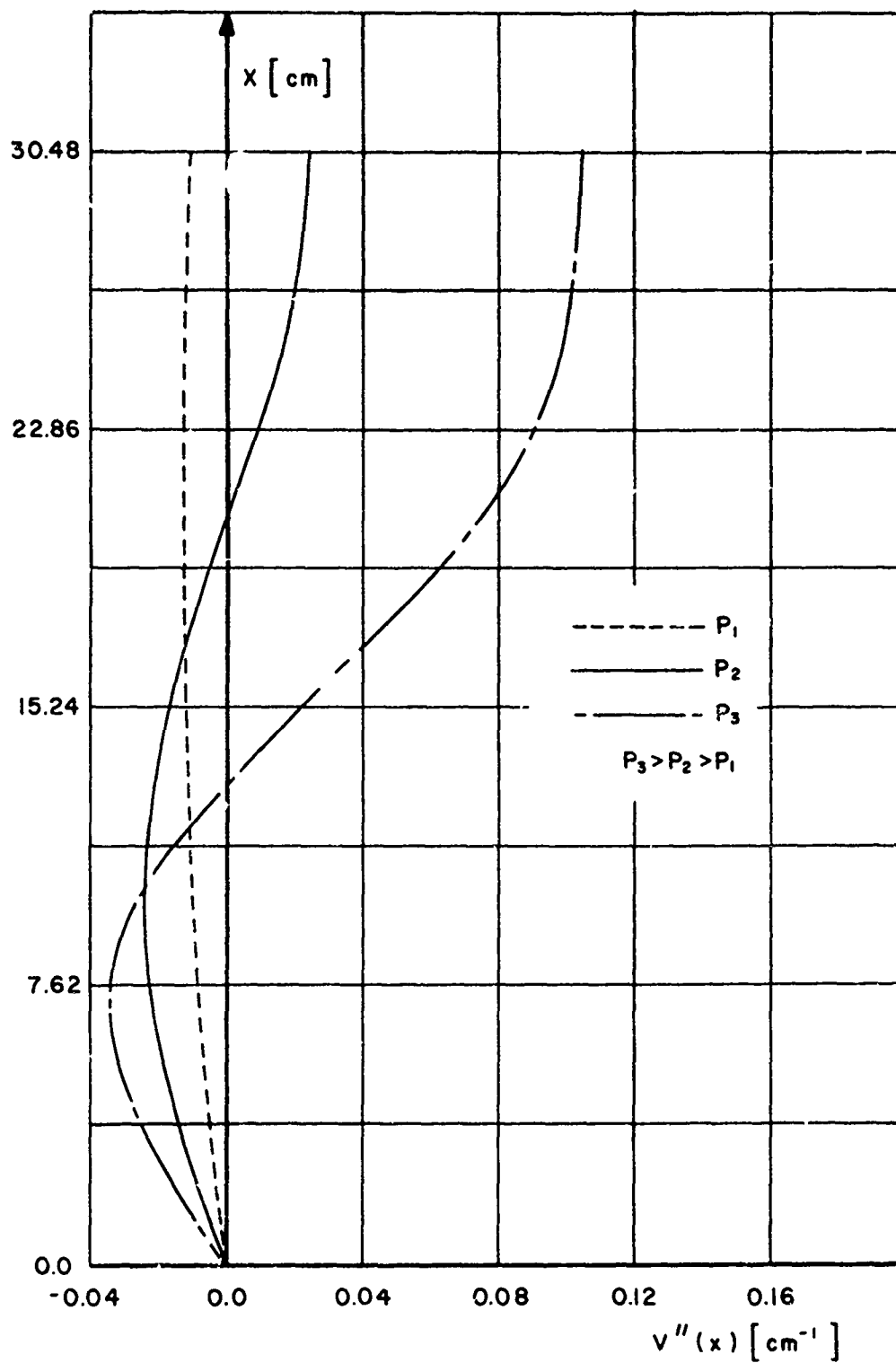


Figure 7. Second Derivative of Eigenfunctions of Unrestrained Spine Model Under Various Longitudinal Loads.

After comparison with the second derivative of the eigenfunction, one would expect the incidence curve of Hirsch and Nachemson to be obtained from cases of relatively small longitudinal loading. The second derivative of the eigenfunction crosses the zero line for two longitudinal loads. This seems to reflect the zero incidence in Higgins' curve around the 4th lumbar vertebra.

### B. Curved Rod

In the previous discussion, we did not consider the right hand side of equation (1). The nonhomogeneous equation cannot be solved exactly by making a product assumption because it is not self adjoint. An approximate solution with such an assumption can be obtained. In this case, the Galerkin method will be applied.

The equation of motion is rearranged to assume the form

$$EI \frac{\partial^4 v}{\partial x^4} + P(t) \frac{\partial^2 v}{\partial x^2} + \mu \frac{\partial^2 v}{\partial t^2} + P(t) \frac{d^2 v_0}{dx^2} = L(v) = 0. \quad (42)$$

A product assumption of the following nature is made

$$\bar{v}(x, t) = \sum_{n=1}^N V_n(x) T_n(t) \quad (43)$$

where the  $V_n(x)$  are the previously determined eigenfunctions. This is substituted into equation (42) which results in

$$L(\bar{v}) = \epsilon(x, t). \quad (44)$$

$\epsilon(x, t)$  is zero if such an assumption can satisfy equation (42) exactly, and it is different from zero if it cannot do that. In this case the error of an approximate solution with this assumption is minimized by imposing the conditions

$$\int_0^l L(\bar{v}) V_n(x) dx = 0 \quad n = 1, \dots, N \quad (45)$$

This requires the error  $\epsilon(x, t)$  along the length of the rod weighted by the eigenfunctions and integrated over  $x$  to be zero. In other words, equation (45) requires orthogonality between the residual and the eigenfunctions.

The variable  $x$  is eliminated through integration and a system of coupled ordinary differential equations with  $t$  as the variable evolves. These equations would not be coupled if the eigenfunctions of the adjoint problem would have been used for weighting functions. The coupled equations are in matrix notation

$$\begin{aligned} \{\ddot{T}_n\} + \frac{1}{\mu} [a_{nj}]^{-1} (EI [b_{nj}] + P(t) [C_{nj}]) \{T_n\} = \\ - P(t) [a_{nj}]^{-1} \{A_n\} \end{aligned} \quad (46)$$

$$\begin{aligned} a_{nj} = \int_0^l V_n V_j dx \quad ; \quad b_{nj} = \int_0^l V_n V_j^{(4)} dx \\ C_{nj} = \int_0^l V_n V_j'' dx \quad ; \quad A_n = \int_0^l \frac{d^2 v_0}{dx^2} V_n dx \end{aligned} \quad (47)$$

The solution of this equation consists of the solution for the homogeneous equation plus a particular solution of the nonhomogeneous equation. An assumption of the type

$$\{T_i\} = \{T_{io}\} e^{i\omega t} \quad (48)$$

for the homogeneous equations, and the usual manipulations, leads to a solution of the type

$$T_n = \sum_{k=1}^N q_k \mu_{nk} \sin(\omega_k t + \psi_k) . \quad (49)$$

The  $\mu_{nk}$  are the amplitude ratios.

The right side of equation (46) is constant. Therefore, a constant can be determined as a particular solution. This solution is

$$\{B_i\} = -P(t) [H]^{-1} [a_{ij}]^{-1} \{A_i\} \quad (50)$$

$$[H] = \frac{1}{\mu} [a_{ij}]^{-1} (EI [b_{ij}] + P(t) [c_{ij}]) \quad (51)$$

The complete solution is then

$$\bar{v}(x, t) = \sum_{n=1}^{\infty} V_n \sum_{k=1}^N (q_k \mu_{nk} \sin(\omega_k t + \psi_k) + B_n) . \quad (52)$$

This can be rearranged and expanded to assume the following form:

$$\begin{aligned} \bar{v}(x, t) = & q_1 [V_1 \mu_{11} + V_2 \mu_{21} + \dots V_n \mu_{n1}] \sin(\omega_1 t + \psi_1) \dots \\ & + q_n [V_1 \mu_{1n} + V_2 \mu_{2n} + \dots V_n \mu_{nn}] \sin(\omega_n t + \psi_n) \\ & + \sum_{n=1}^{\infty} V_n B_n , \end{aligned} \quad (53)$$

The eigenfunctions of the curved rod under the specified boundary conditions can be expressed as series of the eigenfunctions of the straight rod weighted by the amplitude ratios as obtained during the solution for the time distribution.

The  $q_n$  have to be determined using the initial conditions. Various methods can be applied such as subdomain, Galerkin, or a collocation technique. In any case, the  $q_n$  will finally be dependent on the  $V_n$ , that

is the eigenfunctions, and on the  $B_n$  which are determined by the initial curvature. Therefore the amplitudes of the free motions are affected by both the initial curvature and the longitudinal load which is also part of the  $B_n$ 's and the eigenfunctions. The initial curvature of the spine changes between different attitudes of a subject. The difference in response between attitudes can be accounted for through the initial curvature.

### C. Dynamic Instability

The solution for the spatial and time distribution, equation (49), applies only if  $P(t)$  is a constant. The differential equation for the time distribution, equation (46), will have to be solved by procedures such as Hill's method. Of particular interest are areas of possible dynamic instability. These have not been determined for this particular case. However, these areas are usually around the lines of the natural frequencies in Figure 5 and also around curves of twice the natural frequency, fractions of it, and at frequencies that are the sums and differences of the natural frequencies. Some of these conditions of parametric instability are indicated by the broken lines in Figure 5.

## CONCLUSIONS

It was the purpose of this discussion to investigate the possibilities of accounting quantitatively for the effect of longitudinal loads on the natural frequencies of transverse motions of the lumbar spine, as well as for the effects of longitudinal loading and initial curvature on the magnitude and distribution of bending along the lumbar spine.

Longitudinal loads, initial curvature and boundary conditions imposed on the lumbar spine seem to have significant effects on the magnitude and distribution of bending in a dynamic environment. The type of bending distribution curves that have been obtained seem to agree with statistical curves of injury incidence along the lumbar spine. The transverse displacement distribution along the lumbar spine under

longitudinal loads agrees with experimental data. A more detailed numerical adjustment of the model to experimental data will be attempted. In particular, major subsystems that are coupled to the spine will have to be considered for this purpose. Because subsystems have an effect on the boundary conditions and thus on the response of the spine, it seems they have to be included because no experimental data are available that exclude coupling effects.

The natural frequency of transverse spine motions under longitudinal loads is load-dependent. The natural frequency decreases in general with increasing compressive loading and increases with increasing tensile loading. The type of natural frequency - longitudinal load relationship depends to a great degree on the boundary conditions.

Parametric transverse resonances and dynamic instabilities can be expected under a periodic longitudinal load.

#### ACKNOWLEDGEMENTS

This research was jointly sponsored by the 6570th Aerospace Medical Research Laboratories under Air Force Contract F33615-69-C-1681 and the University of Dayton Research Institute (UDRI).

The authors gratefully acknowledge the assistance provided by personnel of the 6570th Aerospace Medical Research Laboratory, Vibration and Impact Branch, and the staff of the University of Dayton Research Institute. The authors are indebted to Dr. Jack Crouch (UDRI) for many suggestions and discussions.

#### REFERENCES

1. Vulcan, A. P., A. I. King and G. S. Nakamura, "Effects of Bending on the Vertebral Column During +  $G_z$  Acceleration," Aerospace Med., 41(3):294-300 (1970).
2. Krause, H., "Das schwingungsmechanische Verhalten der Wirbelsaeule," Int. Z. angew. Physiol. einschl. Arbphysiol, Vol. 20:125-155, (1962).
3. Bolotin, V. V., The Dynamic Stability of Elastic Systems, Holden-Day, Inc., San Francisco, (1964).
4. Hirsch, C. and A. Nachemson, "Clinical Observations on the Spine in Ejected Pilots," Acta Orth. Scand., 31, Fas. 2:135-145 (1961).
5. Moffat, C. A. and R. H. Howard, The Investigation of Vertebral Injury Sustained During Aircrew Ejection, Technology, Inc., San Antonio, Texas, Quarterly Progress Report No. 2, NASA Contract NAS2-5062.
6. Higgins, L. S., S. A. Enfield and R. J. Marshall, Studies on Vertebral Injuries Sustained During Aircrew Ejection, Final Report to Office of Naval Research, Contract No. NONR-4675 (00), Technology, Inc., San Antonio, Texas, (1965).

PAPER NO. 25

NONLINEAR LUMPED PARAMETER MATHEMATICAL MODEL  
OF DYNAMIC RESPONSE OF THE HUMAN BODY

Gordon R. Hopkins

West Virginia University

ABSTRACT

Two nonlinear models of man's dynamic response to low frequency vibration are discussed. The first model uses linear spring and damper elements but accounts for the nonlinear geometry of visceral mass motion. This model adequately reproduces both the input mechanical impedance and vibration transmission characteristics for a seated human subject.

The second model includes the nonlinear effects of the lungs. The influence of this nonlinearity on the dynamic response is discussed and compared to experimental results from tests on animals.

INTRODUCTION

Over the past two decades considerable attention has been paid to the effects of vibration and impact on the human body. As humans are exposed to the implements of modern technology these mechanical stimuli reach magnitudes that can cause physiological damage ranging from mild discomfort to death.

The inaugural research effort in the study of man's dynamic response was to establish human tolerance limits to vibration and impact. Once



these were established, the attention of investigators turned toward the more perplexing problem of understanding the injury mechanisms that set the tolerance.

Using human subjects as test specimens to gather information about the internal dynamics of the body has not always been a gratifying experience. Yet, animal substitutes in most cases have proved equally disappointing. The problems associated with trying to glean information about the dynamics of the internal organs and structural components of the human body is complicated by the necessity of having to gather data without damage to the subject. This limits the types of instruments that may be used as well as severity of the test environment. In effect, investigators have been gathering data about internal dynamics of the human body by sensing only their external effects.

Useful data have been gathered in this manner however. For instance, most of our understanding of the body's dynamic response to low frequency vibration has been based on measurements such as driving point mechanical impedance, external strain, vibration transmission, and cineradiographs.

In order to make the best use of these data, mathematical models have often been employed in the effort to expand our understanding of the human body as a dynamical system.

This report discusses one such model. A nonlinear lumped parameter model that explains phenomena observed during low frequency vibration of a seated man, such as the second and third spinal resonances.

#### BACKGROUND INFORMATION

The rationale of the model is best discussed by first briefly reviewing the experimental data on which it is based.

Mechanical impedance has proved to be a valuable and well used tool in studying the vibration response of biological systems. With its use as a parameter, the dynamic response of a human subject to vibration can be studied as a "black box" much as one would an unknown electrical circuit with input electrical impedance. Although it has limitations, this approach yields much information about man's dynamic response to sinusoidal vibrations by showing system resonances.

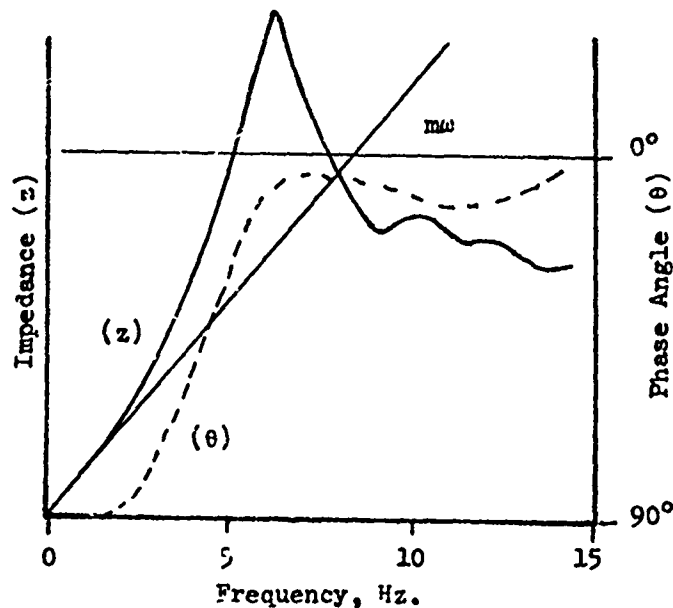


Fig. 1 Mechanical Impedance and Phase Angle for Seated Subject<sup>(1)</sup>

Figure 1 based on the work of Coermann et al.<sup>1,2</sup> illustrates the mechanical impedance of a typical subject to low frequency sinusoidal vibration. The predominant features of this curve are the peaks at 5, 11, and 14 Hz. These peaks suggest points of resonance. As von Gierke<sup>3</sup> suggests, the first peak is due to the abdominal resonance, and the second and third due to some action of the upper torso on the vertebral column.

A second, and equally useful tool used in vibration analysis is vibration transmission, or transmissibility. Again Coermann<sup>1</sup> shows us, and is substantiated by the work of Pradko<sup>4</sup> who used random vibration instead of sinusoidal, that the vibration response of a seated human subject can be characterized by transmissibility. Figure 2 shows this result.

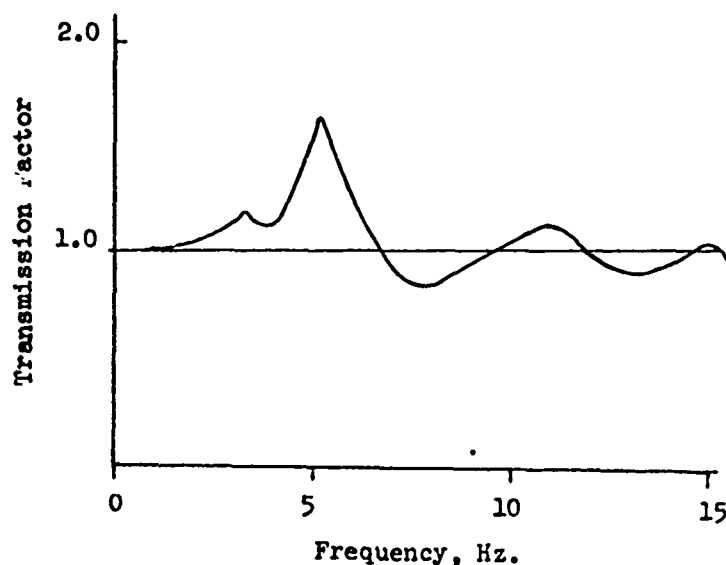


Fig. 2 The Transmission of Vibrations from the Seat to the Head of a Seated Human Subject<sup>(1)</sup>

The transmission factor for a seated subject shows three peaks nominally at 5, 11, and 14 Hz. As with the mechanical impedance, it is hypothesized that these peaks are the result of resonant systems in the body. One should note that the peak corresponding to the abdominal resonance transmits the largest amplitude vibrations to the head.

Another noteworthy set of parameters that characterize the body's dynamic response to low frequency vibration are the strain measurements made by Clark et al.<sup>5</sup> and shown in Figure 3. It is observed from these measurements that the first peak for the upper and lower abdominal strain occur at approximately 1 Hz apart. The implication here is that the visceral mass works against a different spring when it moves toward the head than it does when it moves toward the pelvis.

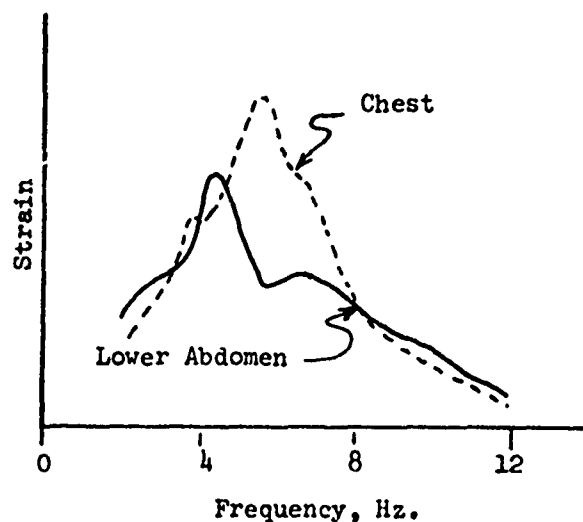


Fig. 3 Strain for Seated Subject During Low Frequency Vibration<sup>(5)</sup>

The final set of measurements to be considered are those made by White et al.<sup>6</sup> of colon pressure during low frequency vibration. As anticipated, these measurements show the effect of the abdominal resonance in agreement with the lower abdominal strain shown in Figure 3. If the second and third peaks of Figures 1 and 2 are due to vertebral column resonances as hypothesized, then the effect on colon pressure would be minimal. As can be seen in Figure 4, this is precisely the case.

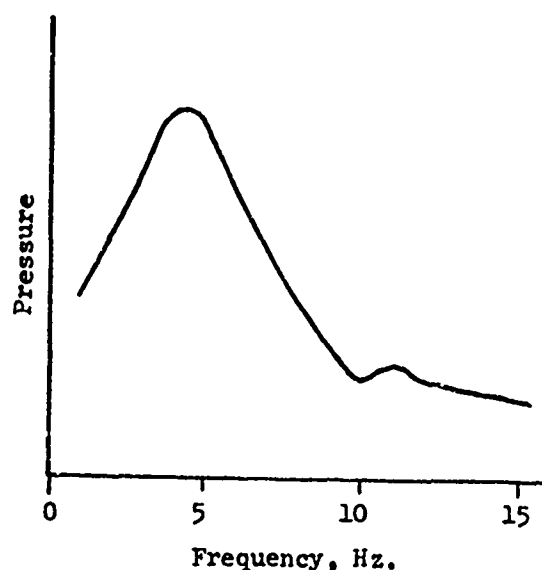


Fig. 4 The "Mean" Colon Pressure During Low Frequency Vibration for a Seated Subject<sup>(6)</sup>

In summary, these experimental measurements require a model to:

1. Have a similar impedance and phase versus frequency relationship as that for a human subject.
2. Demonstrate the same vibration transmission characteristics as does a human subject.

3. Corroborate the organ motions as inferred from the measurements of strain and colon pressure.

#### DEFINITION OF MODEL

It has been demonstrated by Hopkins<sup>7</sup>, Suggs<sup>2</sup>, and others by the construction of mathematical, electric analog, and mechanical models that an uncoupled two degree of freedom system as shown schematically in Figure 5 can adequately simulate the input mechanical impedance of the human body over the 0-15 Hz range. For purposes where only the input impedance is necessary, such as coupling with other machinery for their evaluation, this type of model is sufficient. However, for inquiring into the internal dynamics of the human body, such a model is not satisfactory. It lacks sufficient anatomical similarity to predict injury.

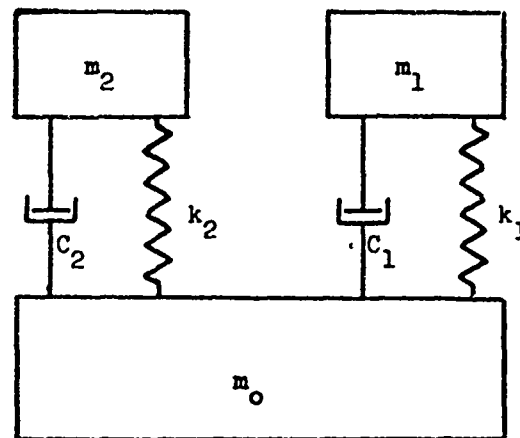


Fig. 5 Uncoupled Two Degree of Freedom Model

There is no way to use this type of model to study the transmission of vibration to various parts of the body or to corroborate such data as transmissibility, strain and internal pressures. This deficiency leads one to consider a coupled mass linear model, such as shown in Figure 6, that could accommodate these considerations.

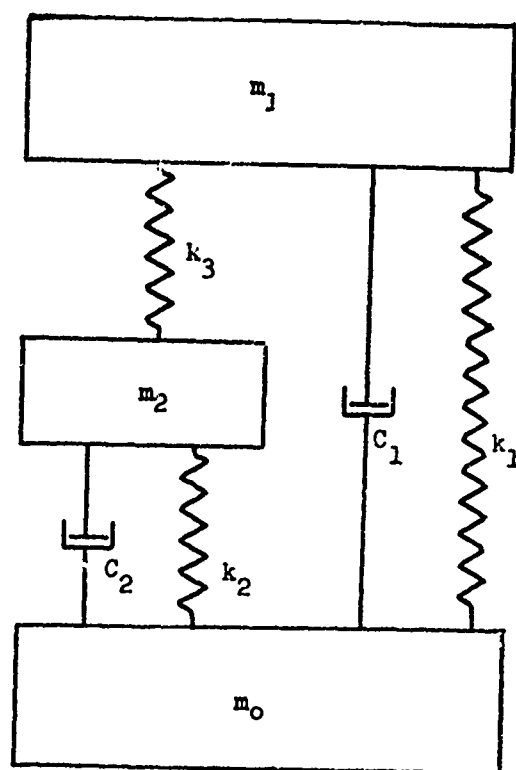


Fig. 6 Linear Coupled Mass Model

The linear coupled mass offers enough geometric similarity to the human body to be able to relate components to their anatomical counterparts. For instance,  $k_1$  and  $C_1$  could represent the vertebral column,  $M_2$  the upper torso mass,  $m_3$  the visceral mass,  $m_1$  the lower torso mass and so on. However, this model does not adequately simulate the input impedance.

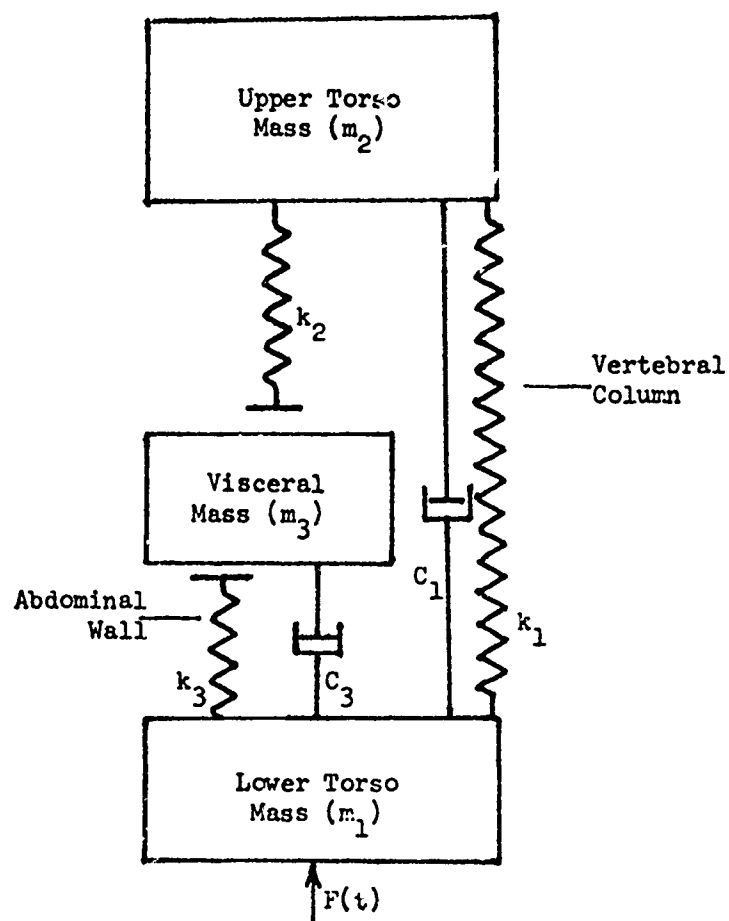


Fig. 7 Nonlinear Geometry Model of Human Body



If one examines the anatomy of the human body in more detail, it may be observed that the visceral organs are not tethered but are supported in the abdominal cavity by the abdominal muscle wall, the pelvis, and the diaphragm. When the visceral mass moves during vibration it exhibits a nonlinear geometry. As the visceral mass moves upward toward the head, it compresses the lungs but does not put tension on the abdominal wall or pelvis since it is not tethered to either. On the other hand, as the mass moves toward the pelvis, it does not put tension on the diaphragm and in turn the lungs.

The simplest model that can accommodate this nonlinear geometry is one with linear elements constructed such that the springs are not rigidly attached to the mass that represents the visceral mass.

This model is shown schematically in Figure 7 where the linear spring,  $k_1$ , and damper,  $C_1$ , represent the vertebral column,  $k_2$ , the abdominal wall,  $k_3$ , the lungs and  $C_2$ , the frictional damping on the internal movement of the organs.

#### DYNAMIC BEHAVIOR OF NONLINEAR GEOMETRIC MODEL

A mathematical model based on the schematic shown in Figure 7 has been formulated and interpreted as a computer model using IBM's Continuous System Modeling Program. The dynamic behavior of this model is shown in Figures 8, 9, and 10.

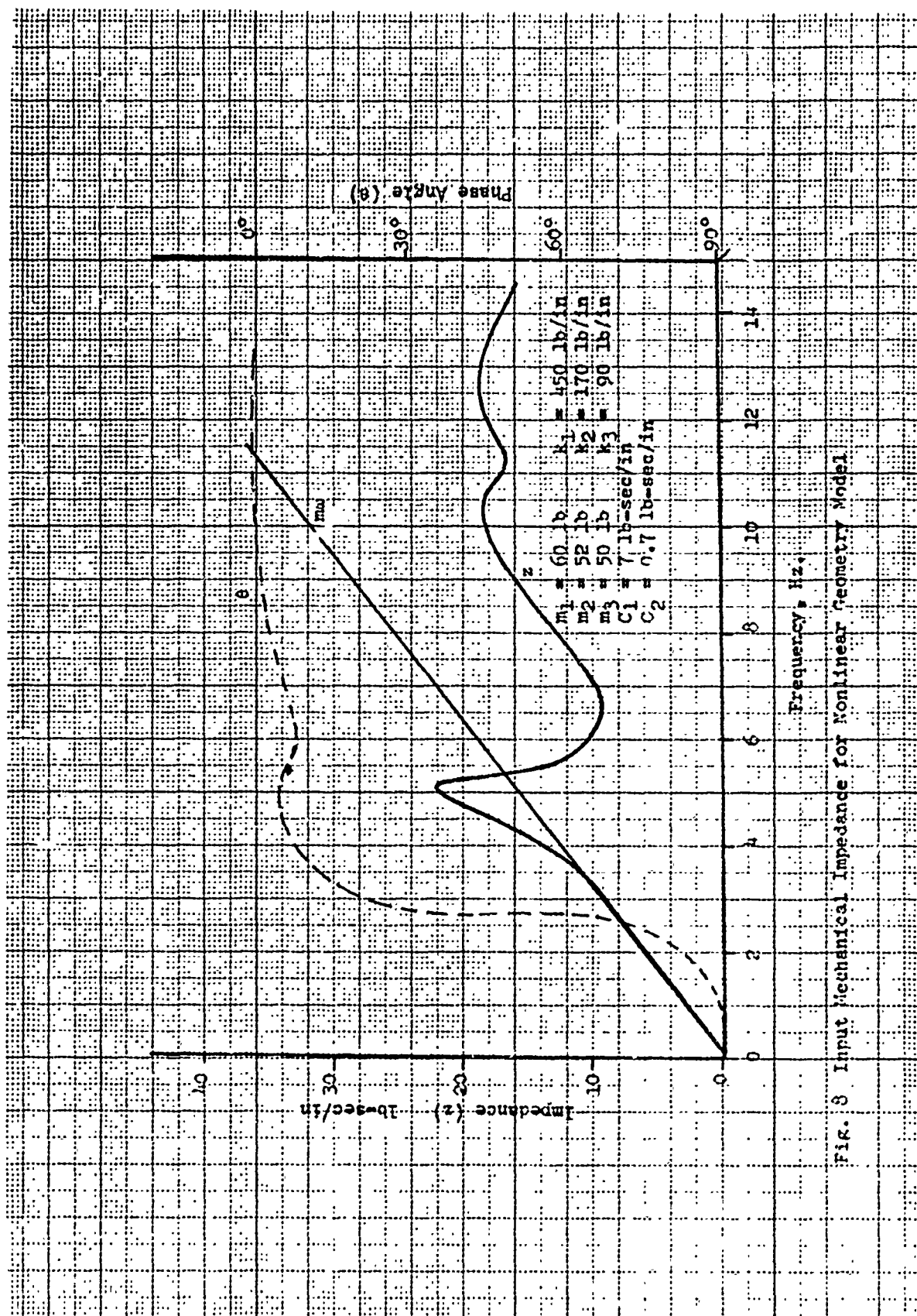


FIG. 3 Input Mechanical Impedance for Nonlinear Geometry Model

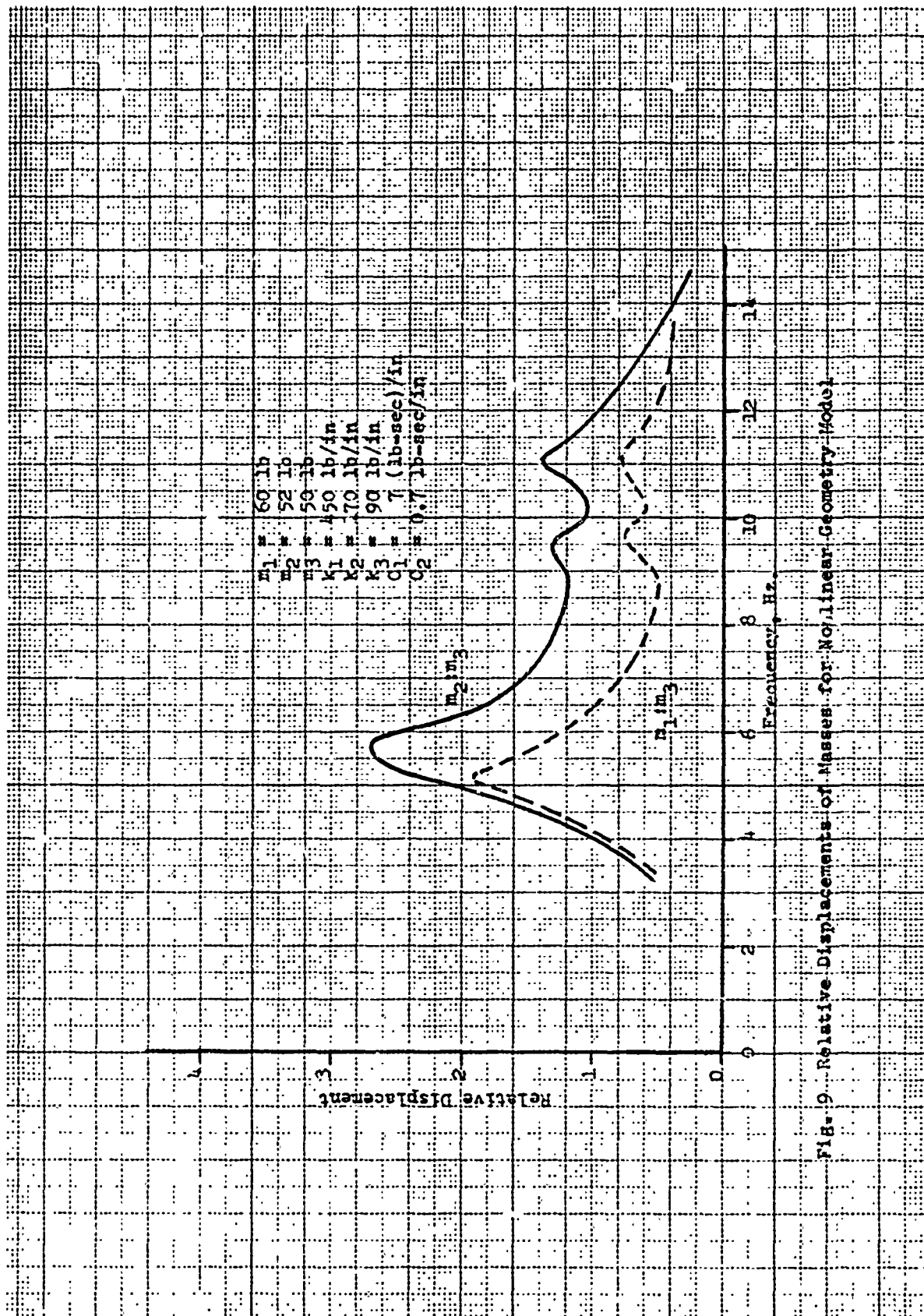


Fig. 9. Relative Displacements of Masses for Nonlinear Geometry Model

## DISCUSSION OF NONLINEAR GEOMETRY MODEL

Comparison of Figures 1 and 8 shows that this two degree of freedom model with nonlinear geometry adequately reproduces the mechanical impedance and phase angle characteristics of the human body; even to displaying the second and third resonant peaks. Comparison of Figures 2 and 9 shows that the model also demonstrates the same general vibration transmission characteristics as the human body.

If one assumes that the displacements of the visceral mass can be related to the external strains on the chest and abdominal wall, then Figure 10 agrees with the strain measurements presented in Figure 3.

It is concluded that the model does satisfactorily demonstrate the same dynamic response to low frequency vibration as does a seated human for small amplitude vibrations.

## NONLINEAR MODEL

Since all the data on which the above model is based was gathered from forced sinusoidal vibration with low amplitude accelerations, from 1/4 to 1/2 g., its use for the study of vibration with higher amplitude acceleration or impact is questionable. Experience with the nonlinear geometry model has shown that its dynamic response is not dependent on the amplitude of the forced vibration.

Krause and Lange<sup>9</sup> have shown with experiments on pigs that mechanical impedance is nonlinear with respect to the acceleration amplitude of the forced vibration. Their results are reproduced in Figure 12.

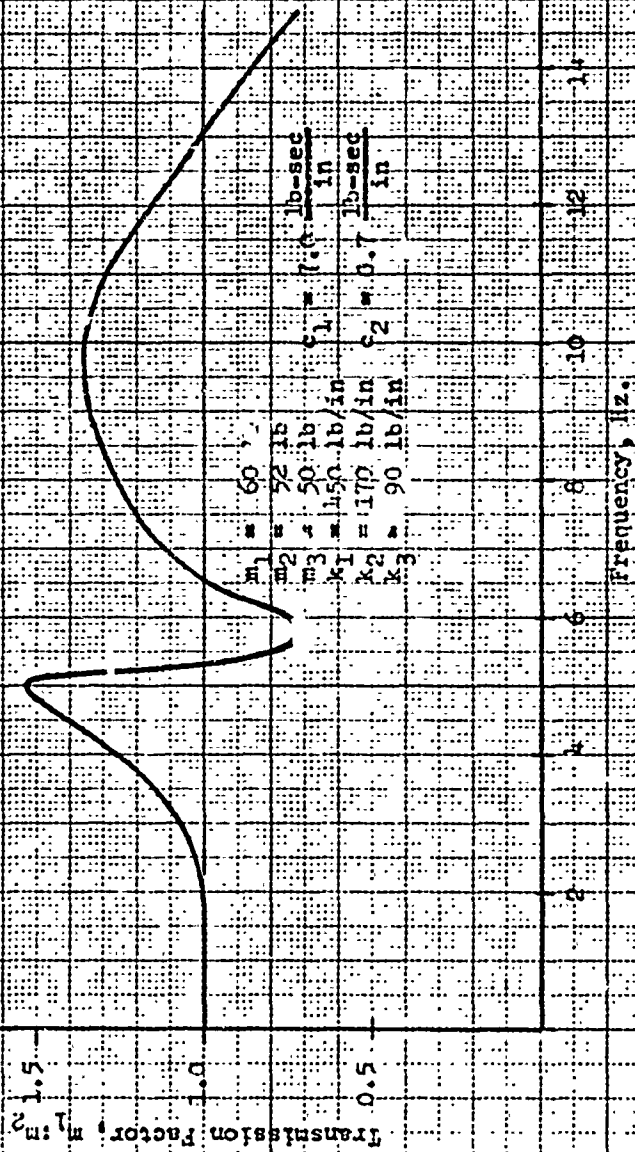


Fig. 10 Transmission of Vibration to Mass  $m_2$  of Nonlinear Geometry Model

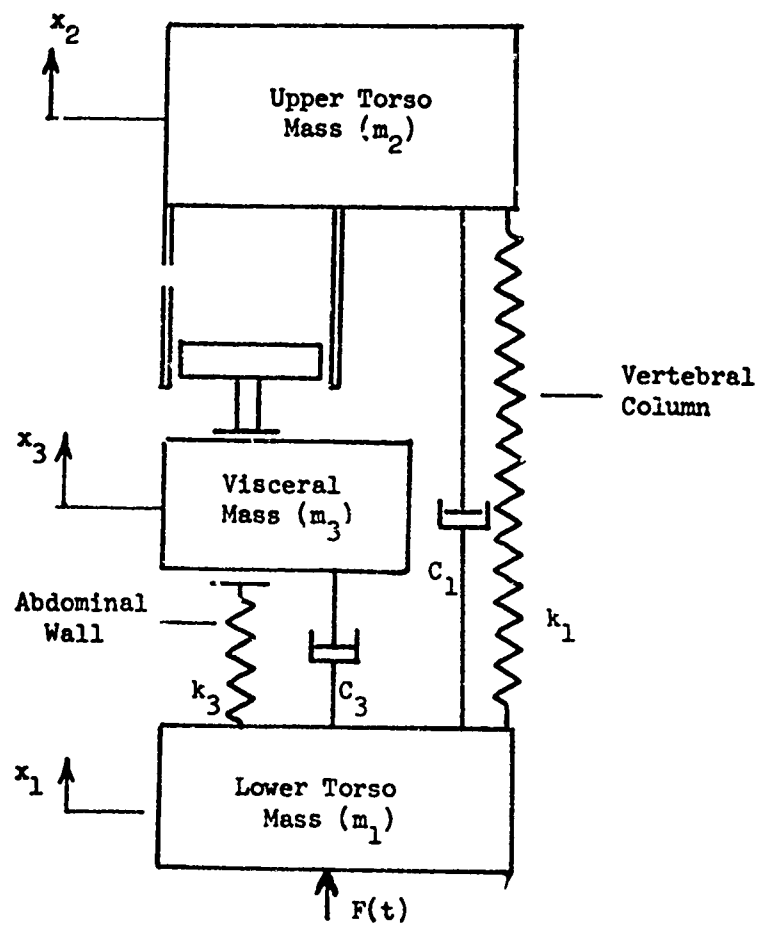


Fig. 11 Nonlinear Dynamic Model of Human Body

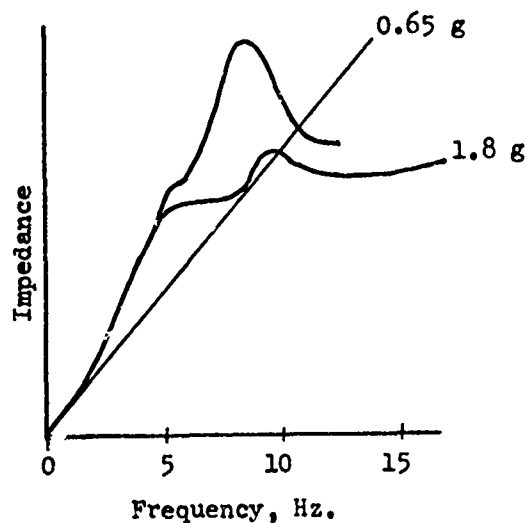


Fig. 12 Impedance of 70-lb Pig<sup>(9)</sup>

If the nonlinear geometry model is slightly sophisticated to include the nonlinear effects of the lungs by modeling them as a piston in a cylinder with an orifice, then the nonlinear behavior of biological systems observed by Krause can be simulated.

The equations of motion for this model, shown in Figure 11, are:

$$m_1 \ddot{x}_1 = k_1(x_2 - x_1) + c_1(\dot{x}_2 - \dot{x}_1) + k_2(x_3 - x_1) + c_3(\dot{x}_3 - \dot{x}_1) \\ + k_3 \delta(x_3 - x_1) + F(t)$$

$$m_2 \ddot{x}_2 = -k(x_2 - x_1) - c_1(\dot{x}_2 - \dot{x}_1) + F_{\text{LUNGS}}$$

$$m_3 \ddot{x}_3 = -k_3 \delta(x_3 - x_1) - C_3(\dot{x}_3 - \dot{x}_1) - F_{\text{LUNGS}}$$

where

$$\delta(x) = \begin{cases} 0 & , \quad x > 0 \\ x & , \quad x \leq 0 \end{cases}$$

The force exerted by the lungs on the visceral mass ( $F_{\text{LUNGS}}$ ) is derived from the model shown in Figure 14.

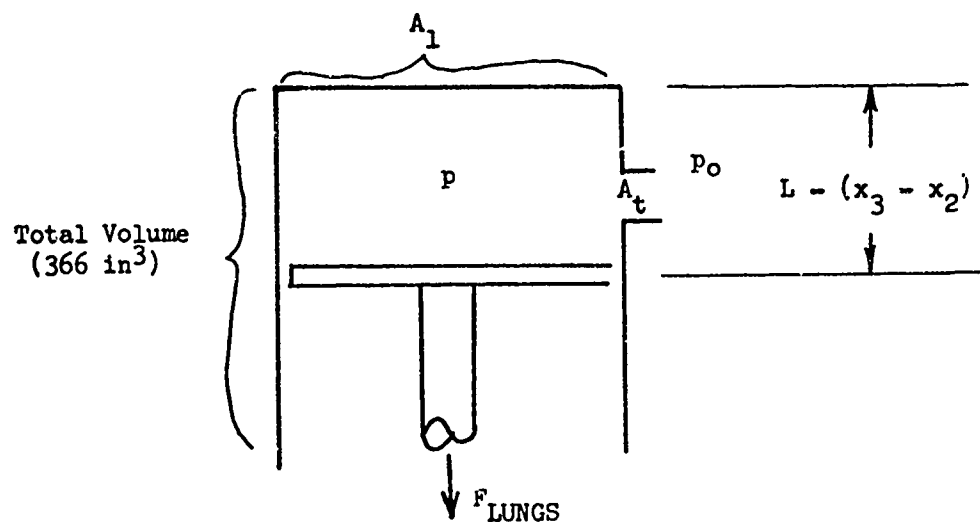


Fig. 14 Lung Model

Assuming isotropic compression, the equation of state  $pV = mRT$  gives the following formulation for  $F_{\text{LUNGS}}$ :



$$p = \int \left\{ c \left( \frac{m}{V} \right)^\delta \left[ \frac{\delta m}{m} - (\delta - 1) \frac{\dot{V}}{V} \right] - \frac{p \dot{V}}{V} \right\} dt$$

where

$$V = A_L [L - (x_3 - x_2)]$$

$$m = A_t \sqrt{\frac{2\delta}{\delta - 1} p_L p_L s \left( \frac{p_s}{p_L} \right)^{2/\delta} \left[ 1 - \left( \frac{p_s}{p_L} \right)^{\frac{\delta-1}{\delta}} \right]} \text{ sign}(p - p_L)$$

where s denotes smaller of p and  $p_L$

and L the larger of the two,

and

$$m = m_{\text{Initial}} - \int \dot{m} dt$$

Then,

$$F_{\text{LUNGS}} = \frac{\delta(x_2 - x_3)}{(x_2 - x_3)} p A_L$$

With this mathematical formulation a digital computer model was constructed using IBM's Continuous System Modeling Program.

The CSMP for this nonlinear model was subsequently used to determine the effects of different amplitude levels of vibration on the mechanical impedance. Figure 15 shows these results.

Although there are no mechanical impedance data available for humans at low frequency vibration level as high as 3 g's., comparison with the results of Krause, Figure 12, shows that the dynamic behavior of the nonlinear model is similar to that of a pig. That is, there is a general stiffening of the system as the acceleration level is increased.

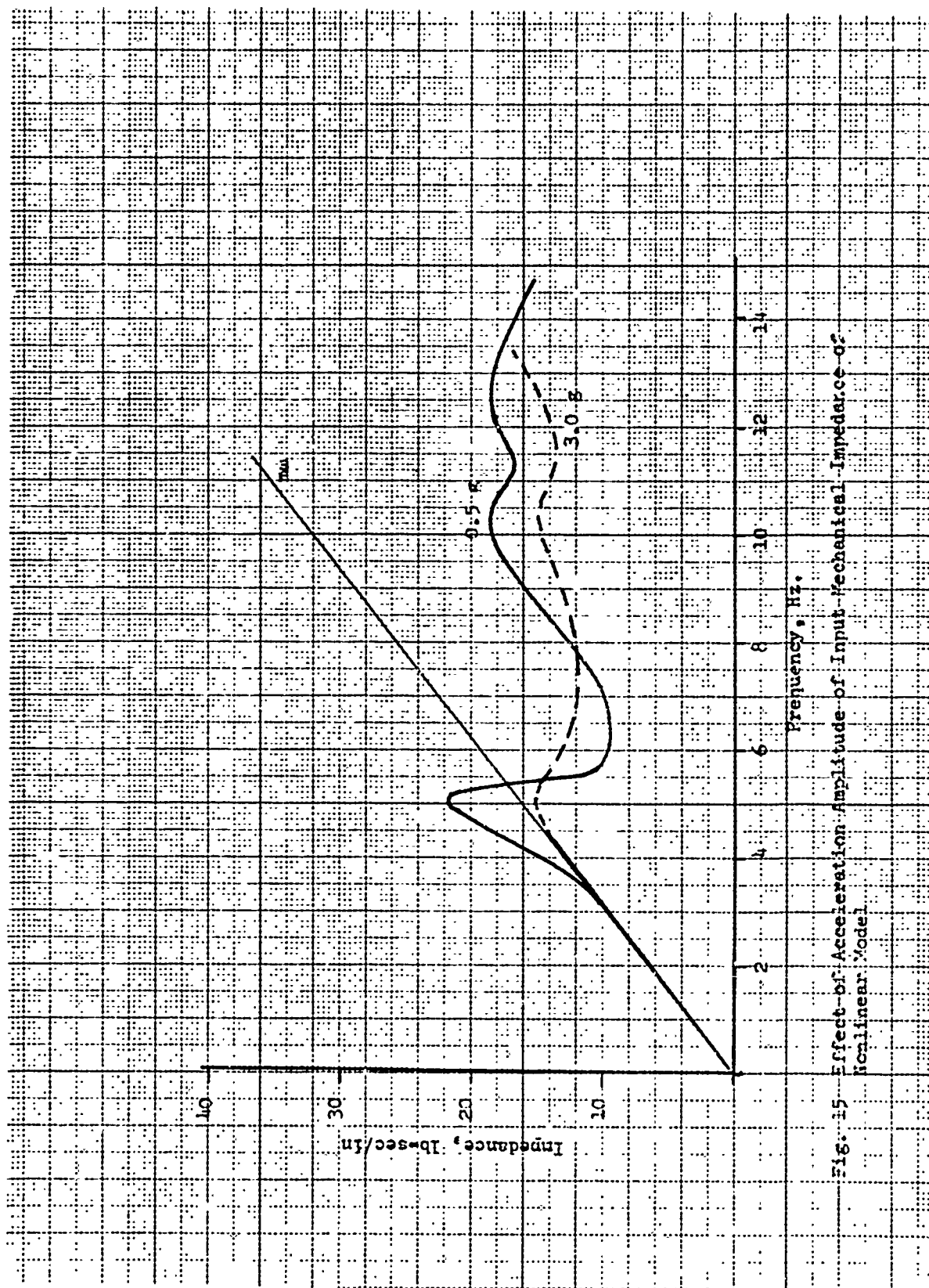


Fig. 15 Effect of Acceleration Amplitude of Input-Mechanical Impedance of Nonlinear Model

## CONCLUSIONS

1. The inclusion of nonlinear geometry in the two degree of freedom model of the human body's dynamic response of the human body improves the dynamic similarity.
2. The nonlinear mechanics of the lungs probably account for most of the body's nonlinear response to low frequency vibration.
3. If sufficient effort were expended to establish the governing parameters of the nonlinearity by vibration tests, nonlinear lumped parameter models could add understanding of the body mechanics during certain impact situations.

# REFERENCES

1. Coermann, R. R. "The Mechanical Impedance of the Human Body in Sitting and Standing Position," Human Factors, Vol. 14, (1963), pp. 227-253.
2. Suggs, C. W., Abrams, C. F. and Stikeleather, L. F. "Application of a Damped Spring-Mass Human Vibration Simulator in Vibration Testing of Vehicle Seats," Ergonomics, Vol. 12, No. 1, (1969), pp. 79-90.
3. Goldman, D. E. and von Gierke, H. E. "Effects of Shock and Vibration on Man," Shock and Vibration Handbook, Vol. 3, McGraw-Hill, (1961).
4. Pradko, F., Lee, R.A. and Greene, J. D. "Human Vibration-Response Theory," Biomechanics Monograph, ASME, (1967), pp. 205-222.
5. Clark, W. S., Lange, K. O. and Coermann, R. R. "Deformation of the Human Body Due to Unidirectional Forced Sinusoidal Vibration," Human Factors, Vol. 19, (1963), pp. 255-279.
6. White, G. H., Lange, K. O., and Coermann, R. R. "The Effects of Simulated Buffeting on the Internal Pressure of Man," Human Factors, Vol. 14, (1963), pp. 275-290.
7. Hopkins, G. R. "The Dynamic Response of the Human Body to Low Frequency Vibration," Masters Thesis, University of Kentucky, (1961).
8. Lange, K. O. and Edwards, R. G. "Force Input and Thoraco-Abdominal Strain Resulting from Sinusoidal Motion Imposed on the Human Body," Aerospace Medicine, (May, 1970), pp. 538-543.
9. Krause, H. E. and Lange, K. O. "The Nonlinear Behavior of Biomechanical Systems," Biomechanics Monograph, ASME, (1967), pp. 57-66.

CONTROL OF THE HUMAN FOREARM DURING ABRUPT ACCELERATION

P. A. Stewart, J. Duffy, J. Soechting, H. Litchman and P. R. Paslay

Center for Biophysical Sciences and Biomedical Engineering,  
Brown University, Providence, R. I.

ABSTRACT

This paper describes research aimed toward the development of a useful mathematical model of the human forearm including the musculature and its neural control. The goals are to provide quantitative bases for both diagnosis and monitoring of therapy in a variety of neuromuscular disease states, and also to improve current understanding of the basic physiological systems involved. Three types of experiments designed to evaluate the parameters in the model have been performed on human subjects. The first, a series of static tests, demonstrates on the basis of the principles of structural mechanics that averaged electromyogram amplitude is directly related to muscle contractile force. This series of tests also provides values for a number of the parameters in the model. The second experiment, a set of constant velocity tests, independently evaluates these same parameters, as well as a damping coefficient. The results show that damping is small. The third, a series of quick release tests, evaluates the control parameters in the model. Results indicate that velocity control is much less important for present experimental conditions than direct proportional control. Work is continuing to improve the quality of the model and its range of applicability.

## INTRODUCTION

This paper describes research aimed toward the development of a useful mathematical model of the human forearm including the musculature and its neural control. Experimental procedures designed to evaluate the parameters in this model are also described. The goals are to provide quantitative bases for both diagnosis and monitoring of therapy in a variety of neuromuscular disease states, and also to improve current understanding of the basic physiological systems involved. In the following sections, the components of the model system will be explained, starting with the mechanics of the forearm. This is followed by descriptions of three types of experiments, some of the results obtained, and our interpretation of them in terms of the model and the goals of the project. Lastly a discussion is given on implementation of the model using the data, and the significance of the results.



FIGURE 1 - INSTRUMENTED SUBJECT READY FOR TESTING

## FOREARM MECHANICS

Figure 1 shows the arm of a subject in the experimental apparatus. An aluminum frame rotates about the elbow with the forearm, and supports a lined wrist collar. This collar limits the motion of the forearm to rotation within a vertical plane about the elbow. A potentiometer located on the axis of rotation of the frame indicates forearm position. Loads, as specified for a particular experiment, are applied to the arm through the wrist collar and measured by a strain gauge load cell. Muscle electrical activity (electromyogram, EMG) is detected by pairs

of electrodes on the skin over the biceps and triceps muscles. The outputs of the arm position potentiometer, the load cell, and the EMG electrodes are all recorded on an oscillograph.

To represent this mechanical system mathematically, several conventional approximations and assumptions are needed, some of which are indicated in figure 2. We first assume that all of the muscles

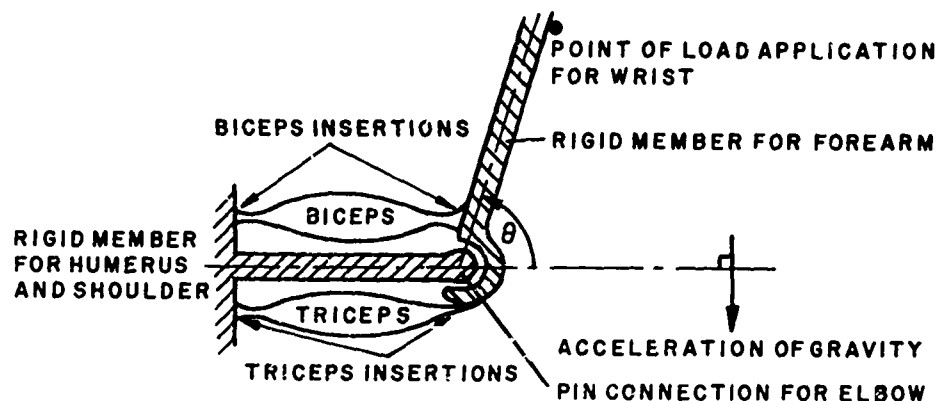


FIGURE 2 - SKETCH OF MECHANICAL MODEL OF SKELETON

which contribute to flexion toward the elbow can be grouped together with the biceps muscle, and that the latter has a single tendon connection into the forearm. Similarly, the triceps is taken to represent all the muscles contributing to outward rotation or extension about the elbow. The antagonistic action of these two muscle masses is an essential feature of the mechanical situation; because of this action, the forearm system is statically indeterminate. In practical terms, this means that to relate force in a muscle to force exerted by the arm, it is not sufficient to study only the action of one muscle, be it biceps or triceps. This important point has frequently been overlooked in earlier studies of this type [1,2].

We do not, however, assume that the geometry of the lines of action of these two muscles about the elbow is as simple as figure 2 might suggest. In the first place, both muscle tendons insert into the forearm bones over finite regions, rather than at single points. In addition, the moment arms are influenced by the geometry of the bones, the action of ligaments and the sizes of the muscles themselves. The moment arms were therefore measured using both embalmed bones and x-rays of subjects' elbows [3]. In the case of the bones, a virtual work method was used to find the moment arms. The bones were mounted in a frame which allowed motion to reproduce as nearly as possible the flexure of the elbow. In the case of the x-rays, measurements were made of the perpendicular distance from the line of action of the muscle to the elbow center of rotation. Figure 2 suggests that moment

arms should vary with the sine of the angle of rotation,  $\theta$ . Figure 3

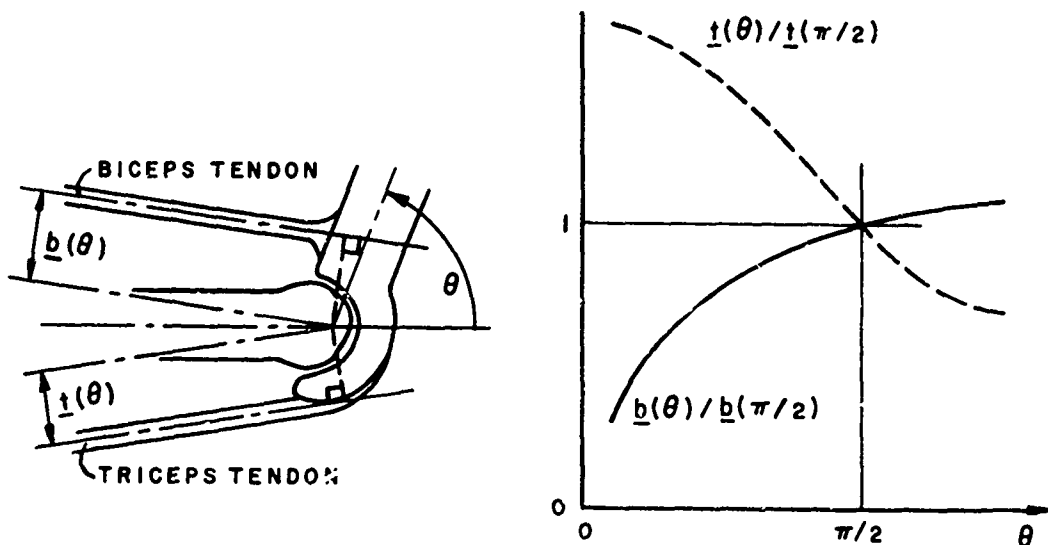


FIGURE 3 - MOMENT ARMS  $\underline{b}(\theta)$  and  $\underline{t}(\theta)$

shows a sketch of the geometry of the elbow joint, and plots of the biceps ( $\underline{b}(\theta)$ ) and triceps ( $\underline{t}(\theta)$ ) moment arms as measured. For the biceps,  $\underline{b}(\theta)/\underline{b}(\pi/2)$  varies as  $\sin\theta$ , but for the triceps,  $(\underline{t}(\theta)/\underline{t}(\pi/2))$  does not. These variations in moment arm with angle are incorporated into all calculations in which  $\theta$  varies over more than a few degrees from  $\pi/2$ .

A similar problem, on a somewhat finer scale, arises with the center of rotation. It was possible to determine from x-rays of elbow joints how the position of this center of rotation changed with forearm angle, and these results have also been incorporated into the calculations wherever appropriate.

The two bones of the forearm, the radius and the ulna, are prevented from relative motion by the wrist collar described above. The forearm can therefore be considered a rigid body with a moment of inertia,  $I$ , about the elbow. Using the methods of dynamic structural analysis, this assumption is reasonable if the natural frequencies of the forearm are lower than the frequencies observed in the motion. The lowest of these natural frequencies will occur in bending of the forearm. For a typical forearm, including tissues, we have shown [4] that this frequency is approximately 40 Hz. All arm movements occurring in this study are sufficiently slow so that no harmonic components of detectable amplitude occur with frequencies greater than 10 Hz, so that the rigidity assumption for the forearm is amply justified.



These assumptions and simplifications can all be summarized in the equation of motion for the forearm in terms of  $\theta$ :

$$-I\ddot{\theta} = + Wa \cos \theta + \text{externally applied moment} + \text{moment developed by muscles} \quad (1)$$

where  $\theta$  = angle shown in figure 2.  
 $I$  = moment of inertia of forearm and attached devices about elbow. This is measured by standard techniques.  
 $W$  = weight of forearm and wrist cuff. This is measured by standard techniques.  
 $a$  = distance from elbow to forearm center of mass.  
 Superposed dots represent derivatives with respect to time  $t$ .

The externally applied moment depends on which experiment is being performed, and may be constant or time-dependent. Three different types of experiments are described below, and the externally applied load is given for each.

If the forces produced by the muscles are  $B$  and  $T$ , then in terms of the moment arms discussed above, the moment developed by the muscles is given by:

$$-B \cdot \underline{b}(\theta) + T \cdot \underline{t}(\theta)$$

Although this expression is written only in terms of biceps and triceps, it represents the total moment developed by all the muscles. The governing equation (1) for the system may then be written

$$-I\ddot{\theta} = Wa \cos \theta + \text{external moments} - B \cdot \underline{b}(\theta) + T \cdot \underline{t}(\theta) \quad (2)$$

If  $B, T, \underline{b}(\theta), \underline{t}(\theta)$  and the externally applied moments can be specified, then equation (2) can be solved to predict  $\theta(t)$  in terms of the model parameters. To evaluate  $B$  and  $T$ , we must consider the mechanical and physiological properties of muscle, as described in the next section, and the physiology of the nervous system, as described in section 4.

#### MUSCLE

Two determinants of muscle action must be considered in this analysis; the mechanical properties of muscle as a substance or tissue, [5] and muscle activation by its nerve supply. Figure 4 indicates the essential mechanical components as they are usually presented. Each of these components displays non-linear behavior under certain conditions, but we have shown that both the damping and parallel spring terms are sufficiently small that they may be taken as linear [3]; in fact, the parallel spring may often be neglected entirely without appreciable error [6,7].

Referring to figure 4, we now define the following symbols for the biceps and triceps muscles:

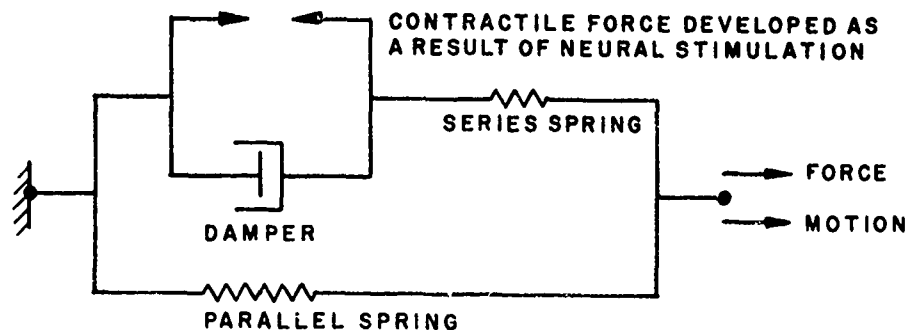


FIGURE 4 - RHEOLOGICAL MODEL FOR MUSCLE

$k_{S_B}, k_{S_T}$  = Series spring constants for biceps and triceps respectively.

$k_{P_B}, k_{P_T}$  = Parallel spring constants for biceps and triceps respectively.

$k/c$  = Ratio of series spring constant to damping constant for both the biceps and triceps. This assumption that both muscles have the same time constant is acceptable physiologically and greatly simplifies the analysis.

$x_B, x_T$  = Elongation of biceps and triceps muscles respectively measured from the resting position.

$P_B, P_T$  = Contractile force developed in biceps and triceps muscles, respectively.

The kinematic relations between  $\dot{x}$  and  $\dot{\theta}$  are:

$$\dot{x}_B = -b(\theta) \cdot \dot{\theta} \quad (3)$$

$$\dot{x}_T = t(\theta) \cdot \dot{\theta} \quad (4)$$

From figure 4, the equations which express the muscle forces ( $B, T$ ) in terms of their elongations ( $x_B, x_T$ ) and contractile activities ( $P_B, P_T$ ) are as follows:

$$\text{Biceps} \quad \dot{B} + \left(\frac{k}{c}\right)B = (k_{S_B} + k_{P_B})\dot{x}_B + k_{P_B}\left(\frac{k}{c}\right)x_B + \left(\frac{k}{c}\right)P_B \quad (5)$$

$$\text{Triceps} \quad \dot{T} + \left(\frac{k}{c}\right)T = (k_{S_T} + k_{P_T})\dot{x}_T + k_{P_T}\left(\frac{k}{c}\right)x_T + \left(\frac{k}{c}\right)P_T \quad (6)$$

In connection with this modeling, an analysis based on a continuum mechanics viewpoint was undertaken to relate single muscle fiber properties to those of whole muscle. One of the surprising results of this study [8] is that for both Hill's [9] and Houk's [10] muscle models, the form of the governing equations for whole muscle can not be the same as the form for single muscle fibers. For the linear model we have adopted here, however, the form for the cell and the whole muscle are the same.

The contractile units of the muscle are activated to generate contractile forces by the arrival of electrochemical impulses, or action potentials, on the surface of the muscle fibers. These action potentials in turn are triggered in a one-to-one relationship by the arrival of similar action potentials in the motor nerve fibers supplying the muscle. The muscle action potentials also produce electrical signals at the surface of the skin over the muscle. These potentials can be measured and processed to produce a signal, the average EMG, whose amplitude indicates the level of motoneuron activity to the muscle.

The greater the frequency of action potentials in a muscle fiber, the greater the contractile force, up to a saturation level called tetanus. In normal physiological activity, including the conditions of our tests, this saturation level occurs well above observed frequencies. It has been shown by several investigators [1,2,3] that over this range, the resultant contractile force in the muscle is proportional to the frequency of motoneuron action potential, and thus to the amplitude of the average EMG. This relationship permits us to replace  $P_B$  and  $P_T$  in equations (5) and (6) above by expressions proportional to the averaged EMG amplitudes,

$$\underline{b}(\theta)P_B = C_B E_B \quad (7)$$

$$\underline{t}(\theta)P_T = C_T E_T \quad (8)$$

where  $C_B$  and  $C_T$  are proportionality constants.

Experimentally, an averaged EMG signal is obtained as follows. The electrical signal from each pair of electrodes is amplified, full-wave rectified and integrated. The output of the integration is recorded by the oscillograph synchronously with the other variables. It is a function which increases monotonically, but sporadically, with time. Over appropriate time intervals, the average slope of this function can be measured on the oscillograph tracing. This slope is then taken as the average EMG amplitude over the interval in question.

#### NEURAL SYSTEM

The "final common pathway" for muscular control by the nervous system is the frequency of action potentials in the motor neurons supplying the muscles [11]. Broadly speaking, these frequencies are

controlled at two levels in the nervous system, depending on the type of muscular activity. At one extreme, higher centers in the brain interact to specify a temporal and spatial pattern of action potentials in appropriate motor neurons so as to bring about a desired voluntary movement. At the other extreme, local connections from muscle stretch receptors activate motor neurons directly to produce reflex responses. These two routes to muscle control can be usefully separated on the basis of response times. When the mechanical situation of a muscle changes abruptly, compensation occurs via the spinal level connections over an initial period of about one-half second, during which there is usually negligible change in the activity of the descending fibers from higher centers. By considering motions only during these short time intervals, therefore, we can effectively eliminate the effects of the complex higher levels of the nervous system, and confine our attention to the control properties of the local spinal circuits [12].

The main skeletal muscle sensory organs are stretch receptors within the muscle spindles, which are in parallel with the main motor fibers of the muscle. The spindles also contain special muscle fibers, the intrafusal fibers, in addition to the stretch receptors and in series with them. Spindle innervation is both afferent (from the stretch receptors to the spinal cord), and efferent ( $\gamma$ -motorneurons fibers from the spinal cord to the intrafusal fibers) [13]. The  $\gamma$ -efferents excite the intrafusal fibers. Their contraction increases tension on the stretch receptors, adjusting their sensitivity to external stretch, and to rate of stretch [14]. The spindle afferents synapse with, and are excitatory to, the  $\alpha$ -motorneurons which innervate the muscle fibers of the same muscle. A stretch of the spindle increases the afferent discharge frequency. As a result, the motorneurons discharge at a higher frequency, causing an increase in contractile force in the muscle, and, if permitted, muscle shortening. Such shortening releases the stretch on the spindle, closing the feedback loop [15,16,17].

The frequency of afferent impulses from the spindle stretch receptor is known from the work of Crowe [18] to be non-linearly dependent on spindle deformation and rate of deformation, but a linear model has been developed by Poppele and Bowman [19] which is appropriate for the condition of our experiments. The effects of muscle length on  $\alpha$ -motorneuron discharge frequency, and therefore on contraction force in the muscle, can thus be represented by two proportionality constants, designated  $\beta$  and  $\gamma$  in the following analysis.  $\beta$  represents the assumed linear relationship between stretch per se and muscle activation, while  $\gamma$  refers to the corresponding relationship between rate of stretch and muscle activation.

Although separate pairs of  $\beta$  and  $\gamma$  parameters could be specified for the biceps and triceps muscles, we have chosen to combine them into a single pair for both muscles. Thus,  $\beta$  and  $\gamma$  represent the total effective control over the net moment produced about the elbow by contractile activity.

A physiological complication is introduced because synaptic delays are involved in all these control loops, so that transmission times between muscle stretch and contractile response must be incorporated into any realistic description of such relationships. The time-delay parameter,  $\tau$ , has therefore been introduced into the mathematical control statements.

When the variations in  $\underline{b}(\theta)$  and  $\underline{t}(\theta)$  are small the net moment produced by both muscles reduces to,

$$(k/c)(P_B \underline{b}(\theta) - P_T \underline{t}(\theta)) = -\beta(\theta(t-\tau) - \bar{\theta}(t-\tau) - \gamma\{\dot{\theta}(t-\tau) - \dot{\bar{\theta}}(t-\tau)\}) \quad (9)$$

where  $\tau$  = delay time  
 $\bar{\theta}$  = desired or target value for angular position of the arm  
 $\beta$  = direct control constant  
 $\gamma$  = rate control constant

The governing equation (2) contains the net moment on the muscles, in terms of  $B$  and  $T$ , rather than the moment produced by the muscles, in terms of  $P_B$  and  $P_T$ . Equations 5 and 6 above can be integrated, however, to eliminate  $B$  and  $T$  in favor of  $P_T$  and  $P_B$ . Equation (9) can then be used to evaluate the moment expression in terms of the parameters  $\beta, \gamma, \tau$  and  $\bar{\theta}$ . The result is a complicated expression, in the variables  $\theta, x$ 's and  $t$ , which is awkward to write and difficult to read, but which can be evaluated by computer whenever needed.

Our first approximation to neural control over short time periods (less than 0.5 seconds) is therefore a direct plus derivative time-delay linear feedback system. We have refrained from introducing any further mathematical complexities into this control system until our experimental results demonstrate the need for them. As indicated below, this relatively simple system is adequate to predict forearm system performance remarkably well for the experiments carried out so far.

#### EXPLICIT STATEMENT OF THE MODEL

By combining the results of the above three sections, we have a set of equations incorporating the assumed properties of the system components, from which we can in principle predict  $\theta(t)$  for any specified experimental conditions.

These equations are listed here for convenience.  
 Governing equation:

$$-I\ddot{\theta} = W a \cos\theta + \text{external moments} - B \underline{b}(\theta) + T \underline{t}(\theta) \quad (2)$$

Kinematics:

$$\dot{x}_B = -\underline{b}(\theta) \dot{\theta} \quad (3)$$

$$\dot{x}_T = \underline{t}(\theta) \dot{\theta} \quad (4)$$

### Muscle Rheology:

$$\dot{B} + \left(\frac{k}{c}\right)B = (k_{S_B} + k_{P_B})\dot{x}_B + k_{P_B}\left(\frac{k}{c}\right)x_B + \left(\frac{k}{c}\right)P_B \quad (5)$$

$$\dot{T} + \left(\frac{k}{c}\right)T = (k_{S_T} + k_{P_T})\dot{x}_T + k_{P_T}\left(\frac{k}{c}\right)x_T + \left(\frac{k}{c}\right)P_T \quad (6)$$

### EMG and Contractile Activity:

$$\underline{b}(\theta)P_B = C_B E_B \quad (7)$$

$$\underline{t}(\theta)P_T = C_T E_T \quad (8)$$

### Neural Control:

$$(k/c)\{P_B \underline{b}(\theta) - P_T \underline{t}(\theta)\} = -\lambda\{\theta(t-\tau) - \bar{\theta}(t-\tau)\} - \gamma\{\dot{\theta}(t-\tau) - \dot{\bar{\theta}}(t-\tau)\} \quad (9)$$

The parameters  $I, W, a, L, \underline{b}(\theta), \underline{t}(\theta)$ , external load  $F, E_B$  and  $E_T$  are measured directly, or can be calculated from direct measurements. The remaining parameters cannot be measured directly, but values must be assigned to them before  $\theta(t)$  can be computed. These initial estimates can then be refined through an iterative procedure which systematically alters these values so as to minimize differences between computed and measured  $\theta(t)$ . In the three experimental situations described below, different loading conditions have been used to isolate and evaluate different groups of these estimated parameters, and to test the validity of the assumptions made in developing the model equations.

## STATIC LOAD EXPERIMENTS

### Theory

In these experiments, the subject is instructed to maintain his forearm at a specified angle (see the sketch in Appendix A), while a static load,  $F$ , is applied to the forearm a distance  $L$  from the elbow. Since measurements are made under static conditions,  $F, \theta, E_B, E_T, P_B$  and  $P_T$  are all constant. As mentioned above,  $k_{P_B}$  and  $k_{P_T}$ , the parallel spring constants are small enough so that they can be neglected. In this case, therefore, equations (2) through (9) become

$$0 = Wa \cos\theta + FL - \underline{b}(\theta)B + \underline{t}(\theta)T \quad (2')$$

$$\dot{x}_B = 0 \quad (3')$$

$$\dot{x}_T = 0 \quad (4')$$

$$B = P_B \quad (5')$$

$$T = P_T \quad (6')$$

$$\underline{b}(\pi/2) P_B = C_B E_B \quad (7')$$

$$\underline{t}(\pi/2) P_T = C_T E_T \quad (8')$$

$$-\beta(\theta - \bar{\theta}) = \text{constant} \quad (9')$$

Equation (9') is not useful in this experiment, however, since the subject can see any discrepancy between the desired and the actual positions and can voluntarily compensate; this test is not suitable for an evaluation of the neural control parameter,  $\beta$ . Equations (2') to (8') may be combined into:

$$\frac{\underline{b}(\theta)}{\underline{b}(\pi/2)} C_B E_B - \frac{\underline{t}(\theta)}{\underline{t}(\pi/2)} C_T E_T - W a \cos \theta - F L = 0 \quad (10)$$

If all the assumptions are valid, and equation (10) is a valid description of the system under these experimental conditions, then values for  $C_B$  and  $C_T$  can be found so that a set of experimental results ( $F, \theta, E_B, E_T$ ) substituted into (10) makes the left side zero.

A measure of the departure from this condition can be defined as the ratio of the value of the left hand side of equation (10) to the total externally applied moment,  $W a \cos \theta + F L$ . We call this ratio the error, ES, where

$$ES = \frac{\frac{\underline{b}(\theta)}{\underline{b}(\pi/2)} C_B E_B - \frac{\underline{t}(\theta)}{\underline{t}(\pi/2)} C_T E_T - W a \cos \theta - F L}{W a \cos \theta + F L} \quad (11)$$

This definition requires that the external moment never be zero, a condition always satisfied in these experiments.

$C_B$  and  $C_T$  are readily evaluated by a least squares method. In our experiments this was performed by a computer program. A number of sets of measurements was made. ES was calculated for each of the sets after  $C_B$  and  $C_T$  were obtained so that the mean of  $E_S$  and standard deviation of  $E_S$  could be found. By selecting different groupings of the data sets, the dependence of  $C_B$  and  $C_T$  on  $\theta$  and on  $F$  may be evaluated. The following notation is therefore employed for reporting the experimental results:

$(C_B)_{\theta_i}$ , $(C_T)_{\theta_i}$	Values of $C_B$ , $C_T$ obtained for least square error fit of all data sets for which $\theta$ is $\theta_i$ .
$(C_B)_{F_i}$ , $(C_T)_{F_i}$	Values of $C_B$ , $C_T$ obtained for least square error fit of all data sets for which $F$ is $F_i$ .
$(C_B)_T$ , $(C_T)_T$	Values of $C_B$ , $C_T$ obtained for least square error fit of all data sets.

#### Experimental Procedure, Static Tests

Measurements were made on three normal male adult subjects, with  $\theta$  equal to  $90^\circ$ ,  $105^\circ$ ,  $120^\circ$ ,  $135^\circ$ ,  $150^\circ$  and  $F$  equal to +25, +47, +69, +91 newtons. (Negative values of  $F$  correspond to loads which tend to flex the elbow.) The sequence of loads and angles was random in order to minimize systematic effects. A total of 160 data sets were obtained for each subject, four for each combination of  $F$  and  $\theta$ . For each subject the experiment required two to three hours, including rest periods.

#### Results and Interpretation, Static Tests

A summary of results is presented in the table in Appendix A. For each subject, values of  $C_B$  and  $C_T$  are reported with groupings of the data as indicated.

$C_T$  and  $C_B$  do not vary systematically with either  $\theta$  or  $F$ . The variations in  $C_B$  are somewhat larger than in  $C_T$ . Because of the appreciable differences between subjects, we suspect this may be related to the shape of the biceps muscle, and work on this aspect of the problem is continuing.

We conclude from these experiments that under static conditions, the magnitude of the averaged EMG is a valid measure of contractile force in muscle. The proportionally constant between contraction force and average EMG magnitude is independent of applied force and muscle length ( $\theta$ ) in any one subject.



## CONSTANT ANGULAR VELOCITY EXPERIMENTS

### Theory

In these experiments, the subject rotates his forearm with a constant angular velocity, while an external load,  $F$ , is applied in such a way that it is perpendicular to the forearm when  $\theta = \pi/2$ . Measured quantities are evaluated only at  $\theta = \pi/2$ . For each external load, measurements are made for a range of angular velocities. Since  $F, \theta, E_B, E_T, P_B$  and  $P_T$  are evaluated at a single point,  $\theta = \pi/2$ , the model equations 2-9 for this experimental situation become:

$$0 = FL - B \underline{b}(\pi/2) + T \underline{t}(\pi/2) \quad (2'')$$

$$\dot{x}_B = -\underline{b}(\pi/2)\dot{\theta} \quad (3'')$$

$$\dot{x}_T = +\underline{t}(\pi/2)\dot{\theta} \quad (4'')$$

$$(k/c)B = k_{S_B} \dot{x}_B + (k/c)P_B \quad (5'')$$

$$(k/c)T = k_{S_T} \dot{x}_T + (k/c)P_T \quad (6'')$$

$$\underline{b}(\pi/2)P_B = C_B E_B \quad (7'')$$

$$\underline{t}(\pi/2)P_T = C_T E_T \quad (8'')$$

$$(k/c)\{\underline{b}(\pi/2)P_B - \underline{t}(\pi/2)P_T\} = -\gamma(\dot{\theta} - \dot{\bar{\theta}}) \quad (9'')$$

The parallel spring constants are neglected, as in the previous case.

Equation (9'') is not applicable, since it cannot be used to evaluate the control parameters. Constant angular velocity motion does not involve the type of abrupt change in conditions which initiates reflex responses. We therefore neglect (9'').

Equations (2'') to (8'') may be combined into:

$$C_B E_B - C_T E_T - [\underline{b}^2(\pi/2)c_B + \underline{t}^2(\pi/2)c_T] \dot{\theta} - FL = 0 \quad (12)$$

The parameter combination  $[\underline{b}^2(\pi/2)c_B + \underline{t}^2(\pi/2)c_T]$  may be interpreted as an effective damping constant for the whole system, since it multiplies  $\dot{\theta}$ . For convenience, it is referred to as  $C_V$  in the sequel.

$C_B, C_T$  and  $C_V$  can be evaluated by a least squares procedure similar to that used in Section 6 above, by substituting measured values for  $\dot{\theta}, E_B, E_T$  and  $F$  into (12). The response of the model can then be compared with that of the real system in terms of an "error",  $EV$ , defined as the ratio of the failure to satisfy (12) to the applied

moment, FL . Thus:

$$EV = \frac{C_B E_B - C_T E_T - C_V \dot{\theta} - FL}{FL} \quad (13)$$

#### Experimental Procedure, Constant Angular Velocity Experiments

Four subjects were tested in these experiments. The subject was asked to vary his forearm angular velocity over as wide a range as reasonable comfort would allow. Loads varied from 11 to 70 Newtons, and a total of 1300 runs was performed. All of the data for each subject were used to compute values for  $C_B$ ,  $C_T$  and  $C_V$ . These values were then substituted into (13) to compute the mean "error", EV, and its standard deviation, for that subject. The results are presented in Appendix B.

#### Results and Interpretation, Constant Angular Velocity Experiments

The small numbers obtained for  $C_V$  indicate that the overall damping moments in this system are small compared to the applied moments under these test conditions. This means that the precise damping mechanisms will be difficult to determine, since their contributions to overall muscle action are small. The usual assumption of linear viscous damping is amply justified by these results.

The values of EV are all negative, and between 10% and 20%. This consistency suggests a systematic inadequacy or inappropriate assumption in the model. Studies aimed at identifying these problems are continuing.

Two of the subjects in these experiments, G and H, are also subjects in the static experiments. In any one test, the difference between subjects'  $C_T$  values may be as great as 100%. For each subject (G or H), however, the difference of  $C_T$  values between tests is very small. This result reinforces our conclusion that contractile activity can be measured by average EMG, and extends the applicability of this measurement to dynamic conditions.

The agreement between the static and dynamic experiment results for  $C_B$  is not as good as for  $C_T$ . This is consistent with the observation in the static experiment that the scatter of the results is much greater for  $C_B$  than for  $C_T$ . As already mentioned, we suspect this large scatter is a function of biceps muscle shape, and are continuing work to elucidate the factors involved.

As was the case in the static experiments, large differences between values for different subjects were found for both  $C_B$  and  $C_T$ . Such differences in muscle training, body size, age, sex and other factors undoubtedly enter. Larger numbers of subjects will be tested to

provide systematic understanding of the effects of such factors. The satisfactory results of these two experiments provide us with the basic tools for such an analysis.

## QUICK RELEASE EXPERIMENTS

### Theory

These experiments, unlike the two previous types, are explicitly designed to evaluate the neural control parameters  $\beta$ ,  $\gamma$ , and  $\tau$ . The subject supports a steady load,  $F$ , at an angle of  $\pi/2$  to his forearm. At an arbitrary zero time, the load is suddenly released, without any cues to the subject. Motion,  $\theta$ , and force,  $F$ , are recorded as functions of time for the first 0.5 sec. after release of the load.

Several simplifications can be introduced into the model equations for this experiment. Since forearm position during the first 0.5 sec. after release is always within  $\pi/12$  ( $15^\circ$ ) of the initial position,  $b(\theta)$  and  $t(\theta)$  can be treated as constants, equal to their values at  $\theta = \pi/2$ .  $\bar{\theta}$  is also constant, at  $\pi/2$ . At the instant of release, we have  $\theta = \pi/2$ ,  $\dot{\theta} = 0$ ,  $\theta = FL/I$ .

Equations (2) - (9) for these conditions then become:

$$-I\ddot{\theta} = -B \underline{b}(\pi/2) + T \underline{t}(\pi/2) \quad (2''')$$

$$\dot{x}_B = -\underline{b}(\pi/2)\dot{\theta} \quad (3''')$$

$$\dot{x}_T = +\underline{t}(\pi/2)\dot{\theta} \quad (4''')$$

$$\dot{B} + (k/c)B = (k_{S_B} + k_{P_B})\dot{x}_B + k_{P_B}(k/c)x_B + (k/c)P_B \quad (5''')$$

$$\dot{T} + (k/c)T = (k_{S_T} + k_{P_T})\dot{x}_T + k_{P_T}(k/c)x_T + (k/c)P_T \quad (6''')$$

$$\underline{b}(\pi/2)F_B = C_B E_B \quad (7''')$$

$$\underline{t}(\pi/2)P_T = C_T E_T \quad (8''')$$

$$(k/c)\{\underline{b}(\pi/2)P_B - \underline{t}(\pi/2)P_T\} = -\beta(\theta(t-\tau) - \pi/2) - \gamma\dot{\theta}(t-\tau) + (k/c)FL \quad (9''')$$

For this experiment, the parallel spring constants  $k_p$  can not be neglected a priori.

Careful inspection of these equations shows that the last term in (9'''),  $(k/c)FL$ , represents the steady-state for the system in terms of the pre-release conditions. During the 0.5 seconds of motion after release, there is no adaptation to a new steady-state condition. We designate the term  $(k/c)FL$  by the symbol  $\delta$ , since it provides a useful check on the adequacy of the model, as pointed out below in 8C.

In this case, (9''') can not be neglected, and (2''') through (9''') must be combined into a system differential equation for  $\theta$ . The result is:

$$\begin{aligned} I\ddot{\theta}(t) + (k/c)I\dot{\theta}(t) + [(k_{S_B} + k_{P_B})\underline{b}^2(\pi/2) + (k_{S_T} + k_{P_T})\underline{t}^2(\pi/2) \\ - Wa]\dot{\theta}(t) + (k/c)[k_{P_B}\underline{b}^2(\pi/2) + k_{P_T}\underline{t}^2(\pi/2) - Wa] \\ \cdot [\theta(t) - \pi/2] = -\gamma\dot{\theta}(t-\tau) - \delta[\theta(t-\tau) - \pi/2] + (k/c)FL \end{aligned} \quad (14)$$

The quantity  $[k_{P_B}\underline{b}^2(\pi/2) + k_{P_T}\underline{t}^2(\pi/2)]$  represents the effect of the parallel spring constants. It is referred to as  $B$  from here on, for convenience. Similarly, the quantity  $[k_{S_B} + k_{P_B})\underline{b}^2(\pi/2) + (k_{S_T} + k_{P_T})\underline{t}^2(\pi/2)]$  represents the effective spring constant for the whole system. It is designated  $A$  in what follows.

Conventional means of solving linear differential equations are not suited to solving (14) due to the presence of  $\theta(t-\tau)$  and  $\dot{\theta}(t-\tau)$ . This type of time delay differential equation has been studied extensively, however, [20] and numerous theorems are available concerning its solution. In general, the presence of  $\tau(>0)$  can be shown to have a destabilizing effect on the solution. (14) can of course be solved by computer-implemented numerical methods, if all the coefficients are known. Alternatively, the measured  $\theta(t)$  can be used to determine appropriate values for some of the otherwise unknown coefficients, a procedure known as an identification scheme.

#### Experimental Procedure, Quick Release Experiments

Measurements were made on six subjects, five of whom were tested on two different occasions separated by several months. Between 4 and 8 quick release tests were carried out on each subject at each sitting, with externally applied moment  $FL$  between -15 and +15 Newton-meters. Coefficients in (14) were determined for each  $FL$  value, and the means and standard deviations for the coefficients computed for each sitting.

The procedure for obtaining coefficients is as follows:

1. Initial values for the coefficient are estimated.
2. (14) is solved numerically for  $0 \leq t \leq 0.5$  sec, yielding predicted values for  $\theta(t)$ .
3. The predicted and measured motions are compared, point by point, to determine an error. A simplex procedure [12] readjusts the coefficient values to decrease the error and, consequently, the difference between predicted and measured  $\theta(t)$ .
4. This procedure is repeated automatically until the change in coefficient values from one cycle to the next is less than a preassigned value. These coefficient values are then printed out as the best

estimate. Since this whole identification procedure is extremely laborious [22], on-line computer processing of the data is currently being implemented in our laboratory.

#### Results and Interpretation, Quick Release Experiments

Eleven data sets were obtained from six subjects. The table in Appendix C presents these measurements, results of the application of the simplex identification scheme, and standard deviations (in parentheses).

Values for  $\tau$ , the delay time control parameter, are almost the same for all subjects, and the standard deviations are small. The overall mean value of 0.12 seconds is consistent with previous work in this area. Since  $\tau$  is a computed parameter in the model, rather than a directly measured quantity, this result provides a significant check on the validity of our measurements and computational procedures.

As expected, the overall elasticity parameter  $A$  is very much larger than the parallel elasticity parameter  $B$ . Although the standard deviations are large for both, the results confirm the usual assumption that the parallel elasticity components are negligible compared to the series components, and justify the omission of the  $k_p$ 's in the first two experiments.

The rate control parameter  $\gamma$  is small but its standard deviation is large. It is in fact not clear from these results that  $\gamma$  is different from zero. This would mean that rate-sensitivity is not a significant feature of muscle control over the first 0.5 seconds under these experimental conditions. The direct control parameter,  $\beta$ , is obviously not negligible, however.

As expected, the values for  $k/c$ , the muscle tissue relaxation time constant, are reasonably consistent between subjects. If the model equation (14) were perfectly valid, and if the identification scheme produced exactly correct values for all the parameters, then the values in the column labelled  $\delta/FL$  should be identical to the  $k/c$  values, since  $\delta = (k/c)FL$ . This is clearly not the case. This disparity thus provides the same sort of information as ES and EV did in the previous sections, and indicates that refinements in the model are necessary.

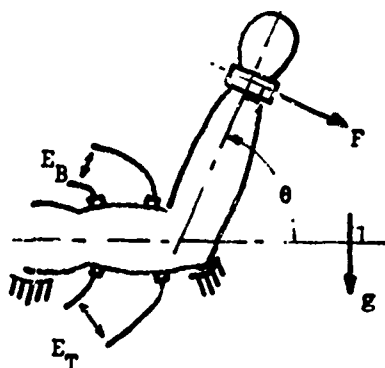
## REFERENCES

1. O. C. J. Lippold, "The Relation between Integrated Action Potentials in a Human Muscle and Its Isometric Tension," J. Physiol., Lond., 117, 492, 1952.
2. V. T. Inman, H. J. Ralston, J. B. Saunders, C. M. Feinstein and E. W. Wright, Jr., "Relation of Human Electromyogram to Muscle Tension," EEG Clin. Neur., 4, 187, 1952.
3. R. H. Messier, J. Duffy, P. A. Stewart, P. R. Paslay and H. M. Litchman, "The Relationship between the Electromyogram and Muscle Tension in the Human Biceps and Triceps," submitted for publication.
4. R. E. Mains, P. R. Paslay, P. A. Stewart and J. Duffy, Mathematical Modeling of Forearm Movements, Brown University Report, Division of Engineering, 1967.
5. D. R. Wilkie, "Facts and Theories about Muscle," Prog. in Biophys., 4, 288, 1954.
6. J. S. Silverberg, J. Duffy, P. A. Stewart, J. F. Soechting and P. R. Paslay, "An Experimental Determination of the Viscous Forces Within Human Biceps and Triceps Muscles Resulting from Forearm Movement," submitted for publication.
7. J. F. Soechting, P. A. Stewart, J. Duffy, R. H. Haw'ey and P. R. Paslay, "Evaluation of Human Neuromuscular Parameters," submitted for publication.
8. P. R. Paslay, J. F. Soechting, P. A. Stewart and J. Duffy, "Constitutive Equations in Muscle Mechanics," submitted for publication.
9. A. V. Hill, "The Heat of Shortening and the Dynamic Constants of Muscle," Proc. Roy. Soc., Ser. B., 126, 136, 1938.
10. J. C. Houk, "A Mathematical Model of the Stretch Reflex in Human Muscle Systems," Master's Thesis, MIT, 1963.
11. E. Gardner, Fundamentals of Neurology, Chapter 10, 4th Ed., W. B. Saunders Co., Philadelphia, 1963.
12. O. J. M. Smith, "Non-linear Computations in the Human Controller," IRE Trans. Bio-Med. Elec., BME-9, 125, 1962.
13. I. A. Boyd, C. Eyzaguirre, P. B. C. Matthews and G. Rushworth, The Role of the Gamma System in Movement and Posture, Assn. for Aid of Crippled Children, New York, 1968.

14. P. B. C. Matthews, "Muscle Spindles and Their Motor Control," Physiol. Rev., 44, 219, 1964.
15. J. R. Swink, "Intersensory Comparisons of Reaction Time Using an Electro-Pulse Tactile Stimulus," Human Factors, 8, 143, 1966.
16. A. Lundberg, "Integration in the Reflex Pathway," in Muscular Afferents and Motor Control, ed. R. Granit, J. Wiley and Sons, New York, 1966.
17. J. Houk and E. Henneman, "Feedback Control of Skeletal Muscles," Brain Research, 5, 433, 1967.
18. A. Crowe and P. B. C. Matthews, "The Effects of Stimulation of Static and Dynamic Fusimotor Fibers on the Response to Stretching of the Primary Endings of Muscle Spindles," J. Physiol., Lond., 174, 109, 1964.
19. R. E. Poppele and R. J. Bowman, "Quantitative Description of Linear Behavior of Mammalian Muscle Spindles," J. Neurophysiol., 33, 59, 1970.
20. J. K. Hale, "Sufficient Conditions for Stability and Instability of Autonomous Functional - Differential Equations," J. Diff. Equas., 1, 213, 1965.
21. J. A. Nelder and R. Mead, "A Simplex Method for Function Minimization," Computer J., 7, 308, 1964.
22. P. R. Paslay, K. Kennedy and R. E. Mains, "The Identification Problem in Nervous System Control of the Skeletal Frame," Proc. Ann. Conf. on Engr. in Med. and Biol., Houston, 1968.

# Appendix A:

## Summary of Static Tests



The constant force  $F$  is applied perpendicular to the forearm while the forearm is held stationary. EMGs indicated by  $E_B$  and  $E_T$  are measured. The test was repeated for values of  $\theta$  and  $F$  indicated in the table.  $(C_B)_M$  and  $(C_T)_M$  are found by minimizing the error defined by (11) with the least squares error technique. The subscript  $M$  indicates the data used in the minimization as follows:

$M = T$ , all data

$M = F$ , all data at force  $F$

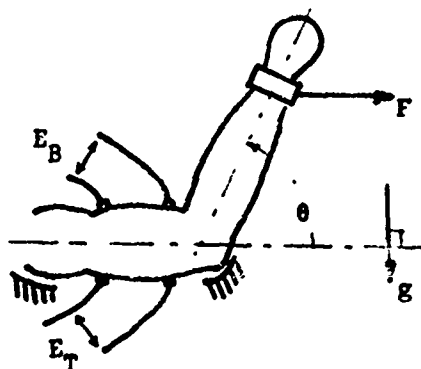
$M = \theta$ , all data at angle  $\theta$

Subject	F	G	H
Total No. Tests	160	160	160
$\bar{C}_B$ N-m/mV	104.	69.	67.
$\bar{C}_T$ N-m/mV	53.	35.	26.
Mean of ES	-.18	-.03	-.15
S.D. of ES	.30	.26	.30
$(C_B)_{30^\circ}$ N-m/mV	105.	76.	85.
$(C_T)_{30^\circ}$ "	79.	31.	22.
$(C_B)_{45^\circ}$ "	93.	81.	72.
$(C_T)_{45^\circ}$ "	54.	40.	24.
$(C_B)_{60^\circ}$ "	116.	68.	80.
$(C_T)_{60^\circ}$ "	67.	40.	33.
$(C_B)_{75^\circ}$ "	110.	62.	72.
$(C_T)_{75^\circ}$ "	45.	37.	32.
$(C_B)_{90^\circ}$ "	129.	57.	47.
$(C_T)_{90^\circ}$ "	45.	33.	31.
$(C_B)_{+25N}$ "	132.	67.	95.
$(C_T)_{+25N}$ "	55.	28.	33.
$(C_B)_{+47N}$ "	129.	64.	83.
$(C_T)_{+47N}$ "	62.	33.	28.
$(C_B)_{+69N}$ "	112.	66.	68.
$(C_T)_{+69N}$ "	48.	34.	28.
$(C_B)_{+91N}$ "	96.	73.	63.
$(C_T)_{+91N}$ "	53.	37.	25.



## Appendix B:

### Summary of Constant Velocity Tests



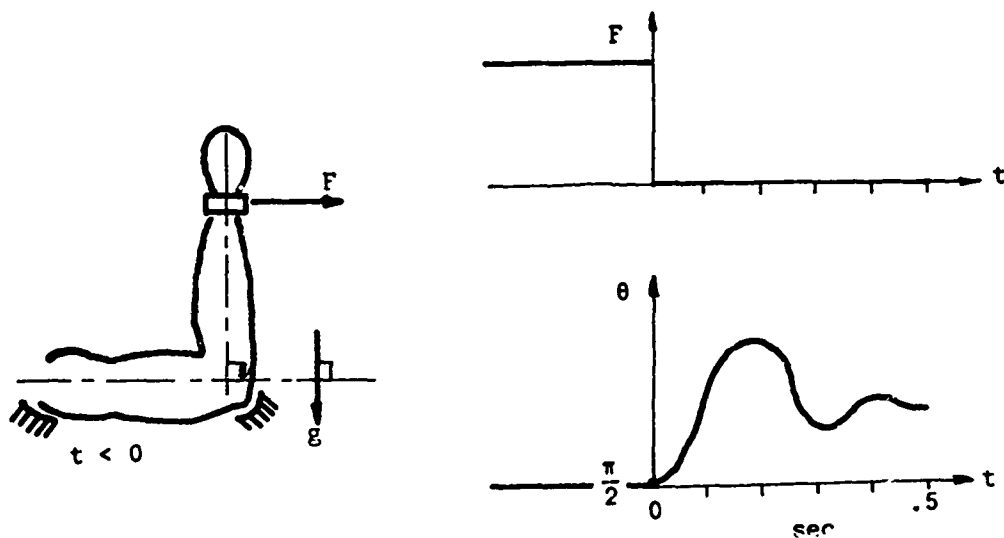
With a constant force  $F$ , the EMGs denoted by  $E_B$  and  $E_T$  are measured for a voluntarily induced constant angular velocity  $\dot{\theta}$  when  $\theta$  passes through  $\pi/2$ . Various combinations of  $F$  and  $\dot{\theta}$  occur in the course of testing a single subject.

Subject	No. Runs	$C_B \frac{N-m}{mV}$	$C_T \frac{N-m}{mV}$	$C_V \frac{N-m-sec}{rad}$	Mean of EV	S.D. of EV
C	312	83.	55.	0.91	-0.18	0.38
D	354	21.	18.	1.20	-0.17	0.38
G	369	40.	41.	1.30	- .19	0.39
H	298.	40.	26.	1.50	-0.13	0.34

$$* C_V = \frac{b^2}{2}(\pi/2) C_B + \frac{t^2}{2}(\pi/2) C_T$$

# Appendix C:

## Summary of Quick Release Tests



Mean Values for Coefficients of Model\*

Subject	No. Tests	$I(\text{kg-m}^2)$	$W$ (N)	$k/c$ ( $\text{sec}^{-1}$ )	$A^{(0)}$ (N-m)	$B^{(0)}$ (N-m)	$\gamma$ (N-m)	$\beta$ (N-m-sec $^{-1}$ )	$\delta/\tau$ (sec $^{-1}$ )	$\tau$ (sec)
A	6	.077	1.81	7.4 (1.6)	54. (13.)	2.1 (1.4)	0.9 (1.0)	180 (78.)	4.1 (2.7)	.14 (.02)
A	7			10.0 (2.2)	42. (11.)	1.2 (.5)	0.9 (.8)	150 (82.)	3.9 (4.5)	.12 (.01)
B	5	.112	2.29	5.0 (3.4)	59. (8.)	2.7 (2.7)	1.5 (1.7)	170 (68.)	0.6 (.5)	.14 (.01)
B	8			11.0 (1.9)	46. (11.)	1.8 (.4)	1.5 (.9)	220 (100.)	2.0 (2.2)	.11 (.01)
C	8	.160	2.26	8.7 (3.0)	60. (7.)	1.8 (.7)	0.9 (.9)	120 (46.)	0.6 (.8)	.12 (.02)
D	7	.071	1.67	11.0 (4.4)	54. (5.)	1.4 (1.3)	1.3 (1.0)	200 (54.)	2.6 (1.6)	.13 (.02)
D	7			7.4 (4.4)	62. (12.)	1.3 (1.4)	2.0 (1.8)	260 (65.)	2.6 (1.8)	.12 (.02)
E	7	.072	1.75	13.0 (3.4)	38. (8.)	4.7 (2.9)	2.4 (2.6)	89 (33.)	-0.2 (.8)	.10 (.01)
E	6			22.0 (3.5)	44. (13.)	3.2 (.5)	2.5 (2.3)	250 (72.)	4.6 (2.6)	.09 (.02)
F	4	.108	2.32	5.3 (1.2)	72. (12.)	1.8 (1.0)	5.4 (5.4)	380 (120.)	1.7 (1.1)	.12 (.02)
F	6			3.0 (1.2)	82. (12.)	2.1 (.6)	1.9 (1.5)	440 (48.)	3.0 (1.5)	.12 (.01)

\* Numbers in parentheses are standard deviations of corresponding mean values.

$$** A = (k_{S_B} + k_{P_B})b^2(\pi/2) + (k_{S_T} + k_{P_T})\tau^2(\pi/2)$$

$$B = k_{P_B}b^2(\pi/2) + k_{P_T}\tau^2(\pi/2)$$

PAPER NO. 27

AN APPROACH TO HEAD IMPACT ANALYSIS

by

Gordon Moskowitz, Ph.D.  
Biomedical Engineering and Science Program  
Mechanical Engineering Department  
Drexel University  
Philadelphia, Pennsylvania 19104

Joseph Rose, Ph.D.  
Mechanical Engineering Department  
Drexel University  
Philadelphia, Pennsylvania 19104

Stephen Gordon, M.S.  
Aerospace Crew Equipment Department  
Naval Air Development Center  
Warminster, Pennsylvania 18974  
Biomedical Engineering and Science Program  
Drexel University  
Philadelphia, Pennsylvania 19104

ABSTRACT

Presently, many mathematical models of response to head impact are based on a thin elastic shell filled with an inviscid fluid. While these models serve as starting points, anatomic and physiologic considerations indicate that many areas for improvement exist. Research has been recently initiated to determine the behavior of the multi-layered viscoelastic and elastic-plastic brain protection system in response to impact loading.

Geometrically simplified layered mathematical models are proposed to evaluate the importance of viscous, plastic, and layering effects within the model. Dynamic material testing has been performed on photoelastic models to demonstrate stress wave propagation through the cavities within the diploe region.

## INTRODUCTION

As a consequence of man's travel at increasing speeds, the incidence and severity of head injuries has also increased. The importance of protecting against head injuries can be readily observed by considering that the present Naval pilot replacement cost is over two million dollars per pilot. A more complete understanding of the mechanical mechanisms involved in impact to the skull will be useful in two ways: 1) explaining the occurrence of post-traumatic symptoms and 2) leading towards the development of a better protective system.

Engin<sup>1</sup>, Benedict<sup>2</sup>, and Advanti and Lee<sup>3</sup> have proposed fluid-filled spherical shell models of the head. These approaches have considered the shell wall, which is analagous to the skull, to be elastic, isotropic, and homogenous. An inviscid compressible fluid represents the brain matter. The Engin<sup>1</sup> and Benedict<sup>2</sup> models consider the walls to be thin, while the Advanti and Lee<sup>3</sup> formulation includes a moderately thick shell with transverse shear and rotary inertia. These shell theories represent useful approaches for indicating areas of potentially dangerous mechanical stress. Engin and Liu<sup>4</sup> suggest a further step would be the inclusion of an opening in the sphere which would simulate the foramen magnum.

Anatomical and physiological considerations suggest that the skull contains three layers of materials which exhibit viscoelastic and elastic-plastic constitutive relationships. A complex CSF-meningeal systems plus an energy absorbing scalp also act to protect the viscoelastic brain. (Figure 1). The various material properties in the many brain protection layers, the ordering of layers, and the coupling between layers are areas of potential importance in head impact analysis. Therefore, it is the object of this study to consider the effects of a multi-layered brain protection system in response to impact loading

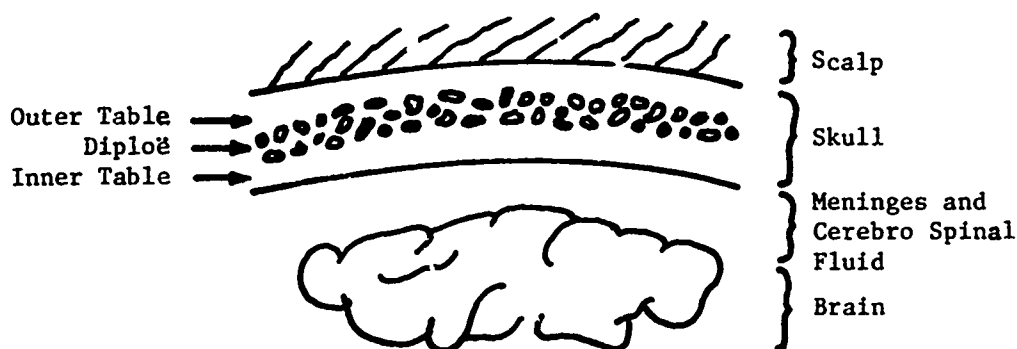


Figure 1. SKETCH OF HEAD CROSS-SECTION

## FORMULATION

As recently as 1968, Ommaya<sup>5</sup> surveyed publications on the mechanical properties of the nervous system. He reported that only three major brain tissue property papers had been presented. Also, very scant findings were given for the other constituents of the nervous system. The material properties of tissues of the head in the present model are based mainly on recent publications and the "Final Report on Determination of the Physical Properties of Tissues of the Human Head" by West Virginia University.<sup>6</sup> As future material information becomes available, it will be incorporated to provide the most realistic results within the framework of the suggested model.

During impact head injury, Galford and McElhaney<sup>7</sup> claim the scalp acts as a cushion in the transmission of the force to the brain. The suggested constitutive relations can be generated by a Maxwell-Kelvin four-parameter model. However, because the four parameter model is not a physical representation of the scalp, individual tests, such as creep compliance or stress relaxation, do not yield a unique model. Galford and McElhaney<sup>7</sup> do not determine any set of parameters for a Maxwell-Kelvin scalp model. Therefore, the present formulation will consider the generalized case with the following governing equation

$$\sigma + p_1 \dot{\sigma} + p_2 \ddot{\sigma} = q_1 \epsilon + q_2 \dot{\epsilon} + q_3 \ddot{\epsilon}$$

Where

$\sigma$  is stress

$\epsilon$  is strain

$\dot{\phantom{x}}$  is 1st time derivative

$\ddot{\phantom{x}}$  is 2nd time derivative

$p_i, q_i$  are material constants.

The skull structure consists of three layers: the outer, the diploë, and the inner table. The outer and inner tables are constructed of hard, dense bone. The diploë consists of bone with fluid-filled interconnected cavities. Strain rate dependence has been demonstrated for hard femur bone<sup>8</sup>. In testing on the human skull, West Virginia University<sup>6</sup> suggests a certain degree of rate sensitivity in the fresher samples; however, the values for the rate dependence are not yet fully evaluated. Because the tables are the most rigid elements in the layered model being considered, the tables will be assumed to act as purely elastic, isotropic, and homogenous materials with a radial compressive elastic modulus of  $5 \times 10^6$  psi and a Poisson's ratio of 0.3.

The random variations in diploë thickness do not have a definite functional relationship<sup>6</sup>. The model considered will be assumed to contain an average hole density. Melvin, Fuller, and Bardawala<sup>9</sup> present graphic relations of compression modulus vs. diploë density and of compression strength vs. diploë density. Using average density values the elastic compressive modulus is  $2 \times 10^5$  psi and the compressive strength is  $6 \times 10^3$  psi. The Poisson's ratio is assumed to be 0.28<sup>6</sup>. There is some

question as to the effects of strain rate on the stress-strain relationships for the diploë. Melvin, et al.<sup>9</sup> indicate very little scatter of the various rate dependent data points in compressive tests on diploë. However, anatomical observations indicate that the fluid-filled diploë cavities would result in strain rate dependence in the *in vivo* skull. At present, we shall assume the diploë layer of the mathematical model to be a continuous, homogeneous, isotropic, and elastic-plastic representation of the physiological diploë region, which is porous and inhomogeneous.

The elastic, elastic-plastic, and elastic representation of the outer table, diploë, and inner table, respectively, serves as a reasonable first approximation of the three layered skull. This present model is very similar to the honeycomb sandwich structure suggested by Melvin, et al.<sup>9</sup>.

The dura will be excluded for the present because of the added mathematical difficulties involved with the inclusion of another layer. The CSF will also be excluded because it has a density and viscosity which are similar to that of the brain. After the mathematical difficulties of a layered viscoelastic model are successfully overcome, the addition of other layers may be accomplished with greater ease.

Brain tissue properties have been investigated recently by several researchers. Mathematical and experimental techniques have been demonstrated for determining the complex shear modulus<sup>10,11</sup>. The brain tissue will be assumed to act as a viscoelastic, isotropic, and homogeneous material. Two possible stress-strain relationships for brain tissue response to compressive loads are found in the literature. Galford and McElhaney<sup>12</sup> suggest a four-parameter Maxwell-Kelvin model as shown below in Figure 2.

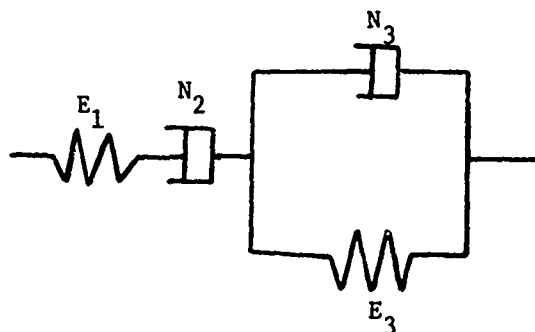


Figure 2. MAXWELL-KELVIN MODEL

The parameters for human brain are given as  $E_1$  (psi) = 3.4,  $E_2$  (psi) = 9.3,  $N_2$  (lb-sec/in<sup>2</sup>) = 257.4, and  $N_3$  (lb-sec/in<sup>2</sup>) = 8.6. Estes and McElhaney<sup>12</sup> describe the following stress-strain relationship:

$$\sigma = e^a \dot{\lambda}^{1-b} \frac{(\lambda-1)^b}{\lambda}$$

Where:  $\lambda = e^{\epsilon}$ ,  $a = 0.50$ , and  $b = 0.782$ .

Besides the constitutive equation, the layers within the mathematical model must satisfy the basic conservation laws of mass, energy, and momentum. In evaluating the importance of material properties, ordering of layers, and coupling between layers, a geometrically simplified finite dimensioned flat plate model will be used. Because reflected stress waves returning from the far end of the brain layer are of lesser importance in demonstrating the effect of layering in the brain protection system, the brain layer will be assumed to be semi-infinite in depth. Eventually, flat sections and future curvilinear segments might be jointed by suturing analogues to form a final closed container model. Figure 3 shows the ordering of material properties for the mathematical model layers.

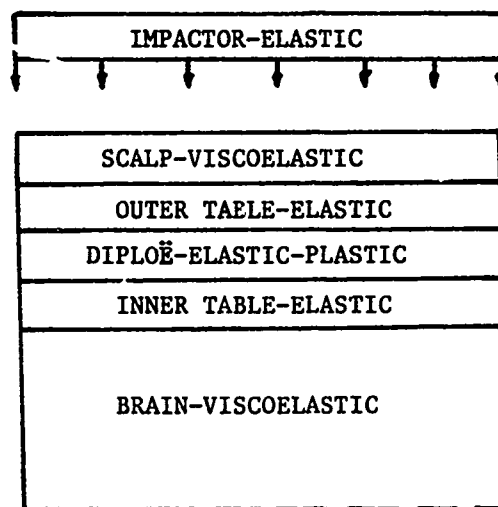


Figure 3. MATERIAL PROPERTIES FOR MODEL LAYERS

The choice of boundary conditions between layers is critical. The three layers of skull material will be rigidly attached to each other. The scalp and brain must be loosely attached to the outer and inner tables. However, it was shown by Janssen and Bowman<sup>14</sup> that the inclusion of a dura attachment to the skull produced results which differed from the unattached tests. Therefore, some partial attachment might be considered.

In general, the solution technique dictates the precise formulation of the problem. At present, there is no definite decision as to which solution approach will be the most advantageous; therefore, a more concise reduction of the equations which must be satisfied will not be presented at this time.

## EXPERIMENTAL METHODS

A representative photoelastic model of the skull was discussed by Melvin et al. and the West Virginia University report. Both studies showed the high stress levels within the diploë region under static compressive loading. A dynamic study of the diploë photoelastic model would be useful in showing how the waves pass through the diploë and indicating any sources of energy loss. To investigate this dynamic situation, the exploding wire facilities of the Drexel University Experiment Wave Propagation Laboratory<sup>15</sup> were used.

A 12.6 mil copper wire  $7\frac{1}{4}$  inches long is exploded by discharging 17,000 volts across the ends. Energy is supplied to the wire from a 14 micro-farad 20,000 volt energy discharge capacitor. The exploding wire applies high pressure gas on the edge of a thin plate, generating plane stress waves in the photoelastic plate specimen. The specimen is mounted in a polariscope and the fringe motion recorded by a Beckman-Whitley model 201 high-speed framing camera. The camera uses an air-turbine mirror system to achieve a framing rate of  $1\mu$ sec between frames. The wave front is observable as a concentration of several fringes in the isochromatic photographs. Light for photographing the stress waves is obtained from an E G and G FX-1C-6 xenon flash tube.

The photoelastic material used was PSM-1 which has an elastic modulus of 340,000 psi and an optical coefficient of 40 psi/in/fringe. The photoelastic model for the three layers of skull is shown in Figure 4. The circular hole is  $7/16$ " diameter. The oblong hole in the lower portion was made with a series of  $7/16$ " diameter holes. Finally, the irregular hole was drilled by a series of  $1/4$ " diameter holes

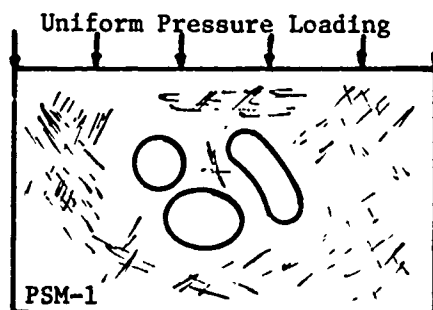
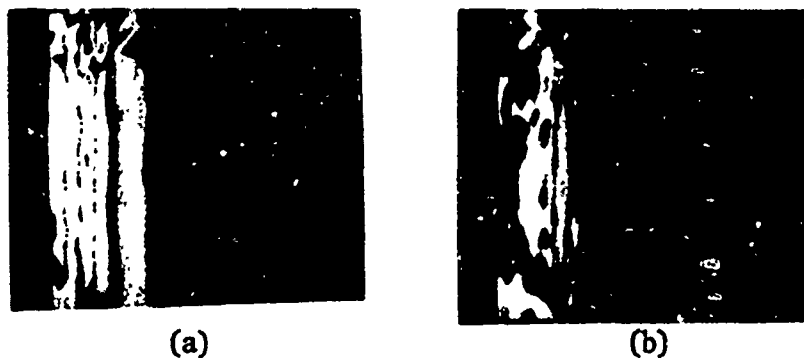


Figure 4. SKETCH OF THE PHOTOELASTIC SKULL MODEL

## EXPERIMENTAL RESULTS

Figure 5 shows the results of one dynamic exploding wire test. The stress wave is traveling from left to right in each of the frames. There is a  $7\mu$ sec time interval between frame (a) and (b).





**Figure 5** Stress waves passing through a photoelastic model of the diploe region. (7μsec between frames)

In Frame (a) the primary wave front is entering the region of the cavity discontinuities. A spherical wave can be seen reflecting from the boundary of the irregularly shaped hole. Frame (b) shows the stress wave as it propagates further into the discontinuity region. A second reflected spherical wave can be observed emanating from the circular hole. As indicated in both frames a portion of the energy is not transmitted through the material; therefore, considerable stress attenuation and wave speed reduction occurs at the wave front.

#### CONCLUDING REMARKS

The work discussed and suggested here is obviously in its initial phases. The main concept is that of approaching the study of head impact analysis by a more complete consideration of the effects of a layered energy absorbing system.

THE BIOMECHANICS OF SPINAL AND HEAD IMPACT:  
PROBLEMS OF MATHEMATICAL SIMULATION

Y. King Liu, Ph.D.  
Assoc. Prof. of Biomechanics  
Tulane University School of Medicine  
New Orleans, Louisiana 70112

ABSTRACT

The present expository paper examines the various mathematical models proposed in impact studies in general and those in connection with spinal and head injuries in particular. First, the concept of injury tolerance surface is introduced. When a complete mapping of this surface is in hand, then the probability of injury due to any acceleration vector can be evaluated. After reviewing a typical single-degree-of-freedom model, a quadrature scheme, based on classical Fourier transform technique, is proposed for obtaining the pulse response from the experimentally determined mechanical impedance. The ignoring of the spatial mass distribution is shown to be the source of many difficulties in simple models. Typical results for the pilot-ejection problem where the spatial mass distribution is accounted for is then given. The determination of input parameters necessary to implement this class of models is also briefly described.

The second part of the paper begins with a review and critique of a promising one-dimensional continuum model of head injury by Hayashi<sup>14</sup>. Exact wave-propagation solutions were obtained for the intracranial pressure and container acceleration. When compared with the approximate solution given previously, both mathematical and physical reasons were advanced for the improvement of this model. The relatively small number of dimensionless parameters of the anticipated improved Hayashi model will make any future discussions of the cavitation theory very much easier. The survey of two- or three-dimensional models is divided into axisymmetric, rotational and nonaxisymmetric versions of fluid-filled spherical shells. A brief summary of the implications of the idealizations discussed above to other critical organs of the human body concludes the paper.

PRECEDING PAGE BLANK

## INTRODUCTION

In the course of daily living, a host of circumstances confront the human body such that a mechanical input is imposed on it. Many are accidental, e.g., athletic injuries, automobile and industrial accidents, while others are preplanned, e.g., ejection from high-speed aircraft, manned launchings and recoveries of aircraft and spaceships on water or land. In either case, the knowledge of the response, tolerance and control of the body is highly desirable, and in many situations, quite imperative. In terms of its response to externally applied forces, the body obeys the laws of mechanics. There is little doubt that this particular structure will be with us for a long time to come. Any understanding or knowledge gained with respect to its structural mechanics will have a continuing significance. The analogy that the skeletal (bone) system corresponds to the main structural members of machines is a plausible one. In that spirit, ligaments and tendons are then cables and tie-bars and muscles are sources of motive power. It is inappropriate to carry the analogy too far. Examples of physiological function which has rare counterparts in machines are: (1) The neuromusculature can shorten as much as 63% of its resting length due to active contraction and generally sustain loads several times more than its bony part. (2) Living bone can repair itself after fracture.

The basic modeling objectives are two-fold: (a) To propose the simplest mathematical description consistent with explaining the physical phenomenon. At the core of the mathematical description, there is the anatomical and/or physiological framework upon which the model rests and, on the other hand, the biomechanical data needed to implement the model. (b) To provide, through the model or its improvement, new insights or predict new phenomena, which serve to indicate where the measuring devices should be placed. The development of meaningful experiments should be guided by some theory, no matter how simple. The construction of a meaningful theory, on the other hand, requires the availability of experimental data and clinical observations. If data are not provided or found, there is always the danger that the theory will be based on how the body could or should respond rather than on how it does.

## INJURY TOLERANCE SURFACES

The mathematical models of the human body subjected to accelerations depend on the direction of the acceleration vector. The applied accelerations range from steady-state oscillations to abrupt pulses. For the sake of uniformity in the discussion to follow, we shall follow the physiological acceleration coordinate (G) system recommended by the Committee on Acceleration of the AGARD Aerospace Medical Panel as reported by Gell<sup>1</sup>.

The fundamental problem in acceleration injury is the construction of tolerance surfaces in the 3-G space with a suitable quantity as parameter. For abrupt pulses, the time of uniform acceleration exposure is an obvious candidate as a parameter. This point of view is easily illustrated in the  $G_x$ - $G_z$  plane. Coincidentally, most of the current

available laboratory data on acceleration injury tolerance are in these directions of impact. In Figure 1 the data of Eiband<sup>2</sup> is replotted for a uniform acceleration duration of 0.05 secs. The axes intercepts correspond to the known tolerance data for  $\pm G_z$ . The straight dotted lines represent the easiest analytical construction of this tolerance curve and is in no way suggestive of reality. In fact, from the F4C aircraft data in which the ejection seat is inclined  $14^\circ$  towards the +x axis, a second-degree hyperbola, shown as a solid curve might be much more appropriate. Tolerance data for combinations of accelerations are woefully lacking even for the plane and is nonexistent for the 3-G space. Many acceleration environments are indeed in this category, e.g., (1) winged-aircraft and automobile collisions are points in the  $G_x$ - $G_y$  plane; (2) helicopter crashes are points in the  $G_z$ - $G_x$ - $G_y$  space. This concept of the tolerance surface is adapted from the theory of yield surfaces (in the principal stress space) in elasticity and plasticity.

#### REVIEW OF SIMPLE LUMPED-PARAMETER MODELS

Given a typical impact situation, one can usually discern the following elements: mass, elasticity, dissipation and the nature of the applied impulse, which contribute to the dynamic response of the body. Assuming linearity of the elements, one can obtain the response of a damped dynamic system to a given acceleration (or force) input,  $a(t)$ , as the solution of the well-known differential equation:

$$\ddot{x} + 2\delta\omega_0\dot{x} + \omega_0^2x = a(t), \quad (1)$$

where  $\omega_0$  is the natural frequency,  $\delta$  is the damping ratio and  $x(t)$  is the relative displacement of the support with respect to the mass. The solution of equation (1) for an arbitrary  $a(t)$  is in the form of Duhamel's integral:

$$x = D \exp \{(-\delta + i \sqrt{1 - \delta^2})\omega_0 t\} + \int a(\tau)h(t - \tau)d\tau, \quad (2)$$

where  $D$  is an arbitrary constant dependent on the initial conditions,  $i = (-1)^{1/2}$ ,  $\exp = e$  and  $h(t)$  is the indicial response, i.e., the response to a Dirac-delta input, of the system. For quiescent initial conditions, it has been shown by many investigators, e.g., von Gierke<sup>3</sup>, Kornhauser<sup>4</sup>, Payne<sup>5</sup>, that the system response can be divided into approximately two regions at a critical pulse duration,  $t_c$ . For  $t < t_c$ , influence on the system occurs only in the pulse area, which is equal to the imposed velocity change. For  $t > t_c$ , the pulse shape is the important factor. If one were to assume that the elastic element always breaks at a given peak force level, the so-called equal tissue strain assumption, it is then possible to relate the damage or injury, through the system response, to the parameters of the input pulse. Typically, the result is a plot of the maximum applied acceleration,  $A_m$ , versus the duration of the pulse,  $t_1$ , on a log-log scale, as shown in Figure 2. In this tolerance graph, the "knee" represents the critical duration,  $t_c$ . To its left, the region is sensitive to velocity-change and to its right, the peak acceleration of the pulse.

An alternative to the above is the use of response to a sinusoidal input to predict system response under arbitrary pulse loading. Let the input be the real part of

$$\tilde{a}(t) = Ae^{i\omega t} \quad (3)$$

where A is a complex constant. The solution to (1) subjected to the input of (3) may be written as:

$$x = B \exp \{(-\delta + i \sqrt{1 - \delta^2} \omega_0) t\} + Ae^{i\omega t}/Z(\omega), \quad (4)$$

where B is a complex constant dependent on the initial conditions,  $Z(\omega)$  is the characteristic impedance and

$$Z(\omega) = m(\omega_0^2 - \omega^2 + 2i\delta\omega_0\omega). \quad (5)$$

The reciprocal of (5), i.e.,  $H(\omega) = 1/Z(\omega)$ , is the transfer function or frequency response function. For steady-state motion, the transfer function is the ratio of the output (displacement) to the input (sinusoidal excitation).

If one attempts to experimentally identify the transfer function, an immediate difficulty arises. Because the human body parts consist of distributed masses, generally no point can be picked where the displacements of the effective mass can be measured. Coermann<sup>6</sup> circumvented this difficulty by adopting the concept of mechanical impedance. Specifically, mechanical or driving point impedance is defined as the ratio of the transmitted force,  $F_{tr}$ , to the velocity,  $\dot{x}$ , of that point where the force is transmitted. It is equivalent to electrical impedance if one were to choose the force-current analogy. This concept of mechanical impedance is not identical to characteristic impedance,  $Z(\omega)$ , defined in (4). To avoid confusion, we denote mechanical impedance by  $Y(\omega)$ , which is easily shown to have the following form:

$$Y(\omega) = \frac{(1 + 2i\delta\omega/\omega_0)m\omega}{\{1 - (\omega/\omega_0)^2\} + 2i\delta\omega/\omega_0} \quad (6)$$

or

$$|Y(\omega)| = |F_{tr}|/|\dot{x}| = m\omega \left\{ \frac{1 + (2\delta\omega/\omega_0)^2}{[1 - (\omega/\omega_0)^2]^2 + (2\delta\omega/\omega_0)^2} \right\}^{1/2} \quad (7)$$

The value of frequency ratio,  $\omega/\omega_0 = p$ , at which the above equation attains its maximum is found by setting  $dY/dp = 0$ . It can be shown to occur at

$$p = \{4\delta^2 + (1 + 8\delta^2)^{1/2}\}/(1 + 8\delta^2 - 16\delta^4)^{1/2}. \quad (8)$$

Using the above model, Coermann<sup>6</sup> vibrated human volunteers, dummies and animals in the sitting and standing position from 1 to 20 hertz. From the experimentally obtained frequency ratio corresponding to the peak of the mechanical impedance curve, he determined the damping ratio,  $\delta$ , with the help of (8).

An interesting question suggests itself at this point: given the frequency response or the mechanical impedance of a system, what can one say about its response to an arbitrary pulse? Define

$$\bar{a}(\omega) = (1/2\pi) \int_0^{\infty} a(t) e^{-i\omega t} dt \quad (9)$$

as the Fourier Transform of  $a(t)$ . Its inverse transform is:

$$a(t) = \int_{-\infty}^{+\infty} \bar{a}(\omega) e^{+i\omega t} d\omega. \quad (10)$$

Implicit in the above definitions is that the conditions for the existence of such a transform pair are satisfied and that  $a(t) = 0$  for  $t < 0$ . The above synthesis when superposed on (4) yields

$$x = B \exp \{ (-\delta + i \sqrt{1 - \delta^2}) \omega_0 t \} + \int_{-\infty}^{+\infty} H(\omega) \bar{a}(\omega) e^{i\omega t} d\omega. \quad (11)$$

In words, the pulse response of system (1) is the sum of the transient solution and the inverse Fourier transform of the product of the frequency response function,  $H(\omega)$  and the frequency spectrum,  $\bar{a}(\omega)$ , of the pulse. To compute the displacement response of the effective mass to an arbitrary pulse based on frequency response data, one needs only to compare (5) and (6) and note that

$$Y(\omega) = m^2 \omega_0^2 \{ 1 + 2i\delta(\omega/\omega_0) \} / Z(\omega). \quad (12)$$

Neglecting the transients, we get

$$x = \int_{-\infty}^{+\infty} \frac{Y(\omega) \bar{a}(\omega) e^{i\omega t} d\omega}{m^2 \omega_0^2 \{ 1 + 2i\delta(\omega/\omega_0) \}}. \quad (13)$$

For specific analytical forms of  $Y(\omega)$  and  $\bar{a}(\omega)$ , it may be possible to obtain an analytical expression for  $x$ . In other instances, the integrand in (13) is so complicated that the evaluation of the integral is a matter of great difficulty. The true value of (13) in the present problem is to use the experimentally determined mechanical impedance,  $Y(\omega)$  to yield information about its response to an arbitrary pulse. For these cases, recourse generally has to be made to numerical methods. To accomplish the complex integration in (13), a feasible approach is to resolve the complex function into separate functions of real and imaginary part and integrate each separately. Rewriting (13) as

$$x(t) = \int_{-\infty}^{+\infty} F(\omega) e^{i\omega t} d\omega, \quad (13')$$

where  $F(\omega) = A(\omega) + iB(\omega)$ . It follows therefore, that

$$x(t) = a(t) + ib(t) = \{ a^2(t) + b^2(t) \}^{1/2} e^{i\phi(t)}, \quad (14)$$

where

$$a(t) = \int_{-\infty}^{+\infty} \{ A(\omega) \cosh \omega t - B(\omega) \sinh \omega t \} d\omega$$

$$b(t) = \int_{-\infty}^{+\infty} \{A(\omega) \sinh \omega t + B(\omega) \cosh \omega t\} d\omega$$

$$\phi = \tan^{-1}(b/a) .$$

The practical difficulty lies in the frequency range to be swept. If the test data obtained is, say, from 0 - 200 hertz, then the Hobson's choice is to sweep from -200 to +200 hertz in evaluating (14). The numerical quadrature required can be achieved through any number of standard integration routines. The use of a hybrid analog-digital computer should also accomplish the task in one operation, i.e., from the data obtained to the final tolerance graph.

The massive experimental program mounted on behalf of the single-degree-of-freedom model served to identify some of the critical organ systems associated with a given force environment. The best understood case is the caudocephalad or +G<sub>z</sub> acceleration where the most critical organ is the spine and the mode of injury is, with few exceptions, compression fracture of the vertebral end-plates. Given this critical injury information, it is possible to refine the model analysis and/or identification of the model parameters. Liu<sup>7</sup> recently reviewed the modelling and experimental progress made for the spine in the dynamic environment with particular emphasis in the +G<sub>z</sub> orientation. A brief summary of his conclusions appear in the next section of this paper.

The critical organs and failure criterion for other orientations of impact are only partially defined. It is in these orientations where the relationships given by equations (2) and (13) are still needed pending additional work which will delineate the failure modes in the critical organs. As an example, consider the dynamics of the head-neck junction, which has major implications in brain injury due either to whiplash or a direct blow to the head. Initially, it can be viewed as a single degree of freedom rotational problem, i.e., the dependent variable in (1) is the angular displacement,  $\theta$ , of the head. The driving point impedance has been determined in detail by Hodgson et al.<sup>8</sup> Assuming a linear, single-degree-of-freedom system the parameters,  $\delta$  and  $\omega_0$ , can be identified from the impedance data and then the response to a pulse is found from (2). Alternately, if one were to compare the experimentally determined impedance data with the response as given in (4), the data will indicate its deviations from the simple model. These deviations can either be due to additional degrees of freedom in the system and/or nonlinear material properties or geometry.

#### MODELS CONSIDERING MASS DISTRIBUTION

Liu<sup>7</sup> recently gave a review and an assessment of the multi-degree-of-freedom, discrete-parameter and continuous-parameter models of the spine under inertial loading and their relationships to the simpler models proposed earlier. The essential points made in that paper were:

- (1) Most of the inconsistencies of the simple models were due to ignoring the spatial mass distribution.
- (2) The possible occurrence of shock waves in a lightly damped nonlinear rod model of the spine is due to an accumulation of small effects.

The shock forms as a result of the steepening of the negatively sloped portion of the input pulse and not as a function of rapid rise time alone as has been suggested in the literature.

(3) That a lumped-parameter equivalent to a continuous segment is valid provided its length is much shorter than the shortest wavelength of interest. If one were to have an understanding of the spinal injury mechanism, the wavelength of interest is, at least, the thickness of the disc.

(4) The initial curvature and the eccentric center of mass of the trunk (anterior to the vertebral bodies) places the spine under complex loading even under normal conditions. For impact loading, the situation is greatly exaggerated.

(5) In order to implement either the multi-degree-of-freedom configuration model of Orne and Liu<sup>9</sup> or the distributed-parameter model of Moffatt<sup>10</sup>, a large amount of biomechanical data is needed, e.g., the inertial-property distribution of the head, neck and trunk, the failure surface of the intervertebral joint under complex loading and the initial configurations of the pilot prior to ejection, etc. Liu et al.<sup>11</sup> recently obtained the inertial properties of a segmented cadaver trunk. Figures 3-5 summarized their results for the distribution of mass, the centers of mass and moments of inertia respectively.

(6) The predominance of anterior-lip and/or compression fractures in the lower thoracic vertebrae during pilot ejection are primarily attributable to the large negative moments there and only secondarily to the axial and shear forces. These summary results are shown in Figures 6-8. The solid curves are the results obtained by using the inertial data of Liu et al.<sup>11</sup> as input to the model by Orne and Liu<sup>9</sup> and the dotted curves were the corresponding results using assumed data. Figure 9 illustrates the time history of the configuration changes of the spine under these same loading conditions.

#### HEAD IMPACT MODELS

The special vulnerability of the head to injury as compared to other parts of the human body is evidenced by the fact that about 75% of the fatalities from all accidents are linked to craniocerebral trauma. The Proceedings of the Conference on Head Injury, edited by Caveness and Walker<sup>12</sup> summarized the spectrum of activities in connection with the problem up to 1966. Recently, Goldsmith<sup>13</sup> reviewed the more current work. It would be superfluous to cite these contributions once more except perhaps in illustrating some inconsistencies which have entered the modeling of intracranial pressure in head impact. The main discussion will deal with models which have entered the literature since 1966.

Mathematical models of the head have been divided in much the same fashion as the major hypotheses proposed to explain head injuries due to impact. One group, the rotational school, has contended that the rotational acceleration induced by impact causes high shear strains in the brain matter, rupturing cerebral blood vessels and tissue. The cavitation school, on the other hand, has claimed that there exist points within the brain where the reduced pressure is sufficient to rupture the capillary walls. The normal transmural pressure of these capillaries is a few mm Hg; however, due to the impact, the transmural pressure is



suddenly increased, bursting the capillary. Of course, when the pressure is reduced to near vapor pressure of the brain substance, cavitation should take place. The catastrophic collapse of the bubbles thus formed is another possible cause of brain damage.

#### ONE DIMENSIONAL CAVITATION MODEL

The most recent one-dimensional continuum model was given by T. Hayashi<sup>14</sup>. The system consists of a rigid but massless vessel (skull) containing elastic fluid (brain and cerebrospinal fluid). The vessel is attached to a linear spring  $k$ , which represents the composite elastic properties of the helmet, skull, hair and elasticity of the wall. Thus, the problem can be simplified to that of a fluid "rod" enclosed in a rigid vessel with an attached spring striking a rigid wall, see Figure 10. The governing nondimensional differential equation is:

$$u_{\tau\tau} + \xi_{\tau\tau} = \xi_{xx}, \quad (16)$$

where the subscript is used to denote partial differentiation with respect to the independent variables,  $x$  and  $\tau$ . The associated initial and boundary conditions are respectively:

$$\zeta(x, 0) = u(0) = 0; \quad \zeta_\tau(x, 0) = 0; \quad u_\tau(0) = V \quad (17)$$

$$\zeta(0, \tau) = \zeta(1, \tau) = 0; \quad u(\tau) = \lambda \{ \zeta_x(0, \tau) - \zeta_x(1, \tau) \}. \quad (18)$$

In terms of the original quantities (with tilde  $\sim$ ), the variables in (16)-(18) have been nondimensionalized as:

$$\begin{aligned} \zeta &= \tilde{\zeta}/\ell; \quad u = \tilde{u}/\ell; \quad x = \tilde{x}/\ell; \quad \tau = c\tilde{\tau}/\ell \\ c &= (B/\rho)^{1/2}; \quad k_f = BA/\ell; \quad \lambda = k_f/k; \quad V = v_0/c, \end{aligned} \quad (19)$$

where  $\tilde{\zeta}(\tilde{x}, \tilde{\tau})$  is the displacement of the fluid at location  $\tilde{x}$  relative to the vessel,  $A$  is the area,  $\ell$  is the length,  $\tilde{\tau}$  is the time,  $\tilde{u}$  is the absolute rigid-body displacement of the vessel,  $v_0$  = velocity of the vessel just prior to impact;  $B$  is the bulk modulus;  $\rho$  is the density;  $c = (B/\rho)^{1/2}$  is the wave speed and  $k_f$  is the stiffness of the fluid. Hayashi<sup>14</sup> utilized a separation of variables technique to obtain an infinite series solution for the vessel displacement and the fluid pressure in the original variables, i.e.,  $\tilde{u}$  and  $\tilde{\zeta}_x$ . In terms of the dimensionless variables given in (19), his solutions can be written as:

$$u(\tau) = 2V \sum_{n=1}^{\infty} \frac{\sin(2\omega_n)}{(2\omega_n)\{2\omega_n + \sin(2\omega_n)\}} \sin(2\omega_n\tau) \quad (20)$$

and

$$\begin{aligned} -P(x, \tau) &= -\frac{\zeta_x(x, \tau)}{B} \\ &= 4V \sum_{n=1}^{\infty} \frac{\sin(\omega_n)}{2\omega_n + \sin(2\omega_n)} \sin\{\omega_n(1-2x)\} \sin(2\omega_n\tau), \end{aligned} \quad (21)$$

where  $\omega_n$  are the  $n$  roots of the characteristic equation:

$$\omega \tan \omega = \frac{1}{4\lambda} \quad (22)$$

The roots of (22) are partially tabulated in the National Bureau of Standards Handbook of Mathematical Functions (edited by Abramowitz and Stegun). Any attempt to perform computations using (20) - (22), however, would show that these infinite series solutions are slowly convergent, if at all, especially for small values of time. In short, while (20) and (21) are nominally "exact" solutions, they are useless in computing numerical results. If, in addition, certain approximations are made in order to make (20) - (22) more pliable, the errors are then compounded as will be shown presently by the exact closed form solution obtained by the author.

Taking the Laplace transform of Equations (16) to (18) yields

$$\bar{\zeta}(x,p) = -\frac{V\{\cosh px - \tanh(p/2) \sinh px - 1\}}{p^2\{1 + 2\lambda p \tanh(p/2)\}} \quad (23)$$

and

$$\bar{u}(p) = \frac{2\lambda V \tanh(p/2)}{p\{1 + 2\lambda p \tanh(p/2)\}} \quad (24)$$

The pressure in the fluid is found from the inversion of:

$$\bar{P}(x,p) = -\bar{\zeta}_x(x,p) = \frac{V\{\sinh px - \tanh(p/2) \cosh px\}}{p\{1 + 2\lambda p \tanh(p/2)\}} \quad (25)$$

The poles of (25) are the characteristic roots of (22). Using the standard contour inversion integral and summing the residues will yield identical results as those shown in (20) and (21). We are back in the same quandary! Under these circumstances, instead of dealing with the entire function, one circumvents the problem by dealing with its expansion, see Carslaw and Jaeger<sup>15</sup>. Expanding the hyperbolic functions in terms of exponentials, we write (25) as:

$$\bar{P}(x,p) = \frac{-V\{e^{-px} - e^{-p(1-x)}\}}{p(1+2\lambda p)\{1 + \epsilon(p)e^{-p}\}} \quad (26)$$

where

$$\epsilon(p) = \frac{2}{1 + 2\lambda p} - 1 \quad (27)$$

Using the binomial theorem, we get

$$\{1 + \epsilon(p)e^{-p}\}^{-1} = 1 + \sum_{n=1}^{\infty} (-1)^n \epsilon^n(p) e^{-np} \quad (28)$$

Observe that

$$(-1)^n \epsilon^n(p) = \left\{1 - \frac{2}{1+2\lambda p}\right\}^n = 1 + \sum_{v=1}^n (-1)^v \binom{n}{v} \lambda^{-v} \left(p + \frac{1}{2\lambda}\right)^{-v} \quad (29)$$

where  $\binom{n}{v} = \frac{n!}{v!(n-v)!}$  are the binomial coefficients.

In view of (28) and (29), (25) becomes

$$\begin{aligned} \bar{P}(x, p) = & \frac{-V}{p(1+2\lambda p)} \left\{ e^{-px} - e^{-p(1-x)} \right\} + \sum_{n=1}^{\infty} e^{-p(n+x)} - \sum_{n=1}^{\infty} e^{-p(n+1-x)} \\ & + \sum_{n=1}^{\infty} \sum_{v=1}^n (-1)^v \binom{n}{v} \lambda^{-v} \left( p + \frac{1}{2\lambda} \right)^{-v} \left\{ e^{-p(n+x)} - e^{-p(n+1-x)} \right\} \end{aligned} \quad (30)$$

The inverse of  $1/p(p + \frac{1}{2\lambda})^{v+1}$  is

$$\frac{1}{2\pi i} \int_{\gamma-i\infty}^{\gamma+i\infty} \left[ e^{p\tau} / p(p + \frac{1}{2\lambda})^{v+1} \right] dp = (2\lambda)^{v+1} \left[ 1 - e^{-\tau/2\lambda} \sum_{\mu=0}^v \frac{\tau^\mu}{(2\lambda)^\mu \mu!} \right] \quad (31)$$

Taking advantage of the shifting theorem, the exact solution to the problem posed by (16) - (18) is:

$$\begin{aligned} - \frac{P(x, \tau)}{V} = & \left[ 1 - e^{-(\tau-x)/2\lambda} \right] H(\tau-x) - \left[ 1 - e^{-(\tau-1+x)/2\lambda} \right] H(\tau-1+x) \\ & + \sum_{n=1}^{\infty} \left[ 1 - e^{-(\tau-n-x)/2\lambda} \right] H(\tau-n-x) - \sum_{n=1}^{\infty} \left[ 1 - e^{-(\tau-n-1+x)/2\lambda} \right] H(\tau-n-1+x) \\ & + \sum_{n=1}^{\infty} \sum_{v=1}^n (-1)^v \binom{n}{v} \frac{1}{\lambda^v (2\lambda)^{-v}} \left\{ \left[ 1 - e^{-(\tau-n-x)/2\lambda} \sum_{\mu=0}^v \frac{(\tau-n-x)^\mu}{\mu! (2\lambda)^\mu} \right] H(\tau-n-x) \right. \\ & \left. - \left[ 1 - e^{-(\tau-n-1+x)/2\lambda} \sum_{\mu=0}^v \frac{(\tau-n-1+x)^\mu}{\mu! (2\lambda)^\mu} \right] H(\tau-n-1+x) \right\} \end{aligned} \quad (32)$$

Where  $H(t)$  is the Heaviside function, i.e., it is zero when  $t < 0$  and unity when  $t > 0$ .

We note that (32) is an odd function about  $x = \frac{1}{2}$ , i.e.,

$$P(x, \tau) = -P(1-x, \tau) \quad (33)$$

and in particular

$$P(0, \tau) = -P(1, \tau). \quad (33')$$

For  $x = \frac{1}{2}$ ,  $P(\frac{1}{2}, \tau) = -P(\frac{1}{2}, \tau)$ , which is possible if and only if  $P(\frac{1}{2}, \tau) \equiv 0$ . Equation (33) states that the pressure at the center is always zero and the pressure variations in time are equal, except for sign, on either side of the center. Further, the solution (32) is valid only prior to rebound which occurs when  $F = k\bar{u} \geq 0$ . In view of (18) and (33'), the rebound condition is

equivalently

$$-P(0, \tau) \geq 0, \quad (34)$$

i.e., when the system returns to the initial position of the container prior to impact. Due to the nature of the Heaviside function, for a given  $x$  and  $\tau$ , only a finite number of terms are needed from (32) to perform the numerical calculations, attesting to its simplicity as well as exactness. For up to 2 wave-transit times even hand calculations would suffice.

The displacement can be found immediately from the boundary condition (18), i.e.,

$$u(\tau) = \lambda \{ \zeta_x(0, \tau) - \zeta_x(1, \tau) \} = -2\lambda P(0, \tau), \quad (35)$$

where use was made of  $P(x, \tau) = -\zeta_x(x, \tau)$  and  $P(0, \tau) = -P(1, \tau)$ . The differentiation in the  $\tau$  domain corresponds to multiplication by  $p$  since the initial displacement is zero, hence

$$pu(p) = 2\lambda V \tanh(p/2) \{1 + 2\lambda p \tanh(p/2)\}^{-1}. \quad (36)$$

To check that the initial velocity is satisfied, we note

$$\begin{aligned} u_\tau(0) &= \lim_{p \rightarrow \infty} p^2 \bar{u}(p) = \lim_{p \rightarrow \infty} \{2\lambda V p \tanh(p/2) [1 + 2\lambda p \tanh(p/2)]^{-1}\} \\ &= \lim_{p \rightarrow \infty} \frac{2\lambda V \tanh(p/2)}{1/p + 2\lambda \tanh(p/2)} = V. \end{aligned} \quad (37)$$

The acceleration is, therefore, the inverse transform of

$$\bar{a}(p) = p^2 \bar{u}(p) - u_\tau(0) = \frac{V \{2\lambda p \tanh(p/2) - 1\}}{1 + 2\lambda p \tanh(p/2)} \quad (38)$$

Through an expansion and inversion procedure similar to (26)-(29), we obtain

$$\begin{aligned} \frac{-2\lambda a(\tau)}{V} &= e^{-\tau/2\lambda} H(\tau) + 2 \sum_{n=1}^{\infty} e^{-(\tau-n)/2\lambda} H(\tau-n) \\ &+ \sum_{n=1}^{\infty} \sum_{v=1}^n (-1)^v \binom{n}{v} \frac{1}{\lambda^v v!} \left[ (\tau-n) e^{-(\tau-n)/2\lambda} H(\tau-n) \right. \\ &\left. - (\tau-n-1) e^{-(\tau-n-1)/2\lambda} H(\tau-n-1) \right]. \end{aligned} \quad (39)$$

Equations (39) and (32) constitute the exact principal results of the model. The corresponding Maayashi approximate results are found from (20), (21) and (22) by the substitution of  $\omega_1 \approx 1/2\lambda^2$  into the infinite series truncated after one term, i.e.,

$$-\frac{2\lambda a}{V} = 2\lambda^{\frac{1}{2}} \sin(\tau/\lambda^{\frac{1}{2}}) \quad (20')$$

$$-\frac{P(x, \tau)}{V} = \frac{(1-2x)}{2\lambda^{\frac{1}{2}}} \sin(\tau/\lambda^{\frac{1}{2}}) \quad (21')$$

Figure 11 is a plot comparing the acceleration of the container as obtained by equation (39) and (20') for different values of stiffness ratio  $\lambda$ . Whereas the exact wave propagation solution has a discontinuous jump at  $\tau = 0$  and "jumps" at  $\tau = 1, 2, \dots$ , the points of wave reflection, in contrast, the Hayashi approximation is a sine wave. The discontinuous jumps shown in Figure 11 have major implications for the infinite series solutions such as (20) and (21). Would the addition of more terms from (21) improve the acceleration result? It is well-known, however, that the partial sums  $S_m(x)$  of a Fourier series for a periodic function  $f$  cannot approach  $f(x)$  uniformly over an interval that contains a point where  $f$  is discontinuous. The nature of the deviation of  $S_m(x)$  from  $f(x)$  on such intervals is known as Gibb's phenomenon, see Carslaw<sup>17</sup>. The pathological nature of the exact acceleration solution was due to the absence of the container mass, which is to be regarded as a weak solution in the sense of Courant and Hilbert<sup>18</sup>.

For the pressure results, two sets of graphical data are of interest: (a) the pressure field variation at given times, and (b) the pressure-time variation at a given location,  $x$ . In Figure 12 is shown the dimensionless contrecoup ( $x = 0$ ) pressure as a function of  $\tau$ . When the contrecoup pressure reaches zero, the solution (32) is no longer valid because of the rebound condition (34). Note that the softer the impact, (increasing  $\lambda$ ) the longer the contact duration,  $\tau_c$ , e.g.,  $\lambda = 1$ ,  $\tau_c \approx 3.275$ , whereas  $\lambda = 0.1$ ,  $\tau_c \approx 1.34$ . For very soft impacts,  $\lambda \gg 1$ , the pressure wave would have traversed the fluid length many times during the time the vessel takes to return to its original position, i.e., just prior to loss of contact. Also shown in Figure 12 is a comparison of the exact wave-propagation solution with the Hayashi approximate solution for various  $\lambda$ . We note with interest that for  $\lambda = 10$  the two results are indistinguishable and that for  $\lambda = 1$ , the approximation is still quite good. It would appear that in all practical cases of interest, the approximate pressure solution would suffice.

Figures 13 and 14 are plots of the pressure fields for time increments,  $\Delta\tau = 0.1$  and  $\lambda = 1$  and  $\lambda = 10$ . Up to  $\tau = 0.5$ , the pressure distribution reflects the wave-propagation nature of the problem. After traversal is completed, i.e.,  $\tau > 0.5$ , the distribution deviates somewhat from the usual experimental observation that the pressure field is linear for any given  $\tau$ , e.g., Roberts et al.<sup>16</sup>

Figure 15 replots the pressure-time variation at a given point for  $\lambda = 0.1, 1$  and  $10$ . The approach to zero pressure at the center of the container is quite abrupt when one considers the amount of pressure fluctuations still present at  $x = 0.4$ .

An overview of Figures 11 - 15 would indicate that the Hayashi approximation for the pressure is excellent for  $\lambda \geq 10$ . To correlate the pressure distribution, however, to a "maximum acceleration", which is due entirely to an approximation, is not self-consistent. The remarkable agreement with experimental data given by Hayashi, reproduced here as Figure 16, should be considered fortuitous at this time. On the other hand, in spite of its analytical pathology, the concept of an acceleration beginning at zero and in phase with the fluid pressure as postulated by Hayashi has intuitive and physical appeal. The weaknesses of the model lie obviously in neglecting the container mass and possibly dissipation. Typically, one can add a damper,  $c$ , in parallel with the spring,  $k$ , and include the vessel mass, i.e., the boundary condition (18) takes the dimensionless form:

$$u + \eta u_{\tau} + \lambda \mu u_{\tau\tau} = \lambda \{ \zeta_x(0, \tau) - \zeta_x(1, \tau) \} , \quad (40)$$

where  $\mu$  is the container to fluid mass ratio and  $\eta$  is a damping parameter. In a preliminary study, the author has shown that the container acceleration is indeed smoother than the "jumps" indicated in Figure 15, e.g., the acceleration has a finite rise time from zero. When these improvements are completed, the model first proposed by Hayashi might indeed still make the discussion of the cavitation model very much easier because of the relatively small number of dimensionless parameters present.

## TWO DIMENSIONAL MODELS

The use of a fluid-filled rigid spherical shell under impact as a model of craniocerebral trauma began with Anzelius<sup>19</sup> and Güttinger<sup>20</sup>. Phenomenologically, this model is not very different from the one-dimensional one just discussed. Because of the rigid assumption, a blow at one point (coup) on the sphere is immediately transmitted to the diametrically opposite pole (contrecoup). Every point on the shell begins to transmit energy at the instant of impact. Goldsmith<sup>13</sup> suggested the obvious necessity of modelling the skull as an elastic shell. Engin and Liu<sup>21</sup> justified the use of a fluid-filled elastic spherical shell as a model for head injury based on neuroanatomical and analytical considerations. They obtained the frequency spectrum for the axisymmetric free vibration of the fluid-solid ensemble and compared the results for the cases of steel and water and skull and water. The axisymmetric response of a thin, elastic, homogeneous and completely closed spherical shell filled with an inviscid and irrotational fluid subjected to a radial impulse was obtained by Engin<sup>22</sup>. The point of view taken is that of a spherical fluid region constrained by very complicated boundary conditions consisting of the two shell differential equations (including both bending and membrane effects) and the continuity of the normal velocity at the fluid-solid interface. Mathematically, this is expressed by satisfying the wave equation in

The pathological nature of these solutions were a consequence of the mathematical formulation of the problem. Wave propagation phenomena are represented by solutions of hyperbolic differential equations with prescribed initial and boundary data. If the given data is discontinuous (e.g., wave motion initiated by an impulse:  $u_\tau(0) = V$ ) the solution is also discontinuous. The function  $f(x + \tau) + g(x - \tau)$  is a genuine solution of the wave equation provided  $f$  and  $g$  are twice differentiable. Otherwise, the function ought to be regarded as a "solution in the general sense" or a weak solution, see Courant and Hilbert.<sup>18</sup>

Because of the inherent weaknesses of the above one-dimensional model due to both the mathematics and obvious geometrical restraints, further improvement of this model appears superfluous. Typically, if one were to add a damping element in parallel or in series with the spring and include the inertia of the container, i.e., boundary condition (18) takes the form:

$$u + \eta u_\tau + \mu u_{\tau\tau} = \lambda \{ \zeta_x(0, \tau) - \zeta_x(1, \tau) \}, \quad (40)$$

where  $\eta$  and  $\mu$  are the dimensionless damping and inertial parameters respectively. A similar analysis as given earlier would yield the presence of a Dirac-delta function in the pressure field, which is physically untenable.

It is indeed regrettable that the one-dimensional continuum model proposed by Hayashi is beset by these mathematical difficulties. The model has the advantage of simplicity. If it had satisfied the test of self-consistency, its small number of dimensionless parameters would have made discussions of the cavitation model very much easier.

## TWO DIMENSIONAL MODELS

The use of a fluid-filled rigid spherical shell under impact as a model of craniocerebral trauma began with Anzelius<sup>19</sup> and Güttinger<sup>20</sup>. Phenomenologically, this model is not very different from the one-dimensional one just discussed. Because of the rigid assumption, a blow at one point (coup) on the sphere is immediately transmitted to the diametrically opposite pole (contrecoup). Every point on the shell begins to transmit energy at the instant of impact. Goldsmith<sup>13</sup> suggested the obvious necessity of modelling the skull as an elastic shell. Engin and Liu<sup>21</sup> justified the use of a fluid-filled elastic spherical shell as a model for head injury based on neuroanatomical and analytical considerations. They obtained the frequency spectrum for the axisymmetric free vibration of the fluid-solid ensemble and compared the results for the cases of steel and water and skull and water. The axisymmetric response of a thin, elastic, homogeneous and completely closed spherical shell filled with an inviscid and irrotational fluid subjected to a radial impulse was obtained by Engin<sup>22</sup>. The point of view taken is that of a spherical fluid region constrained by very complicated boundary conditions consisting of the two shell differential equations (including both bending and membrane effects) and the continuity of the normal velocity at the fluid-solid interface. Mathematically, this is expressed by satisfying the wave equation in

axisymmetrical spherical coordinates for the fluid exactly, i.e., the velocity potential of the fluid in the Laplace-transformed variable is expanded in an infinite series of its characteristic functions. On the other hand, the shell equations are expanded in terms of Legendre and associated Legendre polynomials, which are the characteristic functions for the in-vacuo shell differential equations. The ensuing infinite series solutions have this inherent error of truncation.

The above comments have a familiar ring and one might immediately and legitimately question whether or not the solutions thus obtained fall into the same quagmire as the infinite-series solution in the Hayashi model. There exists no exact solution, such as the wave propagation result, to settle the question definitively. In Engin's solution, the intracranial pressure required the evaluation of 420 residues in order to achieve convergence in the sense of Cauchy. There is every physical reason to believe however, that these solutions will not contain discontinuous jumps. By comparison with the one-dimensional model, the fluid-solid model has the following advantages in this regard:

(a) The container (shell) is elastic and hence it takes a finite time for the stress waves to travel from coup to contrecoup. The instantaneous transmission of pressure waves due to the assumption of rigidity of the container is one contribution to the jump phenomena discussed earlier and also observed in the solutions due to Guttinger<sup>20</sup>.

(b) The load on the shell is spread over a finite area (a polar cap) while in the one dimensional model it is confined to a point, a physically untenable state.

(c) The obvious geometrical advantage in being able to spread the pressure variation as a function of the polar angle, radius and time.

The results of Engin confirmed that most likely locations of skull fracture are away from the impact polar cap. Specifically, for a blow of uniform pressure over a 15° cone angle, the location of high stresses on the skull are immediately below the impact area and in a ring about 45° away from the polar axis. The second interesting result is the pressure distribution in the brain during a closed-head trauma. If one assumes, for the moment, that injury is associated with negative pressure, then the possibility of intermediate coup, i.e., high negative pressures away from the contrecoup point, has been predicted by the model. Liu and Nelson<sup>23</sup> have extended Engin's result and compared the differences in pressure-wave propagation between a Dirac-delta type impulse to a more realistic finite time pulse. Because of the complexity of the wave interaction phenomena, they have produced a "cartoon" type movie showing the progress of the "isobars" in the brain. For the Dirac-delta time function, the frames corresponding to contrecoup and intermediate coup are shown in Figures 17 and 18. In these figures, the symbols +, 0, 1, 2, 3, 4 and 5 represent intervals of increasing negative nondimensional pressure while the symbols -, =, A, B, C, D, E, and F denote increasing positive nondimensional pressures. The dimensionless pressure,  $p_1$  and time  $\tau$  are related to the physical quantities as follows:

$$p_1 = \rho_s(1 - v^2)p/E\rho_f, \quad (41)$$



$$\tau = c_s t/a, \quad (42)$$

where  $\rho_s$  and  $\rho_f$  are the densities of the skull and fluid respectively,  $E$  and  $\nu$  are the Young's modulus and Poisson's ratio of the shell and  $p$  is the magnitude of the externally applied uniform pressure,  $c_s$  is the wave speed in the shell and is equal to  $\{E/\rho_s(1-\nu^2)\}^{1/2}$ ,  $a$  is the radius of the shell and  $t$ , the time.

We note from Figures 17 and 18, the following:

- a) There exists a "ringing" motion in the fluid, i.e., the alternating positive and negative pressures in each frame.
- b) The so-called contrecoup negative pressure is low in magnitude (grade 1) but diffuse over a fairly large area.
- c) The intermediate-coup negative pressure is high in magnitude (grade 5) but extremely well-focused.

The response of the fluid-solid interaction system to a more realistic finite time-varying pulse is obtained by convolution. Using the same spatial distribution as Engin, but instead of the Dirac-delta function, we use

$$T(t) = \exp(-4.73 \times 10^{-6} t^2) \sin(\pi \times 10^{-3} t) \quad (43)$$

The pressure response of the system is similar except that the "ringing" is more pronounced and the contrecoup area less diffused. It was evident from an examination of the frames that the damage criterion for any given location must incorporate the following factor: the time spent beyond a critical negative pressure. Physiological considerations collaborate the above argument. The capillaries will not burst even for a large transmural pressure if the negative pressure is present for only a very short time. Finite time is required for the blood to enlarge the capillary walls to the point of rupture. On the other hand, a small transmural pressure acting over a relatively long period of time can damage the vessel. From simple strength of material, the static hoop stress,  $\sigma$ , for a thin-walled tube is

$$\sigma = \Delta p d/2h, \quad (44)$$

where  $\Delta p$  is the transmural pressure,  $h/d$  is the wall thickness to diameter ratio. According to Burton<sup>24</sup>,  $h/d$  is about 1/8 for a true capillary. Its thickness is practically a single layer of endothelial lining cells. Very little force is required to deform these cells and they are believed to play a very minor role in the total elasticity. Without going into the role of the surrounding tissue, it suffices to note that equation (44) is the basis of those who claim that negative pressure is the damage criterion. Liu and Nelson<sup>23</sup> postulated the following Cumulative Damage Criterion for closed-head brain injuries: The severity of the brain injury at a given location is proportional to the averaged time spent there beyond a critical negative pressure,  $p^*$ . This criterion is illustrated in Figure 19. The negative pressure less than  $p^*$ , at location  $x_0$ , is divided into equal time steps  $\Delta t$  apart. Let  $p_1(x_0, \Delta t_1)$ ,  $p_2(x_0, \Delta t_2)$ , - - -,  $p_i(x_0, \Delta t_i)$  be the lengths of a series of chords representing the discrete pressures at the beginning of its  $\Delta t_i$ , then

the time-averaged pressure  $\bar{p}(x_0, \bar{t})$  is given analytically by:

$$\bar{p}(x_0, \bar{t}) = \sum_{i=1}^n p_i(x_0, \Delta t_i) H(p^* - p_i) / \sum_{i=1}^n \Delta t_i, \quad (45)$$

where  $H(p^* - p_i)$  is the Heaviside function, i.e., it is zero if  $p^* < p_i$  and is unity if  $p^* > p_i$ . The maximum value of  $\bar{p}(x_0, \bar{t})$  is assigned a grade of 5 and a decreasing linear scale is used thereafter for the lower pressures. The computations were terminated at the end of the applied pulse. By the Cumulative Damage Criterion, there appears two foci of intermediate-coup due essentially to the wave propagation and interaction phenomena and contrecoup because of the induced accelerational difference between the shell and the fluid.

The situation appears paradoxical at this point. As the elasticity of the shell is taken into account, the analysis seems to deviate more and more from the comfortable notion of a linear pressure distribution reported by the experimentalists, see, for example, the works of Lingren<sup>25</sup>, Unterharnscheidt and Sellier<sup>26</sup>, and Roberts et al.<sup>16</sup>. The situation is not an unfamiliar one. The experimentalists made measurements without a theoretical model, or at best, the model was constructed from the data a posteriori without much regard for the fundamental requirements of the boundary-value problem. On the other hand, the analysts have not been concerned with the experimental evidence of the suitability of his basic assumptions or if he has, found the experimental situation too difficult to formulate in analytical terms. Hopefully, this disagreement will be resolved as additional experimental and analytical work presently in progress is published.

Recently, Lee and Advani<sup>27</sup> partially extended the model of Engin and Liu<sup>21</sup> to include transverse shear and rotational inertia in the shell approximation. The net effect of this improvement is to include wavelengths of the order of the thickness of the shell. The qualitative differences between their result and Engin's were negligible for radial displacement and fibre stresses. Unfortunately, the boundary-value problem associated with the fluid pressure determination was not solved. It is precisely in the fluid, however, where the "high frequency" effects would be most manifest.

Except for the extremely unusual case in which the blow is delivered such that its resultant force passes through the center of mass of the head, the head will experience both a translation and rotation. In the case of a whiplash-type of injury, one also expects both motions to occur. To assess the relative contributions of each of these proposed damage mechanisms to head trauma, Chan<sup>28</sup> is presently investigating the non-axisymmetric response of a fluid-filled spherical shell. The fluid is considered inviscid and irrotational and an "exact" six mode shell theory is used. The implication of the latter is that the analysis will be valid for a thick shell, i.e., its radius to wall-thickness is between 4 and 10. The loading consists of an axisymmetric pulse perpendicular to the surface and a traction tangential to it.

## ROTATIONAL IMPACT MODELS

Because of the very small shear modulus of the brain compared with its bulk modulus, Holbourn<sup>29</sup> was the first to postulate the possibility of brain damage due to rotational acceleration alone. Von Gierke<sup>3</sup> gave, for soft tissue, a value for volume compressibility of  $2.6 \times 10^{10}$  dyne/cm<sup>2</sup> as compared to a shear elasticity of  $2.5 \times 10^4$  dyne/cm<sup>2</sup>. He further noted that when soft tissue is subjected to a blow most of the energy spreads through the tissue in the form of shear waves and not of compression waves. Only very rapid blows produced compression waves of appreciable magnitude in tissue. The implications for energy transmission in the soft brain tissue is obvious. Engin and Wang<sup>30</sup> gave a theoretical analysis of the driving point impedance test for a continuum model of the brain. Relationships were derived from which some of the viscoelastic parameters can be determined from the experimental data.

Holbourn's observation has been pursued further by Ommaya et al.<sup>31</sup> and Unterharnscheidt and Higgins<sup>32</sup>. The mathematical models used were the single degree of freedom rotational version of equation (1) with the angular head displacement  $\theta$  as the dependent variable and the angular acceleration as input. The motion of the head is modelled as a rigid body constrained by a torsional spring. The failure criterion is a clinical indicator of concussion. The resultant data is correlated with the parameters of the input pulse in a form similar to Figure 3.

Martinez and Garcia<sup>33</sup> used a three-degrees-of-freedom nonlinear model to describe the whiplash phenomena. The head is represented by a mass and the resistance of the neck to rotation and shear are represented by torsional and cantilevered springs respectively. Roberts et al.<sup>34</sup> divided the head into two rigid-body compartments: the skull and the brain. A torsional spring placed at the center of the head simulates the resistance of the brain to rotation relative to the skull. The resistance to linear displacement is simulated by linear spring connecting the brain to the skull. A parametric study was made using many assumed input system constants. Hayashi<sup>35</sup> noted that for very short-duration rotational impact, the severest shear deformation is induced in the boundary layer near the inner surface of the skull. From this observation, he constructed a model consisting of two concentric cylinders, which are connected elastically in shear by the brain material. The cylinders are assumed to be rigid bodies: the outer shell representing the skull and the inner one the essentially undeformed portion of the brain. Using estimated input data and a data point on the tolerance curve due to Ommaya et al.<sup>31</sup>, he obtained through his analysis a tolerance relationship:

$$\ddot{\theta} * t_D^2 = 2.52, \quad (46)$$

where  $\ddot{\theta} *$  is the critical or maximum input angular acceleration and  $t_D$  is the impact duration.

The first two-dimensional continuum model for torsional impact to the head was proposed by Lee and Advani<sup>36</sup>. The model is a linear elastic sphere subjected to a step angular acceleration about a diametrical

axis. The displacement is prescribed to be zero at the surface of the sphere. The results are expressions for the dynamic torsional displacement and shear stress. The maximum torsional displacement occurs approximately at normalized radius  $r = 0.42$ . There is a rapid buildup of shear stresses at the surface of the sphere. If the time for a shear wave to travel from the surface to the center is normalized to unity, then for nondimensional time of less than one ( $t < 1$ ), the shear stress decreases with radius, i.e., reaching zero at the appropriate point. Of course nothing happens prior to the arrival of the stress wave. For  $t > 1$ , the stress distribution is almost linear with respect to the zero at the origin. In addition, the linear viscoelastic response of the sphere is studied by using a superposition principle. The numerical results for a Maxwell fluid model indicate an almost logarithmic attenuation of shear stress with respect to the dimensionless radius.

#### OTHER CRITICAL ORGANS AND CONCLUDING REMARKS

While attention has been focused on the situation where the spine and head are the critical organs, all the perspectives gained hopefully have implications in other impact situations. For instance, the critical organ in human tolerance to blast exposure is most probably the lung. Sass<sup>37</sup> has contended that the lung is the most susceptible organ to injury because of its low density and elasticity and non-rigid envelope, while the brain is the least vulnerable because of its essential incompressibility and rigid enclosure. Experimental and theoretical support for this contention has not been conclusive. Failure criterion in materials, whether biological or not, is given in terms of stresses, which are then related to the strains through constitutive equations. The strain-displacement relationships provide the final link to the relative motion of the body tissues. Unless and until the intermediate relationships are known, excessive displacement or rate of displacement can not by itself be a criterion of injury susceptibility. A good illustrative example is the predominance of compression fracture of the vertebral end-plates and anterior lip fractures in caudocephalad acceleration. Without doubt, in this mode of acceleration, relatively large displacements of the lungs and diaphragm do take place as evidenced by some occurrences of lung and visceral injury in pilot ejection. Of course, these critical organs can be analyzed in a similar way as the spine and head. The question is always one of priority.

A synopsis of the exposure limits for human tolerance to blast will reveal a similar hierarchy of idealizations in the modelling process. The initial linearized model due to von Gierke<sup>3</sup> involved the concept of equal strain in lung tissue. Tolerance curves plotting the maximum overpressure versus the duration of exposure were given. An improved model due to Holladay and Bowen<sup>37</sup> accounted for the nonlinear effects due to large amplitude pressure waves and severe compression of the lung volume. Further refinement of the model probably lies in the continuum notion that there exists a wave transmission through the skin, the neuromusculature, the thoracic cage and the lung tissue while simultaneously the blast wave works its way down the bronchial tree. The possible interaction of these two waves of differing speeds might be reflected in the intrapulmonary pressure measurements.

# REFERENCES

- (1) Gell, C. F., "Table of equivalents for acceleration terminology recommended by the Committee on Acceleration of the AGARD Aerospace Medical Panel". Aerospace Med. 32:1109-1111, 1961.
- (2) Eiband, A. M., "Human tolerance to rapidly applied accelerations: a summary of literature". NASA Memo 5-19-59E. National Aeronautics and Space Administration, Washington, D. C., 1959.
- (3) von Gierke, H. E., "Biodynamic response of the human body", Applied Mechanics Reviews, 17, pp. 961-968, 1964.
- (4) Kornhauser, M., Structural Effects of Impact, Spartan Cleaver-Baltimore, 1962.
- (5) Payne, P. R., Personnel Restraint and Support System Dynamics, TR-65-12F, Aerospace Med. Research Labs., October, 1965.
- (6) Coermann, R. P., "Comparison of the dynamic characteristics of dummies, animals and man" Proc. National Academy of Sciences Symposium on Impact Acceleration Stress, Brooks AFB, San Antonio, Texas, November, 1961.
- (7) Liu, Y. King, "Distributed-parameter dynamic models of the spine". Proc. Workshop on Bioengineering Approaches to the Problems of the Spine, Bethesda, Maryland, September, 1970.
- (8) Hodgson, V. R., Gurdjian, E. S. and Thomas, L. M., "The determination of response characteristics of the head with emphasis on mechanical impedance techniques". 11th Stapp Car Crash Conference, 125-138, 1967.
- (9) Orne, D. and Liu, Y. King, "A mathematical model of spinal response to impact". J. Biomechanics, 4, No. 4, October, 1970. Also as A.S.M.E. preprint No. 70-BHF-1.
- (10) Moffatt, C. A., Private communication, 1970.
- (11) Liu, Y. King, Laborde, J. M. and Van Buskirk, W., "Inertial properties of a segmented cadaver trunk: their implications in acceleration injuries," submitted to Aerospace Medicine for publication.
- (12) Caveness, W. F. and Walker, A. E., eds., Proc. of Head Injury Conference, Lippincott, 1966, University of Chicago.
- (13) Goldsmith, W. "Biomechanics of Head Injury" Symp. on the Foundations and Objectives of Biomechanics, University of California-San Diego, July, 1970.
- (14) Hayashi, T., "Study of intracranial pressure caused by head impact," Jour. Facult. of Engr. Univ. of Tokyo, 30, 59. 1969.

- (15) Carslaw, H. S. and Jaeger, J. C., Operational Methods in Applied Mathematics, 2nd Ed. Oxford University Press, 1948. Also as Dover paperback, 1963.
- (16) Roberts, V., Hodgson, V., and Thomas, L. M. "Fluid pressure gradients caused by impact to the human skull, Biomechanics Monograph ASME: 223, 1967.
- (17) Carslaw, H. S., Theory of Fourier's Series and Integrals, Dover, paperback in 1963.
- (18) Courant, R. and Hilbert, D., Methods of Mathematical Physics, Vol. II: 486 Interscience-Wiley, 1962.
- (19) Anzelius, A., "The effect of an impact on a spherical liquid mass." Acta. Path. Microbiol. Scand. Supplement 48, 1943.
- (20) Güttinger, W. "Der Stosseffect auf eine Flüssigkeitskugel als Grundlage einer Physikalischen Theorie der Entstehung von Gehirnverletzungen," Zeit. f. Naturforschung. 5, 622, 1950.
- (21) Engin, A. E. and Liu, Y. King, "Axisymmetric response of a fluid-filled spherical shell in free vibrations" J. of Biomechanics, Vol. 3, No. 1, 11, January, 1970.
- (22) Engin, A. E., "Axisymmetric response of a fluid-filled spherical shell to a local radial impulse - a model for head injury", J. of Biomechanics, Vol. 2, No. 3, 325, July, 1969.
- (23) Liu, Y. King and Nelson III, J. A., "Intracranial pressure wave propagation in head impact," submitted to J. Neurosurg. for publication.
- (24) Barton, A. C., Physiology and Biophysics of Circulation. Year Book Medical Publishers, Chicago, 1965.
- (25) Lingren, S. O. "Experimental studies of mechanical effects in head injury" Acta Chirurgica Scandinavica, Supp. 360, 1966.
- (26) Unterharnscheidt, F. and Sellier, K. "The mechanics of the impact of violence on the skull" Proc. 3rd Int'l. Cong. of Neuro. Surg., Copenhagen, August, 1965.
- (27) Lee, Y. C. and Advani, S. H., "Forced axisymmetric response of a fluid-filled spherical shell", to appear in 5th Southeast Conf. on Theor. & Appl. Mech., 1970.
- (28) Chan, H. S., pending Ph.D. dissertation, Tulane University, 1970.
- (29) Holbourn, A. H. S., "Mechanics of head injury" Lancet, 11, p. 438, 1943.
- (30) Engin, A. E. and Wang, H. C., "A mathematical model to determine

- viscoelastic behavior of in vivo primate brain", J. of Biomechanics, 3, No. 3, 283, May, 1970.
- (31) Ommaya, A. K., Hirsh, A. E., & Martinez, J., "The role of whiplash in cerebral concussion", Proc. Tenth Stapp Car Crash Conference, New York: Soc. Automotive Engineering, p. 197-203, 1966.
  - (32) Unterharnscheidt, F. & Higgins, L. S., "Pathomorphology of experimental head injury due to rotational acceleration" Acta Neuropathologica, Vol. 12, p. 200-204, 1969.
  - (33) Martinez, J. L. and Garcia, D., "A model for whiplash" J. of Biomechanics, 1, 23-32, 1968.
  - (34) Roberts, S. B., Ward, C. C. and Nahum, A. M., "Head trauma - a parametric dynamic study" J. of Biomechanics, 2, 397-415., 1969.
  - (35) Hayashi, T., "Brain shear theory of head injury due to rotational impact" to appear Jour. of the Faculty of Engineering, Univ. of Tokyo, 31, No. 2, September, 1970.
  - (36) Lee, Y. C. and Advani, S. H., "Transient response of a sphere to torsional loading -- a head injury model" Math. Biosciences, 6, 473-486, 1970.
  - (37) Holladay, A. and Bowen, I. G., "A mathematical model of the lung for studies of mechanical stress" Proc. of the San Diego Symp. for Biomed. Engr., 39-50, 1963.

#### ACKNOWLEDGEMENTS

This paper was written while the author was partially supported by grants No. EC 00402-04 and EC-00087-03 from the National Institute of Environmental Health Service of the U. S. Public Health Service and Contract No. F 33615-70-C-1565 from the Aerospace Medical Research Lab., U. S. Air Force Systems Command.



## LIST OF FIGURES

- Figure 1. Possible injury tolerance curves for the  $G_x$ - $G_z$  plane.
- Figure 2. Typical tolerance graph based on equal tissue strain assumption.  $A_m$  and  $t_1$  are the peak acceleration and duration of the applied pulse respectively.  $t_c$  is the critical pulse duration.
- Figure 3. Mass distribution of the human cadaver trunk. Dotted line is data assumed in Ref. 9.
- Figure 4. Mass eccentricity distribution of the human cadaver trunk. Dotted line is data assumed in Ref. 9.
- Figure 5. Mass moments of inertia distribution of the human cadaver trunk. Dotted line is data assumed in Ref. 9.
- Figure 6. Moment distribution along the spine due to a 10g caudocephalad ( $+G_z$ ) acceleration pulse at 60 and 90 milliseconds. Dotted lines denote result using the data assumed in Ref. 9.
- Figure 7. Axial force distribution along the spine due to a 10g caudocephalad ( $+G_z$ ) acceleration pulse for different times. Dotted lines denote result using data assumed in Ref. 9.
- Figure 8. Shear force distribution along the spine due to a 10g caudocephalad ( $+G_z$ ) acceleration pulse for different times. Dotted lines denote result using data assumed in Ref. 9.
- Figure 9. Time-history of configuration changes of the spine.
- Figure 10. One-dimensional continuum model of head injury by Hayashi<sup>14</sup>.
- Figure 11. Comparisons of the container acceleration for the exact wave propagation solution and the Hayashi<sup>14</sup> approximation.
- Figure 12. Pressure-time variation at contrecoup ( $x=0$ ). Coup ( $x=1$ ) pressure is identical except for sign. The results are not valid for  $-P(0,\tau) = 0$ , the rebound condition.
- Figure 13. Spatial-pressure distribution at a given  $\tau$  for  $\lambda = 1$ .
- Figure 14. Spatial-pressure distribution for a given  $\tau$  for  $\lambda = 10$ .
- Figure 15. Pressure-time variation at a given location  $x$ , for  $\lambda = .1, 1, 10$ .
- Figure 16. Comparison of theory with experiment according to Hayashi<sup>14</sup>,  $P_A$  = pressure at coup;  $P_B$  = pressure at contrecoup.
- Figure 17. Axisymmetric pressure distribution at the time of approximate contrecoup. Note the relatively large diffuse area at grade 1.

Figure 18. Pressure distribution at the time of intermediate coup. Note the sharply-focused area at grades 5, 4, 3 and 2.

Figure 19. Cumulative Damage Criterion for a closed head injury. The damage mechanism is proportional to the averaged time spent at a given location beyond a critical negative pressure,  $p^*$ .

Figure 20. Locations of cumulative brain damage for a time-varying polar-cap load. The most likely location is grade 5, and the least is grade +. The rest of the grades are linearly scaled. Note the absence of contrecoup.

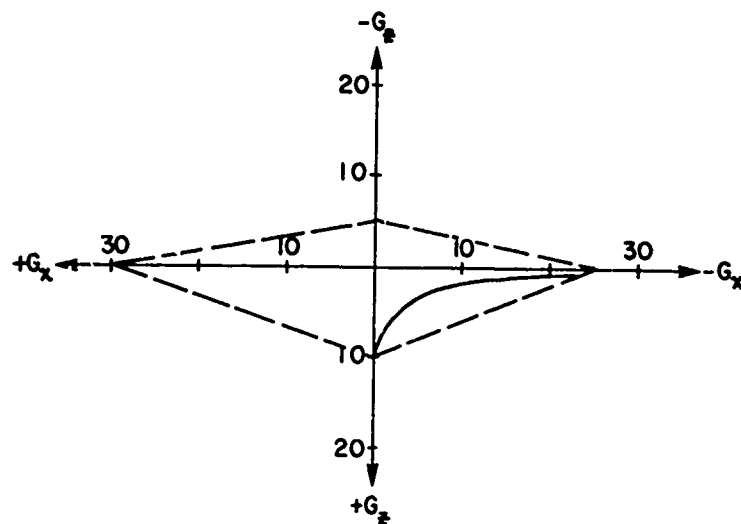


Figure 1. Possible injury tolerance curves for the  $G_x$ - $G_z$  plane.

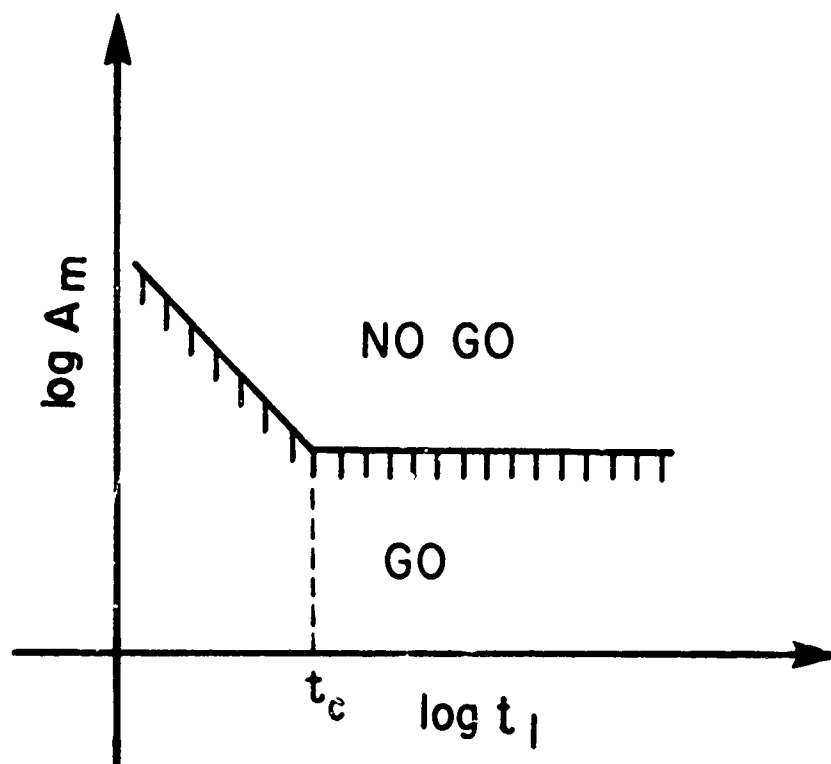


Figure 2. Typical tolerance graph based on equal tissue strain assumption.  $A_m$  and  $t_1$  are the peak acceleration and duration of the applied pulse respectively.  $t_c$  is the critical pulse duration.

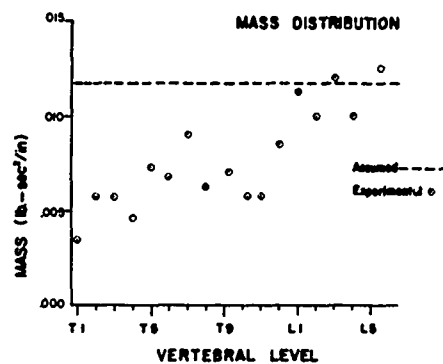


Figure 3. Mass distribution of the human cadaver trunk. Dotted line is data assumed in Ref. 9.

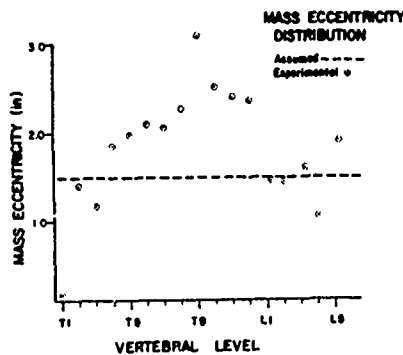


Figure 4. Mass eccentricity distribution of the human cadaver trunk. Dotted line is data assumed in Ref. 9.

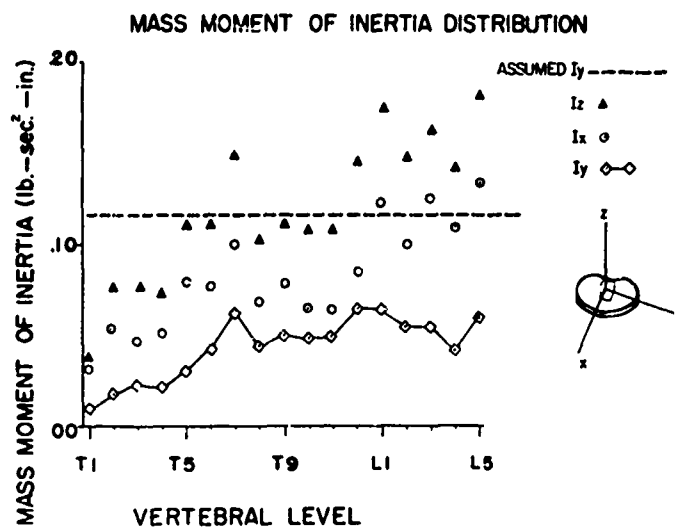


Figure 5. Mass moments of inertia distribution of the human cadaver trunk. Dotted line is data assumed in Ref. 9.

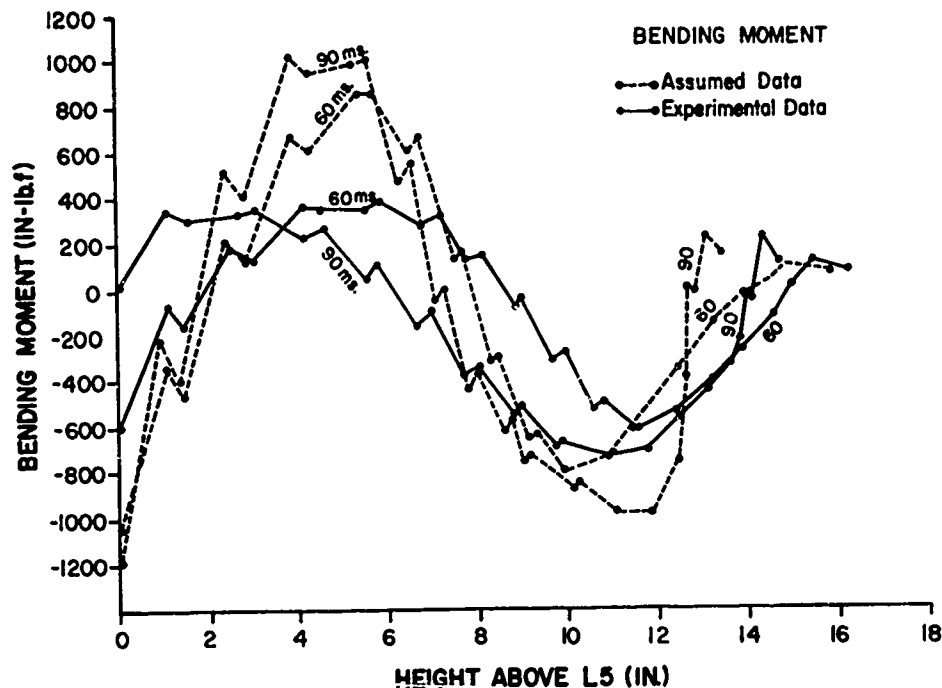


Figure 6. Moment distribution along the spine due to a 10g caudocephalad (+G<sub>z</sub>) acceleration pulse at 60 and 90 milliseconds. Dotted lines denote result using the data assumed in Ref. 9.

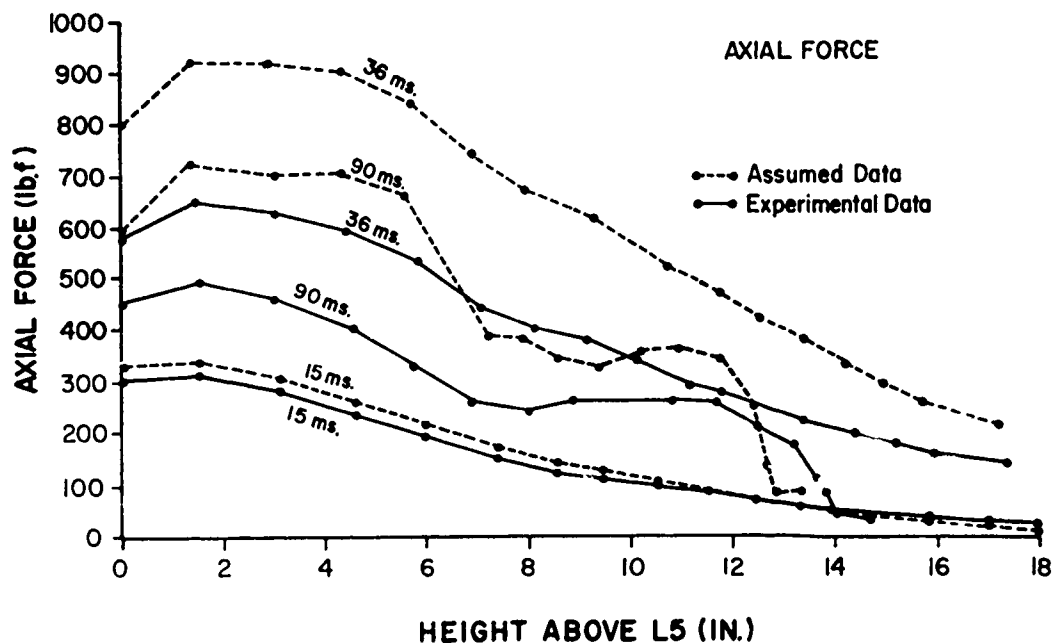


Figure 7. Axial force distribution along the spine due to a 10g caudocephalad (+G<sub>z</sub>) acceleration pulse for different times. Dotted lines denote result using data assumed in Ref. 9.

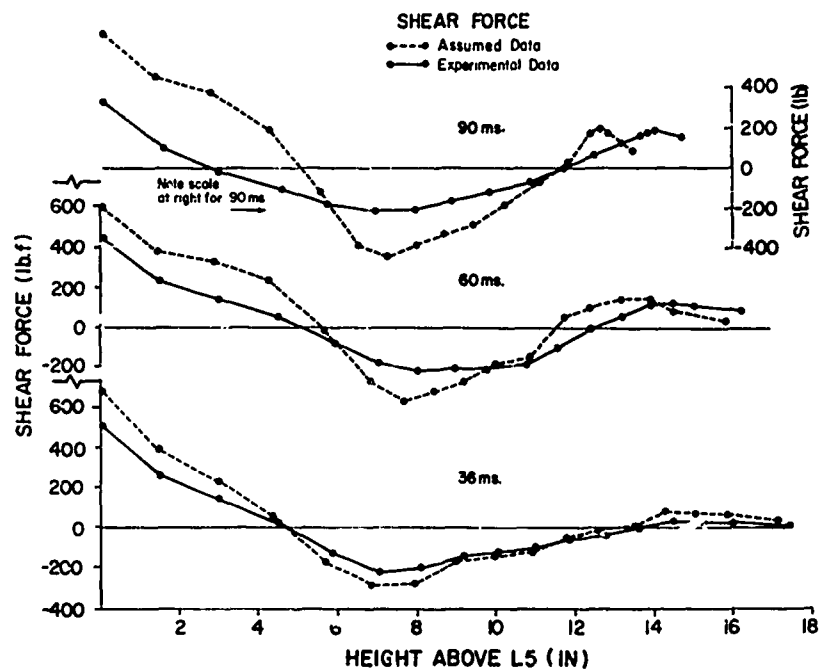


Figure 8. Shear force distribution along the spine due to a 10g caudocephalad ( $+G_z$ ) acceleration pulse for different times. Dotted lines denote result using data assumed in Ref. 9.

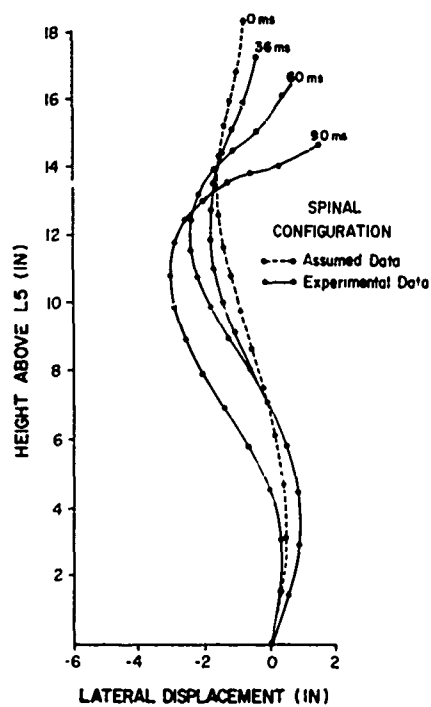
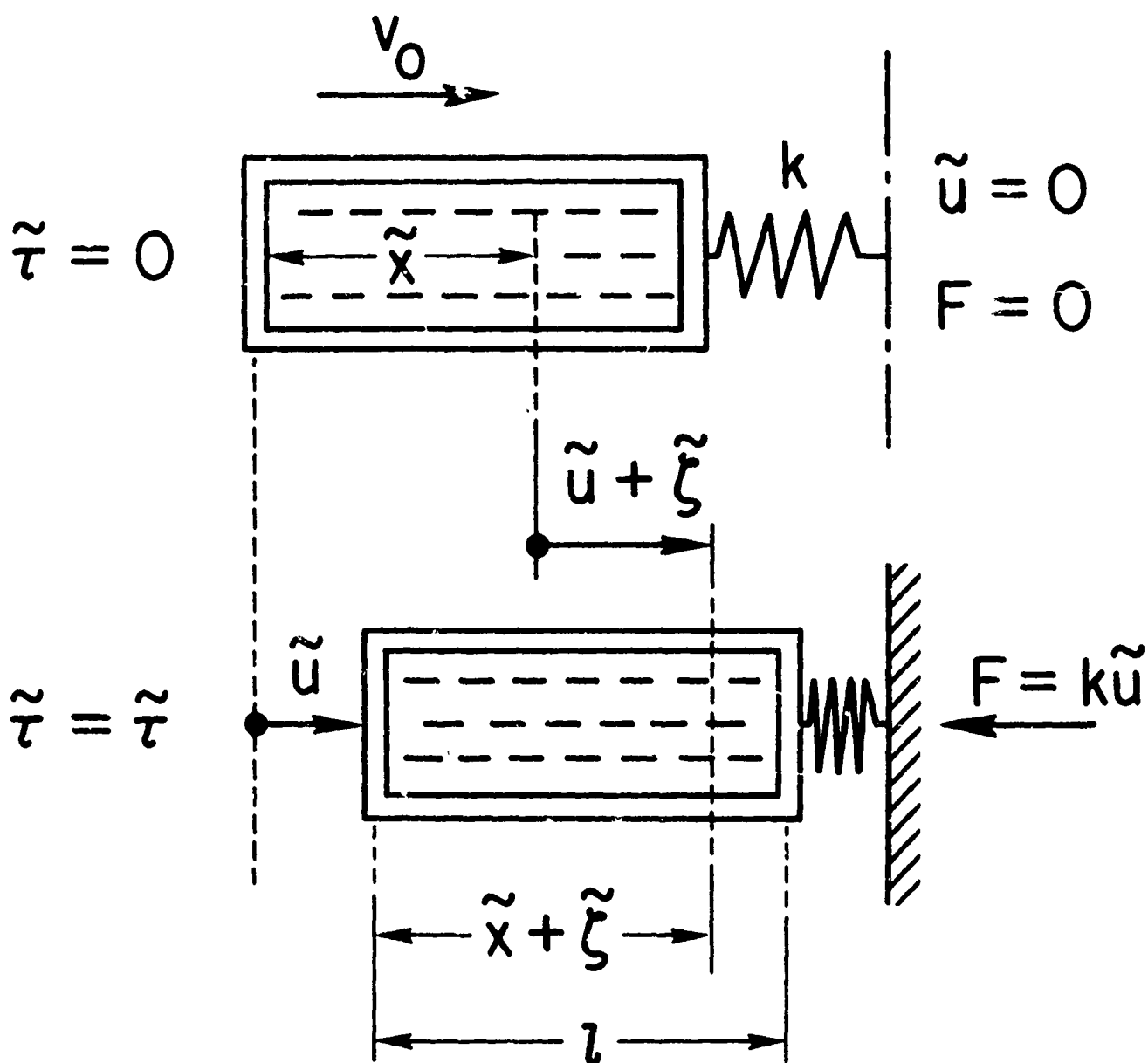


Figure 9. Time-history of configuration changes of the spine.



## HAYASHI MODEL

Figure 10. One-dimensional continuum model of head injury by Hayashi<sup>14</sup>.

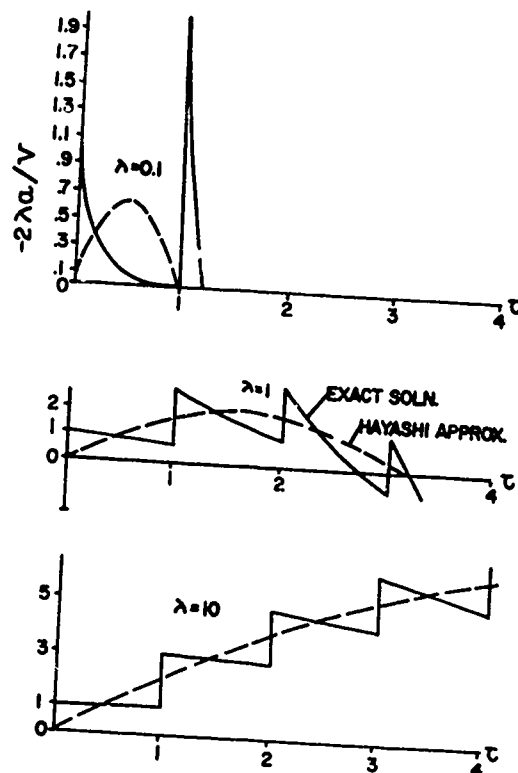


Figure 11

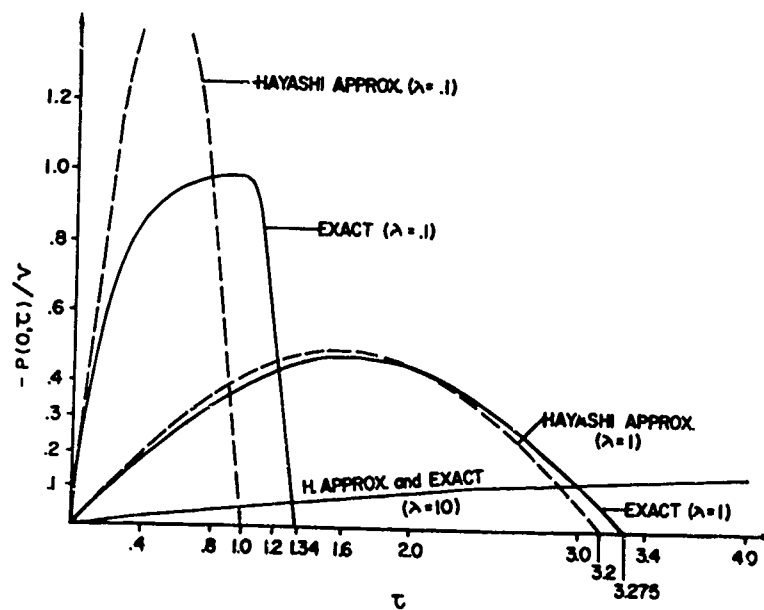


Figure 12



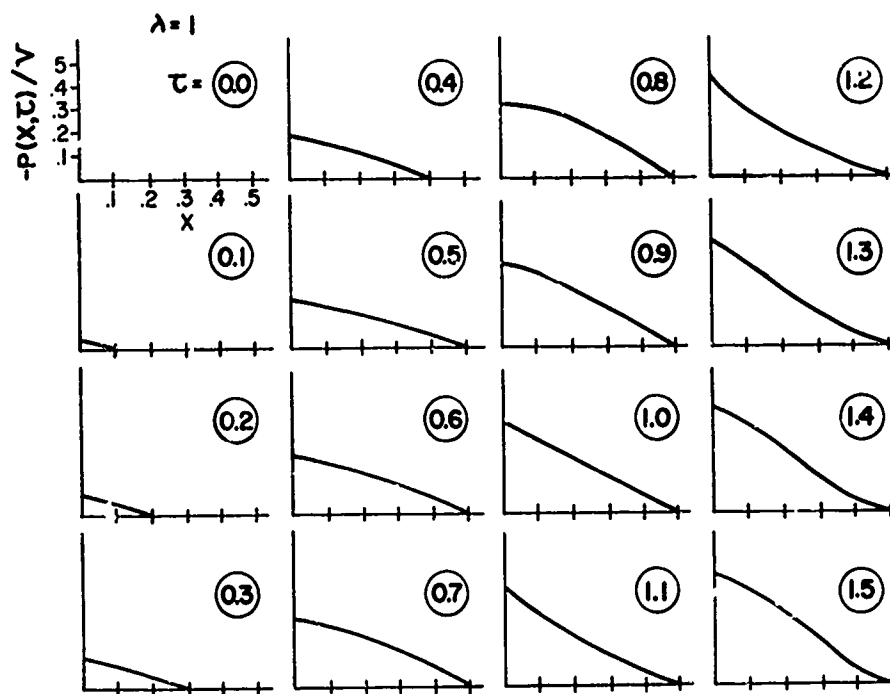


Figure 13

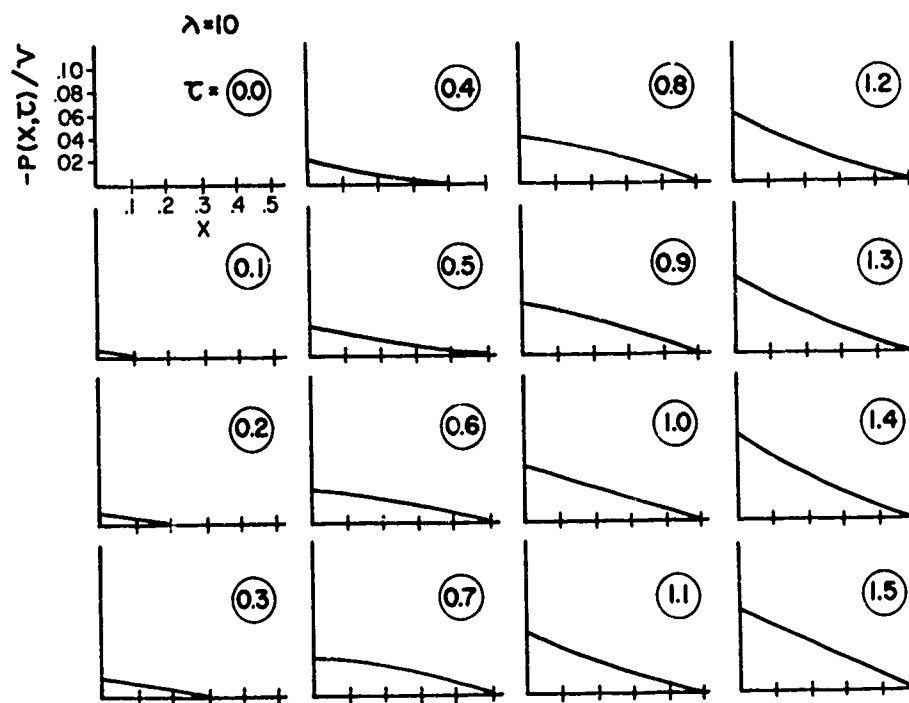


Figure 14

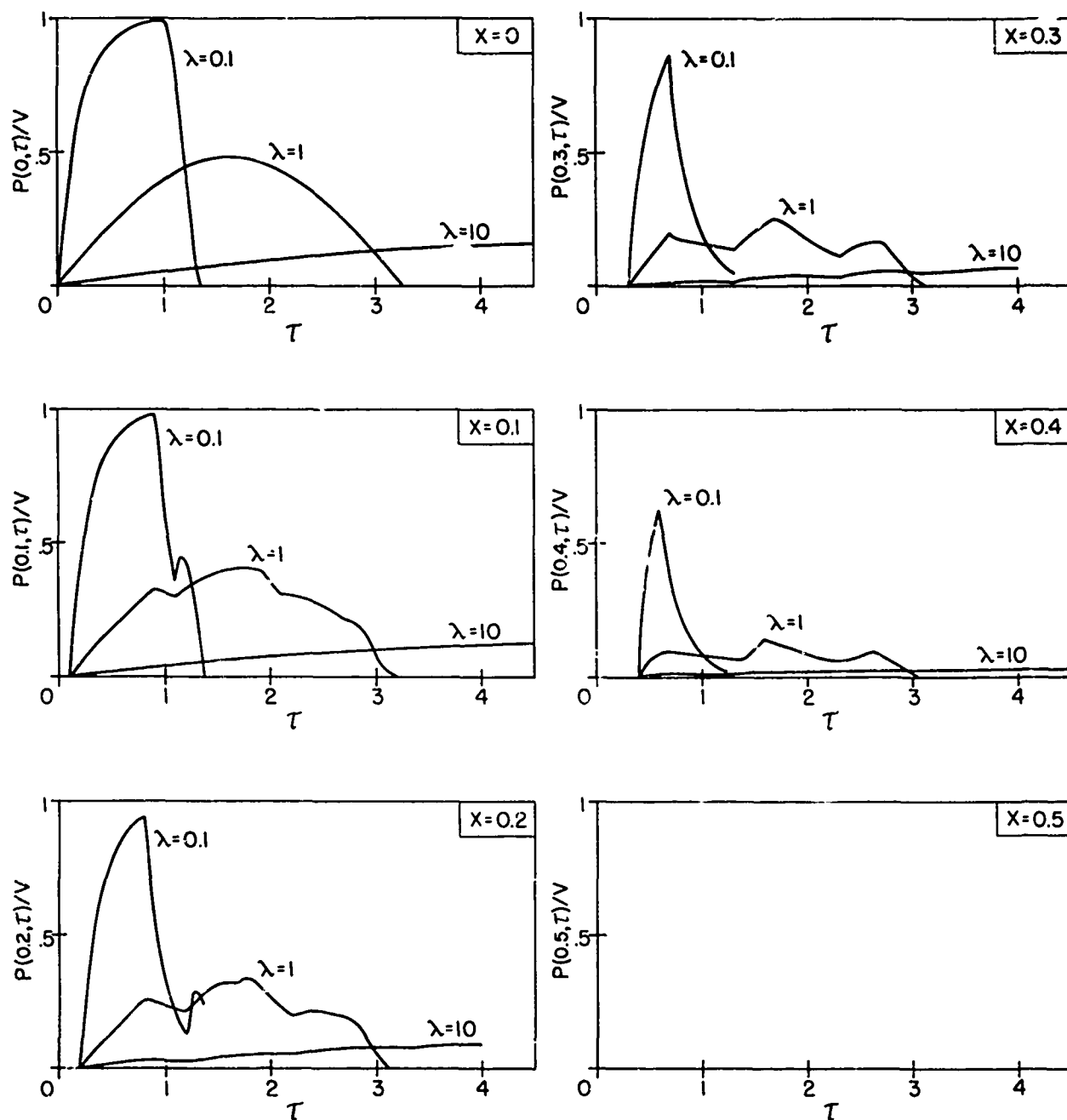


Figure 15

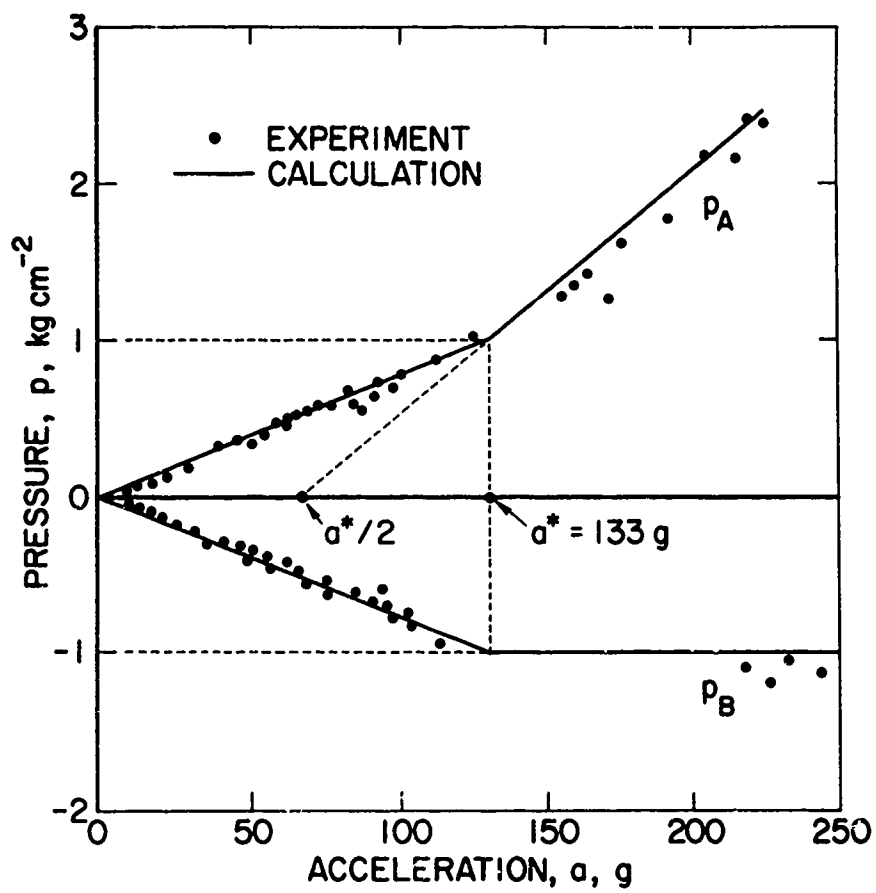


Figure 16. Comparison of theory with experiment according to Hayashi.  
 $P_A$ =pressure at coup;  $P_B$ =pressure at contrecoup.

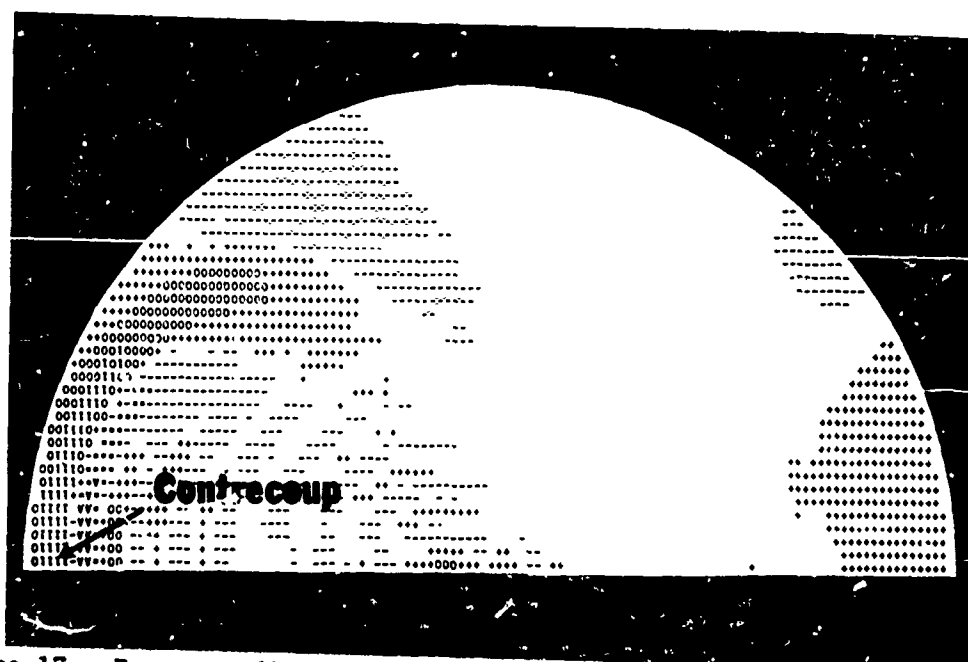


Figure 17. Pressure distribution at the time of approximate contre-coup. Note the relatively large diffuse area at grade 1.

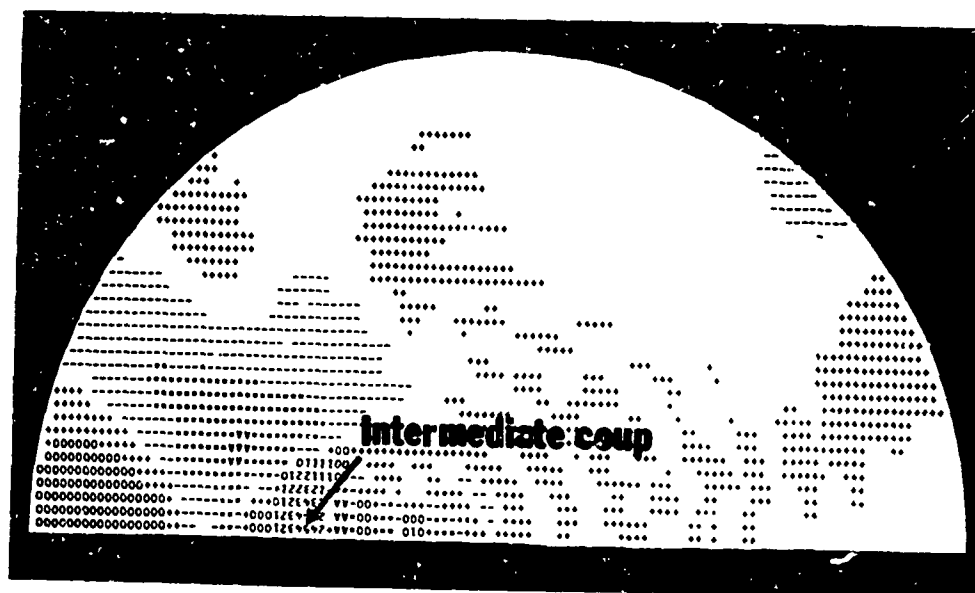


Figure 18. Pressure distribution at the time of intermediate coup. Note the sharply-focused area at grades 5, 4, 3 and 2.

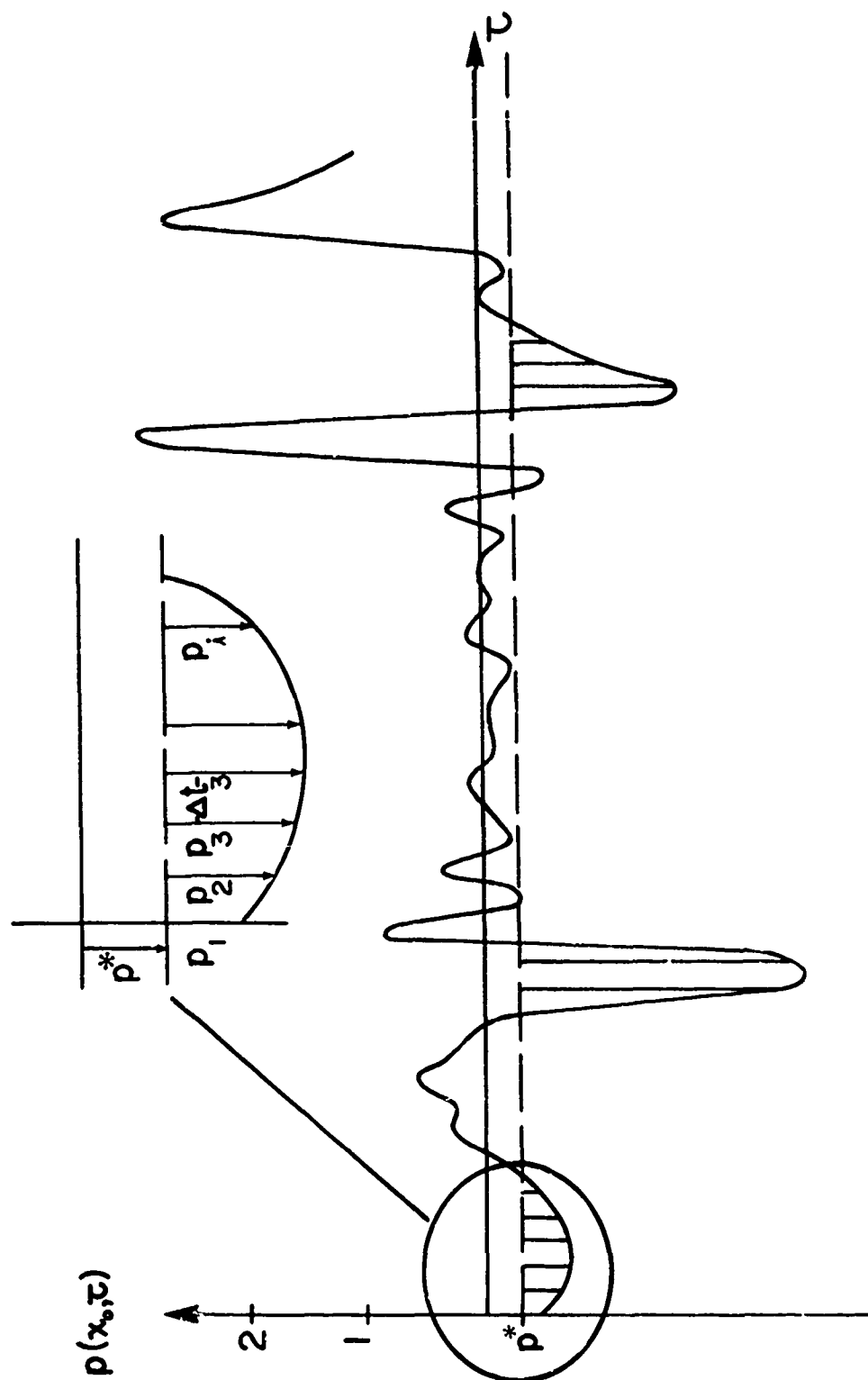


Figure 19. Cumulative Damage Criterion for a closed head injury. The damage mechanism is proportional to the averaged time spent at a given location beyond a critical negative pressure,  $p^*$ .

THE EFFECT OF VIBRATION ON BLOOD FLOW AND PRESSURE IN THE  
MAJOR ARTERIES OF DOGS

by Richard G. Edwards<sup>1</sup>, Charles F. Knapp<sup>1</sup>, Ernest P. McCutcheon<sup>2</sup>,  
Karl O. Lange<sup>1</sup>, and Ward O. Griffen<sup>2</sup>

University of Kentucky, Lexington, 40506

(1) Wenner-Gren Research Laboratory, University of Kentucky

(2) University of Kentucky Medical Center

ABSTRACT

The response of various systems in the human body to forces transmitted from vehicles and machinery has been the object of much research in recent years, but there have been few direct experimental measurements of cardiovascular function in a dynamic environment.

This report describes both in vitro and in vivo approaches to analyzing the cardiovascular effects of vibration. First, a simplified "mechanical" model of the circulatory system was constructed and exposed to sinusoidal vibration. It's purpose was to evaluate the instrumentation required to monitor blood flow rate and pressure during vibration, and to obtain an indication of the magnitudes and mechanisms by which vibration affects these quantities. The results from the mechanical model were compared to those predicted from an existing mathematical model. Next, electromagnetic flow transducers were chronically implanted around the aorta and the pulmonary and carotid arteries of a dog. After recovery the animal was anesthetized, placed in an upright position (spine vertical), and vibra-

ed at 2 to 12 Hz and at 1 to 3G acceleration amplitude in the direction of the gravity vector. Variables measured were blood flow rate, arterial pressure (via acutely positioned catheter-tip or special catheter-manometer pressure transducers), and force transmitted between animal and vibration exciter. The purpose was to determine the maximum and minimum peak flow rates, pressures, and transmitted force during vibration compared to normal levels.

Measurements from the mechanical model were in general agreement with the mathematical model prediction. For any one vibration acceleration amplitude, the largest extremes in peak flow rate occurred at the lowest frequency tested, i.e. at 3 Hz, and decreased to approach the peak flow rate from the non-vibrating model as vibration frequency increased. Data from the model illustrated the importance of the phase relationship between the vibration and cardiac cycles. For example, vibrating the model at 3 Hz with a peak acceleration of 2.5G resulted in a 30% increase in the peak flow rate if "systole" began when the vibration exciter was on it's upward stroke at approximately it's null position. The same vibration reduced the peak flow rate by 75% on a flow cycle initiated at a time when the vibration exciter was on it's downward stroke at approximately the null position.

The animal tests showed that the largest maximum and smallest minimum peak flow rates occurred in the 3 to 9 Hz frequency range for any one acceleration amplitude. The simultaneously measured force transmission data confirmed this range to contain the resonant frequencies of two organ systems, and correlation with aortic pressure confirmed that the motion of internal masses was also reflected in the cardiovascular data. 3G vibration at 4 Hz produced (1) a maximum aortic peak flow rate of more than twice the maximum recorded from the resting animal, and (2) a minimum aortic peak flow rate 90% less than the minimum observed in the resting animal. Such maximum peak flow rates could result in shearing stresses at the vessel wall sufficient to cause damage to the endothelial lining of the vessel if

incurred over long periods of time. Likewise, such minimum peak flow rates, if incurred on successive heart cycles for a period of 10-15 seconds, could reduce sufficiently the blood flow to the head to cause "blackout". (This research was supported in part by Air Force Office of Scientific Research Contract F44620-69-C-0127).

#### SCOPE OF INVESTIGATION

Much research has been directed toward understanding how the various systems in the human body respond to acceleration transmitted from vehicles and machinery. These devices can develop forces which must be isolated or attenuated at their interface with man if his performance or comfort are to be maintained. The problem is to recognize which forces are detrimental, and to which body systems. The magnitude of the problem becomes apparent when one realizes that the human body represents a most intricate composite of mechanical, fluid, electrical, and chemical systems interlaced with multitudes of feedback regulatory mechanisms. In addition, the subjective psychological response as related to real or imagined stress should be included.

It is particularly important to understand any alteration in the "pump and delivery" task of the cardiovascular system caused by vibration, since a loss in this functioning even for a few seconds could result in severe bodily harm to the operator. Few data exist from direct measurements of pertinent parameters associated with cardiovascular function during whole body vibration. The purpose of the present investigation was to gain an understanding of the magnitudes of effects and of the mechanisms by which blood flow rate and pressure in the major arteries of dogs are altered by the application of sinusoidal mechanical vibration. Since it was desired to subject an animal to 31 vibration tests, i.e. 2-12 Hz at 1G and 3-12 Hz at 2 and 3G acceler-



tion amplitude, the duration of each vibration point was limited to 20-30 seconds. For this reason, changes in blood flow rate and pressure in these tests are attributed primarily to "mechanical" mechanisms, i.e. from the direct fluid mechanical effect of vibrating the vascular network, and from effects caused by surrounding resonating organs.

The investigation proceeded in three phases, namely: (1) a theoretical prediction of the effect on blood flow rate of vibration of the vessel wall, (2) subjecting a "mechanical" model to laboratory vibration for the purpose of setting up flow and pressure instrumentation and to give an indication, as did (1) above, of the "fluid mechanical" effects of vibration on flow rate, and (3) to subject to vibration an anesthetized dog with chronically implanted electromagnetic flow transducers and acutely positioned pressure transducers to monitor the resulting arterial flow rates and pressures as a function of the vibration parameters.

#### METHODS & RESULTS

A search of the literature revealed one theoretical investigation concerned with the effect of vibration on the pulsatile flow of an incompressible fluid in a rigid tube. Hooks, Nerem, and Benson (Ref. 1) developed a solution for the resulting flow rate as a function of vibration parameters. Their method assumed a velocity profile adequately defined at any given time by a fourth order polynomial in vessel radius. This equation was combined with the reduced Navier-Stokes equation for axial flow of an incompressible fluid in a "long" rigid cylindrical tube. The coefficients of the series solution were found from appropriate boundary conditions (vibration was introduced by assuming the fluid velocity at the vessel wall to equal the vibration velocity). These investigators presented their results in graphical form as the maximum flow rate occurring on any flow cycle versus vibration frequency equal to the heart frequency. Vibration velocity amplitude and phase angle between heart and vibration frequency were

parameters.

Edwards (Ref. 2) extended the results of Hooks et al (Ref. 1) to present maximum and minimum peak flow rates versus vibration frequency with vibration acceleration amplitude, heart rate, and vessel size as parameters. Figure 1 contains a family of such curves. Notice in this figure that the maximum and minimum peak flow rates occurring on any flow cycle for a given vessel vibration level are normalized by the maximum peak flow rate that occurs without any applied external vibration. These curves are based upon geometrical parameters for a typical large artery of a dog (radius  $R = 1.5$  mm),  $\alpha \equiv C\sqrt{f_h} = 4.2$  ( $C$  is a constant for a given vessel size and fluid properties,  $f_h$  = heart frequency = 2.4 Hz), and a steady state (without vibration) centerline velocity  $U_{10} = 100$  cm/sec. Negative values in this graph correspond to resultant peak flow rates in the direction opposite that in which the pressure gradient propagates. It is important to observe from this figure that, for a given vibration acceleration amplitude, the lowest vibration frequencies produce the greatest change from the control, and as vibration frequency increases the magnitudes of the maximum and minimum peak flow rates decrease to approach the control value at the higher frequencies. In terms of magnitude, it is apparent that this simplified, theoretical model predicts quite large changes in peak flow rate when low frequency vibration is applied, e.g. the model predicts that 3G vibration at 3 Hz will change the "control" peak flow rate by a factor of approximately 15, but the same acceleration amplitude at 12 Hz changes the "control" peak flow rate by a factor of less than 3. The pertinent information gained from this theoretical model may be summarized by stating that for a given vessel size and heart frequency, low vibration frequencies present the greatest potential for amplifying or attenuating the no-vibration flow. As the vibration frequency is increased at a constant acceleration amplitude, this potential decreases and approaches the control value. A theoretical prediction has thus been shown of

# THEORETICAL FLOW CURVES

DOG LARGE ARTERY

$R = 1.5 \text{ mm}$

$\alpha = 4.2$

$U_{10} = 25 \text{ cm/sec}$

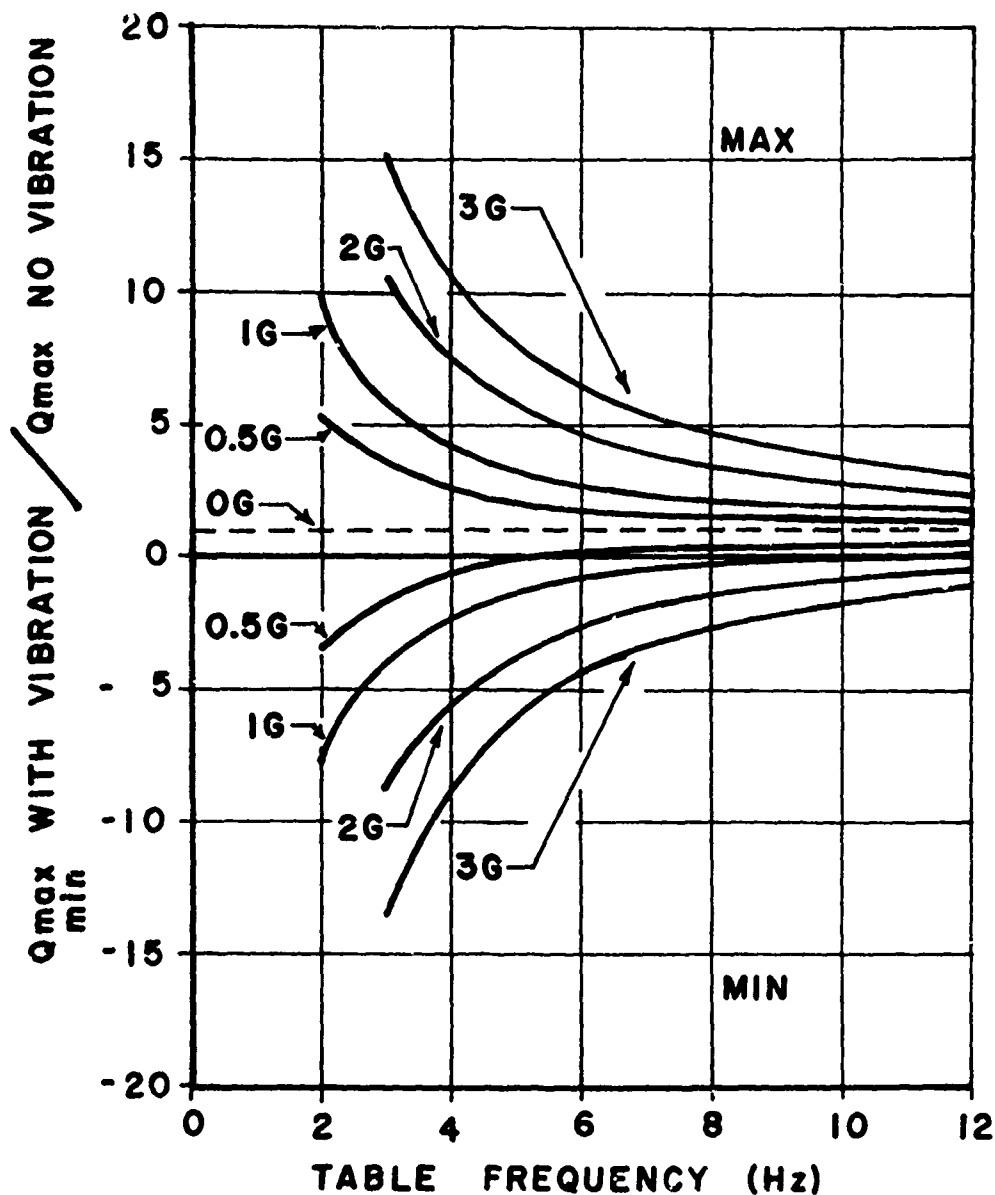


Figure 1. Maximum & Minimum Peak Flow Rate with Vibration, Normalized by the Maximum Peak Flow Rate Without Vibration, Versus Shake Table Frequency with Acceleration Amplitude as a Parameter. Based Upon Theoretical System of Hooks et al (ref. 1) for Flow in a Dog's Large Artery.

how peak flow rate during vibration depends upon the vibration parameters of frequency and acceleration amplitude.

The second phase of this investigation involved the construction of a "mechanical model" incorporating a pressure-diaphragm type pump, unidirectional valves, a two branch circulatory system, and variable "systemic" resistance. Electromagnetic flow transducers were incorporated to record flow rate, and pressure taps were located for monitoring pressures. Figure 2 schematically illustrates the important features of this model. Operation of the pump was as follows (see figure 2). The switching circuit located just beyond the supply air compressor controlled an air pressure of adjustable magnitude to the back side of the pump diaphragm in a 20% "on" - 80% "off" fashion with respect to time, i.e. a preset pressure was applied in step fashion to the diaphragm for 20% of the total pump cycle time and then exhausted to the atmosphere during the remaining 80% of the cycle. These percentages are analogous to the systolic-diastolic time ratio. The "systemic resistance" was adjusted via the metering valves to result in a stroke volume of from 15 to 20 cc, values typically recorded in a resting dog. When pressure was applied during the 20% "on" part of the pump cycle, the upper check valve opened, the lower closed, and a stroke volume of fluid equal to the volume displaced by the diaphragm flowed to the accumulator. The accumulator contained a diaphragm identical to that of the pump to furnish a majority of the required compliance in the circulatory system for accepting the stroke volume (additional "Parallel" compliance was added at the top of the "superior" loop of the circulatory system). When the pump pressure was exhausted during the 80% "off" part of the pump cycle, the pump and accumulator diaphragms returned to their null position, thereby closing the upper unidirectional valve, opening the lower valve, and repriming the pump. The pump frequency for all mechanical model tests was 1 Hz. Figure 3 is a photograph of the model mounted atop the Wenner-Gren Research Laboratory's electrohydraulic vibration exciter.

# SCHEMATIC OF PHYSICAL MODEL ON SHAKETABLE

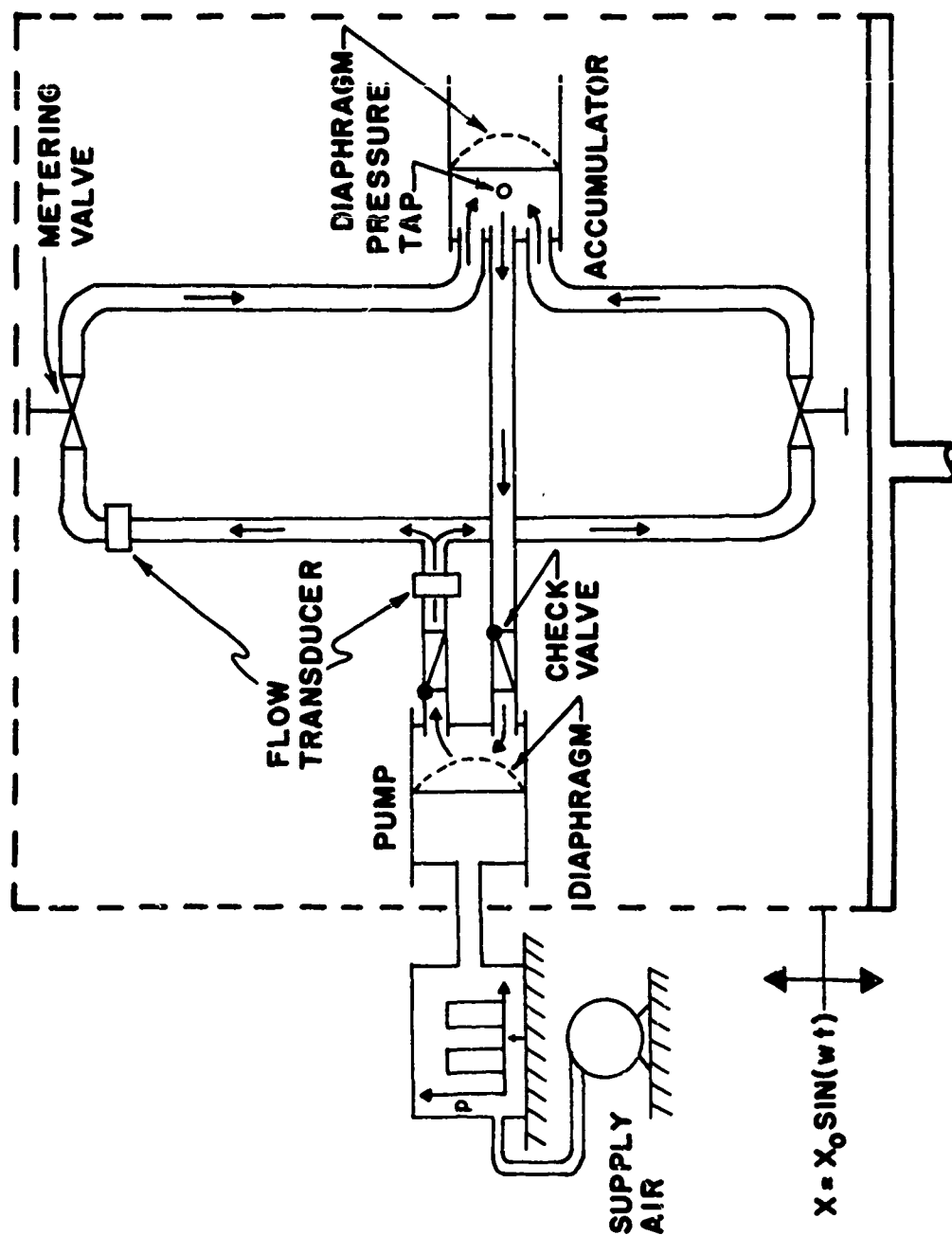


Figure 2. Schematic of Circulatory System Mechanical Model.

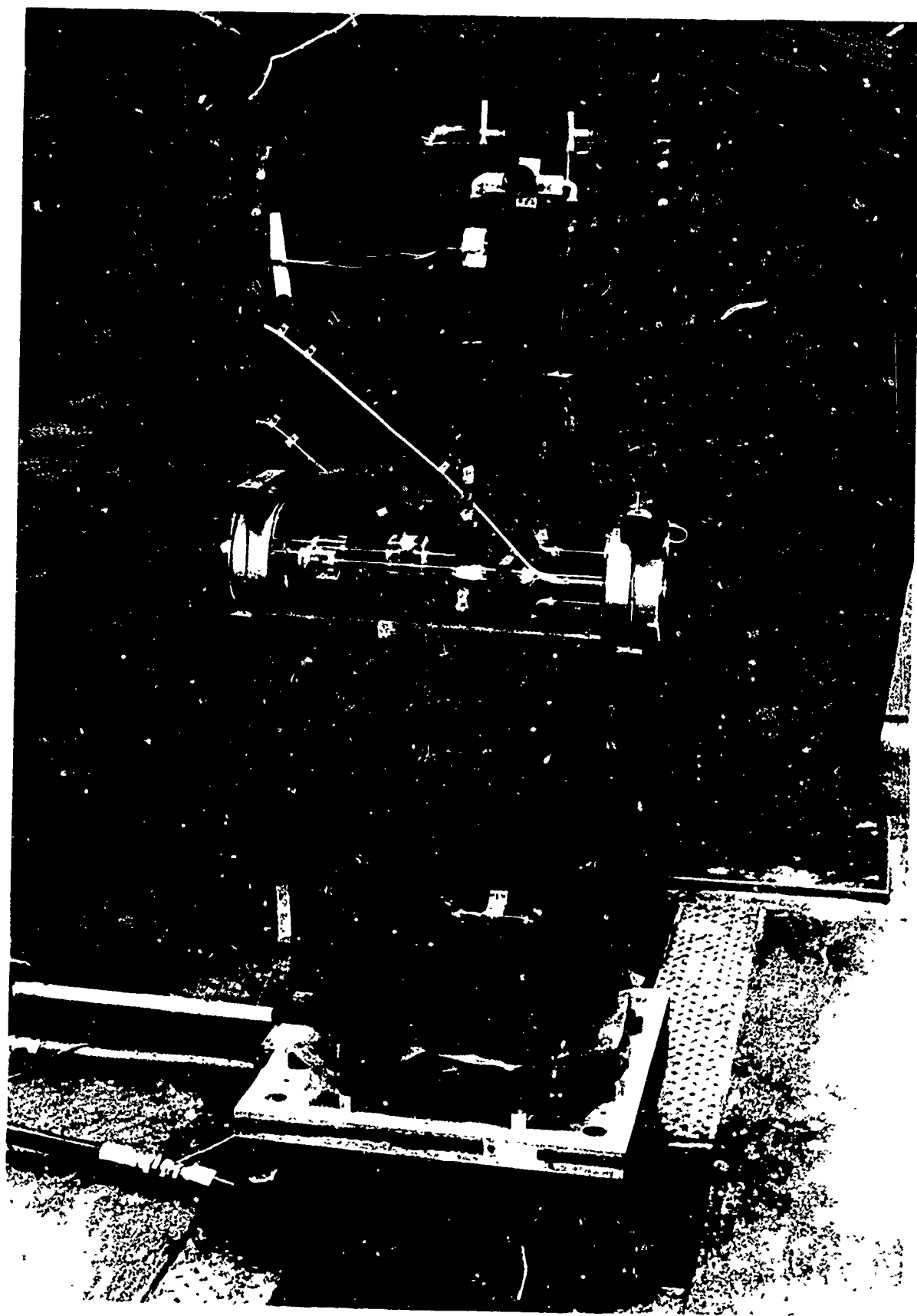


Figure 3. Mechanical Model Mounted Atop Shake Table.

Figure 4 contains tracings of typical recorded curves for the model's "aortic" flow rate and for vibration exciter (shake table) displacement. At the time indicated by the vertical line, pressure was applied to the pump diaphragm and the two curves formed by a dotted line represent flow rate versus time for this condition. The pump was then turned off and 2.5G acceleration amplitude at 3 Hz vibration applied, which induced a flow as represented by the more narrow of the solid lines. For each of these induced flow curves, the table displacement trace immediately below gives the phase relationship between the table motion and the induced flow. The heavy unbroken lines represent the flow when the pump was actuated and the model was simultaneously vibrated. Proper phase relationships between these curves, table displacement, and pump activation time were maintained in this figure. The upper of the heavy unbroken curves corresponds to the maximum flow recorded during the 2.5G-3Hz vibration and it was observed that this maximum peak flow rate occurred when the pump was activated during the upward movement of the table at approximately its null position. Note that the peak of this curve is approximately 30% greater than that from the pump alone. The lower of the heavy unbroken traces represents the minimum flow observed during the same vibration. For this condition the pump was activated when the table was on its downward stroke at approximately the null position, i.e. a difference of  $180^\circ$  in phase from the maximum flow case just considered. For this cycle a 75% reduction in the "no-vibration" peak flow rate occurred. It is thus apparent that a substantial alteration in no-vibration peak flow rate occurred dependent upon the phase between shake table and pump.

In figure 5 the maximum and minimum "aortic" peak flow rates recorded from the model during 2.5G acceleration amplitude vibration are plotted versus table frequency. Operating the model without vibration always produced a peak flow rate that fell within the cross-hatched area labeled "control limits". The graph illustrates that the great-

# EXAMPLES OF FLOWS FROM PHYSICAL MODEL

MAX. FLOW  
AT 2.5 G -  
3 Hz



TABLE DISPLACEMENT



FLOW FROM PUMP ONLY

-----

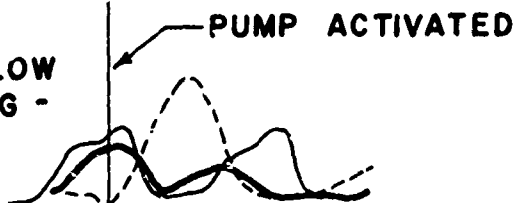
FLOW FROM VIBRATION ONLY

————

FLOW FROM PUMP + VIBRATION

————

MIN. FLOW  
AT 2.5 G -  
3 Hz



PUMP ACTIVATED

TABLE DISPLACEMENT



Figure 4. Example Recordings of Flow Rate From Mechanical Model & Shake Table Displacement Versus Time.



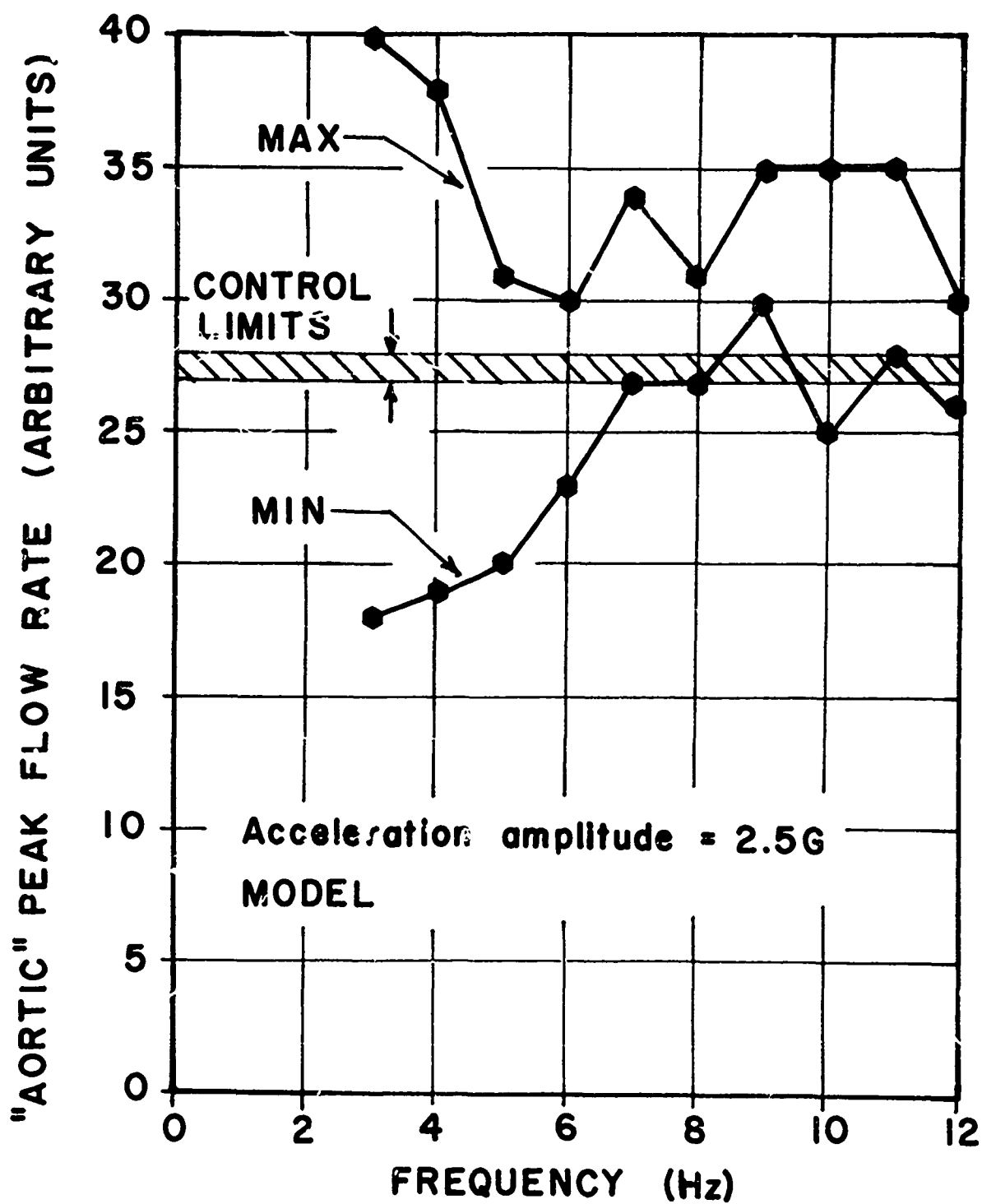


Figure 5. Maximum & Minimum "Aortic" Peak Flow Rate Versus Shake Table Frequency for 2.5G Acceleration Amplitude Vibration of Mechanical Model.

est change in peak flow rate occurred at the lowest frequency (a 45% increase and 35% decrease in peak control flow rate possible at 3 Hz) and decreased as frequency increased. At 12 Hz the control peak flow rate was observed to be changed less than 10% by the 2.5G, 12 Hz vibration. As a function of vibration frequency, these results compare favorably with the trend predicted by the theoretical results presented in figure 1; however, due to the simplifying assumptions required for a solution in the theoretical model, the magnitudes of the predicted curves are much greater than those experimentally recorded.

Completion of the two phases of this investigation just described accomplished two important objectives; namely, (1) to predict, for a given vibration acceleration amplitude, that the greatest change in peak flow rate occurs at the lowest frequency and decreases, approaching the control value, as vibration frequency is increased, and that such changes for a given vibration frequency are a function of the input acceleration intensity as well as the phase between the cardiac (pump) cycle and the vibration displacement cycle, and (2) to complete the instrumentation set-up for the required dynamic measurements to be made from a dog in the next phase of the investigation.

In the final part of this study experiments were designed to record blood flow and pressure in the dog's ascending aorta, common carotid, and pulmonary arteries during vibration. Blood flow rate was measured using a "cuff type" electromagnetic flow transducer (Biotronex Laboratory).

Arterial pressures were monitored using either catheters with the strain gauge mounted at the tip (Whittaker) or Luer-tip gauges connected to a short length of polyethylene tubing.

The flow transducers were surgically implanted around the aorta, carotid, and pulmonary arteries and the pressure transducers were placed at the time of the experiment after the induction of general anesthesia. The minimum recovery time from surgery until experimentation was two weeks.

It was desired to perform the tests with the dog in the upright position since this would result in the greatest changes in blood flow rate and pressure. A support structure to hold the animal in the upright attitude, (figure 6), was constructed with styrofoam sides and wooden top and bottom. Because the animals were vibrated at acceleration amplitudes of up to 3G it was also necessary to restrain them to prevent relative motion between animal and support. A procedure was developed by which the dog was placed in the support box and granular "filler" material poured to completely fill the box and hold the animal in place. Figure 6 is a view of the support structure, with dog inside, mounted atop the shake table and ready for vibration testing. The support structure, less animal, weighed 75 pounds.

Figure 7 is a photograph of the Wenner-Gren Research Laboratory's electrohydraulic shake table (Ref. 3). The double exposure illustrates the table's 10" maximum excursion. An instrumentation schematic for the shake table is given in figure 8. This instrumentation allows direct recording of the force transmitted between vibration exciter and subject (Ref. 4). This force is a measure of the integrated motion of all internal body organ systems. Monitoring this value during vibration located resonant frequencies of internal mass systems. It was anticipated, on the basis of similar previous measurements by Lange & Edwards (Ref. 5), that such relative internal motion might induce pressure and flow changes in the vascular system.

The traces in figure 9 are presented to illustrate the nomenclature. For a given vibration record, figure 9A shows that " $\Delta P_{\max}$ " is the maximum (peak to peak) pressure difference developed during any cycle. Under no-vibration or control conditions,  $\Delta P_{\max}$  is the pulse pressure. Control values were usually 30-40 mm Hg. Figure 9B portrays a flow rate versus time record typical of the aorta or pulmonary artery. Characteristic of this trace is its return to zero after each systole. The "maximum and minimum peak flow rates" that

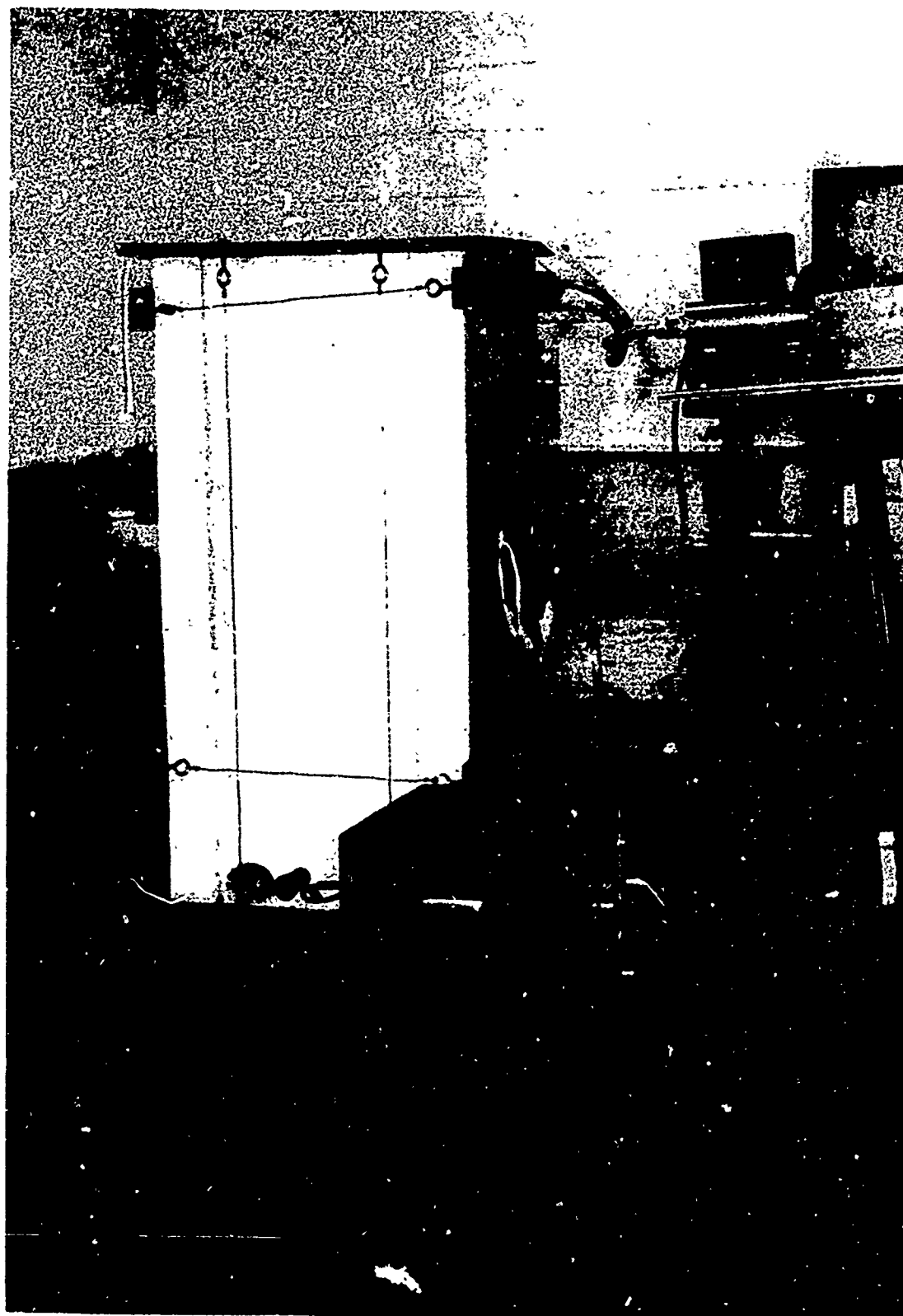


Figure 6. An Overall View of Experimental Set-up Showing Animal Support Structure Atop Shake Table.



Figure 7. Wenner-Gren Research Laboratory's Electrohydraulic Shake Table.

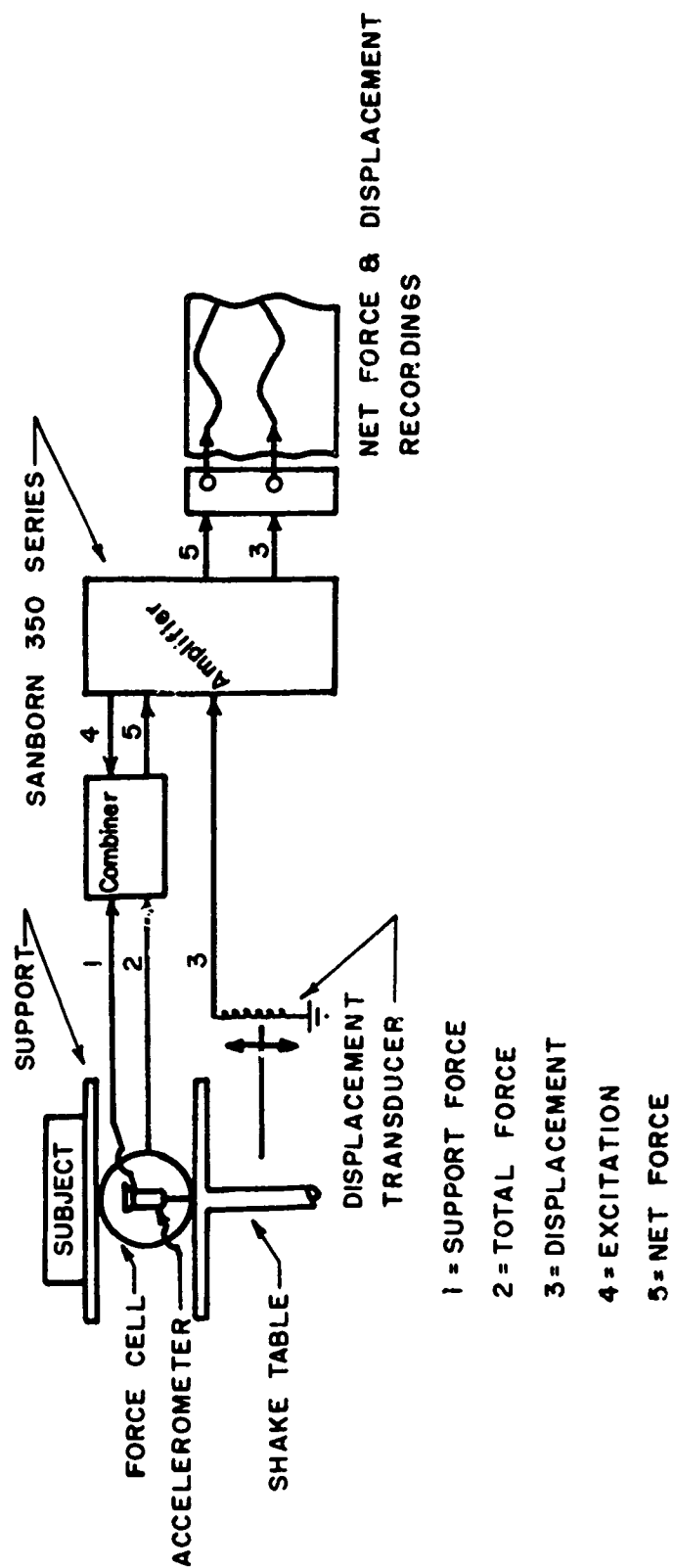


Figure 8. Schematic of Instrumentation for Recording Net Force Transmitted Between Animal and Shake Table.

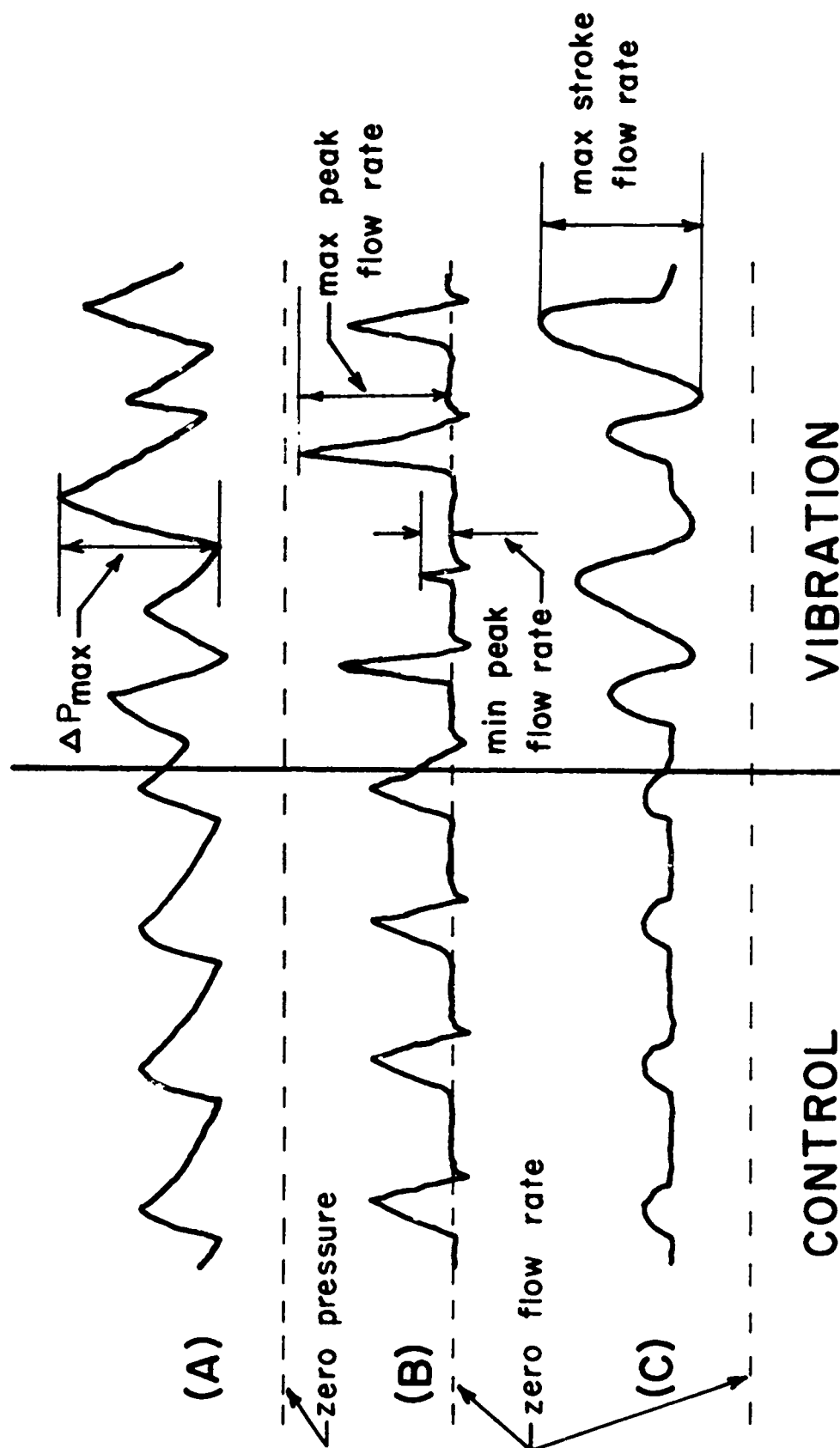


Figure 9. Sketches Illustrating the Nomenclature of this Investigation: (A) Arterial Blood Pressure Versus Time, (B) Aortic or Pulmonary Flow Rate Versus Time, (C) Carotid Flow Rate Versus Time.

occur for a particular measurement are as shown. The trace representing carotid arterial flow rate is shown in figure 9C. This trace differs from the previous one in that the curve does not return to zero after each systolic pulse, i.e. after each flow surge the flow rate assumes a nonzero "bias" value. The difference between this bias and the maximum flow rate observed on any one record is the "maximum stroke flow rate".

The curves in figure 10 were traced directly from strip charts recorded during one animal experiment. The vertical event lines permit observations of the phase relationship between the various recorded values. Two traces are shown for each of the recorded parameters except for shake table displacement. The lower of these two traces represents a no-vibration control recording, while the upper trace is the same measurement during 3G vibration at 3 Hz. Marked changes in peak flow rate and heart frequency are observed by comparing the two aortic flow rate traces. A very regular pattern of control pulmonary arterial flow rate was recorded, with substantial alterations produced by the vibration. The regular stroke flow rate normally recorded in the carotid artery was transformed into an apparent sloshing of the blood back and forth in that vessel when the animal was exposed to vibration. A catheter-tip pressure transducer threaded to a point in the lungs recorded the upper two traces in figure 10. During vibration a "beating" pattern was observed. Comparing the phase of the shake table to that of pulmonary flow rate and pressure, it was observed that when right heart systole (identified from the pulmonary flow rate trace) begins with the table in approximately its upward extreme a large  $\Delta P_{\max}$  was recorded; however, a smaller  $\Delta P_{\max}$  occurred when the table was in some other phase at the onset of right heart systole.

Measuring from flow traces such as those presented in figure 10, the maximum and minimum peak flow rates recorded at each frequency from 2 to 12 Hz at 1, 2, and 3G acceleration amplitude yielded a set



# **EXAMPLES OF DOG RECORDINGS CONTROL AND 3G-3Hz VIBRATION**

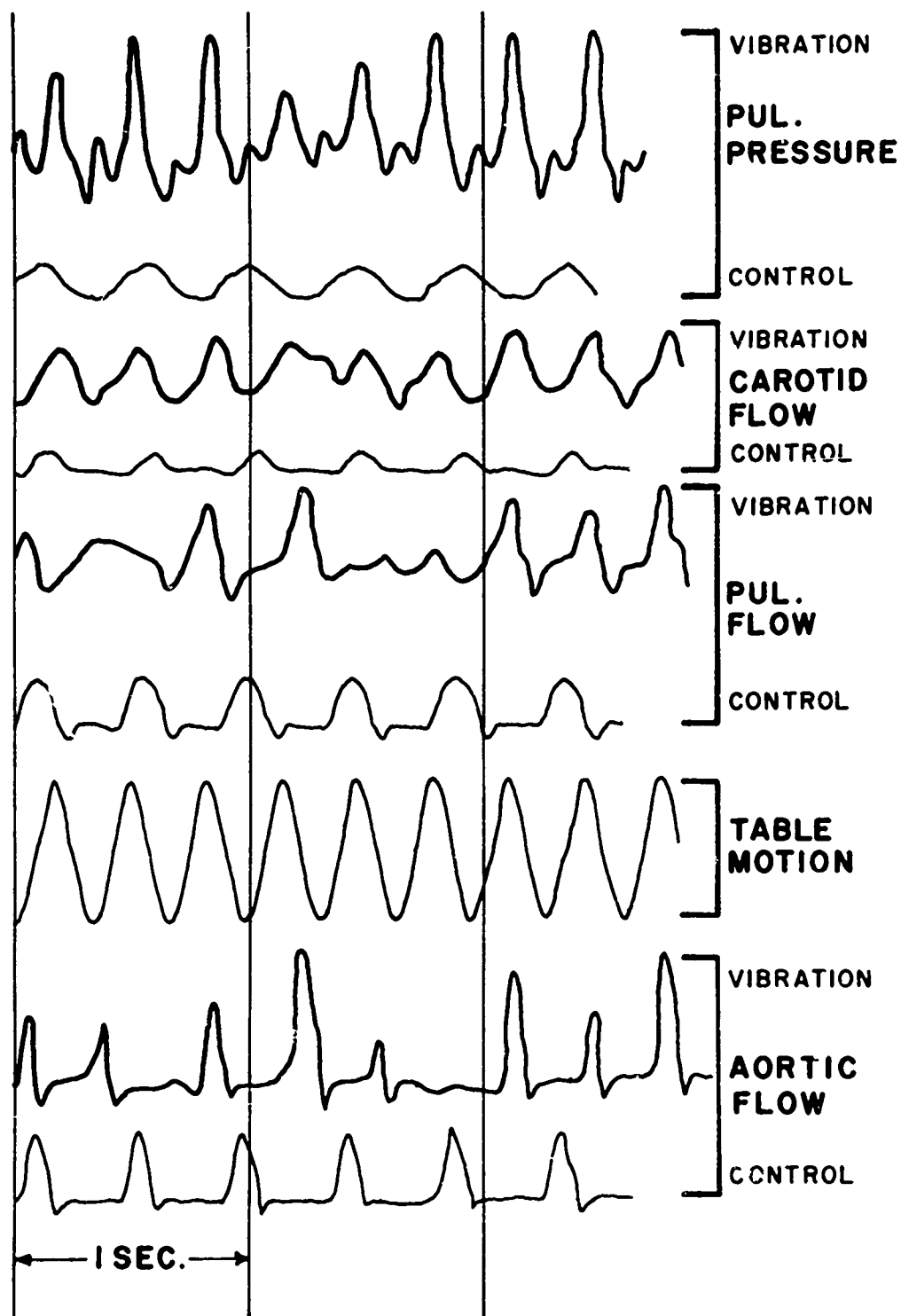


Figure 10. Example Dog Recordings of Flow Rate and Pressure Versus Time.

of curves such as those in the upper graph of figure 11. The points plotted in this graph correspond to recorded maximum and minimum peak flow rates in the dog's aorta, for each table setting. The control limits are shown in this graph as the upper and lower boundaries of the cross-hatched area. For this animal, designated Dog A, an ordered family of curves resulted as a function of the vibration acceleration amplitude. The trend of these curves is for the greatest change in flow rate to occur during the vibration at lower frequencies, and for the effect to decrease as frequency increases such that at 12 Hz the values recorded during vibration approach those occurring without vibration. The frequency where the greatest maximum peak flow rate magnitude occurred decreased with increasing acceleration amplitude, i.e. this frequency for 1G was 8 Hz, for 2G was 6 Hz, and for 3G was 4 Hz.

The maximum stroke flow rates recorded in Dog A's common carotid artery during control and vibration are plotted in the lower graph of figure 11. Again a distinct family of curves resulted demonstrating that the maximum stroke flow rate in the carotid artery increased with increasing table acceleration amplitude and was the greatest for all acceleration amplitudes in the 6 to 9 Hz range. It decreased toward the control value at high frequencies.

Figure 12 contains two additional graphs for the vibration test on Dog A. The lower of these graphs presents pulmonary arterial flow rate in a manner similar to that used in figure 11 for aortic flow. In this graph there is more variation in control peak flow rate than existed for the aortic flow. This is attributed primarily to the effects of respiration. Compared to the graphs of figure 11, vibration had less effect on flow rate in the pulmonary artery than in the aorta or carotid arteries. As was the case for aortic flow, at any vibration intensity the low frequencies produced the greatest effect on peak pulmonary flow rate, and as frequency increased these peak

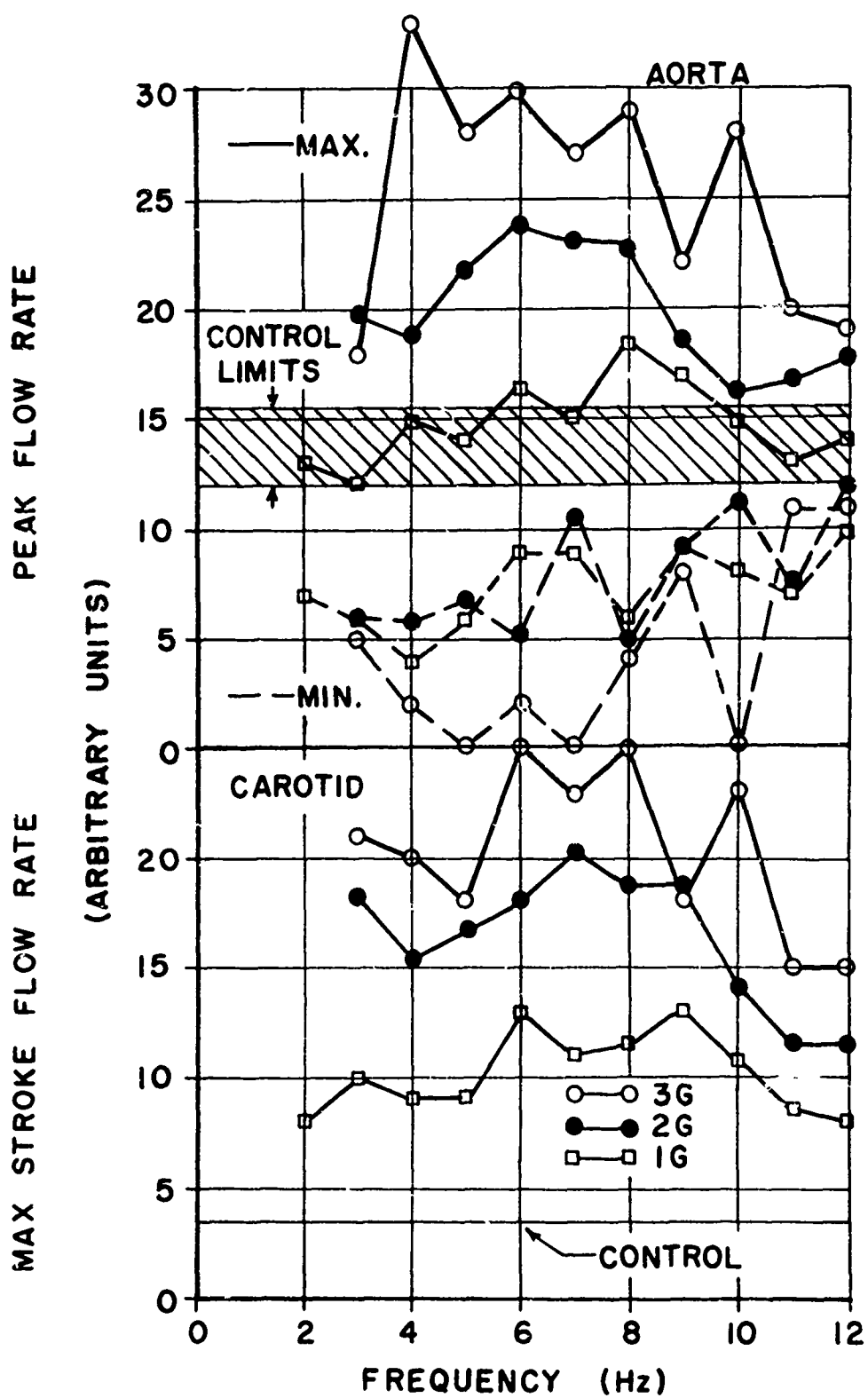


Figure 11. Peak Aortic Flow Rate & Maximum Carotid Stroke Flow Rate Versus Shake Table Frequency with Vibration Acceleration Amplitude as a Parameter, Dog A.

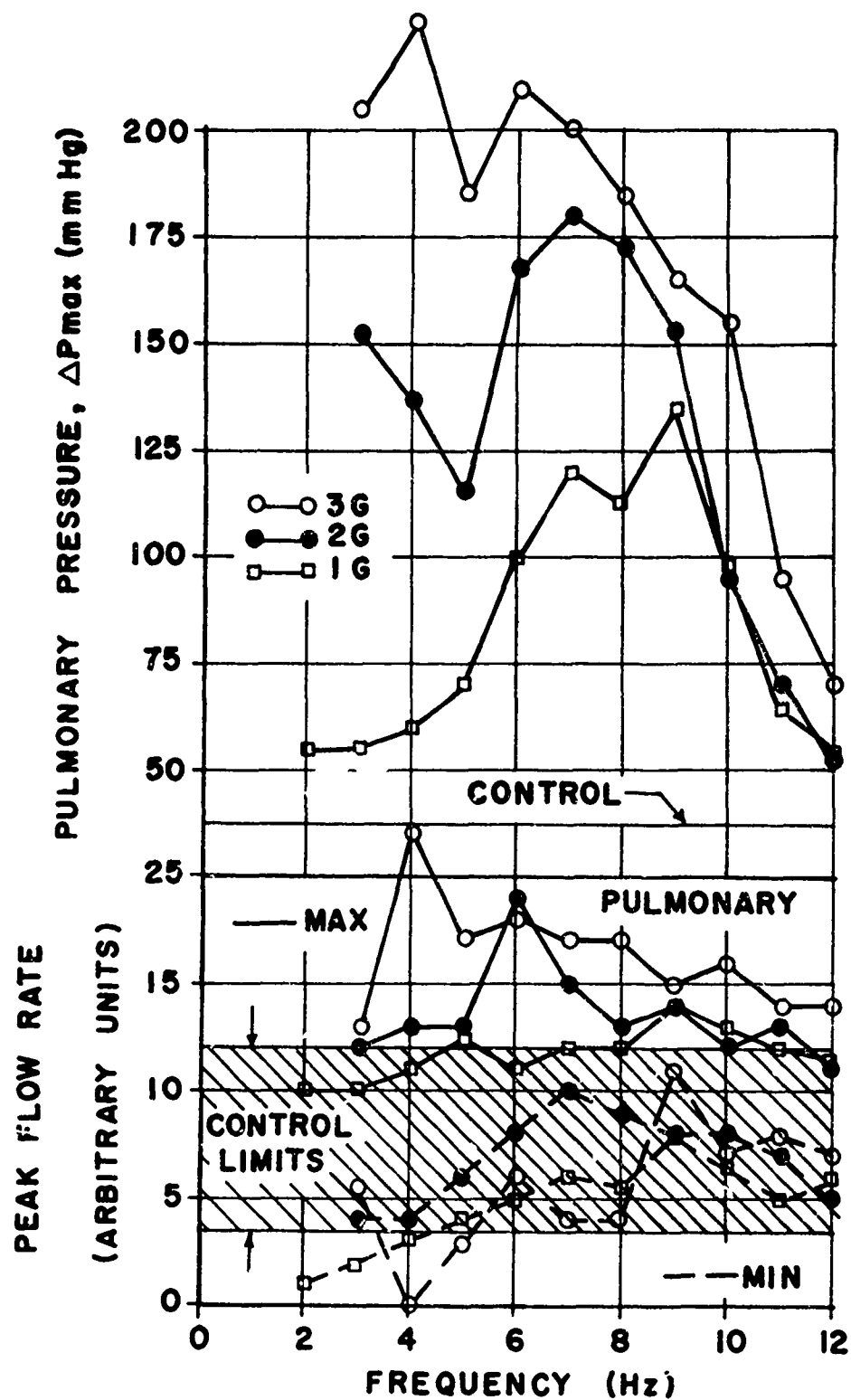


Figure 12. Pulmonary Pressure & Peak Pulmonary Flow Rate Versus Shake Table Frequency with Vibration Acceleration Amplitude as a Parameter, Dog A.

flow rates approached the control values. The curves for maximum peak pulmonary flow rate reach a maximum at a frequency which decreases with increasing acceleration amplitude; i.e., from 9 Hz at 1G, to 6 Hz at 2G to 4 Hz at 3G. This was also the case for the maximum aortic flow rate curves.

Although force transmission was not recorded during the test on Dog A, such data were recorded along with aortic pressure in a test on Dog B. Figure 13 contains the results. Force input (force transmitted between animal and support) is in the upper graph as a function of table frequency at acceleration levels from 0.5 to 3G. For comparison, the input force to an inert mass equal to that of the dog is shown as the four appropriately designated horizontal lines. The graph indicates that one internal organ system resonates at approximately 3 Hz and another, nonlinear and dependent upon the amplitude of input vibration, at 8 Hz for 3G and 2G but not clearly indicated by the curves for 1 and 0.5G. The lower graph of this figure illustrates a definite correlation of the  $\Delta P_{\max}$  developed in the aorta during 3 and 2G vibration with the motion of internal body organ systems as indicated by the input force traces.

#### CONCLUSIONS

This investigation showed that vibration can significantly increase or decrease an animal's peak blood flow rate in a major artery. This alteration depends upon (1) acceleration amplitude and frequency of input vibratory motion, (2) the phase relationship between vibratory motion and repetitive contraction of the heart, and (3) displacement of internal body organ systems induced by (1) above.

Specifically, whole body sinusoidal vibrations of 1 to 3G acceleration amplitude in the 2-12 Hz frequency range produce the following effects with respect to a resting dog's circulatory system:

- (1) For any one of the 1, 2, or 3G acceleration amplitudes, the greatest change in aortic or pulmonary peak flow rate occurs

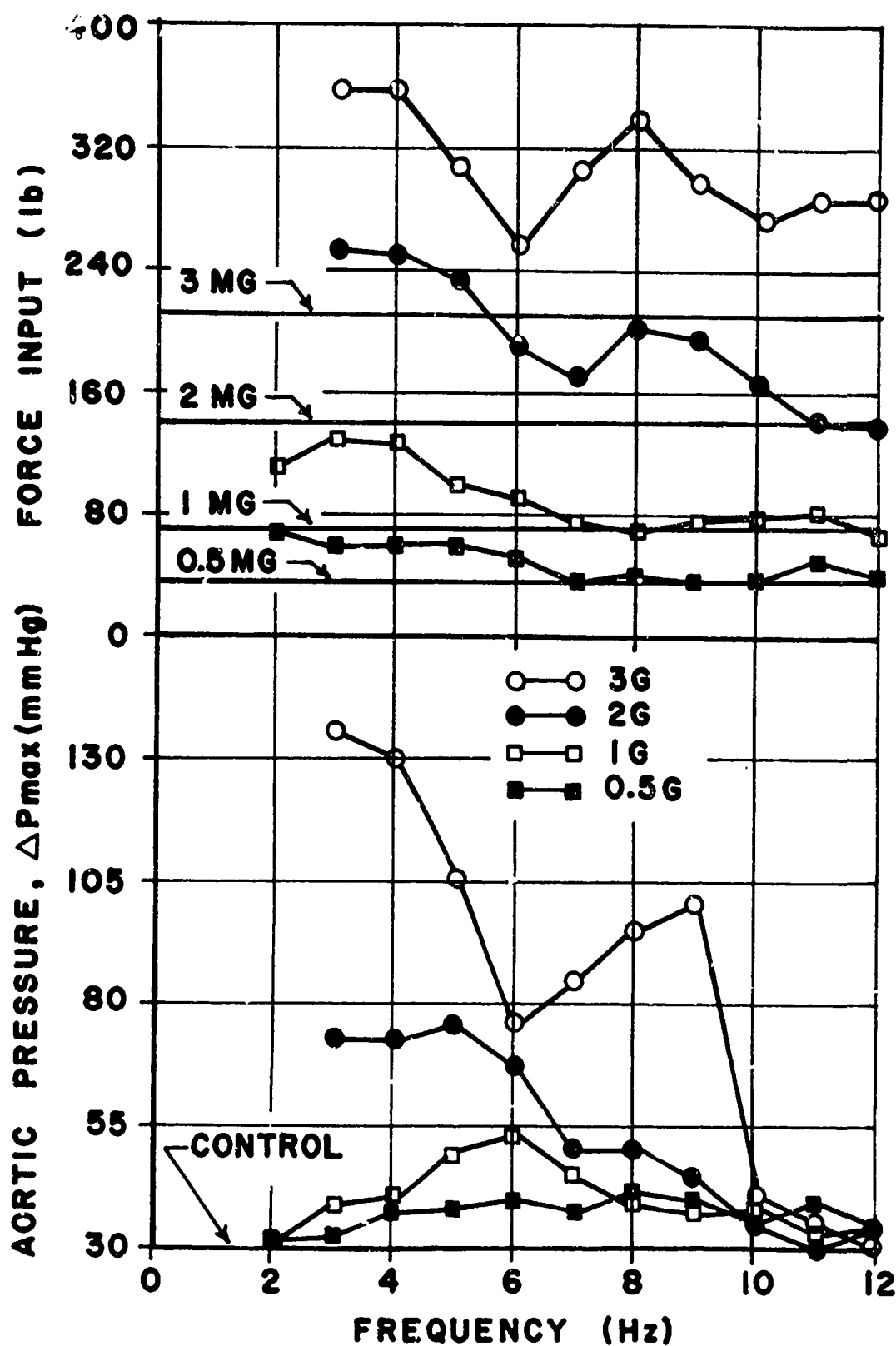


Figure 13. Force Input & Aortic Pressure Versus Shake Table Frequency with Vibration Acceleration Amplitude as a Parameter, Dog B.

in the 3 to 9 Hz frequency interval. 3G vibration at 4 Hz increased the maximum peak flow rate in these arteries by 100%, and decreased the minimum peak flow rate by 90%. Increasing the vibration frequency beyond that which produced the greatest change in peak flow rate, while maintaining a constant peak vibration acceleration, resulted in the aortic and pulmonary maximum and minimum peak flow rates approaching their control values.

- (2) For a given vibration frequency, increasing the acceleration amplitude increased the magnitude of the changes in peak flow rate in the aorta and pulmonary artery. This result, and that in (1) above, were predicted by both mathematical and mechanical models and verified by animal experiments.
- (3) Similar to the effects of vibration on the peak flow rate in the aorta and pulmonary artery, the maximum stroke flow rate in the carotid artery had its greatest change, for a given acceleration amplitude, at frequencies of less than 9 Hz, and approached the control value at higher frequencies. At any chosen frequency, increasing the acceleration amplitude increased the magnitude of the maximum stroke flow rate in the carotid artery. A maximum increase of approximately 6 times the control value occurred with 3G vibration at 6 Hz.
- (4) In general, the trend of the arterial  $\Delta P_{\max}$  versus frequency curves was similar to those for maximum and minimum peak flow rate versus frequency; however, the magnitude of the changes in pressure during vibration was very large. For example, 3G vibration at 4 Hz increased the  $\Delta P_{\max}$  in a resting dog's aorta by a factor of 5. This could be explained by the correlation of the peaks of the pressure curves with resonances of body organ systems. Motion of these systems appears to be one important mechanism altering the blood pressure, and consequently flow rate, during vibration. The force transmission curves show the 3 to 9 Hz

range to contain two resonant frequencies for the upright dog.

- (5) The phase between cardiac and vibration cycles at the onset of systole is another important factor influencing the resultant peak flow rate. A mechanical model showed this relationship to be the mechanism by which the peak flow rate from an analogue without vibration can be increased 30% or decreased 75% when 2.5 G vibration at 3 Hz is applied.
- (6) The stress environment of the tests on dogs produced cardiac arrhythmia. This resulted in a changing relationship between cardiac cycle, input vibration cycle, and movement of internal body masses. Consequently, no significant net changes in blood flow resulted during brief vibration exposure. This also explains why, for a given vibratory motion, maximum and minimum peak flow rates occur instead of regular constant peak pulses.

The significance of the results can be illustrated by considering possible effects of whole body vibration applied over very brief (less than 30 seconds) and very long (months) time periods.

A 90% or greater reduction in cardiac output could result if a near constant phase relationship between input vibration and cardiac cycles (inducing the minimum aortic peak flow rate on each systole) existed for a period of 10 to 15 seconds (such as that for 3 G vibration in the 5 to 7 Hz range shown in figure 11). Blackout, due to reduced blood flow to the head, could occur if such conditions were encountered, for example, by a high speed aircraft pilot during severe buffeting.

Fry (Ref. 6) observed that shear stresses exceeding 300 dynes/cm<sup>2</sup> at the vessel wall for periods as short as one hour could result in a marked deterioration of the endothelial surface of a vessel. Based upon a velocity profile presented by Ling and Atabek (Ref. 7), whereby 90% of the maximum centerline velocity is dissipated in the cylindrical area of one tenth radius from the vessel wall, a maximum wall shearing stress of slightly greater than 300 dynes/cm<sup>2</sup> can be



calculated from the maximum peak flow rate observed in the present investigation during 3 G vibration at 4 Hz. This would indicate that long term exposure to such vibration could indeed damage the lining of the arterial vessel.

#### REFERENCES

1. Hooks, L. E., R. M. Nerem, and T. J. Benson, "A Momentum Integral Solution for Pulsatile Flow in a Rigid Tube with and Without Longitudinal Vibration", Presented At "Engineering Science in Biomedicine" meeting of Society of Engineering Science, Washington University, St. Louis, November, 1969.
2. Edwards, R. G., "Arterial Blood Flow and Blood Pressure in Animals Under Mechanical Vibration", unpublished Ph.D. dissertation, University of Kentucky, Lexington, 1970.
3. Vaught, E. W., "An Electrohydraulic Vibrating Exciting System", Masters Thesis, University of Kentucky, Lexington, 1963.
4. Sharp, T. D., "A Live Load Force Table", Proc. Institute of Environmental Sciences, 1963, pp 129-144.
5. Lange, K. O., and R. G. Edwards, "Force Input and Thoraco-Abdominal Strain Resulting from Sinusoidal Motion Imposed on the Human Body", J. of Aerospace Medicine, May, 1970.
6. Fry, D. L., "Acute Endothelial Changes Associated With Increased Blood Velocity Gradients", Circulation Research, V22, p 165, 1968.
7. Ling, S. C., and H. B. Atabek, "Measurement of Aortic Blood Flow in Dogs by the Hot Film Technique", Engineering in Medicine and Biology, Proceedings of the 19th Annual Conference, p 113, 1966.

AMRL-TR-71-29

SESSION V

PERFORMANCE IN BIODYNAMIC ENVIRONMENTS

Chairman

L. Young  
Massachusetts Institute  
of Technology

Co-chairman

Lt Col C. J. Hodgson  
AMRL

**PRECEDING PAGE BLANK**

INTERFACING MAN-MACHINE CONTROL PERFORMANCE  
IN A BIODYNAMIC ENVIRONMENT

Henry R. Jex\*

ABSTRACT

The purpose of this presentation is to review the state of the art in interfacing man-machine control performance in a biodynamic environment. It is given in three parts:<sup>†</sup> (1) a review of the models which are appropriate for manual control performance and the added elements necessary to deal with biodynamic interfaces, (2) some simplified relationships relating the parameters of the models to the resulting man-machine performance, and (3) a review of some biodynamic interface pilot/vehicle problems which have occurred, been solved, or need to be solved.

MODELS

The types of models evolved in the field of man-machine systems are behavioral (i.e., input-to-output) models rather than mechanistic analog models, although the lumped parameter analog models are often used for particular subsystems within the human operator. The development of these models and empirical data is the result of over two decades of research which received its initial impetus during World War II. The situation is very similar to that in the biodynamic model field, in terms of numbers of workers involved, relative emphasis on theoretical and practical aspects, and to the distribution of sponsorship between military and educational institutions. Manual control technology has been used in numerous practical applications, such as: prediction of military and commercial aircraft handling qualities (and to quantification of the relevant procurement specifications), problems of manned vehicular control systems, and the design of better displays and controls for manned systems (e.g., see Refs. 1-3, and the bibliography in Refs. 1 and 11).

---

\*Principal Research Engineer; Systems Technology, Inc., Hawthorne, California 90250.

<sup>†</sup>For completeness this paper includes several items and a list of references not mentioned in the 20-minute oral presentation.

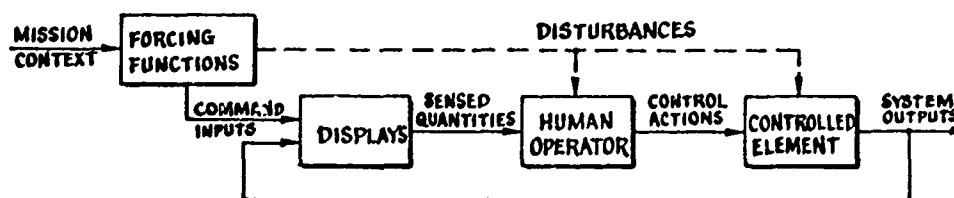
Starting with some basic principles, we will look at an increasingly complex array of models required to interface the man with the machine in a biodynamic environment. Our models are limited to the wide class of tasks which require an operator to act as a very precise sensorimotor link in a closed-loop system. Examples of such tasks are: driving a car, piloting an aircraft, aiming a weapon or telescope, and threading a needle. In such tasks the human operates as an adaptive, learning controller. Subsequent encounters with the same task result in improved behavior which eventually evolves towards that which is most appropriate for the task, and is remarkably consistent from person to person.

Figure 1 shows the "standard" block diagram for man-machine control situations (this diagram is like your seat-spine-head model). Starting from the left, the mission or task context is defined as a set of "forcing functions" comprising command inputs to be followed, and disturbances to be regulated against. Displays couple the command and feedback

Figure 1

## BASIC PRINCIPLES

- **TASKS CONSIDERED REQUIRE THE OPERATOR TO ACT AS A PRECISE, ADAPTIVE, SENSORY-MOTOR LINK IN A CLOSED-LOOP SYSTEM**



- **HUMAN BEHAVIOR IN THESE TASKS DEPENDS ON MANY VARIABLES:**  
TASK, ENVIRONMENTAL, OPERATOR-CENTERED, AND PROCEDURAL
- **SYSTEM OPERATION IS CLOSED-LOOP, SO HUMAN DYNAMIC BEHAVIOR IS QUANTIFIED IN CONTROL TERMS, SUCH AS TIME DELAY, EQUALIZATION, AND OPERATOR-INJECTED NOISE (REMNANT)**

information to the human operator who produces the necessary control actions to operate the controlled element in the desired manner. The output motions of the system are then displayed directly or indirectly to the human operator. This completes a feedback loop in which the goal of the operator is to reduce the observed errors between the actual or implied commands and the outputs. Because human behavior in such tasks evolves towards repeatable forms of response, it is thereby meaningful to measure them, to model them, and to seek their underlying laws.

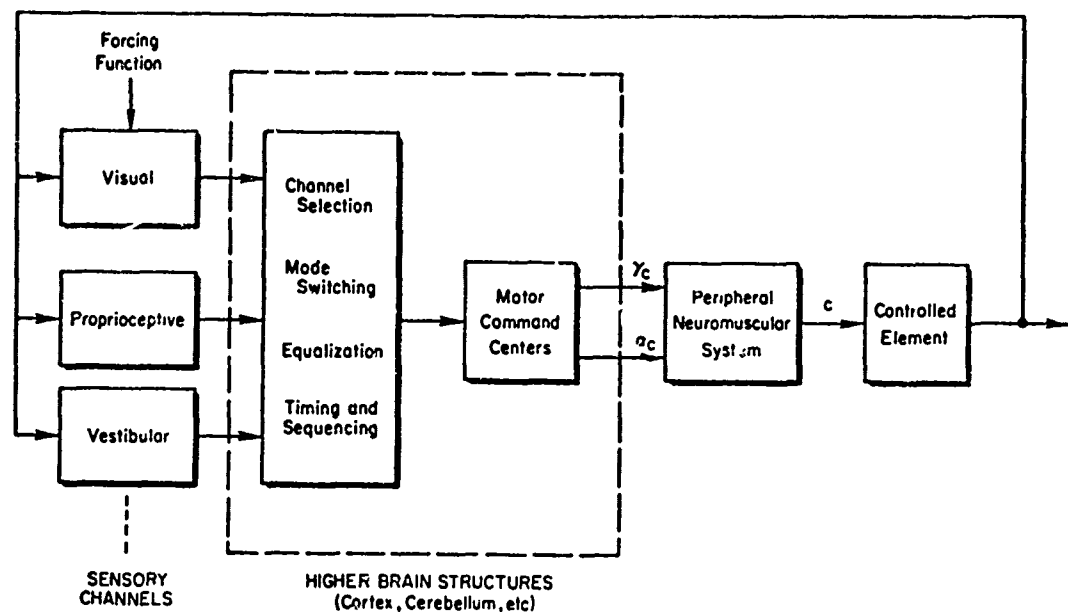
The measured human control behavior in closed-loop tasks has been found to depend on many variables:

- Task variables such as the forcing function displays, control stick, and controlled element.
- Environmental variables such as vibration, temperature, g-level, and breathing atmosphere.
- Operator-centered variables such as anxiety, motivation, workload, and fatigue.
- Procedural variables such as practice, transfer of training, order of presentation, and even the measurement technique.

We generally try to suppress the procedural variables by suitable experimental design and thorough training, so it is the first three which are of main interest. The effects on both models and parameters of the task variables are fairly well understood, but measuring the effects of environmental and operator-centered variables are still in an embryonic status.

Because man-machine control systems generally operate in a closed-loop manner, human control behavior is most suitably quantified in terms of control theory. Such concepts as feedback loops, dynamic stability, dynamic loop delays, equalization, and operator-injected noise ("remnant") are central concepts to all man-machine-control models.

Now let's expand the human operator block of Fig. 1. Here in Fig. 2 we have a more generalized block system diagram. At the left are shown the three main forms of sensory input, i.e., the visual, proprioceptive, and vestibular neural signals. They interact with the higher brain structures in as yet only vaguely understood ways. Within the cortex and the



### GENERALIZED MAN/MACHINE SYSTEM

Figure 2

cerebellum a number of processes occur. Among these are channel selection (when more than one channel must be operated concurrently), mode switching between various types of internal loop structure, equalization (in the form of rate anticipation or smoothing), and the timing and sequencing of various discrete events in cases where that is appropriate. All of these operations take a finite amount of time, but as learning proceeds and the same forcing function is encountered again, less time is taken to handle and command the appropriate motor actions. These emanate from the higher brain structure in the form of alpha and gamma motor neuron signals which operate the neuromuscular servo system. A completely accurate and comprehensive neuromuscular model has yet to be evolved; nevertheless, a lot is known. I will expand on this neuromuscular system model later.

The structure of the models for man-machine control systems is not fixed, but can actually change as learning proceeds. This hierarchy of open- and closed-loop feedback structures has been termed the "Successive Organization of Perception" (SOP) theory of learning (Refs. 4, 5). In Fig. 3 we see that in the most basic phase the operator merely seeks to correct the errors between the command and response. This "compensatory"

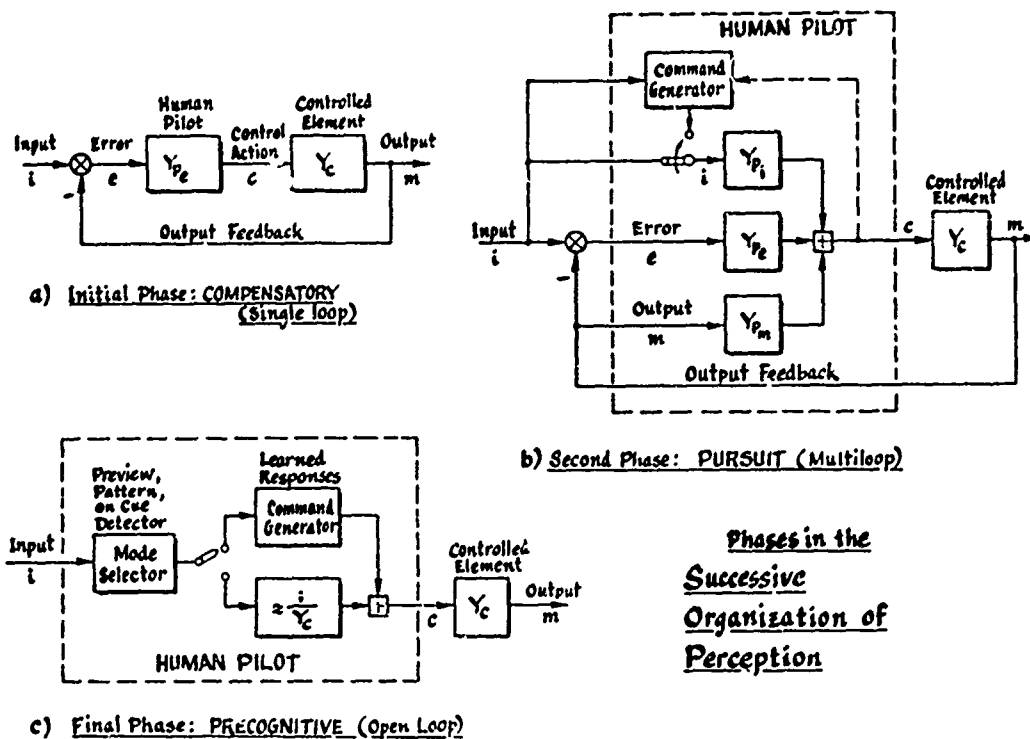


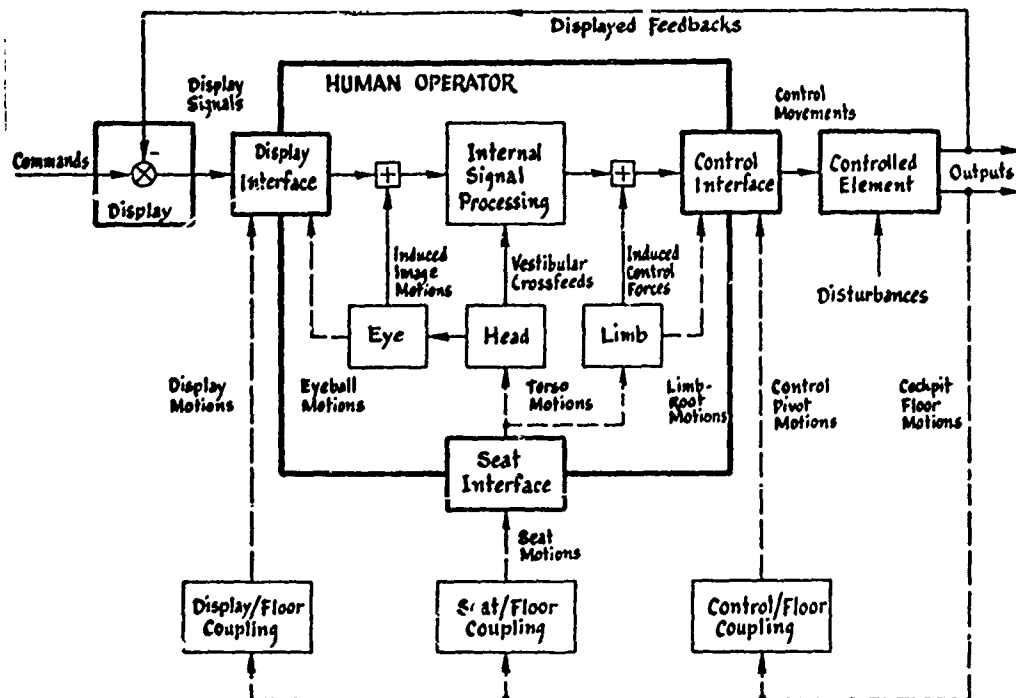
Figure 3

loop structure is the only structure allowed when the input or forcing functions are completely unpredictable.

In the second phase the operator takes advantage of any "coherency," or patterns, in his input (or which he perceives proprioceptively from his control forces) to form other signal paths which can cause the output to follow the input more accurately. Any residual errors are then corrected in a compensatory manner. This so-called "pursuit" loop structure is the most general form of operator control, yet the elements within the blocks at this point can only be inferred, because we have but one input and one output from which the properties of several blocks must be determined. Needless to say, definitive models for the pursuit structures are not well established. Fortunately, it is the error correction portion of this loop which determines the dynamic stability of the man-machine system,



Now consider the additional elements required to interface man and machine in a biodynamic environment. At the top of Fig. 4 is the now-familiar control loop, including display, human operator, controlled element, and feedback. At the bottom are those additional elements

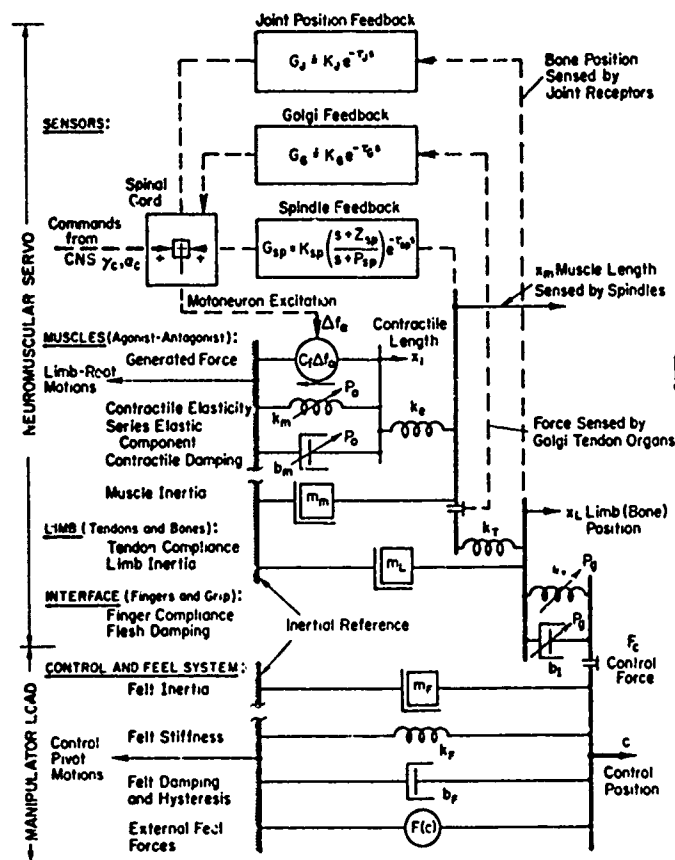


## BIODYNAMIC INTERFACES FOR MAN-MACHINE CONTROL

Figure 4

required in a biodynamic environment. There are three primary biodynamic interfaces of the human operator: at the display, the seat, and the control. Each of these is, in turn, coupled to the structure (floor, say) of the controlled element via passive or possibly active means. An example of active couplings are the vibration isolation seats currently undergoing development at AMRL and NASA.

In a dynamic vibration environment the display, seat, and control can each be vibrating at different large amplitudes and with different phases, so that merely perceiving the display and gripping the stick become difficult in themselves. The human torso, and through it the motions of the head,



## MODEL FOR LIMB/MANIPULATOR INTERFACES

Figure 5

constants are dependent primarily on the tension in the muscle system as set by the gamma motor neuron excitation (see Refs. 8, 9). The resulting muscle actuation forces are coupled elastically through the muscle inertia, then through the tendon compliance into the limb inertia to move the bone. Various sensory paths are shown at the top to complete this actuator loop. We believe the spindle feedbacks play a dominant role in fine control motions, but Golgi-organ feedbacks and joint position receptors are also known to be involved under certain circumstances. The control stick itself is moved through the interface compliance. The picture is not complete without consideration of the feel system dynamic properties, including its effective mass, spring rate, damping, etc.

As any physiologist will tell you, this is a grossly oversimplified neuromuscular model. Nevertheless, we have found it is sufficiently

comprehensive to reveal the various dynamic modes observed in neuromuscular system responses, handle such phenomena as limb tremor (which occurs at frequencies near 10 Hz), and accommodate manipulator feel systems ranging from rigid to free sticks and all forms in between (Ref. 10). This model can also handle situations where: 1) the limb is acting as an additional mass at the end of the feel system, (complicated by its own internal compliances and feedbacks, and 2) the limb-root or pivot are vibrating.

It is easy to draw increasingly complex models to represent increasingly precise details. The art comes in knowing how to extract the essential features from a complex model such as this one in order to use it to solve practical problems. For ordinary manual control purposes we do not need the complete limb/manipulator model shown here. We simply represent its effects by a simple time delay, or at most a third-order system representing its primary lags and resonance. However, under some of the new biodynamic conditions of interest, a model such as this will be essential. It behooves us all to make sure that efficient, yet well validated, biodynamic interface models are available when they are needed.

#### MATHEMATICAL MODELS FOR PERFORMANCE

The previous section has shown the form and structure of the manual control models. To make them quantitatively useful for performance prediction they must be fleshed out in the form of either lumped parameter analogs suitable for simulation, or approximating mathematical functions suitable for computation. To reveal the key parameters and to obtain insight into the tradeoffs among them, simplified mathematical models are essential; yet they must retain the essential features of the man-machine behavior and closed-loop phenomena. A remarkably simple set of such models—the "crossover model" and its refinements—has been evolved and applied (Refs. 1, 7, 12). It is based on a "law" of operator control behavior that has been found to occur in nearly all man-machine closed-loop situations, ranging from aiming weapons at evasive targets to precision

aircraft piloting tasks, to steering a car on a windy day, and to piloting a booster rocket (see Ref. 1 for a bibliography).

The key assumptions are as follows:

1. The inputs are unpredictable, have low bandwidth (below 1 Hz), and are continuous waveforms.
2. The controlled element in a low-order system having no highly resonant modes over the input bandwidth.
3. The display and controls are reasonably well scaled and smooth so as to minimize effects of thresholds, detents, and friction.
4. The other task demands permit the operator to devote the majority of his attention to reducing the displayed errors between the command input and system output in the control loop of interest.

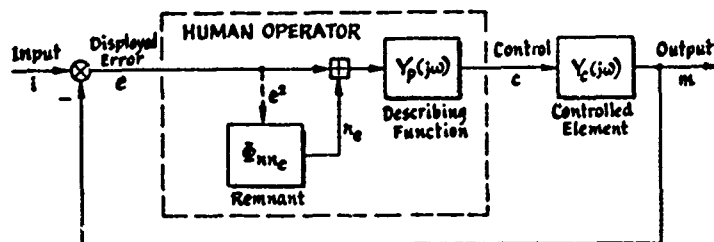
Under these conditions, commonly met in most operational control tasks, both theory and experiments show that the operator tries to compensate or equalize for the properties of the controlled element such that, in the forward (open) loop from displayed error to system output, the combined man-machine system acts roughly like an integrator in series with a delay time. Figure 6 shows this model. The price of increased operator equalization is generally increased delay  $t_d$  and more operator-induced noise or remnant in his control output.

As noted in Fig. 6, the input-dependent compensatory tracking behavior of the operator can be most efficiently represented by a four-parameter open-loop describing function (frequency domain) model:

Refined Crossover Model:

$$Y_{OL}(j\omega) = Y_p(j\omega) \cdot Y_c(j\omega) \doteq \frac{\omega_c}{(j\omega)^N} e^{-j[\tau_e\omega + (\alpha/\omega)]} \quad (1)$$

where  $\omega_c$  is the unity-gain "crossover" frequency;  $\tau_e$  is an effective time delay representing small but cumulative perceptual-motor delays and lags;  $N$  is an amplitude-ratio slope parameter (near 1.0) and  $\alpha$  is a "low frequency phase-droop" parameter ( $\ll 1.0$ ). I call this model the "Refined Crossover Model", as it is based on the "extended" and "modified" models of Refs. 1, 11, 12. It closely matches the describing functions for a large number of practical



CONDITIONS: Unpredictable, low bandwidth inputs  
 Low order controlled element  
 Reasonable controls and displays  
 Prime attention to control task

Then the combined man-machine open-loop describing function is well fitted by:  
 THE REFINED CROSSOVER MODEL:

$$Y_{OL}(j\omega) = \frac{m(j\omega)}{e(j\omega)} = Y_p(j\omega) \cdot Y_c(j\omega) \doteq \frac{\omega_c}{j\omega N} e^{-j(\tau_e\omega + \alpha/\omega)}; .2 < \frac{\omega_c}{\omega_e} < 5$$

where  $\omega_c$  = crossover frequency(gain),  $\tau_e$  = effective delay time,  
 $\alpha$  = low-frequency phase droop, and the operator adopts  
 the necessary equalization(lead, gain, lag) such that  $N \approx 1$ .

The REMNANT looks like low-pass filtered noise, with two components:

$$\hat{G}_{NNc} = e^2 \cdot \hat{G}_{NNc}' + \hat{G}_{NNc}''$$

Processing Remnant,  
 Scales with perceived  
 signal variance

Residual Remnant,  
 depends on thresholds, etc.

### DESCRIBING FUNCTION AND REMNANT MODELS FOR THE PILOT'S BASIC SIGNAL PROCESSING BEHAVIOR

Figure 6

situations. In most cases the operator equalizes the system (to compensate for the controlled element properties), such that the amplitude ratio slope,  $N$ , near crossover frequencies is very nearly 1.0. Further, the small effects of  $\alpha$  on tracking errors can often be neglected without loss of essential trends. With these further simplifications the Simple Crossover Model results:

Simple Crossover Model:

$$Y_{OL}(j\omega) \doteq \frac{\omega_c}{j\omega} e^{-j\tau_e\omega} \quad (1a)$$

A caution is in order here; this model is strictly valid only for continuous, unpredictable inputs, and should not be applied to modeling man-machine step responses or tracking of easily learnable patterns.

The Crossover Model yields an equally simple formula relating the closed-loop tracking performance to the input and behavioral parameters; this is the "One-Third Law" of McRuer, in Ref. 7:

Correlated Error:

$$e_1^2 = \frac{1}{3} \left( \frac{\omega_1}{\omega_c} \right)^2 \sigma_1^2 \quad (2)$$

where  $\omega_1$  is the input spectrum's bandwidth

$\omega_c$  is the crossover frequency

$\sigma_1^2$  is the mean-squared input

$e_1^2$  is the mean-square error coherent with the input

As noted on Fig. 6, the operator-induced remnant is modeled as a bandpassed spectrum of noise  $\phi_{nn_e}(\omega)$  injected at the error node (Refs. 13a, b). It contains a dominant portion due to perceptual and signal processing noise whose variance increases with the displayed signal variance, plus an often negligible residual component due mainly to accumulated thresholds in the perceptual-motor system. The resulting integral equation for the remnant portion of the closed-loop error, with  $\phi_{nn}$  and  $|Y|^2$  both  $f(\omega)$ , is as follows:

Remnant Error:

Processing:

Residual:

$$e_n^2 = e^2 \int_0^\infty \phi'_{nn_e} |Y_{CL}|^2 d\omega + \int_0^\infty \phi_{nn_o} |Y_{OL}|^2 d\omega \quad (3)$$

where:

$$\phi'_{nn_e}(\omega) = \phi_{nn_e}(\omega)/e^2 \quad (\text{See footnote.*})$$

and

$$|Y_{CL}(j\omega)| = Y_{OL}(j\omega)/[1 + |Y_{OL}(j\omega)|] \quad (4)$$

The latter is the fundamental feedback system equation, reflecting the principle that a high open-loop gain causes the closed-loop magnitude to approach unity at that frequency, albeit with some phase error.

The fact that the total error,  $e^2 = e_1^2 + e_n^2$ , also appears in the equation for  $e_n^2$  results in a transcendental equation, and leads to the following expression for the total error variance:

Total Error:

$$e^2 = \frac{e_1^2 + e_{n_o}^2}{1 - \int_0^\infty \phi'_{nn_e} |Y_{CL}|^2 d\omega} \quad (5)$$

The final relationship required connects the closed-loop dynamic stability margins to the Crossover Model parameters of Eq. 1. Feedback

\* $\phi_{nn_e}(\omega)$  and  $\phi_{nn_o}(\omega)$  are "one-sided" power spectral densities, with dimensions of (error units)<sup>2</sup> per (rad/sec).

theory shows that if at some frequency the loop gain is exactly -1.0 ( $|Y_{OL}| = 1.0$ ;  $\angle Y_{OL} = 180^\circ = \pi/2$  radians) the (subtracted) feedback signal will drive the closed-loop system dynamically unstable. Consequently, at the unity gain crossover frequency,  $\omega_c$ , the "phase margin" of stability is given, via Eq. 1, by:

Stability Margin:

$$\phi_M(\text{rad}) = \pi - \frac{\pi}{2} N - \omega_c \tau_e - \frac{\alpha}{\omega_c} \quad (6)$$

Most of the task variables and biodynamic environment effects on the operator will serve to change one or more of the several parameters on the right side of Eqs. 1 and 6. For instance, perceptual blurring due to G-level or vibration will reduce the gain,  $\omega_c$ , and increase the processing remnant spectrum,  $\Phi'_{nn_e}$ , and may increase the effective delay time,  $\tau_e$ . Now we have all the essential phenomena modeled by relatively simple mathematical models, so we can see how such effects interact on performance.

Figure 7

## MAN-MACHINE PERFORMANCE RELATIONSHIPS

### BEHAVIOR (Describing Function)

$$Y_{OL}(j\omega) = Y_P(j\omega) \cdot Y_C(j\omega) = \frac{\omega_c}{(j\omega)^N} e^{-j(\tau_e \omega + \frac{\alpha}{\omega})}$$

$N \neq 1$  ("Crossover Equalization Law")

$$Y_{CL}(j\omega) = \frac{Y_{OL}(j\omega)}{1 + Y_{OL}(j\omega)}$$

### STABILITY (Phase Margin)

$$\phi_M(\text{rad}) = \pi - \frac{\pi}{2} N - \omega_c \tau_e - \frac{\alpha}{\omega_c}$$

### PERFORMANCE (Errors)

Total Errors = Correlated Error + Remnant

$$\bar{e}^2 = \bar{e}_i^2 + \bar{e}_n^2$$

where:

$$\bar{e}_i^2 = \int \frac{\Phi_{ii} d\omega}{|1 + Y_{OL}|^2} \rightarrow \approx \frac{\sigma_i^2 (\omega_i)^2}{3 (\omega_c)^2} \text{ "One-Third Law"}$$

$$\bar{e}_n^2 = \int \overset{\text{Residual Remnant}}{\Phi_{nn_0}} |Y_{CL}|^2 d\omega + \int \overset{\text{Processing Remnant}}{\Phi'_{nn_e}} |Y_{CL}|^2 d\omega$$

Result:

$$\bar{e}^2 = \frac{\bar{e}_i^2 + \bar{e}_n^2}{1 - \int \Phi'_{nn_e} |Y_{CL}|^2 d\omega}$$

Figure 7 summarizes these simplified math models, so that we can trace through some of the conflicting demands of stability versus accuracy. Consider the effect of increased loop gain (represented by  $\omega_c$ ); since this is one variable which is readily adjustable by the pilot over a wide range. From the equations for  $Y_{OL}$ ,  $Y_{CL}$ , and the One-third Law, it is apparent that a high loop gain tends to reduce  $e_i^2$  the mean squared error in following commands (provided the input bandwidth is less than the crossover frequency). But the phase margin equation shows that the gain is always limited by the delay time, through the  $-\omega_c \tau_e$  term. Consequently, the closed loop performance is always constrained by the stability limit allowed by  $\tau_e$ , even without considering the remnant. This is the reason why  $\tau_e$  and  $\omega_c$  are such crucial parameters.

The remnant can be seen to act in two ways, from the expressions for  $e_n^2$  and total  $e^2$ . First there is the direct contribution of residual remnant,  $e_{n0}^2$ , which can excite the system even with no command input! Biodynamic environments often add significantly to  $e_{n0}^2$  by direct mechanical "crosstalk" effects. Even more important is the denominator term in Eq. 5, which results because processing noise affects the net perceived signal including the noise just passed around the loop. For cases where there are large perceptual thresholds or attentional diversions,  $\phi_{nn_e}$  can become so large that the denominator sum can approach zero, causing  $e^2$  to blow up in a closed loop chain reaction of noise-exciting-even-more-noise. This is called "error instability in the mean-square sense." It is not a problem with "good" controlled elements in full attention tasks, but may become the limiting performance factor under high workload or stressful conditions. In such situations, reducing  $\omega_c$  helps because it results in attenuated  $|Y_{CL}|$  in the denominator of Eq. 5. This leads to a reduced processing remnant factor, as well as to lower  $e_{n0}^2$ , which can more than offset the concurrent increase in  $e_i^2$ .

It is really quite remarkable that human operators seem to make these tradeoffs instinctively and quite consistently, given sufficient practice. Even though I have shown the very simplest models here, because they permit insightful analytical formulas to be derived, you should understand that much more accurate and complex models are continually being developed, and that detailed numerical computations can be carried out for any case



you choose, given enough time and computing power. One of the goals of current man-machine research is to discover the laws among these various performance and stability criteria and how they are affected by the numerous tasks and environmental variables. The closed-loop systems approach and the type of describing-function-plus-remnant models I have described are essential ingredients in this search for a comprehensive model of man-machine behavior and performance.

### SOME BIODYNAMIC PROBLEMS AND THEIR STATUS

I'd like to end up this presentation with a review of some specific problems in which biodynamic man-machine interfaces are involved. On the left side of Fig. 8 are some of the important current problem areas, ranging from best to least researched areas. On the right side is my assessment of their status. The first column tells whether sufficiently detailed models are available to represent the phenomena observed. The second column shows by the checks or question marks whether these models have been empirically validated, so that one could have confidence in their use. The last column mentions some of the specific aerospace vehicles on which problems of the type mentioned have occurred, and in some cases solved, by application of biodynamic man-machine models. Let us look at some of these, in succession.

Figure 8

SOME BIODYNAMIC MAN-MACHINE PROBLEMS AND THEIR STATUS

PROBLEM	STATUS		
	MODELS AVAILABLE	MODELS VALIDATED	EXAMPLES
1. <u>Pilot-Induced Oscillations</u>			
a. <u>Limb-balance effects</u>	Good	✓	A-4D, T-38, AH-56
b. <u>Limb-impedance effects</u>	New	?	A-6
2. <u>Effects of Motion Cues on:</u>			
Tracking performance	Good	✓	Ames Centrifuge CAL T-33
3. <u>Bending-Modes excited by:</u>			
Pilot-remnant	Good	✓ (Some)	Saturn-V, B-70, C-5, B-1
4. <u>Vibration effects on:</u>			
a. <u>Tracking performance</u>	Fair	?	UH1-B, A-5
b. <u>Isolation seat design</u>	Partial	Some	Barry Seat
5. <u>Steady-G Effects on:</u>			
a. <u>Tracking performance</u>	Partial	—	Ames F-104B and centrifuge
b. <u>Head-mounted sights</u>	—	—	M-H Sight

## PILOT-INDUCED OSCILLATIONS

Pilot-induced oscillations (PIO) are caused by any of a number of coupling phenomena between the pilot and his vehicle system. By definition, they cease when the pilot releases the controls, or locks them rigidly. Reference 14 gives an overall background of this commonly encountered class of problems. Of the many forms of pilot-induced oscillations, the two of primary interest here are those caused by "limb-bobweight" effects or by "limb-impedance" effects.

Limb-bobweight effects are caused when the accelerations imposed by the control-induced motion of the vehicle are coupled, via the limb's unbalance, back into the control system, thereby forming a closed loop acceleration feedback system. If the mass overbalance of the pilot's arm on the controls has the correct sign and phase lag, this effect can drive the pilot vehicle system to violently unstable oscillations. (For example, in an early T-38, the oscillations reached  $\pm 9 G_z$  at 1.0 Hz! Ref. 15.) This can occur even with the pilot acting as a fairly passive element with his hand resting "loosely" on the stick. Analysis of this type of effect using conventional feedback models of the vehicle system, and relatively crude models for the limb's effective inertia have been performed in connection with a number of specific problems that have occurred during flight tests. Among the earliest work is that of Abzug on the Douglas A-4D, Ref. 16, of the Northrop people and ourselves on the early T-38, Refs. 15 and 17, and more recently by Lockheed on the rigid-rotor AH-56 Helicopter, Ref. 18. One lesson learned from all these analyses is that fairly crude models of biodynamic systems can often be used for these problems, but fairly complete models for the vehicle's control system and the limb/manipulator coupling must be included in order to accurately represent the system dynamics in the frequency range near 1-2 Hz.

In a few instances, simply grabbing the control of an automatic flight control system has caused the system to shake, "quiver," "nibble," or vibrate in some other manner. This is felt to be due to coupling with the limb's complex impedance characteristics, which are included in the model given in Fig. 5. We once did a crude analysis of this effect for the Grumman A-6 aileron "ratchet" problem; nevertheless this is an area

in which little systematic research has been done and still less has been published.

#### EFFECTS OF PERCEIVED MOTION CUES

As illustrated earlier, vehicle motions enter a vehicle control loop through a number of paths, including the vestibular and proprioceptive (seat of the pants) feedbacks which are summed with the visual cues in normal man-machine control. Reasonably good models for the vestibular system crossfeeds now exist. Reference 19 contains a comprehensive review of the vestibular phenomena of interest in man-machine control, and Refs. 20 and 21 summarize some of the recent research on motion cues. There has also been a limited amount of systematic flight research carried out in the Cornell Variable Stability T-33, which is specifically aimed at resolving the motion cue effects on pilot vehicle performance (Ref. 22). Other work is being done on the 5- and 6-degree-of-freedom moving-base simulators at the NASA Ames Research Center (Ref. 23). This is an important problem area which is presently undergoing a very fruitful phase of research.

#### BENDING-MODE EXCITATION

The large aerospace vehicles controlled by pilots are becoming more and more flexible as their length increases and their diameter decreases; for example, the DC8-63 transport, B-70 bomber, and Saturn V booster. The first body-bending modes of these vehicles often lies in the range from 1-5 Hz, and the pilot is usually situated well forward of the vibration node. Movement of the elevator or rudder strongly excites these bending modes, thereby inducing vibrations at the cockpit. This induced vibration acts on the pilot in a number of ways, some mentioned previously. For example, the vibrations can, through limb bobweight effects, couple into a neutral or divergent oscillation. Particularly in the range near 3 Hz, such motions can also involve unpleasant head and torso vibrations. Because the flight path control commands do not demand responses in this frequency range, the pilot does not intentionally excite these bending modes. However, the wideband pilot-induced remnant noise described earlier in this presentation covers a wider frequency range, and it is the primary source of bending excitation.

Recently, good models to detect the existence of a bending mode excitation problem and to guide the solution (in terms of appropriate stick filtering) are available, but little has been done to thoroughly validate these models. One of the better documented cases is the analysis of the manual backup control system for the Saturn V booster reported in Ref. 24. The simulation studies for the vehicle show the dramatic importance of the remnant terms in exciting a 2 Hz body bending mode. Subsequent computer simulations at NASA Ames Research Center showed that the analytical man-machine models, including the remnant inputs, could successfully predict the problem and its solution, even though the magnitudes of remnant-induced bending mode excitation were not accurately predicted (Ref. 25).

#### VIBRATION EFFECTS

Vibration effects on subjective "ride quality" and tolerance of a vibration environment have been well researched and extensively reported (e.g., as summarized in Refs. 26 through 29). Vibration effects on man-machine tracking performance are much more scarce, and they have involved relatively crude measurements compared with the kind of behavioral parameters we have been talking about here (Refs. 30-32). As pointed out in Section II, the net tracking error includes both coherent and remnant contributions, each of which can be influenced in different directions by the direct or indirect effects of vibration. For example, tensing up muscles in the presence of mild vibration reduces the neuromuscular timing delays, thereby tending to increase the system bandwidth, but it may also result in higher gain and reduced stability margins, thereby tending to increase the remnant. Effects of the various vibration parameters on remnant are still unknown. Two of the more recent efforts to use modern manual control measurement and techniques are related to low altitude high speed flight (Ref. 32), and to weapon aiming from a vibrating helicopter (Ref. 33).

There is current interest in the design of "vibration isolation seats" designed to uncouple the pilot from his vibrating cockpit environment. As noted in Fig. 4, this is but one of the three interfaces which must be considered in interfacing man-machine performance with the biodynamic environment, so much remains to be done in modeling and validating this interesting

problem area. Research using an active vibration isolation seat designed by Barry Controls (Ref. 34) is underway both at the 6570th AMRL and at NASA. I strongly urge that complete man-machine system models of the type described here, be applied to this problem area. This work should be carried along in parallel with the experimental research, both to help in the experimental design, selection of measurements and data analysis, and to reveal concurrent technical advances which must accompany such seats (e.g., vibration-compensated displays and controls).

#### STEADY-G EFFECTS

One of the most studied biodynamic inputs is that of steady accelerations on various bodily functions. Various specialized studies have been done in the last two decades on the effective man-machine performance under steady G's (e.g., Refs. 35-38). This line of research seemed to reach a plateau a few years ago and is only recently picking up speed again. The much more comprehensive models which are now available for describing the man-machine performance can guide the selection of tasks measurements, and data reduction analysis procedures (e.g., Ref. 36 is a pioneering example). There is evidence that those involved in centrifuge research, many of whom are medical people, psychologists, or mechanical engineers, have recently begun to include modern man-machine control techniques in their research.

The last, and most fascinating, problem I wish to mention is that of using head-mounted sights under high-G maneuvering conditions. If any of you have tried to track a moving satellite with a pair of binoculars held against your head, you will understand what a frustrating problem this can be. (It's the remnant that blurs the image!) Now imagine doing this if your head and optics weighed 5 times as much, and you will have an idea of the problem of a pilot trying to track an enemy aircraft with a helmet-mounted magnifying sight during a 5 G<sub>z</sub> turn. Some excellent design research has been done on the applications and design features for head-mounted sights (e.g., Ref. 39). Yet, to my knowledge, comprehensive models of the type described here for the combined system of target, sight, head and eye neuromuscular system, vehicle, and maneuver kinematics have not

yet been applied. Here is a problem ideally suited to biodynamic man/machine analysis, and the payoff will be high in terms of: problem areas uncovered and avoided, design parameters delineated, and experimental research guidelines exposed.

#### CONCLUDING REMARKS

In summary, I feel that the field of interfacing man-machine performance in a biodynamic environment is an extremely fertile one, which is about to enter a new and fruitful era. It will have to draw heavily on the classical lumped-parameter biodynamic response models, especially in the representation of body, limb, head and eye coupling effects. In turn, some of the more sophisticated feedback neuromuscular models and measurement techniques should be of value in biodynamic transmittance measurements, particularly where muscle properties have a large influence on the results.

Finally, I hope that some of the new research areas mentioned above will be on their way to the "validated" status by the time of the next Biodynamic Model Symposium.

#### ACKNOWLEDGMENTS

I would like to acknowledge the contributions of my colleagues: Duane T. McRuer who originated much of the research mentioned here, and Raymond E. Magdaleno who is primarily responsible for our neuromuscular models.

## REFERENCES

1. McRuer, D., and D. H. Weir, "Theory of Manual Vehicular Control," Ergonomics, Vol. 12, No. 4, July 1969, pp. 599-634.
2. Young, L. R., "On Adaptive Manual Control," Ergonomics, Vol. 12, No. 4, July 1969, pp. 635-674.
3. Clement, W. F., H. R. Jex, and D. Graham, "A Manual Control Display Theory Applied to Instrument Landings of a Jet Transport," IEEE Trans., Vol. MMS-9, No. 4, Dec. 1968.
4. Krendel, Ezra S., and Duane T. McRuer, "A Servomechanisms Approach to Skill Development," J. Franklin Institute, Vol. 269, No. 1, Jan. 1960.
5. Krendel, Ezra S., and Duane T. McRuer, "Psychological and Physiological Skill Development—A Control Engineering Model," Fourth Annual NASA-University Conference on Manual Control, NASA SP-192, 1969, pp. 275-288.
6. Graham, Dunstan, and Duane McRuer, Analysis of Nonlinear Control Systems, John Wiley and Sons, Inc., New York, 1961.
7. McRuer, Duane, Dunstan Graham, Ezra Krendel, and William Reisener, Jr., Human Pilot Dynamics in Compensatory Systems—Theory, Models, and Experiments with Controlled Element and Forcing Function Variations, AFFDL-TR-65-15, July 1965.
8. McRuer, D. T., L. G. Hoffmann, H. R. Jex, et al., New Approaches to Human-Pilot/Vehicle Dynamic Analysis, AFFDL-TR-67-150, Feb. 1968.
9. Magdaleno, Raymond E., Duane T. McRuer, and George P. Moore, Small Perturbation Dynamics of the Neuromuscular System in Tracking Tasks, NASA CR-1212, Dec. 1968.
10. Magdaleno, R. E., H. R. Jex, and R. W. Allen, Fine Motor Unsteadiness: Models, Data Survey, and Sample Measurements, Systems Technology, Inc., Working Paper 2010-4, Aug. 1970.
11. McRuer, D. T., and J. R. Jex, "A Review of Quasi-Linear Pilot Models," IEEE Trans., Vol. HFE-8, No. 3, Sept. 1967, pp. 231-249.
12. King-Smith, Eric A., "Predictive Compensation in Time-Delay Manual Control Systems," Fourth Annual NASA-University Conference on Manual Control, NASA SP-192, 1969, pp. 253-274.
- 13a. Levison, W. H., S. Baron, and D. L. Kleinman, "A Model for Human Controller Remnant," IEEE Trans., Vol. MMS-10, No. 4, Dec. 1969, pp. 101-107.
- 13b. Jex, H. R., and R. E. Magdaleno, "Corroborative Data on Normalization of Human Operator Remnant," IEEE Trans., Vol. MMS-10, No. 4, Dec. 1969, pp. 137-139.

14. Ashkenas, Irving L., Henry R. Jex and Duane T. McRuer, Pilot Induced Oscillations: Their Cause and Analysis, Systems Technology, Inc., Tech. Rept. No. 239-2 (Northrop-Norair Rept. No. NOR 64-143), 20 June 1964 (AD 481 994).
15. Jex, H. R., Summary of T-38A PIO Analysis, Systems Technology, Inc., Tech. Rept. No. 239-1, 25 Jan. 1963.
16. Abzug, Malcolm J., High-Speed Stability and Control Problems as They Affect Flight Testing, AGARD Rept. 120, 1957.
17. Levi, O. A. and W. E. Nelson, "An Analytical and Flight Test Approach to the Reduction of Pilot-Induced Oscillation Susceptibility," J. Aircraft, Vol. 1, No. 4, July-Aug. 1964, pp. 178-184.
18. "Lockheed Flight Testing AH-56 with Modified Controls, Blades," Av. Week, Vol. 92, No. 13, pp. 66-67.
19. Peters, Richard A., Dynamics of the Vestibular System and Their Relation to Motion Perception, Spatial Disorientation, and Illusions, NASA CR-1309, Apr. 1969.
20. Stapleford, Robert L., Richard A. Peters and Fred R. Alex, Experiments and a Model for Pilot Dynamics with Visual and Motion Inputs, NASA CR-1325, May 1969.
21. Ringland, R. F., R. L. Stapleford and R. E. Magdaleno, Motion Effects on an IFR Hovering Task - Analytical Predictions and Experimental Results, Systems Technology, Inc., Tech. Rept. No. 188-1, Oct. 1970 (forthcoming NASA CR- ).
22. Newell, F. D., "Inflight and Ground Simulation Measurements of Pilot Transfer Characteristics in the Compensatory Roll Tracking Task," Third Annual NASA-University Conference on Manual Control, NASA SP-144, 1967, pp. 99- 119.
23. Dolkas, Constantine B. and John D. Stewart, Effect of Combined Linear and Oscillatory Acceleration on Pilot Attitude-Control Capabilities, NASA TN D-2710, Mar. 1965.
24. Jex, H. R., G. L. Teper, D. T. McRuer and W. A. Johnson, A Study of Fully-Manual and Augmented-Manual Control Systems for the Saturn V Booster Using Analytical Pilot Models, NASA CR-1079, July 1968.
25. Denery, Dallas G. and Brent Y. Creer, Evaluation of a Pilot Describing Function Method Applied to the Manual Control Analysis of a Large Flexible Booster, NASA TN D-5149, Apr. 1969.
26. Roth, Emanuel M., ed., Compendium of Human Responses to the Aerospace Environment, Volume II, Sections 7-9, NASA CR-1205 (II), Nov. 1968.
27. Beaupeurt, J. E., F. W. Snyder, S. H. Brumaghim, et al, Ten Years of Human Vibration Research, Boeing Co., Wichita Div., Rept. No. D2-7888, Aug. 1969.



28. Bryce, W. D., A Review and Assessment of Criteria for Human Comfort Derived from Subjective Responses to Vibration, National Gas Turbine Establishment Rept. No. R. 286, Dec. 1966.
29. von Gierke, H. E., "Response of the Body to Mechanical Forces - An Overview," paper presented at the Conference on Prevention of and Protection Against Accidental Explosion of Munitions, Fuels and Other Hazardous Mixtures, New York Academy of Sciences, New York, 10-13 Oct. 1966.
30. Buckhout, Robert, A Working Bibliography on the Effects of Motion on Human Performance, MRL-TDR-62-77, July 1962.
31. Chiles, W. Dean and Carolyn L. Custer, Summaries of Research on the Human Performance Effects of Vibration, AMRL TR-67-172, Nov. 1963.
32. Soliday, S. M. and B. Schohan, A Simulator Investigation of Pilot Performance during Extended Periods of Low-Altitude, High-Speed Flight, NASA CR-63, June 1964.
33. Rosenberg, Bruce and Robert Segal, The Effects of Vibration on Manual Fire Control in Helicopters, Franklin Institute Research Labs. Tech. Rept. 1-168, Mar. 1966.
34. Schubert, Dale W., Jerome S. Pepi and Frank E. Roman, Investigation of the Vibration Isolation of Commercial Jet Transport Pilots during Turbulent Air Penetration, NASA CR-1560, July 1970.
35. Gillies, J. A., ed., A Textbook of Aviation Physiology, Pergamon Press, New York, 1965.
36. Sadoff, Melvin and C. B. Dolkas, "Acceleration Stress Effects on Pilot Performance and Dynamic Response," Second Annual NASA-University Conference on Manual Control, NASA SP-128, 1966, p. 241-257.
37. Little, V. Z., S. D. Leverett and B. O. Hartman, "Psychomotor and Physiologic Changes During Accelerations of 5, 7, and 9 +G<sub>x</sub>," Aerospace Medicine, Vol. 39, No. 11, Nov. 1968, pp. 1190-1197.
38. Creer, Brent Y., Harald A. Smedal and Rodney C. Wingrove, Centrifuge Study of Pilot Tolerance to Acceleration and the Effects of Acceleration on Pilot Performance, NASA TN D-337, Nov. 1960.
39. Hughes, Robert J., Allen H. Henke, Robert L. Schultz, et al, Helmet-Mounted Sight/Display Applications, Vol. I, Summary and Conclusions, AFFDL-TR-69-118, Apr. 1970.

14. Ashkenas, Irving L., Henry R. Jex and Duane T. McRuer, Pilot Induced Oscillations: Their Cause and Analysis, Systems Technology, Inc., Tech. Rept. No. 239-2 (Northrop-Norair Rept. No. NOR 64-143), 20 June 1964 (AD 481 994).
15. Jex, H. R., Summary of T-38A PIO Analysis, Systems Technology, Inc., Tech. Rept. No. 239-1, 25 Jan. 1963.
16. Abzug, Malcolm J., High-Speed Stability and Control Problems as They Affect Flight Testing, AGARD Rept. 120, 1957.
17. Levi, O. A. and W. E. Nelson, "An Analytical and Flight Test Approach to the Reduction of Pilot-Induced Oscillation Susceptibility," J. Aircraft, Vol. 1, No. 4, July-Aug. 1964, pp. 178-184.
18. "Lockheed Flight Testing AH-56 with Modified Controls, Blades," Av. Week, Vol. 92, No. 13, pp. 66-67.
19. Peters, Richard A., Dynamics of the Vestibular System and Their Relation to Motion Perception, Spatial Disorientation, and Illusions, NASA CR-1309, Apr. 1969.
20. Stapleford, Robert L., Richard A. Peters and Fred R. Alex, Experiments and a Model for Pilot Dynamics with Visual and Motion Inputs, NASA CR-1325, May 1969.
21. Ringland, R. F., R. L. Stapleford and R. E. Magdaleno, Motion Effects on an IFR Hovering Task - Analytical Predictions and Experimental Results, Systems Technology, Inc., Tech. Rept. No. 188-1, Oct. 1970 (forthcoming NASA CR- ).
22. Newell, F. D., "Inflight and Ground Simulation Measurements of Pilot Transfer Characteristics in the Compensatory Roll Tracking Task," Third Annual NASA-University Conference on Manual Control, NASA SP-144, 1967, pp. 99- 119.
23. Dolkas, Constantine B. and John D. Stewart, Effect of Combined Linear and Oscillatory Acceleration on Pilot Attitude-Control Capabilities, NASA TN D-2710, Mar. 1965.
24. Jex, H. R., G. L. Teper, D. T. McRuer and W. A. Johnson, A Study of Fully-Manual and Augmented-Manual Control Systems for the Saturn V Booster Using Analytical Pilot Models, NASA CR-1079, July 1968.
25. Denery, Dallas G. and Brent Y. Creer, Evaluation of a Pilot Describing Function Method Applied to the Manual Control Analysis of a Large Flexible Booster, NASA TN D-5149, Apr. 1969.
26. Roth, Emanuel M., ed., Compendium of Human Responses to the Aerospace Environment, Volume II, Sections 7-9, NASA CR-1205 (II), Nov. 1966.
27. Beaupeurt, J. E., F. W. Snyder, S. H. Brumaghim, et al, Ten Years of Human Vibration Research, Boeing Co., Wichita Div., Rept. No. D2-7888, Aug. 1969.

HUMAN OPERATOR PERFORMANCE  
IN HYPOXIC STRESS

Clyde R. Replogle, Ph.D

Linton L. Kulak, Captain, U.S.A.F., MC

Frank M. Holden, M.D.

F. Joas, M.D.

Robert E. Gold, Major, U.S.A.F., MC      George Potor, Jr., M.D.

Aerospace Medical Research Laboratory  
Aerospace Medical Division  
Air Force Systems Command  
Wright-Patterson Air Force Base, Ohio 45433

ABSTRACT

This experiment was designed to assess the value of several different tracking tasks in quantitatively measuring the effects of hypoxia on human operator performance. Each subject was required to perform three tracking tasks. One was an adaptive first order unstable task. The second represented stable third order longitudinal airframe dynamics. The last was a two axis combination of the first two, with the stable task represented by the vertical display axis and the unstable task on the horizontal axis. Hypoxic stress was simulated by breathing O<sub>2</sub>, N<sub>2</sub> mixtures representing sea level, 12,000 ft and 22,000 ft altitude. The studies employed six well trained subjects breathing the appropriate gas mixtures for two minutes. The experimental factors were randomly ordered with two replications per set of factors. A two by two analysis of variance was employed to provide estimates of the reliability of the measurements. The results indicate that the adaptive unstable task is significantly sensitive to hypoxic stress, whereas to identify similar changes in the stable task requires frequency domain analysis. There is some indication that the unstable task may be sensitive to 12,000 ft simulated hypoxia after only 2 minutes of exposure.

## INTRODUCTION

The capability of a man to effectively control a weapons system is routinely evaluated in terms of the guidance error or the closed loop error. The measurement of closed loop error has been shown to be an effective measure in determining the limits of man's control capability while being exposed to stress in terms of the environment, complexity of task, mission goals, and psychological factors. Closed loop error, however, cannot provide the basis for predictive models of human control capability. The man in a control situation will utilize his maximum capability to reduce or minimize closed loop error until the environment, task, mission goal or psychological factors overwhelm him or terminate the control task.

To evaluate the performance of a man in a control situation, the investigator is obligated to evaluate how the man is achieving effective control. If the stresses upon the man are affecting his ability to control the weapons system and the man can switch to alternative modes of control while maintaining closed loop error at a minimum, then evaluation of the man as an input-output processor will show the changes in his operating behavior while analysis of closed loop error will be uninformative. If changes in the man's mode of control are correlated with the stresses upon the man then they ought to be correlated with the psychological and physiological changes induced by the stresses.

The techniques for evaluating man as an input-output processor have been developed and applied to many operational problems (1,2,3). The majority of these techniques utilize linear systems analysis and systems identification theory. The results of these analyses are phrased in terms of the parameters of the linear system which best describes the man's control behavior. These parameters can be described by the operator's gain, the operator's effective time delay, the operator's phase margin at unity crossover gain, and the power of the uncorrelated signal in the operator's output.

Jex in 1966 described an unstable control task which he claimed was effective in evaluation of the operator's effective time delay (4). The task that Jex described becomes increasingly more difficult as time and the operator's

ability to maintain closed loop error at a minimum progresses. By modifying the task that Jex describes in a manner described below, it is possible to obtain a real time estimate of the operator's effective time delay. The modified unstable tracking task can be used to obtain an estimate of a parameter of the human operator as he performs a controlled task.

This report describes an experiment utilizing standard tracking tasks and the modified unstable tracking task in an attempt to demonstrate that measurement of human operator parameters is a sensitive technique for evaluation of human operator performance under stress.

### EXPERIMENTAL DESIGN

The experiment is designed to evaluate the performance of an operator in a compensatory tracking task at sea level followed by the same task at a simulated altitude of either 12,000 or 22,000 feet. Each run of the experiment consisted of two periods of tracking. Each period was preceded by one minute of prebreathing at the indicated altitude followed by one minute of tracking. Randomization of the order of presentation of the simulated altitudes and tasks to the subjects was done in order to minimize the effects of learning and anticipation of experimental factors.

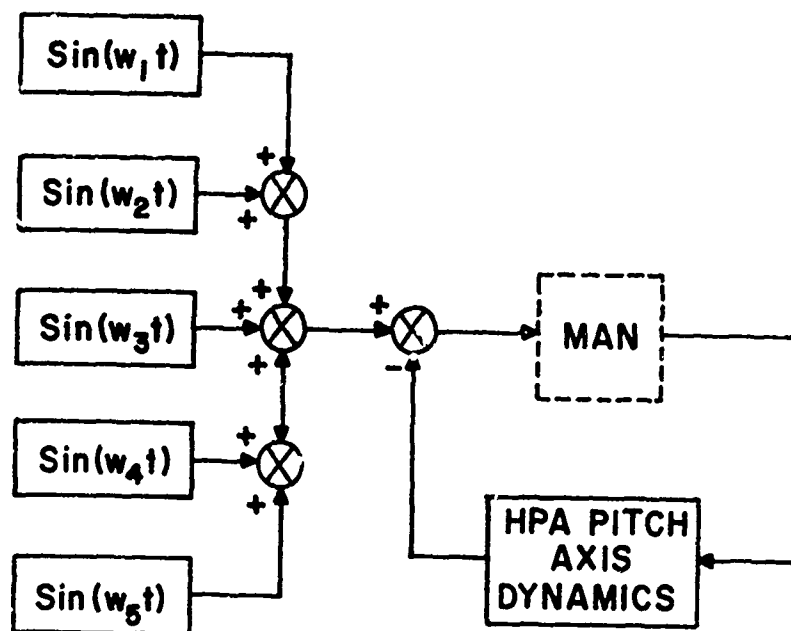
Six subjects were evaluated. Each subject performed the same task on two different occasions. Three compensatory tracking tasks were employed. The first was a single axis stable tracking task. The dynamics of the stable tracking tasks were representative of a high performance aircraft pitch axis control system. The second task was an unstable single axis tracking task modified as described below. The third task consisted of a dual axis tracking task combining the stable tracking task on the vertical axis and the unstable tracking task on the horizontal axis. The data was sampled at a rate of 50 samples per second. The data were reduced by calculating the mean error and the variance of the error for the displayed error signals, and the mean unstable pole and the variance of the unstable pole in the unstable tasks. In addition, empirical probability density functions were generated for the displayed

error and the unstable pole signals. The mean squared error scores and the variance of the mean squared error scores were subjected to analysis of variance utilizing a random variable design.

The stable tracking task was chosen to be representative of the pitch axis dynamics of a high performance aircraft. The dynamics of this stable tracking task are typical of a third order system with a pole at the origin. The forcing function used in the stable tracking task consisted of the sum of five sine waves whose frequencies were chosen to simulate Gaussian white noise buffeting (Figure 1). The operator has no control over the dynamics represented in the stable tracking task. It is, therefore, anticipated that at altitude no effect on RMS error will be observed. If the operator is forced by the affects of altitude to change his internal structure as an operator, he can do so while operating the stable task and maintaining identical or similar mean squared error distribution.

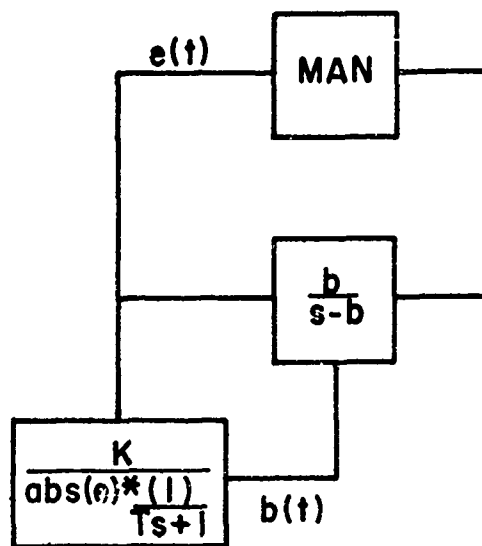
The unstable tracking task is a first order system with a single pole to the right of the imaginary axis. The unstable tracking task as described by Jex et al was modified in the following manner (Figure 2). A norm of the displayed error namely absolute value of the error was filtered with the first order linear filter and then divided into a constant  $K$ . This provides a real time function called  $b$ . The function  $b$  is always positive and is used as a moving pole in the unstable element. By appropriate choices of the values for the constant  $K$  and the time constant in the first order filter, one can prevent skilled trackers from losing control of the task while at the same time forcing him to maintain a low mean squared error.

The above modification of the unstable tracking task provides the following advantages. The operator while controlling such a system can optimize one of two variables. He can either optimize the displayed error which he is instructed to do or he can optimize the difficulty of the controlled element by operating at a point which provides a manageable unstable element. In either case in order for the operator to effectively control the system, he must either



### STABLE TASK

Figure 1 Stable Tracking Task Representative of the Pitch Axis Control System of a High Performance Aircraft



## UNSTABLE TASK

Figure 2 Modified Unstable Tracking Task



adjust his internal gain or he must maintain an effective time delay which is smaller than the value of the unstable pole at all times. Jex et al have observed that the unstable tracking task forces a mode of controlling by the operator which is consistent with pure gain controlling. This is true as long as the operator maintains an effective time delay shorter than the value of the unstable pole. The value of the signal  $b$  or the distribution of his displayed error therefore provides a measure of either the operator's gain or his effective time delay. Jex has shown that in his formulation of an unstable element the critical value of the unstable pole is proportional to the effective time delay of the operator.

If the operator's performance at 22,000 feet is different than his performance at sea level, then the modification of the unstable tracking task as described above should indicate either a change in the mean value of the signal  $b$  or a change in his RMS error. Either of these changes or both in combination indicate that there is an internal change in the structure of the human operator.

## RESULTS

The results are straightforward and require little interpretation. Referring to Table 1, it is apparent that the RMS error in the stable axis was not affected by the 22,000 feet altitude. The RMS error in the unstable tracking task is significantly affected by altitude, and the mean operating point  $b$  in the combined task unstable axis is significantly affected by the altitude of 22,000 feet.

Further analysis of the data will include identification of the linear portion of the human operator as a function of altitude. The analysis of variance will be repeated on the parameters of the operators. It is anticipated that examination of the internal parameters of the operator while performing the stable tracking task will demonstrate an affect due to the simulated altitude. Support for this statement arises as a result of examining the data for the unstable tracking task at 22,000 feet. It is apparent that the majority of the operators in the unstable axis attempted to maintain the average operating points  $b$  at an identical point irrespective of altitude while allowing mean squared error to change.

TABLE I

Results of Analysis of Variance Comparing the Differences in  
the Various Scores at Ground Level and 22,000 Ft Altitude Across Subjects

TASK	SCORE	MAIN EFFECT df = 1	INTERACTIONS df = 5	F RATIO
Stable	RMS error	1.69	11.99	.8457
Unstable	RMS error	0.01	64.97	.00092**
Combined	mean b(t)	6.98	5.54	7.56*

\*\* > p .99

\* > p .95

Examination of the empirical probability density curves (Figures 3-5) verifies that the error curve for the unstable task has a broader variance at altitudes. The b curves however shift their mean to a lower value at higher altitudes. The variance due to interaction was too large to demonstrate significance in the change of the mean b at altitude. If the mean b scores are normalized however a Student's T test shows significance at the .01 level.

Figures 3a and 3b are the empirical probability density functions for the displayed error in the stable tracking task. There is relatively little difference between the curves at the control altitude, sea level, and at the 22,000 feet altitude. Figures 4a and 4b are the probability density functions for both b and e in the unstable tracking task. Not only does the shape of the error curve e change but also the mean of the b curve is lower at 22,000 feet and has a broader variance at 22,000 feet. Figures 5a and 5b are the probability density functions for the combined task at control and at sea level and at 22,000 feet. Again, there is relatively little change in the error curves for the vertical axis whereas the mean value for the b curve shifts to a lower point at 22,000 feet.

## DISCUSSION

The purpose of these experiments is not to evaluate a unique way of identifying a performance measure. Rather, the purpose of these experiments is to demonstrate that control theory principles can be used to identify changes in human operator performance as a result of environmental factors. The data clearly demonstrates that standard measurements of error are insensitive to changes in human operator performance at 22,000 feet. That changes in the human operator occur at 22,000 feet is evidenced by the changes in the unstable tracking task parameters. One of the exciting aspects of the experiments was that the same changes and effects were suggested at 12,000 feet. The effects at 12,000 feet, however, were severely masked by the large amount of subject variance and interaction variance.

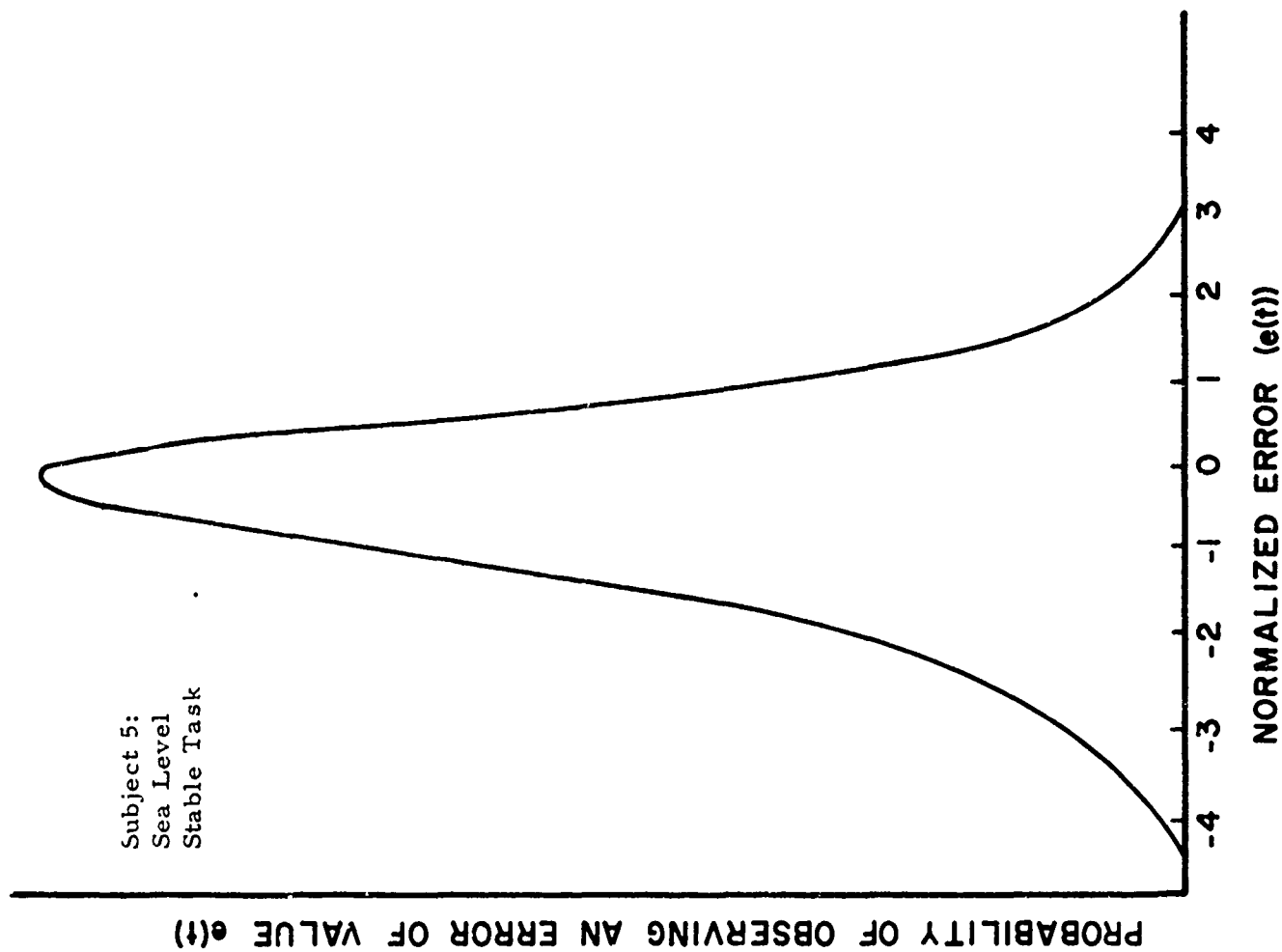


Figure 3a Representative Empirical Probability Density Function of Closed Loop Error  $e(t)$  in the Stable Task at Sea Level

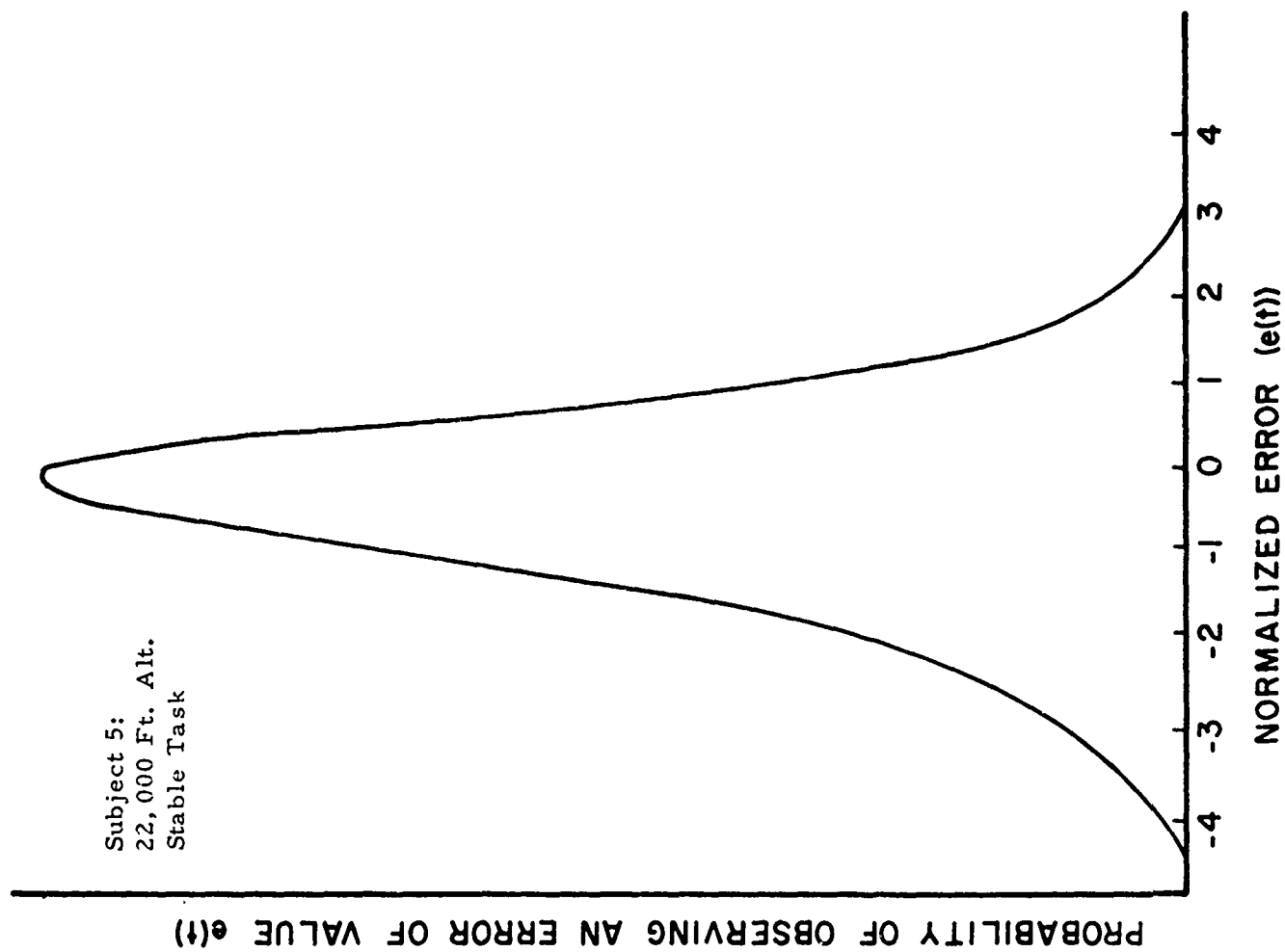


Figure 3b Representative Empirical Probability Density Function of Closed Loop Error  $e(t)$  in the Stable Task at 22,000 Feet.

Subject 5:  
Sea Level  
Unstable Task

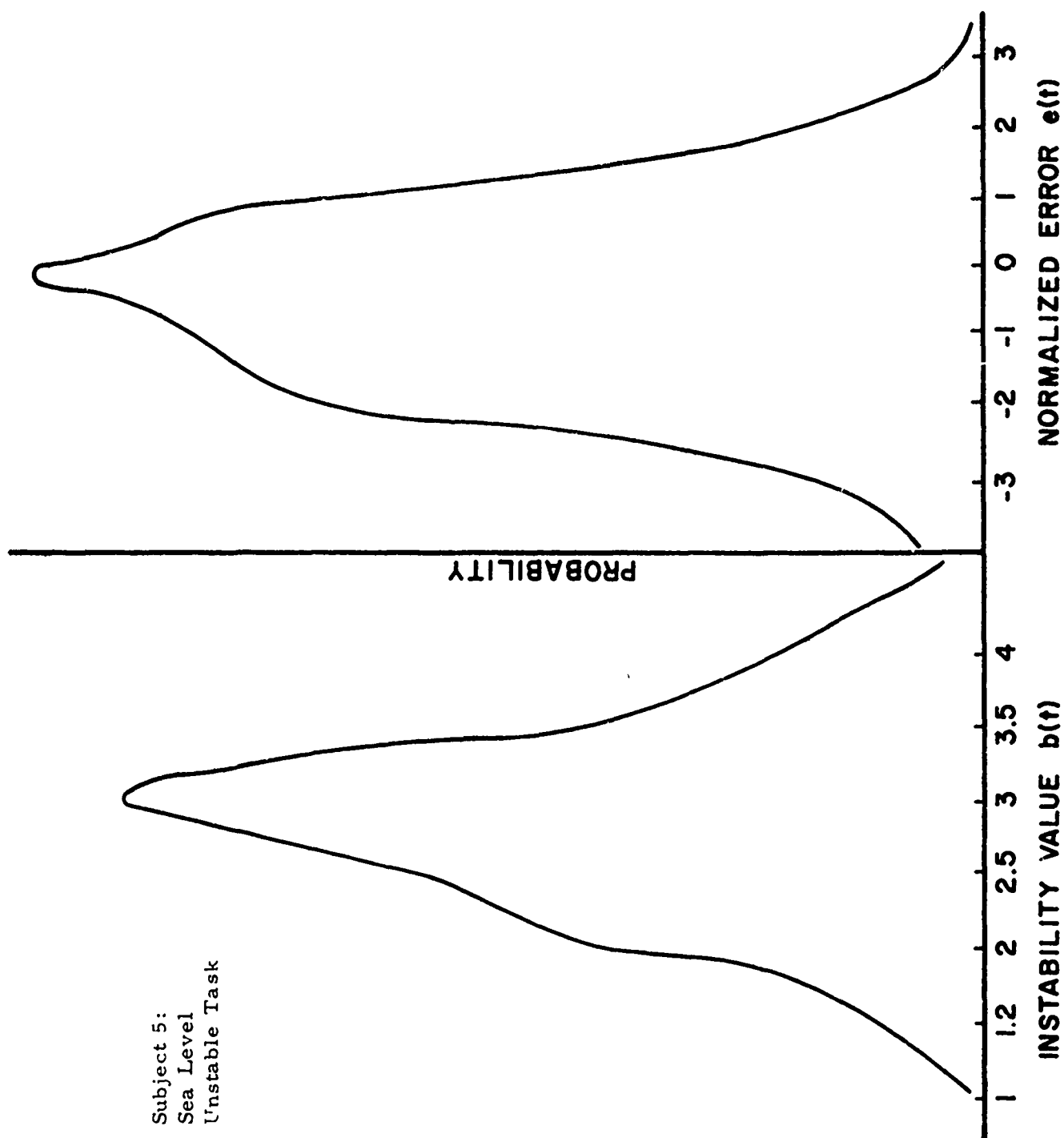


Figure 4a Representative Probability Density Functions for  $b(t)$  and Closed Loop Error  $e(t)$  in the Unstable Task at Sea Level

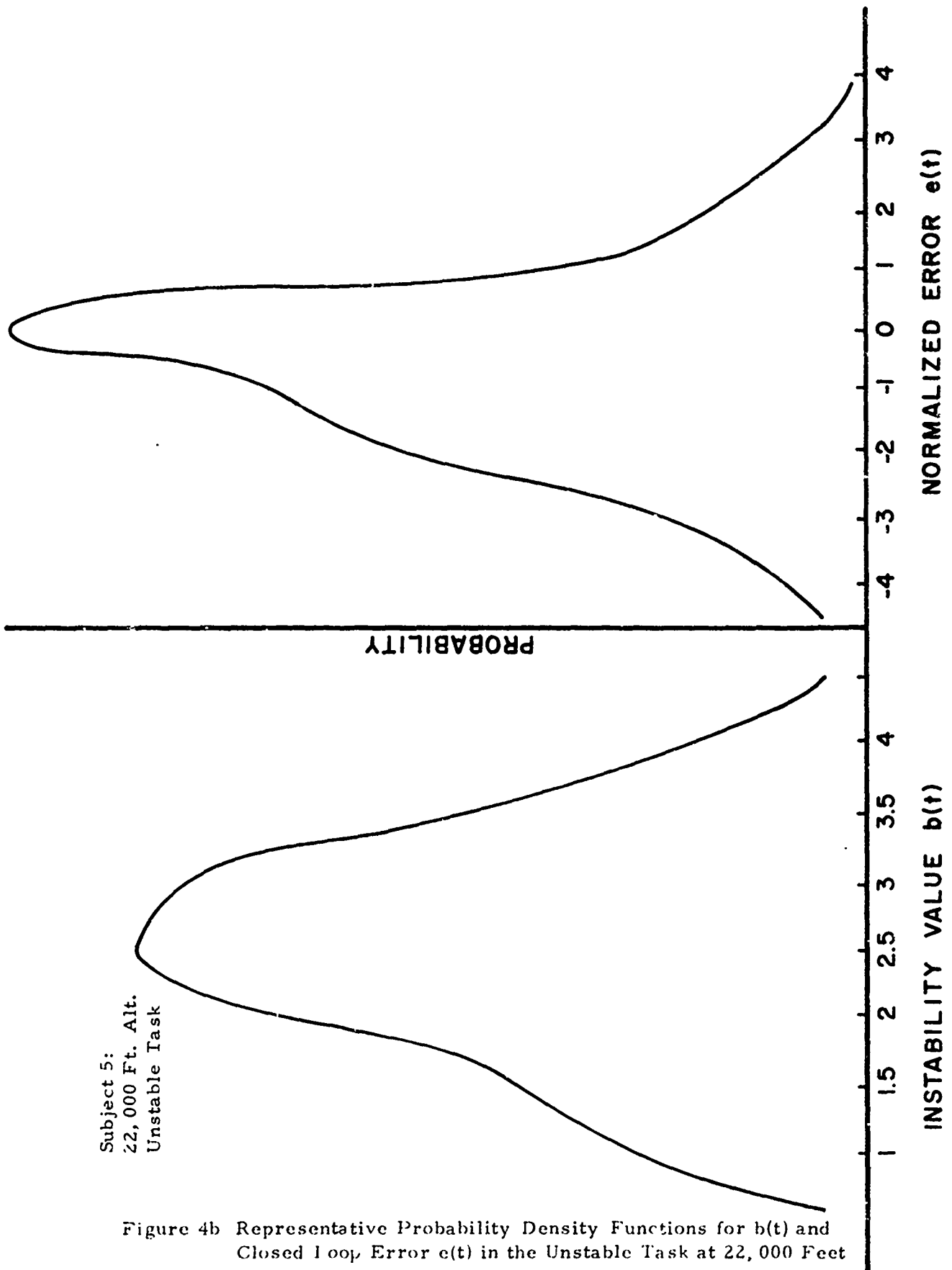


Figure 4b Representative Probability Density Functions for  $b(t)$  and Closed Loop Error  $e(t)$  in the Unstable Task at 22,000 Feet

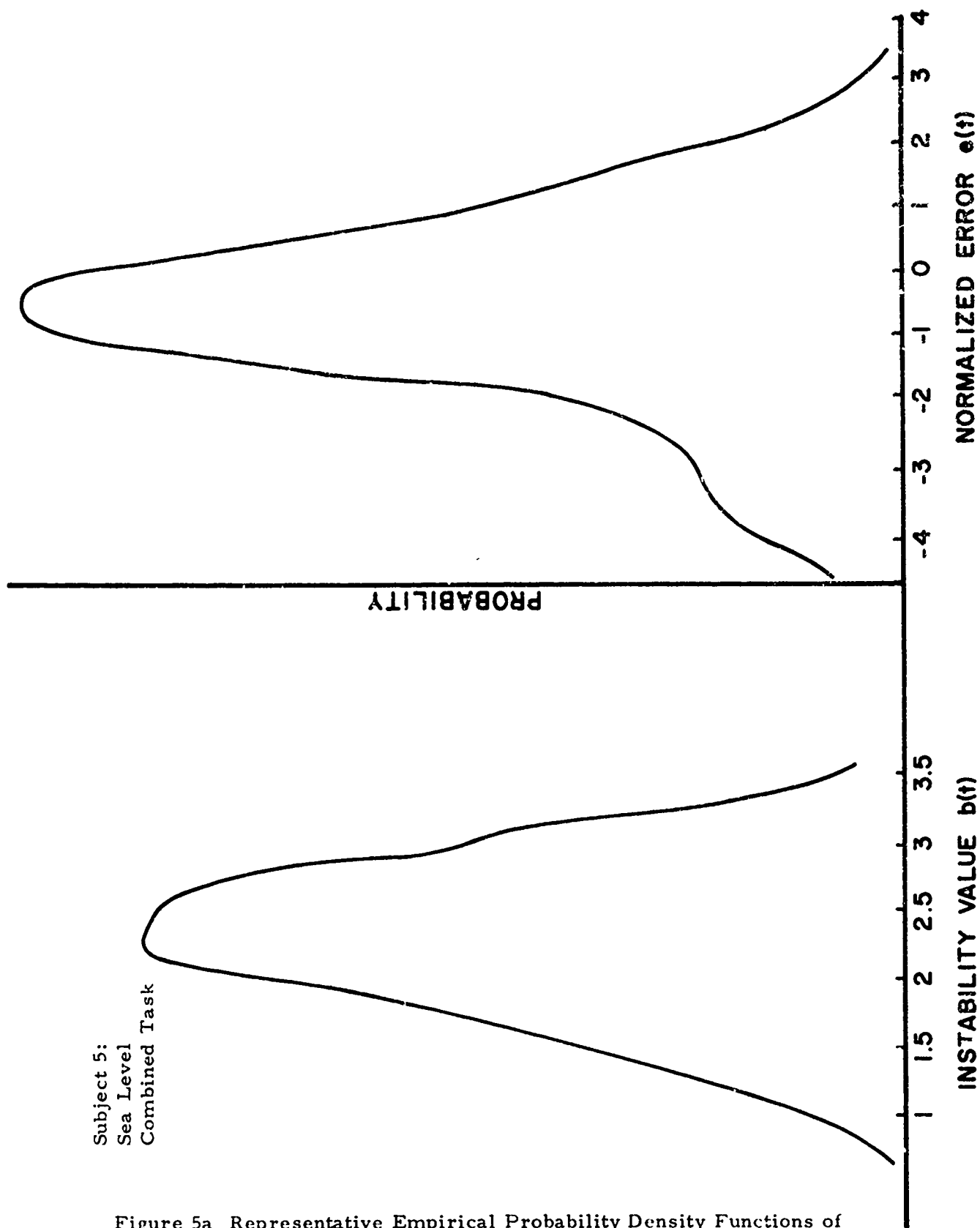


Figure 5a Representative Empirical Probability Density Functions of Vertical Axis Closed Loop Error  $e(t)$  and Horizontal Axis  $b(t)$  Function at Ground Level



Subject 5:  
22,000 Ft. Alt.  
Combined Task

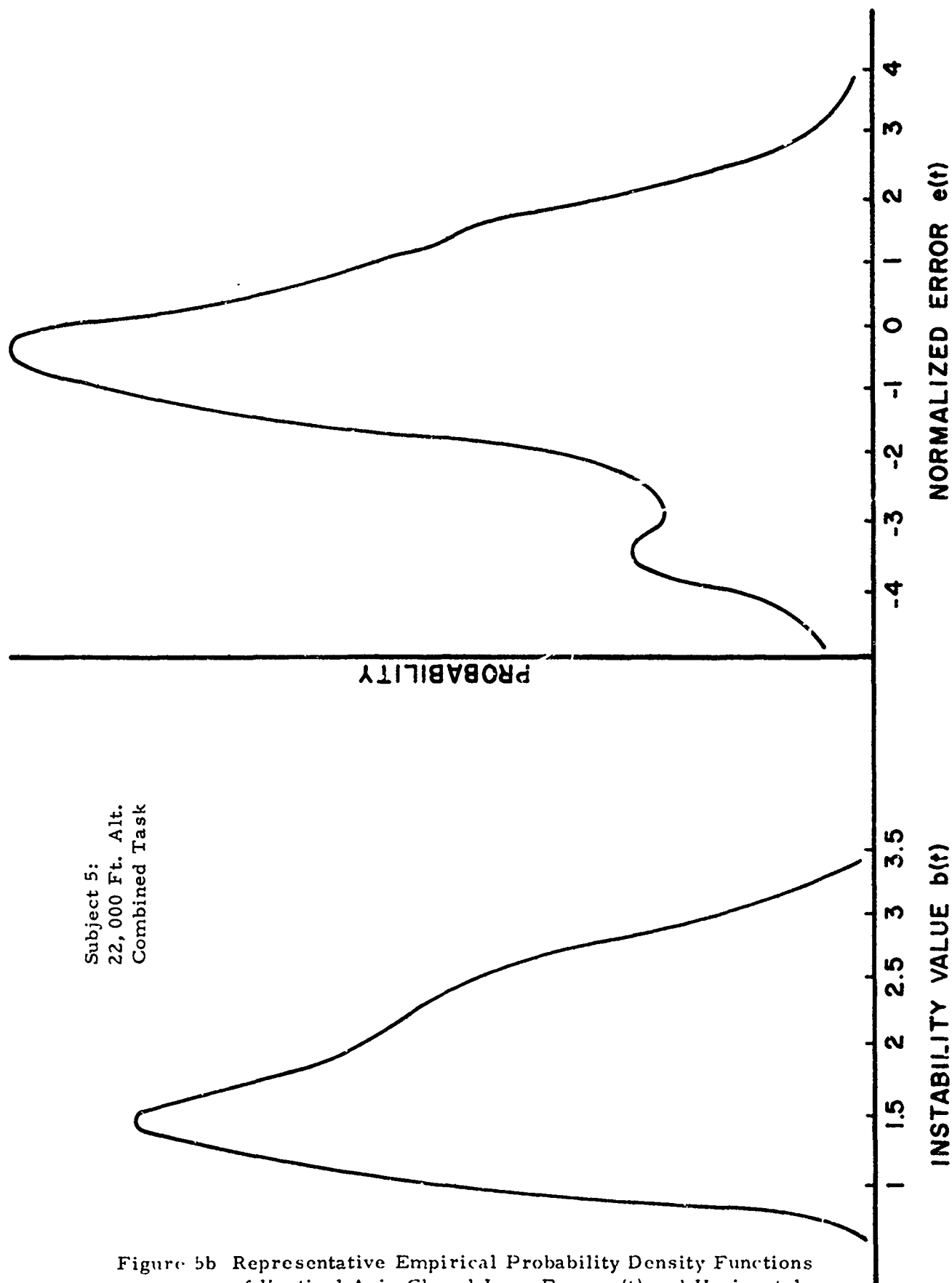


Figure 5b Representative Empirical Probability Density Functions of Vertical Axis Closed Loop Error  $e(t)$  and Horizontal Axis  $b(t)$  Function at 22,000 Feet

## SUMMARY

Although the performance of a man-machine control system is best represented as a function of the closed loop system error, the compensatory actions of the human operator will obscure the effects of stress on the man until the point is reached where his compensation is not effective. In order to predict this point instead of merely observing it, the parameters of the human operator, the effect of stress on these parameters, and the range of control of these parameters must be described.

## REFERENCES

1. McRuer, Duane, Dunstan Graham, Ezra Krendel, and William Reisener, Jr, Human Pilot Dynamics in Compensatory Systems: Theory, Models, and Experiments with Controlled Element and Forcing Function Variations, AFFDL-TR-65-15, Air Force Flight Dynamics Laboratory, Wright-Patterson Air Force Base, Ohio, July 1965.
2. Weir, David H., and Anil V. Phatak, Model of Human Operator Response to Step Transitions in Controlled Element Dynamics, NASA CR-671, National Aeronautics and Space Administration, January 1967.
3. Bekey, C. A., "The Human Operator as a Sampled-Data System," IRE Trans., Vol HFE-3, No. 2 September 1962, 11 43-51.
4. Jex, H. R., J. D. McDonnell, and A. V. Phatak, A Critical Tracking Task for Man-Machine Research Related to the Operator's Effective Delay Time, Part I: Theory and Experiments with a First-Order Divergent Controlled Element, NASA CR-616, National Aeronautics and Space Administration, November 1966.
5. Ali, S. M., "Human Describing Function in Second Order Compensatory Tracking Tasks," Masters Thesis, GGC/EE/70-1, Air Force Institute of Technology, Wright-Patterson Air Force Base, Ohio, 1970.
6. Westbrook, C. B., R. O. Anderson, and P. E. Pietrzak, Handling Qualities and Pilot Workload, AFFDL-FDCC-TM-66-5, Air Force Flight Dynamics Laboratory, Wright-Patterson Air Force Base, Ohio 1966.

PAPER NO. 32

## THE USE OF MODELS IN THE STUDY OF WOUND BALLISTICS

A. A. WOODWARD

Ballistic Research Laboratories  
U.S. Army Aberdeen Research and Development Center  
Aberdeen Proving Ground, Maryland

### ABSTRACT

An overall description is presented of some of the characteristics of a new generalized wound ballistics model that is in the process of development. The model is probabilistic, and it is being formulated so as to allow evolving modifications as improved input data become available or new requirements put on the type of outputs desired. Included are descriptions of a number of modeling methods that are used to generate input data for the generalized model; among these are physical, biological, and mathematical models.

### DISCUSSION

The science of military ballistics deals with the entire phenomenal history of a weapon projectile, beginning with its launching and ending when its effects have been exerted on a target. Our branch of science, wound ballistics, focuses on the effects of weaponry on one specific very complex target, the human body. In brief, we are concerned with casualties, how they are produced, the effectiveness of different weapons (ours and the enemy's) in producing them, and their effects on the military capabilities of men. Ultimately our function is to make predictions of the numbers, types and severity of casualties anticipated among men in combat and of effects of casualties sustained on the ability of the men to accomplish military missions.

Modeling techniques of different kinds are peculiarly useful, and often necessary, tools to us for two primary reasons. On one hand, like others participating in this Symposium, we cannot conduct direct experiments on the phenomena of primary interest to us, the mechanisms of injury production in and the effects of injuries on the functions of

the human body. Modeling methods make possible indirect approaches to the quantitative study of these phenomena. On the other hand, we must deal often with complex multivariant problems: e.g., estimation of casualties of all types, and of their effects, to be expected among soldiers in groups of different sizes performing different kinds of tasks concurrently and in sequence under all kinds of combat conditions while exposed to varying mixes of weaponry. Problems of this kind can be handled by appropriate mathematical models that are practical if one has accumulated sufficient input data and enjoys the support of modern sophisticated computer facilities. At this point one notes that in the discussion that follows the work described is the result of a group effort for which the present author is acting as a reporter.

As a framework within which to discuss some of the ways in which we utilize modeling methods, we may select our currently most significant effort, the development of a completely generalized wound ballistics model. Figure 1 illustrates how the anti-personnel action of a weapon may be analyzed as a multi-stage causal sequence.<sup>1</sup> In this figure the blocks indicate end-points of assessment stages, which are indicated by the connecting arrows. The blocks in this diagram are conceptually important, since they constitute isolating interfaces between assessment methods that are qualitatively different. In addition they represent real observable stages, the transitions between which a useful model must express mathematically. However, the bulk of the effort required to develop a model in working form capable of yielding quantitative evaluations must be spent on the assessment stages.

As a result of the conceptual independence of the assessment stages, research efforts to accumulate data and to develop mathematical formulations defining them can proceed concurrently. Moreover, even though the best available knowledge and methods vary considerably from stage to stage, a model can be designed so that it becomes immediately useful as soon as acceptable formulations are available for each assessment stage. Set up in this manner, the model retains the important characteristic of evolutionary capability; as better assessment techniques become available, they can be substituted for those initially utilized without basic modifications or re-design of the model. These features are lacking in wound ballistics models in current use.

Figure 2 shows part of the same scheme with addition of details on the end-point stages. We can use this to examine how we use specific modeling techniques to solve particular problems only generally inferred above. The Wounding Mechanism block lists the primary means by which contemporary anti-personnel weapons cause damage to living tissue. Any particular weapon may involve only one or any combination of these mechanisms. A high velocity bullet, for example, passes violently through tissues, slowing down as it loses kinetic

energy as a result of the resistance presented by the tissues. In its wake a discreet hole remains, a wound tract of completely destroyed and disintegrated tissue; in addition (as we shall see shortly) it causes a considerable amount of damage at a distance in tissues not directly hit by the passing missile. Because tissues (e.g., bone, muscle, lung) vary in penetrability, the missile will lose kinetic energy at different rates in passing through them, leaving a wound tract of varying cross section area. Since the physical parameters of the missile at the moment of impact can be exactly measured, it is desirable to use energetics as the basis of the trauma (damage producing) assessment stage. This can be done if some measurable characteristic of the damaged tissues can be found that is quantitatively relatable to the energetics of the penetrating missile. The volume of the permanent wound tract is a useful, if less than perfect, measure that is used to give an objective assessment procedure. The wound tract volume, incidentally, thus becomes a conceptual model of damage that permits bypassing of the impossible tasks of analyzing cell by cell the physical events occurring during the actual process of tissue destruction.

The next assessment stage, Medical Assessment, is not now amenable to objective treatment because of the complexity of body architecture and the functional interdependence of its component organs and tissues. The best procedure we can use, in order to let the general model become functional, is to submit descriptions of wound tracts to especially qualified medical assessors and accept their best judgment as the basis for establishing estimates of severity of injury to damaged organic subsystems.

Actual wound tracts in human tissues caused by missiles of known energetics are too rarely available for study, so we resort to one of the simplest models to study penetration phenomena. Missiles of any kind can be fired through blocks of 20 percent gelatin, which has the same density and water content as average human tissues. As a tissue model it is reproducible, inexpensive, and transparent. Figure 3 shows a series of photographs, taken by very high speed photographic techniques of a single high velocity bullet passing through such a block.<sup>2</sup> From such photographs one can make measurements from which equations can be derived for retardation, penetration depth, loss in kinetic energy, etc., that can be used to compare the behavior of any kind of missile impacting at any energetic level. In addition, such phenomena as the effects of yaw and tumbling can be observed and measured. Well illustrated is the phenomenon of cavitation produced by high velocity missiles, in which a large temporary cavity is formed, collapses, and reforms for several cycles. This is the process responsible for tissue damage at a distance from the path of the passing missile, and one can readily understand from this picture some of the problems of estimating quantitatively the degree of damage in a tissue from the permanent wound tract alone.

Although 20 percent gelatin is an adequate model for comparative studies, it differs considerably in microstructure and physical properties of some sorts from any particular real tissue. For this reason it is desirable to make firings through real tissues under controlled firing conditions to get data through which the effects of missile penetration through tissues can be related to more abundant data derived from gelatin block models. For this purpose isolated animal tissues may be used. These become highly specialized models for the study of injury in the human tissues that we cannot study directly.

After sufficient data has been made available from studies as those described above, so that generalized quantitative statements can be formulated, it is possible to use these in a much more sophisticated type of model. One such is the Computer Man Program.<sup>3</sup> Figure 4 is a diagrammatic representation of the anatomical basis for this program. Using the plates of an atlas of cross-sectional anatomy,<sup>4</sup> a given transverse section through an actual human body is subdivided into elements 5 mm. square. Each section is assigned a code reflecting the dominant tissue type contained within. Figure 4 shows the resulting geometric transform. With tissue code and location for each of the elements in the reduced human body form illustrated. Figure 5 is a computer print-out of the same section derived from this program. The program is entered with various input data, such as retardation values for each tissue element, the mass, velocity, and striking angle of an impacting missile of interest, and values for minimum velocity for damage for each tissue type. Then the program can compute penetration paths and depths for any number of random hits from any direction, identifying the tissues identified along the way. In its present form the program proceeds to predict incapacitations within the context of the deterministic wound ballistics model now in use. The program can produce still other types of output, such as probability that a random hit will perforate the whole body at any level hit or that a random hit will strike any particular organ or tissue. Given further input data on the retardation produced by armor materials, it will yield penetration and incapacitation outputs for areas of the body covered by personnel armor. The program is readily adaptable to the new generalized wound ballistics model. Further, it is being updated through acquisition of new sets of body sections more nearly representative of the dimensions of the military population. These will allow the program to take into account variation in body sizes in terms of percentiles of the military population, based on a recent (1966) survey of the anthropometrics of Army personnel.

Figure 6 shows the details of the later stages in the casualty sequence. Let us consider the problems of performance evaluation. Granted any combination of dysfunctions (loss of a hand, of 5 percent of the circulating blood, of hearing in one ear) resulting from injury, how does one assess the resultant decrement in the ability

of the injured man to perform necessary tasks (defined as relatively short sequences of motions)? There is a large body of information on task performance of injured men (industrial workers, athletes, disabled veterans), almost none of which is applicable to the problem of the wounded soldier in combat. If for no other reason, this data is largely invalid because the observations were made on men after they had recovered from the injury to some extent, and had undergone considerable learning in the process. We are concerned with the soldier's ability to perform immediately after injury and during short following intervals. The first step is to simplify the problem; of all the possible things a healthy man can possibly do, a relatively small number of them can account for most of what a soldier is called on to do during the course of combat. This kind of reduction has been done for the case of the foot soldier in the course of development of a Combat Effectiveness Test Facility at Ft. Lee, Virginia,<sup>5</sup> based on interviews with veterans in combat during the three most recent wars. Nearly all of the tasks in the catalogue thus produced have been incorporated into a series of courses provided with a largely automated measuring instrumentation system. The course was designed to test whether individual equipment items (weapons, clothing, etc.) caused any degradation in performance.

We have recently finished a series of pilot studies in which the facility is used in a different way, illustrated in Figure 7. The soldier is in the process of shoveling 1400 lbs. of sand from a concrete pit into a hopper suspended from a load cell, which provides measures of the time required to move successive increments of sand. Two kinds of modeling are illustrated. The task condition is a model of the more familiar task of using an entrenching tool to dig a fox hole, modified in order to provide more reliability and sensitivity of measurement than can be achieved in the digging of actual fox holes. The component courses of the whole test facility are arrays of other types of task modeling; and the entire facility, which takes about 7 hours to run completely and involves about 20 miles of walking, is intended to model a sequence and difficulty of tasks that might be encountered during a day of combat.

In this same photograph one can see that the soldier is restrained by a simple device that denies him the use of his preferred arm (he was right-handed), and the awkwardness of his tool handling is easily observed. We have used a number of such devices, which enable us to use an uninjured man as a model of a man wounded in several ways. The model is imperfect in that it simulates only one aspect of injury, the actual loss of a bodily capability. We are in the process of building up a battery of techniques which can be used to explore other aspects of wound injuries, hoping that the combined results of several such methods will allow us more closely evaluate the effects of actual injury. To our knowledge this has not been attempted in a systematic manner previously under controlled conditions.

We have not yet mentioned one significant characteristic of the new overall wound model we are developing. Most of the models under discussion at this Symposium are almost certainly deterministic in nature; i.e., they deal with a sequence of events related temporarily and causally. Our model is to be wholly probabilistic. Randomness operates widely in the case of a soldier in combat. Whether a man will be hit at all, by what kind of weapon, whether any particular organ is damaged and to what degree, the effects of multiple wounds on ability to perform - all of these are governed by randomness with respect to him. A deterministic model can deal with such problems only by tediously working through large numbers of sequences which have to be reprogrammed as variables are altered in order. Given the proper design and input data, a probabilistic model deals directly with randomness. Figure 8 shows a diagram of the logic of a probabilistic model for evaluation of one type of weapon - a kinetic energy projectile (such as a bullet or a grenade fragment).<sup>6</sup> Seemingly complicated, this schema is made up of a number of YES-NO decisions, with probabilities assigned to each pair of decision alternates. These probabilities themselves can be derived from proper computer processing of data derived from deterministic experimental observations. This yields a model that is conceptually a bit complicated but essentially simple mathematically. The final predictive output consists essentially of the combined probabilities of all the decision elements in the model. It is in this form that we can best use casualty predictions, for our problems involve populations rather than individuals. This is still not the main reason for selecting a probabilistic basis for a generalized wound ballistic model. The reason was mentioned earlier. As better data becomes available from improved assessment methodologies, we can continually evolve an improved model or adapt it to new types of problems by merely inserting into a computer program revised probability data without basically redesigning the entire model.



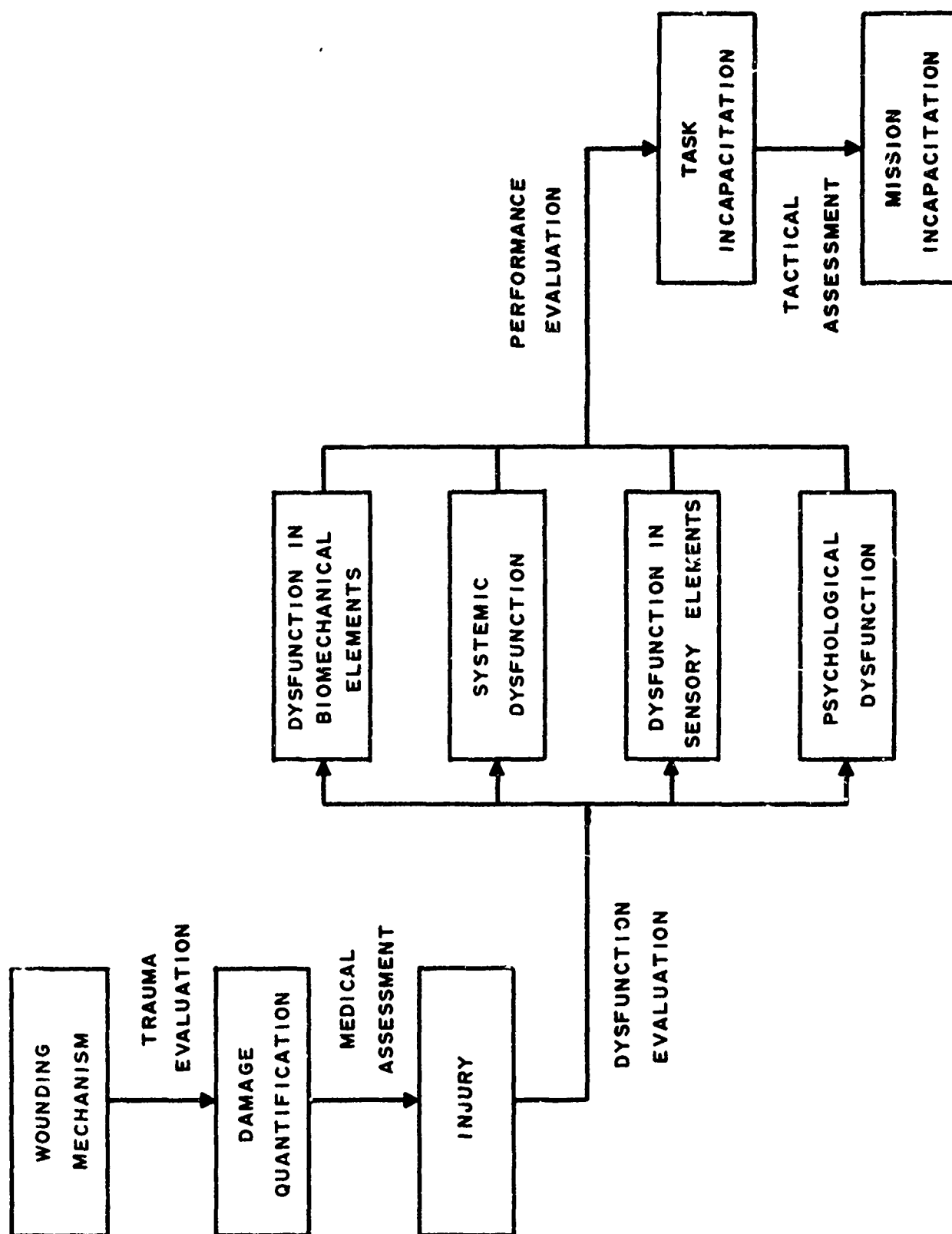


Figure 1. Block diagram of the new wound ballistic model.

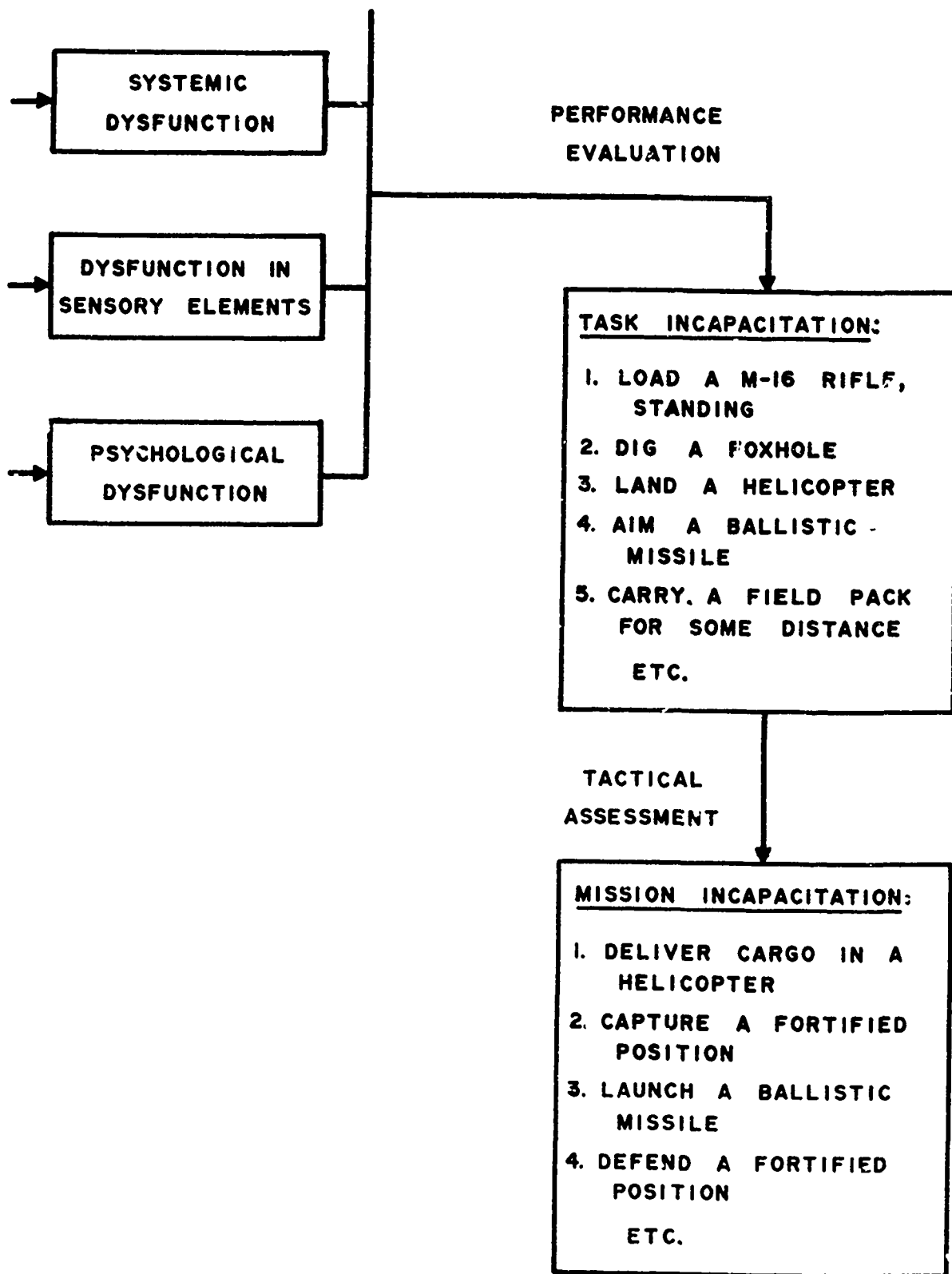


Figure 2. Examples of end-point definitions in the initial stages of the new wound ballistics model.

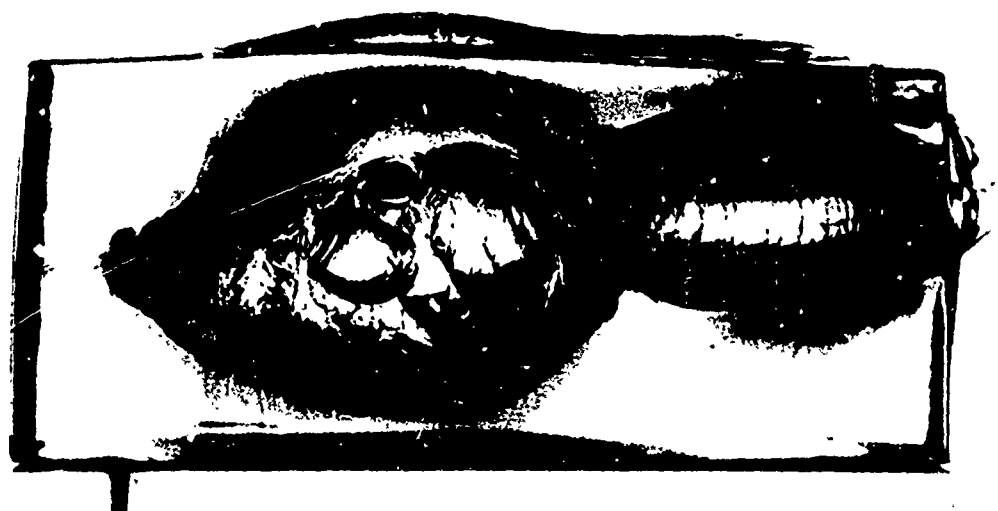
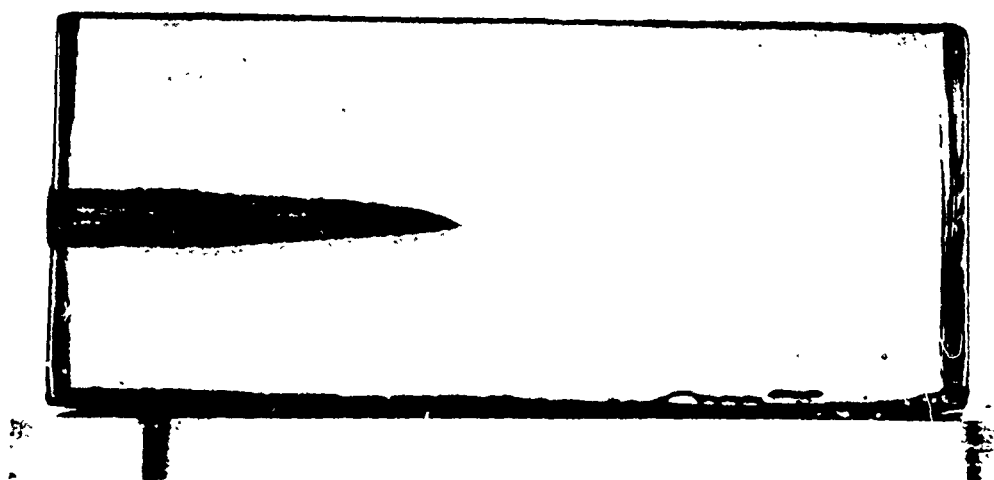
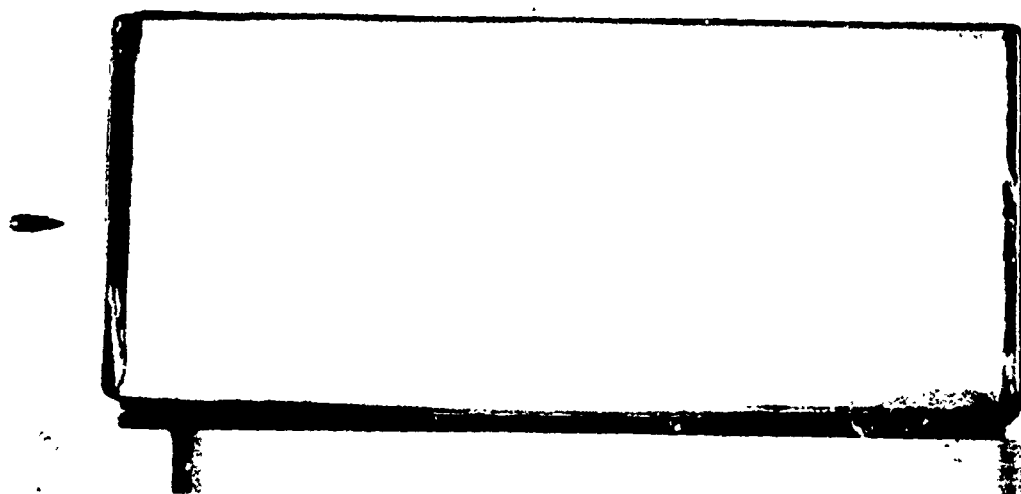


Figure 3. Series of high speed visible light photographs of a single bullet passing through a gelatin block.

# THE COMPUTER MAN

## CROSS SECTION #28

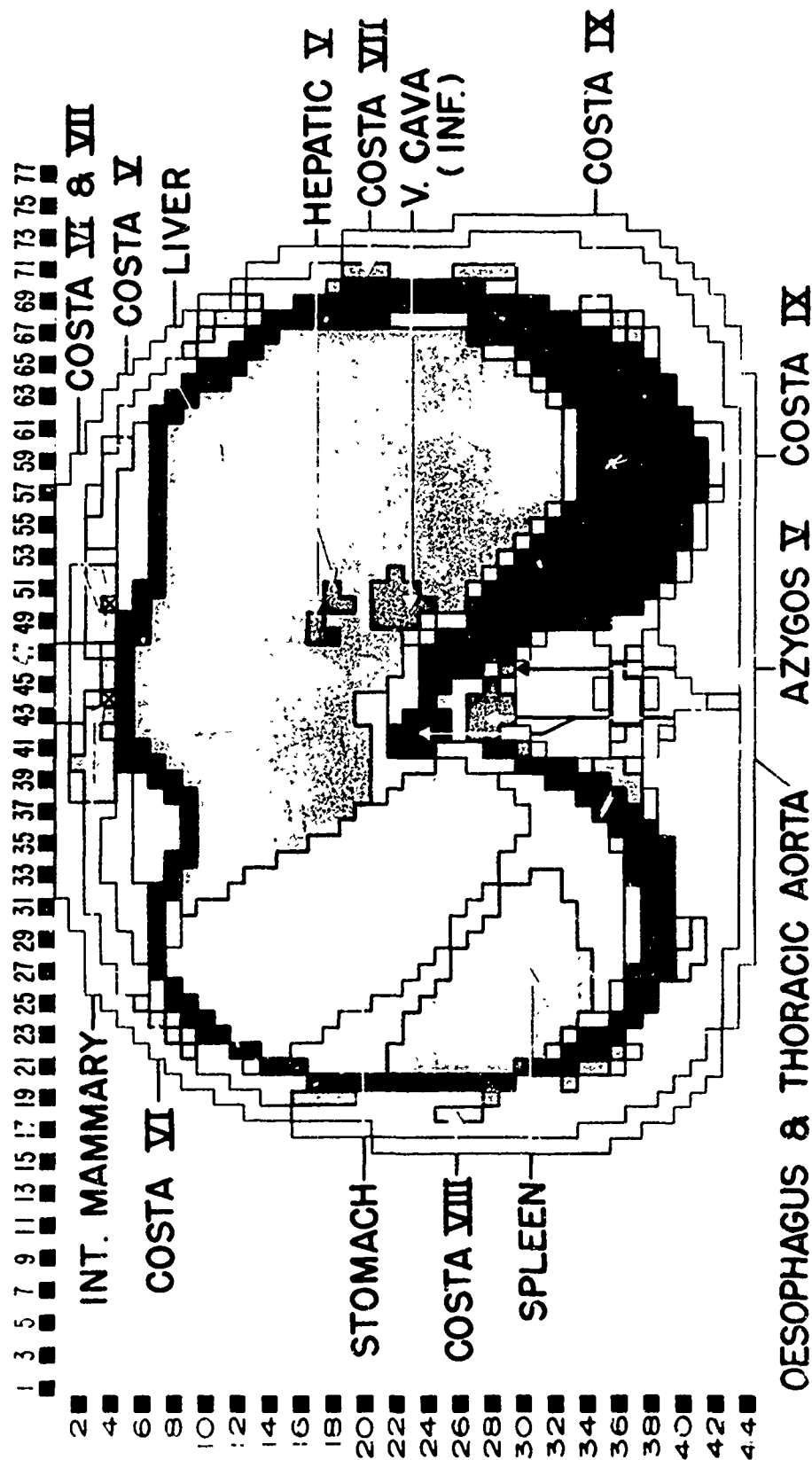


Figure 4. The Computer Man: Diagram of the breakdown of a single human body section into 5 mm. square elements given a single tissue identification.



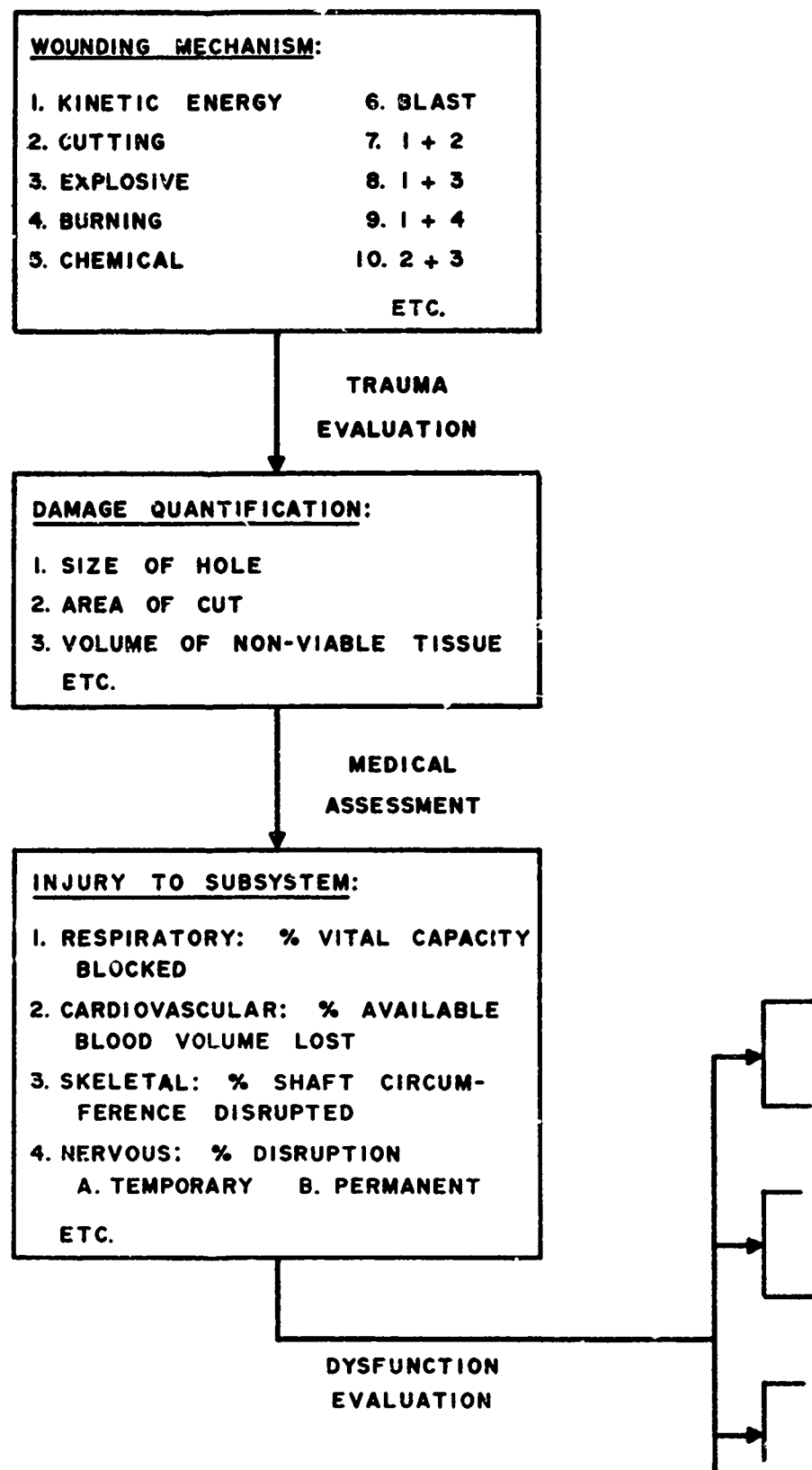


Figure 6. Soldier working at the Hasty Fighting Position course of the Combat Effectiveness Test Facility with one arm completely restrained.



Figure 7. Examples of end-point definitions in the last stages of the new wound ballistics model.

LOGIC FOR DETERMINING THE PROBABILITY OF INCAPACITATING  
A SOLDIER SUBJECTED TO A BATTLEFIELD THREAT

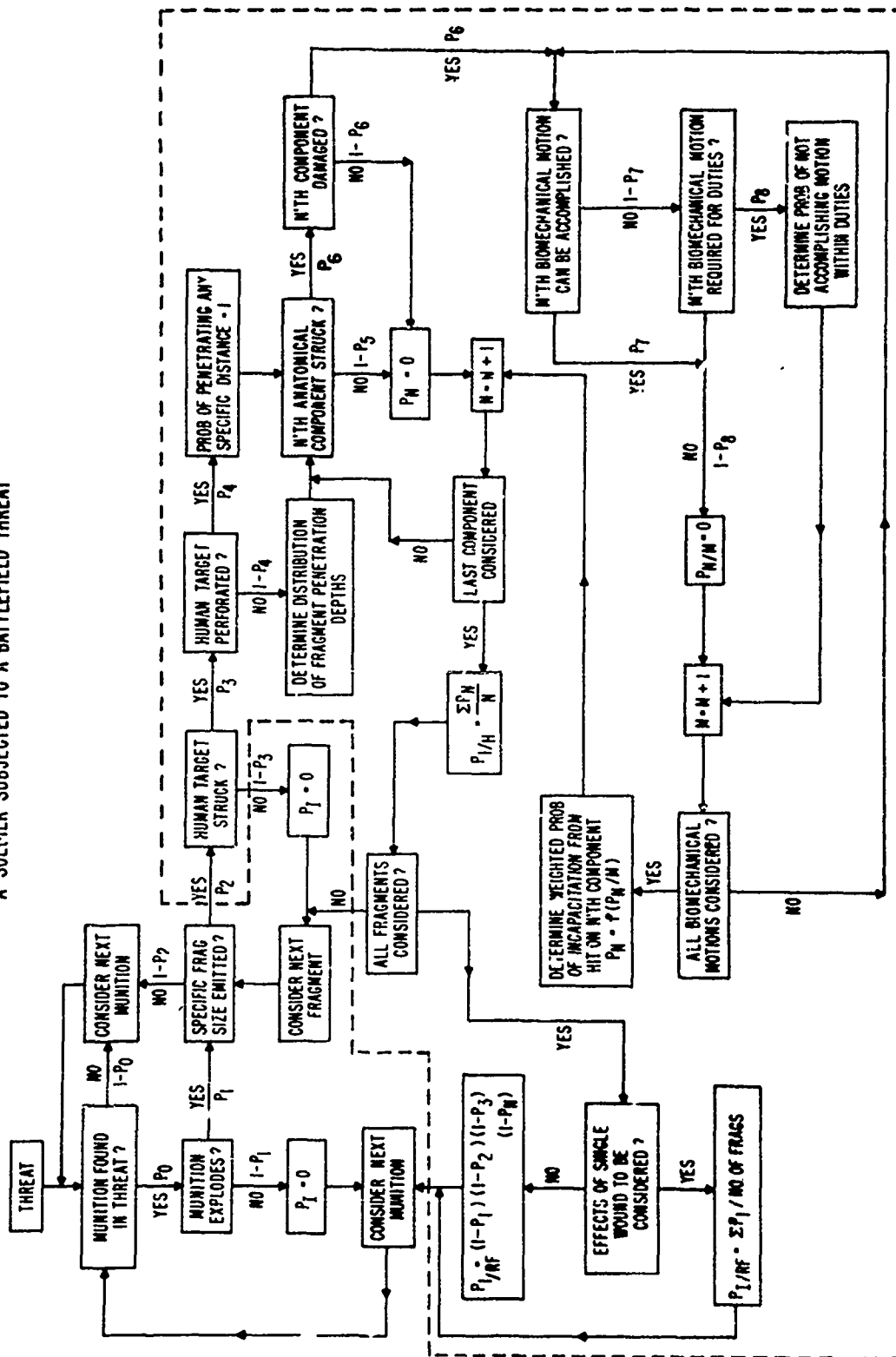


Figure 8. Logic diagram for probabilistic model of incapacitation by kinetic energy missiles.



#### REFERENCES

1. Sturdivan, L.M., Clare, V.R., and Amato, J. J. "New Wound Ballistics Model." Unpublished study paper by joint Committee on New Wound Ballistics Model, Ballistic Research Laboratories, Aberdeen Proving Ground, Maryland and Edgewood Arsenal, Maryland, 1970.
2. High speed photographs taken by Photographic Section, Biophysics Laboratory, Edgewood Arsenal, Maryland 1969.
3. Johnson, W.P., Brown, A., and Kindred, F. A. "Proportions of the Anatomical Components of the Wound Ballistics Computer Man." Ballistic Research Laboratories Memorandum Report No. 1907, March, 1968.
4. Eycleshymer, A.C., and Scjoemaker, D.M. "A Cross-Section Anatomy." New York, 1911.
5. "Development of Methodology for Measuring Effects of Personal Clothing and Equipment on Combat Effectiveness of the Field Soldier." Phase III, Final Report. USATECOM Project Number 803077000-01E. USAGETA, Ft. Lee, Virginia, December 1967.

PAPER NO. 33

ANALYSIS OF GAIT USING A MINIMUM ENERGY APPROACH

R. E. Beckett  
Technical Director, Research & Engineering Directorate

and

K. C. Pan  
Mechanical Engineer, Systems Analysis Directorate  
HQ, U. S. Army Weapons Command, Rock Island, Illinois

ABSTRACT

This paper presents an analysis of the motion of the legs and the center of gravity of the torso in walking. The analysis is based on the hypothesis that the behavior will be such as to minimize the amount of muscle effort and be consistent with constraints imposed by muscle behavior and geometry. The equations of motion are solved by a shooting technique which is made to satisfy conditions imposed at the beginning and end of a step cycle by an interval halving method.

Results give the time phased position of the legs and the torso center of gravity and the moment inputs at the pelvis and the knee. Comparisons of results are made with available experiments and analysis. Results and comparisons are displayed in graphical form.

INTRODUCTION

This paper presents an analysis of the motion of the leg in a step for normal walking on a level surface. It is an extension of work presented in Ref. 1 in that geometric constraints have been more clearly defined and some emphasis has been placed on the computation of the knee moment. The knee moment is a critical parameter in walking and is significantly affected by constraints imposed on the motion.

Equations of motion are developed by using the Lagrangian Method and geometrical constraints are imposed by using the Lagrangian Multipliers. The equations are solved by the fourth order Runge-Kutta Method. Energy considerations are imposed by varying certain parameters such as the toe off velocity of the leg and using the solution satisfying all constraints and involving the least effort imposed by the body muscles.

**PRECEDING PAGE BLANK**

Results for the motion of the leg for the imposed hip moments and the knee moment are given for a man of normal build weighing 150 pounds and walking at rates of 90, 75 and 60 steps per minute.

#### MATHEMATICAL MODEL

The stick diagram in Fig. 1 shows the position of the legs at selected times in a normal walking step. The solid line represents the leg in swing phase while the dotted line represents the leg in the stance phase. Three critical positions for the swing phase are shown. The first is the toe off position just before the foot leaves the floor, the second is the swing through position where the foot comes directly under the hip joint and finally heel strike where the foot reaches the floor to begin the stance phase. From toe off to heel strike the foot will move ahead a distance equal to twice the step size. This motion represents one half of a complete cycle in walking. To complete the cycle the stance leg must swing through to reach the initial toe off position. This paper is concerned with the half cycle illustrated in Fig. 1. For normal walking this half cycle is repeated first with one leg then the other so that it can represent a solution for the gait problem.

Point O in Fig. 1 represents the hip joint. Link 1 is the thigh and is connected by joint O' to link 2 which represents the shank. The foot is connected to link 2 by the ankle joint P. The motion of the hip joint O is prescribed by the forward velocity  $v_0$  which is assumed constant and the vertical motion  $h$ . The angular position of the thigh is denoted by  $\phi$  and is measured from the position of maximum extension. The position of the shank is defined by the angle  $\gamma$  that it makes with the thigh. The angle  $\alpha$  is a measure of the rise of the foot in toe off.

In order to have the motion simulate the swing phase of a typical walking step certain geometrical constraints must be imposed. It is required that the ankle joint move on a prescribed curve denoted by PP' in Fig. 1. The point P' is the ankle position when the thigh reaches maximum flexion and the hip joint reaches its maximum height. It is the time when the foot swings through under the hip and will mark a change in the constraint conditions used to solve the problem. For the remaining part of the swing phase, i.e., until heel strike, the position of the thigh changes little. Small variation in  $\phi$  is admitted to accommodate geometric constraint and to bring the leg smoothly into position for heel strike.

The forces that drive the leg come mainly from two groups of muscles. The quadriceps group provides the acceleration moment over the initial part of the swing phase, and the deceleration moment that acts toward the end of this phase to slow the leg for heel strike is furnished largely by the hamstring group. The effect of these two groups of muscles is a moment acting at the hip joint O. A plot of the equivalent hip moment which approximates the actual behavior of the two groups of muscles is shown as a function of time in Fig. 2. On the basis of available information on the action of these muscle groups the form of the equivalent moment shown in Fig. 2 is a reasonable assumption.

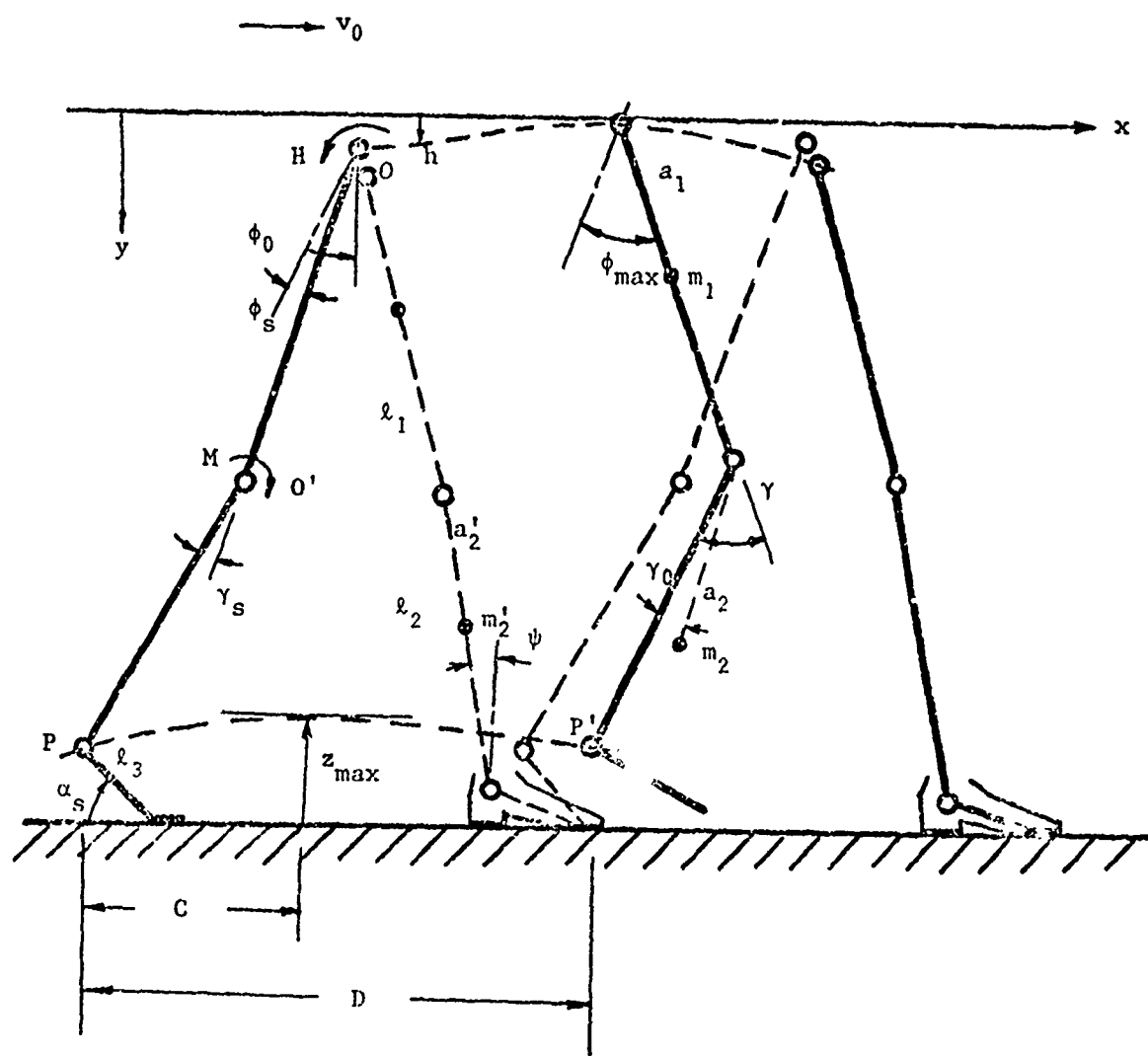


Fig. 1. Position of the Legs in Level Walking

## EQUATION OF BEHAVIOR

The equations of motion are obtained by the Lagrangian Method. This requires appropriate expressions for the kinetic and potential energies of the system and that the constraint condition be in equation form.

It is assumed that the motion is planar and that the position of the hip joint is prescribed. The relative motion between the foot and the shank during the swing phases is small and in this analysis it is ignored. On the basis of these assumptions the kinetic and potential energies can be written as follows, Ref. 1.

$$\begin{aligned}
 T = \frac{1}{2} [ & (m_1 + m_2 + m)(\dot{v}_0^2 + \dot{h}^2) + (\bar{I}_1 + m_2 \ell_1^2) \dot{\phi}^2 \\
 & + \bar{I}_2 (\dot{\phi} - \dot{\gamma})^2 + I_0 \dot{\psi}^2 ] \\
 & + (m_1 a_1 + m_2 \ell_1) \dot{\phi} [v_0 \cos(\phi - \phi_0) - \dot{h} \sin(\phi - \phi_0)] \\
 & + m_2 a_2 (\dot{\phi} - \dot{\gamma}) [v_0 \cos(\phi - \phi_0 - \gamma + \gamma_0) \\
 & - \dot{h} \sin(\phi - \phi_0 - \gamma + \gamma_0)] + m_2 a_2 \ell_1 \dot{\phi} (\dot{\phi} - \dot{\gamma}) \cos(\gamma - \gamma_0)
 \end{aligned} \tag{1}$$

$$\begin{aligned}
 \text{where } \bar{I}_1 &= I_1 + m_1 a_1^2 \\
 \bar{I}_2 &= I_2 + m_2 a_2^2
 \end{aligned} \tag{2}$$

$$\begin{aligned}
 V = & -m_1 g [h + a_1 \cos(\phi - \phi_0)] \\
 & -m_2 g [h + \ell_1 \cos(\phi - \phi_0) + a_2 \cos(\phi - \phi_0 - \gamma + \gamma_0)] \\
 & -mg(h - \epsilon) - m_1 g(h + a_1 \cos\psi) \\
 & -m_2 g[h + (\ell_1 + a_2') \cos\psi]
 \end{aligned} \tag{3}$$

The variables  $\phi$  and  $\gamma$  are defined in Fig. 1. The maximum extension of the thigh  $\phi_0$ , is measured from the vertical axis.  $m_i$ ,  $I_i$  and  $\ell_i$  ( $i = 1, 2$ ) are the mass, the mass moment of inertia about the centroid and the length of links 1 and 2 respectively.  $a_1$  and  $a_2$  are the distances from the joint to the center of mass of the link.  $I_0$  is the mass moment of inertia of the stance leg about the ankle joint and  $\dot{\psi}$  is the rotational velocity.  $m$  is the mass of the trunk and is assumed to move with the hip joint  $O$ .  $m_2'$  and  $a_2'$  are the mass of the shank and the distance from knee joint to the center of mass of the shank respectively for the stance leg  $\epsilon$  is the distance from  $O$  to the center of mass of the trunk.

The conditions of constraint imposed on the system are catalogued into two phases. In Phase I the ankle joint is required to move on the prescribed curve  $PP'$  as shown in Fig. 1. In Phase II the angular position

of the thigh is prescribed to be essentially fixed in maximum flexion while the shank and foot come into position for heel strike.

In Phase I the curve PP' must have a positive slope at toe off to ensure the foot will rise smoothly from the floor. It reaches a maximum height at some horizontal distance C before reaching P' where the foot swings through and mark the end of Phase I. The horizontal distance traveled by the foot Phase I is denoted by D and will depend upon the step size.

It is possible to satisfy the requirements for the curve PP' in Phase I by using a third degree polynomial

$$z = c_0 + c_1x + c_2x^2 + c_3x^3 \quad (4)$$

where  $z$  is measured vertically and  $x$  is horizontally from P.

The four coefficients  $c_0, \dots, c_3$  are chosen to satisfy the following conditions on the curve PP'

$$\begin{aligned} z(0) &= z_0, & z'(0) &= \dot{z}(0)/\dot{x}(0) \\ z'(C) &= 0, & z(D) &= z_D \end{aligned} \quad (5)$$

where  $z_0, z_D$  are the height of the ankle joint above the floor at  $x = 0$  and  $x = D$ .  $\dot{z}(0)$  and  $\dot{x}(0)$  are the velocity components of the ankle joint at toe off. The distances C and D depend upon the step size and the cadence. All these quantities must be determined in order to prescribe the constraint curve PP'.

The constraint conditions for Phase I are written to keep the ankle joint on the curve PP'. In the vertical direction

$$h + \ell_1 \cos(\phi - \phi_0) + \ell_2 \cos(\phi - \phi_0 - \gamma) + z = K_1 \quad (6)$$

and in the horizontal direction

$$v_0 t + \ell_1 \sin(\phi - \phi_0) + \ell_2 \sin(\phi - \phi_0 - \gamma) - x = K_2 \quad (7)$$

where

$$\begin{aligned} K_1 &= h_0 + \ell_1 \cos(\phi_s - \phi_0) + \ell_2 \cos(\phi_s - \phi_0 - \gamma_s) + z_0 \\ K_2 &= \ell_1 \sin(\phi_s - \phi_0) + \ell_2 \sin(\phi_s - \phi_0 - \gamma_s) \end{aligned} \quad (8)$$

From Eqs. (6) and (7) the value of  $z'(0)$  can be found in terms of starting values for  $\phi$  and  $\gamma$ . Furthermore, the constraint condition during Phase I can be expressed entirely in terms of  $\phi$  and  $\gamma$  and arbitrary constants  $c_i$  by replacing  $z$  in Eq. (6) from Eq. (4) and then replacing  $x$  from Eq. (7). Thus

$$\begin{aligned} f(\phi, \gamma) &= h + \ell_1 \cos(\phi - \phi_0) + \ell_2 \cos(\phi - \phi_0 - \gamma) \\ &+ \sum_{i=0}^3 c_i [v_0 t + \ell_1 \sin(\phi - \phi_0) + \ell_2 \sin(\phi - \phi_0 - \gamma) - K_2]^i \\ &- K_1 = 0 \end{aligned} \quad (9)$$

The potential energy function  $V$  is augmented to include the constraint in Eq. (9)

$$\bar{V} = V + \lambda f(\phi, \gamma) \quad (10)$$

The equation of motion for Phase I can now be obtained by using  $T$  and  $V$  in the Lagrangian equations:

$$\frac{d}{dt} \frac{\partial T}{\partial \dot{\phi}} - \frac{\partial T}{\partial \phi} + \frac{\partial \bar{V}}{\partial \phi} = H \quad (11)$$

$$\frac{d}{dt} \frac{\partial T}{\partial \dot{\gamma}} - \frac{\partial T}{\partial \gamma} + \frac{\partial \bar{V}}{\partial \gamma} = M \quad (12)$$

where  $H$  and  $M$  are the hip and knee moments respectively. After carrying out the mathematical operations, Eqs. (11) and (12) become:

$$\begin{aligned} & \ddot{\phi} [\bar{I}_1 + \bar{I}_2 + m_2 \ell_1^2 + 2m_2 a_2 \ell_1 \cos(\gamma - \gamma_0)] \\ & - \gamma [\ddot{I}_2 + m_2 a_2 \ell_1 \cos(\gamma - \gamma_0)] + \dot{\gamma} (\dot{\gamma} - 2\dot{\phi}) m_2 a_2 \ell_1 \sin(\gamma - \gamma_0) \\ & + [(m_1 a_1 + m_2 \ell_1)(g - \ddot{h}) - \lambda \ell_1] \sin(\phi - \phi_0) \\ & + m_2 a_2 (g - \ddot{h}) \sin(\phi - \phi_0 - \gamma + \gamma_0) - \lambda \ell_2 \sin(\phi - \phi_0 - \gamma) \\ & + \lambda [\ell_1 \cos(\phi - \phi_0) + \ell_2 \cos(\phi - \phi_0 - \gamma)] \cdot \sum_{i=1}^3 i c_i [v_0 t \\ & + \ell_1 \sin(\phi - \phi_0) + \ell_2 \sin(\phi - \phi_0 - \gamma) - K_2]^{i-1} = H \end{aligned} \quad (13)$$

$$\begin{aligned} & \ddot{I}_2 \gamma - [\ddot{I}_2 + m_2 a_2 \ell_1 \cos(\gamma - \gamma_0)] \ddot{\phi} \\ & + m_2 a_2 \ell_1 \dot{\phi}^2 \sin(\gamma - \gamma_0) + m_2 a_2 (\ddot{h} - g) \sin(\phi - \phi_0 - \gamma + \gamma_0) \\ & + \lambda \ell_2 \sin(\phi - \phi_0 - \gamma) - \lambda \ell_2 \cos(\phi - \phi_0 - \gamma) \cdot \sum_{i=1}^3 i c_i \\ & [v_0 t + \ell_1 \sin(\phi - \phi_0) + \ell_2 \sin(\phi - \phi_0 - \gamma) - K_2]^{i-1} = M \end{aligned} \quad (14)$$

The constraint condition in Phase II is chosen differently than Phase I. Experiment shows that the thigh rotates very little after reaching maximum flexion. Some rotation is admitted in order to have a smooth transition to heel strike where the foot must touch the ground and have essentially zero forward velocity. The necessary variation in  $\phi$ , the thigh rotation, is given by the following expression

$$\phi = b_0 + b_1 t + b_2 t^2 + b_3 t^3 \quad (15)$$

where  $t$  ranges from the starting of Phase II,  $t = t_1$ , to heel strike  $t = \tau$ . The choice of the coefficients  $b_i$  are made so that

$$\begin{aligned}
\phi(t_1) &= \phi_{\max}, & \dot{\phi}(t_1) &= 0 \\
\ddot{\phi}(t_1) &= \ddot{\phi} \text{ at end of Phase I} \\
\phi(\tau) &= \phi_{\tau}
\end{aligned}
\tag{16}$$

where  $\phi_{\tau}$  is assigned to assure that heel strike is accomplished smoothly. Thus  $\phi$  is assumed to be known during Phase II and the constraint condition in Eq. (9) is not needed. In Eqs. (13) and (14)  $\lambda$  is set equal to zero, and with  $\phi$  known Eq. (13) is used to solve for  $\gamma$ . Eq. (14) is then used to solve for the knee moment.

On the basis of the constraint conditions that are applied and with appropriate starting values for the variables each phase of the problem can be solved numerically.

#### NUMERICAL SOLUTION

The equations of motion are solved by a standard fourth order Runge-Kutta Method. The hip moment that acts in Phase I is assumed to have a constant magnitude. The duration of H in Phase I is 20 percent of the time for one step, i.e.,  $0.20\tau$ , and starts at  $t = 0$ . For Phase II the deceleration moment acts for a time equal to  $0.24\tau$  over the latter part of the phase. The form of the moment curve is assumed to have a trapezoidal profile determined by a slope  $\beta$  and its maximum magnitude (see Fig. 2a). Phase I begins at  $t = 0$  and ends at  $t = t_1 = 0.64\tau$ . Phase II runs from  $0.64\tau$  to  $\tau$ .

The starting conditions on  $\phi$  and  $\gamma$  are obtained from experiment, (Ref. 2)

$$\begin{aligned}
\phi(0) &= \phi_s = 6^\circ \\
\gamma(0) &= \gamma_s = 13^\circ \\
\phi_0 &= 23^\circ
\end{aligned}
\tag{17}$$

On the basis of the analysis of stick diagrams the initial angular velocity of the thigh is small and is taken to be zero. However, the starting rotational velocity of the shank,  $\gamma_s$ , cannot be zero if the toe is to rise off the floor. It turns out that the value assigned to  $\gamma_s$  has considerable influence on the subsequent motion and for this reason, its value is varied within the limits established from experiment to give a smooth motion and the least energy expended.

In order to solve Eqs. (13), (14) and (9) for the unknowns  $\phi$ ,  $\gamma$  and  $\lambda$  it is necessary to know all of the coefficients on  $z$  in Eq. (4) and to know the value of H and M. With initial conditions on  $\phi$  and  $\gamma$  prescribed  $z(0)$  and  $z'(0)$  in Eq. (5) are known. The distance C and D which are related to the step size must be determined and the height of the ankle above the floor on the swing through must be assigned. These quantities are measured from stick diagrams (Ref. 5) and then in the analysis variations are made in the form of the curve PP' to meet constraints at the end of Phase I and to reduce the total energy expended.



Nominal values for  $z_0$ ,  $z_D$  and  $D$  are determined from the following expressions

$$\begin{aligned} z_0 &= l_3 \sin \alpha_s \\ z_D &= K_1 - l_1 \cos(\phi_{\max} - \phi_0) - l_2 \cos(\phi_{\max} - \phi_0 - \gamma_{t_1}) \\ D &= 0.64 v_0 \tau + l_1 \sin(\phi_{\max} - \phi_0) \\ &\quad + l_2 \sin(\phi_{\max} - \phi_0 - \gamma_{t_1}) \cdot K_2 \end{aligned} \quad (18)$$

where  $l_3$  is the rotation arm of the foot when the toe is fixed during toe off,  $l_3 = 7''$  and  $\alpha_s = 45^\circ$  are used in the numerical example.  $C$  is chosen to be 40% of the distance  $D$ .

The vertical motion of the hip joint  $O$  during the half cycle is prescribed by

$$h(t) = h_0 + h_1 t + h_2 t^2 + h_3 t^3 \quad (19)$$

where the coefficients  $h_0, \dots, h_3$  are determined from the following conditions

$$\begin{aligned} h(0) &= h_0, & h(t_1) &= 0 \\ h'(0) &= 0, & h'(\tau) &= h_\tau \end{aligned} \quad (20)$$

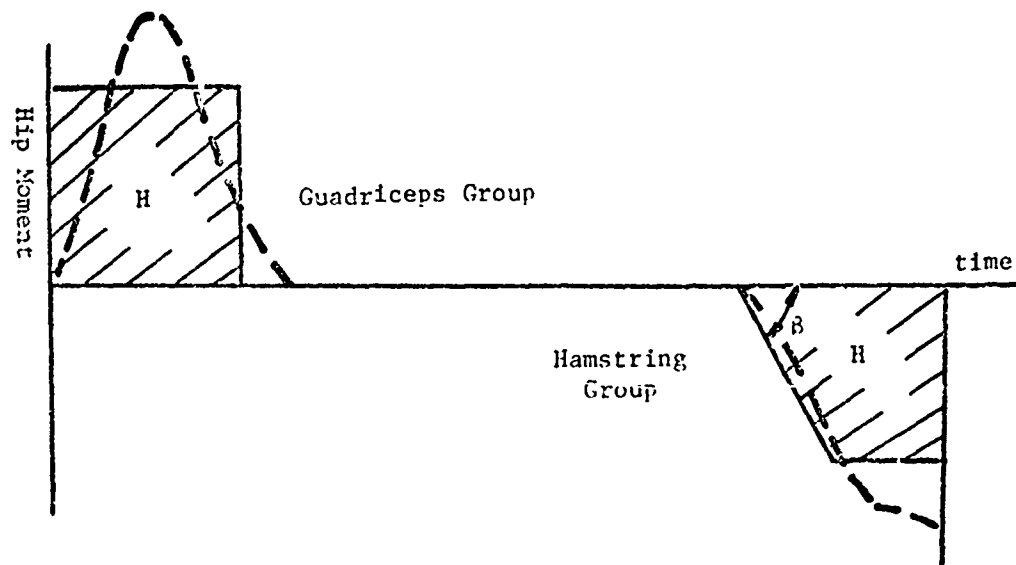
The time  $t_1$  is the end of Phase I and signifies the highest level the hip joint reaches. The initial choice of  $h_0$  and  $h_\tau$  is based on experiment. Some refinement of these values to better meet constraint conditions and to smooth the motion is made by trial and error using the geometric constraints imposed at swing through and a smooth transition to heel strike. Values selected on this basis are

$$h_0 = 0.29 \text{ in.} \quad h_\tau = 0.50 \text{ in.}$$

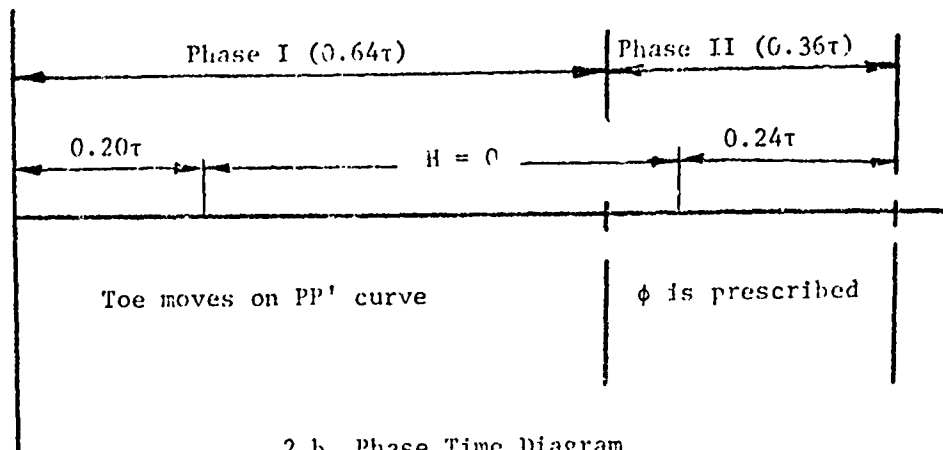
thus,  $h$  is assumed to be known. The value of  $z$  is found as a function of  $x$  from Eqs. (4), (5), (6) and (7) when initial conditions on  $\phi$ ,  $\gamma$ ,  $\phi$ ,  $\gamma$  and the distance  $D$  are given ( $C = 0.40D$ ).

Computations for Phase I are carried out in the following way. A numerical value is chosen for  $H$  and the knee moment is set equal to zero. With the knee moment equal to zero, a value  $\lambda$  is found that will force the ankle to follow the curve  $PP'$ .  $\lambda$  is a fictitious non-work producing force applied at the ankle. Its affect is similar to a groove that holds the ankle on the prescribed curve. The knee moment is then found by computing the equivalent moment at the knee that would equal the restraint offered at the ankle. The computation is then carried to the end of Phase I where certain explicit conditions on  $\phi$  and  $\gamma$  must hold. Experimental information gives estimation on these values and they are refined by trial and error.

$$\phi(t_1) = 43^\circ, \quad \gamma(t_1) = 50^\circ \quad (21)$$



2.a Phase Action of Major Muscle



2.b Phase Time Diagram

Fig. 2. One-Half of a Complete Cycle in Level Walking

The magnitude of the hip moment in Phase I and the form for  $z$  are adjusted in the course of numerical computation so that the conditions, Eq. (21), will be met and simultaneously  $\phi(t_1)$  is near to zero.

Phase II is solved by simply continuing the solution of  $\phi$  and  $\gamma$  from Phase I, but using the constraint condition for Phase II.  $\phi$  is determined from Eqs. (15) and (16) when  $\phi_T$  is explicitly given. The value selected for  $\phi_T$  and for  $\gamma_T$  comes from observation of experiment with refinement by trail and error calculations of the conditions at heel strike.

$$\phi_T = 41^\circ \qquad \gamma_T = 9^\circ \qquad (22)$$

The duration time for the deceleration moment at the hip joint is known. The profile of the hip moment curve is determined by the slope  $\beta$  and the maximum magnitude of the hip moment as shown in Fig. 2a. These two parameters are adjusted in the computation so that the foot will make contact with the ground at the right time with  $\gamma(\tau)$  approximately equal to zero and  $\gamma_T = 9^\circ$ .

For each step the work done is computed according to the expression

$$W = \int_0^\tau |H| |\dot{\phi}| dt + \int_0^\tau |M| |\dot{\gamma}| dt \qquad (23)$$

Absolute values are used for the integrands since they represent effort that is not recoverable. The integration is carried out by a numerical integration scheme.

## RESULTS

Computations have been carried out for the swing phase of a cycle using numerical data for a 150 lb. man walking at 90, 75 and 60 steps per minute. Relevant data is listed below, Ref. 3.

$w = \text{body weight} = 150 \text{ lb.}$	$\ell_1 = 17.4 \text{ in}$
$m_1 = 0.097 w/g$	$\ell_2 = 16.9 \text{ in}$
$m_2 = 0.064 w/g$	$a_1 = 7.53 \text{ in}$
$m = 0.678 w/g$	$a_2 = 9.81 \text{ in}$
$I_1 = 8.6416 \text{ lb-in-sec}^2$	step size = 30 in
$I_2 = 7.0727 \text{ lb-in-sec}^2$	$g = 386.4 \text{ in/sec}^2$
$I_0 = 43.962 \text{ lb-in-sec}^2$	

Results of the computation are presented in both tabular and graphical form. The final solution for the variables  $\phi$ ,  $\gamma$  and the knee moment are shown in Figs. 3 to 7. Fig. 3 gives a plot of the angular displacements  $\phi$  and  $\gamma$  along with a plot of values taken from stick diagrams, Ref. 5. Fig. 4 shows the angular velocity of the thigh and shank versus time. Both the displacement and velocity diagrams are plotted from values obtained with a starting value of  $\gamma_s$  of 1.7 rad/sec and at 90 steps per minute. Small variation around a value of  $\dot{\gamma}_s = 1.7 \text{ rad/sec}$  made little difference in displacement and velocity diagrams. Fig. 5

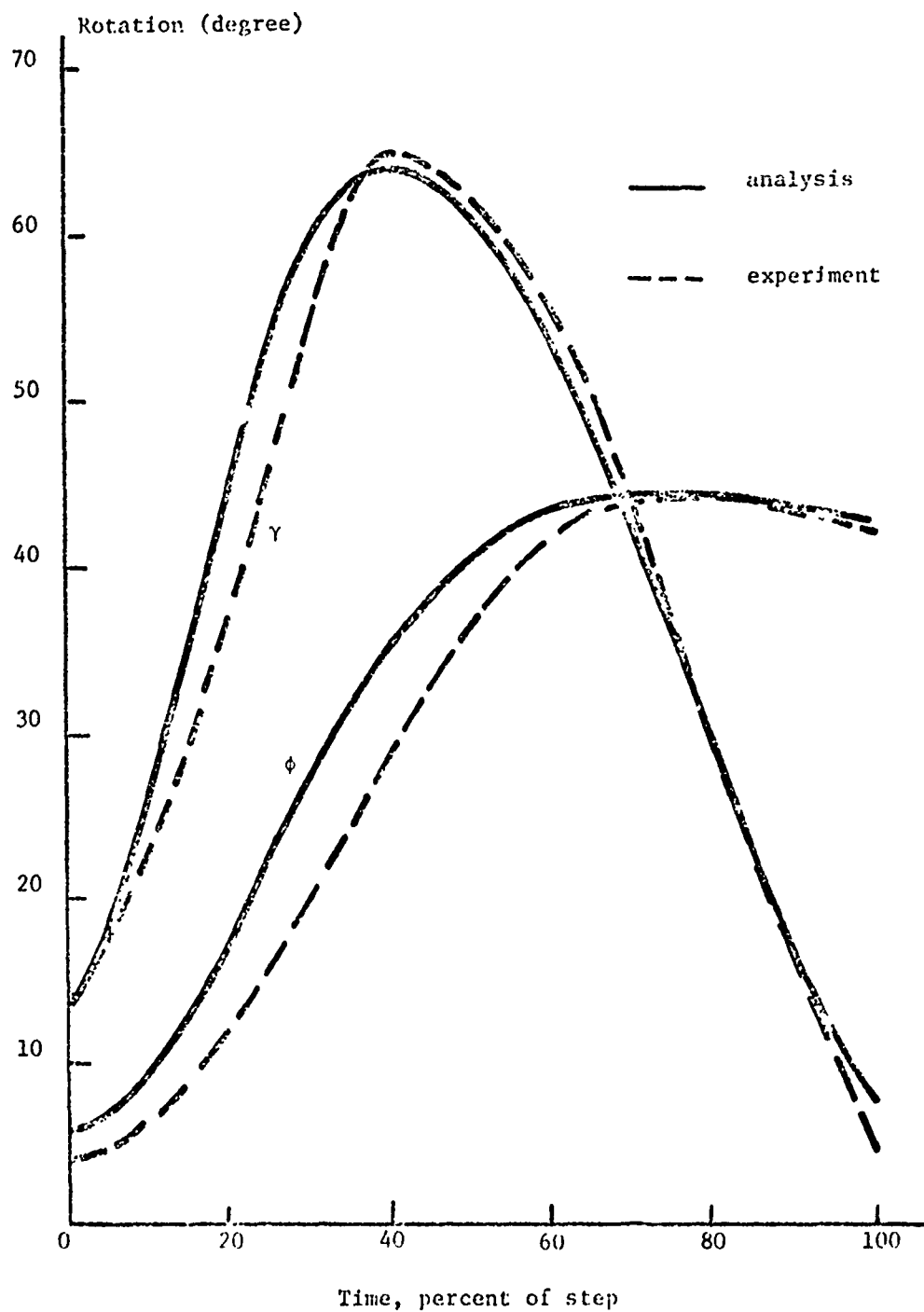


Fig. 3. Rotation Versus Time for the Thigh and Shank (90 steps/min,  $\gamma_s = 1.7$  rad/sec)

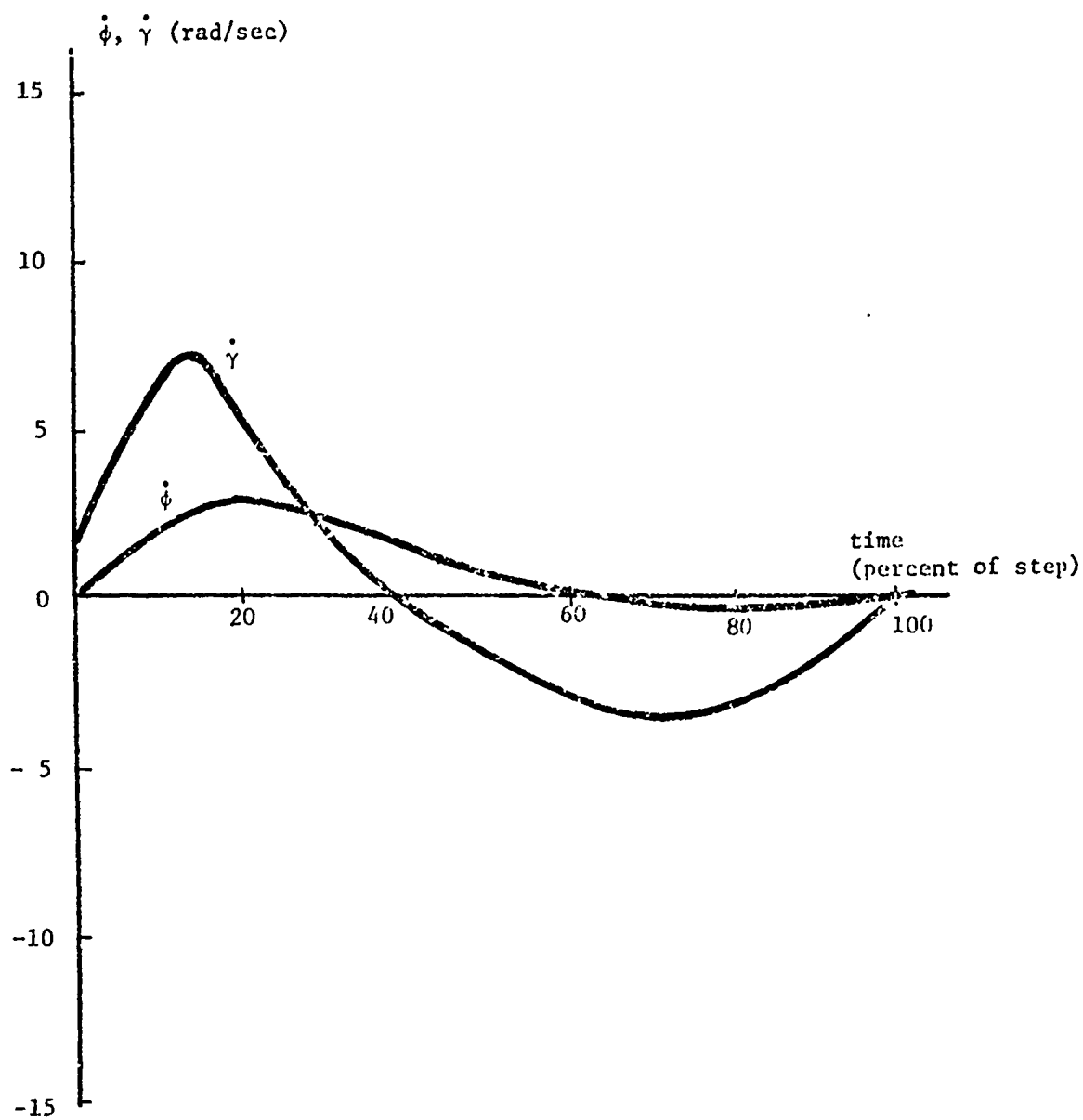


Fig. 4. Velocity Versus Time for the Thigh and Shank (90 steps/min,  $\gamma_s = 1.7$  rad/sec)

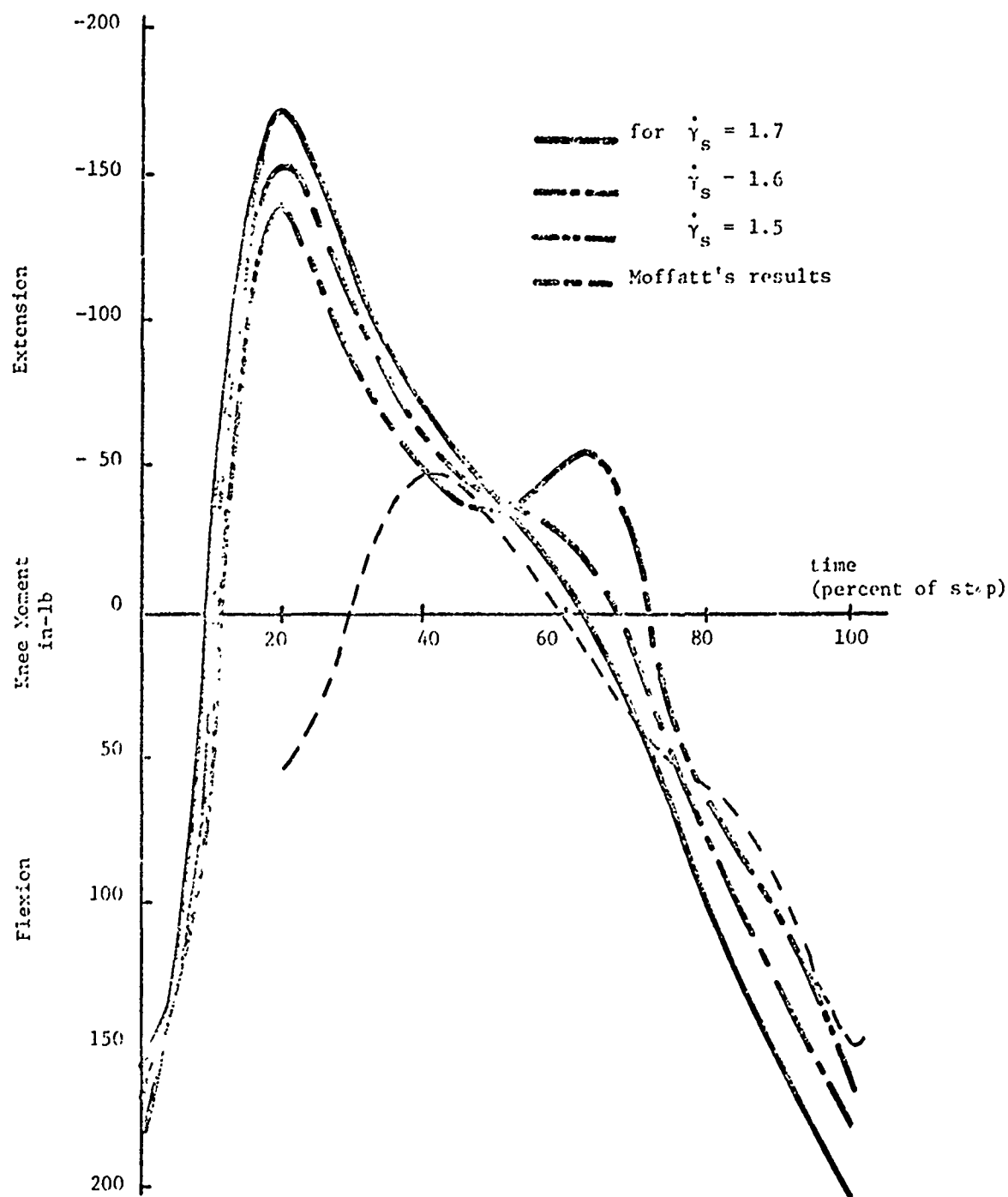


Fig. 5. Knee Moment Versus Time for Constant Magnitude Bip Moment (90 steps/min)

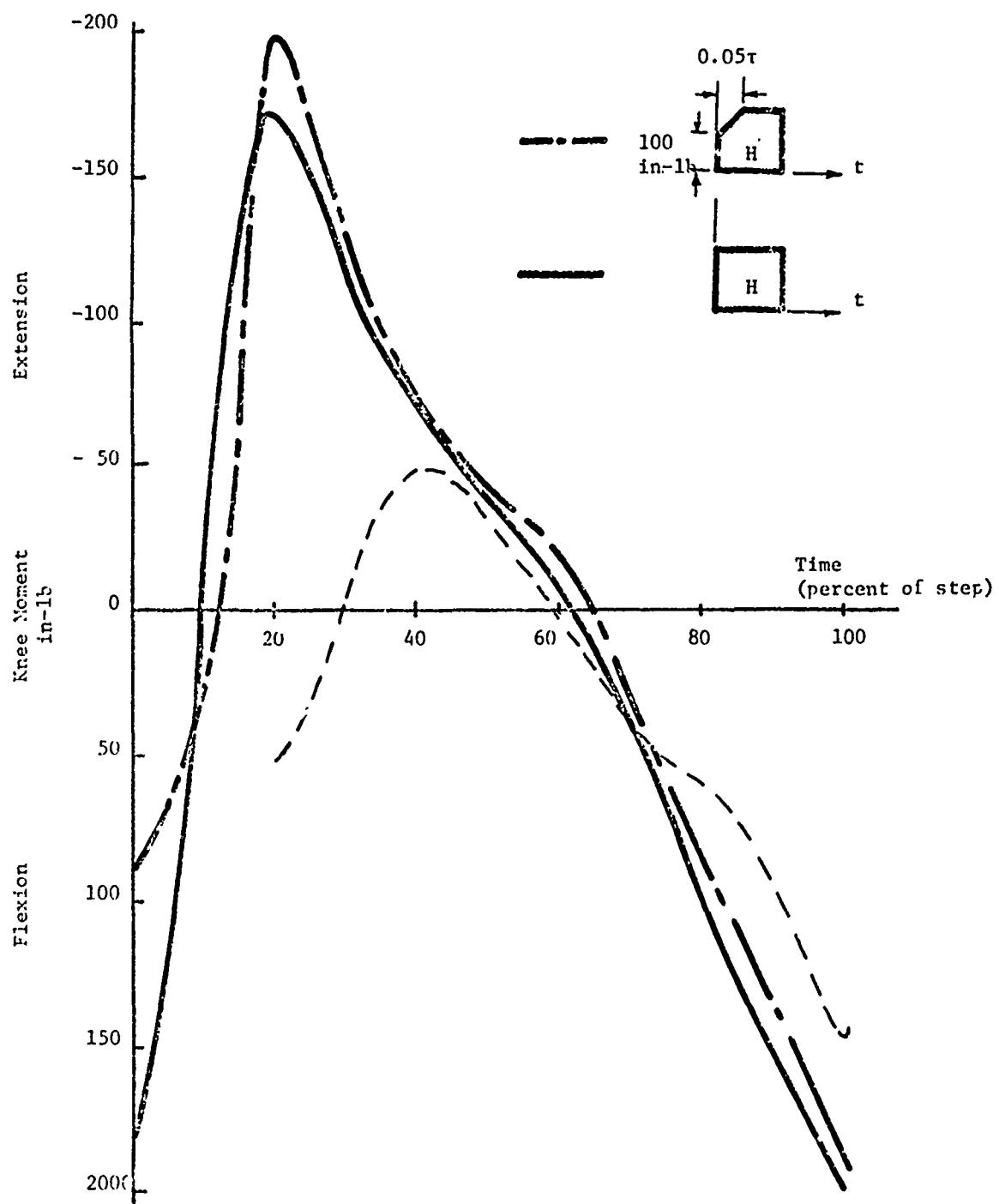


Fig. 6. Knee Moment Versus Time for Variable Profile Hip Moment (90 steps/min)

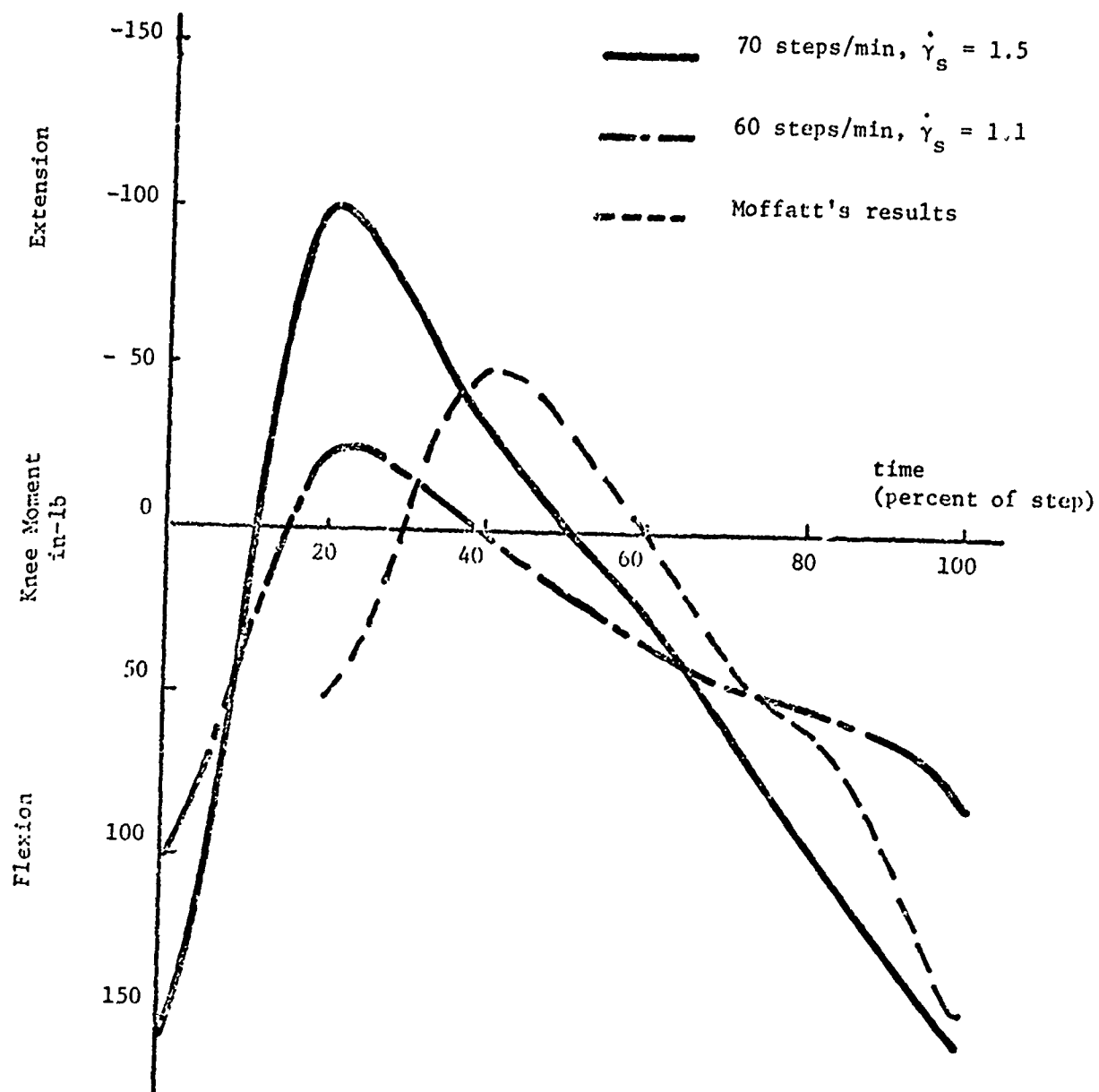


Fig. 7. Knee Moment Versus Time  
for 75, 60 steps/min



shows a plot of the knee moment versus time for a cadence of 90 steps per minute and starting values for  $\dot{\gamma}_s$ . Also shown is an evaluation of the knee moment based on measurements of the acceleration of the thigh and shank carried out by Moffatt, Ref. 4. Fig. 6 shows the variation in the knee moment when the form of the hip moment in Phase I is varied. This is given to illustrate that response is not critically affected by the way in which the hip moment is introduced.

Fig. 7 shows a plot of the knee moment for cadence of 75 and 60 steps per minute. Variation of the cadence has a substantial effect on the knee moment. Fig. 7 shows that the form for the knee moment is very close to the measured results of Moffatt when the cadence is appropriately chosen. The phase difference between the analysis and Moffatt's measurements could be accounted for by a difference in time of toe off.

Fig. 8 shows the effect on the curve PP' of changes in the initial velocity on  $\dot{\gamma}_s$ . Although the curve changes only slightly, the effect on the knee moment is pronounced. Also there is a great effect on the deceleration moment at the hip as is seen from Table 1. Table 1 shows the effect of changing the starting conditions  $\dot{\gamma}_s$  on the hip moments and the total work done in the swing phase. Note that as  $\dot{\gamma}_s$  is decreased, the work done by the hip moments and knee moments is decreased. However, this does not take account of the increasing hip moment during Phase II that essentially acts isometrically to maintain the proper constraint conditions. Application of this high moment would be uncomfortable and tiring, even though little actual work is done. The appropriate value for  $\dot{\gamma}_s$  for the most comfortable walking condition at 90 steps per minute would appear to be about 1.6 rad/sec.

## DISCUSSION

The central objective in this paper is the development of a method of analysis that will give a picture of the motion of the leg and the forces required in normal level walking. There is a great deal of potential freedom in the motion of the leg and hip joint in the swing phase of a step. This potential freedom is reduced to a manageable level by the imposition of constraints. Some of these constraints are more restrictive than the actual case and are made to give a reasonable first approximation to the problem. These constraints are reviewed here with some comment on the validity.

1. The swing phase is assumed to be planar motion. On the basis of motion picture taken along the line of locomotion the leg stays very close to planar motion in swing phase. There is some shifting of body weight perpendicular to the plane of motion but this should have little effect upon the motion of the leg. This assumption greatly simplifies the analysis.

2. The vertical motion of the hip joint is prescribed from experiment and from the rather critical conditions of constraint that require the foot to clear the floor on pass through and to make contact with the ground at heel strike. Anyone who has encountered an unexpected shift of even a small amount in the elevation of the ground at heel strike knows how critical this requirement is for normal walking. This requirement has also influenced the value of  $\phi(\tau)$  and  $\gamma(\tau)$  and to a lesser extent the form of the function for  $\dot{\phi}$  during Phase II.

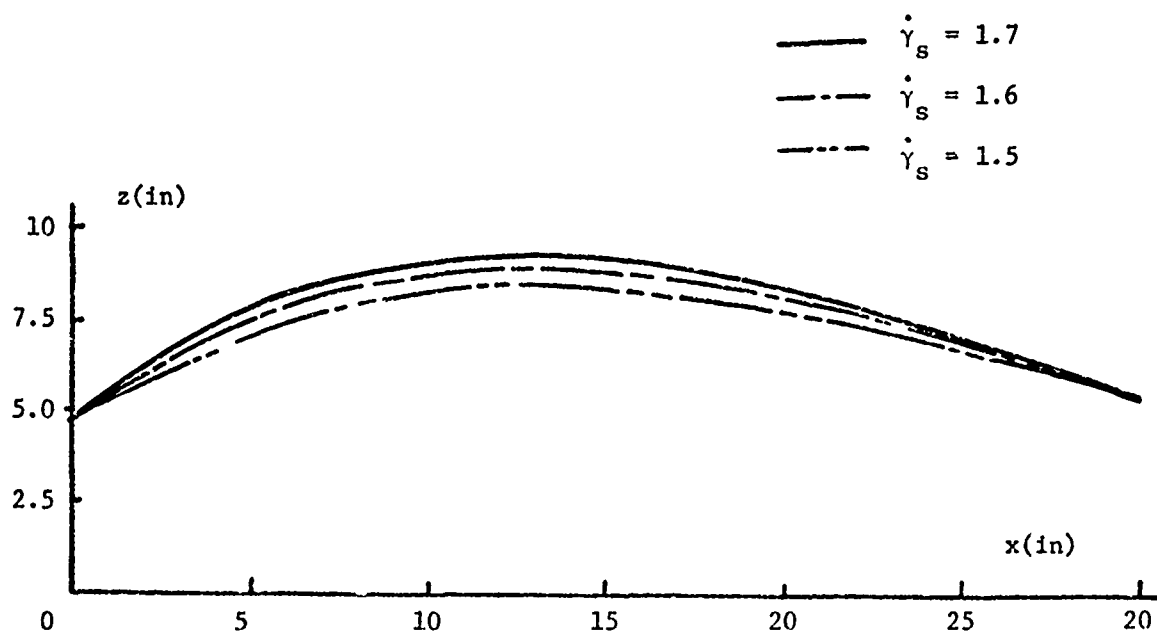


Fig. 8. Constraint Curve for Ankle With Different Initial Velocities (90 steps/min)

3. The position of the leg at the end of Phase I is prescribed in the analysis and forms a constraint on the motion. This constraint ensures that the necessary motion can take place smoothly and the leg come into proper position for heel strike with the correct velocity.

The results of this analysis agree reasonably well with experimental results available from stick diagrams and measured value of the knee moment. Further computations that will give the forces developed in the hip joint, knee joint and the reaction of the floor against the foot for the stance leg can be readily made by an extension of this analysis. Such results will be obtained and compared with available experiment in the near future.

Table 1. Hip Moments and Energy Expended for Slected Run

Steps/min	$\dot{\gamma}_s$ (rad/sec)	Hip Moment (in - lb)		Tctal Energy (in-lb)
		Phase I	Phase II	
90	1.5	307	180	207
90	1.6	320	76	223
90	1.7	330	- 40	245
90	1.7*	372	- 10	253
75	1.5	197	-190	181
60	1.1	60	95	80

\*For trapezoidal profile of hip moment in Phase I.

#### REFERENCES

1. Beckett, R. E. and Chang, K., "An Evaluation of the Kinematics of Gait by Minimum Energy", Journal of Biomechanics, Vol. 1, pp. 147-159, 1968.
2. Bresler, B. and Frankel, J. P., "The Force and Moments in the Leg During Level Walking", Transactions American Society of Mechanical Engineers, 72, pp. 27-36, 1950.
3. Lissner, H. P. and Williams, W., Biomechanics of Human Motion, W. B. Sander, Philadelphia, Penn., 1962.
4. Moffatt, C. A., "An Experimental Determination of Prosthetic Knee Moment for Normal Gait", American Society of Mechanical Engineers, Paper No. 66-WA/BHF-8.
5. Reports of Cissephotographic Studies, Veterans Administration Prosthetic Center, New York, Unpublished.

RESPONSE OF THE SPINE IN BIODYNAMIC  
ENVIRONMENTS

Mehdi Shirazi

University of Dayton Research Institute  
Dayton, Ohio

ABSTRACT

In this report we are concerned with the propagation of longitudinal elastic waves along the spine considered as a thin uniform rod with non-linear elastic parameters. The response of the spine in terms of the dynamic longitudinal deformation of the spine cross section is determined and its variation with respect to axial distance and the applied frequency is noted.

INTRODUCTION

In the dynamic loading of materials and structures, when we are considering the effects of forces which are applied for only very short periods of time or are changing rapidly, we must consider the response of the system in terms of the propagation of stress waves. For much slower loading as compared with the wave propagation time through the body, internal reflections of the stress waves smooth out the stress variations. In this case, a satisfactory approximation to the stress distribution can generally be obtained without an analysis of the wave motion.

**PRECEDING PAGE BLANK**

This report concerns the propagation of longitudinal elastic waves along the spine considered as a thin uniform rod with nonlinear elastic parameters, subjected to periodic displacement. In Section II, we obtain an expression for the dynamic longitudinal deformation of the spine cross section, and note its variation with respect to axial distance and the frequency of the impressed displacement.

## RESPONSE OF THE SPINE TO LONGITUDINAL PERIODIC DISPLACEMENT

We assume that the spine is represented by a thin nonhomogeneous elastic rod (see Figure 1) where the material parameters  $\lambda$  and  $\mu$  vary nonlinearly with respect to distance. If the density  $\rho$  of the material is taken as uniform, the one-dimensional equation governing the longitudinal motion is

$$\frac{\partial}{\partial x} \left[ (\lambda + 2\mu) \frac{\partial u}{\partial x} \right] = \rho \frac{\partial^2 u}{\partial t^2} \quad (1)$$

where

$$\lambda = \lambda_0 e^{\alpha x}, \quad \mu = \mu_0 e^{\alpha x} \quad (2)$$

and  $\alpha > 0$ .

As boundary conditions, we consider a periodic displacement impressed at the end  $x = 0$ . Thus

$$u(x, t) \Big|_{x=L} = u_0 e^{i\omega t} \quad (3)$$

Moreover, at the end  $x = L$ ,

$$\Omega(\lambda + 2\mu) \frac{\partial u}{\partial x} \Big|_{x=0} = -M \frac{\partial^2 u}{\partial t^2} \Big|_{x=0} \quad (4)$$

2017 1819 24010589

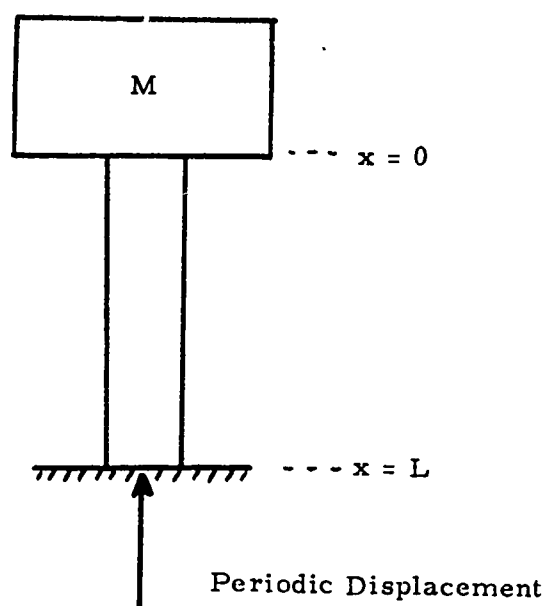


Figure 1.

Combining equations (1) and (2), assuming periodic solutions, and making the necessary transformations, we obtain a Bessel's differential equation of first order whose general solution for small changes in the elastic parameters  $\lambda$  and  $\mu$  may be written in the form

$$u(x, t) = (2c\omega)^{1/2} e^{-\frac{\alpha x}{4}} \left\{ A_1 \sin \left[ (2c\omega)e^{-\frac{\alpha x}{2}} - \frac{1}{4} \right] + A_2 \cos \left[ (2c\omega)e^{-\frac{\alpha x}{2}} - \frac{\pi}{4} \right] \right\} e^{i\omega t}$$

where  $c$  is the velocity of the longitudinal deformation wave and  $\omega$  is the frequency of the displacement. The values of  $A_1$  and  $A_2$  are determined from the boundary conditions (3) and (4).

#### CONCLUSION

The spine has been approximated by a rod of uniform cross section which continuously becomes more rigid toward the base with increasing values of the stiffness parameter  $\alpha$ . Figure 2 is a representative plot of the variation of longitudinal deformation with respect to axial distance, for  $u_0 = 1$ ,  $\alpha = 0.001$ , and for various values of the excitation frequency.

We observe that for small values of the excitation frequency, near  $\omega = 1$  cps, the system responds as a rigid body. Very large values of the longitudinal deformation are obtained, for  $\alpha = 0.001$ , at  $\omega_1 = 12.49$  cps,  $\omega_2 = 25.15$  cps,  $\omega_3 = 37.75$  cps, etc.. For  $\alpha = 0.005$ , these large values occur approximately at  $\omega_1 = 13.30$  cps,  $\omega_2 = 26.80$  cps,  $\omega_3 = 40.40$  cps, etc. and for  $\alpha = 0.01$ ,  $\omega_1 = 14.55$  cps,  $\omega_2 = 27.27$  cps,  $\omega_3 = 43.96$  cps, etc.. These observations may be compared qualitatively with the results of Coerrmann<sup>1</sup>, specially the change in the



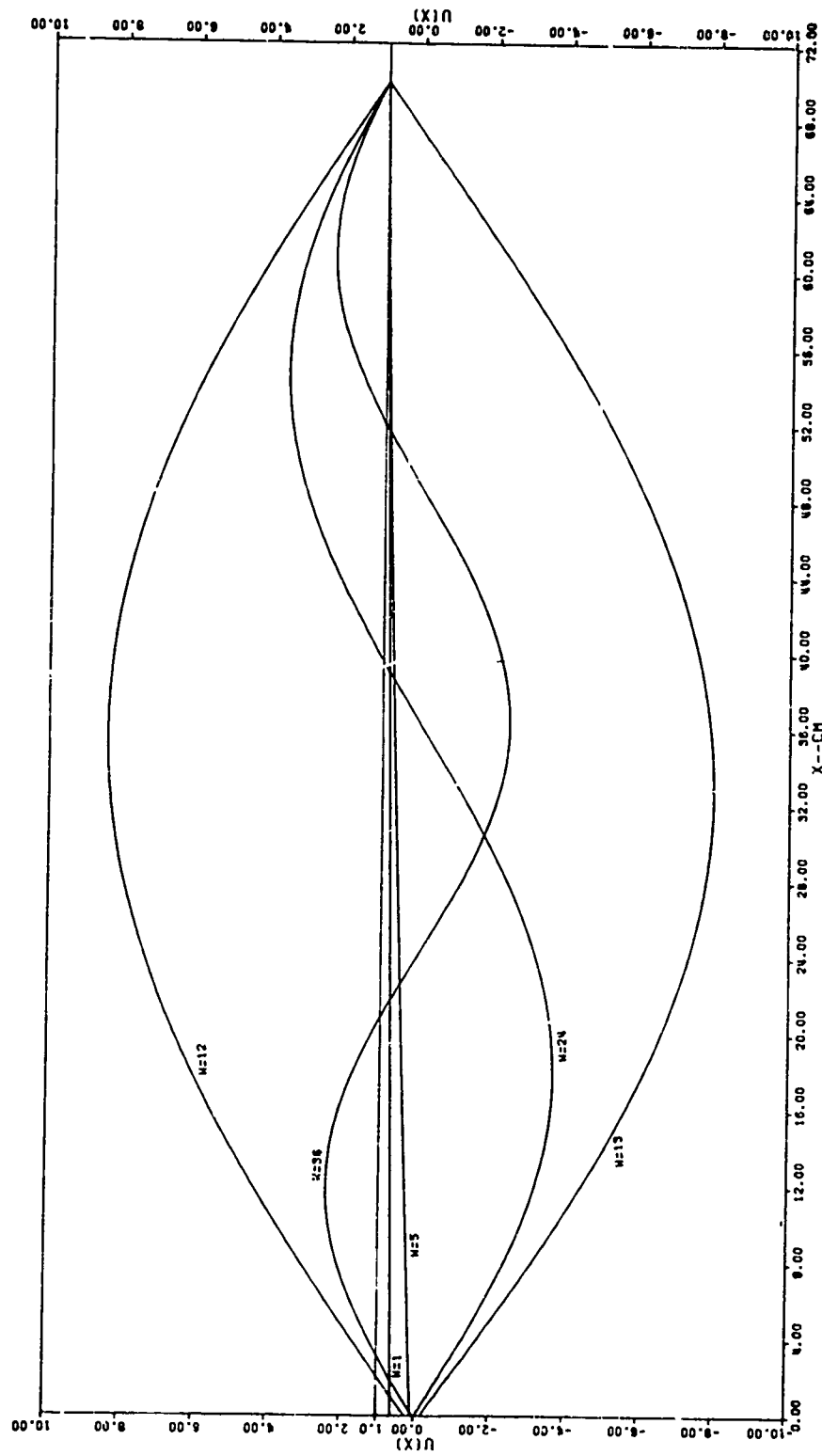


Figure 2.

value of the resonance frequency obtained with posture, and the use of a semi-rigid envelope and a pressure suit.

#### LIST OF SYMBOLS

$A_1, A_2$	coefficients determined from boundary conditions
$c$	velocity of the longitudinal deformation wave
$M$	superimposed mass, (see Figure 1)
$t$	time
$L$	length of rod
$u = u(x, t)$	dynamic longitudinal deformation
$x$	axial distance
$\alpha$	nonlinear parameter
$\lambda, \mu$	elastic parameters
$\lambda_0, \mu_0$	values of $\lambda$ and $\mu$ at $x = 0$
$\omega$	frequency of periodic displacement
$\Omega$	cross section of rod

#### ACKNOWLEDGEMENT

I am indebted to Henry Mohlman for programming effort and to Evie Beyers for her skills in the preparation of this report. This investigation was prepared as part of the internal research program at the University of Dayton Research Institute.

## REFERENCE

Coermann, R. F., "The Mechanical Impedance of the Human Body in Sitting and Standing Position at Low Frequencies," ASD Technical Report 61-492, 1961.

PAPER NO. 35

A DYNAMIC MODEL OF THE SPINE USING A POROUS ELASTIC MATERIAL

by

Edmund F. Rybicki, Ph.D.\*

and

Allen T. Hopper, Ph.D.

BATTELLE MEMORIAL INSTITUTE  
Columbus, Ohio 43201

ABSTRACT

A preliminary investigation of a two-phase solid-fluid continuum model to represent the spinal column subjected to dynamic loadings is presented. The two-fold purpose of this investigation is (1) to examine a simple dynamic model that has a continuum representation and offers a capability to include the inertia and pressure effects of a fluid and (2) to use this model to study what effect the presence of a fluid has on the stresses in the solid material. The model consists of a uniform straight porous elastic column containing a viscoelastic fluid and supporting a mass to represent the head. Loading consists of a constant acceleration at the base of the column. Two types of boundary conditions for the fluid at the upper end of the column are considered. The problem is formulated in terms of two coupled partial differential equations with the displacements of the fluid and the solid material treated as unknowns. Coupling of these equations arises from the coupling in the stress-strain relations and also from the viscosity of the fluid and the permeability of the solid material. An explicit finite difference method is used to obtain solutions for several cases. A comparison of the pressure in the fluid and the stress in the solid material is presented for a range of values of the modulus of the solid material and also for selected values of the viscosity and permeability. Deficiencies of the model as well as tractable extensions are pointed out.

PRECEDING PAGE BLANK

## INTRODUCTION

Knowledge of the response of a human body subjected to vibrations and impact environments is an important input for the design of safety devices used in aircraft and ground vehicles. Mathematical models have displayed a potential to become important engineering tools for studying the biodynamic response of the human body. One part of the body that is susceptible to injury in dynamic environments is the spine. Several models used to predict the dynamic behavior of the spine can be found in the literature. These models include a spring and two masses (Reference 1), several springs, masses, and dashpots (Reference 2), and a continuous uniform elastic rod (Reference 3). Uniform rods with damping (Reference 4), and a mass for the head (Reference 5) have been investigated. A "discrete parameter" model that includes the natural curvature of the spine has also been considered (Reference 6).

The purpose of the model presented here is to include the effect of the porosity and fluid of the spine for dynamic loadings. The spine is modeled as a two-phase media, bone and fluid. Distinct stresses, displacements, and accelerations are associated with each media. The bone is elastic and the fluid is viscoelastic. The equations are based on Biot's equations which have been used to predict behavior of joints where accelerations are neglected (Reference 7). In the present model, the equations are modified to include accelerations.

The spine is modeled as a uniform elastic porous column containing a viscoelastic fluid. The column is 30 inches long, straight, and has a constant cross-sectional area. The fluid completely fills the voids. A mass, to represent the head, is at one end of the column as shown in Figure 1. Two sets of boundary conditions are examined at this end of the column. In the first set of boundary conditions it is assumed that the fluid is stress free and that stress is transmitted to the head through the bone. The second set of boundary conditions examined requires that the fluid remain in contact with the bone at this end of the column and hence the fluid is not stress free. At the lower end of the column the displacement of the fluid equals the displacement of the bone for both sets of boundary conditions.

The first part of the paper is devoted to developing the equations which govern the behavior of the model. Several numerical examples are then considered which pertain to a range of values of the pertinent

---

\* Advanced Solid Mechanics Division, Battelle Memorial Institute, Columbus, Ohio.

100 1000 1000 1000

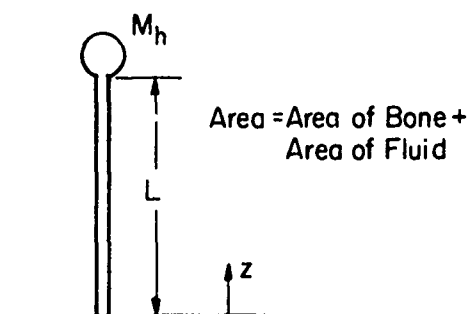


FIGURE 1. POROUS ELASTIC CONTINUUM MODEL OF THE SPINE

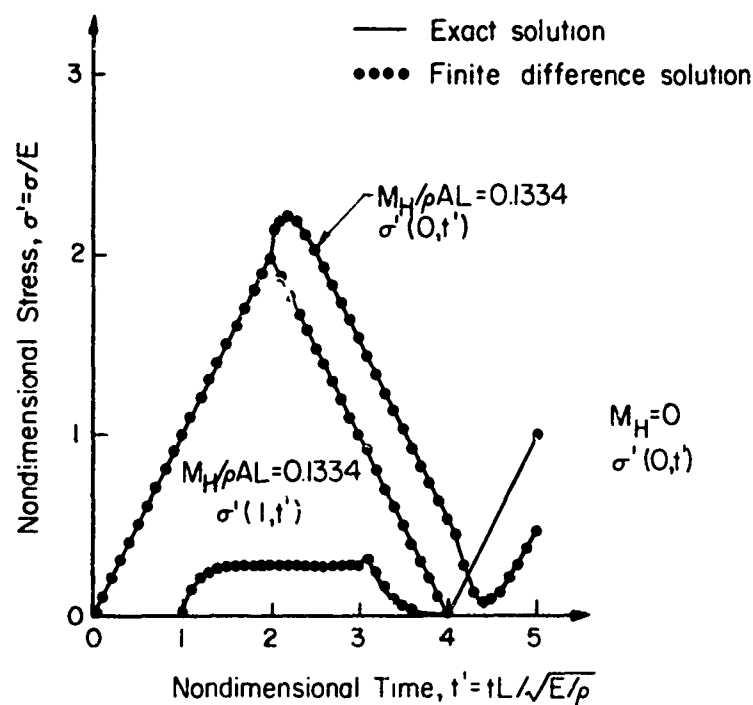


FIGURE 2. COMPARISON OF NONDIMENSIONAL STRESSES OBTAINED FROM EXACT SOLUTION AND BY FINITE DIFFERENCE PROGRAM

parameters. The results of these calculations are summarized and discussed in the final section.

#### Description of The Mathematical Model

The equations governing the behavior of the model can be divided into the following five classifications:

- (1) Equation of motion
- (2) Strain-displacement equations
- (3) Stress-strain relations
- (4) Flow law, and
- (5) Boundary conditions.

The equation of motion for this model is a statement that the sum of the forces acting on a "small" cross-sectional slice of the column is equal to the product of the mass of the bone and the acceleration of the bone plus the mass of the fluid times the acceleration of the fluid. In terms of the stresses that are produced by the prescribed displacements at the base of the column, this equation can be written in the following form.

$$\frac{\partial}{\partial z} (\sigma_z + \sigma) = \rho_B \ddot{u}_B + \rho_F \ddot{u}_F \quad (1)$$

where  $\sigma_z$  and  $\sigma$  are related to the stress in the solid material,  $\sigma_{zB}$ , the pressure of the fluid,  $p$ , and the porosity,  $f$ , in the following manner

$$\sigma = fp \quad (2)$$

$$\sigma_z = (1 - f) \sigma_{zB} \quad (3)$$

The porosity  $f$  is defined as the ratio of volume of fluid to the total volume of the column. The quantities  $\rho_B$  and  $\rho_F$ , in Equation (1) are related to the densities of the solid material,  $\bar{\rho}_B$ , and the fluid,  $\bar{\rho}_F$ , in the following way

$$\rho_B = (1 - f) \bar{\rho}_B \quad (4)$$

$$\rho_F = f \bar{\rho}_F \quad (5)$$

The accelerations of the bone and the fluid are denoted by  $\ddot{u}_B$  and  $\ddot{u}_F$ , respectively.

The strain-displacement relations are linear and applicable for small displacements. These equations are

$$\epsilon_B = \frac{\partial u_B}{\partial z} \quad (6)$$

and

$$\epsilon_F = \frac{\partial u_F}{\partial z} \quad (7)$$

where  $\epsilon_B$  and  $\epsilon_F$  are the strains in the bone and the fluid, respectively, and  $u_B$  and  $u_F$  are the displacements in the bone and fluid, respectively.

The stress-strain relations are given in terms of the effective stresses,  $\sigma_z$  and  $\sigma$ , and the strains,  $\partial u_B/\partial z$  and  $\partial u_F/\partial z$ . These equations are

$$\sigma_z = C \frac{\partial u_B}{\partial z} + Q \frac{\partial u_F}{\partial z} \quad (8)$$

$$\sigma = Q \frac{\partial u_B}{\partial z} + R \frac{\partial u_F}{\partial z} \quad (9)$$

The constant C, Q, and R are evaluated in Appendix B.

The flow law introduces the viscosity of the fluid. This equation is taken to be of the form of Darcy's equation, modified to include an acceleration term. This equation is

$$\frac{\partial \sigma}{\partial z} = fk (\dot{u}_F - \dot{u}_B) + \rho_F \ddot{u}_F \quad (10)$$

where k is a constant characterizing the viscosity of the fluid and the permeability of the solid.

The boundary conditions are a statement of what is happening at the ends of the column. For the cases considered here, the boundary conditions were of the form

$$\left. \begin{aligned} u_B(0,t) &= u(t) \\ u_F(0,t) &= u(t) \end{aligned} \right\} \text{ at } z = 0 \quad (11)$$



with one of the following sets of conditions at  $z = L$

$$\left. \begin{aligned} A(\sigma_z + \sigma) &= -M_H \ddot{u}_B(L, t) \\ u_B(L, t) &= u_F(L, t) \end{aligned} \right\} \text{ at } z = L \quad (12)$$

or

$$\left. \begin{aligned} A\sigma_z &= -M_H \ddot{u}_B(L, t) \\ \sigma &= 0 \end{aligned} \right\} \text{ at } z = L \quad (13)$$

Here  $u(t)$  denotes the prescribed displacement of  $z = 0$ ,  $M_H$  denotes the mass of the head, and  $A$  denotes the cross-sectional area of the column.

#### FORMULATION OF THE PROBLEM

There are four unknown quantities in the governing equations;  $\sigma_z$ ,  $\sigma$ ,  $u_B$ , and  $u_F$ . The problem was formulated in terms of the displacements  $u_F$  and  $u_B$ . The stresses  $\sigma_z$  and  $\sigma$  were eliminated by first substituting the expression for  $\frac{\partial \sigma}{\partial z}$  from Equation (10) into Equation (1). The re-

sult, after canceling like terms with opposite signs and rearranging, is

$$\frac{\partial \sigma_z}{\partial z} = fk(\dot{u}_F - \dot{u}_B) + \rho_B \ddot{u}_B \quad (14)$$

Expressions for  $\frac{\partial \sigma_z}{\partial z}$  and  $\frac{\partial \sigma}{\partial z}$ , in terms of the displacements  $u_B$  and  $u_F$ , are

obtained by differentiating Equations (8) and (9) with respect to  $z$ . Doing this gives

$$\frac{\partial \sigma_z}{\partial z} = c \frac{\partial^2 u_B}{\partial z^2} \quad (15)$$

and

$$\frac{\partial \sigma}{\partial z} = Q \frac{\partial^2 u_B}{\partial z^2} + R \frac{\partial^2 u_F}{\partial z^2} \quad (16)$$

Substituting Equations (15) and (16) into Equations (14) and (10) respectively gives the following 2 equations.

$$C \frac{\partial^2 u_B}{\partial z^2} + Q \frac{\partial^2 u_F}{\partial z^2} = -fk(\dot{u}_F - \dot{u}_B) + \rho_B \ddot{u}_B \quad (17)$$

and

$$Q \frac{\partial^2 u_B}{\partial z^2} + R \frac{\partial^2 u_F}{\partial z^2} = +fk(\dot{u}_F - \dot{u}_B) + \rho_F \ddot{u}_F \quad (18)$$

Solving Equations (17) and (18) for  $\frac{\partial^2 u_B}{\partial z^2}$  and  $\frac{\partial^2 u_F}{\partial z^2}$  gives

$$\frac{\partial^2 u_B}{\partial z^2} = \frac{R\rho_B}{D} \ddot{u}_B + fk \frac{(R+Q)}{D} \dot{u}_B - \frac{Q\rho_F}{D} \ddot{u}_F - fk \frac{(R+Q)}{D} \dot{u}_F \quad (19)$$

and

$$\frac{\partial^2 u_F}{\partial z^2} = \frac{C\rho_F}{D} \ddot{u}_F + fk \frac{(Q+C)}{D} \dot{u}_F - \frac{Q\rho_B}{D} \ddot{u}_B - fk \frac{(Q+C)}{D} \dot{u}_B \quad (20)$$

where

$$D = RC - Q^2 \quad (21)$$

Equations (19) and (20) are two second order linear partial differential equations containing only the displacements of the bone and the fluid. These equations are however coupled by the quantities  $Q$  and  $k$ . If  $Q$  and  $k$  are both zero, Equations (19) and (20) uncouple into two "wave" equations of the type

$$u_{zz} - \frac{1}{v^2} u_{tt} = 0 \quad (22)$$

as would be expected from an examination of Equations (8), (9), and (10).

The complete mathematical statement of the problem is to solve Equations (19) and (20) subject to the boundary conditions given by Equations (11) and (12) or by Equations (11) and (13). The solution method used was finite differences as detailed in Appendix A.

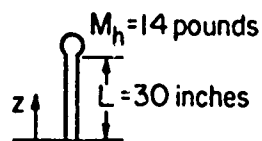
### Numerical Examples

For purposes of checking the numerical algorithms used, two problems for which exact solutions are available were solved. When the column is composed entirely of solid material the equations governing the model simplify and exact solutions of these equations have been investigated in Reference 5. Figure 2 shows the results of the check calculations. In one case the head mass was set to zero while in the second case the mass of the head was 0.1334 times the mass of the column. The results shown compare the obtained stress at the base of the column with the exact solution taken from Reference 5.

The model was then used to predict stresses at the bottom of the column for a range of the modulus of the solid and variations in the permeability and viscosity of the fluid. The modulus of the solid material was given values ranging from 3,000,000 psi to 3,000 psi. These values include the extremes between the modulus of bone (3,000,000 psi) and the modulus of intervertebral discs. Because the model can only be a uniform material, a "composite" modulus representative of the overall stiffness of a spine must be used and it is believed to be in the range examined.

For this range of the modulus, the stresses in the fluid and in the solid material at the lower end of the column are shown in Figures 3 through 6. The prescribed acceleration at the bottom of the column was 4.5 times the acceleration of gravity for all of these cases. Both sets of boundary conditions (Equations (12) and (13)) were examined at the top of the column. However, because of the value selected for Darcy's constant the results obtained were insensitive to the two sets of boundary conditions. The value of  $k$  is the ratio of viscosity to specific permeability and was taken to be  $7,000 \text{ lb sec/in}^4$  for all of these cases. Poisson's ratio for the solid material was taken to be 0.2 while the density of this material was  $1.25 \times 10^{-4} \text{ lb sec}^2/\text{in}^4$ . The fluid density was taken to be  $4.82 \times 10^{-5} \text{ lb sec}^2/\text{in}^4$ .

The results presented in Figures 3 through 6 show that as the modulus of the solid material decreases the stress in the fluid increases while the stress in the solid material decreases. It is noted that the magnitudes of the stresses are essentially insensitive to the modulus of the solid for values of the modulus less than 30,000 psi. The quantities which are dependent on the modulus in this range are the wave speeds. This means that if the stress-time curves for  $E_B = 30,000$  and  $E_B = 3,000$  were plotted on true time scales that the maximum stresses would occur



$$\ddot{u}(0,t) = 4.5g$$

$$\rho_B = 5.2 \text{ slugs/ft}^3 \quad \rho_F = 2.0 \text{ slugs/ft}^3$$

$$\text{Porosity} = 0.5, \quad \text{Area} = 2 \text{ in}^2$$

$$E_B = 3,000,000 \text{ psi}$$

$$k = 7,000 \text{ lb sec/in}^4$$

$$\begin{bmatrix} C & Q \\ Q & R \end{bmatrix} = \begin{bmatrix} 1.52 & 0.05 \\ 0.05 & 0.13 \end{bmatrix} \times 10^6 \text{ psi}$$

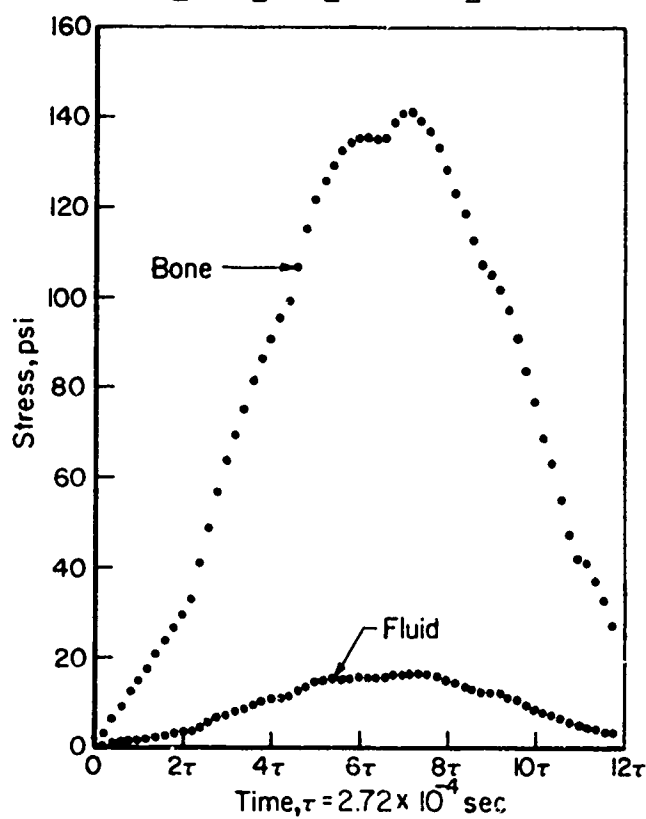
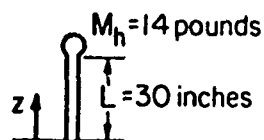


FIGURE 3. STRESSES AT THE LOWER END OF THE COLUMN FOR A MODULUS OF THE SOLID MATERIAL EQUAL TO 3,000,000 psi



$$\ddot{u}(0,t) = 4.5g$$

$$\rho_B = 5.2 \text{ slugs/ft}^3 \quad \rho_F = 2.0 \text{ slugs/ft}^3$$

$$\text{Porosity} = 0.5, \text{ Area} = 2 \text{ in}^2$$

$$E_B = 300,000 \text{ psi}$$

$$k = 7,000 \text{ lb sec/in}^4$$

$$\begin{bmatrix} C & Q \\ Q & R \end{bmatrix} = \begin{bmatrix} 1.59 & 0.24 \\ 0.24 & 0.61 \end{bmatrix} \times 10^5 \text{ psi}$$

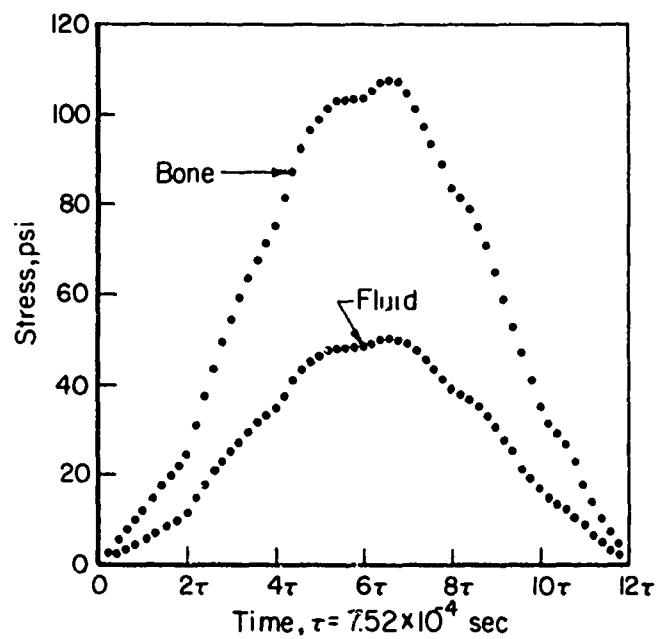


FIGURE 4. STRESSES AT THE LOWER END OF THE COLUMN FOR A MODULUS OF THE SOLID MATERIAL EQUAL TO 300,000 psi

at different times. The unit of time used in the figures is the length of time,  $\tau$ , required for the fastest wave to travel the length of the column.

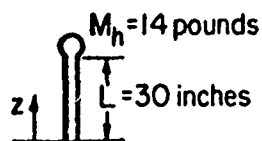
The stresses at the base of the column are periodic functions of time with a period something greater than  $12\tau$  for the cases considered in Figures 3 through 6. This period is determined by the time required for a tension wave to develop at the top of the column. Since the mass of the head is large compared to the mass of the column a relatively large time is needed for the head mass to be displaced sufficiently to cause a tension at the top of the column. In the absence of a head mass the period is  $4\tau$ .

Next the value of  $k$  was decreased to  $10^{-4}$  lb sec/in<sup>4</sup>. The remaining constants retained the values given on Figure 5. This value of  $k$  models a fluid that is very free to flow in the column. Such a fluid is the spinal fluid. Here the boundary conditions on the stress in the fluid at the upper end of the column greatly influenced the pressure in the fluid and the stress in the bone. The results for these problems are compared in Figure 7. When the fluid at the top of the column is stress free the results indicate that the solutions in the solid and fluid materials essentially decouple. That is the response of the solid material is what is expected for a column composed entirely of a solid material with  $E_B = C$  where  $C$  has the value  $1.66 \times 10^4$  psi. Similarly the fluid responds like a column of fluid with no mass at the top end.

To investigate the strength of the coupling between the stresses in fluid and solid materials having the properties given on Figure 5 an additional problem was solved. In this case the column was composed of a solid material having the value of  $1.66 \times 10^4$  psi for  $C$ . No fluid was in the column and this condition was realized in the model by setting  $k$ ,  $Q$ , and  $R$  to zero. In Figure 8, the stress at the bottom of the column for this case is compared with the results of Figure 5. From this figure, it is seen that the stress in the column without fluid is greater than the stress in the solid material containing fluid. However, the value of the stress in the column without fluid cannot be obtained by adding the stresses in the fluid and the solid material for the case shown in Figure 5.

#### SUMMARY AND DISCUSSION OF THE RESULTS

A model of the spine consisting of a continuous porous elastic column containing a viscoelastic fluid has been used to predict the pressure in the fluid for conditions of a constant acceleration at the base of the column and to examine the effect of the presence of the fluid on the stress in the solid material. This model differs from other models



$$\ddot{u}(0,t) = 4.5g$$

$$\rho_B = 5.2 \text{ slugs/ft}^3 \quad \rho_F = 2.0 \text{ slugs/ft}^3$$

$$\text{Porosity} = 0.5, \text{ Area} = 2 \text{ in}^2$$

$$E_S = 30,000 \text{ psi}$$

$$k = 7,000 \text{ lb sec/in}^4$$

$$\begin{bmatrix} C & Q \\ Q & R \end{bmatrix} = \begin{bmatrix} 1.66 & 0.39 \\ 0.39 & 0.97 \end{bmatrix} \times 10^4 \text{ psi}$$

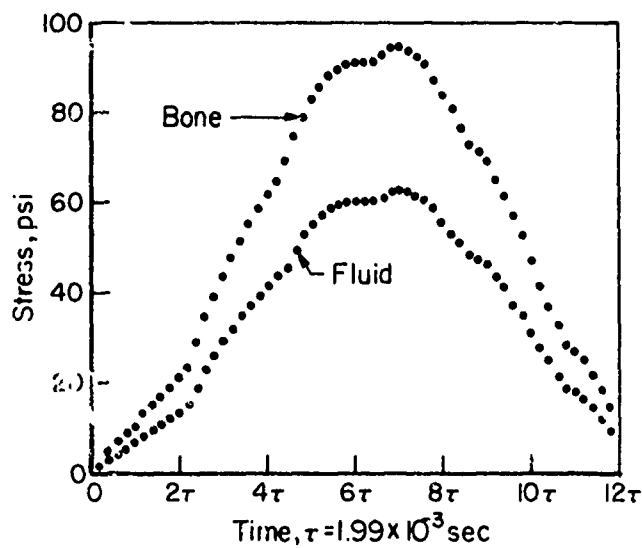
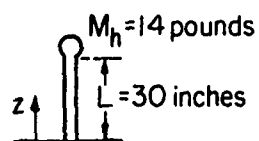


FIGURE 5. STRESSES AT THE LOWER END OF THE COLUMN FOR A MODULUS OF THE SOLID MATERIAL EQUAL TO 30,000 psi



$$\ddot{u}(0,t) = 4.5g$$

$$\rho_B = 5.2 \text{ slugs/ft}^3 \quad \rho_F = 2.0 \text{ slugs/ft}^3$$

$$\text{Porosity} = 0.5, \text{ Area} = 2 \text{ in}^2$$

$$E_B = 3,000 \text{ psi}$$

$$k = 7,000 \text{ lb sec/in}^4$$

$$\begin{bmatrix} C & Q \\ Q & R \end{bmatrix} = \begin{bmatrix} 1.66 & 0.41 \\ 0.41 & 1.03 \end{bmatrix} \times 10^3 \text{ psi}$$

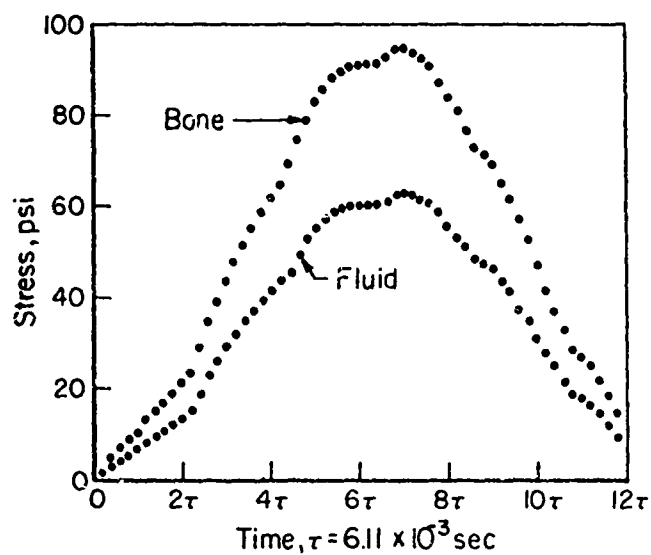
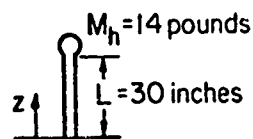


FIGURE 6. STRESSES AT THE LOWER END OF THE COLUMN FOR A MODULUS OF THE SOLID MATERIAL EQUAL TO 3,000 psi





$$\ddot{u}(0,t) = 4.5g$$

$$\rho_B = 5.2 \text{ slugs/ft}^3 \quad \rho_F = 2.0 \text{ slugs/ft}^3$$

$$\text{Porosity} = 0.5, \quad \text{Area} = 2 \text{ in}^2$$

$$E_B = 30,000 \text{ psi}$$

$$k = 0.0001 \text{ lb sec/in}^4$$

$$\begin{bmatrix} C & Q \\ Q & R \end{bmatrix} = \begin{bmatrix} 166 & 0.39 \\ 0.39 & 0.97 \end{bmatrix} \times 10^4 \text{ psi}$$

$$\Delta \sigma(L,t) = 0$$

$$u_B(L,t) = u_F(L,t)$$

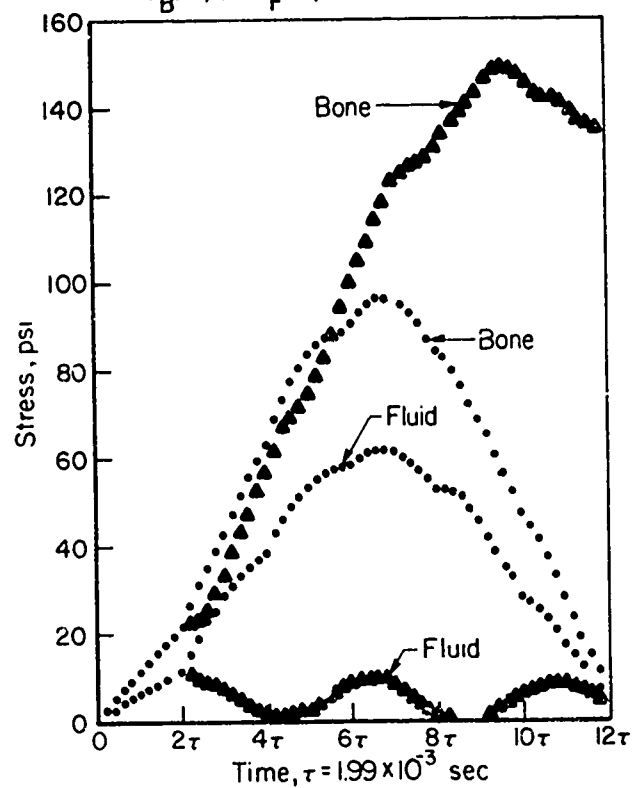
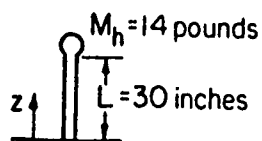


FIGURE 7. EFFECT OF THE BOUNDARY CONDITIONS AT THE TOP OF THE COLUMN ON THE STRESSES AT THE LOWER END FOR A LOW VISCOSITY FLUID IN A PERMEABLE SOLID



$$\ddot{u}(0,t) = 4.5g$$

$$\rho_B = 5.2 \text{ slugs/ft}^3 \quad \rho_F = 2.0 \text{ slugs/ft}^3$$

$$\text{Porosity} = 0.5, \quad \text{Area} = 2 \text{ in}^2$$

• Bone only

$$\begin{bmatrix} C & Q \\ Q & R \end{bmatrix} = \begin{bmatrix} 1.66 & 0 \\ 0 & 0 \end{bmatrix} \times 10^4 \text{ psi}$$

$$\blacktriangle E_B = 30,000 \text{ psi}$$

$$k = 7,000 \text{ lb sec/in}^4$$

$$\begin{bmatrix} C & Q \\ Q & R \end{bmatrix} = \begin{bmatrix} 1.66 & 0.39 \\ 0.39 & 0.97 \end{bmatrix} \times 10^4 \text{ psi}$$

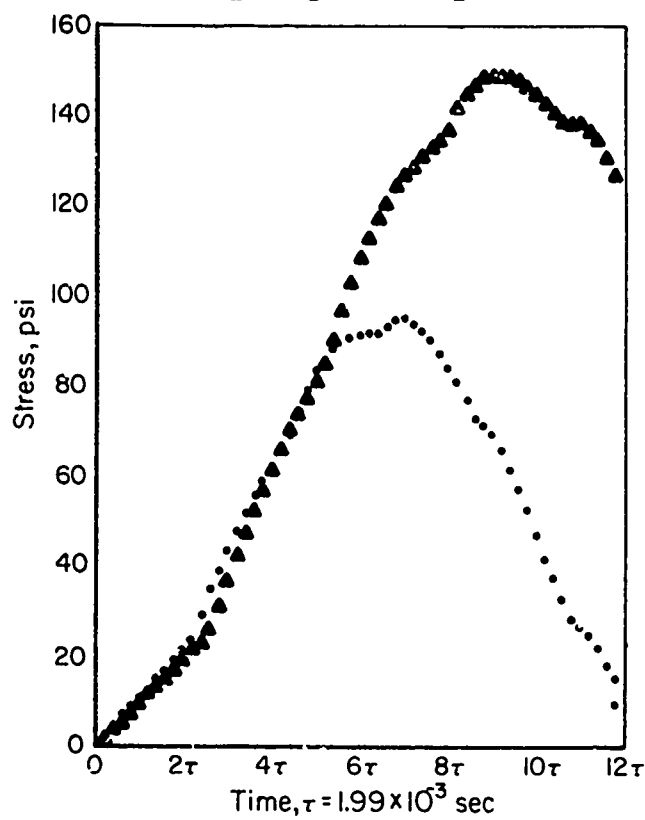


FIGURE 8. COMPARISON OF STRESSES IN THE SOLID MATERIAL FOR THE COLUMN IN FIGURE 5 WITH THOSE FOR THE SAME COLUMN WITHOUT THE FLUID

in the literature in that it contains the effects of pressure in the fluid and the inertia of the fluid. Because the column is treated as a continuum of two distinct media, there are two wave propagation speeds. In general, these speeds are each dependent on all the properties of both materials except  $k$ . If the quantity  $Q$  is zero, then the wave speeds are equal to the Rayleigh speeds of each material.

Another type of coupling between the fluid and the solid occurs through Darcy's constant,  $k$ , as seen by Equations (18) and (19). The magnitude of  $k$  determines the amount of displacement disturbance that is transmitted from one material to the other. The results of the numerical examples revealed that for a value of  $k$  equal to 7,000 lb sec/in<sup>4</sup>, the fluid and solid material had the same displacements. However, for a value of  $k$  equal to 10<sup>-4</sup> lb sec/in<sup>4</sup>, the displacement disturbance in one medium did not appreciably affect the displacement in the other. The larger value of  $k$  corresponds to a fluid that is very viscous or a solid material with a low permeability. The smaller value of  $k$  corresponds to a fluid with low viscosity. For this case the stress in the fluid is dependent on the boundary conditions on the fluid at the top of the column. The reason for this is that equating the fluid and bone displacements at the top of the column creates a compression wave that is not present when the fluid is stress free at the end of the column.

It is noted that the stresses in the fluid were not negligible when compared with the stresses in the bone. Also the results shown in Figures 3 through 6 indicate that the fluid pressure in the intervertebral discs may be higher than the stresses in the vertebrae because the modulus of a disc is lower than that of bone material.

There are several extensions of this model that could be made with reasonable effort and which would make the model more realistic. One of these is to include curvature in the column. Another is to represent the spine as an assemblage of segments to describe the individual vertebrae and discs. Here the area and stiffness could vary throughout the length of the column. The last extension would provide a better estimate of the pressure in the fluid and the stress of the discs.

# APPENDIX A

## METHOD OF SOLUTION

The coupled second order system of Equations (19) and (20), were solved using a forward finite difference method. Because of the "wave" nature of the equations, care must be taken to choose appropriate values for the increments  $\Delta z$  along the column and  $\Delta t$  in time. The needed information can be obtained by examining the characteristics of the system.

Procedures for finding the characteristics of systems of partial differential equations can be found in most textbooks on partial differential equations. For example, see Reference (8). The characteristic equation for Equations (19) and (20) is given by

$$\alpha_1^4 - \frac{1}{D} (R\rho_B + C\rho_F) \alpha_1^2 \alpha_2^2 + \frac{\rho_B \rho_F}{D} \alpha_2^4 = 0 \quad (A-1)$$

where  $\alpha_1$  and  $\alpha_2$  are certain parameters. If it is required that  $\alpha_1^2 + \alpha_2^2 = 1$  in addition, then the  $\alpha_1$  can be interpreted as the cosines of the angles between the  $x$  and  $t$  axes and the normals to a characteristic hyperplane. Setting  $\lambda = \alpha_1/\alpha_2$  and solving Equation (A-1) for  $\lambda^2$  gives

$$\lambda^2 = \frac{1}{2D} \left[ (R\rho_B + C\rho_F) \pm ((R\rho_B + C\rho_F)^2 - 4D\rho_B\rho_F)^{1/2} \right] \quad (A-2)$$

If  $\bar{\lambda}$  denotes the minimum value of  $\lambda$  as determined from Equation (A-2) then the step sizes in  $z$  and  $t$  must satisfy

$$\frac{\Delta t}{\Delta z} < \bar{\lambda}$$

to insure that the numerical process is stepping along faster than the maximum of the disturbance velocities.

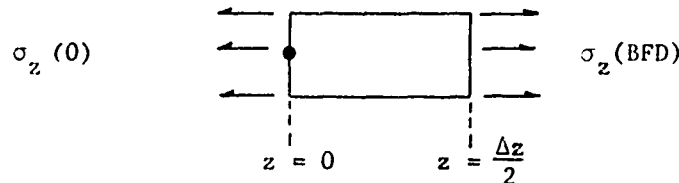
Let the problem region then be discretized by the mesh  $z_i = i\Delta z$   $i = 0, 1, \dots, n$  and  $t_i = i\Delta t$ ,  $i = 0, 1, \dots$ , where  $\Delta t/\Delta z < \bar{\lambda}$ . In terms of the notation  $u(z_i, t_j) = u(i\Delta z, j\Delta t) = u(i, j)$ , the following finite difference approximations were used:

$$\dot{u}(z_i, t_j) = (u(i, j+1) - u(i, j-1))/2\Delta t$$

$$\ddot{u}(z_i, t_j) = (u(i, j+1) - 2u(i, j) + u(i, j-1))/\Delta t^2$$

$$\begin{aligned}
& - \left( \frac{C\rho_F \Delta z^2}{D\Delta t^2} - \frac{(Q+C)fk\Delta z^2}{2D\Delta t} \right) u_F(i,j-1) \\
& - \frac{2Q\rho_B \Delta z^2}{D\Delta t^2} u_B(i,j) - \left( \frac{(Q+C)fk\Delta z^2}{2D\Delta t} - \frac{Q\rho_B \Delta z^2}{D\Delta t^2} \right) u_B(i,j-1)
\end{aligned}$$

The boundary conditions given by either Equations (11) and (12) or Equations (11) and (13) are in terms of displacements and stresses. At the end  $z = 0$  the bone and fluid displacements are prescribed and it is necessary to be able to calculate the stresses in the bone and the fluid there. To accomplish this, the equations of motion for the segment between  $z = 0$  and  $z = \Delta z/2$  are developed.



For the bone, the equation of motion is given by

$$(\sigma_z(\text{BFD}) - \sigma_z(o,t))A = \rho_B \frac{\Delta z}{2} A \ddot{u}(t) \quad (\text{A-5})$$

Here  $\sigma_z(\text{BFD})$  denotes the stress obtained by the finite difference calculation,  $A$  denotes the column area, and  $\ddot{u}(t)$  denotes the known acceleration of the segment between  $z = 0$  and  $z = \frac{\Delta z}{2}$ . Solving Equation (A-5) for the unknown stress,  $\sigma_z(o,t)$ , gives

$$\sigma_z(o,t) = \sigma_z(\text{BFD}) - \rho_B \frac{\Delta z}{2} \ddot{u}(t) \quad (\text{A-6})$$

Reasoning similarly for the fluid yields the equation

$$\sigma(o,t) = \sigma(\text{BFD}) - \rho_F \frac{\Delta z}{2} \ddot{u}(t) \quad (\text{A-7})$$

Equations (A-6) and (A-7) were used to calculate the stresses  $\sigma_z(o,t)$  and  $\sigma(o,t)$ .

At the end  $z = L$  two sets of boundary conditions were considered. The conditions given by Equations (11) and (12) will be treated first. Writing the equations of motion at  $z = L$  gives

$$\frac{\partial^2 u(z_i, t_j)}{\partial z^2} = (u(i-1, j) - 2u(i, j) + u(i+1, j)) / \Delta z^2$$

These approximations, when applied to the system of Equations (19) and (20), yield the difference equations

$$Au_B(i, j+1) + Bu_F(i, j+1) = C_1 \quad (A-3)$$

$$Eu_B(i, j+1) + Fu_F(i, j+1) = C_2 \quad (A-4)$$

where

$$A = \left( \frac{R\rho_B}{D\Delta t^2} + \frac{(R+Q)fk}{2D\Delta t} \right) \Delta z^2$$

$$B = - \left( \frac{Q\rho_F}{D\Delta t^2} + \frac{(R+Q)fk}{2D\Delta t} \right) \Delta z^2$$

$$E = - \left( \frac{Q\rho_B}{D\Delta t^2} + \frac{(Q+C)fk}{2D\Delta t} \right) \Delta z^2$$

$$F = \left( \frac{C\rho_F}{D\Delta t^2} + \frac{(Q+C)fk}{2D\Delta t} \right) \Delta z^2$$

$$\begin{aligned} C_1 = & \left( -2 + \frac{2R\rho_B\Delta z^2}{D\Delta t^2} \right) u_B(i, j) + u_B(i+1, j) \\ & + u_B(i-1, j) - \left( \frac{R\rho_B\Delta z^2}{D\Delta t^2} - \frac{(R+Q)\Delta z^2 fk}{2D\Delta t} \right) u_B(i, j-1) \\ & - \frac{2Q\rho_F\Delta z^2}{D\Delta t^2} u_F(i, j) - \left( \frac{(R+Q)fk\Delta z^2}{2D\Delta t} - \frac{Q\rho_F\Delta z^2}{D\Delta t^2} \right) u_F(i, j-1) \end{aligned}$$

and

$$C_2 = \left( -2 + \frac{2Q\rho_F\Delta z^2}{D\Delta t^2} \right) u_F(i, j) + u_F(i+1, j) + u_F(i-1, j)$$

$$\sigma_z(L,t) = \sigma_z(\text{BFD}) + \rho_B \frac{\Delta z}{2} \ddot{u}_B(L,t) \quad (\text{A-8})$$

and

$$\sigma(L,t) = \sigma(\text{BFD}) + \rho_F \frac{\Delta z}{2} \ddot{u}_F(L,t) \quad (\text{A-9})$$

On substituting Equations (A-8) and (A-9) into the first of Equations (12) and noting that  $u_B(L,t) = u_F(L,t)$  there results

$$\ddot{u}_B(L,t) = - \left[ \sigma_z(\text{BFD}) + \sigma(\text{BFD}) \right] / \left[ \rho_B \frac{\Delta z}{2} + \rho_F \frac{\Delta z}{2} + \frac{M_H}{A} \right] \quad (\text{A-10})$$

Replacing  $\ddot{u}_B(L,t)$  by an appropriate finite difference approximation gives

$$u_B(L,t+\Delta t) = 2u_B(L,t) - u_B(L,t-\Delta t) - \Delta t^2 \left[ \sigma_z(\text{BFD}) + \sigma(\text{BFD}) \right] / \left[ (\rho_B + \rho_F) \frac{\Delta z}{2} + \frac{M_H}{A} \right] \quad (\text{A-11})$$

Equation (A-11) also gives the value of  $u_F(L,t+\Delta t)$  since for this set of boundary conditions

$$u_F(L,t) = u_B(L,t) .$$

For the boundary conditions given by Equations (11) and (13)  $\sigma(L,t) = 0$  so the equation of motion for the fluid becomes

$$\ddot{u}_F(L,t) = - \frac{2}{\rho_F \Delta z} \sigma(\text{BFD}) \quad (\text{A-12})$$

On replacing  $\ddot{u}_F(L,t)$  by a finite difference representation an expression for  $u_F(L,t+\Delta t)$  is obtained. The result is

$$u_F(L,t+\Delta t) = 2u_F(L,t) - u_F(L,t-\Delta t) - \frac{2\Delta t^2}{\rho_F \Delta z} \sigma(\text{BFD}) \quad (\text{A-13})$$

An expression for  $u_B(L,t+\Delta t)$  is similarly obtained from Equation (13) by replacing  $\sigma_B(L,t)$  with the right-hand side of Equation (A-8) and approximating  $\ddot{u}_B(L,t)$  by finite differences. Here the result is

$$u_B(L, t+\Delta t) = 2u_B(L, t) - u_B(L, t-\Delta t) - \Delta t^2 \sigma_z(\text{BFD}) / \left( \rho_B \frac{\Delta z}{2} + \frac{M_H}{A} \right) \quad (\text{A-14})$$

To summarize, the displacements at the end  $z = L$  for the boundary conditions given by Equations (11) and (12) are given by Equation (A-11). The displacements at the end  $z = L$  for the boundary conditions given by Equations (11) and (13) are given by Equations (A-13) and (A-14).



## APPENDIX B

### EVALUATION OF THE CONSTANTS IN THE STRESS STRAIN RELATIONS

The constants C, Q, and R which appear in the stress-strain equations are related to the compressability of the fluid,  $k_F$ , the porosity,  $f$ , Young's modulus of the bone,  $E_B$ , and Poisson's ratio for the bone,  $\nu_B$ . The purpose of this appendix is to derive these relationships.

Let the fluid be given a small fixed displacement  $-\delta$  associated with a pressure  $p > 0$ . Holding the displacement of the bone equal to zero and assuming small strains, it is reasonable to say that

$$\sigma_{xB} = \sigma_{yB} = -p, \quad \epsilon_F = -\delta/l, \quad \text{and} \quad \epsilon_B = \partial u_B / \partial z = 0.$$

The stress-strain equations then assume the form

$$\sigma = R\epsilon_F \quad (B-1)$$

and

$$\sigma_z = Q\epsilon_F \quad (B-2)$$

The fluid compressibility equation is

$$p = -k_F \frac{\Delta V_F}{V_F} \quad (B-3)$$

where  $V_F$  denotes the volume of the fluid. This equation when substituted into Equation (2) and the results substituted into the reduced stress-strain equation (B-1) gives

$$R = f k_F \Delta V_F / (V_F \epsilon_F) \quad (B-4)$$

A similar relation for Q results from first noting that

$$\epsilon_B = \frac{\sigma_{zB}}{E_B} - \nu_B \frac{(\sigma_{xB} + \sigma_{yB})}{E_B} = 0 \quad (B-5)$$

from which

$$\sigma_{zB} = -2\nu_B p \quad (B-6)$$

is obtained. As a result

$$Q = 2(1-f)\nu_B k_F \Delta V_F / (V_F \epsilon_F) \quad (B-7)$$

and it remains to express  $\Delta V_F$  and  $V_F$  in terms of the elastic constants and the geometry.

The change in the fluid volume is conveniently approximated as the fluid area change times the model length plus the original fluid area times the prescribed displacement. Thus

$$\begin{aligned}\Delta V_F &= (\Delta V_F)_L + (\Delta V_F)_A = (\Delta V_F)_L + (\epsilon_x + \epsilon_y) A_B \\ &= (-\delta A_F) + \left( \frac{2p A_B \ell}{E_B} (1 - 2\nu_B)(1 + \nu_B) \right)\end{aligned}\quad (B-8)$$

In deriving the above expression for  $\Delta V_F$ , the assumption was made that for small strains the cross sectional area change of the bone and the fluid are equal in magnitude. Now  $V_F = A_F \ell$  so that

$$\Delta V_F / V_F = \epsilon_F + 2p (1 - 2\nu_B)(1 + \nu_B)(1 - f) / (f E_B) \quad (B-9)$$

Substituting  $-k_F \Delta V_F / V_F$  for  $p$  and rearranging terms gives

$$\Delta V_F / V_F = \epsilon_F / (1 + 2k_F (1 - 2\nu_B)(1 + \nu_B)(1 - f) / f E_B) \quad (B-10)$$

When Equation (B-10) is substituted into Equations (B-4) and (B-7) the following expressions for  $R$  and  $Q$  are obtained:

$$R = \frac{fk_F}{1 + \frac{2k_F}{E_B} (1 - 2\nu_B)(1 + \nu_B) \frac{(1-f)}{f}} \quad (B-11)$$

$$Q = \frac{2(1-f) k_F \nu_B}{1 + \frac{2k_F}{E_B} (1 - 2\nu_B)(1 + \nu_B) \frac{(1-f)}{f}} \quad (B-12)$$

The constant  $C$  is evaluated in a similar fashion. In this case the bone is given a small displacement  $u_B = -\delta$  and  $\epsilon_F = 0$ . Then the stress-strain equations assume the form

$$\sigma_z = C\epsilon_B$$

$$\sigma = Q\epsilon_B$$

Using arguments similar to those used to obtain R and Q, it is found that

$$C = (1-f) \left[ E_B + \frac{4v_B^2 k_F (1-f)}{\left(f + \frac{2k_F}{E_B}\right) (1-2v_B) (1+v_B) (1-f)} \right] \quad (B-13)$$

#### REFERENCES

- (1) Latham, F., "A Study of Body Ballistics: Seat Ejection", Proc. of Royal Society, B, Vol 147 (1957), p 121.
- (2) Weis, E. B., Jr., and Von Gierke, H. E., "A Model of Human Tissue Strain in Mechanical Stress Environments", Presented at the 39th Annual Aerospace Medical Association Meeting (May 6-9, 1968).
- (3) Hess, J. L., and Lombard, C. V., "Theoretical Investigations of Dynamic Response of Man to High Vertical Accelerations", Journal of Aviation Medicine, Vol 29 (1957), p 66.
- (4) Terry, C. T., and Roberts, V. L., "A Viscoelastic Model of the Human Spine Subjected to +gz Accelerations", Journal of Biomechanics, Vol 1, No. 2 (1968), pp 161-168.
- (5) Liu, Y. K., and Murray, J. D., "A Theoretical Study of the Effect of Impulses on the Human Torso", Proc. ASME Symposium on Biomechanics (November, 1966), pp 167-186.
- (6) Orne, D., "A Mathematical Model of Spinal Response to Impact", Doctoral Dissertation, Advisor: Professor Y. K. Liu, University of Michigan, Ann Arbor, Michigan (1969).
- (7) Nowinski, J. L., "Bone Articulations as Systems of Poroelastic Bodies in Contact", Presented at the AIAA 8th Aerospace Sciences Meeting, New York, New York (January 19-21, 1970), Paper No. 70-133.
- (8) Petrovsky, I. G., "Lectures on Partial Differential Equations", Interscience Publishers Inc., New York, New York (1957).

A MATHEMATICAL MODEL FOR THE BEHAVIOR OF THE BRAIN  
WHEN THE HUMAN HEAD IS SUBJECTED TO IMPULSIVE LOADS

by

Ali E. Engin, Ph.D.

and

Verne L. Roberts, Ph.D.

The University of Michigan

ABSTRACT

The subject matter of this paper is concerned with the theoretical determination of the behavior of the brain when the human head is subjected to external impulsive loads. The mathematical analysis is made for the axisymmetric response of an inviscid compressible fluid loaded impulsively by its elastic spherical shell container. The motion of the fluid is assumed to be governed by the linear wave equation. The spherical shell equations include both membrane and bending effects in axisymmetric torsionless motion. In the analysis first the solution for an initial value problem is obtained; later the transient response of the fluid for an arbitrary velocity input of the shell is constructed by means of convolution integral. For the numerical results, a characteristic time is defined and the excess pressure distribution in the fluid is evaluated for various deceleration times comparable with this characteristic time. A description of some of the salient features of the excess pressure distribution is also given in view of the elastic and rigid shell boundary of the fluid. Since the problem is considered from a theoretical point of view to determine some of the causes of the brain damage when the human head is subjected to impulsive loads, in the numerical computations the data is chosen to be suitable to the physical properties of brain and skull.

**PRECEDING PAGE BLANK**

# LIST OF SYMBOLS

- E Young's modulus
- $P_n(\cos \phi)$  Legendre polynomials of the first kind
- $P'_n(\cos \phi)$  Associated Legendre polynomials of the first kind and first order
- V Speed of the fluid-filled shell along an axis passing through the poles
- $\phi$  Velocity potential for the fluid
- $\phi_1$  Nondimensional velocity potential for the fluid,  $\phi/ac_s$
- $\Omega$  Nondimensional frequency,  $\omega a/c$
- a Radius of spherical shell
- $a_0, a_n$  Coefficients of Legendre polynomial expansion of  $\tau$
- $b_n$  Coefficients of Legendre polynomial expansion of  $\psi$
- $c_0, c_n$  Coefficients of velocity potential
- c Compressional wave speed in the fluid
- $c_s$  Apparent wave speed in the shell,  $[E/\rho_s(1-\nu^2)]^{1/2}$
- f Shell-fluid parameter,  $\rho_0 a/\rho_s h$
- h Shell thickness
- $j_n(z)$  Spherical Bessel function,  $(\pi/2z)^{1/2} J_{n+1/2}(z)$
- k Wave number,  $\omega/c$
- p Excess pressure
- $p_1$  Nondimensional excess pressure,  $p/\rho_0 c_s^2$
- $r, \theta, \phi$  Spherical coordinates
- $r_1$  Nondimensional radius,  $r/a$
- s Speed ratio,  $c/c_s$

- t Time
- $t_c$  Characteristic time,  $\frac{2a}{c}$
- $t_0$  Deceleration time
- u Meridional displacement of the shell mid-surface with respect to geometric center of the shell
- w Radial displacement of the shell mid-surface with respect to geometric center of the shell
- $\alpha^2$  Thickness parameter,  $\frac{h^2}{12a^2}$
- $\zeta$  Nondimensional radial displacement,  $w/a$
- $\psi$  Nondimensional meridional displacement,  $u/a$
- $\lambda_n$   $n(n+1)$
- $\nu$  Poisson's ratio
- $\rho_0, \rho_s$  Mass density of fluid and shell respectively
- $\tau$  Nondimensional time,  $c_s t/a$
- $\tau_c$  Nondimensional characteristic time,  $2/s$
- $\tau_0$  Nondimensional deceleration time,  $c_s t_0/a$
- $\omega$  Angular frequency

## INTRODUCTION

This investigation aims at the following two considerations. First, the subject matter is a point of interest in theoretical mechanics due to the fluid-solid interaction nature of the problem. Second, from the application point of view, the impulsive response of the fluid when the enclosing elastic shell is suddenly subjected to a change in its velocity can be taken as a simple but improved theoretical model to determine the formation of brain damage when no local contacts are made on the human head.

The previous studies in the area have been either investigations involving shells in contact externally and/or internally with fluids, especially by researchers in the field of acoustics, or analyses of various head injury models. While studies on these two categories are numerous, only a few representative ones will be mentioned here. Junger<sup>1</sup> investigated the effect of fluid on the natural frequencies of cylindrical and spherical shells freely suspended in a compressible fluid medium. Free and forced oscillations of infinitely long cylindrical shells surrounded by water were studied by Greenspon<sup>2</sup> who treated unpressurized shells by exact elasticity theory and cylindrical shells with fluid by approximate shell theory. Utilizing linear shell theory, which includes both membrane and bending effects, Engin and Liu<sup>3</sup> recently obtained the frequency equation and corresponding frequency spectrum of fluid-filled spherical shells for the axisymmetric and nontorsional motion.

In the literature, the rigorous mathematical treatments of the physical theory of the formation of brain damage was first introduced by Anzelius<sup>4</sup> and Güttinger<sup>5</sup> with their analyses of the impulsive response of an inviscid fluid contained in a rigid closed spherical shell (or container). Their formulations are essentially identical and involve an axisymmetric solution of the acoustic wave equation in



spherical coordinates. In the papers of both authors the eigen values of the problem are determined by requiring the radial component of the fluid velocity to vanish at the interior surface of the rigid spherical shell surrounding the fluid. Hayashi<sup>6</sup> treated a one-dimensional version of the Anzelius-Güttinger model. His model consists of a rigid and massless vessel containing inviscid fluid. The vessel, which is attached to a linear spring, is subjected to impacts with a stationary wall. Approximate solutions were obtained for the limiting cases of soft and very hard impacts. Although this simple model has the advantage of being easy to interpret, it has the similar shortcomings of the Anzelius-Güttinger model, i.e. (a) due to rigidity and geometric assumption there is no way to determine the possible locations of skull fracture and (b) the effects of skull deformation on the intracranial pressure distribution can not be determined. Recently, Engin<sup>7</sup> removed some major restrictions of previous head injury models by obtaining analytical and numerical solutions for the dynamic response of a fluid-filled elastic spherical shell. The loading pattern for his model is taken to be local, radial, axisymmetric and impulsive. Since the load is applied as a force locally on one of the poles of the shell, the combined shell theory which includes both membrane and bending effects of the shell has been used for the proper description of the wave propagation on the shell. The analysis utilizes Laplace transform technique in obtaining the transient response of the system. The conclusions of Engin's paper include the possible locations of brain damage and skull injury on the basis of the numerical computations. As a problem in mechanics, the present investigation is a generalization of the results of Anzelius and Güttinger by removing the restriction of rigidity of the shell surrounding the fluid. Our model consists of an elastic spherical shell filled with inviscid compressible fluid. The shell material and fluid are considered to be homogeneous and isotropic. In the analysis, the fluid-filled shell will be considered to have a

constant translational velocity for  $t < 0$  with respect to an inertial coordinate system. At  $t = 0$  the shell is brought to a sudden stop, i.e. the fluid occupying the interior space of the shell is subjected to a global axisymmetric impulse on its boundary. The determination of the pressure distribution in the fluid for this kind of impulse will help to explain quantitatively the location and the magnitude of brain damage under the conditions in which the application of local forces on the skull is avoided.

# I. EQUATIONS OF MOTION AND THEIR SOLUTIONS

The governing differential equations of motion for a fluid-filled spherical shell were previously obtained in reference 3 by means of Hamilton's Principle. These three partial differential equations, which are coupled in terms of the meridional and radial displacements,  $u$ ,  $w$  of the shell mid-surface and velocity potential,  $\phi$ , of the fluid, are given below in nondimensional form:

$$\alpha^2 \left[ \frac{\partial^2 \psi}{\partial \phi^2} + \cot \phi \frac{\partial \psi}{\partial \phi} - (v + \cot^2 \phi) \psi - \frac{\partial^3 \zeta}{\partial \phi^3} - \cot \phi \frac{\partial^2 \zeta}{\partial \phi^2} + (v + \cot^2 \phi) \frac{\partial \zeta}{\partial \phi} \right] + \frac{\partial^2 \psi}{\partial \tau^2} + \cot \phi \frac{\partial \psi}{\partial \tau} - (v + \cot^2 \phi) \psi + (1+v) \frac{\partial \zeta}{\partial \phi} - \frac{\partial^2 \psi}{\partial \tau^2} = 0, \quad (1)$$

$$\alpha^2 \left[ \frac{\partial^3 \psi}{\partial \phi^3} + 2 \cot \phi \frac{\partial^2 \psi}{\partial \phi^2} - (1+v+\cot^2 \phi) \frac{\partial \psi}{\partial \phi} + (\cot^2 \phi - v + 2) \psi \cot \phi - \frac{\partial^4 \zeta}{\partial \phi^4} - 2 \cot \phi \frac{\partial^3 \zeta}{\partial \phi^3} + (1+v+\cot^2 \phi) \frac{\partial^2 \zeta}{\partial \phi^2} - (2-v+\cot^2 \phi) \cot \phi \frac{\partial \zeta}{\partial \phi} \right] - (1+v) \left( \frac{\partial \psi}{\partial \phi} + \psi \cot \phi + 2 \zeta \right) - \frac{\partial^2 \zeta}{\partial \tau^2} - r \frac{\partial \phi_1(1, \phi, 1)}{\partial \tau} = 0, \quad (2)$$

and

$$\frac{1}{r_1^2} \frac{\partial}{\partial r_1} \left( r_1^2 \frac{\partial \phi_1}{\partial r_1} \right) + \frac{1}{r_1^2 \sin \phi} \frac{\partial}{\partial \phi} \left( \sin \phi \frac{\partial \phi_1}{\partial \phi} \right) - \frac{1}{s^2} \frac{\partial^2 \phi_1}{\partial \tau^2} = 0 \quad (3)$$

where

$$\psi = \frac{u}{a}, \quad \zeta = \frac{w}{a}, \quad \tau = \frac{c_s t}{a}, \quad c_s = \left[ E / \rho_s (1 - \nu^2) \right]^{1/2}, \quad s = \frac{c}{c_s}, \quad r_1 = \frac{r}{a}, \quad \phi_1 = \frac{\phi}{a c_s},$$

$$\frac{\ddot{f}}{f} = \frac{\rho_0 a}{\rho_s h}.$$

Since the deformation of a given shell is usually analyzed in terms of the deformation of its mid-surface, Eqs. 1 and 2 describe the motion of an imaginary boundary of the fluid which is half the shell thickness away from the physical boundary. These shell equations include both membrane and bending effects and they are given for an axisymmetric torsionless motion. Equation 3 is the linear

wave equation describing the motion of small oscillations of inviscid and irrotational fluid.

Consider the following series expansions for the nondimensional radial and tangential displacements of the shell midsurface:

$$z(\phi, \tau) = \sum_{n=0}^{\infty} a_n(\tau) P_n(\cos \phi), \quad (4a)$$

and

$$\psi(\phi, \tau) = \sum_{n=1}^{\infty} b_n(\tau) P'_n(\cos \phi), \quad (4b)$$

where  $P_n(\cos \phi)$  are Legendre polynomials of the first kind and  $P'_n(\cos \phi)$  are associated Legendre polynomials of the first order, first kind. Since the second solutions of the Legendre equations are singular at the poles they are not included in the expansions of  $z$  and  $\psi$ . The requirement of boundedness of solutions and the linearity of Eq. 3 lead to its formal solution:

$$\psi_1(r_1, \phi, \tau) = \sum_{n=0}^{\infty} c_n(\tau) j_n(kar_1) P_n(\cos \phi), \quad (5)$$

where  $j_n(kar_1)$  is spherical Bessel function,  $k=\omega/c$  is the wave number and  $\omega$  is the circular frequency.

The boundary condition between the fluid and shell can be stated as the continuity of normal velocities for all  $\phi$  and  $\tau$ ; that is,

$$\frac{\partial z(\phi, \tau)}{\partial \tau} = \frac{\partial \psi_1(l, \phi, \tau)}{\partial r_1} \quad (6)$$

Substitution of Eqs. 4a and 5 into Eq. 6 yields the following relationship between  $a_n(\tau)$  and  $c_n(\tau)$  for each  $n$ :

$$c_n(\tau) = \frac{1}{ka j'_n(ka)} \frac{da_n(\tau)}{d\tau} \quad (7)$$

It can be shown that substitution of Eqs. 4a, 4b, and Eq. 5, together with Eq. 7 into Eqs. 1 and 2, and the repeated utilization of the differential equations satisfied by  $P_n$  and  $P'_n$  yields the following system of equations for the determination of  $a_n(\tau)$  and  $b_n(\tau)$ :

for  $n=0$ :

$$\left[ 1 + f \frac{j_0(\Omega)}{\Omega j'_0(\Omega)} \right] \frac{d^2 a_0(\tau)}{d\tau^2} + 2(1+\nu) a_0(\tau) = 0, \quad (8)$$

for  $n \geq 1$ :

$$\frac{d^2 b_n(\tau)}{d\tau^2} + [1+\nu-\alpha^2(1-\nu-\lambda_n)] a_n(\tau) - (1-\nu-\lambda_n)(1+\alpha^2) b_n(\tau) = 0, \quad (9)$$

$$\left[ 1 + f \frac{j_n(\Omega)}{\Omega j'_n(\Omega)} \right] \frac{d^2 a_n(\tau)}{d\tau^2} - \left\{ (1+\nu)\lambda_n + \alpha^2 [\lambda_n^2 - \lambda_n(1-\nu)] \right\} b_n(\tau) + \left\{ 2(1+\nu) + \alpha^2 [\lambda_n^2 - \lambda_n(1-\nu)] \right\} a_n(\tau) = 0 \quad (10)$$

where  $\Omega = ka = \frac{\omega a}{c}$  and  $\lambda_n = n(n+1)$ . In reference 3 a description of some of the salient features of the frequency spectrum of a fluid-filled spherical shell is given in detail. There it was also shown that for each mode number,  $n$ , the infinite number of frequencies (or characteristic roots) exists. Thus, the solutions of Eqs. 8, 9 and 10 can be written in the following form:

$$a_0(\tau) = \sum_{m=0}^{\infty} A_{0m} \sin(\Omega_{0m} \tau + \alpha_{0m}), \quad (11)$$

$$a_n(\tau) = \sum_{m=0}^{\infty} A_{nm} \sin(\Omega_{nm} \tau + \alpha_{nm}) \quad (12)$$

and

$$b_n(\tau) = \sum_{m=0}^{\infty} \delta_{nm} A_{nm} \sin(\Omega_{nm} \tau + \alpha_{nm}) \quad (13)$$

where  $A_{0m}$ ,  $A_{nm}$ ,  $\delta_{nm}$  and  $\alpha_{nm}$  are arbitrary constants;  $\Omega_{0m}$  and  $\Omega_{nm}$  are the roots of the following frequency equations respectively

$$\left[1 + f \frac{j_0(\Omega)}{\Omega j_0'(\Omega)}\right] s^2 \Omega^2 - 2(1+\nu) = 0 \quad \text{for } n=0, \quad (14)$$

and

$$\begin{aligned} &\left[1 + f \frac{j_n(\Omega)}{\Omega j_n'(\Omega)}\right] s^4 \Omega^4 + \left\{ \left[1 + f \frac{j_n(\Omega)}{\Omega j_n'(\Omega)}\right] (1-\nu-\lambda_n)(1+\alpha^2) - 2(1+\nu) - \alpha^2 [\lambda_n^2 - \lambda_n(1-\nu)] \right\} s^2 \Omega^2 \\ &- (1+\nu) \left\{ 2(1-\nu-\lambda_n)(1+\alpha^2) + \lambda_n [1+\nu-\alpha^2(1-\nu-\lambda_n)] \right\} - \alpha^2 (2-\lambda_n) [\lambda_n^2 - \lambda_n(1-\nu)] = 0 \end{aligned}$$

(15)

for  $n \geq 1$ .

One of the steps in derivation of Eq. 15 also yields the following expression for  $\delta_{nm}$ :

$$\delta_{nm} = \frac{1+\nu-\alpha^2(1-\nu-\lambda_n)}{s^2 \Omega_{nm}^2 + (1-\nu-\lambda_n)(1+\alpha^2)} \quad \begin{matrix} n=1,2,3,\dots \\ m=0,1,2,\dots \end{matrix}$$

In view of Eqs. 7, 11 and 12 the nondimensional velocity potential,  $\phi$ , now can be written as

$$\phi_i(r_i, \phi, \tau) = \sum_{n=0}^{\infty} \sum_{m=0}^{\infty} A_{nm} s \frac{j_n(\Omega_{nm} r_i)}{j_n'(\Omega_{nm})} \cos(\Omega_{nm} s \tau + \alpha_{nm}) P_n(\cos \phi) \quad (16)$$

Next, let us consider the following physical situation in which a fluid-filled shell is travelling with a constant speed,  $V$ , along an axis passing through the poles. Assume at  $t=0$  it is brought to a sudden stop. Incidentally, this situation can be visualized as the motion of the fluid-filled shell in a force field which can only affect the shell material; the parameters of the force field can be adjusted in such a manner that the desired motion of the shell is obtained. Due to inertia of the fluid particles, at time  $t=0$  they will experience a velocity relative to the coordinate system whose origin is located at the geometric center of the shell. In other words, when the shell surrounding the fluid is brought to a sudden stop at  $t=0$ , the fluid particles occupying the interior space of the

shell are unaware that the motion of shell is arrested. Assuming that the initial excess pressure distribution in the fluid is zero we can now write the following initial conditions on the nondimensional velocity potential  $\phi$ .

$$\phi_1(r_1, \phi, \tau=0) \equiv \phi_0 \frac{V}{c_s} r_1 \cos \phi \quad (17)$$

and

$$\frac{\partial \phi_1}{\partial \tau} = \phi'_0 = 0 \quad \tau=0$$

From the second initial condition, i.e.  $\phi'_0=0$ , we get  $\alpha_{nm}=0$ . The first initial condition is used to obtain the coefficients  $A_{nm}$ . In order to do this let us first write Eq. 16 in the terminology of eigenfunctions by defining  $e_{nm} = j_n(\alpha_{nm} r_1) P_n(\cos \phi)$ :

$$\phi_1(r_1, \phi, \tau) = \sum_{n=0}^{\infty} \sum_{m=0}^{\infty} s A_{nm} e_{nm} \frac{\cos(\alpha_{nm} s \tau)}{j'_n(\alpha_{nm})} \quad (18)$$

Let  $\bar{e}_{nm} = j_n(\alpha_{nm} r_1) P_n(\cos \phi)$  be the conjugate-eigenfunction for  $e_{nm}$ ; having applied the first of the initial conditions on  $\phi_1$  in Eq. 18 and multiplying both sides of the resulting equation by  $\bar{e}_{nm}$  and integrating it over the fluid volume we get

$$A_{nm} = \frac{\int_V \phi_0 \bar{e}_{nm} dv}{\int_V \sum_{n=0}^{\infty} \sum_{m=0}^{\infty} \frac{s}{j'_n(\alpha)} \bar{e}_{nm} e_{nm} dv} \quad (19)$$

To evaluate the integral on the numerator of  $A_{nm}$  we write  $\cos \phi$  as  $P_1(\cos \phi)$  and see that in view of orthogonality of Legendre polynomials in the interval  $[-1, 1]$

$$\int_V \phi_0 \bar{e}_{nm} dv = \int_0^1 \int_0^\pi \int_0^{2\pi} \frac{V}{c_s} (ar_1)^3 j_n(\alpha_{nm} r_1) P_1(\cos \phi) P_n(\cos \phi) \sin \phi d\phi d\theta dr_1 = 0$$

$$\text{for } n \neq 1. \quad (20)$$

Expressing the spherical Bessel functions in terms of fractional order Bessel functions and performing the integration in Eq. 20 yields

$$\int_V \Phi_0 \bar{e}_{nm} dV = \frac{4\pi V}{3} \frac{a^3}{c_s} \frac{a^3}{\Omega_m^{3/2}} J_{5/2}(\Omega_m) \quad (21)$$

where  $\Omega_m \equiv \Omega_{lm}$ . For the evaluation of the integral on the denominator of  $A_{nm}$  we use the following properties of Bessel functions and Legendre polynomials:

$$\int_0^a J_{n+\frac{1}{2}}(k_{nl}r) J_{n+\frac{1}{2}}(k_{nm}r) r dr = \begin{cases} \frac{1}{2} a^2 \left[ J_{n+\frac{1}{2}}^2(k_{nm}a) - J_{n-\frac{1}{2}}(k_{nm}a) J_{n+\frac{3}{2}}(k_{nm}a) \right] & l=m \\ 0 & l \neq m \end{cases}$$

and from the definition of the norm of  $P_n(\cos\phi)$

$$\int_0^\pi P_n^2(\cos\phi) \sin\phi d\phi = \frac{2}{2n+1}.$$

Thus, the value of the integral under consideration becomes

$$\int_V \sum_{n=0}^{\infty} \sum_{m=0}^{\infty} \frac{s}{J_n'(\Omega)} \bar{e}_{nm} e_{nm} dV = \frac{2\pi a^3 s}{2n+1} \frac{\left[ J_{n+\frac{1}{2}}^2(\Omega_{nm}) - J_{n-\frac{1}{2}}(\Omega_{nm}) J_{n+\frac{3}{2}}(\Omega_{nm}) \right]}{\Omega_{nm}^{1/2} \left[ \frac{n}{\Omega_{nm}} J_{n+\frac{1}{2}}(\Omega_{nm}) - J_{n+\frac{3}{2}}(\Omega_{nm}) \right]} \quad (22)$$

From Eq. 20 we see that  $A_{nm}=0$  except  $n=1$ . Let  $A_m \equiv A_{1m}$ , using Eq. 21 and 22 in Eq. 19 we obtain the final expression for  $A_m$ :

$$A_m = \frac{2V J_{\frac{5}{2}}(\Omega_m) \left[ \frac{1}{\Omega_m} J_{\frac{3}{2}}(\Omega_m) - J_{\frac{5}{2}}(\Omega_m) \right]}{c \Omega_m \left[ J_{\frac{3}{2}}^2(\Omega_m) - J_{\frac{1}{2}}(\Omega_m) J_{\frac{5}{2}}(\Omega_m) \right]} \quad (23)$$

where  $\Omega_m$  are the roots of the frequency equation for  $n=1$ . Substitution of Eq. 23 into Eq. 18 after some simplification gives the expression for the nondimensional velocity potential for the fluid

$$\Phi_1(r, \phi, \tau) = \frac{2V}{c_s} \cos\phi \sum_{m=0}^{\infty} \frac{J_{\frac{5}{2}}(\Omega_m) J_{\frac{3}{2}}(\Omega_m r) \cos(\Omega_m s \tau)}{\Omega_m \left[ J_{\frac{3}{2}}^2(\Omega_m) - J_{\frac{1}{2}}(\Omega_m) J_{\frac{5}{2}}(\Omega_m) \right]} r^{1/2} \quad (24)$$

The nondimensional excess pressure,  $p_1$ , is equal to  $-\frac{\partial \Phi_1}{\partial \tau}$  and it is obtainable directly from Eq. 24.



It is interesting to note that the appropriate limiting case of Eq. 24 agrees with the result obtained by Güttinger<sup>5</sup>. When we write Eq. 24 in dimensional form,  $c_s$ , the wave speed on the shell, disappears from the expression of velocity potential. In the case in which the shell surrounding the fluid becomes rigid,  $s \rightarrow 0$ , and Eqs. 14 and 15 degenerate to  $j'_n(\Omega) = 0$ , which is easily shown to be the frequency equation of an ideal fluid contained in a rigid spherical shell. When the shell becomes rigid  $\Omega'_m$ 's in Eq. 24 are taken to be the roots of  $j'_1(\Omega) = 0$  which can also be written in terms of fractional order Bessel functions as  $2\Omega J_{3/2}'(\Omega) - J_{3/2}(\Omega) = 0$ . This last equation was used by Güttinger to obtain the necessary natural frequencies of the fluid for the determination of the impulsive response.

If desired, the transient response of the fluid for an arbitrary velocity input,  $V(\tau)$ , of the surrounding shell can be examined by means of Convolution integral. By the principle of superposition, it can be shown that velocity potential  $\tilde{\phi}_1$ , to an arbitrary shell excitation  $V(\tau)$  can be expressed as

$$\tilde{\phi}_1(r_1, \phi, \tau) = \frac{V(0)}{V} \phi_1(r_1, \phi, \tau) + \int_0^\tau \frac{V'(\xi)}{V} \phi_1(r_1, \phi, \tau - \xi) d\xi, \text{ for } \tau \geq 0. \quad (25)$$

where  $\phi_1(r_1, \phi, \tau)$  is given in Eq. 24 and  $V$  is the constant speed before the sudden stop of the spherical shell.

## II. NUMERICAL RESULTS AND DISCUSSION

For the determination of the numerical values of the excess pressure,  $p_i$ , generated in the fluid we use a different form of Eq. 24 in which the Bessel functions of fractional order are expressed in terms of trigonometric functions. The expression, thus obtained for  $p_i$  is

$$p_i(r_i, \phi, \tau) = \frac{2Vc}{c_s^2} \cos \phi \sum_{m=0}^{\infty} \frac{[3(\sin \Omega_m - \cos \Omega_m) - \Omega_m \sin \Omega_m][\sin(\Omega_m r_i) - \Omega_m r_i \cos(\Omega_m r_i)] \sin(\Omega_m s \tau)}{r_i^2 [\Omega_m^2 + (1 - 3\Omega_m) \sin^2 \Omega_m + \Omega_m \sin \Omega_m \cos \Omega_m]} \quad (26)$$

Here the dimensional excess pressure,  $p$ , can be obtained from  $p = p_i \rho_o c_s^2$ . At  $r_i = 0$  the equation for  $p_i$  is indeterminate; however, application of L'Hospital rule to Eq. 26 once yields  $p_i(0, \phi, \tau) = 0$ . That is, in the equatorial plane which is perpendicular to the direction of impulse, pressure is zero at all times. Since the problem was considered to serve as a theoretical model to determine the formation of brain damage, the numerical values are obtained from the following data suitable to the physical properties of brain and skull:

$$\begin{aligned} \rho_s &= 0.0772 \text{ lbm/in}^3 \\ E &= 2 \times 10^6 \text{ lbf/in}^2 \\ \nu &= 0.25 \\ a &= 3 \text{ in} \\ h &= 0.15 \text{ in} \\ \rho_o &= 0.0362 \text{ lbm/in}^3 \\ c &= 57100 \text{ in/sec.} \end{aligned} \quad (27)$$

The assumptions leading to the above data are discussed in detail in references 7 and 8.

Since the sudden stop of a fluid-filled shell demands an infinite deceleration, it is more reasonable to consider the case where stopping occurs during a finite time  $t_0$  (Nondimensional value,  $\tau_0 = \frac{ct_0}{a}$ ). More specifically let us assume that the shell has the following velocity form

$$V(t) = \begin{cases} V & (t \leq 0) \\ Vt/t_0 & (0 \leq t \leq t_0) \\ 0 & (t \geq t_0) \end{cases} \quad (28)$$

i.e. it is brought to a stop with a constant deceleration during time  $t_0$ . For the numerical results the magnitude of  $V$  is taken to be 528 in/sec. As regards the response of the system, the above situation is identical to that in which the shell and its content are set into motion from rest with the same magnitude of acceleration. Thus, in view of Eq. 25 the expression for the excess pressure can be obtained directly from Eq. 26

$$p_i(r, \phi, \tau) = \sum_{m=0}^{\infty} g_m(\phi, r_i) \left\{ [u(\tau) - u(\tau - \tau_0)] \sin^2 \frac{\Omega_m s \tau}{2} + u(\tau - \tau_0) \sin \frac{\Omega_m s \tau_0}{2} \sin \Omega_m s \left( \tau - \frac{\tau_0}{2} \right) \right\} \quad (29)$$

where

$$g_m(\phi, r_i) = \frac{4V}{c_s \tau_0} \frac{[3(\sin \Omega_m - \cos \Omega_m) - \Omega_m \sin \Omega_m][\sin(\Omega_m r_i) - \Omega_m r_i \cos(\Omega_m r_i)]}{r_i^2 \Omega_m [\Omega_m^2 (1 - 3\Omega_m^2) \sin^2 \Omega_m + \Omega_m \sin \Omega_m \cos \Omega_m]} \cos \phi,$$

and  $u(\tau)$ ,  $u(\tau - \tau_0)$  are the unit step functions. We note that the limiting case of Eq. 29 in fact gives Eq. 26 when  $\tau_0 \rightarrow 0$ . The series in Eq. 29 exhibits much better convergence than the one given in Eq. 26.

Let us define a characteristic time,  $t_c$  (or  $\tau_c = \frac{ct_c}{a}$ , 3.615 for the data given in Eq. 27) to be the time required for a wave in the fluid to travel from one pole to the other. In all the figures the deceleration duration is considered with respect to this characteristic time. Figure 1 shows the plot of the excess pressure at the pole ( $\phi=0$ ) for two different values of deceleration duration. The reduction of the pressure with doubling of the deceleration time is readily apparent. Figures 2 through 8 present the excess pressure distribution along the polar axis for various values of nondimensional radius  $r_1$  and nondimensional time  $\tau$ . From Eq. 29 we see that  $p_1(-r_1, \phi, \tau) = -p_1(r_1, \phi, \tau)$ ; hence, the points located symmetrically with respect to the equatorial plane which is perpendicular to the polar axis always experience the excess pressure of opposite sign. That is, for such a pair of points if one is in a state of compression, the other one will be in a state of dilatation. From Figs. 2 through 8 one can find the magnitude of the excess pressure along any ray extending from the origin by simply multiplying the value with  $\cos\phi$ . In other words, the waves generated on the inner surface of the shell have amplitude factors which attenuate according to the polar angle  $\phi$ . When the deceleration time  $\tau_0 \ll \tau_c$ , sharp extremes in the excess pressure form for  $\tau > \tau_0$ . This fact is illustrated in Fig. 2. A further interesting observation is the comparison of the pressure distributions in the fluid contained in the rigid and the elastic shells. In Figs. 3 through 8 pressure distributions are plotted for both elastic and rigid cases. From these plots we see that the amplitude of the excess pressure wave in the fluid contained in an elastic shell is considerably less than that of the excess pressure wave in the fluid contained in a rigid shell. Local variations of the wave form in the elastic case are also noticeable. When we compare Figs. 5 and 7 and Figs. 6 and 8 we notice that the wave forms are

essentially the same and the amplitudes of pressure for the large value of  $\tau_0$  are much less than those corresponding to a small value of  $\tau_0$  (compare the scales in the figures). In Figs. 7 and 8  $\tau_0=100\tau_c$  corresponds to 502 in/sec<sup>2</sup> (or 130 g's for a deceleration time of 0.0105 sec.) In this case the maximum negative excess pressure generated in the fluid is about 48 psi.

In conclusion, if we seek the brain damage to occur at the points of rarefaction of the fluid, we find this situation arises in maximum magnitudes at the poles and these locations are quite significant for the analytical confirmation of the cavitation theory of brain damage.

#### ACKNOWLEDGEMENT

This investigation was primarily supported by the Biomechanics Department of the Highway Safety Research Institute of The University of Michigan under Contract No. PH-43-67-1136 sponsored by the National Institute for Neurological Diseases and Blindness.

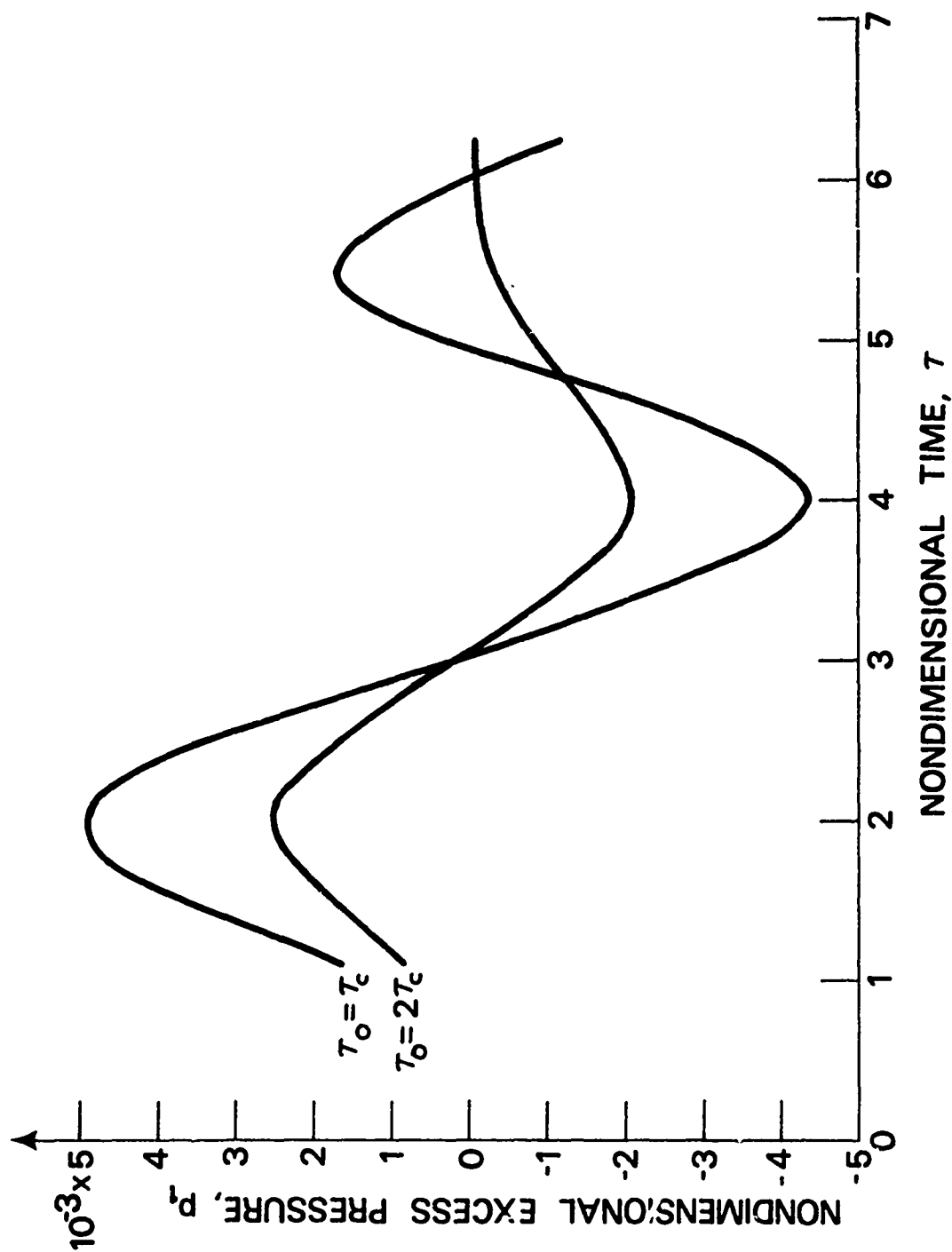


Fig. 1 Nondimensional excess pressure,  $p_1$ , vs. nondimensional time,  $\tau$ , at  $\phi=0$ , (Elastic shell boundary).

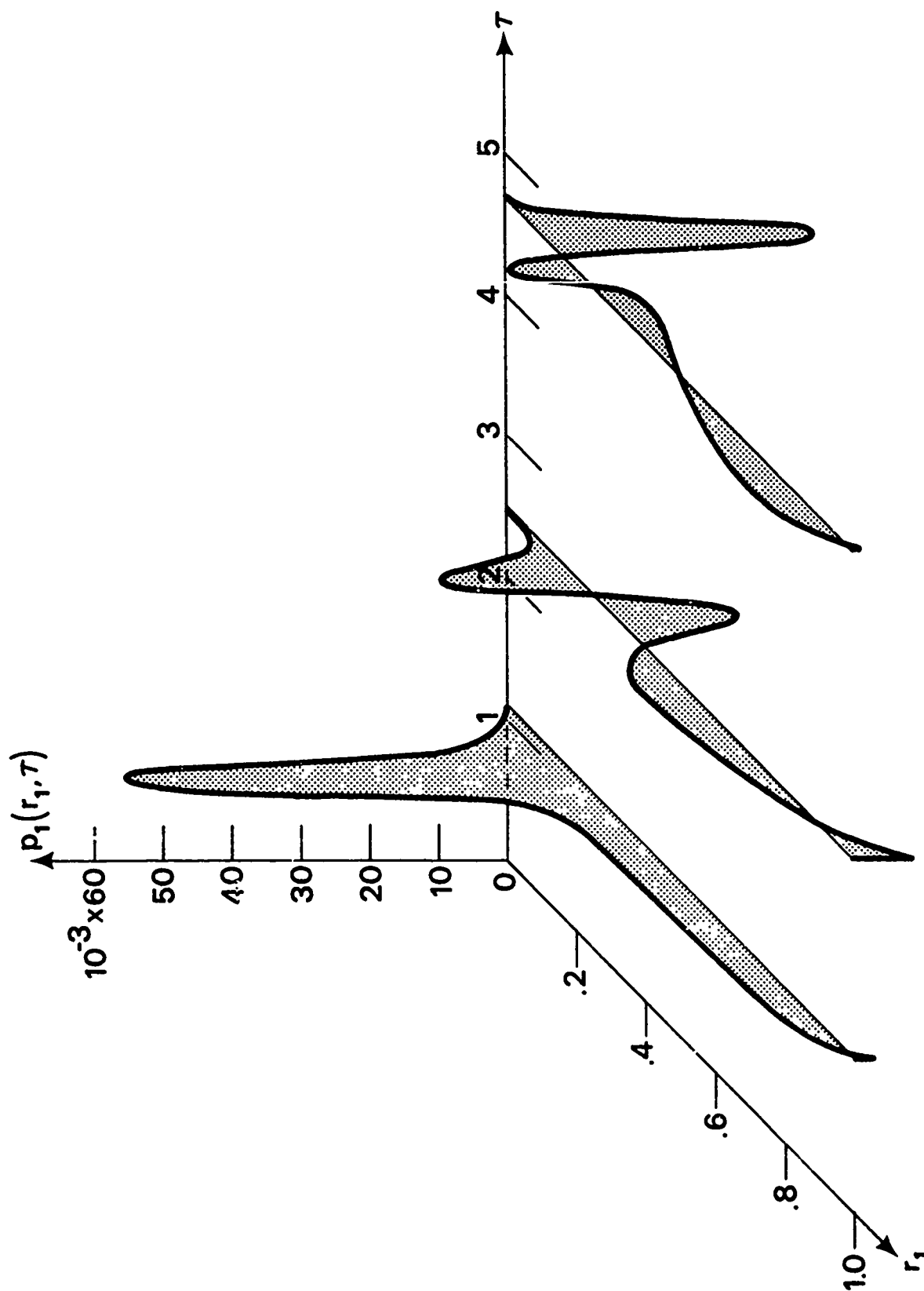


Fig. 2 Nondimensional excess pressure,  $p_1$ , vs. nondimensional time,  $\tau$ , and nondimensional radius,  $r_1$ ;  $\phi=0$  and  $\tau_0=.01\tau_c$ , (Elastic shell boundary).



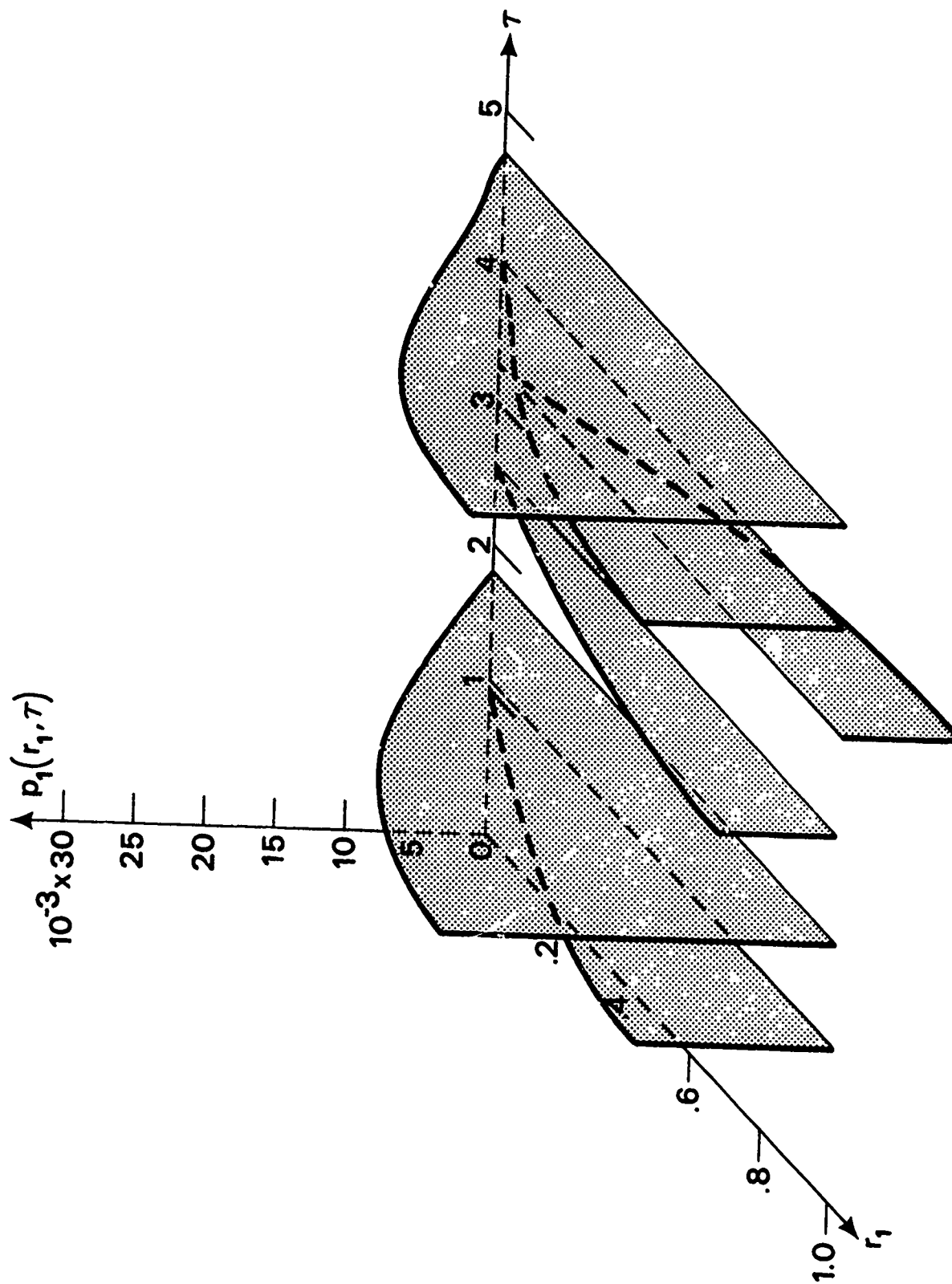


Fig. 3 Nondimensional excess pressure,  $p_i$ , vs. nondimensional time,  $\tau$ , and nondimensional radius,  $r_i$ ;  $\phi=0$  and  $\tau_0=0.5\tau_c$ , (Rigid shell boundary).

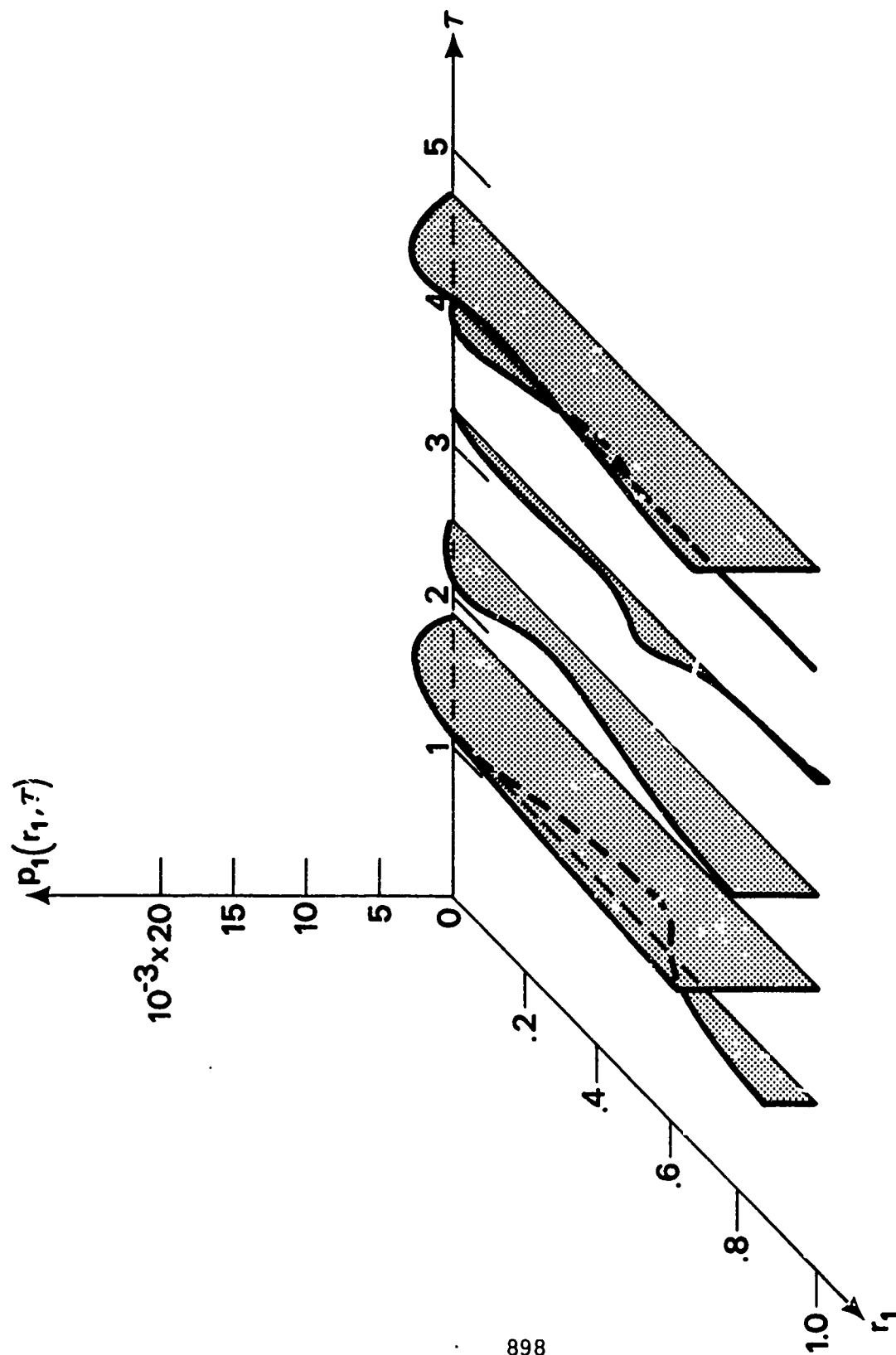


Fig. 4 Nondimensional excess pressure,  $p_i$ , vs. nondimensional time,  $\tau$ , and nondimensional radius,  $r_i$ ;  $\phi=0$  and  $\tau_0=0.5\tau_c$ , (Elastic shell boundary).

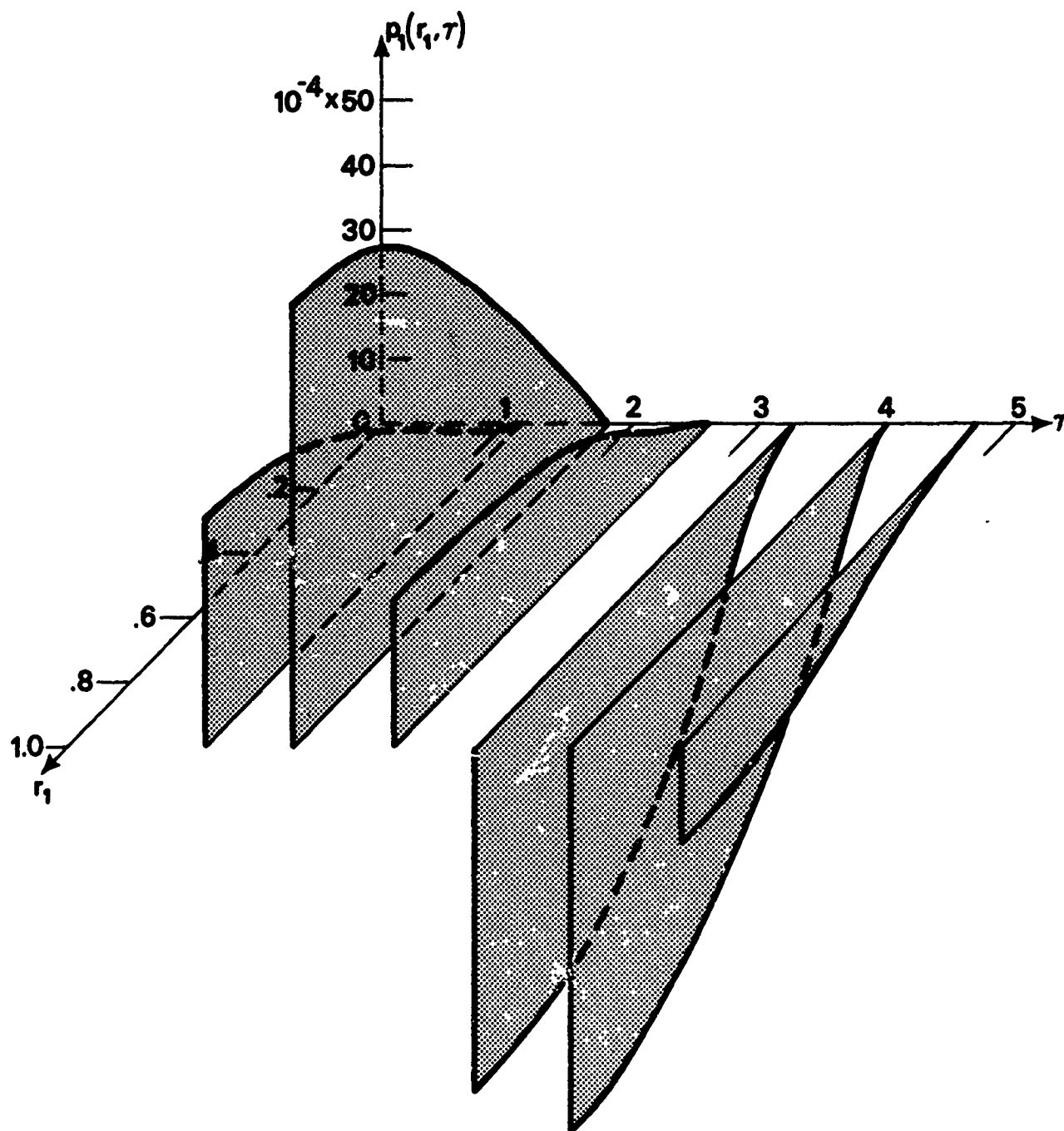


Fig. 5 Nondimensional excess pressure,  $p_1$ , vs. nondimensional time,  $\tau$ , and nondimensional radius,  $r_1$ ;  $\phi=0$  and  $\tau_0=2\tau_c$ , (rigid shell boundary).

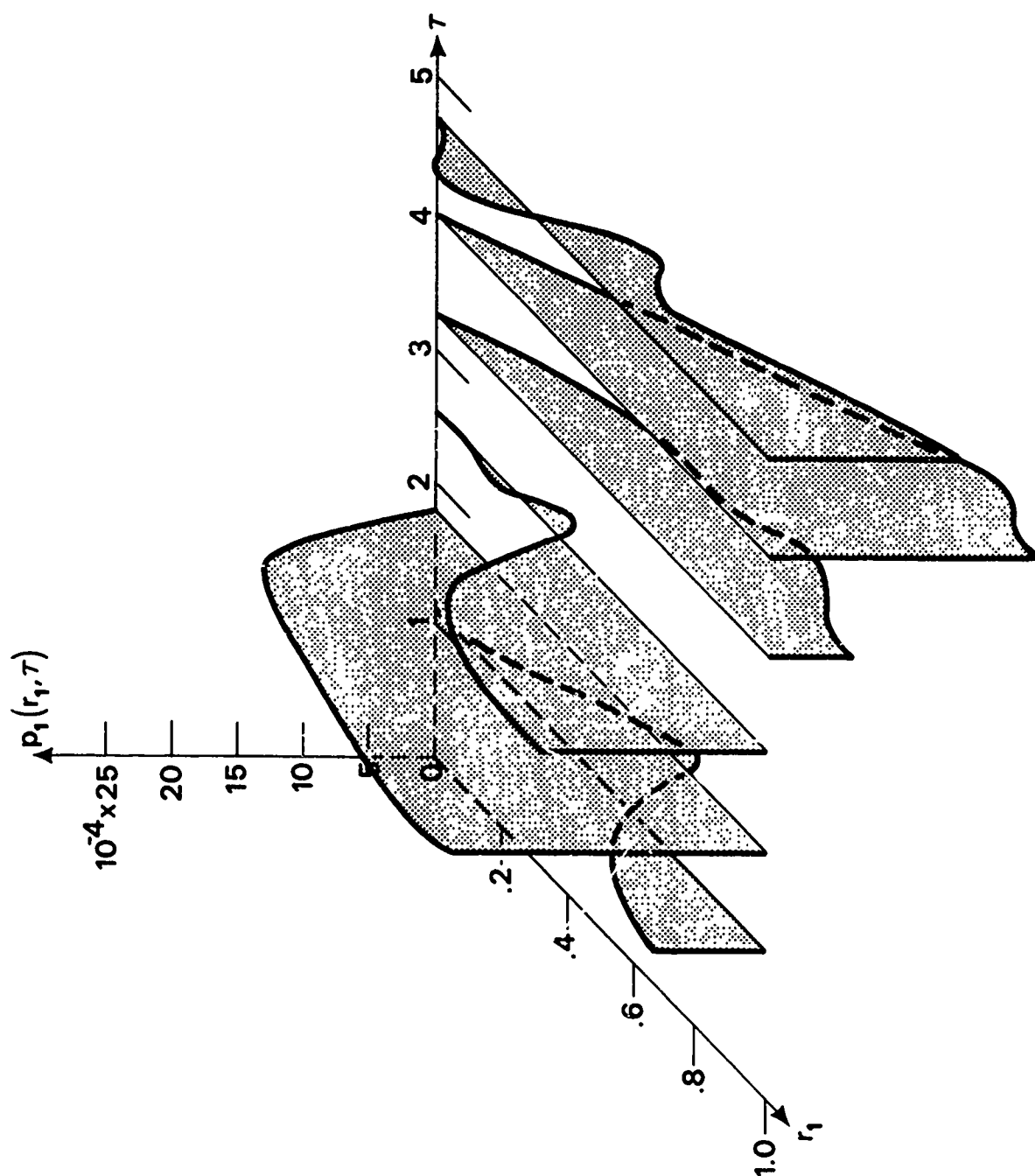


Fig. 6 Nondimensional excess pressure,  $p_1$ , vs. nondimensional time,  $\tau$ , and nondimensional radius,  $r_1$ ;  $\psi=0$  and  $\tau_0=2\tau_c$ , (Elastic shell boundary).

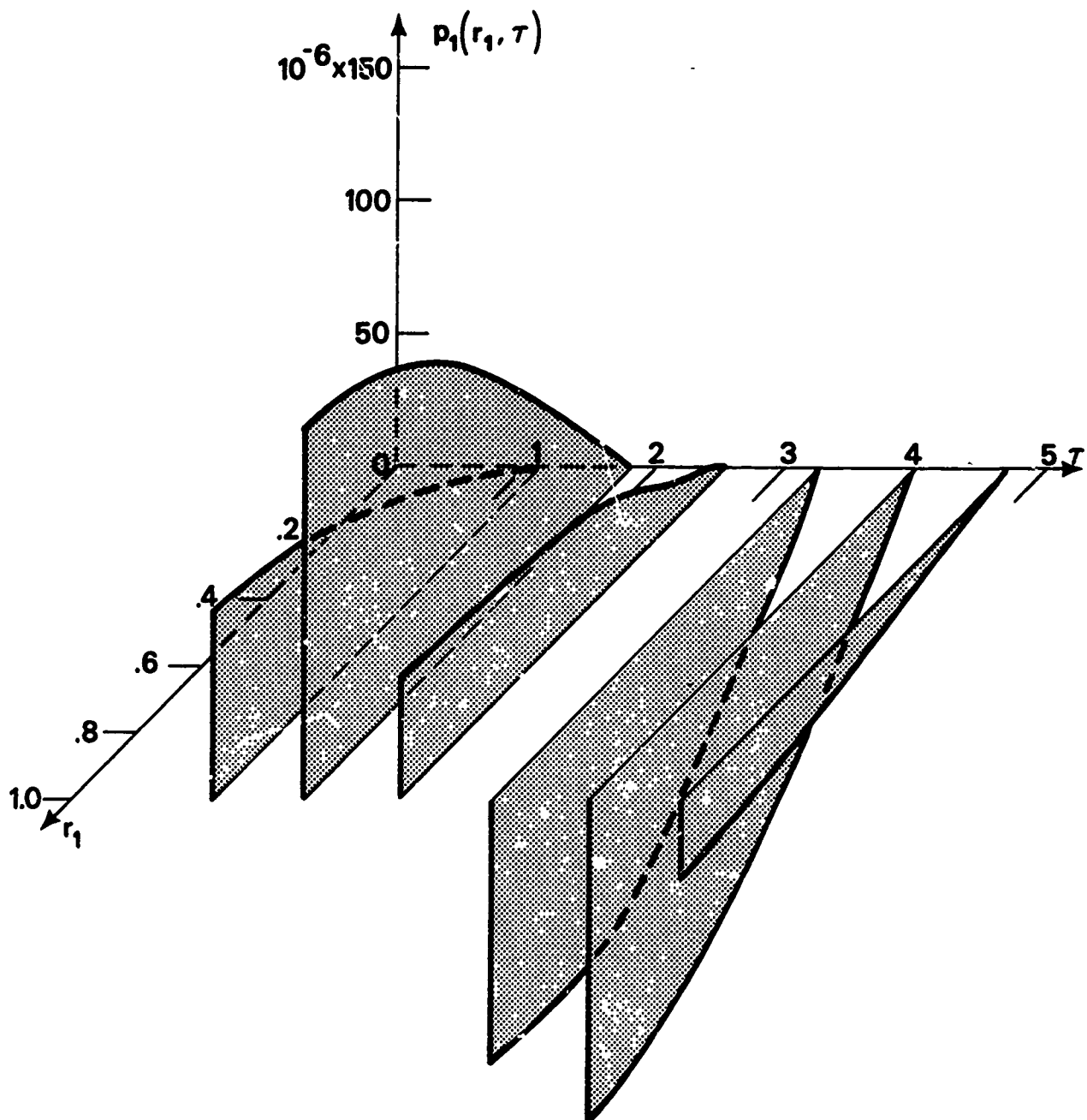


Fig. 7 Nondimensional excess pressure,  $p_1$ , vs. nondimensional time,  $\tau$ , and nondimensional radius,  $r_1$ ;  $\phi=0$  and  $\tau_0=100\tau_c$ , (Rigid shell boundary).

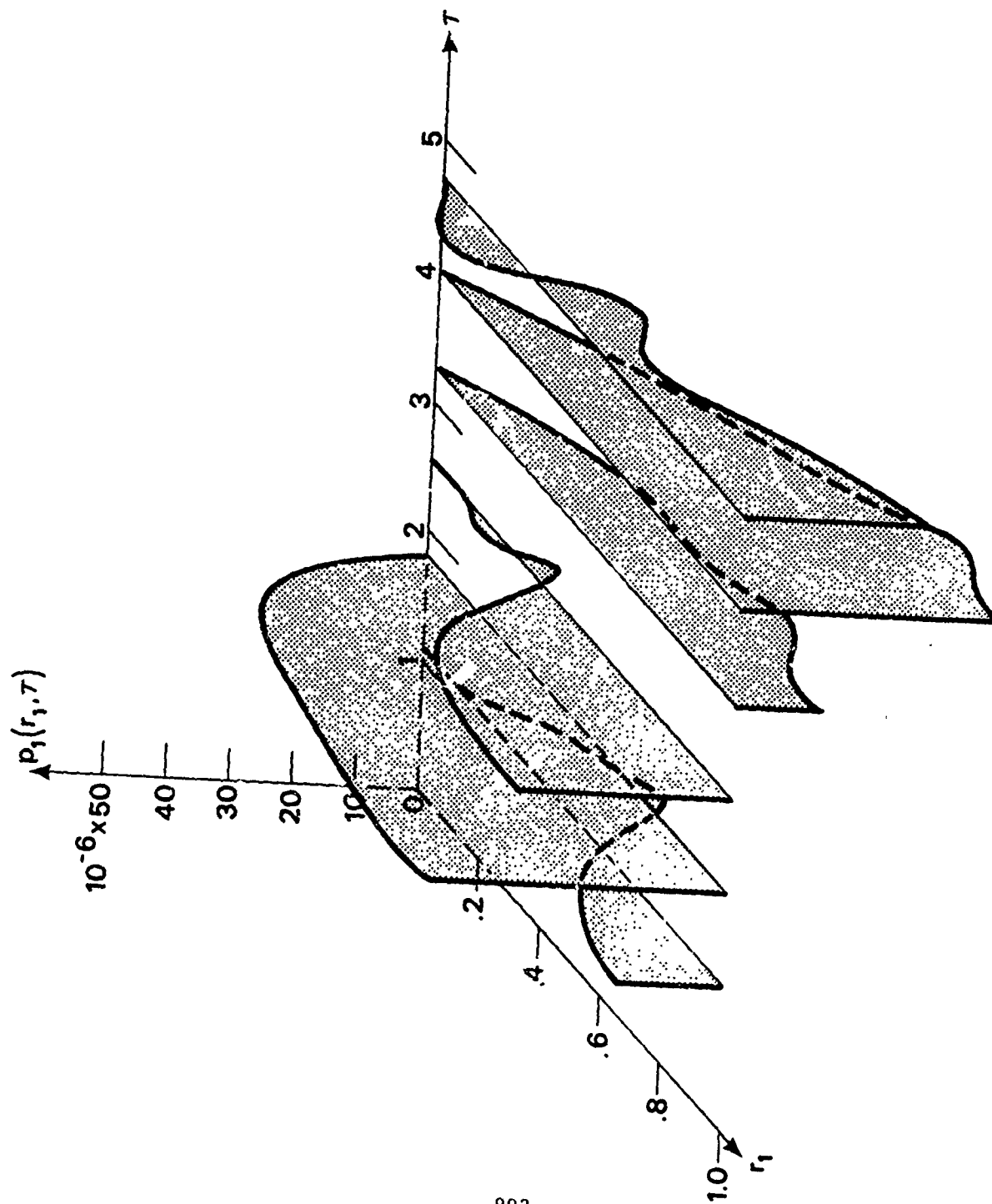


Fig. 8 Nondimensional excess pressure,  $p_1$ , vs. nondimensional time,  $\tau$ , and nondimensional radius,  $r_1$ ;  $\psi=0$  and  $\tau_0=100\tau_c$ , (Elastic shell boundary).

## REFERENCES

1. M. C. Junger, "Vibration of Elastic Shells in a Fluid Medium and Associated Radiation of Sound," J. Appl. Mech. 74, 439-445 (1952)
2. J. E. Greenspon, "Vibration of Thick and Thin Cylindrical Shells Surrounded by Water," J. Acoust. Soc. Amer. 33, 1321-1328 (1961)
3. A. E. Engin and Y.K. Liu, "Axisymmetric Response of a Fluid-Filled Spherical Shell in Free Vibrations" J. Biomech. 3, 11-20 (1970).
4. A. Anzelius, "The Effect of an Impact on a Spherical Liquid Mass" Acta. path. microbiol. scand. Suppl. 48 (1943)
5. W. Güttinger, "Der Stosseffekt auf eine Flüssigkeitskugel als Grundlage einer Physikalischen Theorie der Entstehung von Gehirnverletzungen," Z. Naturforsch. Teil A 5, 622-628 (1950)
6. T. Hayashi, "Study of Intracranial Pressure Caused by Head Impact" 12th Int. Congr. Appl. Mech.
7. A. E. Engin, "The Axisymmetric Response of a Fluid-Filled Spherical Shell to a Local Radial Impulse - A Model for Head Injury" J. Biomech. 2, 325-341 (1969)
8. W. Goldsmith, "The Physical Processes Producing Head Injury" Proceedings of the Head Injury Conference, 350-382, Lippincott, Philadelphia

PAPER NO. 37

A MECHANICAL IMPEDANCE MODEL FOR  
HEAD INJURY DUE TO LINEAR IMPACTS

by

Richard L. Stalnaker  
James H. McElhaney  
Verne L. Roberts

Highway Safety Research Institute  
The University of Michigan  
Ann Arbor, Michigan 48105

ABSTRACT

The mechanical impedance of the human and various other primate species heads was determined over the frequency 30-5000 hertz. A simple model was developed that closely follows the observed impedance characteristics. Spring and damping constants were evaluated and comparisons between species obtained. An impact tolerance curve was computed based on the model predictions with a maximum strain criteria. Various input pulse shapes were analyzed and the effect of pulse shape and duration studied for the different species. Published values of tolerable impulses were examined and compared with the model predictions. Some discrepancies have been noted and analyzed. Particular emphasis in this work has been on linear impacts to the side of the head where angular accelerations do not predominate. Results are presented in the form of tolerable average acceleration versus pulse duration curves for various pulse shapes derived from primate head impacts. A comparison with the Wayne State tolerance curve and Eiband's work of 1959 has also been made.

**PRECEDING PAGE BLANK**



## INTRODUCTION

A critical factor in the design of a motor vehicle interior is the limiting deceleration-time pulse the vehicle can undergo without occupant injury. The type of tolerance data needed for this interior design is not readily available. Although much work has been done in determining tolerances for thoracic and frontal head impacts, much more work is needed to further substantiate existing data and to generate new data for other regions of the body.

The acceleration-time tolerance curve developed at Wayne State University over the past several decades is the only empirically based tolerance curve available for frontal head impacts. Although this curve is widely used as a standard for head injury, the experimental design upon which it is based has been the subject of much controversy. The original Wayne State Tolerance Curve (W.S.T.) (Lissner 1960) consists of six data points, five plotted as peak acceleration and one arbitrarily plotted as the average of the peak acceleration and the average acceleration.

A revised W.S.T. curve was introduced by Patrick (1963). This curve is a composite based on a wide variety of pulse shapes and striker configurations. The failure criteria used was generally skull fracture. In spite of the many interpretive difficulties associated with this curve, it has been in the past the principal source of hard data for human head injury tolerance.

---

The work upon which this paper is based was supported in part by a contract with the Department of Transportation, National Highway Safety Bureau, #FH-11-7288 and a contract with National Institutes of Health, National Institutes of Neurological Diseases and Stroke, #PH-43-67-1136.

Several attempts to generalize the Wayne State Tolerance Curve have been made in the last four years. One such characterization of this curve was set forth by C. W. Gadd (1966), who defines the severity index as:

$$S.I. = \int_0^{\tau} a^n dt \quad (1)$$

where:

a = acceleration, force, or pressure of response function producing threshold or injury of given degree.

n = weighing factor greater than 1.

t = time, seconds

The value for n was obtained from a log-log plot of the Wayne Curve and Eiband's (1969) work for spineward accelerations of seated humans. The limiting index for survival was determined from points on these curves. This severity index is tied very closely to pulse shapes in setting the survival limit.

The J Tolerance value (Slattenschek 1968) or the Vienna Institute index is the newest generalization of the Wayne Curve. In this effort, a single-degree-of-freedom model is assumed and the model constants are determined by fitting a linear differential equation to the Wayne State data. A J Tolerance value is then defined by:

$$J = \frac{X_{max}}{X_{erta}} \quad (2)$$

where:

X<sub>erta</sub> = tolerable amplitude from Wayne State Curve.

X<sub>max</sub> = maximum X generated by putting the acceleration pulse in question into the model differential equation.

thus:

J > 1 Not survivable

J < 1 Survivable

Once more the index is determined from the Wayne State Tolerance Curve.

If the dynamic response of the head is known for a wide range of frequencies and if injury can be related to this response, then a tolerance curve can be generated for all pulse durations, given only one point on the tolerance curve, provided the injury mechanism does not change over that range. This paper is an attempt to investigate this hypothesis from a model based on driving point impedance data from human and other primates.

#### METHOD

The mechanical driving point impedance of human and other primate heads was determined over a frequency range of 30-5000 hertz utilizing the following experimental design.

The primates were anesthetized and a 10 millimeter (mm) circular hole was cored 0.25 inch above the ear canal on the side which was attached to an electromagnetic shaker. The loading fixture was then fastened to the skull at this site. On the opposite side of the skull a similar hole was made and a miniature accelerometer attached (Figure 1).

The sub-human primates skull via the load cell was rigidly attached to the platen of a 200-pound electromagnetic shaker (Figure 2). The bodies were supported in a sling hammock. A servo controller was then set to apply a sinusoidal constant amplitude acceleration of either 10 or 20 g's to the head (Figure 3). In addition, an accelerometer was placed on the free side of the head and the transmitted acceleration recorded.† A sweep oscillator drove the shaker system over a 30 to 5000 Hz cycle range, while an automatic on-line analogue impedance computer was used to convert the force-time and acceleration-time information into a phase and impedance



**RIGHT SIDE VIEW**

**Figure 1. X-ray of Monkey Showing Attachment Point to Shaker**

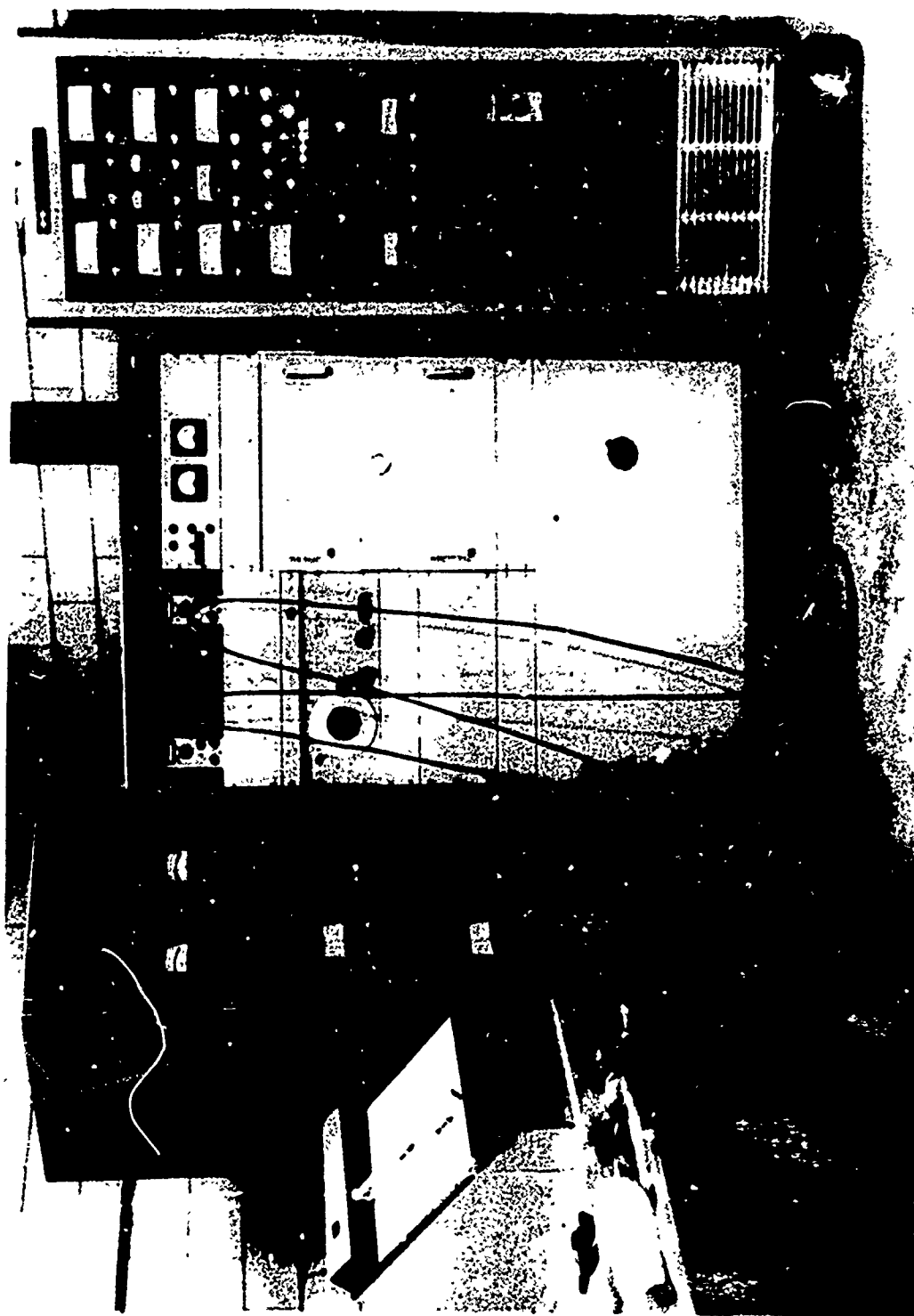


Figure 2. Mechanical Impedance Test Set-Up

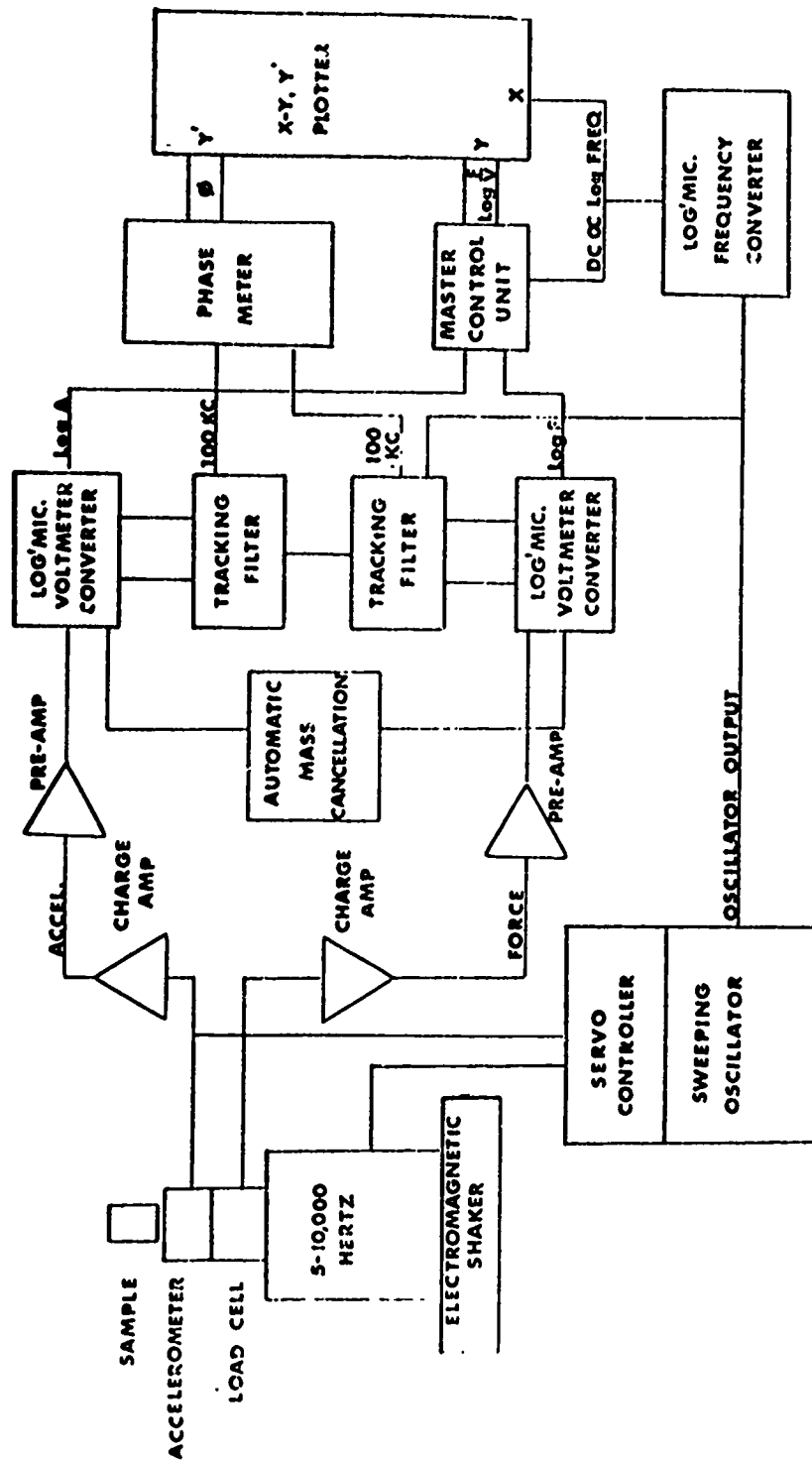


Figure 3. Automatic Impedance Measuring System

versus frequency plot. With this system, the test could be performed in less than one minute (depending on sweep rate) and produces a continuous plot of impedance. Mechanical impedance versus frequency on an  $x, y_1, y_2$  recorder was recorded for the living anesthetized sub-human primates (Figure 4). The primates tested were then sacrificed and the test procedure repeated. The heads were removed from the bodies and the same parameters recorded again. The skin and mandible were removed and the test repeated. The brains were then removed through the foramen magnum and the mechanical impedance and acceleration on the free side of the skulls were recorded (Stalnaker and McElhaney 1970).

The same experiment was performed on an unembalmed 71-year old human male cadaver, who had been dead approximately 5 hours prior to the experiment. Constant accelerations of 1, 5 and 10 g's were applied over the frequency range 30-5000 Hz and the above mentioned mechanical parameters measured.

The two-degree-of-freedom system shown in Figure 5A has been developed to closely approximate the impedance characteristics of the heads as measured in these experiments.

If the system is represented schematically as in Figure 5B, the system elements are combined in parallel and series. Using the rule of parallel systems the impedance at point 4 is

$$z_4 = z_3 + z_2 \quad (3)$$

Using the rule of series system the impedance  $z_2$  at point 2 is

$$\frac{1}{z_2} = \frac{1}{z_1} + \frac{1}{z_k + z_c} \quad (4)$$

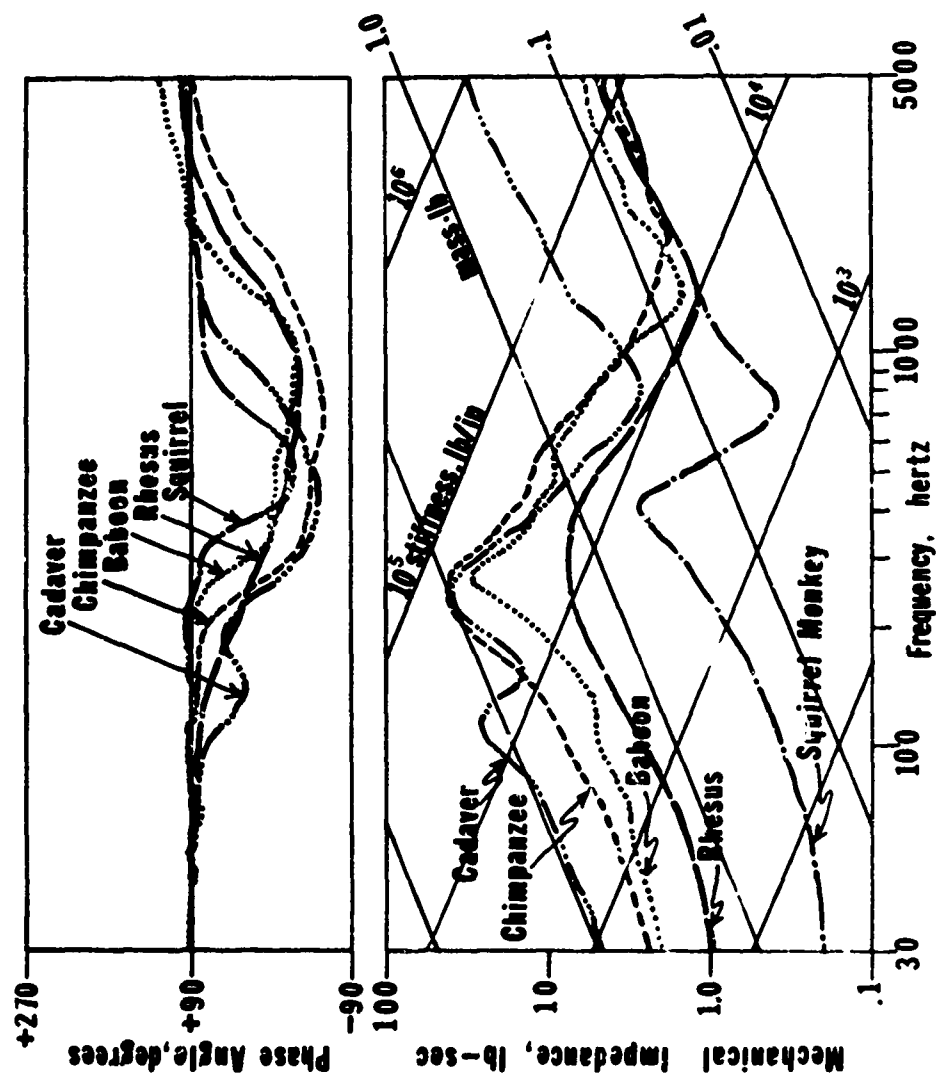


Figure 4. Mechanical Impedance of Primate Head



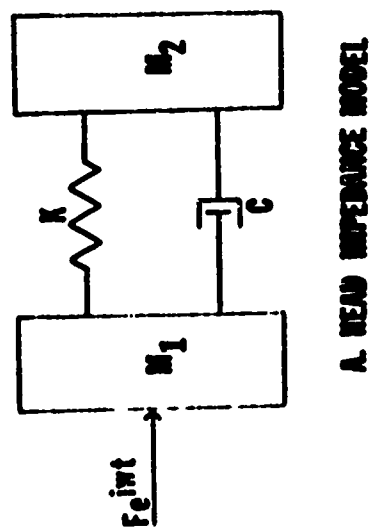
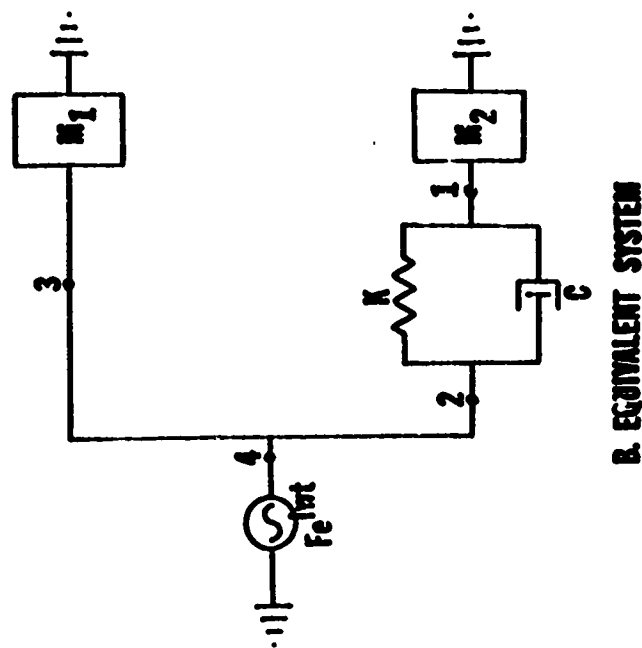


Figure 5. Two-Degree-Of-Freedom System

so now

$$z_4 = z_3 + \frac{1}{\frac{1}{z_1} + \frac{1}{z_k + z_c}} \quad (5)$$

Substituting

$$z_4 = i\omega m_1 + \frac{1}{\frac{1}{i\omega m_2} + \frac{1}{\frac{k}{\omega i} + c}} \quad (6)$$

or

$$z_4 = i\omega(m_1 + m_2) \left[ \frac{1 - \frac{\omega^2 m_1 m_2}{k(m_1 + m_2)} + \frac{i\omega c}{k}}{1 - \frac{\omega^2 m_2}{k} + \frac{i\omega c}{k}} \right] \quad (7)$$

This model has one antiresonance and one resonance. At low frequencies, the system impedance approximates the total mass of the system; at high frequencies it approximates the impedance of the drive mass element  $m_1$ . The phase angle shifts from  $+90^\circ$  through  $0^\circ$  at the antiresonance frequency to  $-90^\circ$ , and from  $-90^\circ$  through  $0^\circ$  at resonant frequency back to  $+90^\circ$ . The height of the peak and the depth of the valley are controlled by the amount of damping. The spring can be approximated for this model by stiffness line going through the inflexion point of the portion of the mechanical impedance curve between the antiresonance and resonance.

This theoretical equation was programmed for the 1130 IBM Digital Computer. By varying the magnitude of the mass, spring, and dash pot of this model a best fit of the mechanical impedance between the model and the Macaca mulatta test data can be approximated (Figure 6). (Stalnaker and McElhanev 1970)

The mechanical impedance of the cadaver head was similar enough to that of the living monkey head so the same model could be used. The model constants that provide a best fit with the cadaver head data are  $m_1 g = .4$  lb,  $m_2 g = 9.0$  lb,  $c = 2.0$  lb/in,  $k = 2.6 \times 10^4$  lb-sec/in., with an antiresonance at 180 hertz and a resonance at 820 hertz (Stalnaker and McElhanev 1970).

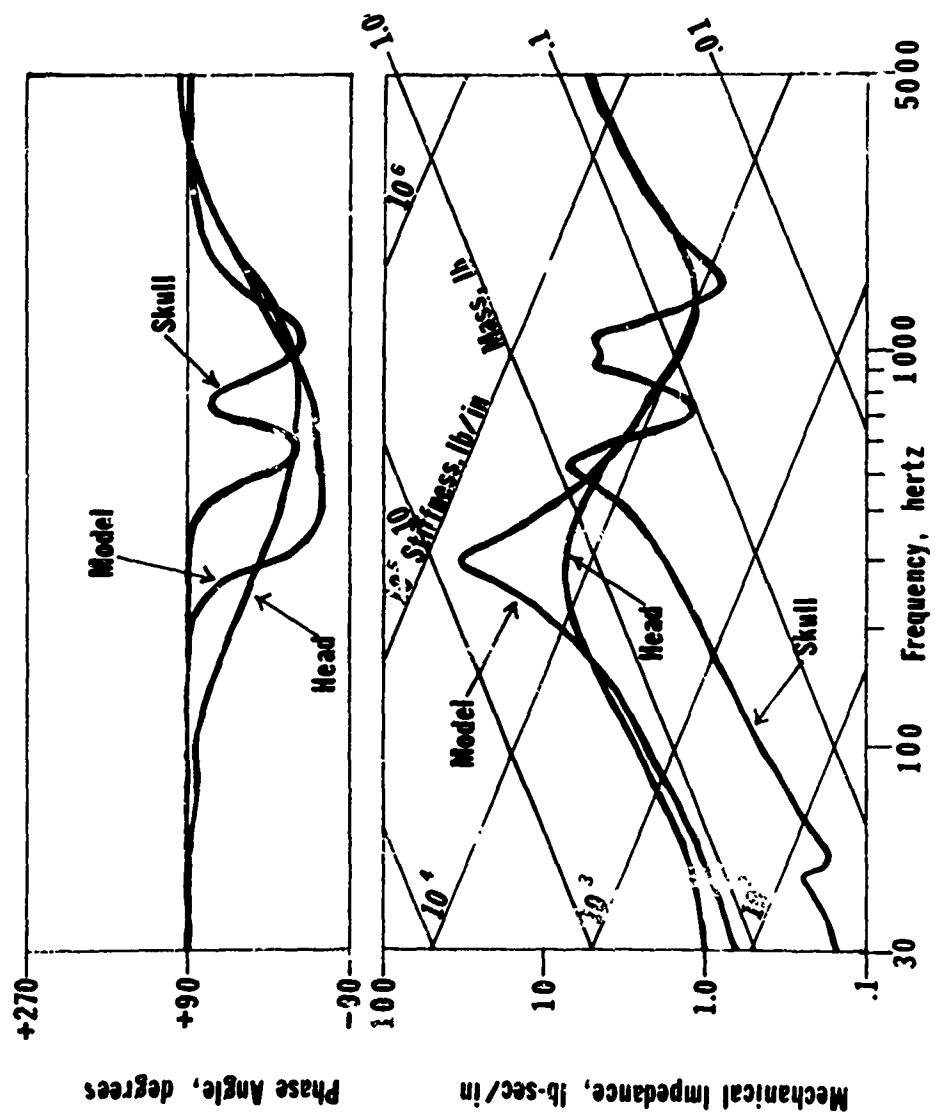


Figure 6. Comparison of Model with Living Rhesus Monkey Head and Skull

In interpreting the model constants, the following considerations apply. The calvarium is divided into approximately four major sections: the frontal bone, left and right parietal bone, and the occipital bone, which in the case of a monkey is almost entirely under the brain. The attachment to the shaker was made through one of the parietal sections. These sections of the skull are connected by sutures which provide isolation from one section to another. This implies that  $m_1$  in the model may be one or more of these sections. The Macaca mulatta parietal sections were found to weigh approximately 0.065 pounds, thus it is believed that  $m_1$  in the model corresponds approximately to the parietal sections of the skull. Comparing the spring constant obtained in the monkey series impedance tests (Stalnaker and McElhanev 1970) ( $1.8 \times 10^4$  lb/in) with the spring constant obtained through the impedance modeling ( $10^4$  lb/in) leads to the conclusion that the spring element in the model corresponds for the most part to the skull stiffness. Comparing the damping constant for the whole head of the Rhesus monkey (1.2 lb-sec/in) with that of the skull alone (0.6 lb-sec/in) indicating that half the damping is due to the skin, muscle and brain (Figure 7).

With this linear two-degree-of-freedom model as a mathematical analogy of the head, many dynamic inputs to the head can be studied. The model response can be expressed in terms of the following linear differential equations (Figure 8):

$$m_1 \ddot{x}_1 = c(\dot{x}_2 - \dot{x}_1) + k(x_2 - x_1) \quad (8)$$

$$m_2 \ddot{x}_2 = -c(\dot{x}_2 - \dot{x}_1) - k(x_2 - x_1) \quad (9)$$

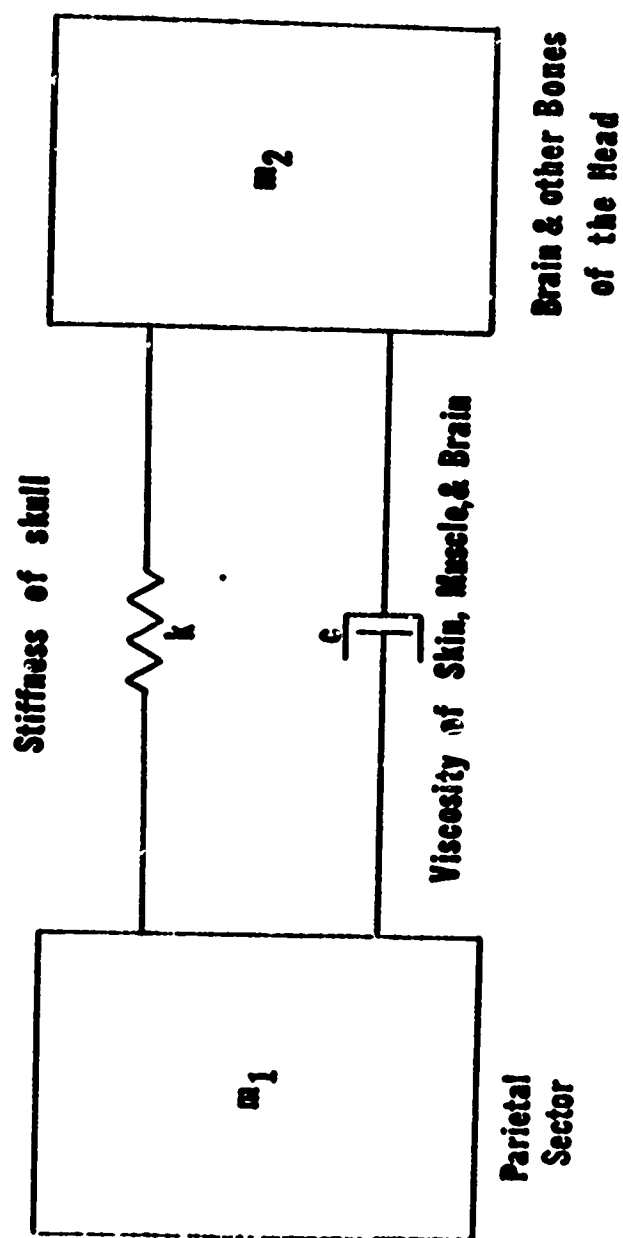


Figure 7. Model of the Head

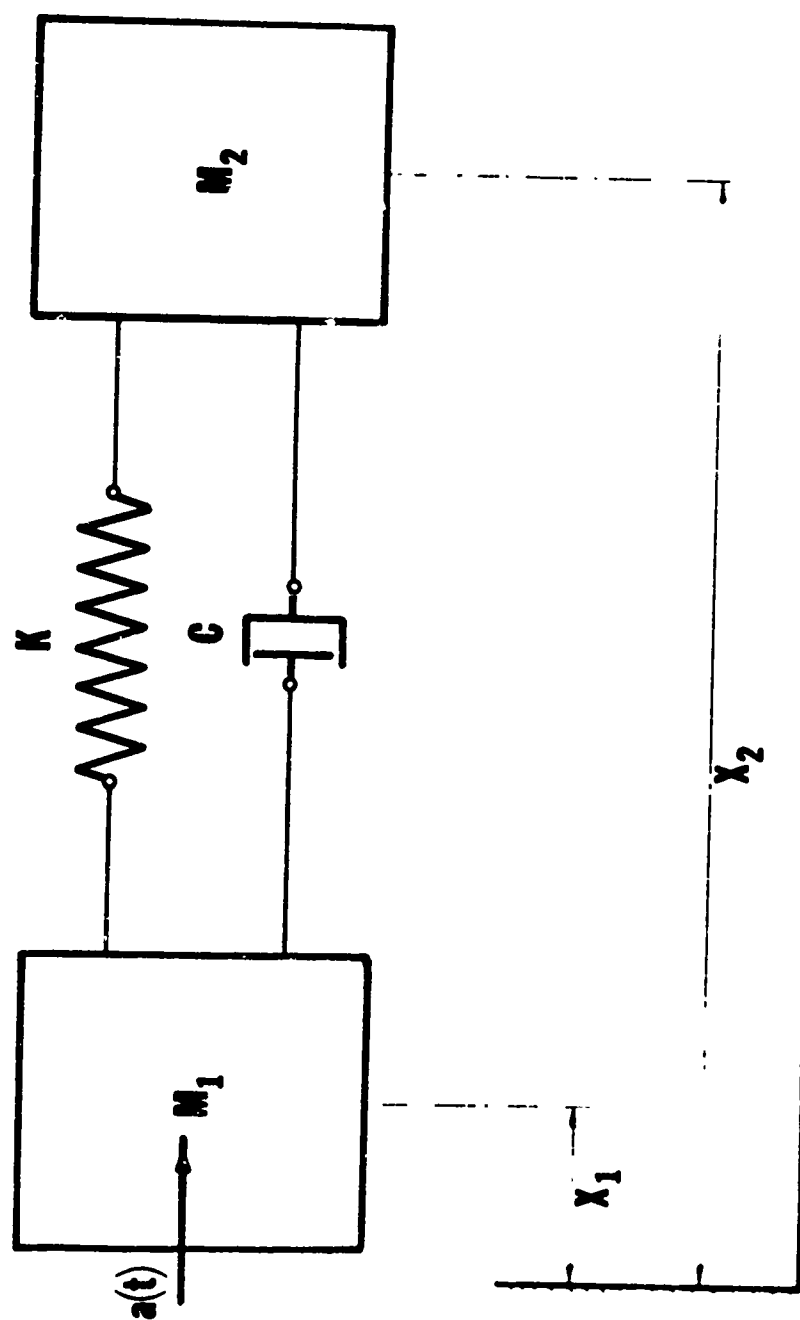


Figure 8. Reference System for Head Model

where

$$\dot{x} = \dot{x}_2 - \dot{x}_1 \quad (10)$$

and

$$x_2 = \dot{x} + x_1 \quad (10a)$$

thus

$$m_2 \ddot{x} + c \dot{x} + kx = -m_2 \ddot{x}_1 \quad (11)$$

Letting

$$\ddot{x}_1 = a(t) \text{ any input acceleration}$$

then

$$\ddot{x} + \frac{c}{m_2} \dot{x} + \frac{k}{m_2} x = -a(t) \quad (11a)$$

Substituting equation (10) into equations (8) and (9) and then substituting equation (9) from equation (8) we finally arrive at

$$\ddot{x} + \left(1 + \frac{m_2}{m_1}\right) \frac{c}{m_2} \dot{x} + \left(1 + \frac{m_2}{m_1}\right) \frac{k}{m_2} x = 0 \quad (12)$$

The required equations of motion of the model are therefore equation (11a) for a forced vibration input and equation (12) for a free vibration. With these two equations and the model constants developed above, the dynamic response of the head model can be studied for a variety of input impulses.

Human tolerance curves have been developed from impedance data for lateral driving point impedance data discussed above and from frontal impedance data compiled by V. R. Hodgson (1968). In addition, the primate lateral impact tolerance curves were obtained from the lateral impedance data. In this way, six data sets were formed (Table I).

	L (inches)	X <sub>max</sub> (inches)	$\epsilon$ in/in	W <sub>1</sub> (lbs.)	W <sub>2</sub> (lbs.)	C ( $\frac{\text{lb-sec}}{\text{in.}}$ )	K (lb/in)	Anti- Resonance Hz	Resonance Hz
1. R.L. Stalnaker Squirrel Monkey Lateral	1.293	0.1131	0.088	0.05	0.20	0.25	4,000.	443	987
2. R.L. Stalnaker Rhesus Monkey Lateral	2.18	0.2143	0.098	0.06	1.20	1.00	10,000.	283	1305
3. R.L. Stalnaker Baboon Lateral	2.758	--	--	0.08	3.46	1.60	30,000.	289	1926
4. R.L. Stalnaker Chimpanzee Lateral	3.504	--	--	0.08	4.75	2.40	35,000.	265	2070
5. R.L. Stalnaker Human Lateral	4.718	0.0155	0.0033	0.40	9.00	2.40	26,000.	167	812
6. V.R. Hodgson Human Longitudinal	5.78	0.0190	0.0033	0.60	10.00	2.00	50,000.	207	923
7. Vienna Inst. of Tech. Human Longitudinal	--	--	--	--	10.00	33.00	10,400.	102	--

Table I. Head Model Parameter.



The criterion for injury was assumed to be the average strain in the brain. This then is the  $X$  in the model normalized by the linear dimensions of the brain at the point of impact and in the direction of the impact.

The maximum deflection  $X$  for human heads in the longitudinal direction was determined from A. M. Eiband's (1959) work on abrupt transverse decelerations (Figure 9). A rectangular pulse of 50 G's for 45 msec. was used as a survival acceleration pulse. This same strain used for the longitudinal direction was assumed as the limit for lateral impact, the underlying assumption here is that the brain is equally vulnerable to strain in all directions.

The maximum  $X$  for sub-human primates was calculated from lateral head impact data (Figure 10). The sub-human primates were impacted on the side of the head with a rigid constant velocity impactor. The extent of the injuries were determined in 72-hour post-impact autopsy. The tolerable impact level for each primate was determined. The acceleration-time pulse for the tolerable impact was then used as the head model data input.

## RESULTS

The results of this study are represented in the form of average acceleration versus pulse duration curves.

The average strain generated by a (50 G, 45 msec) rectangular pulse in the longitudinal direction in the human head was found to be 0.00329 in/in. For the same given strain level a 15 g spread was found above 10 msec. depending on the pulse shape. A minimum was found to occur with a tolerable value of 36 g's at 3.7 msec. in the sine pulse input, and a value of 30 g's at 5.6 msec. in the triangular pulse input. No minimum occurred for the rectangular pulse curve (Figure 11).

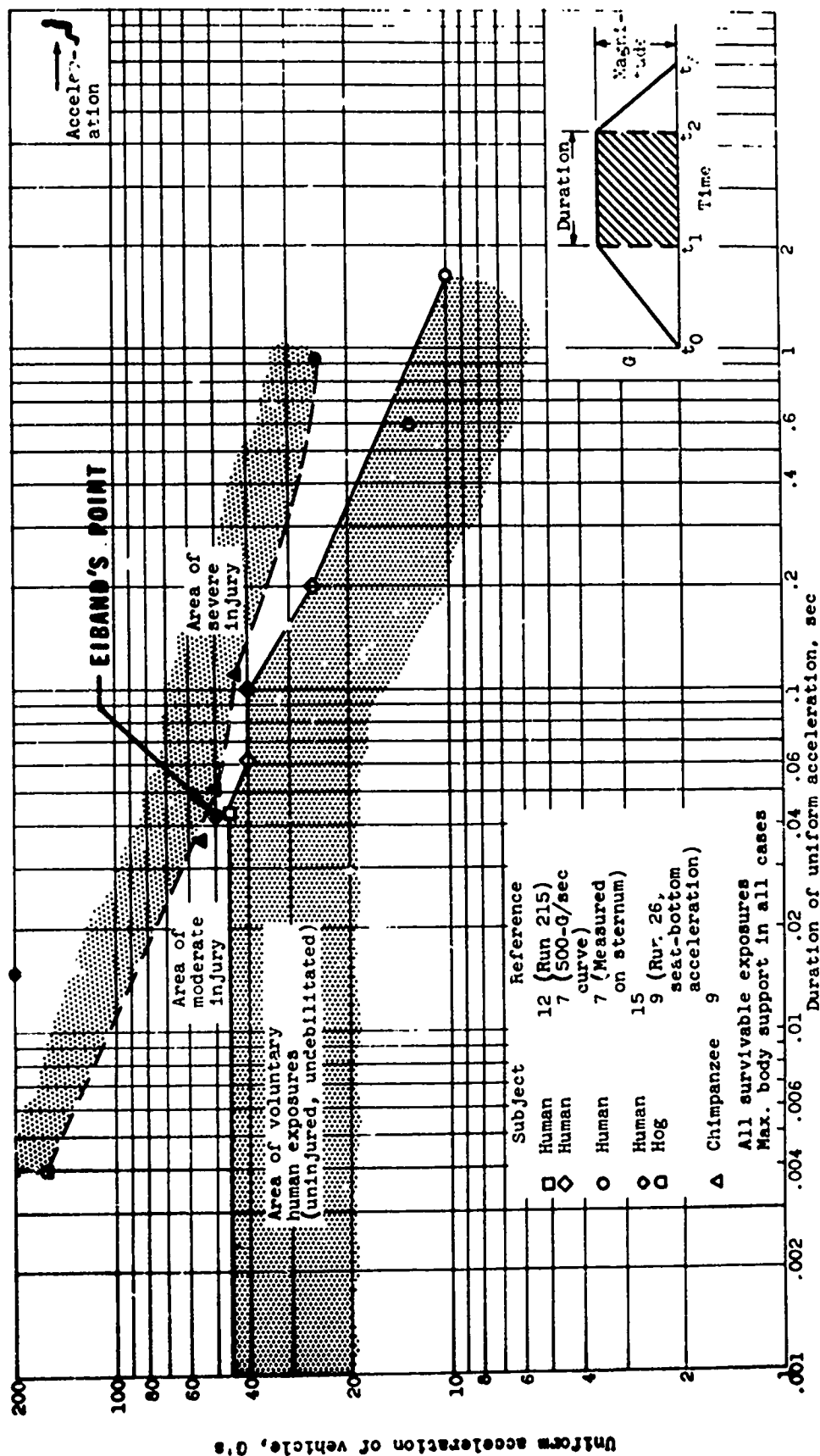


Figure 9. Eiband's Abrupt Transverse Decelerations Endured for Animals and Man

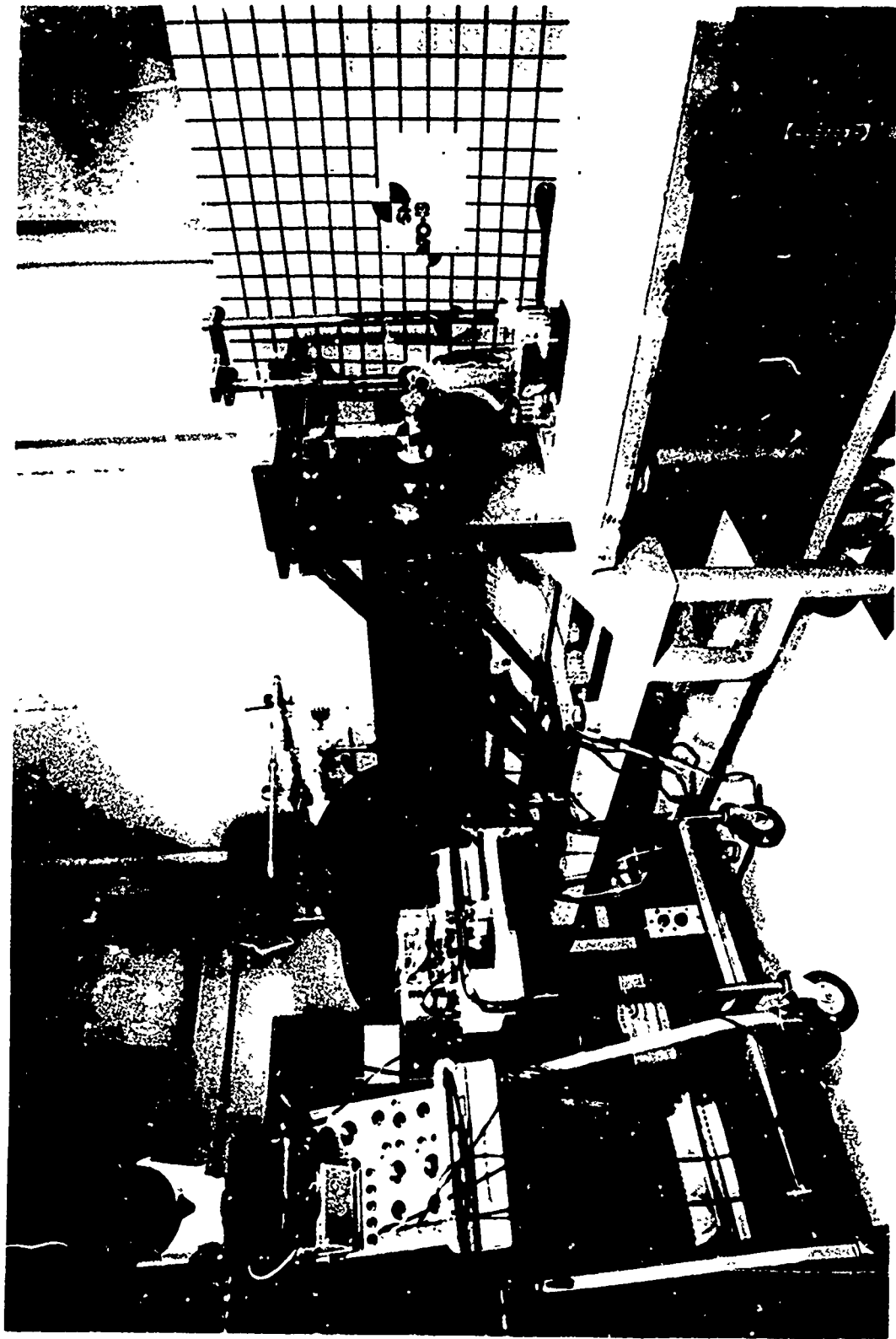


Figure 10. Squirrel Monkey Head Impact Set-Up

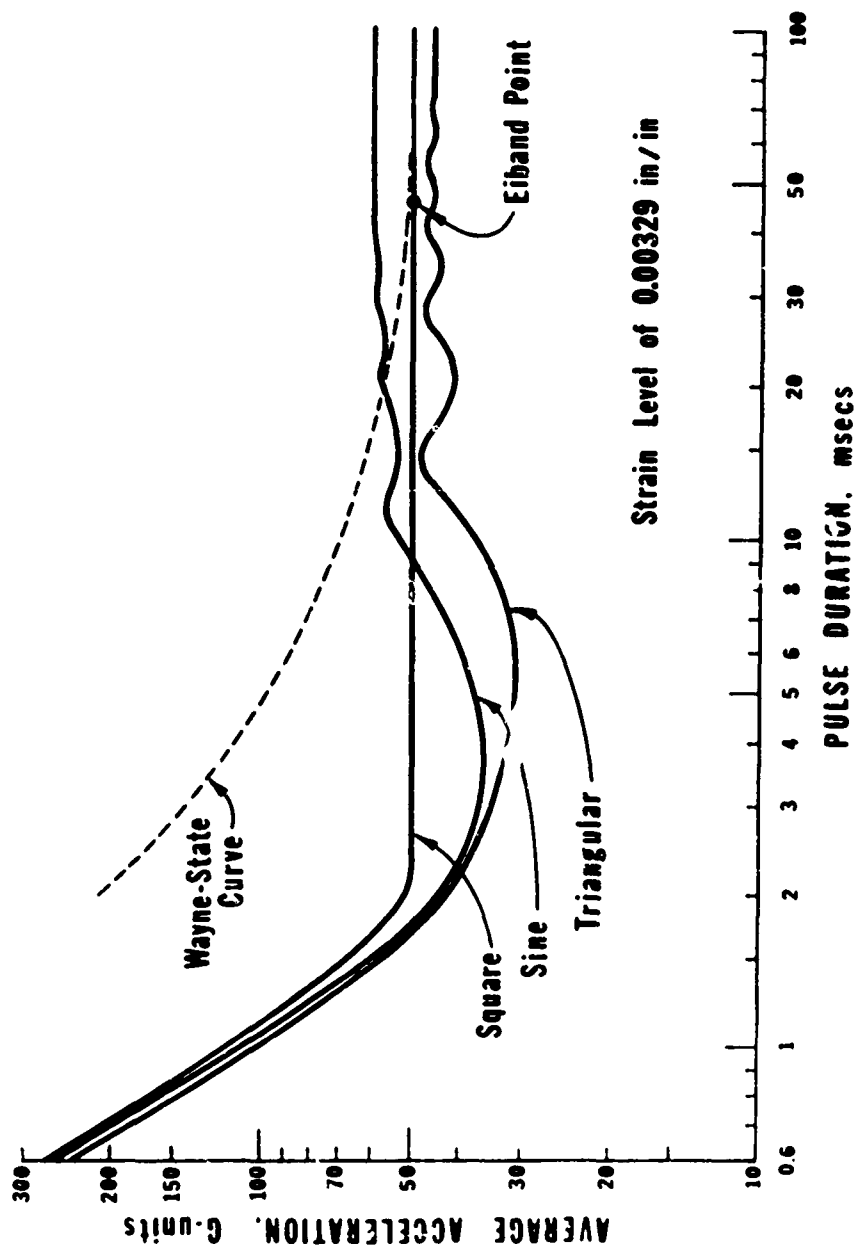


Figure 11. Maximum Strain Criterion Curves for Human Longitudinal Head Impact

The same strain level was used to set the tolerance level for the lateral impacts. The shape of the lateral impact curves were found to be similar to the longitudinal impact curve with a shift of the time and acceleration axis. The spread was only 4 g's above 15 msec., that is, the sine flattens off at 26 g's, the rectangular at 25 g's and the triangular at 22 g's. A dip of 17 g's at 5 msec. occurred for the sine curve and a dip of 15 g's at 7.1 msec. for the triangular, with no dip in the rectangular curve (Figure 12).

The sub-human primate tolerance curves were developed for the squirrel monkey, and the Rhesus monkey from impact tolerance data. Maximum strain levels of 0.089 in/in. and 0.098 in/in. respectively were obtained (Figure 13).

#### CONCLUSIONS

The conclusions of this study indicates that there is a significant difference between the Wayne State Tolerance Curve and the Maximum Strain Criterion (MSC) presented here.

The shape of the input pulse significantly effects the tolerable acceleration for durations greater than 1 msec.

Since  $\Delta v$  is dependent on the pulse duration and shape, a sine pulse is more "tolerable", for large pulse duration, while a rectangular pulse is "tolerable" for short pulse duration.

For pulse durations less than 1 msec the shape and location of the MSC curves are independent only on the model constants.

The human lateral MSC curves were found to be 50% lower than the human longitudinal MSC curve.

The squirrel monkey lateral MSC curve has the highest tolerance level with the Rhesus monkey next. The tolerable strain level for both animals were found to be quite similar. Thus atleast for these two sub-human primates the MSC tolerance concept holds.

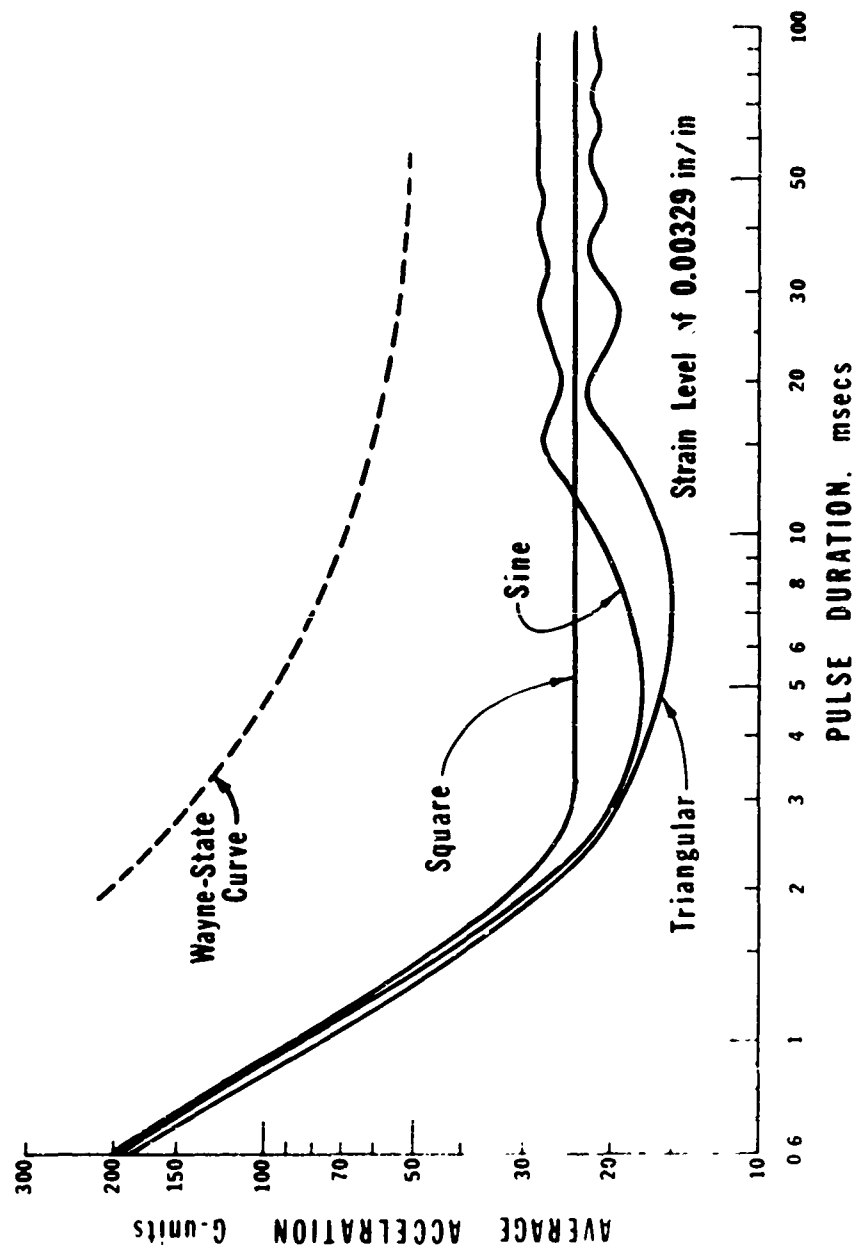


Figure 12. Maximum Strain Criterion Curves for Human Lateral Head Impact

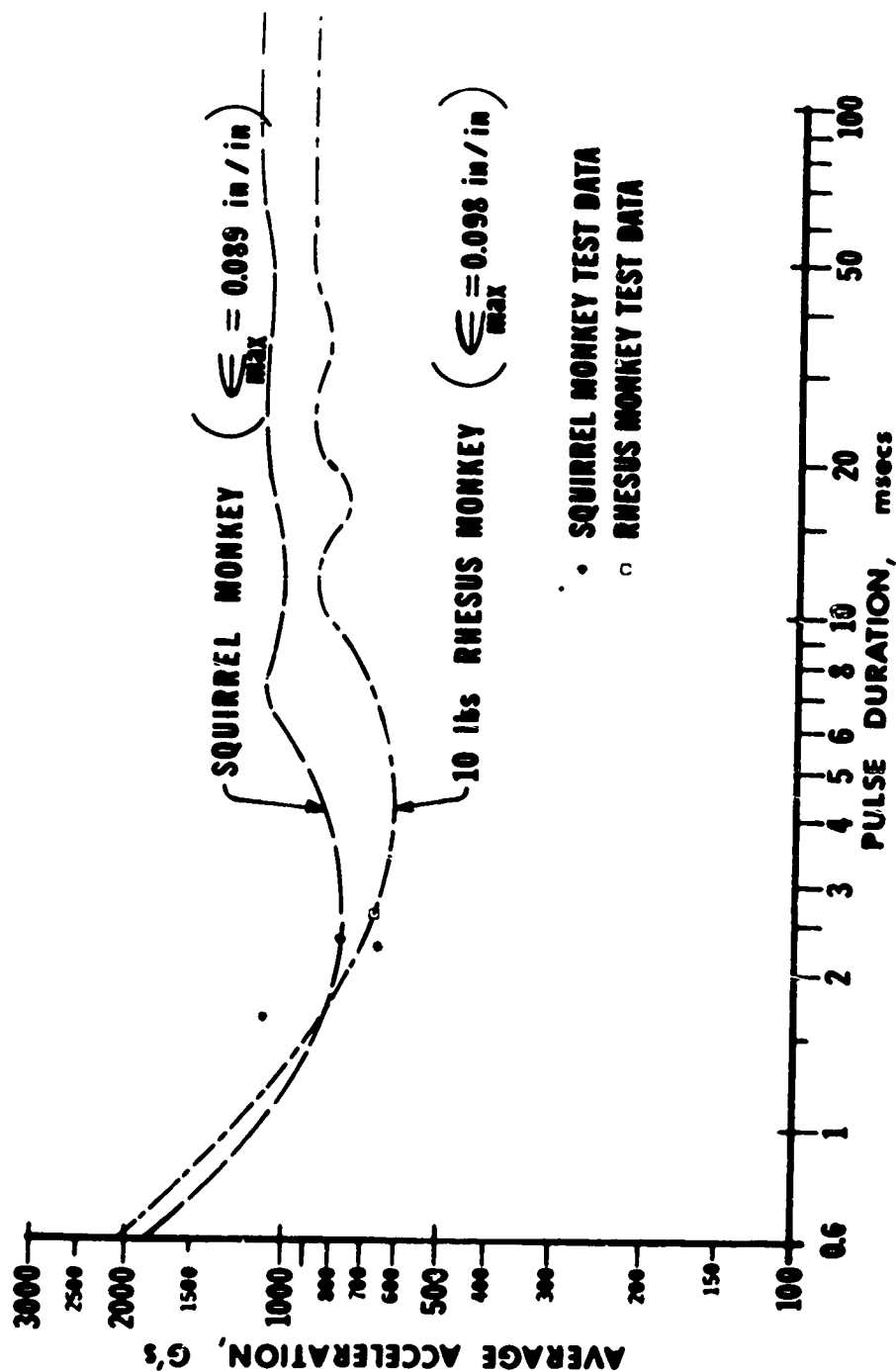


Figure 13. Maximum Strain Criterion Curves for Sub-Human Primates Lateral Head Impact

## NONMENCLATURE

$a$  = acceleration, ft/sec<sup>2</sup>

$c$  = damping constant, lb-sec/in.

$F$  = force, lb

$i = \sqrt{-1}$

$k$  = spring constnat, lb/in.

$m$  = mass, slugs

$t$  = time, sec.

$v$  = velocity, ips

$x$  = displacement, in.

$z$  = mechanical impedance, lb-sec/in.

$\dot{\epsilon}$  = strain rate, 1/sec

$\sigma$  = stress, lb/sq in.

$\phi$  = phase angle, deg.

$\omega$  = frequency, rad/sec



## REFERENCES

1. Eiband, A. M., "Human Tolerance to Rapidly Applied Accelerations: A summary of the Literature," NASA Memorandum, 1959.
2. Franke, E. F., "Response of the Human Skull to Mechanical Vibrations," Journal of the Acoustical Society of America, Vol. 28, 1956, p. 1277.
3. Franke, E. K., "Mechanical Impedance Measurements of the Human Body Surface," USAF Technical Report No. 6469, 1951.
4. Gadd, C. W., "Use of a Weighted-Impulse Criterion for Estimating Injury Hazard," The 10th Stapp Car Crash Conference, 1966.
5. Gurdjian, E. S., Lissner, H. R., Evans, F. G., Patrick, L. M., and Hardy, W. G., "Intracranial Pressure and Acceleration Accompanying Head Impacts in Human Cadavers," Surgery, Gynecology and Obstetrics, Volume 113, 185-190, 1961.
6. Haynes, A. L., and Lissner, H. R., "Experimental Head Impact Studies," The 1st Stapp Car Crash Conference, 1961.
7. Hodgson, V. R., Gurdjian, E. S., and Thomas, L. M., "The Determination of Response Characteristics of the Head with Emphasis on Mechanical Impedance Techniques," The 11th Stapp Car Crash Conference.
8. Hodgson, V. R., and Patrick, L. M., "Dynamic Response of the Human Cadaver Head Compared to a Simple Mathematical Model," The 12th Stapp Car Crash Conference, 1968.
9. Lissner, H. R., Lebow, M., and Evans, F. G., "Experimental Studies on the Relation Between Acceleration and Intracranial Pressure Changes in Man," Surgery, Gynecology and Obstetrics, September 1960.
10. Lombard, C. F., Roy, A., Beattie, J. M., and Advani, S. H., "The Influence of Orientation and Support-Restraint Upon Survival from Impact Acceleration," Report No. ARL-TR-66-20, Aeromedical Air Force Systems Command, November 1966.
11. Mindlin, P. D., Stubner, F. W., and Cooper, H. L., "Response of Damped Elastic Systems to Transient Disturbances," Proc. Soc. Exptl. Stress Anal., 5:2, 69, 1948.
12. Patrick, L. M., Lissner, H. R., and Gurdjian, E. S., "Survival by Design-Head Protection," The 7th Stapp Car Crash Conference.
13. Payne, P. R., "Personnel Restraint and Support System Dynamics," Technical Report AMRL-TR-65-127, At the Wright-Patterson Air Force Base, Ohio, October 1965.

14. Slattenschek, A., "Behavior of Motor Vehicle Windscreens in Impact Tests with a Phantom Head," *Automobiltechnische Zeitschrift*, 70. Jahrgang, Nr. 7, 1968.
15. Slattenschek, A., and Tauffkirchen, W., "Critical Evaluation of Assessment Methods for Head Impact Applied in Appraisal of Brain Injury Hazard, In Particular in Head Impact on Windshields," *The 1970 International Automobile Safety Conf. Compendium*.
16. Stalnaker, R. L. and McElhaney, J. H., "Head Injury Tolerance for Linear Impacts by Mechanical Impedance Methods," *ASME*, 70-WA/BHF-4, 1970.
17. Stalnaker, R. L., Fogle, J. L., and McElhaney, J. H., "Driving Point Impedance Characteristics of the Head," *ASME*, 70-BHF-14, 1970.
18. Tauffkirchen, W., and Slattenschek, A., "Beitrag zur wirklichkeitsnahen Priifung van Kraftfahrzeug-Windschutzscheiben," *Welt Kongress fur Verkehrssicherheit*, Wien, Mai, 1967.
19. Thompson, A. B., "A proposed New Concept for Estimating the Limit of Human Tolerance to Impact Acceleration," *Journal of Aerospace Medicine*, November 1962.

PAPER NO. 38

THE BIOLOGICAL RESPONSE OF THE SPINAL CANAL AND ITS  
CONTENTS TO SURGICAL TRAUMA OF THE AXIAL SKELETON

COMMENTS ON INFRAHUMAN EXPERIMENTATION AND  
BIOSTATISTICS IN CLINICAL ORTHOPEDICS

JOHN HARTLEY MOORE, M.D., F.A.C.S.

ASSOCIATE ATTENDING SURGEON, BRIDGEPORT HOSPITAL  
CLINICAL INSTRUCTOR, YALE UNIVERSITY

ABSTRACT

Ingenious mathematical models that can be applied to the study of loads and input forces relative to the axial skeleton, have been devised by the physicist to study the effects of various modalities of trauma. These studies have greater momentum following a dissertation by Orne and Liu, whose findings show that the incidence of compression fractures (also non-traumatic, pathological fractures) is higher in the thoracic region than in any other area of the spine. Most recently, the study of these forces has entered fully into the clinical area and has been studied in detail by A. White, who has, in a recent thesis, made valuable data available to the clinician.

INTRODUCTION

This presentation deals with the occurring loads or forces (surgical trauma) applied to the canine intervertebral space and its surrounding structures when a surgeon performs a laminectomy with exploration of an interspace. This may also occur when the human disc space is entered, either purposely for diagnosis, such as discoqraphy, or accidentally during the course of spinal anesthesia (rare).

**PRECEDING PAGE BLANK**

The intervertebral space and its contents are an integral part of the axial skeleton that the physicist has carefully studied and reconstructed mathematically. However, there are certain biological forces of unknown etiology that may have little or no relationship to the magnitude, direction, or force input. Yet, in nearly all cases, late biochemical and histological changes are found to occur as a result of trauma to the intervertebral segment when the disc and its space are disrupted.

It is highly improbable that in the erect living human spine, normal or diseased, a state of perfect mathematical equilibrium can be found where the vector sum of all forces acting on it are zero. The spine is eminently equipped to adapt to most input forces and stress loads required in daily living activities. However, it is possible that when a certain vector is applied under specific physiological and/or abnormal conditions to a given spinal anatomical element, biochemical, metabolic and histological changes invariably follow, causing in the human a syndrome-complex that has been called "lumbago", "sacroiliac", and more recently, the "disc" syndrome.

A series of experiments were conducted on dogs, primarily to study the effects of certain modes of electricity on the cauda equina and its somatic efferents. A considerable area of the interspace and annulus was available during the course of these studies, and surgical maneuvers were reproduced in this area with the idea of later examining

the histological results of trauma induced by these procedures. The parameters were simple: to duplicate, in the canine, the routine maneuvers that are performed in operations on a human disc, calibrating all instrumentation in terms of size, shape and length, from the human to the canine spine. These experiments were performed on adult mongrel dogs that were sacrificed at the end of four, eight, and twelve weeks.

In each individual case, the histological changes were amazingly consistent in the chronic phase of the experiment and produced results, especially in the nerve root, that were innocent of prescribed intent and totally unexpected.

In the canine operative procedure, I induced a horizontal vector force in a concentrated manner, and acting at a point with a controlled line of application and sense, but of undetermined magnitude, an ideal situation that seldom occurs in nature. Recently, after studying polode curves in the normal and post-operative dog model to analyze the kinematic motion of the lumbo-sacral motor unit, I was able to duplicate the experiment without externally induced surgical trauma to the interspace. When rotational forces are applied to the vertebral bodies of a given motor segment at controlled rates with a modified Instron testing machine, the cartilaginous plate showed a typical elastic curve and adapted to increasing loads of short duration. Past a certain point, microscopic trauma does occur, creating an anatomical interface and followed

by a reaction at the level of the annulus and the cartilaginous plate, and thereafter by a fairly characteristic and consistent histological sequence. It is now evident that when cartilaginous tissue is injured, it is followed by histochemical changes (hydroxyproline, enzymes, hexosamine, DNA) and metabolic factors (rate of incorporation of thymidine-3H and  $^{35}\text{SO}_4$ ) coupled with unknown serum factors. As applied to the vertebral cartilaginous plate and its rim, injury results in a regional phenomena extending to the total spinal motor unit, including one of its contents: the nerve root.

Historically, this specific element of the intervertebral space has been investigated by a few and I briefly review their work here. Luschka considered the intervertebral segment to be among the amphiarthroses of the human body. To clarify: the nucleus pulposus must be regarded as the articular cavity, the annulus fibrosus as the ligamentous apparatus and the cartilaginous plates equivalent to the articular cartilage.

Junghanns has suggested the name "motor segment or unit" and the disc amphiarthrosis with its two vertebral bodies are of great importance for the clinical appreciation of spinal motion, limitation or absence of motion and also the pathomechanics of nerve root involvement.

Schmorl and other anatomists have clearly demonstrated that the cartilaginous plate and its rim process are in intimate contact with the disc and annulus; thus forming a mechanical unit that contributes to the mobile, elastic, stress-absorbing segments of the vertebral body, and forms also a physiological unit between the rigid vertebral bodies.

Beneke, in 1897, demonstrated that cartilaginous degeneration is preceded by impairment of its main physical properties: elasticity and unit strength. Modern clinical studies of the interspace have been done by investigators who are primarily interested in spinal curvature or scoliosis.

Haas, Nachlas, and Risser have shown that partial suppression of growth of the epiphyseal plate can cause scoliosis.

Mass described the effect of well localized pressure on the plate in contrast to the idea of functional apposition of bone that occurs in deformity according to Wolff's law.

Scaglietti demonstrated that cartilaginous epiphyseal plates are sensitive to constant pressure and respond to it by growth inhibition. The biological implication is that in scoliosis, the lateral deformity with a wedge-shaped vertebra is the product of asymmetrical growth, but the rotary component presupposes overthrow of normal intrinsic equilibrium of the spine, and here the interspace factors are considered of prime importance by some investigators.

Recently, experimental work by Nachemson has demonstrated that in the fused spine (determined by direct intradiscal pressure measurements in vivo), the interspace load decreases by thirty percent. Yet, this most helpful study does not explain the relief, or the persistence, of the back pain syndrome complex.

#### ON THE EFFICACY OF BACK SURGERY

Operative procedures for treatment of back disability are performed daily in most hospitals throughout the country; a raw estimate of monies paid by industry (and, of course, indirectly by the public) is millions of dollars annually.

Despite diagnostic sophistication reflected in tests such as myelography, discography, electromyography, laminography, dynamography, venography, and electric studies (EMG), as well as in the years of diagnostic acumen by surgeons well versed in the field of back surgery, the failure rate is high. Relatively few patients are totally symptom-free and in approximately 17% of those that have submitted to one back operation, recurrence of symptoms are of sufficient intensity to require one or more re-operations.

Years ago, Nachlas asked: "What component of the operation produces the relief?". We simply don't know.

What we consider today to be rational back surgery, as performed daily in nearly every general hospital in this



country, is based on studies published in 1934 by Barr and Mixter, who found that intervertebral disc herniation is a cause of back pain and sciatica.

For those interested in the purely mechanical approach to this condition, a smoldering controversy persists as to whom should operate (neurosurgeon or orthopedist) and, more important, whether a fusion (stabilization of the spine) or a simple laminectomy and disc excision should be performed initially.

#### LIMITATIONS OF STATISTICAL STUDIES

(1) Proponents of one or the other method will quote various statistical studies, some old, some published as recently as last month. (2) Surgeons, third parties, and even patients accept the subtle tyranny of biostatistics applied to orthopedic surgery as basic precept, "the last word." (3) Regrettably, we are reaching a point where statistical creeds are becoming Galenic rituals that, among other things, could impede the progress of science in clinical orthopedics.

It is not my intention to add to the confusion; yet, it would be catastrophic if, when constructing biodynamic models of increasing elegance and sophistication, future mathematicians are delayed or misguided by present day statistical methodology in medicine that, at times, may be subconscious extensions of the "statisticulation" found in mass media.

For this reason, I would like to comment briefly here on an area of study where the mathematician and physicist may find affinity and even sympathy with their colleague, the biostatistician.

Biostatistics entered medicine more than a century ago when Pierre Louis demonstrated, by what he called the "numerical method", that blood letting was useless and even harmful in the treatment of human disease.

Since that time, the influence of mathematics on medicine has been ever-increasing. Perhaps the most striking intellectual change in modern orthopedic surgery over the past few decades has been the frequent conversion of an act of clinical medicine into an act of mathematics. Now we must learn whether a scientific report is an act of science or an exercise in numerology.

Like the physicist, the biostatistician applies mathematical theories of probability, but he is in a clinically nebulous realm when he determines tests, adscribes  $\chi^2$  and P values, wills degree of freedom, applies Poisson distributions, Yates correction, Wilcoxon-Mann-Whitney U tests and other mathematical maneuvers to appraise "statistical significance".

#### PROBLEMS IN USING HUMAN STATISTICAL MODELS

It appears that the larger the statistical study, the more readily it is accepted as basic fact. Closer inspection reveals, however, that most of these studies are

descriptive statistics (simple bookkeeping), confused at times by inferential statistics that ought to be used by the biostatistician only when he is dealing with nonhuman units. The use of "random samples" or "allocations" is proper for infrahuman biological material (crops, animal litter-mates, etc.), but a population of back patients cannot be regarded as a homogeneous entity of identical units. This is particularly evident if one considers that a patient receiving therapy for this condition is the only experimental subject that chooses when, where, and by whom the experiment (therapy) will be performed.

In these statistical studies, it is interesting to note how minimized is information such as: interiatric referrals (which centers, their status, patient's economic level, patient selection, etc.) and iatrotrophic stimuli (type of patient that will see a specific specialist in a given geographical area.)

An index of accomplishment and prognostic distinctions cannot be determined properly with data acquired from this heterogeneous patient group. Biostatisticians frequently categorize patients subjectively, calling them "cured, better, slightly better, or worse." Although such data adscribes values, it is not sufficiently exact to allow for proper application of rigorous statistical analysis.

Sequential analysis is now proposed, resulting in the reduction of the number of patients used in treatment trials, and I seriously question the statistical validity of this method.

An interesting and serious omission in most orthopedic statistical figures is the neglect of co-morbidity, an omission which can be a source of spurious comparisons in evaluation of treated patients. The only co-morbid condition occasionally mentioned is the patient's personality structure in terms of neurotism, psychosomatic or functional overlays, etc.

Acquisition of data through retrospective surveys of information already available in medical records has many pitfalls. For example, the investigator's choice of temporal demarcations varies greatly, even in the same institution. The descriptions of clinical course, specifications or intervals, and follow-up data all vary. Furthermore, such retrospective studies can rarely be applied with good results to patients being followed in the clinics.

The significance of the patient's willingness to follow through with therapy on his ultimate clinical improvement is never evaluated. It is well known that approximately one third of our patients do not follow instructions properly, if at all.

Well-controlled surgical double-blind studies have rarely, if ever, been done in any institution; this method would help eliminate the investigator's bias and would appear to be ideal in assessing results of surgery. It is difficult to apply it in surgical back studies, since not only is the patient population heterogeneous, but the

approach of the individual surgeon in his pre-operative assessment and selection, surgical procedure, and post-operative follow-up varies greatly from one surgeon to the next.

I am also concerned with another source of possible confusion to the mathematician, and that is the simple fact that there are structural, biological, and anatomical differences between the human and the experimental animal. May I hasten to add that although there are few anatomical differences between the spines of the pronograde and orthograde animals, the differences in the mechanical forces applied to these structures are great.

#### THE COMPARISON STUDY

Lovett notes that in the quadruped, the spine is a horizontal sustaining structure arched upward, supported by two anterior and two posterior limbs. The viscera hang directly down from this, being supported by ligaments and attachments at right angles. The angle of the ribs is helpful in inspiration by gravity as the ribs fall into the position of thoracic extension. The ribs must be pulled up to contract the thorax in expiration. Equilibrium is much more easily maintained than in the biped because the supporting base is broad and the weight of the mass to be supported is comparatively small.

He then points out that when this structure, with slight modifications, is set on end to fulfill the functions of a weight-bearing column in a plane at right angles to that for which it is best adapted, certain unfavorable factors are introduced. The column must now bear weight and sustain strains on its long axis; the viscera hang in line with the longitudinal axis to create added strains. The two anterior limbs now hang as dead weights to be supported by the column, and much greater muscle effort is required to maintain equilibrium.

These mechanical differences, as well as the biological changes I will describe, must be taken into consideration in the application of any findings in quadrupeds to problems of the human spine in clinical orthopedics.

## THE DOG EXPERIMENT

In the live specimen, (Figure-1), the dura occupies more space in the spinal canal, due to the distention caused by the cerebrospinal fluid. Note that the nerves emerge close to the horizontal plane and slide under the pedicle in a symmetrical manner at all levels. The course of the nerve in the canal is fairly short (unlike the cat) and I have not encountered an anomalous origin, course, duplication or, for that matter, congenital anomalies of the nerve root--in the dog. The root is in fairly close but not in immediate proximity or intimate contact with the postero-lateral portion of the annulus fibrosus (arrow).

A sagittal section (Figure-2) of the intervertebral space demonstrates that the cartilaginous plates are well defined and cancellous bone has a uniform appearance throughout. The vertebral margin and rim are smooth and even and ligamentous attachments between vertebral bodies are proportionately thinner and smaller than in the human. However, their basic distribution, course, and alignment are fairly similar. The contents of the intervertebral space reveal also a central area that is occupied by avascular muco-protein of the nucleus pulposus, surrounded by the uniform, concentric fibers of the annulus fibrosus that gives this an onion-peel appearance. Note that these fibers are attached intimately to the cartilaginous plate and that the dura lies in close proximity to the annulus posteriorly,



Figure 1





Figure 2

but that the nerve root does so in a more indirect manner with practically no direct contact with this structure.

The annulus was entered posteriorly with a No. 26 gauge needle at exactly the midline (Figure-3), and penetration to the nucleus was carefully measured (average: 4.6 millimeters). The histological changes four weeks later are demonstrated here: there is complete disorganization of the posterior fibers of the annulus, and toward the midportion of the annulus proper, there is the presence of a whitish, amorphous, poorly stained fibrous-like material that has displaced the nucleus anterior. Already, we see changes at the point of insertion of the annular fibers, and at the cartilaginous plate, as well as a discrete reaction underlying the plate proper in subchondral bone. The cancellous bone is not grossly involved here.

This animal was sacrificed at the end of eight weeks (Figure-4) after inserting an No. 18 gauge needle at exactly the midline, introducing it for 4 to 6 millimeters. Gross bleeding was avoided, and an attempt was made to remain at a distance from the cartilaginous plate. In this case, the nonspecific fibrous mass is now clearly visible and its invasive properties can be seen by erosion of both epiphyseal plates with definite changes in the subchondral bone. Again, there is total disruption of the posterior annulus (and also within the substance of the annulus proper) by this invasive, amorphous fibrous material.

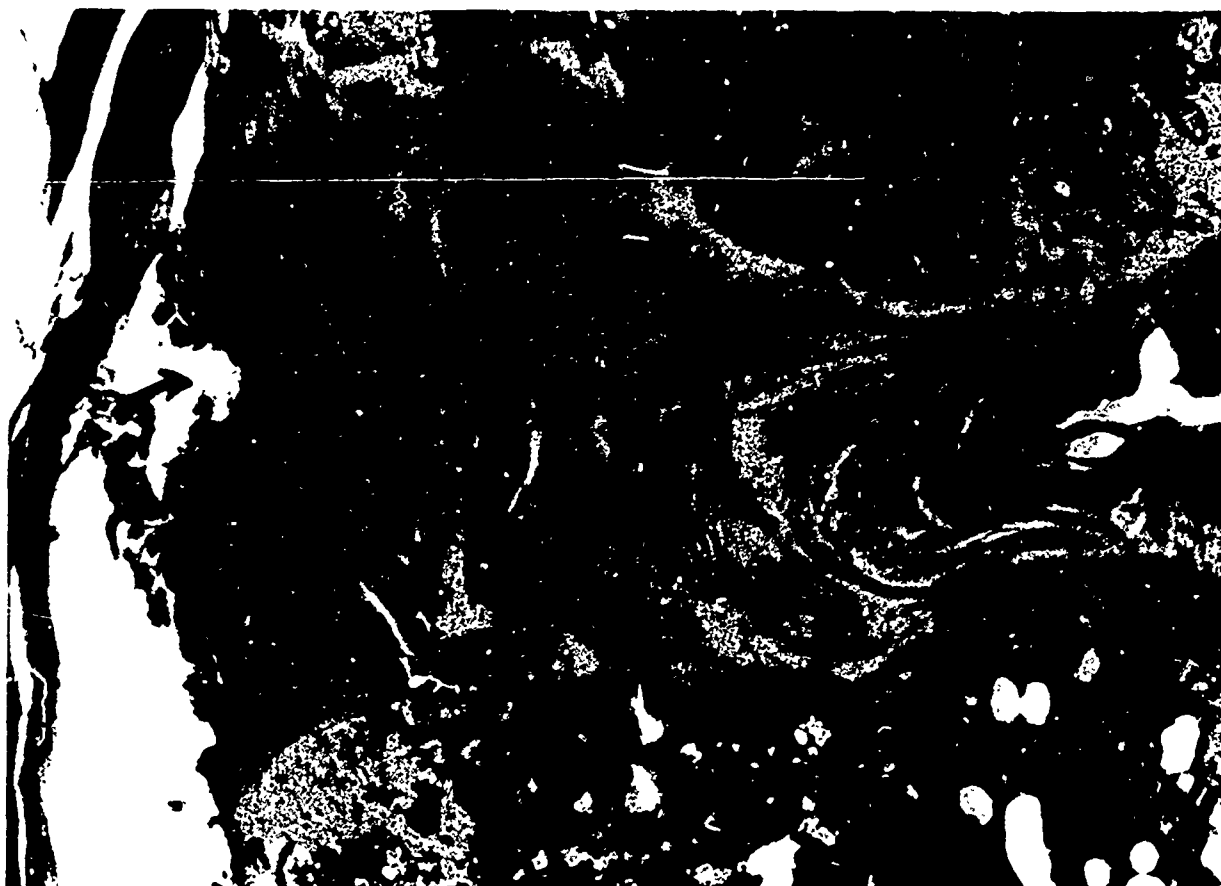


Figure 3



Figure 4

When the dogs were sacrificed approximately 12 weeks (Figure-5) post-operatively, disorganization of the total annulus with slight protrusion into the spinal canal is also found. Outstanding is the presence of osteophytic projections (arrow) anteriorly with hypertrophy and thickening of the anterior portion of the annulus. The upper exostosis is clearly visible and the lower is also evident. In this case, there is little involvement of the plate and subchondral bone. Again, no effort was made to injure the cartilaginous plates.

In the 12 week chronic experiment, (Figure-6), surgical trauma was carefully limited to the proximal cartilaginous plate of the interspace; this was done gently to avoid gross bleeding, although some microscopic bleeding probably occurred. What is demonstrative in this preparation is the hypertrophic, productive changes that project posteriorly, compressing the dura. More important, there is also complete disorganization of the epiphyseal plate and rim, the subchondral bone and the extensive changes on cancellous bone that extend to both the vertebra above and to the one below. Again, the lower epiphyseal plate was not damaged or manipulated surgically. These findings were consistent in this series of experiments.

The pathologist will report these changes as "fibroblastic" or "collagenous hyperplasia" with unusually exuberant repair reaction. There is a possibility of a biological interaction involving serum proteins, factors



Figure 5



Figure 6

within the annulus and also the nucleus pulposus coupled with hitherto unknown material generated by surgical damage or trauma to the vertebral cartilaginous plates. This interaction may, in varying combinations, cause the extensive tissue reaction that not only extends throughout distant areas of the cancellous bone within the vertebral bodies of the motor unit, but also produces exostoses that can be prominent and of uniform appearance in the long-term experiment. Most important are the consistent fibrositic changes observed within the substance of the nerve root. The x-ray films taken in these cases showed what appeared to be normal radiographic bone density and failed to demonstrate the presence of this rather extensive involvement of structures!

On Figure-7, we have a gross specimen that was sectioned longitudinally, including the disc above, for comparison. Note that there is disruption of the interspace proper (with the productive changes mentioned earlier) and projection into the spinal canal, but there is also an increase in the total width of the vertebral body that is obvious when compared with the level above.

Demonstration of the changes that have occurred in this specimen (Figure-8), sacrificed at the end of eight weeks, show again the manifestations mentioned previously, with a fair degree of involvement of the proximal epiphyseal plate and vertebral body.





Figure 7



Figure 8

What may have considerable clinical importance as applied to the human is that x-ray films (Figure-9) taken at the time this dog was sacrificed revealed absolutely no changes in the size, height, or the width of the interspace and, more important, no radiographic evidence of the histological changes that occurred at the level of the cartilaginous plate, subchondral and cancellous bone.

This has special clinical significance since I find, in x-rays of a fairly large number of re-operated backs with continuing pain, discreet evidence of sclerosis and interspace collapse that can be better demonstrated by special radiographic techniques (tomograms). There may be only a decrease in the height of the interspace and negative findings upon re-operation. We assume that these changes are well localized and limited to the interspace itself, and inevitable following surgery. However, these experiments demonstrate that in the dog there invariably is involvement of the cartilaginous plate and subchondral bone and this may have definite clinical implications. X-ray films do not reveal the changes within the nerve root or the contents of the spinal canal.

A frontal view (Figure 10) of a dissected canine spine that did not submit to surgical maneuvers of the interspace, presents a smooth, even, symmetrical and well defined annulus fibrosus anteriorly. The emergence of the nerve roots are horizontal and just proximal to the annulus. The roots are smooth, glistening and of regular, uniform appearance.



Figure 9



Figure 10

When the animals were sacrificed at the end of 12 weeks (Figure-11), the gross preparation revealed the granulomatous, productive and proliferative changes that have occurred on the anterior portion of the lower annulus. Furthermore, the nerve roots follow a course that is somewhat vertical and are intimately attached and incorporated to the scar of the annulus as they emerge from the foramina.

The roots are approximately two or three times larger, thicker and of irregular appearance, with alternating areas of constriction and bulbous enlargement and bound down to the annulus by a regional reaction.

With the spinal canal, as the roots emerge from the dura, they also present a different aspect than the root at the level above and are characterized, again, by thickening and slight irregularity. These findings are more noticeable at the level of the foramina as they emerge from this small canal. It appears that the reaction of the annulus binds the nerve root during its brief course in the foraminal canal. The reaction varies somewhat from dog to dog, but it is greater in those animals that were sacrificed late. The two proximal interspaces are left intact to demonstrate the gross difference from that found at the operated interspace.

Figure-12 reveals the bony components of the foraminal canal and their relation to the nerve root. Note that the root lies in close contact to the pedicle. A portion of the zygoapophyseal joint and its fibrous capsule can be seen on the right, and the distance from the annulus



Figure 11

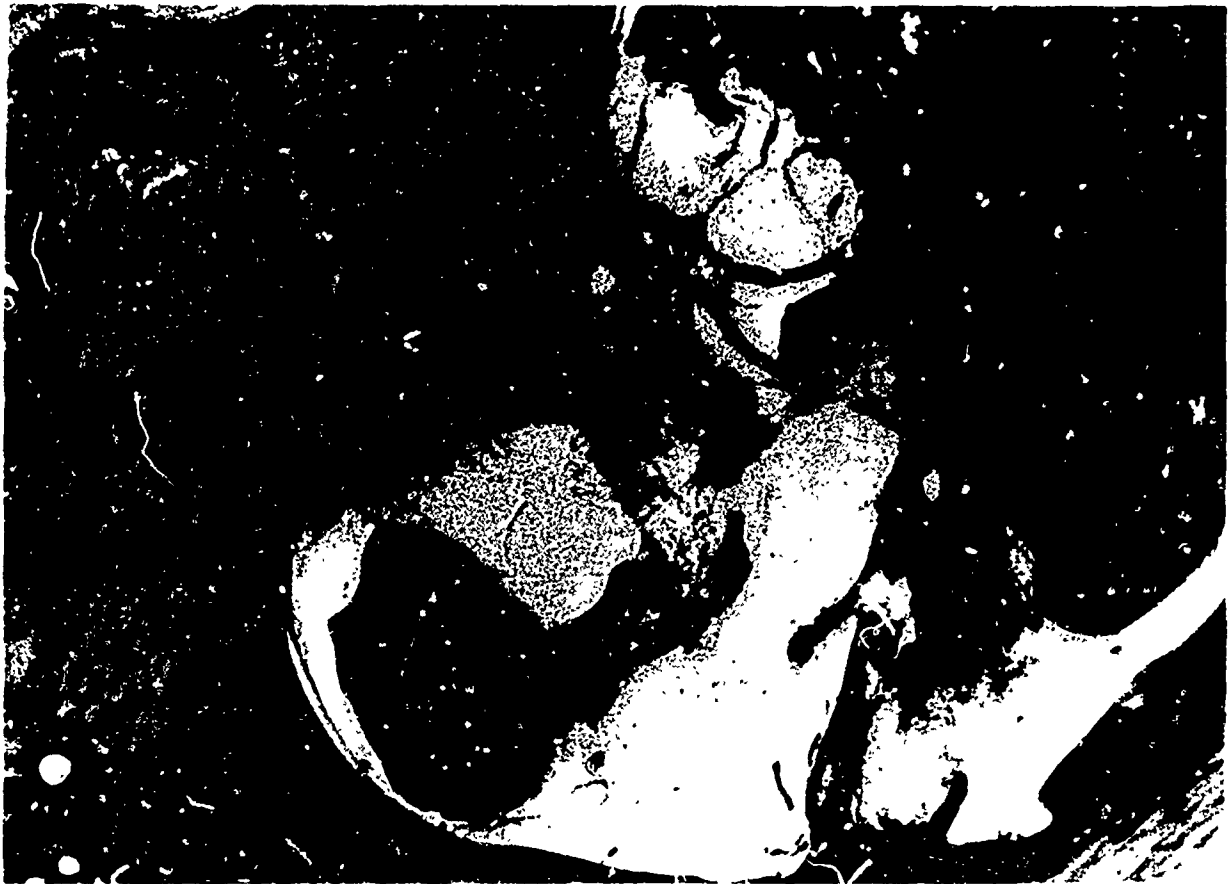


Figure 12



fibrosus (arrow) can be well appreciated. The foramina is primarily occupied with fatty tissue, radicular veins, small arteries and also small nerves.

When the animal was sacrificed at the end of eight weeks, (Figure-13), we can demonstrate the invasion of the foramina by proliferation of the annulus fibrosus that invades the spinal canal and is now found in intimate contact with the nerve root. Compression of the root is now indicated and there already are discreet fibrositic changes within the substance of the root.

Figure-14 demonstrates graphically the problem under discussion. On the left, you will see a cross-section of a normal nerve root of a dog that was obtained at a level above the site of surgery, untouched at the time of the original procedure. On the right is the nerve root on the same animal after it was sacrificed at the end of 14 weeks; the picture was taken at the same side but a level above. Note that the increase in size is 8 to 10 times that of the control root. Note also the extensive infiltration of a fibrositic reaction that literally dissects the individual nerve fiber.

On greater magnification, the only added change is a definite increase in vascularity within the substance of the nerve root proper. In the spinal canal, the root is covered by dura and the watershed of the cerebrospinal fluid, but



Figure 13



Figure 14

as it emerges from the foraminal canal, it is covered by a thin fibrous sheath.

Here is a good case in point that demonstrates the difference between infrahuman biological experimental material and the human patient. Nerve root involvement was observed, to a greater or lesser degree, in every dog that was sacrificed after the sixth or eighth week and yet, this finding is fairly infrequent in the human.

A grossly enlarged, fibrotic nerve root with increased vascularity is found only in 18% of patients that submit to re-operation.

## CONCLUSIONS

When evaluating the application of external forces or measured stress to the vertebral column in infrahuman experiments, the mathematician must take into consideration each anatomical component of the interspace and assess each independently in his calculations. Physical properties change in the pathological state, possibly due to the biological changes mentioned here. These structural changes appear in a consistent sequence in the chronic or long-term phase of the experiment and were not found initially when the input force was studied in the living spine. It is likely that the subsequent histological distortion during repair will change the mathematical equation.

It appears that in the canine spine, when trauma is applied to the cartilaginous plate, an extremely soluble biological material permeates throughout all anatomical elements, crossing all barriers, involving all components of the motor unit, and touching all the elements of the vertebra above that was purposely damaged at surgery. Also permeated was the vertebra below where surgical trauma was avoided. The material created changes in cellular morphology and local staining properties, and also generated productive tissue reaction.

These findings should further refute the purely mechanistic approach to disc excision and should affect therapeutic considerations. From a practical standpoint, I feel now that vigorous scraping of the interspace with excision of "all disc material" should be carefully avoided by surgeons.

It is evident that x-ray studies do not reveal the histological changes present in the dog. Conceivably, these reactions do occur in varying degrees in the human, but we have failed to appreciate this. There may also be a definite correlation between the recurrence or persistence of back pain following surgery and the extent of the hereto radiographically occult histological changes that follow present-day disc surgery. It should be remembered that the animals in the experiment were sacrificed shortly after surgery, and that no information is available on what happens six months or years following these procedures.

It is known today that the presence of abnormal molecular structure of DNA in cartilage may cause an individual to become sensitive to his own tissues. This is the autoimmune state. It is evidenced by the presence of antinuclear antibodies of the Gamma G, A, and M types. When treating collagen diseases, therapy should be directed at both suppression of the immune reaction and control of inflammation.

Also, the complement system consisting of nine globulins, normally present in the body and many autoimmune reactions take place only after the complement fixes. Prevention of such fixation into a substrate stops the immunological reaction from proceeding to cell injury.

This is followed by inflammation that is a protective reaction of the body to injury. The inflammatory process is normally "walled off" by proliferation of fibroblasts and,

If this does not happen, an uncontrolled continuing reaction may occur and the inflammatory process itself may damage the body. Once the inflammatory cycle has begun in autoimmune disease, the host tissue provides an unlimited source of stimuli. For these and other reasons, Azathioprine, an antimetabolite; Epsilon Amino Caproic Acid, a complement inhibitor and anti-inflammatory medication such as glucocorticoids may be of therapeutic value and have a definite role in the treatment of the so-called "disc syndrome".

There is little question that there are humoral mechanisms that operate in the damaged vertebral interspace and, at least in dogs, appear with amazing regularity and consistency when these structures are involved in duplicating the human surgical experiment.

Other humoral mechanisms have been recently described that may give a partial answer to this problem. Bobechko's concept of regional, cell-bound auto-antibodies is ingenious and a novel theory.

According to his hypothesis, vascularization of the nucleus pulposus secondary to any modality of trauma causes release of muco-proteins from the normally well encircled and avascular nucleus pulposus. The release into the general circulation of the otherwise sequestered muco-protein stimulates the production of cell-bound auto-antibodies that cause a reaction (as described by the author) at the level of the nucleus pulposus and also involves the annulus and the cartilaginous plate.

Next, the possibility of an auto-allergic pathogenesis of the nerve root within the spinal canal must be also considered. Waxsman and Adams have created an experimental allergic neuritis model in rabbits. Their research may also serve as an important experimental model of nerve root involvement in the so-called disc syndrome and it certainly deserves additional investigation.

Recently, an enzyme, chymopapain has been introduced in the treatment of disc disease and its hazards and limitations (in the dog) have been studied by Holliand and associates. These authors induced reactive changes within the dura and spinal cord coverings following traumatic punctures of the disc performed transdurally. They have speculated that certain combinations of blood, contrast media, enzyme, cerebrospinal proteins and serum factors generated by interspace damage cause reactive changes within the neural substance proper in dogs following the same unknown biological mechanisms (arachnoiditis, ascending paraplegia, and death).

Other mysteries are still evident and unsolved in the clinical area. I cannot explain why a percentage of patients with acute nerve-root pressure, followed by the typical clinical sequence of body tilt, severe sciatica and pain, respond to nonspecific therapy such as a high caudal anesthesia. Other patients with acute disc extrusions proven at later surgery respond well within 48 to 72 hours to fairly aggressive therapy with large amounts of the hormone, ACTH.



I have also treated patients who demonstrated disc protrusion on myelogram but refused surgery, and I have found that their subsequent condition is of a cyclic nature that is characterized by long periods of nearly complete remissions and then periods of aggravation; yet, the basic pathological process remains constant and unchanged. Furthermore, of these patients who have eventually gone to surgery, all have demonstrated interspace and/or nerve-root pathology.

As the mathematician and the physicist work intimately with the clinician and all become conversant with the experimental models on hand--be they mathematical or biological--the solution to some of the problems related to the low-back syndrome may soon be within our grasp.

## REFERENCES

- AKESON, W.H., et. al.: Experimental Arthroplasty in The Rabbit Metatarsophalangeal Joint. University of Washington, In Proceedings of the Orthopedic Research Society's XVI Annual Meeting (1970).
- BROWN, THORNTON; HANSEN, R.J.; and YORRA, A.J.: "Some Mechanical Tests on the Lumbo-sacral Spine with Particular Reference to the Intervertebral Discs." J. Bone and Joint Surg., 39-A: 1135-1164, Oct. 1957.
- DAVIS, P.R., et. al.: Movements of the Thoracic and Lumbar Spine When Lifting: A Chondro-Cyclophotographic Study. J. Anat. 99:15, 1965.
- EVANS, F.G., and LISSNER, H.R.: Studies on the Energy Absorbing Capacity of Human Lumbar Intervertebral Discs. In Proceedings of Seventh Stapp Car Conference edited by D.M. Severy, Springfield, Illinois, Charles C. Thomas, 1965.
- FARFAN, H.F., et.al.: "The Effects of Torsion on the Lumbar intervertebral Joints: The Role of Torsion in the Production of Disc Degeneration." J. Bone and Joint Surg., 52-A, No. 3, 468-496, April 1970.
- FRANKEL, V.H., and BURSTEIN, A.H.: Biomechanics and Related Bioengineering Topics. In Load Capacity of Tubular Bone pp. 381-396, Edited by R.M. Kenedi. London, Pergamon Press, 1965.
- FUNG, Y.B.: Biomechanics. Its scope, history and some problems of continuum mechanics in physiology. Appl. Mech. Rev., 21: 1-20, 1968.
- GALANTE, J.O.: Tensile Properties of the human Lumbar Annulus Fibrosus. Thesis Acta Orthop. Scand. Suppl. 100, 1967.
- GREGGERSEN, G.G., and LUCAS, D.B.: "An in vivo study of the Axial Rotation of the human Thoraco-lumbar spine." J. Bone and Joint Surg. 49-A: 247, 1967.
- HOWELL, D.S.: Evidence for altered protein polysaccharide Complex (PPC) in fresh osteoarthritic cartilage in human hips. University of Miami, School of Medicine. In Proceedings of Orthopedic Research Society (1970).
- MANKIN, H.: The Biochemical and metabolic changes in the cartilage of the femoral head in patients with osteoarthritis of the hip. Hospital For Joint Diseases. In Proceedings of Orthopedic Research Society's XVI Annual Meeting (1970).
- ORNE, D., and LIU, Y.K.: A mathematical model of spinal response to impact. Thesis 02370, Department of Engineering Mechanics, University of Michigan, 1969.

- PEDPINI-MILLE, A., et. al.: "Chemical studies on the ground substance of human epiphyseal plate cartilage." J. Bone and Joint Surg. 49-A, No. 8, 1628.
- RADIN, E.L.: Force transmission through joints. Massachusetts General Hospital. In Proceedings of XVI Annual Meeting of the Orthopedic Research Society (1970).
- PEPO, P.U.: Tritiated Proline incorporation in normal and injured adult articular cartilage of the rabbit. Royal Victoria Hospital, Montreal, Canada. In Proceedings of Orthopedic Research Society (1970).
- POARK, R.J.: Formulas for stress and strain. Ed. 4, Chap. 9, p. 201. New York, McGraw-Hill, 1965.
- ROSENBERG, L.: Physical characteristics of protein polysaccharides prepared by different methods. New York University Medical Center. In Proceedings of XVI Annual Meeting of the Orthopedic Research Society (1970).
- SCHMORL, G.; and JUNGHANNS, H.: The human spine in health and disease. New York, Grune & Stratton, 1959.
- STEINDLER, A.: Kinesiology of the human body. Springfield, Illinois, Thomas, 1955.
- SYLVEN, BENGT: On the Biology of Nucleus Pulposus. Acta Orthop. Scandinavica, 20: 275-279, 1951.
- VIRGIN, W.J.: "Experimental investigations into the physical properties of the intervertebral disc." J. Bone and Joint Surg. 33-B: 607, 1951.
- WHITE, III, A.A.: Analysis of the mechanics of the thoracic spine in man. Acta Orthop. Scandinavica Suppl. 127, 1969.

## CLOSING REMARKS: THE FUTURE

John P. Stapp, M.D., Ph.D.

National Highway Safety Institute  
Washington, D.C.

Dr. Henning von Gierke has organized and produced an outstanding Symposium on a highly sophisticated subject of great importance to basic science. In the past two and a half days, he has conducted us through thirty-two major presentations by distinguished authorities in mathematical-physical analysis of biological phenomena, with just the right amount of contrapuntal question and answer to clarify the themes while preserving the tempo and balance of the main subject. He has earned our respect and appreciation for this inspiring and informative meeting of so many minds learning from each other.

I share with you the lively creativity and insatiable compulsion to generalize which are characteristic of those who dedicate their lives to science. I am compelled to yield to you in the valor that motivates your choice of a subject for research. What boundless optimism spurs your intrepid assaults on this most obstinate and irregular object you have chosen for mathematical analysis and modeling--MAN! This fifty liter rawhide bag of gas, juices, jellies, gristle and threads moveably suspended on more than 200 bones presided over by a cranium, seldom predictable and worst of all living, presents a challenge to discourage a computer into incoherence. I salute your courage in seeking to make logic out of this seeming chaos through biodynamic mathematical modeling.

The first gain from this endeavor is from organizing the knowledge at your disposal and clarifying your own thinking by the discipline of modeling. This goes beyond the immediate and obvious conclusions derived from inspection of data to the analytical projection of cause and effect within the predictable

scope of interactions. Constructed into a model within parameters, it becomes an instrument to explain and predict biodynamic and biomechanical responses usefully in applied technology. The objectives of applied biodynamic modeling were well described by Colonel Doctor Clarke in his keynote address. The clear thinking and organization achieved through the discipline of modeling is superbly evident in how well and how much speakers communicated in their short ten minutes. This condensation of substantial new data and complex analysis validates the use of models as a system of communication, and sets a standard of scientific excellence.

Two essentially historic reviews provide a perspective on the origins and motivations of biodynamic mathematical modeling. English research dating from the 1940's on mechanical impedance of the human body, described by Sandover, and German anthropometric and biomechanical research since 1870, provided a frame of reference for applied mathematical modeling in the realm of exposure to impact, shock and vibration.

On August 10, 1946, I was assigned to the Special Projects Unit of the Aeromedical Laboratory of Wright Field. My chief, Dr. Harvey Savely, who is with us at this Conference, did not consider me qualified to begin work on ejection seat research until I had read the works of Ruff, Geertz, Stewart, Pekarek, Dubois, and DeHaven among others.

That Biodynamic Modeling is not an esoteric mathematical game is amply demonstrated in the scope of subjects covered by the authors of this Symposium. Their themes include: (1) Scaling, analoging, and projecting responses of experimental animals, cadavers, anthropometric dummies and man to provide models that will make optimum use of experimental data and conserve on hazardous experiments. (2) Modeling of impact accelerations of body parts. (3) Mathematical projection of injury criteria. (4) Mathematical modeling of tissue biomechanics. (5) Mathematical modeling applied to impact protection systems. (6) Human mechanical impedance, and (7) closed circuit models.

Mathematical modeling provides logical organization of data with analogs of real time functions describing complex interactions accurately and clearly. Where equations resort to too many constants and relate to inadequate premises or meagre data, mathematical biodynamic models begin to depart from reality. Erratic, nonlinear systems become difficult to model with any useful accuracy. I will not bore you with the parable of the six blind Hindu scientists and their monographs on the elephant model. However, it is prudent to note some of the hazards of data interpretation. Two country boys in Arkansas on their first train ride bought their first coca colas. As one of them raised the bottle to his lips, the train entered a tunnel. "Joe, Joe," he cried, "don't drink this stuff. I had one swallow, and I am blind as a bat."

The growing accuracy of correlation between real time performance and predictions by mathematical models, frequently demonstrated in computer runs, is an impressive and encouraging achievement that itself predicts a great future for modeling. How this applies to man rated designing of machines and to analysis of environmental factors affecting human health and well being, to the diagnosis and treatment of disease, and to preventive and protective measures against accidental death and injury becomes more evident with every day of progress.

This aspect of modeling has not escaped the attention of industry in sponsoring research, for example, for safer automotive design. The excellent paper presented by Dr. Lange, sponsored by a major European automobile industry, is a case in print. The Max-Planck Institute is developing into a center of excellence in biodynamic research on impact injury. No less excellence is demonstrated in the work of Dr. Kenedi from Scotland, in applying structural analysis techniques to microanatomy of the skin under the electron microscope and stress analysis to provide data for producing realistic models of this remarkable organ.

Necessity dictates the priority of models to be investigated and developed, accounting for involvement with staggeringly complex models of open systems with multitudes of interacting variables, and the application of resulting incomplete solutions without waiting for perfection in the pursuit of urgently needed answers to real time problems.

Nevertheless, the invited paper by Dr. Julia Apter, (whose name may be comparative, but whose presentation was superlative), on a mathematical model of the mammalian circulation, demonstrates what can be done with a closed biological system. Relatively long range prediction of the consequences of interaction between combinations of variables was well demonstrated. Even longer range and more subtle consequences of fluid mechanical factors in production of aneurysms and hypertensive changes in vessel walls may yet be predicted with just such models.

The bound proceedings of this Symposium attest that these papers speak for themselves and need no further extolling of their merits beyond the examples cited. How does the composite pattern of thinking in biodynamic mathematical modeling predict the future developments of this field of research? Inherent in the very nature of modeling is a selective survey of phenomena that discriminates priorities by a sort of operations research approach. The saving in effort and cost of research by such screening of the inconsequential and non-productive emancipates scientists from the random pursuit of serendipities. Blind alleys and involitional preoccupation with ever narrower horizons are avoided by constant recalibrations of models with reality and relative to the whole problem.

Retrospectively, research was the lifelong dedication of individual effort resulting in monographs with comprehensive bibliographies and detailed protocols of each experiment, by which the investigator became an authority in his field. The exponential growth of research shifted the emphasis to teams of specialists turning out frequent synoptic publications and abstracts, tabulating results without protocols, other than illustrative examples, and

limited to references instead of bibliographies. The volume of literature and vast quantities of data generated has led to the science of information retrieval, which barely copes with the information explosion, and data gathered at great expense is hurriedly processed for the limited objectives of the authors. Multiple repetitions of the same experiments for data to support slightly different conclusions represent an enormous waste. Computers provide a way of avoiding this waste by setting up centers where protocols of experiments and original data can be accumulated in data banks in statistical quantities. Such banks can provide answers by computer runs on statistically valid samples to questions that may never have occurred to the original performers of the experiments. An example of such an approach is in the data system of the Armed Forces Institute of Pathology where more than a million human autopsies have been stored as data bits in a computer memory. Digital readouts can be run off in a matter of minutes on any selection of factors. Runs can be programmed for consecutive regressions of any discriminators selected for a statistical sample of cases. An analogous approach is being undertaken at the National Bureau of Standards, where protocols of more than four thousand experiments on human volunteers exposed to impact and deceleration on test sleds will be stored in a data bank for similar availability for digital retrieval and analysis.

A third important area of endeavor began in May of 1968, in a joint effort by the Society of Automotive Engineers, the National Highway Safety Bureau and the Bureau of Standards, to develop anthropometric dummy reference standards for the 95th and 50th percentile male, the 5th percentile female, the 30 pound and the 50 pound child. Dimensional, dynamic, and instrumentation specifications are being formulated and eventually type specimen models will be maintained for calibration of corresponding test dummies for use in research and industrial compliance testing. Eventually, they will serve as measuring devices to man rate the machines, work space and living environment of man. The only occasion where an engineering project ever



began by measuring the men and designing the vehicles to fit them was National Aeronautics and Space Administration's Mercury Project. It is devoutly to be hoped that Mathematical Biodynamic Modeling will bring to an early end the practice of designing an occupant space in a vehicle or machine and defying human engineers to fit a human in it.

You have in your hands a concept that can multiply the effectiveness of research effort in the same way that computers compress the time and work of data handling and calculations. Progress is only limited by the intelligence, industry and funding you are able to apply to this critically important field of research. Thank you for the information and inspiration of communicating with you and learning from you during these two and a half days. It is a necessity to be reminded occasionally that we are not alone in struggling toward difficult goals. May you have ever increasing success in achieving your objectives.